
ELEVENTH SYMPOSIUM ON

turbulent shear flows

Grenoble, France
September 8-10, 1997

DISTRIBUTION STATEMENT A

Approved for public release
Distribution Unlimited

19971209 070

VOLUME 1
SESSIONS 1-10
POSTER SESSION 1



SPONSORED BY:

- **Association Universitaire de Mécanique**
- **Centre National de la Recherche Scientifique**
Département Sciences de l'Ingénieur
- **Direction Générale de l'Armement**
Direction des Systèmes de Forces et de la Prospective
- **Electricité de France**
- **European Research Office**
United States Army and Air Force
- **Gaz de France**
- **Institut National Polytechnique de Grenoble**
- **Laboratoire des Ecoulements Géophysiques et Industriels**
- **Rank Xerox**
- **Université Joseph Fourier**

ORGANIZING COMMITTEE

F. Durst
Lehrstuhl für Strömungsmechanik
Cauerstraße 4
8520 Erlangen, Germany

B. E. Launder
Department of Mechanical Engineering
UMIST
Manchester, M60 1QD, UK

F. W. Schmidt (Secy.)
Department of Mechanical Engineering
The Pennsylvania State University
University Park, PA 16802, USA

J. H. Whitelaw
Department of Mechanical Engineering
Imperial College
London, SW7 2BX, UK

PAPERS COMMITTEE

M. Lesieur (Chairman)
Laboratoire des Ecoulements Géophysiques
et Industriels
Institut Universitaire de France
BP 53
38041 Grenoble cedex 9, France

B. E. Launder

G. Binder
Laboratoire des Ecoulements Géophysiques
et Industriels
Centre National de la Recherche Scientifique
BP 53
38041 Grenoble cedex 9, France

J. H. Whitelaw

LOCAL ARRANGEMENTS COMMITTEE

G. Binder (Chairman)

PREFACE

These proceedings contain the papers presented at the Elenventh Symposium on Turbulent Shear Flows held at the Institut National Polytechnique and the Université Joseph Fourier of Grenoble, France, September 8-10, 1997. The purpose of these biennial international symposia is to provide a forum for presentation and discussion of new developments in the field of turbulence, especially as related to shear flows of importance in engineering and geophysics.

The previous TSF conferences took place respectively at Pennsylvania State University, USA, in 1977, at Imperial College, London, England, 1979, at the University of California, Davis, USA, in 1981, at the University of Karlsruhe, Germany, 1983, at Cornell University, Ithaca, USA, 1985, at the University Paul Sabatier, Toulouse, France, 1987, at Stanford University, USA, 1989, at the Technical University of Munich, Germany, 1991, at Kyoto University, Japan 1993 and again at Pennsylvania State University in 1995 for the tenth anniversary of the series.

In response to a call for papers, 304 abstracts were submitted to the Symposium Papers Committee composed of Marcel Lesieur (chairman), Gilbert Binder, Brian Launder and James H. Whitelaw. Each abstract was evaluated by two members of the Advisory Committee and by at least one member of the Papers Committee. From the consensus of these evaluations, papers were selected for presentation at the Symposium either for stand-up or poster sessions. No such selection process can ever be perfect and we appreciate the understanding of colleagues whose papers were not included in the program.

All authors were requested to prepare a manuscript of six pages for inclusion in the Symposium Proceedings. These are organized in three volumes, one for each day of the Symposium.

The Organizing Committee wishes to acknowledge the financial help of various organizations. At the time the Proceedings went to press, financial support was confirmed from Laboratoire des Ecoulements Géophysiques et Industriels, Institut National Polytechnique de Grenoble, Université Joseph Fourier, Association Universitaire de Mécanique.

Finally, the Organizing Committee is most appreciative of the efforts of the Local Arrangements Committee, chaired by Gilbert Binder, which did much to ensure the success of the Symposium. It is especially gratefull to Michel Favre-Marinet and Geneviève Chavand for their help in processing the material for the publication of these Symposium Proceedings.

Franz Durst
Brian E. Launder
Frank W. Schmidt
James H. Whitelaw

ORGANIZING COMMITTEE

F. Durst
B. E. Launder

F. W. Schmidt (Secy.)
J. H. Whitelaw

PAPERS COMMITTEE

M. Lesieur (Chairman)
G. Binder

B. E. Launder
J. H. Whitelaw

LOCAL ARRANGEMENTS COMMITTEE

G. Binder (Chairman)
S. Anquetin
J.- P. Chollet
P. Comte

M. Favre- Marinet
O. Metais
S. Tardu

ADVISORY COMMITTEE

R. J. Adrian, USA
H. Alfredsson, Sweden
H. Andersson, Norway
F. Anselmet, France
R. A. Antonia, Australia
B. Aupoix, France
G. Bergeles, Greece
J. P. Bertoglio, France
R. W. Bilger, Australia
J. P. Bonnet, France
J. G. Brasseur, USA
S. Candel, France
I. P. Castro, UK
J. M. Chomaz, France
P. Comte, France
J. Cousteix, France
M. P. Escudier, UK
J. F. Foss, USA
R. Friedrich, Germany
T. Gatski, USA
W. K. George, USA
S. E. Gutmark, USA
H. HaMinh, France
K. Hanjalic, Netherlands
T. J. Hanratty, USA
M. Heitor, Portugal
K. Hishida, Japan
J.A.C. Humphrey, USA
F. Hussain, USA
A. Johansson, UK

J. Jovanovich, Germany
N. Kasagi, Japan
J. Kim, USA
T. Kobayashi, Japan
S. Komori, Japan
D. Laurence, France
M. A. Leschziner, UK
J. L. Lumley, USA
J. Magnaudet, France
O. Metais, France
P. Monkewitz, Switzerland
Y. Nagano, Japan
F. Nieuwstadt, Netherlands
W. Nitsche, Germany
M. Oberlack, Germany
W. C. Reynolds, USA
W. Rodi, Germany
R. Schiestel, France
G.-X. Shen, Beijing, China
R. L. Simpson, USA
A. J. Smits, USA
R.M.C. So, Hong Kong
M. Sokolov, Israel
M. Sommerfeld, Germany
J. Sommeria, France
C. G. Speziale, USA
H. J. Sung, Korea
K. Suzuki, Japan
A.M.K.P. Taylor, UK
M. Wolfshtein, Israel
J. Wyngaard, USA

ELEVENTH SYMPOSIUM ON TURBULENT SHEAR FLOWS
Institut National Polytechnique
Université Joseph Fourier
Grenoble, September 8-10, 1997

CONTENTS OF VOLUME 1
SESSIONS 1 - 10
POSTER SESSION 1

SESSION 1 - PLENARY SESSION	1-1
Large eddy simulation of a boundary layer flow passing over a groove <i>Y. Dubief, P. Comte</i>	1-1
Uniformly sheared turbulent flow under the effect of solid-body rotation <i>M. Tanaka, S. Yanase, S. Kida, G. Kawahara,</i>	1-7
Computational modelling of highly-loaded compressor cascade flows <i>W. L. Chen, F. S. Lien, M. A. Leschziner</i>	1-13
The effect of Reynolds number on boundary layer turbulence <i>D.B. deGraaff, D.R. Webster, J.K. Eaton</i>	1-19
 SESSION 2 - FREE FLOWS I	 2-1
The effect of the Reynolds number on the turbulence structure in a circular cylinder farwake <i>Y. Zhou, R. A. Antonia, W. K. Tsang</i>	2-1
A study of coherent structures in the near wake of a heated cylinder at $x/D=30$ <i>M. D. Pons, J. A. Ferre</i>	2-7
Turbulent dissipation rate measurements in a plane wake flow <i>J. Jovanovic, Q.-Y. Ye, F. Durst</i>	2-13
An experimental study on unsteady turbulent near wake of rectangular cylinder in a channel flow <i>S. Nakagawa, M. Senda, K. Yamagami, K. Nitta</i>	2-19
On the three-dimensional evolution of a wake subjected to cross-shear <i>S. Beharelle, J. Delville, J.-P. Bonnet</i>	2-25
 SESSION 3 - INTERNAL AERODYNAMICS	 3-1
Simulation of flow through circular to rectangular transition duct using non-linear second- order moment closures <i>C. Eifert, D. G. Pfuderer, J. Janicka</i>	3-1
The use of linear and non-linear low Reynolds number models in the calculations of flow in a RAE M2129 S-duct <i>A. J. Marquis, L. Y. Ong</i>	3-7

Computation of film cooling by lateral injection using a multi-block technique	3-13
<i>D. Lakehal, G. S. Theodoridis, W. Rodi</i>	
Computation of flow and heat transfer through rotating ribbed passages	3-19
<i>H. Iacovides</i>	
Calculation of gas turbine combustor flows using an adaptive grid redistribution method .	3-25
<i>W. P. Jones, K. R. Menzies</i>	

SESSION 4 - FUNDAMENTALS I

4-1

A parametric study of Rayleigh-Benard convection using a Karhunen-Loeve basis	4-1
<i>I. H. Tarman, L. Sirovich</i>	

Relation between third-order and second-order velocity structure functions for axisymmetric turbulence	4-7
<i>M. Ould-Rouis, R. A. Antonia, Y. Zhu, F. Anselmet</i>	

Intermittency and wavelet analysis of one-point turbulence data	4-13
<i>F. Nicolleau, J. C. Vassilicos</i>	

Scaling law of coherent fine scale structure in homogeneous isotropic turbulence	4-17
<i>M. Tanahashi, T. Miyauchi, J. Ikeda</i>	

Investigation of renormalization group methods for the numerical simulation of isotropic turbulence	4-23
<i>W. D. McComb, T. J. Yang, A. Young, L. Machiels</i>	

SESSION 5 - FREE FLOWS II

5-1

Interaction of the wake of a circular cylinder and a plane mixing layer	5-1
<i>D. Heitz, J. Delville, G. Arroyo, J.-H. Garem, J.-P. Bonnet, P. Marchal</i>	

Quasi-2D MHD turbulent shear layers	5-7
<i>T. Alboussiere, V. Uspenski, R. Moreau</i>	

Examination of LSE-based velocity field estimations using instantaneous, full field measurements in an annular mixing layer	5-12
<i>D. Ewing, J. H. Citriniti</i>	

POD coefficient interaction and its relation to structure evolution in a turbulent axisymmetric shear layer	5-18
<i>J. H. Citriniti</i>	

The joint probability functions of the measured velocity and vorticity components in a plane wake	5-24
<i>P. N. Nguyen</i>	

SESSION 6 - EXTERNAL AERODYNAMICS

6-1

Utilization of the Garteau swept wing data base for turbulence models evaluation in boundary layer calculations	6-1
<i>M. Doussinault, C. Gleyzes, B. Aupoix, J. Cousteix, J. H. M. Gooden</i>	

Numerical study of flow past a wing-body junction with a realizable nonlinear eddy-viscosity model	6-7
<i>S. Fu, T. Rung, F. Thiele, Z. Zhai</i>	
Large eddy simulation of the three-dimensional turbulent boundary layer over a swept bump	6-13
<i>X. Wu, K. D. Squires</i>	
Non-linear v2-f modeling with application to aerodynamic flows	6-19
<i>F. S. Lien, P. A. Durbin, S. Parneix</i>	
A new low-Re non-linear two-equation turbulence model for complex flows	6-25
<i>D. D. Apsley, M. A. Leschziner</i>	

SESSION 7 - CLOSURES I

7-1

Particle and one-point structure-based modeling of slow deformations of homogeneous turbulence	7-1
<i>S. C. Kassinos, W. C. Reynolds</i>	
Analytical constraints for single point closures in geophysical turbulence	7-7
<i>J. R. Ristorcelli</i>	
Low-Reynolds-number second-moment closure without wall-reflection redistribution terms	7-12
<i>N. Shima</i>	
A two-scale model for a passive scalar field undergoing a spherical compression	7-18
<i>J. Pinheiro, M. Gonzalez, R. Borghi</i>	
On the modelling of conditional scalar dissipation in locally self-similar flows	7-24
<i>A. Kronenburg, R. W. Bilger, J. H. Kent</i>	

SESSION 8 - HEAT AND MASS TRANSFER

8-1

Measurements and modelling of heat-flux transport in a heated cylinder wake	8-1
<i>P. M. Wikstrom, M. Hallback, A. V. Johansson</i>	
DNS of turbulent heat transfer in channel flow with low to medium-high Prandtl number fluid	8-7
<i>H. Kawamura, K. Ohsaka, K. Yamamoto</i>	
Turbulent heat flux measurements on a rotating disk	8-13
<i>C.J. Elkins, J.K. Eaton</i>	
Joint scalar-scalar dissipation measurements at the exit of a turbulent jet	8-19
<i>K. Sardi, A. M. K. P. Taylor</i>	
High-Schmidt number mass transfer through turbulent gas-liquid interfaces	8-24
<i>I. Calmet, J. Magnaudet</i>	

SESSION 9 - FLOW MANAGEMENT	9-1
Control of drag by time-space periodical suction and blowing	9-1
<i>S. Tardu</i>	
Turbulence modification with streamwise-uniform sinusoidal wall-oscillation	9-7
<i>Y. Mito, N. Kasagi</i>	
Optimum feedback control of vortex shedding from a circular cylinder by rotary oscillations using a neural network	9-13
<i>N. Fujisawa, T. Nakabayashi</i>	
Active flow control with neural network and its application to vortex shedding	9-18
<i>Y. Suzuki, N. Kasagi</i>	
The influence of polymer stresses in drag-reduction	9-24
<i>T. J. Hanratty, M. Warholic, H. Massah</i>	
 SESSION 10 - FUNDAMENTALS II	 10-1
Stretching of vorticity gradients in two-dimensional wake flow	10-1
<i>B. Protas, J. E. Wesfreid</i>	
Hyperviscous dynamics of two-dimensional turbulence	10-7
<i>V. Herbert, M. Larcheveque, C. Staquet</i>	
Model of two-dimensional turbulence for liquid metal flows in a magnetic field	10-11
<i>J. Sommeria, T. Dumont, R. Robert</i>	
Vorticity measurements in a turbulent grid flow	10-16
<i>Y. Zhu, T. Zhou, R. A. Antonia</i>	
Generalized theory for symmetries in inhomogeneous turbulent shear flows	10-21
<i>M. Oberlack</i>	

POSTER SESSION 1

P1-1

Numerical prediction of turbulent heat transfer in a rotating square duct with nonlinear $k-\epsilon$ model P1-1

A. F. Abdel Gawad, O. E. Abdel Latif, S. A. Ragab, M. R. Shaalan,

Exploiting the flexibility of unstructured grids for computing complex flow patterns more precisely P1-7

C.-H. Rexroth, R. Koch, S. Wittig

Computation of the unsteady and laminar-turbulent flow in a low-pressure turbine P1-11

F. Eulitz, K. Engel

Steam turbine-rotor blade oscillation P1-18

R. S. Amano, B. Lin

Effects of first-order turbulence models applied to flows around lifting airfoils P1-19

S. Khris, J. Marcillat

Investigation of the turbulence wind on the aerodynamics characteristics of windturbines and sails P1-25

C. Breard, S.G. Voutsinas, F. Hauville, S. Huberson

3D direct simulation of the shock-boundary layer interaction and von Karman instability in transonic flow around a wing P1-31

A. Bouhadji, M. Braza

Effects of blowing/suction from a spanwise slot on a turbulent boundary layer flow P1-37

H. Choi, J. Park, S. Hahn

Suboptimal turbulence control with the body force of selective velocity damping localized to the near-wall region P1-43

S. Satake, N. Kasagi

Turbulent characteristics in transition region of dilute surfactant drag reducing flows P1-49

Y. Kawaguchi, H. Daisaka, A. Yabe, K. Hishida, M. Maeda

Kinetic energy balance in a turbulent boundary layer disturbed by a circular cylinder: classical and conditional approach P1-55

F. de Souza, J. Delville, J.-P. Bonnet

Verification of a turbulent dispersion model through comparison with the results of a field tracer experiment in a complex terrain P1-61

Y. Ichikawa, K. Sada, K. Asakura

A modified continuous in time stochastic mixing model: application to a simple atmospheric chemical reaction P1-67

C. Michelot, S. Simoens, M. Ayrault, V. Sabelnikov

Turbulent flow and heat transfer from an oblique flat plate to a two-dimensional wall attaching offset jet P1-71

H. B. Song, D. S. Kim, S. H. Yoon, D. H. Lee

Concentration fluctuation characteristics around a cubic obstacle P1-77

R. Yasuda, Y. Ikeda

Turbulent wall shear flow in a vertical tube with combined heat and mass transfer	P1-83
<i>S. He, P. An, J. Li, J. D. Jackson</i>	
Velocity measurements in the wake of a pair of cylinders in high interaction configuration	P1-89
<i>C. Brun, M. Picut</i>	
On the configuration of three-dimensional intermittent turbulent bulges in a far wake	P1-95
<i>G. A. Kopp, F. Giralt, J. F. Keffer, J. A. Ferre</i>	
Low dimensional description of large scale structures dynamics in a plane turbulent mixing layer	P1-101
<i>L. Cordier, J. Delville, C. Tenaud</i>	
Dangers of turbulence description by means of Navier-Stokes solutions with a priori symmetry restrictions	P1-102
<i>V.G. Priymak, T. Miyazaki</i>	
Coupled resonant triads interactions in phase-locked evolution	P1-106
<i>G. Sciortino, M. A. Boniforti, M. Morganti</i>	
Computation of turbulent channel flow using PDF method	P1-112
<i>J. P. Minier, J. Pozorski</i>	
Dynamical system analysis of Reynolds stress closure equations	P1-118
<i>S. S. Girimaji</i>	

ELEVENTH SYMPOSIUM ON TURBULENT SHEAR FLOWS
Institut National Polytechnique
Université Joseph Fourier
Grenoble, September 8-10, 1997

CONTENTS OF VOLUME 2
SESSSIONS 11 - 22
POSTER SESSION 2

SESSION 11 - WALL FLOWS I	11-1
On clustering of quasi-streamwise vortices in near-wall turbulence	11-1
<i>Y. Miyake, K. Tsujimoto, T. Yoshikawa, T. Morikawa</i>	
Scaling of the viscous wall layer	11-7
<i>T. J. Hanratty, D. V. Papavassiliou</i>	
Experimental study of a turbulent Couette flow at low-Reynolds number	11-10
<i>K. Nakabayashi, O. Kitoh, F. Nishimura</i>	
Application of oil-surface visualisation and topology principles to identify the flow patterns around wall-mounted cubes	11-16
<i>E. R. Meinders, R. J. Martinuzzi, K. Hanjalic</i>	
Large eddy simulation of annular duct flow	11-22
<i>H. Xu, A. Pollard</i>	
 SESSION 12 - VARIABLE DENSITY FLOWS	 12-1
Reaction of near wall turbulence to strong density gradients	12-1
<i>S. Tardu, M. Favre Marinet, J. L. Harion</i>	
Monte Carlo computations of turbulent variable density jets	12-6
<i>J. P. H. Sanders, I. Gokalp</i>	
Experimental determination of some characteristic scales in variable density turbulent jets	12-12
<i>J. Page, Y. Haidous, B. Sarh, I. Gokalp</i>	
Velocity statistics associated with scale distributions in variable density turbulent jets	12-18
<i>L. Pietri, J. F. Lucas, M. Amielh, F. Anselmet</i>	
Variable density mixing in kinematically homogeneous turbulence.....	12-24
<i>P. Chassaing, S. Castaldi, G. Haran, L. Joly</i>	
 SESSION 13 - CLOSURES II	 13-1
Realizability of non-linear stress-strain relationships for Reynolds-stress closures	13-1
<i>S.R. Fu, T. Rung, F. Thiele</i>	

Predicting non-inertial effects with algebraic stress models which account for dissipation rate anisotropies	13-7
<i>T. Jongen, L. Machiels, T. B. Gatski</i>	
A new explicit algebraic Reynolds stress turbulence model for 3D flow	13-13
<i>S. Wallin, A. V. Johansson</i>	
Nonlinear eddy viscosity modelling with a transport equation for Lumley's stress flatness parameter	13-18
<i>K. Suga</i>	
Development of the the k - j turbulence model	13-24
<i>J. Cousteix, V. Saint Martin, R. Messing, H. Beazard, B. Aupoix</i>	

SESSION 14 - WALL FLOWS II

	14-1
Comparison between directly simulated numerical and experimental data of the unsteady turbulent channel flow	14-1
<i>M. Hartmann, C. Völtz, D. Ronneberger</i>	
Second-moment modelling of periodic and transient pipe flow	14-6
<i>M. A. Cotton, A. W. Guy, B. E. Launder</i>	
Relaxation process of 2D asymmetric turbulent channel flow subjected to sudden replacement of smooth and rough walls	14-12
<i>M. Miyata</i>	
Turbulence Measurements in a rough wall boundary layer	14-18
<i>S. Young, D.J. Bergstrom</i>	
Drag reduction in turbulent MHD pipe flows	14-22
<i>P. Orlandi</i>	

SESSION 15 - APPLICATIONS I

	15-1
Combined P.I.V. and L.D.V. analysis of the evolution and breakdown of a compressed tumbling vortex	15-1
<i>D. Marc, J. Boree, R. Bazile, G. Charnay</i>	
Compression of a turbulent vortex flow	15-7
<i>O. Le Roy, L. Le Penven</i>	
Analytical and direct numerical study of the evolution and breakdown of a compressed tumbling vortex	15-13
<i>J. Boree, A. Corjon, D. Marc</i>	
Evolution of cylinder spin-down turbulence subjected to a single-stroke compression: experiments and modelling	15-19
<i>K. Hanjalic, S. Jakirlic, C. Tropea, J. Volkert</i>	
A model defroster flow	15-25
<i>K. Willenborg, J.F. Foss, R. AbdulNour, J.J. McGrath, B. AbdulNour</i>	

SESSION 16 - DNS AND LARGE EDDY SIMULATION - I	16-1
Stimulated small scale SGS model and its application to channel flow <i>K. B. Shah, J. H. Ferziger</i>	16-1
Subgrid-scale modeling based on the generalized scale-similarity models <i>K. Horiuti</i>	16-7
A subgrid-scale model for nonpremixed turbulent combustion <i>A. W. Cook, J. J. Riley, S. M. deBruynKops</i>	16-13
Large-eddy simulation of turbulent reactive flows <i>F. Mathey, J.P. Chollet</i>	16-19
A priori testing of subgrid-scale models in anisotropic homogeneous turbulence <i>A. Juneja, J. G. Brasseur</i>	16-25
 SESSION 17 - INSTABILITY AND TRANSITION	17-1
Large-scale instability and small-scale transition in vortex pairs <i>T. Leweke, C. H. K. Williamson</i>	17-1
Transition to turbulence in the wakes of axisymmetrical objects <i>M. Provansal, D. Ormieres</i>	17-7
Distinct modes of small-scale instability in wake transition <i>C. H. K. Williamson, T. Leweke</i>	17-12
Absolute instability of round heated air jet <i>A. Boguslawski, S. Drobniak</i>	17-18
Instability induced by a roughness <i>K. Ono, T. Motohashi</i>	17-24
 SESSION 18 - COMBUSTION I	18-1
Reynolds stress closures for strongly swirling combustng jets <i>T. Landefeld, A. Kremer, E. P. Hassel, J. Janicka</i>	18-1
A multi-scalar PDF method for SI engine combustion simulation <i>R. Tatschl</i>	18-7
Turbulence statistics and scalar transport in highly-sheared premixed flames <i>D. Duarte, P. Ferrao, M. V. Heitor</i>	18-13
An experimental study on the consecutive and competing reaction in a turbulent liquid jet by the light absorption spectrometric method <i>Y. Sakai, I. Nakamura, T. Kubo</i>	18-19
Extended self-similarity and intermittency in turbulent combustion <i>D. Queiros-Conde</i>	18-25

SESSION 19 - APPLICATIONS II	19-1
Vortex formation processes in open channel flows with a side discharge by using the nonlinear k- ϵ model	19-1
<i>T. Hosoda, Y. Muramoto, I. Kimura</i>	
Numerical simulation and experimental validation of the turbulent combustion and perlite expansion processes in an industrial perlite expansion furnace	19-7
<i>A. Klipfel, M. Founti, K. Zahringer, J. P. Martin, J. P. Petit</i>	
Generation of longitudinal vortices in internal flows with an inclined impinging jet and enhancement of target plate heat transfer	19-13
<i>K. Suzuki, K. Nakabe, A. Higashio, J. S. Acton, W. Chen</i>	
Physical and numerical modeling of turbulent flow over complex topography	19-19
<i>A. Nakayama, H. Noda</i>	
Experimental investigation of flow near friction screens	19-25
<i>P. Sullivan, T. Oshinowo, D. C. S. Kuhn, Z. Huang</i>	
SESSION 20 - STRATIFIED FLOWS	20-1
The effect of stable density stratification on the dynamics of turbulent channel flow	20-1
<i>O. Iida, N. Kasagi, Y. Nagano</i>	
Heat Transfer in a stably stratified shear flow	20-7
<i>T. Kanzaki, Y. Ichikawa</i>	
Importance of third-moment modelling in horizontal, stably stratified flows	20-13
<i>T. J. Craft, J. Kidger, B. E. Launder</i>	
Modeling of turbulent transport in PBL with third-order moments	20-19
<i>B.B. Ilyushin, A.F. Kurbatskii</i>	
Mixing in a stably-stratified shear layer	20-25
<i>C. Staquet, K. B. Winters</i>	
SESSION 21 - COMBUSTION II	21-1
Large eddy simulation of a turbulent non-premixed flame	21-1
<i>N. Branley, W. P. Jones</i>	
Analysis of flame surface density concepts in non-premixed turbulent combustion using direct numerical simulations	21-7
<i>E. Van Kalmthout, D. Veynante</i>	
Large eddy simulations of turbulent premixed flames based on the G-equation and a flame front wrinkling description	21-13
<i>J. Piana, F. Ducros, D. Veynante</i>	
Modeling of turbulent convection in joint pdf equation. Applications for turbulent premixed combustion	21-19
<i>F. Galzin, T. Mantel, G. Borghi</i>	

Effects of unstable stratification and mean shear on the chemical reaction in grid-generated turbulence	21-25
<i>S. Komori, K. Nagata</i>	

SESSION 22 - JETS I	22-1
----------------------------	-------------

Measured Reynolds stress distributions and energy budgets of fully pulsed round free jets and comparisons with k-e model predictions	22-1
<i>K. Bremhorst, P. Gehrke, S. He</i>	
Vortical structure of an acoustically forced plane jet: bi-orthogonal eddies vs. physical eddies	22-7
<i>D. Faghani, A. Sevrain, H.-C. Boisson</i>	
Entrainment and mixing patterns in coflowing forced jets subjected to axial and azimuthal forcing	22-12
<i>K. P. Prestridge, J. C. Lasheras</i>	
Sensitivity of impinging turbulent jets to the external disturbances	22-18
<i>S. V. Alekseenko, A. V. Bilski, D. M. Markovich, V. I. Semenov</i>	
Large eddy simulation of plane impinging jets	22-24
<i>M. Tsubokura, T. Kobayashi, N. Taniguchi</i>	

POSTER SESSION 2

	P2-1
New first-order closure models for stably stratified flows	P2-1
<i>B. Abart, J.-F. Sini</i>	
Numerical simulation of diurnal atmospheric flow variations in a coastal complex terrain area and comparison of results with field observations	P2-7
<i>K. Sada, Y. Ichikawa, K. Asakura</i>	
Experimental study of internal waves in the stratified shear flow between two immiscible layers	P2-13
<i>M. Keicher, A. M. K. P. Taylor</i>	
Numerical prediction of performance of annular jet pump	P2-19
<i>N. Namiki, O. Kitamura, M. Yamamoto</i>	
Fuel-air ratio influence on mixing processes in turbulent premixed acetylene flame	P2-25
<i>V. V. Bakic, S. N. Oka, A. A. Acanski, M. M. Stefanovic</i>	
Role of mean strain and turbulent diffusion in early turbulent premixed flame growth	P2-30
<i>T. Mantel, F. Galzin, R. Borghi</i>	
Modelling of variable density effects in the second moment and dissipation equations in turbulent premixed flames	P2-36
<i>R. P. Lindstedt, E. M. Vaos</i>	
Direct numerical simulation of 2-D compressible chemically reacting mixing layer with compact difference scheme	P2-42
<i>G. Cai, F. Zhuang, D. Fu</i>	
Two-point velocity measurements in nonreacting and reacting turbulent stagnation flows	P2-43
<i>E. Bourguignon, Y. Michou, I. Gokalp</i>	
Characteristics of the turbulent flow in pipes with helical turbulence promoters	P2-49
<i>K. F. F. Vicari, S. V. Möller</i>	
Turbulent structure of an intermittent region of the turbulent boundary layer interacting with controlled longitudinal vortex arrays	P2-55
<i>C. Fukushima, H. Osaka, G. Nedelcu</i>	
Effect of local blowing on the instability of channel flow	P2-61
<i>Y. M. Chung, H. J. Sung, A. V. Boiko</i>	
Turbulent velocity profiles in gravel bed rivers	P2-67
<i>G. M. Smart</i>	
Computation with the k-e model with turbulent mass transfer in the wall-region	P2-71
<i>B. Chaouat</i>	
Investigation of the bursting phenomenon in transitional boundary layers	P2-77
<i>V. Uruba, P. Jonas, O. Mazur</i>	
Computation of turbulent flows using upwind-bias 5th order schemes	P2-83
<i>P.G.Huang</i>	
Development of a non-linear, strain-sensitive k-w turbulence model	P2-89
<i>D. Sofialidis, P. Prinos</i>	

Proposal of a low-Reynolds-number two-equation model to predict dynamic and thermal field	P2-95
<i>C. B. Hwang, C. A. Lin</i>	
Near wall modellization for dissipation equation in second-moment turbulence closures .	P2-101
<i>G. B. Deng, M. Visonneau</i>	
Calibration of models for the slow pressure-strain rate using LES	P2-107
<i>K. Alvelius, M. Hallbäck, A. V. Johansson</i>	
L.R.N. k-e model for prediction of turbulent boundary layers, developing under strong pressure gradient conditions	P2-113
<i>E. V. Shishov, A. I. Leontiev, A. V. Gerasimov</i>	
Experimental and computational study of pressure effects on turbulent flow in an asymmetric plane diffuser	P2-114
<i>L. Brunet, J. B. Cazalbou, P. Chassaing, L. Jervase</i>	
Mixing in coaxial jets with large density differences	P2-120
<i>M. Favre-Marinet, E. B. Camano, J. Sarboch</i>	
Simulation of two-dimensional structures in variable density coaxial jets	P2-126
<i>P. Reynier, A. Kourta, H. Ha Minh</i>	

ELEVENTH SYMPOSIUM ON TURBULENT SHEAR FLOWS
Institut National Polytechnique
Université Joseph Fourier
Grenoble, September 8-10, 1997

CONTENTS OF VOLUME 3
SESSSIONS 23 - 34
POSTER SESSION 3

SESSION 23 - BUOYANT FLOWS	23-1
The influence of shear number in stably stratified turbulent shear flow	23-1
<i>F. G. Jacobitz, S. Sarkar</i>	
DNS of natural convection between two vertical, differentially heated walls	23-7
<i>F. T. M. Nieuwstadt, T. A. M. Versteegh</i>	
Turbulent energy transport in non-neutral shear flows	23-13
<i>S. Heinz, A. Cadiou, K. Hanjalic</i>	
Turbulent convection at low Prandtl number	23-19
<i>S. Cioni, J. Sommeria, S. Ciliberto</i>	
LES of buoyant cavity: subgrid scale models for inhomogeneous flows	23-24
<i>X. Huang, D.J. Bergstrom</i>	
 SESSION 24 - TWO PHASE FLOWS I	 24-1
Sedimentation of small particles through the two-dimensional plane mixing layer	24-1
<i>T. M. Dreier, M. Virant, W. Kinselbach</i>	
Dispersion of small, heavy, spherical particles in a three-dimensional, temporally developing mixing layer	24-5
<i>B. Marcu, E. Meiburg</i>	
Lagrangian statistics of fluid/particle correlated motion in channel flow	24-11
<i>Y. Sato, I. Hayashi, K. Hishida</i>	
Simulation and Reynolds stress modeling of particle-laden turbulent shear flows	24-17
<i>D. B. Taulbee, F. Mashayek, P. Givi, C. Barré</i>	
Numerical study of particle motion in a turbulent mixing layer using the discrete vortex method	24-23
<i>E. Ory, R. J. Perkins</i>	
 SESSION 25 - JETS II	 25-1
Investigation of mixing in a coaxial jet configuration	25-1
<i>M. V. Salvetti, G. Lombardi, A. Talamelli</i>	
Flow regimes and mixing in the near field of large velocity ratio coaxial jets	25-7
<i>H. Rehab, E. Villermaux, E. J. Hopfinger</i>	

On similarity of a plane turbulent jet in a co-flowing stream	25-11
<i>J. C. LaRue, H. Rahai, T. Ly, P. Y. Jan</i>	
The influence of inlet conditions on a large eddy simulation of a turbulent plane jet	25-17
<i>C. Weinberger, J. Rewerts, J. Janicka</i>	
Large eddy simulations of three-dimensional spatially evolving round jets	25-23
<i>G. Urbin, C. Brun, O. Metais</i>	

SESSION 26 - SEPARATED FLOWS I 26-1

Large eddy simulation: A dynamic one-equation subgrid model for three-dimensional recirculating flow	26-1
<i>L. Davidson</i>	
Numerical and modelling influences on large eddy simulations for the flow past a circular cylinder	26-7
<i>M. Breuer</i>	
Response of separated flows over a backward-facing step to local forcing	26-13
<i>K. B. Chun, H. J. Sung</i>	
An experimental investigation of the flow around a two-dimensional square prism in the proximity of a solid wall: Effect of the gap size	26-18
<i>R. J. Martinuzzi, K. C. Q. Wu</i>	
Topology of coherent vortices in the reattachment region of a backward-facing step	26-24
<i>F. Delcayre</i>	

SESSION 27 - TWO PHASE FLOWS II 27-1

Primary instability in liquid-gas shear layers	27-1
<i>L. Raynal, E. Villermaux, J. Lasheras, E. J. Hopfinger</i>	
On the analysis of shear-driven liquid break-up processes	27-6
<i>I. S. Carvalho, M.V. Heitor, D. Santos</i>	
Dispersion of bubbles in a shear flow	27-12
<i>C. Martinez, J.C. Lasheras</i>	
Large eddy simulation of turbulent gas-solid flows in a vertical channel and evaluation of second-order models	27-18
<i>Q. Wang, K. D. Squires, O. Simonin</i>	
Numerical investigation of turbulent heat transfer mechanisms at a gas-liquid interface ...	27-24
<i>V. De Angelis, P. Lombardi, S. Banerjee</i>	

SESSION 28 - DNS AND LARGE EDDY SIMULATION - II 28-1

Large-eddy simulations of compressible flows on hybrid meshes	28-1
<i>F. Ducros, F. Nicoud, T. Schönfeld</i>	

Spectral-dynamic model for LES of free and wall shear flows	28-7
<i>E. Lamballais, M. Lesieur, J. H. Silvestrini</i>	
Large eddy simulation of turbulent channel flows	28-13
<i>C. Fureby, A. D. Gosman, G. Tabor, H. G. Weller, N. Sandham, M. Wolfshtein</i>	
A numerical simulation on the interaction between tangled polymers and turbulent structures	28-19
<i>Y. Hagiwara, Y. Takashina, M. Tanaka, H. Hana</i>	
Identification of vortical structures by a non-local criterion: Application to PIV measurements and DNS-LES results of turbulent rotating flows	28-25
<i>M. Michard, L-Graftieaux, L. Lollini</i>	
 SESSION 29 - COMPRESSIBLE FLOWS I	 29-1
Mixing enhancement in supersonic rectangular jets	29-1
<i>M. Samimy, J.-H. Kim, P. Clancy</i>	
Amplification/attenuation of turbulence in a heated jet/shock wave interaction	29-7
<i>L. Jacquin, P. Geffroy</i>	
Localization and analysis of large scale structures by a wavelet transform technique in a supersonic turbulent mixing layer	29-8
<i>P. Dupont, P. Muscat, J. P. Dussauge</i>	
Validation of a pseudo-sound theory for the pressure-dilatation in DNS of compressible turbulence	29-14
<i>J. R. Ristorcelli, G. A. Blaisdell</i>	
Prediction of 3D supersonic flows including crossflow separation using low Reynolds number turbulence models	29-19
<i>H. Deniau, F. Thivet, J. M. Moschetta</i>	
 SESSION 30 - SEPARATED FLOWS II	 30-1
Measurements in an unsteady separated flow using hot wire rakes	30-1
<i>S. Aubrun, P. Carles, H. Ha Minh, J. Coulomb, H. Boisson</i>	
An investigation on the fluctuations of the reattachment point downstream a backward facing step using particle tracking velocimetry	30-7
<i>G. P. Romano, S. Pomponio, G. Querzoli</i>	
Direct and Reynolds-averaged numerical simulations of a transitional separation bubble .	30-13
<i>Ph. R. Spalart, M. Kh. Strelets</i>	
Computations of separating and reattaching flows using a low-Reynolds-number second-moment closure	30-19
<i>T. J. Craft</i>	
Large eddy simulation of perturbed turbulent wall flows	30-25
<i>A. Dejoan, E. Vedy, R. Schiestel</i>	

SESSION 31 - ROTATION AND CURVATURE FLOWS I	31-1
Modeling of turbulent swirling flows	31-1
<i>T.-H. Shih, J. Zhu, W. W. Liou, K. H. Chen, N.-S. Liu, J. L. Lumley</i>	
EDQNM and DNS predictions of rotation effects in strained axisymmetric turbulence	31-7
<i>O. Leuchter, C. Cambon</i>	
Experiments for the effects of curvature and pressure-gradient on the turbulent wake of a flat plate	31-13
<i>A. R. Starke, R. A. W. M. Henkes, M. J. Tummers</i>	
Calculations of the flow through a U-bend	31-19
<i>M. M. Gibson, R. D. Harper</i>	
The dissipation rate transport equation and subgrid-scale models in rotating turbulence ...	31-25
<i>R. Rubinstein, Y. Zhou, B. A. Younis</i>	
 SESSION 32 - COMPRESSIBLE FLOWS II	 32-1
Computations of compressible turbulent shear flows with multiple-time-scale models	32-1
<i>A. Hadjadj, D. Vandromme, L. De Chanterac</i>	
Modeling of inhomogeneous compressible turbulence using a two-scale statistical theory	32-7
<i>F. Hamba</i>	
An improved two-point closure for weakly compressible turbulence and comparisons with large-eddy simulation	32-13
<i>G. Fauchet, L. Shao, R. Wunenburger, J. P. Bertoglio</i>	
Validation of linear and non-linear low-Re turbulence models in shock/boundary layer interaction	32-19
<i>G. Barakos, D. Drikakis</i>	
Computation of turbulent shock waves using second-moment closures	32-25
<i>G. Brun, J. M. Herard, D. Jeandel, M. Uhlmann</i>	
 SESSION 33 - WALL FLOWS III	 33-1
Direct numerical simulation of decelerated wall-bounded shear flows	33-1
<i>G.N. Coleman, J. Kim, P. R. Spalart</i>	
Structure of turbulent boundary layer subjected to adverse pressure gradient	33-7
<i>Y. Nagano, T. Tsuji, T. Houra</i>	
Application of turbulence models to equilibrium boundary layers under adverse pressure gradient	33-13
<i>R. A. W. M. Henkes, M. Skote, D. S. Henningson</i>	
On the turbulence structure in solid and permeable pipes	33-19
<i>C. Wagner, R. Friedrich</i>	

On the large scale organization of a turbulent boundary layer disturbed by a circular cylinder	33-25
<i>F. de Souza, J. Delville, J. Lewalle, J.-P. Bonnet</i>	

SESSION 34 - ROTATION AND CURVATURE II	34-1
---	-------------

Performance of the subgrid-scale algebraic stress model for turbulent flows in a rotating frame	34-1
<i>Y. Shimomura</i>	
Statistics of rapidly rotating turbulent plane couette flow	34-6
<i>H. I. Andersson, K. H. Bech</i>	
Modelling near-wall effects in axially rotating pipe flow by elliptic relaxation	34-12
<i>B. A. Pettersson, H. I. Andersson, A. S. Brunvoll</i>	
Importance of a local Rossby number for turbulence in a wake submitted to rotation	34-18
<i>L. Tarbouriech, D. Renouard</i>	
Transition to 3-D vortex breakdown in a closed cylinder with a rotating endwall	34-24
<i>F. Sotiropoulos, Y. Ventikos</i>	

POSTER SESSION 3	P3-1
Blowing with gas or water <i>J. Bellettre, F. Bataille, A. Lallemand,</i>	P3-1
Numerical study of bubble and particle motion in wall turbulence <i>I. A. Joia, T. Ushijima, R. J. Perkins</i>	P3-6
Turbulence modeling and first numerical simulations in turbulent two-phase flows <i>C. Morel</i>	P3-10
Statistical description of the bubble motion in a turbulent boundary layer <i>S. Tran-Cong, J. L. Marie, R. J. Perkins</i>	P3-16
Large eddy simulation and modelling of inter-particle collision influence in gas-solid turbulent shear flows <i>E. Deutsch, J. Lavieville, M. Sakiz, O. Simonin</i>	P3-22
The effect of turbulence modelling on turbulence modification in two-phase flows using the Euler-Lagrange approach <i>G. Kohnen, M. Sommerfeld</i>	P3-23
Extended algebraic stress models for prediction of three-dimensional and separating turbulent flow <i>R. J. A. Howard, N. D. Sandham</i>	P3-29
Computation of unsteady flows by using a semi-deterministic approach with nonlinear turbulence model <i>A. Kourta</i>	P3-35
Swirl flow simulation by means of Reynolds stress turbulent modelling <i>M. Sijercic, S. Nemoda</i>	P3-41
Modeling turbulent flow in curved duct of square cross section <i>Y. D. Choi, J. K. Shin, K. H. Chun, J. A. C. Humphrey</i>	P3-47
Coherence of vortices in a rotating fluid <i>S. Leblanc, F. S. Godefert</i>	P3-53
Computations of strongly swirling flows with quadratic pressure-strain model <i>J. C. Chen, C. A. Lin</i>	P3-59
Repartition of the energy in compressible turbulence <i>F. Bataille, Y. Zhou, J. P. Bertoglio</i>	P3-65
Modelling of extra-compressibility terms in high speed turbulent flows <i>C. Lejeune, A. Kourta</i>	P3-71
Assessment of an implicit, parallel, multigrid diven algorithm for large eddy simulation <i>E. Arad, L. Martinelli</i>	P3-77
Numerical methods for DNS of flow past a square cylinder <i>R. W. C. P. Verstappen, A. E. P. Veldman</i>	P3-83
Generation of initial and boundary conditions for large-eddy simulations of wall-bounded flows <i>D. C. Weatherly, J. M. McDonough</i>	P3-89

On optimum filter size and efficient numerical viscosity for large eddy simulation of complex flows around a square cylinder	P3-95
<i>K. Nozawa, T. Tamura</i>	
Wavelet velocity correlation analysis in a plane turbulent jet	P3-101
<i>H. Li</i>	
Turbulence characteristics of a three-dimensional turbulent boundary layer on a rotating disk with an impinging jet	P3-107
<i>H. S. Kang, J. Y. Yoo, H. Choi</i>	
An axisymmetric wall jet with its axis removed from the wall and the effect of the wall on the evolution of coherent structures	P3-113
<i>A. Benaissa, D. Ewing, A. Pollard</i>	
Velocity structure functions in a turbulent plane jet	P3-117
<i>B. R. Pearson, R. A. Antonia</i>	
Numerical study of the detaching flow aerodynamical sound	P3-122
<i>S. Huang, C. Beguier</i>	

AUTHOR INDEX

**VOLUME 1: SESSIONS 1 - 10
 POSTER SESSION 1 (P1)**

**VOLUME 2 : SESSIONS 11 - 22
 POSTER SESSION 2 (P2)**

**VOLUME 3 : SESSIONS 23 - 34
 POSTER SESSION 3 (P3)**

Abart B. , P2.1
 Abdel Gawad A. F., P1.1
 Abdel Latif O. E., P1.1
 AbdulNour B., 15.25
 AbdulNour R., 15.25
 Acanski A. A., P2.25
 Acton J. S., 19.13
 Alboussiere T., 5.7
 Alekseenko S. V., 22.18
 Alvelius K., P2.107
 Amano R. S., P1.18
 Amielh M., 12.18
 An P., P1.83
 Andersson H. I., 34.6, 34.12
 Anselmet F., 4.7, 12.18
 Antonia R. A., 2.1, 4.7, 10.16, P3.117
 Apsley D. D., 6.25
 Arad E., P3.77
 Arroyo G., 5.1
 Asakura K., P1.61, P2.7
 Aubrun S. , 30.1
 Aupoix B., 6.1, 13.24
 Ayrault M., P1.67
 Bakic V. V., P2.25
 Banerjee S., 27.24
 Barakos G., 32.19
 Barré C., 24.17
 Bataille F., P3.1, P3.65
 Bazile R., 15.1
 Bech K. H., 34.6
 Beguier C., P3.122
 Beharelle S., 2.25
 Bellettre J., P3.1
 Benaissa A., P3.113
 Bergstrom D. J., 14.18, 23.24
 Bertoglio J. P., 32.13, P3.65
 Bezard H., 13.24
 Bilger R. W., 07.24
 Bilski A. V., 22.18
 Blaisdell G. A., 29.14
 Boguslawski A., 17.18
 Boiko A. V., P2.61
 Boisson H.-C., 22.7, 30.1
 Boniforti M. A., P1.106
 Bonnet J.-P., 2.25, 5.1, 33.25, P1.55
 Boree J., 15.1, 15.13
 Borghi R., 7.18, 21.19, P2.30
 Bouhadji A., P1.31
 Bourguignon E., P2.43
 Branley N., 21.1
 Brasseur J. G., 16.25
 Braza M., P1.31
 Breard C., P1.25
 Bremhorst K., 22.1
 Breuer M., 26.7
 Brun C., 25.23, P1.89
 Brun G., 32.25
 Brunet L., P2.114
 Brunvoll A. S., 34.12
 Cadiou A., 23.13
 Cai G., P2.42
 Calmet I., 8.24
 Camano E. B., P2.120
 Cambon C., 31.7
 Carles P., 30.1
 Carvalho I. S., 27.6
 Castaldi S., 12.24
 Cazalbou J. B., P2.114
 Chaouat B., P2.71
 Charnay G., 15.1
 Chassaing P. , 12.24, P2.114
 Chen J. C., P3.59
 Chen K. H., 31.1
 Chen W., 19.13
 Chen W. L., 1.13
 Choi H., P1.37, P3.107
 Choi Y. D., P3.47
 Chollet J. P., 16.19
 Chun K. B., 26.13
 Chun K. H., P3.47
 Chung Y. M., P2.61
 Ciliberto S., 23.19
 Cioni S., 23.19
 Citriniti J. H., 5.12, 5.18
 Clancy P., 29.1
 Coleman G. N., 33.1
 Comte P., 1.1
 Cook A. W., 16.13
 Cordier L., P1.101
 Corjon A., 15.13
 Cotton M. A., 14.6
 Coulomb J., 30.1
 Cousteix J., 6.1, 13.24
 Craft T.J., 20.13, 30.19
 Daisaka H., P1.49
 Davidson L., 26.1
 De Angelis V., 27.24
 De Chanterac L., 32.1
 de Souza F., 33.25, P1.55
 deBruynKops S. M., 16.13
 deGraaff D. B., 1.19
 Dejoan A., 30.25
 Delcayre F., 26.24
 Delville J., 2.25, 5.1, 33.25, P1.55, P1.101
 Deng G. B., P2.101
 Deniau H., 29.19
 Deutsch E., P3.22
 Doussinault M., 6.1
 Dreier T. M., 24.1
 Drikakis D., 32.19
 Drobniak S., 17.18
 Duarte D., 18.13

Dubief Y., 1.1
 Ducros F., 21.13, 28.1
 Dumont T., 10.11
 Dupont P., 29.8
 Durbin P. A., 6.19
 Durst F., 2.13
 Dussauge J. P., 29.8
 Eaton J. K., 1.19, 8.13
 Eifert C., 3.1
 Elkins C. J., 8.13
 Engel K., P1.11
 Eulitz F., P1.11
 Ewing D., 5.12, P3.113
 Faghani D., 22.7
 Fauchet G., 32.13
 Favre Marinet M., 12.1, P2.120
 Ferrao P., 18.13
 Ferre J. A., 2.7, P1.95
 Ferziger J. H., 16.1
 Foss J. F., 15.25
 Founti M., 19.7
 Friedrich R., 33.19
 Fu D., P2.42
 Fu S., 6.7
 Fu S. R., 13.1
 Fujisawa N., 9.13
 Fukushima C., P2.55
 Fureby C., 28.13
 Galzin F., 21.19, P2.30
 Garem J.-H., 5.1
 Gatski T. B., 13.7
 Geffroy P., 29.7
 Gehrke P., 22.1
 Gerasimov A. V., P2.113
 Gibson M. M., 31.19
 Giralt F., P1.95
 Girimaji S. S., P1.118
 Givi P., 24.17
 Gleyzes C., 6.1
 Godeferd F. S., P3.53
 Gokalp I., 12.6, 12.12, P2.43
 Gonzalez M., 7.18
 Gooden J. H. M., 6.1
 Gosman A. D., 28.13
 Graftieaux L., 28.25
 Guy A. W., 14.6
 Ha Minh H., 30.1, P2.126
 Hadjadj A., 32.1
 Hagiwara Y., 28.19
 Hahn S., P1.37
 Haidous Y., 12.12
 Hallback M., 8.1, P2.107
 Hamba F., 32.7
 Hana H., 28.19
 Hanjalic K., 11.16, 15.19, 23.13

Hanratty T. J., 9.25, 11.7
 Harion J. L., 12.1
 Harper R. D., 31.19
 Harran G., 12.24
 Hartmann M., 14.1
 Hassel E. P., 18.1
 Hauville F., P1.25
 Hayashi I., 24.11
 He S., 22.1, P1.83
 Heinz S., 23.13
 Heitor M. V., 18.13, 27.6
 Heitz D., 5.1
 Henkes R. A. W. M., 31.13, 33.13
 Henningson D. S., 33.13
 Herard J. M., 32.25
 Herbert V., 10.7
 Higashio A., 19.13
 Hishida K., 24.11, P1.49
 Hopfinger E. J., 25.7, 27.1
 Horiuti K., 16.7
 Hosoda T., 19.1
 Houra T., 33.7
 Howard R. J. A., P3.29
 Huang P. G., P2.83
 Huang S., P3.122
 Huang X., 23.24
 Huang Z., 19.25
 Huberson S., P1.25
 Humphrey J. A. C., P3.47
 Hwang C. B., P2.95
 Iacovides H., 3.19
 Ichikawa Y., 20.7, P1.61, P2.7
 Iida O., 20.1
 Ikeda J., 4.17, P1.77
 Ilyushin B. B., 20.19
 Jackson J. D., P1.83
 Jacobitz F. G., 23.1
 Jacquin L., 29.7
 Jakirlic S., 15.19
 Jan P. Y., 25.11
 Janicka J., 3.1, 18.1, 25.17
 Jeandel D., 32.25
 Jervase L., P2.114
 Johansson A. V., 8.1, 13.13, P2.107
 Joia I. A., P3.6
 Joly L., 12.24
 Jonas P., P2.77
 Jones W. P., 3.25, 21.1
 Jongen T., 13.7
 Jovanovic J., 2.13
 Juneja A., 16.25
 Kang H. S., P3.107
 Kanzaki T., 20.7
 Kasagi N., 9.7, 9.18, 20.1, P1.43
 Kassinos S. C., 7.1

Kawaguchi Y., P1.49
 Kawahara G., 1.7
 Kawamura H., 8.7
 Keffer J. F., P1.95
 Keicher M., P2.13
 Kent J. H., 7.24
 Khris S., P1.19
 Kida S., 1.7
 Kidger J., 20.13
 Kim D. S., P1.71
 Kim J., 33.1
 Kim J. H., 29.1
 Kimura I., 19.1
 Kinselbach W., 24.1
 Kitamura O., P2.19
 Kitoh O., 11.10
 Klipfel A., 19.7
 Kobayashi T., 22.24
 Koch R., P1.7
 Kohnen G., P3.23
 Komori S., 21.25
 Kopp G. A., P1.95
 Kourta A., P2.126, P3.35, P3.71
 Kremer A., 18.1
 Kronenburg A., 7.24
 Kubo T., 18.19
 Kuhn D. C. S., 19.25
 Kurbatskii A. F., 20.19
 Lakehal D., 3.13
 Lallemand A., P3.1
 Lamballais E., 28.7
 Landenfeld T., 18.1
 Larcheveque M., 10.7
 LaRue J. C., 25.11
 Lasheras J. C., 22.12, 27.1, 27.12
 Launder B. E., 14.6, 20.13
 Lavieville J., P3.22
 Le Penven L., 15.7
 Le Roy O., 15.7
 Leblanc S., P3.53
 Lee D. H., P1.71
 Lejeune C., P3.71
 Leontiev A. I., P2.113
 Leschziner M. A., 1.13, 6.25
 Lesieur M., 28.7
 Leuchter O., 31.7
 Lewalle J., 33.25
 Leweke T., 17.1, 17.12
 Li H., P3.101
 Li J., P1.83
 Lien F. S., 1.13, 6.19
 Lin B., P1.18
 Lin C. A., P2.95, P3.59
 Lindstedt R. P., P2.36
 Liou W. W., 31.1

Liu N.-S., 31.1
 Lollini L., 28.25
 Lombardi G., 25.1, 27.24
 Lucas J. F., 12.18
 Lumley J. L., 31.1
 Ly T., 25.11
 Machiels L., 4.23, 13.7
 Maeda M., P1.49
 Magnaudet J., 8.24
 Mantel T., 21.19, P2.30
 Marc D., 15.1, 15.13
 Marchal P., 5.1
 Marcillat J., P1.19
 Marcu B., 24.5
 Marie J. L., P3.16
 Markovich D. M., 22.18
 Marquis A. J., 3.7
 Martin J. P., 19.7
 Martinelli L., P3.77
 Martinez C., 27.12
 Martinuzzi R. J., 11.16, 26.18
 Mashayek F., 24.17
 Massah H., 9.24
 Mathey F., 16.19
 Mazur O., P2.77
 McComb W. D., 4.23
 McDonough J. M., P3.89
 McGrath J. J., 15.25
 Meiburg E., 24.5
 Meinders E. R., 11.16
 Menzies K. R., 3.25
 Messing R., 13.24
 Metais O., 25.23
 Michard M., 28.25
 Michelot C., P1.67
 Michou Y., P2.43
 Minier J. P., P1.112
 Mito Y., 9.7
 Miyake Y., 11.1
 Miyata M., 14.12
 Miyauchi T., 4.17
 Miyazaki T., P1.102
 Möller S. V., P2.49
 Moreau R., 5.7
 Morel C., P3.10
 Morganti M., P1.106
 Morikawa T., 11.1
 Moschetta J. M., 29.19
 Motohashi T., 17.24
 Muramoto Y., 19.1
 Muscat P., 29.8
 Nagano Y., 20.1, 33.7
 Nagata K., 21.25
 Nakabayashi T., 9.13, 11.10
 Nakabe K., 19.13

Nakagawa S., 2.19
 Nakamura I., 18.19
 Nakayama A., 19.19
 Namiki N., P2.19
 Nedelcu G., P2.55
 Nemoda S., P3.41
 Nguyen P. N., 5.24
 Nicolleau F., 4.13
 Nicoud F., 28.1
 Nieuwstadt F. T. M., 23.7
 Nishimura F., 11.10
 Nitta K., 2.19
 Noda H., 19.19
 Nozawa K., P3.95
 Oberlack M., 10.21
 Ohsaka K., 8.7
 Oka S. N., P2.25
 Ong L. Y., 3.7
 Ono K., 17.24
 Orlandi P., 14.22
 Ormieres D., 17.7
 Ory E., 24.23
 Osaka H., P2.55
 Oshinowo T., 19.25
 Ould-Rouis M., 4.7
 Page J., 12.12
 Papavassiliou D. V., 11.7
 Park J., P1.37
 Parneix S., 6.19
 Pearson B. R., P3.117
 Perkins R. J., 24.23, P3.6, P3.16
 Petit J. P., 19.7
 Pettersson B. A., 34.12
 Pfuderer D. G., 3.1
 Piana J., 21.13
 Picut M., P1.89
 Pietri L., 12.18
 Pinheiro J., 7.18
 Pollard A., 11.22, P3.113
 Pomponio S., 30.7
 Pons M. D., 2.7
 Pozorski J., P1.112
 Prestridge K. P., 22.12
 Prinos P., P2.89
 Priymak V.G., P1.102
 Protas B., 10.1
 Provansal M., 17.7
 Queiros-Conde D., 18.25
 Querzoli G., 30.7
 Ragab S. A., P1.1
 Rahai H., 25.11
 Raynal L., 27.1
 Rehab H., 25.7
 Renouard D., 34.18
 Rewerts J., 25.17

Rexroth C. H., P1.7
 Reynier P., P2.126
 Reynolds W. C., 7.1
 Riley J. J., 16.13
 Ristorcelli J.R., 7.7, 29.14
 Robert R., 10.11
 Rodi W., 3.13
 Romano G. P., 30.7
 Ronneberger D., 14.1
 Rubinstein R., 31.25
 Rung T., 6.7, 13.1
 Sabelnikov V., P1.67
 Sada K., P1.61, P2.7
 Saint Martin V., 13.24
 Sakai Y., 18.19
 Sakiz M., P3.22
 Salvetti M. V., 25.1
 Samimy M., 29.1
 Sanders J. P. H., 12.6
 Sandham N., 28.13
 Sandham N. D., P3.29
 Santos D., 27.6
 Sarboch J., P2.120
 Sardi K., 8.19
 Sarh B., 12.12
 Sarkar S., 23.1
 Satake S., P1.43
 Sato Y., 24.11
 Schiestel R., 30.25
 Schönfeld T., 28.1
 Sciortino G., P1.106
 Semenov V. I., 22.18
 Senda M., 2.19
 Sevrain A., 22.7
 Shaalan M. R., P1.1
 Shah K. B., 16.1
 Shao L., 32.13
 Shih T.-H., 31.1
 Shima N., 7.12
 Shimomura Y., 34.1
 Shin J. K., P3.47
 Shishov E. V., P2.113
 Sijercic M., P3.41
 Silvestrini J. H., 28.7
 Simoens S., P1.67
 Simonin O., 27.18, P3.22
 Sini J. F., P2.1
 Sirovich L., 4.1
 Skote M., 33.13
 Smart G. M., P2.67
 Sofialidis D., P2.89
 Sommerfeld M., P3.23
 Sommeria J., 10.11, 23.19
 Song H. B., P1.71
 Sotiropoulos F., 34.24

Spalart Ph. R., 30.13, 33.1
 Squires K. D., 6.13, 27.18
 Staquet C., 10.7, 20.25
 Starke A. R., 31.13
 Stefanovic M. M., P2.25
 Strelets M. Kh., 30.13
 Suga K., 13.18
 Sullivan P., 19.25
 Sung H. J., 26.13, P2.61
 Suzuki Y., 9.18, 19.13
 Tabor G., 28.13
 Takashina Y., 28.19
 Talamelli A., 25.1
 Tamura T., P3.95
 Tanahashi M., 4.17
 Tanaka M., 1.7, 28.19
 Taniguchi N., 22.24
 Tarbouriech L., 34.18
 Tardu S., 9.1, 12.1
 Tarman I. H., 4.1
 Tatschl R., 18.7
 Taulbee D. B., 24.17
 Taylor A. M. K. P., 8.19, P2.13
 Tenaud C., P1.101
 Theodoridis G. S., 3.13
 Thiele F., 6.7, 13.1
 Thivet F., 29.19
 Tran-Cong S., P3.16
 Tropea C., 15.19
 Tsang W. K., 2.1
 Tsubokura M., 22.24
 Tsuji T., 33.7
 Tsujimoto K., 11.1
 Tummers M. J., 31.13
 Uhlmann M., 32.25
 Urbin G., 25.23
 Uruba V., P2.77
 Ushijima T., P3.6
 Uspenski V., 5.7
 Van Kalmthout E., 21.7
 Vandromme D., 32.1
 Vaos E. M., P2.36
 Vassilicos J. C., 4.13
 Vedy E., 30.25
 Veldman A. E. P., P3.83
 Ventikos Y., 34.24
 Verstappen R. W. C. P., P3.83
 Versteegh T. A. M., 23.7
 Veynante D., 21.7, 21.13
 Vicari K. F. F., P2.49
 Villiermaux E., 25.7, 27.1
 Virant M., 24.1
 Visonneau M., P2.101
 Volkert J., 15.19
 Völtz C., 14.1
 Voutsinas S. G., P1.25
 Wagner C., 33.19
 Wallin S., 13.13
 Wang Q., 27.18
 Warholic M., 9.24
 Weatherly D. C., P3.89
 Webster D. R., 1.19
 Weinberger C., 25.17
 Weller H. G., 28.13
 Westfreid J. E., 10.1
 Wikstrom P. M., 8.1
 Willenborg K., 15.25
 Williamson C. H. K., 17.1, 17.12
 Winters K. B., 20.25
 Wittig S., P1.7
 Wolfshtein M., 28.13
 Wu K. C. Q., 26.18
 Wu X., 6.13
 Wunenburger R., 32.13
 Xu H., 11.22
 Yabe A., P1.49
 Yamagami K., 2.19
 Yamamoto K., 8.7
 Yamamoto M., P2.19
 Yanase S., 1.7
 Yang T. J., 4.23
 Yasuda R., P1.77
 Ye Q. Y., 2.13
 Yoo J. Y., P3.107
 Yoon S. H., P1.71
 Yoshikawa T., 11.1
 Young A., 4.23
 Young S., 14.18
 Younis B. A., 31.25
 Zahringer K., 19.7
 Zhai Z., 6.7
 Zhou T., 10.16
 Zhou Y., 2.1, 31.25, P3.65
 Zhu J., 31.1
 Zhu Y., 4.7, 10.16
 Zhuang F., P2.42

PLENARY SESSION

Large Eddy Simulation of a boundary layer flow passing over a groove

Y. Dubief, P. Comte
LEGI/IMG-MOST, BP53, 38041 Grenoble-Cedex 09, France.

ABSTRACT

The boundary layer flow passing over a groove is investigated by means of large eddy simulation. A first simulation is performed with a mean turbulent velocity profile perturbed by small-amplitude white noise. The skin friction is found to be reduced downstream of the groove. The shear layer developing above the groove generates spanwise vortices which in turn create low- and high-velocity streaks. The vortical structure of the flow downstream of the groove could be a key factor of the drag reduction mechanism for the flow under consideration. A method based on the work of Lund *et al.* (1996) is then used in order to generate more realistic inlet conditions. This method proves to be fairly accurate and allows the generation of turbulent boundary layer flows at low numerical cost.

INTRODUCTION

The effect of a spanwise groove (whose dimensions are typically of the order of the boundary layer thickness) on the vortical structure of a turbulent boundary layer flow has recently regained interest in the field of turbulence control (Choi & Fujisawa (1993) and Pearson *et al.*, 1996). The groove belongs to the category of passive devices capable of reducing skin friction in turbulent boundary layer flow. Tani *et al.* (1987) experimentally showed that the turbulent skin friction over a d -type rough surface (sparsely spaced transverse grooves in this case) is less than that over a smooth wall. Choi & Fujisawa (1993) observed a small reduction in the skin friction over $100d$ downstream of a single square groove of depth d . Also for a single groove, Pearson *et al.* (1996) found a local maximum of skin friction reduction (about 50%), one boundary layer thickness δ_0 downstream of the groove. They also indicated that the skin friction coefficient slowly relaxes back to its smooth wall value in an oscillatory manner. Pearson *et al.* (1996) observed injections and

ejections of fluid at the downstream edge of the groove emphasizing the existence of an important communication between the groove flow and the boundary layer flow. They established that the ejection of low-speed fluid out of the groove is responsible for an increase of the magnitude of decelerating events downstream of the groove. There is a wide agreement to associate this kind of event with low-speed streaks.

Even though the effect of the groove is quite limited in space and the resulting drag reduction is small, the study of a boundary layer passing over a groove could be very useful to understand the mechanism involved in drag generation and control as discussed by Pearson *et al.* (1996). We present a large eddy simulation of a groove embedded in a flat plate (see figure 1). The flow is weakly compressible ($M_\infty = 0.5$). The Reynolds number of the flow based on the free stream velocity U_0 and the groove depth (or the boundary layer thickness, since $d = \delta_0$) is 5100. It corresponds to the numerical simulation of a turbulent boundary layer performed by Spalart (1988) at $R_\theta = 670$ (where θ is the momentum thickness of the flow). The Reynolds number is also roughly the same as that of Pearson *et al.* (1996)'s experiment ($R_\theta = 700$ for the flow visualization and 1320 for the measurements). The code and subgrid-scale model are similar to the ones used by Ducros *et al.* (1996). Ducros *et al.* (1996) successfully simulated the transition to turbulence of a boundary layer developing spatially over a smooth wall by using a modified version (called the filtered structure-function model) of the structure function model of Métais & Lesieur (1992). The filtered structure-function model proved to be superior to the structure-function model and Smagorinsky's model to solve a transitional boundary layer (for a review on subgrid models, see Lesieur & Métais, 1996). The boundary layer manipulated by a groove has first been investigated with a mean turbulent velocity profile perturbed by weak white noise as inlet conditions. The second part of

this paper discusses the generation of more consistent inflow condition thanks to an auxiliary calculation of a turbulent boundary layer developing spatially. This inflow generation is based on the method of Lund *et al.* (1996).

CALCULATION PROCEDURE

The simulation is carried out using a multi-domain compressible code described in Comte *et al.* (1995). It is based on a McCormack-type finite-difference scheme which is second order accurate in time and fourth order accurate in space. Curvilinear coordinates can be used in the streamwise and vertical directions. Periodicity is assumed in the spanwise direction. Non reflective boundary conditions (based on the Thompson characteristic method, Thompson, 1987) are prescribed at the outlet and the upper boundaries. The Filtered Structure-Function Model (Ducros *et al.*, 1996) consists of filtering out the large-scale fluctuations of the resolved velocity field before computing its second-order structure function at the cut-off scale, on a plane parallel to the wall. This corresponds to the four-neighbour version of the model. Variable-density eddy-viscosity and eddy-diffusivity coefficients are then derived assuming Kolmogorov's law.

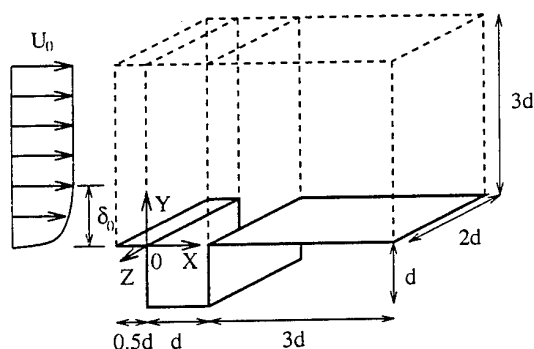


Figure 1: Sketch of the computational domain. Dashed lines bound the three different domains.

The streamwise, vertical and spanwise directions are noted x , y and z respectively. All dimensions are normalized by the groove depth d . The coordinate system used is located at the upstream edge of the groove (see figure 1). The inflow consists of the mean turbulent velocity profile obtained by Spalart at $Re_\theta = 670$, plus white noise of amplitude $10^{-3} U_0$, regenerated every timestep. The computational domain (figure 1) is decomposed into three blocks. The ratio groove depth over upstream boundary layer thickness, d/δ_0 is 1. The resolution for the inlet, the groove and the downstream flat plate blocks are, respectively, $21 \times 51 \times 40$, $41 \times 101 \times 40$ and $121 \times 51 \times 40$. The minimal grid spacing at the wall in the vertical direction corresponds to $\Delta y^+ = 1.2$. The streamwise grid spacing goes from $\Delta x^+ = 3.2$ near the groove edges to 20 at the outlet. The spanwise resolution is $\Delta z^+ = 16$. The grid is stretched by an hyperbolic tangent-type transformation similar to that used by Le & Moin (1994) for a backward-facing step flow. The simulation has been performed on a Cray C98 of the CNRS national com-

puting center IDRIS. The data presented in this paper have been collected over 16 characteristic times (based on d and U_0) sampled at a frequency of $1200 U_0/d$. The data collection amounted to 20 hours of CPU time.

FLOW OVER AND DOWNSTREAM OF A SQUARE GROOVE

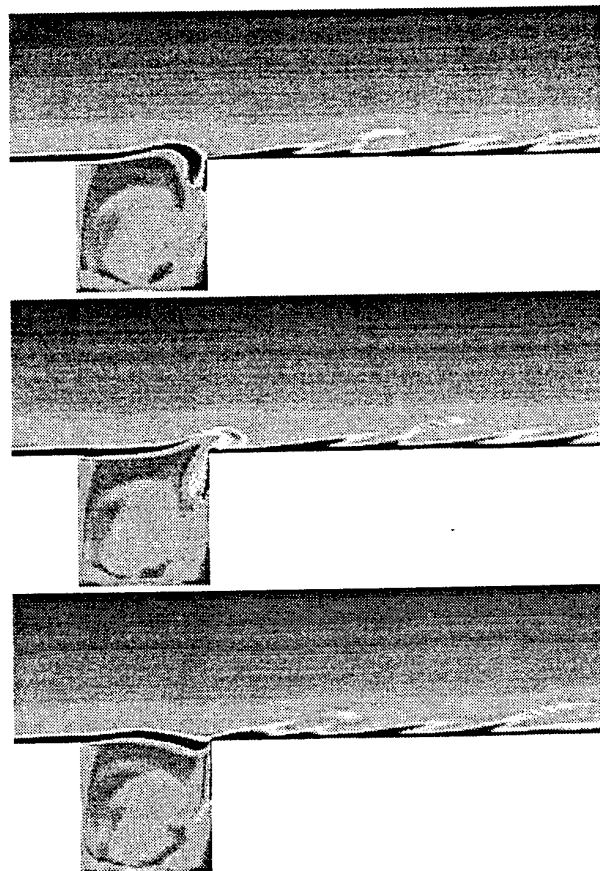


Figure 2: A time sequence showing a typical wrapping and impingement of the shear layer which develops above the groove. The images are taken at $tU_0/d = 0$, $tU_0/d = 0.8$ and $tU_0/d = 2.4$. They represent isocontours of the instantaneous vorticity in the plane $z/d = 0.25$. The domain is truncated at $y/d = 1.1$.

Figure 2 shows a time sequence of instantaneous vorticity contours in a (x,y) plane. The boundary layer flow which separates at the upstream edge of the groove develops a shear layer above the groove. The shear layer rolls-up into a spanwise vortex which impinges the downstream edge of the groove and flaps periodically. The impingement frequency is evaluated by spectral analysis of the flow (see figure 5). The Strouhal number of vortex impingement is about 0.33. It corresponds to the most energetic peak in the energy spectrum of the flow at the downstream edge. This frequency is slightly larger than that of the vortex shedding in a backward-facing step flow (Delcayre, 1997). The vortex is split in two by the downstream edge. The lower part of the vortex dissipates in the recirculation flow inside the groove. Its upper part is convected downstream and produces the tilted waves of high vorticity shown in figure 2. These waves ap-

pear to be stretched upwards. Yet the perturbations generated by the impingement of vortices are confined to the near-wall region of the flow, as illustrated by the evolution of mean velocity profiles in the streamwise direction (figure 3). Figure 3 indicates that mean velocity profiles depart from the smooth wall profile in the range $0 \leq y/d \leq 0.2$. For $x/d = 1$ (i.e., at the downstream edge), the flow is accelerated in a thin layer above the flat plate and eventually decelerated up to $y/d = 0.2$. At $x/d = 3.5$, the velocity of the flow for $y/d \leq 0.2$ is considerably less than that at the inlet. It should be noted that $y/d = 0.2$ corresponds to the vertical extent of instantaneous vorticity perturbations visualized in figure 2.

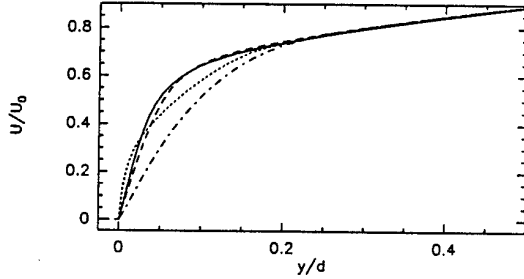


Figure 3: Mean streamwise velocity profiles at the inlet. —, $x/d = -0.5$; ---, $x/d = 0$; ···, $x/d = 1$; -·-·, $x/d = 3.5$.

As expected from the evolution of mean velocity profiles, the skin friction coefficient:

$$C_f = \frac{(\mu \frac{\partial U}{\partial y})_{wall}}{\frac{1}{2} \rho_0 U_0^2},$$

normalized by its inlet value, experiences a sharp rise at the downstream edge and rapidly falls below unity (figure 4). The overshoot at $x/d = 1$, which has a magnitude of 3, is caused by the stagnation point due to the edge. The fluid which impinges the downstream edge has gained momentum as it passes over the groove thanks to the recirculation vortex. Therefore the wall gradient at the edge is considerably larger than at the inlet. Downstream of the groove, C_f/C_{f0} rapidly reaches a plateau region $C_f/C_{f0} \approx 0.5$. Also plotted in figure 4, the experimental values of Pearson *et al.* (1996) are comparable to that calculated in the present study. As the groove studied by Pearson *et al.* (1996) is much smaller ($d/\delta_0 = 0.17$) than ours, the agreement between their data and ours needs further investigation to be discussed.

Three-dimensionalisaty of the flow

As the flow moves downstream of the groove, the structure associated with the impingement of vortices (i.e., the remainder of spanwise vortices) lose their energy as shown by the time spectrum of the kinetic energy (figure 5). Meanwhile the high-frequency part is shifted upwards, which denotes the appearance of small scales. Figure 2 clearly shows that the vorticity perturbations grow as they are convected downstream. The dissipative process could be viewed in the present study as the onset of a turbulent production which

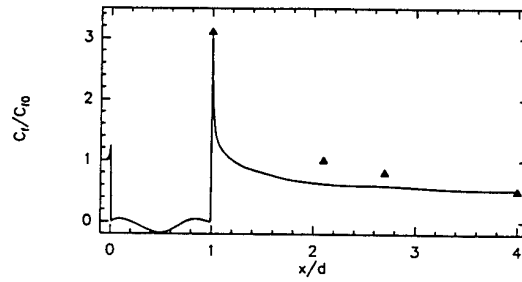


Figure 4: Streamwise evolution of the skin-friction coefficient normalized by its inlet value, C_{f0} . Symbols correspond to the measurements of Pearson *et al.*, 1996

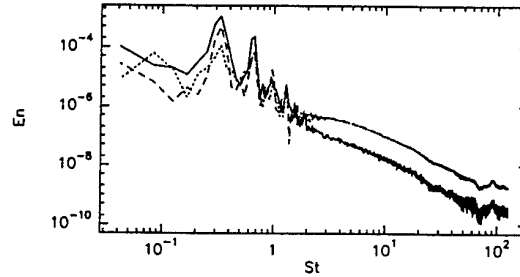


Figure 5: Time spectra of the kinetic energy at different streamwise locations. —, $x/d = 0.9$; ---, $x/d = 1.5$; ···, $x/d = 3.5$. The data has been collected at $y/d = 0.05$.

is missing in the inlet condition. This speculation is confirmed by three dimensional visualisations of instantaneous vorticity isosurfaces. The following visualizations correspond to the same instant of the simulation: $tU_0/d = 2.4$ (i.e. the last image of figure 2). This instant has been chosen because the spanwise vortex has already impinged the edge. The other reason for this choice is that this particular sequence gathers all the structures of the flow. Figure 6 reveals the existence of longitudinal structures in the shear layer developing above the groove. The wavelength of these structures is approximately $0.5d$. When a spanwise vortex impinges the wall, the longitudinal structures cross over the edge and develop over the flat plate. Figure 6 shows that the remainder of the spanwise vortex which impinges the wall at $tU_0/d = 0.8$ is highly distorted in the spanwise direction (structures which are located approximately one groove length after the groove). Further away the vortical organisation is clearly longitudinal.

Figure 7 shows the evolution of longitudinal structures downstream of the groove. Three stages of evolution are present in this figure. The first stage is the generation of the spanwise oscillation which occurs in the shear layer of the groove. The second stage is the patch of longitudinal structures located approximately one groove length after the edge. Structures of alternate vorticity have been created to satisfy the sudden change in boundary condition, i.e. the appearance of a no-slip condition imposed by the wall. These structures correspond to the convected part of the spanwise

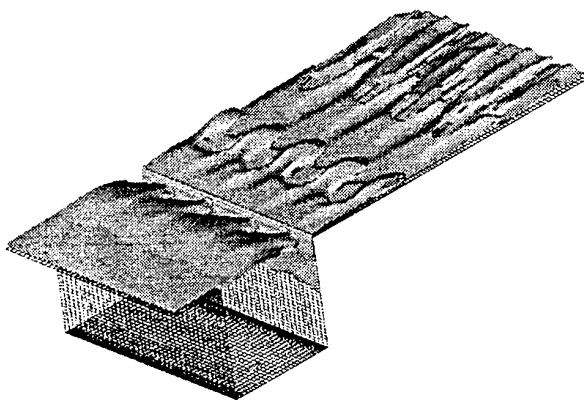


Figure 6: Isosurfaces of the norm of vorticity. $\omega = 0.3\omega_i$, where ω_i is the initial vorticity modulus. $tU_0/d = 2.4$

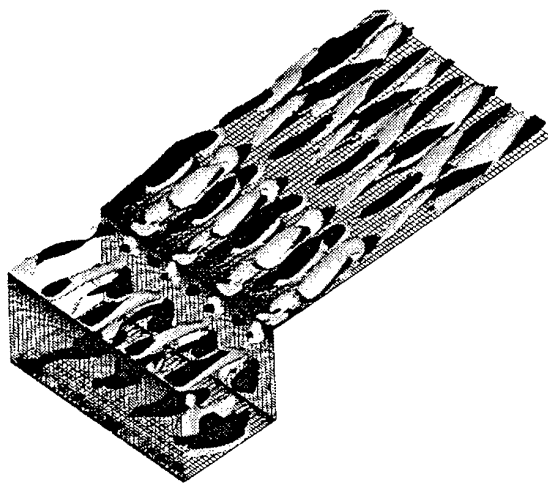


Figure 7: Isocontours of the streamwise vorticity. $\omega_x = -0.08\omega_i$ (dark), $\omega_x = +0.08\omega_i$ (grey). $tU_0/d = 2.4$

vortex which has just impinged. Finally, the third stage, near the downstream end of the domain indicates the arrangement of longitudinal vorticity into Λ -shaped structures, similar to those found by Ducros *et al.* (1996) in transitional boundary layers.

The vortical structure of the flow downstream of the groove results in a streaky like velocity field (figure 8) with low- and high-speed streaks. Immediately downstream of the edge, the flow is dominated by high-speed streaks which slowly vanish as they are convected by the flow. The remainder of the spanwise vortex gives birth to low-speed streaks at the wall. The low- and high-speed streaks have the same spanwise wavelength which is approximately 90 wall units (to be compared to 100 wall units in turbulent boundary layers). Near the downstream end of the domain, figure 8 shows that low-speed streaks are tilted upwards. Their vertical extent reaches $y/d \approx 0.2$.

TURBULENT BOUNDARY LAYER DEVELOPING SPATIALLY

In the above simulation, the upstream flow is deprived of coherent longitudinal vorticity. In order to

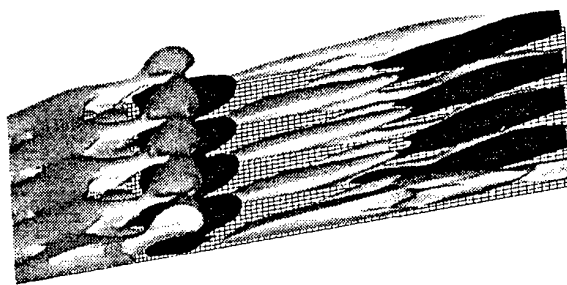


Figure 8: Isosurfaces of the streamwise fluctuating velocity above the downstream plate. $u' = -0.07$ (dark), $u' = 0.07$ (grey). The flow goes from left to right. $tU_0/d = 2.4$

understand the role played by the structures discussed in the previous section on drag reduction mechanism, it is necessary to compute a turbulent boundary layer upstream of the groove at the lowest possible cost. The method of Lund *et al.* (1996) seems the most appropriate for this purpose.

At each time step, the mean and fluctuating velocities, temperatures and pressures are extracted from a plane, called the recycling plane and rescaled at the appropriate inlet scaling. This method is based on the inner and outer scaling laws, where the variables scale with (u_τ, ν) and (u_τ, δ) , respectively. The inlet solution is then a composite solution of the inner and outer profile obtained as follows (Lund *et al.*, 1996):

$$q_i = (Q_i^I + q_i^{I'}) (1 - W(\eta)) + (Q_i^O + q_i^{O'}) W(\eta),$$

where $\eta = y/\delta_0$. q_i is either a velocity, pressure or temperature variable. Q_i and q_i' are the mean and fluctuating value of q_i . The superscripts I and O refer to a rescaling and interpolation performed on the basis of the inner or outer scaling. The recycling plane should be far enough from the inlet to avoid any forcing of the flow (*i.e.* more than one streamwise correlation length).

A simulation of a turbulent boundary layer using the method described above has been carried out over a domain $10\delta_0$ long. The recycling plane is $6.5\delta_0$ (≈ 2000 wall units) downstream of the origin. The height of the domain is $3\delta_0$. Its width is $1\delta_0$, *i.e.* 300 wall units. The minimal grid spacing Δx^+ and Δy^+ are 1.5 and 1, respectively. The grid is uniform in the streamwise and spanwise directions with $\Delta x^+ = 30$ and $\Delta z^+ = 10.8$. The total resolution is $101 \times 61 \times 30$. Despite an evident lack of convergence, the statistics near the wall are in fairly good agreement with the direct numerical simulation of a turbulent boundary layer performed by Spalart (1988) at the same Reynolds number $Re = 5100$. An overall view of the streak system is given in figure 9. Figures 10 and 11 show the distributions of mean velocity, root mean square of u , v and w at $6.5\delta_0$ from the inlet. Actually the domain could be shortened to $8\delta_0$ in the streamwise direction without affecting the result.

Reynolds shear stress distribution in wall coordinates.



Figure 9: Spatial turbulent boundary layer. Isosurfaces of the streamwise fluctuating velocity. $u' = -0.15$ (dark), $u' = 0.15$ (grey). The flow goes from left to right.

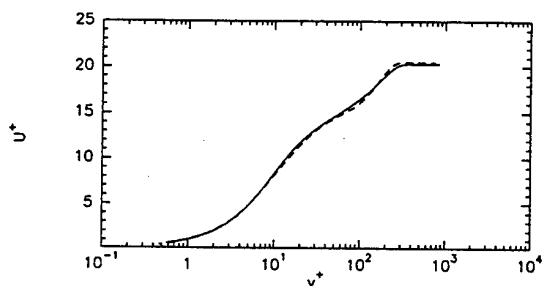


Figure 10: Mean streamwise velocity profiles in wall coordinates. DNS of Spalart $Re = 5100$, —; present study $x/\delta_0 = 6.5$, ----.

CONCLUSION

A large eddy simulation of a boundary layer passing over a groove has been performed with a mean turbulent velocity profile perturbed by a weak white noise. On the flat plate downstream of the groove, the skin friction coefficient is first higher than its inlet value and rapidly decreases to reach a plateau region around $x/d = 2$. The reduction for $x/d \geq 2$ is approximately 50% and is similar to that obtained experimentally by Pearson *et al.* (1996) with a smaller groove. For the present simulation, three types of structures have been identified:

- spanwise Kelvin-Helmholtz vortices within the groove shed at a Strouhal number 0.33. They are distorted three-dimensionally at a spanwise wavelength $0.5d$, maybe by translatative instability (Pierrehumbert & Widnall, 1982) or Görtler instability during their ascending motion.
- remains of these, downstream of the groove, after impingement.
- low- and high-speed streaks whose streamwise vorticity contributes to less than 30% of the total vorticity. Their spanwise spacing is also $0.5d$, that is 90 wall units.

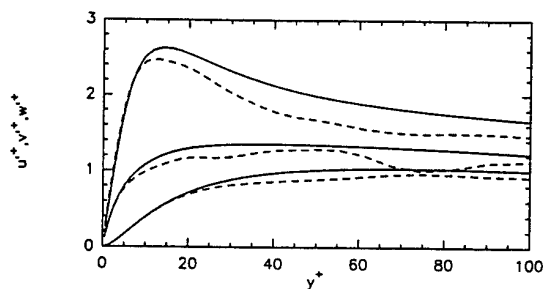


Figure 11: RMS u (upper curves) v (middle curves) w (lower curves) distributions in wall coordinates. DNS of Spalart $Re = 5100$, —; present study $x/\delta_0 = 6.5$, ----.

The origin of the three-dimensionality of the flow remains unclear. Calculation with more realistic upstream conditions are in progress. The simulation of a turbulent boundary layer developing spatially has been then presented in the scope of the generation of realistic inflow conditions. The method proposed by Lund *et al.* (1996) has proved to be efficient and accurate. It has been found that a small domain ($\approx 8\delta_0$) is sufficient to generate a realistic turbulent boundary layer. The full simulation including the groove will be presented at the conference.

ACKNOWLEDGMENTS

The CPU time used for this study was allocated by the French national computing center IDRIS.

REFERENCES

- Choi, K. S. and Fujisawa N., 1993, "Possibility of drag reduction using a d -type roughness", *App. Sci. Res.*, 50, pp. 315-324.
- Comte, P., Silvestrini, J.H. and Lamballais, E. 1995, "A Straightforward 3D Multiblock Unsteady Navier-Stokes Solver for Direct and Large-Eddy Simulations of Transitional and Turbulent Compressible Flows, 77th. AGARD Fluid Dynamic Panel Symposium "Progress and Challenges in CFD Methods and Algorithms", Seville, pp. 2-5.
- Delcayre, F., 1997, "Topology of Coherent Vortices in the Reattachment Region of a Backward-Facing Step Flow", *Presented at Turbulent Shear Flows 11*.
- Ducros, F., Comte, P. and Lesieur, M. 1996 Large-Eddy Simulation of Transition to Turbulence in a Boundary Layer Developing Spatially Over a Flat Plate", *J. Fluid Mech.*, 326, pp.1-36.
- Le, H. and Moin, P., 1995, "Direct Numerical Simulation of a Turbulent Backward-Facing Step", *NASA Report*, TF 58.
- Lesieur, M., and Métais, O., 1995, "New Trends in Large-Eddy Simulations of Turbulence", *Ann. Rev. Fluid Mech.*, 28.
- Lund, T. S., Wu, X., and Squires, K. D., 1996, "On the Generation of Turbulent Inflow Conditions for Boundary Layer Simulations", *Annual Research Briefs*, Center for Turbulence Research, pp. 287-295.
- Métais, O., and Lesieur, M., 1992, "Spectral Large-Eddy Simulation of Isotropic and Stably Stratified Turbulence", *J. Fluid. Mech.*, 239, pp. 157-194.
- Pearson, B. R., Elavarasan, R. and Antonia, R. A. 1996,

"The Response of a Turbulent Boundary Layer to a Square Groove", *To be published in J. Fluids. Eng.*.

Pereira, J.C.F., Sousa, J.M.M., 1994: Large-Eddy Simulation of Turbulent Flow Over a Cavity, 74th. AGARD Fluid Dynamics Symposium on "Application of Direct and Large-Eddy Simulation to Transition and Turbulence", Chania, April 1994.

Pierrehumbert, R. T., and Widnall, S. E., 1982, "The Two- and Three-Dimensional Instabilities of a Spatially Periodic Shear Layer. *J. Fluid Mech.*, 114, pp. 59-82.

Spalart, P., 1988, "Direct Numerical Simulation of a Turbulent Boundary Layer up to $Re_\theta = 1410$ ", *J. Fluid Mech.*, 187, pp. 61-98.

Tani, I., Munakata, H., Matsumoto, A. and Abe, K., 1987, "Turbulence Management by Groove Roughness", in *Turbulence Management and Relaminarisation*, Liepman, H. W., and Narasimha, R. (eds), Berlin Springer Verlag (1987), pp 161-172.

Thompson, K. W., 1987, "Time Dependent Boundary Conditions for Hyperbolic Systems", *J. Comp. Phys.*, 68, pp. 506-517.

UNIFORMLY SHEARED TURBULENT FLOW UNDER THE EFFECT OF SOLID-BODY ROTATION

M. Tanaka⁽¹⁾, S. Yanase⁽²⁾, S. Kida⁽³⁾, G. Kawahara⁽⁴⁾

⁽¹⁾ Department of Mechanical and System Engineering, Kyoto Institute of Technology
Sakyo-ku, Kyoto-shi, Kyoto 606, Japan

⁽²⁾ Department of Engineering Sciences, Okayama University
3-1-1 Tsushima-naka, Okayama-shi, Okayama 700, Japan

⁽³⁾ Theory and Computer Simulation Center, National Institute for Fusion Science
322-6 Oroshi-cho, Toki-shi, Gifu 509-52, Japan

⁽⁴⁾ Department of Mechanical Engineering, Ehime University
3 Bunkyo-cho, Matsuyama-shi, Matsuyama 790-77, Japan

ABSTRACT

Rotating homogeneous turbulence with and without uniform shear flow is investigated numerically. In the first part of the paper, two-dimensionalization process in a rotating turbulence is examined and a remarkable increase in size of the vortex structures is observed. In the second part, the change of the vortical structures is studied for cyclonic, non-rotating and anti-cyclonic turbulent flows. The results show that a distinct coherent structure develops when the solid-body rotation cancels the shear vorticity.

INTRODUCTION

The effect of solid-body rotation on shear flow turbulence has become one of the central issues of fluid mechanics not only because it is closely related to geophysical and astrophysical phenomena but also because it is thought to give a useful insight for developing the method of drag reduction in engineering applications through controlling vortex structures.

Recently it has been well understood that the direction of rotation of vortex tubes against that of solid-body rotation is important for the development of the coherent structure in rotating turbulence. Cyclonic vortices can keep two-dimensional coherent structures but anti-cyclonic ones become highly three-dimensional if the magnitude of the solid-body rotation is small (Lesieur *et al.* 1991, Yanase *et al.* 1993 and Métais *et al.* 1995). The idea of cyclonic and anti-cyclonic vortices is also important for understanding wall-shear-flow turbulence (Kawahara *et al.* 1997). A vortex tube whose vorticity is parallel to the direction of the vorticity associated with the mean shear is called cyclonic, and that of the opposite vorticity, anti-cyclonic. It was shown that cyclonic vortex tubes predominate anti-cyclonic ones because the growth rate of the former is larger than the latter. Therefore, it is likely to observe more cyclonic eddies than anti-cyclonic ones in fully developed turbulence. In the present paper, we study fully developed rotating turbulence with a uniform shear rather than wall-shear-flow turbulence.

It is commonly believed that Taylor-Proudman's theo-

rem ensures the two-dimensionalization of turbulence under strong solid-body rotation. However, there are few works which demonstrate the approach to two-dimensional turbulence by the action of uniform rotation (for example Bartello *et al.* 1994, Hossain 1994), and the physical interpretation of these phenomena seems to be poor. In order to understand the dynamics of vortex tubes in the shear flow turbulence under a solid-body rotation, it is necessary to clarify the process of two-dimensionalization.

In the present paper, we investigate numerically homogeneous turbulence with and without uniform shear in a rotating frame. We pay our attention to energy development and vortical structures in the rotating shear-flow turbulence.

FORMULATION

Basic Equations

Consider a unidirectional flow along the x_1 -axis sheared in the x_2 -axis, $\mathbf{U} = (Sx_2, 0, 0)$, under a solid-body rotation around the x_3 -axis (see Fig.1). The equations for velocity u_i and vorticity ω_i of the fluctuation flow are written in the rotating frame as

$$\frac{\partial u_i}{\partial t} + Sx_2 \frac{\partial u_i}{\partial x_1} + u_k \frac{\partial u_i}{\partial x_k} = -Su_2 \delta_{i1} + f \epsilon_{ij3} u_j - \frac{\partial p}{\partial x_i} + \nu \nabla^2 u_i, \quad (1)$$

$$\begin{aligned} \frac{\partial \omega_i}{\partial t} + Sx_2 \frac{\partial \omega_i}{\partial x_1} + u_k \frac{\partial \omega_i}{\partial x_k} \\ = S\omega_2 \delta_{i1} + (f - S) \frac{\partial u_i}{\partial x_3} + \omega_k \frac{\partial u_i}{\partial x_k} + \nu \nabla^2 \omega_i, \end{aligned} \quad (2)$$

which are supplemented by solenoidal condition $\partial u_j / \partial x_j = 0$. Here, $f = 2\Omega$, Ω being the angular velocity of the solid-body rotation. We can assume that $f \leq 0$ (S can be negative) without loss of generality owing to the flow symmetry. In order to eliminate the spatial coordinate x_2 in Eqs.(1) and (2), we introduce a coordinate system

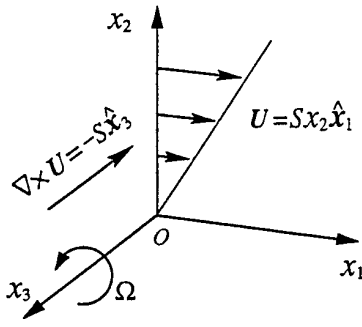


Figure 1 Configuration of rotating uniform shear flow.

moving with the uniform shear flow as follows (Kida and Tanaka 1994):

$$\xi_1 = x_1 - Stx_2, \quad \xi_2 = x_2, \quad \xi_3 = x_3, \quad \tau = t. \quad (3)$$

The vorticity equation is written in the moving coordinate as

$$\frac{\partial \omega_i}{\partial \tau} + u_k \frac{\partial \omega_i}{\partial \xi_k} = S\omega_2 \delta_{i1} + (f - S) \frac{\partial u_i}{\partial \xi_3} + \omega_k \frac{\partial u_i}{\partial \xi_k} + \nu \nabla^2 \omega_i. \quad (4)$$

The linear stability characteristics of the sheared flow with solid-body rotation was discussed by Bradshaw (1969). He introduced the non-dimensional number

$$B = f(f - S)/S^2 \quad (5)$$

by taking an analogy between rotating and density-stratified flows into consideration. This analogy led him to a conclusion that the effect of rotation on three-dimensional motions should be stabilizing for $B > 0$ and destabilizing for $B < 0$ with the growth rate of the fluctuation being $(-B)^{1/2}$.

Turbulence Energy

For homogeneous turbulence the time-evolution of the turbulence energy per unit mass $E(t) = \frac{1}{2} \langle |u|^2 \rangle (\equiv \frac{1}{2} u'^2(t))$ is described by

$$\frac{dE}{dt} = -S \langle u_1 u_2 \rangle - \nu Q, \quad (6)$$

where $Q(t) = \langle |\omega|^2 \rangle (\equiv \omega'^2(t))$ is the turbulence enstrophy per unit mass. The first and second terms in the right-hand side of Eq.(6) represent the Reynolds shear stress and the viscous dissipation, respectively. It should be noted that the system rotation affects significantly the growth of turbulence energy by changing the Reynolds shear stress and the energy dissipation rate, though it does not appear explicitly in Eq.(6). Equation (6) is rewritten in terms of the anisotropy tensor, $b_{ij} = \langle u_i u_j \rangle / u'^2 - (1/3) \delta_{ij}$, of the turbulent velocity as

$$\frac{1}{E} \frac{dE}{dt} = -2Sb_{12} - \nu \frac{Q}{E}. \quad (7)$$

Parameters

There are four time scales which characterize uniform shear flow turbulence subjected to a solid-body rotation. The time scales associated with the solid-body rotation and the mean shear are given by $1/f$ and $1/|S|$, respectively. Those of the large and the small eddies are u'^2/ϵ and $1/\omega'$, respectively, where $\epsilon = \nu \omega'^2$ is the energy dissipation rate.

The large-scale motions in a uniformly rotating turbulence are characterized by the large-scale Rossby number

$$Ro^{(u)}(t) = \frac{\nu \omega'^2}{f u'^2}, \quad (8)$$

while the small-scale by the small-scale Rossby number

$$Ro^{(\omega)}(t) = \frac{\omega'}{f}, \quad (9)$$

The relative importance of the uniform shear to the solid-body rotation is represented by the shear Rossby number

$$Ro^{(S)}(t) = \frac{-S}{f}. \quad (10)$$

The Taylor micro-scale Reynolds number $R_\lambda(t) = u' \lambda / \nu$, where $\lambda = u' / \omega'$, and the shear rate parameter $S^*(t)$ (Kida and Tanaka 1992), are expressed by these Rossby numbers as

$$R_\lambda(t) = Ro^{(\omega)} / Ro^{(u)}, \quad S^*(t) = -Ro^{(S)} / Ro^{(u)}. \quad (11)$$

Hereafter, we simply call R_λ the Reynolds number.

RAPID DISTORTION THEORY (RDT)

First we examine the linearized version of Eqs.(1) and (2). For the case without solid-body rotation, $f = 0$, an analytical solution can be obtained for each Fourier coefficient $\hat{u}(\mathbf{k})$. Taking an average over all directions, we find the Reynolds stress for the turbulent velocity field in the Fourier space as

$$\hat{R}_{ij}(\mathbf{k}) \equiv \text{Re} [\langle \hat{u}_i(\mathbf{k}) \hat{u}_j^*(\mathbf{k}) \rangle] = \frac{1}{2} \left(\delta_{ij} - \frac{k_i k_j}{|\mathbf{k}|^2} \right) \langle |\hat{u}(\mathbf{k})|^2 \rangle, \quad (12)$$

where $*$ denotes the complex conjugate. If the initial field is randomly distributed, we can calculate $\hat{R}_{ij}(\mathbf{k})$ at any time t (Townsend 1976).

If a solid-body rotation is present, however, we may not be able to obtain any analytical solutions in general form. For $|St| \ll 1$ and $\nu = 0$ and if the initial field is isotropic, each component of the Reynolds stress, R_{ij} , can be calculated in the power series of St . The Reynolds stress is positive ($\propto S^2 t$) at an initial period irrespective of the rate of rotation, which leads to an increase of turbulence energy.

Although it is not easy to extract asymptotic properties of turbulence from RDT for $f \neq 0$, some interesting results are obtained for the following two special cases.

Case(i) $f = S$ (see Eq.(4)): The directions of the quasi-streamwise vortex tube and its associated vorticity coincide with each other because the deviation of their directions is created only by the linear term $(f - S) \partial u_i / \partial x_3$ in Eq.(2) which vanishes for $f = S$ (Tanaka 1994).

Case(ii) $f \gg S$: The phase scrambling effects (Mansour et al. 1991) lead to a relation between b_{ij} and y_{ij} as

$$b_{ij} = b_{ij}^{(S)} \equiv -\frac{1}{2} y_{ij}, \quad (13)$$

where y_{ij} is defined in terms of the Fourier component of the velocity field $\hat{u}_i(\mathbf{k})$ by

$$y_{ij} = \frac{Y_{ij}}{Y_{kk}} - \frac{1}{3} \delta_{ij}, \quad Y_{ij} = \int \frac{k_i k_j}{k^2} |\hat{u}(\mathbf{k})|^2 d\mathbf{k}. \quad (14)$$

It should be remarked that Eq.(12) holds for this case.

Finally, we note that the Fourier modes except for those of $k_1 = k_2 = 0$ do not necessarily develop as $|\hat{u}(\mathbf{k})| \propto \exp [(-B)^{1/2} |St|]$ which is predicted by the linear stability analysis by Bradshaw (see Métais et al. 1992).

run group	$R_\lambda(0)$	grids (box-size)	k_0	S	f
A	16	$64^2 \times 128$ ($2\pi^2 \times 4\pi$)	3.87	0	0, 0.25 0.5, 1 2, 4
B	32	$128^2 \times 256$ ($2\pi^2 \times 4\pi$)	5.48	0	0 1 0.5
C	16	128^3 ($4\pi \times 2\pi^2$)	6.83	1	0
				1	1
				1	2
				0	0
		128^3 ($2\pi^3$)	4.10	1	0.5

Table 1 Parameters for numerical simulations.

DIRECT NUMERICAL SIMULATION(DNS)

Numerical Methods

Equation (1) is solved numerically in a coordinate system which is advected by the uniform shear flow (Kida and Tanaka 1994). The computation is carried out by using the Fourier spectral/Runge-Kutta-Gill scheme. The initial velocity field is given by the Fourier coefficients with specified energy spectrum

$$E(k) = c k^4 \exp(-2k^2/k_0^2), \quad (15)$$

and with random phase. Here, c is a constant and k_0 is a wavenumber at which the energy spectrum takes the maximum.

Many runs were performed for different combinations of values of c , k_0 , S , f and the initial Reynolds number $R_\lambda(0)$. The parameters in the runs employed here are summarized in Table 1. In the present paper, the time scale is normalized by $\omega'(0)$. We put $c = \frac{128}{15} \sqrt{\frac{2}{\pi}} k_0^{-7}$ so that $\omega'(0) = 1$. Statistical properties and vortical structures without rotation have already been investigated in Kida and Tanaka (1992, 1994).

Shearless Case

First, we study the case without shear. We here focus our attention to the two-dimensionalization of turbulence by the solid-body rotation. In order to find the rotation rate at which the effect of rotation on turbulence is strongest, calculations with lower resolution ($64 \times 64 \times 128$) were performed for several values of f and for a low Reynolds number $R_\lambda(0) = 16$, starting with the same initial condition (see group A in Table 1). Simulations were executed until $t = 50$.

The time-evolution of turbulence kinetic energy of three-dimensional modes, $E_{3d} = \frac{1}{2} \sum_{k_3 \neq 0} |\hat{u}(k)|^2$, and two-dimensional one, $E_{2d} = \frac{1}{2} \sum_{k_3=0} |\hat{u}(k)|^2$, are respectively plotted in Figs. 2(a) and 2(b) for $Ro^{(\omega)} = \infty$ (non-rotating case), 4, 2, 1, 0.5, and 0.25. It is seen that the decay rate of E_{3d} decreases monotonically with the Rossby number (Bardina *et al.* 1985). On the other hand, the decay rate of E_{2d} decreases as $Ro^{(\omega)}$ at first, but it turns to increase as $Ro^{(\omega)}$ becomes smaller than about unity, which suggests that the energy transfer from three-dimensional (3D) to two-dimensional (2D) modes is most active for $Ro^{(\omega)} \approx 1$ (Mansour *et al.* 1992).

Figure 3 shows the time-evolution of (a) E_{2d}/E_{3d} and (b) Q_{2d}/Q_{3d} for various values of the Rossby number, which are normalized by those for the non-rotating case in order to extract the effect of rotation. Here, Q_{2d} and Q_{3d} respectively stand for the two- and three-dimensional modes of the enstrophy which are defined in a similar way as E_{2d} and

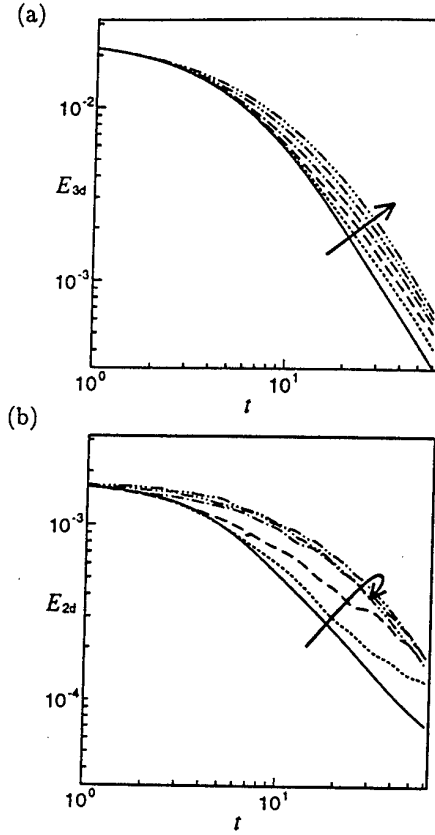


Figure 2 Time-evolution of (a) three and (b) two dimensional parts of energy. — non-rotating case, ... $Ro^{(\omega)} = 4$, -- $Ro^{(\omega)} = 2$, - . - $Ro^{(\omega)} = 1$, - - - $Ro^{(\omega)} = 0.5$, - - - - $Ro^{(\omega)} = 0.25$.

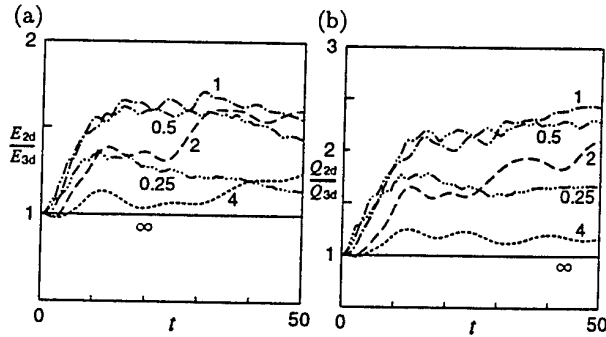


Figure 3 Time-evolution of (a) E_{2d}/E_{3d} and (b) Q_{2d}/Q_{3d} for the same cases as in Fig.2

E_{3d} . They give a measure of two-dimensionalization of the velocity and the vorticity fields respectively. It is seen in Fig.3 that both E_{2d}/E_{3d} and Q_{2d}/Q_{3d} are largest around $Ro^{(\omega)} = 1$, which suggests that two-dimensionalization is taking place most actively at this Rossby number. A similar behavior was found in Bartello *et al.* (1994). It must be remarked that the rapid increases of E_{2d}/E_{3d} and Q_{2d}/Q_{3d} take place only in the initial period. In later periods when turbulence continuously decays, on the other hand, they grow more slowly probably because the effect of the rotation is excessively dominant against the nonlinear effect which is capable of two-dimensionalization through the energy transfer from 3D to 2D modes. In order to examine the vortical structures in more detail, we performed larger simulations ($128 \times 128 \times 256$) for a higher Reynolds number

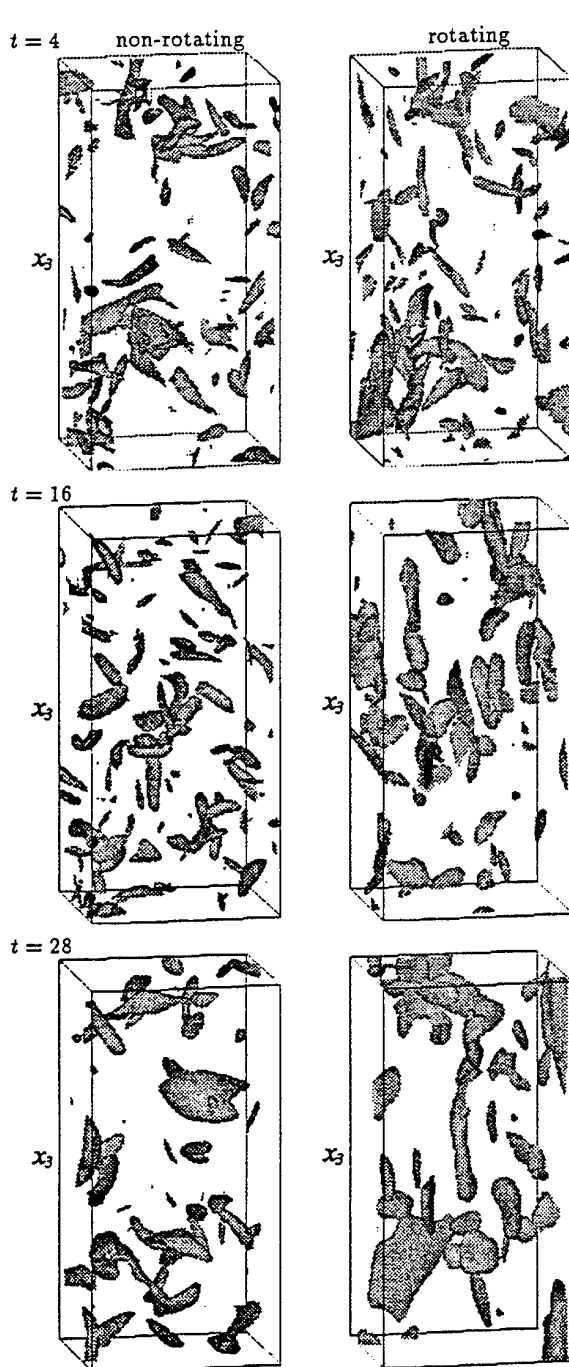


Figure 4 Regions of high-vorticity magnitude at $t = 4, 16, 28$ for the non-rotating and the rotating cases.

$R_\lambda(0) = 32$. For the purpose of realizing strong two-dimensionalization, we took $Ro^{(\omega)} = 1$. A simulation without rotation was done with the same initial condition and the same Reynolds number for comparison.

Figure 4 shows the regions of high-vorticity magnitude at $t = 4, 16, 28$ for both the rotating and the non-rotating cases. Numerical domains of $\pi \times \pi \times 2\pi$ ($64 \times 64 \times 128$ grids) in the x_1 -, x_2 - and x_3 -directions are displayed. We observe apparent vorticity structures at $t = 4$ both in the rotating and the non-rotating cases. Incidentally, the enstrophy takes its maximum value at about $t = 2.8$.

For the rotating case, we see thin vortex tubes at $t = 4$ which are aligned in the direction of the rotating axis. As

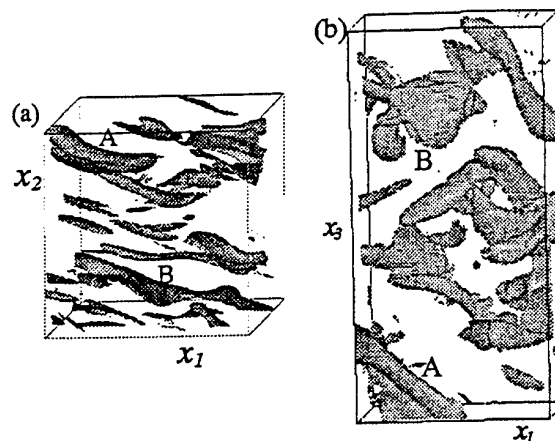


Figure 5 Regions of high-vorticity magnitude ($|\omega| \geq 1.68$) at $t = 12$ for $Ro^{(S)} = 1$.

time proceeds, the field is filled with larger vortex structures which are elongated tubes in the rotation direction or vortex sheets (Bardina et al. 1985, Bartello et al. 1994). The difference between the rotating and the non-rotating cases is obvious at later times.

Cyclonic Case

Next, we examine vortical structures in the cyclonic case. We have performed a simulation for $f = -S = 0.5$ ($Ro^{(S)} = 1$) with the same initial condition as the two larger simulations mentioned above (see group B in Table 1). Note that the flow is linearly stable according to Bradshaw (1969) ($B > 0$). In Fig. 5, the regions of $|\omega| \geq 1.68$ at $t = 12$ in the domain of $\pi \times \pi \times 2\pi$ are viewed from the positive (a) x_3 - and (b) x_2 -directions. Two typical structures are recognized: the *oblique vortex tubes* which are inclined from the x_3 -direction toward the x_1 -direction (see e.g. A in Fig. 5) and the *pancake like structures* which are thin in the x_2 -direction and spread both in the x_1 - and x_3 -directions (see e.g. B in Fig. 5). The oblique vortex tubes decay gradually as time goes on by emitting inertia waves due to the phase scrambling effect. The pancake like structures, on the other hand, remain coherent for a long time.

Comparing Fig. 5 with Fig. 4, we notice that the growth in size of vortical structures in the x_3 -direction in this case is comparable to that in the rotating turbulence without shear. From the results of many other simulations that we have done, we conjecture that the average absolute vorticity $f - S$ is one of the most important factors of the vorticity growth.

Anti-cyclonic Case

Figure 6 shows the time-evolution of the turbulence kinetic energy for the sheared turbulence at $Ro^{(S)} = \infty$ (non-rotating case), -2 , -1 and -0.5 with $S = 1$ and the isotropic turbulence with $f = S = 0$ (see group C in Table 1). It is found that the kinetic energy increases rapidly as $\exp(\alpha t)$, $\alpha \approx 0.4$ for the most unstable anti-cyclonic case ($Ro^{(S)} = -2$) of the linear stability analysis. Therefore, it can be concluded that the three-dimensional linear instability of anti-cyclonic eddies leads to an increase of turbulence energy. In the non-rotating case, the energy also increases exponentially though the growth rate is not large (~ 0.15 , Kida and Tanaka 1992). For another neutral case ($B = 0$), $Ro^{(S)} = -1$, turbulence energy stays around the equilibrated value. It is remarkable that the energy growth rate for this case is lower than that for the

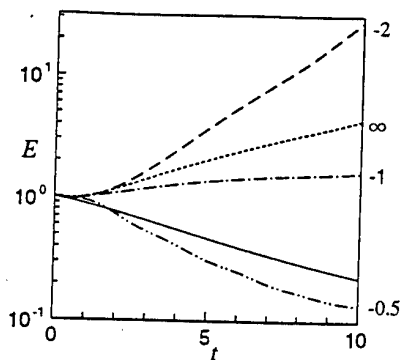


Figure 6 Time-evolution of turbulence energy. — $f = S = 0$, ... $Ro^{(S)} = \infty$, -- $Ro^{(S)} = -2$, -.- $Ro^{(S)} = -1$, --- $Ro^{(S)} = -0.5$.

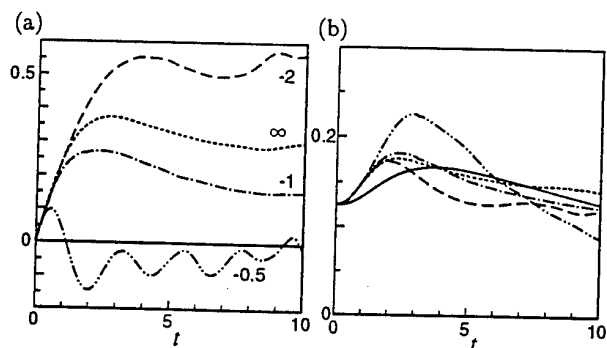


Figure 7 Time-evolution of (a) the relative Reynolds stress and (b) the relative energy dissipation rate for the same cases as in Fig.6.

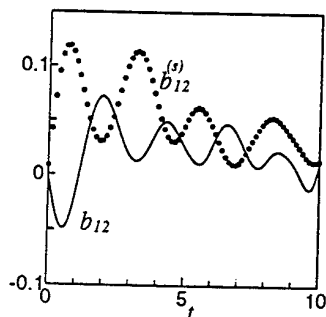


Figure 8 Time-evolution of b_{12} and $b_{12}^{(s)}$ for $Ro^{(S)} = -0.5$.

non-rotating case and that the decay rate for the stable anti-cyclonic case, $0 > Ro^{(S)} > -1$, is in general larger than that for the cyclonic case with the same Bradshaw number B . This indicates that the symmetry predicted by Eq.(5) is broken. For $Ro^{(S)} = -0.5$, turbulence energy decrease as time goes on. It is interesting to note that the energy decays more rapidly than that in the freely decaying isotropic turbulence. These results are consistent with those obtained by RDT (Bertoglio 1982) and a large-eddy simulation (Bardina *et al.* 1983).

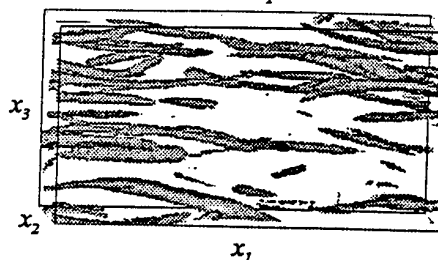
Figure 7 shows the time-evolution of (a) the relative Reynolds stress $-2Sb_{12}$ and (b) the relative energy dissipation rate $\nu Q/E$ (see Eq.(7)) for the same cases as in Fig.6. The relative Reynolds stress strongly depends on the Rossby number $Ro^{(S)}$, and it takes the largest value (≈ 0.6) for $Ro^{(S)} = -2$. Note that the Fourier modes of $k_1 = k_2 = 0$ grow rapidly as

(a) $Ro^{(S)} = -1$

(side)

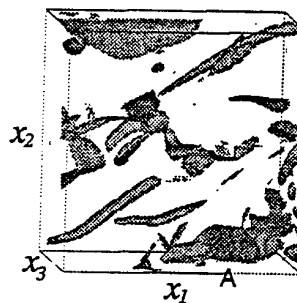


(top)

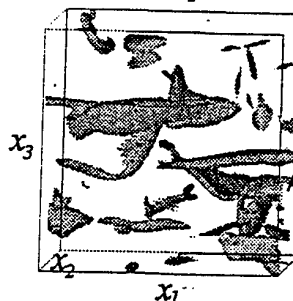


(b) $Ro^{(S)} = -2$

(side)

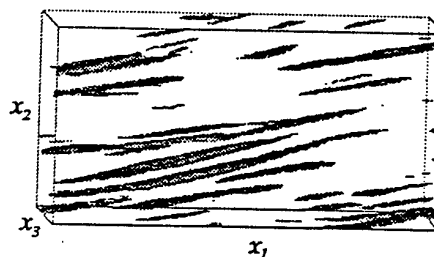


(top)



(c) $Ro^{(S)} = -0.5$

(side)



(top)

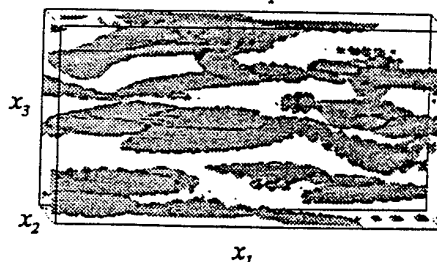


Figure 9 Regions of high-vorticity magnitude. (a) $Ro^{(S)} = -1$, $|\omega| \geq 2.3\omega' = 2.92$, (b) $Ro^{(S)} = -2$, $|\omega| \geq 2.5\omega' = 8.62$, (c) $Ro^{(S)} = -0.5$, $|\omega| \geq 2.1\omega' = 0.85$.

$|\hat{u}(\mathbf{k})|^2 \propto \exp[2(-B)^{1/2}St]$ and that the corresponding relative Reynolds stress, $-2S[\hat{u}_1(\mathbf{k})\hat{u}_2(\mathbf{k})/|\hat{u}(\mathbf{k})|^2]$, evolve as $\tanh(2t)$ (≈ 1 for $t \gg 1$) for $Ro^{(S)} = -2$ and $S = 1$. For $Ro^{(S)} = -0.5$, the relative Reynolds stress takes negative values, which contributes to the rapid decay of turbulence energy together with the energy dissipation.

Negative Reynolds stress reflects the oblique structures of the shear flow turbulence. For $S > 0$ (anti-cyclonic case), flow structures are inclined from the x_1 -direction toward the positive x_2 -direction, which means that the Fourier spectrum spreads in the upper-left and lower-right in the (k_1, k_2) -plane, that is $Y_{12} < 0$. Under the action of the phase scrambling due to the rotation, $b_{12} \approx b_{12}^{(S)}$ and therefore the Reynolds stress becomes negative ($-S\langle u_1 u_2 \rangle \approx SY_{12}/2 < 0$; see Eqs.(13) and (14)). Figure 8 shows the time-evolution of b_{12} and $b_{12}^{(S)}$. They develop in a similar way except at an initial period, indicating that the phase scrambling effect is really working. The structures incline more and more toward the x_1 -direction, which reduces $|y_{12}|$ and then b_{12} and $b_{12}^{(S)}$.

Figure 9 shows the regions of high-vorticity magnitude at $St = \omega'(0)t = 8$ for (a) $Ro^{(S)} = -1$, (b) $Ro^{(S)} = -2$ and $Ro^{(S)} = -0.5$. The side view from the x_3 -direction and the top view from the x_2 -direction are displayed for all the cases. A cubic domain of sides $(105/128) \times 2\pi$ is shown for Fig.9(b), while rectangular domains of $(63/128) \times 4\pi$, $(63/128) \times 2\pi$ and $(63/128) \times 2\pi$ for Figs.9(a) and 9(c).

Very coherent vortical structures of the turbulent vorticity field are clearly observed for neutral case of $Ro^{(S)} = -1$. All of the vortex tubes are inclined at $15^\circ \sim 30^\circ$ from the x_1 -direction. This structure is similar to that obtained by Métais et al. (1995) where the simulation started from the tanh-type mean shear flow with three-dimensional random noise and the value of the local Rossby number approached -1 asymptotically.

For the most unstable case of $Ro^{(S)} = -2$, the vorticity field is quite complicated. In addition to three typical vortical structures which appear in uniformly sheared turbulence without rotation (longitudinal vortex tubes directed nearly to the x_1 -direction, lateral vortex tubes along the x_3 -direction, and the vortex layers with the x_3 -component of vorticity), there exist vortex layers the planes of which are perpendicular to the x_3 -axis (see e.g. A in Fig.9(b)). It is expected that this vortex layer grows faster than the other vortical structures because it corresponds to the rapidly growing Fourier modes of $k_1 = k_2 = 0$.

For the stable case of $Ro^{(S)} = -0.5$, there exist ribbonlike structures but no tubular structure. The ribbons are extended in the x_3 -direction compared with the vortex tubes for $Ro^{(S)} = -1$. The inclination angles of vortical structures to the x_1 -direction are large for $Ro^{(S)} = -2$ but small for $Ro^{(S)} = -0.5$. But they seem to depend on the Reynolds number.

CONCLUDING REMARKS

Energy development and vortical structure are investigated for uniformly sheared turbulent flows under solid-body rotation by use of RDT and DNS. It is found that for the most unstable case of the linear stability analysis, turbulence energy grows fastest, that is, the linear instability mechanism proves to contribute turbulence energy production for this case. For a neutral case, $Ro^{(S)} = -1$, turbulence energy stays around the equilibrated value and coherent structures are generated. For the stable anti-cyclonic case, on the other hand, turbulence energy decays rapidly due to the negative Reynolds stress and ribbonlike structures appear.

There appear vortex tubes and layers elongated in the

direction of the rotating axis for the shearless case. For the cyclonic case, oblique vortex tubes and pancake like structures come out, which may correspond to the tubes and the layers in the shearless case. In later periods, the oblique tubes decays due to the phase scrambling effects, while the pancakes are elongated in the streamwise direction by the mean shear as in the stable anti-cyclonic case.

For the physical understanding of the phenomena obtained by DNS, some vortex models are needed. We have made a vortex layer model which is an extension of that by Métais et al. (1992). We hope it can describe vortical structures in uniformly sheared rotating turbulence.

REFERENCES

- Bardina J., Ferziger, J.H. and Rogallo, R.S., 1985, "Effect of rotation on isotropic turbulence: computation and modelling", *J. Fluid Mech.*, Vol. 154, pp. 321-336.
- Bardina J., 1983, Report No. TF-19, Thermoscience Division, Department of Mechanical Engineering, Stanford University, Stanford, CA.
- Bartello, P., Métais, O., and Lesieur, M., 1994, "Coherent structures in rotating three-dimensional turbulence", *J. Fluid Mech.*, Vol. 273, pp. 1-29.
- Bertoglio, J.P., "Homogeneous Turbulent field within a Rotating Frame", *AIAA J.*, Vol. 20, pp. 1175-1181.
- Bradshaw, P., 1969, "The analogy between streamline curvature and buoyancy in turbulent shear flow", *J. Fluid Mech.*, Vol. 36, pp. 177-191.
- Hossain, M., 1994, "Reduction in the dimensionality of turbulence due to a strong rotation", *Phys. of Fluids*, Vol. 6, pp. 1077-1080.
- Kawahara, G., Kida, S., Tanaka, M. and Yanase, S., 1997, "Wrap, tilt and stretch of vorticity lines around a strong thin straight vortex tube in a simple shear flow", submitted to *J. Fluid Mech.*
- Kida, S. and Tanaka, M., 1992, "Reynolds stress and vortical structure in a uniformly sheared turbulence", *J. Phys. Soc. Japan*, Vol. 61, pp. 4400-5517.
- Kida, S. and Tanaka, M., 1994, "Dynamics of vortical structures in a homogeneous shear flow", *J. Fluid Mech.*, Vol. 274, pp. 43-68.
- Lesieur, M., Yanase, S. and Métais, O., 1991, "Stabilizing and destabilizing effects of a solid-body rotation upon quasi-two-dimensional shear layers", *Phys. of Fluids A*, Vol. 3, pp. 403-407.
- Mansour, N.N., Shih T.-H. and Reynolds, W.C., 1991, "The effects of rotation on initially anisotropic homogeneous flows", *Phys. of Fluids A*, Vol. 3, pp. 2421-2425.
- Mansour, N.N., Shih T.-H. and Reynolds, W.C., 1992, *Studies in Turbulence*, Springer-Verlag, pp. 59-75.
- Métais, O., Flores, C., Yanase, S., Riley, J.J. and Lesieur, M., 1995, "Rotating free-shear flows. Part 2: numerical simulations", *J. Fluid Mech.*, Vol. 239, pp. 47-80.
- Métais, O., Yanase, S., Flores, C., Bartello, P. and Lesieur, M., 1992, "Reorganization of coherent vortices in shear layers under the action of solid-body rotation", Selected proceedings of the *Turbulent Shear Flows VIII*, Springer-Verlag, pp.415-430.
- Tanaka M., 1994, "Vortical structure in homogeneously sheared turbulence subjected to background rotation", *J. Phys. Soc. Japan*, Vol. 63, pp. 3914-3918.
- Townsend, A.A., 1976, *The structure of turbulent shear flow* 2nd ed., Cambridge Univ. Press.
- Yanase, S., Flores, C., Métais, O. and Riley, J.J., 1993, "Rotating free shear flows Part 1: Linear stability analysis", *Phys. of Fluids A*, Vol. 5, pp. 2725-2737.

COMPUTATIONAL MODELLING OF HIGHLY-LOADED COMPRESSOR CASCADE FLOWS

W.L. Chen, F.S. Lien & M.A. Leschziner

UMIST, Mechanical Engineering Department,
PO Box 88, Manchester, M60 1QD, UK

ABSTRACT

A computational study is presented which examines the predictive performance of non-linear eddy-viscosity models (EVMs) and second-moment closure when applied to two blade geometries: a controlled-diffusion (CD) and a double-circular-arc (DCA) compressor blade, both operating at off-design conditions that include laminar leading-edge separation and transition. The study demonstrates that both the non-linear EVM and second-moment closure possess characteristics which enable the models to give, at least for some important flow properties, superior predictive performance relative to a reference linear EVM. However, in the case of DCA compressor blade, only the second-moment closure captures the substantial trailing-edge separation on the suction side and gives a credible representation of the boundary layers.

INTRODUCTION

The flow in a lightly-loaded turbomachine cascade operating in its design conditions is largely dominated by inviscid processes, whereas turbulence transport affects principally the relatively thin near-wall layers. In high-load and off-design conditions, however, the boundary layers on the blades and end walls grow rapidly, separation can occur on both suction and pressure sides (depending on the blade geometry and inlet angle of incidence), and there arises a strong interaction between the boundary layers and the main passage flow. In such circumstances, turbulence transport has a major effect on the primary flow properties that are of direct consequences to operational parameters of the cascade. The sensitivity of the flow to turbulence is especially high when the flow enters the blade passage at an angle which departs significantly from the design value, thus causing leading-edge separation and high flow displacement, followed by transition in the separated shear layer. Transition tends to be an influential process, especially in off-design flows, in that its location and evolution contribute to the sensitive two-way interaction between the boundary layers and the pressure field.

The importance of turbulence in off-design conditions provides strong motivation for the use of advanced turbulence models in computational schemes required to predict the consequences of off-design operation, especially if the determination of the loss level is an important objective. A model is not merely required to return the correct level of the Reynolds shear stress in thin shear-flow conditions - which most well-calibrated models readily do - but must give the correct sensitivity of the shear stresses to streamline

curvature, resolve realistically the very different response of turbulence to shear and normal straining and reproduce the interaction between viscosity and turbulence associated with the transition process.

Conventional eddy-viscosity models which employ linear relationships between stresses and strains are not adequate in the present context. They fail to resolve turbulence anisotropy and to represent correctly the effects of normal straining and curvature on the turbulence stresses. It is now generally accepted that the strong variability in the strength of interaction between different strain types and turbulence stresses can only be resolved in any fundamentally rigorous sense through the use of second-moment closure. However, this type of closure is complex, poses particular challenges in respect of its stable integration into general computational schemes and is costly to apply in practice. A simpler and more economical alternative - albeit one which rests on a weaker fundamental foundation - is to use non-linear stress-strain relation which can be made to return, upon the introduction of physical constraints and careful calibration, some of the predictive capabilities of second-moment closure. The present paper considers both types of closure and their performance in flows which pertain to off-design conditions in linear compressor cascades.

TURBULENCE MODELLING

The turbulence models investigated here are the low-Re non-linear eddy viscosity model of Craft *et al.* (1993) and the second-moment closure of Gibson & Launder (1978), the latter coupled to the Launder-Sharma (1974) linear eddy-viscosity model which is used in the semi-viscous sublayer. The performance of both is contrasted against that of the linear Launder-Sharma model applied on its own. The non-linear model is based on the cubic constitutive relationship:

$$\begin{aligned} & \frac{\mu}{\rho} \frac{2}{3} \delta_{ij} k - \nu S_{ij} \\ & + c_1 \nu \frac{k}{\epsilon} (S_{ik} S_{kj} - \frac{1}{3} S_{kk} S_{ij} \delta_{ij}) + c_2 \nu \frac{k}{\epsilon} (\Omega_{ik} S_{kj} + \Omega_{jk} S_{ki}) \\ & + c_3 \nu \frac{k}{\epsilon} (\Omega_{ik} \Omega_{kj} - \frac{1}{3} \Omega_{kk} \Omega_{ij} \delta_{ij}) + c_4 \frac{\nu k^2}{\epsilon^2} (S_{ik} \Omega_{kj} + S_{jk} \Omega_{ki}) S_{ij} \\ & + c_5 \frac{\nu k^2}{\epsilon^2} S_{ij} (S_{ik} S_{kj} - \Omega_{ik} \Omega_{kj}) \end{aligned} \quad (1)$$

The turbulence energy k and its (homogeneous) dissipation $\bar{\epsilon}$ are

obtained from related transport equations. The coefficients c_μ (appearing in ν_t), c_1 , c_2 and c_{ϵ_1} and c_{ϵ_2} (the last two appearing in the ϵ equation) are either numerically constant or functions of strain and vorticity invariants and the turbulence Reynolds number.

The second moment closure consists of the set of stress-transport equations:

$$\frac{D\overline{u_i u_j}}{Dt} = D_{ij} P_{ij} + \Phi_{ij} - \epsilon_{ij} \quad (2)$$

with Φ_{ij} approximated as a sum of the linear Rotta model for the slow term, the linear "Isotropisation of Production" model for the rapid term and wall-reflection corrections for both. Dissipation is assumed isotropic and diffusion is approximated by Daly & Harlow's GGDH.

Model properties of major interest in the context of the present blade flow are the response to irrotational straining at stagnation regions (here, the leading edge of blades), the response to curvature, especially the stabilisation of turbulence on convex surfaces (here, the blade suction side), and the representation of bypass transition. The last process is closely linked to the first, as a misrepresentation of the turbulence level at the leading edge will prevent transition downstream of the leading edge from being returned correctly.

While both types of closure contain terms or model elements expected to correctly represent the response of turbulence to irrotational straining and curvature, these mechanisms are fundamentally quite different in nature. In the case of second-moment closure, the weak response of turbulence to irrotational straining is inherent in the manner in which stresses interact with strains within the production mechanism which is represented exactly in a formal sense. Similarly, curvature effects are represented principally through the interaction of the stresses with the curvature strain. For example, in the case of a fully-developed curved channel flow,

$$P_{\theta r} = -\overline{u_r^2} \frac{\partial U_\theta}{\partial r} - (2\overline{u_\theta^2} - \overline{u_r^2}) \frac{U_\theta}{r} \quad (3)$$

which demonstrates the disproportionately important role of the curvature strain on the production of the shear stress and the significance of its sign. In contrast, equation (1) can be shown to yield for the same flow:

$$\overline{u_\theta u_r} = -\nu \left(1.4 c_s \frac{k^2}{\epsilon^2} \frac{\partial U_\theta}{\partial r} \frac{U_\theta}{r} \right) \left(\frac{\partial U_\theta}{\partial r} \frac{U_\theta}{r} \right) \quad (4)$$

Thus, if c_s is negative, as is the case with Craft *et al.*'s model, $\frac{\partial U_\theta}{\partial r}$ is positive on the convex (suction) side, and the shear stress is reduced. Similarly an increase is provoked on the concave (pressure) side.

In common with linear eddy-viscosity models, non-linear forms resting on (1) are fundamentally unable to represent the weak response of turbulence to irrotational straining. Here then, the correct response hinges on sensitising c_μ to strain and vorticity invariants so as to depress c_μ in stagnation regions. For example, Craft *et al.*'s non-linear model uses:

$$c_\mu = \frac{0.3}{1 + 0.35[\max(\tilde{S}, \tilde{\Omega})]^{1.5}} \left\{ 1 - \exp\left[\frac{-0.36}{\exp(-0.75\max(\tilde{S}, \tilde{\Omega}))} \right] \right\} \quad (5)$$

in which \tilde{S} and $\tilde{\Omega}$ are dimensionless strain and vorticity invariants.

As regards bypass transition, the present hybrid implementation of the second-moment closure does not permit this process to be captured when transition is preceded by impingement, principally as a consequence of defects in the linear model. An appropriate low-Re form is needed, one that gives a quantitatively accurate

level of turbulence in the stagnation region close to the wall. The non-linear model of Craft *et al.* returns transition well in flat-plate flow subjected to relatively weak pressure gradient, but has been found by Chen *et al.* (1996) to delay transition unduly in the free shear layer of laminar separation bubbles ensuring from curved leading edges, especially at low-Re numbers. This defect has been traced to the strong functional dependence in the model of ν_t on the turbulence Reynolds number, via a Re-dependent damping function f_μ multiplying c_μ .

COMPUTATIONAL APPROACH

Calculations reported herein have been performed with a multi-block version of the general non-orthogonal, fully collocated finite-volume approach 'STREAM' (Lien & Leschziner, 1994a; Lien *et al.*, 1996). Convection of mean-flow as well as turbulence quantities is approximated by the second-order TVD scheme 'UMIST' (Lien & Leschziner, 1994b) or a variant of the 'MUSCL' scheme (van Leer, 1979). Since the predicted onset and evolution of transition and the leading-edge separation bubble have been observed to be extremely sensitive to numerical details, the retention of second-order accuracy for turbulence convection is essential, even when very fine grids are used.

The transport solutions and the pressure-correction equation are solved sequentially and iterated to convergence, defined by reference to Euclidean residual norms for mass and momentum components.

RESULTS

This section presents selected results for two blade geometries for which extensive experimental data are available: a controlled-diffusion (CD) blade examined by Elazar and Shreeve (1990) and a double-circular-arc (DCA) blade investigated by Zierke and Deutsch (1989). For both cases, surface pressure, wake and boundary-layer measurements are available, and these allow comprehensive comparisons with computational results to be made. Preliminary quasi-3D computations were performed and demonstrated that effects arising from spanwise confinement were marginal, and hence the detailed follow-up computations, giving rise to the results presented below, were two-dimensional.

CD Blade

The multi-block grid used for the computation of the CD blade flow is shown in Fig. 1. This contains 48,000 nodes, with 400 nodes distributed along the blade surfaces and 200 grid nodes covering the flow passage in the pitchwise direction. The necessity of using such a fine mesh was established through grid-independence tests with grids of 25200, 48000 and 58000 nodes.

The most challenging flow condition among those examined is that for a design inlet angle of 46° , a departure of more than 6° from the design value. Even at this extremely high incidence angle, the flow on the suction side does not separate at the trailing edge, signifying the favourable aerodynamic characteristics of this particular blade geometry. However, a substantial leading-edge separation bubble occurs on the suction side, stated by Elazar to occupy at least the first 20% of the chord. In addition, the flow on the suction side is subjected to a strong adverse pressure gradient, which would result, on its own, in a thick boundary layer towards the trailing edge.

Results arising from the eddy-viscosity models and second-moment closure are shown in Figs. 2-4. The measured pressure distribution, given in Fig. 2(a), suggests the existence of a substantial leading-edge separation bubble on the suction side,

which tends to diminish the steep adverse pressure gradient at that location. The non-linear EVM resolves this separation and thus returns far better agreement with the data at the leading edge. This is confirmed by the velocity distribution at 5% of the chord, shown in Fig. 2(b). In contrast, the other two models fail to predict separation, and hence return a much too steep rise in pressure. Associated with the extensive differences in model performance at the leading edge are the significant discrepancies observed in the trailing-edge region. The leading-edge bubble results in a considerable initial thickening of the boundary layer, and this has a substantial influence on the boundary-layer structure further downstream, even if other response mechanisms in the attached flow portion are ignored. As the flow develops along the suction side, the mixing level predicted by the non-linear EVM in the outer part of the boundary layer appears to be too weak (Fig. 2(c)), and the boundary layer recovers too slowly from the upstream separation process. Further downstream, towards the trailing edge, the computed boundary layer is closer to separation than the measured one. Although the linear EVM does not capture the leading-edge separation, it returns a thick initial boundary layer, due to excessive turbulence energy being generated during the impingement and deflection process (Fig. 2(c)). Towards the trailing, however, the model gives rise to a boundary layer which is too strongly attached, due to insufficient initial displacement, excessive mixing and insensitivity to curvature and adverse pressure gradient. The second-moment closure fails to predict the leading-edge separation, probably owing to defects in the linear EVM used in the semi-viscous sub-layer. The development of the downstream boundary layer is broadly in line with the experiment. This reflects the model's superior response to streamline curvature and adverse pressure gradient.

The comparisons for boundary-layer parameters, given in Fig. 3, demonstrate perhaps most strikingly the significant differences in the predictive performance among the three models. The most encouraging feature in relation to the non-linear EVM is its ability to give a credible representation of the suction-side peak in the displacement thickness that is associated with the leading-edge separation. Agreement is also good further downstream. However, as the trailing edge is approached, the displacement thickness grows too quickly as a result of insufficient mixing in the boundary layer and hence excessive sensitivity to the adverse pressure gradient, which drives the flow towards separation. In contrast to the overestimation of the displacement thickness on the rear portion of the suction side, the momentum thickness in this region is under-predicted. Thus, the shape factor returned by the non-linear EVM in the rear portion of the suction side is excessive, indicating that the boundary layer is too close to separation, and this is confirmed by the velocity distributions shown in Fig. 2(b). As regards the performance of the linear EVM, it is clear that this model fails to give a credible description of the suction-side boundary layer: the leading-edge separation is not resolved, and the rate of increase in the displacement thickness is far too low. The second-moment closure returns fairly good agreement with the data for the displacement thickness, apart from missing the peak on the suction side associated with leading-edge separation. The momentum thickness is also well predicted up to about 85% of the chord, where the growth becomes too slow. Therefore, the shape factor is underestimated near the leading edge and is slightly too high as the trailing edge is approached. This suggests that, although this model does not capture the initial thickening of the boundary layer, its sensitivity to curvature and adverse pressure gradient provokes a rapid growth of the displacement thickness, and this eventually drives the boundary layer to a state which is less attached than the real flow.

The only major comment which can be made in relation to the pressure side is that the shape-factor distributions imply that all models predict too early transition. It must be recognised, however, that the experimental shape-factor data may be subject to significant error, especially in the vicinity of the leading-edge, because these were determined from very low values of displacement- and momentum-thickness data.

Results for the wake are given in Fig. 4. Here, both the non-linear EVM and the second-moment closure give much better accord with the experimental data for the velocity than the linear EVM, owing principally to their ability to resolve the displacement of the suction-side boundary layer more faithfully. In particular, the wake width and its lateral location are well represented. In terms of turbulence intensity, both the non-linear EVM and the second-moment closure yield substantially higher levels of turbulence intensity than the linear EVM in the boundary layers, hence resulting in two distinctive peaks in the wake, one emanating from the suction side and the other from the pressure side. The measurements show that the turbulence intensity in the fluid emanating from the pressure side is much higher than that in the suction-side fluid, a behaviour consistent with a lower boundary-layer thickness and turbulence-destabilising curvature. The non-linear EVM gives the opposite trend. This suggests that, while the model captures the effect of curvature on the mean flow - via the strain and vorticity invariants, it does not correctly represent the interaction between curvature and turbulence energy.

DCA Blade

The DCA blade is especially challenging because of its intense curvature and the fact that separation is provoked at the rear part of the suction side, even when the flow is close to the design state. On the suction side, there exists a small leading-edge separation bubble, and this causes the flow to become turbulent within 3% of the chord. At about 80% of the chord, the turbulent boundary layer separates, forming a substantial recirculation zone which extends well beyond the trailing edge. Thus, to predict this flow accurately, all features associated with separation must be captured, since they either provoke transition or produce a large boundary-layer displacement.

A multi-block grid similar to that shown in Fig. 1 was used for the computation of the present flow, and Figs. 5-7 show selected results for an incidence angle which departs by -1.5° from the design state. The pressure distributions given in Fig. 5(a) demonstrate that the second-moment closure performs much better than the linear and non-linear EVMs, especially near the trailing edge where separation occurs. The streamwise velocity profiles given in Fig. 5(b) confirm that only the second-moment closure resolves the trailing-edge separation. The success of this model may again be attributed to its inherent sensitivity to streamline curvature and adverse pressure gradient, causing a rapid thickening of the boundary layer on the suction side and leading to trailing-edge separation. The non-linear EVM, whilst also capable of representing this sensitivity to some extent, fails to capture the trailing-edge separation. The main reason appears to be that the model overestimates the leading-edge separation bubble, resulting in a substantial delay in the onset of transition and thus returning a relatively thin boundary layer upstream of the trailing edge, which resists separation. This delay in transition is readily identified from the streamwise turbulence-intensity profiles at 7.3% of chord, shown in Fig. 5(c). The linear EVM predicts the initial boundary layer fairly well. However, it also fails to capture the trailing-edge separation because of excessive turbulent mixing in the suction-side boundary layer.

Variations of boundary-layer quantities are given in Fig. 6(c). On the suction side, the small leading-edge separation bubble is barely

resolved by the measurement, its existence being reflected by the slightly elevated momentum thickness and shape factor. The steep rise in the shape factor beyond 75% of chord indicates the presence of the trailing-edge separation. Only the second-moment closure gives a credible prediction of the boundary-layer quantities on the suction side. A significant discrepancy can only be observed in relation to the shape factor near the leading edge on the suction side, reflecting a failure of the model to capture the small leading-edge separation bubble. Clearly, the most serious predictive defect of the other two models is their failure to reproduce the trailing-edge separation, and this is reflected by the substantial discrepancies between the predicted and measured displacement thickness and shape factor.

The comparisons for velocity and turbulence intensity in the wake, given in Fig. 7, serve to amplify earlier observations on the predictive performance of the three models, especially in respect of the suction-side boundary layer. The experimental data clearly indicate the presence of reverse flow in the wake and identify the massive displacement arising from the suction-side separation. As only the second-moment closure predicts the trailing-edge separation, the wake profiles returned by this model are in much better accord with the experiment than those obtained with the other two models. However, the results also suggest that even this model underestimates the trailing-edge separation bubble and hence the width of the wake.

CONCLUSIONS

The paper investigated the performance of three turbulence models when applied to physically complex flows over two highly loaded compressor-cascade blades, one a CD and the other a DCA geometry. In the former case, the non-linear EVM and the second moment closure yield superior results to those returned by the linear model, reflecting the ability of the first two models to represent more realistically the growth of the boundary layer subject to adverse pressure gradient and streamline curvature. Only the non-linear EVM resolves the substantial leading-edge separation present in the CD blade, which has important consequences to the pressure and boundary-layer structure further downstream. In the case of the DCA blade, the second-moment closure performs far better than the other two models, mainly due to its ability to capture the extensive trailing-edge separation, which is the most important feature in this flow. The failure of the non-linear EVM in this flow can be attributed to the model predicting an inappropriate delay in the transition within the separated shear layer emanating from the leading edge. This then results in a thin boundary layer further downstream, which resists separation as it approaches the trailing

edge.

ACKNOWLEDGEMENTS

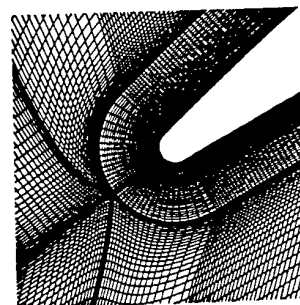
The writers are grateful for the financial support provided by Rolls Royce plc to the first-named author.

REFERENCES

- Chen, W.L., Lien, F.S. and Leschziner, M.A., 1996, "Turbulence Modelling of Transitional Flows Pertinent to Turbomachine Cascade Aerodynamics", *Internal Report TFD/96/06, UMIST, Manchester, UK*.
- Craft, T.J., Launder, B.E. and Suga, K., 1993, "Extend the Applicability of Edd-Viscosity Model Through the Use of Deformation Invariant and Non-linear Elements", *Proc. 5th Int. Symp. Refined Flow Modelling and Turbulence Measurements*, pp. 125-132.
- Elazar, Y. and Shreeve, R.P., 1990, "Viscous Flow in a Controlled Diffusion Compressor Cascade with Increasing Incidence", *ASME J. of Turbomachinery*, Vol. 112, pp. 256-266.
- Gibson, M.M. and Launder, B.E., 1978, "Ground Effects on Pressure Fluctuations in the Atmospheric Boundary Layer", *J. Fluid Mech.*, Vol. 86, pp. 491-511.
- Launder, B.E. and Sharma, B.I., 1974, "Application of the Energy-Dissipation Model of Turbulence to the Calculation of Flow near a Spinning Disc", *Int. Journal of Heat Mass Transfer*, Vol. 1, pp. 131-138.
- Lien, F.S. and Leschziner, M.A., 1994a, "A General Non-orthogonal Collocated FV Algorithm for Turbulent Flow at All Speeds Incorporating Second-Moment Turbulence-Transport Closure, Part 1: Computational Implementation", *Comp. Meth. Appl. Mech. Eng.*, Vol. 114, pp. 123-148.
- Lien, F.S. and Leschziner, M.A., 1994b, "Upstream Monotonic Interpolation for Scalar Transport with Application to Complex Turbulent Flows", *Int. J. Num. Meth. Fluids*, Vol. 19, pp. 527-548.
- Lien, F.S., Chen, W.L. and Leschziner, M.A., 1996, "A Multi-Block Implementation of a Non-orthogonal, Collocated FV Algorithm for Complex Turbulent Flows", *Int. J. Num. Meth. Fluids*, Vol. 23, pp. 567-588.
- van Leer, 1979, "Towards the Ultimate Convection Diffusion Scheme V: A Second-Order Sequel to Godunov's Method", *J. Comp. Phys.*, Vol. 32, pp. 101-136.
- Zierke, W.C. and Deutsch, S., 1989, "The Measurement of Boundary Layers on a Compressor Blade in Cascade", *NASA CR-185118*.



Overall mesh



Grid near the leading edge

Fig 1. CD COMPRESSOR BLADE, COMPUTATIONAL MESH.

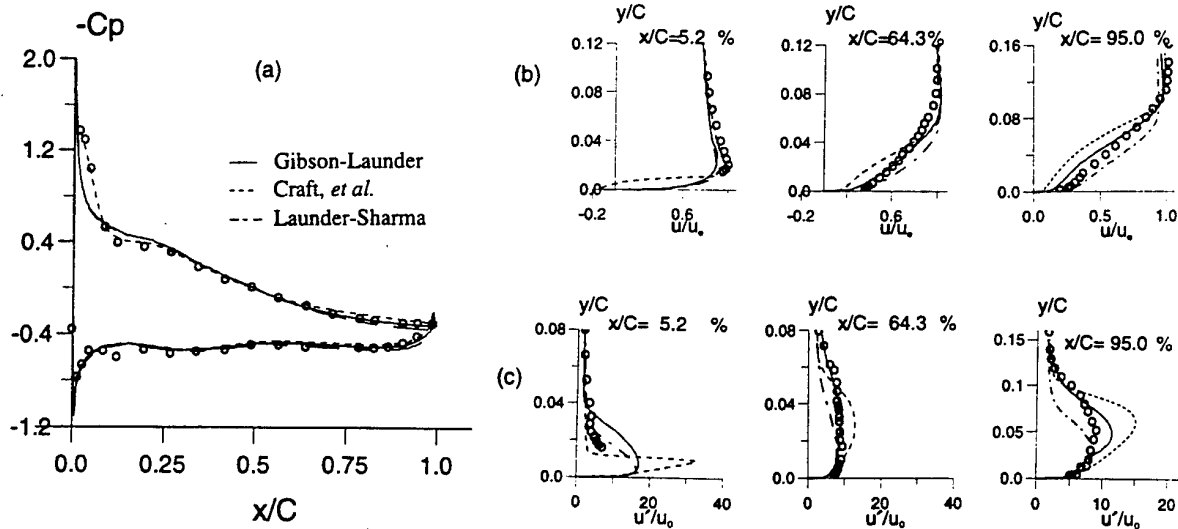


Fig 2. CD COMPRESSOR BLADE, DISTRIBUTIONS OF (a) PRESSURE COEFFICIENT, (b) SUCTION-SIDE STREAMWISE VELOCITY AND (c) TURBULENCE INTENSITY AT $\beta=46^\circ$.

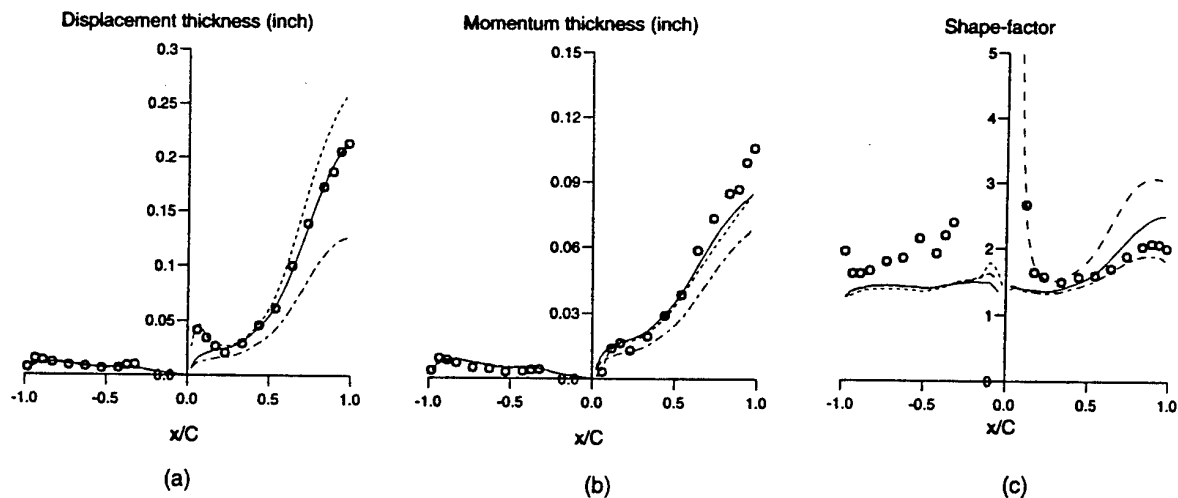


Fig 3. CD COMPRESSOR BLADE, DISTRIBUTIONS OF (a) DISPLACEMENT THICKNESS, (b) MOMENTUM THICKNESS AND (c) SHAPE FACTOR AT $\beta=46^\circ$; legend as in Fig 2.

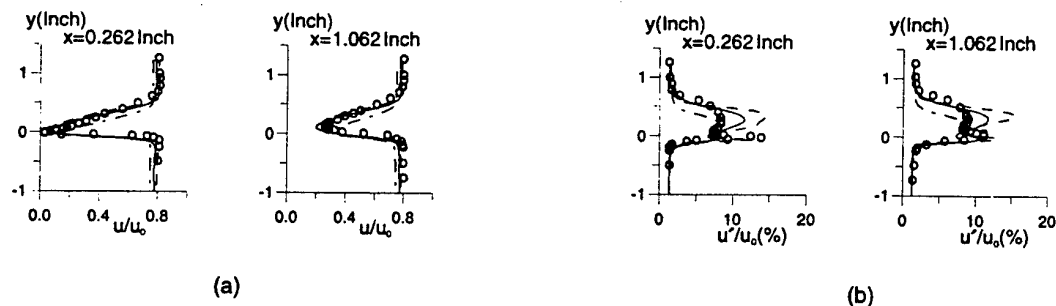


Fig 4. CD COMPRESSOR BLADE, DISTRIBUTIONS OF (a) WAKE VELOCITY AND (b) TURBULENCE INTENSITY AT $\beta=46^\circ$; legend as in Fig 2.

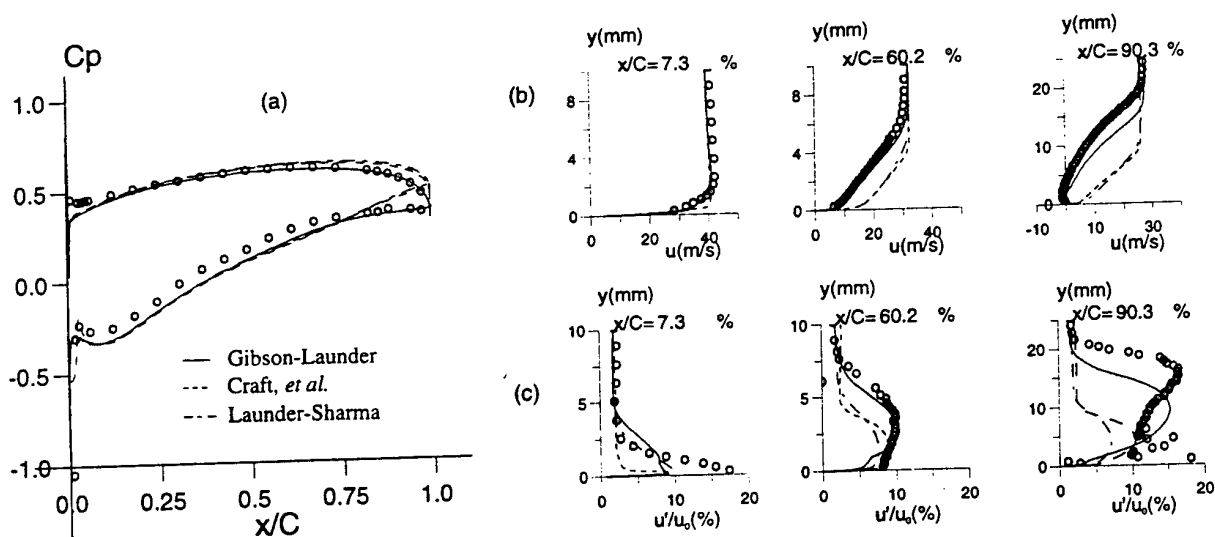


Fig 5. DCA COMPRESSOR BLADE, DISTRIBUTIONS OF (a) PRESSURE COEFFICIENT, (b) SUCTION-SIDE STREAMWISE VELOCITY AND (c) TURBULENCE INTENSITY AT $i=-1.5^\circ$.

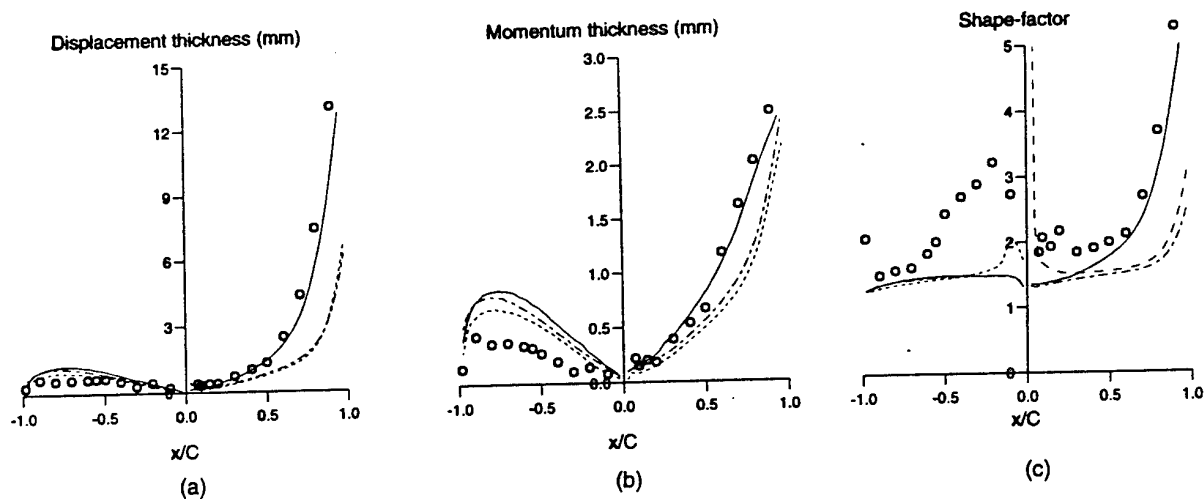


Fig 6. DCA COMPRESSOR BLADE, DISTRIBUTIONS OF (a) DISPLACEMENT THICKNESS, (b) MOMENTUM THICKNESS AND (c) SHAPE FACTOR AT $i=-1.5^\circ$; legend as in Fig 5.

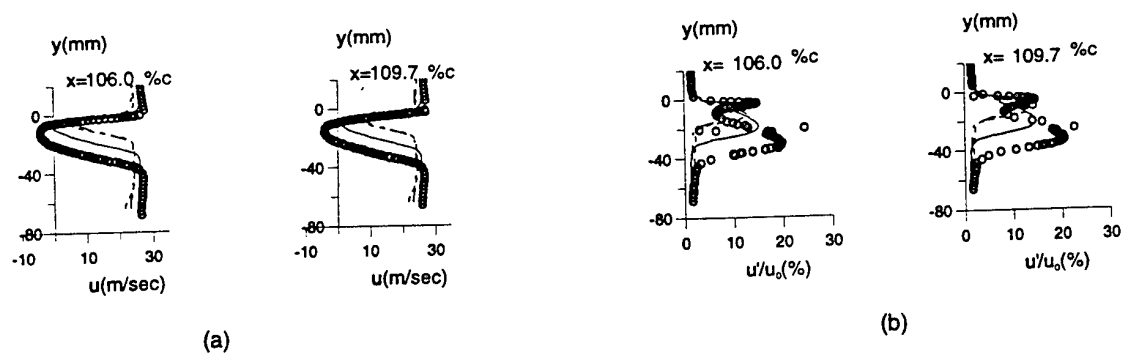


Fig 7. DCA COMPRESSOR BLADE, DISTRIBUTIONS OF (a) WAKE VELOCITY AND (b) TURBULENCE INTENSITY AT $i=-1.5^\circ$; legend as in Fig 5.

THE EFFECT OF REYNOLDS NUMBER ON BOUNDARY LAYER TURBULENCE

David B. DeGraaff, Donald R. Webster*, and John K. Eaton

Department of Mechanical Engineering

Stanford University

Bldg. 500

Stanford, CA 94305-3030

U.S.A.

*Present address: Dept. of Aerospace Eng.

University of Minnesota

U.S.A.

ABSTRACT

A new facility for studying high Reynolds number, incompressible turbulent boundary layer flows has been constructed. It consists of a moderately sized wind tunnel, completely enclosed by a pressure vessel, which can raise the ambient air pressure in and around the wind tunnel to 8 atmospheres. This results in a Reynolds number range of about 20:1, while maintaining incompressible flow. Results are presented for the zero pressure gradient flat plate boundary layer over a momentum thickness Reynolds number range of 1500 to 15000. Scaling issues for high Reynolds number non-equilibrium boundary layers are discussed, with data comparing the three dimensional turbulent boundary layer flow over a swept bump at Reynolds numbers of 3800 and 8600. It is found that successful prediction of these types of flows must include length scales which do not scale on Reynolds number, but are inherent to the geometry of the flow.

INTRODUCTION

It has long been assumed that boundary layer turbulence approaches an asymptotic state for momentum thickness Reynolds numbers above 6000. This has led to the incorporation of dimensionless structure parameters measured at relatively low Reynolds numbers into turbulence models which are then used to predict much higher Reynolds number flows. For example, the constants in advanced models are generally tuned to match low Reynolds number experimental data because of its high resolution, or low Reynolds number numerical data bases from Spalart (1988) or Kim et al. (1987) because of the detailed information available.

Because the dominant flow structures in the inner and outer layers of the boundary layer are so different, it is likely that there are significant Reynolds number effects on the dimensionless structural parameters. The inner region is dominated by long streamwise low-speed streaks and longitudinal vortices, which scale on the viscous length scale (ν/U_τ). The outer region contains more three dimensional structures often characterized as hairpin vortices, which scale on outer length scales, such as the boundary layer thickness (See review by Robinson (1991)). Since the viscous length scale decreases rapidly with Reynolds number,

and the outer length scales are only a weak function of Reynolds number, the inner and outer scales become increasingly disparate with increasing Reynolds number. For example, at a momentum thickness Reynolds number of 1000, the region below $y^+ = 100$ occupies approximately 14% of the total boundary layer thickness, and accounts for almost all of the turbulence production. At a Reynolds number of 6000, this region occupies only about 4% of the total boundary layer thickness and still accounts for a large fraction of the total turbulence production. However, at a Reynolds number of 20000, the region below $y^+ = 100$ occupies only about 1.5% of the boundary layer thickness, and accounts for only a small fraction of the total turbulence production. It therefore seems appropriate to examine high Reynolds number turbulent boundary layers in the same detail as we have studied lower Reynolds number flows to determine if the models we are presently using are really capable of accurately predicting high Reynolds number flows.

Several recent studies have provided high Reynolds number data for the canonical flat plate zero pressure gradient boundary layer (see Saric (1996), Gad-el-Hak and Bandyopadhyay (1994), Fernholz and Finley (1996)). These data collapse well in traditional inner/outer scaling with the appropriate scaling variables in the inner region being the skin friction and the kinematic viscosity, and the outer layer scale being dictated by the boundary layer thickness and the wake velocity deficit. These scaling parameters are simple known functions of only the Reynolds number (Coles and Hirst (1968)), and extrapolation of the existing behavior from low and moderate Reynolds number experiments to much higher Reynolds numbers thus appears to be appropriate.

More complex turbulent flows, however, are often not well described by the Reynolds number alone. These non-equilibrium flows have additional length or time scales introduced by the geometry or dynamics of the system. For example, a rapid change in wall curvature, pressure gradient, or wall roughness causes the formation of an internal layer. This layer is in equilibrium with the boundary condition at the wall, and then evolves outward to eventually bring the rest of the boundary layer into equilibrium with

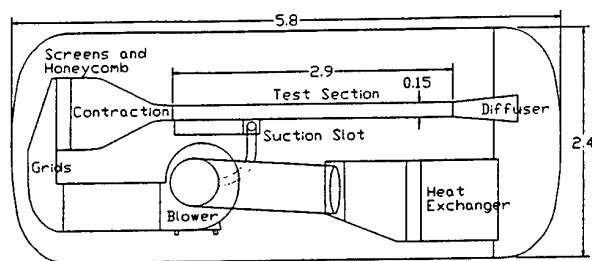


Figure 1: Wind tunnel schematic. Outer shell is the pressure vessel. All dimensions are in meters.

the modified boundary condition. The distance from the wall to the interface between the internal layer and outer boundary layer provides an additional length scale that is not a simple function of the Reynolds number.

A geometric length scale is important in most separated flows and particularly in the flow over a step or cavity where the geometric scale dominates the flow development. Such a scale does not change with Reynolds number while the length scale of near-wall structures in the same flow changes rapidly. The interaction of the near-wall structures with large vortices formed in the separated flow thus would be expected to be dependent on the Reynolds number.

The introduction of a spanwise pressure gradient or wall shear causes a two-dimensional boundary layer to become three dimensional with a mean crossflow relative to the free stream direction. This introduces another length scale, namely the height of the peak in the cross flow profile. At low Reynolds number this peak may occur as low as y^+ of 20 meaning that the cross flow has a strong interaction with near wall structure. At high Reynolds numbers, the peak is much farther from the wall when measured in inner coordinates (Eaton (1995)).

It is clear that non-equilibrium turbulent flows have additional length and/or time scales that must be considered. These scales do not evolve with Reynolds number in the same way as the traditional inner and outer scales. One might guess then that the dimensionless structure parameters might continue to change in non-equilibrium flows up to very high Reynolds number.

The objectives of the present work are to examine the effects of varying Reynolds numbers on non-equilibrium turbulent boundary layers. A new facility was constructed allowing a wide variation in Reynolds number in a flexible, moderate scale wind tunnel. As a test of the facility, and to corroborate previous data, two dimensional boundary layer data are presented for Reynolds numbers ranging from 1500 to 15000. The effects of Reynolds number on a non-equilibrium boundary layer developing over a swept bump are also examined.

EXPERIMENTAL APPARATUS AND TECHNIQUES

The experiments were performed in the tunnel floor boundary layer of a wind tunnel which is completely enclosed in a pressure vessel as shown in Figure 1. This facility provides a wide Reynolds number range by regulating the ambient pressure from one to eight atmospheres. In this approach, the tunnel walls need only support the dynamic pressure loads of the flow and not the absolute pressure. Thus, typical construction materials for atmospheric pressure wind tunnels can be used, and the tunnel can be modified easily for visual or probe access. A total Reynolds number range of approximately 20:1 is possible by varying both the flow speed and density. Additionally, the flow maintains a low Mach number (approximately 0.04), and

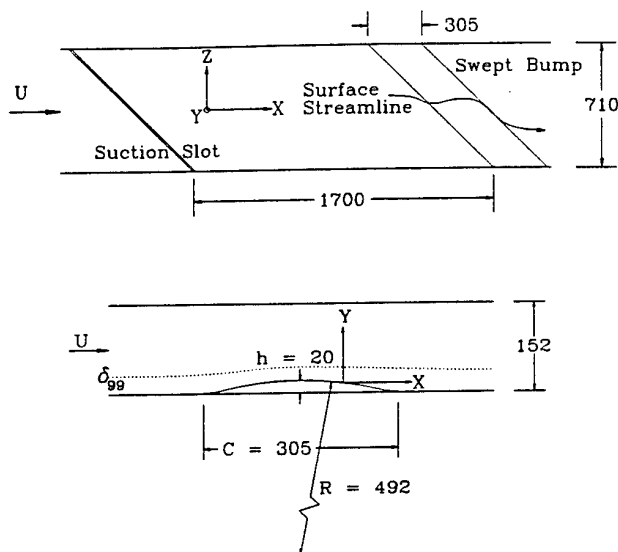


Figure 2: Top view of test section, and side view of bump. All Dimensions are in millimeters.

can therefore be modeled as incompressible.

The closed circuit wind tunnel was designed with a very short flow conditioning section and uses the curved door of the pressure vessel as a turning duct, in order to maximize the test section length. The test section is 2.9 m long, with a 150 by 710 mm rectangular test section. The nominal operating velocity is 15 m/s, with a free stream turbulence level of 0.2%.

Velocity measurements were performed with the single-wire and cross-wire probes described in Littell and Eaton (1994). The probes were strung with 2.5 micron platinum-coated tungsten wire which was copper plated and etched for an active length to diameter ratio of 250. The spacing between the cross-wires was 0.35 mm. The probes were connected to TSI constant temperature anemometers (model IFA-100), operating with a resistance overheat ratio of 1.8. The effective wire angles were found using a yawing procedure described in Westphal and Mehta (1984). The probes were positioned using a two axis traverse, and zeroed by contact with the conducting floor of the test section. Data acquisition was performed with a 486 PC clone and National Instruments AT-MIO-16 and GPIB-PCII boards. An external simultaneous sample and hold circuit was used to collect cross-wire voltages. Further details of the operation of these probes can be found in Webster et al. (1996a). The mean velocity uncertainty is estimated to be 3% of the streamwise velocity, the normal stress uncertainty is 5% of the local value of u'^2 , and the shear stress measurements have an uncertainty of 10% of the local value of $u'v'$.

This paper presents data from two different experimental setups. The first is flat plate data from the test section floor. The second is the non-equilibrium boundary layer flow over a bump swept at 45 degrees with respect to the freestream velocity vector. The bump shape is described by three tangential circular arcs, and is illustrated in figure 2. The initial boundary layer thickness to bump height ratio was 1.5, and the boundary layer thickness to convex radius of curvature was 0.06. The boundary layer originates at a suction slot which is swept parallel to the leading edge of the bump. A parallel boundary layer trip insures that the boundary layer is uniform along lines parallel to the bump. Mean velocity and skin friction measurements showed excellent uniformity across the span so only cen-

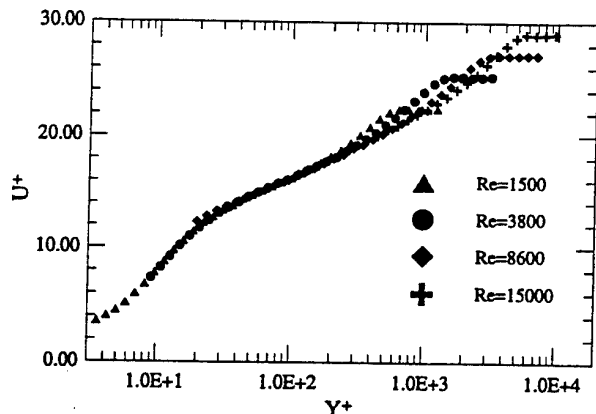


Figure 3: Mean streamwise velocity profiles at different momentum thickness Reynolds numbers: inner coordinates.

terline measurements are reported here. All measurements are reported in the coordinate system shown on Fig. 2, with x , y , and z , being the streamwise, wall normal, and spanwise directions, respectively. The y -axis is maintained normal to the flat plate tunnel floor, with its origin on the tunnel floor or the bump surface.

RESULTS AND DISCUSSION

Part One: The Flat Plate

Figure 3 shows mean streamwise velocity measurements on a flat plate for Reynolds numbers from 1500 to 15000, plotted in inner coordinates, and figure 4 shows the same data plotted in outer coordinates. For the lower two Reynolds numbers, data extend into the sub layer, while only the log region is attained for the higher Reynolds numbers. The inner layer collapses very well on the standard log law of the wall. This is perhaps not surprising since the wall velocity used in scaling the plots was derived by fitting the data to the log law. As many investigators have noted previously, the constant shear stress region of the log law increases in length with increasing Reynolds number, and the wake decreases. The data agree well with data compiled by Fernholz and Finley (1996) in their extensive review of incompressible zero pressure gradient turbulent boundary layers.

Figure 4 shows excellent collapse of the data in the outer region. The x -axis is now linear to emphasize that the outer region occupies a large fraction of the boundary thickness at high Reynolds number.

Figure 5 shows the streamwise normal stresses, in inner coordinates. For the lower Reynolds number cases, the near wall peak is resolved. The data collapse at the near wall peak at y^+ of 12 to 15, with a magnitude of about 2.7. The higher Reynolds number hot-wire measurements clearly show the effects of poor measurement resolution near the wall, as they are not collapsing on the same near wall peak with the lower two Reynolds number cases. Mockizuki et al. (1996) compiled 47 near-wall data sets which demonstrate the peak height is Reynolds number independent, and the distance of the peak from the wall in viscous lengths is a very weak function of Reynolds number.

Resolution of the turbulence is a fundamental problem for most high Reynolds number experiments. In this study

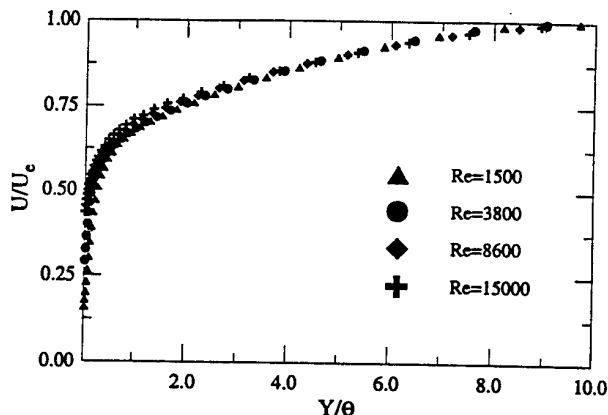


Figure 4: Mean streamwise velocity profiles at different momentum thickness Reynolds number: outer coordinates.

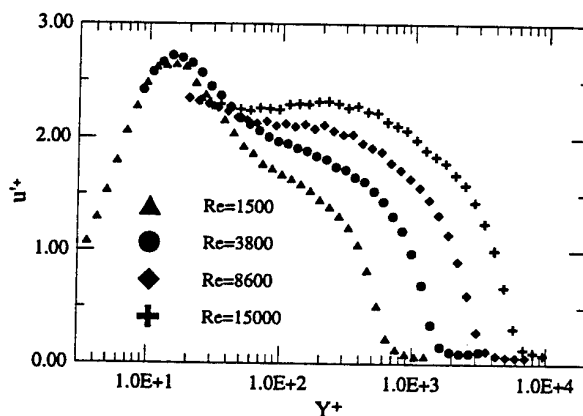


Figure 5: RMS streamwise velocity profiles at different momentum thickness Reynolds numbers: inner coordinates.

the near-wall turbulence data are only well resolved for the lower two Reynolds number cases, since the length of the hot wire in viscous units is 4, 11, 25, and 45 for Reynolds numbers of 1500, 3800, 8600, and 15000, respectively.

Figure 6 shows the streamwise normal stress in outer coordinates, which collapses fairly well for y/θ larger than one. The present data both corroborate the previous measurements and serve as a check on our facility. As a further check, we repeated one Reynolds number case by raising the ambient pressure, and compensating by reducing the freestream velocity. The dimensionless data were identical for the two cases.

Part Two: The Swept Bump

In order to study non-equilibrium effects, a swept bump was installed on the test section floor as shown in figure 2. The flow over the bump is subjected first to a short length of concave curvature with a mildly adverse pressure gradient, then a long convex curvature over the top of the bump, with a strongly favorable streamwise pressure gradient on the upstream side, followed by a strongly adverse

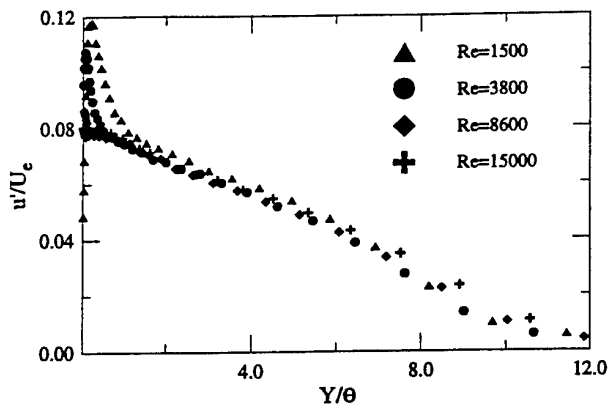


Figure 6: RMS streamwise velocity profiles at different momentum thickness Reynolds numbers: outer coordinates.

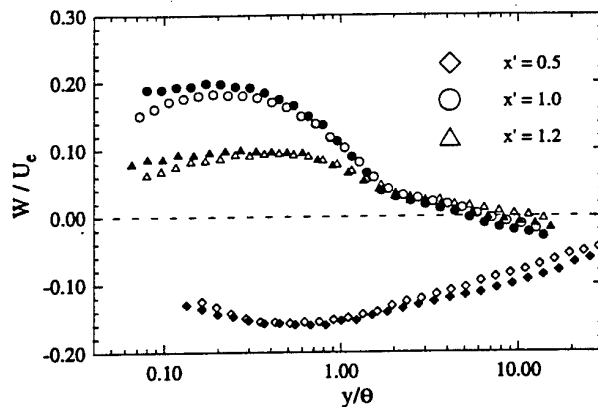


Figure 9: Mean spanwise velocity profiles at different x -locations. Open symbols are $Re_\theta = 3800$, filled symbols are $Re_\theta = 8600$.

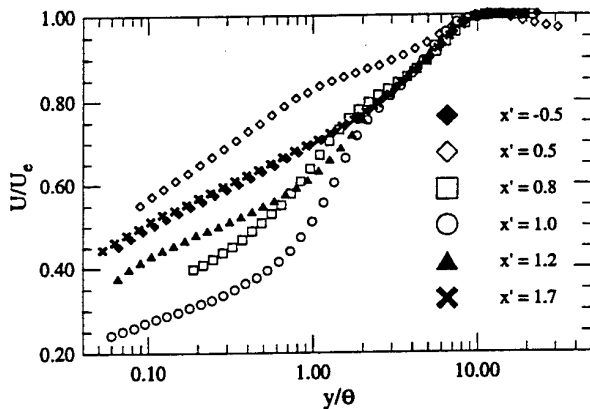


Figure 7: Mean streamwise velocity profiles at different x -locations, for $Re_\theta = 8600$.

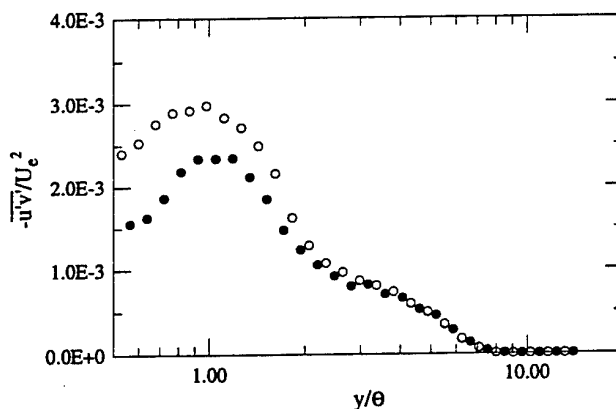


Figure 10: Shear Stress Profiles at the bump trailing edge ($x' = 1.0$). Open symbols are $Re_\theta = 3800$, filled symbols are $Re_\theta = 8600$.

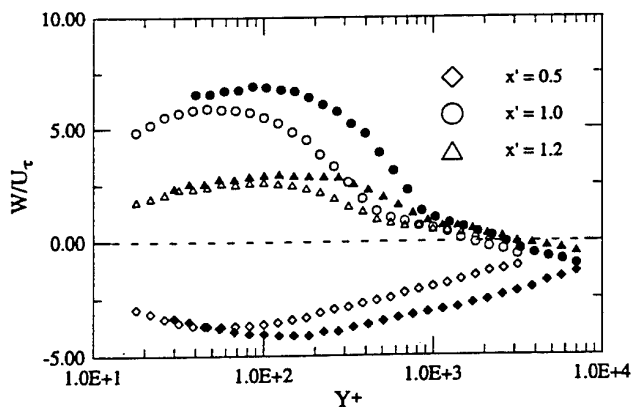


Figure 8: Mean spanwise velocity profiles at different x -locations. Open symbols are $Re_\theta = 3800$, filled symbols are $Re_\theta = 8600$.

streamwise pressure gradient on the downstream side of the bump. Finally, a short length of concave curvature and mild favorable pressure gradient at the rear of the bump brings the flow back to the flat test section floor downstream of the bump. The curvature and alternating signs of streamwise pressure gradient have a profound effect on the mean streamwise velocity. Profiles at different streamwise locations are shown in figure 7. The x' coordinate is the distance from the bump leading edge normalized by the bump cord. The incoming boundary layer is significantly thinned at the apex of the bump ($x' = 0.5$), and the log region is destroyed by the rapid acceleration. The boundary layer is thickest at the trailing edge of the bump ($x' = 1.0$), and then shows a rapid recovery. The last profile ($x' = 1.7$) is only 0.7 cord lengths behind the bump, and the profile lies almost on top of the incoming flat plate boundary layer profile ($x' = -0.5$). Flow visualization and shear stress measurements using an oil interferometry technique confirmed there was no separation on the back of the bump. Further details can be found in Webster et al. (1996b).

Because of the 45 degree sweep angle of the bump, span-

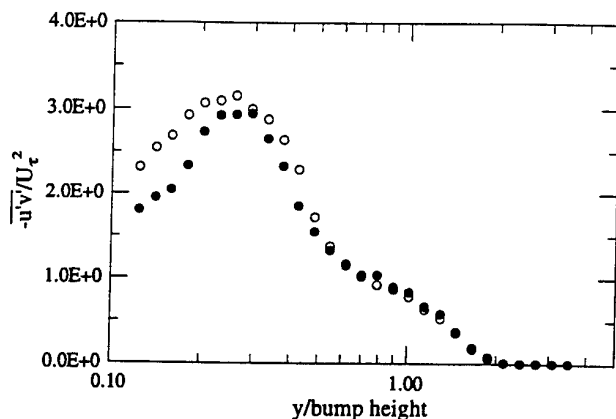


Figure 11: Shear Stress Profiles at the bump trailing edge ($x'=1.0$). Open symbols are $Re_\theta = 3800$, filled symbols are $Re_\theta = 8600$.

wise pressure gradients caused significant skewing of the mean velocity vector near the wall. The top view of the test section in figure 2 shows the direction of shear stress near the wall with a surface streamline drawn on the bump. Along the leading edge of the bump, the spanwise flow is initially in the direction of the sweep of the bump, and then turns into the sweep as the flow goes over the bump apex. Along the trailing edge of the bump the shear stress vector is nearly parallel to the bump trailing edge, due to the combined effects of the spanwise pressure gradient, and deceleration of the flow from the adverse streamwise pressure gradient. This behavior is shown in inner coordinates in figure 8, for three streamwise locations. The profile at the apex has a negative near-wall peak, and the profile at the trailing edge has a large positive near-wall peak. The same data are plotted in figure 9, using the local freestream velocity and bump height for normalization. Clearly there is much better collapse of the data for the two Reynolds numbers. In this Reynolds number range, the height of the peak crossflow is a constant distance from the wall, independent of Reynolds number. Thus, the bump has introduced another length scale which is necessary to properly scale this flow.

Similar scaling arguments can be made based on the behavior of the principal shear stress behind the bump. Figures 10 and 11 compare shear stress data taken at the trailing edge of the bump, for two different Reynolds numbers. Figure 10 is in outer coordinates, and shows strong Reynolds number dependence on the peak shear stress when normalized by the local freestream velocity. Figure 11 is in mixed coordinates, with the friction velocity normalizing the shear stress magnitude (an inner variable), and the bump height normalizing the distance from the wall (an outer variable). With this scaling the data collapse reasonably well. Note that in the log region, the shear stress normalized by the wall velocity is near unity for a standard two dimensional turbulent boundary layer, where $\overline{u'v'}$ is the only shear stress. It is remarkable that in this highly perturbed flow, where $\overline{u'v'}$ is augmented by a factor of three, and the other Reynolds shear stresses are significant, that the friction velocity is the appropriate scaling.

CONCLUSIONS

A unique facility for studying boundary layers over a

wide range of Reynolds numbers has been developed. Measurements for a zero pressure gradient turbulent boundary layer agree well with standard log law and inner/outer scaling. This suggests that computations of these flows at Reynolds numbers significantly higher than those used to calibrate the turbulence models will be successful.

The three dimensional turbulent boundary layer over a swept bump has been discussed with regard to scaling arguments. This is a typical non-equilibrium flow, in which new length scales are introduced by the geometry, which are necessary to scale both mean and turbulence quantities. It is clear that models which hope to accurately predict such flows need to include these additional scales.

Further investigation of the scaling issues in non-equilibrium flows requires turbulence measurements at higher Reynolds numbers. This will require either very large facilities or high resolution measurement systems. Development of the latter is imperative.

ACKNOWLEDGMENTS

We gratefully acknowledge support of the The Office of Naval Research under grant number N0001494-1-0070, monitored by Dr. L. P. Purtell.

REFERENCES

- Coles, D. A., and Hirst E. A., 1968, "The Young Person's Guide to the Data," AFOSR-IFP-Stanford Conference, Vol. 2.
- Eaton, J. K., 1995, "Effects of Mean Flow Three Dimensionality on Turbulent Boundary-Layer Structure," *AIAA J.*, Vol. 33, No. 11, pp. 2020-2025.
- Fernholz, H. H., and Finley, P. J., 1996, "The Incompressible Zero Pressure Gradient Turbulent Boundary Layer: An Assessment of the Data," *Prog. Aerospace Sci.*, Vol. 32, pp. 245-311.
- Gad-el-Hak, M., and Bandyopadhyay, P. R., 1994, "Reynolds Number Effect in Wall-Bounded Turbulent Flows," *Applied Mech. Rev.*, Vol. 47, No. 8, pp. 307-365.
- Kim, J., Moin, P., and Moser, R. D., 1987, "Turbulence Statistics in Fully-Developed Channel Flow at Low Reynolds Number," *J. Fluid Mech.*, Vol. 177, pp. 133-166.
- Littell, H. S., and Eaton, J. K., 1994, "Turbulence Characteristics of the Boundary Layer on a Rotating Disk," *J. Fluid Mech.*, Vol. 266, pp. 175-207.
- Mochizuki, S., and Nieuwstadt, F. T. M., 1996, "Reynolds Number Dependence of the Maximum in the Streamwise Velocity Fluctuations in Wall Turbulence," *Exp. in Fluids*, Vol. 21, pp. 218-226.
- Robinson, S. K., 1991, "Coherent Motions in the Turbulent Boundary Layer," *Annual Rev. Fluid Mech.*, Vol. 23, pp. 601-639.
- Saric, W. S., 1996, "Turbulent Boundary Layer in Subsonic and Supersonic Flow," AGARDograph No. 335.
- Spalart, P. R., 1986, "Direct Simulation of a Turbulent Boundary Layer up to $Re_\theta=1410$," NASA Tech. Memorandum No. TM-89407, Wash. D.C.
- Webster, D., DeGraaff, D. B., and Eaton, J. K., 1996a, "Turbulent Characteristics of a Boundary Layer over a Two-Dimensional Bump," *J. Fluid Mech.*, Vol. 320, pp. 53-69.
- Webster, D., DeGraaff, D. B., and Eaton, J. K., 1996b, "Turbulent Characteristics of a Boundary Layer over a Swept Bump," *J. Fluid Mech.*, Vol. 323, pp. 1-22.
- Westphal, R. V., and Mehta, R. D., 1984, "Crossed Hot-Wire Data Acquisition and Reduction System," NASA TM No. 85871.

SESSION 2 - FREE FLOWS I

THE EFFECT OF THE REYNOLDS NUMBER ON THE TURBULENCE STRUCTURE IN A CIRCULAR CYLINDER FAR-WAKE

Y. Zhou

Department of Mechanical Engineering
The Hong Kong Polytechnic University, Hung Hom, Hong Kong

R.A. Antonia

Department of Mechanical Engineering
University of Newcastle, N.S.W., 2308, Australia

W.K. Tsang

Department of Mechanical Engineering
The Hong Kong Polytechnic University, Hung Hom, Hong Kong

Abstract

The effect of the Reynolds number in a turbulent plane far-wake has been investigated for two values of Re_θ (based on the free stream velocity and the momentum thickness), i.e. 1350 and 4600, using two orthogonal arrays of sixteen X-wires, eight in the (x, y)-plane and eight in the (x, z)-plane. It is observed that as the Reynolds number increases the magnitudes of the measured Reynolds stresses increase, as does the size of two-point correlation iso-contours. Discernible differences are also observed in probability density function, spectra and three-dimensional topologies. The Reynolds number dependence seems to vanish when $Re_\theta \geq 5000$.

1. Introduction

It is now well established that turbulence does not entirely "forget" its origins and the concept of a self-preserving state implying asymptotic independence on initial conditions is not strictly valid. There is a significant amount of evidence which points to the persistence of initial conditions in the self-preserving regions of plane and axisymmetric wakes (e.g. Bevilacqua and Lykoudis, 1978; Bonnet et al., 1985; Wygnanski et al., 1986; Louchez et al., 1988; George, 1989; Zhou and Antonia, 1995).

One would expect that the Reynolds number effect persists in turbulent shear flows. Tong and Warhaft (1995) noted, in the context of a turbulent jet, that the cross-correlation between the square of the scalar derivative and the scalar itself, which is essentially a measure of the interdependence of small- and large-scales, decreased as the jet Reynolds number (on the jet diameter and jet velocity) increased from 2800 to 18000. The effect of Reynolds number on a turbulent boundary layer has been considered by a number of investigators with various degrees of detail. Coles (1962) provided a measure of the effect of Re_θ (the Reynolds number based on the free stream velocity U_∞ and the momentum thickness θ) on the so called "strength of the wake" or maximum departure of the mean velocity from the logarithmic distribution. Antonia et al. (1990a) considered the effect of Re_θ on the topology of the organised motion in a

turbulent boundary layer, using an array of X-wires in the (x, y)-plane or mean shear plane. Although the wake has often been compared to the outer region of the boundary layer, the effect of Re_θ on the far-wake structure, e.g. Reynolds stresses, spectra and flow topology, does not seem to have been investigated.

The main objective of the present paper is to provide information on possible changes, associated with Re_θ , in the far-wake turbulent structure. The experimental investigation uses two orthogonal arrays of sixteen X-wires, eight in the (x, y)-plane and eight in the (x, z)-plane. The two arrays allow velocity data to be obtained simultaneously in the two planes. Measurements were made at $x/\theta = 580$ (x is the streamwise distance downstream of the cylinder) and $Re_d (\equiv U_\infty d/\nu, \text{ where } d \text{ is the cylinder diameter}) = 2800 \text{ and } 9750$ respectively: the corresponding values of Re_θ are 1350 and 4600. On the basis of these data, we have documented the dependence of various quantities on the Reynolds number. These quantities include Reynolds stresses, probability density function(PDF), spectra, vorticity and two-point correlations.

2. Experimental Details

Experiments were carried out in an open return low turbulence wind tunnel with a 2.4 m long working section (0.35 m x 0.35 m). The bottom wall was tilted to achieve a zero streamwise pressure gradient. A circular cylinder ($d=6.35$ mm) was installed in the mid-plane and spanned the full width of the working section, 20 cm from the exit plane of the contraction. This resulted in a blockage of about 1.8% and an aspect ratio of 55. Measurements were made at constant free-stream velocities of 6.7 m/s and 23 m/s respectively. Table 1 presents the characteristic parameters of the wakes, where L is the half-width and U_1 the maximum velocity defect. In the free stream the longitudinal and lateral turbulence intensities were about 0.05% and 0.08% respectively.

Using two orthogonal arrays, each comprising eight X-wires (Figure 1), velocity fluctuations u, v in the (x, y)-plane and u, w in the (x, z)-plane were simultaneously obtained. The

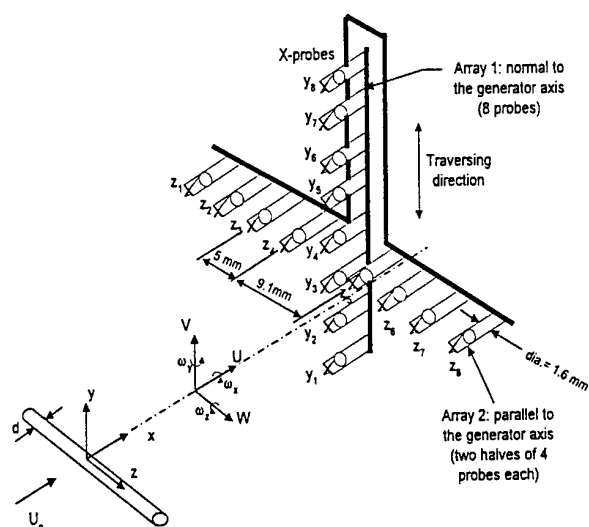


Figure 1 Experimental arrangement.

Table 1. Characteristic parameters of the wakes

Re_d	Re_θ	L (mm)	U_1 (m/s)	U_1/U_∞	x/θ
2,800	1,350	26.1	0.47	6.9	580
9,750	4,600	26.7	1.49	6.5	580

nominal spacing between X-wires in both planes was about 5 mm except for a relatively large gap ($= 9.1$ mm) between the fourth and fifth X-wires in the (x, z) -plane. The arrays were attached to separate traversing mechanisms and could be moved independently of each other. The eight X-wires in the (x, y) -plane were fixed with the second X-wire (from the bottom) positioned approximately on the centreline; the eight X-wires in the (x, z) -plane could be displaced in the y direction. The physical blockage caused by these arrays, cables and supports was estimated to be about 3%. Several types of measurements (Zhou & Antonia, 1994) indicated that the interference to the flow due to the two arrays was negligible.

Wollaston (Pt-10% Rh) wires, 5 μ m in diameter and about 1 mm in working length, were operated with constant temperature circuits. Signals from the circuits were offset, amplified and then digitized using two 16 channel (12bit) A/D boards and two personal computers at a sampling frequency of 3.5 kHz per channel. Data acquisition by the two computers was synchronized using a common external trigger pulse (the configuration is shown in Krogstad et al., 1992). The wires were calibrated for velocity and yaw, and continuously checked for drift. (Velocity calibration was done separately for different free stream velocities). Using velocity and yaw calibrations, signals proportional to u , v and w , together with the local mean velocities U , V (≈ 0) and W (≈ 0), were formed on digital tape. The duration of each record was about 38 s. Subsequent data processing was done on a VAX computer.

3. Results

Distributions of the measured mean velocity and Reynolds stresses are shown in Figure 2. The mean velocity profiles appear to be insensitive to the Reynolds number, probably because of the use U_1 and L as the normalizing parameters.

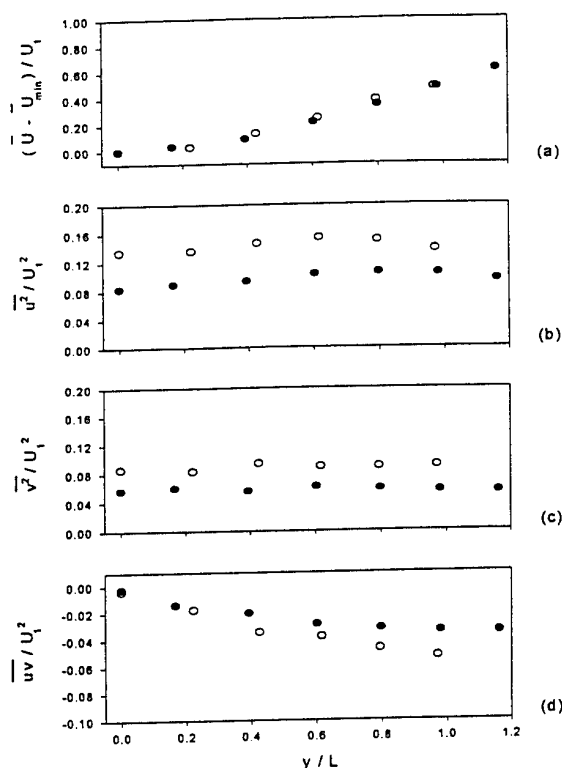


Figure 2 Mean velocity and Reynolds stress distributions. \bullet , $Re_d = 2800$ ($Re_\theta = 1350$); \circ , $Re_d = 9750$ ($Re_\theta = 4600$). (a) $(\bar{U} - \bar{U}_{min})/U_1$; (b) \bar{u}^2/U_1^2 ; (c) \bar{v}^2/U_1^2 ; (d) \bar{uv}/U_1^2 .

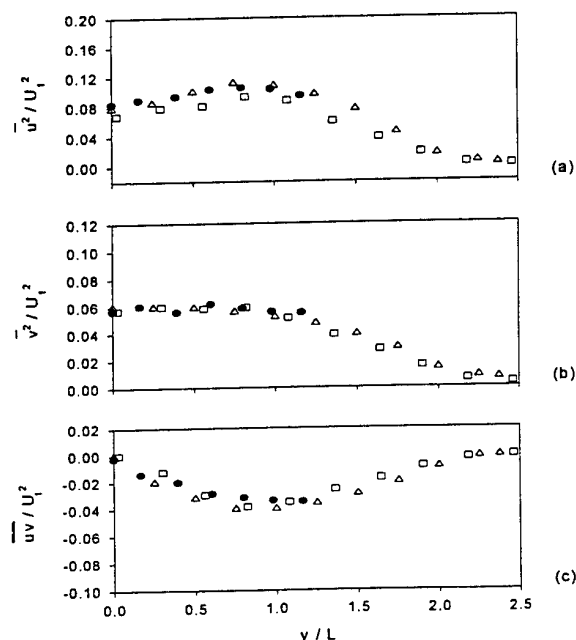


Figure 3 Distributions of \bar{u}^2/U_1^2 , \bar{v}^2/U_1^2 and \bar{uv}/U_1^2 : a comparison between the present (\bullet , $Re_d = 2800$) and published data (Δ , $Re_d = 1170$, Bisset et al. 1990; \square , $Re_d = 2800$, Fabris, 1979).

However, the magnitudes of the Reynolds stresses are clearly larger for $Re_d = 9750$ than for $Re_d = 2800$. It has been confirmed that the values of U_1 are in excellent agreement with Browne and Antonia (1986)'s measurement and with the relation $U_1 / U_\infty = 1.58 (\theta / x)^{1/2}$ (Tennekes & Lumley, 1972). The distributions for $Re_d = 2800$ agree reasonably well with those of comparable Reynolds numbers previously published for nominally self-preserving wakes (Figure 3). This agreement is consistent with self-preservation (George, 1989). For $Re_d = 9750$, $U_\infty^2 / \overline{u^2}$ (see Figure 4), where $\overline{u^2}$ is measured on the centreline (at $x/\theta = 580$), seems to agree with Champagne (1978)'s result ($Re_d = 18,000$).

The ratio $U_\infty^2 / \overline{u^2}$, available in the literature, is plotted in Figure 4 and shows a variation with Re_d .

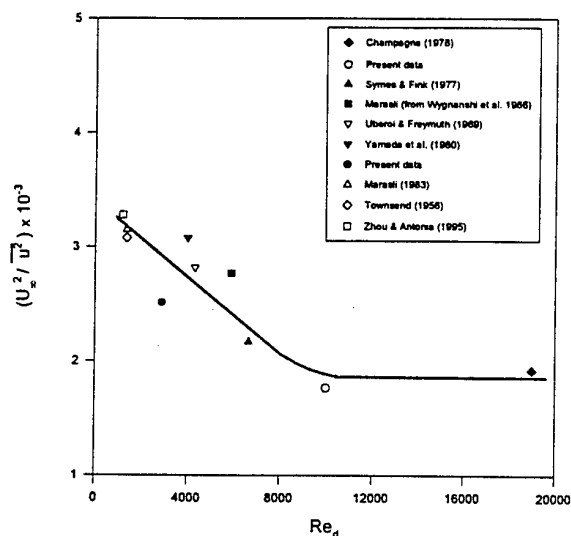


Figure 4 Dependence on Re_d of $U_\infty^2 / \overline{u^2}$ on the centreline ($x/\theta = 580$).

The relationship between $U_\infty^2 / \overline{u^2}$ and Re_d is equivalent to that between $U_1^2 / \overline{u^2}$ and Re_θ since $Re_\theta / Re_d \approx 0.5$ and U_1 / U_∞ at the same value of x/θ does not vary with Re_d or Re_θ . The figure indicates that the value of $U_1^2 / \overline{u^2}$ decreases as Re_d increases and the Reynolds number dependence disappears only when Re_d exceeds about 10000, or $Re_\theta > 5000$. The effect of Reynolds number on the near-wake turbulence has been documented extensively in the literature, including the mean base pressure, fluctuating lift, vortex formation length and topology (e.g. Gerrard, 1965; Roshka & Fiszdon, 1969; Zdravkovich, 1988; and Lin et al., 1995); this effect is particularly significant in the range of $Re_d = 10^3$ to 10^4 . This range interestingly coincides with that in the far-wake.

Tong and Warhaft (1995) investigated the effect of Re_d in the self-preserving region ($x/d = 30, 40$) of a turbulent round jet ($2800 < Re_d < 18000$). The correlation between the square of the temperature fluctuation and the square of the temperature difference, which is essentially proportional to the scalar dissipation rate, varied with Re_d and became negligible only for $Re_d > 10000$. Namer and Ötügen (1988) measured the longitudinal velocity in a turbulent plane jet using both hot wire and laser Doppler anemometry. They observed in the self-preserving region a higher turbulence intensity as the jet

Reynolds number was decreased from 7000 to 1000. A similar observation was also made by Heskestad (1965) in a turbulent plane jet when the jet Reynolds number was varied between 4700 and 36,900. The observations are opposite to that in a turbulent plane wake.

It is noted that the PDF of v/v' (Figure 5), where prime denotes rms value, is relatively symmetrical with respect to $v = 0$ at $Re_d = 9750$ but skewed towards negative values at $Re_d = 2800$, indicating a better mixing associated with the higher Re_d . This is also probably true in the case of a jet. In a turbulent jet, the mixing brings in still (low momentum) fluid from the surrounding. It seems plausible that the low momentum fluid has an inclination to be influenced by the

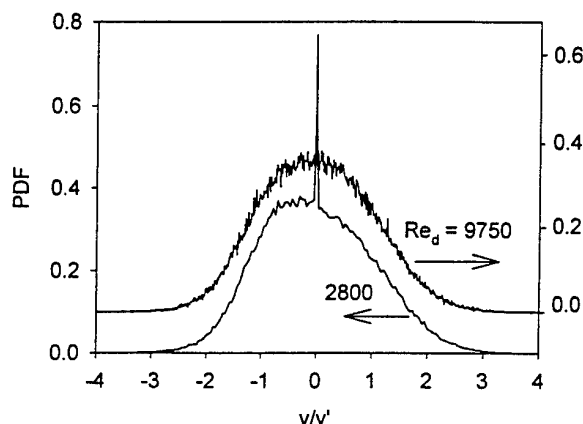


Figure 5 Probability density function of v/v' at $y/L \approx 0.6$.

viscous effect; more fluid of low momentum, brought in by mixing, associated with a higher Re_d may thus result in a larger dissipation rate of turbulence energy. Therefore, the turbulence intensity in a jet decreases with the increase of Re_d , as Heskestad (1965) and Namer & Ötügen (1988) observed. In a wake, however, the mixing brings in high speed (high momentum) fluid from the free stream. The high momentum fluid may be less influenced by the viscous effect; more fluid of high momentum associated with a higher Re_d may therefore lead to a relatively smaller dissipation rate of turbulence energy, as corroborated later by the calculation of the normalized energy dissipation rate $\overline{\epsilon L} / U_1^3$. Consequently, as Re_d increases, the turbulence intensity in a wake increases.

The u and v spectra (Figure 6) measured at $y/L \approx 1$ exhibit discernible differences. The main peak occurs at a lower frequency for $Re_d = 9750$ than $Re_d = 2800$; the higher Reynolds number spectra cross those at the lower Reynolds number at $fL / U_1 \approx 10^{1.6} \approx 40$, suggesting that small scale structures at $Re_d = 9750$ extend to higher frequencies. This is consistent with the notion that the separation of scales increases with Re_d .

The instantaneous lateral and spanwise components of vorticity can be approximated as follows

$$\omega_y \approx \frac{\Delta U}{\Delta z} - \frac{\Delta W}{\Delta x}$$

$$\omega_z \approx \frac{\Delta V}{\Delta x} - \frac{\Delta U}{\Delta y}$$

where $U = \overline{U} + u$, $V = v$ and $W = w$. Δy or Δz (≈ 5 mm) is

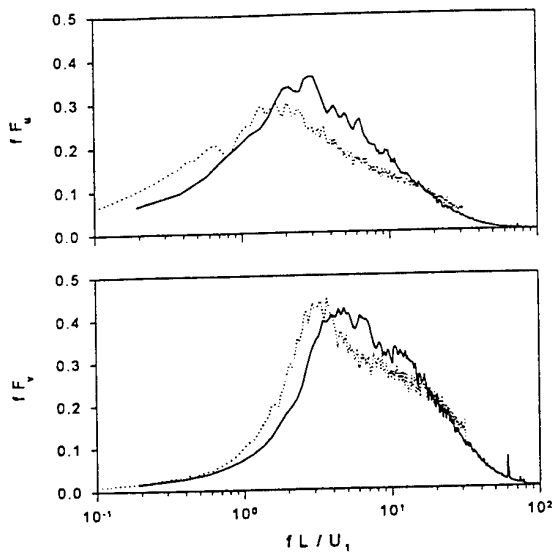


Figure 6 Spectra (smoothed) of longitudinal and lateral velocity fluctuations u and v at $y/L \approx 1.0$. —, $Re_d=2800$; ---, $Re_d=9750$.

the spacing between X-wires and $\Delta x \approx -\Delta t \bar{U} (= 1.8 \sim 1.9$ mm for $Re_d = 2800$ and $6.3 \sim 6.5$ mm for $Re_d = 9750$), where Δt is the time interval. In computing vorticity, the central difference approximation (e.g. Hussain and Hayakawa, 1987) was used so that the array of eight X-wires in each plane gave the instantaneous vorticity at each of the seven midpoints between adjacent X-wires. The relatively large spacing between X-wires degraded the spatial resolution of vorticity. (The Kolmogorov length at the centreline is about 0.45 mm for $Re_d = 2800$ and 0.30 mm for $Re_d = 9750$). This is not critical in the context of comparing the rms vorticity between different Reynolds numbers since the degradation should be roughly the same in each case.

The distribution of ω_z' is shown in Figure 7. It is evident that $(U_1 L / \nu)^{-1/2} (\omega_z' L / U_1)$ (see Antonia et al., 1996 for the scaling of vorticity) varies little, at least, when $y/L \leq 1.0$ and decreases as the Reynolds number increases. Since the

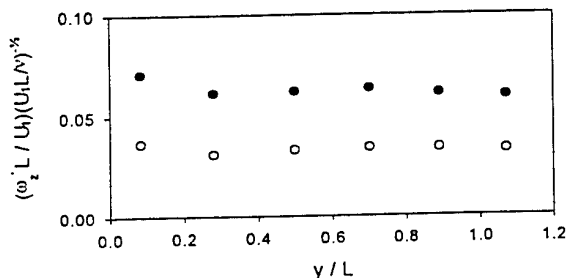


Figure 7 Lateral distributions of the root mean square spanwise vorticity. Symbols are as in Figure 2.

value of $\omega_y' L / U_1$ does not vary greatly with y/L when $y/L \leq 1.0$ (Marasli et al., 1993; Antonia et al., 1988), $(U_1 L / \nu)^{-1/2} (\omega_y' L / U_1)$ was estimated at $y/L \approx 0.5$. The variation between the Reynolds numbers is negligible; the magnitude of $(U_1 L / \nu)^{-1/2} (\omega_y' L / U_1)$ is about 0.065 for $Re_d = 2800$ and 0.035 for $Re_d = 9750$. Note that $(U_1 L / \nu)^{-1/2} (\omega_y' L / U_1)$ is

comparable in magnitude to $(U_1 L / \nu)^{-1/2} (\omega_z' L / U_1)$ (\approx), as observed by Zhou & Antonia (1995), that is, the spanwise vorticity does not dominate over the lateral vorticity. Recent unpublished measurements by Zhu & Antonia indicate that $(U_1 L / \nu)^{-1/2} (\omega_x' L / U_1)$ is comparable in magnitude to $(U_1 L / \nu)^{-1/2} (\omega_y' L / U_1)$ or $(U_1 L / \nu)^{-1/2} (\omega_z' L / U_1)$.

Figure 8 shows contours for the two-point u-correlation coefficient in the (x, y) -plane (the u-signal at $y/L \approx 1.0$ is the reference signal), viz. $\rho(\Delta y) = \overline{u_{y/L=1} u(\Delta y)} / \overline{u'_{y/L=1} u'(\Delta y)}$, and $\rho(\Delta x) = \overline{u_{y/L=1} u(\Delta x)} / \overline{u'_{y/L=1} u'}$. It appears that the major axis of the contours is inclined with respect to the y direction and the

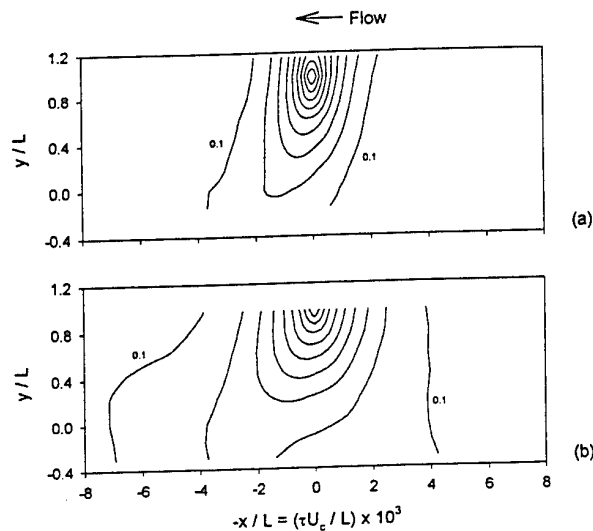


Figure 8 Contours of two-point u-correlation coefficients in the (x, y) -plane ($U_c = 0.95 U_\infty$ is the convection velocity of vortices and $\tau = 0$ is the time at which ρ is maximum). (a) $Re_d = 2,800$; (b) $Re_d = 9750$. (Contour levels = 0.1 to 0.9, increment = 0.1).

inclination for $Re_d = 9750$ is noticeably larger than for $Re_d = 2800$, suggesting a topological difference in organised motion

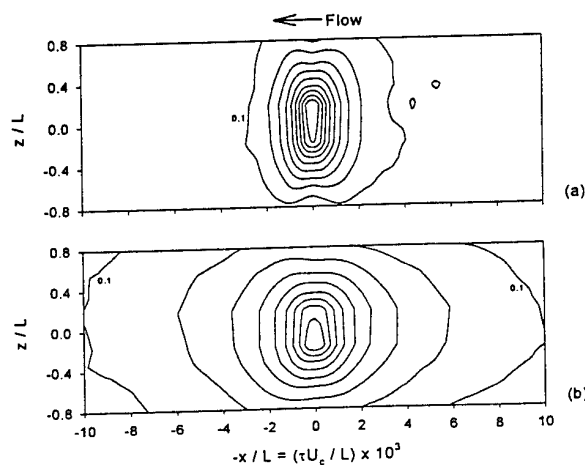


Figure 9 Contours of two-point u-correlation coefficients in the (x, z) -plane. (a) $Re_d = 2,800$; (b) $Re_d = 9,750$. (Contour levels = 0.1 to 0.9, increment = 0.1).

between the Reynolds numbers. In addition, the same contour levels show a greater spatial streamwise extent for $Re_d = 9750$ than for $Re_d = 2800$. A similar observation is made from the contours (Figure 9) for the two-point u -correlation coefficient in the (x, z) -plane (the u -signal at $y/L \approx 0.35$ in the (x, y) -plane, which is closest to the (x, z) -plane, is used for reference). The correlation coefficient is defined by $\rho(\Delta z) = \overline{u_{y/L=0.35}(\Delta z) u'_{y/L=0.35}(\Delta z)}$, and $\rho(\Delta x) =$

$\overline{u_{y/L=0.35}(\Delta x) u'_{y/L=0.35}(\Delta x)}$. The iso-level contours are more widely spread, not only in the streamwise but also the spanwise direction, for $Re_d = 9750$ than $Re_d = 2800$. The difference in spatial extent implies an increase in size of the organised structures as Re_d increases. This increase is supported by the observation that the peaks of the u and v spectra (Figure 6) occur at a lower frequency for $Re_d = 9750$ than $Re_d = 2800$. The difference in size also seems consistent with the difference in the magnitude of the Reynolds stresses, given that organised structures contribute significantly to the Reynolds stresses (Zhou & Antonia, 1995).

Figure 10 shows contours for the two-point v -correlation coefficient in the (x, y) -plane (the v -signal at $y/L \approx 1.0$ is used for reference), viz. $\rho(\Delta y) = \overline{v_{y/L=1}(\Delta y) v'_{y/L=1}(\Delta y)}$, and $\rho(\Delta x) = \overline{v_{y/L=1}(\Delta x) v'_{y/L=1}(\Delta x)}$. The iso-contours are

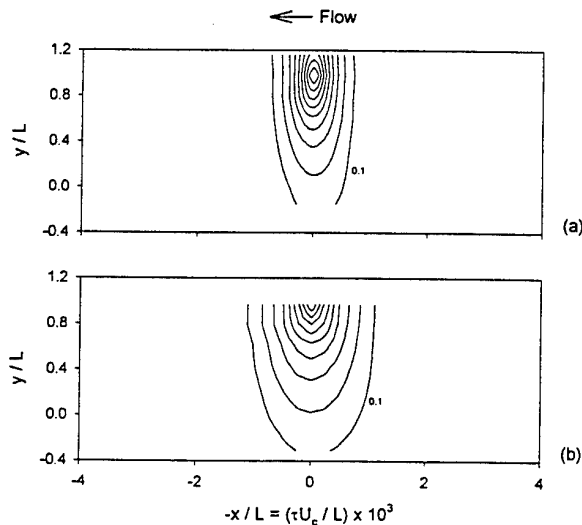


Figure 10 Contours of two-point v -correlation coefficients in the (x, y) -plane. (a) $Re_d = 2,800$; (b) $Re_d = 9,750$. (Contour levels = 0.1 to 0.9, increment = 0.1).

significantly smaller than the u -correlation contours (Figure 7); the streamwise extent, for example, for $\rho = 0.2$, is about one third of that of the u -correlation contours at both Reynolds numbers. This indicates a difference in length scales with which

u and v are associated, as exhibited by $\overline{u^2}$ and $\overline{v^2}$. The major axis of the v -correlation contours, unlike that of the u -correlation contours, coincides with the y direction. Note that, as in Figures 8 and 9, the higher Reynolds number corresponds to a greater streamwise extent for the same level contours.

Figure 11 shows the contours of correlation coefficient between the v signal at $y/L \approx 0.35$ in the (x, y) plane and w -signals in the (x, z) plane, i.e. $\rho(\Delta z) = \overline{v_{y/L=0.35}(\Delta z) w'_{y/L=0.35}(\Delta z)}$, and $\rho(\Delta x) =$

$\overline{v_{y/L=0.35}(\Delta x) w'_{y/L=0.35}(\Delta x)}$. The contours exhibit a clover-leaf pattern. This is probably a consequence of the dominance of counter-rotating vortices, as observed by Zhou and Antonia (1995). Once again, the iso-level contours are larger in the streamwise extent for $Re_d = 9750$ than $Re_d = 2800$. In addition, the four 'leaves' (Figure 11a) are clearly separate, but the two positive leaves (Figure 11b) appear connected to each other, indicating a difference in topology between the Reynolds numbers.

The results obtained to date indicate that the wake does not reach its asymptotic state before $Re_d \approx 10000$ (or $Re_\theta \approx 5000$). This Re_θ limit is similar to that previously documented for the outer region of the boundary layer. There seems to be

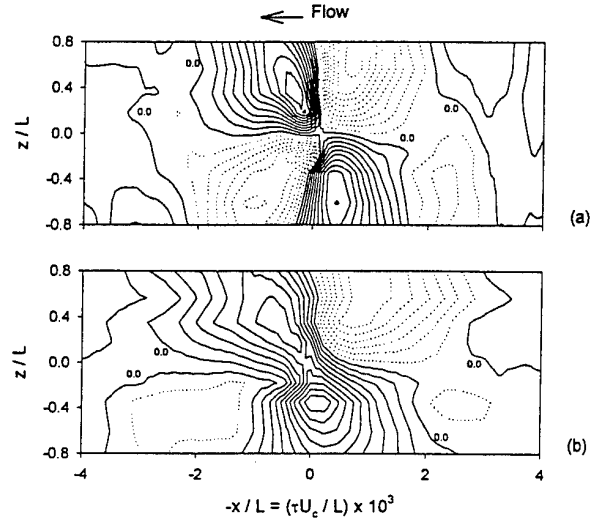


Figure 11 Contours of two-point vw correlation coefficients in the (x, z) -plane. (a) $Re_d = 2,800$; (b) $Re_d = 9,750$. Contour levels = -0.1 to 0.9 (dotted lines) and 0 to 0.9 (solid lines), increment = 0.1.

however an important difference in the Re_d effects between the two flows. Two-point u -correlations in the boundary layer (Antonia et al., 1990b) suggest that contours are larger, with respect to x and z , as Re_θ decreases, i.e. a trend opposite to that observed in the wake. The boundary layer behaviour is reasonable since the separation between the wall length scales, responsible for most of the turbulent energy production, and the outer length scales reduces as Re_θ decreases, the turbulence energy thus being more readily transported from the inner region into the outer layer. In the wake, the normalized energy dissipation rate $\overline{\epsilon} L / U_1^3$ can be approximated using the

assumption of isotropy, i.e. $\overline{\epsilon} = 15 \nu \overline{\left(\frac{\partial u}{\partial x}\right)^2} \approx 15 \nu \overline{\left(\frac{\Delta u}{-\Delta t}\right)^2}$,

where ν is the kinematic viscosity and Δt the time interval, equal to the inverse of the sampling frequency. The magnitude of $\overline{\epsilon} L / U_1^3$ is 0.024 at $Re_d = 2800$ and 0.0048 at $Re_d = 9750$, a difference of about five. The result may not be conclusive in terms of quantifying the relationship between the Reynolds number and energy dissipation rate because of the insufficient resolution, as dictated by the data sampling rate (3500 Hz), of the Kolmogorov length scales. Nevertheless, it indicates that $\overline{\epsilon} L / U_1^3$ tends to decrease as Re_d increases, resulting in larger

and more energetic structures with longer life spans. As Re_δ increases, so does the decoupling between the far-wake structure and the initial conditions. This is consistent with the establishment of an asymptotic state at a sufficiently large Re_δ .

4. Conclusions

The effect of Re_δ on Reynolds stresses, spectra, vorticity and two-point correlation, has been investigated in the far-wake of a circular cylinder. It has been observed that, as Re_δ increases, the magnitude of the Reynolds stresses increases, as does the size of large-scale organised structures. This may be attributed to a reduced normalized energy dissipation rate as Re_δ increases. There is a discernible difference in the measured PDF, spectra and topology of the organised structures. The Reynolds number dependence appears to be negligible for $Re_\delta \geq 5000$.

Acknowledgments

RAA is grateful for the continuing support of the Australian Research Council. YZ acknowledges the support of a research grant of The Hong Kong Polytechnic University.

References:

- Antonia, R.A., Browne, L.W.B. and Shah, D.A.: 1988. Characteristics of vorticity fluctuations in a turbulent wake, *J. Fluid Mech.*, **189**, 349-365.
- Antonia, R.A., Bisset, D.K. and Browne, L.W.B.: 1990a. Effect of Reynolds number on the topology of the organised motion in a turbulent boundary layer, *J. Fluid Mech.*, **213**, 267-286.
- Antonia, R.A., Browne, L.W.B. and Bisset, D.K.: 1990b. Effect of Reynolds number on the organised motion in a turbulent boundary layer, in S.J.Kline and N.H.Afgan (eds.) *Near-wall turbulence*. New York, Hemisphere, 488-506.
- Antonia, R.A., Rajagopalan, S. & Zhu, Y.: 1996. Scaling of mean square vorticity in turbulent flows, *Expts. in Fluids*, **20**, 393-394.
- Bevilaqua, P.M. and Lykoudis, P.S.: 1978. Turbulence memory in self-preserving wakes, *J. Fluid Mech.*, **80**, 589-606.
- Bisset, D.K., Antonia, R.A. & Browne, L.W.B.: 1990. Spatial organisation of large structures in the turbulent far wake of a cylinder, *J. Fluid Mech.*, **218**, 439-461.
- Bonnet, J-P., Delville, J. and Garem, H.: 1986. Space and space-time longitudinal velocity correlations in the turbulent far wake of a flat plate in incompressible flow, *Expts. in Fluids*, **4**, 189-196.
- Browne, L.W.B. and Antonia, R.A.: 1986. Reynolds shear stress and heat flux measurements in a cylinder wake, *Phys. Fluids*, **29**, 709-713.
- Champagne, F.H.: 1978. The fine-scale structure of the turbulent velocity field, *J. Fluid Mech.*, **86**, 67-108.
- Coles, D.: 1962. The turbulent boundary layer in a compressible fluid, *Rand Corp. Rep. R-403-PR, ARC 24478*.
- Fabris, G.: 1979. Conditional sampling study of the turbulent wake of a cylinder. Part 1. *J. Fluid Mech.*, **94**, 673-709.
- George, W.K.: 1989. The self-preservation of turbulent flows and its relation to initial conditions and coherent structures, in W.K.George and R.Arndt (eds.). *Advances in Turbulence*, Berlin, Springer: 39-74.
- Gerrard, J.H.: 1965. A disturbance-sensitive Reynolds number range of flow past a circular cylinder. *J. Fluid Mech.*, **22**, 187-196.
- Heskestad, G.: 1965. Hot-wire measurements in a plane turbulent jet, *J. Applied Mech.*, **115**, 721-734.
- Hussain, A.K.M.F. and Hayakawa, M.: 1987. Eduction of large-scale organised structures in a turbulent plane wake, *J. Fluid Mech.*, **180**, 193-229.
- Krogstad, P-A., Antonia, R.A. and Browne, L.W.B.: 1992. Structure investigation in a turbulent boundary layer using orthogonal X-wire arrays, in M.R.Davis and G.J.Walker (eds.) *Proc. Eleventh Australian Fluid Mechanics Conference*. Hobart, 251-254.
- Lin, J.-C., Towfighi, J. & Rockwell, D.: 1995. Instantaneous structure of the near-wake of a circular cylinder: on the effect of Reynolds number, *J. Fluids and Structures*, **9**, 409-418.
- Louchez, P.R., Kawall, J.G. and Keffer, J.F.: 1987. Detailed spread on characteristics of plane turbulent wakes, *Proc. 5th Symposium on turbulent shear flows*, Lecture Notes in Physics, Springer, 98-109.
- Marasli, B.: 1983. Master's thesis, AME Dept., University of Arizona.
- Marasli, B., Nauyen, P. and Wallace, J.M.: 1993. A calibration technique for multiple-sensor hot-wire probes and its application to vorticity measurements in the wake of a circular cylinder, *Expts. in Fluids*, **15**, 209-218.
- Namer, I. & Ötügen, M.V.: 1988. Velocity measurements in a plane turbulent air jet at moderate Reynolds numbers, *Expts. in Fluids*, **6**, 387-399.
- Roshko, A. & Fiszdon, W.: 1969. On the persistence of transition in the near-wake. *Problems of Hydrodynamics and Continuum Mechanics*, 606-616. S.I.A.M.
- Symes, C.R. & Fink, L.E.: 1977. In *Structures and Mechanisms of Turbulence I*, proceedings. Berlin. 86.
- Townsend, A.A.: 1956. *The Structure of Turbulent Shear Flow*. Cambridge University Press.
- Tennekes, H. and Lumley, J.L.: 1972. *A First Course in Turbulence*. The MIT Press.
- Tong, C. & Warhaft, Z.: 1995. Passive scalar dispersion and mixing in a turbulent jet. *J. Fluid Mech.*, **292**, 1-38.
- Uberoi, M.S. & Freymuth, P.: 1969. Spectra of turbulence in wakes behind circular cylinders, *Phys. Fluids*, **12**, 1359-1363.
- Wyganski, I., Champagne, F. and Marasli, B.: 1986. On the large-scale structures in two-dimensional, small-deficit, turbulent wakes, *J. Fluid Mech.*, **168**, 31-71.
- Yamada, H., Kawata, Y., Osaka, H. & Kageyama, Y.: 1980. Tech.Rep., Yamaguchi University, Japan, vol. 2, no. 4.
- Zdravkovich, M.M.: 1988. Conceptual overview of laminar and turbulent flows past smooth and rough circular cylinders. *International colloquium on Bluff-Body Aerodynamics and its applications*, Oct. 17-20, Kyoto, Japan.
- Zhou, Y. & Antonia, R.A.: 1994. Critical points in a turbulent near-wake, *J. Fluid Mech.*, **275**, 59-81.
- Zhou, Y. & Antonia, R.A.: 1995. Memory effects in a turbulent plane wake. *Expts in Fluids*, **19**, 112-120.

A STUDY OF COHERENT STRUCTURES IN THE WAKE OF A HEATED CYLINDER AT $x/D=30$

M.D. Pons and J.A. Ferré
Departament d'Enginyeria Mecànica
Universitat Rovira i Virgili
Carretera de Salou s/n
43005 TARRAGONA
Spain

ABSTRACT

Temperature, θ , and two components of velocity, either u & v or u & w , are measured simultaneously in a turbulent wake 30 diameters downstream of a slightly heated cylinder in order to study the topology of the Kármán vortex street. A procedure for the complete 3D reconstruction of the dynamic (u , v and w) and thermal (θ) field of coherent motions using a limited set of sensors is developed, and the main features of the Kármán vortices are obtained. The velocity and temperature footprints of the Kármán vortices are obtained in a vertical plane. Also 3D maps of temperature and ω_z vorticity are presented. Finally, the internal circulation of the Kármán vortices is examined using artificial flow visualization by particle tracking.

INTRODUCTION AND OBJECTIVES

The coherent structures in the near wake of a circular cylinder have been investigated by several researchers. Hayakawa and Hussain (1989), using a procedure based on the detection of peaks of vorticity in the signals sensed by an array of aligned hot wires, studied the organized structures in the turbulent Kármán vortex street, from $x/D=10$ to $x/D=40$ at $Re=13000$. They hypothesized that the Kármán vortices, which they call "rolls", could be interconnected with "ribs" or secondary vortices with streamwise (ω_x) vorticity. Antonia (1991) identified the spatial arrangement of structures about the centerline, i.e. the antisymmetric (alternating) or symmetric (opposing) mode. He obtained that the ratio of the relative frequencies of these modes decreases with increasing distance from the cylinder. Matsumura and Antonia (1993) studied the organized structures in the intermediate wake ($x/D=10$ to $x/D=40$) and quantified the contribution from the coherent motions to several averaged quantities (momentum and heat transport). The results indicated that the vortices transport heat more effectively than momentum, especially at $x/D=10$ and 20.

In this paper we present the results obtained from the simultaneous measurement of temperatures and velocities in the near region ($x/D=30$) of the heated wake generated by a circular cylinder at $Re=9000$. The purpose of the experiments is to develop a procedure for the complete 3D reconstruction of the dynamic (u , v and w) and thermal (θ) field of coherent motions using a limited set of sensors, and to obtain the main features of the Kármán vortices.

EXPERIMENTAL DETAILS

A cylinder of diameter $D=21$ mm, fitted with an electrical resistance, was placed in the open-return wind tunnel at the Universitat Rovira i Virgili. The wind tunnel has a test section 60×60 cm square and 300 cm of length, thus the aspect ratio was 38 and the tunnel blockage was 3.5%. The free stream turbulence intensity was less than 0.4%. The electrical resistance provided a maximum mean temperature of 3°C at the measurement location. The external velocity was $U_o=6.5$ m/s ($Re=9000$) and at $x/D=30$ the half-width of the wake was $l_o=32$ mm. Then $X^*=\Delta t \cdot U_o/l_o$, $Y^*=y/l_o$ and $Z^*=z/l_o$.

A set of experiments using 16 anemometers arranged in four different rake configurations (see Fig. 1) was performed. Rake BH and BV contained 6 temperature sensors and 5 x -wires. Rake AH and AV contained 4 temperature sensors in a horizontal plane and 6 x -wires spanning either the horizontal or vertical plane. Rake BV and AV were fixed. Rake BH was moved from $Y^*=-2.25$ to $Y^*=2.44$ and the velocity probes in rake AH were also moved from $Y^*=-2.25$ to $Y^*=2.44$ while the temperature probes were fixed always at $Y^*=1.0$. For any of this configurations the x -wires were rotated $\pi/2$ in order to measure u & v or u & w at the same spatial points in successive experiments. Therefore the data files obtained contain always velocity and temperature data, either u & v & θ or u & w & θ .

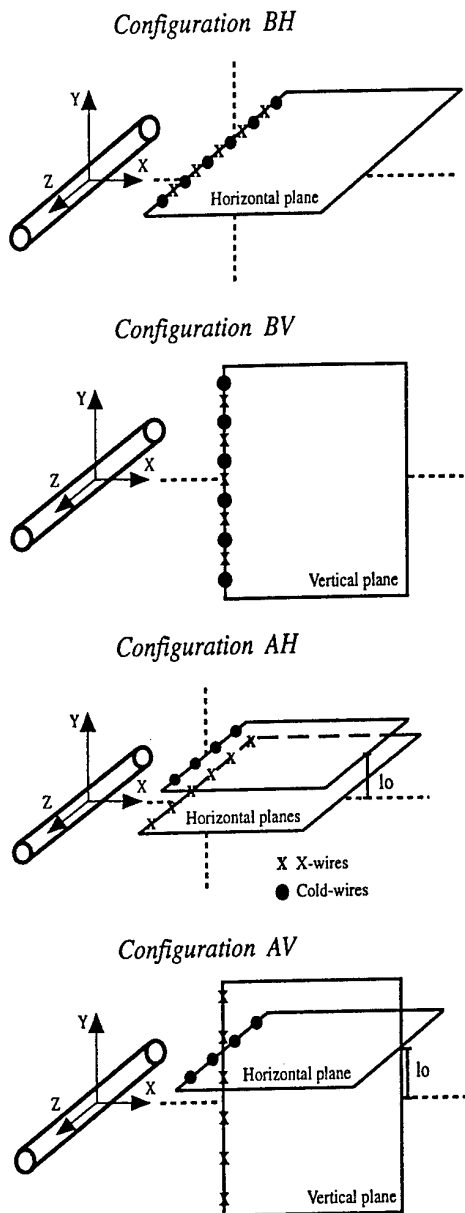


FIGURE 1. DEFINITION SKETCH AND EXPERIMENTAL CONFIGURATIONS

The voltage signals from each anemometer were low-pass filtered at 2 kHz, sampled at 5 kHz per channel ($\Delta t = 0.2$ ms) during 40 seconds using a 12 bit A/D converter, and stored on a magnetic disc for later processing.

RESULTS AND DISCUSSION

Data analysis was performed using a mixture of *pattern recognition* and *conditional averaging* (Pons, 1996) to obtain ensemble-averages of the u , v , w & θ footprints of the Kármán vortices over the three-dimensional domain $X^* = -4.4$ to 4.4, $Y^* = -2.25$ to 2.44 and $Z^* = -1.25$ to 3.44. The instantaneous signals are always centered to zero by

subtracting from each of them its mean value. Therefore, the u , v , w & θ signals that we refer to are always fluctuations.

Pattern recognition and conditional averaging

The pattern recognition technique has been presented elsewhere (Ferré and Giralt, 1989), and is briefly described here. An initial template aimed to represent the velocity (or temperature) footprint of the Kármán vortices is cross-correlated with the recorded velocity (or temperature) data. The positions where the cross-correlation attain a maximum and exceeds some threshold level identify the appearance of individual events that are similar to the template. These events are selected and ensemble-averaged. When this ensemble-average is used again as a new template, and the procedure is iterated until no changes between two consecutive ensemble-averages are observed, we call this technique *pattern recognition*. Because the process is iterated until no further changes are observed, the final ensemble-average obtained becomes independent of the initial template and can be interpreted as the "mean" or "average" structure of the flow (see Kopp et al., 1997).

In addition, during the last iteration of the pattern recognition analysis of the $u&v$ or $u&w$ velocities recorded in the turbulent wake, an ensemble-average of the associated temperature signals recorded in the same file is obtained, simultaneously with the conventional ensemble-average of the velocities.

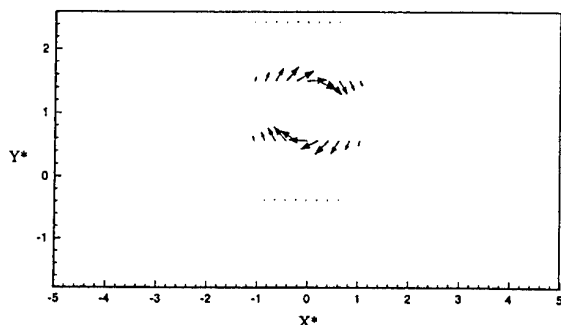
Moreover, if the pattern recognition is carried out over the temperature signals, then during the last iteration an extra ensemble-average containing velocities is obtained. In this way, the whole pattern recognition procedure always yields a $u&v&\theta$ or $u&w&\theta$ "slice" through the Kármán vortices (see, for example, Fig. 3), irrespective whether the iteration has been performed over velocity or temperature data.

If the procedure described above as *pattern recognition* stops just after the first ensemble-average has been computed, then the output from this process becomes a *conditional averaging* analysis of the data, where the condition used to average the data is the similarity between the initial template and the data as measured by the cross-correlation between these two sets. In this work *pattern recognition* and *conditional averaging* have been combined in several ways as described below.

The vertical plane at $Z^* = 0$

The first part of the analysis was directed to obtain the ensemble-average of the $u&v$ velocities and temperature footprints of the Kármán vortices in the X^*-Y^* (vertical) plane, using the files obtained from configuration BV. The analysis was performed by *pattern recognition*, iterating over the $u&v$ data, and adding during the last iteration the temperature data to the ensemble-average.

The initial template used is shown in Fig. 2. Figure 3 shows the output from this procedure after 5 iterations, displaying the typical velocity and temperature footprints of the Kármán vortices in the X^*-Y^* plane at $Z^* = 0.2$, with the flow moving from left to right. In this and subsequent plots we have added to the ensemble-averaged u -velocity fluctuations the measured mean U -velocity profile, and after we have subtracted a convection velocity $U_c = 0.9U_0$. Therefore, the Kármán vortices are displayed as could be seen by an observer moving at $0.9U_0$. The ensemble-average is



Initial Template

FIGURE 2. INITIAL TEMPLATE

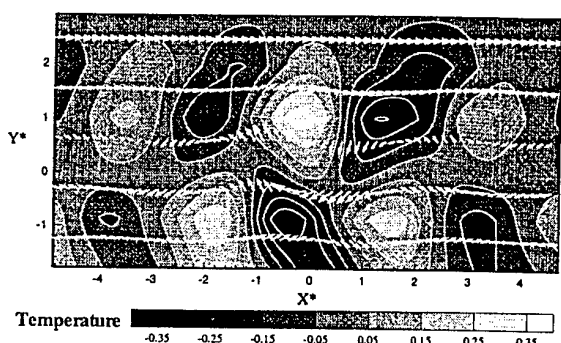


FIGURE 3. ENSEMBLE-AVERAGE OF VELOCITIES AND TEMPERATURE IN THE X^*-Y^* PLANE AT $Z^*=0.2$.

obtained over 1600 individual events, accounting for about 47 % of the data analyzed.

These Kármán vortices are similar to those shown by other authors (Antonia 1987, Matsumura and Antonia 1993). Notice that the centers of the vortices do not match exactly the hotter or colder spots in the wake, where "hotter" or "colder" mean exactly "hotter than the mean temperature" or "colder than the mean temperature", because the temperature data has also been centered to zero like velocities.

Figure 4 shows the histogram of the detection frequency of the Kármán vortices, in 3 Hz steps. The dominant frequency (63 Hz) matches the expected $St=0.21$. However it is interesting to note that the peak at 63 Hz is broad band, and also that other broad band harmonics appear at $63/2=31.5$ Hz and at $63/3=21$ Hz. The result can be interpreted taking into account that only a fraction of the vortices shed from the cylinder are detected at $x/D=30$ because some of the vortices have been destroyed under the dissipation effects of turbulence.

The same sort of analysis was performed over the files generated from configuration AV. However now the temperature footprints obtained during the last iteration are those left by the Kármán vortices in the X^*-Z^* (horizontal) plane at $Y^*=1.0$. Figure 5 displays this ensemble-average, that appears as a succession of cold and hot temperature strips due to the two-dimensionality of the Kármán vortices in this plane.

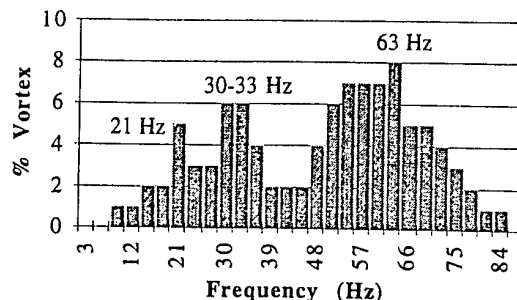


FIGURE 4. DETECTION FREQUENCY OF KÁRMÁN VORTICES.

Three-dimensional reconstruction of the vortices

The sudden cold-to-hot transition of the temperature signals that in Fig. 3 appears at $X^*=0.6$ and $Y^*=1$, and in Fig. 5 appears at $X^*=0.6$ for any Z^* , was used as the triggering signal for the *conditional averaging* analysis of the velocity data obtained from configuration AH, with the temperature probes held fixed at $Y^*=1.0$ but with the velocity probes sensing u & w at $Y^*=-2.25, -1.31, -0.38, 0.56, 1.50$ and 2.44 . This process yielded several ensemble-averages of u & w data that sliced the Kármán vortices in horizontal planes. The same analysis was repeated now over the files containing u & v data. Notice that although in this case the velocity probes span horizontal planes, the velocities sensed are u & v . Finally, the u & v ensemble-averages were used to conditionally average the temperature of the files recorded with configuration BH which contained u & v & θ . The final result was the reconstruction of the conditionally-averaged 3D velocity (u, v and w) and thermal (θ) field of the prototypical Kármán vortex street at $x/D=30$.

The process described above slices the flow in horizontal planes. In order to check if this process is reliable, the data from this set of horizontal slices was sorted to reconstruct the X^*-Y^* (vertical) plane at $Z^*=0.6$; this is shown in Fig. 6a. This has to be compared with Fig. 6b, which displays the

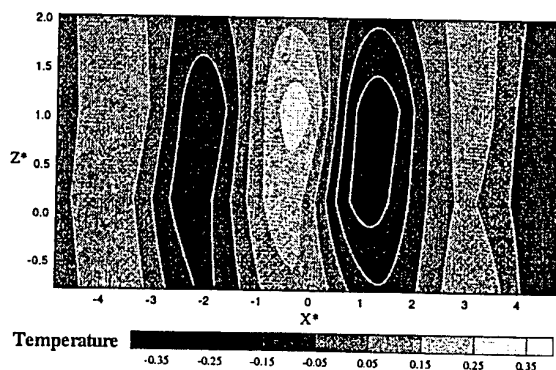
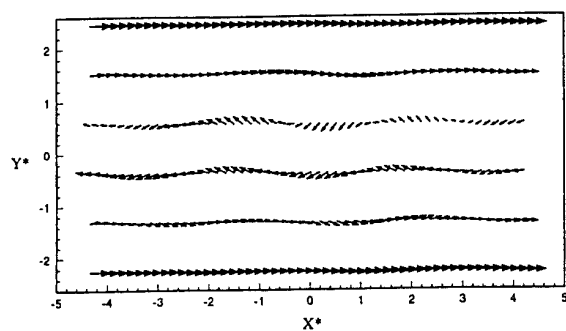
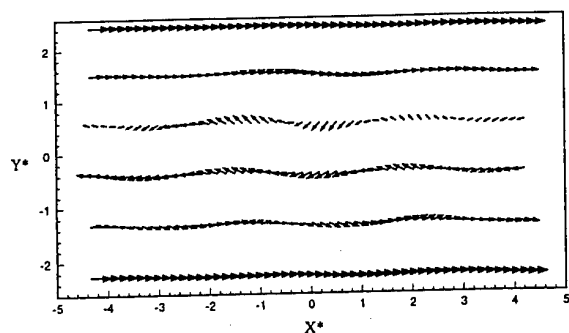


FIGURE 5. ENSEMBLE-AVERAGE OF TEMPERATURE IN THE X^*-Z^* PLANE AT $Y^*=1.0$.



(a)



(b)

FIGURE 6. ENSEMBLE-AVERAGE OF VELOCITIES.
(A) IN THE X^*-Y^* RECONSTRUCTED PLANE AT $Z^*=0.6$.
(B) IN THE X^*-Y^* PLANE AT $Z^*=0.2$.

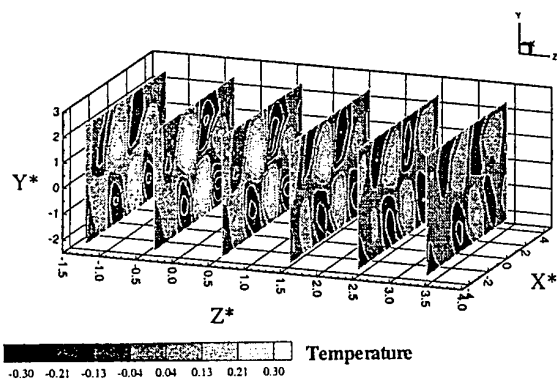


FIGURE 7. TEMPERATURE CONTOURS IN THE X^*-Y^* PLANES AT $Z^*=-1.25, -0.31, 0.63, 1.56, 2.50$ AND 3.44 .

conditional average of the u & v footprint of the Kármán vortices obtained directly from configuration AV. Because the agreement between this two figures is very good, we can assert that the 3D reconstruction of the velocity and thermal field of the Kármán vortices from horizontal slices is reliable.

Figure 7 shows the 3D temperature field obtained by the above mentioned procedure. Planes at $Z^*=-0.3$ and $Z^*=0.6$ agree very well with the results previously displayed in Fig. 3 ($Z^*=0.2$). The plane at $Z^*=3.44$, the one that is farther

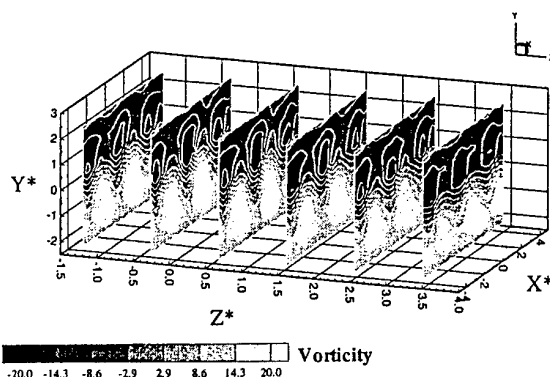


FIGURE 8. SPANWISE (ω_z) VORTICITY CONTOURS IN THE X^*-Y^* PLANES AT $Z^*=-1.25, -0.31, 0.63, 1.56, 2.50$ AND 3.44 .

from the triggering probes, shows weaker signals, as a consequence of the three-dimensional features of the instantaneous events that are ensemble-averaged.

In Fig. 8 we present the spanwise vorticity (ω_z) contours in six different planes. This vorticity has been calculated from the ensemble-averaged velocities as seen by an observer moving at $U_c=0.9U_0$. While the time step used to sample the data ensures no aliasing in the X^* coordinate, our grid is necessarily coarse in the Y^* and Z^* coordinates. Therefore the vorticity that we can compute is some sort of "large-scale" vorticity but not "point" vorticity.

Both figures 7 and 8 show that the Kármán vortices at this station are still fairly well aligned with the z -axis within the spatial domain covered by the rake of anemometers. However we can not say that they are very two-dimensional, because the vertical planes show some differences that are stronger in the thermal field. Vorticity in the upper half wake is always negative (clockwise) and positive (anti-clockwise) in the lower half wake. In the core of the Kármán vortices, vorticity attain local extrema (minimum or maximum) and temperature fluctuations are positive-valued (over the mean). In either the half upper or half lower wake, and between two consecutive Kármán vortices, the vorticity has lower values, without changing sign, and at the same spatial position the ensemble-averaged temperature fluctuations exhibit values below the mean, signaling that at this point colder fluid is being engulfed into the turbulent wake.

It is also possible to compute the ω_x and ω_y vorticity components from the ensemble averaged u & v & w data. This two components are a factor of ten below the ω_z component and do not show any evidence of ribs connecting consecutive Kármán vortices, as has been postulated by other authors (Hayakawa and Hussain, 1989). However this fact can not be taken as experimental evidence against the existence of this kind of vortices because, first, their size could be well below the probe spacing, and second, the conditional averaging process used "locks" better the X^* position of the Kármán vortices than their Z^* alignment, due to the two-dimensionality of the template shown in Fig. 5.

Particle Tracking

Vorticity is a point property and circulation is a line property. Vorticity is linked to circulation through the

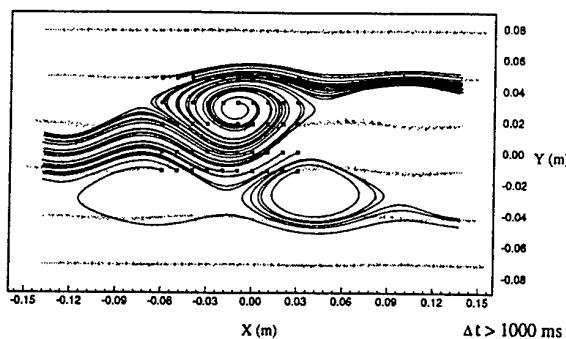


FIGURE 9. PARTICLE TRACKING.

Stoke's theorem. However it is easy to recognize that some flows can exhibit both vorticity and circulation without showing particle paths that close over itself. This is the reason why particle tracking has also been used to visualize the behavior of the Kármán vortices in this turbulent wake. Figure 9 shows the result from such an artificial "flow visualization". A set of 5 rows of 10 particles was positioned at $Z^*=0.6$ ($Z=0.02$ m), with $X^*=-2$ to 1 ($X=-0.064$ m to 0.032 m) and $Y^*=-0.5$ to 1.5 ($Y=-0.016$ m to 0.048 m). The particles were allowed to move under the effect of the same three-dimensional velocity field that was used to compute the vorticity shown in Fig. 8, until they disappeared from the window ($\Delta t > 1000$ ms). The trajectories followed by the particles are spiraling, some of them exit the window running faster than the observer that is moving at $U_c=0.9U_o$, while others exit the frame running slower. This is an interesting observation: the particle paths captured by our virtual camera depend on the convection velocity of the observer. If this velocity is increased, more particles exit the window by the left, because they run slower than the camera, while a decrease in the convection velocity implies that more particles exit the window by the right, because they run faster than the camera. If the particles paths are projected over the X^*-Z^* plane, it can be observed that they are almost two-dimensional because their Z^* displacement is below probe spacing.

The convection velocity used to display results in this paper was selected from a set of trials made at $U_c=0.86, 0.88, 0.90, 0.92, 0.94$ times the free stream velocity U_o , while at the center of the wake the mean U -velocity is just below $0.80U_o$. In this case, this narrow range of values suffices to display a set of different behaviors, as described above. The final value $U_c=0.9U_o$ was selected because it represents an intermediate situation. In addition this value matches very well the convection velocity measured using an independent method by Zhou and Antonia (1992).

The artificial flow visualization presented in Fig. 9 is unrealistic in the sense that the time that the particles were allowed to move under the effect of the velocity field is much larger than the significant convection times in this turbulent wake. That is, the Kármán vortices shown in all the figures presented in this paper are those existing at $x/D=30$. These vortices are significantly different from those that could be detected at $x/D=40, 50$ or 60. But with a convection velocity

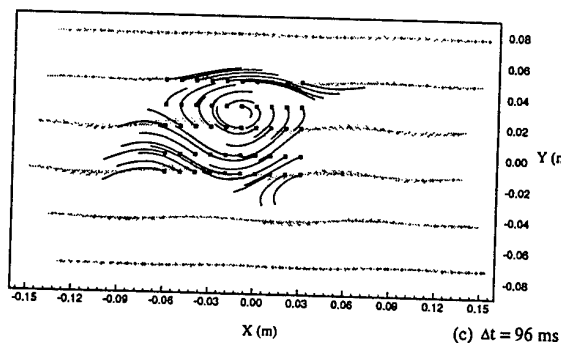
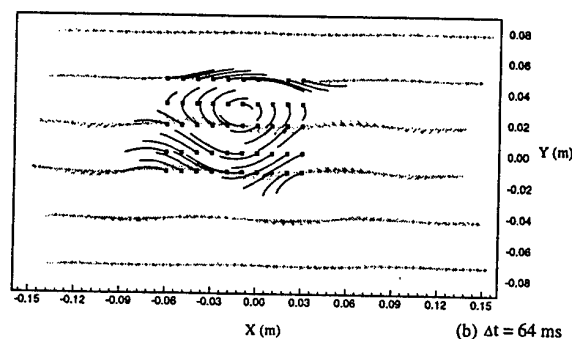
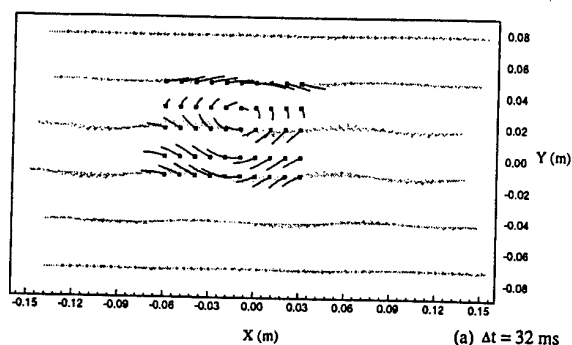


FIGURE 10. PARTICLE TRACKING. (A) $\Delta T=32$ MS. (B) $\Delta T=64$ MS. (C) $\Delta T=96$ MS.

$U_c=0.9U_o=5.9$ m/s, the Kármán vortices reach this stations in only 32, 64 and 96 ms, respectively. Figures 10a, 10b and 10c have been obtained using the same procedure as in Fig. 9, but stopping at $\Delta t=32, 64$ and 96 ms, respectively.

It is interesting to note that the internal circulation times of the Kármán vortices are much longer than their convection times, that is, they translate much faster than they rotate. But we know that translation of the Kármán vortices mean essentially transformation, because the vortices are shed at $x/D=0$, they are easily detected until $x/D=40$ (Hayakawa and Hussain, 1989) and virtually disappear beyond $x/D=60$ (Budny et al., 1979). Therefore, a particle enclosed in a Kármán vortex that could travel from $x/D=0$ to $x/D=60$ (remember that only a small fraction of the Kármán vortices shed by the cylinder reach the station $x/D=60$, see Ferré &

Giralt, 1989) probably would never be allowed to describe a closed loop. From this point of view the Kármán vortices can be better described as "traveling waves" rather than as "translating vortices". This is consistent with the fact that their apparent internal rotation disappears easily if they are observed at convection velocities lower than the velocity at the wake center-line, which is just below $0.8U_0$.

FINAL DISCUSSION

From Fig. 4 and the ensemble averages displayed in Figs. 3, 5, 6, 7 and 8 we can conclude that the reconstruction of the Kármán vortex street at $x/D=30$ has been successful because the pattern recognition approach that we have used allows the individual detection of the vortices, but does not attempt to make use of their periodicity, that is very weak at this station. In fact Fig. 4 allows us to give an explanation to this lack of periodicity. Some of the vortices shed by the cylinder at $x/D=0$ are destroyed before they arrive at $x/D=30$. When this happens to a single vortex, then the apparent frequency goes down from 63 Hz to $63/2=31.5$ Hz. But if this happens to two consecutive vortices, then the apparent frequency goes down from 63 Hz to $63/3=21$ Hz. In addition, the voids left by these missing vortices allow the surviving vortices to gain randomness in the streamwise direction, which translates in producing broad band peaks. This whole picture suggests that the Kármán vortex street disappears beyond $x/D=60$ not only by a general weakening of all the vortices, but by the individual destruction of all (or almost all) of them under secondary instabilities.

The three-dimensional reconstruction of the wake shows that at $x/D=30$ the Kármán vortices are still fairly two-dimensional because ω_z vorticity is much stronger than either ω_x or ω_y vorticity. Probably, our grid resolution does not allow us to solve other secondary structures, as could be the ribs connecting two consecutive Kármán vortices. However, it has to be noted that even in the case that this point could be solved, it can not be taken for sure that the ribs could be observed from our pattern recognition/conditional averaging results if they do not appear always riding over the Kármán vortices at the same Z^* position. If the ribs connecting the individual Kármán vortices were de-localized in the Z^* coordinate, then their footprint after ensemble averaging would always be smeared out, unless we were able to effectively "lock" the Z^* alignment of the Kármán vortices. But this is a feature that our pattern recognition/conditional averaging procedure does not yet guarantee.

The results obtained from the artificial flow visualization produced by particle tracking put some important warnings in the explanation of experimental flow visualization results. It is easy to imagine what would be the appearance of Fig. 10a if instead of a grid of 5×10 points with $\Delta t=32$ ms a grid of 100×100 with $\Delta t=3$ ms was used, for example. Despite the individual particle paths were very short, nice closed loop lines would be displayed, because the short trajectories described by the particles from neighbor rows would appear connected to the eyes of the observer. Therefore, it would be interesting to re-understand some of the most popular flow visualizations (Van Dike, 1982, for example) taking into account this fact.

REFERENCES

- Antonia R.A., Browne L.W.B., Bisset D.K., and Fulachier L., 1987, "A description of the organized motion in the turbulent far wake of a cylinder at low Reynolds number", *Journal of Fluid Mechanics*, Vol. 184, pp 423-444.
- Antonia R.A., 1991, "Organization in a turbulent near-wake", *Fluid Dynamics Research*, Vol. 7, pp 139-149.
- Budny R.S., Kawall J.G., and Keffer J.F., 1979, "Vortex street evolution in the wake of a circular cylinder", *Symposium on Turbulent Shear Flows 2th*, July 2-4, Imperial College, London.
- Ferré J.A., and Giralt, F., 1989, "Pattern-recognition analysis of the velocity field in plane turbulent wakes", *Journal of Fluid Mechanics*, Vol. 198, pp 27-64.
- Hayakawa M., and Hussain A.K.M.F., 1989, "Three-dimensionality of organized structures in a plane turbulent wake", *Journal of Fluid Mechanics*, Vol. 206, pp 375-404.
- Kopp, G.A., Ferré, J.A., and Giralt, F., 1997, "The use of PR and POD in identifying the structure of fully developed free turbulence", *Journal of Fluids Engineering* (in press).
- Matsumura M., and Antonia R.A., 1993, "Momentum and heat transport in the turbulent intermediate wake of a circular cylinder", *Journal of Fluid Mechanics*, Vol. 250, pp 651-668.
- Pons, M.D., 1996, "Estudi de les estructures coherents dels fluxos turbulents tipus estela", Ph. D. Thesis, Universitat Rovira i Virgili.
- Van Dyke, M., 1982. "An Album of Fluid Motion", The Parabolic Press, Stanford, California.
- Zhou Y., and Antonia R.A., 1992, "Convection velocity measurements in a cylinder wake", *Experiments in Fluids*, Vol. 13, pp 63-70.

ACKNOWLEDGEMENTS

This work was financed under grants DGICYT PB91-0551 and DGICYT PB93-0656-C02-01.

TURBULENT DISSIPATION RATE MEASUREMENTS IN A PLANE WAKE FLOW

J. Jovanović* Y.-Q. Ye** F. Durst*

*Lehrstuhl für Strömungsmechanik
Universität Erlangen-Nürnberg
Erlangen Germany

**Institut für Reaktorsicherheit
Forschungszentrum Karlsruhe
Karlsruhe Germany

ABSTRACT

The paper reports on the validation of the modeled equations for prediction of the dissipation rate correlations, using the experimental data obtained in a plane wake flow behind a circular cylinder in cross flow. Good spatial resolution of the measurements was ensured by measuring in the far wake where the turbulence level was only a few percent of the mean velocity and by running the experiment at low Reynolds numbers ($Re \approx 40-80$). Data is provided for all quantities involved in the balance of the turbulent kinetic energy, including the components of the stress and dissipation tensors as well as the triple correlations. The gradients of fluctuating velocity in the normal and lateral directions, which contribute to the dissipation rate correlations, were measured using three different configurations of a pair of either single or cross hot-wire probes. Taylor's hypothesis was used to determine the fluctuating velocity derivatives in the streamwise direction.

in turbulence originates from the nonlinearity of the basic equations that govern fluid flow. The most widely explored approach to define turbulence closure is based on the equations for the moments of fluctuating flow quantities. This line of research was established by Chou (1945), who formulated the turbulence closure for dynamic equations for moments.

In the equations for moments, Chou (1945) identified three different types of unknowns that need to be closed: higher-order velocity correlations, velocity/pressure gradient correlations and dissipation correlations. For all of these unknown quantities he formulated a systematic statistical closure, utilizing the two-point correlation technique, assumption of local homogeneity of turbulence at small scales, and a truncation approximation for the treatment of the higher-order velocity correlations. The work of Chou (1945) is a cornerstone of second moment turbulence closure.

It is recognized nowadays that the treatment of dissipation rate correlations is the weakest link in the development of the Reynolds stress closure. In part this is due to the lack of adequate data which could be used to validate the fundamental issues of the closure assumptions used to approximate the individual terms in the budget of the turbulent dissipation rate. For nearly all the required quantities experimental measurements are extremely difficult or even impossible.

The authors (Jovanović, Ye and Durst 1995; Jovanović, Ye, Jakirlić and Durst 1996) used the two-point correlation technique and invariant theory to study turbulence closure for the dissipation rate correlations. The influence of flow inhomogeneity, the anisotropy of turbulence, and the secondary role of the mean flow deformation on the dynamics of the

INTRODUCTION

Turbulence closure has been of considerable interest to modern fluid mechanics and numerous investigations have been carried out. The closure problem

dissipation rate correlations were among the issues analysed in detail. A critical evaluation of the closure assumptions was performed against databases of direct numerical simulations for a variety of turbulent shear flows. Good agreement between the analytically derived closure and the numerical databases was obtained. The results of the analysis are consistent with the suggestion made by Lumley (1978) that the anisotropy of turbulence plays an important role in the budget of the dissipation rate correlations.

The main objective of the present paper is to validate the closure developed by the authors for the dynamics of the stress dissipation, using the experimental data measured in a plane wake flow.

ANALYTICAL BACKGROUND

The approximate equations governing the dynamics of the dissipation rate correlations, derived by Jovanović *et al.* (1996) are

$$\epsilon = \frac{1}{2} \nu \Delta_x k + \epsilon_h \quad (1)$$

$$\begin{aligned} \frac{\partial \epsilon_h}{\partial t} + U_k \frac{\partial \epsilon_h}{\partial x_k} = & -2A \frac{\epsilon_h \overline{u_k u_s}}{k} \frac{\partial U_s}{\partial x_k} - \psi \frac{\epsilon_h^2}{k} + \\ & \frac{\partial}{\partial x_k} \left(C_\epsilon \frac{k}{\epsilon_h} \overline{u_k u_l} \frac{\partial \epsilon_h}{\partial x_l} \right) + \frac{1}{2} \nu \Delta_x \epsilon_h \end{aligned} \quad (2)$$

$$\epsilon_{ij} = \frac{1}{4} \nu \Delta_x \overline{u_i u_j} + (\epsilon - \frac{1}{2} \nu \Delta_x k) \left\{ \frac{1}{3} (1-A) \delta_{ij} + A \frac{\overline{u_i u_j}}{q^2} \right\} \quad (3)$$

$$\begin{aligned} \epsilon_{ij} &= \nu \frac{\partial u_i}{\partial x_k} \frac{\partial u_j}{\partial x_k} & \epsilon &= \nu \frac{\partial u_i}{\partial x_k} \frac{\partial u_i}{\partial x_k} \\ q^2 &= \overline{u_s u_s} & k &= \frac{1}{2} \overline{u_s u_s} \\ a_{ij} &= \frac{\overline{u_i u_j}}{q^2} - \frac{1}{3} \delta_{ij} & A_2 &= a_{ij} a_{ji} \\ A_3 &= a_{ik} a_{kj} a_{ji} & \Delta_x &= \frac{\partial^2}{\partial x_l \partial x_l} \\ \epsilon_h &= 5 \nu \frac{q^2}{\lambda^2} & R_\lambda &= \frac{q \lambda}{\nu} \end{aligned}$$

$$f_\epsilon = \frac{54\sqrt{3}}{7} [1 - 0.222 \exp(-0.07505 R_\lambda)]$$

$$C_\epsilon \simeq 0.18$$

$$\psi = (1-F)(\psi)_{2C} + F(\psi)_{axi}.$$

$$\begin{aligned} (\psi)_{axi} &= 1.4 + \{1 - 9[\frac{3}{4}(\frac{4}{3}|A_3|)^{2/3} - A_3]\} \times \\ & \left(\frac{7\sqrt{3}}{90} f_\epsilon - 1.4 \right), III_a \geq 0 \end{aligned}$$

$$\begin{aligned} (\psi)_{axi} &= 1.2 + \{1 - 9[\frac{3}{4}(\frac{4}{3}|A_3|)^{2/3} - A_3]\} \times \\ & \left(\frac{7\sqrt{3}}{90} f_\epsilon - 1.2 \right), III_a < 0 \end{aligned}$$

$$(\psi)_{2C} = 0.0517 R_\lambda$$

$$A = (1-F) + 9[\frac{3}{4}(\frac{4}{3}|A_3|)^{2/3} - A_3] F$$

$$F = \frac{1 - 9[\frac{1}{4}(\frac{1}{3}A_2 - A_3)]}{1 - 9[\frac{3}{4}(\frac{4}{3}|A_3|)^{2/3} - A_3]}$$

According to (1), the turbulent dissipation rate ϵ is composed of an inhomogeneous part $1/2 \nu \Delta_x k$ and homogeneous part ϵ_h . The inhomogeneous part of (1) plays an important role only in the near-wall region of wall-bounded flows.

The first term on the right side of (2) approximates the production by the mean velocity gradient and the mixed production of the equation for the homogeneous part of the turbulent dissipation rate. The firm analytic proof for the closure of these terms is given in the paper of Chou (1945). The proposed closure implies that the production of ϵ_h due to the mean velocity gradient vanishes as the anisotropy of the turbulence vanishes; a similar but not identical conclusion was also reached by Kolmogorov (1942) and Lumley and Khajeh-Nouri (1972).

The second term in (2) stands for the difference of the turbulent production and viscous destruction the two predominant terms in the budget of the dissipation equation. At infinite Reynolds number, these two terms dominate in the budget of the turbulent dissipation rate. Following a practice first introduced by Davidov (1961), these terms are exclusively determined from the laws of the decay of grid turbulence. However, as shown by Hanjalić and Launder (1976), the closure deduced from grid turbulence requires further semi-empirical modifications for near-wall applications. The invariant approach was used to formulate ψ from the limiting states of turbulence in order to extend the classical closure of the sink term to account for the anisotropy of turbulence.

The third term in (2) accounts for the diffusive transport of ϵ_h . The adopted closure for this term is analogous to that of the similar term in the equation for turbulent kinetic energy.

The last term on the right side of (2) is the viscous diffusion. We may note that the factor $1/2$ arises from the splitting of ϵ into homogeneous and inhomogeneous parts.

Lumley (1978), and the follow-up contributions to models for the dissipation rate equation would argue that the modern models are for the entire right hand side of (2) and not the individual terms in the dissipation rate equation.

Equation (3) defines the partition of the dissipation tensor. It shows a linear relation between the anisotropies of the stress and dissipation tensors. For turbulence with a moderate mean flow deformation level, Kolmogorov (1941) would have argue that the anisotropy in ϵ_{ij} decreases with increasing Reynolds number. Analytical considerations, based on various asymptotic states of the turbulence, permitted construction of the invariant function A , which is used to predict the components of ϵ_{ij} . In homogeneous turbulence equipartition of ϵ_{ij} is obtained for $A = 0$. In two-component turbulence, $A = 1$.

EXPERIMENTAL INVESTIGATIONS

Wind tunnel and measuring section

The experimental investigations were carried out in the closed test section of a return-type wind tunnel at the Lehrstuhl für Strömungsmechanik. It consists of a well designed settling chamber with wire meshes, followed by a contraction with an area ratio of 5:1. The test section, shown in Fig.1 was 1.87m wide, 1.40m high and 2.0m long. The flow uniformity and two-dimensionality were systematically investigated before performing the measurements. The free stream turbulence level in the empty test section was approximately $T_u \approx 0.07\%$ at all flow velocities.

The wake was generated by a steel tube of diameter $d=3\text{mm}$ that was installed horizontally at the mid plane of the tunnel test section. The velocity U_∞ in the free stream was 6.65m/s, corresponding to Reynolds number based on the cylinder diameter of $Re_d=1290$. All measurements reported herein were done at the nominal measuring station $x/d \approx 400$ downstream from the cylinder where the wake reached its self-preserving state. A more detailed description of the flow conditions and measuring equipment can be found in Ye (1996).

Hot-wire equipment

The measurements were made using standard DANTEC hot-wire probes operated with DISA M10 and DANTEC 56C constant temperature anemometers at an overheat ration of 0.6. The output signals from the anemometers were passed through the back-up amplifiers, low-pass filtered, and then digitized into an HP-1000 computer. The measured signals were stored on streaming tapes for further processing. The recorded signals were subsequently analysed by employing special software programs written for evaluation of hot-wire signals.

Single hot-wire probes (DANTEC 55P15) were used to measure mean velocity profiles and the streamwise intensity component. X-wire probes (DANTEC 55P61) were employed for measurements of the normal and lateral intensity components and shear stress profile. The triple velocity correlations, which contribute to the balance of the turbulent kinetic energy, were also measured with the above mentioned X-wire probes using the method developed by Townsend (1949) and Wygnanski and Fiedler (1969).

The gradients of fluctuating velocity in the normal and lateral directions, which contribute to the dissipation rate correlations, were measured using the difference technique by employing three different configurations of a pair of either single or X-wire probes as described by Browne, Antonia and Shah (1987). The probes are shown in Fig.2. Taylor's hypothesis was used to determine the fluctuating velocity deriva-

tives in the streamwise direction from recorded time traces of the velocity fluctuations.

Two single hot-wire probes (DANTEC 55P14 and DANTEC 55P11) were used to measure $(\partial u/\partial y)^2$ and $(\partial u/\partial z)^2$. The distance between the hot-wires was about 1.5mm, corresponding to 2-3 Kolmogorov microscales. The data from these measurements were also used to determine the separation between the sensors when using two X-wire probes for derivative measurements.

Two different configurations of X-wire probes (DANTEC 55P64+55P61 and DANTEC 55P63+55P61) were used to measure $(\partial v/\partial y)^2$, $(\partial v/\partial z)^2$, $(\partial w/\partial y)^2$ and $(\partial w/\partial z)^2$. The distance between the wires was approximately the same as for the pair of single hot-wires.

The hot-wires were calibrated in the free stream in the range 5-10m/s to yield less than 0.2% deviations when computed by the King's calibration law. Yaw calibration was performed as proposed by Bradshaw (1972) to obtain the effective angles between the hot-wires.

RESULTS

Anisotropy invariant map

Recent results obtained from direct numerical simulations are heavily in support of the conclusion reached by Lumley (1978) that anisotropy plays an important role in the dynamics of turbulence. The tensor

$$a_{ij} = \frac{\overline{u_i u_j}}{q^2} - \frac{1}{3} \delta_{ij}, \quad (4)$$

which was introduced by Lumley and Newman (1977) and its scalar invariants $II_a = a_{ij}a_{ji}$ and $III_a = a_{ij}a_{ik}a_{jk}$ are usually used to quantify the anisotropy and to define the state of the turbulence. A plot of II_a versus III_a in axisymmetric turbulence $II_a = \frac{3}{2}(\frac{4}{3}|III_a|)^{2/3}$ and two-component turbulence $II_a = \frac{3}{2} + 2III_a$ defines the anisotropy invariant map, which, according to Lumley (1978), bounds all physically realizable turbulence. This plot is shown in Figure 3 together with the measured data in a plane wake flow and the data from the direct numerical simulation of plane turbulent channel flow by Kim, Moin and Moser (1987).

Near the wake centreline the data indicate an approach towards isotropic flow conditions. Away from the wake centreline, up to the point $x_2/L \approx 1$ (where L is the half width of the wake), the invariants follow the right boundary of the anisotropy invariant map, which characterizes axisymmetric turbulence. The behaviour of the invariants is similar to the joint variation of II_a and III_a in the logarithmic region of turbulent channel flow. In the intermittent region of the wake flow $x_2/L > 1$ the data lie within

the map and tend to move towards the bound that corresponds to two-component turbulence. The data for the stress components are in good agreement with those reported by Browne, Antonia and Shah (1987).

The scalar function A

The distribution of A across the wake, calculated from the measured data, is shown in Fig. 4. At the wake centerline, $A \simeq 0$, it increases moving towards the outer intermittent flow region. At $x_2/L \simeq 1.5$ A attains its maximum of 0.7 and decreases thereafter towards a very small value in the free stream.

Equation (2) shows that the anisotropy directly affects the production and destruction terms in the transport equation for the turbulent dissipation rate. It must be pointed out in connection with this issue that most turbulence models are adjusted to reproduce the wall flows but ignore the influence of the anisotropy on the dynamics of ϵ . However, it appears that some of the most important turbulence functions vanish with vanishing anisotropy of the turbulence.

Partition of the dissipation tensor

We used (3) and the experimental data for ϵ and $\overline{u_i u_j}$ in order to predict the partition of the dissipation tensor on its components. Figure 5 shows the comparisons between predictions and measurements. The results show satisfactory agreement across the entire wake.

The budget of the dissipation rate

Figure 6 shows the budget of the classical equation for ϵ :

$$\frac{\partial \epsilon}{\partial t} + U_k \frac{\partial \epsilon}{\partial x_k} = -C_{\epsilon 1} \frac{\overline{\epsilon u_i u_k}}{k} \frac{\partial U_i}{\partial x_k} - C_{\epsilon 2} \frac{\epsilon^2}{k} + \frac{\partial}{\partial x_k} \left(C_{\epsilon} \frac{k}{\epsilon} \overline{u_k u_l} \frac{\partial \epsilon}{\partial x_l} \right) + \nu \Delta_x \epsilon, \quad (5)$$

$$C_{\epsilon 1} \simeq 1.44, \quad C_{\epsilon} \simeq 0.18,$$

computed from the experimental data. The terms in the budget are normalized by the centreline mean-velocity defect U_0 (which is the difference between the free stream and local mean velocities) and the length scale L defined at the position in the wake where the mean-velocity defect reaches $0.5U_0$.

At the wake centerline, convection balances the sink term. Moving towards the edge of the wake, the production term becomes equally as important as the convection term. Both of these terms contribute to the production of ϵ . Compared with other terms involved in (2), turbulent transport plays a rather passive role.

The large positive imbalance in the data from Fig. 6 is a clear indication of failure in the production term of (5). Figure 6 also shows, in contrast to the finding

mentioned above, that the budget of ϵ_h (2) is satisfied to an acceptable degree of accuracy across the entire wake. We see that inclusion of the anisotropy in the production of dissipation is of substantial importance. Since

$$0 \leq 2A \leq 2 \quad (6)$$

the suggested closure for production of ϵ_h can accommodate nearly all proposals reported in the literature so far ($2A \simeq 1.44$, Hanjalić and Launder 1972; $2A \rightarrow 0$, Launder, Reece and Rodi 1975, footnote on p. 547; $2A \simeq 0.475$, Zeman and Lumley 1979; $2A \simeq 1$, Launder 1995).

ACKNOWLEDGEMENTS

The authors acknowledge the support (Jo 240/1-2) given to us by the Deutsche Forschungsgemeinschaft (DFG). The work was supported in part from Max-Planck-Forschungspreis given to FD by the Alexander von Humboldt-Foundation.

REFERENCES

- Bradshaw, P. 1971 "An Introduction to Turbulence and its Measurement", Pergamon Press.
- Browne, L.W., Antonia, R.A. and Shah, D.A. 1987 Turbulent energy dissipation in a wake. *J. Fluid Mech.* **179**, 307-326.
- Chou, P.Y. 1945 On the velocity correlation and the solution of the equation of turbulent fluctuation. *Quart. Appl. Math.* **3**, 38-54.
- Davidov, B.I. 1961 On the statistical dynamics of an incompressible turbulent fluid. *Doklady Akad. Nauk SSSR* **136**, 47-50.
- Hanjalić, K. and Launder, B.E. 1972 A Reynolds-stress model of turbulence and its application to thin shear flows. *J. Fluid Mech.* **52**, 609-638.
- Hanjalić, K. and Launder, B.E. 1976 Contribution towards a Reynolds-stress closure for low Reynolds number turbulence. *J. Fluid Mech.* **74**, 693-610.
- Jovanović, J., Ye, Q.-Y. and Durst, F. 1995 Statistical interpretation of the turbulent dissipation rate in wall-bounded flows. *J. Fluid Mech.* **293**, 321-347.
- Jovanović, J., Ye, Q.-Y., Jakirlić, S. and Durst, F. 1996 Turbulence closure for dissipation rate correlations. Submitted to *J. Fluid Mech.*
- Kim, J., Moin, P. and Moser, R. 1987 Turbulence statistics in a fully developed channel flow at low Reynolds numbers. *J. Fluid Mech.* **177**, 133-166.
- Kolmogorov, A.N. 1941 Local Structure of turbulence in an incompressible fluid at very high Reynolds numbers. *Doklady Akad. Nauk SSSR* **30**, 299-303.
- Kolmogorov, A.N. 1942 Equation of turbulent motion of an incompressible fluid. *Izv. Akad. Nauk SSSR, Ser. Fiz.* **6**, 56-58.
- Launder, B.E., Reece, G.J. & Rodi, W. 1975 Progress

in the development of a Reynolds stress turbulence closure. *J. Fluid Mech.* **68**, 537-566.

Launder, B.E. 1995 Turbulence modelling. Lecture notes for the Short Course on the Calculation of Turbulent Flows. Institut für Schiffbau, Hamburg, pp.36-37.

Lumley, J.L. and Khajeh-Nouri, B. 1972 Computational modeling of turbulent transport. *Adv. Geophys.* **A18**, 169-192.

Lumley, J.L. and Newman, G. 1977 The return to isotropy of homogeneous turbulence. *J. Fluid Mech.* **82**, 161-178.

Lumley, J.L. 1978 Computational modeling of turbulent flows. *Advances in Applied Mechanics* **18**, 123-176.

Townsend, A.A. 1949 The fully developed turbulent wake of a circular cylinder. *Australian J. Sci. Res.* **2**, 451-468.

Wyganski, I and Fiedler, H. 1969 Some measurements in the self-preserving jet. *J. Fluid Mech.* **38**, 577-612.

Ye, Q.-Y. 1996 Die turbulente Dissipation mechanischer Energie in Scherschichten. Ph.D. Thesis, Universität Erlangen-Nürnberg.

Zeman, O. and Lumley, J.L. 1979 Buoyancy effects in entraining turbulent boundary layers: a second-order closure study. In *Turbulent Shear Flows I* (ed. Durst et al), pp. 295-306. Springer, Berlin.

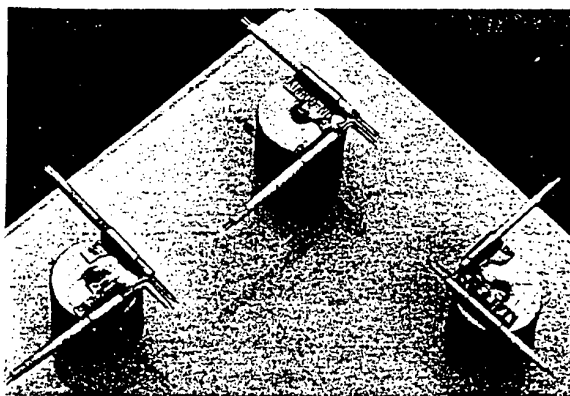


Figure 2: Photograph of the hot-wire probes used for turbulent dissipation rate measurements.

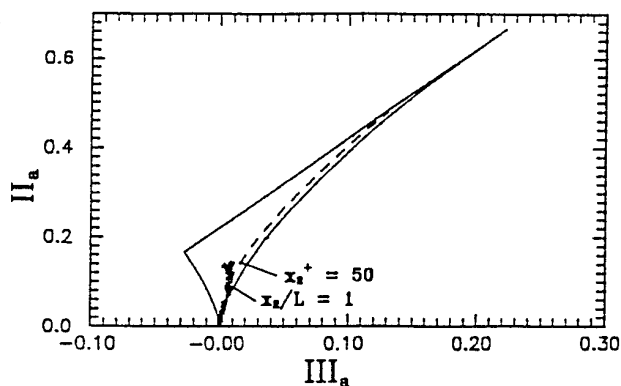


Figure 3: Anisotropy invariant map of the stress tensor. ----, channel flow; *** wake flow.

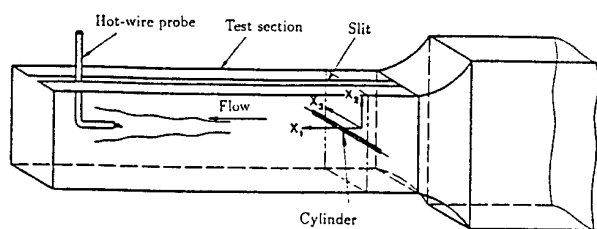


Figure 1: Sketch of wind tunnel test section.

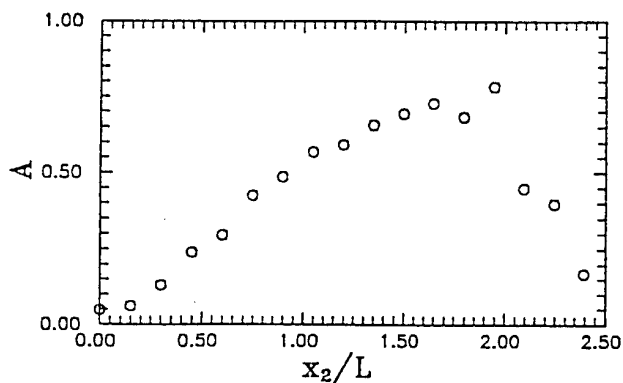


Figure 4: Distribution of the scalar function A across the wake.

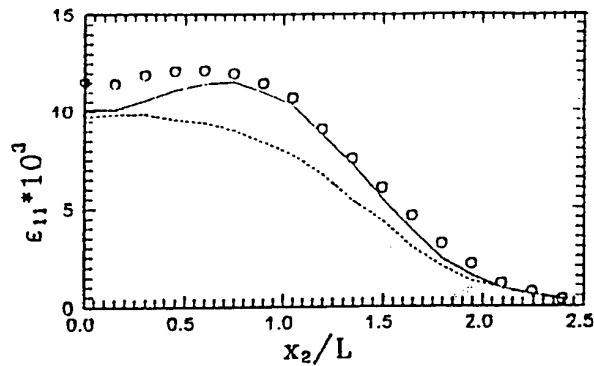


Figure 5(a)

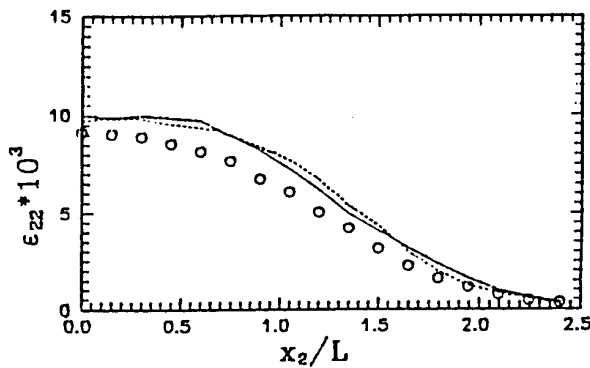


Figure 5(b)

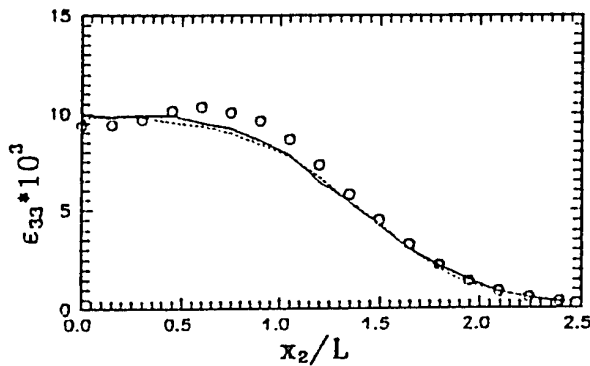


Figure 5: Comparisons between measured and computed components of the dissipation tensor. The dissipation rate components are normalized by the centerline mean-velocity defect U_0 and the length scale L defined at the position in the wake where the mean-velocity defect reaches $0.5U_0$. $\circ \circ \circ$, measurements; —, computations using Eq.(3); ----, isotropic split $\epsilon_{ij} = \frac{1}{3}\epsilon\delta_{ij}$.

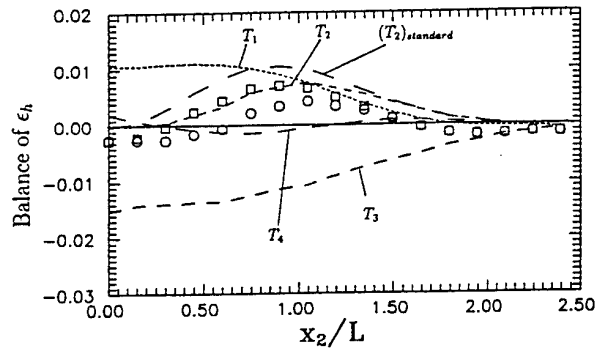


Figure 6: Terms in the budget of Eq.(2) deduced from the experimental data. The normalization of the measurements was performed using U_0 and L as velocity and length scales respectively.

----, convection term ($T_1 = U_k \frac{\partial \epsilon_h}{\partial x_k}$);

-----, production term ($T_2 = -2A \frac{\epsilon_h u_k u_l}{k} \frac{\partial U_x}{\partial x_k}$);

-----, sink term ($T_3 = -\psi \frac{\epsilon_h^2}{k}$)

-----, transport term

($T_4 = \frac{\partial}{\partial x_k} (C_\epsilon \frac{k}{\epsilon_h} \overline{u_k u_l} \frac{\partial \epsilon_h}{\partial x_l})$);

-----, production term ($(T_2)_{standard} =$

$-1.44 \frac{\epsilon_h u_k u_l}{k} \frac{\partial U_x}{\partial x_k}$);

$\circ \circ \circ$, sum of terms $T_1 + T_2 + T_3 + T_4$;

$\square \square \square$, sum of terms $T_1 + (T_2)_{standard} + T_3 + T_4$.

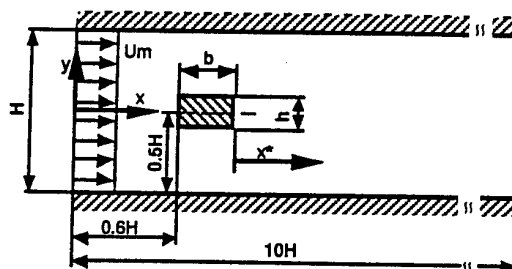
Shinji Nakagawa, Mamoru Senda, Kenji Yamagami and Kenji Nitta
Department of Mechanical Engineering
Doshisha University
Kyotanabe, Kyoto, 610-03
Japan

Unsteady turbulent near wake of rectangular cylinder in a channel flow was studied experimentally with a laser Doppler velocimetry. The time-averaged and phase-averaged statistics were measured for the cylinders having the various width-to-height ratios. Streamwise and normal turbulent intensities on the centerline of the channel have their maxima near the rear stagnation point of the recirculation region. The peaks of the phase-averaged vorticity coincide with the relevant centers of streamline in the reference frame moving with the vortices. The kinetic energy of the mean flow transfers mainly to the coherent structure near the cylinder and then the coherent vortices feed the incoherent turbulence in the cases of $b/h=0.5, 1$ and 3 , while the vorticity of $b/h=2$ is rather weak due to the intermittent change of flow pattern around the cylinder.

Separated flows often appear in many engineering equipment as seen, for example, in the flows over steps and fences, and around bluff bodies. A great number of studies have been carried out extensively from the view point of the turbulence promoter in heat transfer. In a channel flow with rectangular cylinder, it has been confirmed by Yao et al. (1994) and Nakagawa et al. (1996) that the periodically shed vortices from the rectangular cylinder enhance heat transfer at the downstream region of the cylinder. In order to clarify the mechanism of heat transfer enhancement, detailed measurement of the flow field is indispensable. In addition, it has been also revealed (Nakagawa et al. (1996)) that the flow pattern around and downstream of the cylinder changes depending on the width-to-height ratio, b/h , of the cylinder. In the cases of $b/h=2$ and 3, the separated flows at the leading edge reattach to the side walls of the cylinder, while they don't reattach to the side walls and are entrained immediately behind the cylinder for $b/h=0.5$ and 1. In the case of $b/h=2$, in particular, the simultaneous reattachment to the upper and lower side surfaces occurs intermittently,

Therefore, it is our purpose to investigate the flow field in detail in the near wake of the cylinder by a laser Doppler velocimetry and to clarify the velocity characteristics between the different flow patterns. Since the flow field under consideration, in which the large-scale organized motion exists, is unsteady due to the periodically shed vortices, a phase-averaged measurement as well as a time-averaged one was carried out.

A schematic diagram of the test section and the definitions of the coordinates and nomenclature are shown in Fig. 1. Experiments were made in a closed water channel, in which the rectangular cylinder was installed symmetrically. The height, h , of the cylinder was 10mm and we varied the width b of the cylinder with the width-to-height ratio being 0.5, 1, 2 and 3. The cylinder was 350mm long and completely spanned the channel. Water supplied by a constant head tank passed through the contraction and the uniform flow came into the test section with the mean velocity U_m . Reynolds number, which is defined by the cylinder height and U_m , is 3000 and Reynolds number based on the channel height ($H=50\text{mm}$) is 15000. A two-



2-19

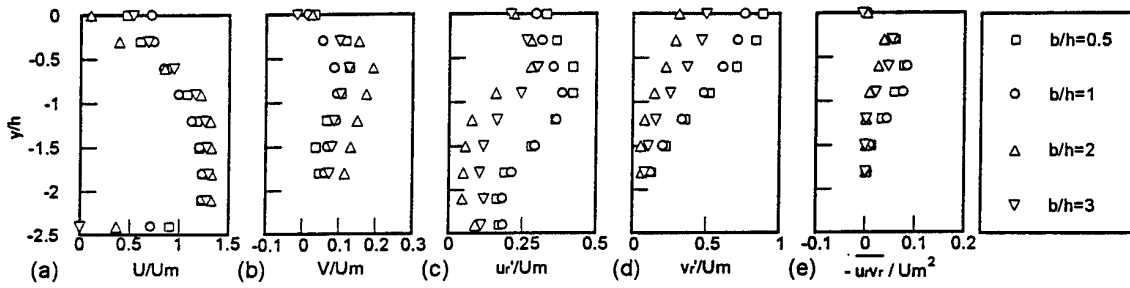


FIG.2 PROFILES OF TIME-AVERAGED VELOCITY CHARACTERISTICS AT $x^*/h=2.0$; (a) STREAMWISE VELOCITY; (b) NORMAL VELOCITY; (c) STREAMWISE TURBULENT INTENSITY; (d) NORMAL TURBULENT INTENSITY; (e) REYNOLDS SHEAR STRESS

color four-beamed laser Doppler velocimetry (KANOMAX 9100-7) with sensitivity to the flow direction provided by Bragg cells has been used and the streamwise and normal velocity components have been measured simultaneously. A backward scattering optical arrangement has been employed and the output signals of the photomultiplier have been processed by a frequency counter.

Experimental Procedure

Phase-averaged flow field was measured by using the signal of a hot film sensor as the phase reference. The hot film sensor was located outside of the separated shear layer, but just behind the cylinder. A total number of 20 phase bins was used. Strouhal number, which is based on the frequency of the vortex shedding, the height of the cylinder and the sectional mean velocity at the cylinder inserted, is 0.15, 0.13, 0.19 and 0.20 for $b/h=0.5, 1, 2$ and 3 , respectively. The number of samples used in the ensemble average is about 3000 per phase bin. Measurements were confined to the lower half of the flow region and it was assumed that the flow in the upper half could be obtained by reflecting the measured lower flow about the centerline (Lyn et al. (1996)).

Analytic Treatment

Instantaneous signal, f , is conventionally decomposed into the time-averaged, F , and the fluctuating, f_r , components (Reynolds decomposition) as

$$f = F + f_r \quad (1)$$

Because of the large-scale organized motion in the near wake of the cylinder, the decomposition expressed by eq.(1) is not adequate. The instantaneous signal is now considered to consist of three components as

$$f = F + f_p + f_i \quad (2)$$

where f_p is the periodic or coherent contribution and f_i corresponds to the turbulent or incoherent motion (Reynolds and Hussain (1972)). The phase average is defined as

$$\langle f \rangle = F + f_p \quad (3)$$

Since $f_r = f_p + f_i$ from eqs.(1) and (2), a correlation of f_r , like Reynolds shear stress, consists of the coherent and incoherent contributions as follows,

$$-\overline{u_r v_r} = -\overline{u_p v_p} - \overline{u_i v_i} \quad (4)$$

The relevant equations for such a flow were given by Hussain (1983).

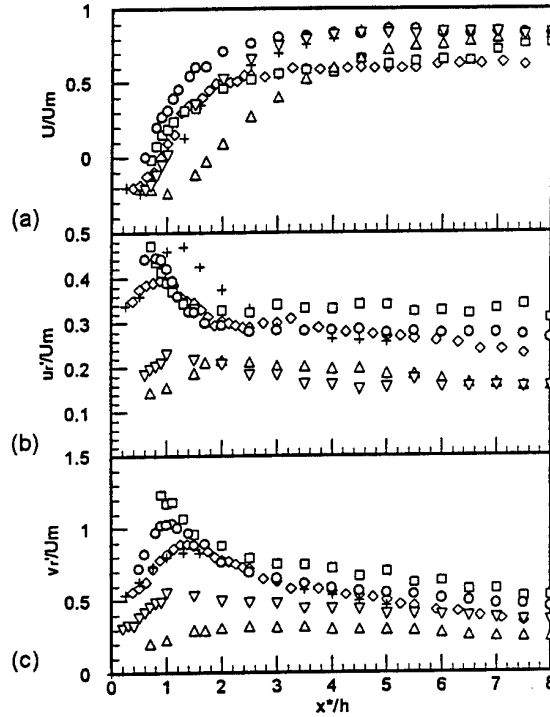


FIG.3 CENTERLINE DISTRIBUTIONS OF VELOCITY CHARACTERISTICS; (a) STREAMWISE VELOCITY; (b) STREAMWISE TURBULENT INTENSITY; (c) NORMAL TURBULENT INTENSITY; + Durao et al.(1988); \diamond Lyn et al.(1995); \square $b/h=0.5$; \circ $b/h=1$; \triangle $b/h=2$; ∇ $b/h=3$

RESULTS AND DISCUSSION

Time-averaged Flow Field

At first the time-averaged turbulent characteristics are discussed. Profiles of time-averaged velocities, turbulent intensities and Reynolds shear stress at the position of $x^*/h=2$ are shown in Fig.2. The profiles of U (Fig.2(a)) show the defect of velocity near the centerline. Maximum values of the normal turbulent intensity are large compared to those of the streamwise turbulent intensity. The time-averaged turbulent quantities differ in profile depending on b/h . Turbulent intensities and Reynolds shear stress for $b/h=0.5$ and 1 are larger over the cross section than those of the other cases, which implies the shedding of strong vortices from the cylinder.

The distributions of velocity characteristics on the centerline are shown in Fig.3 together with the results for

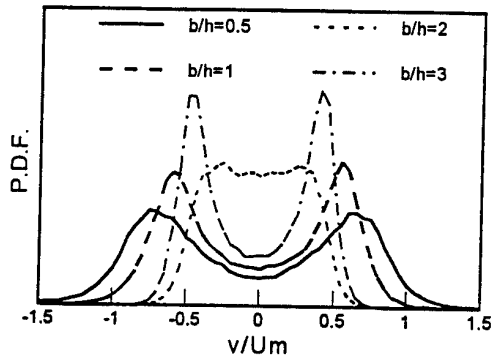


FIG.4 PROBABILITY DENSITY FUNCTION PROFILES OF NORMAL VELOCITY AT $x^*/h=5$ AND $y/h=0$

the square cylinder by Durao et al. (1988) and Lyn et al. (1995). In this figure, the abscissa is the non-dimensional streamwise distance from the rear surface of the cylinder. There is the recirculation region, in which U is negative, just behind the cylinder and the streamwise length of this region, L_r , depends on b/h . In the case of $b/h=1$, L_r obtained by Durao et al. (1988) and Lyn et al. (1995) is larger than that of ours. The discrepancy may be explained by the difference in the blockage ratio of the cylinder height to the channel height. The blockage ratio of 20 % in our experiment is greater than that of 13% (Durao et al. (1988)) and 7% (Lyn et al. (1995)). The large blockage ratio prevents the separated shear layers from moving outwards. Therefore, the entrainment behind the cylinder is intense in the present study, and the normal turbulent intensity is augmented near the cylinder as shown in Fig.3(c).

The streamwise and normal turbulent intensities have their maxima near the rear stagnation point of the recirculation region. A vortex formation length, L_f , is often defined as the downstream position of the cylinder where the streamwise velocity fluctuation level has grown to a maximum. An increase in L_f is associated with a decrease in the turbulent intensities and a decrease in the base suction (Williamson (1996)). In the case of $b/h=0.5$, a recovery of the velocity defect is relatively slow though L_f and L_r are small. This would be attributed to the strong shed vortices which persist downstream and enhance heat transfer at farther downstream region compared to the other cases (Nakagawa et al. (1996)). The extent of the recirculation region of $b/h=2.0$ is larger than those of the other cylinders and this indicates the weak entrainment behind the cylinder as seen from the small turbulent

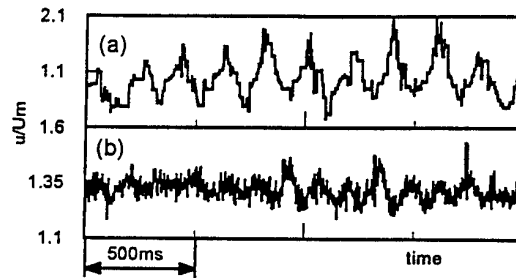


FIG.5 STREAMWISE VELOCITY FLUCTUATIONS AT $x^*/h=2$ AND $y/h=-1.8$; (a) $b/h=1$; (b) $b/h=2$

intensities of Figs.3(b) and (c).

The profiles of probability density function of normal velocity are shown in Fig.4. Two hump profiles are obtained except for the case of $b/h=2$, indicating that the periodically shed vortices move across the centerline of the channel alternately. Fig.5 shows the streamwise velocity signals of $b/h=1$ and 2. The streamwise velocity fluctuates periodically in the wake of the square cylinder, while the irregular fluctuations appear intermittently between the periodic ones in the case of $b/h=2$. These peculiar features of $b/h=2$ seems to be caused by the flow pattern change (intermittent appearance of narrow and wide width of the wake), which is described in detail based on the flow visualization by Nakagawa et al. (1996).

Phase-averaged Flow Field

Fig.6 shows the variations of u_p , v_p , and turbulent kinetic energy, k_t , with the phase bins for $b/h=1$ at $x^*/h=1.5$. In the present study, k_t is defined as $k_t = (\overline{u'^2} + \overline{v'^2})/2$. The present results agree well with those of Lyn et al. (1995), though they used the pressure signal measured at the side surface of the cylinder as the phase reference. This figure confirms the present experimental procedure to be valid. The variation on the centerline, which is different from that of $y/h=-1.5$, can be accounted for by the fact that the two vortices from the upper and lower halves of the flow region come across the centerline during one cycle period, while, at $y/h=-1.5$ the effect of vortex shed in the upper half of the flow region becomes much less (see Fig.7).

Contours of the phase-averaged vorticity, $\langle \omega \rangle / (U_m / h)$, is shown in Fig.7 for the square cylinder, where $\langle \omega \rangle = \partial \langle v \rangle / \partial x - \partial \langle u \rangle / \partial y$, and the shed vortices and their movement are clearly observed. Normal velocity near the wall could not be measured in this experimental setup because of the constraint on optical access. Consequently,

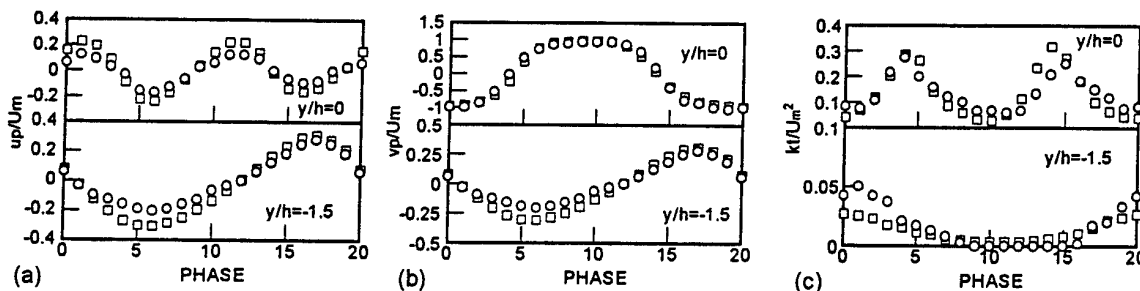


FIG.6 VARIATIONS OF VELOCITY CHARACTERISTICS WITH PHASE; COHERENT COMPONENTS OF (a) STREAMWISE VELOCITY AND (b) NORMAL VELOCITY; (c) TURBULENT KINETIC ENERGY; □ PRESENT RESULT; ○ Lyn et al. (1995)

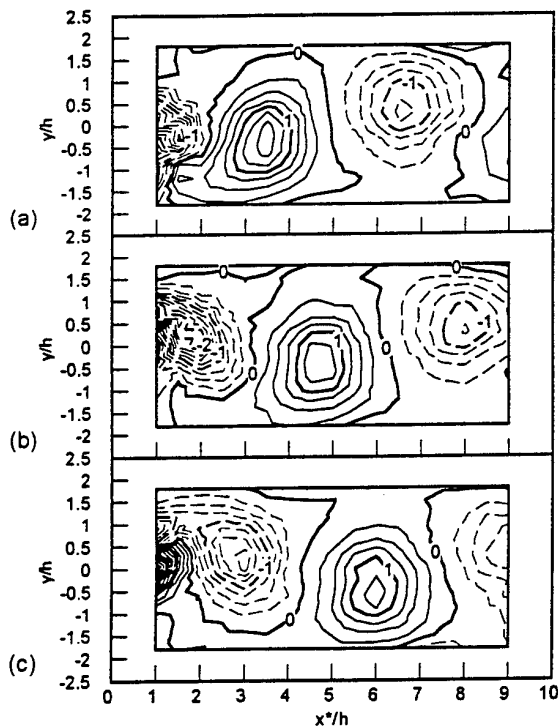


FIG.7 CONTOURS OF COHERENT VORTICITY FOR $b/h=1$; (a) PHASE(2,12); (b) (6,16); (c) (10,20); —, POSITIVE VALUES; ---, NEGATIVE VALUES

the region, in which the vorticity is calculated, is restricted to $|y/h| \leq 1.8$. In this figure, phase (2,12) means that the lower half of the flow region is at phase 2 and the upper half is at phase 12 (a total of 20 phase bins was used for one cycle period.). The vortex is shed from the upper side at phase (2,12) and travels downstream as the phase moves forward. The high vorticity region extends from the cylinder to the downstream region and then the successive vortex is formed from the lower side at phase (10,20).

Figure 8 shows the contours of the coherent vorticity for 4 types of the cylinder. The peak vorticity is considerably large for $b/h=0.5$ and small for $b/h=2$. The shape of shed vortex in the vorticity contour is nearly circular in the cases of $b/h=0.5, 1$ and 3 , and the vortices move deep into the rear of the cylinder. On the other hand, the vortices for $b/h=2$ are elongated in the streamwise direction and the line of zero-vorticity is waving around the centerline. Therefore, the vortex shed from the upper side may exert less effect on the lower flow region, and vice versa. The peculiar feature discussed above with Figs.4 and 5 is attributed to this weak vortex, and the observed feature of the vortices in Fig.8 agrees well with the flow visualization results (Nakagawa et al.(1996)). In addition, the region, in which the absolute value of the coherent vorticity is high, extends further downstream in the case of $b/h=2$ compared to the other cases. The elongated vortices, being formed just behind the cylinder, will reduce the streamwise velocity on the centerline, which results in the largest recirculation region for $b/h=2$ mentioned above.

The streamlines in the reference frame moving with the vortices are shown in Fig.9. In order to clarify the vortical structure in the streamline, the convection velocity of the vortex, U_c , has to be chosen as the reference frame. U_c has

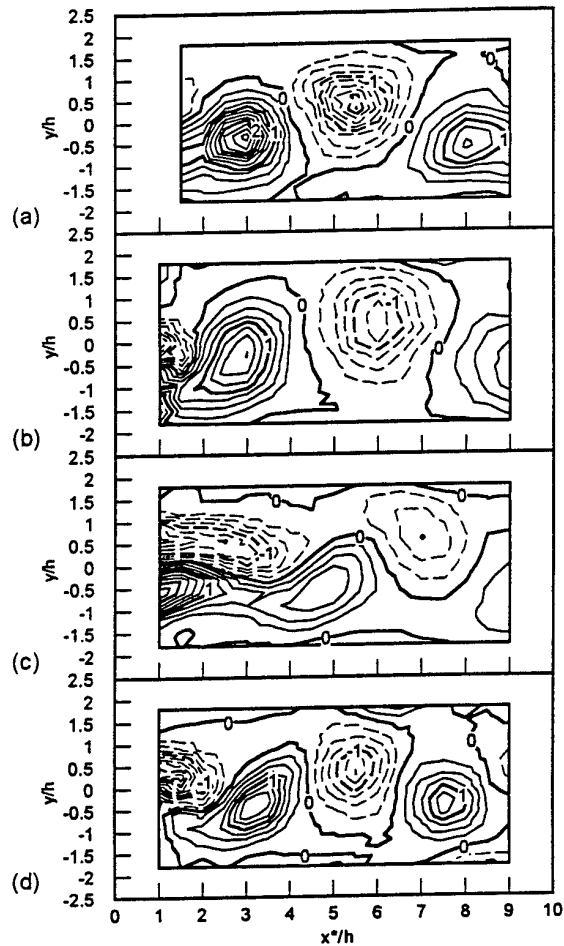


FIG.8 CONTOURS OF COHERENT VORTICITY AT PHASE (0,10); (a) $b/h=0.5$; (b) $b/h=1$; (c) $b/h=2$; (d) $b/h=3$; —, POSITIVE VALUES; ---, NEGATIVE VALUES

been defined here as the streamwise velocity of the movement of the vorticity peak. It is seen that the streamline centers coincide with the relevant vortex peaks in Fig.8. The present result of U_c is nearly equal to U_m ($0.95U_m < U_c < 1.05U_m$), which is slightly larger than that of Taniguchi et al. (1988). This may be also due to the difference in blockage ratio. As seen from Fig.2(a), the large blockage ratio brings about a maximum of the sectional velocity up to about $1.3U_m$.

Contour plot of the turbulent kinetic energy, k_t/U_m^2 , at phase (0,10) is shown in Fig.10. The kinetic energy is large at the position where the absolute value of the coherent vorticity is great. This fact suggests that the coherent structure organizes the incoherent turbulence spatially as indicated by Hussain (1983).

A representative contour plot of incoherent Reynolds shear stress, $(-u_t v_t)/U_m^2$, is shown in Fig.11 for $b/h=0.5$. The centers of streamline, which also correspond to the center of the vortex, are plotted in this figure. A high $(-u_t v_t)$ region is located at $x^*/h=3$ and $y/h=0.9$ and away from the streamline center. Another peak of $(-u_t v_t)/$ is situated at $x^*/h=3$ and $y/h=-0.6$. As the phase is advanced, the value of the former peak decreases and that of the latter increases. Such double-peak structure and its evolution are seen in Lyn et al. (1995) for the square cylinder, though the

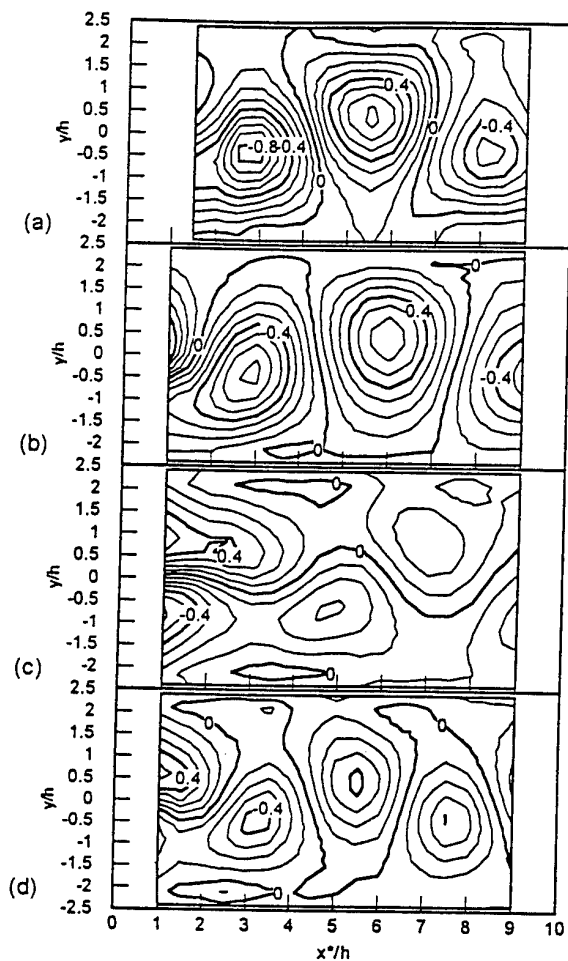


FIG.9 STREAMLINES AT PHASE (0,10); (a) $b/h=0.5$; (b) $b/h=1$; (c) $b/h=2$; (d) $b/h=3$

high $\langle -u_t v_t \rangle$ regions are observed near the streamline saddle for the circular cylinder (Hussain and Hayakawa (1987)). When the streamline center comes on $x^*/h > 3$, its position corresponds with that of the peak of $\langle -u_t v_t \rangle$ as seen in this figure at $x^*/h=5.5$ and $y/h=0.3$.

Comparison between Coherent and Incoherent Contributions

Reynolds shear and normal stresses and kinetic energy, which are estimated by using the Reynolds decomposition, consist of the periodic or coherent component and turbulent or incoherent component as shown in eq.(4). Contributions of each component to the time-averaged quantities are shown in Fig.12. From this figure the distinguishing characteristics are observed in the wake of the cylinder for $b/h=2$. The coherent component is significantly smaller than the turbulent component, although the coherent component is dominant in the other cases

Figure 13 shows the production of kinetic energy. Large values near the centerline are due to the normal stress production. In the cases of $b/h=0.5, 1$ and 3 , P_p is larger than P_t and P_{pt} at $x^*/h=2$ (the definitions of P_p , P_t and P_{pt} are shown in the figure). This indicates that the kinetic energy of the mean flow mainly transfers to the coherent kinetic energy. As a result, the coherent structure will develop or

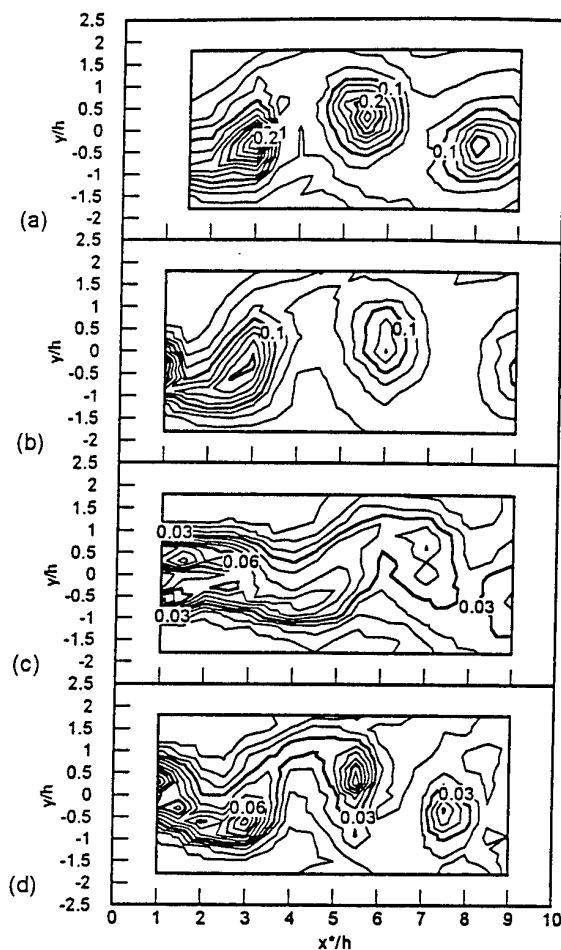


FIG.10 CONTOURS OF TURBULENT KINETIC ENERGY AT PHASE (0,10); (a) $b/h=0.5$; (b) $b/h=1$; (c) $b/h=2$; (d) $b/h=3$

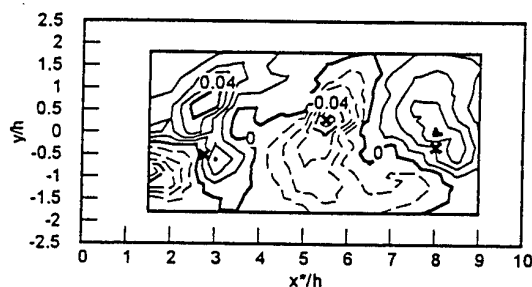


FIG.11 INCOHERENT REYNOLDS SHEAR STRESS FOR $b/h=0.5$ AT PHASE(0,10); \times , POSITION OF STREAMLINE CENTER; —, POSITIVE VALUES; ---, NEGATIVE VALUES

maintain itself. As x^*/h increases, P_p and P_t decrease and P_t becomes smaller than P_{pt} , and the energy of coherent structure given from the mean flow is transferred to the incoherent turbulent flow field. In other words, the coherent structure feeds the turbulence and collapses. In the case of $b/h=2$, P_t is comparable to P_p , which is consistent with the result that the shed vortices are weak as shown above in Fig.8.

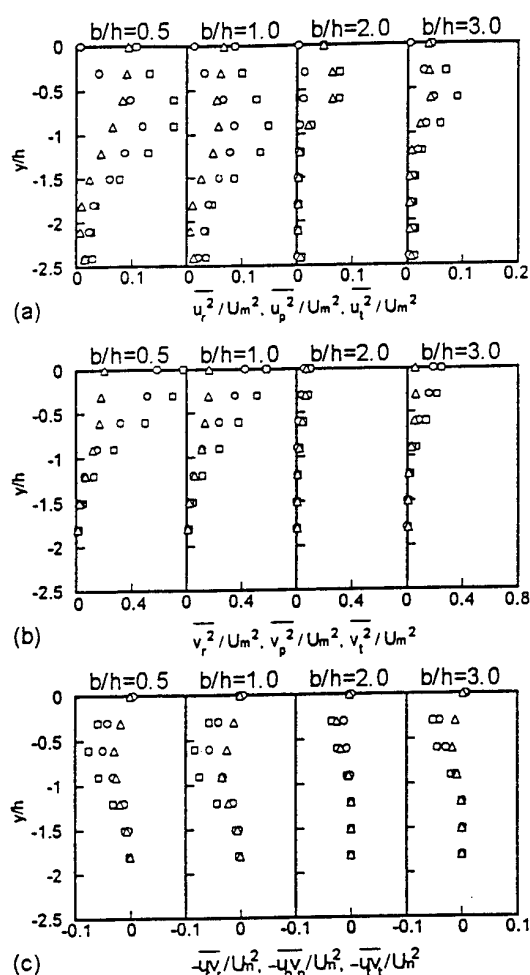


FIG.12 COMPARISON BETWEEN COHERENT AND TURBULENT COMPONENTS AT $x^*/h=2$; REYNOLDS NORMAL STRESSES IN (a) STREAMWISE AND (b) NORMAL DIRECTIONS; (c) REYNOLDS SHEAR STRESS; \square REYNOLDS DECOMPOSED VALUE; \circ COHERENT COMPONENT; \triangle TURBULENT COMPONENT

CONCLUSIONS

Unsteady turbulent near wake of rectangular cylinder in a channel flow was studied experimentally by obtaining the phase-averaged statistics with a laser Doppler velocimetry. The following is a summary of the main results.

- (1) Streamwise and normal turbulent intensities on the centerline of the channel have their maxima near the rear stagnation point of the recirculation region. The recovery of the velocity defect is slowest in the case of $b/h=0.5$ and the extent of the recirculation region of $b/h=2$ is largest.
- (2) Contours of the phase-averaged vorticity and the streamline in the reference frame moving with the vortices have been reproduced clearly. The vortex peaks coincide with the relevant streamline centers.
- (3) Contribution of the coherent components of Reynolds stresses to the time-averaged ones is dominant in the cases of $b/h=0.5, 1$ and 3 , compared to the incoherent components. It is shown from the investigation on the production term that the kinetic energy of the mean flow transfers mainly to the coherent structure near the cylinder and that the coherent vortices feed the incoherent turbulence at the

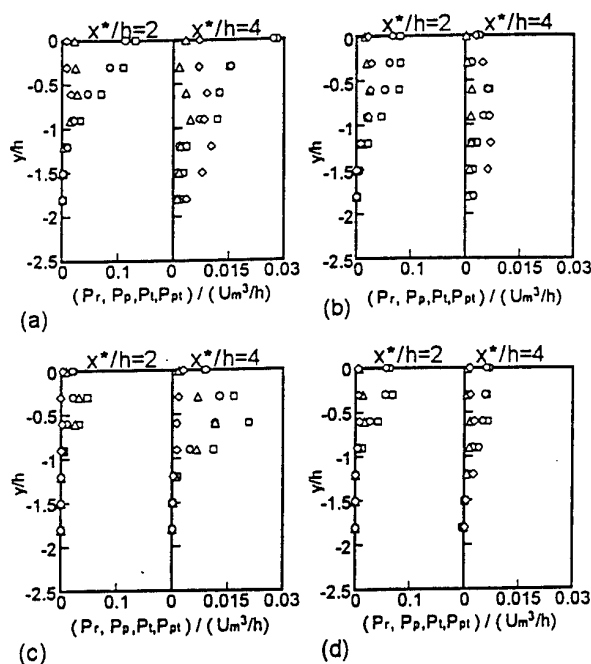


FIG.13 PRODUCTION OF KINETIC ENERGY;

(a) $b/h=0.5$; (b) $b/h=1$; (c) $b/h=2$; (d) $b/h=3$;

\square $P_r = -\overline{u_{ri} u_{rj}} \frac{\partial U_i}{\partial x_j}$; \circ $P_p = -\overline{u_{pi} u_{pj}} \frac{\partial U_i}{\partial x_j}$;

\triangle $P_t = -\overline{u_{ti} u_{tj}} \frac{\partial U_i}{\partial x_j}$; \diamond $P_{pi} = -\overline{\langle u_{ti} u_{tj} \rangle} \frac{\partial U_i}{\partial x_j}$

downstream region.

- (4) In the case of $b/h=2$, the periodic components of Reynolds stresses are less than those of turbulence and the vorticity is rather weak. This is consistent with our flow visualization study (Nakagawa et al.(1996)), which shows the intermittent appearance of the narrow- and wide-width wake due to the change of flow pattern of separated shear layers around the cylinder.

REFERENCES

- Durao, D.F.G., Heitor, M.V., and Pereira, J.C.F., 1988, *Experiments in Fluids*, Vol.6, pp.298-304.
- Hussain, A.K.M.F., 1983, *Physics of Fluids*, Vol.26, pp.2816-2850.
- Hussain, A.K.M.F. and Hayakawa, M., 1987, *Journal of Fluid Mechanics*, Vol.180, pp.193-229.
- Lyn, D.A., Einav, S., Rodi, W. and Park, J.H., 1995, *Journal of Fluid Mechanics*, Vol.304, pp.285-319.
- Nakagawa, S., Senda, M., Kikkawa, S., Wakasugi, H. and Hiraide, A., 1996, *Proceedings, 3rd KSME-JSME Thermal Engineering Conference*, Vol.1, pp.501-506.
- Reynolds, W.C. and Hussain, A.K.M.F., 1972, *Journal of Fluid Mechanics*, Vol.54, pp.263-288.
- Taniguchi, S., Deguchi, A., Miyakoshi, K. and Dohda, S., 1988, *Transactions of the Japan Society of Mechanical Engineers, Ser.B*, Vol.54, No.498, pp.256-264.
- Williamson, C.H.K., 1996, *Annual Review of Fluid Mechanics*, Vol.28, pp.477-539.
- Yao, M., Nakatani, M., Senoo, T. and Suzuki, K., 1994, *Transactions of the Japan Society of Mechanical Engineers, Ser.B*, Vol.60, No.576, pp.2819-2825.

ON THE THREE-DIMENSIONAL EVOLUTION OF A WAKE SUBJECTED TO CROSS-SHEAR

S. BEHARELLE, J. DELVILLE and J. -P. BONNET

LEA/CEAT
43 Route de l'Aérodrome
86036 Poitiers Cédex
France

INTRODUCTION

The investigation of coaxial jets with weak counter-swirl can allow the influence of the transverse instabilities on wake or mixing layer developments to be better understood. The understanding of these phenomena is of primordial importance for the improvement of many industrial applications such as combustors, industrial burners, trailing vortices of aircraft... In addition, these rather simple geometric arrangements are useful for code validations.

We focus here on the analysis of the influence of the transverse shear on the development of wake flows. Several experiments are carried out in a specially designed wind tunnel allowing to generate two coaxial jets with counter-swirl. The swirl level that introduces the transverse shear $\Delta \bar{W}$, and the exit velocity can be independently adjusted for each jet.

By setting the same longitudinal component velocity (U_e) to the two jets, a wake-like flow can be observed immediately downstream of the trailing edge. By imposing to these two flows a counter-swirl, a constant shear in the radial direction is created. Thus a wake flow is obtained that develops in the midst of constant shear perpendicular to the direction of the global convection (Fig. 1).

EXPERIMENTAL SET-UP

The wind tunnel consists of two coaxial plenum chambers with attached swirl generators and contractions. Each swirl generator is constituted of 36 orientable radial inlet vanes and is far upstream of the jet exits to reduce the turbulence level (see Nayeri et al (1996)). The contraction ratios are 1:9.8 for the inner jet and 1:12 for the annular one. The turbulent mixing zone which develops downstream the inner cylindrical splitting plate is investigated (Fig. 1).

The diameters of the inner and the outer jets are respectively 24 cm and 40 cm. The diameter D of the inner jet is large compared to the momentum thickness θ of the boundary layer at the trailing edge ($\theta/D \simeq 0.004$), in such a way that the axisymmetric shear layer can then be assumed to behave like in a plane configuration (Michalke (1971)).

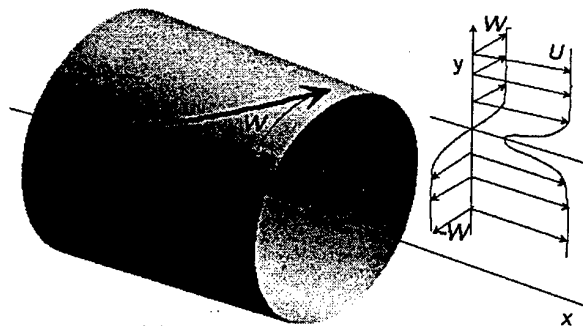


Figure 1: Schematic of the investigated flow.

A cylindrical test section of diameter 40 cm and length 1.5 m, made of plexiglass, is mounted flush to the exit of the external jet in order to shield the flow from external perturbations. The boundary layers are tripped to provide a complete transition and to be turbulent at the trailing edge of the axisymmetric splitter plate.

The exit flows conditions were determined by single hot-wire constant temperature anemometry measurements. The main characteristics of the flow under study are:

- mean axial velocities of the inner and outer jets are both equal to $U_e = 27$ m/s.

- the exit turbulence level in the core of the two jets are less than 0.5%.

- the momentum thicknesses θ of the two jets are respectively 0.9 mm for the outer jet and 1.1 mm for the inner. These values allow to obtain the Reynolds numbers based on the momentum thickness: $Re = 1714$ for the outer jet and $Re = 2266$ for the inner jet.

The velocity component along the streamwise direction x is noted U . The radial direction, perpendicular to the trailing edge is noted y and the corresponding velocity component V . The third axis, z , is tangent to the trailing edge.

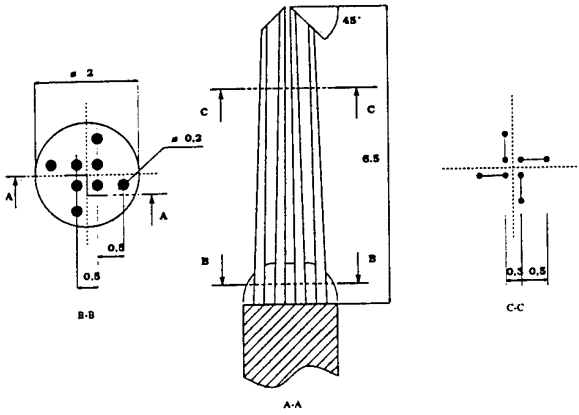


Figure 2: Diagram of the four hotwire probe (all dimensions in mm).

The corresponding velocity component is W and can be adjusted from 0 to 15 m/s by varying the angle of the radial blades. The origins are $x = 0$ and $y = 0$ at the trailing edge.

The resulting flow is built from the superimposition of a wake and a mixing layer. In a similar way than in the case of plane wake configurations, the local velocity defect of the streamwise velocity is noted $\bar{U}_s(x)$, and the wake thickness b is defined by:

$$(\bar{U}_e - \bar{U}_s(x=b))/\bar{U}_s(x) = 0.61.$$

The characteristic scale corresponding to the mixing layer is $\Delta\bar{W}$, the difference of azimuthal velocities. This quantity is found to be independent of the streamwise location. The usual vorticity thickness can be defined by:

$$\delta_{\omega_x}(x) = \Delta\bar{W} / \left(\frac{\partial \bar{W}(x)}{\partial y} \right)_{max}$$

MEASUREMENT TECHNIQUE

In order to address the highly three-dimensional character of the flow, the measurements were performed by using a home-made four-wire probe (see e.g. Jacquin et al (1995), Bruun (1995)). The probe is built of four slanted (45°) sub-miniature probes (micro-welded $2.5\mu\text{m}$ Platinum-plated Tungsten wires with approximatively 0.7 mm length). The four wires are oriented following a pyramidal distribution (Fig. 2). The diameter of the probe body is 2 mm and the measuring volume can be approximately included in a sphere with 1.3 mm diameter.

The calibration procedure consists, first, in placing the probe at zero yaw and pitch, in the center of the potential core of a calibration jet. Varying the jet velocity, a set of $\{(anemometer\ voltage\ e_i), (velocity\ Q_i)\}$ pairs is obtained for each wire i which allows to calculate, by a least square method, the King's law (1) coefficients a_i , b_i , n_i . The voltages issued from the anemometers are then related to the effective jet velocity Q by:

$$e_i^2 = a_i + b_i Q_i^{n_i} \quad (1)$$

In a second step, the yaw (α) and pitch (β) angles are varied for different velocity levels. Using the a_i , b_i , n_i coefficients determined in the first step, equivalent velocities $V_i = ((e_i^2 - a_i)/b_i)^{1/n_i}$ can be determined for each angular position and velocity level. From these velocities and using a method similar to the one followed by Jacquin et

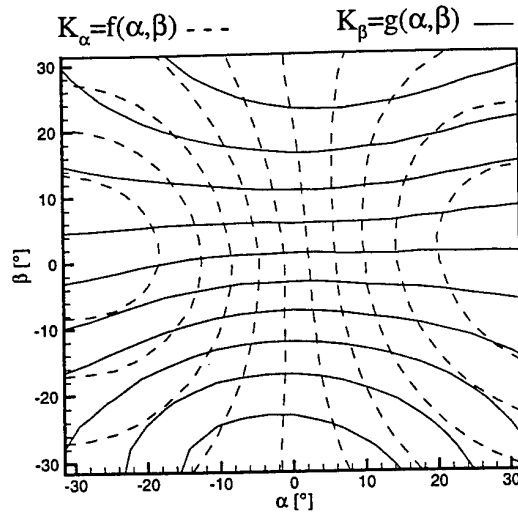


Figure 3: Calibration chart: yaw and pitch sensitivities.

al (1995), two angular coefficients $K_\alpha(\alpha, \beta)$, $K_\beta(\alpha, \beta)$ (related to the normalized difference of equivalent velocities Q_i for opposite wires) and a correction factor $C_q(\alpha, \beta)$ for the modulus of velocity are calculated. Figure 3 shows the iso-values of K_α and K_β as a function of (α, β) and a typical example of the sensitivity of the probe to the flow direction. The calibration is carried out over a mesh of 19×19 angular positions (yaw and pitch angles between -31.5° and 31.5°) and 15 velocity levels ($8 < Q < 34$ m/s). The typical duration of probe calibration is about 6 hours. In order to accelerate the data analysis, preliminary interpolations on the calibration meshes are carried out, making possible the use of the Look-Up-Method on regular meshes with dimension 100×100 . The calibration method used allows to avoid the "a priori" knowledge of the wires orientation and does not need to introduce for example a Jørgensen equation (e.g. Bruun (1995)) to express the effective velocity. The validation of the probe has been achieved by comparing several velocity profiles measured by cross hotwire probe and LDA, in a reference flow (see Béharelle (1996)).

RESULTS

A first set of experiments was carried out to obtain different velocity profiles downstream of the trailing edge for different levels of the transverse shear ($\Delta\bar{W} = 0, 2, 4, 7, 8.5, 10$ and 15 m/s). These measurements were achieved for 16 longitudinal positions: $x = 10, 50, 100, 150, 200, 250, 300, 350, 400, 450, 500, 600, 700, 800, 900$ and 1000 mm ($0.041 \leq x/D \leq 4.16$). For each location, 51 positions were acquired in the radial direction y with 20480 samples per point of measurements. These measurements allowed us to obtain characteristic thicknesses (momentum, vorticity, wake thickness...), to reveal the evolution of the mean and turbulent fields, and to establish the kinetic energy balance.

Mean velocity profiles.

The evolution of two characteristic configurations are depicted here: $\Delta\bar{W} = 0$ and $\Delta\bar{W} = 10$ m/s. The first case $\Delta\bar{W} = 0$ allows to validate the flow by comparison with the classical plane wake and the second case $\Delta\bar{W} = 10$ m/s shows the effects due to the transverse shear, mainly the creation of a mixing layer in the azimuthal direction. The

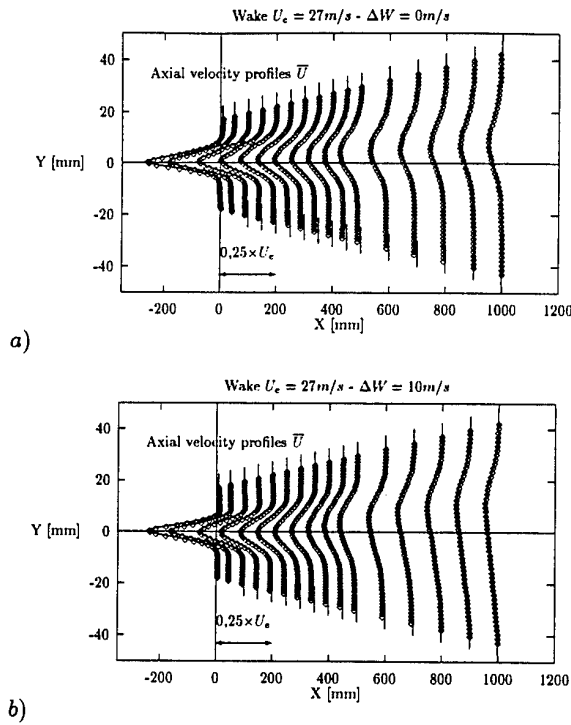


Figure 4: Evolution of \bar{U} a) without transverse shear and b) with transverse shear.

other cases with transverse shear having a similar behavior than the case $\Delta\bar{W} = 10\text{m/s}$, they are not described in this section.

Mean streamwise component.

Figures 4.a and 4.b show some examples of the streamwise evolution of the longitudinal velocity profiles with and without cross-shear. We can observe that, whatever the studied case is (with or without transverse shear), all the profiles are characteristic of a wake evolution.

The influence of the transverse shear on the deficit of the longitudinal velocity component is negligible. However, the thickness $2b$ is slightly increased when a transverse shear is applied.

With transverse shear, in the similarity region, the present results no longer correspond to those found by Hackett and Cox (1970) in their theoretical study of the three-dimensional mixing layer between two grazing perpendicular streams. Indeed, these authors obtain constant velocity profiles for the component \bar{U} .

In our cases, the velocity profiles correspond to those observed in regular plane wake case, with an evolution of the form:

$$\frac{\bar{U}_e - \bar{U}}{\bar{U}_e} = e^{-\frac{1}{2}c\xi^2} \quad (2)$$

where \bar{U}_e is the convective velocity, ξ the similarity variable (here y/b). c is a constant.

Mean azimuthal component.

When the transverse shear is added, the downstream evolution of the azimuthal profiles (Fig. 5) shows that the value of $\Delta\bar{W}$ remains constant along x . The shape of the profiles is in agreement with those suggested by Hackett

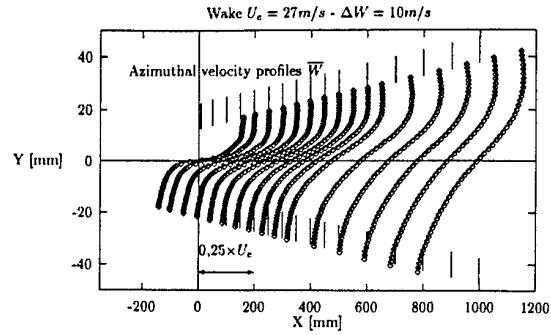


Figure 5: Evolution of \bar{W} with transverse shear.

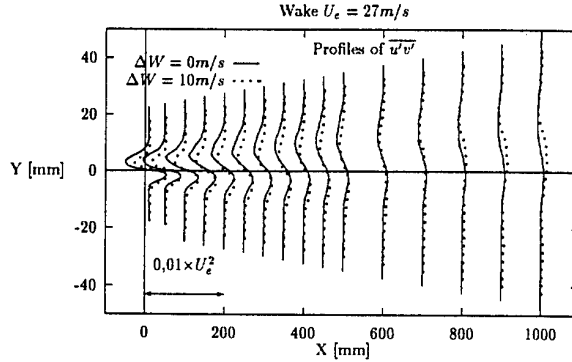


Figure 6: $\overline{u'v'}$ evolution with and without transverse shear.

and Cox (1970) concerning the evolution of \bar{W} in the region of similarity. This behavior corresponds to the typical evolution of a regular mixing layer:

$$\frac{\bar{W}}{\bar{W}_e} = \text{erf}(\sigma\eta) \quad (3)$$

where $\eta = \frac{y}{x}$ and σ is a constant.

Thus, the transverse shear creates a constant shear mixing layer in the azimuthal direction z . This shear layer is superimposed on the wake still developing in the downstream direction x . When the wake effect vanishes as it develops downstream, the flow generated is a mixing layer in the $y-z$ plane convected downstream in the x direction.

In its last part ($x \geq 600$), the flow can be viewed as a temporally evolving mixing layer, providing that the convection velocity (\bar{U}) is quasi constant and normal to the constant mean shear obtained with opposite equal velocities. The application of the Taylor hypothesis is in this case straightforward.

Second order moments.

$\overline{u'v'}$ profiles.

$u'v'$ is the cross momentum which allows to characterize the streamwise velocity gradient in the y direction. One can observe in Fig. 6 that without transverse shear, the shapes of the velocity profile are typical of a plane wake.

In the case with transverse shear (Fig. 6), the evolution of $\overline{u'v'}$ remains close to that of a plane wake, with a small decaying level.

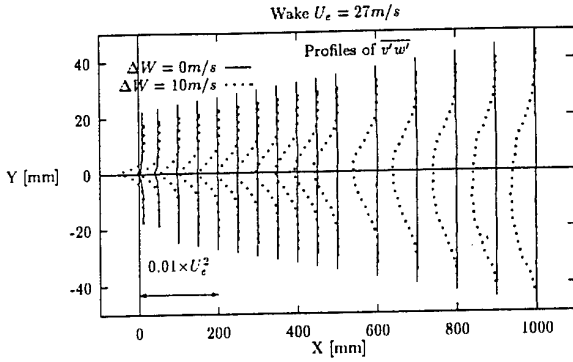


Figure 7: $\overline{v'w'}$ evolution with and without transverse shear.

$\overline{v'w'}$ profiles.

$\overline{v'w'}$ is the cross momentum which allows to quantify the azimuthal shear. We can observe in Fig 7, in the case without transverse shear, that $\overline{v'w'}$ profiles are almost zero.

At the contrary, in the case of cross-shear, the shear stress $\overline{v'w'}$ corresponds to the primary mean shear stress of a plane mixing layer (Fig. 7). Its maximum value remains constant, as it is the case for self-similar flows.

Considerations on the Reynolds tensor structure.

The comparison of the terms $\overline{u'^2}$, $\overline{v'^2}$, $\overline{w'^2}$ gives a good approach of the flow behavior in the similarity region.

In free shear flows, for a gradient $\partial \overline{U}/\partial y$, the experimental results of the literature show a consensus with the following relations:

$$\overline{u'^2} \simeq 1.7 \overline{v'^2} \simeq 1.4 \overline{w'^2} \quad (4)$$

Using this relation, we can define the two following quantities:

$$\psi_1 = \frac{\overline{w'^2}}{\overline{u'^2}} \simeq \frac{1}{1.4} \simeq 0.71, \quad \psi_2 = \frac{1.4 \overline{w'^2} + 1.7 \overline{v'^2}}{2 \overline{u'^2}} \simeq 1 \quad (5)$$

We can observe in Figs. 8-a) and 8-b) that the case without transverse shear ("pure wake") is in good agreement with the values given in (5).

In the case with transverse shear $\partial \overline{W}/\partial y$, the role of \overline{U} and \overline{W} are somewhat inverted. Consequently, we can guess the following relations:

$$\frac{1}{\psi_1} = \frac{\overline{w'^2}}{\overline{u'^2}} \simeq 1.4, \quad \psi_3 = \frac{1.4 \overline{u'^2} + 1.7 \overline{v'^2}}{2 \overline{w'^2}} \simeq 1 \quad (6)$$

The experimental results can be observed in Figs. 8-a) and 8-c). When the transverse shear is important, the quantity $\overline{w'^2}/\overline{u'^2}$ tends towards 1.4 and the ratio $\frac{1.4 \overline{u'^2} + 1.7 \overline{v'^2}}{2 \overline{w'^2}}$ towards 1.

Mixing lengths.

From $\overline{u'v'}$ and $\overline{v'w'}$, two mixing lengths l_{m12} and l_{m23} can be defined. The first one is associated with the wake and the other with the mixing layer. A simple Boussinesq's hypothesis can be applied:

$$\overline{u'u_j} = -\nu_{ij} \left(\frac{\partial \overline{U}_i}{\partial x_j} + \frac{\partial \overline{U}_j}{\partial x_i} \right) \quad (i, j) = (1, 2) \text{ and } (2, 3)$$

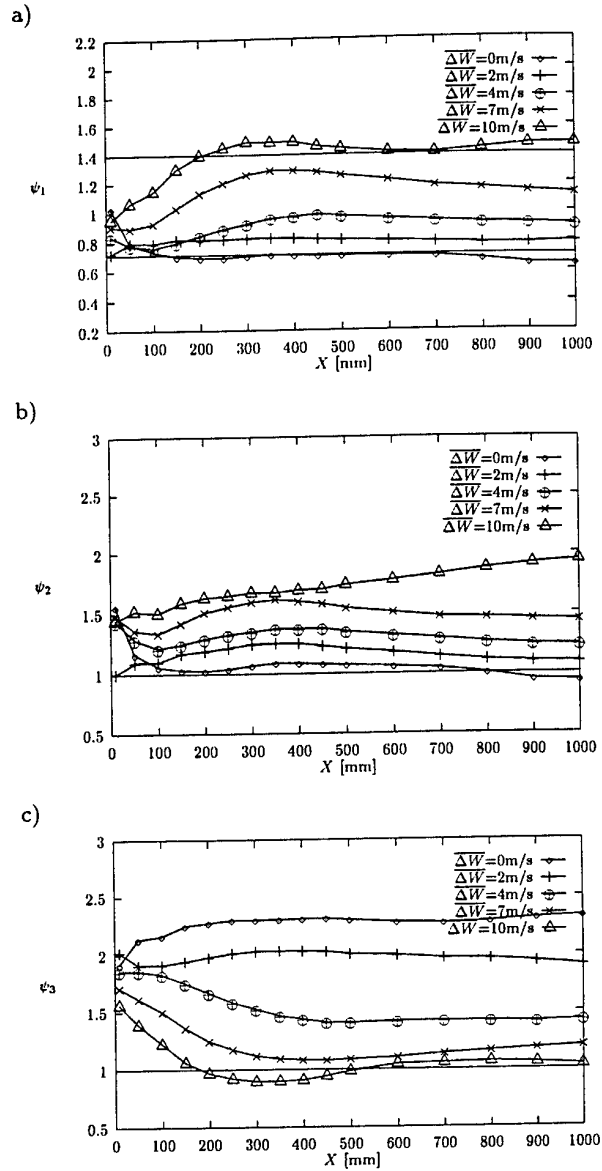


Figure 8: Order of magnitude between $\overline{u'^2}$, $\overline{v'^2}$, $\overline{w'^2}$.

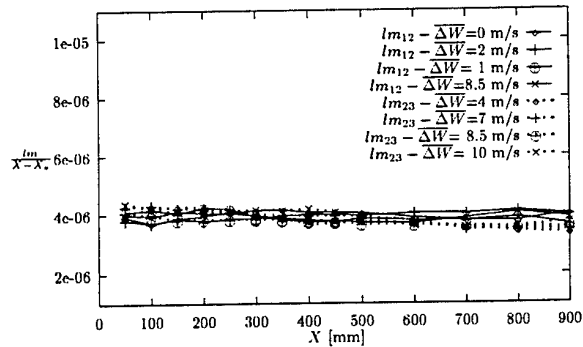


Figure 9: Evolution of the mixing lengths $l_{m12}/(x - x_o)$ and $l_{m23}/(x - x_o)$ with downstream distance x .

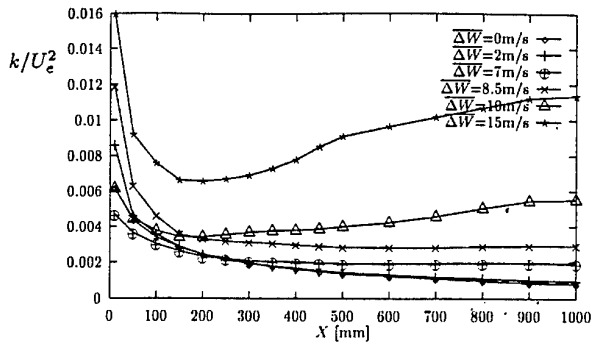


Figure 10: Evolution of maximum T.K.E (k) for various transverse shear

Where:

$$\nu_{12} = l_{m12}^2 \left| \frac{\partial \bar{U}}{\partial y} \right| \quad \nu_{23} = l_{m23}^2 \left| \frac{\partial \bar{W}}{\partial y} \right| \quad (7)$$

The downstream evolutions of the mixing lengths determined at the maximum radial gradient location are plotted in Fig. 9 for several values of transverse shear. The values are non-dimensionalized with the streamwise distance from the trailing edge. These two quantities characterizing the longitudinal shear (l_{m12}) and the transverse shear (l_{m23}), present rather small variations and converge towards a common value. The similar evolution for the mixing length l_{m12} and l_{m23} seems to indicate a similar growth for the two superimposed flows (wake and mixing layer) and a common turbulent length scale in the downstream and transverse directions.

Turbulent kinetic energy (T.K.E.).

Figure 10 represents the evolution of the maximum of the turbulent kinetic energy ($k = 1/2 (\overline{u'^2} + \overline{v'^2} + \overline{w'^2})$). The values are non-dimensionalized by the convective velocity U_e . In the similarity region, we observe that the value of k_{max} increases with the rate of transverse shear. Nevertheless, for each studied configuration, we notice a stabilization of this maximum beyond a certain distance. The final value is higher when the transverse shear is high.

Kinetic energy balance.

For the free shear flows, the T.K.E. equation can be schematically expressed as:

$$CONVECTION = PRODUCTION + DIFFUSION + REMAINDER$$

where

$$REMAINDER = DISSIPATION + PRESSURE TRANSPORT$$

The terms of convection, production and diffusion have been directly computed from the four-hot-wire probe data. The "remainder" has been evaluated by balancing the T.K.E. equation. Taking into account the highly 3D character of the flows, no attempt was made to estimate the dissipation. For example, the assumptions of isotropy of dissipative domain are not proven to be valid and the technique proposed by Wygnanski and Fiedler (1969) can be questionable for this flows.

Two characteristic balances are shown in Figs. 11 and 12. The first case, without transverse shear ($\Delta \bar{W} = 0$ m/s) has been chosen as a reference data that can be compared with the "classical" plane wake. The second case ($\Delta \bar{W} =$

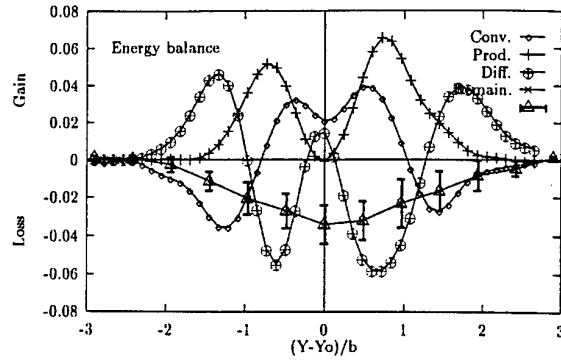


Figure 11: Kinetic energy balance without transverse shear.

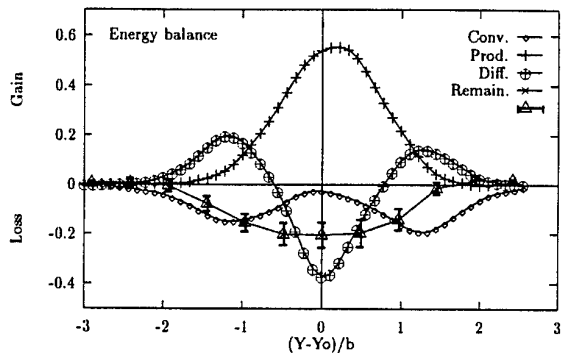


Figure 12: Kinetic energy balance with transverse shear.

10m/s) is used to evaluate the influence of the transverse shear on the development of a "wake" type flows. Each term has been non-dimensionalized by the ratio $b / \Delta \bar{U}^3$.

We can check in Fig. 11 that the overall behavior of the balance for the case $\Delta \bar{W} = 0$ is similar to the one obtained in the developed region of a plane wake (see Rodi (1975)). In particular, a negligible production can be observed at the location where the mean velocity deficit is maximum (here the axis). When transverse shear is added, dramatic modifications of the T.K.E. balance are observed, as plotted in Fig. 12. The shape of the different terms seems to be then similar to the one observed in a "classical" mixing layer (see Rodi (1975)). Moreover, it should be noticed that the level of the terms of the balance are increased by a factor 10. This change of behavior implies for example, that without transverse shear, the convection term is mainly a gain of energy when, with transverse shear, it becomes a loss. In the same way, the production of T.K.E., which is zero at the location $y = 0$ in the case where $\Delta \bar{W} = 0$ m/s, becomes the most important term when a transverse shear is imposed. This behavior is due to the fact that the gradient $\partial \bar{W} / \partial y$ is maximum at this location. The energy losses due to the diffusion in the external parts are maximum when the shear are maxima. Thus, in the case without transverse shear, the term of diffusion is maximum at $\frac{y - y_0}{b} \simeq \pm 1,5$ and at the location $y = 0$ for the case with transverse shear.

CONCLUSION

This study contributes to a better understanding of the complex phenomena produced by addition of a transverse shear on the development of the free shear flows.

That configuration allows to built an experimental data base on the evolution of the axisymmetric mixing layer between coaxial jets with swirl.

Among all the possibilities given by the facility, only the "wake" configuration has been studied. Thus in all the investigations achieved, the exit velocities of the two jets are equal and only the swirl number of the inner and external flows are changed (in opposite sense).

The results show from the mean velocity profiles, the second order momentum and the energy balances a change of state when a transverse shear is applied. In the near field, the flow is dominated by the trailing edge effects then can be seen as a wake flow under transverse shear. In the far field, when the wake deficit has nearly vanished, we observe a transition which brings the flow to a state similar to a mixing layer. This flow can be seen as a temporally evolving mixing layer, where the quasi-uniform convection velocity plays the exact role of time with a Taylor hypothesis. This detailed investigation of a "pure shear layer" allows to provide a data base that can be directly compared with theoretical or numerical simulations.

Acknowledgements: Professor H.E. Fiedler and C.N. Nayeri are gratefully acknowledged for fruitful comments and enlightening discussions

REFERENCES

S. Béharelle, Oct. 1996, "Réalisation et mise en œuvre d'une sonde anémométrique à quatre fils chauds", *tech. rep. LEA - CEAT Poitiers*.

H. H. Bruun, 1995, "Hot-wire Anemometry - Principles and signal analysis", *Oxford university press*, Three-component velocity measurements, pages 177-207.

J. E. Hackett and D.K. Cox, 1970, "The three-dimensional mixing layer between two grazing perpendicular streams", *J. of Fluid Mech*, Vol. 43, part 1, pp 77-96.

J.O. Hinze, 1975, "Turbulence", McGraw-hill Series in Mechanical Engineering, *Kingsport Press*, second edition.

L. Jacquin, O. Leuchter, and P. Geffroy, 1995, "Use of quadripole hotwire probes for studying turbulent flows", *La Recherche Aéronautique*, Vol. 6, pp 427-444.

A. Michalke, 1971, "Instabilität eines kompressiblen runden freistrahls unter berücksichtigung des einflusses der strahlgrenzschichtdicke", *Z. Flugwiss*, Vol. 19, pp 319-328.

C. Nayeri, S. Béharelle, J. Delville, J.-P. Bonnet, and H.E. Fiedler, 1996, "Experimental investigation of the axisymmetric shear layer between coaxial jets with swirl", *In Proc. ETC-VI*, Kluwer Academic Publishers.

W. Rodi, 1975, "A Review of Experimental Data of Uniform Density Free Turbulent Boundary Layers", *Theory, Measurement and Applications*, Academic Press, ed. B.E. Launder, Vol. 1, pp 79-165.

I. Wygnanski and H.E. Fiedler, 1969, "The two-dimensional mixing region", *J. of Fluid Mech*, Vol. 41, part 2, pp 327-361.

SESSION 3 - INTERNAL AERODYNAMICS

SIMULATION OF FLOW THROUGH CIRCULAR TO RECTANGULAR TRANSITION DUCT USING NON-LINEAR SECOND ORDER MOMENT CLOSURES

Claus Eifert, Dirk G. Pfuderer, Johannes Janicka

Fachgebiet Energie- und Kraftwerkstechnik

Technische Hochschule Darmstadt

Petersenstr. 30

D-64287 Darmstadt

Germany

ABSTRACT

A computational study of turbulent three-dimensional flow in a circular to rectangular transition duct has been undertaken. Four non-linear second moment closures are examined. The models differ mainly by the order of approximations in terms of the Reynolds stress anisotropy tensor of the slow-part and the rapid-part of pressure strain correlation. The computation of the complex flow field has been carried out with a numerical code that applies generalized curvilinear coordinates. The investigation reveals, that those non-linear closures which perform well in rapidly distorted flows, are superior in predicting the mean flow field and the turbulence field of the transition duct. This emphasizes the need for closures, which account for rapid strain, since such situation may also occur in technical flows.

INTRODUCTION

Recent developments in second order moment closure (SMC) modeling demonstrated that non-linear dependency of pressure-strain correlation approximations on the anisotropy tensor seems to be required, if basic turbulent flow behaviors are to be properly described, i.e. i) the non-linear return to isotropy, ii) the bifurcation effects under system rotation, iii) the realizability constraints and iv) the rapid distortion limit.

Hitherto the performance of non-linear SMC's was mainly tested for homogeneous axisymmetric strain and plane strain, rotating and non-rotating shear flows, pipe/plane channel flow and plane/axisymmetric free shear flows. For such simple two-dimensional flows the programming effort is tolerable and theoretical knowledge can be used for the analysis, e.g. long-time equilibrium states or self-preserving states. These studies revealed that non-linear SMC's can capture most of the basic and simple flows better than the linear ones, see Speziale et al. (1991), Johansson and Hallbäck (1994), Pfuderer et al. (1996) and (1997).

Four models that showed the best predictive capabilities are scrutinized in this paper for complex three-dimensional flow. The SMC's by Speziale et al. (1991) (SSG), by Launder and coworkers (cf. Launder and Li (1994)) (LL), by Hallbäck and Johansson (Johansson and Hallbäck (1994) and Hallbäck et al. (1995)) (HJ) and a model by the present authors Pfuderer, Eifert and Janicka (1997) (PEJ) are investigated. The SSG model as well as a truncated form of the LL model performed best in predicting plane and round jets (Pfuderer et al. (1996)) and in the

calculations of plane channel flow and mixing layer (Demuren and Sarkar (1993)). The PEJ model is realizable and is superior to the SSG model in basic flows. The HJ model is of the highest accuracy in the rapid distortion limit compared to other SMC's.

The effort of implementation prevented their application in a fully elliptic three-dimensional code. One notable exception is the use of the LL model (Iacovides et al. (1996)). Better results compared to a linear SMC are reported for the turbulence field and heat transfer in a flow through a U-bend.

An experimental investigation which was comprehensive enough to be applied as benchmark test for SMC's was the report by Davis and Gessner (1992), who measured a circular to rectangular transition duct at a Reynolds-number $Re = 390,000$. Fields of application for ducts with changing cross-section area are passages of combustion chambers or ventilation systems. This duct has nearly constant cross-section-area, while changing from a circular to a rectangular shape. Since the upper wall converges while the other diverges convex and concave streamline curvature appears which attenuates and amplifies turbulence. The secondary flow arises from transverse pressure gradients. Near the sidewalls it develops two vortex pairs which distort the streamwise velocity profiles.

This flow was computed by Demuren (1993), Lien and Leschziner (1993) and Sotiropoulos and Patel (1994). Demuren as well as Lien and Leschziner reported that the standard k - ϵ -model does not capture the distortion of streamwise velocity profile, because the secondary flow was underpredicted. The same was shown by Demuren (1993) for the linear SMCs. Sotiropoulos and Patel (1994) used a linear low-Reynolds-number SMC including explicitly geometry dependent wall reflection terms. Despite satisfying results of the meanflow quantities, the decay of turbulence was stronger than indicated by the experiment.

This work pursues to investigate, whether the four mentioned non-linear SMC's (SSG, LL, HJ and PEJ) are of advantage in simulating and predicting transition duct flows.

TURBULENCE CLOSURES

The transport equation for the Reynolds-stress tensor for incompressible flow can be written as:

$$D\overline{u_i u_j} / Dt = P_{ij} + \Pi_{ij}^{(r)} + \Pi_{ij}^{(s)} + T_{ij} + D_{ij} - E_{ij}. \quad (1)$$

The closed terms are the production

$$P_{ij} = -(\overline{u_i u_k} U_{j,k} + \overline{u_j u_k} U_{i,k}) \quad (2)$$

and the molecular diffusion

$$D_{ij} = (\nu (\overline{u_i u_j})_{,k})_{,k} \quad (3)$$

The non-closed terms are the pressure-strain, divided into slow part $\Pi_{ij}^{(s)}$ and rapid part $\Pi_{ij}^{(r)}$ (omitting special treatment of the surface integral), the turbulent transport term T_{ij} and the mechanical dissipation rate tensor E_{ij} . It is useful to decompose the dissipation rate tensor into an isotropic and an anisotropic part:

$$E_{ij} = \frac{2}{3} \varepsilon \delta_{ij} + E_{ij}^{(dev)} \quad \text{with} \quad E_{ij}^{(dev)} = \varepsilon e_{ij}, \quad (4)$$

where ε is half the trace of ε_{ij} and e_{ij} is the dimensionless anisotropic part of ε_{ij} . The analysis of the transport equation of the turbulent kinetic energy k , which is half the trace of $\overline{u_i u_j}$, reveals that e_{ij} and Π_{ij} only redistribute the Reynolds-stresses, i.e. these terms can be modeled simultaneously.

Pressure-strain correlation modeling assumes, that the integrals arising as solution for this term can be sufficiently described linear in terms of k/ε , the strain-tensor $S_{ij} = 0.5 (U_{i,j} + U_{j,i})$ and the rotational-tensor $\Omega_{ij} = 0.5 (U_{i,j} - U_{j,i})$ and non-linear in terms of the anisotropy tensor $a_{ij} = \overline{u_i u_j}/k - 2/3 \delta_{ij}$, and its invariants $II = a_{ij} a_{ji}$, $III = a_{ij} a_{jk} a_{ki}$. Hence the most general form of the rapid pressure-strain part is

$$\begin{aligned} \Pi_{ij}^{(r)} = & k \cdot S_{pq} [Q_1 \delta_{ip} \delta_{jq} \\ & + Q_2 (a_{ip} \delta_{jq} + a_{jp} \delta_{iq} - 2/3 a_{pq} \delta_{ij}) + Q_3 a_{pq} a_{ij} \\ & + Q_4 (a_{iq} a_{jp} - 1/3 a_{pk} a_{kq} \delta_{ij}) + Q_5 a_{pl} a_{lq} a_{ij} \\ & + (Q_5 a_{pq} + Q_6 a_{pl} a_{lq}) (a_{ik} a_{kj} - 1/3 II \delta_{ij})] \\ & + k \cdot \Omega_{pq} [Q_7 (a_{ip} \delta_{jq} + a_{jp} \delta_{iq}) \\ & + Q_8 a_{pk} (a_{jk} \delta_{iq} + a_{ik} \delta_{jq}) \\ & + Q_9 a_{pk} (a_{jk} a_{iq} + a_{ik} a_{jq})] \end{aligned} \quad (5)$$

Commonly the slow pressure-strain part is modeled together with the energy interchanging deviatoric part of the mechanical dissipation rate tensor using the general form

$$\Pi_{ij}^{(s)} - E_{ij}^{(dev)} = -\varepsilon [C_1 a_{ij} + C_2 (a_{ik} a_{kj} - 1/3 II \delta_{ij})], \quad (6)$$

assuming that both are associated with the same turbulent length and time scales and the anisotropy a_{ij} .

The turbulent transport consists of the velocity triple correlations and the pressure diffusion terms. For confined flows the model of Mellor and Herring (1973),

$$T_{ij} = (C_s k^2 / \varepsilon [\overline{u_i u_j k} + \overline{u_k u_j i} + \overline{u_i u_k j}])_{,k}, \quad (7)$$

was preferred, because it yields better results for the plane channel flow than other proposals. The model constant C_s is calculated from the consistency condition,

$$C_s / C_s = 10 \left(\sqrt{4C_s^2 + 1} - 2C_s \right) \quad (8)$$

developed by Lele (1985).

The modeled transport equation of the dissipation rate is given by

$$D\varepsilon/Dt = \left([C_\varepsilon k^2 / \varepsilon + \nu] \varepsilon_{,k} \right)_{,k} + \varepsilon / k (C_{\varepsilon_1} P_{kk} / 2 - C_{\varepsilon_2} \varepsilon). \quad (9)$$

This implies the assumption that the dissipation takes place at small scales, which are locally isotropic at high Reynolds-numbers, hence $E_{ij} = 2/3 \varepsilon \delta_{ij}$ and $E_{ij}^{(dev)} = 0$. C_ε was chosen to

be consistent with the law of the wall for a plane boundary layer in turbulent equilibrium ($P_{kk}/2 = \varepsilon$) with constant anisotropy levels, i.e.

$$C_\varepsilon = (C_{\varepsilon_1} - C_{\varepsilon_2}) \frac{a_{12}^3}{\kappa^2} \quad \text{with} \quad a_{12} = -0.3. \quad (10)$$

Here $\kappa = 0.4$ is the von Kármán constant.

The selected SMC's for the present test case are the model by Speziale et al. (1991) (SSG), the model used by Launder and Li (1994) (LL), the model of Hallböck and Johansson (Johansson and Hallböck (1994) and Hallböck et al. (1995)) (HJ) and a closure by the present authors Pfuderer, Eifert and Janicka (1996) (PEJ). For details about the performance of these models in simple shear flows the reader is referred to Demuren and Sarkar (1993) and Pfuderer et al. (1996). The model coefficients are summarized as follows, with $Re_\tau = 4k^2/(9\varepsilon)$ and $F = 1 + 9/8(III - II)$:

SSG: $C_\varepsilon = 0.066$, $C_{\varepsilon_1} = 1.44$, $C_{\varepsilon_2} = 1.83$, $C_1 = 1.7$, $C_2 = -1.05$, $Q_1 = 0.8 - 0.65\sqrt{II}$, $Q_2 = 0.625$, $Q_3 = 0.9$, $Q_7 = -0.2$, $Q_4 = Q_5 = Q_6 = Q_8 = Q_9 = 0$

LL: $C_\varepsilon = 0.085$, $C_{\varepsilon_1} = 1.0$, $C_{\varepsilon_2} = 1.92/(1 + 0.7F\sqrt{II})$, $C_1 = 1 + 3.1\sqrt{F \cdot II}$, $C_2 = 3.72\sqrt{F \cdot II}$, $Q_1 = 0.751 + 0.146II + 0.11III$, $Q_2 = 0.71 + 0.138II$, $Q_3 = 0.748$, $Q_4 = 0.115$, $Q_5 = -0.275$, $Q_6 = 0$, $Q_7 = -0.952 - 1.063II$, $Q_8 = -0.512$, $Q_9 = -4.15$

HJ: $C_\varepsilon = 0.066$, $C_{\varepsilon_1} = 1.44$, $C_{\varepsilon_2} = 1.83$, $C_1 = 2.4(Re_\tau/(20\pi) + 9[0.00775Re_\tau/\pi]^2)^{0.5} - 0.0558Re_\tau/\pi + 0.5 + 3II/8$, $C_2 = -0.75$, $Q_1 = 0.8 - 0.243II - 1.01II^2 - 0.146III$, $Q_2 = 1.71 - 0.682II - 5.58III$, $Q_3 = -1.98 + 4.05II$, $Q_4 = 4.57 - 7.92II$, $Q_5 = 0.365$, $Q_6 = 14$, $Q_7 = 0.865II - 1.23III$, $Q_8 = -1.83 + 2.03II$, $Q_9 = 3.94$

PEJ: $C_\varepsilon = 0.066$, $C_{\varepsilon_1} = 1.44$, $C_{\varepsilon_2} = 1.83$, $C_1 = 3.83 + 1.25II$, $C_2 = -2.5$, $Q_1 = 0.8 - 0.259II - 0.449III^2 - 0.279III$, $Q_2 = 1.18 - 0.206II - 2.83III$, $Q_3 = -1.71 + 1.79II$, $Q_4 = 2.48 - 2.31II$, $Q_5 = -0.697$, $Q_6 = -5$, $Q_7 = -0.419 - 2II - 1.09III$, $Q_8 = -1.41 - 0.897II$, $Q_9 = -6$

NUMERICAL PROCEDURE

Setup

The calculations were performed with XSTREAM, which is a modified extension of a k - ε -model version of the STREAM code developed by Lien and Leschziner (1994). The transport equations are written in generalized curvilinear coordinates with dependent tensorial variables kept in cartesian components. The code uses the finite volume method and a single block structured collocated grid arrangement for all dependent variables. The convection terms are discretized with the aid of a second order accurate bounded TVD/MUSCL scheme by van Leer (1979). The pressure and velocity fields are achieved by the use of a pressure correction algorithm. Chequerboard oscillations of the pressure and velocity field are avoided applying of the non-linear interpolation method of the cell face velocities by Rhie and Chow (1983) in a form proposed by Majumdar (1988), which is independent of the underrelaxation parameter of the iterative velocity calculation. To prevent the same stability problems with the Reynolds-stresses in the momentum equations a similar interpolation method to the above mentioned is applied (cf. Obi et al. (1991)). Apparent viscosities deduced from the Reynolds-stress equations eliminate the decoupling of the Reynolds-stresses and the velocity components. All equations are segregated solved using the alternate-direction-implicit (ADI) method embedded in an iterative process.

Boundary Conditions and Grid

The test case considered is a circular to rectangular transition duct. Measurements of the velocity, pressure and turbulence field were carried out by Davis and Gessner (1992) using HWA and

Pitot tubes. Due to flow symmetry only a quarter of the duct has been discretized. The computational domain, the measurement stations as well as a typical cross-sectional view of the grid are plotted in Fig. 1.

Inlet (Station 1) conditions for the velocity and the Reynolds-stress have been extracted from experimental data. The measurements indicate, that the law of the wall is valid in a small region, i.e. $30 \leq y^+ \leq 80$. Therefore all near wall grid points are carefully set to justify the wall-function approach. The Reynolds-stresses in the near wall cells are calculated by solving the k -equation for the near wall cells and by assuming the anisotropy levels of a plane channel boundary layer in turbulent equilibrium, i.e. $P_{kk}/2 = \epsilon$. At the cross sections $y = 0$ and $z = 0$ symmetry conditions have been applied. Finally, at the exit (Station 6) the streamwise gradients for all variables have been set to zero.

Test calculations were performed on three grids with $(45 \times 20 \times 20)$, $(50 \times 30 \times 35)$ and $(60 \times 35 \times 40)$ cells. Nearly no differences are found between the results of the medium and the finest grid. Hence the use of the medium grid seems to be appropriate. These calculations are presented in the following.

RESULTS AND DISCUSSION

All models reproduce the shape of the measured pressure profiles in the transition duct, see Fig. 2, but the computed overall pressure drop along the duct is slightly higher than measured.

The computed and measured skin-friction coefficient $c_f = \tau_{\text{wall}} / (1/2 \rho U_b^2)$ distributions along the wall at stations 5 and 6 are depicted in Fig. 3. It should be noted that the skin-friction was measured by using a Preston tube, a method which relies on the assumption that the flow obeys the law of the wall. Due to the use of the log-law assumption the calculated wall shear stresses are directly tied to the turbulent kinetic energy in the wall cells. At station 5 the HJ predicts best the skin-friction, whereas it yields as well as the LL model lower values at station 6, i.e. the turbulent kinetic energy decays too fast at the upper duct wall. All models reveal fairly close the measured peak value ($s/s_{\text{ref}} \approx 0.85$) near the vortex at the sidewall.

The transverse pressure gradients force the fluid to move sideways and hence may essentially cause a skew-induced contra-rotating vortex pair near each diverging sidewall. These vortices transport low axial momentum fluid from the boundary layer along the semi major axis to duct center and, thus, flatten the axial velocity profile. This process is depicted in Fig. 4. The flat spot of the axial velocity profile starts at station 5 and increases to station 6. While all models lead to similar and satisfying results at stations where no vortex is present, none of the models reproduce the correct axial velocity profile at station 5. At station 6 the influence of the vortex on the axial velocity profile is evident. The HJ model performs best followed by the LL and PEJ model, while the SSG model returns a far too weak vortex to cause a noticeable distortion of the axial velocity profile, see Fig. 5. In contrast to the measurements all models predict a second weak counterrotating vortex at the upper left of each duct quarter in Fig. 5. This turbulence driven vortex arrangement is typical for non-circular duct flows.

Besides the mean flow the turbulence field is also distorted by extra rates of strain associated with the vortex pairs. In Fig. 6 and Fig. 7 the non-zero Reynolds-stresses and the turbulent kinetic energy are plotted along the semi major axis. At station 5 the turbulent kinetic energy and all Reynolds-stresses exhibit a second maximum beyond the boundary layer in the center of the vortex pair. This is not returned by the computations, since all models insufficiently predict the onset of the main vortex. At station 6 the maxima of Reynolds stresses and kinetic energy are further amplified and are shifted towards the center of the duct. This is reproduced by the SMC's but position and magnitude of the peak are not correct. It is also evident, that the different magnitudes of the peaks of the normal stresses, $\overline{uu} > \overline{vv} > \overline{ww}$, are not captured by the models. Especially the \overline{ww} peak is strongly underpredicted.

Overall, the LL model performs the best. Surprisingly the HJ predictions show the largest deviations from experiments in the

Reynolds stresses although the vortex and mean velocities are well reproduced.

Since the mean flow is strongly strained in the transition section, it is expected that the rapid-part dominates in the pressure strain correlation. This may be confirmed by computed values of the strain parameter $S = \sqrt{2S_{ij}S_{ji}}k/\epsilon$, see Fig. 8. For each model $S \approx 20$ at Station 4 in the core region of the duct. At Station 5 the core value decayed to $S \approx 6$ while in the vortex region $S \approx 5$. At Station 6 the rate of strain in the duct core diminishes continuously and $S \approx 8$ in the vortex near the wall. There is some kind of relaxation, since the geometrical distortion section of the duct ends at station 5. Thus, the fairly good prediction of the mean flow components by HJ model compared to the LL model and PEJ model seems to root in the rapid part modeling, since $S \approx 20$ is 5 to 10 times higher than in typical shear flow situations, except the near wall region. The HJ model was calibrated by the use of the rapid distortion theory.

Obviously the secondary flow and hence the depression of the axial velocity profile is sensitive to the turbulence structure of the flow, i.e. the anisotropy. However, due to the non-linear interaction of pressure driven and turbulence driven vortex generation it is not possible to separate these contributions quantitatively.

CONCLUSIONS

Three-dimensional finite volume computations on a collocated grid using generalized curvilinear coordinates have been performed for a circular to rectangular transition duct flow with a rapidly distorted mean flow. This flow shows causes a pressure-driven cross-flow inducing a counter rotating vortex pair. Four non-linear Reynolds-stress closures were examined for this challenging flow case. The comparison of the models with the experimental data and previously reported calculations (Lien and Leschziner (1993), Demuren (1993)) revealed that the mean flow distortion can be better predicted with an non-linear SMC than with the k - ϵ -model or a linear SMC. The HJ model performs best for mean flow field quantities and the SSG model worst. However, the LL or PEJ model, which are almost close to the HJ-predictions, are recommended. Both SMC's were developed under the primary objective to describe as much different states of turbulent flows as possible, while the rapid-part of the HJ model was only calibrated to the rapid distortion limit.

However, some weaknesses of the current investigated models are evident. In contrast to the experimental findings the predicted turbulent kinetic energy maximum decays for all models too fast. The underpredicted values of the turbulent energy in the vortex core might be related to deficiencies in the ϵ -equation which is mainly developed for non-rotating flows with moderate strain. Generally, the pressure-strain modeling should be more sensitized to rapid distortion effects.

Although the law of the wall was applied the mean flow distortion effect due to the vortex pairs can be qualitatively captured with a well-calibrated non-linear SMC. Hence, the correct calculation of the redistribution of the Reynolds-stress tensor components away from the wall is also important in such flows. The linear SMC of Sotiropoulos and Patel (1994) needed a low-Reynolds-number correction and extra wall reflection terms to reproduce the mean flow distortion. The present results indicate that the ambiguous wall reflection term modeling can be replaced by non-linear redistribution term modeling.

Finally, these findings should provide encouragement for the application of non-linear SMC's to computations involving complex geometries of technical interest.

Acknowledgements : The authors are grateful to Dr. D.O. Davis (NASA Lewis Research Center) and Prof. F.B. Gessner (University of Washington) for kindly providing us their experimental data of flow through a circular to rectangular transition duct.

This work was supported by the Deutsche Forschungsgemeinschaft under contract number JA 544/8-1.

Station 5 ($x/R = 4$)

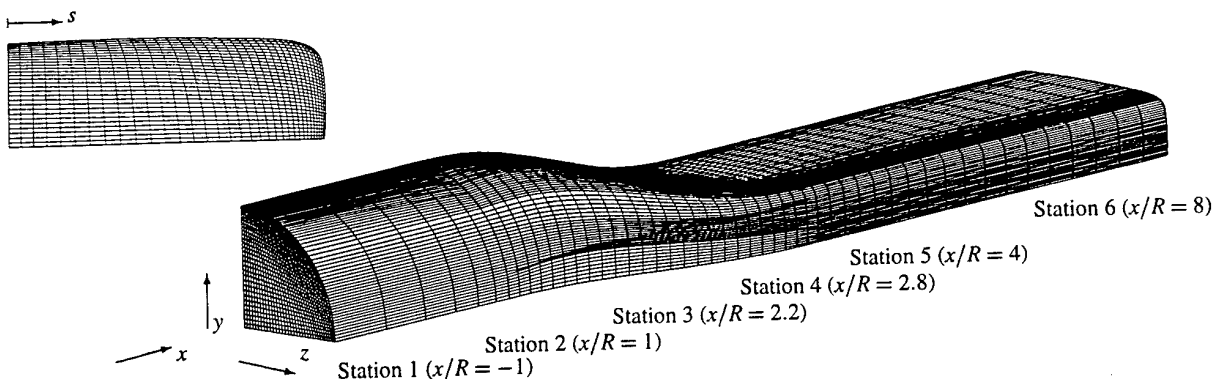


FIGURE 1. CIRCULAR TO RECTANGULAR TRANSITION DUCT: COMPUTATIONAL DOMAIN ($-1 \leq x/R \leq 8$), MEASUREMENT STATIONS, MESH AT CROSS-SECTION $x/R = 4$ (STATION 5).

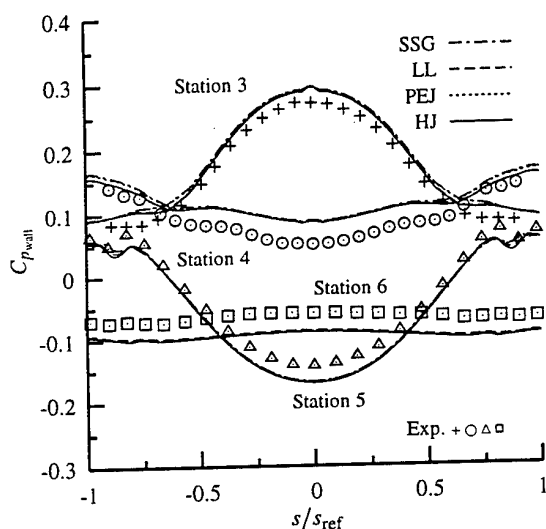


FIGURE 2. WALL PRESSURE COEFFICIENTS AT 4 AXIAL POSITIONS (s = WALL COORDINATE WITH $s = 0$ AT THE MAJOR SYMMETRY PLANE ($z = 0$), $s_{ref} = 1/4$ OF CIRCUMFERENTIAL DUCT LENGTH OF THE CORRESPONDING STATION).

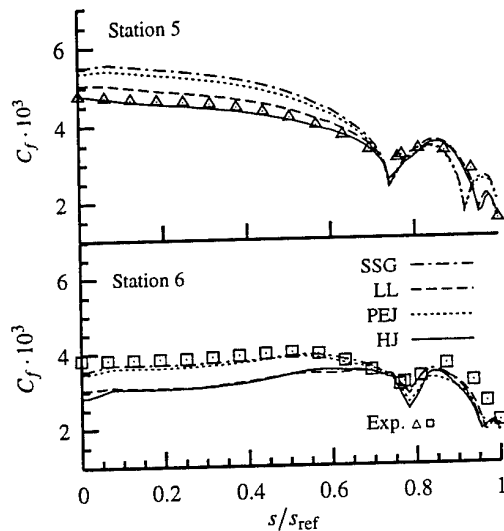


Figure 3. SKIN-FRICTION COEFFICIENTS (SEE FIG. 2 FOR DEFINITION OF s/s_{ref})

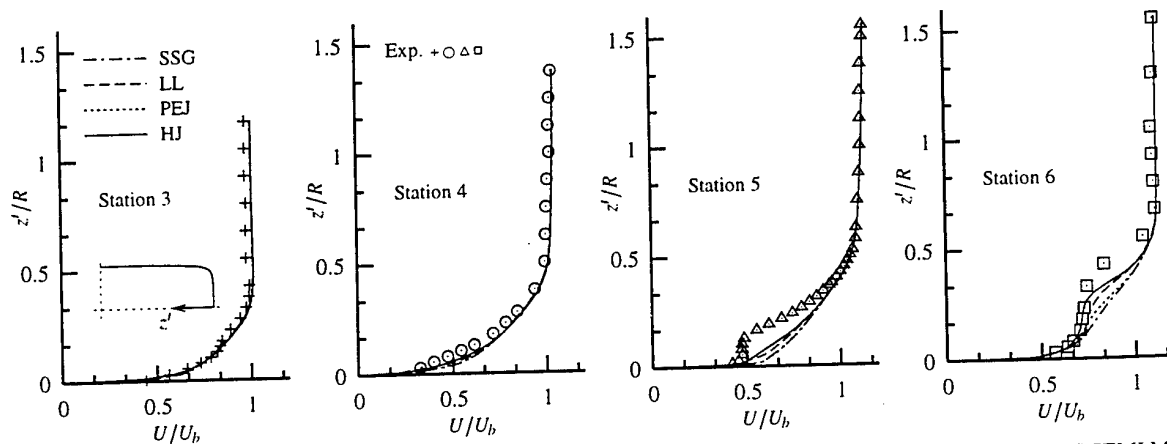


FIGURE 4. NORMALIZED STREAMWISE MEAN VELOCITY PROFILES (U_b = BULK VELOCITY) ALONG THE SEMI MAJOR AXIS AT 4 AXIAL POSITIONS.

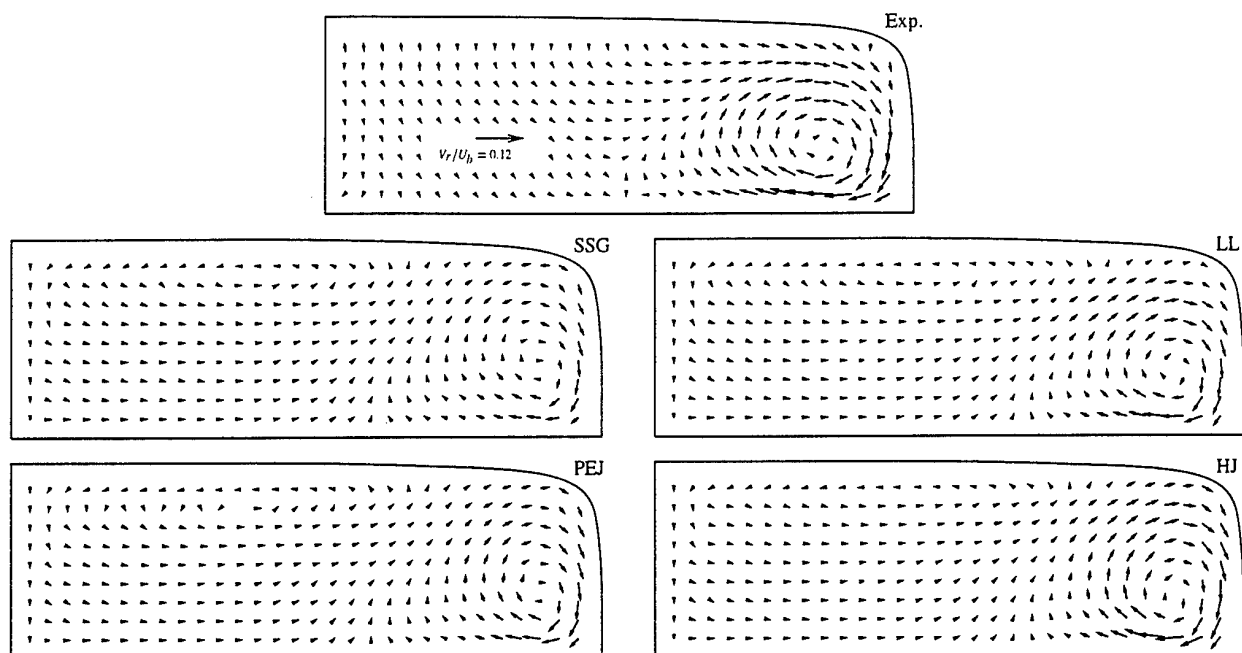


FIGURE 5. NORMALIZED CALCULATED AND MEASURED TRANSVERSE MEAN VELOCITY FIELD AT STATION 6 (U_b =BULK VELOCITY).

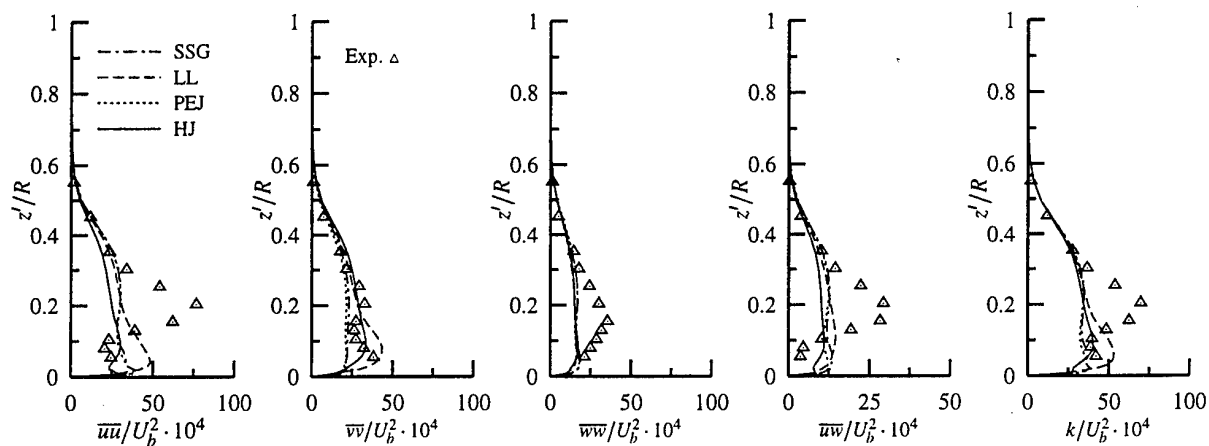


FIGURE 6. NORMALIZED REYNOLDS-STRESS TENSOR AND TURBULENCE KINETIC ENERGY PROFILES ALONG THE SEMI MAJOR AXIS AT STATION 5.

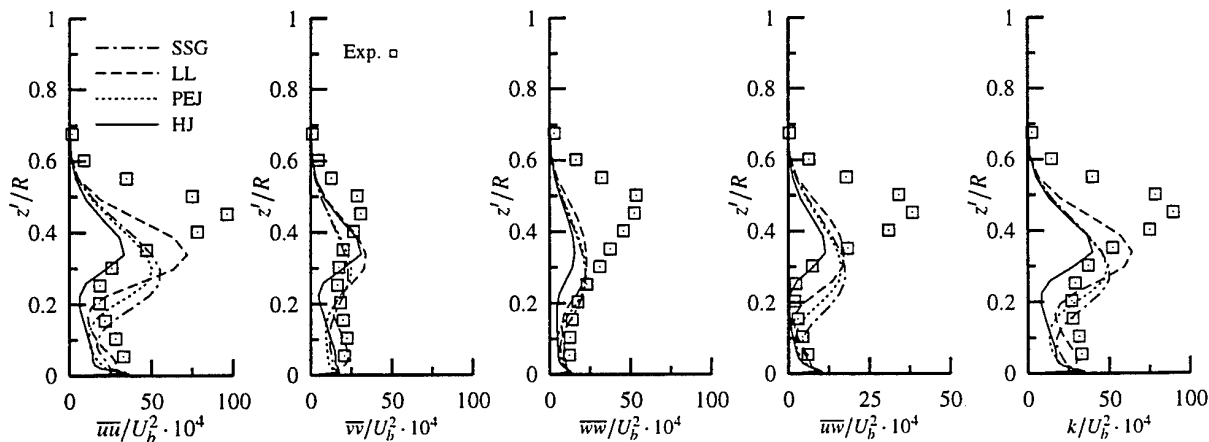


FIGURE 7. NORMALIZED REYNOLDS-STRESS TENSOR AND TURBULENCE KINETIC ENERGY PROFILES ALONG THE SEMI MAJOR AXIS AT STATION 6.

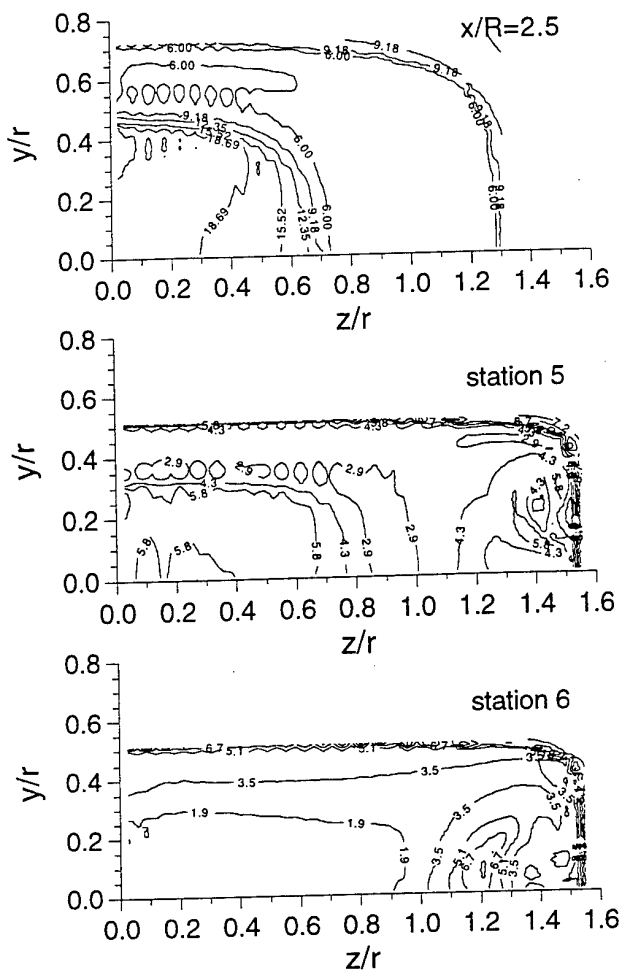


FIGURE 8. CALCULATED STRAIN PARAMETER $S = \sqrt{2S_{ij}S_{ij}} k / \epsilon$ AT THREE DIFFERENT STATIONS.

REFERENCES

- Davis, D.O. and Gessner, F.B., 1992, "Experimental investigation of turbulent flow through a circular-to-rectangular transition duct," *AIAA J.*, Vol. 30, pp. 367-375.
- Demuren, A.O., 1993, "On the generation of secondary motion in circular-to-rectangular transition ducts," AIAA-93-0681, AIAA.
- Demuren, A.O. and Sarkar, S., 1993, "Study of second-moment closure models in computations of turbulent shear flows," In Rodi, W., Martelli, F., editor, *Engineering Turbulence Modelling and Experiments 2*, pp. 53-62, Elsevier, Amsterdam.
- Hallböck, M., Sjögren, T. and Johansson, A.V., 1995, In Durst, F., Friedrich, R., Launder, B.E., Schmidt, F.W., Schumann, U. and Whitelaw, J.H., editor, *Turbulent Shear Flows 9*, Selected Papers from the 8th International Symposium on Turbulent Shear Flows, chapter Part I, Closures and Fundamentals, pp. 21-32, Springer-Verlag, Berlin.
- Iacovides, H., Launder, B.E. and Li, H.Y., 1996, "Second-moment computations of flow and heat transfer through U-bends of moderate curvature," In Rodi, W., Bergeles, G., editor, *Engineering Turbulence Modelling and Experiments 3*, pp. 29-38, Elsevier, Amsterdam.
- Johansson, A.V. and Hallböck, M., 1994, "Modelling of rapid pressure-strain in Reynolds-stress closures," *J. Fluid Mech.*, Vol. 269, pp. 143-168.
- Launder, B.E. and Li, S.-P., 1994, "On the elimination of wall-topography parameters from second-moment closure," *Phys. Fluids A*, Vol. 6, pp. 999-1006.
- Lele, S.K., 1985, "A consistency condition for Reynolds stress closures," *Phys. Fluids*, Vol. 28, pp. 64-68.
- Lien, F.-S. and Leschziner, M.A., 1993, "Computational modelling of 3d turbulent flow in s-diffuser and transition ducts," In Rodi, W., Martelli, F., editor, *Engineering Turbulence Modelling and Experiments 2*, pp. 217-228, Elsevier, Amsterdam.
- Lien, F.S. and Leschziner, M.A., 1994, "A general non-orthogonal collocated FV algorithm for turbulent flow at all speeds incorporating second-moment closure," *Comp. Meths. Appl. Mech. Eng.*, Vol. 114, pp. 123-148.
- Majumdar, S., 1988, "Role of underrelaxation in momentum interpolation for calculation of flow with nonstaggered grids," *Num. Heat Trans.*, Vol. 13, pp. 125-132.
- Mellor, G.L. and Herring, H.J., 1973, "A survey of the mean turbulent closure models," *AIAA J.*, Vol. 11, pp. 590-599.
- Obi, S., Perić, M. and Scheuerer, G., 1991, "Second-moment calculation procedure for turbulent flows with collocated variable arrangement," *AIAA J.*, Vol. 29, pp. 585-590.
- Pfuderer, D.G., Eifert, C. and Janicka, J., 1996, "A comparison of linear and non-linear second-order closure models applied to plane and round jets," In Rodi, W., Bergeles, G., editor, *Engineering Turbulence Modelling and Experiments 3*, pp. 19-28, Elsevier, Amsterdam.
- Pfuderer, D.G., Eifert, C. and Janicka, J., 1997, "A non-linear second moment closure consistent with shear and strain flows," *AIAA J.*, in press.
- Rhie, C.M. and Chow, W.L., 1983, "Numerical study of the turbulent flow past an airfoil with trailing edge separation," *AIAA J.*, Vol. 21, pp. 1525-1532.
- Sotiropoulos, F. and Patel, V.C., 1994, "Prediction of turbulent flow through a transition duct using a second-moment closure," *AIAA J.*, Vol. 32, pp. 2194-2204.
- Speziale, C.G., Sarkar, S. and Gatski, T., 1991, "Modelling the pressure-strain correlation of turbulence: an invariant dynamical systems approach," *J. Fluid Mech.*, Vol. 227, pp. 245-272.
- van Leer, B., 1979, "Towards the ultimate conservative difference scheme. V. A second-order sequel to Godunov's method," *J. Comp. Phys.*, Vol. 32, pp. 101-136.

The Use of Linear and Non-linear Low Reynolds Number Models in the Calculations of Flow in a RAE M2129 S-Duct

A. J. Marquis⁽¹⁾ and L. Y. Ong⁽²⁾

Department of Mechanical Engineering
Imperial College of Science, Technology and Medicine
Exhibition Road
London SW7 2BX, England

(1) Lecturer; e-mail: a.marquis@ic.ac.uk

(2) Research Student; presently at Singapore Technologies Aerospace, Singapore

INTRODUCTION

In typical high performance multi-role fighter aircraft, engines are usually installed in the fuselage to ensure longitudinal and directional stability. In addition, the need to reduce the infra-red signature of the aircraft by shielding the engine's face from the free-stream necessitates the use of high-offset S-shaped diffusing duct. S-ducts of circular and rectangular cross-sections are popular configurations employed in many experimental and numerical studies to investigate the complex flow-field within the intake. However, the use of conformal inlet shapes produces lower drag and better stealth characteristics, and hence, from an aerodynamics view-point, there are needs to evaluate inlet shapes other than the square and circular cross-sections.

The RAE M2129 semi-circular-to-circular diffusing duct investigated here is one of the AGARD-AR-270 (1991) research test-cases. The incompressible velocity field has been measured by Ong (1997) using a refractive-index matching LDV technique at a Reynolds number in excess of 33 000. Initial calculations using the Launder-Sharma $k-\epsilon$ model and the Gibson-Dafa'Alla $q-\zeta$ model have also been performed by Marquis and Ong (1996). Although both models have demonstrated their superiority over the standard wall-functions treatment in capturing the separation region, the extent of the separation was still far from satisfactory.

This paper summarises further attempts (see Ong (1997) for details) to model this flow, and the results using the Gibson and Dafa'Alla (1994) linear $q-\zeta$ model, the Cotton and Kirwin (1995) $k-\epsilon$ model (CK) with and without Yap's Correction (Launder (1988)), a non-linear $q-\zeta$ model (Ong (1997)) and a Reynolds stress model with wall-functions are presented and discussed.

LOW REYNOLDS NUMBER TWO EQUATION MODELS

The linear Boussinesq stress-strain constitutive relation is a well established algebraic formulation to model the Reynolds stress tensor. However, there is no reason why such a relationship should be linear, and Pope (1975) has shown that the Reynolds stress can be expressed as the sum of finite set of higher-order strain and vorticity invariants

using the Cayley-Hamilton theorem. Shih et al. (1993) applied the Schwarz inequality as realisability constraints to derive the coefficients of the invariants. The final form implemented and utilised here follows the re-arrangement of Lien et al. (1996):

$$-\left(\frac{\widetilde{u'_i u'_j}}{k} - \frac{2}{3}\delta_{ij}\right) = \underbrace{C_\mu f_\mu \frac{k}{\epsilon}}_{\text{Linear term}} - \underbrace{\frac{k^2}{\epsilon^2} Q_{ij}}_{\text{Quadratic term}} \quad (1)$$

where the superscript * denotes the inclusion of deviatoric part in order to obtain a consistent zero-trace stress tensor, i.e.,

$$S_{ij}^* = S_{ij} - \frac{1}{3}\delta_{ij} S_{kk}; \quad S_{ij} = \frac{1}{2} \left(\frac{\partial U_i}{\partial x_j} + \frac{\partial U_j}{\partial x_i} \right)$$

$$Q_{ij}^* = Q_{ij} - \frac{1}{3}\delta_{ij} Q_{kk}; \quad \Omega_{ij} = \frac{1}{2} \left(\frac{\partial U_i}{\partial x_j} - \frac{\partial U_j}{\partial x_i} \right)$$

The quadratic terms, Q_{ij} , are defined as:

$$Q_{ij} = q_1 S_{ik} S_{jk} + q_2 (S_{ik} \Omega_{jk} + S_{jk} \Omega_{ik}) + q_3 \Omega_{ik} \Omega_{jk}$$

and q_1 , q_2 and q_3 are $C_{\tau 1} + 2C_{\tau 2} + C_{\tau 3}$, $q_2 = C_{\tau 1} - C_{\tau 3}$, and $C_{\tau 1} - 2C_{\tau 2} + C_{\tau 3}$ respectively. By defining the following invariant strain terms where $\bar{S} = \frac{k}{\epsilon} \sqrt{2S_{ij} S_{ij}}$, $\bar{\Omega} = \frac{k}{\epsilon} \sqrt{2\Omega_{ij} \Omega_{ij}}$, and $A_1 = 2.5$, the models coefficient are given by:

$$f(\bar{S}) = 1000 + \bar{\Omega}^3, C_\mu = \frac{2/3}{A_1 + f_\mu \bar{S} + 0.9 f_\mu \bar{\Omega}}$$

$$C_{\tau 1} = \frac{13}{f(\bar{S})}, C_{\tau 2} = \frac{-4}{f(\bar{S})}, C_{\tau 3} = \frac{-2}{f(\bar{S})}$$

$$q_1 = \frac{3}{f(\bar{S})}, q_2 = \frac{15}{f(\bar{S})}, q_3 = \frac{19}{f(\bar{S})} \quad (2)$$

A_1 was originally proposed as 1.25 by Shih et al. Lien et al. (1996) suggested that a value of 4 was more appropriate for computing the flow-over-the-hill case. The

current computation has discovered that the value of 4 was too high for a case where separated flow is expected to emanate from a surface of milder adverse pressure gradient, and a value of 2.5 seems more appropriate. In the linear model, C_μ remains as a constant of 0.09.

The turbulence time and length-scales needed in the above constitutive equations were provided by solving the low Reynolds number two-equation models. The Cotton-Kirwin $k - \varepsilon$ model, equations 3 and 4, was used for the linear stress-strain relationship, and was selected because of its ability to capture the near-wall turbulence kinetic energy peak in a channel flow without using the wall distance in its damping terms. Yap's length-scale correction was also added to the ε -equation to examine its influence on the model. The $q - \zeta$ model of Gibson and Dafa'Alla (1994), equations 5 and 6, was used in the non-linear constitutive model as it has demonstrated better computational efficiency than its $k - \varepsilon$ counterpart (Gibson and Dafa'Alla (1994)). The f_μ damping term adopted was similar to that of the Cotton-Kirwin model.

The Low Reynolds Number $k - \varepsilon$ Model

$$\mu_t = \rho C_\mu f_\mu (Re_t) \frac{k^2}{\varepsilon}$$

$$\frac{\partial \rho k}{\partial t} + \frac{\partial \rho U_i k}{\partial x_i} = \frac{\partial}{\partial x_i} \left\{ \left(\mu + \frac{\mu_t}{\sigma_k} \right) \frac{\partial k}{\partial x_i} \right\} + \rho P - \rho (\tilde{\varepsilon} + D) \quad (3)$$

$$\frac{\partial \rho \tilde{\varepsilon}}{\partial t} + \frac{\partial \rho U_i \tilde{\varepsilon}}{\partial x_i} = \frac{\partial}{\partial x_i} \left\{ \left(\mu + \frac{\mu_t}{\sigma_\varepsilon} \right) \frac{\partial \tilde{\varepsilon}}{\partial x_i} \right\} + \rho \frac{\tilde{\varepsilon}}{k} \{ C_{\varepsilon 1} f_1 P - C_{\varepsilon 2} f_2 \tilde{\varepsilon} \} + \rho E + \rho S_\varepsilon(\gamma C) \quad (4)$$

The Gibson-Dafa'Alla $q - \zeta$ Model

$$\mu_t = \rho C_\mu f_\mu (Re_t) \frac{q^3}{2\zeta}$$

$$\frac{\partial \rho q}{\partial t} + \frac{\partial \rho U_i q}{\partial x_i} = \frac{\partial}{\partial x_i} \left\{ \left(\mu + \frac{\mu_t}{\sigma_q} \right) \frac{\partial q}{\partial x_i} \right\} + \rho \frac{P}{2q} - \rho \zeta \quad (5)$$

$$\frac{\partial \rho \zeta}{\partial t} + \frac{\partial \rho U_i \zeta}{\partial x_i} = \frac{\partial}{\partial x_i} \left\{ \left(\mu + \frac{\mu_t}{\sigma_\zeta} \right) \frac{\partial \zeta}{\partial x_i} \right\} + \rho \frac{\zeta}{q} \left\{ C_{\zeta 1} f_{\zeta 1} \frac{P}{2q} - C_{\zeta 2} f_{\zeta 2} \zeta \right\} + \rho E \quad (6)$$

where $q = \sqrt{k}$, $\zeta = \frac{\varepsilon}{2q}$, $c_l = C_\mu^{-3/4} \kappa$, $\sigma_q = 1.0$, $\sigma_\zeta = 1.3$, $C_{\zeta, m} f_{\zeta, m} = 2C_{\varepsilon, m} f_{\varepsilon, m} - 1$, $P = -u_i'' u_j'' (\frac{\partial U_i}{\partial x_j})$, and $S_\varepsilon(\gamma C) = \text{Max} \left[0.83 \left(\frac{\varepsilon^2}{k} \right) \left(\frac{k^{3/2}/\varepsilon}{c_l y} - 1 \right) \left(\frac{k^{3/2}/\varepsilon}{c_l y} \right)^2, 0 \right]$.

Model	D	E
CK	$2\nu \left(\frac{\partial \sqrt{k}}{\partial x_i} \right)^2$	$1.3\nu \nu_t \left(\frac{\partial^2 U_i}{\partial x_k \partial x_j} \right) \left(\frac{\partial^2 U_i}{\partial x_k \partial x_j} \right)$
$q - \zeta$	0.0	$2\nu \frac{\nu_t}{2q} \left(\frac{\partial^2 U_i}{\partial x_k \partial x_j} \right) \left(\frac{\partial^2 U_i}{\partial x_k \partial x_j} \right)$
NLR $q - \zeta$	0.0	$2\nu \frac{\nu_t}{2q} \left(\frac{\partial^2 U_i}{\partial x_k \partial x_j} \right) \left(\frac{\partial^2 U_i}{\partial x_k \partial x_j} \right)$

Model	f_μ
CK	$1.0 - 0.97 \exp\left(-\frac{Re_t}{160}\right) - 0.0045 Re_t \exp\left(-\left(\frac{Re_t}{200}\right)^3\right)$
$q - \zeta$	$\exp\left[\frac{-6.0}{(1 + Re_t/50)^2}\right]$
NLR $q - \zeta$	$1.0 - 0.97 \exp\left(-\frac{Re_t}{160}\right) - 0.0045 Re_t \exp\left(-\left(\frac{Re_t}{200}\right)^3\right)$

Model	$f_{\varepsilon 1}$	$f_{\varepsilon 2}$	$\tilde{\varepsilon}$ or ζ B.C.
CK	1.0	$1.0 - 0.3 \exp(-Re_t^2)$	0.0
$q - \zeta$	1.0	$1.0 - 0.3 \exp(-Re_t^2)$	0.0
NLR $q - \zeta$	1.0	$1.0 - 0.3 \exp(-Re_t^2)$	0.0

In the Reynolds stress model, the Jones and Musonge (1988) pressure-strain correlation was employed.

NUMERICAL PROCEDURE

The basic computational framework was provided by BOFFIN (Jones (1988)), which employs the SIMPLE-type of pressure correction numerical procedure. The convection terms of all the transport equations were discretised using the Total Variational Diminishing (TVD) scheme of van Leer (1974) in order to ensure a spatially second-order accurate solution.

RESULTS AND DISCUSSION

The physical domain, figure 1, has a semi-circular inlet of radius 34 mm, an exit diameter of 57 mm, and a length of 170.4 mm. Consistent with measurements of Ong (1997), the inlet boundary layer thickness was 10% of the local duct height. The size of discretised domain was 65 (circumferential) by 41 (radial) by 59 (streamwise) in the Low Reynolds number cases. In the radial direction, 5 to 10 points were inserted in the viscous sub-layer ($y^+ \leq 11$), with the first grid-point positioned at $y^+ \leq 1$. Mesh generation involved using a combination of algebraic and elliptic methods, whose detail can be found in Marquis and Ong (1996).

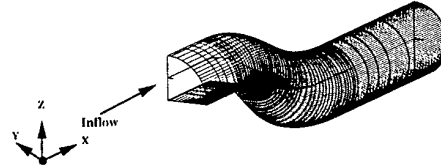


Figure 1: The Computational Mesh (65x41x59)

Flow Separation in the Symmetry Plane

The measurements indicated the presence of flow separation (figure 2), where the onset of separation occurred just after the first bend on the suction (lower) surface at $X/D_{exit} \approx 0.4$, and the re-attachment location at around $X/D_{exit} = 2.25$. The height of the recirculating zone and the magnitude of the reverse flow reached a maximum of $0.15D_{exit}$ and $0.34U_{bulk}$ respectively near the plane of inflexion, station 6, where U_{bulk} is the reference bulk velocity calculated at the station 1 for both the experiment and computations. Figure 3 presents the computed axial mean velocity profiles, where the experimental data are represented by the square symbols. The separation bubble predicted was identified by joining the locations of zero mean axial velocity along the successive profiles, and to facilitate discussion, a ruler normalised by the exit diameter was included such that stations 2 (inlet) and 10 (exit)

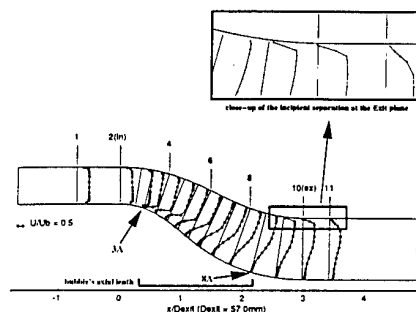


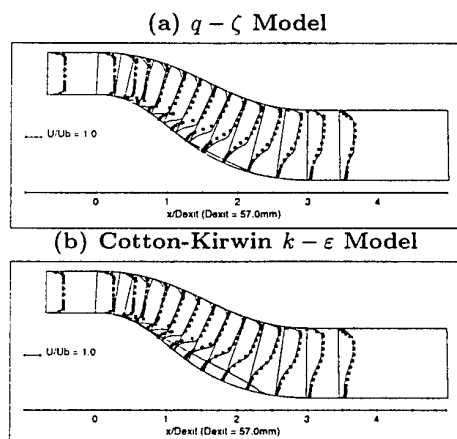
Figure 2: LDV Measurements: Mean Velocity Profiles in the Symmetry Plane

Turbulence Model	Bubble Length, X/D_{exit}		Max Ht/Local Ht at X/D_{exit}
	Onset	Re-attachment	
Expt	0.40	2.25	18%@1.05
$q-\zeta$	1.11	2.23	4.7%@1.67
CK	0.68	2.43	16.5%@1.60
CK+YC	0.25	2.62	18.7%@1.44
NLR $q-\zeta$	0.36	2.70	22.5%@1.97
RSM+WF	1.17	1.66	7.26%@1.55

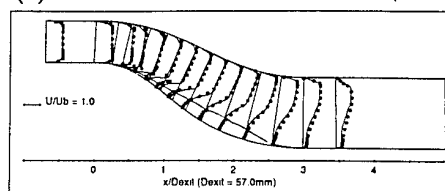
Table 1: The Sizes of the Measured and Predicted Separation Bubbles

corresponded to the axial locations of $X/D_{exit} = 0$ and $X/D_{exit} \approx 3$ respectively.

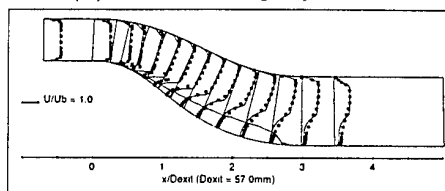
Table 1 presents a summary of the predicted locations and sizes of the separation bubbles. The predictions of the low Reynolds number models (figures 3(a)-(d)) were better than that of the Reynolds stress model in general. The onset location predicted by the $q-\zeta$ model (figure 3(a)) was around $X/D_{exit} = 1.1$, and the flow re-attached at ≈ 2.2 . Compared with the experimental data, the onset location was over-predicted and consequently, the size and magnitude of the recirculating bubble were under-estimated. The Cotton-Kirwin model in figure 3(b) shows a vastly improved prediction when compared to the $q-\zeta$ model: the onset occurred at $X/D_{exit} \approx 0.7$ and re-attached at approximately 2.4. The use of Yap's Correction in figure 3(c) moves the onset of separation to $X/D_{exit} \approx 0.25$, and delays re-attachment point to $X/D_{exit} \approx 2.6$. The prediction using the non-linear $q-\zeta$ model (figure 3(d)) shows that the onset of separation occurred at $X/D_{exit} \approx 0.4$, and the re-attachment was over-estimated at $X/D_{exit} \approx 2.7$.



(c) Cotton-Kirwin $k-\epsilon$ Model + YC



(d) Non-Linear $q-\zeta$ Model



(e) RSM Model + WF

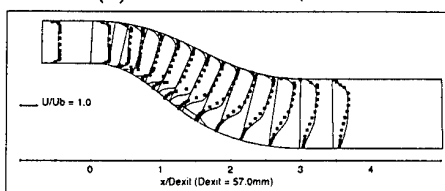


Figure 3: Axial Velocity Profiles in the Plane of Symmetry

All the low Reynolds number models have over-predicted the locations of maximum reverse flow velocity, and consequently, the axial locations of maximum flow reversal were predicted to occur later than the measurements. In the experiment, maximum flow reversal occurred at $X/D_{exit} \approx 1.05$ near station 6, while in the simulations, the locations of maximum flow reversal were *over-predicted* by between $0.4D_{exit}$ in the case of Cotton-Kirwin model with Yap's correction, and $0.9D_{exit}$ in the case of non-linear $q-\zeta$ model. The cause for a generally later predicted re-attachment location of the separation bubble can be investigated by examining the shear stress contours in figure 4. Two possible mechanisms affect the re-attachment location (Lien and Leschziner (1994)): the entrainment of turbulence across the free shear-layer via the production term, and the anisotropy near the wall. The former mechanism is more likely to affect the location of maximum flow reversal and the height of the separation bubble, while the latter will influence the shape of the separation bubble at the re-attachment location. The comparison of the shear stress contour shows that the level predicted by the Reynolds stress model was comparable to the low Reynolds number eddy viscosity models, in spite of the grossly under-predicted separated region. The shows that despite the low strain rate predicted, probably due to the wall functions treatment, the transport of the Reynolds stress has played a crucial part in the shear stress development in this duct. In the eddy viscosity models, the shear stress developed is only dependent on the strain rates, and thus, the maximum shear stress was positioned near the re-attachment location, where the strain rate, $\frac{\partial U}{\partial z}$, was highest. The entrainment of energy via the turbulence production mechanism was likely to be under-predicted because local equilibrium is assumed for all the eddy viscosity models. Hence, the low Reynolds number Reynolds stress models may be required to model separated flow in the present duct or in intake ducts of similar complexity because the transport of Reynolds stresses is important.

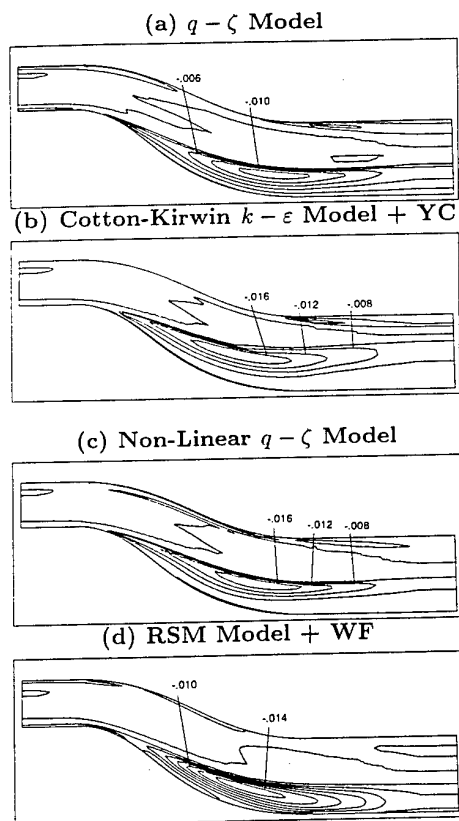


Figure 4: Normalised Shear Stress (global coordinate system), $\overline{u''w''}/U_{bulk}^2$

Cross-Sectional Velocity Components

The axial and secondary velocities predicted by the Cotton-Kirwin $k-\epsilon$ model with Yap's correction and the non-linear $q-\zeta$ models are presented in figures 5 to 7, which corresponded to stations 6 (inflexion), 8 and 10 (exit). All the velocity components were normalised by the bulk velocity calculated at station 1.

At the plane of inflexion, the measurements in figure 5(a) indicate a large reverse flow region, whose height was about 17% of the local duct height and was located on the bottom surface along the centreline. The maximum strength of the reverse flow was larger than $0.2U_{bulk}$, and due to the accumulation of low momentum fluid on the bottom surface that resulted in the reduction of effective area, the high speed core was displaced towards the top surface with an average magnitude of $1.1U_{bulk}$. The height and shape of the recirculating flow region predicted by the Cotton-Kirwin model (figure 5(b)) were in good accord with the measurements, whilst the non-linear $q-\zeta$ model (figure 5(c)) predicted a wider region of separation, and a lower reverse flow magnitude of around $0.1U_{bulk}$. At station 8 in the second bend, the measurements show that the recirculation region was still present but with diminishing size and strength. The sizes of the separation bubble predicted by the Cotton-Kirwin and non-linear $q-\zeta$ models (figures 6 (b) and (c)) were larger than the measurements, and the magnitudes of flow reversal were over-predicted by at least $0.1U_{bulk}$. The spanwise velocity gradient, $\frac{\partial U}{\partial y}$, in the low momentum region was more pronounced than that of the measurements. At station 10 (exit) in figure 7(a), the measurements indicate that the high speed core was positioned between $Z^* = 0.3$ and 0.8 with a magnitude of $1.0U_{bulk}$, while in the low momentum region, the gradient in the radial direction was fairly uniform. In the case of Cotton-Kirwin model (figure 7(b)), the distribu-

tions of the axial contours show a larger distortion than the measurements, and in the case of the non-linear $q-\zeta$ model (figure 7(c)), the size of the high-speed core was over-predicted, and this was due primarily to the over-prediction of the size of the separation bubble.

In terms of the development of the secondary flow, the Cotton-Kirwin and non-linear $q-\zeta$ models have predicted the presence of the circulation near the bottom surface, while in the measurements, such circulation was non-existent. Based on the formulation of Squire and Winter (refer to Taylor et al. (1982)), the change in the streamwise vorticity depends on:

$$\begin{aligned}\Delta\omega_s &= -2\omega_n\Delta\theta \\ &= -2\left(\frac{\partial U}{\partial y} - \frac{1}{R}\frac{\partial V}{\partial\theta}\right)\Delta\theta\end{aligned}\quad (7)$$

where ω_s and ω_n are the components of the vorticity along and normal to the flow streamlines, and $\Delta\theta$ is the change in turning angle of the bend. Since $\frac{\partial U}{\partial y} \gg \frac{1}{R}\frac{\partial V}{\partial\theta}$ Taylor et al. (1982), the development of the streamwise vorticity is strongly related to the spanwise gradient of the axial velocity distribution, $\frac{\partial U}{\partial y}$. An anti-clockwise vorticity in the left-hand-side of the cross-section, i.e. $Y^* > 0$, is negative, and thus, a positive $\frac{\partial U}{\partial y}$ would enhance the development of the circulation developed in the first bend. At station 8, figure 6, the measurements indicated that the separation bubble was approaching its re-attachment, while the predictions show that their respective locations of maximum reverse flow and maximum separation bubble height occurred around station 8 (see table 1). Due to the varying cross-sectional shapes and sizes of the separation bubble, the distortions in $\frac{\partial U}{\partial y}$ were different. The Cotton-Kirwin $k-\epsilon$ model with Yap's correction returned a larger distortion in the $\frac{\partial U}{\partial y}$ gradient than the non-linear $q-\zeta$ model, and hence the circulation developed in the first bend could continue to develop in the low momentum region close to the bottom surface. At the exit plane, there is a good correlation between the $\frac{\partial U}{\partial y}$ gradient and the development of circulation in the low momentum region. The Cotton-Kirwin and non-linear $q-\zeta$ models have predicted a substantial $\frac{\partial U}{\partial y}$ gradient as a result of the later re-attachment of the separation, and thus, produced fairly significant circulation.

CLOSURE

The streamwise separation detected in the LDV measurements has been modelled with varying degree of success by the low Reynolds number models, of which the Cotton-Kirwin $k-\epsilon$ model with Yap's correction produced the best agreement with respect to the onset and re-attachment of separation. The non-linear $q-\zeta$ model predicted a similar location for the onset of separation, but the re-attachment location has been over-predicted. The regions of maximum reverse flow velocity have been significantly over-predicted by the two low Reynolds number eddy viscosity models tested in the present work. Analysis of the shear stress contours shows that the transport of Reynolds stresses is important in modelling the present separated flow, as the Reynolds stress field is more likely to be non-equilibrium. Hence, for configurations with strong separation emanating from a smooth surface with high curvature, the use of low Reynolds number Reynolds stress models may be the best approach to adopt in future.

The trend in the development of the secondary flow patterns and distortion of the axial velocity profiles were dependent on the extent of separation in the streamwise direction. Although the Cotton-Kirwin and non-linear $q-\zeta$ models have predicted a separation bubble of almost similar length to that of the experiment, the reverse flow regions were located further downstream. This resulted in

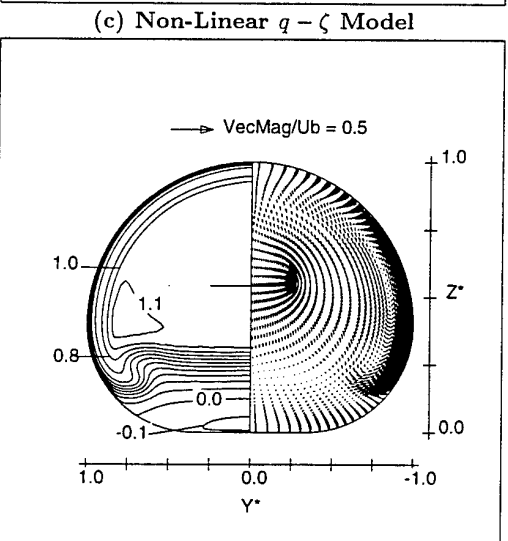
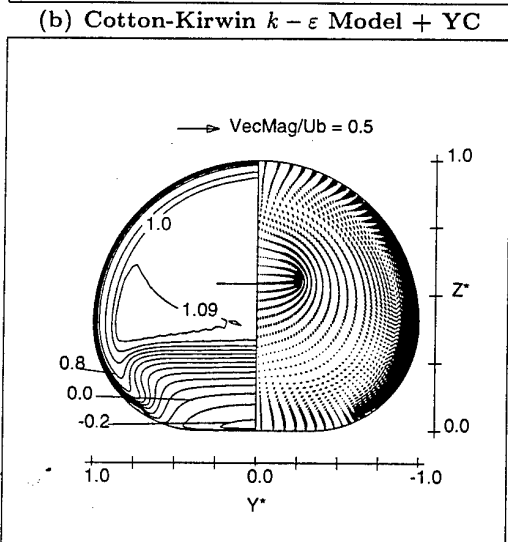
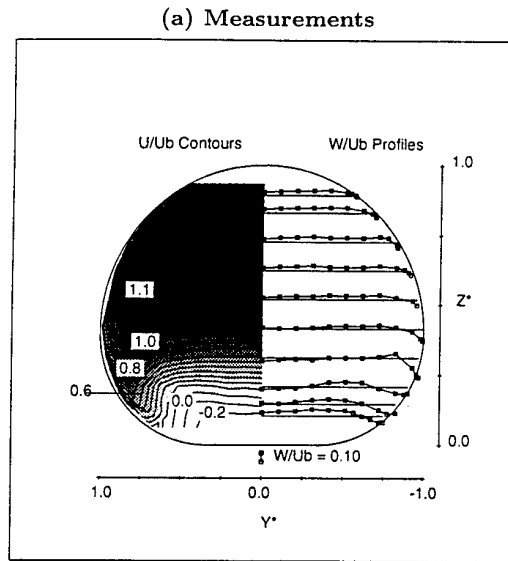


Figure 5: Axial and Secondary Velocity at Station 6 (Plane of Inflexion)

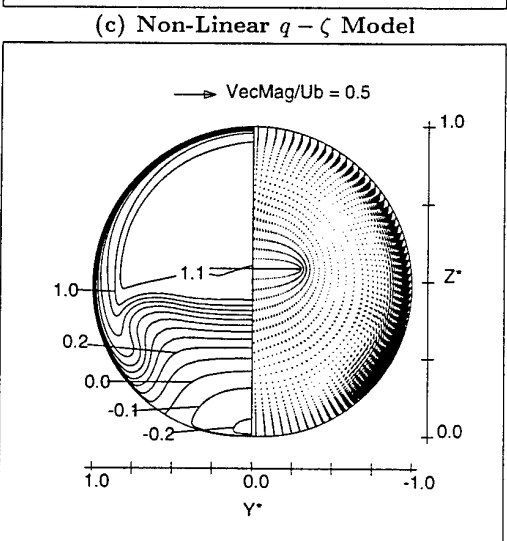
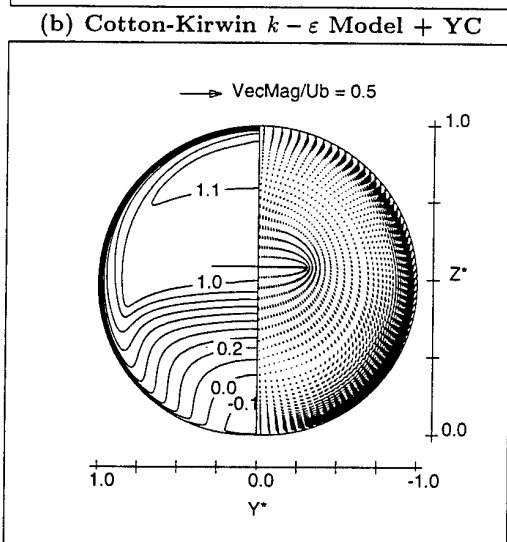
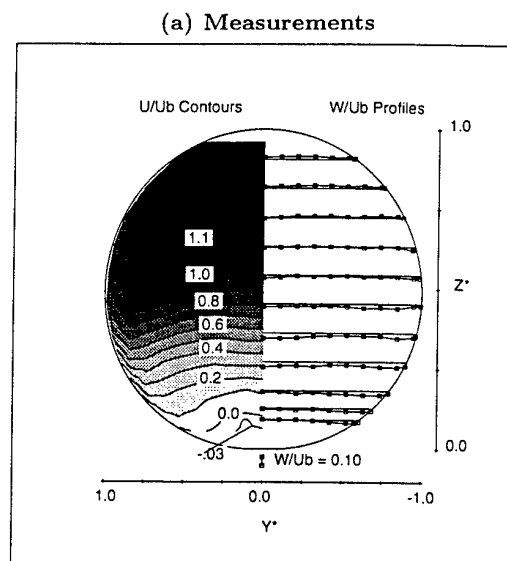


Figure 6: Axial and Secondary Velocity at Station 8 (In the Second Bend)

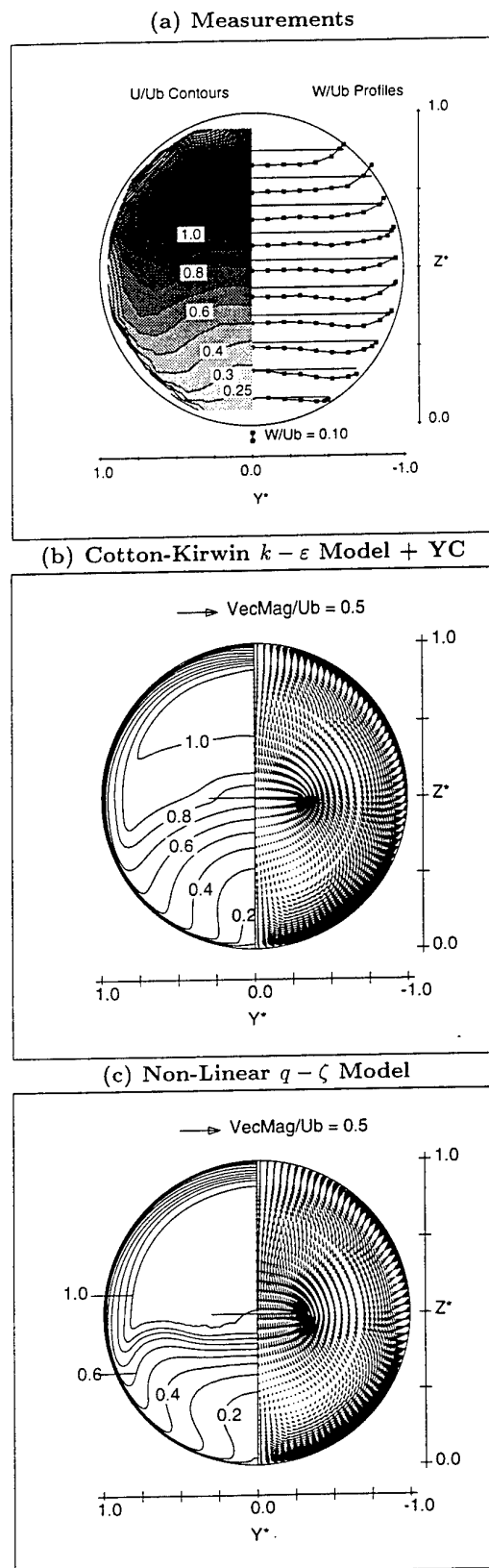


Figure 7: Axial and Secondary Velocity at Station 10 (Exit)

the distortion of axial flow in the low momentum region, and produced the spanwise distortion gradient $\frac{\partial U}{\partial y}$, leading to the development of the circulation in the low momentum region at the exit plane.

ACKNOWLEDGEMENTS

This work has been carried out with the support of the Defence Research Agency at Bedford (UK) acting on behalf of the Ministry of Defence (UK). The authors would like to acknowledge the many useful discussions with Dr J Gibb and Mr J Hodges of Defence Research Agency at Bedford, UK.

REFERENCES

- AGARD-AR-270 September 1991 "Air Intakes for High Speed Vehicles",.
- Cotton, M. A. and Kirwin, P. J., 1995, "A Variant of the Low-Reynolds-Number Two-Equation Turbulence Model Applied to Variable Property Mixed Convection Flows", *International Journal Heat and Fluid Flow*, 16, pp.486-492.
- Gibson, M. M. and Dafa'Alla, A. A., 1994, "Two-Equation Model for Turbulent Wall Flow", *Journal of AIAA*, 33(8), pp.1514.
- Jones, W. P. and Musonge, P., 1988, "Closure of the Reynolds Stress and Scalar Flux Equations", *Physics of Fluids*, 31(12), pp.3589-3604.
- Jones, W. P., 1988 "BOFFIN: A Computer Program for Flow and Combustion in Complex Geometries", Technical report, Department of Chemical Engineering, Imperial College of Science, Technology and Medicine.
- Launder, B. E., 1988, "On the Computation of Convective Heat Transfer in Complex Turbulent Flows", *Transactions of the ASME*, 110, pp.1112-1128.
- Lien, F. S. and Leschziner, M. A., 1994, "Assessment of Turbulent-Transport Models Including Non-Linear RNG Eddy-Viscosity Formulation and Second-Moment Closure For Flow Over a Backward-Facing Step", *Computers and Fluids*, 23(8), pp.983-1004.
- Lien, F. S., Chen, W. L., and Leschziner, M. A., 1996 "Low Reynolds-Number Eddy-Viscosity Modelling Based on Non-Linear Stress-Strain/Vorticity Relations", 3rd International Symposium on Engineering Turbulence Modelling and Measurements, Crete, Greece.
- Marquis, A. J. and Ong, L. Y., 1996 "Computation of Incompressible Flow in a RAE M2129 Semi-Circular to Circular Diffusing Duct", Third ECCOMAS Computational Fluid Dynamics Conference, Paris, France.
- Ong, L. Y., 1997 *Experimental and Numerical Studies of S-shaped Diffusing Ducts* PhD thesis, Department of Mechanical Engineering, Imperial College of Science, Technology and Medicine, University of London.
- Pope, S. B., 1975, "A More General Effective-Viscosity Hypothesis", *Journal of Fluid Mechanics*, 72, pp.331-340.
- Shih, T. H., Hsu, A. T., and Lumley, J. L., 1993 "A Realisable Reynolds Stress Algebraic Equation Model", NASA TM-105993, 9th Symposium on Turbulent Shear Flows, Kyoto, Japan.
- Taylor, A. M. K. P., Whitelaw, J. H., and Yianneski, M., 1982, "Developing Flow in S-shaped Ducts, Part II: Circular Cross-Section Duct", *NASA CR 3759 under Contract NASW-3435*.
- van Leer, B., 1974, "Towards the Ultimate Conservative Difference Scheme", *J. Comp. Physics*, 14, pp.361-370.

COMPUTATION OF FILM COOLING BY LATERAL INJECTION USING A MULTI-BLOCK TECHNIQUE

D. Lakehal *
G.S. Theodoridis **
W. Rodi

Institute for Hydromechanics
University of Karlsruhe
Karlsruhe
Germany

ABSTRACT

Film cooling effectiveness of a flat plate by a row of laterally injected jets is investigated using a Navier-Stokes equation solver which employs a finite-volume method with a multi-block technique. The paper compares measured and calculated temperature and velocity fields obtained with the $k - \epsilon$ based two-layer turbulence model for various blowing rates. The resolution of the viscosity-affected near-wall region with a one equation turbulence model yielded a noticeable improvement in the prediction of film-cooling effectiveness compared to results obtained with wall functions. Furthermore, results of additional calculations using the *ad-hoc* correction proposed by Bergeles et al. (1978), which attempts to promote the lateral diffusivity, combined with the two-layer model indicate that this anisotropy correction enhances indeed the spanwise spreading, but its application very close to the wall needs additional calibration.

INTRODUCTION

The thermal performance of modern gas turbines, used either in aircraft engines or power-production systems, depends primarily on the level of temperature at the inlet to the turbine section. Despite the noticeable progress in blade-metallurgy, a reasonable lifetime of turbine blades can be ensured only by an efficient surface-cooling mechanism. Film cooling is one of the most efficient cooling methods; it is generally more efficient than internal convection cooling because of the relatively poor heat-transfer characteristics of air. In film cooling, cool air is discharged from rows of holes to form a thin film on the surface acting as a buffer between the hot gas and the blade. The efficiency of such a technique can be influenced by several parameters, among them the discharge geometry, ejection angle, blowing rate, blade geometry, density and temperature ratio, and reliable prediction methods are

needed to optimize the design. In practice often lateral injection is used since with this the cooling film covers better the area to be cooled. The present paper aims to contribute to the development of a prediction method for this situation and to the understanding of the cooling behaviour.

The test case studied here represents film cooling of a flat plate by a row of laterally injected jets. The on-coming flow is that of a fully turbulent boundary layer, and the flow configuration is displayed in Fig. 1. The test case was studied experimentally in detail by Honami and al. (1992), and the inflow conditions are well defined. In their experimental investigation, the authors have measured simultaneously velocity and temperature fields using a double-wire probe. The tests were conducted at three mass flux ratios $M = \rho_j U_j / \rho_s U_s = 0.5, 0.85$ and 1.2 , (U_j and ρ_j are respectively the injected-jet velocity and density and U_s and ρ_s the primary-stream velocity and density). Although this configuration has a simple geometry, it offers most of the complex features observed in turbo-machinery flows, such as the strongly three dimensional nature of the flow and temperature field, caused by the interaction between the primary and coolant streams. Also, the lateral injection causes an asymmetric behaviour of the flow. In all cases, the temperature difference between primary stream and coolant was 55° .

Two-equation turbulence models employing wall-functions as near-wall treatment bridging the viscous sublayer are known to be inaccurate in predicting certain flows, in particular when heat transfer is involved. The assumptions on which such near-wall treatment is based are not generally valid; an example is the case in which secondary flows extend into the sublayer (Rodi, 1991). Resolving the viscous sublayer by Low Reynolds number $k - \epsilon$ models was found to require very high numerical resolution near the walls, in order to deal with the steep gradients of the dissipation rate ϵ . As an alternative, the two-layer approach has recently become popular, in which only the core flow outside the viscosity-affected near-wall region is

* Present address: Technical University of Berlin, Germany

** Present address: University of Thessaloniki, Greece

simulated by the $k - \varepsilon$ model. The viscous sublayer is resolved by a simpler model, notably a one-equation model in which the length-scale distribution is prescribed and an ε -equation is not solved. Such models therefore require considerably fewer grid points in the viscous sublayer and are hence more suitable for complex situations involving more than one wall for which the near-wall regions have to be resolved. Also, because of the fixed length-scale distribution near the wall, these models have been found to give better predictions for adverse pressure gradient boundary layers than pure $k - \varepsilon$ models. In jet-in-a-cross-flow situations, isotropic eddy viscosity/diffusivity models are known to underpredict the lateral spreading of the jet and of passive scalars. Hence, the *ad-hoc* measure proposed by Bergeles et al. (1978), which attempts to increase the lateral eddy viscosity and diffusivity, combined here with the two-layer model, is tested in further calculations.

THE $k - \varepsilon$ BASED TWO-LAYER TURBULENCE MODEL

The standard $k - \varepsilon$ model of Launder and Spalding (1974) employs the Boussinesq eddy-viscosity concept and characterizes the turbulence through the turbulent kinetic energy (k) and its rate of dissipation (ε). It employs the following relation for determining the isotropic eddy-viscosity ν_t

$$\nu_t = C_\mu k^2 / \varepsilon \quad (1)$$

The distributions of k and ε are determined from the following model transport equations solved together with the mean-flow equations:

$$\frac{1}{J} \frac{\partial}{\partial x_m} \left[u_m \phi - \frac{\Gamma_\phi}{J} \left(\beta_i^j \beta_i^m \frac{\partial \phi}{\partial x_m} \right) \right] = S_\phi \quad (2)$$

ϕ stands for either k or ε , and the equation is written in a general co-ordinate system. u stands for the contravariant velocity expressed in terms of its Cartesian components U_i by $u_m = \beta_j^m U_j$, where β_j^i is the cofactor of the Jacobian $J (= \partial y_j / \partial x_i)$. Γ_ϕ is the diffusion coefficient which involves the molecular and turbulent viscosities ν and ν_t through $\Gamma_\phi = (\nu + \nu_t) / \sigma_\phi$. The net source/sink term S_ϕ is given for the k and ε equations by $(G - \varepsilon)$ and $(C_1 G - C_2 \varepsilon) \varepsilon / k$ respectively. G represents the rate of production of turbulent kinetic energy resulting from the interaction of the turbulent motions and velocity gradients:

$$G = \frac{\nu_t}{J^2} \left(\frac{\partial U_i}{\partial x_n} \beta_j^n \right) \left(\frac{\partial U_i}{\partial x_n} \beta_j^n + \frac{\partial U_j}{\partial x_m} \beta_i^m \right) \quad (3)$$

The standard values are assigned for the constants appearing in this model, namely $C_\mu = 0.09$; $C_1 = 1.44$; $C_2 = 1.92$; $\sigma_k = 1.$, $\sigma_\varepsilon = 1.3$ and the turbulent Prantl number $\sigma_\phi = 0.9$.

The two-layer approach adopted here consists of resolving the viscosity-affected regions close to walls with a one-equation model, while the outer core flow is resolved with the standard $k - \varepsilon$ model described above. In the one-equation model, the eddy viscosity is made proportional to a velocity scale and a length scale l_μ . The distribution of l_μ is prescribed algebraically while the velocity scale is determined by solving the k -equation (Eq. (2)). The dissipation rate ε appearing as sink term in the k -equation is related to k and a dissipation length scale l_ε which is also prescribed algebraically. The different two-layer versions available in the literature differ in the use of the velocity scale and the way l_μ and l_ε are prescribed. It

should be mentioned that in the fully turbulent region the length scales l_μ and l_ε vary linearly with distance from the wall. However, in the viscous sublayer l_μ and l_ε deviate from the linear distribution in order to account for the damping of the eddy viscosity and the limiting behaviour of ε at the wall. The one-equation model employed is due to Norris and Reynolds (1975) and reads:

$$\nu_t = C_\mu k^{1/2} l_\mu; \quad l_\mu = C_l y_n \left[1 - \exp \left(- \frac{R_y}{A_\mu} \frac{25}{A^+} \right) \right];$$

$$R_y = \frac{k^{1/2} y_n}{\nu} \quad (4)$$

$$\varepsilon = k^{3/2} / l_\varepsilon; \quad l_\varepsilon = \frac{C_l y_n}{1 + 13.2 / (R_y C_l)} \quad (5)$$

Note that the length scale l_μ is damped in a similar way as the Prandtl mixing length by the Van Driest function. The constant C_l is set equal to $\kappa C_\mu^{-3/4}$ to conform with the logarithmic law of the wall ($\kappa =$ von Kármán constant). The empirical constants appearing in the damping function are assigned the values $A_\mu = 50.5$ and $A^+ = 25$ (Rodi, 1991). The outer $k - \varepsilon$ and the near-wall model are matched at a location where the damping function (term in brackets) reaches the value 0.95, i.e. where viscous effects become negligible.

Due to the isotropic eddy-viscosity assumption on which two-equation turbulence models are based, computations of jet-in-cross flow, in particular the transport of passive scalars, reveal systematically an under-prediction of the lateral spreading. In order to account for the anisotropy of the turbulent exchange processes in these flows, Bergeles et al. (1978) proposed to substitute the eddy-viscosity μ_t appearing in the lateral components of the Reynolds stresses and scalar fluxes

$$-\rho \overline{u'w'} = \mu_t \frac{\partial U}{\partial z}; \quad -\rho \overline{w'\phi'} = \frac{\mu_t}{\delta_\phi} \frac{\partial \theta}{\partial z} \quad (6)$$

by an increased value determined by

$$\mu_t^a = \mu_t [1.0 + f(1.0 - y/\delta)] \quad (7)$$

in which μ_t is the eddy viscosity determined by the basic turbulence model. δ denotes the local boundary layer thickness. Relation (7) was derived from model transport equations for the Reynolds stresses by assuming local equilibrium of turbulence and neglecting the stress $\overline{v'w'}$ against $\overline{u'v'}$ and $\overline{u'w'}$. The ratio of eddy viscosities/diffusivities for the stresses and heat fluxes in the lateral and normal direction was found to be equal to the ratio of the fluctuating velocities w'^2/v'^2 , which was assumed to vary linearly from a near-wall value f to 1 at the outer edge of the boundary layer. The coefficient f was given the value 3.5 in the original paper. Within the viscous sublayer it may however reach considerably higher values.

THE COMPUTATIONAL METHOD

The numerical procedure applied to calculate the test case is based on a finite-volume approach for solving implicitly the incompressible averaged Navier-Stokes equations on arbitrary non-orthogonal grids, employing a cell-centered grid arrangement. A detailed description of the computer program FAST-3D is reported in Majumdar et al. (1992). Furthermore, and because of the geometrical complexity of

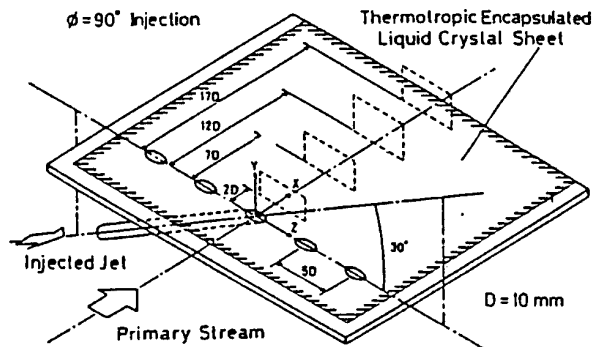


Fig. 1: Experimental apparatus from Honami et al. (1992)

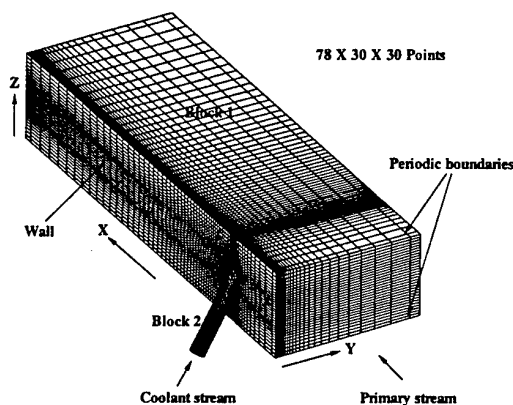


Fig. 2: The computational grid

film-cooling problems, a multi-block technique is introduced into the method, which reduces significantly the core memory needed for computation, and gives more freedom in generating the grid. This technique allows to generate separately grids for the different parts of the flow domain, namely the region above the blade surface to be cooled, inside the discharge pipe and in the associated plenum if needed, which are finally assembled into one array forming the grid for the complete computational domain (see Fig. 2). The computation is performed within each block, with the linkage achieved through special mapping conditions. The momentum-interpolation technique of Rhie and Chow (1983) is used to prevent pressure-field oscillations. The pressure-velocity coupling is achieved using the SIMPLEC algorithm of Van Doormal and Raithby (1984). Different higher order schemes can be used to approximate the convection fluxes, i.e. the second order schemes QUICK and HPLA (Zhu, 1991). The achievement of numerical stability when employing the two-layer model has required the application of the HPLA scheme to the k and ϵ -equations, while the momentum equations could be solved with the QUICK scheme. The resulting system of difference equations is solved using the SIP algorithm of Stone (1968).

GRIDS AND BOUNDARY CONDITIONS

The computational domain with the various boundaries is shown in Fig. 2. Grid sensitivity studies indi-

cated that with the standard $k - \epsilon$ model using wall functions, grid-independent results could be obtained with $78 \times 30 \times 30$ grid points in the x -, y - and z -directions as shown in Fig. 2. A finer mesh consisting of $94 \times 42 \times 42$ grid points is required for the two-layer computations. The grids were considerably refined in the near-wall regions and in the vicinity of the injection hole. The lateral injection of coolant from a row of discrete holes leads to spanwise periodicity and consequently periodicity conditions were used at the lateral boundary planes midway between two holes. The first cells adjacent to the walls were set with respect to the criteria required for the individual near-wall treatment, i.e. using the two-layer approach, the width of the first grid-cell was set equal to $0.01D$, which corresponds to $0.5 < y^+ < 4$. The number of grid points placed in the viscous sublayer was in most regions typically 10 to 15. The boundary conditions employed are as follows: On the ground plate and the pipe walls, either wall functions were employed or the no-slip condition and $k = 0$ in the two-layer calculations, while at the upper boundary of the domain, a zero flux condition was employed. At the inflow boundary, a streamwise velocity profile deduced from the power-law approximation $U_{in} = U_s \times (y/\delta)^{1/7}$ with $\delta = 0.011m$ was applied to reproduce the measured fully turbulent boundary layer. The k and ϵ -profiles were specified using uniform distributions corresponding to a freestream turbulence intensity of $T_u = 5\%$ a ratio $\nu_t/\nu = 50$. The discharge pipe was $8D$ long, and the velocity profile at the inlet was determined using the common distribution of turbulent flow in a pipe, which reads $U_{in} = 1.26U_j \times (2.z/D)^{1/6}$, z being the distance to the pipe wall. Here also, uniform distributions of k and ϵ were specified, based on a turbulence intensity of $T_u = 5\%$ and a length scale of $k^{3/4}/\epsilon = 0.5D$.

RESULTS AND DISCUSSION

In Figs. 3 and 4, the contours of the non-dimensional velocity U/U_∞ and temperature $\eta = (\theta - \theta_\infty)/(\theta_j - \theta_\infty)$ computed with the standard $k - \epsilon$ model are compared for the mass flux ratio $M = 0.5$ with the corresponding experimental data at various streamwise locations. The centre of the jet as characterised by the lowest velocities and highest temperatures can be seen to move in the spanwise injection direction with increasing streamwise distance from the hole. The injection-hole centre is located at $z = 0$ and an arrow in Fig. 4 indicates the orientation of the injection. The contours are clearly asymmetrical, with high-momentum and low-temperature fluid penetrating underneath the jet on its left side (viewed downstream). This is caused by a counter-clockwise rotating secondary-flow vortex at the left side of the jet as typically found in jets in cross flow. In jets with streamwise injection there is a counter-rotating vortex on the other side; together the two vortices cause the typical, symmetrical kidney shape of the temperature contours. In the case with lateral injection considered here, the counter-rotating vortex on the right side of the jet appears to be absent, probably because it is counter-acted by the velocity of the jet and of the primary-stream fluid displaced by the jet in the spanwise (positive z) direction. Hence there is no ambient fluid pushed underneath the jet on its right side, leading to the asymmetric behaviour of the velocity and temperature contours. Due to turbulent mixing, the peak temperature in the jet decreases rapidly near the injection hole and more slowly in the downstream

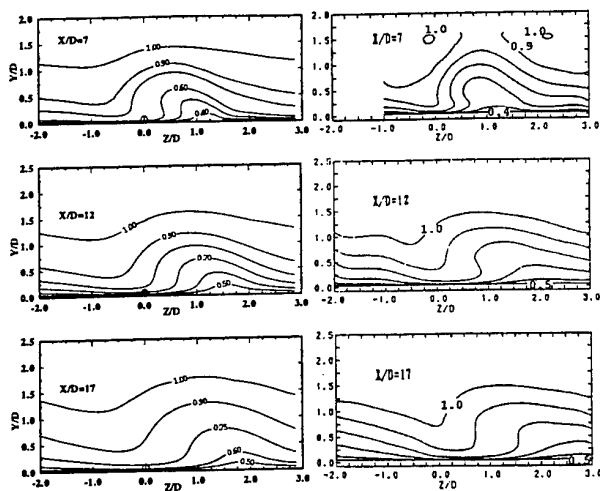


Fig. 3: U/U_∞ -contours; left: Calc.; right: Exp.
(a) $M = 0.50$; $k - \epsilon$ WF

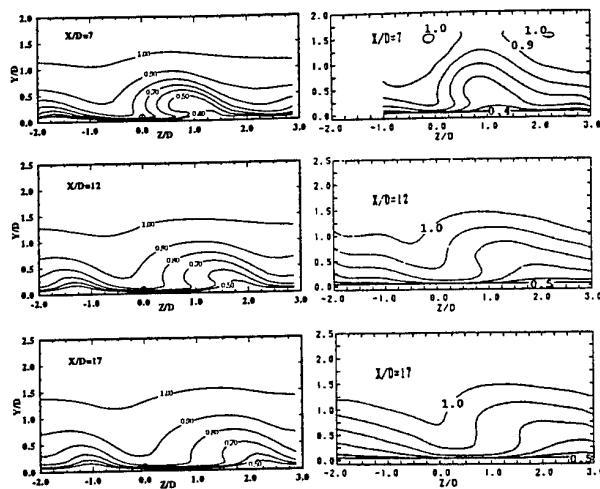


Fig. 5: U/U_∞ -contours; left: Calc.; right: Exp.
(a) $M = 0.50$; $k - \epsilon$ two-layer

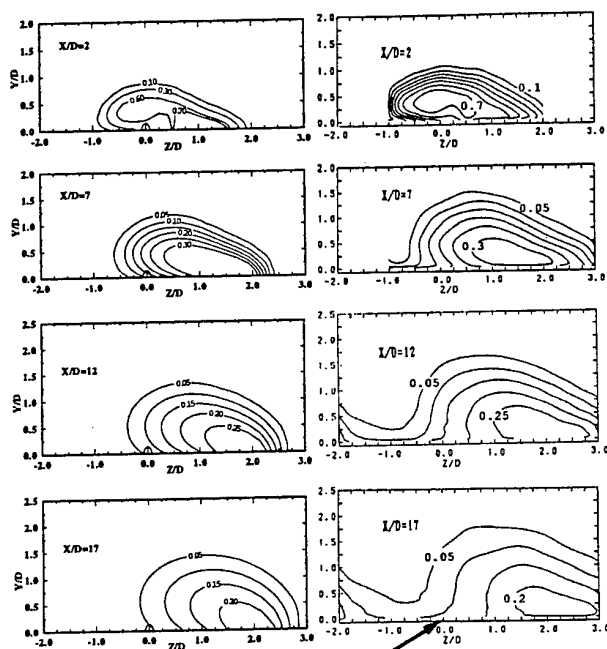


Fig. 4: η -contours; left: Calc.; right: Exp.
(a) $M = 0.50$; $k - \epsilon$ WF

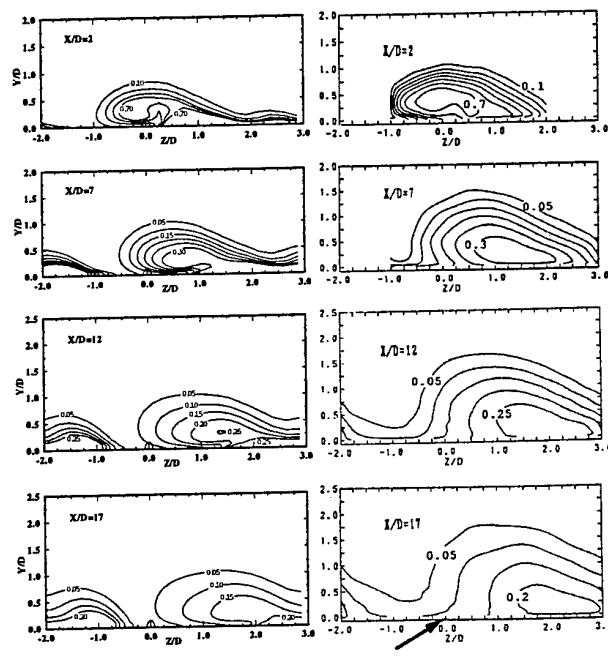


Fig. 6: η -contours; left: Calc.; right: Exp.
(a) $M = 0.50$; $k - \epsilon$ two-layer

region. In general, the behaviour described above is predicted by the standard $k - \epsilon$ model in fairly good agreement with the experiments, but the model underpredicts the lateral and vertical spreading of the passive scalar and, judging from the velocity contours, the strength of the secondary-flow vortex is also underpredicted.

For the same blowing rate, Figs. 5 and 6 compare the results obtained with the two-layer model for U/U_∞ and η respectively with the experimental data. It can be seen that the model enhances the lateral spreading compared with the standard model, but the spreading in the vertical direction is suppressed. Judging again from the velocity contours, it seems that the secondary-flow vortex is more pronounced when the two-layer model is used. This results in a sharper deformation of the velocity contours predicted with this model. The η -contours clearly show more lateral dif-

fusion of temperature which is brought about both by resolving better the important near-wall region and also promoting the strength of the secondary-flow vortex. However, the better lateral spreading is achieved at the expense of a reduced vertical spreading of temperature, and the decay of the peak temperature is now somewhat too fast in the downstream region.

Figs. 7 and 8 compare the computed and measured velocity and temperature contours for a mass flux ratio of $M = 0.85$. The calculations were obtained with the two-layer model. The velocity contours agree fairly well, even though the boundary-layer thickness on the left side of the jet is underpredicted. Closer inspection of the velocity contours at $x/D = 7$ indicates that there is more than one secondary-flow vortex present in this case. This is confirmed by the secondary-flow velocity vectors plotted at this station in Fig. 9, which shows a much weaker counter-rotating vortex on

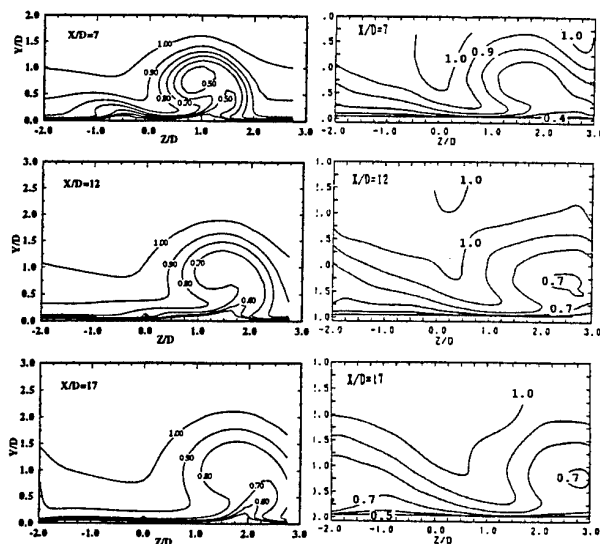


Fig. 7: U/U_∞ -contours; left: Calc.; right: Exp.
(b) $M = 0.85$; $k - \epsilon$ two-layer

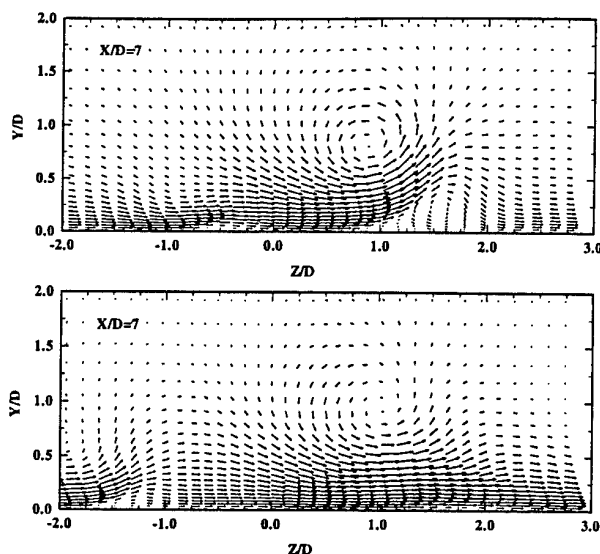


Fig. 9: velocity vectors, $w-v$; (b) $M = 0.85$
upper: 2-l ($f = 0$); lower: 2-l ($f = 4$)

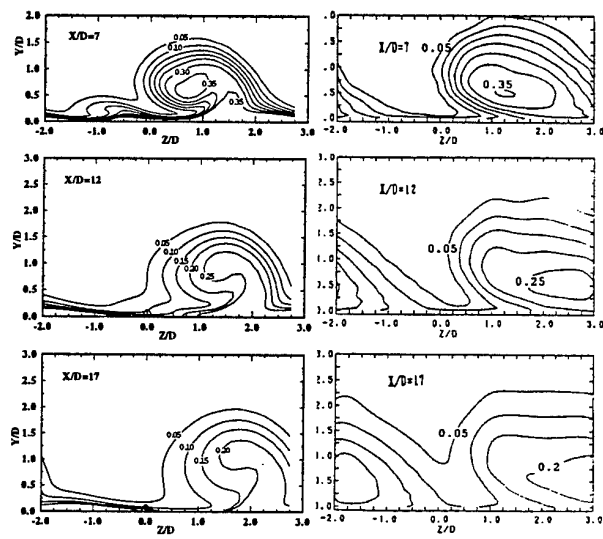


Fig. 8: η -contours; left: Calc.; right: Exp.
(b) $M = 0.85$; $k - \epsilon$ two-layer

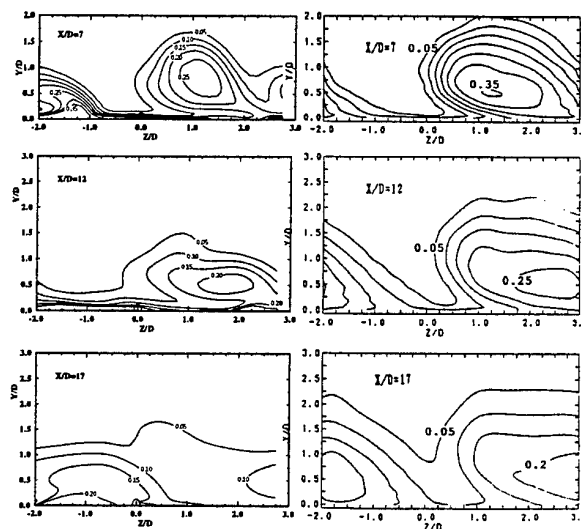


Fig. 10: η -contours; left: Calc.; right: Exp.
(b) $M = 0.85$; $k - \epsilon$ two-layer; $f = 4$

the right and also traces of another counter-rotating vortex on the left of the main vortex. These additional vortices may originate from the horse-shoe vortex which the jet obstructing the oncoming boundary layer may produce. There is no indication from the experiments that these vortices exist; they may be a result of the particular turbulence model used. The temperature contours in Fig. 8 indicate that the temperature in the core is fairly well predicted but that the spanwise spreading to the right-hand side is severely underpredicted. In order to test whether the Bergeles et al modification would remove this deficiency, this case was also calculated using the formula (7) for increasing the eddy viscosity/diffusivity for the momentum and heat transfer in the lateral direction, with the factor f chosen as 4. The resulting secondary velocity vectors at $x/D = 7$ are shown in Fig. 9 and the temperature contours in Fig. 10. It can be seen that the counter-rotating vortex on the right side of the jet has disappeared and the lateral velocity at the

wall is larger in this region. This, together with the increased eddy diffusivity for the lateral transport, has led to significantly increased lateral spreading of the temperature contours, at least at $x/D = 7$. There, the agreement with the measurements is fairly good, whereas it deteriorates further downstream ($x/D = 12$ and 17), and there is no clear overall improvement due to the Bergeles et al correction, even though the lateral spreading is clearly increased.

The results of the computation with the two-layer model for the case of the highest mass flux ratio ($M = 1.2$) are compared with the experiments in Figs. 11 and 12. It is clear that in this case the jet lifts off more from the wall so that the penetration of the fluid from the primary stream on the left of the jet is stronger. On the whole, this is predicted quite well by the model with roughly the correct decay in peak temperature, but again the lateral spreading is not as strong as in the experiments.

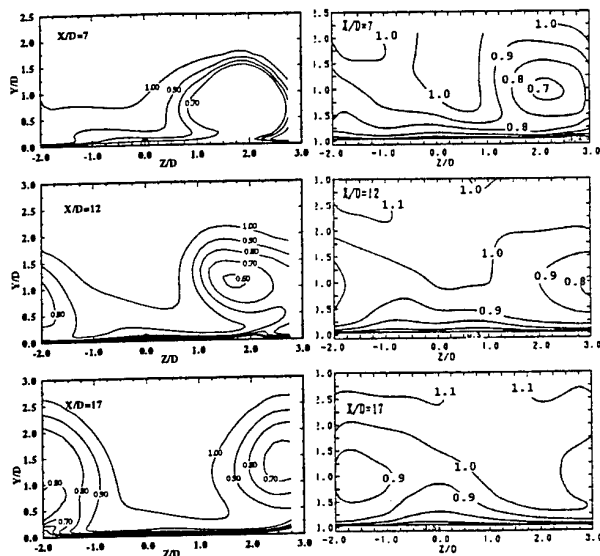


Fig. 11: U/U_∞ -contours; left: Calc.; right: Exp.
(c) $M = 1.20$; $k - \epsilon$ two-layer

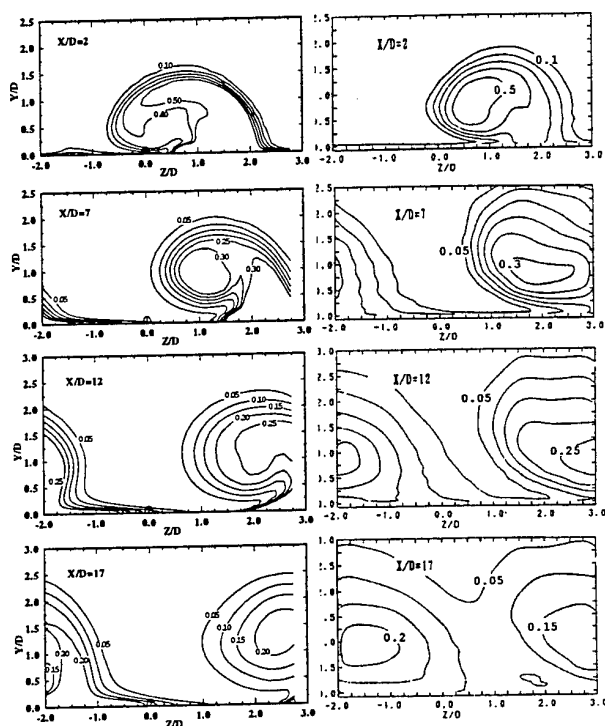


Fig. 12: η -contours; left: Calc.; right: Exp.
(c) $M = 1.20$; $k - \epsilon$ two-layer

CONCLUSIONS

Calculations were conducted of the 3D flow arising from lateral injection of jets into flow over a flat plate using a refined near-wall treatment. The computations underline the need for a resolution of the secondary-flow and heat-transfer mechanisms occurring in the viscosity-affected near-wall layer. Already the standard $k - \epsilon$ model with wall functions was found capable of capturing many of the complex features of the flow, like the asymmetric behaviour due to the injection-induced secondary-flow vortex on the left side and its absence on the right side of the jet and the initial-

ly strong and then slower decay of the temperature in the core of the jet; but the lateral jet spreading is underpredicted considerably by this model and so is somewhat also the strength of the vortex. Resolving the viscosity-affected near-wall region with a one-equation model in a two-layer approach increases the vortex strength and also the lateral spreading, but at the same time reduces the vertical spreading. In fact the strength of the secondary motion is now found to be overpredicted while the lateral spreading in the direction of the injection is still not sufficiently strong. This may be due to the use of the same eddy viscosity and diffusivity for the lateral and normal momentum and heat fluxes, while experiments have indicated that the lateral values should be higher. The Bergeles et al (1978) correction introducing such higher viscosity/diffusivity for the momentum and heat fluxes in the lateral direction did increase the lateral spreading, but met only with partial success. It appears that further calibration of this correction is necessary since it has been developed originally only for the fully turbulent flow region and not for the viscous sublayer in which it was also used here.

The secondary-flow vortex moves primary-stream fluid underneath the coolant jet on its left side, which undermines the film-cooling effectiveness. This important process and also the decay of peak temperature could be simulated quite well by the computational model for all mass flux ratios investigated. The applications should now be extended to real blade situations.

ACKNOWLEDGEMENTS

This work was sponsored by the German Federal Ministry of Education, Science, Research and Technology through programme TURBOTHERM under contract No. 0326760D.

REFERENCES

- Bergeles, G., A.D., Gosman, B.E., Launder.: *The turbulent jet in a cross stream at low injection rates: a three-dimensional numerical treatment*, Num. Heat Transfer, 1, 217-242, (1978).
- Honami, S., Shizawa, T., Uchiyama, A.: *Behaviors of the Laterally injected jet in film cooling: Measurements of surface temperature and velocity/Temperature field within the jet*, ASME paper, 92-GT-180, (1992).
- Launder, B.E., and Spalding, D.B.: *The numerical computation of turbulent flows*, Comput. Meths. Appl. Mech. Eng., 3, pp.269-289, (1974).
- Majumdar, S., Rodi, W., Zhu, J.: *Three-dimensional finite-volume method for incompressible flows with complex boundaries*, J. Fluid Eng., 114, 496-503, (1992).
- Norris, L.H. and Reynolds, W.C.: *Turbulent channel flow with a moving wavy boundary*, Rept. No. FM-10, Stanford University, Dept. Mech. Eng., (1975).
- Rhie, C.M., and Chow, W.L.: *A numerical study of the turbulent flow past an isolated airfoil with trailing edge separation*, AIAA-J., 21, 1225-1532, (1983).
- Rodi, W.: *Experience with two-layer models combining the $k - \epsilon$ model with a one-equation model near the wall*, paper AIAA-91-0216, (1991).
- Stone, H.L.: *Iterative solution of implicit approximations of multidimensional partial differential equations*, SIAM J. on Num. Anal., 5, 530-558, (1968).
- Van Doormal, J.P., and Raithby, G.D.: *Upstream weighted differencing schemes and their application to elliptic problems involving fluid flow*, Computers and Fluids, 2, 191-220, (1984).
- Zhu, J.: *A low-diffusive and oscillating-free convective scheme*, Communications in Applied Num. Meth., 7, 225-232, (1991).

COMPUTATION OF FLOW AND HEAT TRANSFER THROUGH ROTATING RIBBED PASSAGES

Hector Iacovides
Department of Mechanical Engineering
UMIST
P.O.Box 88
Manchester, M60 1QD
UK

ABSTRACT

This study focuses on the computation of periodic flow and heat transfer through stationary and rotating ducts of square cross-section, with rib-roughened walls. Square-sectioned ribs, normal to the flow direction are employed along two opposite walls. Flow comparisons are presented for a duct under stationary and rotating conditions, with ribs in a staggered arrangement. The rib-height-to-diameter ratio is 0.1 and the rib-pitch-to-rib-height ratio is 10. Heat transfer comparisons are shown for a stationary duct with in-line ribs. The rib-height-to-diameter ratio is 0.0675 and the rib-pitch-to-rib-height ratio is 10. Body-fitted grids are employed and two zonal models of turbulence are tested; a $k-\epsilon$ with the 1-eqn model of k transport across the near-wall regions and a low-Re version of the basic DSM model, in which in the near-wall regions the dissipation rate, ϵ , is obtained from the wall distance. The numerical approach adopted is found to lead to the efficient discretization of flows through ribbed ducts. Both models return satisfactory mean flow predictions and the DSM is also able to reproduce most of the features of the turbulence field, under both stationary and rotating conditions. Though the computations of the coefficient of wall heat transfer are not as close to the data as the flow predictions, the DSM thermal computations are clearly superior to those of the $k-\epsilon/1$ -eqn.

1. INTRODUCTION

Heat-transfer-enhancing ribs are often employed in blade cooling and also in other cooling applications. In the case of blade cooling, such ribs are employed along the surfaces of internal passages within rotating blades and nozzle-guide vanes. As intended, the presence of surface ribs leads to flow separation, on either side of each rib, and to a general rise in turbulence and heat transfer levels. Moreover, the blade rotation produces a Coriolis force normal to the main flow direction, which in turn generates secondary motion across the passage (Moon, 1964). The Coriolis force also directly influences the turbulence field, raising the turbulence levels along the pressure (trailing) side of the rotating passage (Johnston et al 1972). The resulting flow is consequently three-dimensional, highly turbulent and, as shown in earlier studies of smooth rotating passages, Iacovides and Launder (1995), influenced by secondary motion that is stronger along the near-wall regions. In blade cooling

passages, consequently, the thermal behaviour would be influenced by the presence of secondary motion, rib-induced separation and also by the effects of the Coriolis force on turbulence. As far as the computation of such flows is concerned, the implication is that the turbulence model employed needs to be able to cope with the presence of secondary motion, the presence of flow separation and also be sensitive to the effects of the Coriolis force on turbulence. Moreover, the elliptic nature of such flows requires the use of fine three-dimensional grids and, as recent studies suggest (Bo et al, 1995), use of high order schemes for the discretization of convective transport.

As shown in earlier studies (Choi et al, 1989 and Besserman and Tanrikut, 1991), the resolution of the secondary motion requires the integration of the mean flow equations across the wall sub-layer, making the wall function approach inappropriate. Subsequent work on flows through rotating ducts, Bo et al (1995) and through U-ducts of strong curvature, Iacovides et al (1995), revealed that use of low-Re second-moment closures further improves predictions of flows affected by orthogonal rotation and also by the combined presence of secondary motion and flow separation.

Similarly extensive numerical studies of the flow and thermal development in rotating ribbed ducts have not until recently been possible, because of the understandable absence of detailed experimental data. Recent experimental work at UMIST, Iacovides et al (1996) has produced detailed LDA measurements for flow through rotating ducts with ribbed surfaces, thus providing the necessary validation data for the present study.

This study has been confined to the computation of flows through passages that are long enough for repeating flow conditions to prevail over each rib interval. Flow through only one rib-interval has consequently been examined, using periodic flow boundary conditions. The objective has been to apply effective-viscosity and also simple second-moment closures to the computation of flow and heat transfer through such passages, in order to assess their effectiveness.

2. FLOW EQUATIONS

All equations are expressed here in Cartesian tensor notation, for a rotating frame of reference.

2.1 Mean Motion.

Continuity
$$\frac{\partial}{\partial x_i}(\rho U_i) = 0$$

Momentum Transport

$$\frac{\partial}{\partial x_j}(\rho U_i U_j) = -\frac{\partial P}{\partial x_i} - \frac{\partial}{\partial x_j} \left[\mu \left(\frac{\partial U_i}{\partial x_j} + \frac{\partial U_j}{\partial x_i} \right) - \rho \overline{u_i u_j} \right] - 2\rho \epsilon_{ij} \Omega_j U_i - \rho [\Omega_j X_j \Omega_i - \Omega_j Y_i \Omega_j]$$

Enthalpy
$$\frac{\partial}{\partial x_j}(\rho U_j T) = \frac{\partial}{\partial x_j} \left[\frac{\mu}{Pr} \frac{\partial T}{\partial x_j} - \rho \overline{u_j T} \right]$$

2.2 Turbulent Flow Equations

The earlier studies, discussed in Section 1, suggest that a low-Reynolds-number model of turbulence needs to be employed across the near-wall regions and that the use of second-moment closures is also desirable. In order to reconcile these requirements with the need for grid economy, two zonal models have been selected: the high-Re version of the $k-\epsilon$ matched to a low-Re one-equation model of k transport and a simple version of the stress transport model, arising from a low-Re ASM closure employed in earlier computations of flow and heat transfer through smooth rotating ducts (Bo et al, 1995), in which across the near-wall regions the dissipation rate of turbulence is obtained from the wall distance. These models have also been recently applied to the computation of heat transfer in two-dimensional ribbed passages, with reasonable success, Iacovides and Raisee (1997).

Effective Viscosity Model (EVM)

$$\rho \overline{u_i u_j} = \frac{2}{3} k \delta_{ij} - \mu_t \left(\frac{\partial U_i}{\partial x_j} + \frac{\partial U_j}{\partial x_i} \right) \quad \text{and} \quad \mu_t = \rho c_\mu \frac{k^2}{\epsilon}$$

$$\frac{\partial}{\partial x_j}(\rho U_j k) = \frac{\partial}{\partial x_j} \left[(\mu + \mu_t) \frac{\partial k}{\partial x_j} \right] + P_k - \rho \epsilon \quad P_k = -\rho \overline{u_i u_j} \left(\frac{\partial U_i}{\partial x_j} \right)$$

$$\frac{\partial}{\partial x_j}(\rho U_j \epsilon) = \frac{\partial}{\partial x_j} \left[(\mu + \mu_t) \frac{\partial \epsilon}{\partial x_j} \right] + c_{\epsilon 1} \frac{\epsilon}{k} P_k - \rho c_{\epsilon 2} \frac{\epsilon^2}{k}$$

Across the near-wall regions (Wolfshtein, 1969):

$$\epsilon = \frac{k^{3/2}}{\ell_\epsilon} \quad \text{and} \quad \mu_t = \rho c_\mu \ell_\mu \sqrt{k}$$

The length scales ℓ_ϵ and ℓ_μ are obtained from the near-wall distance Y , according to:

$$\ell_\epsilon = 2.55 Y [1 - \exp(-0.263 y^*)]$$

$$\ell_\mu = 2.55 Y [1 - \exp(-0.016 y^*)]$$

Where $y^* = Y k^{1/2} / \nu$ is the dimensionless wall distance.

Low-Re Differential Stress Model (DSM)

$$\frac{\partial}{\partial x_k}(\rho U_k \overline{u_i u_j}) = \frac{\partial}{\partial x_k} \left[(\mu + \mu_t) \frac{\partial \overline{u_i u_j}}{\partial x_k} \right] + P_{ij} - \rho \epsilon_{ij} + \Phi_{ij} - \left[H_{ij} - \frac{1}{3} H_{kk} \delta_{ij} \right] + J_{ij}$$

$$P_{ij} = -\left[\overline{u_i u_k} \frac{\partial U_j}{\partial x_k} + \overline{u_j u_k} \frac{\partial U_i}{\partial x_k} \right] - 2\Omega_p \left(\epsilon_{ipq} \overline{u_q u_j} + \epsilon_{jpq} \overline{u_q u_i} \right)$$

$$\epsilon_{ij} = \frac{2}{3} (1 - f_\epsilon) \epsilon \delta_{ij} + f_\epsilon \frac{\overline{u_i u_j}}{k} \epsilon$$

$$\Phi_{ij} = c_1 \frac{\epsilon}{k} (\overline{u_i u_j} - \frac{2}{3} k \delta_{ij}) - c_2 (P_{ij} - \frac{2}{3} P_k \delta_{ij}) + f_w (\Phi_{ij1}^* + \Phi_{ij2}^*)$$

The conventional wall reflection terms are used, which rely on the wall distance x_n and the unit vector normal to the wall n .

$$\Phi_{ij1}^* = c_1 \frac{\epsilon}{k} \left(\overline{u_k u_n} n_k n_j \delta_{ij} - \frac{3}{2} \overline{u_k u_i} n_k n_j - \frac{3}{2} \overline{u_k u_j} n_k n_i \right) \left(\frac{k^{1.5}}{\epsilon c_\mu x_n} \right)$$

$$\Phi_{ij2}^* = c_2 \frac{\epsilon}{k} \left(\overline{\phi_{km} n_k n_m} \delta_{ij} - \frac{3}{2} \overline{\phi_{km} n_k n_j} - \frac{3}{2} \overline{\phi_{km} n_k n_i} \right) \left(\frac{k^{1.5}}{\epsilon c_\mu x_n} \right)$$

$$\Phi_{ij2} = -c_2 (P_{ij} - \frac{2}{3} P_k \delta_{ij})$$

The low-Re terms H_{ij} and J_{ij} are defined as

$$H_{ij} = f_H \frac{\nu}{k} \left(\overline{u_i u_k} \frac{\partial \sqrt{k}}{\partial x_j} \frac{\partial \sqrt{k}}{\partial x_i} + \overline{u_j u_k} \frac{\partial \sqrt{k}}{\partial x_i} \frac{\partial \sqrt{k}}{\partial x_j} \right)$$

$$J_{ij} = f_J k \left(\frac{\partial U_i}{\partial x_j} + \frac{\partial U_j}{\partial x_i} \right)$$

The damping functions that appear in the above terms have the following expressions

$$f_\epsilon = \exp(-y^*/3)$$

$$f_w = [1 - \exp(-0.12 y^*)] [1 + \exp(-0.03 y^*)]$$

$$f_j = 0.06 \exp(-y^*/3)$$

$$f_H = (10.2 + 7.5 y^*) \exp(-y^*/20)$$

The dissipation rate equation is identical to that used in the EVM model. In the near-wall regions, the dissipation rate, ϵ , is also obtained from a prescribed length scale ℓ_ϵ , obtained from:

$$\ell_\epsilon = 2.55 Y [1 - \exp(-0.236 y^*)]$$

Turbulent Heat Fluxes

The same approximation has been employed for both stress models, namely the effective diffusivity approximation.

$$\rho \overline{u_i T} = -\frac{\mu_t}{\sigma_T} \frac{\partial T}{\partial x_i}$$

3. NUMERICAL ASPECTS

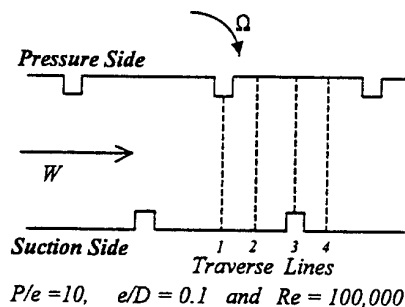
A three-dimensional non-orthogonal finite volume solver, STREAM, was employed, developed at UMIST, which solves for the Cartesian velocity components. A collocated grid is employed with mass flux modification to prevent pressure checkerboarding. In the case of the DSM model, use of the apparent viscosity concept prevents numerical oscillations arising from the explicit presence of the Reynolds stress gradients in the momentum transport equations. For the discretization of convective transport, a bounded form of the quadratic upstream interpolation scheme (QUICK) is employed in the solution of all transport equations, details of which are provided by Iacovides (1997).

In the heat transfer computations constant wall heat flux thermal

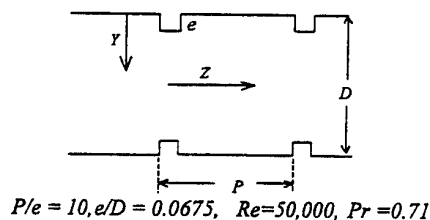
boundary conditions were employed.

4. CASES COMPUTED

Flow computations through two types of ribbed passages have been obtained, both of square cross-section: a passage with staggered square ribs along two opposite walls, Figure 1(a) and a passage with in-line square ribs along opposite walls, Figure 1(b). For the former type, flow computations have been obtained with the passage either stationary, or orthogonally rotating about an axis parallel to the ribs and comparisons have been carried out with the LDA data of Iacovides et al, 1996. For the latter type, heat transfer computations have also been obtained, using air ($Pr=0.7$) as the working fluid and comparisons have been carried out with the Nusselt number measurements of Baughn and Yan (1992).



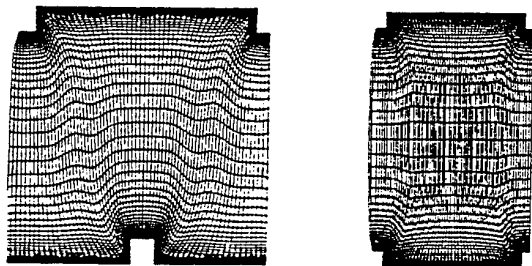
(a) Square duct with staggered ribs



(b) Square duct with in-line ribs

Figure 1. Flow geometries and conditions.

In order to minimise the number of grid nodes required, body-fitted grids, shown in Figure 2, have been employed. This approach, allows for a more efficient distribution of the grid nodes and a more effective resolution of the near-wall regions. Both grids shown in Figure 2, consisted of $76 \times 64 \times 30$ nodes, along the streamwise direction, between the ribbed walls and between the symmetry plane and the smooth wall respectively.



(a) Staggered Ribs

(b) In-line Ribs

Figure 2. Body-fitted grids employed, $76 \times 64 \times 30$ nodes

For the duct with staggered ribs, a coarser $38 \times 32 \times 15$ mesh was also used, shown in Figure 3, for grid sensitivity comparisons. Comparisons of the resulting EVM predictions along the symmetry plane, traverse lines 1 and 2, for the stationary case, are shown in Figure 4. The mean velocity profiles obtained with the two grids are practically identical and are also in close agreement with the LDA data. These comparisons provide some support for the numerical and gridding strategy adopted.

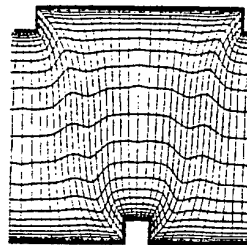


Figure 3.
Coarse mesh employed for grid
sensitivity comparisons.
 $38 \times 32 \times 15$ nodes

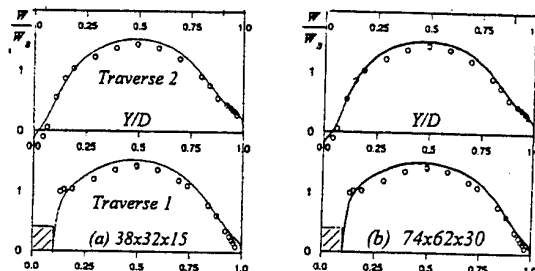


Figure 4. EVM computations of the streamwise velocity for a stationary passage with staggered Ribs

5. RESULTS AND DISCUSSION

5.1 Flow in a Square Duct with Staggered Ribs

Figure 5 shows the mean flow development along the symmetry plane of a stationary duct. The separation bubble downstream of each rib extends to almost half the inter-rib distance. Profile comparisons along traverse lines 1 and 2 of the duct symmetry plane, are presented in Figure 6. As already commented, the EVM computed velocity profiles are in close agreement with the measurements. The DSM comparisons return a somewhat faster core flow, which appears to be consistent with the fact, shown later in Figure 11, that the DSM model returns a significant turbulence-driven secondary motion. The comparisons of the stress profiles show that both models reproduce the high turbulence levels measured. The DSM model tested is also found able to reproduce the levels of the individual stresses, in the streamwise and cross-duct directions, with reasonable accuracy. The experimental distribution of the turbulent

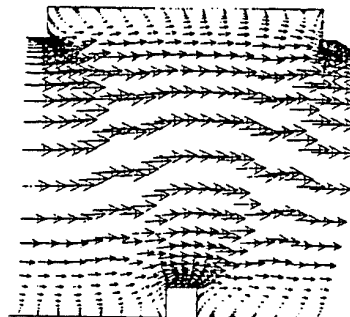
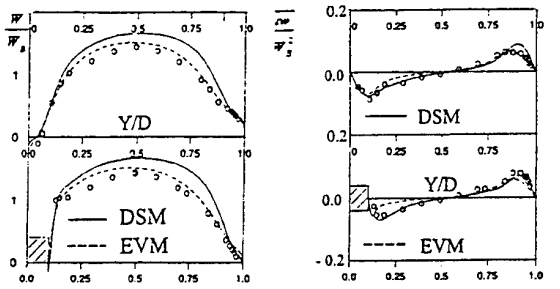


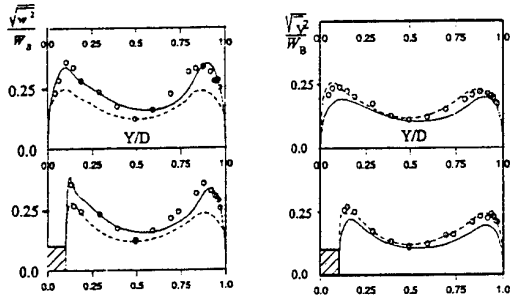
Figure 5.
Mean flow along
the symmetry
plane, for a
stationary duct.

shear stress is also well reproduced, especially by the DSM model. The corresponding EVM predictions are also not far from the LDA data, but under-predict shear stress levels over the rib.



(a) Streamwise Velocity

(b) Turbulent Shear Stress



(c) Streamwise Intensity

(d) Cross-Duct Intensity

Figure 6. Profile comparisons for stationary passage with staggered ribs.

For the rotating case at a rotation number ($Ro = QD/W_s$) of 0.2, the mean flow development along the symmetry plane is shown in Figure 7. Flow separation along the pressure (trailing) side is attenuated, while along the suction side the separation bubbles are enlarged. Mean-velocity profile comparisons along the symmetry-plane traverse lines 1 to 4 are shown in Figure 8. The mean flow measurements indicate that the Coriolis-induced secondary motion convects the faster fluid toward the pressure (trailing) side of the duct. The mean velocity field is well reproduced by both models. Moreover, because the Coriolis-driven secondary motion is a mean flow phenomenon, differences between the DSM and EVM predictions have diminished.

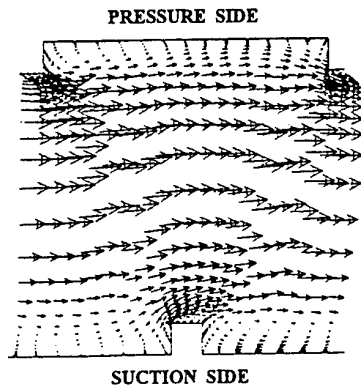
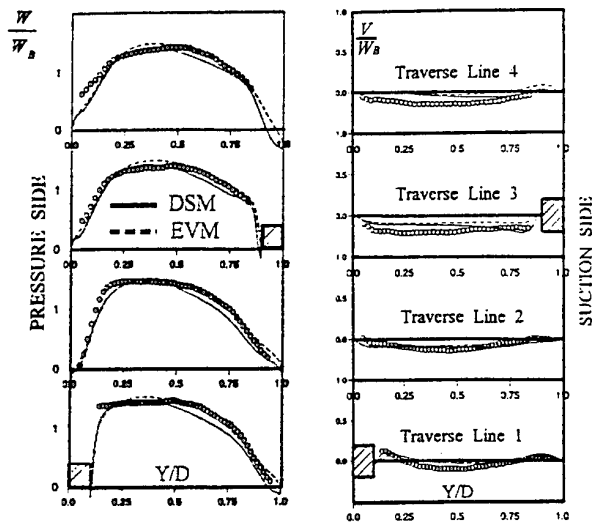


Figure 7.
Mean flow along the symmetry plane, for a rotating duct, at $Ro=0.2$.

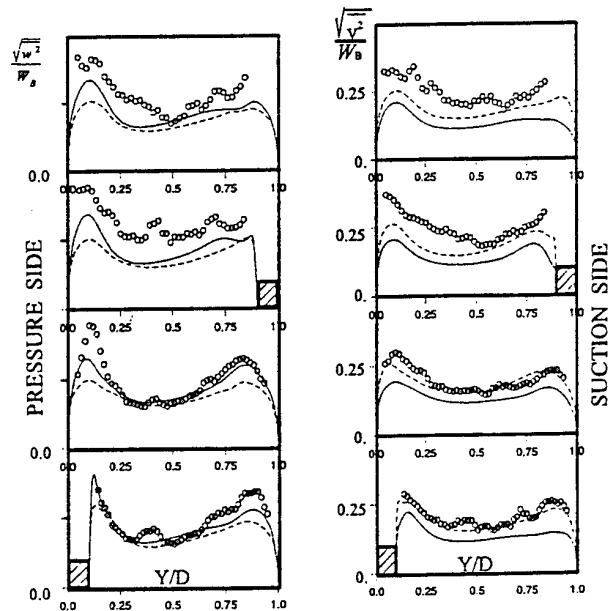


(a) Streamwise Velocity

(b) Cross-Duct Velocity

Figure 8. Mean flow comparisons for rotating passage with staggered ribs, at $Ro=0.2$.

The corresponding stress comparisons are shown in Figure 9. As expected, rotation raises the levels of all measured components of the Reynolds stress tensor along the pressure side of the duct. Some of this rise in the pressure-side turbulence levels is reproduced even by the EVM model, indicating that it is partly caused by the secondary motion. The DSM model produces a stronger variation in the levels of the normal stresses across the duct and the computed distribution of the streamwise component is in good accord with the data. The cross-duct component is somewhat under-predicted by the DSM model, while both models return shear stress levels



(a) Streamwise Intensity

(b) Cross-Duct Intensity

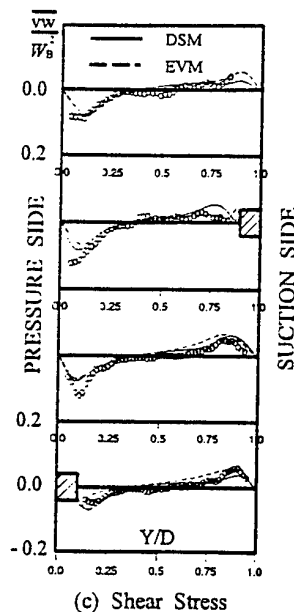


Figure 9. Turbulence field comparisons for rotating passage with staggered ribs, at $Ro=0.2$.

comparable to those measured. The DSM model returns a shear stress distribution that is in closer overall agreement with the measurements than that of the EVM model.

On the whole, the main effects of rotation on the turbulence field are reproduced by the DSM model employed, but agreement with measurements is not as close as in the stationary case.

5.2 Heat Transfer in a Square Duct with In-Line Ribs

The flow development for this case is shown in the symmetry-plane vector plots of Figure 10, where the separation bubbles on

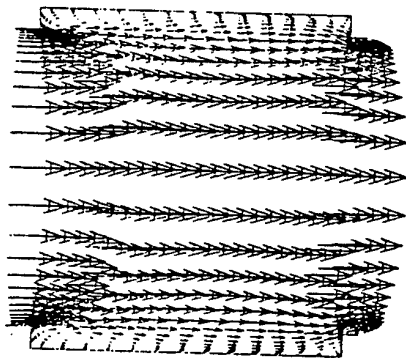
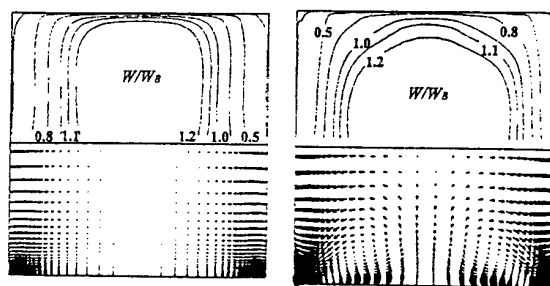


Figure 10. Mean flow along symmetry plane of square duct with in-line ribs.

either side of each rib are clearly visible. The cross-duct vector plots of Figure 11, at a plane half-way between the ribs, show that, as commented earlier, the DSM model produces a turbulence-driven secondary motion that influences the distribution of the streamwise velocity.



(a) EVM Computations (b) DSM Computations
Figure 11. Predicted flow field across the duct, half-way between the in-line ribs.

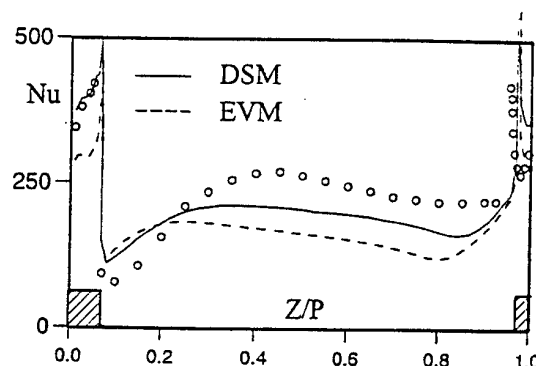


Figure 12. Local Nusselt number comparisons along the centre line of the ribbed wall of a passage with in-line ribs.

Comparisons between the computed and measured distributions of the local Nusselt number, along the centre line of the ribbed wall, are shown in Figure 12. Both the level and distribution of the local Nusselt number, are better reproduced by the second-moment closure, though there is still scope for further improvement. The stronger secondary motion returned by the DSM must be at least partly responsible for the higher Nusselt number levels returned by this model, which in places are still as much as 20% lower than the experimental ones. It is especially noteworthy that over the rib, while the EVM model under-predicts the high Nusselt number values measured, the DSM values are close to the experimental levels. This is consistent with the earlier finding that over the rib, the EVM model also under-predicts the turbulent shear stress.

The plots of the local Nusselt number contours along the ribbed wall, shown in Figure 13, also show that the DSM model reproduces the experimental distribution more faithfully over the entire ribbed wall. The EVM model returns a faster recovery downstream of the rib, which is at variance with the data and also fails to return the dip found in the corner region, upstream of the rib. As also shown in Figure 12, near the symmetry plane, both models and especially the EVM, show a gradual rise in Nusselt number levels ahead of the rib, not present in the data.

The heat transfer comparisons thus reveal that the models tested are less successful in reproducing the thermal behaviour than they are in returning the flow development in ribbed ducts. The comparisons also reveal that there are important differences between the thermal predictions of the DSM and the EVM models, suggesting that a second-moment closure produces significant predictive improvements.

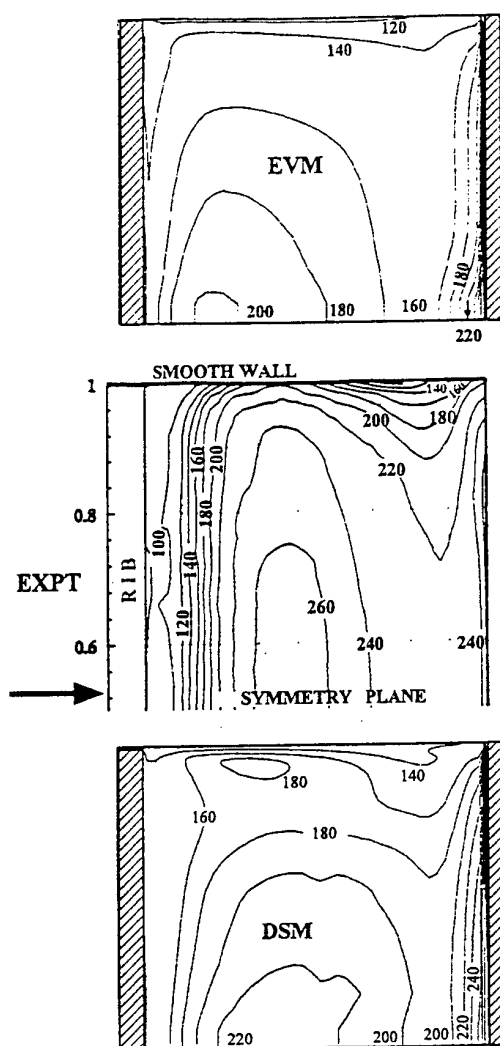


Figure 13. Contours of the local Nusselt number, along the ribbed wall, for a square duct with in-line ribs.

6. CONCLUDING REMARKS

From the comparisons carried out, a number of conclusions can be drawn regarding the computation of flow and heat transfer through ribbed and rotating passages.

The use of body-fitted grids and high-order discretization schemes for the convective transport leads to the efficient resolution of flow through ribbed ducts.

The mean flow development in stationary ribbed ducts is well predicted by the zonal $k-\epsilon/1$ -eqn model, while the rather simple low-Re DSM employed somewhat over-predicts the strength of the turbulence-driven secondary motion. Both models return the high turbulence levels measured, and the DSM model also returns satisfactory predictions of the anisotropy of turbulence and, in contrast to the EVM model, predicts the correct shear-stress levels over the ribs.

In ribbed ducts rotating orthogonally, both the above models reproduce well the mean flow development. The effects of rotation on turbulence are well reproduced by the DSM model, but agreement with the measurements is not as close as in the stationary case.

The thermal behaviour in ribbed ducts, is not well predicted by the $k-\epsilon/1$ -eqn model. Introduction of a simple low-Re DSM, in which the near-wall dissipation rate is obtained from the wall distance, improves thermal predictions, because of its ability to predict the turbulence-driven secondary motion and also because it is able to return the correct turbulence field over the ribs. More refined turbulence models are however necessary to achieve the close agreement with the experimental data, observed in the hydrodynamic comparisons.

ACKNOWLEDGEMENTS

The author wishes to express his gratitude to his colleague Prof. B.E. Launder for his support and encouragement. Support for this work has been provided by Rolls-Royce plc and DRA Pyestock. The helpful input of Mr J. Coupland, of Rolls-Royce plc is greatly acknowledged. Thanks are also due to Dr. Y-M Yuan at UMIST for making available the experimental data in digital form.

REFERENCES

- Baughn J W and Yan X, 1992, "Local heat transfer measurements in square ducts with transverse ribs.", ASME, National Heat Transfer Conference.
- Besserman D L and Tanrikut S, 1991, "Comparison of heat transfer measurements with computations for turbulent flow around a 180° bend." ASME Paper 91-GT-2, Int. Gas-Turbine and Aero Congress, Orlando FL.
- Bo T, Iacovides H and Launder B E, 1995, "Developing buoyancy-modified turbulent flow in ducts rotating in orthogonal mode.", ASME, J. Turbomachinery, **117**, 474-484.
- Bo T, Iacovides H and Launder B E, 1995, "Convective discretization schemes for the turbulence transport equations in flow predictions through sharp U-bends.", Int. Journal of Numerical Methods in Heat and Fluid Flow, **5**, pp 33-48.
- Choi Y-D, Iacovides H. and Launder B E, 1989, "Numerical computation of turbulent flow in a square-sectioned 180-deg bend.", ASME J Fluids Engrg, **111**, pp 59-68.
- Iacovides H, 1997, "The computation of turbulent flow through stationary and rotating u-bends of with rib-roughened surfaces." 11th Int Conf on Lam and Turb. Flows, Swansea.
- Iacovides H. and Launder B E, 1995, "Computational fluid dynamics applied to internal cooling of gas-turbine blade cooling: a review.", Int of Journal Heat and Fluid Flow, **16**, 454-470.
- Iacovides H, Jackson D C, Ji H, Kelemenis G, Launder B E and Nikas K, 1996, "LDA study of flow development through an orthogonally rotating U-Bend of strong curvature and rib-roughened walls.", Paper No ASME-96-GT-476, Int. Gas-Turb and Aero Congress, Birmingham, UK.
- Iacovides H and Raisee M, 1997, "The computation of flow and heat transfer in two-dimensional rib-roughened passages.", 2nd Int. Symp. on Turbulence Heat and Mass Transfer, Delft.
- Johnston J P, Halleen R M and Lezius D K, 1972, "Effects of spanwise rotation on the structure of two-dimensional fully developed turbulent channel flow.", JFM, **56**, 533-557.
- Moon I M, 1964, "Effects of Coriolis force on turbulent boundary layers in rotating fluid machines.", MIT Gas-Turbine Laboratory, Report No 74.
- Wolfstein M, 1969, "The velocity and temperature distribution in one-dimensional flow with turbulence augmentation and pressure gradient.", Int. J. Heat and Mass Transfer, **12**, 301.

CALCULATION OF GAS TURBINE COMBUSTOR FLOWS USING AN ADAPTIVE GRID REDISTRIBUTION METHOD

W. P. Jones

Department of Chemical Engineering and Chemical Technology,
Imperial College of Science, Technology and Medicine,
London SW7 2BY
United Kingdom

K. R. Menzies

Combustion Engineering,
Rolls-Royce plc,
P. O. Box 3,
Filton, Bristol BS12 7QE
United Kingdom

ABSTRACT

A three-dimensional adaptive grid redistribution scheme is described and applied to the calculation of the reacting flow in a gas turbine combustion chamber. The adaptive grid method is coupled to a three-dimensional flow solver employing the $k-\epsilon$ turbulence model and a conserved scalar description of combustion. The results of the calculations on different grid sizes are shown and are compared to measurements. The adaptive grid scheme is shown to improve the results of the calculations by reducing numerical errors.

INTRODUCTION

In calculating the flows in typical gas turbine combustion chambers it is often very difficult to ensure that the number of grid nodes is sufficient to entirely eliminate grid related errors in the computation. The complexity of the flow is such that the computer time and memory required to achieve a grid independent solution can be impractical for routine calculations even on present computers. In order to take advantage of sophisticated turbulence and combustion models it is necessary to have high numerical accuracy which demands making the best use of the finite number of nodes available.

If grid related errors in the computation cannot be eliminated then there should be an optimum distribution of the grid nodes which yields the lowest numerical error for the specified grid size. In the present work the grid generation is coupled to the underlying velocity field which allows the nodes to be automatically distributed to reduce the numerical error. This also allows the code user to be freed from 'hand-tuning' the grid. The velocity field is obtained from a three-dimensional finite volume CFD solver suitable for low Mach number turbulent reacting flows.

MODELLING APPROACH FOR COMBUSTION SYSTEMS

The flow in a gas turbine combustion chamber is three-dimensional, recirculating, turbulent and displays large density variations as a result of combustion. The flow is in general also contained within a domain of complex shape and so the simulation must employ turbulence and combus-

tion models capable of describing the flow and numerical techniques capable of resolving the domain.

Computer limitations preclude the use of techniques such as Large Eddy Simulation for routine combustor CFD in an industrial design environment and consequently the approach adopted here is based upon the density weighted or Favre averaged forms of the conservation equations for reacting flow. In the present work turbulent transport has been modelled using the high Reynolds number $k-\epsilon$ model of Jones and Launder (1972) with wall functions to represent the viscous sublayer arising adjacent to solid surfaces. A conserved scalar combustion model has been used based on the normalised carbon element mass fraction (mixture fraction) \bar{f} along with a laminar flamelet description of the thermochemistry employing the global hydrocarbon reaction mechanism of Jones and Lindstedt (1987). An unstrained laminar propane-air flamelet was used to obtain the thermochemical state as a function of mixture fraction. Turbulence-chemistry interaction was represented using a presumed shape probability density function (here a β -function) specified in terms of the mean mixture fraction and its variance \bar{f}''^2 .

Since the primary aim of the present work was to demonstrate the improvement in numerical accuracy which could be obtained for a complex reacting flow by use of adaptive grid redistribution the use of more advanced turbulence and combustion models was not felt justified. However, the results presented here though should carry over to situations where more sophisticated models are used.

NUMERICAL IMPLEMENTATION

The modelled equations are cast into a three-dimensional nonorthogonal coordinate system ξ^i employing a fixed cartesian basis for the velocity components \tilde{u}_i . The general transport equation transforms to equation (1) where β_i^j denotes the cofactor of $\partial x_i / \partial \xi^j$ in the inverse transformation Jacobian:

ϕ	Γ_ϕ	S_ϕ
1	0	0
\bar{u}_i	μ_T	$-\frac{\partial}{\partial \xi^j} (\bar{p} \beta_i^j) + \frac{\partial}{\partial \xi^j} \left(\frac{\mu_T}{J} \beta_i^m \beta_k^j \frac{\partial \bar{u}_k}{\partial \xi^m} \right)$
k	μ_T / σ_k	$\mathcal{P}_k - \bar{p} \epsilon$
ϵ	μ_T / σ_ϵ	$C_{\epsilon 1} \frac{\epsilon}{k} \mathcal{P}_k - C_{\epsilon 2} \bar{p} \frac{\epsilon^2}{k}$
f	μ_T / σ_f	0
\bar{f}''^2	μ_T / σ_{fv}	$2 \bar{p} \frac{\mu_T}{\sigma_{fv}} \frac{1}{J^2} \beta_m^j \beta_m^j \frac{\partial \bar{f}''^2}{\partial \xi^m} \frac{\partial \bar{f}''^2}{\partial \xi^m} - C_D \bar{p} \frac{\epsilon}{k} \bar{f}''^2$

Table 1: Diffusion Coefficients and Source Terms for Governing Equations

C_μ	$C_{\epsilon 1}$	$C_{\epsilon 2}$	C_D	σ_k	σ_ϵ	σ_f	σ_{fv}
0.09	1.44	1.92	2.00	1.00	1.30	0.70	0.70

Table 2: Model Constants

$$\frac{\partial}{\partial t} (\bar{p} \bar{\phi}) + \frac{\partial}{\partial \xi^j} (\bar{p} \bar{u}_m \beta_m^j \bar{\phi}) - \frac{\partial}{\partial \xi^j} \left(\frac{\Gamma_\phi}{J} \beta_k^m \beta_k^j \frac{\partial \bar{\phi}}{\partial \xi^m} \right) = S_\phi J \quad (1)$$

The appropriate values for the diffusion coefficients Γ_ϕ and source terms S_ϕ for each equation are given in Table 1. In Table 1, $\mu_T = C_\mu k^{3/2} / \epsilon$ is the turbulent viscosity and \mathcal{P}_k the production of turbulence energy.

The values of the constants in these equations are listed in Table 2:

The governing equations were discretised using a finite volume approach on a structured nonorthogonal grid. A co-located variable arrangement was employed along with the momentum interpolation procedure of Rhie and Chow (1982) to prevent pressure-velocity decoupling. The Total Variation Diminishing (TVD) scheme of van Leer (1974) was used to discretise the convection terms in all of the equations, implemented in the manner described by Alvarez (1994). All other spatial derivative terms were discretised using standard second order accurate central differences. The coupled system of equations was solved using a pressure correction method as described by Jones (1994). This algorithm solves the governing equations in time dependent form using an approximate factorisation technique; the solution is advanced through time until a steady state is reached. The system of linear equations arising at each time step for transported variables were solved using a line Gauss-Seidel matrix solution algorithm whereas a preconditioned conjugate gradient solver was used for the pressure.

THE ADAPTIVE GRID METHOD

There are two distinct possible approaches to generating a solution adaptive grid. Resolution of important features of the solution may be increased either by adaptively redistributing the existing grid lines so that the grid remains structured or by adaptively refining regions of the solution by adding new nodes. In the present work the first approach has been used.

The adaptive redistribution of the grid is achieved by clustering nodes in regions where an adaptive monitoring parameter or *weight function* is large, to equi-distribute the monitoring parameter over the adapted grid (see for example Eiseman (1987) and Thompson *et al* (1985)). This monitoring parameter should indicate regions where the numerical error in the approximation is large, either directly by measurement of the discretisation error, or indirectly by considering the variation of the solution variables on the grid; the numerical error is likely be large where the

dependent variables change rapidly over a few grid lines. It is difficult to obtain an effective a-priori measure of discretisation error, particularly with coarse grids - a mesh sufficiently fine to resolve the leading terms of the error would be required - and so the indirect error measure approach has been adopted in the present work. To achieve this it is important to note that it is not sufficient to simply detect high-gradient regions of selected variables in the solution since this may result in too severe a depletion of nodes in regions where the solution varies slowly and around extrema. The adaptive monitor used is therefore based on an arc-length formulation. It remains to choose the solution variable to be used to construct the monitor and of the many variables available, a velocity based measure seems the most promising, particularly considering the importance of convective transport in combustor flows. Since there is no predominant direction in the flow-field it is not appropriate to favour one velocity component over another so the magnitude of the velocity vector has been selected. The adaptive monitoring parameter is then defined as

$$w_i = \sqrt{1 + \left(\frac{\partial |\mathbf{v}|}{\partial s_i} \right)^2} \quad (2)$$

where $|\mathbf{v}|$ is the magnitude of the velocity vector and s_i is the arc length in the ξ^i direction.

A grid generation system based on the solution of elliptic partial differential equations (as described by Thompson *et al* (1985)) has been used to generate the adaptive grids. The basic generating system is written in the form

$$\nabla^2 \xi^i = g^{ii} P_i \quad (\text{no summation on } i) \quad (3)$$

where the g^{ii} are the contravariant metric tensor components and the P_i are the grid control functions, used to influence the grid node distribution. Interchanging dependent and independent variables gives

$$g^{ij} \frac{\partial^2 x_l}{\partial \xi^i \partial \xi^j} + g^{kk} P_k \frac{\partial x_l}{\partial \xi^k} = 0 \quad (4)$$

which is solved on a uniform grid in computational space. To couple this grid generation system to the adaptive information from the solution it is necessary to define the control functions P_i from the adaptive weight functions w_i :

$$P_i = \frac{1}{w_i} \frac{\partial w_i}{\partial \xi^i} \quad (\text{no summation on } i) \quad (5)$$

The adaptive control functions from the interior field are projected onto the boundary in order to reduce grid distortion next to solid walls.

More details on the adaptive grid method are available in Menzies (1997).

THE MODEL COMBUSTOR

The combustor geometry used for this study is a model can-type combustor, as shown in Figure 1, for which detailed internal temperature and species measurements are available (Bicen *et al* (1988)). The combustor comprises a hemispherical head, 75mm diameter circular barrel and a circular to rectangular discharge nozzle, all fabricated from porous metal sheet. The combustor barrel contains six 10mm diameter primary holes and six 20mm diameter dilution holes which are staggered half a pitch from the primary holes. The combustor head includes an air swirler and a fuel injector; propane is used as fuel. Figure 1 also illustrates the air flow splits for the various combustor features.

Experimental data is available for this configuration for a variety of air swirlers, overall air-fuel ratio values and inlet

temperatures, all at approximately atmospheric pressure. The conditions chosen for the present study corresponds to a 45° air swirler, an air-fuel ratio of 57 and an air inlet temperature of 315K. The temperature measurements used for comparison were made using 80µm bare wire digitally compensated thermocouples and so are close to unweighted mean temperatures.

The measured temperature fields for these conditions in the mid-vertical and mid-horizontal planes are shown in Figures 2 and 3 respectively. A major feature to be noted is the high temperature region in the primary zone (upstream of the first row of jets) on the fuel injector centreline which is terminated by the primary jet flows. Downstream of the primary jets the maximum gas temperatures are found closer to the walls of the combustor with a relatively cool zone on and around the combustor centreline. The dilution jets, which do not penetrate to the combustor centreline, can also be seen in Figure 2.

CALCULATIONS

Calculations have been made on a variety of grid sizes for the combustor using both unadapted (generated by transfinite interpolation with elliptic smoothing) and adapted grids. Results for two grid sizes are shown here; more detailed results are available in Menzies (1997). The calculated results presented here have been obtained with grids of 20,000 nodes and 65,000 nodes; a fine grid calculation with a grid of 235,000 nodes has also been performed. The coarse grid would normally be too sparse to consider for practical calculations of combustion systems but has been performed in order to assess the improvement in accuracy available with the adaptive grid scheme on a very coarse grid.

All of the results to be presented were obtained using the methods and models described earlier.

RESULTS

The results of the calculations are presented as contours of unweighted temperature on the mid-vertical and mid-horizontal planes which can be compared with the experimental data of Figures 2 and 3. It should be noted that in all cases the temperature levels are over predicted. This is thought to be a consequence of ignoring radiative heat losses in the laminar flamelet calculation; given the size of the combustor and the operating conditions (atmospheric pressure) then radiation losses may become important in this configuration.

The temperature fields obtained with the coarse unadapted grid are shown in Figures 4 and 5. While the general shape of the measured temperature field has been captured, the primary jets do not penetrate far enough into the crossflow and consequently the low temperature region formed downstream of the jet impingement point is not formed in the calculations. However, the movement of the high temperature gas towards the combustor walls has been correctly reproduced.

Figures 6 and 7 show the same views for the medium grid calculation. Here the primary jets penetrate more strongly than in the coarse grid case; consequently the calculations correctly reproduce the high temperature zone on the fuel injector centreline upstream of the primary jets and the low temperature region on the combustor centreline downstream of the jets.

Adaptively redistributing the grid for this flow gives a modified coarse grid as shown in Figure 8. The grid has concentrated around the fuel injector efflux and the jets. The solution obtained on this grid is shown in Figures 9 and 10 which should be compared with the previous results. The adapted grid calculation displays an improved penetration of the primary jets compared to the unadapted coarse grid with the low temperature zone on the com-

busator centreline downstream of the primary jets being detected similar to the medium grid. The high temperature region upstream of the jets on the centreline is also more distinct than in the unadapted coarse grid calculation. The adapted grid prediction shows a lower temperature downstream of the dilution jets than the coarse grid, which is also consistent with the medium grid calculation. The adaptive grid calculation can therefore be seen to provide results which are much closer to the finer grid than the initial unadapted grid results. Even on so coarse an initial grid the use of adaptive redistribution has been beneficial.

Note that since the cost of performing a calculation of this type varies roughly with the square of the number of grid nodes, the coarse grid results require about 10% of the computational time as the medium grid calculations.

CONCLUSIONS

An adaptive grid redistribution method has been presented which is suitable for complex low Mach number flows and has been applied to the calculation of the reacting flow in a model can-type gas turbine combustion chamber. Comparing the predictions to internal temperature measurements shows that while an unadapted grid of 20,000 nodes is less able to predict the major features of the flow than an (unadapted) grid of 65,000 nodes, using the adaptive redistribution method allows the (adapted) 20,000 node grid to produce results comparable to the finer grid calculation but at a much lower computational cost. It is of course likely that much finer grids will be required to resolve all of the important features of the combustor flow presently considered. However the adaptive method described should allow this to be achieved with a minimum grid size and computational resource.

Acknowledgements : The authors would like to thank Rolls-Royce plc for supporting this work and for permission to publish.

REFERENCES

- Alvarez, J.E., 1994, "Calculation of the Velocity and Temperature Fields in a Jet in Cross-Flow", Ph.D. Thesis, University of London
- Bicen, A.F., Tse, D.G.N. and Whitelaw, J.H., 1988, "Combustion Characteristics of a Model Can-type Combustor", Department of Mechanical Engineering Fluids Section Report FS/87/28 (Revised), Imperial College of Science and Technology, London
- Eiseman, P.R., 1987, "Adaptive Grid Generation", *Computer Methods in Applied Mechanics and Engineering* vol 64, p 321
- Jones, W.P., 1994, "Turbulence Modelling and Numerical Solution Methods for Variable Density and Combusting Flows", in *Turbulent Reactive Flows* (P.A.Libby and F.Williams, eds), Academic Press, New York
- Jones, W.P. and Launder, B.E., 1972, "The Prediction of Laminarisation with a Two-Equation Model of Turbulence", *International Journal of Heat and Mass Transfer* vol 15 p 301
- Jones, W.P. and Lindstedt, R.P., 1987, "Global Reaction Schemes for Hydrocarbon Combustion", *Combustion and Flame* vol 73 pp 233-249
- Menzies, K.R., 1997, Ph.D Thesis, University of London (in preparation)
- Thompson, J.F., Warsi, Z.U.A. and Mastin, C.W., 1985, *Numerical Grid Generation - Foundations and Applications*, North Holland, New York
- Van Leer, B., 1974, "Towards the Ultimate Conservative Differencing Scheme II - Monotonicity and Conservation Combined in a Second-Order Scheme", *Journal of Computational Physics* vol 14 p 361

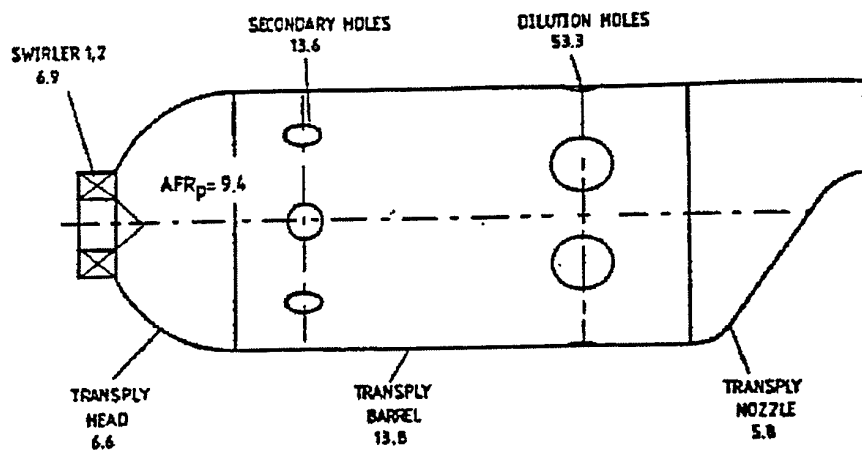


Figure 1: THE MODEL COMBUSTOR GEOMETRY AND FLOW SPLITS

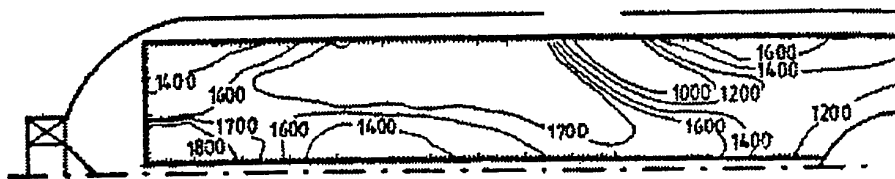


Figure 2: MEASURED TEMPERATURES IN MID-VERTICAL PLANE

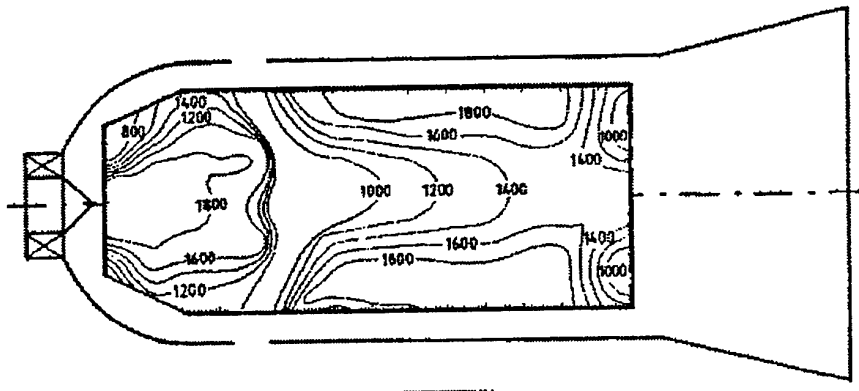


Figure 3: MEASURED TEMPERATURES IN MID-HORIZONTAL PLANE

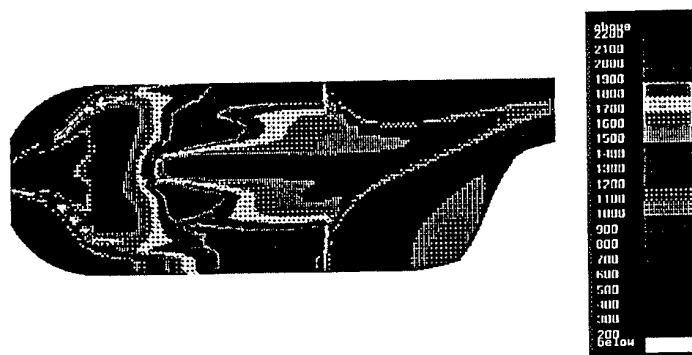


Figure 4: COARSE GRID: PREDICTED TEMPERATURES IN MID-VERTICAL PLANE

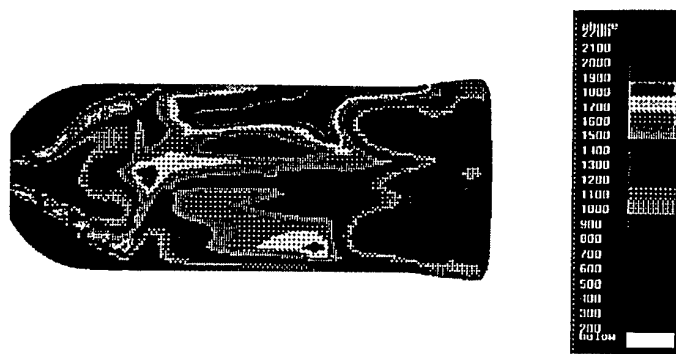


Figure 5: COARSE GRID: PREDICTED TEMPERATURES IN MID-HORIZONTAL PLANE

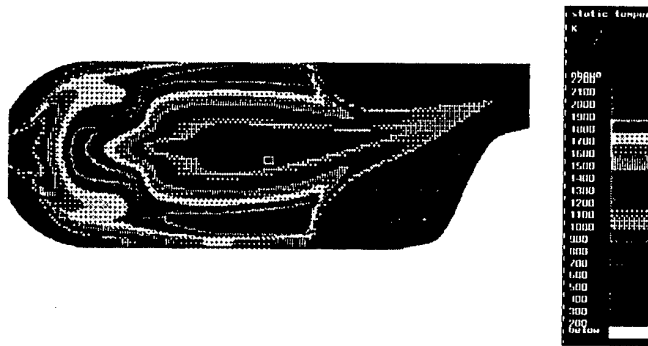


Figure 6: MEDIUM GRID: PREDICTED TEMPERATURES IN MID-VERTICAL PLANE

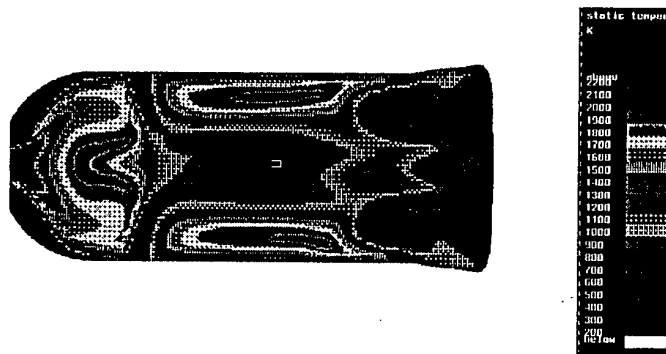


Figure 7: MEDIUM GRID: PREDICTED TEMPERATURES IN MID-HORIZONTAL PLANE

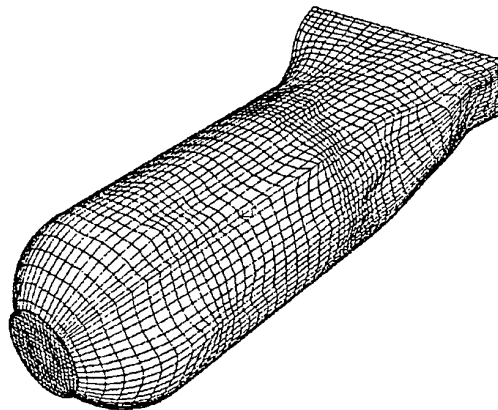


Figure 8: ADAPTED COARSE GRID

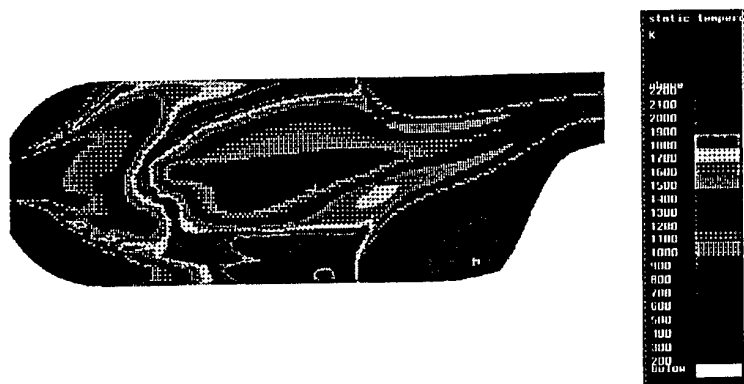


Figure 9: ADAPTED COARSE GRID: PREDICTED TEMPERATURES IN MID-VERTICAL PLANE

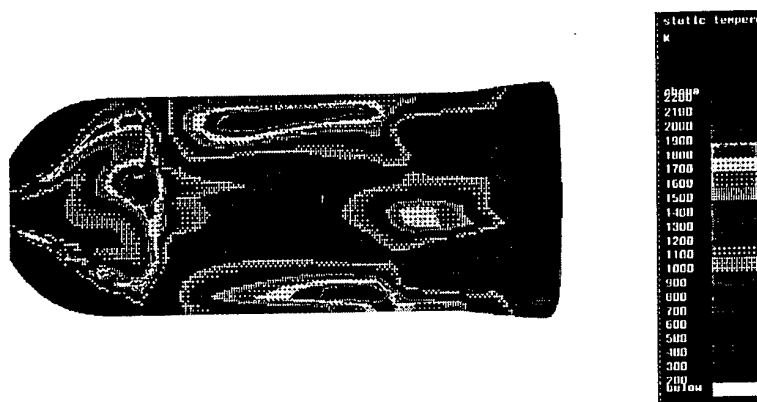


Figure 10: ADAPTED COARSE GRID: PREDICTED TEMPERATURES IN MID-HORIZONTAL PLANE

SESSION 4 - FUNDAMENTALS I

A PARAMETRIC STUDY OF RAYLEIGH-BENARD CONVECTION USING A KARHUNEN-LOEVE BASIS

Hakan I. Tarman

Department of Mathematical Sciences
King Fahd University of Petroleum and Minerals
Dhahran 31261
Saudi Arabia

Lawrence Sirovich

Laboratory of Applied Mathematics
CUNY / Mt. Sinai
Box 1012
New York City 10029
USA

ABSTRACT

A parametric study of Rayleigh-Benard thermal convection is performed for varying control parameter, Rayleigh number, while the Prandtl number and aspect ratio of the convective box are fixed at 0.72 (for air) and $2\sqrt{2}$, respectively. This study is based on the numerical integration of a relatively low dimensional approximation of the governing Boussinesq equations by amplitude equations obtained from a Galerkin projection using the Karhunen-Loeve basis. This basis is empirically generated from a numerical database obtained from a numerical simulation of the Boussinesq equations at Rayleigh number about 10,000 in a horizontal periodic convective box bounded vertically by a free surface. Steady, periodic, quasi-periodic and non-periodic regimes after a weakly frequency-locked state are observed as Rayleigh number is increased passed its critical value from the linear stability theory.

INTRODUCTION

The transition to chaos in the case of Rayleigh-Benard thermal convection takes the form of discrete steps as the forcing parameter, Rayleigh number (Ra), is gradually increased passed the critical value. The first step, in this transition, has been shown analytically by Busse (1972) to be in the form of traveling waves imposed on the two dimensional rolls at low Prandtl number (Pr) with stress-free boundary conditions. Further, numerical studies by McLaughlin & Orszag (1982) in air with rigid boundary conditions and Curry *et al.* (1984) at high Prandtl number with stress-free boundary conditions have shown that transition follows a route consistent with the scenario of Ruelle *et al.* (1978), namely, that the appearance of a third oscillatory mode in a nonlinearly coupled system likely leads to broadband frequency excitations and

chaos. Gollub & Benson (1980) found experimentally several other routes of transition to chaos under various fluid conditions and geometries. More recently, Meneguzzi, *et al.* (1987) observed period doubling in their numerical simulations at low Prandtl number with stress-free boundary conditions.

In the present work, the Karhunen-Loeve (K-L) basis is used to reduce the Boussinesq equations to a set of amplitude equations by means of Galerkin projection. The truncated amplitude equations are used to follow the flow transition. As we show, the K-L basis decomposes the flow into physically meaningful *flowlets* that satisfy the boundary conditions, symmetries of the flow and are divergence-free, thus these carry the structure of the flow and provides a criterion for systematic inclusion of flowlets in the truncated system. Numerous prior studies have adopted the K-L procedure in a variety of low dimensional dynamical studies (Sirovich & Rodriguez 1987, Aubry *et al.* 1988, Deane *et al.* 1991, Rajaei *et al.* 1994, Rempfer & Fasel 1994).

A Rayleigh-Benard thermal convection database which was generated by numerical integration of the Boussinesq equations at the parameter values $Pr = 0.72$ and $Ra = 15 \times Ra_c$, has been utilized to create a K-L basis. This K-L basis, evaluated at a particular value of the parameter set, is then used for a range of parameter values. In the present formulation unlike the previous treatments (Sirovich *et al.* 1989, Tarman 1996), the K-L decomposition technique is applied separately to the mechanical and thermal components of the solution field resulting in two orthonormal K-L basis sets and the mean field is not subtracted off from the solution field prior to the generation of the bases, thus removing the need to treat the mean field separately in the low dimensional simulation (Tarman & Sirovich 1997). This treatment leads to a more robust formulation which is better suited for the parametric study to be undertaken.

RAYLEIGH-BENARD CONVECTION

Thermal convection in the presence of gravity is governed by the Boussinesq equations,

$$\nabla \cdot \mathbf{u} = 0 \quad (1a)$$

$$\frac{\partial \mathbf{u}}{\partial t} + \mathbf{u} \cdot \nabla \mathbf{u} = -\nabla p + \text{Ra Pr} \mathbf{e}_z + \text{Pr} \Delta \mathbf{u} \quad (1b)$$

$$\frac{\partial T}{\partial t} + \mathbf{u} \cdot \nabla T = w + \Delta T \quad (1c)$$

All quantities have been made dimensionless by the standard normalization, e.g. the box height, H , is used to normalize \mathbf{x} . The dependent flow variables $\mathbf{u} = (u, v, w)$ and T represent the velocity and temperature, respectively. p is the pressure and \mathbf{e}_z is the unit vector antiparallel to the direction of gravity. The two dimensionless parameters are Prandtl number, $\text{Pr} = \nu/\kappa$ and Rayleigh number, $\text{Ra} = g\beta H^4 \alpha / \kappa \nu$.

The flow takes place in a box of dimensions $L \times L \times H$. The boundary conditions are imposed as the stress-free flow conditions

$$w = T = \frac{\partial u}{\partial z} = \frac{\partial v}{\partial z} = 0 \text{ at } z = 0, 1 \quad (1d)$$

in the vertical and periodic in the horizontal x and y variables.

The database generated earlier was obtained by numerically integrating the Boussinesq equations using a Fourier-collocation spectral method on a $20 \times 20 \times 20$ grid at $\text{Pr} = 0.72$, $\text{Ra} = 15 \times \text{Ra}_c$ and $A = L/H = 2\sqrt{2}$. The critical Rayleigh number in this case is $\text{Ra}_c = 27\pi^4/4$ and the aspect ratio corresponds to the wavelength of maximum linear instability.

K-L FORMULATION

K-L Basis (Lumley 1970, Sirovich 1987, Berkooz *et al.* 1993)

A K-L basis can be generated from an ensemble of snapshots of realizations. The elements of the basis set are the eigenfunctions of the integral equation,

$$\int \mathbf{R}(\mathbf{x}, \mathbf{x}') \Psi^{\mathbf{k}}(\mathbf{x}') d\mathbf{x}' = \lambda_{\mathbf{k}} \Psi^{\mathbf{k}}(\mathbf{x}) \quad (2)$$

the kernel of which is the two-point correlation tensor

$$R_{ij}(\mathbf{x}, \mathbf{x}') = \langle v_i(\mathbf{x}, t) v_j(\mathbf{x}', t) \rangle. \quad (3)$$

Generally three indices are required to specify a basis set in three spatial dimensions. \mathbf{k} represents these indices (see below).

The angle bracket denotes ensemble average. If the process is statistically stationary, ergodicity permits replacement of the ensemble average by an average over time. The existence of a countably infinite number of orthogonal eigenfunctions spanning the space follows from Hilbert-Schmidt theory. An element of the space can be expressed in the form of a modal decomposition

$$\mathbf{v}(\mathbf{x}, t) = \sum_{\mathbf{k}} a_{\mathbf{k}}(t) \Psi^{\mathbf{k}}(\mathbf{x}) \quad (4)$$

and the expansion coefficients are statistically orthogonal

$$\langle a_{\mathbf{k}}(t) a_{\mathbf{l}}^*(t) \rangle = \lambda_{\mathbf{k}} \delta_{\mathbf{k}\mathbf{l}} \quad (5)$$

For \mathbf{v} representing the flow, each eigenvalue, $\lambda_{\mathbf{k}}$, represents the mean energy of the flow projected on the direction $\Psi^{\mathbf{k}}$ in the function space.

Symmetries

The governing system of equations (1) is invariant under a discrete symmetry group in the form of reflectional and rotational symmetries in the horizontal and reflectional symmetry in the vertical mid plane as well as a continuous symmetry group in the form of translational invariance in the horizontal directions.

Homogeneity in the horizontal directions leads to the translational invariance,

$$R_{ij}(\mathbf{x}, \mathbf{x}') \equiv R_{ij}(\mathbf{x} - \mathbf{x}', y - y', z, z'), \quad (6)$$

which in turn implies that the eigenfunctions are in the form

$$\Psi_j^{\mathbf{k}}(\mathbf{x}) \equiv \Psi_j(k_x, k_y, n; \mathbf{x}) = \Phi_j^{\mathbf{k}}(z) e^{ik_x x} e^{ik_y y} \quad (7)$$

where $\mathbf{k} = (k_x, k_y, n)$, n is the vertical quantum number and

$\alpha = \pi/\sqrt{2}$. Due to the reflectional and rotational symmetries, the eigensolutions come with a maximum 8-fold degeneracy, i.e.

$$\lambda_{(\pm k_x, \pm k_y, n)} = \lambda_{(\pm k_x, \mp k_y, n)} = \lambda_{(\pm k_y, \pm k_x, n)} = \lambda_{(\pm k_y, \mp k_x, n)} \quad (8)$$

Since the planform is a square, the reflectional and rotational symmetries in the horizontal plane form the dihedral group D_4 containing eight elements. The reflectional symmetry in the vertical mid plane $z = 1/2$, renders the individual functions either odd or even in $z = 1/2$ (Sirovich 1987-part 2). These lead to a more convenient representation of the flow in terms of *flowlets*, $\mathbf{v}^{\mathbf{k}}$,

$$\mathbf{v}(\mathbf{x}, t) = \sum_{\mathbf{k}} \mathbf{v}^{\mathbf{k}} = \sum_{\mathbf{k}} \left\{ a_{\mathbf{k}}(t) \Psi^{\mathbf{k}}(\mathbf{x}) + a_{\mathbf{k}^*}(t) \Psi^{\mathbf{k}^*}(\mathbf{x}) \right\} \quad (9)$$

where the summation index \mathbf{k} runs through the conjugate pairs of the K-L modes $\{\mathbf{k}, \mathbf{k}^*\}$ defined by

$$\mathbf{k} = (k_x, k_y, n) \text{ and } \mathbf{k}^* = (-k_x, -k_y, n) \quad (10)$$

where

$$\Psi^{\mathbf{k}^*} = (\Psi^{\mathbf{k}})^* \text{ and } a_{\mathbf{k}^*} = a_{\mathbf{k}}^* \quad (11)$$

with

$$a_{\mathbf{k}} = (\Psi^{\mathbf{k}}, \mathbf{v}) = \int \sum_i v_i(\mathbf{x}, t) (\Psi_i^{\mathbf{k}}(\mathbf{x}))^* d\mathbf{x}. \quad (12)$$

$()^*$ represents complex conjugation. We will use the notation $\{k_x, k_y, n\}$ to represent a conjugate pair.

K-L Representation

We use this formalism to create two ensembles, containing separately the mechanical $\mathbf{u} = (u, v, w)$ and thermal T components of the flow. The two orthonormal K-L basis sets are denoted by $\{\mathbf{U}^{\mathbf{k}}\}$ and $\{\Theta^{\mathbf{k}}\}$, so that the mechanical component is represented by,

TABLE 1: THE K-L EIGENVALUES FOR THE FIRST TEN DEGENERATE MECHANICAL AND THERMAL MODES. THE ORDERING IS BASED ON THE EIGENVALUES WHICH ARE SCALED BY THE LARGEST. THE DEGENERACY IMPLIES FOR EXAMPLE THAT $[0,1,1]$ STANDS FOR THE DEGENERATE FAMILY $\{(0,1,1), (0,-1,1), (1,0,1), (-1,0,1)\}$ AS DEFINED BY (8)

Mechanical Modes				
index	k	eigenvalue	degeneracy	% energy
1	[0 1 1]	1.0000	4	51.39
2	[1 1 1]	0.2639	4	64.95
3	[0 1 2]	0.1654	4	73.45
4	[0 0 1]	0.0637	2	75.09
5	[1 2 1]	0.0435	8	79.57
6	[0 2 1]	0.0379	4	81.52
7	[1 1 2]	0.0338	4	83.26
8	[1 1 3]	0.0181	4	84.19
9	[0 3 1]	0.0179	4	85.11
10	[1 2 2]	0.0167	8	86.83
Thermal Modes				
1	[0 0 1]	1.0000	1	53.86
2	[0 1 1]	0.1272	4	81.27
3	[1 1 1]	0.0320	4	88.17
4	[0 2 1]	0.0048	4	89.19
5	[1 2 1]	0.0042	8	91.00
6	[0 2 2]	0.0042	4	91.89
7	[0 1 2]	0.0037	4	92.70
8	[0 0 2]	0.0036	1	92.90
9	[0 3 1]	0.0033	4	93.61
10	[0 1 3]	0.0025	4	94.15

$$\mathbf{u}(\mathbf{x}, t) = \sum_{\mathbf{k}} \mathbf{u}^{\mathbf{k}} = \sum_{\mathbf{k}} \left\{ \mathbf{b}_{\mathbf{k}}(t) \mathbf{U}^{\mathbf{k}}(\mathbf{x}) + \mathbf{b}_{\mathbf{k}}^*(t) \mathbf{U}^{\mathbf{k}*}(\mathbf{x}) \right\} \quad (13)$$

and thermal component by,

$$T(\mathbf{x}, t) = \sum_{\mathbf{k}} T^{\mathbf{k}} = \sum_{\mathbf{k}} \left\{ c_{\mathbf{k}}(t) \Theta^{\mathbf{k}}(\mathbf{x}) + c_{\mathbf{k}}^*(t) \Theta^{\mathbf{k}*}(\mathbf{x}) \right\} \quad (14)$$

It follows that

$$\langle \mathbf{b}_{\mathbf{k}}(t) \mathbf{b}_{\mathbf{l}}^*(t) \rangle = \mu_{\mathbf{k}} \delta_{\mathbf{k}\mathbf{l}} \quad \text{and} \quad \langle c_{\mathbf{k}}(t) c_{\mathbf{l}}^*(t) \rangle = \eta_{\mathbf{k}} \delta_{\mathbf{k}\mathbf{l}} \quad (15)$$

with

$$\mathbf{b}_{\mathbf{k}} = (\mathbf{U}^{\mathbf{k}}, \mathbf{u}) \quad \text{and} \quad c_{\mathbf{k}} = (\Theta^{\mathbf{k}}, T) \quad (16)$$

The eigenvalues corresponding to the K-L decomposition of the mechanical and thermal components for the first ten K-L modes are shown in table 1. As mentioned in the introduction the mean temperature is not subtracted from the thermal field, thus the energy content of the thermal K-L mode $[0,0,1]$ is substantial and is close in value to the mean. Note that K-L modes belonging to the same degenerate family are grouped together. We will use the notation $[k_x, k_y, n]$ to represent a degenerate family.

Galerkin Projection

Next, Galerkin projection is applied to the Boussinesq equations. To accomplish this, we introduce the truncated K-L representations,

$$\mathbf{u}(\mathbf{x}, t) \approx \sum_{\mathbf{k} \in U_c} \mathbf{u}^{\mathbf{k}} \quad \text{and} \quad T(\mathbf{x}, t) \approx \sum_{\mathbf{k} \in T_c} T^{\mathbf{k}}. \quad (17)$$

Each summation is over a suitable class of flowlets, denoted by U_c and T_c . In choosing these classes we respect the symmetries carried by the degeneracies shown in (8).

Under projection, the resulting amplitude equations have the form,

$$\frac{d\mathbf{b}_{\mathbf{k}}}{dt} = \text{Ra Pr } B_{\mathbf{k}\mathbf{p}} c_{\mathbf{p}} + \text{Pr } D_{\mathbf{k}\mathbf{p}} b_{\mathbf{p}} + Q_{\mathbf{k}\mathbf{p}\mathbf{q}} b_{\mathbf{p}} b_{\mathbf{q}} \quad (18)$$

$$\frac{dc_{\mathbf{k}}}{dt} = B'_{\mathbf{k}\mathbf{p}} b_{\mathbf{p}} + D'_{\mathbf{k}\mathbf{p}} c_{\mathbf{p}} + Q'_{\mathbf{k}\mathbf{p}\mathbf{q}} b_{\mathbf{p}} c_{\mathbf{q}} \quad (19)$$

with the summation convention over repeated indicies, and only over flowlet sets U_c and T_c . The coefficients are defined for $\mathbf{p} = \{p_x, p_y, n_p\}$, $\mathbf{q} = \{q_x, q_y, n_q\}$ and $\mathbf{k} = \{k_x, k_y, n_k\}$ as follows:

$$B_{\mathbf{k}\mathbf{p}} = (\mathbf{U}^{\mathbf{k}}, T^{\mathbf{p}} \mathbf{e}_z) \quad \text{and} \quad D_{\mathbf{k}\mathbf{p}} = (\mathbf{U}^{\mathbf{k}}, \Delta \mathbf{u}^{\mathbf{p}}) \quad (20)$$

$$B'_{\mathbf{k}\mathbf{p}} = (\Theta^{\mathbf{k}}, w^{\mathbf{p}}) \quad \text{and} \quad D'_{\mathbf{k}\mathbf{p}} = (\Theta^{\mathbf{k}}, \Delta T^{\mathbf{p}}) \quad (21)$$

with $p_x = k_x$ and $p_y = k_y$,

$$Q_{\mathbf{k}\mathbf{p}\mathbf{q}} = -\frac{1}{2} \left(U_i^{\mathbf{k}}, u_j^{\mathbf{p}} \frac{\partial u_i^{\mathbf{q}}}{\partial x_j} + u_j^{\mathbf{q}} \frac{\partial u_i^{\mathbf{p}}}{\partial x_j} \right) \quad (22)$$

$$Q'_{\mathbf{k}\mathbf{p}\mathbf{q}} = - \left(\Theta^{\mathbf{k}}, u_j^{\mathbf{p}} \frac{\partial T^{\mathbf{q}}}{\partial x_j} \right) \quad (23)$$

with $p_x + q_x = k_x$, $p_y + q_y = k_y$. Diffusive terms are designated D or D' depending on whether they arise in the momentum or thermal equations and similarly for the bouyancy terms, B and B' . Quadratic terms are denoted by Q and Q' , also depending on whether they arise in the momentum or thermal equations. Observe that quadratic cross-coupling only appears in the thermal equation where it is the only nonlinearity.

RESULTS

The issue of the inclusion of modes in the truncated system is dealt with in a systematic manner. The truncation will be governed by the parameter pair (M, N) which specifies the degenerate family of modes to be included as

$$\left\{ [k_x, k_y, n] \mid \sqrt{k_x^2 + k_y^2} \leq M \quad \text{and} \quad 1 \leq n \leq k \cdot N \right\} \quad (24)$$

where $k = 4$ for mechanical and 2 for thermal modes, respectively. This is based on two observations. It is observed that the family of modes identified by $[k_x, k_y, n]$ that resolve certain amount of energy, say, nearly 90% of the mean energy at $r \equiv \text{Ra}/\text{Ra}_c = 15$ in table 1, can be included effectively by

the criterion $\sqrt{k_x^2 + k_y^2} \leq 3$. It is also observed that as n increases, a well defined symmetry pattern is spanned cyclically by sets of 4 mechanical and 2 thermal modes while (k_x, k_y) is fixed. The number of cycles of this symmetry pattern is denoted by N . Two typical cycles ($N=2$) are shown by the vertical profiles of the mechanical and thermal modes

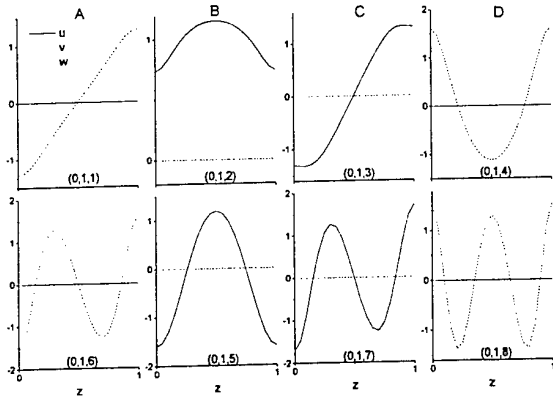


FIGURE 1: THE VERTICAL PROFILES OF THE MECHANICAL K-L EIGENFUNCTIONS FOR THE FAMILY OF MODES (0,1,n) TRUNCATED AT N=2.

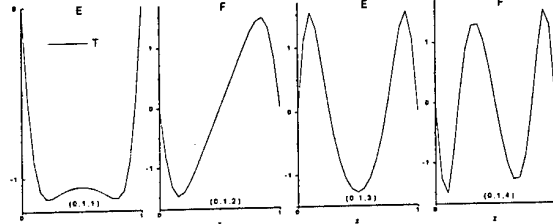


FIGURE 2: THE VERTICAL PROFILES OF THE THERMAL K-L EIGENFUNCTIONS FOR THE FAMILY OF MODES (0,1,n) TRUNCATED AT N=2.

($k_x = 0, k_y = 1, n$) in figures 1&2, respectively. As it is shown the mechanical modes $\{(0,1,1), (0,1,2), (0,1,3), (0,1,4)\}$ span one cycle (Four classes in each cycle are labeled by A & B & C & D) while $\{(0,1,6), (0,1,5), (0,1,7), (0,1,8)\}$ span the second cycle with increasing zero crossings (sequency). Similarly, the thermal modes $\{(0,1,1), (0,1,2)\}$ and $\{(0,1,3), (0,1,4)\}$ span the respective cycles (Two classes in each cycle are labeled by E & F).

A revealing characterization of the modes belonging to each symmetry class can be achieved by the following representation of the divergence-free velocity field

$$\mathbf{u} = \delta \mathbf{v} + \varepsilon \mathbf{w} \quad (25)$$

where the operators δ and ε are defined by

$$\delta \mathbf{v} \equiv \nabla \times (\nabla \times \mathbf{v} \mathbf{e}_z), \quad \varepsilon \mathbf{w} \equiv \nabla \times \mathbf{w} \mathbf{e}_z. \quad (26)$$

In general, flowlet $\mathbf{u}^{\mathbf{k}} = \delta \mathbf{v}^{\mathbf{k}} + \varepsilon \mathbf{w}^{\mathbf{k}}$ and $T^{\mathbf{k}}$ in this representation for a conjugate pair of modes $\mathbf{k} = \{k_x, k_y, n\}$ is for each symmetry class A,B,C,D and E,F in the form:

$$\begin{Bmatrix} v_A^{\mathbf{k}} \\ v_B^{\mathbf{k}} \\ v_C^{\mathbf{k}} \\ v_D^{\mathbf{k}} \end{Bmatrix} = \|b^{\mathbf{k}}(t)\| \begin{Bmatrix} \sum_{k_z, \text{odd}} \hat{A}_{k_z}^{\mathbf{k}} \sin(\pi k_z z) \\ 0 \\ 0 \\ \sum_{k_z, \text{even}} \hat{D}_{k_z}^{\mathbf{k}} \sin(\pi k_z z) \end{Bmatrix} \cos((k_x x + k_y y)\alpha + ph) \quad (27)$$

TABLE 2: THE INTERVAL FOR τ IN WHICH THE TRANSITION TO THE INDICATED STATES OCCUR FOR SOME SELECTED TRUNCATION PARAMETER PAIRS (M, N).

(M, N)	periodic state	quasi-periodic state
(3, 2)	(1.9, 2.0)	(2.9, 3.0)
(3, 3)	(1.8, 1.9)	(2.7, 2.8)
(4, 2)	(2.0, 2.1)	(2.7, 2.8)
(5, 2)	(1.9, 2.0)	(2.8, 2.9)

$$\begin{Bmatrix} w_A^{\mathbf{k}} \\ w_B^{\mathbf{k}} \\ w_C^{\mathbf{k}} \\ w_D^{\mathbf{k}} \end{Bmatrix} = \|b^{\mathbf{k}}(t)\| \begin{Bmatrix} 0 \\ \sum_{k_z, \text{even}} \hat{B}_{k_z}^{\mathbf{k}} \sin(\pi k_z z) \\ \sum_{k_z, \text{odd}} \hat{C}_{k_z}^{\mathbf{k}} \sin(\pi k_z z) \\ 0 \end{Bmatrix} \cos((k_x x + k_y y)\alpha + ph) \quad (28)$$

and,

$$\begin{Bmatrix} T_E^{\mathbf{k}} \\ T_F^{\mathbf{k}} \end{Bmatrix} = \|c^{\mathbf{k}}(t)\| \begin{Bmatrix} \sum_{k_z, \text{odd}} \hat{E}_{k_z}^{\mathbf{k}} \sin(\pi k_z z) \\ \sum_{k_z, \text{even}} \hat{F}_{k_z}^{\mathbf{k}} \sin(\pi k_z z) \end{Bmatrix} \cos((k_x x + k_y y)\alpha + ph) \quad (29)$$

where $\|\cdot\|$ and ph are the magnitudes and the phase of the complex K-L expansion coefficient, respectively. The notation for the Fourier expansion coefficients is selected to be indicative of the symmetry class labels. The visible characterization of the symmetry classes as shown in figures 1&2 are the odd or even symmetry at the mid-plane $z = 1/2$ as well as the absence of the vertical velocity component in classes B&C of the mechanical modes which we will term them as *parasitic* modes since they do not contribute to the convective heat flux and are sustained only by their nonlinear interactions with other modes. Furthermore, since w component in the representation (25) is associated with the vertical vorticity component, the modes in classes A&D have vanishing vertical vorticity component. On the other hand, the modes in classes B&C with nonzero vertical vorticity component are further characterized by having nonzero mean component independent of the vertical coordinate z in B while none in C.

We have performed numerical experiments by integrating the truncated amplitude equations for some selected truncation parameter pairs. The numerical integration is performed by starting from the initial conditions set as zero for the amplitudes of the mechanical modes and small random numbers for those of the thermal modes for the initial run. For the subsequent runs with increasing τ only the amplitudes of the thermal field are perturbed randomly by a small amount. We have compared the parameter ranges that the transition to various regimes occurred as shown in table 2. For the indicated range of selection we have observed a satisfactory qualitative agreement. Thus we have selected the truncation parameter pair of (3, 2) for a qualitative study of the transition, considering large number of runs are needed for the subsequent study. This truncation corresponds to the inclusion of 232+116 (mechanical + thermal) K-L modes.

TABLE 3: THE K-L MODES THAT ARE INCLUDED FOR THE SELECTED TRUNCATION PARAMETER PAIR ($M=3$, $N=2$). HOWEVER ONLY THOSE MODES FOR $N=1$ ARE LISTED FOR BREVITY. THE BOLDFACE INDEX IS USED IN THE IDENTIFICATION OF THE MODES IN THE K-L POWER SPECTRUM PLOTS AND IS ARBITRARY OTHERWISE.

A	B	C	D
1 {0 1 1}	3 {0 1 2}	5 {0 1 3}	7 {0 1 4}
2 {1 0 1}	4 {1 0 2}	6 {1 0 3}	8 {1 0 4}
9 {1 1 1}	11 {1 1 2}	13 {1 1 3}	15 {1 1 4}
10 {1 -1 1}	12 {1 -1 2}	14 {1 -1 3}	16 {1 -1 4}
17 {1 2 1}	21 {1 2 2}	25 {1 2 4}	29 {1 2 3}
18 {1 -2 1}	22 {1 -2 2}	26 {1 -2 4}	30 {1 -2 3}
19 {2 1 1}	23 {2 1 2}	27 {2 1 4}	31 {2 1 3}
20 {2 -1 1}	24 {2 -1 2}	28 {2 -1 4}	32 {2 -1 3}
33 {0 2 1}	35 {0 2 2}	37 {0 2 4}	39 {0 2 3}
34 {2 0 1}	36 {2 0 2}	38 {2 0 4}	40 {2 0 3}
41 {0 3 1}	43 {0 3 2}	45 {0 3 4}	47 {0 3 3}
42 {3 0 1}	44 {3 0 2}	46 {3 0 4}	48 {3 0 3}
49 {2 2 1}	51 {2 2 2}	53 {2 2 3}	55 {2 2 4}
50 {2 -2 1}	52 {2 -2 2}	54 {2 -2 3}	56 {2 -2 4}
57 {0 0 1}			59 {0 0 3}
58 {0 0 2}			60 {0 0 4}
E	F	E	F
61 {0 1 1}	63 {0 1 2}	65 {1 1 1}	67 {1 1 2}
62 {1 0 1}	64 {1 0 2}	66 {1 -1 1}	68 {1 -1 2}
69 {1 2 1}	73 {1 2 2}	77 {0 2 2}	79 {0 2 1}
70 {1 -2 1}	74 {1 -2 2}	78 {2 0 2}	80 {2 0 1}
71 {2 1 1}	75 {2 1 2}	81 {0 3 1}	83 {0 3 2}
72 {2 -1 1}	76 {2 -1 2}	82 {3 0 1}	84 {3 0 2}
85 {2 2 1}	87 {2 2 2}	89 {0 0 2}	90 {0 0 1}
86 {2 -2 1}	88 {2 -2 2}		

Various numerical tests on the truncated amplitude equations with the selected truncation at and around the transition to the convective motion at $r = 1$ have shown satisfactory sharpness. It is also observed that the sharpness can be further increased by increasing the truncation parameter N from 2 to 3 while keeping M fixed at 3. The K-L power spectrum plot at $r = 1.9$ in figure 3 shows that the two dimensional roll solutions are dominant as shown by the physical manifestation of this spectrum in figure 4. The alignment of the rolls is in the y -direction which evolved from randomly selected initial conditions. The K-L modes excited in this steady state regime have the common parity that $k_x + k_z$ is even.

As r is increased from 1.9 to 2.0, transition to a periodic-state occurs. The appearance of the fundamental oscillation frequency f_1 is shown in figure 5 at $r = 2.9$. All the newly excited modes as shown in the K-L power spectrum plot in figure 3 still have the common parity that $k_x + k_z$ is even. The functional dependence of v, w, T of these newly excited K-L modes on the horizontal x and y variables and time are, in general, of the form $\cos(k_x \alpha x) \cos(k_y (\alpha y + 2\pi f_1 t))$ or $\sin(k_x \alpha x) \sin(k_y (\alpha y + 2\pi f_1 t))$ where the time dependence enters through the phase of the complex K-L expansion coefficients while their magnitudes are constant in time. This indicates periodic translation of the modes in the y -direction which is perpendicular to the roll axis. Since the modes that formed the two dimensional roll solution in the steady state regime still have no time dependence in this periodic state, the motion manifests itself as traveling waves superimposed onto

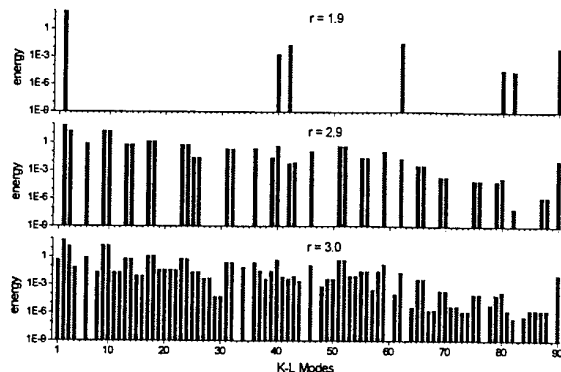


FIGURE 3: THE MAGNITUDES (AVERAGED IN TIME) OF THE COMPLEX EXPANSION COEFFICIENTS OF THE K-L MODES EXCITED AT THE INDICATED r VALUES. THE INDEXING OF THE MODES IS BASED ON TABLE 3.

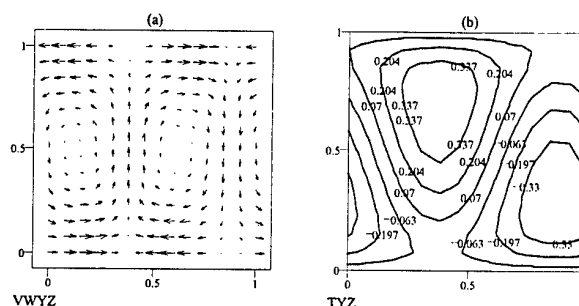


FIGURE 4: THE TWO DIMENSIONAL ROLLS (a) AND THE CORRESPONDING TEMPERATURE DISTRIBUTION (b) IN THE x - z PLANE AS THE PHYSICAL MANIFESTATION OF THE MODES EXCITED AT $r=1.9$ AS SHOWN IN FIGURE 3.

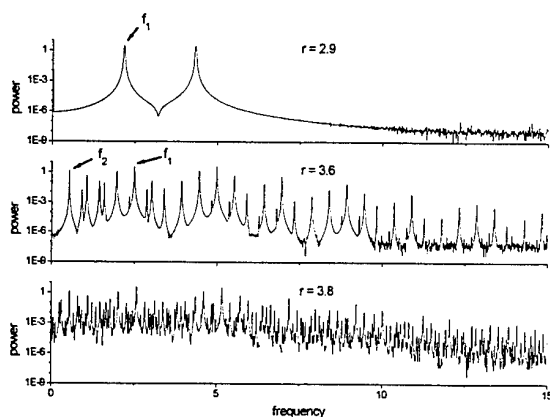


FIGURE 5: THE FREQUENCY SPECTRUM CORRESPONDING TO THE TIME SERIES GENERATED BY SAMPLING THE VERTICAL VELOCITY COMPONENT w AT A PARTICULAR SPATIAL LOCATION. THESE ARE TYPICAL AT THE PERIODIC, DOUBLY PERIODIC AND AT THE START OF THE NON-PERIODIC REGIMES.

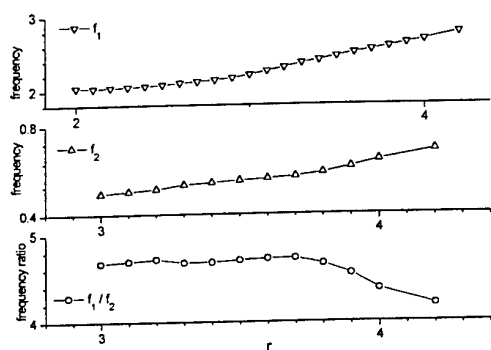


FIGURE 6: THE TWO PRIMARY FREQUENCY VALUES AND THEIR RATIOS FOR A RANGE OF r AT WHICH THE IDENTIFICATION OF THE PRIMARY FREQUENCIES WAS POSSIBLE.

the rolls. The functional dependence above for those conjugate pairs with $k_x, k_y \neq 0$ represents the combined motion of $\{k_x, k_y, n\} + \{k_x, -k_y, n\}$ since their corresponding complex K-L expansion coefficients have equal magnitudes as can be seen in the K-L power spectrum plot in figure 3 and their phases are related. The most energetic mode that contributes to the generation of vertical vorticity in this regime is the mode $\{0, 1, 2\}$ which is of class B and, thus, has nonzero mean component independent of the vertical coordinate z . This is consistent with the linear stability analysis of Busse (1972) that reported the z -independent component of the vertical vorticity as a cause of the oscillatory behaviour.

Transition to a doubly periodic state (quasi-periodic) is observed as r is increased from 2.9 to 3.0. The appearance of the second incommensurate frequency f_2 is shown in figure 5. The newly excited modes in this regime as shown in the K-L power spectrum plot in figure 3 have the common parity that $k_x + k_z$ is odd which breaks the spectral even parity of the previous regime.

The two primary frequencies f_1 and f_2 are shown to increase monotonically with r in figure 6. The evolution of the ratio f_1/f_2 with r as shown in figure 6 appears to be in a weakly frequency-locked state as the ratio takes values between 4.67 and 4.73 at selected points in a range of r from 3.0 to 3.7. As the ratio starts to decrease at $r = 3.8$, the frequency spectrum develops a marked change towards non-periodicity as shown in figure 5. Further increase in r results in broadband spectral excitation in the spectrum. This transition seems to agree with *route-1* transition scenario as it is termed in Gollub & Benson (1980) based on the experimental observations. However, it does not rule out a transition as in the numerical studies by McLaughlin & Orszag (1982) and Curry *et al.* (1984) based on the predictions of Ruelle *et al.* (1978) since the non-periodicity is started to develop after the appearance of the quasi-periodic regime. Our observation that the transition to the quasi-periodic and then to non-periodic state coincides with the appearance of the modes with opposite spectral parity may be consistent with the observation in McLaughlin & Orszag (1982)

that implicates the broken spectral parity with the onset of chaos.

One of us (I.H.T.) would like to acknowledge the support given by King Fahd University of Petroleum and Minerals.

REFERENCES

- Aubry, N., Holmes, P., Lumley, J.L. and Stone, E. 1988, "The dynamics of coherent structures in the wall region of a turbulent boundary layer", *J. of Fluid Mech.*, **192**, 115.
- Berkooz, G., Holmes, P. and Lumley, J.L. 1993, "The Proper Orthogonal Decomposition in the analysis of turbulent flows", *Annual Review Fluid Mechanics*, **25**, 539.
- Busse, F. H., 1972, "The oscillatory instability of convection rolls in a low Prandtl number fluid", *J. Fluid Mech.*, **52**, 97-112.
- Curry, J. H., Herring, J. R., Loncaric, J. & Orszag, S. A., 1984, "Order and disorder in two- and three-dimensional Benard convection", *J. Fluid Mech.*, **147**, 1-38.
- Deane, A.E., Kevrekidis, I.G., Karniadakis, G.E. and Orszag, S.A. 1991, "Low-dimensional models for complex geometry flows: Application to grooved channels and circular cylinders", *Physics of Fluids*, **3**, (10), 2337.
- Gollub, J. P. & Benson, S. V., 1980, "Many routes to turbulent convection", *J. Fluid Mech.*, **100**, 449-470.
- Lumley, J.L. 1970, 'Stochastic Tools in Turbulence', Academic Press, New York.
- McLaughlin, J. B. & Orszag, S. A. 1982, "Transition from periodic to chaotic thermal convection", *J. Fluid Mech.*, **122**, 123-142.
- Meneguzzi, M., Sulem, C., Sulem, P. L. & Thual, O. 1987, "Three-dimensional numerical simulation of convection in low-Prandtl-number fluids", *J. Fluid Mech.*, **182**, 169-191.
- Rajasee, M., Karlsson, S.K.F. and Sirovich, L. 1994, "Low-dimensional description of free-shear-flow coherent structures and their dynamical behaviour", *J. Fluid Mech.*, **258**, 1.
- Rempfer, D. and Fasel, H.F. 1994, "Dynamics of three-dimensional coherent structures in a flat plate boundary layer", *J. Fluid Mech.*, **275**, 257.
- Ruelle, D., Takens, F. & Newhouse, S. E. 1978, "Occurrence of strange axiom A attractors near quasi periodic flows on T^m , $m \geq 3$ ", *Commun. Math. Phys.*, **64**, 35-40.
- Sirovich, L. 1987, "Turbulence and the dynamics of coherent structures, Parts 1-3", *Q. Appl. Math.*, **45**, 561.
- Sirovich, L., Maxey, M. and Tarman, I. H. 1989, "Analysis of turbulent thermal convection", In *Sixth Symposium on Turbulent Shear Flow*, Toulouse, France, p. 68, Springer.
- Sirovich, L. and Rodriguez, J.D. 1987, "Coherent structures and chaos: A model problem", *Phys. Lett. A*, **120**, 211-214.
- Tarman, I. H. 1996, "A Karhunen-Loeve based Galerkin approximation to Boussinesq equation", *Comp. Meth. in Appl. Mech. and Eng.*, **137**, (3-4), 275-284.
- Tarman, I. H. and Sirovich, L. 1997, "Extensions to Karhunen-Loeve based approximation of complicated phenomena", *Comp. Meth. in Appl. Mech. and Eng.*, (to appear).

RELATION BETWEEN THIRD-ORDER AND SECOND-ORDER VELOCITY STRUCTURE FUNCTIONS FOR AXISYMMETRIC TURBULENCE

M. Ould-Rouis

Université de Marne la Vallée, Génie des Procédés,
93166 Noisy le Grand Cedex - France

R.A. Antonia and Y. Zhu

University of Newcastle, Department of Mechanical Engineering,
NSW 2308 - Australia

F. Anselmet

IRPHE - 12, Avenue Général Leclerc,
13003 Marseille - France

ABSTRACT

An equation relating third-order and second-order velocity increments at two points separated by a distance r is derived using the assumption of axisymmetric turbulence. This assumption is more constraining than homogeneity, but less restrictive than isotropy. When the separation is along the axis of symmetry, the equation predicts a linear behaviour for inertial range separations, just like Kolmogorov's well known equation for isotropic turbulence. Plane jet data at a moderately high turbulence Reynolds number support the new relation marginally better than Kolmogorov's equation.

INTRODUCTION

Statistics associated with velocity increments have been widely used for describing the small scale structure of turbulence. In particular, the expression, commonly referred to as Kolmogorov's equation, relating third-order and second-order moments of the longitudinal velocity increment $\Delta u_1 (= u_1(x+r) - u_1(x))$, where r denotes a separation, usually taken along the longitudinal direction) is very important since it is directly obtained from the Navier-Stokes equations (ϵ_{iso} denotes the isotropic mean dissipation rate of the turbulent kinetic energy):

$$\langle (\Delta u_1)^3 \rangle = 6\nu \frac{\partial}{\partial r} \langle (\Delta u_1)^2 \rangle - \frac{4}{5} r \epsilon_{iso} \quad (1)$$

I

II

This equation was originally written by Kolmogorov (1941) using the Kármán-Howarth equation (1938) as point of departure. It is usually derived using the

assumption of isotropy or local isotropy (i.e. Monin and Yaglom, 1975), but there is a suspicion, backed by plausible arguments, that even local isotropy is not essential for $\langle (\Delta u_1)^3 \rangle$ to vary linearly with r for inertial range scales (Frisch, 1995; Antonia et al., 1997).

Equation (1) has received considerable experimental attention and, surprisingly, the linear inertial range evolution of $\langle (\Delta u_1)^3 \rangle$ appears to be reasonably satisfied at relatively small Reynolds numbers and for conditions which depart significantly from isotropy. However, the value of the inertial range constant is generally smaller than 4/5; alternately, the estimated value of ϵ using 4/5 is larger than that determined by means other than equation (1) (e.g. Antonia et al., 1983; Saddoughi and Veeravalli, 1994; Mydlarski and Warhaft, 1996).

The objective of the present paper is to establish a relation similar to equation (1), but using less restrictive assumptions. In particular, the assumption of isotropy is relaxed to an assumption of axisymmetry (without mean rotation). Axisymmetric turbulence was first analyzed by Batchelor (1946) who could express the two-point correlation tensor $R_{ij}(\vec{r}) (= \langle u_i(\vec{x}) u_j(\vec{x} + \vec{r}) \rangle)$ in terms of four scalar functions of $r=|\vec{r}|$ and $\mu=\vec{r} \cdot \vec{\lambda}/r$, where $\vec{\lambda}$ is a unit vector along the direction of symmetry. The recent developments by Lindborg (1995) provide a framework which allows axisymmetric tensors, such as the two-point second- and third-order correlation tensors, to be expressed in terms of measurable scalar functions, which was not possible for Batchelor's work.

We first follow Lindborg's approach to obtain axisymmetric forms of the second- and third-order tensors for velocity structure functions, as well as of the

dissipation rate of turbulent kinetic energy, in order to derive the axisymmetric relation equivalent to (1). Measurements in a plane jet at a moderate Reynolds number seem to validate our new relation.

MONIN'S EQUATION FOR HOMOGENEOUS TURBULENCE

To derive the new relation equivalent to (1), we must first consider the Navier-Stokes equations at two positions \bar{x} and \bar{x}_0 separated by \bar{r} ($= \bar{x} - \bar{x}_0$). Only homogeneity is required to obtain the non-projected equation from which (1) was then deduced using isotropic approximations for the tensorial contractions (Frisch, 1995; Antonia et al., 1997) :

$$\frac{\partial}{\partial r_\alpha} D_{ij\alpha} = 2\nu \frac{\partial^2}{\partial r_\alpha^2} D_{ij} - \frac{4}{3} \varepsilon \delta_{ij}, \quad (2)$$

where r_α stand for the components of \bar{r} . $D_{ij\alpha}$ and D_{ij} are respectively the third- and second-order correlation tensors associated with velocity increments (e.g. $D_{ij} = \langle \Delta u_i \Delta u_j \rangle$), whereas $\varepsilon = \nu \langle (\nabla_\alpha u_i)^2 \rangle$ is the dissipation rate of kinetic energy. Contribution from the pressure term, $\langle \Delta u_i \partial_j \Delta p \rangle$ vanishes because of continuity. Note that Monin (see Monin and Yaglom, 1975) had first derived this equation, but with the requirement of local isotropy.

Therefore, we are now left with the problem of computing for axisymmetric turbulence the expressions associated with the three quantities appearing in (2).

SECOND-ORDER TENSOR D_{ij} FOR AXISYMMETRIC TURBULENCE

We consider a system of orthogonal unit vectors $(\bar{\lambda}, \bar{e}_2, \bar{e}_3)$, where $\bar{\lambda}$ is along the axis of symmetry, in similar fashion to Lindborg (1995) (Figure 1, where point P is at location \bar{x} and P' is its image with respect to the plane normal to the axis $\bar{\lambda}$). For axisymmetric turbulence without mean rotation, the most general representation of D_{ij} can be expressed as a function of four independent scalar quantities (Ould-Rouis et al., 1996) which depend only on $\rho = |\bar{r} \times \bar{\lambda}|$ and $z = \bar{r} \cdot \bar{\lambda}$:

$$D_{ij}(\bar{r}) = \lambda_i \lambda_j D_1 + e_{2i} e_{2j} D_2 + e_{3i} e_{3j} D_3 + (\lambda_i e_{3j} + \lambda_j e_{3i}) D_4, \quad (3)$$

with $D_1(\rho, z) = \langle (\Delta u_1)^2 \rangle$, $D_2(\rho, z) = \langle (\Delta u_2)^2 \rangle$, $D_3(\rho, z) = \langle (\Delta u_3)^2 \rangle$ and $D_4(\rho, z) = \langle \Delta u_1 \Delta u_3 \rangle$. Note that D_1 , D_2 and D_3 are even in z while D_4 is odd with respect to z . As noted by Lindborg (1995), reflectional symmetry about a plane containing the axis of symmetry, for example the $(\bar{\lambda}, \bar{r})$ plane, implies that the skew tensors are zero. This is true when there is no rotation about the axis of symmetry.

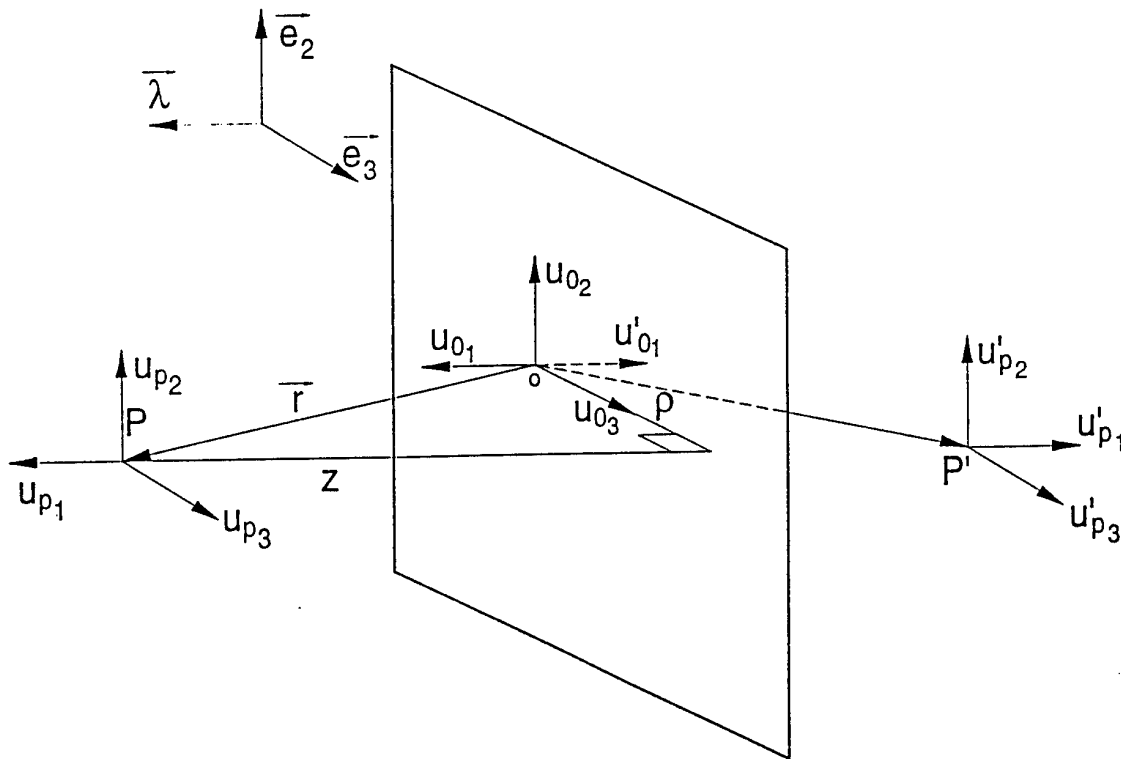


FIGURE 1. CARTESIAN CO-ORDINATE SYSTEM SHOWING VELOCITY COMPONENTS.

Relations between D_1 , D_2 , D_3 and D_4 follow from continuity, $\frac{\partial}{\partial r_j} D_{ij}(\bar{r}) = \frac{\partial}{\partial r_i} D_{ij}(\bar{r}) = 0$. Using standard

relations for the various derivatives (Lindborg, 1995; Ould-Rouis et al., 1996), we then obtain :

$$\frac{\partial}{\partial \rho} (\rho D_4) + \rho \frac{\partial}{\partial z} (D_1) = 0$$

and

$$\frac{\partial}{\partial \rho} (\rho D_3) + \rho \frac{\partial}{\partial z} (D_4) = D_2.$$

In order to check that these results are compatible with the well-known isotropic relations between $D_{LL}(r)$ ($= \langle (\Delta u_1(r))^2 \rangle$) and $D_{NN}(r)$ ($= \langle (\Delta u_2(r))^2 \rangle$), let us project the second-order isotropic tensor

$$D_{ij}(\bar{r}) = (D_{LL} - D_{NN}) \frac{r_i r_j}{r^2} + D_{NN} \delta_{ij} \quad (5)$$

onto the tensors $\lambda_i \lambda_j$, $e_{2i} e_{2j}$, $e_{3i} e_{3j}$, and $\lambda_j e_{3i}$.

We then obtain :

$$D_1 = \frac{z^2}{r^2} D_{LL} + \frac{\rho^2}{r^2} D_{NN} \quad D_2 = D_{NN},$$

and

$$D_3 = \frac{\rho^2}{r^2} D_{LL} + \frac{z^2}{r^2} D_{NN} \quad D_4 = \frac{\rho z}{r^2} (D_{LL} - D_{NN}),$$

which finally gives the isotropic result,

$$D_{NN}(r) = (1 + \frac{r}{2} \frac{\partial}{\partial r}) D_{LL}(r). \quad (7)$$

When \bar{r} is parallel to $\bar{\lambda}$, $\rho = 0$, $D_2 = D_3$ and $D_4 = 0$, and we infer from (3) that :

$$D_{ij}(\bar{r}) = \lambda_i \lambda_j D_1 + D_2 (\delta_{ij} - \lambda_i \lambda_j), \quad (8)$$

which is similar in form to the isotropic relation (5). However, whereas D_{LL} and D_{NN} are related through (7), D_1 and D_2 are two independent functions which remain to be determined, for instance by experiment.

THIRD-ORDER TENSOR D_{ijk} FOR AXISYMMETRIC TURBULENCE

For the third-order tensor D_{ijk} , the general axisymmetric form (without rotation about the axis of symmetry) involves six independent functions :

$$D_{ijk}(\bar{r}) = \lambda_i \lambda_j \lambda_k T_1 + T_2 (\lambda_j e_{2i} e_{2k} + \lambda_i e_{2j} e_{2k} + \lambda_k e_{2i} e_{2j}) + T_3 (\lambda_j e_{3i} e_{3k} + \lambda_i e_{3j} e_{3k} + \lambda_k e_{3i} e_{3j}) + T_4 (\lambda_i \lambda_k e_{3j} + \lambda_i \lambda_j e_{3k} + \lambda_j \lambda_k e_{3i}) + e_{3i} e_{3j} e_{3k} T_5 + T_6 (e_{2i} e_{2k} e_{3j} + e_{2i} e_{2j} e_{3k} + e_{2j} e_{2k} e_{3i}), \quad (9)$$

where the scalar functions are given by :

$$T_1(\rho, z) = \langle (\Delta u_1)^3 \rangle, \quad T_2(\rho, z) = \langle (\Delta u_2)^2 \Delta u_1 \rangle, \\ T_3(\rho, z) = \langle (\Delta u_3)^2 \Delta u_1 \rangle, \quad T_4(\rho, z) = \langle (\Delta u_1)^2 \Delta u_3 \rangle, \\ T_5(\rho, z) = \langle (\Delta u_3)^3 \rangle \text{ and } T_6(\rho, z) = \langle (\Delta u_2)^2 \Delta u_3 \rangle.$$

This tensor is symmetric in its three indices and it can readily be shown that

$$D_{ijk} = 2B_{ij,k} + 2B_{ik,j} + 2B_{jk,i} \quad (10)$$

and

$$\frac{\partial^3 D_{ijk}}{\partial r_i \partial r_j \partial r_k} = 0, \quad (11)$$

where $B_{ij,k}(\bar{r})$ is the third-order correlation tensor, $B_{ij,k}(\bar{r}) = \langle u_i(\bar{x}_0) u_j(\bar{x}_0) u_k(\bar{x}) \rangle$. Relation (11) is inferred from the property that each of the third-order correlation tensors in (10) is solenoidal in one index, i.e. $\partial B_{ij,k} / \partial r_k = 0$. From these relations and the definition (9) of the tensor D_{ijk} , we obtain expression (12) relating the six scalar functions T_1, \dots, T_6 :

$$\frac{\partial^3 T_1}{\partial z^3} - \frac{3}{\rho} \frac{\partial^2}{\partial \rho \partial z} T_2 + \frac{3}{\rho} \frac{\partial^3}{\partial \rho^2 \partial z} (\rho T_3) + \frac{3}{\rho} \frac{\partial^3}{\partial z^2 \partial \rho} (\rho T_4) + \frac{1}{\rho} \frac{\partial^3}{\partial \rho^3} (\rho T_5) - \frac{3}{\rho} \frac{\partial}{\partial \rho} \left(\frac{1}{\rho} + \frac{\partial}{\partial \rho} \right) T_6 = 0 \quad (12)$$

Note that a single equation relates T_1, \dots, T_6 , whereas the two relations in Eq. (4) connect the four scalar functions involved in the second-order tensor $D_{ij}(\bar{r})$.

As in the previous section, it is possible to establish relations between the axisymmetric scalar functions T_1, \dots, T_6 and the isotropic third-order functions D_{LNN} and D_{LLL} . The third-order isotropic tensor can be written as follows :

$$D_{ijk}(\bar{r}) = (D_{LLL} - 3D_{LNN}) \frac{r_i r_j r_k}{r^3} + D_{LNN} \left(\frac{r_i}{r} \delta_{jk} + \frac{r_j}{r} \delta_{ik} + \frac{r_k}{r} \delta_{ij} \right). \quad (13)$$

After projecting this tensor onto the tensors $\lambda_i \lambda_j \lambda_k$, $\lambda_k e_{2i} e_{2j}$, $\lambda_k e_{3i} e_{3j}$, $\lambda_i \lambda_j e_{3k}$, $e_{3i} e_{3j} e_{3k}$ and $e_{2i} e_{2j} e_{3k}$ which correspond to T_1, T_2, T_3, T_4, T_5 and T_6 respectively, we obtain the following relations :

$$T_1 = (D_{LLL} - 3D_{LNN}) \frac{z^3}{r^3} + D_{LNN} \left(\frac{3z}{r} \right),$$

$$T_2 = \frac{z}{r} D_{LNN},$$

$$T_3 = (D_{LLL} - 3D_{LNN}) \frac{z \rho^2}{r^3} + D_{LNN} \left(\frac{z}{r} \right),$$

$$T_4 = (D_{LLL} - 3D_{LNN}) \frac{z^2 \rho}{r^3} + D_{LNN} \left(\frac{\rho}{r} \right),$$

$$T_5 = (D_{LLL} - 3D_{LNN}) \frac{\rho^3}{r^3} + D_{LNN} \left(\frac{3\rho}{r} \right),$$

$$T_6 = \frac{\rho}{r} D_{LNN}.$$

Note that when $\bar{\lambda}$ and \bar{r} are parallel, i.e. when $\rho = 0$, $T_2 = T_3$ and $T_4 = T_5 = T_6$.

With the help of these six relations, we can verify that equation (12) reduces, in the case of isotropic turbulence, to the well-known relation between the isotropic scalar functions of the tensor $D_{ijk}(\bar{r})$:

$$(1 + \frac{r}{3} \frac{\partial}{\partial r}) \frac{\partial}{\partial r} [\frac{1}{6} (1 + r \frac{\partial}{\partial r}) D_{LLL} - D_{LNN}] = 0. \quad (14)$$

And, using Monin and Yaglom's argument, the only solution of (14) which does not have a singularity at $r=0$ is $D_{LNN} = \frac{1}{6} (1 + r \frac{\partial}{\partial r}) D_{LLL}$, i.e. the isotropic result (e.g. Monin and Yaglom, 1975).

AXISYMMETRIC DISSIPATION RATE

The dissipation term in equation (2) is defined, for homogeneous turbulence, by $\varepsilon = \nu \langle (\nabla_\alpha u_i)^2 \rangle$. For isotropic turbulence, this relation reduces to

$$\varepsilon_{iso} = 15 \nu \langle (\frac{\partial u_1}{\partial x_1})^2 \rangle. \quad (15)$$

The general form for homogeneous turbulence is in fact given (Batchelor, 1946) by :

$$\varepsilon_{ij} = -\nu \langle \frac{\partial^2 B_{ij}(\bar{r})}{\partial r_n^2} \rangle_{r=0} = \nu \langle \frac{\partial u_i}{\partial x_n} \frac{\partial u_j}{\partial x_n} \rangle. \quad (16)$$

For axisymmetric turbulence, in the $(\lambda_i, e_{2i}, e_{3i})$ co-ordinate system, equation (16) becomes, when $i=j$:

$$\varepsilon = -\nu \langle (\frac{1}{\rho} \frac{\partial}{\partial \rho} + \frac{\partial^2}{\partial \rho^2} + \frac{\partial^2}{\partial z^2}) B_{ii}(\bar{r}) \rangle_{r=0}, \quad (17)$$

where $B_{ij}(\bar{r})$ is defined in similar fashion to $D_{ij}(\bar{r})$, Eq. (3) :

$$B_{ij}(\bar{r}) = \lambda_i \lambda_j B_1 + e_{2i} e_{2j} B_2 + e_{3i} e_{3j} B_3 + (\lambda_i e_{3j} + \lambda_j e_{3i}) B_4, \quad (18)$$

with $B_1(\rho, z) = \langle u_1(\bar{x}_0) u_1(\bar{x}) \rangle$, $B_2(\rho, z) = \langle u_2(\bar{x}_0) u_2(\bar{x}) \rangle$, $B_3(\rho, z) = \langle u_3(\bar{x}_0) u_3(\bar{x}) \rangle$, $B_4(\rho, z) = \langle u_1(\bar{x}_0) u_3(\bar{x}) \rangle$, and $B_{ii}(\bar{r}) = B_1 + B_2 + B_3$.

Using the relation between the correlation $B_{ii}(\bar{r})$ and the structure function $D_{ii}(\bar{r})$, $D_{ii}(\bar{r}) = 2B_{ii}(0) - 2B_{ii}(\bar{r})$, and considering also that $D_2 = D_3$, an approximation for ε_{axi} can be obtained, viz.

$$\varepsilon_{axi} = 3 \nu \langle (\frac{\partial u_1}{\partial x_1})^2 \rangle + 6 \nu \langle (\frac{\partial u_2}{\partial x_1})^2 \rangle. \quad (19)$$

This relation reduces to the isotropic form, Eq. (15), since, in that case, $2 \langle (\frac{\partial u_1}{\partial x_1})^2 \rangle = \langle (\frac{\partial u_2}{\partial x_1})^2 \rangle$.

AXISYMMETRIC FORM OF KOLMOGOROV'S EQUATION

After substituting into equation (2) the expressions for $D_{ii\alpha}(\bar{r})$ (Eq. (9)), $D_{ij}(\bar{r})$ (Eq. (3)) and the dissipation, the result (Ould-Rouis et al., 1996) is :

$$\begin{aligned} & \frac{\partial}{\partial z} (T_1 + T_2 + T_3) + (\frac{1}{\rho} + \frac{\partial}{\partial \rho}) (T_4 + T_5 + T_6) = \\ & 2 \nu (\frac{\partial^2}{\partial z^2} + \frac{\partial^2}{\partial \rho^2} + \frac{1}{\rho} \frac{\partial}{\partial \rho}) (D_1 + D_2 + D_3) - 4 \varepsilon_{axi}. \end{aligned} \quad (20)$$

The isotropic equation equivalent to (1) is therefore obtained (Ould-Rouis et al., 1996) when λ is allowed to assume any direction :

$$\begin{aligned} & (\frac{2}{r} + \frac{\partial}{\partial r}) (4 + r \frac{\partial}{\partial r}) \dots\dots \\ & \dots\dots [\frac{1}{3} D_{LLL} - 2 \nu \frac{\partial}{\partial r} D_{LL} + \frac{4}{15} \varepsilon_{iso} r] = 0, \end{aligned} \quad (21)$$

since, using the same argument from Monin and Yaglom (1975) as for equation (14), we can then write :

$$D_{LLL} = 6 \nu \frac{\partial}{\partial r} D_{LL} - \frac{4}{5} \varepsilon_{iso} r. \quad (22)$$

For axisymmetric turbulence, when \bar{r} is parallel to $\bar{\lambda}$, an equation corresponding to (1) may be written, with all the scalar functions being directly measurable in both dissipative and inertial ranges. We then obtain :

$$\begin{aligned} & (\frac{2}{r} + \frac{\partial}{\partial r}) (T_1 + 2 T_2) = \\ & 2 \nu (\frac{\partial^2}{\partial r^2} + \frac{2}{r} \frac{\partial}{\partial r}) (D_1 + 2 D_2) - 4 \varepsilon_{axi}, \end{aligned} \quad (23)$$

with $T_1 = D_{LLL}$, $T_2 = D_{LNN}$, $D_1 = D_{LL}$, $D_2 = D_{NN}$ and ε_{axi} defined by equation (19), which yields after integration :

$$\begin{aligned} & D_{LLL} + 2 D_{LNN} = 2 \nu \frac{\partial}{\partial r} (D_{LL} + 2 D_{NN}) \dots\dots\dots \\ & \text{I} \qquad \qquad \qquad \text{II} \\ & \dots\dots\dots - \frac{4}{3} r \varepsilon_{axi}. \end{aligned} \quad (24)$$

This equation can be verified by experiment. In particular, for inertial range scales, the viscous term is negligible and the linear variation with r of the quantity I should have more general validity than the classical four-fifths law for isotropic turbulence.

LIMITING FORM OF EQUATION (24) WHEN $r \rightarrow 0$

Using Taylor series expansions of the two quantities $D_{LLL} + 2 D_{LNN}$ and $\frac{\partial}{\partial r} (D_{LL} + 2 D_{NN})$ about $r=0$, we obtain (Ould-Rouis et al., 1996) :

$$\begin{aligned} & \langle (\frac{\partial u_1}{\partial x_1})^3 \rangle + 2 \langle (\frac{\partial u_1}{\partial x_1}) (\frac{\partial u_2}{\partial x_1})^2 \rangle = \\ & - \frac{2}{3} \nu \langle (\frac{\partial^2 u_1}{\partial x_1^2})^2 \rangle - \frac{4}{3} \nu \langle (\frac{\partial^2 u_2}{\partial x_1^2})^2 \rangle. \end{aligned} \quad (25)$$

This equation is to be compared to the usual isotropic formulation,

$$\langle (\frac{\partial u_1}{\partial x_1})^3 \rangle = -2 \nu \langle (\frac{\partial^2 u_1}{\partial x_1^2})^2 \rangle, \quad (26)$$

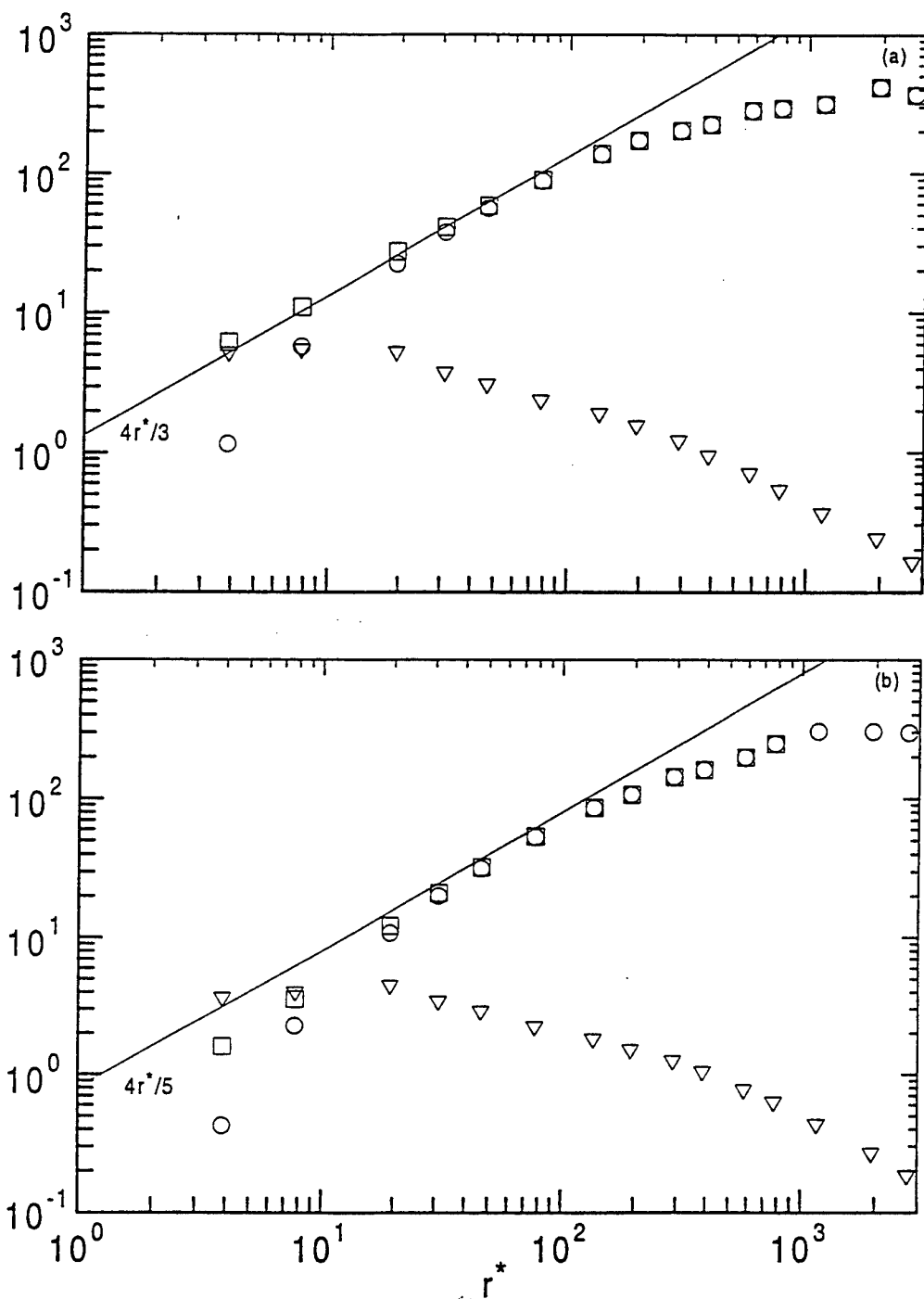


FIGURE 2. EXPERIMENTAL VERIFICATION OF THE AXISYMMETRIC, EQ. (24), AND ISOTROPIC, EQ. (1), FORMS OF THE RELATION BETWEEN THIRD-ORDER AND SECOND-ORDER VELOCITY STRUCTURE FUNCTIONS.
(a) AXISYMMETRY, \square , $-I+II$, \circ , $-I$, ∇ , II , —, $4r^*/3$; (b) ISOTROPY, \square , $-I+II$, \circ , $-I$, ∇ , II , —, $4r^*/5$.

which expresses the isotropic form of the vorticity budget.

EXPERIMENTAL VERIFICATION OF EQUATION (24)

To check the validity of equation (24), we use X-wire (diameter $2.5 \mu\text{m}$, nominal length 0.5 mm) data obtained on the centreline of a plane jet at a distance from the nozzle equal to $53d_j$ (d_j , the nozzle width, is equal to

42 mm). The Taylor microscale Reynolds number was 600. The anemometer signals were digitized at a frequency of 25 KHz, compared with a Kolmogorov frequency of 15 KHz. Taylor's hypothesis was used to convert temporal increments into spatial increments.

Figure 2 shows all three terms in both equation (24) (Fig. 2.a) and equation (1) (Fig. 2.b). Asterisks denote normalization by the Kolmogorov velocity scale $(\nu\epsilon)^{1/4}$ and the Kolmogorov length scale $(\nu^3/\epsilon)^{1/4}$: first note that the magnitude of ϵ_{axi} is about 12% larger than that of ϵ_{iso} , which is in qualitative agreement with previously reported results. When r^* is sufficiently small, both Eqs. (24) and (1) should be satisfied by the data since, in the limit $r^* \rightarrow 0$, the equations reduce to the definitions for ϵ_{axi} and ϵ_{iso} . For inertial range values of r^* , the contributions from the viscous terms become negligible. Over this range, the data appear to be closer to Eq. (24) (Fig. 2.a) than to Eq. (1) (Fig. 2.b).

CONCLUSION

A new equation relating third-order and second-order velocity structure functions has been derived. The new relation, Eq. (24), is based on less restrictive assumptions than Eq. (1), since only axisymmetry about a preferred direction λ was assumed. When the separation \bar{r} is along the axis of symmetry, all terms in equation (24) are amenable to experimental verification.

The plane jet data analyzed in this paper indicate encouraging support for the inertial range behaviour of equation (24). The implication seems to be that local isotropy cannot be a strong condition for the linear dependence of $\langle (\Delta u_1)^3 \rangle$ in the inertial range. Note that a similar conclusion is implicit in Benzi et al.'s ESS approach (1993), where $\langle |\Delta u_1|^3 \rangle$ is used as the basic quantity for determining structure function scaling exponents at low-to-moderate Reynolds numbers. In this case, dissipation range effects as well as the departure from isotropy prevent strong hypotheses, such as those used by Kolmogorov (1941) for writing equation (1), from being valid. However, the behaviour of $\langle |\Delta u_1|^3 \rangle$ is roughly linear over a range of scales which defines the "inertial zone".

Another implication of the present study would be that the value of the constant in the inertial range linear scaling law for third-order structure functions would be more "universal" for axisymmetry ($\approx 4/3$) than for isotropy ($\approx 4/5$). A similar trend was already observed for velocity and temperature derivative moments at one point in space (e.g. Antonia et al., 1991; George and Hussein, 1991). More data would obviously be desirable, over a range of Reynolds numbers and possibly different flows, to provide stronger support for this claim.

ACKNOWLEDGEMENTS

We are most grateful to Dr H.S. Shafi for his contribution to the jet experiments. R.A.A. acknowledges the support of the Australian Research Council.

REFERENCES

- Antonia, R.A., Chambers, A.J. and Browne, L.W.B., 1983, "Relations between structure functions of velocity and temperature in a turbulent jet", *Expts. in Fluids*, Vol. 1, pp. 213-219.
- Antonia, R.A., Kim, J. and Browne, L.W.B., 1991, "Some characteristics of small-scale turbulence in a turbulent duct flow", *J. Fluid Mech.*, Vol. 233, pp. 369-388.
- Antonia, R.A., Ould-Rouis, M., Anselmet, F. and Zhu, Y., 1997, "Analogy between predictions of Kolmogorov and Yaglom", *J. Fluid Mech.*, Vol. 332, pp. 395-409.
- Batchelor, G.K., 1946, "The theory of axisymmetric turbulence", *Proc. R. Soc. Lond.*, Vol. A186, pp. 480-502.
- Benzi, R., Ciliberto, S., Baudet, C., Chavarria, G.R., Tripiccone, R., 1993, "Extended self-similarity in the dissipation range of fully developed turbulence", *Europhys. Letters*, Vol. 24, pp. 275-278.
- Frisch, U., 1995, "Turbulence, The legacy of A.N. Kolmogorov", Cambridge University Press.
- George, W.K. and Hussein, H.J., 1991, "Locally axisymmetric turbulence", *J. Fluid Mech.*, Vol. 233, pp. 1-23.
- Kármán, T. von and Howarth, L., 1938, "On the statistical theory of isotropic turbulence", *Proc. Roy. Soc.*, Vol. A164, pp. 192-215.
- Kolmogorov, A.N., 1941, "Energy dissipation in locally isotropic turbulence", *Dokl. Akad. Nauk. SSSR*, Vol. 32, pp. 19-21.
- Lindborg, E., 1995, "Kinematics of homogeneous axisymmetric turbulence", *J. Fluid Mech.*, Vol. 302, pp. 179-202.
- Monin, A.S. and Yaglom, A.M., 1975, "Statistical fluid mechanics", MIT Press.
- Mydlarski, L. and Warhaft, Z., 1996, "On the onset of high-Reynolds number grid-generated wind tunnel turbulence", *J. Fluid Mech.*, Vol. 320, pp. 331-368.
- Ould-Rouis, M., Antonia, R.A., Zhu, Y and Anselmet, F., 1996, "The axisymmetric form of Kolmogorov's equation", Tech. Note n° 96/2, Dept. Mech. Eng., University of Newcastle (Australia).
- Saddoughi, S.G. and Veeravalli, S.V., 1994, "Local isotropy in turbulent boundary layers at high Reynolds number", *J. Fluid Mech.*, Vol. 268, pp. 333-372.
- Townsend, A.A., 1976, "The structure of turbulent shear flow", Cambridge University Press.

INTERMITTENCY AND WAVELET ANALYSIS OF ONE-POINT TURBULENCE DATA

F. Nicolleau⁽¹⁾ and J.C. Vassilicos⁽¹⁾

⁽¹⁾ Department of Applied Mathematics and Theoretical
Physics, University of Cambridge, Silver Street,
Cambridge CB3 9EW, U.K.

INERTIAL RANGE INTERMITTENCY AND EDDY CAPACITY

The intermittency of a statistically homogeneous and isotropic velocity field $u(x)$ is often characterised by the flatness

$$F(r) = \frac{\langle \Delta u^4(r) \rangle}{\langle \Delta u^2(r) \rangle^2} \quad (1)$$

where $\Delta u(r) = u(x+r) - u(x)$, $u(x)$ is one arbitrary component of the velocity field $u(x)$, x and r are measured along the direction of this component u and the brackets $\langle \dots \rangle$ denote an ensemble average. A signal is often said to be intermittent when $F(r)$ increases with decreasing r .

$F(r)$ is a global statistical quantity obtained by an averaging procedure. However, we show that it is determined by the local geometry of the *intermittency* of the signal. This geometry is captured by D_E the Kolmogorov capacity of the zero-crossings of the *second derivative* of the signal. Indeed D_E which is called eddy capacity verifies

$$F(r) \sim r^{D_E-1}, \quad (2)$$

for a broad class of signals (see figure 1).

D_E has the following properties:

- D_E can be measured in practise. A β -model's result is similar to (2):

$$F(r) \sim r^{D-1}$$

where D is a Kolmogorov capacity defined in terms of the volume-fraction $p(r)$ of eddies of size r (see [Frish (1995)]). However, in the β -model the concept of an eddy of size r remains abstract, no operative definition and no algorithm are given by which to identify such an eddy. Whereas D_E is practically defined as the Kolmogorov capacity of the zero-crossings of the second derivative of the signal.

- D_E is a measure of intermittency whereas D'_K is not. the Kolmogorov capacity D'_K of the zero-crossings of the signal is in general different from D_E . It influences the scalings of power spectra but the scalings of higher-order structure functions, and in particular that of the flatness factor, depend on the eddy capacity D_E which is a direct measure of intermittency. Non-intermittent signals are such that $D_E = 1$ but the Kolmogorov capacity D'_K of their zero-crossings can take any value between 0 and 1.
- D_E can be a better measure of intermittency than $F(r)$. We find numerically that accurate measurements of D_E require significantly smaller data sets with significantly lower resolution than necessary for converged and accurate measurements of $F(r) \sim r^{-q}$.

We measure D_E and $F(r)$ on two high-resolution one-point turbulent velocity signals obtained by Y. Gagne and his team in Grenoble. The first experimental signal was measured in a jet, its Reynolds number based on the Taylor microscale is $Re_\lambda = 835$ and its resolution is 2η where η is the Kolmogorov length scale. The second experimental signal was measured in a grid turbulence and has a higher Reynolds number ($Re_\lambda = 3050$) and a higher resolution (1.2η).

In the inertial range (the range of length-scales where Kolmogorov's law $E(k) \sim k^{-5/3}$ is valid), results indicate that $D_E = 0.95$ and $F(r) \sim r^{-0.11}$. Inertial range turbulence is therefore intermittent, albeit weakly. However, the relation

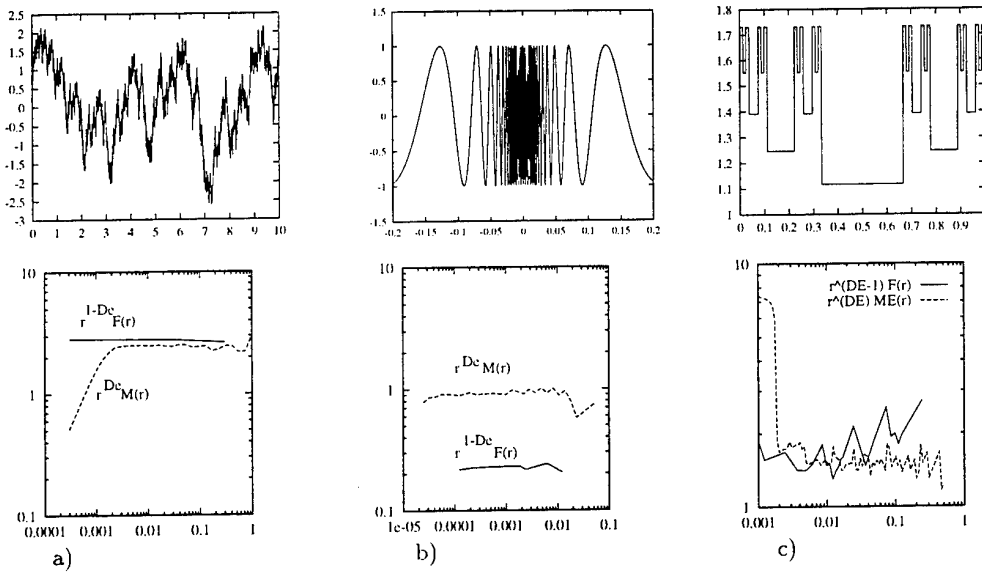


Figure 1: Comparison of $r^{DE} M_E(r)$ and $r^{1-DE} F(r)$ as functions of r . $M_E(r)$ is the number of boxes of size r needed to cover the zero-crossings of the second derivative of u a) - The Weierstrass function b) - $\sin(1/x)$ c) - An intermittent fractal signal

$F(r) \sim r^{DE-1}$ is not obeyed in the inertial range of high-Reynolds number turbulence, and signals such as those of figure 1 are therefore not good models of turbulence fluctuations. Future modelling of turbulence fluctuations should perhaps consider multifractal and multispiral assemblies of the relatively simple model signals of figure 1.

The inertial range does not extend all the way down to the Kolmogorov length-scale η but down to a scale that seems closer to λ and is significantly larger than η in the data sets studied here.

INTERMITTENCY IN THE DISSIPATION RANGE

We call dissipation range the range of length-scales below the inertial range but above η .

We have defined intermittency by the condition $DE < 1$. However, such a property does not shed much light on the actual topology of the signal's intermittency. In this section we introduce distinctions between different topologies of intermittency which can give rise to the same flatness properties. It is therefore impossible to discriminate between them on the sole basis of $F(r)$. [Hunt & Vassilicos (1991)] emphasize that turbulence signals must contain singularities (or rather near-singularities if we take into account the small-scale smoothing effect of viscosity) that can be qualitatively classified as follows:

- isolated cusp singularities such as $1/x^\alpha$,
- isolated accumulating singularities such as $\sin(1/x)$ (see figure 1b),
- and non-isolated singularities such as fractal signals (see figures 1c).

It is of some importance to develop practical methods by which to distinguish between them, future small-scale turbulence modelling may depend on a good understanding of the topology of small-scale intermittency. We use and refine the average wavelet method introduced by [Kevlahan & Vassilicos (1994)].

This method is based on the wavelet transform $\tilde{u}(x_0, a)$ of the signal $u(x)$. The definition of $\tilde{u}(x_0, a)$ is

$$\tilde{u}(x_0, a) = a^{-3} \int u(x) \psi^* \left(\frac{x - x_0}{a} \right) dx, \quad (3)$$

where $\psi(x)$ is a 'mother-wavelet' (ψ^* its complex conjugate), and $\tilde{u}(x_0, a)$ is a function of position x_0 and length-scale a .

The average wavelet transform $\tilde{U}_N(x_0, a)$ of the wavelet transforms $\tilde{u}_r(x_0, a)$ of N different realisation $u_r(x)$ ($r = 1, 2, \dots, N$) of a stochastic signal is

$$\tilde{U}_N(x_0, a) = \frac{1}{N} \sum_{r=1}^N \tilde{u}_r(x_0, a). \quad (4)$$

The average wavelet method is based on the quantity

$$\sigma_a(N) = \int |\tilde{U}_N(x_0, a)| dx_0. \quad (5)$$

The averaging procedure is linked to the topology of the signal. The average depends on N according to the way that the wavelet transform of the signal fills the wavelet space (see figure fig2). This filling process can be measured by N_{max} ,

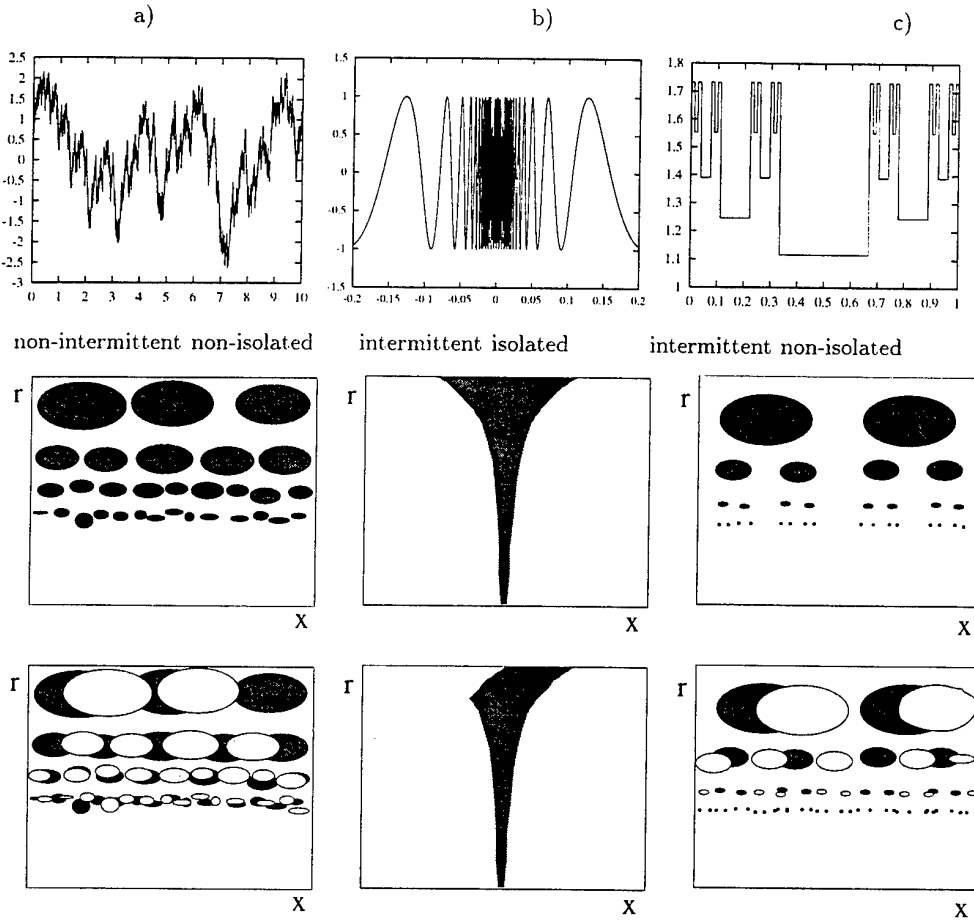


Figure 2:

the maximum number of wavelet transforms $\tilde{u}_r(x_0, a)$ that can be superimposed without cancellations. N_{max} is defined for a fixed scale a as follows:

$$\begin{aligned} \sigma_a(N) &\sim \text{constant} & \text{if } N < N_{max} \\ \sigma_a(N) &= O(N^{-\frac{1}{2}}) & \text{if } N > N_{max} \end{aligned} \quad (6)$$

We make the following distinctions:

(i) for any signal with space-filling non-isolated singularities (figure 1a and 2a).

$$N_{max} = 1 \quad \forall a.$$

We call these signals non-intermittent signals.

(ii) For signals with a finite number of randomly located isolated accumulating singularities (figure 1b and 2b), and for sufficiently small value of a

$$N_{max}(a) \sim a^{D_E-1}$$

where D_E is the eddy capacity of the signal.

(iii) The situation is much the same, albeit for different reasons, for intermittent signal with non-isolated singularities ($D_E \neq 1$, figure 1c and 2c): $N_{max}(a) \sim a^{D_E-1}$.

(iv) Differences between non-isolated and isolated singularities may be detected, however, in the limit $D_E \rightarrow 1$. Non-isolated singularities then tend to non-intermittency (i) whereas isolated accumulating singularities tend to isolated space-filling singularities. Isolated space-filling singularities are defined by:

$$N_{max}(a) \sim a^0$$

and in contrast with (i), $N_{max} > 1$.

(v) The average wavelet method can also distinguish between isolated space-filling singularities and isolated cusp singularities. We find for signals with a finite number of cusp singularities x^s that N_{max} is *not* independent of a , for all value of s (see table 1).

function $u(x)$	D_E	$D_E - 1$	slope of $N_{max}(a)$
$\sin(1/x^{0.5})$	0.33	-0.66	-1.16
$\sin(1/x)$	0.50	-0.50	-0.54
$\sin(1/x^3)$	0.75	-0.25	~ 0
$1/x^{0.5}$	0.00	-1.00	-1.58
$1/x$	0.00	-1.00	-1.43
Cantor set	0.63	-0.37	-0.33

Table 1: N_{max} as a function of a

The average wavelet method can therefore distinguish in practise between cusp signals, non-intermittent signals and signals with isolated space-filling singularities.

When applied to the turbulence data measured in Modane, The average wavelet method shows that turbulence small-scales are intermittent in a stronger sense than large-scales and share intermittency properties of signals having isolated space-filling singularities (iv) (see figure 3).

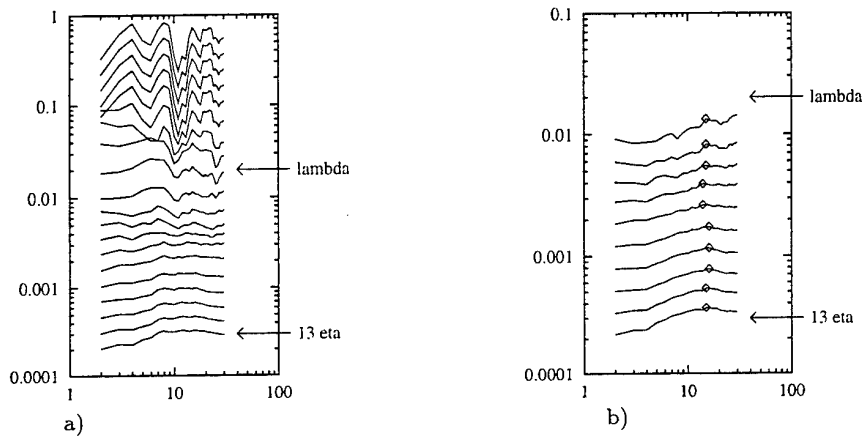


Figure 3: Average Wavelet method applied to 0.5 integral length scale long samplings of grid turbulence signal: a) Full results. b) Details of the small-scales.

REFERENCES

- Frish, U., 1995, "Turbulence", Cambridge University Press.
- Hunt, J. C. R., and Vassilicos, J. C., 1991, "Kolmogorov's contribution to the physical and geometrical understanding of small-scale turbulence", *Proc. R. Soc. Lond. A*, **434**, 183-210.
- Kevlahan, N., and Vassilicos, J. C., 1994, "The space and scale dependencies of the self-similar structure of turbulence", *Proc. R. Soc. Lond. A* **447**, 341-363.

SCALING LAW OF COHERENT FINE SCALE STRUCTURE IN HOMOGENEOUS ISOTROPIC TURBULENCE

M. Tanahashi, T. Miyauchi, J. Ikeda
Department of Mechano-Aerospace Engineering
Tokyo Institute of Technology
2-12-1 Ookayama, Meguro-ku
Tokyo 152
Japan

ABSTRACT

Scaling law of coherent fine scale structure in turbulent flow was investigated by using a DNS data base of decaying homogeneous isotropic turbulence up to $Re_\lambda = 87.9$. To identify the coherent fine scale structure, a new identification scheme that uses local flow patterns to determine the axis of fine scale structure was employed. The coherent fine scale structures of turbulence, which show tube-like features, can be scaled by Kolmogorov microscale and r.m.s. of velocity fluctuation. Mean diameter of the structures is close to 12 times of Kolmogorov microscale and maximum of mean azimuthal velocity is close to r.m.s. of velocity fluctuation, where the mean azimuthal velocity profile can be approximated by a Burgers' vortex. Diameter of the coherent fine scale structure shows an asymptotic behavior with the increase of second invariant and reaches about 6 ~ 8 times of Kolmogorov microscale. These characteristics do not depend upon Reynolds number. A simple description of the coherent fine scale structures were presented based on Burgers' vortex model and Reynolds number dependence of intense coherent fine scale structures are specified. Circulation of most intensified coherent fine scale structures increases with the increase of turbulent Reynolds number, while probability density functions of circulation of all coherent fine scale structures do not depend upon the turbulent Reynolds number.

INTRODUCTION

Theories of fine scale structure in turbulence have been developed by many researchers (Townsend 1951, Corrsin 1962, Tennekes 1968, Lundgren 1982, Pullin and Saffman 1993, Saffman and Pullin 1994, Pullin 1995). These theories are based on an assumption that many tube-like or sheet-like vortices are embedded in turbulence randomly. Each vortex is considered to be an analytical solution of Navier-Stokes equations; for example a Burgers vortex. Recently, from the results of direct numerical simulations, it is shown that there are high vorticity regions in homogeneous turbulence, which are supposed to be a candidate of fine scale structure in turbulence (Kerr 1985, She et al. 1990, Vincent and Meneguzzi 1991, Ruetsch and Maxey 1991, 1992, Jimenez et al. 1993, Vincent and Meneguzzi

1994). Observed high vorticity regions show tube-like features, but the definition depends upon the threshold. Most of studies have employed magnitude of vorticity to educe fine scale structure. Jimenez et al. (1993) have reported that high vorticity regions occupy a few percents of the total volume and these tube-like structures actually produce intermittent characters in the velocity field. However, the high vorticity regions do not always correspond to the universal fine scale structures in turbulence.

The purpose of this study is to specify fine scale structures in homogeneous isotropic turbulence and to investigate a scaling law and Reynolds number dependence of fine scale structures. DNS database of decaying homogeneous isotropic turbulence are analyzed by using a new identification method of fine scale structures (Tanahashi et al. 1997a). Tanahashi et al. (1997a) have found that homogeneous isotropic turbulence consists of a lot of similar tube-like structures and that mean azimuthal velocity profiles of those structures agree with that of a Burgers' vortex. As these fine scale structures have similar mean azimuthal velocity profiles and distinct axis, these eddies can be called as 'coherent fine scale structure' in turbulence.

IDENTIFICATION OF COHERENT FINE SCALE STRUCTURES IN TURBULENCE

DNS of Homogeneous Isotropic Turbulence

Direct Numerical Simulations of decaying homogeneous isotropic turbulence are conducted by using a spectral method with 216^3 grid points. Aliasing errors due to nonlinear interactions are fully removed by a 3/2 rule, which result in 216^3 active modes. Numerical conditions are listed in Table 1. For two lower Reynolds number cases, calculations are conducted with the same conditions that have reported by Comte-Bellot and Corrsin (1971) for grid turbulence. Statistical properties obtained by these DNSs show a good agreement with the experimental results. Flatness and skewness factors of the velocity derivatives for the highest Reynolds number case coincide with previous experimental and numerical results (Van Atta and Antonia 1980, Jimenez et al. 1993).

Table 1: DNS database of decaying homogeneous isotropic turbulence. Re_λ : Reynolds number based on Taylor microscale, Re_l : Reynolds number based on integral length scale, Re_k : Reynolds number based on Kolmogorov microscale and r.m.s. of velocity fluctuation, N : number of grid points, $S_{u'}$: skewness of longitudinal velocity derivative, $F_{u'}$: flatness of longitudinal velocity derivative.

ID	Re_λ	Re_l	Re_k	N	$S_{u'}$	$F_{u'}$
1	37.1	163	3.10	216^3	-0.487	4.14
2	66.1	580	4.15	216^3	-0.495	4.52
3	87.9	700	4.78	216^3	-0.483	4.97

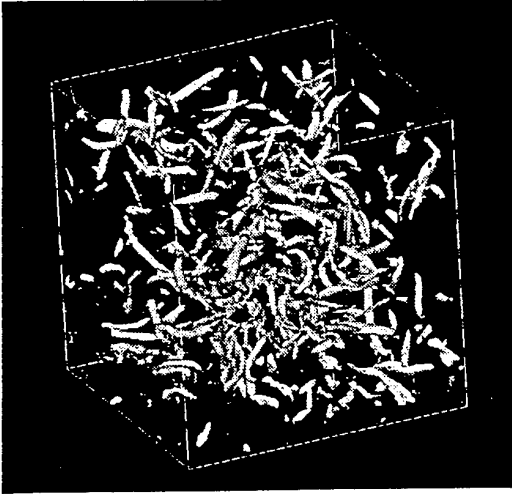


Figure 1: Contour surfaces of normalized second invariant of the velocity gradient tensor ($Q^* = 0.03$) for the case of $Re_\lambda = 87.9$. Visualized region is $1/27$ of the whole calculation domain. Second invariant is normalized by Kolmogorov microscale and r.m.s. of fluctuating velocity.

Identification Scheme

In previous studies, high vorticity or enstrophy regions have been used to identify intermittent fine scale structures of homogeneous turbulence (Kerr 1985, She et al. 1990, Vincent and Meneguzzi 1991, Ruetsch and Maxey 1991, 1992, Jimenez et al. 1993, Vincent and Meneguzzi 1994). However, high vorticity regions may represent tube-like structures and sheet-like structures simultaneously. For the case with a strong mean shear like the flow near the wall or center of free shear flows, employment of high vorticity or enstrophy regions fail to educe coherent structures.

In this work, to avoid this confusion, a new identification scheme that has proposed by Tanahashi et al. (1997a) is used. In this scheme, local streamline patterns are directly used to find out the coherent fine scale structures in turbulence. The identification scheme is summarized as follows (Tanahashi et al. 1997a):

- Evaluation of $Q = -(S_{ij}S_{ij} - W_{ij}W_{ij})$ at each collocation point from the results of DNS. Q is second invariant of characteristic equations for the velocity gradient tensor $A_{ij} = S_{ij} + W_{ij}$ ($S_{ij} = (\partial u_i / \partial x_j + \partial u_j / \partial x_i) / 2$ and $W_{ij} = (\partial u_i / \partial x_j - \partial u_j / \partial x_i) / 2$).
- Probability of existence of positive maximals of Q near the collocation points is evaluated at each collocation point from Q distribution. The case that a maximal of Q coincides with a collocation point is very rare, so it is necessary to define probability on collocation points.
- Collocation points with high possibility of existence

Table 2: Characteristic length scales and mean diameter of the coherent fine scale structure. l : integral length scale, λ : Taylor microscale, $l_{D.M.}$: dissipation maximum scale, D_m : mean diameter of the coherent fine scale structure, V : investigated volume, n : number of detected coherent fine scale structure. Listed length scales are normalized by Kolmogorov microscale and investigated volume is represented in an integral length scale unit.

Re_λ	l^*	λ^*	$l_{D.M.}^*$	D_m^*	V	n
37.1	52.6	12.0	24.7	11.8	30.8	195
66.1	140	15.9	29.2	12.7	27.9	733
87.9	147	18.4	34.9	12.3	29.3	921

are selected to survey actual maximals of Q . Locations of Q maximals are determined by applying a three dimensional cubic spline interpolation to DNS data.

- At the maximal second invariant point, a horizontal plane perpendicular to the vorticity vector is defined and a cylindrical coordinate system setting the maximal point as the origin is considered. The velocity vectors are transformed on this coordinate and mean azimuthal velocity is calculated.
- Point that has minimum variance of azimuthal velocity is surveyed near the maximal point. In this process, a new cylindrical coordinate system is always defined around a newly searched point.
- Statistical properties are calculated around the point.

Detail descriptions have been given by Tanahashi et al. (1997a).

Figure 1 shows contour surfaces of normalized second invariant ($Q^* = 0.03$) for the case of $Re_\lambda = 87.9$. Here, an asterisk denotes normalization by Kolmogorov microscale (η) and r.m.s. of velocity fluctuation (u_{rms}). This normalization is due to the results described below. Tube-like structures are randomly oriented in homogeneous isotropic turbulence as was shown in the previous studies by She et al. (1990), Vincent and Meneguzzi (1991) and Jimenez et al. (1993). Note that positive Q regions are corresponding to solid body rotations where rotation rate ($= W_{ij}W_{ij}$) exceed strain rate ($= S_{ij}S_{ij}$). By the above described identification scheme, points on the axis of tube-like structure can be specified. Tanahashi et al. (1997a) have reported three-dimensional structure along the axis by extending above scheme. In this study, however, we restricts our discussions to two-dimensional characters on the sections including points where variance of azimuthal velocity becomes minimum.

SCALING LAW OF COHERENT FINE SCALE STRUCTURES OF TURBULENCE

Figure 2 shows a mean azimuthal velocity profile of fine scale structures for the case of $Re_\lambda = 87.9$. The average was taken over 921 samples. Symbols in Fig.2 show an azimuthal velocity profile of a Burgers' vortex:

$$v_\theta = \frac{\Gamma}{2\pi r} [1 - \exp(-\frac{\alpha r^2}{4\nu})], \quad (1)$$

$$v_z = \alpha z, \quad (2)$$

where Γ is a circulation and α is a stretching parameter. Mean azimuthal velocity profile of the coherent fine scale structures shows a good agreement with that of a Burgers' vortex. In Table 2, characteristic length scales of turbulence and mean diameters of the coherent fine scale structures are listed for three different Reynolds numbers, where

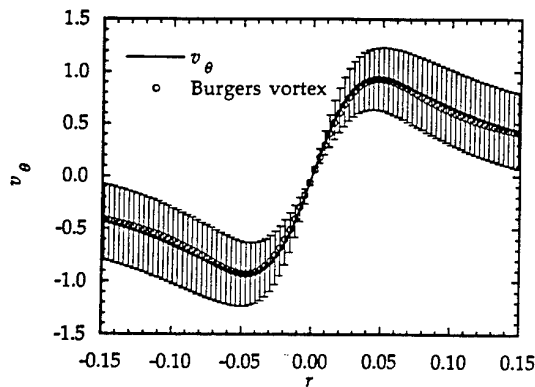


Figure 2: Mean azimuthal velocity profile of the coherent fine scale structure for the case of $Re_\lambda = 87.9$. Symbols: velocity profile of a Burgers' vortex. Error bars denote variances of azimuthal velocity.

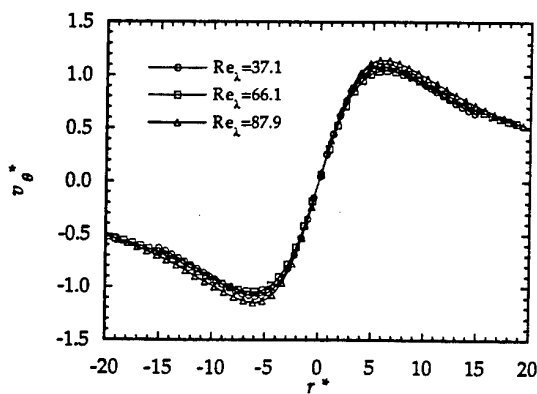


Figure 3: Mean azimuthal velocity profiles of the coherent fine scale structure normalized by Kolmogorov microscale and r.m.s. of fluctuating velocity.

length scales are normalized by Kolmogorov microscale. Investigated volumes for each Reynolds number case are selected to be $\approx 30l^3$ and number of detected coherent fine scale structures is 195 for $Re_\lambda = 37.1$, 733 for $Re_\lambda = 66.1$ and 921 for $Re_\lambda = 87.9$. These investigated volumes and samples are enough to discuss the statistical characters of the coherent fine scale structures. In this study, radius of the coherent fine scale structures is determined by a distance between the center and location where the mean azimuthal velocity reaches the maximum value.

Taylor microscale and dissipation maximum scale nondimensionalized by the Kolmogorov microscale become large with the increase of Reynolds number. However, mean diameters of the coherent fine scale structures are about 12 times of Kolmogorov microscale and does not depend on turbulent Reynolds number. She et al. (1990), Vincent and Meneguzzi (1991) and Jimenez et al. (1993) have shown that high vorticity regions in homogeneous turbulence are scaled by Kolmogorov microscale and the scale of high vorticity regions are order of Kolmogorov microscale. The diameters of those high vorticity regions are slightly smaller than present results of the coherent fine scale structures, while their observation that the high vorticity regions can be scaled by Kolmogorov microscale coincide with our results.

In Fig.3, mean azimuthal velocity profiles normalized by Kolmogorov microscale and r.m.s. of velocity fluctuation are shown for three different Reynolds number cases. Mean azimuthal velocity profiles coincide very well for different Reynolds number. The maximums of mean azimuthal velocity profiles are close to u_{rms} . This results show that

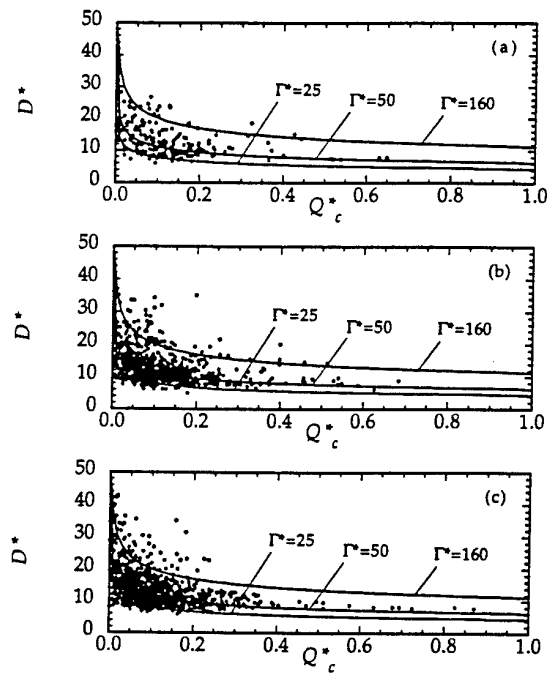


Figure 4: Scatter plots of diameters of the coherent fine scale structure with respect to second invariant of the velocity gradient tensor. All variables are normalized by Kolmogorov microscale and r. m. s. of fluctuating velocity. (a) $Re_\lambda = 37.1$, (b) $Re_\lambda = 66.1$, (c) $Re_\lambda = 87.9$. Solid lines denote relations between diameter and second invariant of Burgers' vortices for $\Gamma^+ = 25, 50, 160$.

mean diameter and intensity of the coherent fine scale structures can be scaled by Kolmogorov microscale and r.m.s. of fluctuating velocity in these Reynolds number range. These coherent fine scale structures have high and very thin energy dissipation regions around them and these regions contribute to total energy dissipation significantly (Tanahashi et al. 1996).

Figure 4 shows relation between diameter and second invariant at the center of each coherent fine scale structure. Diameters and second invariants are also normalized by Kolmogorov microscale and r.m.s. of velocity fluctuation. Distributions of diameter as a function of second invariant show good agreement with each other. Variance of the diameter is relatively large for low second invariant and small for large second invariant. Most of coherent fine scale structures have relatively low second invariant ($Q^+ < 0.3$). Asymptotic value of diameter for large second invariant is 6 ~ 8 times of Kolmogorov microscale, which is also a lower limit of those diameters for all range of second invariant.

Maximums of mean azimuthal velocity are plotted in Fig.5 with respect to the second invariant. For all cases, maximum values reach 2.0 ~ 2.5 times of u_{rms} . Asymptotic behaviors are also observed for the intensity of the azimuthal velocity. The asymptotic values seem to depend on Reynolds number: 1.5 times of u_{rms} for $Re_\lambda = 37.1$, 2.0 times of u_{rms} for $Re_\lambda = 66.1$ and 2.4 times u_{rms} for $Re_\lambda = 87.9$. The reason of the Reynolds number dependence is discussed in the next section. The coherent fine scale structures produces large velocity differences (about 5 times of u_{rms}) in a very small spatial region (about 12η). This character suggest that the coherent fine scale structures are directly related to the intermittency of the velocity fields in small scales.

Figure 6 shows relations between enstrophy and second invariant at the center of coherent fine scale structure for the case of $Re_\lambda = 87.9$. The coherent fine scale structures with large azimuthal velocity and small radius correspond

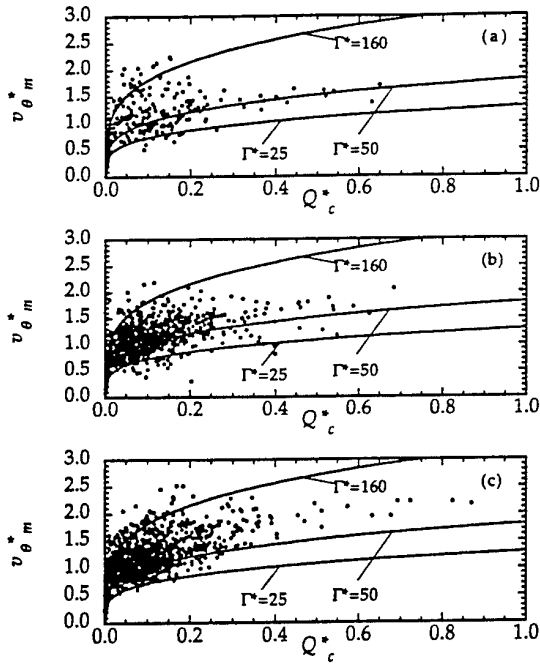


Figure 5: Scatter plots of maximum of mean azimuthal velocity with second invariant of the velocity gradient tensor. All variables are normalized by Kolmogorov microscale and r.m.s. of fluctuating velocity. (a) $Re_\lambda = 37.1$, (b) $Re_\lambda = 66.1$, (c) $Re_\lambda = 87.9$. Solid lines denote relations between maximum azimuthal velocity and second invariant of Burgers' vortices for $\Gamma^* = 25, 50, 160$.

to the high enstrophy regions that have reported by previous studies (She et al. 1990, Vincent and Meneguzzi 1991, Jimenez et al. 1993). Jimenez et al. (1993) have reported that high vorticity regions in statistically steady homogeneous turbulence have a radius of about 4 times of Kolmogorov microscale. Their result coincide very well with present asymptotic values ($3 \sim 4\eta$) as shown in Fig.4. The high vorticity regions in turbulence are frequently called as 'worms' (Yamamoto and Hosokawa 1988) or 'sinews' (Moffatt et al. 1994). Present results suggest that 'worms' or 'sinews' reflect one aspect of the coherent fine scale structures in turbulence.

Scatter plots of second and third invariants at the center of the coherent fine scale structures are shown in Fig.7. Here third invariant of velocity gradient tensor is defined by $R = -(S_{ij}S_{jk}S_{ki} + 3W_{ij}W_{jk}S_{ki})/3$. By using second and third invariants, we can determine a local flow pattern. In the case of incompressible flows, local flow patterns are classified into four categories: stable focus-stretching, unstable focus-compressing, stable node-saddle-saddle and unstable node-saddle-saddle (Chong 1990). The coherent fine scale structures detected in this work have positive Q and positive/negative R . In these regions, local streamline patterns are classified into stable focus-stretching and unstable focus-compressing. In these topologies, streamlines show spiral features because two eigenvalues of the velocity gradient tensor are complex value. Figure 8 shows histogram of third invariant for the case of $Re_\lambda = 87.9$. A large part of the coherent fine scale structures have negative third invariant. Hence, most of structures are stretched in the axial direction and stably exist in turbulence.

SIMPLE DESCRIPTION OF COHERENT FINE SCALE STRUCTURE

In this section, we discuss about a description of the co-

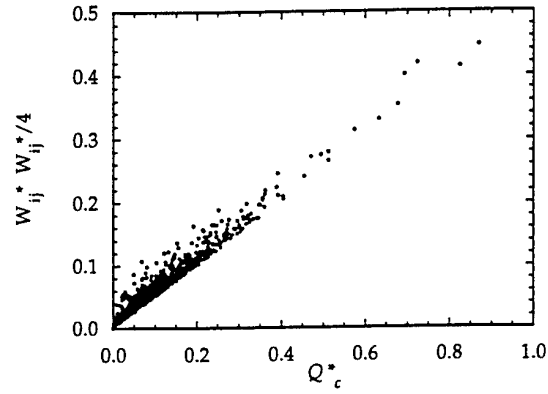


Figure 6: Relation between second invariant and enstrophy at the center of the coherent fine scale structure ($Re_\lambda = 87.9$).

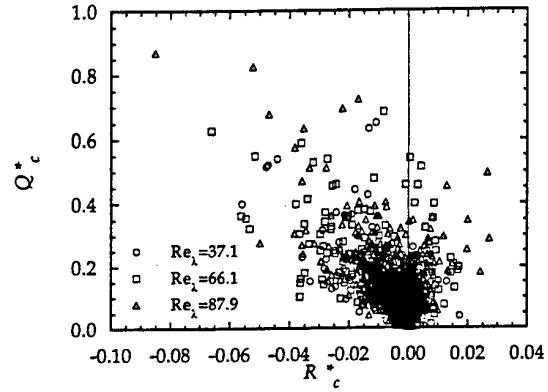


Figure 7: Distributions of coherent fine scale structures on $Q-R$ plane for the case of $Re_\lambda = 87.9$.

herent fine scale structures based on Burgers' vortex. As shown in Figs.2 and 3, mean azimuthal velocity profile of the coherent fine scale structures can be approximated by that of a Burgers' vortex. However, for the approximation of coherent fine scale structures by a Burgers' vortex, each coherent fine scale structure should be represented by a Burgers' vortex. Figure 9 shows a mean azimuthal velocity profile obtained by other definition of the average for the case of $Re_\lambda = 87.9$. In this average, mean azimuthal velocity is first normalized by maximum azimuthal velocity and radius of each coherent fine scale structure. Symbols in Fig.9 show an azimuthal velocity profile of a Burgers' vortex. Note that the azimuthal velocity profiles of Burgers' vortices become independent of Γ and α by this normalization. From Fig.9, it is obvious that the mean azimuthal velocity profile of each coherent fine scale structure can be approximated by that of Burgers' vortex. Figure 10 shows fluctuating energy of azimuthal velocity in k_θ mode for the case of $Re_\lambda = 87.9$. Near the center of the coherent fine scale structures, fluctuating energy of azimuthal velocity is relatively small and energy in $k_\theta = 1$ is dominant. This result coincide with an analysis of a Burgers' vortex by Moffatt et al. (1994). Departing from the center, energies in high wave number increase, while maximum energy in fluctuating modes is about 30% of mean azimuthal velocity.

From above results, we can assume that each of the coherent fine scale structure can be approximated by a Burgers' vortex defined by Eqs.4 and 5, and embedded in flow field with Γ and α . Present results described above allow us the normalization by η and u_{rms} . Diameters and maximum azimuthal velocity of Burgers' vortices can be

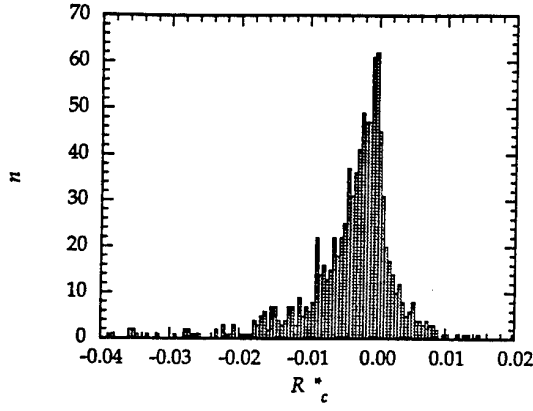


Figure 8: Histogram of third invariant of the center of the coherent fine scale structures for $Re_\lambda = 87.9$.

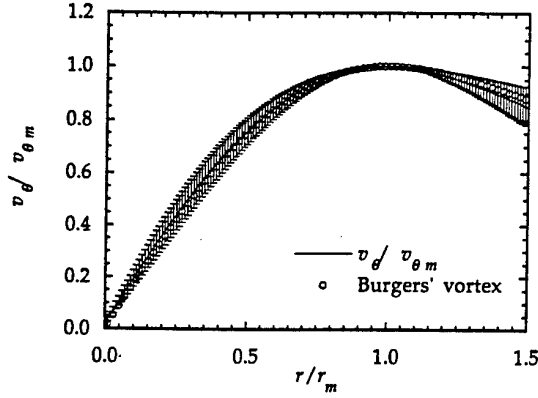


Figure 9: Mean azimuthal velocity profile of the coherent fine scale structures ($Re_\lambda = 87.9$). The average is taken after a normalization by maximum azimuthal velocity and radius of each coherent fine scale structure. Error bars denote variances of azimuthal velocity.

represented as follows:

$$D_m^* = 2A^{-1/4} Q_c^{*-1/4}, \quad (3)$$

$$v_{\theta m}^* = \frac{\Gamma^*}{2\pi} A^{-1/4} [1 - \exp(-s_m)] Q_c^{*-1/4}, \quad (4)$$

$$A = \left[\frac{1}{4\pi^2} (\Gamma^* Re_k)^2 - 12 \right] \left(\frac{s_m}{Re_k} \right)^2, \quad (5)$$

where s_m is a value that satisfy $2s + 1 = \exp(s)$: $s_m = 1.2564\dots$ and Re_k denotes Reynolds number based on u_{rms} and η . In Figs.4 and 5, solid lines represent behaviors of diameter and maximum azimuthal velocity of Burgers' vortices for normalized circulation $\Gamma^* = 25, 50, 160$. Here, Re_k is set equal to the results of DNS. This Reynolds number is very important for the description of the coherent fine scale structures by Burgers' vortices and about 3 ~ 5 for these Reynolds number regions as listed in Table 1. Figures 4 shows that dependence of diameters of coherent fine scale structures on second invariant are represented very well by that of Burgers' vortices. Since diameters of Burgers' vortices show $-1/4$ power law for the second invariant, differences of diameter of Burgers' vortices for different Γ^* are large for low Q^* and small for large Q^* . Variances in distributions of maximum azimuthal velocities are also represented by Burgers' vortex model as shown in Fig.5.

To show the effectiveness of the Burgers' vortex model in detail, maximum azimuthal velocities of coherent fine scale structures that have $64 < \Gamma^* < 81$ and $81 < \Gamma^* < 100$ are

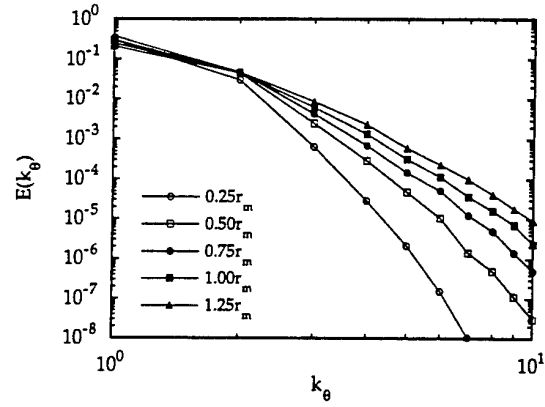


Figure 10: Fluctuating energy in azimuthal velocity ($Re_\lambda = 87.9$). k_θ is wave number of azimuthal modes. Spectrums are plotted at 5 radius with an interval $0.25r_m$.

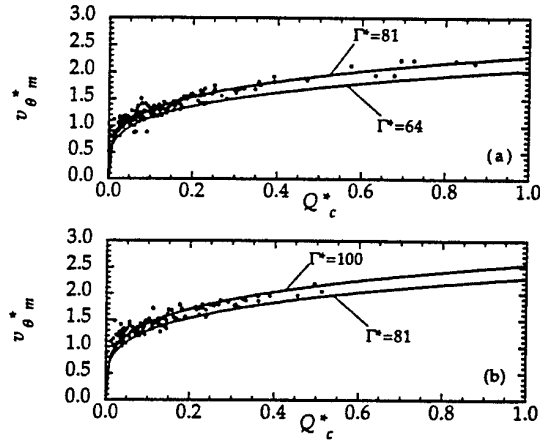


Figure 11: Relation between maximum azimuthal velocity and second invariants ($Re_\lambda = 87.9$). Symbols: coherent fine scale structures, Solid lines: Burgers' vortices. (a) $64 < \Gamma^* < 81$, (b) $81 < \Gamma^* < 100$.

shown in Fig. 11 for the case of $Re_\lambda = 87.9$. Circulation of coherent fine scale structures are determined by fitting with a Burgers' vortex. Maximum azimuthal velocities of coherent fine scale structures show similar characters of Burgers' vortices having the same circulation. As mentioned above, the asymptotic values of maximum azimuthal velocity depend on Reynolds number. This Reynolds number dependence is due to circulation of coherent fine scale structures at large second invariant. Intense coherent fine scale structures show $\Gamma^* \approx 50$ for $Re_\lambda = 37.1$, ≈ 70 for $Re_\lambda = 66.1$ and ≈ 80 for $Re_\lambda = 87.9$.

For the intense vorticity regions in homogeneous turbulence, Jimenez et al (1993) have reported that circulation $|\Gamma/\nu|$ of the intense tube-like structures increase with turbulent Reynolds number. Note that $|\Gamma/\nu|$ can be related to Γ^* by $|\Gamma/\nu| = \Gamma^* Re_k$. Therefore, intense coherent fine scale structures show that $|\Gamma/\nu|$ is about 150 for $Re_\lambda = 37.1$, about 200 for $Re_\lambda = 66.1$ and about 380 for $Re_\lambda = 87.9$. The tendency that circulation of intense tube-like structures increase with Reynolds number coincide with the results by Jimenez et al. (1993). However, magnitude of circulation's that have reported by Jimenez et al. (1993) is slightly smaller than our results. This discrepancy in the magnitude of circulation may be attributed to the identification method of the fine scale structures and definition of circulation. Figure 12 shows probability density functions of Γ^* for three Reynolds number cases. In spite of Reynolds number dependence of the intense co-

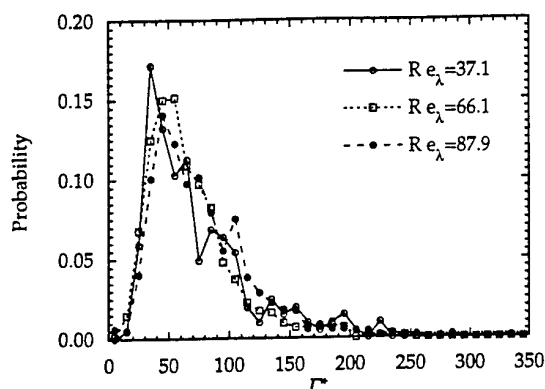


Figure 12: Probability of circulation of the coherent fine scale structure. Circulation is normalized by Kolmogorov microscale and r.m.s. fluctuating velocity.

herent fine scale structures, pdfs of Γ^* constructed by all structures coincide very well and show a peak at $\Gamma^* \approx 50$.

CONCLUSIONS

In this study, scaling law of coherent fine scale structure in turbulent flow was investigated by using a DNS data base of decaying homogeneous isotropic turbulence up to $Re_\lambda = 87.9$. To identify the coherent fine scale structure, a new identification scheme that uses local flow patterns to determine the axis of fine scale structure was employed. Statistical characters of educed fine scale structure in turbulence were discussed.

The detected coherent fine scale structures of turbulence, which show tube-like features, can be scaled by Kolmogorov microscale and r.m.s. of velocity fluctuation. Mean diameter of the structures is close to 12 times of Kolmogorov microscale and maximum of mean azimuthal velocity is close to r.m.s. of velocity fluctuation. Mean azimuthal velocity profiles can be approximated by a Burgers' vortex. Diameters of the coherent fine scale structures show asymptotic behaviors with the increase of second invariant and reaches about 6 ~ 8 times of Kolmogorov microscale. The asymptotic values is a lower limit of diameters of the coherent fine scale structures. These characteristics do not depend upon Reynolds number.

A simple description of the coherent fine scale structures were presented based on Burgers' vortex model. From the comparison between Burgers' vortices and the coherent fine scale structures, Reynolds number dependence of intense coherent fine scale structures are specified, which results in the asymptotic values of maximum azimuthal velocity. Circulation of mostly intensified coherent fine scale structures increase with turbulent Reynolds number, while probability density functions of circulation of all coherent fine scale structures are identical.

Our findings imply that turbulence is composed of fine scale structures which show universal character. To prove this universality, detail characteristics of coherent fine scale structures should be investigated in higher Reynolds number cases and in other turbulent flows. Our resent work in turbulent mixing layers (Tanahashi et al. 1997b) shows the evidence of a universal coherent fine scale structure in turbulence.

Acknowledgments : This work is partially supported by the Kawakami memorial foundation.

REFERENCES

Chong, M. S., Perry, A. E. and Cantwell, B. J., 1990,

"A general classification of three-dimensional flow field". *Phys. Fluids*, Vol. A2, pp.765-777.

Comte-Bellot, G. and Corrsin, S., 1971, "Simple eulerian time correlation of full- and narrow-band signals in grid-generated 'isotropic' turbulence", *J. Fluid Mech.*, Vol. 48, pp. 273-337.

Corrsin, S., 1962, "Turbulent Dissipation Fluctuations", *Phys. Fluids*, Vol. 10, pp. 1301-1302.

Jimenez, J., Wray, A. A., Saffman, P. G. and Rogallo, R. S., 1993, "The structure of intense vorticity in isotropic turbulence", *J. Fluid Mech.*, Vol. 255, pp. 65-90.

Kerr, R. M. V., 1985, "Higher-order derivative correlations and the alignment of small-scale structures in isotropic numerical turbulence", *J. Fluid Mech.*, Vol. 153, pp. 31-58.

Lundgren, T. S., 1982, "Strained Spiral vortex model for turbulent fine structure", *Phys. Fluids*, Vol. 25, pp. 2193-2203.

Moffatt, H. K., Kida, S. and Ohkitani, K., 1994, "Stretched vortices - the sinews of turbulence; large-Reynolds-number asymptotics", *J. Fluid Mech.*, Vol. 259, pp.241-264.

Pullin, D. I. and Saffman, P. G., 1993, "On the Lundgren-Townsend model of turbulent fine scales", *Phys. Fluids*, Vol. A5, pp. 126-145.

Pullin, D. I., 1995, "Pressure spectra for vortex models of fine-scale homogeneous turbulence", *Phys. Fluids*, Vol. A7, pp. 849-856.

Ruetsch, G. R. and Maxey, M. R., 1991, "Small-scale features of vorticity and passive scalar fields in homogeneous isotropic turbulence", *Phys. Fluids*, Vol. A3, pp. 1587-1597.

Ruetsch, G. R. and Maxey, M. R., 1992, "The evolution of small-scale structures in homogeneous isotropic turbulence", *Phys. Fluids*, Vol. A4, pp. 2747-2760.

Saffman, P. G. and Pullin, D. I., 1994, "Anisotropy of the Lundgren-Townsend model of fine-scale turbulence", *Phys. Fluids*, Vol. A6, pp. 802-807.

She, Z. -S., Jackson, E. and Orszag, S. A., 1990, "Intermittent vortex structures in homogeneous isotropic turbulence", *Nature*, Vol. 344, pp. 226-228.

Tennekes, H., 1968, "Simple model for the small-scale structure of turbulence", *Phys. Fluids*, Vol. 11, pp. 669-761.

Tanahashi, M., Miyauchi, T. and Yoshida, T., 1996, "Characteristics of small scale vortices related to turbulent energy dissipation", *Proc. 9th Int. Symp. Transport Phenomena*, Vol. 2, pp. 1256-1261.

Tanahashi, M., Miyauchi, T. and Ikeda, J., 1997a, "Identification of coherent fine scale structure in turbulence", to be appeared in *IUTAM Symposium on Simulation and Identification of Organized Structures in Flows*.

Tanahashi, M., Miyauchi, T. and Matsuoka, K., 1997b, "Coherent fine scale structures in temporally developing turbulent mixing layers", to be appeared in *2nd International Symposium on Turbulence, Heat and Mass Transfer*.

Townsend, A. A., 1951, "On the fine-scale structure of turbulence", *Proc. R. Soc. Lond.*, Vol. A208, pp. 534-542.

Van Atta, C. W. and Antonia, R. A., 1980, "Reynolds number dependence of skewness and flatness factors of turbulent velocity derivatives", *Phys. Fluids*, Vol. 23, pp. 252-257.

Vincent, A. and Meneguzzi, M., 1991, "The spatial structure and statistical properties of homogeneous turbulence", *J. Fluid Mech.*, Vol. 225, pp. 1-20.

Vincent, A. and Meneguzzi, M., 1994, "The dynamics of vorticity tubes in homogeneous turbulence", *J. Fluid Mech.*, Vol. 258, pp. 245-254.

Yamamoto, K. and Hosokawa, I., 1988, "A decaying isotropic turbulence pursued by the spectral method", *J. Phys. Soc. Japan*, Vol. 57, pp.1532-1535.

INVESTIGATION OF RENORMALIZATION GROUP METHODS FOR THE NUMERICAL SIMULATION OF ISOTROPIC TURBULENCE

David McComb, Taek-Jin Yang, Alistair Young

Department of Physics and Astronomy

University of Edinburgh

James Clerk Maxwell Building

Mayfield Road

Edinburgh EH9 3JZ

United Kingdom

Luc Machiels

Laboratory of Fluid Mechanics

Swiss Federal Institute of Technology

CH-1015 Lausanne

Switzerland

INTRODUCTION

Over the years, our research into turbulence at Edinburgh has concentrated on the application of renormalization methods to the prediction of the energy spectrum of isotropic turbulence. General discussions of this work will be found elsewhere (McComb 1990, 1995), while accounts of specific progress have been given previously in this conference series (McComb & Shanmugasundaram 1983, McComb, Filipiak, Roberts & Watt, 1991).

From a practical point of view, the most promising development in this area is undoubtedly Renormalization Group or RG. If we work in the Fourier representation, in principle, this involves the progressive averaging out of high-wavenumber modes in bands, with rescaling at each step, until a fixed point is reached. The result is, in effect, a 'subgrid model' for large-eddy simulation.

RG has enjoyed its successes in other areas of statistical physics. However, its application to turbulence faces several technical difficulties, which have to be circumvented by uncontrolled approximations. Indeed, in view of the deterministic nature of the Navier-Stokes equations, it is clear that the operation of averaging out the high-wavenumber modes while keeping the low-wavenumber modes constant, cannot be done rigorously and in itself can only be an approximation.

With points like this in mind, we have recently adopted direct numerical simulation as a tool for probing the basic feasibility of using RG techniques to reduce the number of degrees of freedom requiring to be numerically simulated. In this paper, we present some of the first results of this approach. We begin by discussing the RG approach in detail.

RENORMALIZATION GROUP THEORY

Basic Equations

Working in Fourier-wavevector (k) space and restricting our attention to turbulent velocity fields which are homogeneous, isotropic and stationary, we may write the pair-correlation of velocities as

$$\langle u_\alpha(k, t) u_\alpha(k', t') \rangle = Q(k, t - t') D_{\alpha\beta}(k) \delta(k - k'), \quad (1)$$

where $Q(k, t - t')$ is the spectral density and the projector $D_{\alpha\beta}(k) = \delta_{\alpha\beta} + k_\alpha k_\beta k^{-2}$ arises due to the incompressibility condition. Thus, the energy spectrum $E(k) = 4\pi k^2 Q(k)$ with $Q(k) = Q(k, 0)$ and the maximum cut-off wavenumber, k_0 , is defined via the dissipation integral

$$\epsilon = \int_0^\infty dk \, 2\nu_0 k^2 E(k) \simeq \int_0^{k_0} dk \, 2\nu_0 k^2 E(k), \quad (2)$$

where ϵ is the dissipation rate, ν_0 is the kinematic viscosity, and k_0 is of the same order of magnitude as the Kolmogorov dissipation wave-number.

Renormalization Group Theory

Taking our goal to be the calculation of the energy spectrum $E(k)$, our intermediate objective is to find an analytical method of reducing the number of degrees of freedom (or Fourier modes), in order to make the numerical solution of the equations of motion a practical proposition. Let us consider how this might be done by using RG.

First, we divide up the velocity field at $k = k_1$ as $u_\alpha(k, t) = u_\alpha^-(k, t)$ for $0 < k < k_1$ and $u_\alpha(k, t) = u_\alpha^+(k, t)$ for $k_1 < k < k_0$, where $k_1 = (1 - \eta)k_0$ and the bandwidth parameter η satisfies the condition $0 < \eta < 1$. Working with the standard form of the solenoidal Navier-Stokes equation in k -space, we may write the evolution of the low- k velocity field for $0 < k < k_1$ as

$$\begin{aligned} & \left[\frac{\partial}{\partial t} + \nu_0 k^2 \right] u_\alpha^-(k, t) \\ &= M_{\alpha\beta\gamma}^-(k) \int d^3 j \left[u_\beta^-(j, t) u_\gamma^-(k - j, t) \right. \\ &+ \left. 2u_\beta^-(j, t) u_\gamma^+(k - j, t) + u_\beta^+(j, t) u_\gamma^+(k - j, t) \right], \quad (3) \end{aligned}$$

and the evolution of the high- k velocity field for the first shell, $k_1 < k < k_0$, as

$$\begin{aligned} & \left[\frac{\partial}{\partial t} + \nu_0 k^2 \right] u_\alpha^+(k, t) \\ &= M_{\alpha\beta\gamma}^+(k) \int d^3 j \left[u_\beta^-(j, t) u_\gamma^-(k - j, t) \right. \end{aligned}$$

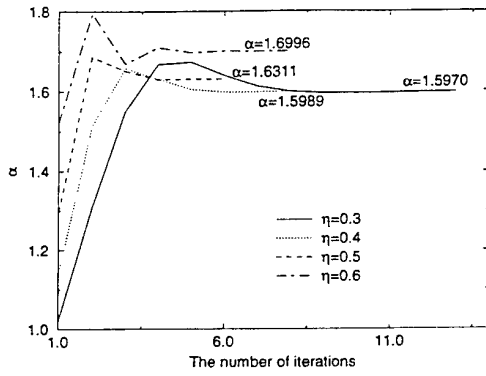


Figure 1: Convergence of the Kolmogorov spectral constant α to the fixed points for several values of the bandwidth parameter η .

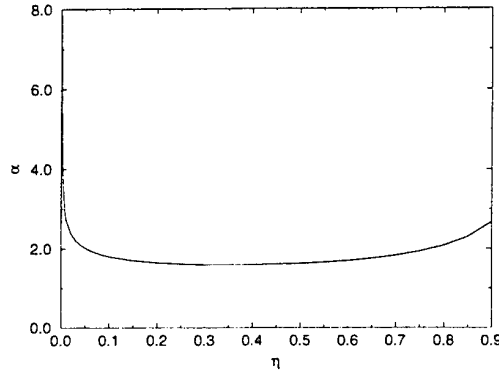


Figure 2: Dependence on the bandwidth parameter η of the calculated values of the Kolmogorov spectral constant α based on equation (6).

$$+ 2u_{\beta}^{-}(\mathbf{j}, t)u_{\gamma}^{+}(\mathbf{k} - \mathbf{j}, t) + u_{\beta}^{+}(\mathbf{j}, t)u_{\gamma}^{+}(\mathbf{k} - \mathbf{j}, t)], \quad (4)$$

where the superscripts $+$ and $-$ on $M_{\alpha\beta\gamma}(\mathbf{k})$ have the same significance as for $u_{\alpha}(\mathbf{k}, t)$, and the symmetrized inertial transfer operator $M_{\alpha\beta\gamma}(\mathbf{k}) = (2i)^{-1}[k_{\beta}D_{\alpha\gamma}(\mathbf{k}) + k_{\gamma}D_{\alpha\beta}(\mathbf{k})]$.

In principle, the RG approach involves two stages: (i) Eliminate the high- k modes, u^{+} , which appear in equation (3) for $0 < k < k_1$, by solving for the mean effect of the high- k field. This results in an increment to the viscosity, i.e. $\nu_0 \rightarrow \nu_1 = \nu_0 + \delta\nu_0$. (ii) Rescale the basic variables, so that the Navier-Stokes equation for $0 < k < k_1$ looks like the original Navier-Stokes equation for $0 < k < k_0$.

Although this procedure is appealingly simple and has a clear physical interpretation, it has not proved easy to put into practice in the turbulence problem. A typical approach is to eliminate all the high- k effects in equation (3), by substituting the solution of equation (4), directly into the u^{+} modes in the u^{-} equation. However, problems are then encountered because of the mode coupling between u^{-} and u^{+} . Even if one succeeds in carrying out the first part, the further problem of averaging out the high- k modes arises immediately, because u^{-} and u^{+} are not statistically independent. This problem was avoided by Foster, Nelson and Stephen (1977; hereafter referred to as FNS) in their pioneering study of stirred fluid motion, as they restricted their attention to stirring forces which were multivariate normal and excluded the effects of the turbulence cascade. However, it has been shown that the use of a 'filtered' average by FNS to eliminate the u^{-} equation is really an uncontrolled approximation (Eyink, 1994).

Iterative-Averaging RG with Results

Here, we follow the method of iterative averaging, which is based upon the derivation of a recurrence relation and, in principle, eliminating finite blocks of modes (i.e. high- k modes) while maintaining the form invariance of the dynamical equation. Apart from the work of FNS, elimination procedures can be performed by 'conditional' averaging, first introduced by McComb (1982). Further details about the conditional average have been given elsewhere (McComb, Robert and Watt, 1992). The basic ansatz of a conditional average is that a small uncertainty (Φ^{-} , say) at the cutoff wavenumber will generate chaotic behaviour for the high- k modes. Although the introduction of Φ^{-} has been accepted, mainly due to the chaotic nature of the Navier-Stokes equations, it might be interesting to see how 'rapidly' chaotic behaviour develops from the given small

Φ^{-} by numerical simulation. This aspect is one of our current tasks and the results will be reported in due course.

The current result of the iterative-averaging calculation for the Navier-Stokes equations after first eliminating the high- k effects is

$$\left[\frac{\partial}{\partial t} + \nu_1 k^2 \right] u_{\alpha}^{-}(\mathbf{k}, t) = M_{\alpha\beta\gamma}^{-}(\mathbf{k}) \int d^3 \mathbf{j} u_{\beta}^{-}(\mathbf{j}, t) u_{\gamma}^{-}(\mathbf{k} - \mathbf{j}, t), \quad (5)$$

where $\nu_1 = \nu_0 + \delta\nu_0(k)$ and

$$\delta\nu_0(k) = -\frac{1}{k^2} \int d^3 \mathbf{j} Q_v^{+}(\mathbf{j}) \times \frac{\frac{4}{d-1} \text{Tr} [M_{\alpha\beta\gamma}^{-}(\mathbf{k}) M_{\gamma\rho\sigma}^{+}(\mathbf{k} - \mathbf{j}) D_{\beta\sigma}(\mathbf{j})]}{\nu_0 j^2 + \nu_0 |\mathbf{k} - \mathbf{j}|^2}. \quad (6)$$

Here, we consider space dimension $d = 3$. This result can be extended to further shells, and we have shown elsewhere (McComb and Watt, 1992) that a fixed point is reached under numerical iteration of the recursion relations (see also Figure 1). In Figure 2, we show a calculation of the Kolmogorov constant $\alpha = 1.60 \pm 0.01$ independent of the bandwidth of modes being eliminated for bandwidths in the range $0.25 \leq \eta \leq 0.45$, in agreement with experiment.

NUMERICAL SIMULATIONS

Two programmes of numerical simulation are being carried out — one at the University of Edinburgh in the United Kingdom, the other at the Swiss Federal Institute of Technology, Lausanne. A large number of runs have already been carried out at Lausanne, and this paper presents some of the results obtained so far.

The simulations themselves are very similar, while the computer systems on which they are run differ greatly. At Edinburgh, work is carried out on a parallel machine, the Cray T3D, while in Lausanne a parallel-vector machine, the NEC SX-4, is used.

The simulations discussed in this paper were carried out at a resolution of 256^3 , requiring approximately 14 seconds of SX-4 time per time-step on a single processor.

The general method of such simulations has been well established. We follow the work of Orszag for the construction of initial velocity fields (1969) and in the use of a pseudospectral method (1971). The time integration scheme is a second-order Runge-Kutta method and partial dealiasing is achieved by way of a random-shifting method (see, for example, Rogallo, 1981).

Δt	T	ν_o	k_f	k_o
10^{-3}	113.5	10^{-3}	1.5	120

ϵ	R_λ	L	λ	τ_E	s_3	s_4
.15	190.606	1.431	.246	1.853	-.51	6.053

Table 1: Characteristics of the simulation

Initial Conditions

The simulations are started with an initial energy spectrum of the form

$$E(k, 0) = 16(2/\pi)^{1/2} u_0^2 k_p^{-5} k^4 \exp[-2(k/k_p)^2] \quad (7)$$

where k_p is the location of the spectrum's maximum and u_0 is the required initial r.m.s. velocity.

Forcing

Stationary turbulence is obtained by use of a deterministic forcing term

$$f_\alpha(k, t) = \begin{cases} \epsilon u_\alpha(k, t)/(2E_f(t)) & \text{if } 0 < k < k_f, \\ 0 & \text{otherwise,} \end{cases} \quad (8)$$

where ϵ is the mean dissipation rate, and

$$E_f(t) = \int_0^{k_f} E(k, t) dk. \quad (9)$$

There is no preferred direction in this forcing and the turbulence rapidly reaches a statistically isotropic and steady state.

Statistics

While our simulations are entirely conventional, we do not rely solely on the usual practice (as justified by isotropy) of averaging over shells in wavenumber space in order to obtain statistical quantities, but also generate many realizations in order to increase our sample size.

The main characteristics of the simulation are reported in Table 1, where Δt is the time step, T is the integration time, ν_o is the molecular viscosity, k_f is defined in (8), k_o is the ultraviolet cut-off, ϵ is the mean dissipation rate, R_λ is the Reynolds number based on the Taylor microscale, L is the integral scale, λ is the Taylor microscale, τ_E is the turnover time and s_3 and s_4 are respectively the skewness and flatness of the velocity derivative.

The equations have been integrated for more than 60 turnover times and about 200 box-realizations of each component of the velocity field have been stored in a database. Since these box-realizations are separated by $\approx \tau_E/4$ they can be considered statistically independent for the middle-range-scales and the small-scales.

RESULTS

We wish to assess the freedom to carry out conditional averages of the type required by RG. In principle we may do this by extracting, from an ensemble of realizations of the velocity field

$$\mathcal{X} = \{X_\alpha^{(n)}(k, t) | \alpha = 1, 2, 3; t \in [0, T]; 0 \leq |k| \leq k_o; n = 1, \dots, N\}, \quad (10)$$

two disjoint subensembles \mathcal{Y} and \mathcal{Z} chosen such that, for a prescribed $\zeta > 0$,

$$\frac{|Y^{(m)}(k, t) - Z^{(m)}(k, t)|^2}{2(|Y^{(m)}(k, t)|^2)} \leq \zeta$$

$$\text{for all } 0 \leq |k| \leq k_c; m = 1, \dots, M; t \in [0, T], \quad (11)$$

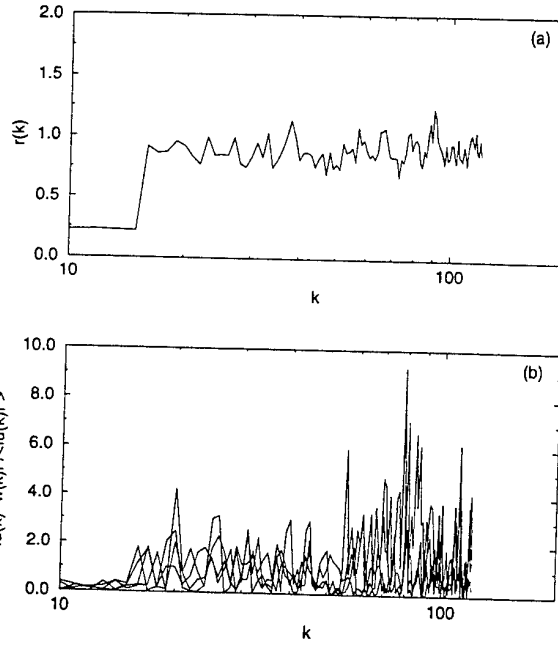


Figure 3: (a) Relative energy error for $k_b = 10$, $k_c = 15$, $\zeta = 0.5$ and $\alpha = 1$. (b) A selected set of realizations showing strong fluctuations for $k \geq 15$.

for each realization $Y^{(m)} \in \mathcal{Y}$ and $Z^{(m)} \in \mathcal{Z}$. We may then define the relative energy of the error

$$r(|k|) = \frac{\langle (u(k, t) - w(k, t))^2 \rangle}{2\langle u(k, t)^2 \rangle}, \quad (12)$$

where $u(k, t) \in \mathcal{Y}$ and $w(k, t) \in \mathcal{Z}$. (It is important to note that the averages in the definition (12) are, in this context, subensemble averages defined on \mathcal{Y} and \mathcal{Z} and not ensemble averages on \mathcal{X} .) In equation (12) and subsequently, we assume that the fields are statistically stationary and isotropic, therefore r depends only on $|k|$. Since the two fields are very close when $0 \leq |k| \leq k_c$, $r(|k|)$ will be much smaller than 1 in this interval, indicating that the fields are almost completely correlated. If the error between the fields grows in such a way that they become decorrelated, we will have $r(|k|) \rightarrow 1$ as $|k| \geq k_c$ increases.

In practice, our 200 box-realizations are not sufficient for the above analysis and we shall describe how we have extracted, using a partial sampling technique, enough realizations to compute the relative energy of the error defined by (12).

In order to this, we have performed the following partial Fourier transform of one component of the velocity field

$$u_\alpha(x, y, k) = \frac{1}{2\pi} \int u_\alpha(x, y, z) e^{ikz} dz, \quad (13)$$

then we have selected, for each box-realization, a set of realizations, say $u_\alpha(x_i, y_i, k)$, where the spacing $\delta x = |x_{i+1} - x_i| = |y_{i+1} - y_i|$ is chosen such that the realizations are (approximately) independent for the range of k we consider (if we consider only the scales such that $k \geq k_b$, then $\delta x = 2\pi/k_b$). The union of all these realizations obtained for each of the box-realizations will constitute our ensemble \mathcal{X} . The subensemble \mathcal{Y} is formed by choosing an arbitrary subensemble of \mathcal{X} . To select the subensemble \mathcal{Z} , we impose the condition

$$\frac{|Y^{(m)}(k) - Z^{(m)}(k)|^2}{2(|Y^{(m)}(k)|^2)} \leq \zeta \quad \text{for all } k_b \leq k \leq k_c; m = 1, \dots, M. \quad (14)$$

Note that the time dependence does not appear in the equations since all the box-realizations used to form the ensemble \mathcal{X} are taken in the statistically steady regime. Figure 3(a) shows the relative energy error

$$r(k) = \frac{\langle (u(k) - w(k))^2 \rangle}{2\langle u(k)^2 \rangle}, \quad (15)$$

where $u \in \mathcal{Y}$ and $w \in \mathcal{Z}$ for $k_b = 10$, $k_c = 15$, $\zeta = 0.5$ and $\alpha = 1$. The number of realizations M is 2533. Though the number of realizations is not large enough to have a smooth converged solution, one can see that the relaxation to a chaotic regime is indeed very fast. Figure 3(b) shows a selected set of realizations for which one can observe that the constraint imposed for $10 \leq k \leq 15$ does not prevent strong fluctuations for $k \geq 15$. The convergence of $r(k)$ is difficult to improve, due to the restriction on the number of realizations available for a given constraint.

Another natural way in which the small-scale properties of a conditional subensemble may be investigated is by studying the probability density functions (pdfs) of velocity increments. In physical-space, we can use homogeneity in the three dimensions and have sufficiently large subensembles to compute high-order statistics and pdfs. The velocity increments are defined by the following relation

$$\delta u(\mathbf{x}, \mathbf{h}) = u(\mathbf{x} + \mathbf{h}) - u(\mathbf{x}), \quad (16)$$

where \mathbf{h} is a displacement vector and \mathbf{x} the position. Since the fields are statistically isotropic, we can restrict ourselves to the study of the longitudinal velocity increment $\delta v_L(\mathbf{h})$ which is the projection of $\delta u(\mathbf{h})$ on the direction of the vector \mathbf{h} and the lateral velocity increment $\delta v_T(\mathbf{h})$ which is the projection of $\delta u(\mathbf{h})$ on a direction perpendicular to \mathbf{h} . For the purpose of this paper, we have only studied the longitudinal velocity increment $\delta v_L(\mathbf{h})$. We have selected two scales, $h_1 = \lambda/1.26$ and $h_2 = \lambda/5.01$ (λ is the Taylor micro-scale, therefore h_1 is a typical scale in the inertial subrange and h_2 is in the dissipation subrange). The selection of the subensembles is performed using conditions of the type $a < \delta v_L(h_1) < b$. The pdfs of $\delta v_L(h_2)$ for the unconditional ensemble and for the subensembles are then compared. Figure 4 gives the normalized pdf (σ is the standard deviation of $\delta v_L(h)$) of the unconditional ensemble for $h = h_1$ and $h = h_2$. We observe the classical result that the tails of the pdfs are growing as the scale is decreased which is the signature of growing intermittency. The pdf also shows a negative skewness which is a direct consequence of the nonlinear dynamics of the Navier-Stokes equations. Figure 5, shows the pdfs of the unconditional ensemble and of a subensemble defined by the constraint $-1 < \delta v_L(h_1) < 0$. The pdfs are almost superimposed, showing that the flow at scale h_2 is unaffected by the condition imposed at scale h_1 . Figure 6 is a case for which the subensemble is much smaller due to a more restrictive condition, $1 < \delta v_L(h_1) < 4$. However, the general behavior of the pdf supports the view that the chaotic dynamics of the Navier-Stokes equations tends to restore the original distribution. Note that the skewness is incorrectly predicted and seems to be correlated with the sign of $\delta v_L(h_1)$. Figure 7 presents a case with a very strong condition, $-7 < \delta v_L(h_1) < -2$. Though the number of realizations is small, we observe that the top of the pdf is quite accurately reproduced.

CONCLUSION

These results, although preliminary in nature, offer crucial support to the hypothesis that a conditional average may be used to reduce the number of degrees of freedom required for the numerical simulation of turbulence. Work is continuing to make a more stringent assessment of the validity of such averages for turbulence and this includes

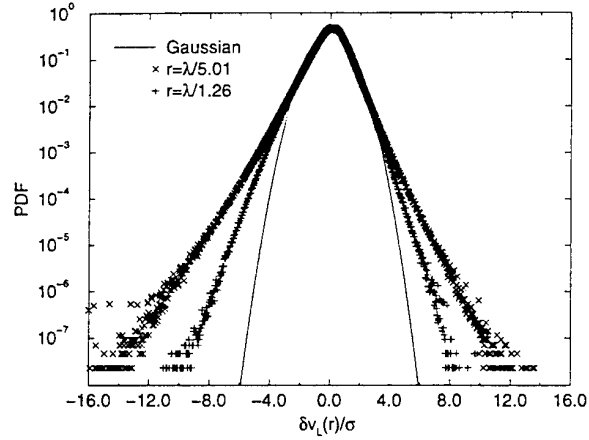


Figure 4: Normalized pdf of the unconditional ensemble.

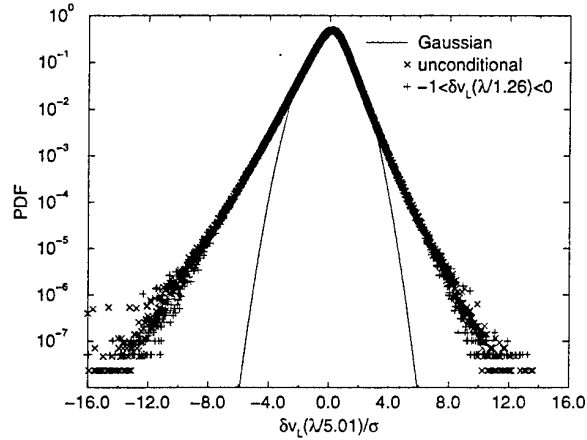


Figure 5: The pdfs of the unconditional ensemble and a subensemble defined by the constraint $-1 < \delta v_L(h_1) < 0$.

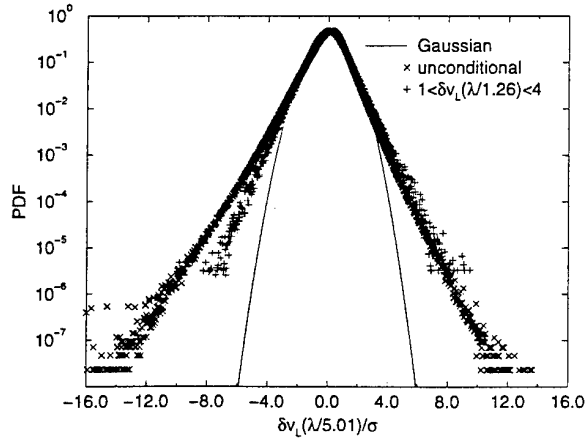


Figure 6: The pdfs of the unconditional ensemble and a subensemble defined by the constraint $1 < \delta v_L(h_1) < 4$.

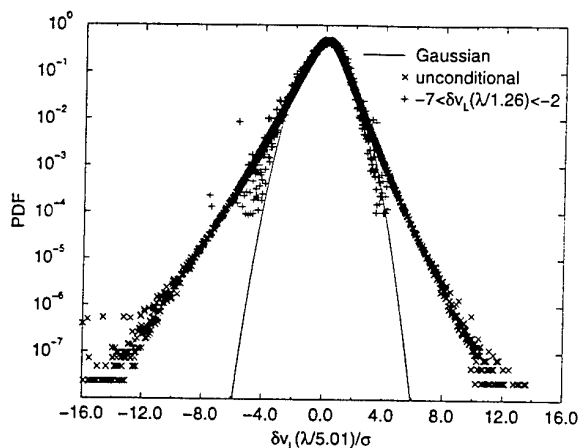


Figure 7: The pdfs of the unconditional ensemble and a subensemble defined by the constraint $-7 < \delta v_L(h_1) < -2$.

carrying out simulations at higher numerical resolution. At present we are working on a 512^3 simulation and hope to present results from this at the conference.

Acknowledgements: The simulation presented in this paper has been performed on the computers of the Swiss Center for Scientific Computing, Manno. The research of L. Machiels is supported by the Swiss National Foundation for Scientific Research.

REFERENCES

- Eyink, G. L., 1994, "Renormalization group method in statistical hydrodynamics", *Phys. Fluids*, Vol. 6, pp. 3063-3078.
- Forster, D., Nelson, D. R. and Stephen, M. J., 1977, "Large-distance and long-time properties of a randomly stirred fluid", *Phys. Rev. A*, Vol. 16, pp. 732-749.
- McComb, W. D., 1982, "Reformulation of the statistical equations for turbulent shear flow", *Phys. Rev. A*, Vol. 26, pp. 1078-1094.
- McComb, W. D. 1990, *The Physics of Fluid Turbulence*, Oxford University Press.
- McComb, W. D. 1995, "Theory of Turbulence", *Rep. Prog. Phys.*, Vol. 58, No. 10, pp. 1117-1205.
- McComb, W. D., Robert, W. and Watt, A. G., 1992, "Conditional-averaging procedure for problems with mode-mode coupling", *Phys. Rev. A*, Vol. 45, pp. 3507-3515.
- McComb, W. D. and Shanmugasundaram, V. 1983, "Some developments in the application of renormalization methods to turbulence theory". Paper presented to the *Fourth Symp. on Turb. Shear Flows*, Karlsruhe, Germany September 12-14, 1983.
- McComb, W. D., "Some recent developments in the application of renormalization methods to problems in turbulence." Paper presented to the *Eighth Symp. on Turb. Shear Flows*, Munich, Germany, September 9-11, 1991.
- McComb, W. D. and Watt, A.G., 1992, "Two-field theory of incompressible-fluid turbulence", *Phys. Rev. A*, Vol. 46, pp. 4797-4812.
- Orszag, S., 1969, "Numerical Methods for the Simulation of Turbulence," *Phys. Fluids (suppl. 2)*, Vol. 12, pp. 250-257.
- Orszag, S., 1971, "Numerical Simulation of Incompressible Flows Within Simple Boundaries. I. Galerkin (Spectral) Representations," *Stud. Appl. Maths.*, Vol. 50, No. 4, pp. 293-327.
- Rogallo, R.S., 1981, "Numerical Experiments in Homogeneous Turbulence," NASA TM-81315.

SESSION 5 - FREE FLOWS II

INTERACTION OF THE WAKE OF A CIRCULAR CYLINDER AND A PLANE MIXING LAYER

[†]D. Heitz, [‡]J. Delville, [†]G. Arroyo, [‡]J.-H. Garem, [†]J.-P. Bonnet, [†]P. Marchal

[†]Cemagref

French Institute of Agricultural and environmental engineering research

Food processes engineering research group

17, avenue de Cucillé 35044 RENNES cedex

France

[‡]LEA (UMR CNRS 6609)

Laboratoire d'Etudes Aérodynamiques

43, route de l'aérodrome 86036 POITIERS cedex

France

ABSTRACT

The interaction of the wake of a circular cylinder and a plane mixing layer were studied experimentally in a wind tunnel at low air speed (2 – 3 m/s). Investigation has been carried out involving hot wire anemometry and flow visualisations. Results show a fluid motion in the wake formation zone, from the low to the high velocity side.

INTRODUCTION

In the Food Industry the protection of food products against contamination by airborne particles is generally ensured by ultraclean air flows inside clean rooms. Some new technologies are now emerging which restrict the protected area to a limited volume around the product by means of a localized clean air flow. One of the main challenges in this field is to maintain the efficiency of such protection in situations where the protected volume remains open to the ambient air and where machine or human arms may penetrate through the interface between the clean and the polluted air. An effective approach to this problem is to study the interaction between the wake of a cylinder and a plane mixing layer. The cylinder can be taken as a generic shape for the arms, while the interface between the clean and the polluted air can be considered correctly represented, for the flows that we judge of technological interest, by a mixing layer with high speed on the clean side. To resolve most of industrial situations, we have to understand three dimensional dynamics of the flow past the cylinder.

Earlier studies took an interest in a wake of a cylinder placed perpendicular to a turbulent shear flow (see Maull and al. 1973 and Mair and al. 1975, Tavoularis and al. 1987). Their results showed the occurrence of spanwise cells with nearly constant shedding frequency. The presence of strong shear and turbulence appears, in general, to cause a strong spanwise variation of the local base pressure coefficient and an appreciable decrease of the Strouhal number. To date we didn't find any bibliographic references dealing with the study of a cylinder wake placed perpendicular to a turbulent shear flow with presence of coherent structures.

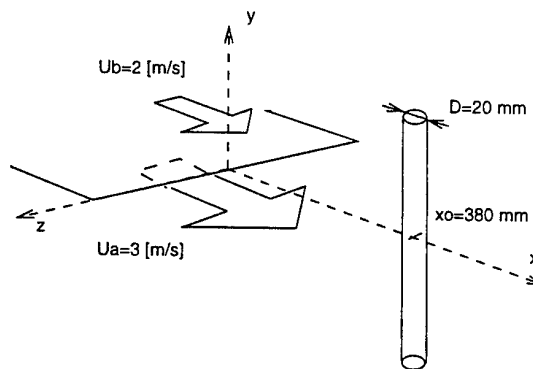


Figure 1: Schematic of the flow facility.

EXPERIMENTAL CONDITIONS

Flow facility

Experiments were carried out in the working section (300 × 300 mm², 200 cm long) of the subsonic wind-tunnel E300 of the LEA. Wind-tunnel ceiling was tilted to achieve a zero streamwise pressure gradient. The mixing layer is initially turbulent. Its velocity ratio $r = Ub/Ua$ (with $Ua = 3$ m/s high velocity of the mixing layer and $Ub = 2$ m/s low velocity of the mixing layer) is equal to 0.67. The circular cylinder of cross-sectional diameter $D = 20$ mm and of $L = 300$ mm long, applied a blockage ratio of 6.7 % with an aspect ratio of 15. The presents experiments were performed with the cylinder ends fastened on the wind-tunnel walls without end-plates. The cylinder was positioned so as to get equality between its diameter and the vorticity thickness. From the study of the mixing layer alone, the location satisfying that condition was found at $x_0 = 380$ mm ($x_0/D = 19$) downstream of the trailing of the splitter plate (cf Fig. 1).

The Reynolds numbers, based on the cylinder diameter, were respectively 2200 and 3300 for each side of the mixing layer. The free stream turbulence intensity $\sqrt{u'^2}/U$ was

less than 2 % (minimum measurable value of 4 cm/s rms). The same level had been measured with the mixing layer alone, before positioning the cylinder.

Velocity measurements involved hot-wire anemometry. Modified DANTEC (55P11) single tungsten hot-wire, 2.5 μm in diameter and 0.5 mm in working length, was operated with constant temperature anemometer TSI 1750 (CTA). Measurements have been carried out in x planes, with the wire parallel to the cylinder-axis. They determined the mean velocities and corresponding rms values.

Flow visualizations with laser tomography gave qualitative informations about velocity distribution and flow dynamic in the wake of the cylinder.

Calibration at low velocities

In low velocity range (< 3 m/s), hot-wire anemometry requires not only a special calibration method, but also good knowledge of heat-transfer from the hot-wire probe (see Bruun 1995). In the conventional calibration methods the velocity is evaluated from a pressure difference reading, Δp , using a pitot-static tube. However, when the velocity becomes smaller than about 3 m/s, the value of Δp in air flows becomes so small ($\Delta p < 1$ mmH₂O) that it is difficult to obtain accurate velocity results by these methods. Thus, we made a calibration device that use the conservation of mass principle. The probe and the pitot-static tube were respectively upstream and downstream of a contraction. By this method we obtained a speed reduction of 14.5. The loss of speed due to boundary layer growth in the calibration section was taken into account.

Generally, the assumption is made that the whole of the electrical energy provided to the hot-wire is transferred to the fluid by convection. Analytical correlations (e.g. equation of Collis et Williams 1959) used for calibration are approximated with that assumption and others that are valid only inside the limits of numerical or analytical calculation of the convective heat transfer from horizontal cylinders (i.e. an infinitely long cylinders, two-dimensional flow and uniform temperature distribution). However, under a certain velocity, assumptions are not sufficient. Stengetle & Rath (1994), determined with microgravity experiments that free convective flow affects the heat transfer only up to a critical Reynolds number (based on the wire) of $Re = 0.0045$ (i.e. about 3.3 cm/s for our hot-wire). Nevertheless, due to three-dimensional heat transfer, they stated that $Re = 0.02$ makes the end of the validity of the given correlations. In our experiments, because of the low velocity range, resulting in high sensitivity to temperature (-17 cm/s/°C), we applied a polynomial corrected with temperature. The calibration was systematically made for a range of temperatures (18 °C to 30 °C). We applied :

$$u = \sum_{i=0}^N a_i \left[\frac{e}{\sqrt{T_{\text{wire}} - T_a}} \right]^i$$

- u : velocity normal to the hot-wire.
- e : anemometer voltage.
- T_{wire} : hot-wire temperature.
- T_a : ambient air temperature.

Oncoming flow

The growth of the mixing layer without the cylinder is plotted in the form of the lateral (y) locations where $\frac{U - U_b}{U_a - U_b}$ is 0.9, 0.5 and 0.1 in z -fixed plans (Fig. 2). A quasi-linear increase for the flow investigated is observed.

The location of the virtual origin x_{virt} is at $x_{\text{virt}}/D \approx 3.75$. The boundary layers are turbulent at the exit of the

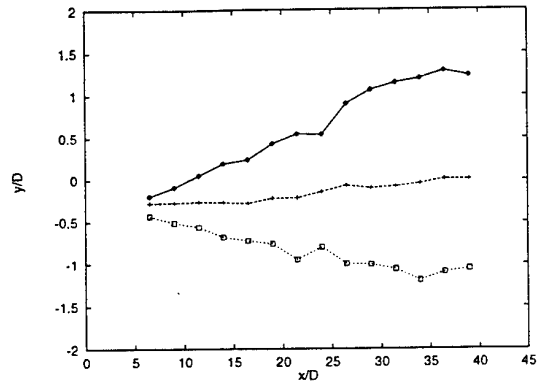


Figure 2: Growth of the mixing layer without the cylinder (\diamond : $\frac{U-U_b}{U_a-U_b} = 0.1$; $+$: $\frac{U-U_b}{U_a-U_b} = 0.5$; \square : $\frac{U-U_b}{U_a-U_b} = 0.9$).

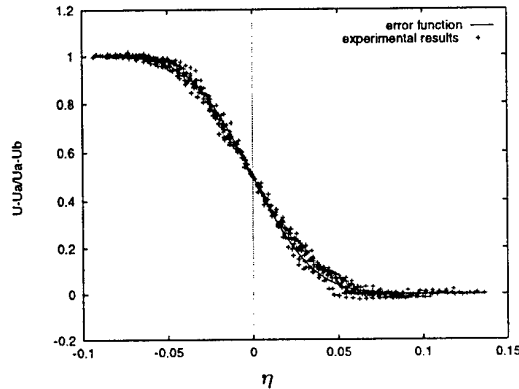


Figure 3: Mean velocity profiles for the mixing layer without the cylinder ($\frac{U-U_b}{U_a-U_b} = f(\eta)$ with $\eta = (y - y_{0.5})/(x - x_{\text{virt}})$).

splitter plate. The rate of spread $d\delta/dx$ ($\delta = y_{0.1} - y_{0.9}$) and the spreading parameter σ characterize mixing layer self-similarity. As usual, σ is defined in such a way that it brings the velocity profiles closest to the error function Φ (see e.g. Spencer & Jones 1971) :

$$\Phi = \frac{U - U_b}{U_a - U_b} = \frac{1}{2}(1 + \text{erf}(\sigma\eta))$$

with :

$$\text{erf}(x) = \frac{2}{\sqrt{\pi}} \int_0^x e^{-t^2} dt$$

and η is the spatial similarity variable : $\eta = \frac{y - y_{0.5}}{x - x_{\text{virt}}}$.

We obtain $\sigma = 23.9$ and $d\delta/dx = 0.067$ which are consistent with Mills (1968) results ($\sigma = 25.0$ and $d\delta/dx = 0.07$). Experimental results and error function are plotted with $\sigma = 23.9$ (Fig. 3).

The low value of the spreading parameter may be due to the dramatic influence of free-stream turbulence (relatively high in our configuration) as is emphasized by Rodi 1975.

RESULTS AND DISCUSSIONS

The complete flow (mixing layer interacting with the cylinder) is investigated. Single hot-wire anemometry results show the wake and its formation zone. Borders of that zone can be seen in particular on Fig. 4, with two

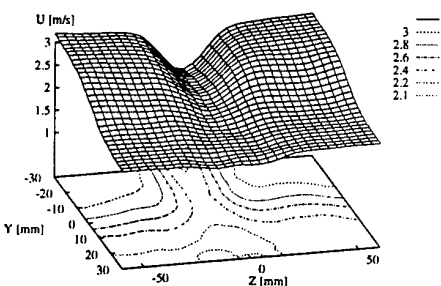
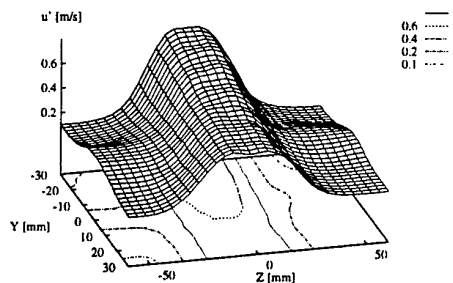
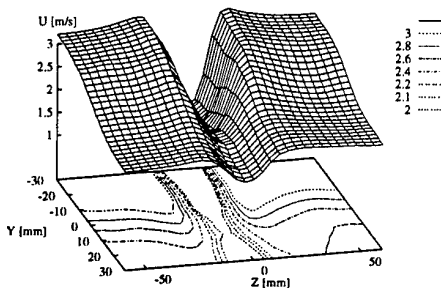
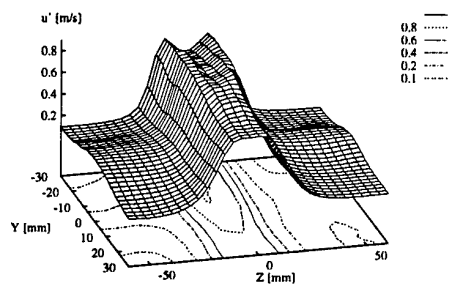
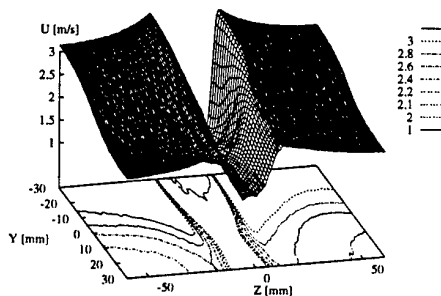
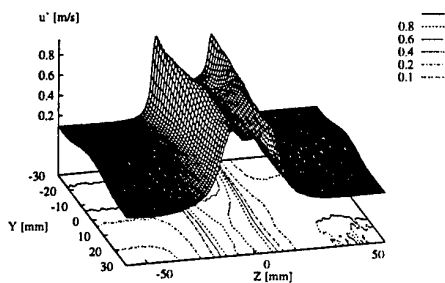
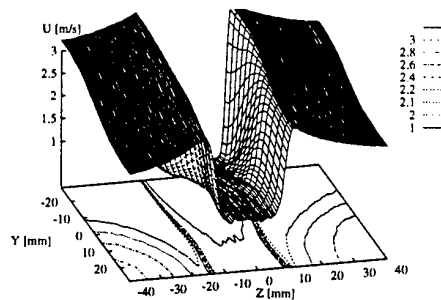
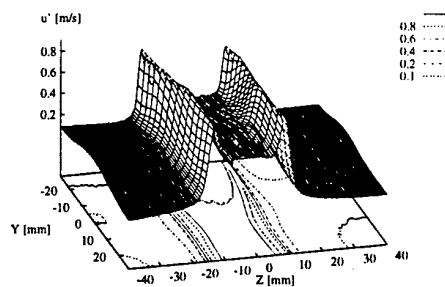


Figure 4: Velocity fluctuation profiles downstream of the cylinder. $(x - x_0)/D$ from 1.25 to 3.6.

Figure 5: Mean velocity profiles downstream of the cylinder. $(x - x_0)/D$ from 1.25 to 3.6.

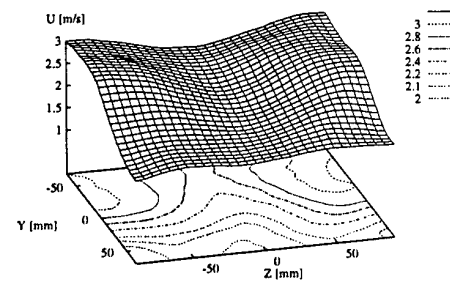
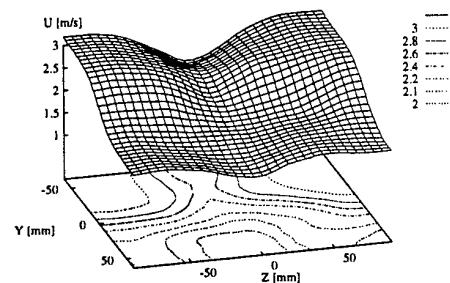
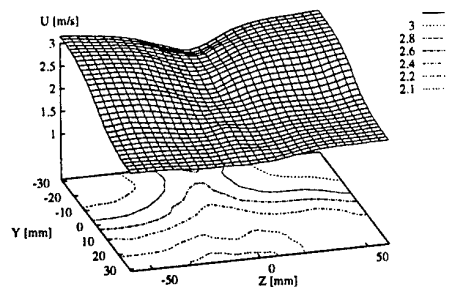
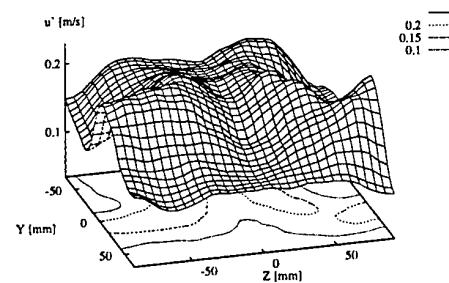
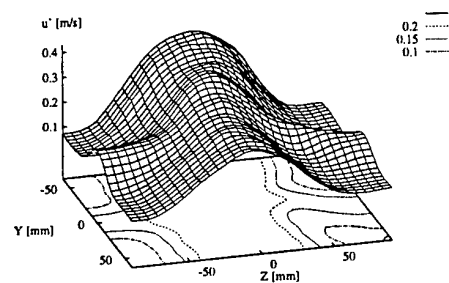
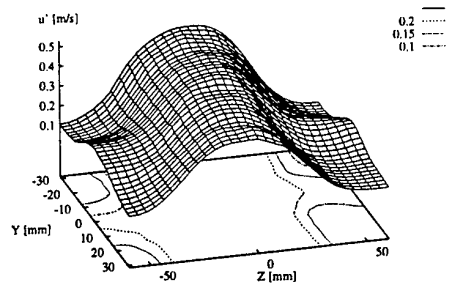


Figure 6: Velocity fluctuation profiles downstream of the cylinder. $(x - x_0)/D$ from 5.04 to 45.1.

Figure 7: Mean velocity profiles downstream of the cylinder. $(x - x_0)/D$ from 5.04 to 45.1.

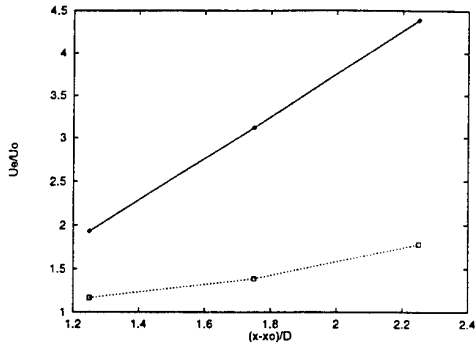


Figure 8: Mean velocity loss in the wake formation zone. (—: $y/D = +1.5$ low velocity; - - : $y/D = -1.5$ high velocity).

sharp crests of rms values. This enables us to locate the very exact location of the maximum of turbulence (with an accuracy better than 0.4 mm). The formation zone is of particular interest for the present study. Two distinct phenomena appear in it. First, a contraction is observed. Second, the wake formation zone follows an unusual behavior.

Flow visualization as well as hot-wire measurements, show that the location of the mixing layer is clearly identified through a contraction of this formation zone (see iso-velocity lines on Fig. 5 and 4 for $(x-x_0)/D < 3$). This behavior can be attributed to the fact that, since the mixing layer upstream of the cylinder is turbulent, the boundary layers separate later than in the flow outside the mixing layer. For both sides of the mixing layer, the Reynolds number is such that the boundary layers are still laminar when they separate.

Downstream of the cylinder a singular behavior appears. It is well known that, for the present range of Reynolds number, the formation length decreases when the Reynolds number increases (e.g. A. Roshko 1955). In our experiment we observed the contrary: the vortex formation zone becomes longer on the high velocity side of the mixing layer. This can be seen qualitatively by observing the velocity defect U_0 (difference between U_e velocity outside of the wake and the velocity on the axis of the wake, i.e. $U_0(x_1, y_1, z) = U_e(x_1, y_1, z) - U(x_1, y_1, 0)$ at $x = x_1$ and $y = y_1$ fixed values). From Fig. 5, it appears that, for $(x-x_0)/D < 5$, U_0 is always longer on the high velocity side than on the low velocity side. In a more explicit way, we plot on the same graphic the ratio U_e/U_0 for the low ($y/D = +1.5$) and high ($y/D = -1.5$) velocity sides of the mixing layer for $(x-x_0)/D < 5$. The difference between the gradient of the two curves shows that the defect velocity is reduced faster for the low velocity side (Fig. 8).

That region just downstream of the cylinder appears to be also characterized by an inversion of the velocity gradient between the velocity profile $U_e((x_1-x_0)/D, y/D, z_{\max}/D)$ outside of the wake and the velocity profile $U((x_1-x_0)/D, y/D, 0)$ on the wake axis (Fig. 9a). Such profiles plotted in the far wake haven't an inversion of the velocity gradient (Fig. 9c). Between these two longitudinal locations the gradient recovers its normal sign faster in the low velocity side (i.e. for $y/D > 0$) (Fig. 9b and 9c).

Transition between the formation zone and the wake takes probably place at the location of reorientation of the velocity gradient. This particular aspect may be due to fluid transfer along the formation zone from the low to the high velocity side of the mixing layer. We get more information about this phenomenon by visualizing the flow. Photos taken in the $z = 0$ plane show the motion (Fig. 10).

The fluid motion through the formation zone from the

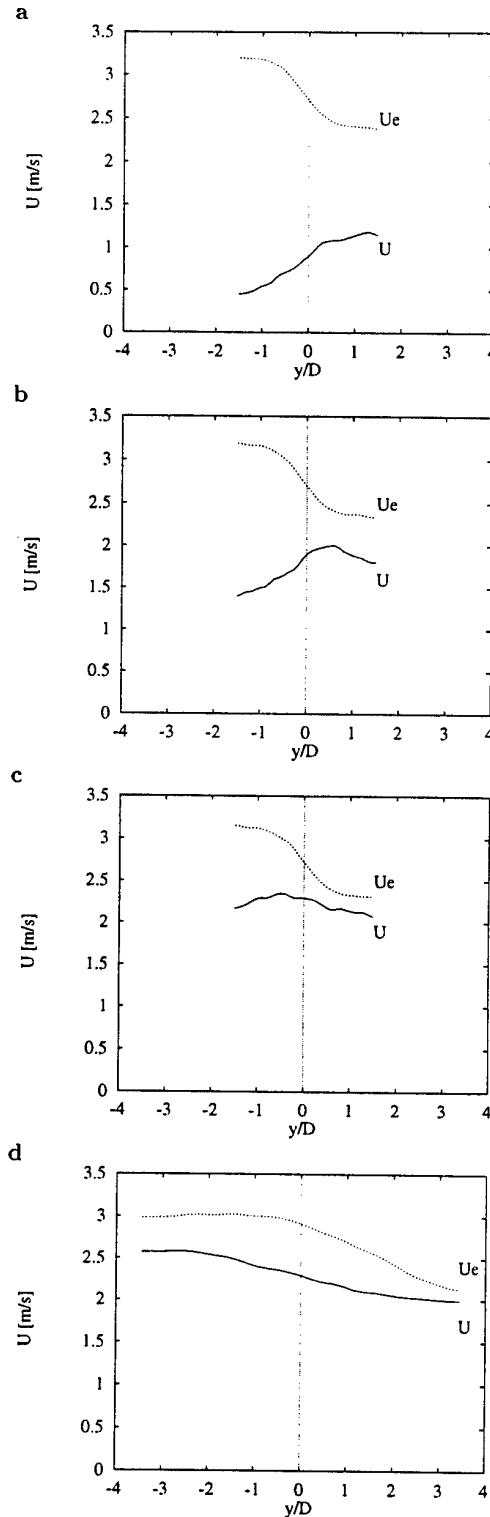


Figure 9: Mean velocity loss in the wake formation zone for $(x-x_0)/D$: a) 1.25; b) 2.25; c) 3.6; d) 45.1. (- - : $U_e((x_1-x_0)/D, y/D, z_{\max}/D)$; — : $U((x_1-x_0)/D, y/D, 0)$).

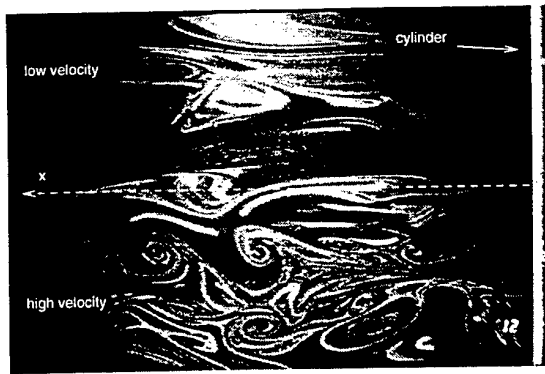


Figure 10: Visualization in the plane $z = 0$; flow is from right to left.

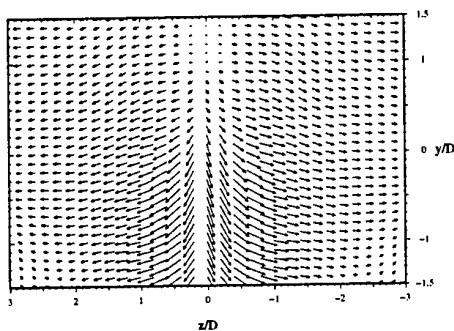


Figure 11: Vectors field at $(x - x_0)/D = 3.6$ (four-wire probe).

low to the high velocity is opposed by the motion due to end effects initiated at the wind tunnel wall (for end effects see Miller and al. 1994). The union of these two motions results in a double vortex street which is located on the high velocity side. Preliminary measurements in that flow, with four-wire probes (see S. Béharelle 1997 for four-wire probe anemometry), validated single-wire measurements and particularly the fluid motion in the formation zone (Fig. 11 presents vectors field obtained at $(x - x_0)/D = 3.6$).

In the developed wake, further downstream, the Kármán vortex street is present up until twenty diameters away from the cylinder. Analysis of the rms velocity fluctuations shows that, as the turbulence due to the Kármán vortex street is convected downstream, it progressively loses its dominance to the turbulence generated by the mixing layer (Fig. 7 and 6). At about forty diameters downstream of the cylinder, the wake vanishes more rapidly on the low velocity side, while the wake that remains on the high velocity side interacts with the mixing layer. At this location, the turbulence intensities arising from the wake and from the mixing layer are of the same order of magnitude (8%).

CONCLUSIONS

Understanding three dimensional dynamics in the interaction of the wake of a circular cylinder and a plane mixing layer is of high interest for localized food protection. Fluid movements in the formation zone seem to be especially important in this context. Indeed, flow visualization and hot-wire anemometry have shown that there is a motion from the low to the high velocity side of the mixing layer, in this zone. Results suggest that such a flow, although sheared in

two perpendicular directions, has an eddy structure that is essentially dominated by the mixing layer.

REFERENCES

- S. Tavoularis, H. Stapountzis & U. Karnik, 1987, "Vortex shedding from bluff cylinders in strongly sheared turbulent streams", *Journal of Wind Engineering and Industrial Aerodynamics*, Vol. 26, pp. 165-178.
- D.J. Maull & R.A. Young, 1973, "Vortex shedding from bluff bodies in a shear flow", *Journal of Fluid Mechanics*, Vol. 60, pp. 401-409.
- W.A. Mair & P.K. Stansby, 1975, "Vortex wakes of bluff cylinders in shear flow", *SIAM Journal of Applied Mathematics*, Vol. 28, pp. 519-540.
- H.H. Bruun, 1995, "Hot-wire anemometry - Principles and signal analysis", *Oxford Science Publications*.
- D. Collis & M.J. Williams, 1959, "Two-dimensional convection from heated wires at low Reynolds numbers", *Journal of Fluid Mechanics*, Vol. 6, pp. 357-384.
- F.R. Stengele & H.J. Rath, 1994, "Influence of free convection on the heat transfer from hot-wire probes", *Wärme und stoffübertragung*, Vol. 29, pp. 299-307.
- B.W. Spencer & B.G. Jones, 1971, "Statistical investigation of pressure and velocity fields in the turbulent two-stream mixing layer", *AIAA 4th Fluid and Plasma Dynamics conference*.
- R.D. Mills, 1968, "Numerical and experimental investigations of the shear layer between two parallel streams", *Journal of Fluid Mechanics*, Vol. 33, pp. 591-616.
- W. Rodi, 1975, "A review of experimental data of uniform density free turbulent boundary layers", *Studies in Convection - theory, measurement and Applications*. Vol 1. ed. B.E. Launder. Academic Press pp. 79-165.
- A. Roshko, 1955, "On the wake and drag of bluff bodies", *J. Aero. sci.*, Vol. 22, pp. 124-132.
- Miller G.D. & Williamson C.H.K., 1994, "Control of three-dimensional phase dynamics in a cylinder wake", *Experiments in Fluids*, Vol. 18, pp. 26-35.
- Béharelle S., Delville J. & Bonnet J.-P., 1997 "On the three-dimensional evolution of a wake subjected to cross-shear", *Eleventh symposium on Turbulent Shear Flows*.

Quasi-2D MHD turbulent shear layers

T. Alboussière ⁽¹⁾, V. Uspenski ⁽²⁾ and R. Moreau ⁽¹⁾

⁽¹⁾ Lab. EPM-MADYLAM
ENSHM de Grenoble
BP 95, 38402 St-Martin d'Hères
France

⁽²⁾ Visitor from Institute of Mechanics
Univ. of Moscow
Michurinskii Pr. 1, 119899 Moscow
Russia

ABSTRACT

An experiment has been carried out to investigate the properties of 2D turbulence in a mercury layer in the presence of a steady magnetic field. Visualizations of the vortices were possible *via* the observation of the image of a regular grid mesh reflected on the free surface. In parallel, quantitative measurements of the velocity were recorded with the use of potential probes located at the bottom of the fluid layer. The basic flow consists in a shear flow. The mean part of the turbulent flow and the spectrum of its fluctuations are characterized. The global influence of turbulence on both momentum and heat transfers is examined.

INTRODUCTION

MHD turbulence exhibits quite specific properties associated with its tendency to become two-dimensional (Sommeria and Moreau, 1982; see also Moreau, 1990, p. 272-304). But, so far, most of the experiments performed with electrically conducting fluids in the presence of a uniform magnetic field were devoted to homogeneous turbulence (except within the thin Hartmann layers), so that the need of knowledge and understanding of the behaviour of quasi-2D turbulence in MHD shear layers is still enormous. As a matter of fact, those layers, which develop along the walls parallel to the magnetic field or from any kind of singularity (either geometrical, such as a sharp angle, or electrical, such as a jump in the electrical conductivity) in the direction of the magnetic field, are of special interest because all sorts of transport phenomena take place there. The first observation, purely qualitative, of the turbulent character of these layers is due to Lehnert (1955) and the first quantitative description of their properties is due to Kljugin and Kolesnikov (1989). However, to our knowledge, nothing is known on the transport of a scalar quantity, such as heat, by this kind of turbulent flow, and its dynamics is still

far from being well understood. Of course, none of the available models for ordinary turbulent shear flows can be applied to this quasi-2D turbulence. The purpose of this paper is therefore to present new experimental results which might be used as a reference to be compared with predictions of adequate modeling. Another paper in this conference (Dumont et al., 1997) presents an attempt to model this 2D turbulence by using a maximum entropy theory, initially proposed by Robert and Sommeria (1991). The equipment has been realized with a special care to insure the stability and uniformity of all the control parameters and to select a combination of them which guarantees the two-dimensional character of this turbulence. And a special effort has been made to improve the accuracy of the diagnostic techniques, based on the measurements of temperatures and electric potential differences.

APPARATUS AND MEASUREMENT TECHNIQUES

The working fluid is a layer of mercury. It is located in a horizontal circular cell (internal diameter 22 cm) above an electrically insulating bottom plate. The upper boundary may be, either a free surface, allowing to observe the deformation produced by the turbulent eddies, or an insulating horizontal plate, to privilege the two-dimensionality when the quantitative measurements are performed. This cell is located in a vertical coil which generates a uniform vertical magnetic field. Both the depth of the fluid layer and the strength of the magnetic field are adjusted in such a way that the typical time scale to establish a good two-dimensionality, $\tau_{2D} = (\rho H^2) / (\sigma B_0^2 l^2)$ (ρ stands for density, σ for the electrical conductivity, B_0 for the magnetic field, H for the fluid depth and l for the typical horizontal length scale of a turbulent eddy) is much smaller than the typical turnover time $\tau_{tu} = l/u$ (u stands for a typical velocity scale). Typically, with $H = 9.4 \text{ mm}$ and $B_0 = 0.17 \text{ T}$, which are the val-

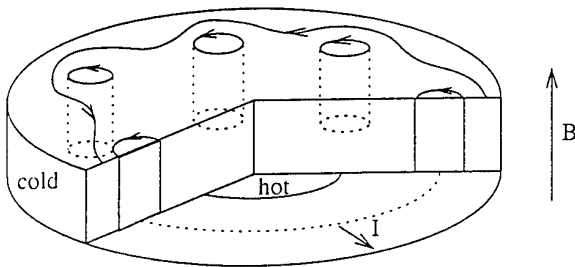


Figure 1: Structure of the electrically driven 2D turbulent shear flow (the control parameter I is the intensity of the electric current passing from the ring of electrodes to the external vertical wall)

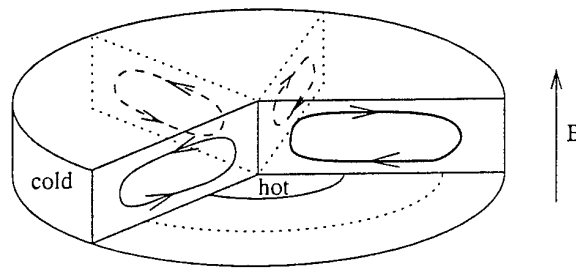


Figure 2: Structure of the buoyant axisymmetric flow generated by heating the center of the bottom plate

ues selected for all the results presented in this paper, $\tau_{2D} \sim 10^{-2} s$ whereas $\tau_{tu} \sim 1 s$, so that two-dimensionality is well achieved. At this stage, it may be noticed that, because the energy transfer is directed towards the large scales in 2D turbulence, this condition is well satisfied as soon as it is satisfied for the length scale of the forcing mechanism.

On the bottom plate a set of 292 small electrodes are located on a circle of radius $9.3 cm$ and make an anode from which the electric current I arrives, whereas the electrically conducting external vertical plate collects this electric current. Because the Hartmann number Ha is significantly larger than one (42 with the chosen values), this radial electric current is passing through the Hartmann layers which behave like an electric motor and drive the fluid in rotation. From the theory of the Hartmann layer, if the flow was laminar, the core velocity between two Hartmann layers should be $V_0 = I / (2\pi r \sqrt{\sigma \rho \nu})$, where r denotes the distance from the center of the cell and ν the kinematic viscosity. This means that a shear is necessarily established between the rotating external annulus and the central core region which stays at rest in a laminar regime. The typical maximum velocity which is expected is of the order of $40 cm/s$. And, if the flow was laminar, the typical thickness of the circular shear layer above the ring of electrodes, would be of the order of $0.15 cm$. But, as expected, this circular shear (or mixing) layer is unstable. Two-dimensional columnar eddies aligned with the applied magnetic field develop, with an initial wave length which corresponds to the most linearly unstable disturbances (close to $2 cm$), and interact. These structures remain 2D since any 3D disturbance induces an electric current and a damping Lorentz force (2D eddies do not induce any current). Therefore, an energy transfer towards the large scale feeds larger and larger vortices, until the largest allowed scale which is the cells radius ($11 cm$). This arrangement and the 2D shear flow are sketched on fig. 1.

Besides, a central part of the bottom plate (radius $3.65 cm$) made of a thick copper piece (but electrically insulated from the mercury) may be heated from below at a given power (0 or $8 W$, in this paper) whereas the external vertical wall is maintained at a given and precisely controlled temperature (with fluctuations less than $0.02^\circ C$). This allows to study how a 2D tur-

bulent shear flow transports a scalar quantity such as heat, as well as angular momentum (fig. 1). On the contrary, if the central part of the bottom plate was heated without passing any electric current, the apparatus would give the possibility to study an axisymmetric convective flow such as the one sketched on fig. 2. This is not the case in this paper which focuses on the behaviour of the 2D shear flow with or without heating. It has been checked that the convective flow is always masked by the electrically driven shear flow.

The temperature measurements are easy to perform with thermocouples. To measure the two velocity components in the radial and azimuthal directions, electric potential sensors were used. Between two such sensors close enough to each other, the electric potential difference is equal to the product of the velocity component in the direction perpendicular to the sensors line times the magnetic field B_0 and the distance between these sensors. We have nevertheless developed a significant originality in these techniques, since our sensors are in the same time thermocouples and velocity probes. Each sensor is made of two small wires, one made of platinum and the other of constantan, both of diameter $0.2 mm$. A cylinder of alumina whose external diameter is $0.9 mm$ containing two holes of diameter $0.2 mm$ is used to electrically insulate the two wires and to maintain them in place. Each probe, located at the bottom boundary of the fluid, behaves like a Pt-Cst thermocouple and provides the local temperature. Measuring the electric potential between the Pt surfaces of two neighbouring probes gives the local and instantaneous velocity. Platinum was chosen as one of these materials precisely because it has almost the same absolute thermoelectric power as mercury, in order to minimize to error due to the addition of a thermoelectric Pt-Hg contribution to the MHD electrical potential difference. All the results presented in this paper have been obtained with such sensors inserted in the insulating bottom plate. Their total number is 88. They are located, either on some radial lines (to provide the angular velocity component), or on some circles (to provide the radial velocity component).

A flow visualization may also be realized when a free surface is present, either using tracers moving with the free surface of mercury, or looking at the image of a regular grid reflected by the mercury free surface. Each eddy capable to locally depress the plane surface yields a disturbance of the image. It can be

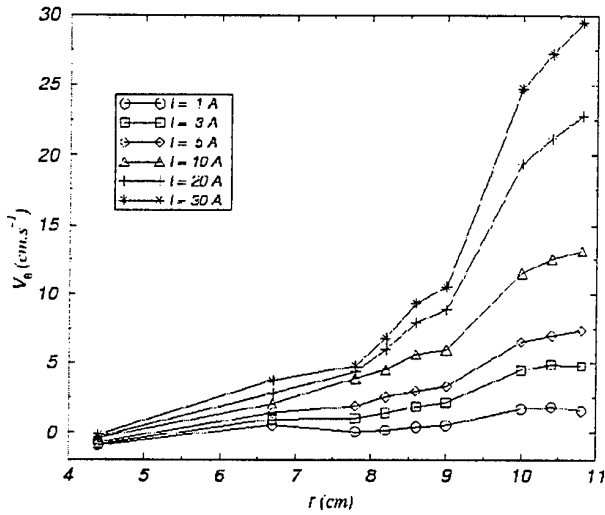


Figure 3: Profiles of the mean angular velocity component for different values of the control parameter I ($B_0 = 0.17T$)

proved for small deformations, that a linear dependency of the area of the mesh elements exists with respect to the Laplacian of the surface height: the area decreases for a depression (light rays are focussed) and increases for a hump. On the video shown during the oral presentation of this paper, it is clear that the initial instability of the mixing layer (made of about 30 periodic eddies of typical length scale of the order of 2 cm) rapidly feeds an inverse cascade. At high values of the electric current (of the order of 20 or 30 Amp) only a small number of large coherent structures (2 or 3 structures with length scales of the order of 10 cm) moving around the cell at a velocity smaller than the maximum fluid velocity by about one order of magnitude are present.

RESULTS AND INTERPRETATION

The mean velocity profiles are shown of fig. 3. It is remarkable that, whereas the wall shear layer thickness is almost the same as in a laminar regime (estimated at about 2 mm), the free shear layer thickness is increased by about one order of magnitude. It also noticeable that the maximum angular velocity is nearly half that predicted for the laminar regime. For instance, the expression predicts a velocity of 43 cm/s for $I = 20$ Amp, but the measured value is close to 23 cm/s. And, consistently, a significant angular momentum is present in the central part of the cell where no electric current is flowing within the Hartmann layers. This illustrates the turbulent transport of angular momentum by the turbulence. If one would wish to derive a thickness for the turbulent free shear layer from the maximum slope of the mean velocity profile, one would get values of the order of 3 cm (instead of 0.15 cm in a laminar regime).

In exactly the same conditions, the mean temperature profiles are shown on fig.4. At low electric current (0 or 1 Amp), the angular velocity of the rotating annulus is quite small. Similarly, the buoyant flow due to

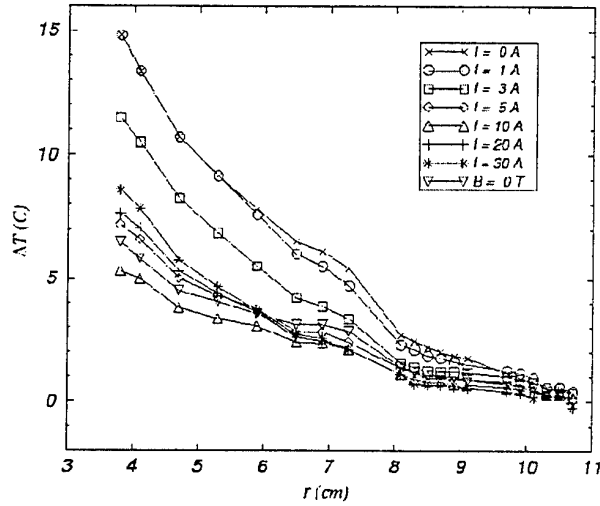


Figure 4: Mean temperature profiles for different values of the control parameter I ($B_0 = 0.17T$)

the heating is efficiently damped by the applied magnetic field. One may therefore consider that the temperature profiles measured at $I = 0$ and 1 Amp, which are indeed very close to each other, correspond to almost pure thermal conduction. This means that the observed temperature difference between the central part and the external wall (14.5 K) may be associated with a Nusselt number close to unity. When the electric current (and the velocity) increases to 10 Amp, the maximum temperature difference reduces to 5.2 K, which is the minimum value ever observed and corresponds to a Nusselt number of nearly 2.8. Then, if the electric current still increases to 30 Amp, the maximum temperature difference increases again to about 8.6 K, which corresponds to a Nusselt number of 1.7. This result, which has been repeatedly checked, seems to be quite important: the Nusselt number is not a monotonic function of the Reynolds number. In other words, whereas the quasi-2D turbulence transports momentum with a good efficiency, heat transfer is not very efficient. This means that none of the usual turbulence models, which all consider turbulence as a kind of universal mixer, could succeed in modeling this flow. Now, if we look more locally at the slopes of the mean temperature profiles, it seems clear that the slope remains significantly smaller in the free shear layer (between $r = 8$ cm and $r = 11$ cm) than in the central part of the cell where the mean velocity is small (but the turbulence intensity high).

Precisely, fig. 5 and 6 show the profiles of the rms values of the fluctuations of the two velocity components V'_θ and V'_r . The first point to notice is the importance of the turbulence level: the ratio V'_θ/V_θ is of the order of 10 to 12 % in the free shear layer and goes to values of the order of 35 % in the central part. Indeed, the rms of the azimuthal velocity fluctuation is almost uniform all over the cell, whatever the value of the mean velocity. One may also notice that the rms of the radial velocity fluctuation is about half that of the angular fluctuation. And, finally, the almost linear increase of V'_r with the distance from the wall when we

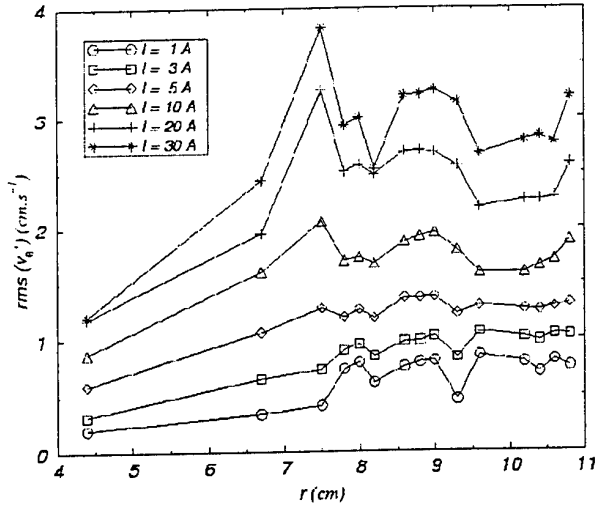


Figure 5: Profiles of the rms of the velocity fluctuations for different values of the control parameter I ($B_0 = 0.17 T$); angular velocity component

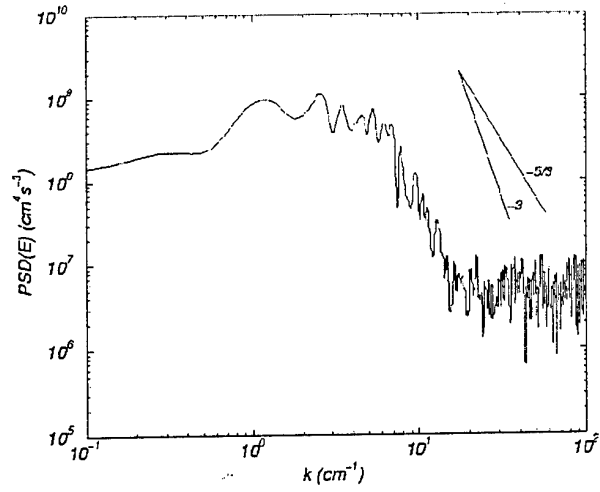


Figure 7: One-dimensional energy spectra of V_θ at $r = 96 \text{ mm}$ for $I = 3 \text{ Amp}$.

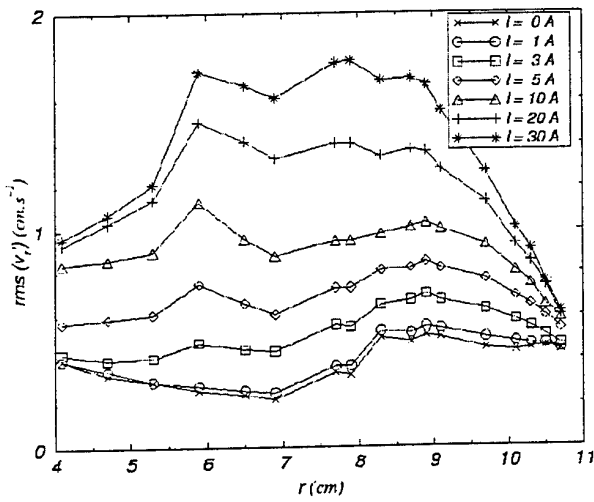


Figure 6: Profiles of the rms of the velocity fluctuations for different values of the control parameter I ($B_0 = 0.17 T$); radial velocity component

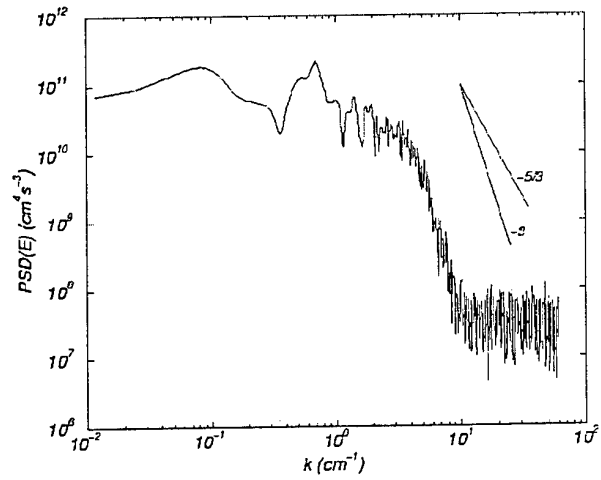


Figure 8: One-dimensional energy spectra of V_θ at $r = 96 \text{ mm}$ for $I = 20 \text{ Amp}$.

move from the external wall towards the centre, seems to be quite consistent with continuity.

Two typical energy spectra are shown on fig. 7 (for a moderate electric current $I = 3 \text{ Amp}$) and 8 (for a high value of the electric current $I = 20 \text{ Amp}$). Both figures show nice signatures of the large coherent structures illustrated on the video, in the forms of peaks in a range of small wave numbers. The first peak corresponds to the largest length scale, namely the diameter of the cell. For $I = 3 \text{ Amp}$, other individual peaks can be identified, corresponding to smaller structures (vortices). The spectra were produced from temporal records of the velocity and transformed in spatial spectra using the Taylor hypothesis. The peaks correspond to the distance between a vortex and itself (after one turn), to a vortex and the one before it, etc. About seven peaks can be seen. The smallest well defined structure (distance between two neighbouring vortices) is about 3 cm . For $I = 20 \text{ Amp}$, only three peaks can be identified. The smallest well defined structure is about 7 cm . This shows clearly the increase of the size of the large coherent structures (or the reduction of their number) when the kinetic energy of the turbulence increases.

At larger wave numbers, but before those dominated by the noise, an inertial range seems to be well defined, although it starts with a clear reminiscence of the peaks. In both cases ($I = 3 \text{ Amp}$ and $I = 20 \text{ Amp}$) a power law fits well with the measurements, but the exponent should be close to $-5/3$ at low electric current (or low kinetic energy) and close to -3 at high electric current (or high kinetic energy). These results are in agreement with previous measurements. Sommeria *et al.* (1989) had also measured $k^{-5/3}$ spectra in a 2D homogeneous turbulence dominated by an inverse energy cascade. And many authors, in Riga (see Lielausis, 1975), in Purdue (Brouillette and Lykoudis, 1967; Gardner and Lykoudis, 1971) and in Grenoble (Alemany *et al.*, 1979) had previously reported k^{-3} energy spectra in MHD turbulence, but in quite different conditions (see a discussion of these conditions in Moreau, 1990). It is important to discuss the origin of the k^{-3} slope for the energy spectrum. It is commonly argued that it results from dimensional analysis of the enstrophy cascade to the small scales in 2D-turbulence. It must be added that MHD flows have their own reasons to display k^{-3} slopes, which is the possibility of a quasi-steady equilibrium between the inertial transfer mechanisms and the damping mechanisms. The first one has a typical time scale $1/(u k)$, whereas the second one has a typical time scale $(H\sqrt{\rho})/(B_0\sqrt{\sigma\nu})$, which is k independent (Sommeria and Moreau, 1982). This damping, which takes place within the Hartmann layers, and which results from both viscous and ohmic effects (it results from the Hartmann layer theory that they are equal to each other) is the only dissipation suffered by this 2D turbulence.

The transition between the $k^{-5/3}$ and the k^{-3} energy spectral slope can also be believed as dependent on the relative importance of energy dissipation *versus* enstrophy dissipation. When the turnover time scale is longer than the damping time due to the Hartmann layer, energy dissipation is important and leads to its $k^{-5/3}$ spectrum. When the turnover time scale is much less than the dissipation time, energy can be considered as conserved, whereas enstrophy is still dissipated.

The enstrophy cascade towards small scales leads to a k^{-3} spectrum for energy and feeds also large scales, by conservation of energy.

CONCLUDING REMARKS

A mercury cell located in a vertical magnetic field is used to observe the singular properties of quasi-2D turbulent shear layers. A number of striking results have been obtained, among which the most noticeable seem to be the following:

a) The velocity field is dominated by a number of large coherent structures fed from the instability of the shear layer via a energy transfer towards the large scales.

b) This kind of turbulence is, as expected, a good way to efficiently transport the momentum, but it seems to have a much lower efficiency to transport a scalar quantity such as heat. This point is particularly noticeable since it suggests that the turbulent Prandtl number should not tend to unity.

c) The energy spectrum exhibits peaks (at low wave numbers) corresponding to the large structures and an inertial range (at higher wave numbers) whose typical law is $k^{-5/3}$ or k^{-3} depending on the time scale of energy transfer compared to the time scale of dissipation in the Hartmann layer. Two possible mechanisms are a quasi-steady equilibrium of energy transfer and dissipation in the Hartmann layer at all scales, or an enstrophy cascade.

Acknowledgement: the present work was supported by the European contract N° CIPA-CP-0080.

REFERENCES

- Alemany A., Moreau R., Sulem P. and Frisch U., 1979, *J. de Méca. Théor. et Appl.*, vol. 18, p. 277-313
- Brouillette E. C. and Lykoudis P. S., 1967, *Phys. Fluids*, vol. 10, p. 995-1001
- Dumont T., Robert R. and Sommeria J., 1997, paper presented to this *11th Symp. on Turbulent Shear Flows*
- Gardner R. A. and Lykoudis P. S., 1971, *J. Fluid Mech.*, vol. 47, p. 737-764
- Kljukin A. A. and Kolesnikov Yu. B., 1989, in *Liquid Metal Magnetohydrodynamics*, eds. Lielpeteris J. and Moreau R., *Kluwer Acad. Pub.*, p.449-454
- Lehnert B., 1955, *Proc. Royal Soc. London*, A 233, p. 299
- Lielausis O. A., 1975, *Atomic Energy Review*, vol. 13, p. 527
- Moreau R., 1990, *Magnetohydrodynamics*, *Kluwer Acad. Pub.*
- Robert R. and Sommeria J., 1991, *J. Fluid Mech.*, vol. 229, p. 291-310
- Sommeria J. and Moreau R., 1982, *J. Fluid Mech.*, vol. 118, p. 507-518
- Sommeria J., Nguyen Duc J. M. and Caperan P., 1989, in *Liquid Metal Magnetohydrodynamics*, eds. Lielpeteris J. and Moreau R., *Kluwer Acad. Pub.*, p. 441-448

Examination of LSE-based velocity field estimations using instantaneous, full field measurements in an annular mixing layer

Daniel Ewing
Department of Mechanical Engineering
Queen's University
Kingston, Ont. Canada.

Joseph H. Citriniti
Thermo- and Fluid Dynamics
Chalmers University of Technology
S-412 96 Goteborg, Sweden

Abstract

The data base measured by Citriniti (1995) is used to examine the accuracy of using Linear Stochastic Estimation to estimate the velocity field in the annular mixing layer. This data base is used to compute the velocity field that would be measured if the field was measured on two radial rings in the shear layer and the velocities on four other rings were estimated using Linear Stochastic Estimation. This result is compared to the actual velocity field measured at 138 points on the 6 radial positions by Citriniti (1995). The estimated and actual velocity fields are projected onto the orthogonal basis deduced by Citriniti (1995) and only the information from the most energetic modes are retained. It is found that the estimated field is capable of accurately reproducing the gross features of both the ring structures and the inter-ring regions found in the shear layer.

Introduction

It is widely recognized that large energetic structures play an important role in the dynamics of the near field in many free-shear flows, such as the axisymmetric shear layer occurring near the exit of a round jet. Although there are many different techniques that can be used to identify the coherent structures (*cf* Bonnet and Glauser 1994), only a few of these can be used to study the dynamics of the structures. One technique that can be used for this purpose is the Proper Orthogonal Decomposition (POD) technique introduced by Lumley (1967).

One of the primary difficulties of studying the *instantaneous* dynamics of the large structures with this technique (and others) is that it requires the simultaneous measurement of the velocity over the region of interest. As a result, there have been few attempts to experimentally study the instantaneous dynamics of

the structures on an entire plane in a free-shear flow. In one attempt to investigate these features Citriniti (1995) simultaneously measured the velocity field at 138 points in a high-Reynolds-number annular shear layer using hot-wire anemometers. Using the POD technique he found evidence that the shear layer was made up of both ring vortices and streamwise rib vortices that occur between the vortex rings, similar to the streamwise vortices that occur in the planar mixing layers braid region (*cf* Rogers and Moser 1994). The experimental evidence also suggests that these streamwise modes may entrain more ambient air into the shear layer than the ring vortices (the commonly assumed entrainment mechanism).

Although this experiment yielded very useful physical information about the axisymmetric shear layer, the effort required to perform the experiment effectively precludes its use on a wide variety of flows. One alternative approach suggested by Bonnet *et al.* (1994) is to measure the velocity at a small number of points and use Linear Stochastic Estimation to approximate velocity over the rest of the field. This estimated velocity field could then be used as an input into POD technique and an estimate for the dynamics of the large structures could be deduced. Bonnet *et al.* (1994) demonstrated that this technique was capable of accurately reproducing the dynamics of the large structures when applied to one non-homogeneous direction in a shear layer. They also suggested that the method could be extended to more spatial dimensions in a flow, however as yet, there has not been an attempt to confirm this.

The objective of this investigation is to examine if LSE can be used in conjunction with the POD technique to produce an accurate estimate of the dynamics of the large structures on a full $r - \theta$ plane in the axisymmetric shear layer. The predictions for the dy-

namics of the structures from the estimated field are compared with the results reported by Citriniti (1995) to determine how well the technique reproduces the dynamics of both the ring and inter-ring regions.

Background

Annular Shear Layer Data Base

In order to study the large structures in the axisymmetric shear layer Citriniti (1995)¹ constructed an array of 138 single-wire transducers that was placed at a distance of 3 diameters downstream of a round jet. Glauser (1987) had shown previously that the large structures in flow could be resolved using the POD if the velocity was measured at 6 radial positions across the layer at $r/d = 0.15, 0.28, 0.41, 0.54, 0.67$, and 0.80 . He also found that the azimuthal dependence of the structures could be recovered if the velocity was measured at 6 azimuthal positions at the inner most radial position and 12, 24, 32, 32, and 32 positions at the other 5 radial positions, respectively. This information was used to locate the probes within the 138 wire array. The mean velocity normalized by the exit velocity ranged from 0.9 to 0.15 over these 6 radial points indicating that array of hot wires measured the streamwise velocity component in a region that spanned most of the shear layer.

The exit velocity profile of the jet was top hat within 0.1% with a turbulence intensity of 0.35%. The outlet velocity of the jet was set such that the exit Reynolds number based on the nozzle diameter, d , was 80,000. For these conditions, Glauser (1987) demonstrated that the large structures could be well resolved in the first 800 Hz of the spectra so the signals from all of the wires in the array were filtered at 800 Hz and simultaneously sampled at 2,028 Hz. The data was gathered in 300 blocks of 1024 points, which allowed the accurate computation of spectral information.

Proper Orthogonal Decomposition

Lumley (1967) argued that the functions used to represent the large structures in a turbulent flow should be defined in an objective manner using information from the flow only. For example, Lumley suggested these functions could be defined as those that make the largest contribution to the turbulent energy in the region of interest. Using this definition, it can be shown that functions for the homogeneous and stationary directions are simply Fourier modes so these directions can be transformed out the problem in the standard manner.

For the axisymmetric shear layer, the functions to represent the information in the radial direction that satisfy this definition, $\Phi^n(r, m, f)$, are solutions to the integral eigenvalue problem given by (Citriniti 1995)

$$\int_0^\infty \psi(r', m, f) \Phi^n(r', m, f) r' dr' = \lambda^n(m, f) \Phi^n(r, m, f), \quad (1)$$

where $\psi(r, m, f)$ is the Fourier transform of the two-point velocity correlation in both the azimuthal di-

rection and time, m is the azimuthal mode number and f is the frequency. It is straightforward to show that these functions are orthogonal (cf Lumley 1967). Thus, the integral eigenvalue can be solved using only statistical measures of the flow to yield an orthogonal basis to optimally describe the flow in the radial direction.

The information about the dynamics of the field is, however, contained in the coefficients of the orthogonal basis which are given by

$$a^n(m, f) = \int_0^\infty \hat{u}(r, m, f) \Phi^n(r, m, f) r dr, \quad (2)$$

where $\hat{u}(r, m, f)$ is the Fourier transform of the *instantaneous* velocity field in the azimuthal direction and time. Thus, it is necessary to simultaneously sample the velocity field over the entire domain of interest in order to determine these coefficients.

Once the coefficients for the orthogonal functions are determined, the dynamics of the large-scale structures in the field can then be studied by reconstructing the Fourier coefficients; *i.e.*,

$$\hat{u}_{rec}(r, m, f) = \sum_{n=1}^N a^n(m, f) \Phi^n(r, m, f), \quad (3)$$

where N is a user specified parameter. If all the available modes are used (*i.e.*, N is set to its highest value) then all the information from the original signal can be recovered. If on the other hand N is set to a small number then only the information from the most energetic modes is retained, thus reducing the small-scale information in the signal. The amount of small-scale information in the reconstructed velocity field can be further reduced by including the information from only a small number of azimuthal modes. The coefficients for the other modes are set to zero in order to remove them from the signal. This reduced signal can then be inverse Fourier transformed in time and the azimuthal direction to yield a low-order model for the instantaneous velocity field in the axisymmetric shear layer.

Citriniti (1995) demonstrated that the dynamics of the large-scale structures could be modeled if only the first POD mode is used (*i.e.*, $N=1$) and only the coefficients for azimuthal mode numbers 0 and 3–6 are retained in the reconstructed field. Examples of the reconstructed instantaneous fluctuating velocity fields computed using these modes are shown in figures 1 and 2. In both of these figures the colour scale corresponds to the value of the instantaneous fluctuating velocity. The light colours correspond to velocities that are larger than the local mean while the dark colours correspond to velocities less than the local mean.

It is clear that there is a band of faster-than-average moving fluid inside a band of slower-than-average moving fluid in figure 1, which is consistent with the pattern one would expect with the passage of a vortex ring like structure. On the other hand there are neighbouring regions of fast and slow moving fluid in figure 2, suggesting that regions of fast flow moving out of the core neighbour regions of slow moving fluid being entrained into the core. This is consistent with the pattern one would expect in a braid region of counter-rotating streamwise vortices. Thus, the velocity field

¹ See also the paper by Citriniti in this volume.

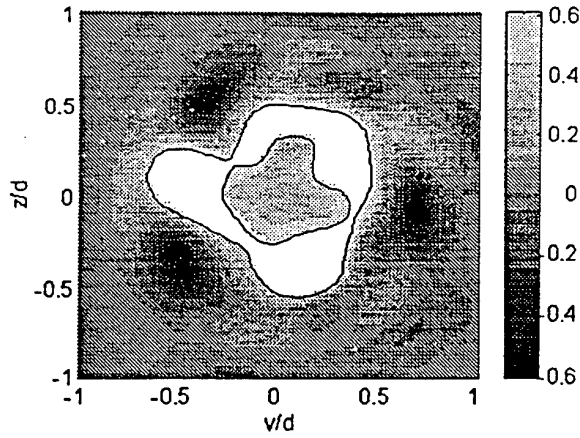


Figure 1: Ring-like structure from the low-order reconstruction of the axisymmetric shear layer.

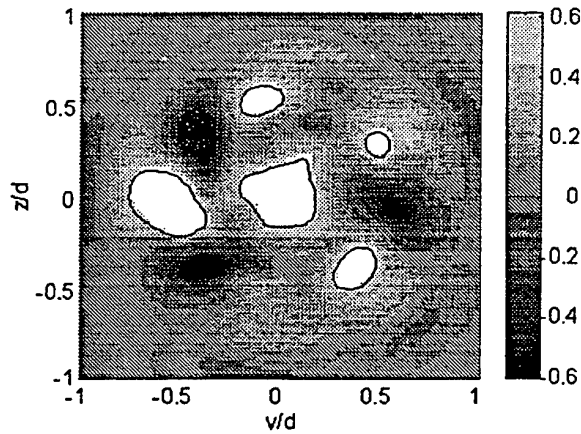


Figure 2: The inter-ring region that appears to contain a series of counter-rotating streamwise vortices.

reconstructed with only a few modes on the $r-\theta$ plane showed evidence of both ring vortices and streamwise vortices in the inter-ring regions.

Linear Stochastic Estimation

Although these results shed insight into the dynamics of the structures in the axisymmetric shear layer, it is not trivial to simultaneously measure the velocity field at 138 points in the field. Thus, as Bonnet *et al.* (1994) suggested, it would be very useful if a similar picture of this flow (and others) could be deduced by applying the POD to an instantaneous field that was measured at a smaller number of points and estimated at the other points necessary to resolve the POD coefficients. Bonnet *et al.* suggested using Linear Stochastic Estimation to extrapolate information from the measured points and fill out the field sufficiently to use the POD.

In this approach, the instantaneous velocity at a position x_n is approximated as a linear combination of the velocities at the points where it is measured

(x', x'', \dots) ; i.e.,

$$u_e(x_n) = A(x_n)u(x') + B(x_n)u(x'') + \dots \quad (4)$$

The coefficients, $A(x_n), B(x_n), \dots$ are then determined by minimizing the mean square error in the estimated velocity; i.e., $(u_e(x_n) - u(x_n))^2$.

For the current application, it is more useful to estimate the Fourier coefficients $\hat{u}(r, m, f)$ at a radius in the axisymmetric shear layer using the Fourier coefficients measured at one or two radial positions. If the Fourier coefficients are measured at a single radial position it follows that the Fourier coefficients at the other positions can be approximated as

$$\hat{u}_e(r_n, m, f) = C(r_n, m, f)\hat{u}(r', m, f), \quad (5)$$

where $\hat{u}(r', m, f)$ are the Fourier coefficients at the measured points. In this case, the mean square error in the estimated Fourier coefficient, $(\hat{u}_e - \hat{u})(\hat{u}_e - \hat{u})^*$, is minimized if

$$C(r_n, m, f) = \frac{F(r_n, r', m, f)}{F(r', r', m, f)}, \quad (6)$$

where $F(r_n, r', m, f) = \overline{\hat{u}_e(r_n, m, f)\hat{u}^*(r', m, f)}$. Thus, the coefficients used to estimate the velocity are determined using statistical measures of the flow that can be easily measured with a small number of hot-wires.

If the Fourier coefficients are measured at two radial positions it follows that the coefficients at the other radial positions can be approximated as

$$\hat{u}_e(r_n, m, f) = A(r_n, m, f)\hat{u}(r', m, f) + B(r_n, m, f)\hat{u}(r'', m, f), \quad (7)$$

where $\hat{u}(r', m, f)$ and $\hat{u}(r'', m, f)$ are the measured Fourier coefficients. In this case, the error in the estimated coefficients are minimized if

$$A(r_n, m, f) = \frac{F(r_n, r')F(r'', r'') - F(r_n, r'')F(r', r')}{F(r', r'')F(r'', r') - |F(r'', r')|^2} \quad (8)$$

and

$$B(r_n, m, f) = \frac{F(r_n, r'')F(r', r') - F(r_n, r')F(r'', r'')}{F(r'', r'')F(r', r') - |F(r'', r')|^2}. \quad (9)$$

The dependence of F on m and f has been left out of these last equations in order to shorten their length.

Results

In the axisymmetric shear layer, the LSE technique could be used to interpolate or extrapolate information in two different spatial directions, r or θ . Since the signals are correlated over a greater distance in the radial direction than the azimuthal direction (relative to the characteristic length scales in those directions), it follows that the LSE should work more effectively in radial direction than in the azimuthal direction. Thus, the first step in this investigation was to examine how effectively the LSE could interpolate or extrapolate information in the radial direction. It was assumed

that the Fourier coefficients $\hat{u}(r, m, f)$ are known at one or two radial positions. This information is then used to estimate the Fourier coefficients at the other radial positions. Physically, this corresponds to doing the experiment carried out by Citriniti (1995) using only one or two rings of hot-wires instead of the 6 used in that experiment.

A number of different configurations were examined in order to determine which radial positions were the optimal to use. Initially the suitability of different positions was examined by considering the value of the means square error in the estimated coefficient normalized by the mean square value of the actual coefficients; i.e.,

$$\frac{|\hat{u}_e(r_n, m, f) - \hat{u}(r_n, m, f)|^2}{F(r_n, r_n, m, f)}$$

It was found that none of the individual radial positions could be used to extrapolate the Fourier coefficients for both the 0 mode and modes 3 – 6. The mean square error in the estimated Fourier coefficient for the 0 mode was generally small over the dominant energy frequencies when a point on the inner or high-speed side of the layer was used as the measured point. This was not unexpected since the ring vortex structure, which contributes to the 0 mode, is the most dominant feature of the inner radial positions. Similarly, the normalized error in the Fourier coefficients for modes 3 – 6 was significantly lower when a point on the outer or slow speed side of the layer was used as the measured point. Again, this is expected since the inter-ring region is more dominant on the outside of the layer than the inside.

Thus, it was suspected that the most accurate estimated coefficients could be derived if two measuring points were used, with one on each side of the shear layer. A variety of combinations of these points were studied. It was found that there was little variation in the accuracy of the estimated Fourier coefficients (at least from the perspective of the normalized mean square error) when the two measured points were situated on opposite sides of the mixing layer. The best results, however, seemed to occur when the two radial positions are chosen near center of the shear layer, $r/d = 0.41$ and $r/d = 0.67$, which is analogous to the result deduced by Bonnet *et al.* (1994). The normalized mean square error in the estimated Fourier coefficients for azimuthal modes 0 at the other four radii in the shear layer are shown in figure 3. It is important to note the spectra for the 0 mode has a dominant peak at approximately 100 hz so this is the region where the Fourier coefficients need to be well predicted. It is clear that this occurs for all the radial positions except for the position at the center of the mixing layer. It is not clear why the prediction at this point is so poor however, a similar result was noted by Bonnet *et al.* when they used the LSE in a single non-homogeneous direction.

The normalized mean square error in the Fourier coefficients for azimuthal mode 5 are shown in figure 4. The error is only shown for the outer three positions because the Fourier coefficient for mode 5 is not measured in the inner most radius. The spectra for this mode peaks at the lowest frequency measured so it is

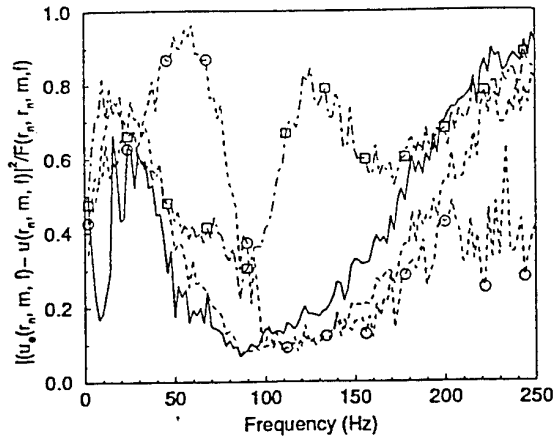


Figure 3: Normalized mean square error in the coefficients for azimuthal mode number 0. — $r_1/d = 0.15$, ---- $r_2/d = 0.28$, -.- $r_4/d = 0.54$, and $r_5/d = 0.8$.

important that the Fourier coefficients for this mode number are accurately predicted in this region. Although the normalized mean square error is higher for these Fourier coefficients than for the 0 mode, the level of the error is still small in the low frequency region at the outer radial positions where the higher modes play a large role in the dynamics of the flow.

Although these results show that the normalized mean square errors in the estimated coefficients are small for the important ranges of frequencies, they do not provide any information about how well the instantaneous coefficients are predicted. In order to examine this question the estimated and actual coefficients were projected onto the orthogonal basis deduced by Citriniti (1995) to determine the coefficients for the POD modes. Following the same procedure outlined by Citriniti (1995), the coefficient of the first POD mode computed from the estimated field was used to generate a partial reconstruction of the field. The information from azimuthal modes 0, 3, 4, 5, and 6 were retained and the resulting coefficients were inverse Fourier transformed in time and the azimuthal direction in order to produce a low-order estimate of the velocity field.

A comparison of several realizations from the estimated and original fields are shown in figures 5 - 10. The realizations from the estimated field are shown in figures 5 - 7 while corresponding realizations from the original field are shown in figures 8 - 10. The colour is again used to denote the level of the instantaneous fluctuating velocity with light colours corresponding to velocities larger than the local mean and dark colours corresponding to velocities less than the local mean.

Comparing figures 5 and 8 it is clear that the estimated realization has almost all of the gross features of the original field. As one would expect the estimated field appears to be a filter version of the original field, removing some of the finer features of the flow and smoothing the topology. This is evident if the highest speed contour from the two realizations are

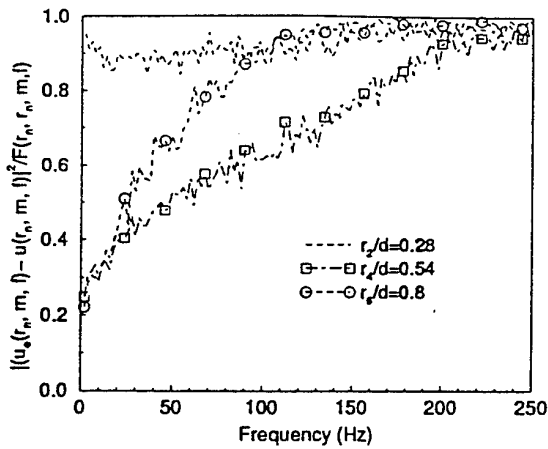


Figure 4: Normalized mean square error in the coefficients for azimuthal mode number 5. ---- $r_2/d = 0.28$, ---- $r_4/d = 0.54$, and ---- $r_5/d = 0.8$.

compared. The shape of the contour is smoother for the realization from the estimated field. Two different realizations in the inter-ring region are compared in figures 6 and 9 and figures 7 and 10. It can be seen that the overall levels of the fluctuating velocity in the estimated field are smaller than the levels in the actual field. However, the topology of the structures in the region are well preserved showing the distinctive feature characteristic of the streamwise vortices. Thus, the estimated field seems to be quite capable of reproducing the major features of the shear layer.

Summary

The accuracy of using estimated velocity fields to study the dynamics of the large structures in the axisymmetric shear layer is examined using the data base measured by Citriniti (1995). It was found that the dynamics of the ring vortices and the inter-ring regions could be well reproduced if the Fourier coefficients are measured on 2 radii and estimated on 4 others. This reduced the number of probes necessary to carry out the experiment from 138 to 56, thus effecting a 60 percent savings in the number of probes. Further refinement of the estimation technique will be considered in order to try to increase the savings in the number of probes. In particular interpolation in the azimuthal direction will be considered.

Acknowledgements

The work was funded in part by a NSERC postdoctoral fellowship.

References

- Bonnet, J. P. and Glauser, M. N. (1994). *Eddy Structure Identification in Free Turbulent Shear Flows*. Kluwer Academic Press.
- Bonnet, J. P., Cole, D. R., Deville, J., Glauser, M. N., and Ukeiley, L. S. (1994). Stochastic estimation

and proper orthogonal decomposition: Complementary techniques for identifying structure. *Expts. in Fluids* 17, 307-314.

Citriniti, J. (1995), *Experimental investigation into the large structures of the axisymmetric mixing layer using the Proper Orthogonal Decomposition*. PhD thesis, State University of New York at Buffalo.

Glauser, M. N. (1987), *Coherent Structures in the Axisymmetric Turbulent Jet Mixing Layer*. PhD thesis, State University of New York at Buffalo.

Lumley, J. L. (1967). The structure of inhomogeneous turbulence. In Yaglom, A. M. and Tatarski, V. I., editors, *Atmospheric Turbulence and Wave Propagation*, pages 166-178. Nauka, Moscow.

Rogers, M. M. and Moser, R. D. (1994). Direct simulation of a self-similar turbulent mixing layer. *Phys. Fluids* 6 (2), 903-923.

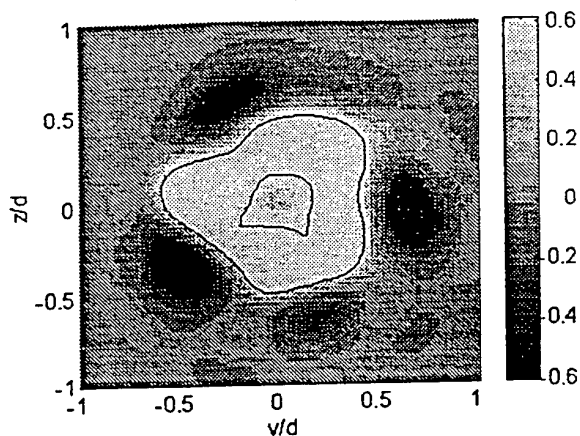


Figure 5: Ring-like structure from the low-order reconstruction produced using the estimated field.

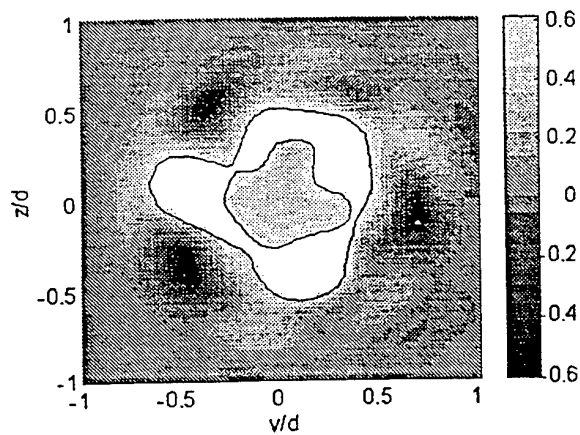


Figure 8: Ring-like structure from the low-order reconstruction produced using the original field.

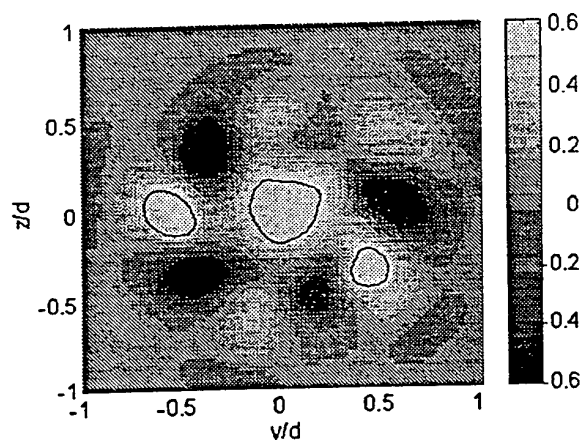


Figure 6: The inter-ring region from the low-order reconstruction produced using the estimated field. Appears to be a series of counter-rotating vortices.

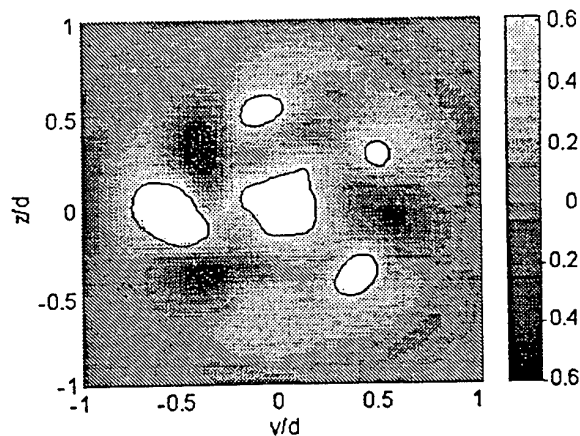


Figure 9: The inter-ring region from the low-order reconstruction produced using the original field. Appears to be a series of counter-rotating vortices.

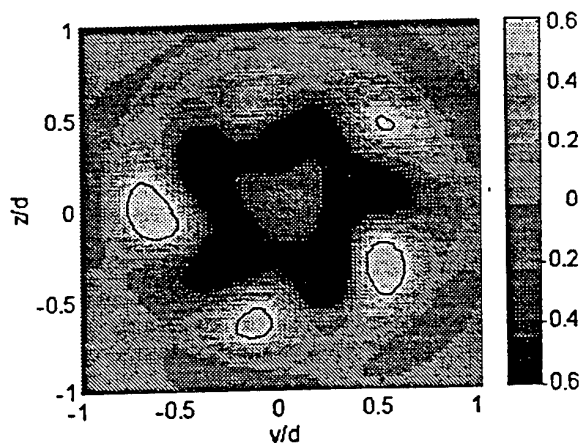


Figure 7: A second realization in the inter-ring region from the low-order reconstruction produced using the estimated field.

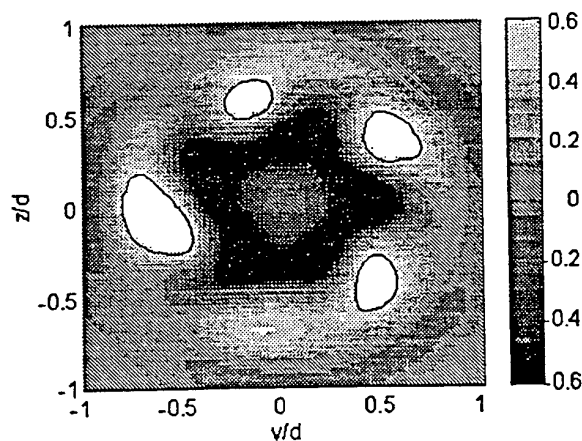


Figure 10: A second realization in the inter-ring region from the low-order reconstruction produced using the original field.

POD coefficient interaction and its relation to structure evolution in a turbulent axisymmetric shear layer

Joseph H. Citriniti
Thermo- and Fluid Dynamics
Chalmers University of Technology
S-412 96 Göteborg, Sweden

Abstract

The coefficients of the orthogonal basis obtained from the application of the Proper Orthogonal Decomposition (POD) to the streamwise velocity field in the axisymmetric mixing layer are presented. The coefficients are utilized to explain the interaction between azimuthal modes in the shear layer and their relation to the large scale structure at a position 3 diameters downstream from the exit of a round jet. The large scale structure in the axisymmetric mixing layer has been found to be well represented by the first radial POD mode and a further breakdown of the structure into azimuthal modes reveals more insight into the structure dynamics. It is shown that higher azimuthal Fourier mode structures ($m = 3, 4, 5$ and 6) interact in the layer and a proposed phase relationship between these structures at different parts of the layer is discussed.

Introduction

The POD technique has been used in the eduction of coherent structures in the axisymmetric mixing layer by Glauser (1987). These experiments showed conclusively that only three POD modes were necessary to describe the *radial* dependence of all but the smallest structures present in the flow. Moreover, only a single POD mode captured all the essential characteristics of the large scale structure. A surprising result of the Glauser experiment, however, was that the *azimuthal* Fourier modes necessary to describe the flow varied greatly with radial position. (Note that the periodicity of the flow in the azimuthal direction, θ , dictates that the azimuthal POD modes are Fourier modes.) Specifically, near the potential core, the 0-azimuthal mode contained almost all the energy, while outside the energy was distributed in modes centered around mode-5.

The short-coming of the Glauser experiment was

that although it was able to determine which modes were important *to* the flow, it could not determine *how* they were assembled *in* the flow. For example, it was not possible to tell whether the mode-0 (which dominated the statistics of the inner shear layer and core region) occurred simultaneously with the mode-5 contributions on the outside, with a time lag, or simply randomly phased with respect to it. This could only have been determined if the eigenfunctions could have been projected back onto the entire profile to determine the coefficients for a single ensemble. And this would have been possible only if all the measurements at *all* locations had been made *simultaneously*. The coefficients so determined could then have been used to reconstruct the instantaneous spatial and temporal flow at the cross-section, one mode at a time.

The experiment of Citriniti (1996) was designed specifically to provide the missing information to find out how the radial POD and azimuthal Fourier modes fit together in time. This was a non-trivial undertaking, even by comparison to the Glauser experiment since what was required was simultaneous measurement in an entire cross-section of a very high Reynolds number flow. And, most importantly, the measurements had to have sufficient spatial resolution to avoid aliasing the higher spatial azimuthal and POD modes into the lower ones which were of primary interest.

The results of this effort to obtain the dynamical relationships between azimuthal Fourier modes in the axisymmetric shear layer are presented below. Specifically, the phase relationship between azimuthal modes 0, 3, 4, 5 and 6 in the inner and outer portions of the layer are determined.

Methods

Proper Orthogonal Decomposition

The present investigation uses the POD-

reconstructed velocity database obtained in the experiment of Citriniti (1996). In that experiment, the POD technique was applied to an ensemble of realizations of the streamwise velocity field, three diameters downstream from the exit of a round jet. The velocity field was reconstructed using the calculated eigenfunctions and random coefficients.

The structure, in the POD application, is assumed to be represented by the first of an ordered set of orthogonal eigenfunctions, $\vartheta_i(\vec{x}, t)$, that are defined by the maximization of their normalized mean square projection on the velocity vector, $u_i(\vec{x}, t)$ (Lumley, 1970). The maximization is performed via the calculus of variations and the result is an integral eigenvalue equation of the Fredholm type (Lumley, 1970),

$$\int R_{i,j}(\vec{x}, \vec{x}', t, t') \vartheta_j(\vec{x}', t') d\vec{x}' dt' = \lambda \vartheta_i(\vec{x}) \quad (1)$$

where the symmetric kernel of this equation is the two point correlation tensor

$$R_{i,j}(\vec{x}, \vec{x}', t, t') = \langle u_i(\vec{x}, t) u_j(\vec{x}', t') \rangle \quad (2)$$

and ϑ_j are the eigenfunctions and λ is the eigenvalue.

Solution of this equation produces the eigenfunctions and Galerkin projection of the instantaneous velocity on the set determines the coefficients of the eigenfunctions. The velocity field can then be reconstructed and the form of this equation for the axisymmetric mixing layer, $(x_1, x_2, x_3) = (x, r, \theta)$, is (Citriniti and George, 1997),

$$\hat{u}_i^{nmf}(r, m, f) = \sum_{n=1}^N \hat{a}_n(m, f) \phi_i^{(n)}(r, m, f) \quad (3)$$

where $n = 1, 2, 3 \dots$ represents the discrete nature of the solution set and $\phi_i^{(n)}(r, m, f)$ and $\hat{a}_n(m, f)$ are the POD eigenfunctions and coefficients, respectively, decomposed in frequency, f , and azimuthal mode number, m . An equation for the coefficients is obtained by using the orthogonality of the eigenfunctions, *i.e.*

$$\hat{a}_n(m, f) = \int \hat{u}_i^{nmf}(r, m, f) \phi_i^{(n*)}(r, m, f) dr. \quad (4)$$

Performing partial sums in equation 3, *i.e.* $N = 1, 2, 3, \dots$, provides a way to visualize different energy weighted views of the flow. It has been shown, *v. Citriniti and George (1997)*, that setting $N = 1$ effectively filters out the small scale structure and leaves an unobscured view of the large scale, or coherent, structure in the axisymmetric mixing layer. Also, since the eigenfunctions are made orthonormal, the magnitude of the streamwise velocity is determined by the coefficients. Therefore, by studying the instantaneous coefficient dynamics on a mode-by-mode basis, a clear view of the structure interaction is obtained.

Experiment

The flow field at 3 diameters downstream of the nozzle is representative of the fully developed mixing layer. At this position, it has been shown that 138 measuring positions is sufficient to properly resolve the flow field for the application of the POD to the streamwise velocity field (Citriniti and George, 1996). The hot-wire probes are distributed across the mixing layer

at 6 radial position with the azimuthal distribution of probes on the 6 radii, starting at the center and proceeding outward, 6, 12, 24, 32, 32, 32 thus totalling 138 positions. The transducers were simultaneous operating, single-wire, hot-wire anemometer probes powered by in-house anemometers, *v. Citriniti et al. (1994)*. The sampling rate of each of the hot-wires was set at 2,048 Hz to satisfy the Nyquist criterion which must be greater than twice the 800 Hz corner frequency on the low-pass anti-alias filters. There were 300 blocks of 1024 samples producing a bandwidth of 2 Hz and a block length of 0.5 s.

The Reynolds number based on nozzle diameter, d , for the jet is 80,000. The free-stream turbulence intensity at the jet exit is 0.35% and the boundary layer at the jet exit was turbulent with an approximate thickness of 1.2 mm. The mean velocity profile was flat to within 0.1%.

The statistics of the streamwise velocity field, as measured by the sampling grid, demonstrate that an axisymmetric shear layer has been formed, *i.e.* the mean and rms contours are circular *v. Citriniti (1996)*. The mean velocity normalized by the exit velocity is about 0.9 at the inner radius of the sampling array and falls to 0.15 at the outside of the mixing layer. The spectral character of the velocity field demonstrates the fully developed, turbulent character of the mixing layer, *v. Citriniti (1996)*.

Coefficient Dynamics

The magnitude and phase of the random coefficients are shown in sequential order in figure 1 to figure 3. The first column shows the temporal evolution of the magnitude of the first radial POD coefficient while the second shows its phase angle. The third column is a plot of the reconstructed velocity field by the POD (*v. equation 3*) with $N = 1$ and using the first 7 azimuthal modes, $m = 0, 1, 2, 3, 4, 5, 6$. The third column shows the effect the large scale structures on the streamwise velocity field in the mixing layer. Each row in the 3 figures represents one step in the temporal evolution of the structures. There is no discontinuity between figures so they could, in essence, be placed top to bottom to obtain 12 straight time steps in the flow evolution. Each row is separated by about 1 ms in real time.

In figure 1 the amplitude of the sixth azimuthal mode is first seen to grow and then begin to decay (column 1). Directly following the peak in this mode, there appears to be a mode-transfer process that begins with the increase in the amplitude of mode 5 and proceeding to modes 4, 3 and 2. This transfer is interesting because it suggests that the smaller length scale modes may act as triggers, or perhaps indicators, for the emergence of the lower, more energetic mode-number structures in the mixing layer. This mode interplay has also been observed in the POD-based dynamical system simulations of Glauser *et al.* (1992).

Citriniti and George (1997) have shown that the higher azimuthal mode structure is associated with streamwise vortices which advect high-momentum fluid from the potential core to the outside of the layer and low-momentum, ambient fluid toward the potential core. The fact that the mode-6 structures precede the lower mode structures indicates that these streamwise vortices are important players in the en-

ergy cascade process of turbulence. It is interesting to note that the mode-6 structure, which is correlated over a shorter spatial scale than the mode-4 structure, should be the trigger mechanism since this would imply that the energy cascade proceeds from smaller to larger scales. However, it should be noted that these temporal visualizations do not follow individual energy paths but rather the entire field so the mode-6 trigger may just be the consequence of the temporal sequencing of the large scale structure in the layer at $x/d = 3$. These results are consistent both with the low-mode dynamical systems models of Glauser *et al.* (1992) as well as the proposed mechanism for turbulent structure interaction in the mixing layer proposed by Glauser and George (1987). This model proposes that the dynamics of the large scale structure in the layer parallels the leapfrog mechanism of two interacting vortex rings.

The phase of the random coefficients also shows interesting trends. A pattern of large phase lag followed by a continuous evolution toward zero phase and then to large phase lead is seen at all azimuthal modes indicating a highly repetitive pattern of structures exists in the layer.

Other useful measures of the large scale structure in the turbulence are evident in the movies generated by the sequential plotting of the figures presented earlier. In these movies, the true evolution of the large scale structures is evident. Especially the bursting of a highly coherent ring-like structure near the potential core of the layer. This event is seen in the third row of figure 2 and is followed (and proceeded because of the repetitive nature of the flow) by the straining of streamwise structures which are believed to be formed by the breakup of the Kelvin-Helmholtz rings formed at the edge of the shear layer.

References

- Citriniti, J.H. and George, W.K. (1996). Experimental investigation into the dynamics of the axisymmetric jet mixing layer. In Begell, William, editor, *Turbulence, Heat and Mass Transfer*, New York, NY. Begell House.
- Citriniti, J.H. and George, W.K. (1997). An application of the proper orthogonal decomposition to the axisymmetric mixing layer. part 2: reconstruction of the global velocity field. *J. Fluid Mech.* . Submitted for publication.
- Citriniti, J.H., Taulbee, K.D., Woodward, S.H., and George, W.K. (1994). Design of multiple channel hot-wire anemometers. In *Fluid Measurement and Instrumentation 1994*, pages 67-73, ASME FED-Vol. 183.
- Citriniti, J.H. (1996), *Experimental Investigation Into the Dynamics of the Axisymmetric Mixing Layer Utilizing the Proper Orthogonal Decomposition*. PhD thesis, State University of New York at Buffalo.
- Glauser, M.N. and George, W.K. (1987). An orthogonal decomposition of the axisymmetric mixing layer utilizing cross-wire measurements. In F. Durst *et al.* , editor, *Turbulent Shear Flows 6*, page 10.1.1. Springer Verlag.
- Glauser, M.N., Zheng, X., and Doering, C. (1992). A low-dimensional dynamical systems description of the axisymmetric mixing layer. *Clarkson University Report MAE-427* .
- Glauser, M.N. (1987), *Coherent Structures in the Axisymmetric Turbulent Jet Mixing Layer*. PhD thesis, State University of New York at Buffalo.
- Lumley, J. L. (1970). *Stochastic Tools in Turbulence*. Academic Press.

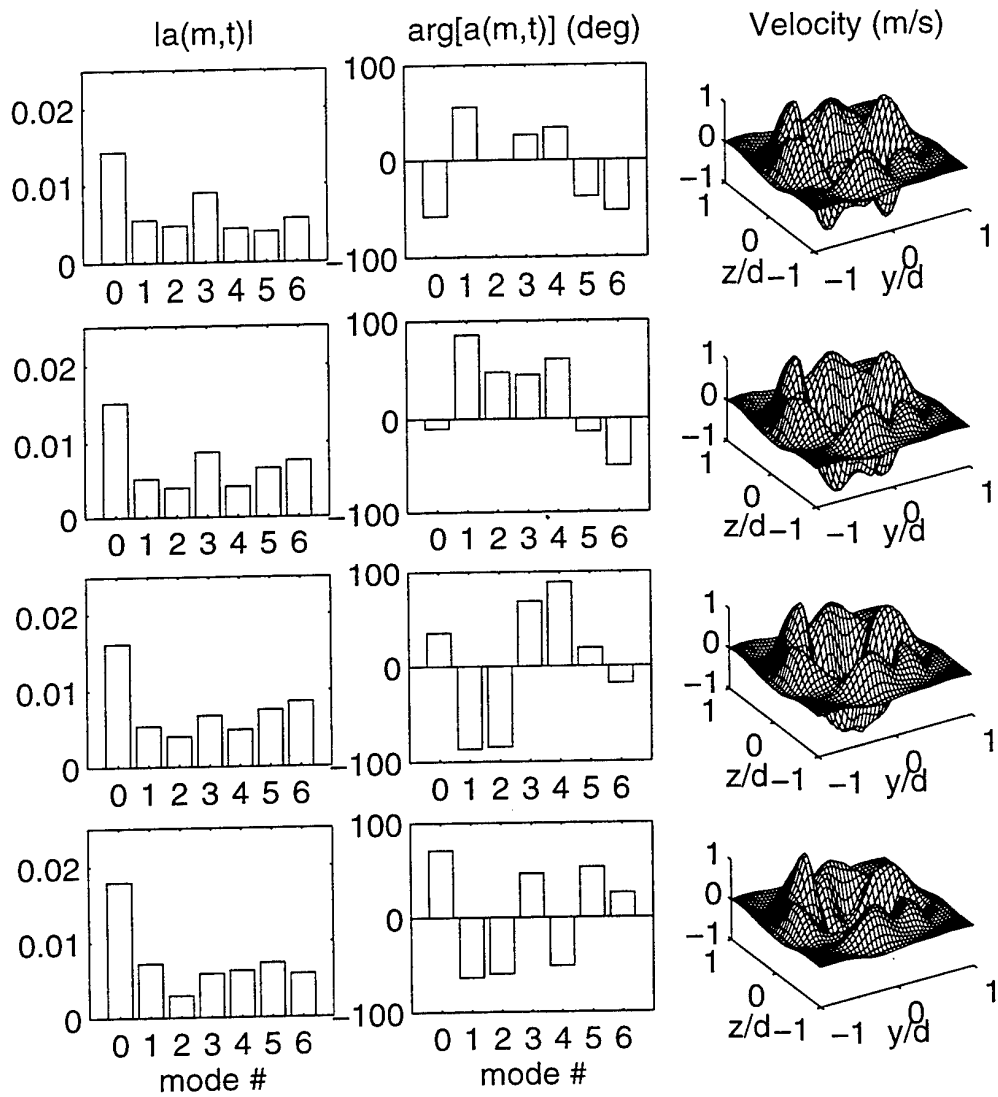


Figure 1: See figure 3 for extended caption

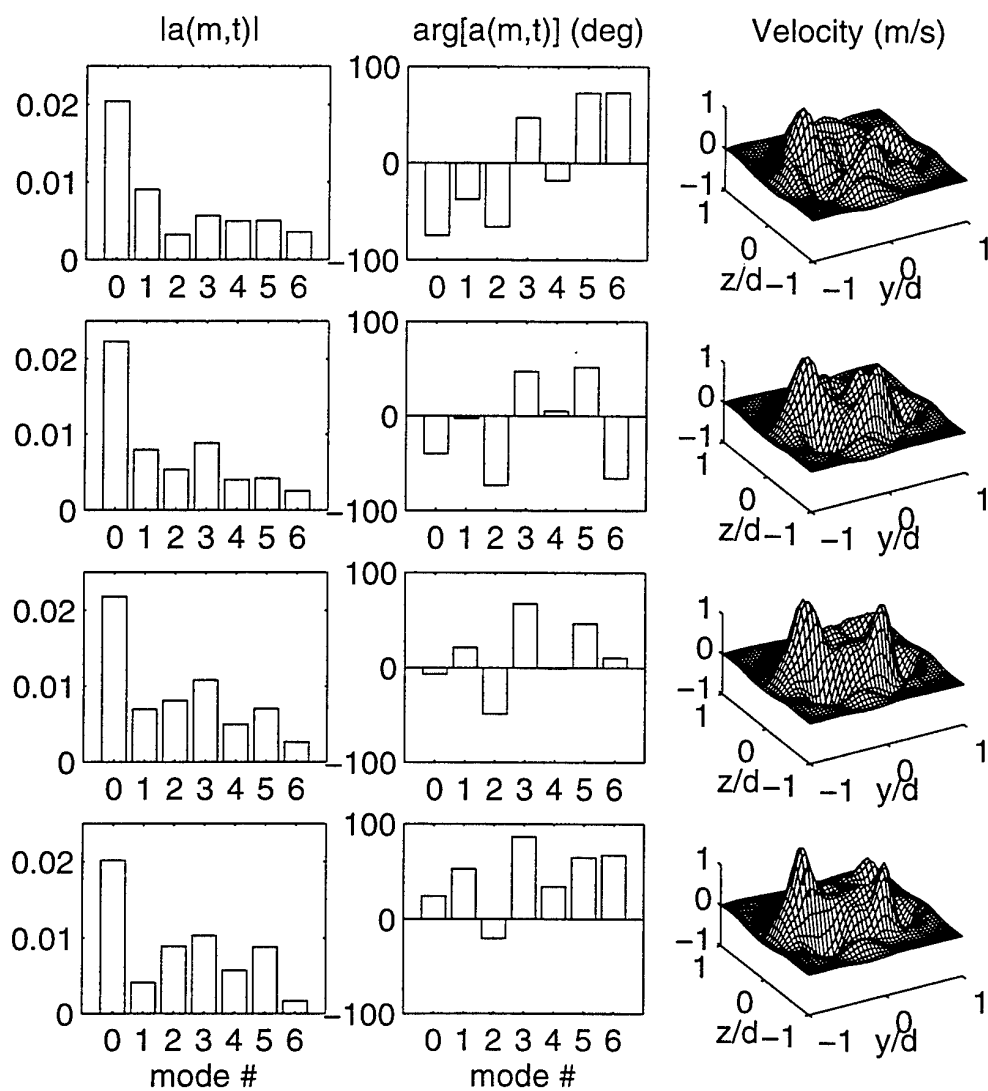


Figure 2: See figure 3 for extended caption

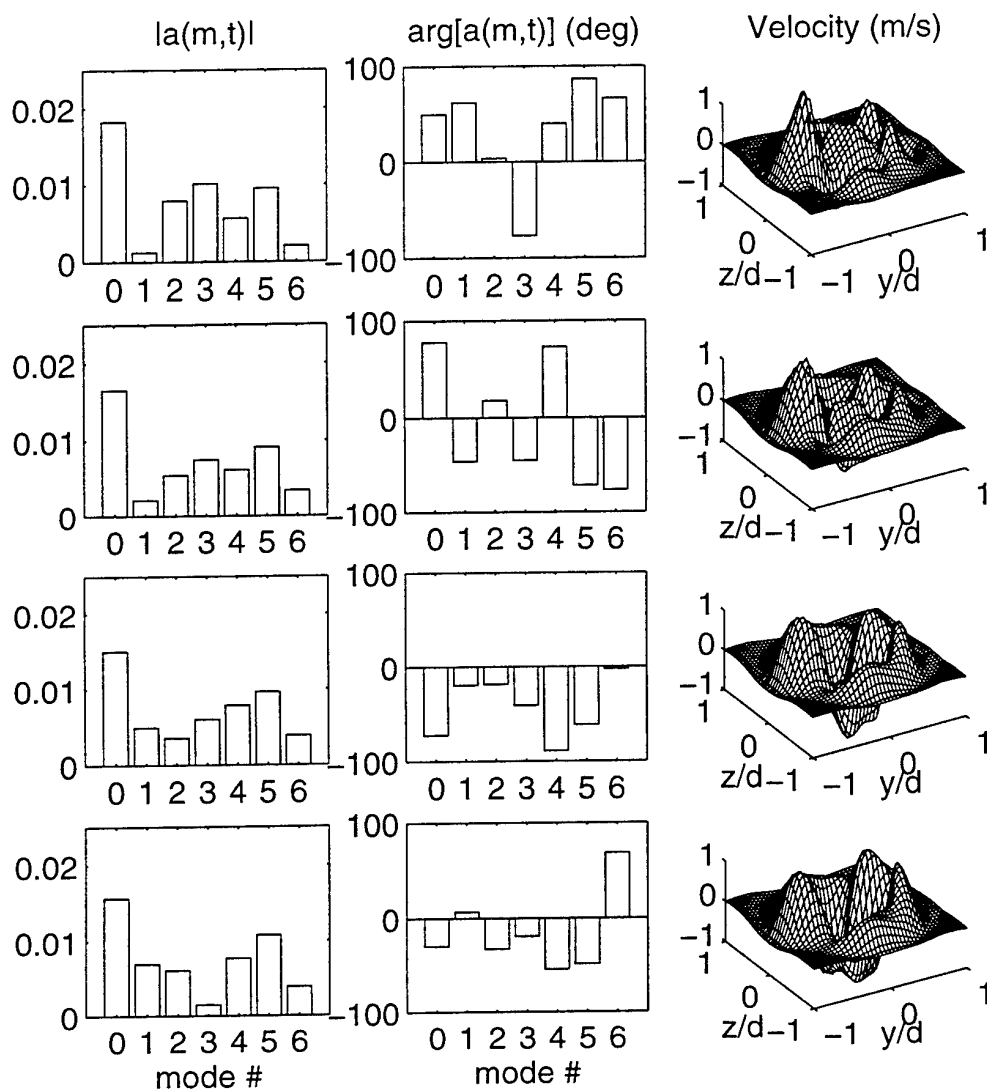


Figure 3: Sequential plots of the coefficient magnitude and phase and the projected velocity for the first POD mode and azimuthal modes 0-6. Column 1: magnitude of the first 6 azimuthal modes. Column 2: phase angle of the first 6 azimuthal modes. Column 3: projection of the streamwise velocity field using the first POD mode and azimuthal modes 0-6 (v , equation 3). The rows display the temporal evolution of the various quantities and are separated in real time by approximately 1 ms.

THE JOINT PROBABILITY FUNCTIONS OF THE MEASURED VELOCITY AND VORTICITY COMPONENTS IN A PLANE WAKE

Phuc N. Nguyen
Propulsor Department
David Taylor Model Basin
9500 MacArthur Blvd.
Bethesda, Maryland 20817-5700, USA

ABSTRACT

This paper illustrates the preferred orientation of the vortical structure in a plane wake by analysis of the joint distribution functions of the velocity components or the vorticity components. The quadrant contributions are calculated to quantify the preferred states of these variables. These characteristics are revealed through the simultaneous measurements of all velocity components and all vorticity components.

INTRODUCTION

The joint probability density functions (JPDFs) of two variables, $P(v_1, v_2)$, indicate the probability of the two variables having specified values at the same time. The orientation of the JPDF contours reflects the preferred simultaneous states of the two variable fields. Thus, some turbulence structure information can be deduced, even from single-point measurements. JPDF analysis was utilized by Wallace & Brodkey [7] to examine the structure of the correlation \bar{uv} in a turbulent channel flow.

For plane wake flows, much knowledge about turbulence structures has been obtained, but the lack of detailed vorticity data hinders understanding of the dynamics of these vortical structures. Previous attempts to measure vorticity components with X-wires in a cylinder wake have been reported by Hussain & Hayakawa [2] and Antonia et al. [1]. These X-wire measurements give only one component at a time due to the extreme difficulty of multi-component velocity measurement with a small probe. The present results are the first simultaneous measurements of all three components of the velocity and vorticity vectors in a wake flow.

RESULTS AND DISCUSSION

The experiment was performed with a cylinder $d = 6.3$ mm at a free-stream speed of 5.0 m/s ($Re_d \approx 2000$). For the $x/d=30$ measurement station, the wake half-width L_o was 8.5 mm, and the centerline wake deficit u_o was 0.82 m/s. A 12-sensor probe, built by P. Vukoslavčević as an extension of the nine-sensor probe [6], was used. The probe consists of three four-sensor arrays which have centroids at the corners of an equilateral triangle. Each array has two pairs of mutually perpendicular V-probes, with prong spacings of about 0.45 mm. The data were reduced with an iterative error-minimization technique. The velocity and vorticity statistics of these measurements have been shown to have relatively high accuracy [4].

The JPDFs for all combinations of the velocity components have been determined for six locations across the wake. Numerical values of the contributions from all four quadrants, Q1, Q2, Q3 and Q4, of the two velocity component hodograph plane are also presented. The quadrant definition is: Q1= (+, +), Q2= (-, +), Q3= (-, -), and Q4= (+, -). The streamwise velocity is u , the cross-stream velocity v , and the spanwise velocity w . All velocity components are nondimensionalized by u_o .

Fig. 1 shows the JPDF, $P(u, v)$, and the covariance integrand contours, $uvP(u, v)$, for nondimensionalized wake positions $\eta \equiv y/L_o = -1.65$ to 1.29. For the lower wake, the JPDF contours show a preferred orientation of $+45^\circ$ from the horizontal axis u . The covariance integrand contours show this even more clearly with the contribution coming more from Q1 and Q3 than from Q2 and Q4 in the lower wake. Furthermore, the Q3 activity has lower probability but larger fluctuations than the Q1 activity; this will result in larger contribution to the total covariance from Q3. The Q2 and Q4 contributions will be smallest. In the centerline region ($\eta = 0.12$) the contours are symmetric in v but not in u , as

expected. The upper wake has a preferred Reynolds stress orientation of -45° from the horizontal axis, and most of the activity is in Q4 and Q2. Here, the vortical structure is a mirror image of that in the lower wake. Therefore, the contribution to \overline{uv} will be more from Q2 and Q4 than from Q1 and Q3.

For $P(u, w)$, the JPDF and covariance integrand contours are symmetric with respect to w , which must be the case for a two-dimensional mean flow. The symmetry in w results in the nearly zero \overline{uw} , and \overline{vw} covariances across the wake. Due to space limitation, these JPDFs are not illustrated.

The preferred $\pm 45^\circ$ angles of the JPDF contours could indicate a tendency to maximize generation of \overline{uv} . The following illustration explains why. For a unit two-dimensional vector with angle α , the x and y components are, respectively,

$$v_1 = \cos \alpha,$$

$$v_2 = \sin \alpha.$$

The product of these two components is

$$v_1 v_2 = \cos \alpha \sin \alpha.$$

Since the right-hand-side can be expressed as

$$\cos \alpha \sin \alpha = \frac{1}{2} \sin(2\alpha),$$

maximizing the product $v_1 v_2$ is equivalent to maximizing the function $\sin(2\alpha)$. This function is maximum at 90° which makes $\alpha = 45^\circ$.

The JPDF contours of the streamwise and transverse vorticity components $P(\omega_x, \omega_y)$, and the covariance integrand $\omega_x \omega_y P(\omega_x, \omega_y)$ are shown in Fig. 2 for wake positions $\eta = -1.65$ to 1.29 . the vorticity components are nondimensionalized by u_0 and L_0 . The contours of the JPDFs are inclined about the horizontal axis by approximately -45° for the lower wake, and about $+45^\circ$ for the upper wake. The contours of the covariance integrand offer the additional information that there is a greater contribution to the covariance $\overline{\omega_x \omega_y}$ from Q2 and Q4 than from Q1 and Q3 for the lower wake, and vice versa for the upper wake.

Fig. 2 also shows that the projection of the vorticity vector on the $x - y$ plane has a preferred orientation in the direction of the mean shear. This quantitatively illustrates the presence of vortical structures that are most probably inclined at approximately $\pm 45^\circ$ from the wake centerline, which is consistent with the simulation results of Meiburg & Lasheras [3]. They showed that flow structures with streamwise vortices interact with the Kármán vortices to produce three-dimensional closed vortex loops. For these vortex loops, the preferred orientation is along the diverging legs (or braids) of the wake vortical structure, which is also parallel to the axis of the maximum positive strain rate. Approximately perpendicular to this is the preferred orientation for the JPDFs of uv , which are along the converging legs.

Fig. 3 quantifies the quadrant contributions for the velocity covariance, and Fig. 4 for the vorticity covariance. These contributions are calculated by integrating the covariance integrand over the respective quadrants. In the lower wake region ($\eta < 0$) of Fig. 3, the larger magnitudes of Q1 and Q3 compared to Q2 and Q4 come from the higher activity (more occurrence and larger fluctuations) in those former states (see the discussion on Fig. 1). Furthermore, for the outer part of the lower wake, the Q3 activity has lower probability but larger fluctuations than the Q1 activity; thus, Q3 becomes the greatest contributor to the \overline{uv} covariance. It is also observed that the Q3 curve crosses the Q1 curve at $\eta \approx -0.7$ (similarly, Q4 crosses Q2 at $\eta \approx 0.7$); this phenomenon cannot be explained at current writing.

The upper wake sees the opposite trend with Q2 and Q4 playing the bigger role. These observations reveal why the covariance \overline{uv} is positive in the lower wake, near zero in the centerline region, and negative in the upper wake. They also reveal the mechanism for the momentum deficit transport of the streamwise momentum from the centerline region to the outer wake.

Fig. 4 shows that the covariance $\overline{\omega_x \omega_y}$ is positive for the upper wake because Q1 and Q3 contributions are larger than those for Q2 and Q4. This can be traced back to the higher correlation of same-sign ω_x and ω_y for the upper wake in Fig. 2. Other vorticity covariances are about zero across the wake due to symmetry; they cannot be illustrated due to space limitation.

The positive values of $\overline{\omega_x \omega_y}$ in the upper wake could indicate that the diverging leg is the preferred orientation of the vortical structure on the $x - y$ plane, and has a larger contribution than the converging leg. The upper wake can be related to a turbulent boundary-layer in which the positive values of $\overline{\omega_x \omega_y}$ is interpreted by Ong [5] to be an indication of the "hairpin" vortex structures.

CONCLUSION

Discussion of the above results demonstrates that:

- the JPDFs of uv show preferred orientations at $+45^\circ$ from the centerline for the lower wake and at -45° for the upper wake. These flow regions are along the direction normal to the mean shear.

- the JPDF contours of $\omega_x\omega_y$ show a preferred orientation along the direction of the mean shear. The preferred $\pm 45^\circ$ angles of these JPDF contours show consistency with direct simulation results and could indicate a tendency to maximize the generation of $\overline{\omega_x\omega_y}$.

ACKNOWLEDGEMENTS

The author wants to thank Professors Jim Wallace and Barsam Marasli of the University of Maryland, Drs. Frank Peterson and Bruce Douglas of the David Taylor Model Basin, and Dr. Pat Purtell of the Office of Naval Research.

REFERENCES

1. Antonia, R.A., Browne, L.W.B., and Shah, D.A., 1988, "Characteristics of Vorticity Fluctuation in a Turbulent Wake," *J. Fluid Mech.* **189**, pp. 349-365.
2. Hussain, A.K.M.F., and Hayakawa, M., 1987, "Eduction of Large-Scale Organized Structures in a Turbulent Plane Wake," *J. Fluid Mech.* **180**, pp. 193-229.
3. Meiburg, E., and Lasheras, J.C., 1988, "Experimental and Numerical Investigation of the Three-Dimensional Transition in Plane Wakes," *J. Fluid Mech.* **190**, pp. 1-37.
4. Nguyen, P.N., 1993, "Simultaneous Measurements of the Velocity and Vorticity Vector Fields in the Turbulent Near Wake of a Circular Cylinder," PhD Thesis, University of Maryland (USA).
5. Ong, L., 1992, "Visualization of Turbulent Flows with Simultaneous Velocity and Vorticity Measurements," PhD Thesis, University of Maryland (USA).
6. Vukoslavčević, P., Wallace, J.M., and Balint, J.L., 1991, "The Velocity and Vorticity Vector Fields of a Turbulent Boundary Layer. Part 1. Simultaneous Measurement by Hot-Wire Anemometry," *J. Fluid Mech.* **228**, pp. 25-51.
7. Wallace, J.M., and Brodkey, R.S., 1977, "Reynolds Stress and Joint Probability Density Distributions in the $u-v$ Plane of a Turbulent Channel Flow," *Phys. Fluids* **20** (3), p. 351.

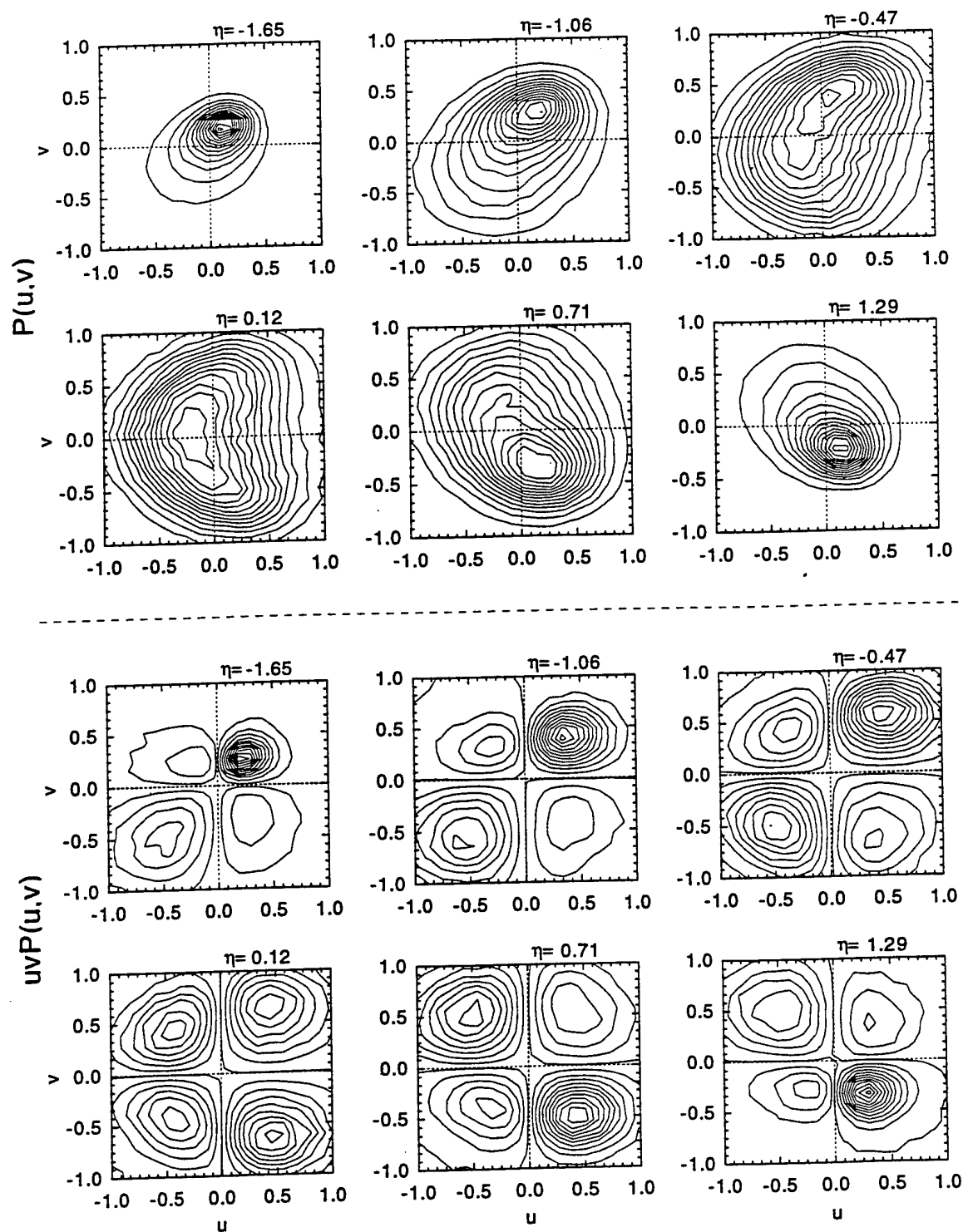


FIGURE 1. JPDF (TOP) AND COVARIANCE INTEGRAND (BOTTOM) CONTOURS FOR THE u AND v VELOCITY COMPONENTS.

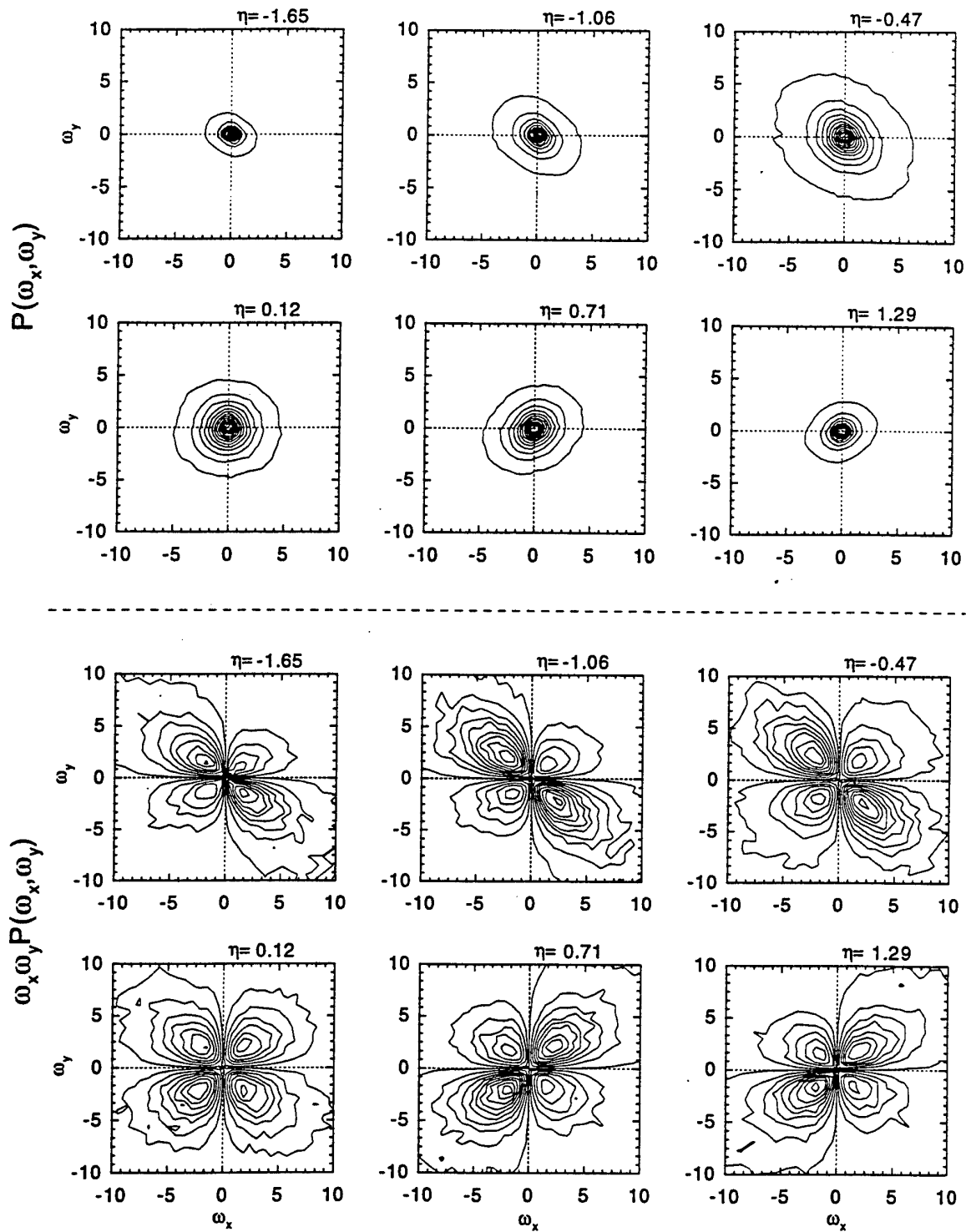


FIGURE 2. JPDF (TOP) AND COVARIANCE INTEGRAND (BOTTOM) CONTOURS FOR THE ω_x AND ω_y VORTICITY COMPONENTS.

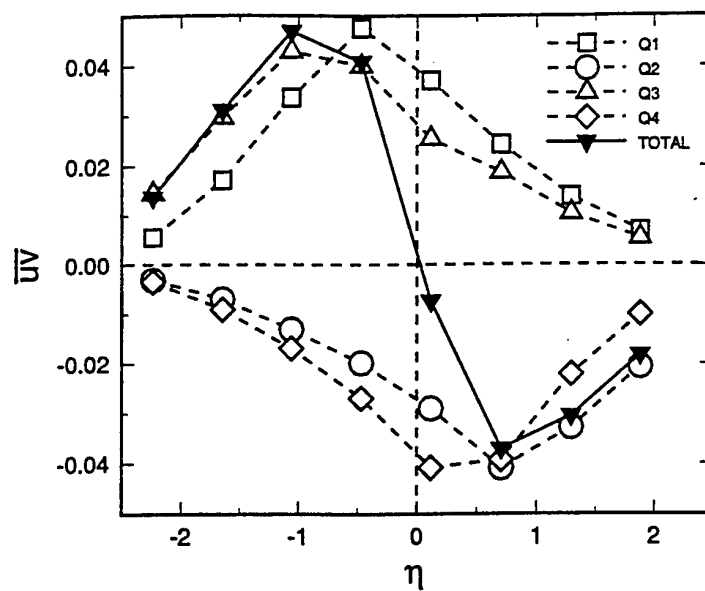


FIGURE 3. QUADRANT ANALYSIS FOR THE CORRELATION \overline{uv} .

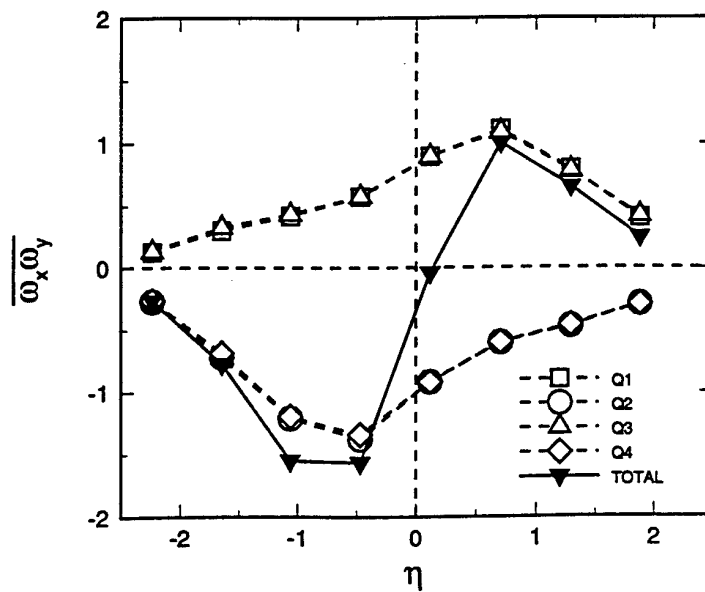


FIGURE 4. QUADRANT ANALYSIS FOR THE CORRELATION $\overline{\omega_x \omega_y}$.

SESSION 6 - EXTERNAL AERODYNAMICS

UTILIZATION OF THE GARTEUR SWEEP WING DATA BASE FOR TURBULENCE MODELS EVALUATION IN BOUNDARY LAYER CALCULATIONS

M. Doussinault, C. Gleyzes, B. Aupoix
ONERA/CERT/DERAT
P.O.Box 4025 - 31055 Toulouse Cédex 04
France

J.H.M Gooden
NLR/NOP
P.O.Box 153 - 8300 AD Emmeloord
The Netherlands

ABSTRACT

Three-dimensional flows are difficult test cases for boundary layer turbulence modeling. Algebraic, two and five-equation models are tested here, in one or two-layer approaches, on the suction and the pressure side of the GARTEUR AD/AG07 wing. Initial and boundary conditions are defined, in direct and inverse mode. Some examples of results are shown (skin friction coefficients, shape factors, turbulence kinetic energy profiles) at 68% of span where the flow is near separation at the suction side trailing edge, and accelerated in the last 30% of chord at the pressure side. The mixing-length model gives good skin friction predictions for this type of three-dimensional flow. The two-layer approach (algebraic - five-equation) and the $k-\epsilon$ models are disappointing. The model proposed by MENTER (derived from WILCOX $k-\omega$ model), used in inverse mode, is the most efficient of the tested models, but has also some difficulties to predict with accuracy this type of flow.

REFERENCE FRAMES AND NOTATIONS

The reference Cartesian coordinate system is noted (X_R, Y_R, Z_R) . X_R and Z_R are in the plane of the tunnel wall on which the model is mounted, Z_R being normal to the tunnel longitudinal axis. Y_R is the incidence rotation axis of the model. For a given section at constant span, C_S is the local chord and X_S is the distance from the leading edge in the reference coordinate system, so that $X^1 = X_S/C_S$ is the dimensionless chord. The dimensionless span $X^2 = Y_R/S$ is also defined, where S is the span of the wing. At last, (X_B, Y_B, Z_B) is the local boundary layer coordinate system. Z_B is the normal direction to the surface of the wing at the considered point. X_B is tangent to the surface, pointing towards the trailing edge in the direction $X^2 = \text{constant}$. Y_B completes this Cartesian system. (U, V, W) and (u', v', w') are the mean and fluctuating components of the velocity the mean magnitude of which is G and deviation angle from $X^2 = \text{constant}$ lines is noted β . Subscripts e and w stand for edge flow and wall conditions, and the subscript 1 means that the velocity is expressed in the boundary layer frame in which the X direction follows the local external streamwise direction.

INTRODUCTION

Experimental data upon three-dimensional turbulent flows close to practical applications are rare. A GARTEUR action group led parallel experiments on this type of flow in the LST wind tunnel of NLR and the F2 one of ONERA. The model is a swept wing on which the pressure distribution in incompressible flow conditions is similar to the one of supercritical transonic wings (FERMIN *et al.*, VAN DEN BERG, GLEYZES *et al.*). Boundary layers are tripped on both sides of the model. The Reynolds number based on the mean chord C is $3.3 \cdot 10^6$, and the incidence is 0.5° . For these experiments, pressure probes (noted S2T in figures), two and four hot-wire probes (respectively noted S2F and S4F), as well as 3D-LDA were used to allow cross-checking. Within the GARTEUR framework, this very detailed database is being used to study performances of classical turbulence models on this type of steady 3D turbulent shear flow.

The suction side is characterized by a strong adverse pressure gradient which leads to a nearly separated flow. The three-dimensional character of the flow is very important : wall deviation is about 50° at the trailing edge. On the pressure side, the flow is decelerated only between 30 and 70% of chord. Downstream, the acceleration induces a nearly collateral flow at the trailing edge. Despite these two different behaviors, the lag of the shear stress vector behind the mean strain rate vector can be observed on both sides of the wing.

The calculation domain is limited from 20 to 95% in chord, and from 8 to 92% in span on the pressure and the suction sides. Each side is calculated separately.

BOUNDARY CONDITIONS

A three-dimensional boundary layer code, 3C3D, has been developed at ONERA/CERT/DERAT since 1990 by HOUEVILLE and MALECKI. The originality of this code is to solve first order boundary layer equations in a local Cartesian system which allows not to compute Christoffel coefficients. Boundary layer equations are discretized following the local streamlines to take strictly into account the influence-dependence domains. It is possible to run calculations in direct or inverse mode.

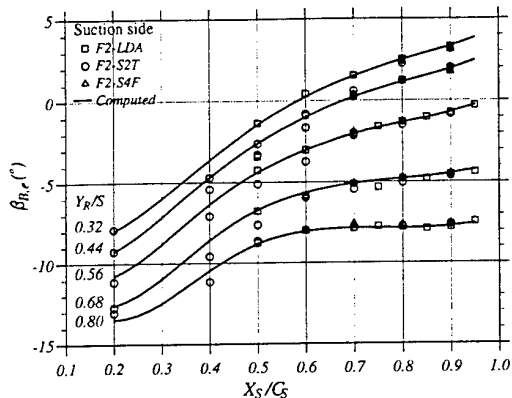


Figure 1: Edge flow conditions : suction-side deviation.

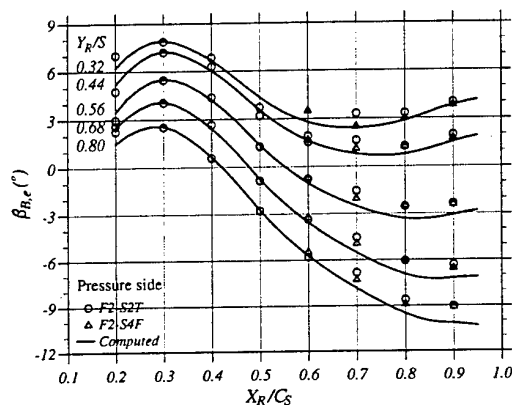


Figure 2: Edge flow conditions : pressure-side deviation.

Direct mode : Edge flow velocity

In this case, edge flow conditions are the velocity magnitude (G_e) and direction ($\beta_{R,e}$). Unfortunately, measured edge flow velocity field is not available on all the surface of the wing. Assuming that the normal pressure gradient is zero, the inviscid wall flow is computed using the experimental wall pressure coefficients and solving the Euler equations on the surface of the wing. This method gives good results on the suction side where the normal pressure gradient is effectively negligible. Mean quadratic differences between calculated edge flow angles and measured ones (0.1° for LDA, 0.5° for S2T) are lower than the accuracy of measurement techniques (Fig. 1). On pressure side, the relatively strong curvature of the wing induces a small normal pressure gradient which might explain that results are not as good as on the suction side (Figure 2) : up to 1° difference between computed and experimental deviations. However, boundary layer thickness is sufficiently thin to neglect the normal pressure gradient in boundary layer calculations.

Inverse mode : Displacement thicknesses

Inverse mode is an interesting approach for nearly separated flows. Longitudinal δ_1 and transverse δ_2 displacement thicknesses deduced from experimental velocity profiles are imposed here as boundary conditions. These thicknesses are not known on a grid fine enough for calculations. They were interpolated at the desired points. The 10 first percent after the initialization line (from 20 to 30% of chord) are calculated in direct mode, and then the calculation is switched to inverse mode.

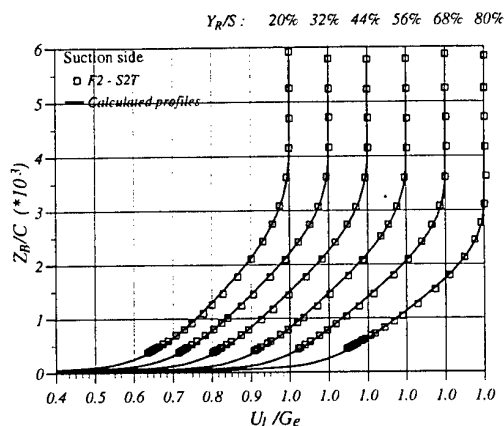


Figure 3: Initial longitudinal velocity profiles. Suction-side.

Lateral conditions

Experimental side boundary conditions are not imposed at the borders of the calculation domain (8 and 92% of span). Conditions imposed on the lateral borders of the calculation domain are those of an infinite swept wing : it is assumed that the flow is invariant in the spanwise direction, that is to say, $\partial/\partial X^2 = 0$. Comparisons with experiments have to be made out of the domain of influence of lateral borders. One can deduce from external and wall streamlines that the domain of validity of the calculation at the trailing edge is reduced and extends from 38 to 74% of span on the suction side and from 26 to 74% on the pressure side.

INITIAL CONDITIONS

To start boundary layer calculations, initial velocity profiles are imposed at 20% of chord. Experimental profiles can not be used directly (because of scatter and lack of measurement points near the wall). Longitudinal profiles are built from the shape factor H and the integral thickness θ_{11} using the GALBRAITH and HEAD analytical expressions. Starting from estimated H and θ_{11} deduced from experimental velocity profiles, H and θ_{11} are optimized in an iterative process to minimize the quadratic error between calculated and experimental profiles (Figure 3, dimensionless longitudinal velocity U_1/G_e function of dimensionless distance normal to the wall Z_B/C). Transverse profiles are built using the integral thickness θ_{21} and the cross-flow angle at the wall β_0 , and assuming they are triangular in polar plots. This assumption is not always verified on the suction side, but cross-flow magnitude is weak compared to edge velocity magnitude (lower than 2%) and does not significantly influence calculations downstream.

TURBULENCE MODELS

Algebraic model

The GARTEUR action group decided that a simple turbulence model should be used by all the participants to facilitate calculation comparisons. The chosen model is an algebraic eddy viscosity model derived from the CEBECI-SMITH mixing length model (noted LMS). It is a two-layer approach model. In the inner layer a mixing-length formulation is used with the VAN DRIEST damping function to express the eddy viscosity $\nu_{t,i}$. In the outer region, eddy viscosity $\nu_{t,o}$ is expressed as a function of the external velocity, the longitudinal displacement thickness and the Klebanoff intermittency function. No junction point is needed as the final expression for the eddy viscosity is :

$$\nu_t = \nu_{t,o} \tanh \left(\frac{\nu_{t,i}}{\nu_{t,o}} \right)$$

Two-layer : algebraic - five-equation model

This model (noted LMS/IP-GL) is also a two-layer model. The LMS model is used in the inner part of the boundary layer. In the outer region, the isotropization of production model (IP) proposed by NAOT *et al.* is used for the redistribution term. The GIBSON-LAUDER damping function (GL) is also used in this model. Five equations are solved (in addition to the momentum and continuity equations) : for the kinetic turbulent energy k , for the dissipation ϵ , for the longitudinal and transverse Reynolds stresses $u'w'$ and $v'w'$ and for the normal Reynolds stress w'^2 . With the thin layer approximation and the IP model, only these three Reynolds stresses are needed for calculation. The junction point is fixed at $z_B^+ = 60$ in wall units. Equations of this model will not be detailed in this paper. For further informations, see MALECKI *et al.* for example.

Two-equations k - ϵ model

The SO-ZHANG-SPEZIALE model (noted k - ϵ SZS in figures) will be the only k - ϵ model presented here. This model gives slightly better results than the other k - ϵ models implemented in 3C3D code in the case of the GARTEUR AD/AG07 wing.

Two-equation k - ω models

A second popular two-equation model is the k - ω model proposed by WILCOX (noted k - ω W88 in figures). The equation for the dissipation ϵ is replaced by an equation for the specific dissipation rate $\omega = \frac{\epsilon}{C_\mu k}$ with $C_\mu = 0.090$.

The advantage of this model is that there is no damping function near the wall and that it performs better in adverse pressure gradient conditions than k - ϵ model. However, MENTER showed that the results of this model depend on the free-stream values of the specific dissipation imposed outside the boundary layer. In the 3C3D code, the imposed value is :

$$\omega_e = \frac{20\sqrt{k_e}}{C_\mu \delta}$$

which has a good numerical behavior, and gives satisfactory results for most of the boundary layer calculations tested. As it is difficult to rely on results that depend so strongly on the value of ω_e , this model is presented for information.

To remove the dependency of the k - ω model to the edge condition, MENTER proposed a new model (noted k - ω SST). Including a cross-diffusion term ($\frac{\partial k}{\partial z} \frac{\partial \omega}{\partial z}$) in the equation for the specific dissipation rate, and using appropriate blending functions, this model behaves like the k - ω model near the wall and like the k - ϵ model in the outer part of the boundary layer. The edge condition is then:

$$\omega_e = \frac{G_0}{L}$$

where G_0 is the upstream free-stream velocity and L is the length of the calculation domain. Taking 0.1 or 10 times the recommended value does not change the solution.

RESULTS AND DISCUSSION

General trends

Some examples of results concerning skin friction and shape factor at 68% of span in direct and inverse mode are given in figures 5 and 6 for suction and pressure side respectively. General trends emerge from these figures. The skin friction is over-estimated, and models are not able to reproduce the plateau between 60 and 100% of chord on the suction side, and to reach the minimum of C_f at 60%

of chord on the pressure side. Inverse mode improves the results. Models underrate the shape factor, even in inverse mode. The wall shear stress deviation (not shown here) is also underestimated in direct mode, but is quite well estimated in inverse mode by LMS and SST models.

Concerning turbulence, dimensionless kinetic energy k/G_0^2 profiles in inverse mode are presented in figures 5e and 6e. Results of Wilcox k - ω model are not presented on these figures because they are similar to SST model ones. Some discrepancies are seen between LDA and hot-wire measurements. Interference between the probe-support and the model, combined with a high local turbulence level may explain these differences. LDA data seem to be more reliable than hot-wire ones. In direct mode (not shown here), turbulence quantities are quite well estimated up to 60% of chord, but downstream, their level decreases to reach an underestimation of 40% on k at 90% of chord. The turbulent layer thickness is also underestimated near the trailing edge. Results obtained on $u'w'$ in direct mode do not differ much with the models (excepted at 80 and 90% of chord on the pressure side) and are 30 to 40% lower than LDA measurements. Inverse mode has an important effect on LMS and LMS/IP-GL models and increases the level of turbulent quantities, which are still lower than experimental ones. The boundary layer thickness is also increased. On other models, inverse mode has not such important effects.

LMS model

On both sides, the algebraic model (solid lines in figures) yields the best prediction as far as the C_f is concerned in direct and inverse mode (Fig. 5a-b, 6a-b). Unfortunately, the shape factor (Fig. 5c-d) and the deviation are largely underestimated on the suction side, and even if inverse mode seems to give better results it is because the external velocity magnitude is underestimated by nearly 10% at 90% of chord (Fig. 4) and induces a more decelerated flow than in the experiment. On the suction side, as all the other models, the turbulent kinetic energy is underestimated (for this model, the kinetic energy is estimated using the turbulence structural parameter, which is supposed to be constant). Till 70% of chord on the pressure side (decelerated part of the flow), the model has the same behavior as on the suction side, but the prediction of the shape factor is better than on the suction side (Fig. 6c-d). Near the trailing edge, the acceleration induces a fall in the turbulence quantities much more important than reported by the experiment (Fig. 6e).

The LMS model seems to be a reasonably good first approach for skin friction estimate in this type of flow. However, it is important to moderate the good results obtained in inverse mode because external conditions are then not well predicted.

LMS/IP-GL model

The two-layer approach with 5 equations in the outer part of the boundary layer (long dashed lines in figures) is somewhat disappointing. It gives reasonably good results for turbulent quantities especially in inverse mode (Fig. 5e, 6e). The general shape of the evolutions of C_f and H is quite well reproduced, but the level of these quantities are not the good ones. Inverse mode improves calculations as it is particularly visible on skin friction coefficient predictions (Fig. 5b, 6b), but the calculated shape factor is still 15% lower than the experimental one (Fig. 5d, 6d). As for the LMS model, the prediction of boundary layer edge conditions are not well predicted in inverse mode.

Even though LMS and LMS/IP-GL have the same turbulence model near the wall, these models do not give the same C_f evolutions. Outer region turbulence model plays an important part in wall shear stress predictions.

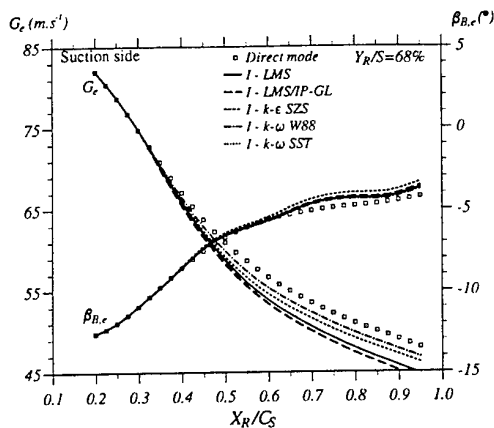


Figure 4: Chord-wise evolution of edge flow velocity (magnitude and direction) calculated in inverse mode. Comparison with direct mode imposed values. 68% of span, suction-side.

k - ϵ SZS model

The k - ϵ model (in short dashed lines in figures) gives, for this flow, quite poor results. The skin friction coefficient is largely overestimated, even in inverse mode (Fig. 5a-b, 6a-b). This induces a great increase of k near the wall. On the suction side, the slope of the H evolution from 40 to 90% is nearly constant in direct and inverse mode whereas there is an experimental break at 60% of chord (Fig. 5c-d). The difficulties of k - ϵ models in adverse pressure-gradient conditions are well illustrated in this flow.

As k - ϵ model results were disappointing, an anisotropic eddy viscosity was introduced in this model following the ROTTA formulation. The value of the anisotropy factor T is taken lower than 1 to create artificial anisotropy. The effect of T factor is important on the wall shear stress direction but is scarcely visible on other quantities, even for weak values of T such as 0.5.

k - ω models

On the suction side, there is scarcely no difference between k - ω W88 (mixed lines) and SST (dot lines) models (Fig. 5). In inverse mode, edge flow computed conditions are the same for both models (Fig. 4). The choice of the external value ω_e for W88 model seems to be appropriate for this case.

In direct mode, k - ω models give the same C_f evolution as LMS model (Fig. 5a) but yields much better shape factor prediction (Fig. 5c). In inverse mode external velocity conditions are quite well predicted (less than 2% of difference between direct and inverse mode edge flow velocity (Fig. 4)). Inverse mode also improves calculations for the friction coefficient and the shape factor (Fig. 5b, 5d). The maximum difference between experimental and calculated shape factor goes from 20 to 8% using direct or inverse mode. For kinetic turbulent energy (Fig. 5e), calculations results are still more than 30% lower than LDA measurements (for the maximum value of k in the boundary layer at 90% of chord). But, contrary to other models, the boundary layer thickness is not overestimated.

On the pressure side (Fig. 6), W88 and SST models do not give the same results particularly for the shape factor (Fig. 6c, 6d). The differences become important downstream of 50% chord. Inverse mode improves moderately the results on SST model (Fig. 6b, 6d) and the edge flow velocity is within 2% of the direct mode one. As the flow is accelerated (70 to 90% of chord) the kinetic energy becomes underestimated, as well as the boundary layer thickness which even decreases between 80 and 90% whereas it goes on increasing (moderately) experimentally.

CONCLUSION

This study points out that first order closure turbulence models (used in industry) are not able to foresee with accuracy this type of practical turbulent shear flow. It seems that, on suction side, turbulence modeling difficulties are principally due to the strong adverse pressure gradient, and to a lower degree, to the anisotropy of eddy viscosity. Taken as a whole, k - ω SST model in inverse mode is the best of the tested models, whereas k - ϵ model gives poor results.

Reynolds Stress Models, which may take into account the lag of the turbulent shear stress direction behind the viscous one, will be tested in this flow soon.

Acknowledgments : Financial support of the ONERA/CERT contribution was provided by the French government agency STPA.

REFERENCES

- B. van den Berg, 1988, "A European collaborative investigation of the three-dimensional turbulent shear layers of a swept wing", AGARD-CP-438.
- T. Cebeci and A.M.O. Smith, 1974, "Analysis of turbulent boundary layers", In *Applied Mathematics and Mechanics*, Vol. 15, Academic Press.
- M.C.P. Firmin and M.A. McDonald, 1988, "The design of the Garteau low aspect-ratio wing for the use in validation of shear layer and overall flow prediction methods", In *FDP Symposium on "Validation of Computational Fluid Dynamics"*, AGARD CP 437 (GARTEUR AD(AG07) TP032), Lisbonne, 2-5 May.
- M.M. Gibson and B.E. Launder, 1978, "Ground effects on pressure fluctuation in the atmospheric boundary layer", In *J. Fluid Mech.*, Vol. 86, n° 3, pp491-511.
- C. Gleyzes, Y. Maciel, J. Cousteix, J.H.M. Gooden, W. Reinders, and B. van den Berg, 1993, "Three-dimensional turbulent flow around the GARTEUR swept wing. Selected features", In *Proceedings of the Ninth Symposium on "Turbulent Shear Flows"*, Kyoto, Japan.
- R. Houdeville, 1992 "Three-dimensional boundary layer calculation by a characteristic method", In *Proceedings of the Fifth Symposium of "Numerical and Physical Aspects of Aerodynamic Flows"*, Long Beach.
- P. Malecki, 1994, "Etude de modèles de turbulence pour les couches limites tridimensionnelles", PhD thesis, EN-SAE, Toulouse.
- P. Malecki, J. Cousteix and R. Houdeville, 1993, "Three-dimensional boundary layer calculations with two-layer turbulence models", 5th IAHR Int. Symposium on Refined Flow Modelling and Turbulence Measurements - Paris, Ed. ENPC, 7-10 Sept.
- F.R. Menter, 1993, "Zonal two equation k - ω turbulence models for aerodynamic flows", *AIAA Paper* 93-2906, 24th Fluid Dynamics Conference, Orlando, FL.
- D. Noat, A. Shavit and M. Wolfshtein, 1973, "Two-point correlation model and the redistribution of Reynolds stresses", *The Physics of Fluids*, Vol. 16, n° 6, pp 738-743.
- J.C. Rotta, 1977, "A family of turbulence models for three-dimensional thin shear layer", In *Proceedings of the First Symposium on "Turbulent Shear Flows"*, University Park, Pennsylvania.
- R.M.C. So, H.S. Zhang, and C.G. Speziale, 1991, "Near wall modeling of the dissipation rate equation", *AIAA Journal*, Vol 29, n° 12, pp 2069-2076.
- D.C. Wilcox, 1988, "Reassessment of the scale-determining equation for advanced turbulence models", *AIAA Journal*, Vol. 26, n° 11, pp 1299-1310.

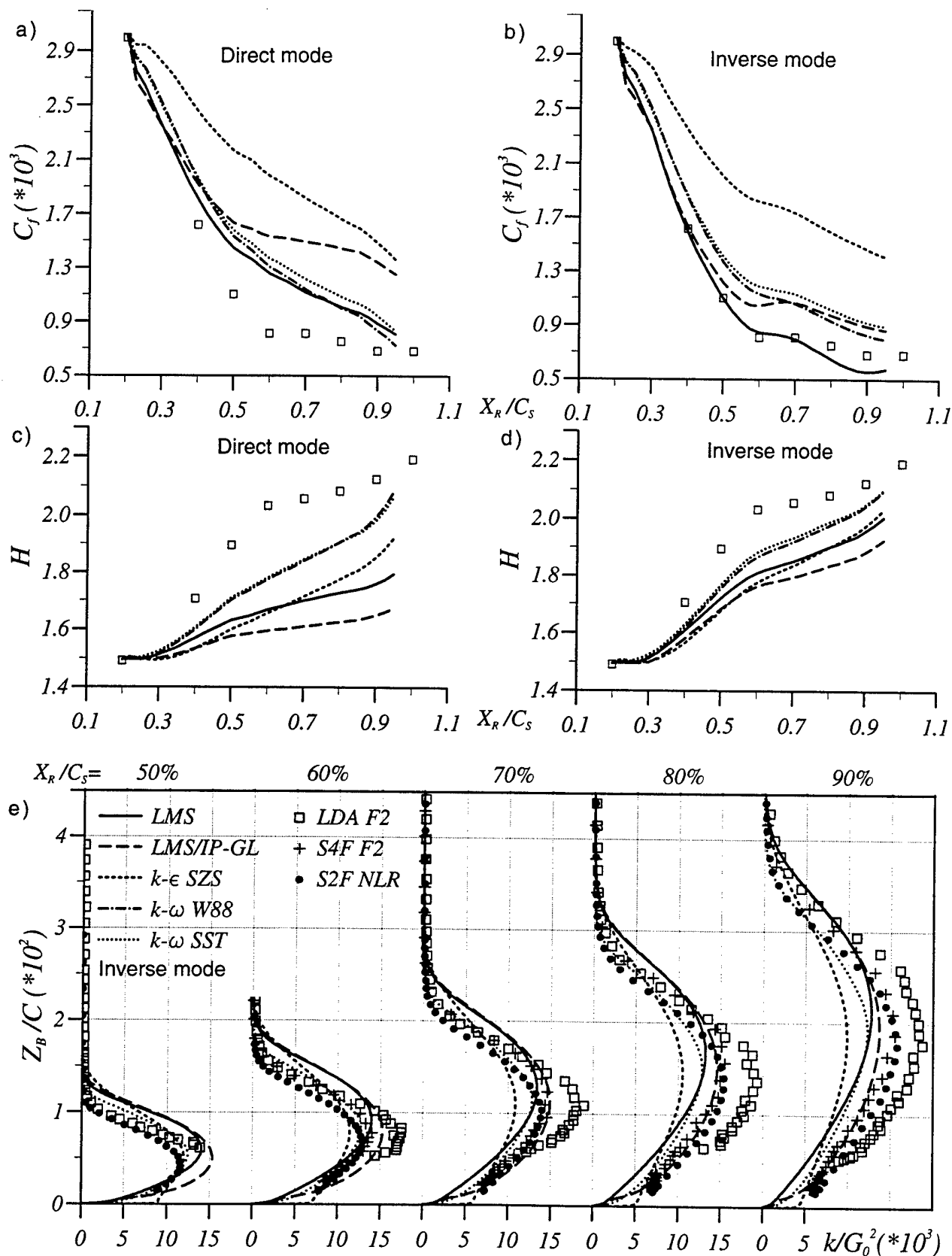


Figure 5: Comparison of different turbulence models with experience at 68% of span. Suction-side. Friction coefficient : a) direct mode; b) inverse mode. Shape factor : c) direct mode; d) inverse mode. e) Kinetic turbulent energy profiles from 50 to 90% of chord in inverse mode.

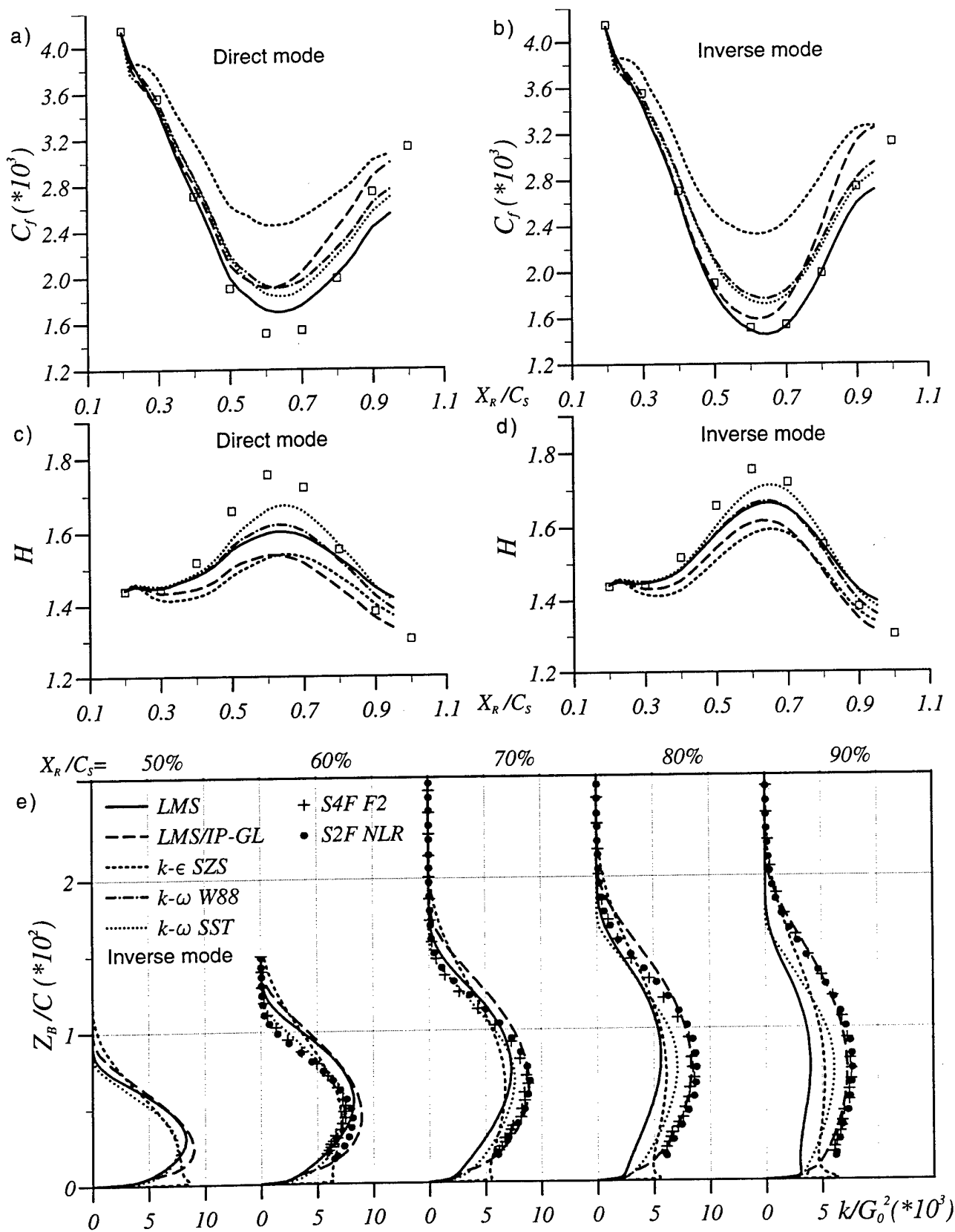


Figure 6: Comparison of different turbulence models with experience at 68% of span. Pressure-side. Friction coefficient : a) direct mode; b) inverse mode. Shape factor : c) direct mode; d) inverse mode. e) Kinetic turbulent energy profiles from 50 to 90% of chord in inverse mode.

Numerical Study of Flow Past a Wing-Body Junction with a Realizable Nonlinear EVM

S. Fu and Z. Zhai

Department of Engineering Mechanics, Tsinghua University
Beijing 100084, PRC

T. Rung and F. Thiele

Hermann-Foettinger Institut fuer Stroemungsmechanik
Technische Universitaet Berlin, D-100623 Berlin, Germany

ABSTRACT

The flow passing a wing-body junction exhibits a number of interesting and important flow physics. In the nose region flow separation occurs and translates into a pair of horse-shoe vortices along the junction as the flow moves downstream. In the downstream tail region separation may occur again due to flow expansion. This study will calculate this flow with three EVMs, the standard BVM and two nonlinear EVMs based on the explicit ASM. Computation Results show that the nonlinear EVMs give more favourable comparison with experiment than the linear EVM.

INTRODUCTION

The present study is a numerical investigation of the characteristics of an incompressible 3-D turbulent boundary layer generated by a wing-body junction flow. Existing studies have shown that the linear eddy-viscosity models (EVM) were found to produce excessive eddy viscosity in regions of strong surface curvature, significant vortical motion or flow acceleration. The physical deficiency in the linear EVM can be attributed to the isotropic assumption of the eddy viscosity which is often incorporated in the linear stress/strain relation leading to the resultant Reynolds shear stress direction same as the local mean velocity gradient angle. Numerous experimental studies on 3-D turbulent boundary layers have indicated that the turbulence structure in this case, with its length and velocity scales, lags the mean flow behavior. Mathematically, this skewness is the inequality of the flow-gradient angle, γ_g , and the turbulent shear-stress angle, γ_r , which are defined as

$$\gamma_g = \tan^{-1} \frac{\partial W / \partial y}{\partial U / \partial y}, \quad \gamma_r = \tan^{-1} \frac{\overline{vw}}{\overline{uv}}. \quad (1)$$

Obviously, the equality of these two parameters is the direct consequence of the linear isotropic EVM.

In order to improve the predictive capability for the wing-body junction flow, progress has been achieved recently to employ advanced turbulence closures which can more accurately resolve the Reynolds-stress anisotropy for complex 3-D flows involving large surface curvatures and strong vortical motions. In particular the second-moment closure of SSG type has been successfully applied to such flow that clearly demonstrated the superior predictive capability in comparison with the performance of simple eddy-viscosity model.

The present work is an attempt to explore the capability of a nonlinear eddy-viscosity model in this complex 3-D boundary layer prediction. The advantage of the nonlinear EVM is that it can reflect more turbulent physics than that returned by the linear EVM while greatly saving the extra amount of computation time required by the second-moment closure as compared with, for instance, model computation. Further, the present nonlinear EVM represents an explicit form of algebraic-stress model derived by Gatski and Speziale [4]. It therefore embodies the important stress production and redistribution mechanisms present in the second-moment closures. The original form of the GS model however violates realizability principle in a manner of giving rise to negative turbulence energy component in many cases especially in regions of significant flow acceleration. This feature obviously represents a major defect in the original ASM and hence in the GS model.

In a recent analysis Fu, Rung and Thiele [3] modified the GS model to remedy this unphysical model behavior. It was shown that the FRT nonlinear eddy viscosity model preserved the realizability property in shear flow, flow with curvature effects as well as in the flow with large distortion. While the analysis made there was mainly for these simple flows but bearing fundamental physics which commonly occur in complex flows, the predictive performance of the model in a real complex flow, such as the flow past a wing-body junction, is still unclear. The objective of the

present work is therefore to further demonstrate the predictive quality of the FRT model. Computation results obtained with the FRT nonlinear eddy viscosity indeed give favorable agreement with experiments over the linear EVM.

MATHEMATICAL FORMULATION

The present study assumes the flow to be incompressible, isothermal and in steady state. For brevity and clarity, the governing equations are written in Cartesian tensor forms.

Mean Flow Equations

The governing equations of the mean flow field, obtained with ensemble-averaging of the Navier-Stokes and continuity equations, consist of:

Reynolds Equation

$$\frac{DU_i}{Dt} = -\frac{1}{\rho} \frac{\partial P}{\partial x_i} + \frac{\partial}{\partial x_j} \left[\nu \left(\frac{\partial U_i}{\partial x_j} + \frac{\partial U_j}{\partial x_i} \right) - \overline{u_i u_j} \right] \quad (2)$$

Continuity

$$\frac{\partial U_i}{\partial x_i} = 0 \quad (3)$$

The Reynolds stresses, $\overline{u_i u_j}$, represent the influence of turbulence on the mean flow field. They are unknowns and need to be evaluated for the momentum equation (2) to be closed, i.e., they need to be modelled.

The GS Model

The derivation of the GS model is based on the equilibrium turbulence assumption from which Rodi (Rodi 1976) proposed the algebraic-stress model. The algebraic form of the Reynolds-stress equation can be written as

$$P_{ij} + \phi_{ij} - \epsilon_{ij} = \frac{\overline{u_i u_j}}{k} (P - \epsilon), \quad (4)$$

where, $P_{ij} = -\overline{u_i u_k} \partial U_j / \partial x_k - \overline{u_k u_j} \partial U_i / \partial x_k$ representing the generation rate of the Reynolds stresses, $P = P_{kk}/2$ and ϕ_{ij} , the pressure-strain correlations representing the mechanism of turbulence redistribution and relaxation. In the linear ϕ_{ij} models the following expression is common to all,

$$\begin{aligned} \phi_{ij} = & -2C_1 \epsilon b_{ij} + C_2 k S_{ij} \\ & + C_3 k (b_{ik} S_{kj} + b_{jk} S_{ki} - \frac{2}{3} \delta_{ij} b_{lk} S_{kl}) \\ & - C_4 (b_{ik} W_{kj} + b_{ik} W_{kj}) \end{aligned} \quad (5)$$

with $b_{ij} = (\overline{u_i u_j} / 2 - \delta_{ij} k / 3) / k$ and

$$S_{ij} = \frac{1}{2} \left(\frac{\partial U_i}{\partial x_j} + \frac{\partial U_j}{\partial x_i} \right) \quad W_{ij} = \frac{1}{2} \left(\frac{\partial U_i}{\partial x_j} - \frac{\partial U_j}{\partial x_i} \right)$$

representing the anisotropy tensor of Reynolds stresses, mean strain rate and vorticity tensors, respectively.

It was shown by Pope [7] from the principle of rational mechanics that, if the turbulence energy and its dissipation rate, or, more precisely, their ratio, k/ϵ , the turbulence time scale, is known or can be otherwise determined, eq.(4) can be solved to provide the analytical solution in which the Reynolds stress $\overline{u_i u_j}$ and strain rate S_{ij} and vorticity W_{ij} are explicitly related as

$$\overline{u_i u_j} = \sum_{\lambda} G^{\lambda} T_{ij}^{\lambda}. \quad (6)$$

Here, T_{ij}^{λ} denote to the tensor expansion in power series with respect to S_{ij} and W_{ij} with the G^{λ} to be the coefficients which are functions of the irreducible invariants of S_{ij} and W_{ij} [7,4]. Because of the solution complexity Pope was then only able to present this expression for 2-D flows (more precisely, for two-component turbulence) by adopting LRR pressure-strain model. The 3-D relation of eq.(6) was later completed by Gatski and Speziale with the aid of a symbolic manipulator [4].

The 3-D explicit formulation of the ASM is however considered to be too elaborate as compared with the 2-D counterpart, for this reason Gatski and Speziale generalized the 2-D relation as a quadratic eddy-viscosity model which reads, after regularization, as

$$\begin{aligned} \overline{u_i u_j} = & \frac{2}{3} \delta_{ij} k - 2\nu_t \left[S_{ij} + \beta_2 \frac{k}{\epsilon} (S_{ik} W_{kj} + S_{jk} W_{ki}) \right. \\ & \left. - \beta_3 \frac{k}{\epsilon} \left(S_{ij}^2 - \frac{1}{3} \delta_{ij} S_{kk}^2 \right) \right] \end{aligned} \quad (7)$$

where, $S_{ij}^2 = S_{ik} S_{kj}$, $S_{kk}^2 = S_{lk} S_{kl}$ and

$$\nu_t = C_{\mu}^* \frac{k^2}{\epsilon}, \quad C_{\mu}^* = \frac{3\beta_1(1+\eta^2)}{3+\eta^2+6\xi^2(1+\eta^2)} \quad (8)$$

and

$$\left. \begin{aligned} \beta_1 &= (2/3 - C_2/2)/g, & \beta_2 &= (1 - C_4/2)/g; \\ \beta_3 &= (2 - C_3)/g, & g &= C_1 + C_5 - 1; \\ \eta^2 &= (\beta_3 S)^2/8, & \xi^2 &= (\beta_2 \Omega)^2/2 \\ S &= (k/\epsilon) \sqrt{2S_{kk}^2} & \Omega &= (k/\epsilon) \sqrt{-2W_{kk}^2} \end{aligned} \right\} \quad (9)$$

The term quadratic to the vorticity tensor is not included in the GS model for the authors found it to be inappropriate in predicting rotating flows.

The RQEVm

The present RQEVm adopts the same mathematical form as that of the GS model but satisfying the realizability principle for a class of fundamental flows. The realizability principle requires that a turbulence model must always provide turbulence quantities satisfying the fundamental physics of turbulence. Specifically, all the kinetic turbulence energy components

should always remain non-negative, i.e.,

$$\overline{u_\alpha^2} \geq 0 \quad (10)$$

must be always true. Any model violating this constraint is said to be *unrealizable*. Apparently, the realizability principle represents the very basic quality on turbulence modelling, however, many of the well-known turbulence models provide, indeed, unrealistic turbulence such as the negative normal stress components. For instance, in the BVM,

$$\overline{u_i u_j} = \frac{2}{3} \delta_{ij} k - 2\nu_t S_{ij}, \quad (11)$$

it is easily seen that the energy component $\overline{u_1^2} = 2k/3 - \nu_t S_{11}$ will be negative in the case of large positive strain rate S_{11} .

However, studies on realizable eddy-viscosity models had received relatively less attention. A reason may be that the explicit stress-strain relation in the eddy-viscosity approach requires the realizability constraint, eq.(10), to be casted in forms of strain rates and vorticities. It is unclear how these mean flow quantities will affect the turbulence realizability. In the development of the RQEVm, a set of fundamental flows, considered to be representative of flow physics, such as plane and curved shear flows, shear flows in noninertial frames and flows under strong stretching, are selected for the realizability analysis on the GS model. While the detailed analysis is omitted here (but can be found in [3]), the RQEVm coefficients are summarized in the following table together with the coefficients relating GL, LRR and SSG models.

Model	β_1	β_2	β_3
RQEVm	0.12	0.21	0.46
GL	2/21	1/7	2/7
LRR	1.07	0.14	0.1
SSG	0.11	0.19	0.18

The governing transport equations for the turbulence kinetic energy k and the dissipation rate ϵ take the conventional form. The nonlinear stress-strain relation (7) however leads to a different expression for the turbulence energy production term G . Here, by definition,

$$G = -\overline{u_i u_j} \frac{\partial U_i}{\partial x_j} = 2\nu_t \left(S_{kk}^2 - \beta_3 \frac{k}{\epsilon} S_{kk}^3 \right). \quad (12)$$

Mathematically, G is not necessarily always positive contrary to the case in the linear EVM. This property shows that the nonlinear EVM is able to reflect relaminarization process which may occur in practice. The coefficients in these equations are the same as the ones proposed by the originators with respect to the Reynolds-stress closures. But in the present RQEVm Fu *et al.* [3] proposed the values for the coefficients $C_{\epsilon 1}$ and $C_{\epsilon 2}$ in the ϵ -equation to be 1.42 and 1.83, respectively.

NUMERICAL IMPLEMENTATION

The present computation adopts the non-staggered grid strategy on a non-orthogonal curvilinear coordinate system. In the solution procedure the partial differential equations for all the transport quantities are written in the following general form:

$$\partial(C_i \phi - D_{i\phi}) / \partial \xi_i = J S_{i\phi} \quad (13)$$

where the coefficients C_i represents convection, $D_{i\phi}$ denotes to diffusion and $S_{i\phi}$ are the source terms with respect to the variable ϕ . J is the Jacobian of the coordinate transformation between the general curvilinear coordinate system ξ_i and a reference Cartesian system x_i with $x_1 = x$, $x_2 = y$ and $x_3 = z$ in the streamwise, normal and spanwise direction respectively. Eq.(13) uses the velocity components defined in coordinates x_i instead of along the grid-aligned directions ξ_i . While the detailed expressions for each component in eq.(13) are written in the same manner as that in Zhu's report [8] for the standard $k - \epsilon$ (linear) EVM, it is worthwhile to highlight here the methodology in which the present nonlinear EVMs are implemented.

Since the Reynolds stresses appear in the diffusion term, thus, denoting the diffusion term in eq.(2) by D_i and substituting the nonlinear stress-strain relation (7) it can be written for the nonlinear EVMs as

$$\begin{aligned} D_i = & \frac{\partial}{\partial x_j} \{ 2\nu_e S_{ij} \\ & + 2\nu_t (k/\epsilon) [\beta_2 (S_{ik} W_{kj} + S_{jk} W_{ki}) \\ & - \beta_3 (S_{ij}^2 - (1/3) \delta_{ij} S_{kk}^2)] \}. \end{aligned} \quad (14)$$

In the curvilinear coordinates, then,

$$\begin{aligned} D_i = & \frac{1}{J} \frac{\partial}{\partial \xi_p} \left\{ \nu_e \frac{B_j^p B_j^q}{J} \frac{\partial U_i}{\partial \xi_q} + \nu_e B_j^p (S_{ij} - W_{ij}) \right. \\ & + 2\nu_t (k/\epsilon) B_j^p [\beta_2 (S_{ik} W_{kj} + S_{jk} W_{ki}) \\ & \left. - \beta_3 (S_{ij}^2 - (1/3) \delta_{ij} S_{kk}^2)] \right\} \end{aligned} \quad (15)$$

with ν_e representing the effective viscosity ($\nu + \nu_t$) and B_j^i the cofactor of the coordinate relation $\partial \xi_i / \partial x_j$ in the Jacobian J .

It is clear in (15) that the first line is identical to the linear EVM formulation while the second and third lines elucidate the nonlinear stress-strain relation. From the numerical computation view point the addition of the nonlinear terms requires no significant effort for the strain rates and vorticities have already occurred in the linear EVM expression in the first line. These strain rates and vorticities are calculated on the control volume faces in a staggered manner to ensure second order accuracy and solution smoothness.

For the boundary conditions no special treatment is required. The present work still adopts the wall function approach to resolve the near-wall turbulence effect.

RESULTS AND DISCUSSION

The flow past a wing-body junction had been studied quite extensively experimentally especially by R. L. Simpson and his coworkers [2,6,5]. The present study attempts to focus on the case in which the wing configuration consists of a 3:2 elliptical-nose NACA 0020 tail body standing on a flat plate with maximum thickness 7.17cm. The nominal reference velocity of the air is $U_{ref} = 27.5\text{m/s}$ and the Reynolds number based on momentum thickness Re_θ is 5940 at 0.75 chord upstream of the nose of the wing on the centreline [6]. This case was chosen for computation is because of the detailed measurement data for all the Reynolds stresses are available at seven stations in the nose region (the detailed location is referred to [6]).

The computation has been performed with three $k - \epsilon$ EVMs, a linear and two nonlinear models, namely, the standard linear EVM with Boussinesq hypothesis, GS-model with SSG coefficients and RQEVM. Fig.1 and Fig.2 give the velocity vectors of the linear EVM and RQEVM results on the computational plane closest to the flat plate and on the symmetry plane ahead of the nose. It is seen that recirculation occurs in the vicinity of the nose and the flat plate. This is consistent with the oil flow visualization in the experiment and the similar computation of Chen [1] with the $k - \epsilon$ model. In Chen's work the computation with second-moment closure revealed a separation prior to the leading edge recirculation, this is however not observed here. The difference between the linear EVM and RQEVM flow patterns is not significant.

Fig.3-Fig.5 show the profiles of mean flow velocities and Reynolds stresses at three stations 3, 5 and 7 representing locations at (-1.33, -2.04), (0.33, -2.94) and (2.17, -3.53) in inches on $x-z$ plane perpendicular to the wing with the x coordinates positive to the downstream and the origin at the nose edge. All quantities in these figures have been nondimensionalized with the local free stream velocity and the maximum wing thickness. The profiles for the streamwise velocity are almost identical among the three model calculations, but apparent difference exists between the computations and experiment. This difference decreases as the flow moves downstream. The agreement in the spanwise velocity profiles is however much better. The difference in the streamwise velocities may be attributed partly to the uncertainties in the inlet conditions in the calculations in which the inlet profiles are taken from boundary layer calculation by matching the momentum thickness. It is not clear whether this is identical to the experimental values.

Unlike the mean-flow velocities the Reynolds-stress profiles differ significantly among computation results. While the uncertainties in the inlet profiles inevitably lead to the discrepancies in the Reynolds stresses especially at upstream locations, at the down-

stream locations the nonlinear EVMs provide overall better agreement with the experiment than that returned by the linear EVM. In fact, the RQEVM results appear to be marginally better than the GS-model results.

Concerning the skewness between the flow-gradient angle γ_g and the shear-stress angle γ_τ , it seems that the differences between $\bar{u}\bar{v}$ and $\bar{v}\bar{w}$ profiles in the linear and nonlinear EVMs represent such behaviour. However, it can be shown analytically that in a genuine 3-D boundary layer flow, where $\partial U/\partial y$ and $\partial W/\partial y$ are the principal velocity gradients, the all the quadratic nonlinear EVMs gives the $\bar{u}\bar{v}$ and $\bar{v}\bar{w}$ shear-stress expressions the same as in the linear model. Thus, the apparent difference in the shear stresses arises due to some other secondary velocity gradients other than the 3-D boundary layer effects. The nonlinear EVMs in the quadratic form can not truly resolve the 3-D boundary layer effects.

CONCLUSION

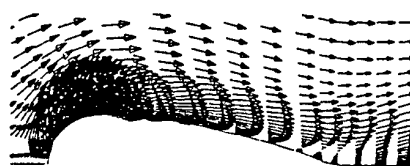
The flow around a wing-body junction has been studied in this work numerically with the standard linear EVM and two nonlinear models namely GS-SSG and RQEVM. All the three models give close results for the mean-flow velocities, but significant differences appear in the Reynolds stresses. The two nonlinear EVMs provide overall better performance than the linear version with the RQEVM marginally superior. But, the 3-D boundary layer skewness is not appropriately captured in the present computation indicating that such 3-D anisotropic effects can not be resolved at the quadratic level for the stress-strain relations.

Acknowledgment The first author appreciates the support of NSFC, State Education Commission of China and Tsinghua University.

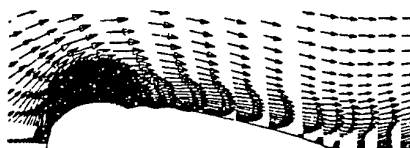
References

- [1] Hamn-Ching Chen. Assessment of a reynolds stress closure model for appendage-hull junction flows. *J. Fluids Engng.*, 117():557-563, 1995.
- [2] R. L. Devnport, W. J. and Simpson. Flow past a wing-body junction-experimental evaluation of turbulence models. *AIAA J.*, 30():873-881, 1983.
- [3] S. Fu, T. Rung, and F. Thiele. *On the realizability of the nonlinear stress-strain relationship for Reynolds-stress closures*. Technical Report, HFI, TU-Berlin, 1996.
- [4] T. B. Gatski and C. G. Speziale. On explicit algebraic stress models for complex turbulent flows. *J. Fluid Mech.*, 254:59-78, 1993.

- [5] S. M. Olcmen and R. L. Simpson. Evaluation of algebraic eddy-viscosity models in 3-d turbulent boundary layer flows. *AIAA J.*, 31():1545-1554, 1993.
- [6] S. M. Olcmen and R. L. Simpson. An experimental study of a three-dimensional pressure-driven turbulent boundary layer. *J. Fluid Mech.*, 290():225-262, 1995.
- [7] S. B. Pope. A more general effective viscosity hypothesis. *J. Fluid Mech.*, 72:331-340, 1975.
- [8] J. Zhu. *FAST-2D: A computer program for numerical simulation of two-dimensional incompressible flows with complex boundaries*. 1991.

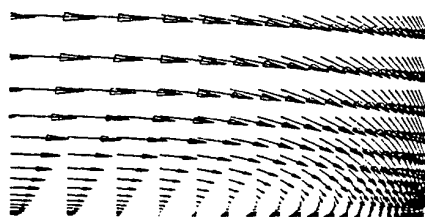


(a) Linear EVM

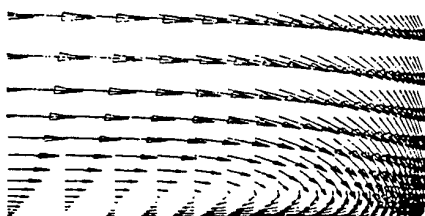


(b)RQEVm

Fig.1 Velocity vectors of flow around a wing-body junction on at a plane near the flat plate.



(a)Linear EVM



(b)RQEVm

Fig.2 Velocity vectors of flow around a wing-body junction on at the symmetry plane ahead of the nose.

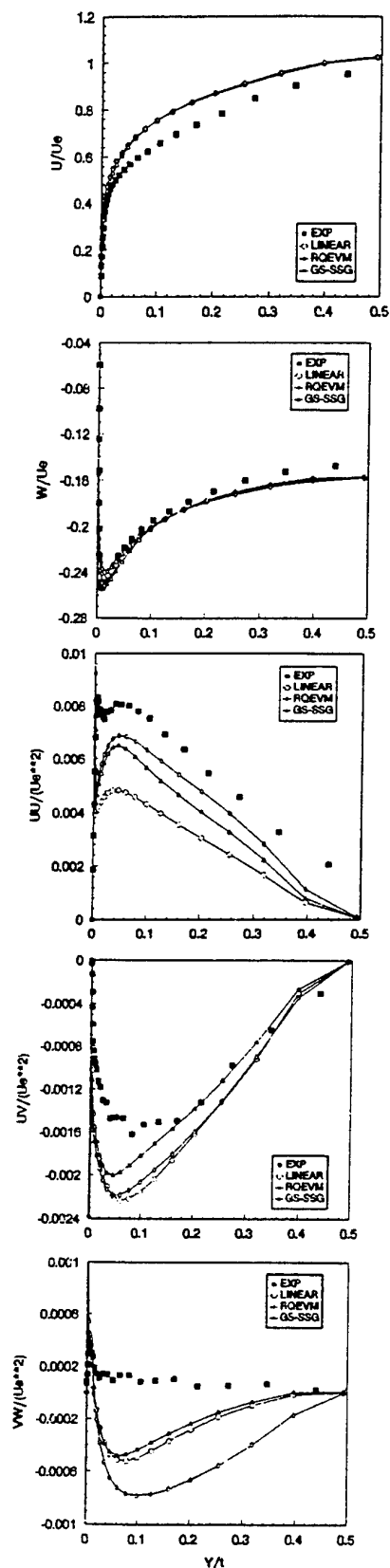


Fig.3 Profiles of mean velocities and Reynolds stresses at station 3.

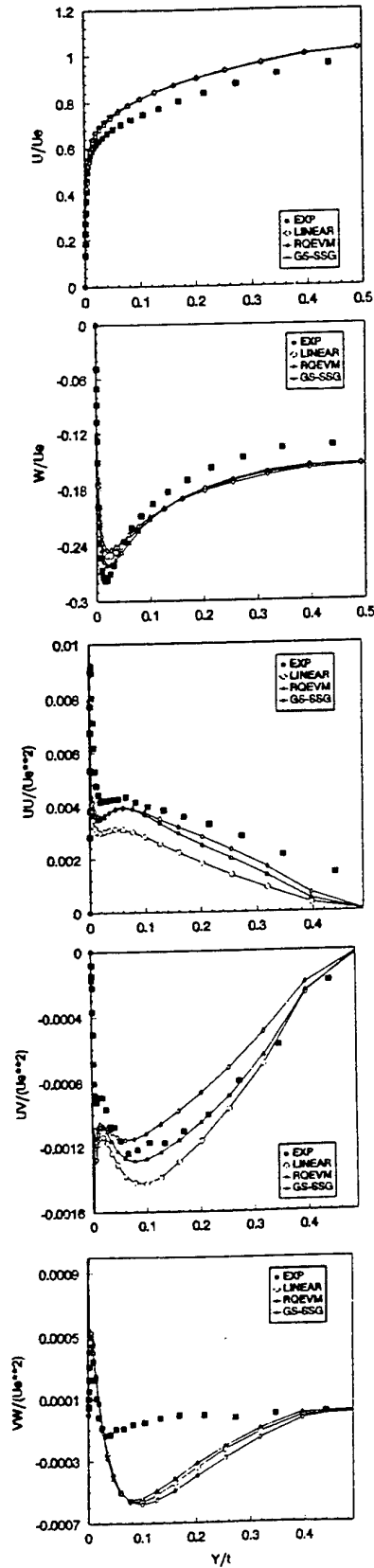


Fig.4 Profiles of mean velocities and Reynolds stresses at station 5.

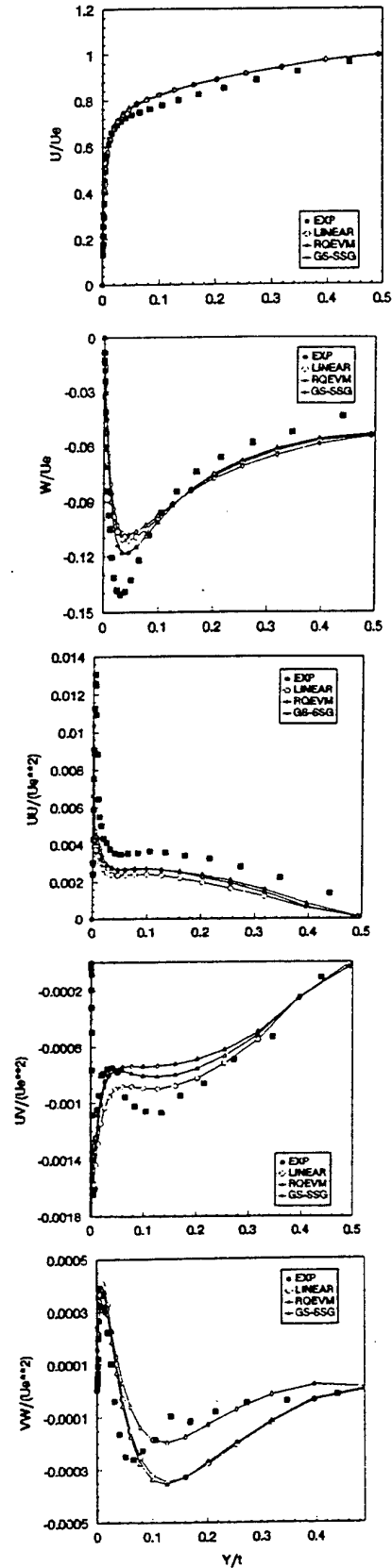


Fig.5 Profiles of mean velocities and Reynolds stresses at station 7.

LARGE EDDY SIMULATION OF THE THREE-DIMENSIONAL TURBULENT BOUNDARY LAYER OVER A SWEEPED BUMP

Xiaohua Wu and Kyle D. Squires

Department of Mechanical and Aerospace Engineering
Arizona State University
Tempe, Arizona 85287-6106, USA

ABSTRACT

Large eddy simulation (LES) and the dynamic eddy viscosity model has been used for prediction of a spatially developing three-dimensional turbulent boundary layer (3DTBL). The 3DTBL is formed when an initially two-dimensional boundary layer encounters a bump swept at 45° with respect to the upstream flow. In the calculations, a zero-pressure gradient, statistically two-dimensional boundary layer at momentum thickness Reynolds number 3800 is introduced one-half chord length upstream of the onset of curvature. The flow is statistically homogeneous along the coordinate parallel to the bump axis and is subject to combined perturbations in streamwise pressure gradient, spanwise pressure gradient, and surface curvature. The angle formed by the mean velocity vector measured with respect to the upstream flow changes sign twice due to the alternating spanwise pressure gradient. Results are presented for a range of grid resolutions and with/without the SGS model. LES predictions are validated through comparison to the experimental measurements of Webster *et al.* (1996). The mean streamwise velocity, the Reynolds normal stresses, the 12 (primary) and 23 (secondary) Reynolds shear stresses are all in excellent agreement with measurements. The mean crossflow velocity and the 13 (secondary) Reynolds shear stress are less accurately predicted.

INTRODUCTION AND BACKGROUND

Spatially developing 3DTBLs are important to a variety of applications, e.g., the boundary layer over a swept wing, around a submerged vehicle, and the flow over turbine or compressor blades. In applications, 3DTBLs are often generated due to a streamwise variation in geometry. A spanwise pressure gradient develops which skews the flow, with the crossflow velocity increasing from zero at the boundary layer edge to a maximum and then back to zero at the wall to satisfy the no-slip condition. The turning of the velocity vector is measured by the angle between the wall shear stress and direction of the freestream flow. In some spatially developing 3DTBLs, this angle will reverse sign with downstream evolution (e.g., see Johnston & Flack 1996, Webster *et al.* 1996). In addition, among the other complicating features of 3DTBLs which have been measured in experiments and direct numerical simulations are that the vector formed by the turbulent stress parallel to the wall is not aligned with the mean strain rate in the outer layer and there is a reduction in the stress-intensity ratio as compared to two-dimensional boundary layers (e.g.,

see Anderson & Eaton 1989, Schwarz & Bradshaw 1994, Simpson & Olcmen 1995, Moin *et al.* 1990, Coleman *et al.* 1996).

These and other features challenge turbulence models and therefore accurate prediction of 3DTBLs remains difficult and continues to be a pacing item for application of computational fluid dynamics to complex flows. Large eddy simulation should be a viable approach for prediction of 3DTBLs since the large, energy-containing scales of motion are computed and only the smallest (subgrid) scales of motion are modeled. This should be an advantage in simulation of complex flows such as 3DTBLs since, although the large eddies may be altered by mean-flow three-dimensionality, streamwise pressure gradient, and other effects resulting from variations in geometry such as curvature, the small eddies probably respond more rapidly to perturbations. Therefore, it is still reasonable to model the small scales using simple closures, especially closures sensitive to local properties of the flow such as dynamic models. In dynamic modeling, the SGS eddy viscosity is calculated using the resolved field rather than being provided as input in advance. This feature allows the model to respond naturally to changes in the turbulence caused by external perturbations. LES and dynamic SGS models have been successfully applied to prediction of a variety of flows (e.g., Germano *et al.* 1991, Meneveau *et al.* 1996, Akselvoll & Moin 1996). Application to complex, spatially developing flows is needed to further advance the technique.

Therefore, the specific aim of this paper is to apply LES to prediction of a complex, spatially developing 3DTBL. In addition, it is also of interest to examine convergence of the LES calculations with changes in grid resolution as well as the role of the dynamic model in the simulations. The main objective is to establish the reliability of the calculations in a complex flow for which high-quality experimental measurements exist. The particular flow considered in this work the boundary layer over a bump swept at 45° with respect to the upstream two-dimensional boundary layer. The bump is formed by three tangential circular arcs (Figure 1). The configuration shown in Figure 1 is considered since boundary layer properties have been reported by Webster *et al.* (1996) and provide a means for evaluation of simulation results. In the experiments a suction slot parallel to the spanwise axis of the bump was used to maintain a direction of statistical homogeneity. A canonical zero-pressure gradient boundary layer at a momentum thickness Reynolds number $Re_{\theta,ref} = 3800$ is introduced one-half chord length upstream of the onset of curvature (the *ref* subscript is used throughout the paper to denote

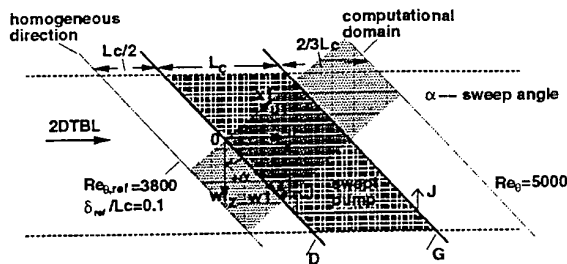


Figure 1: Top view of the computational domain; for bump dimensions, see Webster *et al.* (1996).

values at the upstream reference station). The boundary layer then experiences alternating signs of streamwise pressure gradient, surface curvature, as well as spanwise pressure gradient.

SIMULATION OVERVIEW

The SGS stress tensor appearing in the filtered incompressible momentum equations is closed using the dynamic eddy viscosity model of Germano *et al.* (1991). The model coefficient in the expression for the eddy viscosity is calculated by averaging over the homogeneous spanwise direction in order to eliminate numerical instabilities arising from small values of the denominator (see Meneveau *et al.* 1996 for further discussion). Therefore, the coefficient is time-dependent and a function of the two inhomogeneous coordinates. A clipping function was used to ensure non-negative values following the spanwise averaging.

The origin of the streamwise (x) coordinate is at the onset of curvature (Figure 1). The bump chord/height ratio (L_c/h) is 15.2:1. The height of the computational domain is $10h$ measured from the flat plate ($y = 0$). The length of the upstream and downstream flat plates are $1/2L_c$ and $2/3L_c$, respectively. Because the flow field is homogeneous along the coordinate parallel to the bump axis, LES calculations were actually performed using dependent variables ($u1, v, w1$) in the $(x1, y, z1)$ plane (see Figure 1). Results were then projected back to the experimental (x, y, z) coordinate system.

Measurements from Webster *et al.* (1996) showed that the bump caused a relatively small distortion of the flow at a location one-half chord length upstream of the onset of curvature ($x/L_c = -1/2$ in Figure 1). In order to compare LES predictions to experimental measurements it is necessary to specify in the simulations a realistic, two-dimensional boundary layer at the same location. In the current study, a time-dependent velocity field at the inflow boundary was obtained through a separate LES pre-calculation of a flat plate boundary layer over a continuous momentum thickness Reynolds number range $3600 \leq Re_\theta \leq 4200$ (see Lund *et al.* 1997). As in the experiments of Webster *et al.* (1996), the inlet boundary layer thickness $\delta_{ref} = 1.5h$. At the exit plane a convective boundary condition was used together with a correction on the streamwise velocity to ensure global mass conservation. Over the top surface of the computational domain $\partial u1/\partial y = 0$, $\bar{v} = 0$, $\partial w1/\partial y = 0$ were applied. Periodic boundary conditions were applied in the spanwise direction.

The numerical methodology adopted to solve the momentum and continuity equations is the generalized semi-implicit fractional step method (e.g., see Choi *et al.* 1993). The computational domain is transformed from the Cartesian $(x1, y, z1)$ system to a body-fitted curvilinear nonorthogonal system $(\xi, \eta, z1)$ where η is the coordinate normal to the flat plate. The test filtering operation required in the dynamic modeling procedure was performed

in physical space on the coordinate plane $\eta = \text{constant}$ using a top-hat filter of width equal to two computational mesh spacings. Test filtering is performed numerically by applying Simpson's rule of integration.

In the present LES, the near-wall flow ($0 \leq y_{ref}^+ \leq 25$) was modeled using approximate boundary conditions. The instantaneous wall stress is assumed to be in phase with and proportional to the local velocity at the first plane of grid points (e.g., see Piomelli *et al.* 1989). The instantaneous wall stresses $\tau_{\xi,w}$ and $\tau_{z1,w}$ are calculated from,

$$\tau_{q,w} = \frac{\bar{u}_q(x1, y, z1, t)}{\langle \bar{u}_q \rangle(x1, y, t)} \langle \tau_{q,w} \rangle, \quad q = \xi, z1 \quad (1)$$

where the mean wall stresses $\langle \tau_{\xi,w} \rangle$ and $\langle \tau_{z1,w} \rangle$ were prescribed through interpolation of the experimental skin-friction data of Webster *et al.* (1996). The mean velocities, $\langle \bar{u}_\xi \rangle(x1, y, t)$ and $\langle \bar{w}1 \rangle(x1, y, t)$, are obtained by performing spanwise averaging at each time step during the calculation.

LES predictions were obtained using two grid sizes: $586 \times 51 \times 65$ (referred to as LES1) and $391 \times 51 \times 33$ (referred to as LES2) in the streamwise, wall-normal, and spanwise directions, respectively. In LES1 the length of the computational domain in the spanwise direction is $0.20L_c$ (about two reference boundary layer thicknesses), compared to $0.15L_c$ in LES2 in order to ensure that the spanwise size of the domain was large enough to accurately accommodate large-scale motions. Thus, although the number of grid points along the spanwise direction is decreased by a factor of two from LES1 to LES2, the actual spanwise grid spacing in LES2 is $2/3$ that in LES1. The streamwise grid spacing in LES2 is also $2/3$ of that used in LES1. Based on the friction velocity at the inlet, the spatial resolution in LES1 is $\Delta x^+ = 60$, $\Delta y_{min}^+ > 25$, and $\Delta z^+ = 50$. In LES2 the spatial resolution is $\Delta x^+ = 90$, $\Delta y_{min}^+ > 25$, and $\Delta z^+ = 75$. To assess the overall effect of the model, the LES2 calculation was repeated with the no subgrid model (referred to as LES2n). Using the inlet profile as the initial condition, the flow was allowed to evolve for $100\delta_{ref}/U_{ref}$ at a time step $dt = 0.01\delta_{ref}/U_{ref}$ and statistics were then collected for a period of $200\delta_{ref}/U_{ref}$. Turbulence statistics in the (x, y, z) , $(x1, y, z1)$, (n, s, z) , and $(\xi, \eta, z1)$, and coordinate systems were obtained using standard tensor algebra operations.

RESULTS AND DISCUSSION

The measurements of Webster *et al.* (1996) show that the streamwise pressure gradient $\partial p/\partial x$ changes sign three times over the bump surface, i.e., and favorable near the bump leading/trailing edge, and adverse to adverse at the summit. Because the flow remains homogeneous along the $z1$ axis, the streamwise and spanwise pressure gradients are related via $\partial p/\partial z = -\partial p/\partial x \tan \alpha$. Thus, as the flow passes over the bump, an alternating spanwise pressure gradient causes substantial skewing of the boundary layer, resulting in two sign changes of the near-wall mean flow skewing angle. Figure 2a shows the instantaneous streamlines near the plane of $0.05\delta_{ref}$. Near the leading edge of the bump negative $\partial p/\partial z$ deflects the streamlines towards the direction of $z > 0$ (c.f., Figure 1). The deflection can also be seen in Figure 2b where the mean flow skewing angle, $\tan[\langle w \rangle / \langle u_s \rangle]$, is shown (the s subscript denotes the direction tangent to the bump surface). Because the flow is not directly resolved below $y_{ref}^+ = 25$, Figure 2b only shows contours of the skewing angle above this plane. Over the upstream surface of the bump, the spanwise pressure gradient reverses sign and becomes positive. As a result, near-wall streamlines are skewed towards the negative z direction. Contours of the mean flow skewing angle presented in Figure 2b show that for $1/6 < x/L_c < 5/6$, the

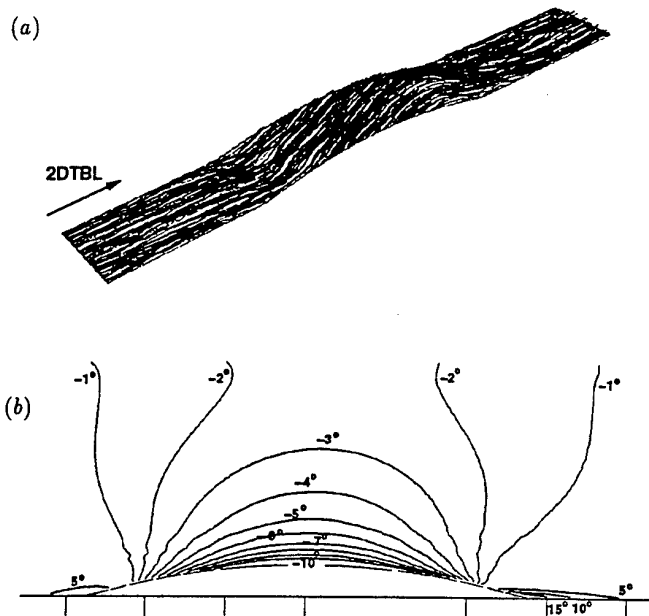


Figure 2: (a) 3D view of instantaneous streamlines near the plane of $y/\delta_{ref} = 0.05$ (LES1); (b) mean velocity skewing angle (LES1).

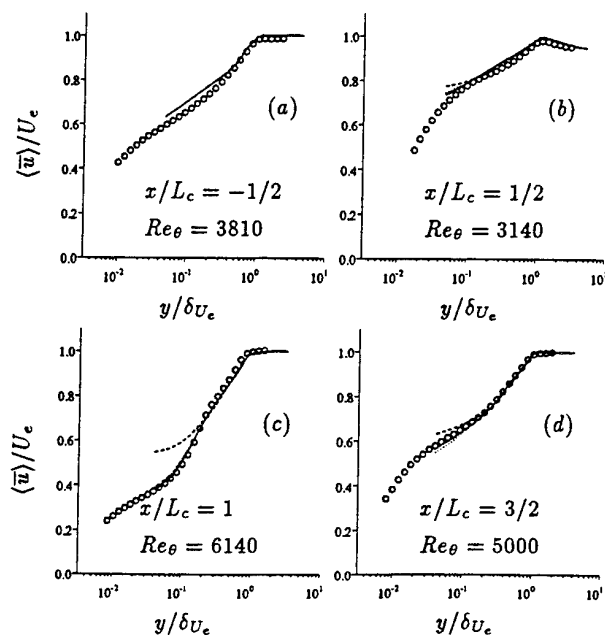


Figure 3: Streamwise mean velocity along vertical traverses. \circ Webster *et al.* (1996), — LES2, LES1, ---- LES2n.

mean crossflow velocity $\langle w \rangle < 0$. It is interesting to note from Figure 2b that near $x/L_c = 1/6$ and $5/6$ there exist two regions where the skewing angle changes sign along the wall-normal direction, which indicates an S-shaped crossflow velocity profile. Near the trailing edge of the bump the spanwise pressure gradient undergoes a step-change from positive to negative. The near-wall streamlines are deflected accordingly towards the positive z direction. Over the downstream flat plate, the boundary layer gradually relaxes towards an equilibrium two-dimensional flow.

Profiles of the mean horizontal velocity $\langle \bar{u} \rangle / U_e$ are shown in Figure 3. The first station ($x/L_c = -1/2$) is at the inflow boundary and the next three stations are downstream of the bump summit. Figure 3a shows the LES pre-computation used to generate the inflow condition yields a mean velocity profile in reasonable agreement with the experiments. When scaled using the friction velocity the predicted inflow velocity exhibits the same logarithmic slope as the experimental measurements but with a slightly higher intercept. As the flow passes the bump, the mean streamwise velocity profile is strongly distorted by pressure gradients and curvature. Distortion of the mean profile is accurately captured in LES1 and LES2 (Figure 3b,c). After the perturbations are removed, the mean streamwise velocity profile over the downstream flat plate quickly relaxes towards the inlet profile (Figure 3d).

At all four stations, predictions of the mean velocity $\langle \bar{u} \rangle$ from LES1 and LES2 also collapse, indicating that the predicted mean streamwise velocity has converged with respect to improved grid resolution. Predictions of $\langle \bar{u} \rangle / U_e$ from case LES2n, using no SGS model, are visibly different from the profiles obtained in LES1 and LES2. Without the subgrid model, the mean flow is over-predicted in the region $y < 0.25\delta_{U_e}$.

LES predictions of the mean spanwise velocity are compared with experiments in Figure 4. In the calculations using the dynamic model (LES1 and LES2), the agreement with measurements is excellent upstream of the bump trailing edge ($x/L_c = 1$), and fairly good at and after the trailing edge. The under prediction of $\langle \bar{w} \rangle$ is probably due to the use of approximate boundary condition, since the peak of $\langle \bar{w} \rangle$ is determined by the combined effects of the no-slip condition and spanwise pressure gradient. The no-slip condition is not enforced for the spanwise velocity, i.e., the approximate boundary condition is applied in order to determine the wall shear stress. It is interesting to note that $\langle \bar{w} \rangle$ changes sign over bump surface downstream of the summit. This sign reversal in the mean spanwise velocity arises because the streamwise variation in geometry results in a streamwise change in the sign of the spanwise pressure gradient (see Johnston & Flack 1996 for further discussion). Similar to the mean streamwise velocity, predictions at the different grid resolutions used in LES1 and LES2 collapse, again indicating adequate resolution of the mean flow. LES2n (no model) predictions exhibit a noticeable difference from those predicted with the model. At the trailing edge the $\langle \bar{w} \rangle$ profile in LES2n deviates from those predicted with model in the region of $y < 0.5\delta_{U_e}$, indicating a stronger effect of the model on the mean spanwise velocity than on the streamwise velocity.

Resolved turbulence intensities are compared with the experimental measurements in Figures 5-7. At the finer resolution used in LES1 the normal stresses \bar{u}'_{rms} , \bar{v}'_{rms} , and \bar{w}'_{rms} are slightly larger than predicted using the coarser resolution in LES2, consistent with the fact that a larger fraction of turbulence kinetic energy is captured with increasing grid resolution. The figures show that both LES1 and LES2 predictions are in excellent agreement with the data of Webster *et al.* (1996). As also noted in Webster *et al.* (1996), profiles of turbulent fluctuations at $x/L_c = 3/2$ have quickly asymptoted towards the upstream unperturbed distributions, indicating a relatively

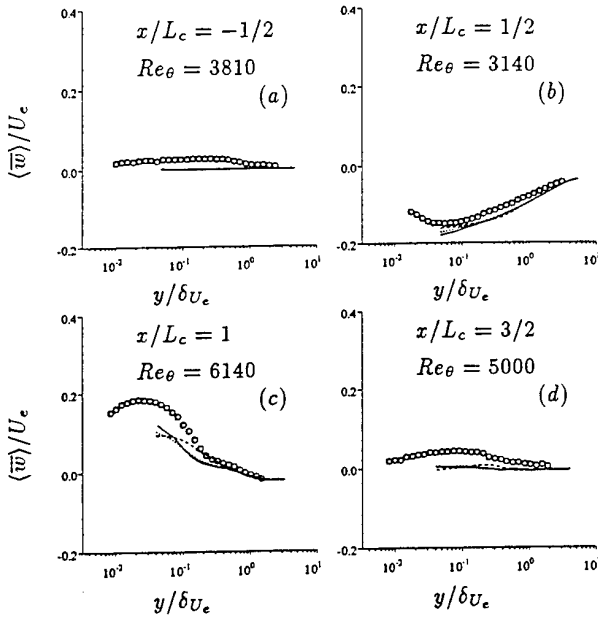


Figure 4: Spanwise mean velocity along vertical traverses. Legend same as Figure 3.

quick return to equilibrium. The rapid relaxation of the turbulence intensities following the removal of perturbations in streamwise pressure gradient and surface curvature has been accurately captured in the LES (e.g., see Figures 6a,d). In the companion two-dimensional boundary layer over the bump, the rapid return occurs through the initiation of an internal layer which is generated near the trailing edge of the bump. A similar effect is apparent in the 3DTBL (see also Webster *et al.* 1996). Turbulence intensities obtained with no SGS model (LES2n) are significantly inaccurate compared to those obtained with the dynamic model (LES1 and LES2). The vertical fluctuations \bar{v}'_{rms} , for example, are over-predicted in LES2n at all stations. Similar over predictions are also apparent in \bar{u}'_{rms} and \bar{w}'_{rms} , although to a lesser degree. These results help to illustrate that the energy transfer accounted for by the dynamic model is crucial to obtaining accurate predictions of the turbulent fluctuating velocities.

Figure 8 shows the resolved part of the primary turbulent shear stress, $-\langle \bar{u}' \bar{v}' \rangle$. Excellent agreement with the experimental data is obtained for both LES1 and LES2, with slightly higher shear stress levels obtained at the finer resolution. It is very significant to note that the LES predictions correctly reproduce the three essential features in the streamwise evolution of the primary turbulent shear stress, i.e., suppression at the summit, elevation near the trailing edge, and rapid return to equilibrium over the downstream flat plate. The strong suppression of $-\langle \bar{u}' \bar{v}' \rangle$ at $x/L_c = 1/2$ is due to the combined effects of convex curvature and favorable pressure gradient. The significant enhancement of the shear stress shown in Figure 8c is due to a large adverse pressure gradient and, to a lesser extent, the downstream concave curvature. As also discussed in Webster *et al.* (1996), the rapid return to equilibrium over the trailing flat results from the growth of an internal layer initiated near the bump trailing edge. Figure 8 also shows without the SGS model (LES2n), the peak value is over-predicted prior to the trailing edge, and under-predicted at and after $x/L_c = 1$.

The secondary turbulent shear stress $\langle \bar{v}' \bar{w}' \rangle$ is compared with the measurements of Webster *et al.* (1996) in Figure 9. Comparison of Figure 8 and Figure 9 shows that the mag-

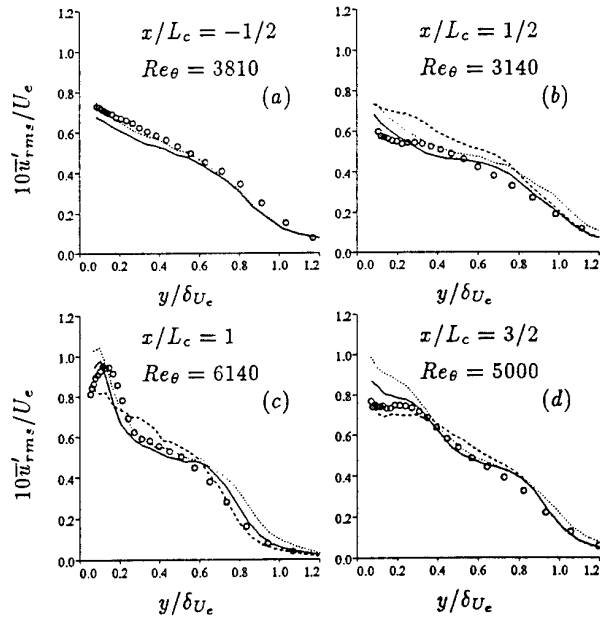


Figure 5: Streamwise turbulence intensity along vertical traverses. Legend same as Figure 3.

nitude of this secondary stress is much smaller than the primary shear stress $-\langle \bar{u}' \bar{v}' \rangle$. Predictions from LES1 and LES2 of $\langle \bar{v}' \bar{w}' \rangle$ are in excellent agreement with the experimental measurements, except for the coarse resolution calculation where a higher peak at the trailing edge is predicted. Figure 8b and Figure 8c indicates near the wall there exist a negative and positive peak in $\langle \bar{v}' \bar{w}' \rangle$ at the summit and the trailing edge, respectively. The behavior of $\langle \bar{v}' \bar{w}' \rangle$ is dominated by its primary production term $\bar{v}'^2 \partial \langle \bar{w} \rangle / \partial y$ (see also Webster *et al.* 1996). This is consistent with the mean spanwise velocity distribution presented in Figure 4, i.e., according to Figure 4, near the wall $\partial \langle \bar{w} \rangle / \partial y < 0$ at $x/L_c = 1/2$, and $\partial \langle \bar{w} \rangle / \partial y > 0$ at $x/L_c = 1$. Figure 9 also shows secondary shear stress levels from LES2n are not as accurate as those obtained using the dynamic model.

Shown in Figure 10 is a comparison of the other secondary shear stress $\langle \bar{u}' \bar{w}' \rangle$. Similar to $\langle \bar{v}' \bar{w}' \rangle$ shown in Figure 9, this component of the shear stress tensor is nearly zero except near the bump trailing edge. Webster *et al.* (1996) pointed out that such a weak magnitude in the secondary shear stresses is an indication that the crossflow has a relatively mild effect. However, it should be noted that at $x/L_c = 1$ both the 23 and 13 components show relatively large peaks, comparable to the primary shear stress level at the inlet, suggesting that mean-flow three-dimensionality has a large local effect. Prior to the trailing edge, the predicted profiles are in good agreement with the experimental measurements. Downstream of the trailing edge, this shear stress component is not as accurately predicted. As discussed in Webster *et al.* (1996), the important production terms for $\langle \bar{u}' \bar{w}' \rangle$ include $\langle \bar{v}' \bar{w}' \rangle \partial \langle \bar{u} \rangle / \partial y$ and $\langle \bar{u}' \bar{v}' \rangle \partial \langle \bar{w} \rangle / \partial y$. Since these quantities are themselves predicted in the LES, inaccuracies in the prediction of the mean spanwise velocity and $\langle \bar{v}' \bar{w}' \rangle$ near the trailing edge of the bump can result in a relatively large error in the predicted $\langle \bar{u}' \bar{w}' \rangle$ component shown in Figure 10c. It is worth noting that in boundary layer analysis the contribution from this secondary stress component is usually neglected (e.g., see Bradshaw 1987, Spalart 1989).

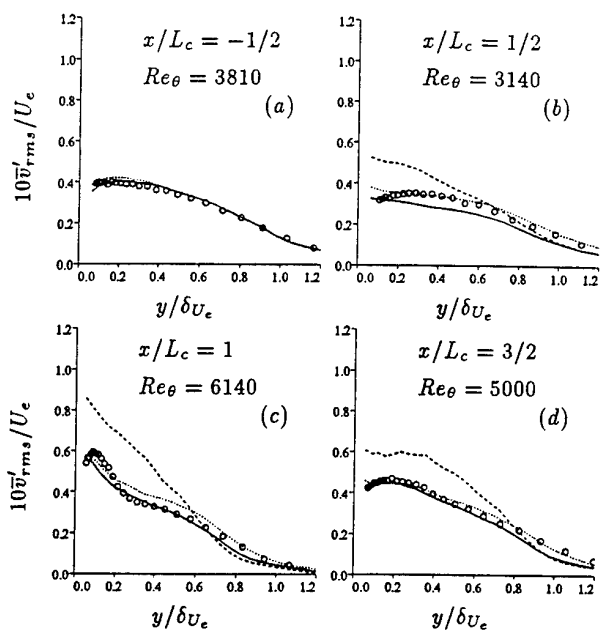


Figure 6: Vertical turbulence intensity along vertical traverses. Legend same as Figure 3.

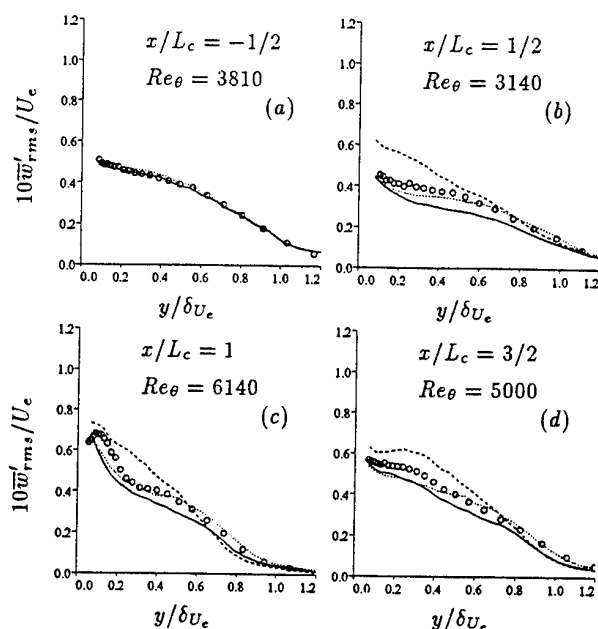


Figure 7: Spanwise turbulence intensity along vertical traverses. Legend same as Figure 3.

SUMMARY

Large eddy simulation and the dynamic eddy viscosity model has been applied to prediction of a spatially developing 3DTBL over a swept bump. Approximate boundary conditions were used to model the near-wall layer. The inflow condition was obtained from a separate pre-calculation of a spatially developing boundary layer and fed into the bump flow simulation. The boundary layer is then strongly distorted by combined perturbations in streamwise pressure gradient, spanwise pressure gradient, and surface curvature.

In general, LES predictions are in very good agreement with the experimental measurements of Webster *et al.* (1996). Strong distortions of the mean flow and turbulence intensities are accurately captured in the calculations. The LES also accurately predicts the strong distortions of the primary turbulent shear stress $-\langle \bar{u}' \bar{v}' \rangle$, e.g., substantial suppression at the summit by convex curvature and favorable pressure gradient, elevation near the trailing edge due to strong adverse pressure gradient, and rapid return towards the (equilibrium) upstream profile over the trailing flat plate following the removal of the perturbations. Compared to the streamwise component, the mean crossflow velocity is not as accurately predicted. Since the crossflow profile is dependent on both the no-slip condition and spanwise pressure gradient, the approximate boundary conditions used in the LES may have a stronger, and possibly more adverse, effect on the spanwise velocity. The secondary shear stress $\langle \bar{w}' \bar{v}' \rangle$ is accurately predicted in the LES and in excellent agreement with the experimental measurements of Webster *et al.* (1996). LES predictions of $\langle \bar{u}' \bar{w}' \rangle$ are less accurate downstream of the trailing edge of the bump in the region where the boundary layer is recovering from perturbations in pressure gradient and curvature. Production of this stress is dependent on the gradient of the mean spanwise velocity and $\langle \bar{w}' \bar{v}' \rangle$. It is possible that combinations of small inaccuracies in these quantities manifest themselves in a relatively larger error in the 13 shear stress.

Finally, simple approximate boundary conditions were used in the LES calculations to model the near-wall layer. The particular form used in this work requires specifica-

tion of the mean wall stresses, which were prescribed using the experimental measurements of Webster *et al.* (1996). Approximate boundary conditions in which the mean wall stress is predicted, rather than prescribed, are currently being implemented and tested. The goal is to further advance LES as a viable tool for prediction of complex flows at high Reynolds number in which it is not possible to directly resolve the near-wall flow.

Acknowledgments

This work is supported by the U.S. Office of Naval Research (Grant Numbers N00014-94-1-0047 and N0014-94-1-1053), Program Officer: Dr. L. Patrick Purtell). The authors gratefully acknowledge valuable discussions with Prof. J.K. Eaton, Dr. T.S. Lund and Dr. D.R. Webster, and Mr. D.A. Degraaff. Simulations were performed on the Cray C90 and T90 at the U.S. Department of Defense High Performance Computing Major Shared Resource Centers (CEWES and NAVO).

REFERENCES

- [1] Anderson, S.D. & Eaton, J.K., 1989, "Reynolds stress development in pressure-driven three-dimensional turbulent boundary layers", *J. Fluid Mech.*, **202**, 263-294.
- [2] Akselvoll, K. & Moin, P., 1996, "Large-eddy simulation of turbulent confined coannular jets", *J. Fluid Mech.*, **315**, 387-411.
- [3] Bradshaw, P., 1987, "Turbulent secondary flows", *Ann. Rev. Fluid. Mech.*, **19**, 53-74.
- [4] Choi, H., Moin, P. & Kim, J., 1993, "Direct numerical simulation of turbulent flow over riblets", *J. Fluid Mech.*, **255**, 503-539.
- [5] Coleman, G.N., Kim, J. & Spalart, P., 1996, "Direct numerical simulation of strained three-dimensional wall-bounded flows", *Exp. Therm. Fluid Sci.*, **13**, 239-251.
- [6] Germano, M., Piomelli, U., Moin, P. & Cabot, W.H., 1991, "A dynamic subgrid-scale eddy viscosity model", *Phys. Fluids A*, **3**(7), 1760-1765.

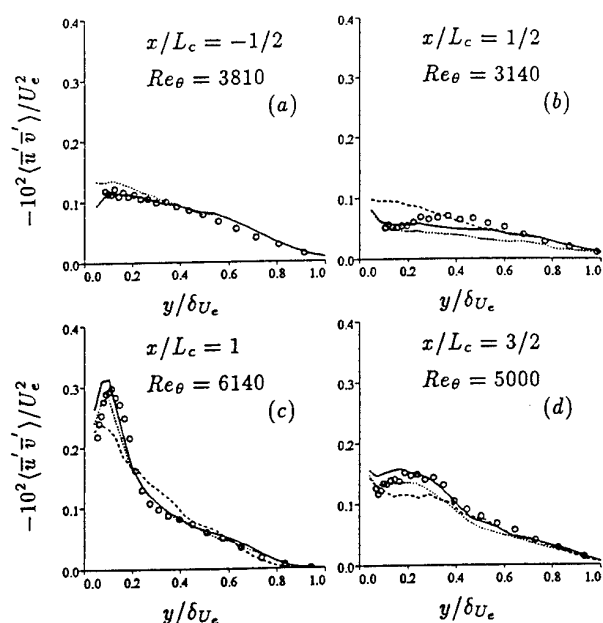


Figure 8: Primary turbulent shear stress along vertical traverses. Legend same as Figure 3.

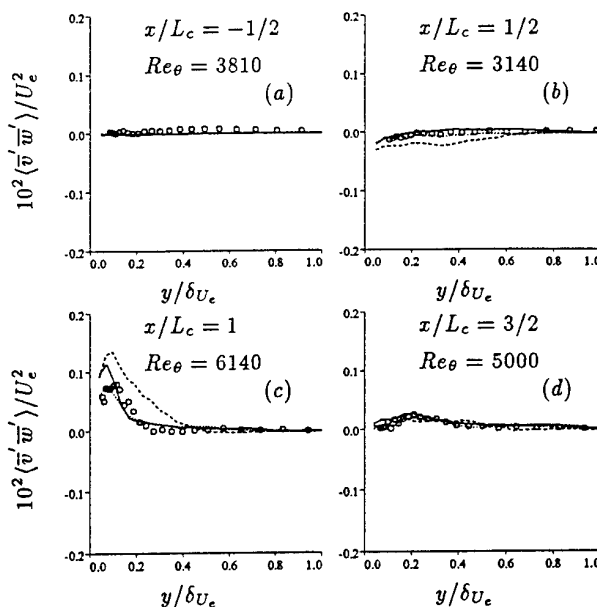


Figure 9: Secondary turbulent shear stress along vertical traverses. Legend same as Figure 3.

- [7] Johnston, J.P. & Flack, K.A., 1996, "Review-advances in three-dimensional turbulent boundary layers with emphasis on the wall-layer regions", *J. Fluids Eng.*, **118**, 219-232.
- [8] Lund, T.S., Wu, X. & Squires, K.D., 1997, "Generation of turbulent inflow data for spatially developing boundary layer simulations", *J. Comp. Phy.*, accepted.
- [9] Meneveau, C., Lund, T.S. & Cabot, W., 1996, "A Lagrangian dynamic subgrid-scale model of turbulence", *J. Fluid Mech.*, **319**, 353-385.
- [10] Moin, P., Shih, T.H., Driver, D. & Mansour, N.N., 1990, "Direct numerical simulation of a three-dimensional turbulent boundary layer", *Phys. Fluids A*, **2**, 1846-1853.
- [11] Piomelli, U., Ferziger, J. & Moin, P., 1989, "New approximate boundary conditions for large eddy simulations of wall-bounded flow", *Phy. Fluids A*, **1**, 1061-1068.
- [12] Schwarz, W.R. & Bradshaw, P., 1994, "Turbulence structural changes for a three-dimensional turbulent boundary layer in a 30° bend", *J. Fluid Mech.*, **272**, 183-209.
- [13] Simpson, R.L. & Olcmen, S.M., 1995, "An experimental study of a three-dimensional pressure-driven turbulent boundary layer", *J. Fluid Mech.*, **290**, 225-262.
- [14] Spalart, P., 1989, "Theoretical and numerical study of a three-dimensional turbulent boundary layer", *J. Fluid Mech.*, **205**, 319-340.
- [15] Webster, D., Degraaff, D. & Eaton, J.K., 1996, "Turbulence characteristics of a boundary layer over a swept bump", *J. Fluid Mech.*, **320**, 1-22.
- [16] Wu, X. & Squires, K.D., 1997, "Large eddy simulation of an equilibrium three-dimensional turbulent boundary layer", *AIAA J.*, **35**, 67-74.

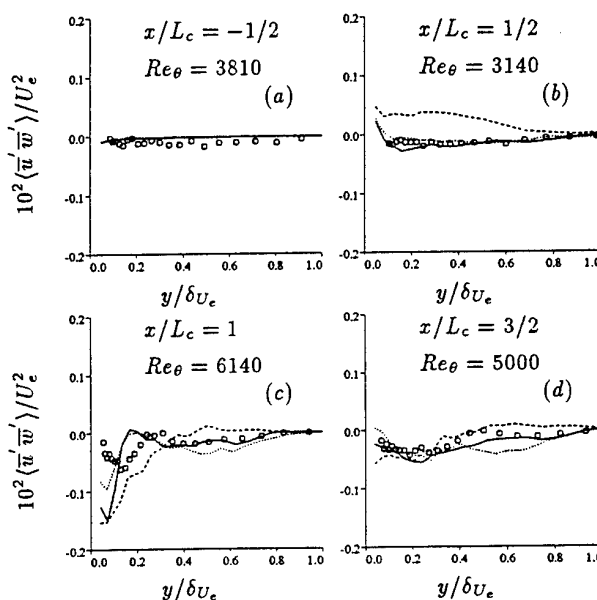


Figure 10: Secondary turbulent shear stress along vertical traverses. Legend same as Figure 3.

NON-LINEAR $\overline{v^2} - f$ MODELLING WITH APPLICATION TO AERODYNAMIC FLOWS

F.S. Lien⁽¹⁾, P.A. Durbin⁽²⁾, S. Parneix⁽²⁾

⁽¹⁾ University of Manchester Institute of Science and Technology
UK

⁽²⁾ Stanford University
USA

ABSTRACT

The $\overline{v^2} - f$ (or $k - \varepsilon - \overline{v^2}$) model has been investigated to quantify its predictive performance on two high-lift configurations: 2D flow over a single-element aerofoil, involving closed-type separation; 3D flow over a prolate spheroid, involving open-type separation. A 'code-friendly' modification has been proposed, which enhances the numerical stability, in particular, for explicit and uncoupled flow solvers. As a result of introducing Reynolds-number dependence into a coefficient of the ε -equation, the skin-friction distribution for the by-pass transitional flow over a flat plate is better predicted. In order to improve deficiencies arising from the Boussinesq approximation, a non-linear stress-strain constitutive relation was adopted, in which the only one free constant is calibrated on the basis of DNS data, and the Reynolds-stress anisotropy near the wall is fairly well represented.

1. INTRODUCTION

Eddy-viscosity models based on the linear Boussinesq relations are known to be afflicted by numerous weaknesses, including an inability to capture normal stress anisotropy, insufficient sensitivity to secondary strains, seriously excessive generation of turbulence at impingement zones and a violation of realizability at large rates of strain. Notwithstanding these defects, eddy-viscosity models remain popular, and their use in complex flows is widespread due, principally, to their formalistic simplicity, numerical robustness, and computational economy. Second-moment closure, on the other hand, accounts for several of the key features of turbulence that are misrepresented by linear eddy-viscosity models, but is considerably more complex and can suffer from poor numerical stability due to the lack of dominance of second-order fragments in the set of terms representing diffusion. As a result, the CPU requirements for second-moment closure models can be high, especially in 3D flows.

A potential alternative to second-moment closure, but one which retains advantageous elements of the linear eddy-viscosity framework, is to use a constitutive relation that equates the Reynolds-stresses to a non-linear expansion in powers of the mean rate of strain and rate of ro-

tation tensors. This may be cast in the form of a sum of terms, each pre-multiplied by an apparent viscosity — hence the term 'non-linear eddy-viscosity models'. Examples include the models of Speziale (1987), Shih et al (1993), Durbin (1995a), Craft et al (1995) and Lien et al (1996).

In Craft et al's $k - \varepsilon - A_2$ model, the A_2 value — the second Reynolds-stress invariant — is obtained by solving a related transport equation as follows:

$$\partial_t A_2 + U \cdot \nabla A_2 = -2 \frac{A_2}{k} (d_k + P_k - \varepsilon) + 2 \frac{a_{ij}}{k} (d_{ij} + P_{ij} + \phi_{ij} - \varepsilon_{ij}), \quad (1)$$

with fragments consistent with second-moment closure. The major drawback with this model is the high level of sensitivity to the near-wall grid parameters, including resolution, distribution and aspect ratio. The $\overline{v^2}$ -equation in Durbin's $\overline{v^2} - f$ model, to be addressed in Section 2, was simplified from second-moment closure on the basis of the IP pressure-strain model in conjunction with elliptic relaxation. This approach is algorithmically simple, applicable to the low-Re region and naturally mimics the kinematic blocking effect on the turbulence of a solid wall.

Another important feature which distinguishes Durbin's model from most others is the expression of eddy-viscosity ν_t , which plays an important role in determining the correct level of shear stress. In Craft et al's model,

$$\nu_t = 0.734 \frac{r_\eta (1 - \exp\{-0.36 \exp(0.75\eta)\})}{1 + 0.35\eta^{1.5}} \times \frac{\sqrt{\varepsilon/\varepsilon} \{1 - 0.8 \exp(-\tilde{R}_t/30)\}}{1 + 0.6A_2 + 0.2A_2^{3.5}} (kT) \quad (2)$$

where

$$r_\eta = 1 + \left[1 - \exp\left(-\frac{A_2^3}{0.125}\right) \right] \left[1 + 4 \sqrt{\exp(-\tilde{R}_t/20)} \right],$$

$$\eta = \max(\tilde{S}, \tilde{\Omega}) r_\eta, \quad (3)$$

and \hat{S} and $\hat{\Omega}$ are strain and vorticity invariants. While in Durbin's model,

$$\nu_t = 0.19 \frac{\overline{v^2}}{k} (kT). \quad (4)$$

One distinct difference between Eqs. (2) and (4) is that the latter does not require any damping function: a result of using $\overline{v^2}$ as the velocity scale in the direction of the wall. The former, on the other hand, sensitizes ν_t to \hat{S} , $\hat{\Omega}$, \hat{R}_t (i.e., Reynolds number) and A_2 , with the functional dependency being carefully calibrated on a range of flows, including straining flow, channel flow, impinging jet and transitional flow. However when this model was tested for turbomachinery flows at (and near) off-design conditions, the size of the leading-edge separation bubble was over-estimated and, in some cases, no converged solution could be obtained. This is due to η (strain and vorticity) and A_2 being too large along the curved shear layer. As a result of both parameters appearing in the denominator of ν_t expression, the level of shear stress was significantly under-predicted (Chen, 1996).

In the present work, the $\overline{v^2} - f$ model of Durbin (1995b) is applied to high-lift configurations, both 2D and 3D. In the course of this study, numerical instability arising from the boundary condition at wall was encountered, due to our use of a solution algorithm that uncouples the $\overline{v^2}$ and f -equations. A 'code-friendly' modification is introduced, which not only circumvents this numerical difficulty, but also gives better predictions for transitional flows. This variant is then combined with the non-linear stress-strain constitutive equation with the aim of improving the near-wall behaviour of normal-stress anisotropy.

2. $\overline{v^2} - f$ MODEL

The turbulence model uses the standard $k - \varepsilon$ equations:

$$\partial_t k + U \cdot \nabla k = P_k - \varepsilon + \nabla \cdot \left[\left(\nu + \frac{\nu_t}{\sigma_k} \right) \nabla k \right], \quad (5)$$

$$\partial_t \varepsilon + U \cdot \nabla \varepsilon = \frac{C_{\varepsilon 1} P_k - C_{\varepsilon 2} \varepsilon}{T} + \nabla \cdot \left[\left(\nu + \frac{\nu_t}{\sigma_\varepsilon} \right) \nabla \varepsilon \right]. \quad (6)$$

On no-slip boundaries, $y \rightarrow 0$,

$$k = 0, \quad \varepsilon \rightarrow 2\nu \frac{k}{y^2}. \quad (7)$$

The $\overline{v^2}$ transport equation is

$$\partial_t \overline{v^2} + U \cdot \nabla \overline{v^2} = kf - n \overline{v^2} \frac{\varepsilon}{k} + \nabla \cdot \left[(\nu + \nu_t) \nabla \overline{v^2} \right], \quad (8)$$

where kf represents redistribution of turbulence energy from the streamwise component. Non-locality is represented by solving an elliptic relaxation equation for f :

$$L^2 \nabla^2 f - f = \frac{1}{T} \left[(C_1 - n) \frac{\overline{v^2}}{k} - (C_1 - 1) - \frac{2}{3} \right] - C_2 \frac{P_k}{k}, \quad (9)$$

where

$$T = \max \left[\frac{k}{\varepsilon}, 6 \left(\frac{\nu}{\varepsilon} \right)^{1/2} \right], \quad L = C_L \max \left[\frac{k^{3/2}}{\varepsilon}, C_\eta \left(\frac{\nu^3}{\varepsilon} \right)^{1/4} \right]. \quad (10)$$

The Boussinesq approximation is used for the stress-strain relation:

$$a_{ij} = \frac{\overline{u_i u_j}}{k} - \frac{2}{3} \delta_{ij} = -\frac{\nu_t}{k} S_{ij}, \quad (11)$$

where the eddy viscosity is given by

$$\nu_t = C_\mu \overline{v^2} T. \quad (12)$$

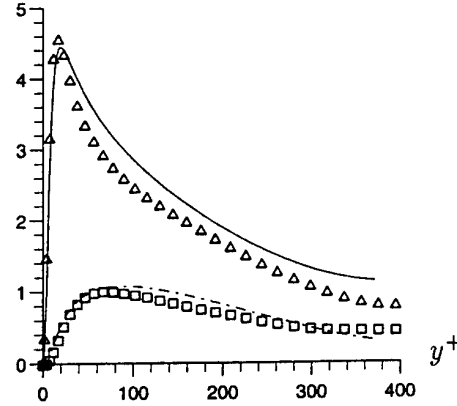


Figure 1: Channel flow: profiles of k and $\overline{v^2}$. DNS: $\triangle k$; $\square \overline{v^2}$.

The constants of the model are:

$$C_\mu = 0.19, \quad \sigma_k = 1, \quad \sigma_\varepsilon = 1.3,$$

$$C_{\varepsilon 1} = 1.55, \quad C_{\varepsilon 2} = 1.9$$

$$C_1 = 1.4, \quad C_2 = 0.3, \quad C_L = 0.3, \quad C_\eta = 70. \quad (13)$$

As $y \rightarrow 0$ — y being the minimum distance to walls — and $k \rightarrow (1/2\nu)\varepsilon y^2$, Eq. (8) becomes:

$$\nu \partial_y^2 \overline{v^2} - 2n\nu \frac{\overline{v^2}}{y^2} = kf. \quad (14)$$

The viscous and kinematic conditions at the wall show that $\overline{v^2}$ should be $O(y^4)$ as $y \rightarrow 0$. In the original $\overline{v^2} - f$ model, $n = 1$, yielding the boundary condition for f

$$f(0) = -\frac{(24 - 4n)\nu^2 \overline{v^2}}{\varepsilon(0)y^4} \Big|_{n=1} = -\frac{20\nu^2 \overline{v^2}}{\varepsilon(0)y^4}. \quad (15)$$

on no-slip walls.

2.1 Code-friendly Modification

Eq. (15) works fairly well for coupled, implicit solvers [e.g. INS2D code of Rogers & Kwak (1990)]. However, for explicit and uncoupled schemes, numerical instability, arising from y^4 in the denominator of Eq. (15), sometimes occurs. Therefore, a code-friendly modification is made here by setting $n = 6$, which allows $f(0) = 0$ to be imposed as the boundary condition. In addition, $C_{\varepsilon 1}$ and $C_{\varepsilon 2}$ are replaced by

$$C_{\varepsilon 1} = 1.55 + \exp(-A_\varepsilon R_y^2) \Big|_{A_\varepsilon=0.00285}, \quad C_{\varepsilon 2} = 1.92, \quad (16)$$

where $R_y = y\sqrt{k}/\nu$, and the other model constants are:

$$C_\mu = 0.19, \quad \sigma_k = 1, \quad \sigma_\varepsilon = 1.5,$$

$$C_1 = 1.4, \quad C_2 = 0.3, \quad C_L = 0.17, \quad C_\eta = 70. \quad (17)$$

Fully-developed Channel Flow.

The model constants, in particular $A_\varepsilon = 0.00285$ and $C_L = 0.17$, were first calibrated with the channel-flow DNS data of Kim et al (1987) and then optimized on the basis of 2D/3D separated flows to be presented later. As seen in Fig. 1, the turbulence profiles of k and $\overline{v^2}$ agree reasonably well with the data.

Transitional Flow over a Flat Plate.

The second case examined here is the flow over a flat plate with free-stream turbulence intensity $T_u = 3\%$ and dissipation length scale $\ell_\varepsilon^\infty = 10$ mm. The experimental

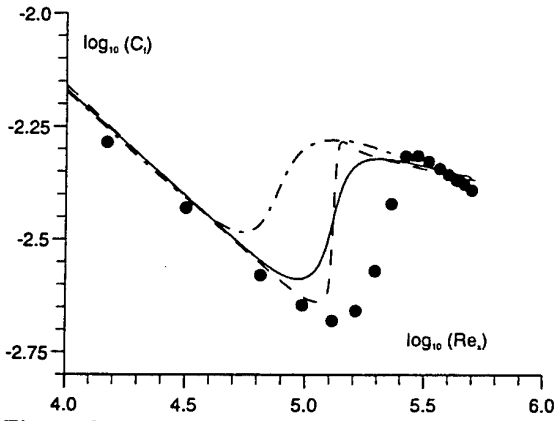


Figure 2: Flat plate: skin-friction distributions. • expt.; ---- $k-\epsilon$; -.-.- original \bar{v}^2-f ; — modified \bar{v}^2-f .

study was conducted at Rolls Royce Aeroengines in Derby, UK. The skin-friction distributions, obtained with the original and code-friendly \bar{v}^2-f variants and Launder-Sharma model (1974), are shown in Fig. 2. As seen, introducing the Re_τ -dependency in $C_{\epsilon 1}$ for the code-friendly variant improves transition predictions. Although the resulting onset of transition is slightly earlier than that returned by the Launder-Sharma model, the length of transition is better represented.

2.2 Non-linear Constitutive Relation

A general constitutive relation of the type proposed by Pope (1975) can be written as:

$$a_{ij} = \frac{\bar{u}_i \bar{u}_j}{k} - \frac{2}{3} \delta_{ij} = \sum_{\lambda=1}^{10} G^\lambda(S_{ij}, \Omega_{ij}, \bar{v}^2/k, T) T_{ij}^\lambda. \quad (18)$$

where $T_{ij}^1 = S_{ij}$, $T_{ij}^2 = S_{ik} \Omega_{kj} - \Omega_{ik} S_{kj}$, $T_{ij}^3 = S_{ik} S_{kj} - \frac{1}{3} \delta_{ij} S_{ik} S_{kl} \dots$. Truncating at the third term for simplicity gives rise to

$$a_{ij} = -\frac{\nu_t}{k} S_{ij} + G^2(S_{ik} \Omega_{kj} - \Omega_{ik} S_{kj}) + G^3(S_{ik} S_{kj} - \frac{1}{3} \delta_{ij} S_{ik} S_{kl}), \quad (19)$$

where

$$S_{ij} = \frac{\partial U_i}{\partial x_j} + \frac{\partial U_j}{\partial x_i}, \quad \Omega_{ij} = \frac{\partial U_i}{\partial x_j} - \frac{\partial U_j}{\partial x_i}. \quad (20)$$

Two constraints for parallel flow will be imposed:

$$a_{22} = a_{\bar{v}^2}, \quad a_{11} = \alpha a_{22} = \alpha a_{\bar{v}^2}, \quad (21)$$

where $a_{\bar{v}^2} = \frac{\bar{v}^2}{k} - \frac{2}{3}$. These yield

$$G^2 = \frac{1}{4} \frac{(1-\alpha)a_{\bar{v}^2}}{S^2} \left(\frac{k}{\epsilon}\right)^2, \quad G^3 = \frac{3}{2} \frac{(1+\alpha)a_{\bar{v}^2}}{S^2} \left(\frac{k}{\epsilon}\right)^2, \quad (22)$$

where $S = \frac{k}{\epsilon} \left| \frac{\partial U}{\partial y} \right|$ or $(= \frac{k}{\epsilon} \sqrt{S_{ij} S_{ij}/2})$, in general). The remaining unknown, α , can be evaluated from DNS data of channel flow (Kim et al, 1987) and boundary-layer flow (Spalart, 1988). As seen in Fig. 3,

$$\alpha = -1 - \frac{6S}{15 + 10S} \quad (23)$$

fits DNS data reasonably well. In order to apply Eq. (19) to mean-flow prediction, while preventing computational intractability, the S^2 in the coefficients G^2 and G^3 above needs to be replaced by $S^2 + 1$.

3. NUMERICAL METHOD

All flows have been computed with the STREAM general geometry, block-structured, finite-volume code (Lien

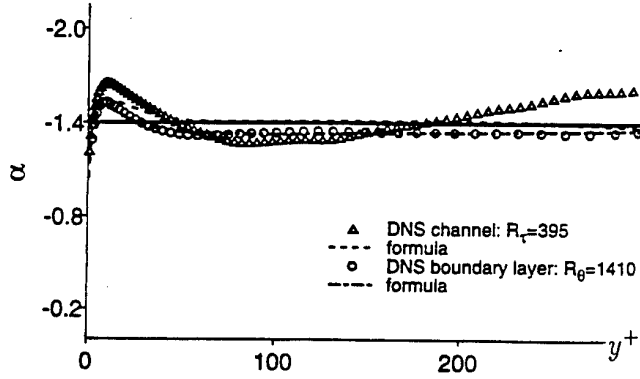


Figure 3: Correlation of α in the non-linear constitutive equation with DNS data. DNS channel ($Re_\tau = 395$) Δ ; formula, ----. DNS boundary layer ($Re_\theta = 1410$): \circ ; formula, -.-.-.

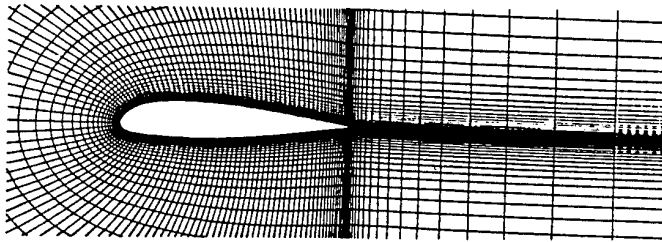


Figure 4: A-aerofoil: geometry and partial grid

& Leschziner, 1994a). Advection is approximated by a TVD scheme with the UMIST limiter (Lien & Leschziner, 1994b). To avoid checkerboard oscillations within the co-located storage arrangement, the "Rhie and Chow" interpolation method (1983) is used. The solution is effected by an iterative pressure-correction SIMPLE algorithm, applicable to both subsonic and transonic conditions.

4. RESULTS AND DISCUSSION

4.1 Aerospatiale A-aerofoil

Computations for the A-aerofoil have been performed at 13.3° incidence, with transition on the suction side prescribed at 12% of chord. The geometry and a partial view of the grid are given in Fig. 4. The Reynolds number, based on free-stream velocity and chord length, is 2.1×10^6 . Solutions have been obtained on a grid containing 177×65 lines, extending to 10 chords into the free stream.

In total, four turbulence-model variants have been applied to this case [comparisons to second-moment closure can be found in Lien & Leschziner (1995)]:

1. the low-Re $k-\epsilon$ model of Lien & Leschziner (1993);
2. the original $k-\epsilon-\bar{v}^2$ model of Durbin (1995b);
3. the code-friendly variant;
4. the above variant combined with the non-linear stress-strain relation.

The skin-friction and wall-pressure distributions obtained with three linear eddy-viscosity models, one $k-\epsilon$ and two \bar{v}^2-f , are compared in Fig. 5. These, as well as the associated profiles of streamwise velocity and shear stress on the suction side in Fig. 6, clearly demonstrate the

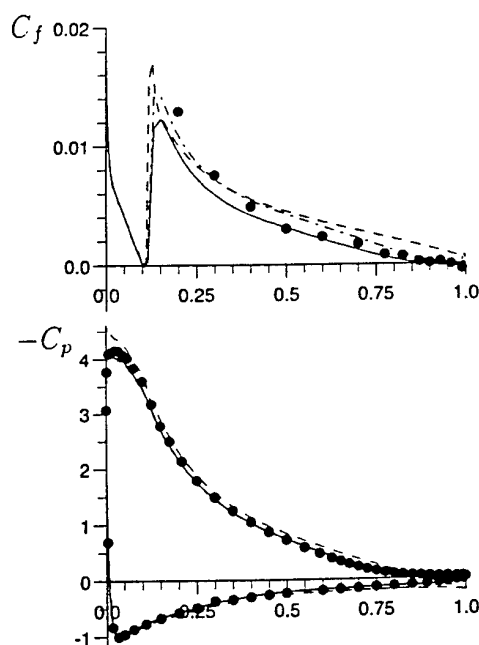


Figure 5: A-aerofoil: (Top) skin friction; (Bottom) pressure coefficient. • expt.; ---- $k - \epsilon$; — original $\overline{v^2} - f$; -.- modified $\overline{v^2} - f$.

superiority of $\overline{v^2} - f$ variants relative to the conventional $k - \epsilon$ model.

Attention is turned next to comparisons between linear and non-linear $\overline{v^2} - f$ models in Fig. 7 for profiles of streamwise velocity and Reynolds normal-stresses. It is found from these figures that the Reynolds-stress anisotropy is fairly well predicted by the non-linear model at $x/c=0.5$, which is consistent with the constraints in Eq. (21) imposed on the constitutive equation. As the flow approaches the trailing edge, streamline curvature arising from secondary strain becomes important and the omission of its production term ($\sim \frac{\partial v}{\partial x}$) in the $\overline{v^2}$ -equation is no longer valid, resulting in large discrepancies between predictions and data at $x/c=0.9$.

4.2 DLR Prolate Spheroid

An overview of the geometry, including the surface streaklines, is conveyed in Fig. 8. The Reynolds number, based on the chord, is 6.5×10^6 . Computations have been performed at 30° incidence in which transition is free. The solution domain, containing $64 \times 128 \times 64$ lines, extends 10 chords into the outer stream.

Numerical solutions have been obtained with two models:

- the low-Re $k - \epsilon$ model of Lien & Leschziner (1993);
- the code-friendly non-linear $\overline{v^2} - f$ variant in conjunction with Launder and Kato's modification in the turbulence production P_k (1993).

A well-known defect of any conventional, linear eddy-viscosity model is that it predicts excessive levels of turbulence energy in impingement regions, due to the fact that the irrotational strains appearing in the turbulence-energy equation ($\sim S_{ij}S_{ij}$) act to generate turbulence irrespective of their signs. The rationale behind Launder & Kato's proposal is to partially replace the strain by the vorticity,

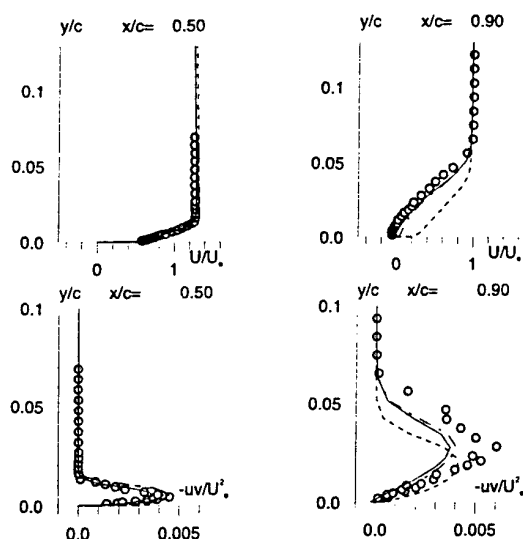


Figure 6: A-aerofoil: (Top) profiles of streamwise velocity; (Bottom) profiles of shear-stress. o expt.; ---- $k - \epsilon$; — original $\overline{v^2} - f$; -.- modified $\overline{v^2} - f$.

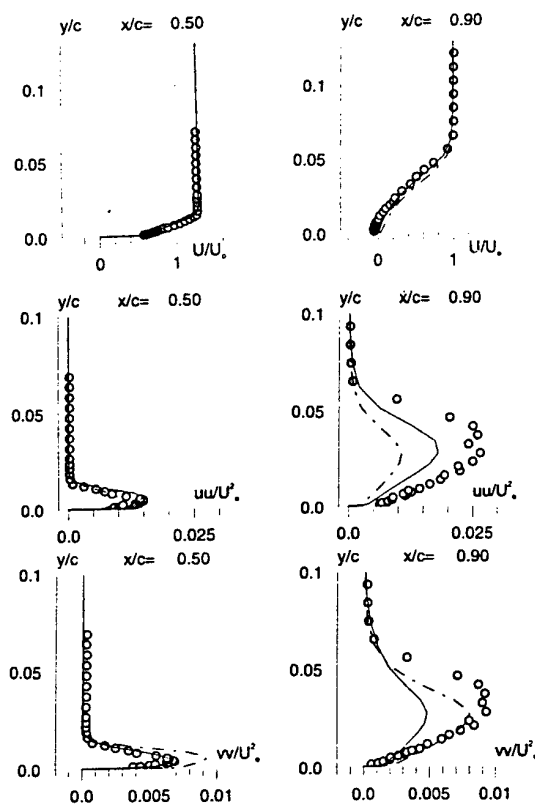


Figure 7: A-aerofoil: (Top) profiles of streamwise velocity; (Middle) profiles of streamwise normal stress; (Bottom) profiles of transverse normal stress; o expt.; ---- linear $\overline{v^2} - f$; — non-linear $\overline{v^2} - f$.

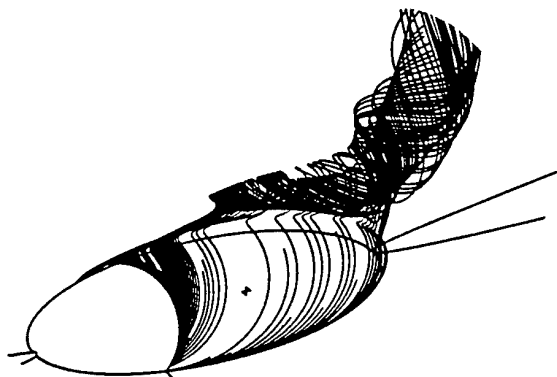


Figure 8: Prolate spheroid: geometry and streaklines.

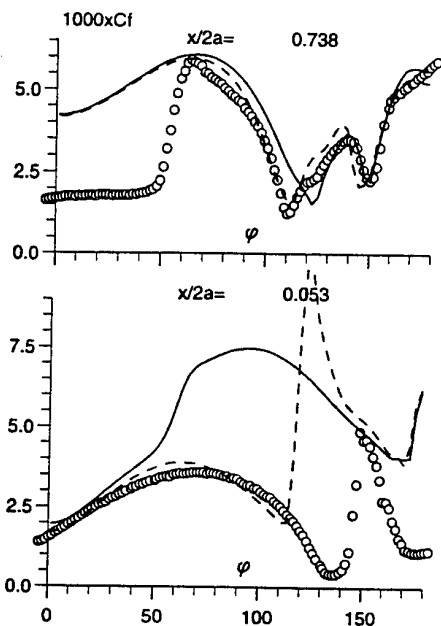


Figure 9: Prolate spheroid: skin-friction magnitude. \circ expt.; $—$ $k - \epsilon$; $----$ non-linear $\overline{v^2} - f$.

i.e.

$$P_k = 0.5\nu_t S_{ij}\Omega_{ij}. \quad (25)$$

A similar idea, based on 'realizability' constraints on the turbulence time scale, has been suggested recently by Durbin (1996), in which an upper bound to k/ϵ proportion to $\sqrt{2/S_{ij}S_{ij}}$ was introduced.

Azimuthal variations of skin-friction magnitude at two streamwise locations are shown in Fig. 9, and the circumferential distributions of wall pressure are given in Fig. 10. As seen at $x/2a=0.053$, the non-linear $\overline{v^2} - f$ model in conjunction with Launder & Kato's modification returns a transition-like behaviour in the boundary layer close to the windward side. Although the model is unable, on fundamental grounds, to predict any aspect of *natural* transition, the predicted transitional phenomenon is mainly due to a strong suppression of turbulence energy at the impingement regions, in which the flow becomes 'laminar', combined with the fact that the free-stream turbulence diffuses into the boundary layer, and ultimately triggers transition. It is clear from Fig. 10 that the extent of pressure plateau at $x/2a=0.73$, signifying the azimuthal extent of separation zone, is better predicted by the non-linear $\overline{v^2} - f$ variant than the $k - \epsilon$ model.

5. CONCLUSIONS

A computational study has been undertaken to investi-

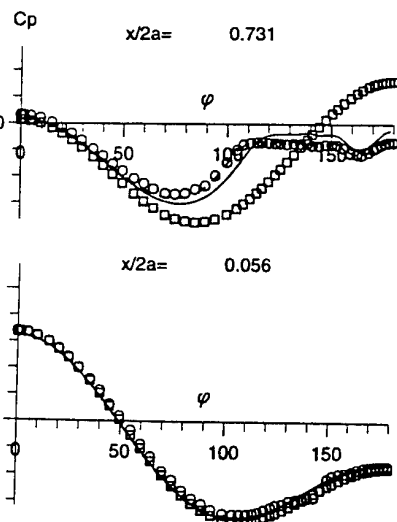


Figure 10: Prolate spheroid: pressure coefficient. \circ expt.; \square inviscid solution; $—$ $k - \epsilon$; $----$ non-linear $\overline{v^2} - f$.

gate the predictive capabilities of $\overline{v^2} - f$ variants when applied to high-lift configurations, including 2D aerofoil and 3D prolate spheroid. Both the linear and non-linear stress-strain constitutive relations are examined. The outcome of the present study may be summarized as follows:

1. The $\overline{v^2} - f$ model and its variants, whether linear or non-linear, return superior predictions relative to the conventional $k - \epsilon$ model.
2. This superiority can be attributed to the use of $\overline{v^2}$ as the velocity scale in the eddy-viscosity expression without resorting to an *ad hoc* damping function.
3. A code-friendly modification is proposed here, including the assurance of the near-wall behaviour $\overline{v^2} \sim O(y^4)$ as $y \rightarrow 0$, the introduction of R_y -dependency in $C_{\epsilon 1}$ and the use of $f = 0$ as the boundary condition on no-slip boundaries. As a result, the numerical stability, in particular, for the uncoupled solution procedure used herein is greatly enhanced.
4. The introduction of R_y in $C_{\epsilon 1}$ yields improved results for the transitional flow. However, it requires the minimum distance to walls, which can be difficult to apply to complex geometries.
5. In order to overcome the above drawback, a first attempt suggested by Durbin & Laurence (1996) was adopted:

$$C_{\epsilon 1} = 1.44(1 + 0.0333\sqrt{k/\overline{v^2}}), \quad C_{\epsilon 2} = 1.85,$$

$$C_L = 0.188,$$

and results for flows over a flat plate and the A-aerofoil are given in Figs. 11–12. As seen, the use of $\sqrt{k/\overline{v^2}}$ returns very similar mean-velocity profiles for the A-aerofoil case. However, the onset of transition for the flat-plate case is too early and the length of transition is too long.

6. The level of normal stress anisotropy returned by the non-linear model is fairly well represented at the mid-chord of A-aerofoil, where the curvature effect is unimportant. Close to the trailing

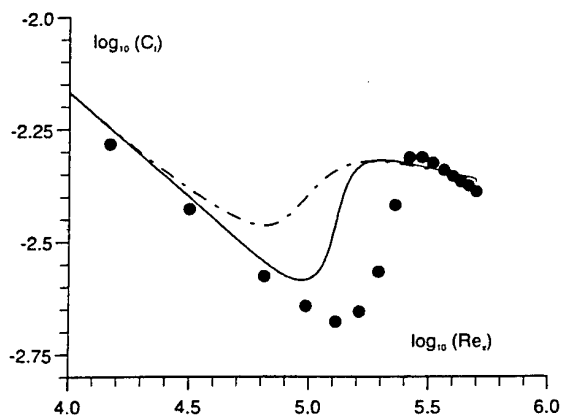


Figure 11: Flat plate: skin friction. • expt.; — based on R_y ; --- based on $\sqrt{k/v^2}$.

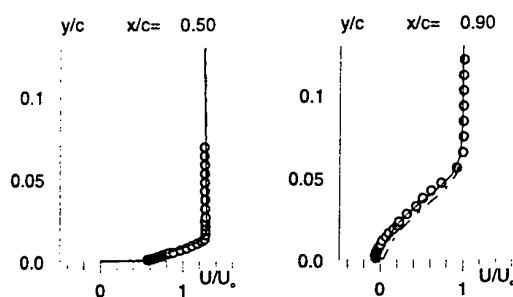


Figure 12: A-aerofoil: profiles of streamwise velocity. o expt.; — based on R_y ; --- based on $\sqrt{k/v^2}$.

edge, however, both $\overline{u^2}$, $\overline{v^2}$ and, consequently, k and its production P_k are under-predicted. Since $P_k = \nu_t \left(\frac{\partial U}{\partial x_j} + \frac{\partial U_j}{\partial x_i} \right) \frac{\partial U}{\partial x_j} + \dots$ and the mean-velocity profile and, hence, its gradient at $x/c=0.9$ are in good agreement with the data, this indicates that ν_t is too low, which is consistent with the under-estimation of $\overline{v^2}$ at the same location.

7. To ensure a wide range of applicability of the non-linear model, the free coefficients and their associated functional forms need to be more carefully optimized by reference to different types of flow, featuring separation, impingement, swirl, rotation and transition.

Acknowledgements : The first author would like to express his gratitude to CTR, UMIST and the Royal Academy of Engineering in the UK for their financial support. Part of the computations were performed on the CRAY T3D at the Edinburgh Parallel Computing Centre via the CCAF programme, with allocations granted by the UK Engineering and Physical Sciences Research Council.

REFERENCES

- Chen, W.L., 1996, "Turbulence modelling for highly-loaded cascade blades", Ph.D Thesis, UMIST, Manchester, UK.
- Craft, T.J., Launder, B.E. & Suga, K., 1995, "A non-linear eddy viscosity model including sensitivity to stress anisotropy", *Proc. 10th Symp. on Turbulent Shear Flows*, Vol. 2, pp. 23.19-23.24.
- Durbin, P.A., 1995a, "Constitutive equation for the $k - \epsilon - \overline{v^2}$ model", *Proc. 6th Int. Symp. on Computational Fluid Dynamics*, Vol. 1, pp. 258-262.
- Durbin, P.A., 1995b, "Separated flow computations with the $k - \epsilon - \overline{v^2}$ model", *AIAA J.*, Vol. 33, pp. 659-664.
- Durbin, P.A., 1996, "On the $k - \epsilon$ stagnation point anomaly", *Int. J. Heat and Fluid Flow*, Vol. 17, pp. 89-90.
- Durbin, P.A. & Laurence, D., 1996, "Non-local effects in single point closure", *Advances in Turbulence Research*, Seoul, Korea, May 17, 1996, pp. 109-120.
- Launder, B.E. & Kato, M., 1993, "Modeling flow-induced oscillations in turbulent flow around a square cylinder", *ASME FED*, Vol. 157, pp. 189-199.
- Launder, B.E. & Sharma, B.I., 1974, "Application of energy-dissipation model of turbulence to the calculation of flow near a spinning disc", *Letters in Heat and Mass Transfer*, Vol. 1, pp. 131-138.
- Lien, F.S. and Leschziner, M.A., 1993, "A pressure-velocity solution strategy for compressible flow and its application to shock/boundary-layer interaction using second-moment turbulence closure", *ASME J. Fluids Engineering*, Vol. 115, pp. 717-725.
- Lien, F.S. and Leschziner, M.A., 1994a, "A general non-orthogonal collocated finite volume algorithm for turbulent flow at all speeds incorporating second-moment closure, Part 1: Computational implementation, Part 2: Application", *Comput. Methods Appl. Mech. Eng.*, Vol. 114, pp. 123-167.
- Lien, F.S. and Leschziner, M.A., 1994b, "Upstream monotonic interpolation for scalar transport with application to complex turbulent flows", *Int. J. Numer. Methods Fluids*, Vol. 19, pp. 527-548.
- Lien, F.S. & Leschziner, M.A., 1995, "Modeling 2D separation from a high-lift aerofoil with a non-linear eddy-viscosity model and second-moment closure", *Aeronautical J.*, Vol. 99, pp. 125-144.
- Lien, F.S., Chen, W.L. & Leschziner, M.A., 1996, "Low-Reynolds-number eddy-viscosity modeling based on non-linear stress-strain/vorticity relations", *Engineering Turbulence Modeling and Experiments 3*, W. Rodi & G. Bergeles (eds.), Elsevier Science Publishers B.V., pp. 91-101.
- Kim, J., Moin, P. & Moser, R.D., 1987, "Turbulence statistics in fully-developed channel flow at low Reynolds number", *J. Fluid Mech.*, Vol. 177, pp. 133-166.
- Pope, S.B., 1975, "A more general effective-viscosity hypothesis", *J. Fluid Mech.*, Vol. 72, pp. 33-340.
- Rhie, C.M. & Chow, W.L., 1983, "Numerical study of the turbulent flow past an airfoil with trailing edge separation", *AIAA J.*, Vol. 21, pp. 1525-1532.
- Rogers, S.E. & Kwak, D., 1990, "Upwind differencing scheme for the time-accurate incompressible Navier-Stokes equations", *AIAA J.*, Vol. 28, pp. 253-262.
- Shih, T.H., Zhu, J. and Lumley, J.L., 1993, "A realisable Reynolds stress algebraic equation model", *NASA TM-105993*.
- Spalart, P.R., 1988, "Direct simulation of a turbulent boundary layer up to $Re_\theta = 1410$ ", *J. Fluid Mech.*, Vol. 187, pp. 61-98.
- Speziale, C.G., 1987, "On non-linear $k - l$ and $k - \epsilon$ models of turbulence", *J. Fluid Mech.*, Vol. 178, pp. 459-475.

A NEW LOW-RE NON-LINEAR TWO-EQUATION TURBULENCE MODEL FOR COMPLEX FLOWS

David D. Apsley and Michael A. Leschziner

Department of Mechanical Engineering

UMIST

P.O. Box 88

Manchester, M60 1QD

England

ABSTRACT

A new low- Re , non-linear k - ϵ turbulence model is proposed and tested. The stress-strain relationship is derived by iterative solution of an algebraic stress model. Truncation of the process at the third iteration yields a stress-strain relationship which is cubic in the mean-velocity gradients and circumvents the singular behaviour which afflicts the exact solution at large strains. Free coefficients are calibrated - as functions of y^+ - by reference to DNS data for a channel flow, and are extended to non-equilibrium conditions by consideration of their P/ϵ dependence. The model performance is investigated for two 2D separated flows.

1. INTRODUCTION

Whilst Reynolds-stress transport models (RSTMs) are widely perceived as the statistical closures offering the greatest prospect for generality when modelling complex flows, limited computer resources often demand the adoption of lower-order closures. This is most keenly felt in numerical calculations of 3D and low- Re flows.

First-order closures assume an explicit algebraic relationship between the Reynolds stresses and the mean strain. Linear eddy-viscosity models (EVMs) are the simplest members of this group and have proved successful in attached, fully-turbulent boundary layers subject to weak pressure gradients, but display important weaknesses in flows with complex strain, where components other than a single shear stress are dynamically significant. The pioneering proposal of Pope (1975) was that greater sensitivity to complex strain could be achieved by including higher-order products of mean-velocity gradients in the stress-strain constitutive relationship. This is the basis of *non-linear eddy-viscosity models* (NLEVMs). Specifically, the addition of quadratic terms imparts normal-stress anisotropy (Speziale, 1987), whilst cubic terms introduce a sensitivity to streamline curvature and swirl (Craft et al., 1997).

In this paper, a new cubic k - ϵ turbulence model is proposed for incompressible flow. A novel feature of the model is that

successive higher-order terms in the stress-strain relationship are generated by successive iterative approximations to the solution of an algebraic Reynolds-stress model. The model coefficients are calibrated by reference to DNS data for a simple shear flow.

2. MODEL CONSTRUCTION

In what follows, cartesian tensors of rank 2 are identified by bold, non-italic symbols (e.g. \mathbf{T}) and their components are italicised; e.g., T_{ij} . Contracted products are written as for matrix multiplication; e.g., $(\mathbf{ST})_{ij} \equiv S_{ik}T_{kj}$. The trace, T_{kk} , of a tensor is denoted by $\{\mathbf{T}\}$, and the second and higher invariants by $T_2 \equiv \{\mathbf{T}^2\} \equiv T_{ij}T_{ji}$, $T_3 \equiv \{\mathbf{T}^3\} \equiv T_{ij}T_{jk}T_{ki}$, etc. Components of mean velocity are denoted by U_i and turbulent fluctuations by u_i . The turbulent kinetic energy is $k \equiv \frac{1}{2}\overline{u_i u_i}$ and its production and dissipation rates are P and ϵ , respectively. The anisotropy tensor \mathbf{a} is defined by

$$a_{ij} = \frac{\overline{u_i u_j}}{k} - \frac{2}{3}\delta_{ij} \quad (1)$$

and the non-dimensionalised mean strain and vorticity tensors by

$$s_{ij} = \frac{1}{2}(U_{i,j} + U_{j,i})\frac{k}{\epsilon}, \quad \omega_{ij} = \frac{1}{2}(U_{i,j} - U_{j,i})\frac{k}{\epsilon} \quad (2)$$

In a RSTM, the pressure-strain interaction is typically decomposed into slow ($\Phi^{(1)}$) and rapid ($\Phi^{(2)}$) parts. Adopting a linear model for each, these may be written:

$$\begin{aligned} \Phi^{(1)}/\epsilon &= -c_1 \mathbf{a} \\ \Phi^{(2)}/\epsilon &= c_{01} \mathbf{s} + c_{11}(\mathbf{as} + \mathbf{sa} - \frac{2}{3}\{\mathbf{as}\}\mathbf{I}) + c_{12}(\omega \mathbf{a} - \mathbf{a} \omega) \end{aligned} \quad (3)$$

For example, the widely-used "return-to-isotropy/isotropisation-of-production" model of Launder et al. (1975) can be written in this form, with $c_1=1.8$, $c_{01}=0.8$, $c_{11}=c_{12}=0.6$. By making the algebraic-stress approximation (Rodi, 1976) $D/Dt(\overline{u_i u_j}) - \text{diff}(\overline{u_i u_j}) = (\overline{u_i u_j}/k)[Dk/Dt - \text{diff}(k)]$, and assuming isotropic dissipation, the Reynolds-stress transport equations can be reduced to the algebraic system:

$$\mathbf{a} = -\alpha \mathbf{s} - \beta(\mathbf{s}\mathbf{a} + \mathbf{a}\mathbf{s} - \frac{2}{3}\{\mathbf{a}\mathbf{s}\}\mathbf{I}) - \gamma(\omega\mathbf{a} - \mathbf{a}\omega) \quad (4)$$

The coefficients α , β and γ derived from the RSTM are

$$\alpha = \frac{4/3 - c_{01}}{c_1 + P/\varepsilon - 1}, \quad \beta = \frac{1 - c_{11}}{c_1 + P/\varepsilon - 1}, \quad \gamma = \frac{1 - c_{12}}{c_1 + P/\varepsilon - 1} \quad (5)$$

The system (4) can be solved (Pope, 1975; Gatski and Speziale, 1993) to yield tensorially quadratic and quintic NLEVMs in 2D and 3D flows, respectively. The finite order is imposed by the finite number of independent products of \mathbf{s} and ω , which may be deduced as a consequence of the Cayley-Hamilton theorem of matrix algebra.

The model to be presented here differs from those above in two fundamental respects. Firstly, it does not attempt to solve (4) exactly, but generates terms of successive order in a NLEVM by successive iterative approximations. Amongst other benefits this removes the singularities which arise in the exact solution at large strain rates. Secondly, the RSTM fixes the *relative* values of the NLEVM coefficients, but the actual values of α , β and γ are determined (as functions of $y^* = y_n k^{1/2}/\nu$, with y_n the distance from the wall) from DNS data for a simple shear flow. This makes the model immediately applicable to low- Re , near-wall conditions.

In detail, (4) is treated as an algebraic system

$$\mathbf{a} = \mathbf{b} + \mathbf{f}(\mathbf{a}) \quad (6)$$

to be "solved" by the iterative procedure

$$\mathbf{a}^{(1)} = \mathbf{b}; \quad \mathbf{a}^{(n)} = \mathbf{b} + \mathbf{f}(\mathbf{a}^{(n-1)}), \quad n = 2, 3, \dots \quad (7)$$

Thus, the first iterate is a linear EVM:

$$\mathbf{a}^{(1)} = -\alpha \mathbf{s} \quad (8)$$

The second iterate is a quadratic NLEVM:

$$\begin{aligned} \mathbf{a}^{(2)} &= -\alpha \mathbf{s} - \beta(\mathbf{s}\mathbf{a}^{(1)} + \mathbf{a}^{(1)}\mathbf{s} - \frac{2}{3}\{\mathbf{a}^{(1)}\mathbf{s}\}) - \gamma(\omega\mathbf{a}^{(1)} - \mathbf{a}^{(1)}\omega) \\ &= -\alpha \mathbf{s} + 2\alpha\beta(\mathbf{s}^2 - \frac{1}{3}\mathbf{s}_2\mathbf{I}) + \alpha\gamma(\omega\mathbf{s} - \mathbf{s}\omega) \end{aligned} \quad (9)$$

and the third, obtained in a similar manner, is

$$\begin{aligned} \mathbf{a}^{(3)} &= -\alpha \mathbf{s} + 2\alpha\beta(\mathbf{s}^2 - \frac{1}{3}\mathbf{s}_2\mathbf{I}) + \alpha\gamma(\omega\mathbf{s} - \mathbf{s}\omega) \\ &\quad - 4\alpha\beta^2(\mathbf{s}^3 - \frac{1}{3}\mathbf{s}_3\mathbf{I} - \frac{1}{3}\mathbf{s}_2\mathbf{s}) - 3\alpha\beta\gamma(\omega\mathbf{s}^2 - \mathbf{s}^2\omega) \\ &\quad - \alpha\gamma^2(\omega^2\mathbf{s} + \mathbf{s}\omega^2 - 2\omega\mathbf{s}\omega) \end{aligned} \quad (10)$$

By application of the Cayley-Hamilton theorem, the cubic terms can be simplified and rearranged to yield

$$\begin{aligned} \mathbf{a}^{(3)} &= -\alpha \mathbf{s} + 2\alpha\beta(\mathbf{s}^2 - \frac{1}{3}\mathbf{s}_2\mathbf{I}) + \alpha\gamma(\omega\mathbf{s} - \mathbf{s}\omega) \\ &\quad - \frac{2}{3}\alpha\beta^2\mathbf{s}_2\mathbf{s} - 2\alpha\gamma^2\omega_2\mathbf{s} \\ &\quad - 3\alpha\gamma^2(\omega^2\mathbf{s} + \mathbf{s}\omega^2 - \omega_2\mathbf{s} - \frac{2}{3}\{\omega\mathbf{s}\omega\}) \\ &\quad - 3\alpha\beta\gamma(\omega\mathbf{s}^2 - \mathbf{s}^2\omega) \end{aligned} \quad (11)$$

The grouping of cubic terms - for example, the appearance of $\omega_2\mathbf{s}$ in two separate elements - is for convenience: the last two terms vanish in 2D incompressible flow.

The iterative process is terminated at this level. To determine α , β and γ , consider the three independent anisotropy components in simple shear:

$$\begin{aligned} a_{11} &= \overline{u^2}/k - 2/3 = \frac{1}{6}(\alpha\beta + 3\alpha\gamma)\sigma^2 \\ a_{22} &= \overline{v^2}/k - 2/3 = \frac{1}{6}(\alpha\beta - 3\alpha\gamma)\sigma^2 \\ a_{12} &= \overline{uv}/k = -\frac{1}{2}\alpha\sigma[1 + (\frac{1}{3}\beta^2 - \gamma^2)\sigma^2] \end{aligned} \quad (12)$$

where $\sigma = (s_{ij}s_{ij} + \omega_{ij}\omega_{ij})^{1/2} = (k/\varepsilon)\sqrt{(\partial U/\partial y)^2}$ here reduces to $(k/\varepsilon)(\partial U/\partial y)$. Given the components a_{ij} as functions of y^* from DNS data (distinguished henceforth by a tilde: \tilde{a}_{ij}) and σ either from DNS data ($\tilde{\sigma}(y^*)$) or from the local flow, (12) consists of three equations for the three unknowns α , β and γ . The process bears some resemblance to the *calibration* (although not the *derivation*) of Speziale's (1987) quadratic model, although in that high- Re model the calibration is based upon a single point, rather than as a function of y^* .

Figure 1 shows the variation of the normal stresses and shear parameter in the DNS data for a zero-pressure-gradient boundary layer (Spalart, 1988) and channel flow (Kim et al., 1987), together with the following curve fits to the latter:

$$\begin{aligned} \overline{u^2}/k &= 1.0 + 0.42\exp(0.30y^{*1/2} - 0.040y^*) \\ \overline{v^2}/k &= 0.40[1 - \exp(-0.001y^* - 0.00015y^{*2})] \\ -\overline{uv} &= 0.3[1 - \exp(-0.0044y^{*1/2} - 0.019y^*)] \\ \tilde{\sigma} &= 3.3[1 - \exp(-0.45y^*)][1 + 0.28y^{*3/2}\exp(-0.088y^*)] \end{aligned} \quad (13)$$

These have the correct behaviour at small y^* and in the log-law

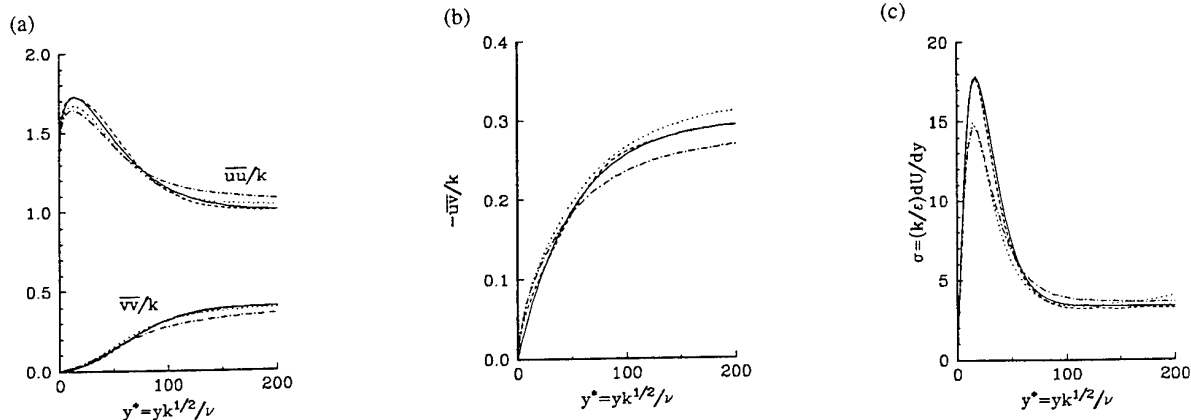


Figure 1. DNS data for (a) normal stresses, (b) shear stress, (c) shear parameter. Key: - boundary layer ($Re_\theta=670$); - - - - boundary layer ($Re_\theta=1410$); - . - . channel flow ($Re_c=7890$); - - - curve fit.

region. Using the shear parameter from DNS data, (12) can be inverted to give

$$\begin{aligned}\alpha\bar{\sigma} &= -\bar{a}_{12} + \sqrt{\bar{a}_{12}^2 + (\bar{a}_{11} - \bar{a}_{22})^2 - 3(\bar{a}_{11} + \bar{a}_{22})^2} \\ \beta\bar{\sigma} &= \frac{3(\bar{a}_{11} + \bar{a}_{22})}{\alpha\bar{\sigma}}, \quad \gamma\bar{\sigma} = \frac{\bar{a}_{11} - \bar{a}_{22}}{\alpha\bar{\sigma}}\end{aligned}\quad (14)$$

Considering first the high- Re regime (i.e. letting $y^* \rightarrow \infty$ in (13)), and denoting this limit by a subscript ∞ , gives

$$\bar{\alpha} = \alpha_{\infty} \bar{\sigma}_{\infty} = 0.96, \quad \bar{\beta} = \beta_{\infty} \bar{\sigma}_{\infty} = 0.21, \quad \bar{\gamma} = \gamma_{\infty} \bar{\sigma}_{\infty} = 0.62 \quad (15)$$

A feature of the present model is that both linear and cubic terms contribute to the shear stress in simple shear. If α , β and γ are evaluated according to (14) for all y^* it is found that both the linear term ($-\alpha\bar{\sigma}$) and the cubic terms are $O(1)$ as $y^* \rightarrow 0$ and only in combination do they yield an expression for a_{12} which vanishes as $y^* \rightarrow 0$. To ensure that each individually vanishes as $y^* \rightarrow 0$, we replace β and γ in the cubic terms by β' and γ' , such that

$$\beta'\bar{\sigma} = \bar{\beta} = 0.21, \quad \gamma'\bar{\sigma} = \bar{\gamma} = 0.62 \quad (16)$$

Clearly, outside the semi-viscous sublayer, $\beta' = \beta$ and $\gamma' = \gamma$. The expression for α in (14) must then be amended to read

$$\alpha = -2 \frac{\bar{a}_{12}}{\bar{\sigma}} (1 + \frac{1}{3} \bar{\beta}^2 - \bar{\gamma}^2)^{-1} \quad (17)$$

The shear parameter in (12) could equally be regarded as the invariant $\sigma = (s_{ij}s_{ij} + \omega_{ij}\omega_{ij})^{1/2}$ computed from the flow. One may, of course, multiply α , β and γ by $f_p(\sigma/\bar{\sigma})$, where $f_p(1) = 1$, without changing the calibration. A function $f_p(\xi)$ which decays as $O(1/\xi)$ as $\xi \rightarrow \infty$ will ensure that in flows with large strain, far from equilibrium, the Reynolds stresses are bounded (although not necessarily realisable). Such a function may be constructed by noting that the values of α , β and γ from the RSTM (equation (5)) have a non-equilibrium dependence through the factor $(c_1 + P/\epsilon - 1)^{-1}$. This suggests the multiplicative factor

$$f_p = \frac{c_1 - \bar{a}_{12}\bar{\sigma} - 1}{c_1 + P/\epsilon - 1} \quad (18)$$

which, on approximating P/ϵ by $C_\mu \sigma^2$, where $C_\mu = f_p(-\bar{a}_{12}/\bar{\sigma})$, and solving for f_p , yields

$$f_p = \frac{2f_0}{1 + \sqrt{1 + 4f_0(f_0 - 1)(\sigma/\bar{\sigma})^2}}, \quad f_0 = \frac{c_1 - \bar{a}_{12}\bar{\sigma} - 1}{c_1 - 1} \quad (19)$$

where $c_1 = 1.8$.

To summarise, the new cubic stress-strain relationship may be written in the following canonical form:

$$\begin{aligned}a &= -2Cs \\ &+ q_1(s^2 - \frac{1}{3}s_2I) + q_2(\omega s - s\omega) + q_3(\omega^2 - \frac{1}{3}\omega_2I) \\ &- \gamma_1 s_2 s - \gamma_2 \omega_2 s - \gamma_3(\omega^2 s + s\omega^2 - \omega_2 s - \frac{2}{3}\{\omega s \omega\}I) \\ &- \gamma_4(\omega s^2 - s^2 \omega)\end{aligned}\quad (20)$$

where

$$C = \frac{1}{2} \alpha f_p$$

$$q_1 = \frac{6(\bar{a}_{11} + \bar{a}_{22})}{\bar{\sigma}^2} f_p^2, \quad q_2 = \frac{\bar{a}_{11} - \bar{a}_{22}}{\bar{\sigma}^2} f_p^2, \quad q_3 = 0 \quad (21)$$

$$\begin{aligned}\gamma_1 &= \frac{2}{3} \alpha (\bar{\beta}/\bar{\sigma})^2 f_p^3, \quad \gamma_2 = 2\alpha (\bar{\gamma}/\bar{\sigma})^2 f_p^3, \quad \gamma_3 = 3\alpha (\bar{\gamma}/\bar{\sigma})^2 f_p^3, \\ \gamma_4 &= 3\alpha (\bar{\beta}\bar{\gamma}/\bar{\sigma}^2) f_p^3\end{aligned}$$

α is given by (17), $\bar{\beta}$ and $\bar{\gamma}$ by (16), f_p by (19) and the curve fits for \bar{a}_{ij} and $\bar{\sigma}$ by (13). Note that the ω^2 term is zero and, since $\gamma_1 \neq \gamma_2$, cubic terms do not cancel in simple shear. In 2D flows the stress-strain relationship reduces to

$$a = \left\{ \frac{1 + [\frac{1}{3}\bar{\beta}^2(2s_{ij}s_{ij}/\bar{\sigma}^2) - \bar{\gamma}^2(2\omega_{ij}\omega_{ij}/\bar{\sigma}^2)] f_p^2}{1 + \frac{1}{3}\bar{\beta}^2 - \bar{\gamma}^2} \right\} \bar{a}_{12} f_p \frac{2s}{\bar{\sigma}} + q_1(s^2 - \frac{1}{3}s_2I) + q_2(\omega s - s\omega) \quad (22)$$

Finally, transport equations must be solved for k and ϵ . These are modelled as

$$\frac{Dk}{Dt} = \nabla \cdot \left[\left(\nu + \frac{\nu_t}{\sigma_k} \right) \nabla k \right] + P - \epsilon \quad (23)$$

$$\frac{D\epsilon}{Dt} = \nabla \cdot \left[\left(\nu + \frac{\nu_t}{\sigma_\epsilon} \right) \nabla \epsilon \right] + [C_{\epsilon 1} P - C_{\epsilon 2} (\epsilon - D\epsilon_w)] \frac{\epsilon}{k}$$

Here, the eddy viscosity ν_t is given by the isotropic model

$$\nu_t = C_\mu \frac{k^2}{\epsilon}, \quad C_\mu = \frac{-\bar{a}_{12} f_p}{\bar{\sigma}} \quad (24)$$

and the rate of production of turbulent kinetic energy by

$$P \equiv -\overline{u_i u_j} \frac{\partial U_i}{\partial x_j} = \epsilon \{ -as \} \quad (25)$$

The free constants are $C_{\epsilon 1} = 1.44$, $C_{\epsilon 2} = 1.83$ (a value which is being increasingly used in preference to the more familiar 1.92) and $\sigma_k = 1.0$. $\sigma_\epsilon = k^2 / C_{\mu \infty} (C_{\epsilon 2} - C_{\epsilon 1}) = 1.37$ to be consistent with the log law of the wall. ϵ_w and D appear only in combination, so that we may take ϵ_w as the theoretical near-wall variation of ϵ :

$$\epsilon_w = \frac{2\nu k}{y_n^2} \quad (26)$$

To balance source and sink terms in the ϵ equation, DNS data gives $D = \max(1 - y^*/12, 0)$. Computation of plane channel flow, however, gives better results with the slightly modified form

$$D = \exp(-y^*/12) \quad (27)$$

The boundary condition is $\epsilon = \epsilon_w$ at the near-wall node.

3. MODEL APPLICATION

The new model has been applied to a number of complex 2D flows (although its tensorial formulation makes it equally valid in 3D). Calculations were performed with a modified version of the finite-volume code STREAM (Lien and Leschziner, 1994), using co-located variable storage on single-block, structured, non-orthogonal grids. The steady-state, incompressible-flow equations for primitive variables were solved iteratively, using the SIMPLE pressure-correction algorithm and line-iterative procedures to solve the matrix equations. A third-order, upwind-biased, bounded advection scheme was employed and the mass fluxes on cell faces obtained by the Rhie-Chow interpolation procedure. The performance of the present non-linear $k-\epsilon$ model

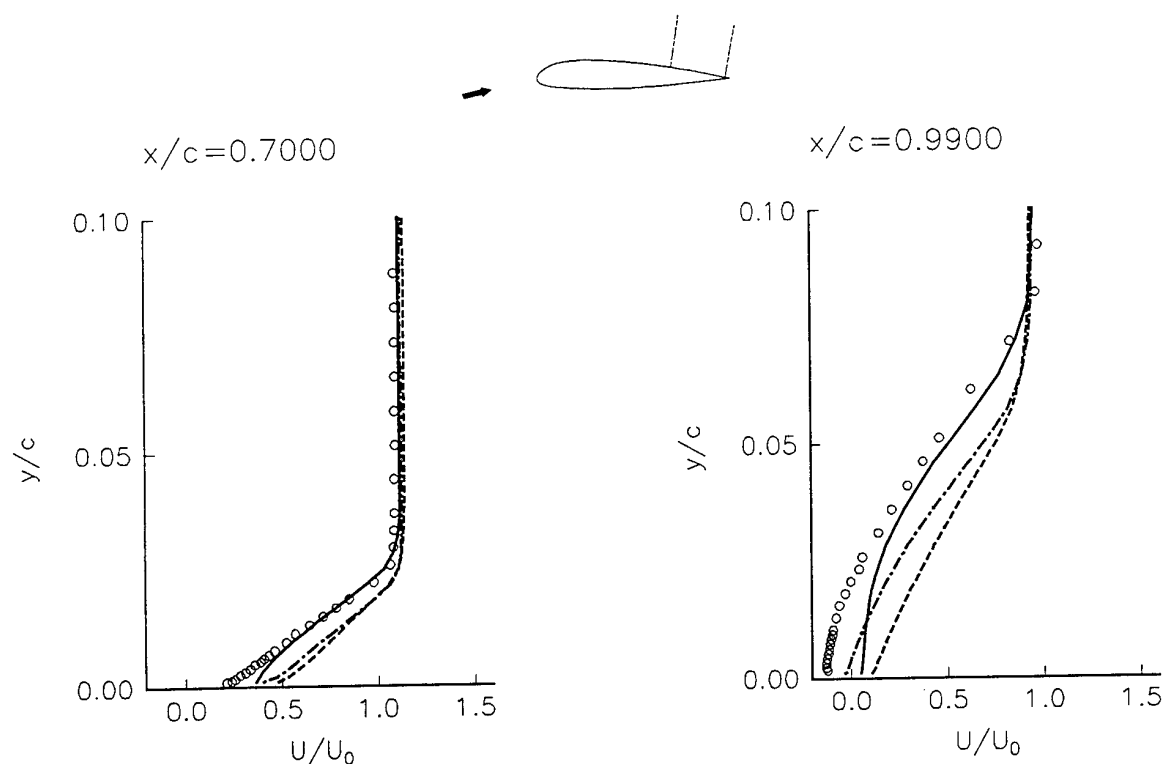


Figure 2. Mean flow profiles on the aerofoil suction surface at 70% and 99% chord. Key:- o experiment; ----- linear $k-\epsilon$ (Lien and Leschziner, 1993); RSTM (Speziale et al., 1991); ——— new cubic $k-\epsilon$ model.

is here compared to that of the low- Re linear $k-\epsilon$ model of Lien and Leschziner (1993) and the Reynolds-stress-transport model of Speziale et al. (1991). In the latter case, a one-equation eddy-viscosity model is used to resolve the near-wall sublayer.

3.1 High Lift Aerofoil (Piccin and Cassoudealle, 1987)

The Aerospatiale-A aerofoil test case is an example of a single-element aerofoil operating at or beyond stall. The Reynolds number based on chord and free-stream velocity is 2.1×10^6 and the Mach number is 0.15. Calculations have focused on an incidence angle (corrected for blockage effects) of 13.3° , at which the flow was observed to separate. A C-type grid of 352×64 control volumes extending to 10 chord lengths from the aerofoil and with minimum finite-volume height corresponding to y^+ values of order 1 was employed in the computations. Transition was fixed at experimentally-determined locations of 12% and 30% chord on suction and pressure surfaces, respectively.

Figure 2 shows mean velocity profiles on the suction surface at 70% and 99% chord. Both Reynolds-stress-transport and non-linear $k-\epsilon$ models show much better response than the over-diffusive linear $k-\epsilon$ model to the adverse pressure gradient (although failing to predict the observed separation). The magnitude of the wall-normal velocity fluctuations are also well predicted by the cubic $k-\epsilon$ model (Figure 3).

3.2 Plane Asymmetric Diffuser (Obi et al., 1993)

In this 2D test case, fully-developed channel flow enters a diffuser section with one plane wall, the diffusing section having length $21H$ (where H is the inlet height) and overall expansion

ratio 4.7. The Reynolds number based on upstream centre-line velocity and H is 21200. The flow was observed to separate half-way along the angled wall due to the adverse pressure gradient. Computational predictions were made on a mesh of

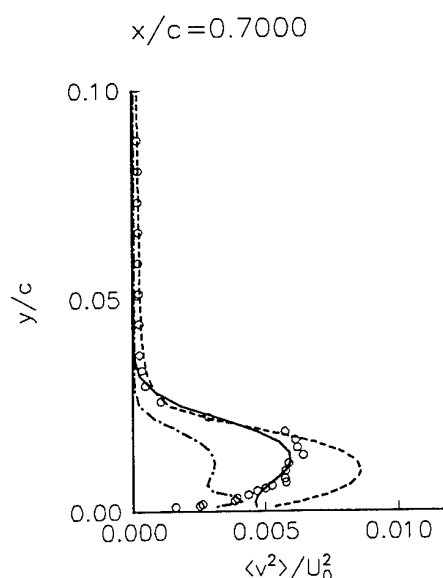


Figure 3. Wall-normal velocity fluctuations computed on the aerofoil suction surface. Key as for Figure 2.

270×80 control volumes, extending $11H$ upstream and $40H$ downstream of the diffuser section. Results have been compared with LDA profiles at various streamwise stations.

The general behaviour of the turbulence models tested is illustrated by Figures 4 and 5. The linear EVM fails to generate any cross-channel asymmetry. In contrast, both the new cubic NLEV and the RSTM predict the asymmetric mean velocity and shear-stress profiles well, with a clear velocity maximum in the lower half of the channel, preceding flow separation from the upper wall (which is, however, slightly delayed). The anisotropy of the normal stresses is well-predicted by both RSTM and NLEV, although there is an unexplained tendency of the new cubic model to exaggerate anisotropy very close to the bottom wall.

4. CONCLUSIONS

A new non-linear, low- Re k - ϵ model has been described. The main features of the model are its construction by iterative solution of an algebraic stress model, y^+ -dependent coefficients calibrated against DNS data for channel flow and a strain-dependent factor which accounts for departures from equilibrium and which ensures bounded anisotropy components.

The new model has been successfully applied to separated, 2D flows. Since two of the cubic terms vanish in these conditions, future testing in 3D flows would be desirable. Key elements in its successful prediction of non-parallel flows are the non-linear terms (providing a better representation of individual stress components) and the non-equilibrium factor, f_p , which effectively provides a limiter for the Reynolds stresses.

ACKNOWLEDGEMENTS

The financial support of Audi, BMW, Mercedes-Benz, Opel, Porsche and Renault, is gratefully acknowledged.

REFERENCES

- Craft, T.J., Launder, B.E. and Suga, K., 1997, "Prediction of turbulent transitional phenomena with a non-linear eddy-viscosity model", *International Journal of Heat and Fluid Flow*, Vol. 18, pp. 15-28.
- Gatski, T.B. and Speziale, C.G., 1993, "On explicit algebraic stress models for complex turbulent flows", *Journal of Fluid Mechanics*, Vol. 254, pp. 59-78.
- Kim, J., Moin, P. and Moser, R., 1987, "Turbulence statistics in fully developed channel flow at low Reynolds number", *Journal of Fluid Mechanics*, Vol. 177, pp. 133-166.
- Launder, B.E., Reece, G.J. and Rodi, W., 1975, "Progress in the development of a Reynolds stress closure", *Journal of Fluid Mechanics*, Vol. 68, pp. 537-566.
- Lien, F.-S. and Leschziner, M.A., 1993, "A pressure-velocity solution strategy for compressible flow and its application to shock/boundary-layer interaction using second-moment turbulence closure", *Journal of Fluids Engineering*, Vol. 115, pp. 717-725.
- Lien, F.-S. and Leschziner, M.A., 1994, "A general non-orthogonal collocated finite volume algorithm for turbulent flow at all speeds incorporating second-moment turbulence-transport closure, Part I: computational implementation", *Computer Methods in Applied Mechanics and Engineering*, Vol. 114, pp. 123-148.
- Obi, S., Aoki, K. and Masuda, S., 1993, Experimental and computational study of turbulent separating flow in an asymmetric plane diffuser, *Proceedings, 9th Symposium on Turbulent Shear Flows*, Kyoto.
- Piccin, O. and Cassouesalle, D., 1987, "Etude dans la soufflerie F1 des profils AS239 et AS240", ONERA technical report, PV 73/1685 AYG.
- Pope, S.B., 1975, "A more general effective-viscosity hypothesis", *Journal of Fluid Mechanics*, Vol. 72, pp. 331-340.
- Rodi, W., 1976, "A new algebraic relation for calculating the Reynolds stresses", *Z. angew. Math. Mech.*, Vol. 56, pp. 219-221.
- Spalart, P.R., 1988, "Direct numerical simulation of a turbulent boundary layer up to $R=1410$ ", *Journal of Fluid Mechanics*, Vol. 187, pp. 61-98.
- Speziale, C.G., 1987, "On nonlinear K-1 and K- ϵ models of turbulence", *Journal of Fluid Mechanics*, Vol. 178, pp. 459-475.
- Speziale, C.G., Sarkar, S. and Gatski, T.B., 1991, "Modelling the pressure-strain correlation of turbulence: an invariant dynamical systems approach", *Journal of Fluid Mechanics*, Vol. 227, pp. 245-272.

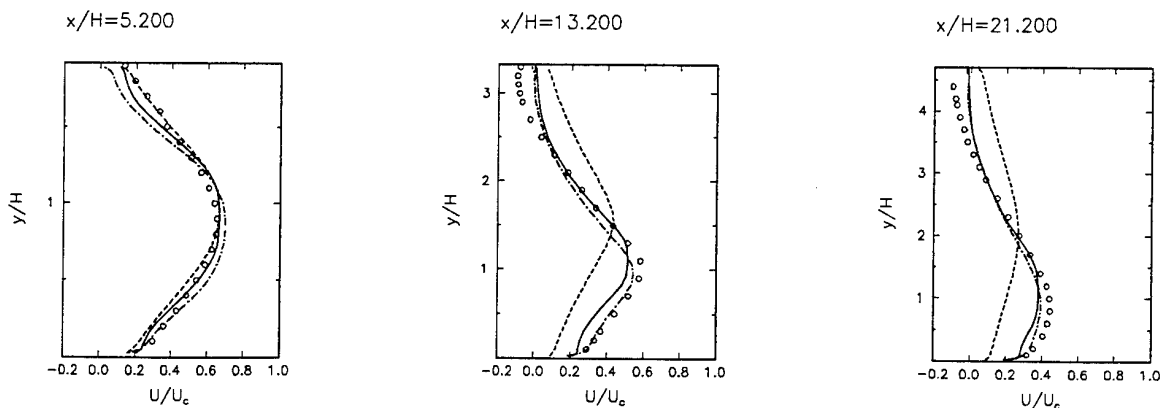
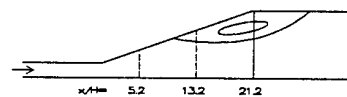


Figure 4. Development of the mean-velocity profile along the diffuser. Key as for Figure 2.

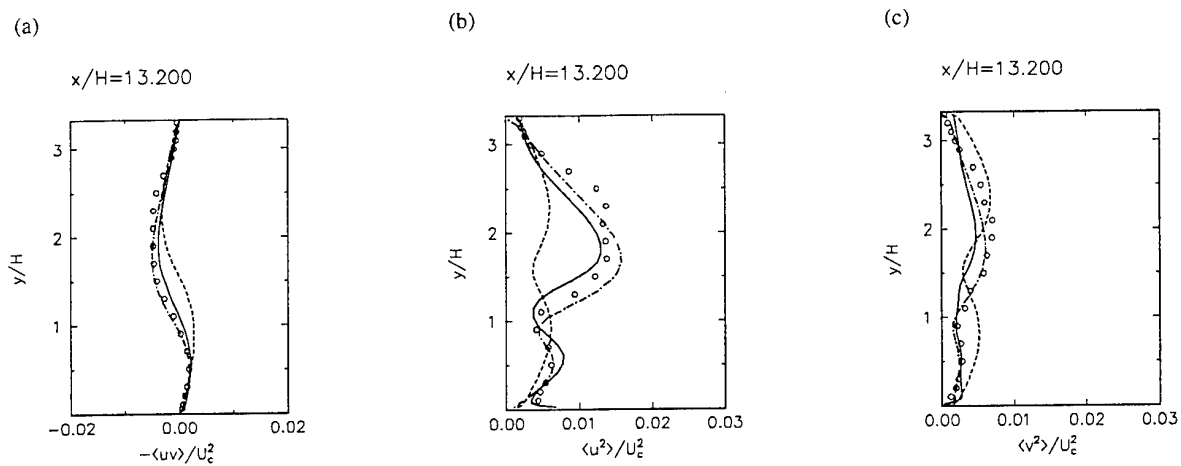


Figure 5. Profiles of Reynolds stresses near the centre of the diffuser: (a) shear stress; (b) streamwise fluctuations; (c) cross-stream fluctuations. Key as for Figure 2.

SESSION 7 - CLOSURES I

PARTICLE AND ONE-POINT STRUCTURE-BASED MODELING OF SLOW DEFORMATIONS OF HOMOGENEOUS TURBULENCE

Stavros C. Kassinos, William C. Reynolds, and Carlos A. Langer

Department of Mechanical Engineering
Stanford University
Stanford, California 94305
USA

ABSTRACT

The response of turbulence to mean deformation is viscoelastic, *i.e.* it depends on the rate of deformation: in *rapidly* deformed turbulence the turbulent stresses are determined by the *total* mean deformation whereas in *slowly* deformed turbulence the stresses are determined by the applied deformation *rate*. Both types of deformation are encountered in modern engineering flows that must be predicted in order to advance technology, and a good engineering model should reflect the viscoelastic response of turbulence to applied deformation. Under non-equilibrium conditions the structure of the turbulence plays a key role in the evolution of the turbulent stresses. Models based solely on the stress R_{ij} cannot handle mean rotation properly (Reynolds & Kassinos 1995). Hence modeling of non-equilibrium turbulence must be *structure-based*. Here a new structure-based particle representation model (PRM) is introduced, which is exact in the RDT limit and remarkably accurate in the prediction of slow deformations of homogeneous turbulence. Results are shown for several cases involving complex combinations of mean rotation and strain. A one-point structure-based model follows directly from the new PRM. Here the formulation of the one-point model is outlined for the case of irrotational mean deformation. Results from the one-point model demonstrate that accuracy comparable to that of the PRM can be achieved by the one-point model.

1. INTRODUCTION

Reynolds-averaged turbulence models are the primary engineering tool for the analysis of complex turbulent flows. A good model should reflect the viscoelastic character of turbulence. For example in simple flows, with mild mean deformation rates, the turbulence has time to come to equilibrium with the mean flow, and the Reynolds stresses are determined by the applied strain *rate*. In these flows, it

is often adequate to relate the Reynolds stresses to the mean deformation through an eddy-viscosity approximation. Flows encountered in modern engineering applications often involve very rapid deformations. In these flows the structure of the turbulence plays an important role in determining the transport of the Reynolds stresses, and because the turbulence structure takes sometime to respond to the imposed deformation, an eddy-viscosity representation is not appropriate.

The response of turbulence to rapid deformations is given by rapid distortion theory (RDT). Under RDT the nonlinear effects due to turbulence-turbulence interactions are neglected, but even when linearized in this fashion, the governing equations are unclosed at the one-point level due to the non-locality of the pressure fluctuations.

Our goal has been the development of an engineering *one-point* model of turbulence that has the correct viscoelastic character. Guidance in developing a good one-point structure-based model has been obtained from a viscoelastic model based on a particle representation method (PRM). In a particle representation method, a number of key properties and their evolution equations are assigned to hypothetical particles. The idea is to follow an ensemble of "particles", determine the statistics of the ensemble and use those as the representation for the one-point statistics of the corresponding field.

We have already used the rapid PRM to formulate a successful one-point structure-based model of RDT (Reynolds and Kassinos 1995). Here we first focus on the structure-based modeling of the nonlinear effects in the PRM. We show that even with relatively simple models, the extended PRM produces remarkably accurate predictions for a wide range of slow deformations of homogeneous turbulence. Finally, we show how a consistent *one-point* model for the slow deformation of homogeneous turbulence follows from the PRM. For irrotational deformations, the accuracy of

the one-point model and the PRM are found to be comparable.

2. PARTICLE REPRESENTATION MODELS

The Interacting Particle Representation Model (IPRM) presented here introduces three important innovations; (a) the recognition that the linearity of the RDT governing equations makes it possible to emulate exactly the RDT for homogeneous turbulence using a particle method *without any modeling assumptions*; (b) the use of the newly-introduced structure tensors in the closure of the non-linearity; (c) the use of cluster-averaged governing equations for greater numerical efficiency.

The IPRM is a viscoelastic structure-based model at what one may call "quasi-one-point level". Unlike spectral methods, which provide complete two-point information, the IPRM provides information only about the directional dependence of the real part of the spectrum of homogeneous turbulence; yet, this is sufficient to remove the closure problem associated with the non-locality of the pressure fluctuations. Hence, unlike one-point models, the IPRM bypasses the closure problem due to *non-locality* (RDT) and it does so at minimum additional expense relative to a one-point approach. The IPRM is exact for RDT, but still modeling is required even in the IPRM in order to deal with *nonlinearity*, important whenever the mean deformation is mild.

2.1 Emulation of Rapid Distortion Theory with a PRM

The following properties are assigned to each of the hypothetical particles:

- **V** velocity vector
- **W** vorticity vector
- **S** stream function vector
- **N** gradient vector
- **P** pressure.

The evolution of the vector properties assigned to each particle are governed by ordinary differential equations based on the Navier-Stokes equations. For example, a kinematic analysis leads to the RDT evolution equation for **N**

$$\dot{N}_i = -G_{ki} N_k, \quad (2.1)$$

which shows that **N** plays a role similar to that of the wavenumber vector **k**. Here $G_{ij} = U_{i,j}$ is the mean velocity gradient tensor. The unit vector $n_i = N_i / \sqrt{N_k N_k}$ satisfies

$$\dot{n}_i = -G_{ki} n_k + G_{km} n_k n_m n_i. \quad (2.2)$$

The PRM evolution equation for **V** is

$$\dot{V}_i = -G_{ik} V_k + 2G_{km} \frac{V_m N_k N_i}{N^2}. \quad (2.3)$$

The familiar Poisson equation for the rapid pressure is the basis for the analogous definition

$$P = -2G_{km} \frac{V_m N_k}{N^2}. \quad (2.4)$$

Using (2.4) and (2.3), one obtains

$$\dot{V}_i = -G_{ik} V_k - P N_i \quad (2.5)$$

by analogy to the fluctuation momentum equation under RDT.

2.2 Representations for One-point Statistics

The Reynolds stress $R_{ij} = \overline{u'_i u'_j}$ is represented as

$$R_{ij} = \langle V_i V_j \rangle = \langle V^2 v_i v_j \rangle, \quad (2.6)$$

where the angle brackets denote averaging over an ensemble of particles. Two one-point turbulent tensors that carry useful structure information are the structure *dimensionality* and *circulicity*, defined by

$$D_{ij} = \overline{\Psi'_{n,i} \Psi'_{n,j}} \quad F_{ij} = \overline{\Psi'_{i,n} \Psi'_{j,n}}.$$

Here Ψ'_i is the turbulent stream function vector, which satisfies

$$u'_i = \epsilon_{its} \Psi'_{s,t} \quad \Psi'_{i,i} = 0 \quad \Psi'_{i,nn} = -\omega'_i$$

and ω'_i is the fluctuation vorticity. In the IPRM formulation the structure tensors are represented as

$$D_{ij} = \langle S_n S_n N_i N_j \rangle = \langle V^2 n_i n_j \rangle \quad (2.7)$$

$$F_{ij} = \langle N_n N_n S_i S_j \rangle = \langle V^2 s_i s_j \rangle$$

where $s_i = S_i / \sqrt{S_k S_k}$ and $v_i = V_i / \sqrt{V_k V_k}$. A consequence of the orthogonality of the three vectors n_i , v_i , and s_i is that, for homogeneous turbulence, the three second-rank tensors satisfy the constitutive equation

$$R_{ij} + D_{ij} + F_{ij} = q^2 \delta_{ij}. \quad (2.8)$$

Here $q^2 = 2k = R_{ii}$. For homogeneous turbulence $D_{ii} = F_{ii} = q^2$ and it is possible to normalize (2.8) so that

$$r_{ij} + d_{ij} + f_{ij} = \delta_{ij} \quad (2.9)$$

where

$$r_{ij} = R_{ij}/q^2 \quad d_{ij} = D_{ij}/q^2 \quad f_{ij} = F_{ij}/q^2. \quad (2.10)$$

The tensor anisotropies $\tilde{r}_{ij} = r_{ij} - \frac{1}{3}\delta_{ij}$, $\tilde{d}_{ij} = d_{ij} - \frac{1}{3}\delta_{ij}$ and $\tilde{f}_{ij} = f_{ij} - \frac{1}{3}\delta_{ij}$ satisfy

$$\tilde{r}_{ij} + \tilde{d}_{ij} + \tilde{f}_{ij} = 0. \quad (2.11)$$

2.3 Cluster-Averaged Equations

The cluster-averaged implementation of the PRM offers a better computational efficiency. The idea is to do the averaging in two steps, the first step being done analytically. First, an averaging is done over particles that have the same $\mathbf{n}(t)$, followed by an averaging over all particles with different $\mathbf{n}(t)$. The one-point statistics resulting from the first (cluster) averaging are conditional moments, which will be denoted by

$$R_{ij}^{|\mathbf{n}} \equiv \langle V_i V_j | \mathbf{n} \rangle \quad D_{ij}^{|\mathbf{n}} \equiv \langle V^2 n_i n_j | \mathbf{n} \rangle = \langle V^2 | \mathbf{n} \rangle n_i n_j$$

and

$$F_{ij}^{|\mathbf{n}} \equiv \langle V^2 s_i s_j | \mathbf{n} \rangle. \quad (2.12)$$

The conditionally-averaged stress evolution equation

$$\dot{R}_{ij}^{|\mathbf{n}} = -G_{ik} R_{kj}^{|\mathbf{n}} - G_{jk} R_{ki}^{|\mathbf{n}} + 2G_{km} (R_{im}^{|\mathbf{n}} n_k n_j + R_{jm}^{|\mathbf{n}} n_k n_i) \quad (2.13)$$

is obtained by using the definition (2.12) along with (2.3). Note that (2.13) and (2.2) are *closed* for the conditional stress tensor $R_{ij}^{|\mathbf{n}}$ and n_i . That is, they can be solved without reference to the other conditioned moments.

2.4 Particle Representation Model for Slow Deformations

Whenever the time scale of the mean deformation is large compared to that of the turbulence the nonlinear turbulence-turbulence interactions become important in the governing field equations. In the context of the Interacting Particle Representation Model (IPRM), these nonlinear processes are represented by a model for the particle-particle interactions.

Direct numerical simulations (Lee and Reynolds 1985) show that under weak strain the structure dimensionality D_{ij} remains considerably more isotropic than does the Reynolds stress R_{ij} . This leads to counter-intuitive R_{ij} behavior in axisymmetric expansion flows, supported by experiments (Choi 1983). Hence we modify the basic evolution equations (2.2) and (2.3) to account for these effects. The resulting cluster-averaged evolution equations are

$$\dot{n}_i = -G_{ki}^n n_k + G_{kr}^n n_k n_r n_i \quad (2.14)$$

$$\begin{aligned} \dot{R}_{ij}^{\text{In}} = & -G_{ik}^v R_{kj}^{\text{In}} - G_{jk}^v R_{ki}^{\text{In}} - C_r [2R_{ij}^{\text{In}} - R_{kk}^{\text{In}} (\delta_{ij} - n_i n_j)] \\ & + [G_{km}^n + G_{km}^v] (R_{im} n_k n_j + R_{jm} n_k n_i). \end{aligned} \quad (2.15)$$

Note that the mean velocity gradient tensor G_{ij} that appeared in (2.2) and (2.13) has been replaced by the *effective* gradient tensors G_{ij}^v and G_{ij}^n . These are defined by

$$G_{ij}^n = G_{ij} + \frac{C_n}{\tau} r_{ik} d_{kj} \quad G_{ij}^v = G_{ij} + \frac{C_v}{\tau} r_{ik} d_{kj}. \quad (2.16)$$

Here $r_{ij} = R_{ij}/q^2$ and $d_{ij} = D_{ij}/q^2$ where $q^2 = 2k = R_{ii}$. The two constants are taken to be $C_n = 2.2C_v = 2.2$. The different values for these two constants account for the different rates of return to isotropy of \mathbf{D} and \mathbf{R} . The time scale of the turbulence τ is evaluated so that the dissipation rate in the IPRM

$$\epsilon^{\text{PRM}} = q^2 \frac{C_v}{\tau} r_{ik} d_{km} r_{mi} \quad (2.17)$$

matches that obtained from a modified model equation for the dissipation rate,

$$\dot{\epsilon} = -C_0(\epsilon^2/q^2) - C_s S_{pq} r_{pq} \epsilon - C_\Omega \sqrt{\Omega_n \Omega_m d_{nm}} \epsilon. \quad (2.18)$$

The last term in (2.18) accounts for the suppression of ϵ by mean rotation. Here Ω_i is the mean vorticity vector, and the constants are taken to be

$$C_0 = -\frac{11}{3} \quad C_s = -3.0 \quad \text{and} \quad C_\Omega = 0.01.$$

Mean rotation acting on the particles tends to produce rotational randomization of the \mathbf{V} vectors around the \mathbf{n} vectors (Mansour *et al.* 1991, Kassinos and Reynolds 1994). The third (bracketed) term in (2.15), is the *slow rotational randomization model*, which assumes that the effective rotation due to nonlinear particle-particle interactions, $\Omega_i^* = \epsilon_{ipq} r_{qk} d_{kp}$, should induce a similar randomization effect, while leaving the conditional energy unmodified. Based on dimensional considerations and requirements for material indifference to rotation (Speziale 1981), we take

$$C_r = \frac{8.5}{\tau} \Omega^* f_{pq} n_p n_q, \quad \Omega^* = \sqrt{\Omega_k^* \Omega_k^*}, \quad \Omega_i^* = \epsilon_{ipq} r_{qk} d_{kp}. \quad (2.19)$$

The rotational randomization coefficient C_r is sensitized to the orientation of the \mathbf{n} vector, so that the slow rotational randomization vanishes whenever the large-scale circulation is confined in the plane normal to \mathbf{n} .

The pressure P is determined by the requirement that $V_k N_k = 0$ is maintained by (2.14) and (2.15). This determines the effects of the slow pressure strain-rate-term without the need for further modeling assumptions

$$P = \underbrace{-2G_{mk} \frac{V_k N_m}{N^2}}_{\text{rapid}} - \underbrace{\frac{(C^v + C^n)}{\tau} r_{mt} d_{tk} \frac{V_k N_m}{N^2}}_{\text{slow}}. \quad (2.20)$$

3. A ONE-POINT STRUCTURE-BASED MODEL BASED ON THE IPRM

A one-point structure-based model for the deformation of homogeneous turbulence can be derived directly from the IPRM formulation. At the one-point level, additional modeling assumptions must be introduced in order to deal with the non-locality of the pressure fluctuations. Here we limit the formulation of the one-point model to the case of irrotational deformation of homogeneous turbulence and discuss briefly the more general case.

As a result of the constitutive equation (2.8), a *structure-based* one-point model must carry the transport equations for only two of the three second-rank tensors. Here we propose a model based on the R_{ij} and D_{ij} equations, which are the one-point analogs of (2.14) and (2.15). Using the definitions (2.12) and the evolution equations (2.14) and (2.15), and averaging over all clusters, one obtains

$$\dot{D}_{ij} = -D_{ik} G_{kj}^n - D_{jk} G_{ki}^n + 2q^2 G_{km}^n Z_{kmi}^d - 2G_{km}^v M_{mkij} \quad (3.1)$$

and

$$\begin{aligned} \dot{R}_{ij} = & -G_{ik}^v R_{kj} - G_{jk}^v R_{ki} \\ & - \hat{C}_r f_{pq} [2M_{ijpq} - (\delta_{ij} D_{pq} + q^2 Z_{ijpq}^d)] \\ & + [G_{km}^n + G_{km}^v] (M_{imki} + M_{jmki}). \end{aligned} \quad (3.2)$$

Here G_{ij}^n and G_{ij}^v are as defined for the IPRM in (2.16), and $\hat{C}_r = 8.5\Omega^*/\tau$ where Ω^* is given in (2.19). The fourth-rank tensors

$$Z_{ijk m}^d = \langle V^2 n_i n_j n_k n_m \rangle / q^2 \quad \text{and} \quad M_{ijpq} = \langle V^2 v_i v_j n_p n_q \rangle \quad (3.3)$$

must be modeled. Note that \mathbf{Z} is the fully symmetric, energy-weighted fourth moment of a single vector, for which we have been able to construct a good model. What is more, one can use an exact decomposition based on group theory (see Kassinos & Reynolds 1994) to express M_{ijpq} in terms of fourth moments of a single vector and the second-rank tensors R_{ij} and D_{ij} :

$$\begin{aligned} M_{ipqj} = & \frac{1}{2} q^2 (Z_{ipqj}^f - Z_{ipqj}^r - Z_{ipqj}^d) + \frac{1}{6} [-3\delta_{ip}\delta_{qj}q^2 \\ & + 4(\delta_{qj}R_{ip} + \delta_{ip}D_{qj}) + 2(\delta_{qj}D_{ip} + \delta_{ip}R_{qj})]. \end{aligned} \quad (3.4)$$

Note that in the presence of mean rotation (3.4) involves additional terms that require modeling of the *stropholysis* effects (see Reynolds and Kassinos 1995). Here

$$Z_{ijpq}^r = \langle V^2 v_i v_j v_p v_q \rangle / q^2 \quad \text{and} \quad Z_{ijpq}^f = \langle V^2 s_i s_j s_p s_q \rangle / q^2. \quad (3.5)$$

Substituting (3.4) in (3.1) and (3.2) and using the definitions (2.10), one obtains

$$\begin{aligned} \dot{d}_{ij} = & -d_{jk}G_{ki}^n - d_{ik}G_{kj}^n + 2G_{km}^v r_{km}(d_{ij} - \frac{2}{3}\delta_{ij}) \\ & - \frac{2}{3}G_{km}^v d_{mk}\delta_{ij} + G_{kk}^v(\delta_{ij} - \frac{4}{3}d_{ij} - \frac{2}{3}r_{ij}) \\ & + (2G_{km}^n + G_{km}^v)Z_{kmij}^d + G_{km}^v Z_{mkij}^r - G_{km}^v Z_{mkij}^f \end{aligned} \quad (3.6)$$

and

$$\begin{aligned} \dot{r}_{ij} = & \frac{1}{3}(G_{mj}^v + G_{mj}^n)(2d_{mi} + r_{mi}) \\ & + \frac{1}{3}(G_{mi}^v + G_{mi}^n)(2d_{mj} + r_{mj}) \\ & + \frac{1}{3}G_{jm}^v(d_{mi} - r_{mi}) + \frac{1}{3}G_{im}^v(d_{mj} - r_{mj}) \\ & + \frac{1}{3}G_{jm}^n(d_{mi} + 2r_{mi}) + \frac{1}{3}G_{im}^n(d_{mj} + 2r_{mj}) \\ & + 2G_{km}^v r_{km} r_{ij} - \frac{1}{2}(G_{ij}^v + G_{ji}^v + G_{ij}^n + G_{ji}^n) \\ & + (G_{mk}^v + G_{mk}^n)(Z_{ikmj}^f - Z_{ikmj}^r - Z_{ikmj}^d) \\ & - \dot{C}_r f_{pq}[Z_{ijpq}^f - Z_{ijpq}^r + \frac{2}{3}\delta_{pq}(r_{ij} - f_{ij}) \\ & + \frac{1}{3}\delta_{ij}(r_{pq} - f_{pq})]. \end{aligned} \quad (3.7)$$

Closure of (3.6) and (3.7) in the irrotational case requires a consistent model for the fully symmetric tensors Z_{ijpq}^n , Z_{ijpq}^r , and Z_{ijpq}^f . We have constructed a model for the energy-weighted fourth moment of any vector t_i in terms of its second moment t_{ij} that allows the successful closure of (3.1) and (3.2) while maintaining *full realizability*. The same model can be used for each of the three vectors v_i , n_i , and s_i and their moments and has the general form

$$\begin{aligned} Z_{ijpq}^t = & \langle V^2 t_i t_j t_p t_q \rangle / q^2 = C_1 \mathbf{i} \circ \mathbf{i} + C_2 \mathbf{i} \circ \mathbf{t} \\ & + C_3 \mathbf{t} \circ \mathbf{t} + C_4 \mathbf{i} \circ \mathbf{t}^2 + C_5 \mathbf{t} \circ \mathbf{t}^2 + C_6 \mathbf{t}^2 \circ \mathbf{t}^2. \end{aligned} \quad (3.8)$$

Here \mathbf{i} and \mathbf{t} stand for δ_{ij} and $t_{ij} = \langle V^2 t_i t_j \rangle / q^2$ respectively. Extended tensor notation is used in (3.8), where the fully symmetric product of two second-rank tensors \mathbf{a} and \mathbf{b} is denoted by

$$\mathbf{a} \circ \mathbf{b} \equiv a_{ij}b_{pq} + a_{ip}b_{jq} + a_{jp}b_{iq} + a_{iq}b_{jp} + a_{jq}b_{ip} + a_{pq}b_{ij}.$$

The coefficients C_1 - C_6 are functions of the invariants of t_{ij} and determined by enforcing the trace condition $Z_{ijkk}^t = t_{ij}$, 2D realizability conditions for the case when the vectors t_i lie in a plane, and an important identity,

$$\mathbf{Z}^a = \frac{1}{16}\mathbf{i} \circ \mathbf{i} - \frac{1}{8}\mathbf{i} \circ \mathbf{b} + \frac{3}{8}\mathbf{Z}^b, \quad (3.9)$$

which applies between the fourth moments of two vectors a_i and b_i when a_i is randomly distributed about b_i . Kassinos & Reynolds (1994) gave an earlier \mathbf{Z} model that does not exactly satisfy (3.9). The new coefficients will be published separately.

Next, we consider the performance of the interacting particle representation and one-point models for two cases of irrotational mean deformation. In addition, the IPRM is evaluated for the case of homogeneous shear.

3. EVALUATION OF THE IPRM AND ONE-POINT MODELS

In this section, the IPRM based on (2.14), (2.15), (2.17), and (2.18) and the one-point model based on (3.6), (3.7), and (3.8) are evaluated for several cases of deformation of homogeneous turbulence. The examples considered here show that, even with a relatively simple closure for non-linearity, both models achieve remarkably accurate predictions.

For example, results for the case of irrotational axisymmetric expansion with an initial $Sq_0^2/\epsilon_0 = 0.82$ are shown in Figure 1. Here the axis of symmetry is taken to be x_1 . The predictions of the IPRM (solid lines) and those of the one-point model (dashed lines) are compared with the direct numerical simulation (DNS) of Lee & Reynolds (1985), shown as symbols. The evolution histories are plotted against

$$C = \exp\left(\int_0^t |S_{\max}(t')| dt'\right),$$

where S_{\max} is the largest principal value of the mean strain tensor. As discussed in Kassinos & Reynolds (1995), the axisymmetric expansion flows exhibit counter-intuitive behavior, where a weaker mean deformation rate produces a level of stress anisotropy \bar{r}_{ij} that exceeds the one produced under RDT. This effect, which is also supported by the experiments of Choi (1983), is triggered by the different rates of return to isotropy in the r and d equations, but it is dynamically controlled by the rapid terms. The net effect is a growth of \bar{r}_{ij} in expense of \bar{d}_{ij} , which is strongly suppressed. As shown in Figure 1, the predictions of the IPRM and one-point models are almost indistinguishable from each other, and both are able to capture these intriguing effects quite accurately. The predictions of both models for the evolution of the normalized turbulent kinetic energy and dissipation rate are also in good agreement with the DNS.

Figure 2 shows evolution histories for the three tensor anisotropies, and for k and ϵ , for a case of weak irrotational plane strain ($Sq_0^2/\epsilon_0 = 1.0$). The mean deformation is in the x_2 - x_3 plane. Again, the IPRM predictions are shown as solid lines and those of the one-point model as dashed lines. Comparison is made with the 1985 DNS of Lee & Reynolds (symbols). Note how the predictions of the one-point model are practically indistinguishable from those of the IPRM and how both models are in excellent agreement with the DNS results for all predictions.

Next, we consider the case of homogeneous shear flow with an initial $Sq_0^2/\epsilon_0 = 4.73$, where S is the shear rate. In this case the evaluation is restricted to the IPRM because the formulation of the one-point model was presented only for irrotational deformations. The IPRM predictions for the components of the normalized Reynolds stress tensor r_{ij} are shown in Figure 3a. The symbols are from the DNS of Rogers and Moin (1986). The agreement between the IPRM predictions and the DNS results is good, but the IPRM somewhat overpredicts r_{11} and underpredicts r_{22} . Figure 3b shows the prediction for the components of the normalized dimensionality tensor d_{ij} , where again the IPRM achieves a satisfactory level of accuracy. The evolutions of the normalized turbulent kinetic energy and dissipation rate are shown in Figure 3c. The IPRM does predict the correct growth rates for both k/k_0 and ϵ/ϵ_0 , but the agreement between actual values is moderate. Figure 3d shows the evolution of the dimensionless parameters P/ϵ and Sk/ϵ , where P is the production of k . The IPRM predictions (lines) are in good agreement with DNS results (symbols), especially in the period $8 \lesssim St \lesssim 15$ where the DNS was fully developed. The same equilibrium values are predicted for the two dimensionless parameters by both the DNS simulation and the IPRM.

CONCLUSION

One-point turbulence models must reflect the viscoelastic response of turbulence to mean deformation. Models based solely on R_{ij} cannot do that. Under non-equilibrium conditions (e.g. rapid deformation) models must include information on the structure of the turbulence. Here we outlined the formulation of a successful interacting particle representation model (IPRM) for the deformation of homogeneous turbulence. The IPRM is exact in the RDT limit and quite accurate for slow deformations, including flows with strong mean rotation effects. A consistent one-point model follows directly from the IPRM formulation. Here the construction of the one-point structure-based model was outlined for the case of irrotational mean deformation. We have found that under irrotational strain the one-point model achieves accuracy that is comparable to that of the IPRM. Extensions of the one-point model for more general flows require additional modeling to deal with the *stropholysis* effects arising due to the breaking of reflectional symmetry by mean rotation. A general one-point model for inhomogeneous turbulence using the scheme outlined here is currently under development.

ACKNOWLEDGMENTS

This work has been supported by the Air Force Office of Scientific Research (Dr. James McMichael and Dr. Mark Glauser).

REFERENCES

- Choi, Kwing-So., 1983, "A study of the return to isotropy of homogeneous turbulence," Technical report, Sibley School of Mechanical and Aerospace Engineering, Cornell University, New York.
- Kassinos, S. C. & Reynolds, W. C., 1995, "An extended structure-based model based on a stochastic eddy-axis evolution equation," *Annual Research Briefs 1995*, Center for Turbulence Research, 133-148.
- Kassinos, S. C. & Reynolds, W. C., 1994, "A structure-based model for the rapid distortion of homogeneous turbulence," Report TF-61, Thermosciences Division, Department of Mechanical Engineering, Stanford University.
- Lee, M. J. & Reynolds, W. C., 1985, "Numerical experiments on the structure of homogeneous turbulence," Report TF-24, Thermosciences Division, Department of Mechanical Engineering, Stanford University.
- Mansour, N. N., Shih, T.-H., & Reynolds, W. C., 1991, "The effects of rotation on initially anisotropic homogeneous flows," *Phys. Fluids A* **3**, 2421-2425.
- Reynolds, W. C. & Kassinos, S. C., 1995, "One-point modelling of rapidly deformed homogeneous turbulence," *Proceedings of the Royal Society of London A*, **451**, 87-104.
- Rogers, M. M. & Moin, P., 1987, "The structure of the vorticity field in homogeneous turbulent flows," *J. Fluid Mech.* **176**, 33-66.
- Speziale, C. G. 1981 "Some interesting properties of two-dimensional turbulence," *Phys. Fluids* **24**(8), 1425-1427.

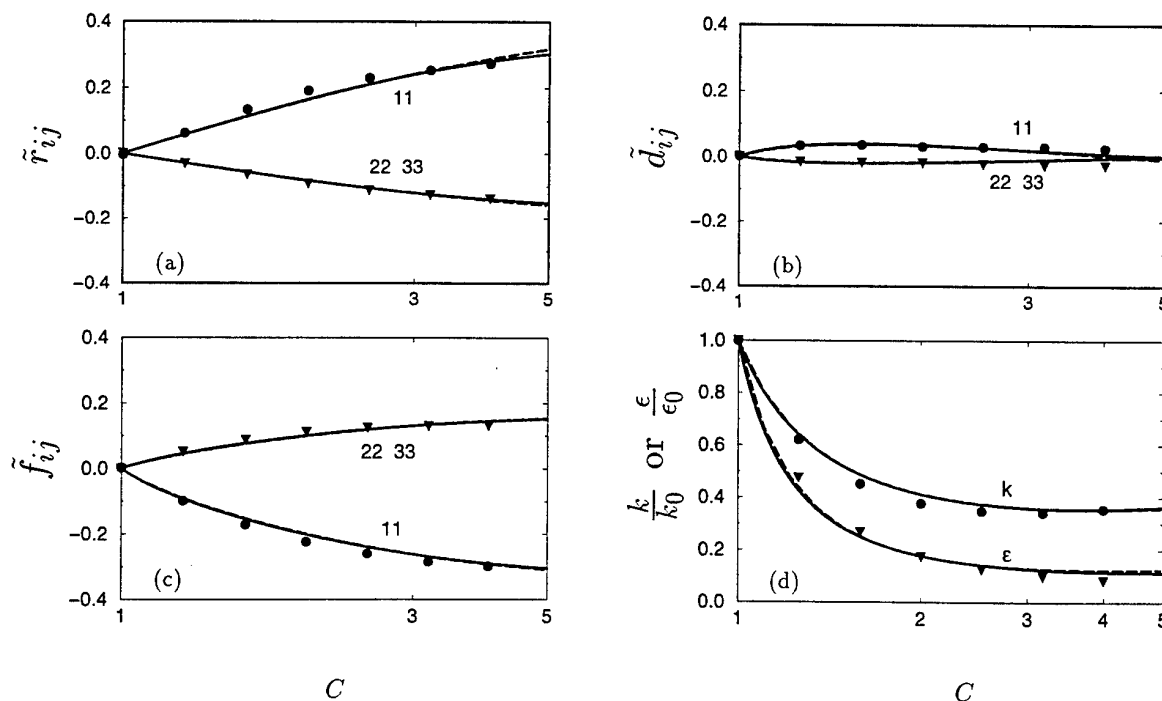


FIGURE 1. Comparison of the one-point model predictions (dashed lines) with the IPRM results (solid lines) and the 1985 DNS of Lee & Reynolds (symbols) for axisymmetric expansion case EXO ($Sq_0^2/\epsilon_0 = 0.82$). (a)-(c) evolution of the Reynolds stress, dimensionality, and circulatory anisotropies; 11 component (\bullet), 22 and 33 components (\blacktriangledown). (d) evolution of the normalized turbulent kinetic energy (\bullet) and dissipation rate (\blacktriangledown).

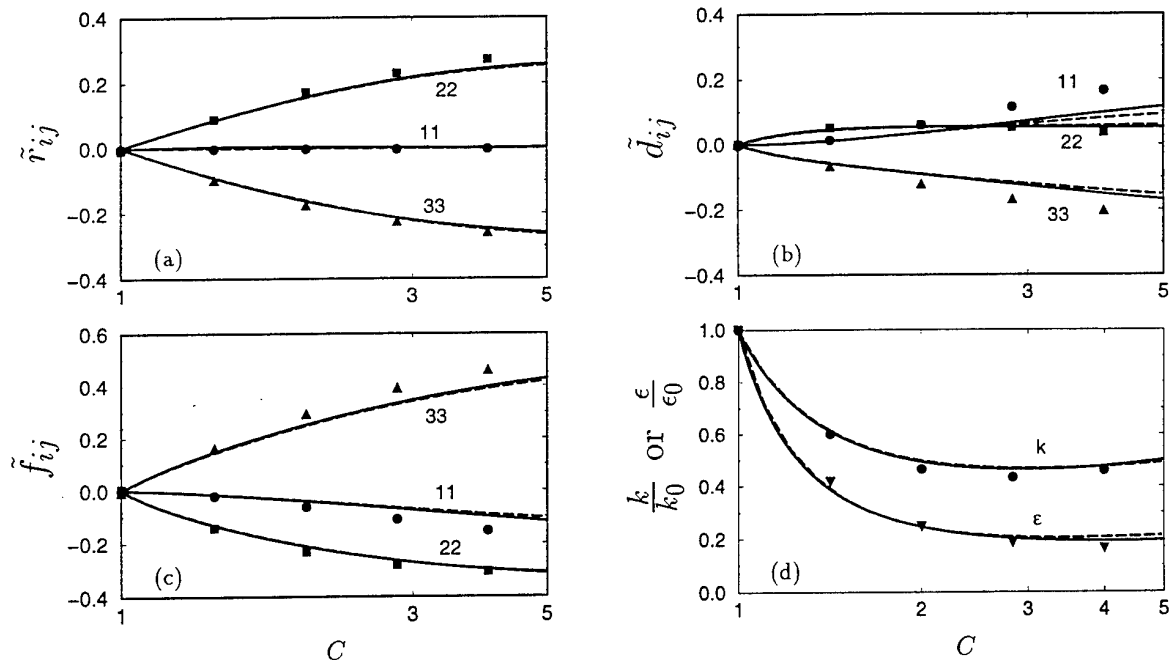


FIGURE 2. Comparison of the one-point model predictions (dashed lines) with the IPRM results (solid lines) and the 1985 DNS of Lee & Reynolds (symbols) for plane strain case PXA ($Sq_0^2/\epsilon_0 = 1.0$). (a)-(c) evolution of the the Reynolds stress, dimensionality, and circuality anisotropies; 11 component (\bullet), 22 component (\blacksquare), and 33 component (\blacktriangledown). (d) evolution of the normalized turbulent kinetic energy (\bullet) and dissipation rate (\blacktriangledown).

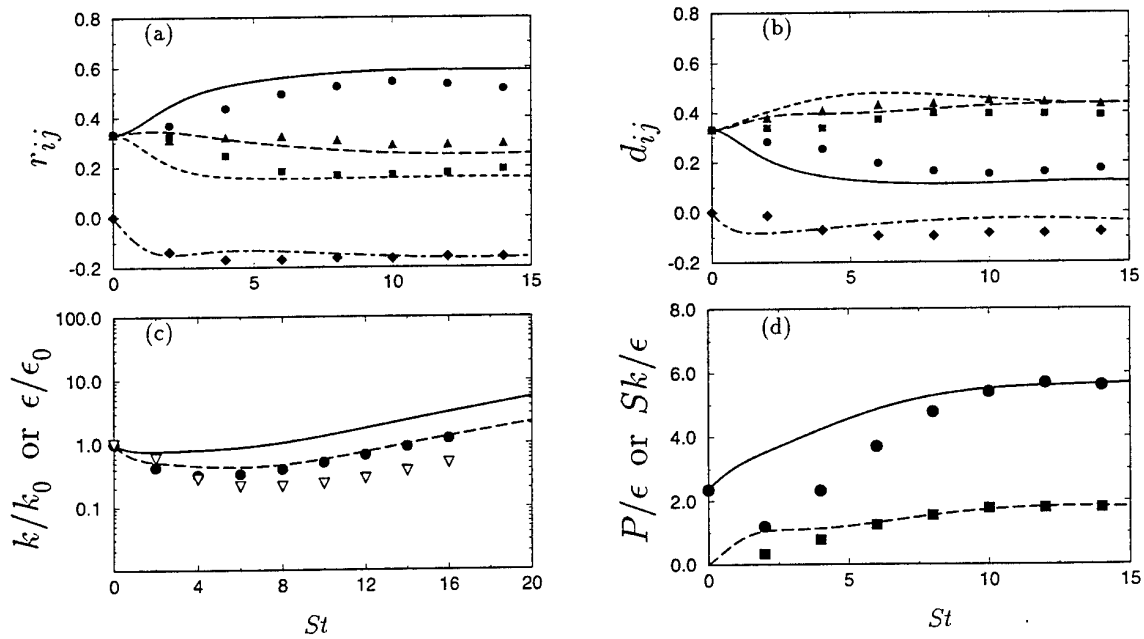


FIGURE 3. Comparison of IPRM predictions (shown as lines) with the DNS of Rogers and Moin (1986) for homogeneous shear ($Sq_0^2/\epsilon_0 = 4.73$). (a) and (b) evolution of the normalized Reynolds stress and dimensionality tensors; 11 component (—, \bullet), 22 component (---, \blacksquare), 33 component (---, \blacktriangledown), 12 component (—, \blacklozenge). (c) evolution of the normalized turbulent kinetic energy (—, \bullet) and dissipation rate (---, \blacktriangledown). (d) evolution of the dimensionless parameters P/ϵ (---, \blacksquare) and Sk/ϵ (—, \bullet).

Analytical constraints for single-point closures in geophysical turbulence

J.R. Ristorcelli

Institute for Computer Applications in Science and Engineering
NASA Langley Research Center
Hampton, Virginia 23693
USA

Introduction

In many rapidly rotating turbulent flows the largest scales of the motion are in approximate geostrophic balance. Unfortunately most single-point turbulence closures cannot reflect such a geostrophic balance. This article addresses and resolves the possibility of constitutive relation procedures for single-point second-order closures for a specific class of flows that include rapidly rotating flows, flows with large stable stratification and also flows that satisfy the shallow layer approximation. Physical situations in which the geostrophic balance is attained are described. Closely related issues of frame-indifference, horizontal nondivergence, Taylor-Proudman theorem and two-dimensionality are, in the context of both the instantaneous and averaged equations, discussed. It is shown that *in the absence of vortex stretching along the axis of rotation that turbulence is frame-indifferent*. This physical fact leads to what has been called the geostrophic constraint, Ristorcelli (1987), on the rapid-pressure covariance. A derivation and discussion of the geostrophic constraint which the second-order moment equations must satisfy for turbulence approaching a frame-indifferent limit as is likely in many geophysical applications.

These flow situations, which include rotating and *nonrotating* stratified flows, are slowly evolving flows in which the constitutive relation procedures are useful, Lumley (1970), Ristorcelli (1996, 1997). A nonlinear non-constant coefficient representation for the rapid-pressure strain covariance appearing in the Reynolds stress and heat flux equations consistent with the geostrophic balance is possible, Ristorcelli *et al.* (1995). The rapid-pressure strain model coefficients are not constants determined by numerical optimization but are functions of the state of the turbulence as parameterized by the Reynolds stresses and the turbulent heat fluxes.

Frame-indifference and horizontal divergence

It is shown that horizontally-divergent-free flows have evolution equations that are frame-indifferent. The Navier-Stokes equations, in the Boussinesq approximation, are

$$\frac{D}{Dt} u_i + 2\epsilon_{ikp} \Omega_k u_p = -p_{,i} + g\beta_i \theta + \nu \omega_{i,jj}. \quad (1)$$

The pressure has been normalized by the constant density. For simplicity it shall be assumed that the rotation and gravity are along the "3" axis. The curl of the Navier-Stokes equations produces the vorticity equation

$$\frac{D}{Dt} \omega_i = (\omega_j + 2\Omega_j) u_{i,j} + \epsilon_{imq} g \beta_q \theta_{,m} + \nu \omega_{i,jj}. \quad (2)$$

where $\omega_k = \epsilon_{kqi} u_{i,q}$. Inspection shows that it is frame-invariant if there is no axial stretching of vorticity, $\Omega_j u_{i,j} = 0$. In a wide class of geophysical flows the dynamically significant component of the vorticity is vertical and thus $\Omega_j u_{3,j} = 0$. A horizontally-divergent-free flow has $-w_{,z} = u_{,x} + v_{,y} = 0$; thus a horizontally divergence free flow, $\Omega_j u_{3,j} = 0$, is frame-indifferent *for arbitrary rotation rate*.

The geostrophic balance of the horizontal momentum equations indicates

$$2\epsilon_{ikp} \Omega_k u_p = -p_{,i} \quad (3)$$

which allows a representation $u_p = \epsilon_{pqk} \hat{\Omega}_k \psi_{,q} + w \delta_{i3}$, and the pressure plays the role of a streamfunction. Such of representation includes a horizontal turbulence whose velocity components lie in planes perpendicular to the axis of rotation as well as three-dimensional velocity fields that are independent of the coordinate along the axis of rotation. There are several geophysical situations in which the horizontal divergence $\Omega_j u_{3,j} \rightarrow 0$ can vanish; these include flows described by the shallow water equations as well as stably stratified or rapidly rotating flows and also baroclinic flows.

Taylor Proudman flows

For rapidly rotating flows the Taylor-Proudman limit, for those portions of the flow whose frequency is slow with respect to the rotation of the frame, is obtained from the vorticity equation,

$$\Omega_j u_{i,j} \rightarrow 0 \quad (4)$$

as $\Omega_j \rightarrow \infty$. This implies $u_p = \epsilon_{pqk} \hat{\Omega}_k \psi_{,q} + w \delta_{i3}$ with $\psi = \psi(x, y)$ and $w = w(x, y)$. The motions of a fluid

undergoing rapid rotation is the same in planes perpendicular to the axis of rotation. The Taylor-Proudman result which indicates that portions of the motion with time scales slow compared to the rotational period become horizontally divergent free: the vorticity generation mechanisms of stretching along the axis of rotation $\Omega_3 s_{33}$ (and rotating into the axis of rotation $\Omega_3 w_{\alpha 3}$, ($\alpha = 1, 2$)) are absent. Here $s_{ij} = \frac{1}{2}[u_{i,j} + u_{j,i}]$ and $w_{ij} = \frac{1}{2}[u_{i,j} - u_{j,i}]$.

The rotating tank: Greenspan (1968), has tentatively summarized the major effects of rotation as being the tendency of the flow to become two-dimensionalized in planes perpendicular to the axis of rotation, the occurrence of inertial wave for frequencies, $\omega < 2\Omega$ and the rapid spin up of fluid elements or creation of intense vortices. These three regimes are seen in the rotating grid generated turbulence studied by Hopfinger, Browand and Gagne (1982). The rotating tanks is an inhomogeneous turbulence with no mean flow; an isotropic turbulence is generated at an oscillating grid placed at the bottom of the rotating tank. This flow is a graphic demonstration of the effects of rotation as a function of the local turbulent Rossby number, $Ro_t = \bar{u}/2\Omega\ell$, which changes in the inhomogeneous (axial) direction. The axial coordinate is a proxy for the Rossby number which decreases with from distance from the grid as, near the grid, $\bar{u} \sim z^{-1}$ and $\ell \sim z$ and $Ro_t \sim z^{-2}$.

The grid is oscillated at a frequency much larger than $f > 2\Omega$. Near the grid one obtains an isotropic three-dimensional turbulence unaffected by rotation as seen in inertial systems. This is a region of large Ro_t ; as long as the turbulence frequency $\bar{u}/\ell > 2\Omega$ the usual three-dimensional turbulence exists.

Further from the oscillating grid, $Ro_t < 0.4$, there is a transitional zone in which the largest scales of the motion are two-dimensional over which are superposed smaller scale ageostrophic motions. In this region the energy decay is substantially diminished; this is due to a reduction of vortex stretching and thus the reduction of the cascade from the energy containing two-dimensional scales. The smaller ageostrophic motions continue to lose energy through the cascade and dissipation. The fluctuating field is composed of inertial waves and turbulence.

Further past the transitional zone there is a third region in which the turbulence, now almost purely two componential is independent of the axial coordinate, two-dimensional - "2D-2C", Reynolds (1987). The transition to this flow takes place abruptly at $Ro_t = 0.2$. The flow is composed of thin coherent columnar vortices whose lifespans are very large compared to the rotation period, $(2\Omega)^{-1}$ and the eddy turnover time, ℓ/\bar{u} . The flow, in this region, is consistent with the Taylor-Proudman theorem:

$$\Omega_j u_{i,j} \rightarrow 0. \quad (5)$$

In this region of the flow both energy and enstrophy conserved quantities and as a consequence the transfer of energy from a larger to a smaller scale of the flow is accompanied by transfer from smaller to larger wavenumber. The "inverse cascade" imposes a powerful constraint on nonlinear interactions between different scales of the motion. It is accompanied, as is well known, by vortex merging phenomenon. The vorticity of the vortices can be two orders of magnitude larger than the background rotation.

Baroclinic flows

Flows with buoyancy (unstable) and rotation also have features leading to frame-indifferent conditions. For baroclinic flows the thermal wind balance of the vorticity equation, in the limit of large rotation, is

$$2\Omega_j u_{i,j} = -\epsilon_{imq} g \beta_q \theta_{,m}. \quad (6)$$

The individual components of the vorticity equation require, for $i = 1, 2$, $2\Omega_j u_{i,j} = -\epsilon_{imq} g \beta_q \theta_{,m}$, and for $i = 3$,

$2\Omega_j u_{3,j} = 0$. The velocity field, to lowest order in Ro_t , is described by a streamfunction

$$u_p = \epsilon_{pqk} \hat{\Omega}_k \psi_{,q} + w \delta_{i3} \quad (7)$$

$$\psi_{,p} = \epsilon_{qp k} \hat{\Omega}_k u_q + \hat{\Omega}_p \hat{\Omega}_q \psi_{,q} \quad (8)$$

where $\psi = \psi(x, y, z)$. The carat indicates a unit vector. This is easily seen by contracting on the geostrophic balance: $\epsilon_{ijq} \Omega_q [2\epsilon_{ikp} \Omega_k u_p = -p_{,i} + g\beta_i \theta]$. Carrying through the mathematics one obtains $\psi = -p/2\Omega$. The streamfunction and pressure field are proportional and the isobars and streamlines are aligned. Thus $u \sim -p_{,y}$ and $v \sim p_{,x}$ and to lowest order $u_{,x} + v_{,y} = 0$. The hydrostatic balance, $p_{,3} = g\beta\theta$ leads to $\theta = \frac{-2\Omega}{g\beta} \psi_{,3}$. The vertical velocity is then obtained diagnostically from the energy equation, $\frac{D}{Dt} \theta = 0$. The vorticity is related to the streamfunction, $\psi = \psi(x, y, z)$, by

$$\omega_i = \hat{\Omega}_i \psi_{,il} - \hat{\Omega}_i \psi_{,qq}. \quad (9)$$

The vertical component of the vorticity is given by the horizontal Laplacian of the streamfunction $\omega_3 = -\nabla_H^2 \psi$ which evolves according to

$$\dot{\omega}_3 + u_j \omega_{3,j} = (\omega_j + 2\Omega_j) u_{3,j} + \nu \omega_{3,jj}. \quad (10)$$

This is then the prognostic equation for the streamfunction and it is closed with respect to the streamfunction. It is frame indifferent if the velocity field is horizontally divergent-free.

The differentially heated rotating annulus: This is an example of a flow in which both buoyancy and rotation are important. This experimental set up simulates the transport of heat in the atmosphere (*modulo* the beta effect) from the warm equatorial regions to the poles: the heated outer cylinder representing the equatorial regions, the cool inner cylinder the polar regions, the azimuthal direction represents the zonal (east-west) flows. A horizontal temperature gradient is impressed across a rotating annulus. Under the action of strictly gravitation torques the fluid elements undergo an overturning motion and the differential heating produces a stably stratified meridional circulation. The mean vorticity is azimuthal. At zero and low rotation rates the flow is an "ageostrophic" thermal turbulence (provided the Grashof number is high enough). As the annulus is rotated more rapidly several things occur: Coriolis forces inhibit the meridional flow, vertical component of the velocity is reduced, and an azimuthal component to the mean velocity is induced. The Coriolis force that inhibits the overturning motion in the meridional planes and promotes a different kind of convection called sloping convection, Hide and Mason (1975): fluid elements have trajectories with very small angles to the horizontal. This is a manifestation of baroclinic waves. The waves transfer heat and momentum perpendicular to the shear.

Some of the features of this sequence of transitions, more comprehensively described in Ristorcelli (1996, 1997), can be understood from the thermal wind balance. The momentum equations, in this limit, reflect the geostrophic and hydrostatic balances,

$$2\Omega_3 U_2 \simeq p_{,1}, \quad 2\Omega_3 U_1 \simeq p_{,2}, \quad g\beta T \simeq -p_{,3}. \quad (11)$$

Here the coordinates $[x_1, x_2, x_3]$ are the cartesian equivalents to the cylindrical system $[r, \theta, z]$. The comma indicates differentiation with respect to the subscripted variable. The basic state represents a balance between buoyancy, Coriolis and pressure forces in the interior of the fluid. The equations for the azimuthal and vertical components of the vorticity become

$$2\Omega_3 U_{2,3} \simeq g\beta T_{,2}, \quad 2\Omega_3 U_{3,3} \simeq 0. \quad (12)$$

If the basic state of the temperature field is assumed to be of the form $T(x_1, x_3) = x_3 - x_1 \tan(\theta)$ the balance requires

an azimuthal shear, $U_2 = \frac{g\beta T}{2\Omega} z$. This is the basic state that is used in the Eady model for the analysis of the baroclinic instability, Hide and Mason (1976). It is valid when the Ekman and Rossby numbers are small. The baroclinic instability is the instability of the vertically sheared zonal current, $U_2 = \frac{g\beta T}{2\Omega} z$.

For a given Prandtl number the flow can be characterized by two nondimensional numbers: the thermal Rossby number, $Ro_{th} = g\beta\Delta TH/\Omega^2(R_o - R_i)^2$, and a Taylor number, $Ta = 4\Omega^2(R_o - R_i)^2/\nu^2$ where R_o and R_i are the outer and inner radii of the annulus. The different flow states as a function of these two external flow parameters reflecting the size of the impressed horizontal temperature gradient and the rate of rotation is of interest. The complex sequence of intermediate flow states, associated with the baroclinic instability, are nicely illustrated in the heated rotating annulus flows of Buzyna, Pfeffer and King (1984), Fein and Pfeffer (1976) and Hide and Mason (1975). In this brief communication only the low rotation and high rotation rates are described.

Thermal turbulence: At large values of the Rossby number, $Ro_{th} \gg 1$ (low rotation rates) the flow in the annulus is essentially buoyancy driven with a unicellular meridional circulation. The flow field is axisymmetric and the mean vorticity is azimuthal. As the rotation increases Coriolis forces reduce the azimuthal component of the mean vorticity, the vertical component of the velocity is reduced, and the mean velocity becomes zonal. This is accompanied by a reduction in heat transfer across the annulus. In addition, the stable stratification (associated with the meridional circulation driven by the horizontal heat flow) decreases, the temperature fluctuations decrease and conduction becomes a much more important component of the heat transfer.

Geostrophic turbulence: When $Ro_{th} < 0.1$ the flow is spatially (in the horizontal) and temporally uncorrelated; the flow is perfectly correlated in the vertical. The temperature spectrum is broad and relatively featureless. The heat flux across the annulus undergoes a sudden decrease as the flow becomes a geostrophic turbulence; essentially composed of random unsteady baroclinic waves. With increasing rotation more baroclinic waves of higher azimuthal wavenumber appear; this is a necessary prerequisite for the transition to a baroclinic turbulence which requires an inverse cascade and cannot occur until there are enough small scales for a spectral flux to larger scales.

Stably stratified flows

In the previous sections the flows approached frame-indifference due to the constraints imposed on the dynamics by the rapid rotation limit of the vorticity equation. Now the stable stratification, as quantified by the mean density gradient, plays a role analogous to the rotation. Like the baroclinic flow the additional degree of freedom of the system – the temperature or the density – is linked to the dynamics through the hydrostatic balance of the vertical momentum equation. In the baroclinic flows the vertical velocity is not zero. In stably stratified flows, on the time scale of the turbulence, the vertical velocity vanishes and, consequently, the horizontal divergence is small.

A scale analysis of the continuity and vorticity equations can be used to scale the relative magnitudes of the vertical and horizontal components of velocity. Linearizing around the basic stratified state the continuity equation becomes,

$$u_j \rho_{,j} + u_3 \frac{d\rho_0}{dz} = 0 \quad \Rightarrow \quad \rho \sim \frac{u_3 \ell}{u_H} \frac{d\rho_0}{dz}. \quad (13)$$

The balance in the vorticity equation produces

$$\rho_0(u_j \omega_{i,j} - \omega_j u_{i,j}) = \epsilon_{imq} g_{q,m} \Rightarrow \rho \sim \rho_0 \frac{u_H^2}{g\ell}. \quad (14)$$

Combining the two estimates produces

$$\frac{u_3}{u_H} \sim \rho_0 \frac{u_H^2}{g\ell} \left| \frac{d\rho_0}{dz} \right|^{-1} \sim \frac{1}{Ri}. \quad (15)$$

Ri is the Richardson number. As the stable stratification increases Ri increases and $u_3 \rightarrow 0$ and the turbulence becomes a horizontal or pancake turbulence. For arbitrary rotation the axial stretching of the vertical vorticity goes to zero, $2\Omega_3 u_{3,3} \rightarrow 0$ as $u_3 \rightarrow 0$. The interested reader is referred to Ristorcelli (1996, 1997) for additional details.

The turbulence collapse: These scalings are consistent with the observation of the turbulence collapse for grid turbulence under stable stratification, Browand and Hopfinger (1982) and Browand, Guyomar and Yoon (1987), observed to take place when

$$\frac{\tilde{u}}{N\ell} < 0.3, \quad N^2 = \frac{g}{\rho_0} \left| \frac{d\rho_0}{dz} \right|. \quad (16)$$

This is analogous to the collapse of the two-dimensional flow seen far from the grid in the rotating tank flows, Hopfinger, Browand and Gage (1982). The Brunt-Väisälä frequency now plays the role the Coriolis frequency, 2Ω ; N^2 and 2Ω both represent upper bounds on the frequency range of gravity and inertial waves. They approximate the frequency with which a particle displaced from its equilibrium position oscillates. A similar collapse is seen in the wake of a sphere in a stably stratified environment: a fully three-dimensional turbulent wake collapses to create a two-dimensional wake, in the plane of the stratification, similar to the two-dimensional von Karman vortex street behind a cylinder. Some of these wake issues are summarized in Thorpe (1987) and Hopfinger (1987). Lin and Pao (1979) and Xu, Fernando and Boyer (1995) provide more detail.

Shallow water flows

In the shallow water flows the depth of the fluid is the dependent variable that plays the role of the pressure and thus streamfunction. The vertical velocity is small scaling with the aspect ratio of the domain. The horizontal divergence is a result of the changes in fluid depth due to the wave motion or topographical features and not the vertical variation of the vertical velocity. The vorticity equation, in the shallow water limit, can be written,

$$\begin{aligned} \omega_3 + u_j \omega_{3,j} &= (\omega_j + 2\Omega_j) u_{3,j} + \dots \\ &= -2\Omega_3 \frac{1}{h} \frac{D}{Dt} h + \dots \end{aligned} \quad (17)$$

The relationship between the horizontal divergence and the changes in fluid depth come from a first integral of the continuity equation and appropriate application of boundary conditions, Gill (1982). The leading order balance of the horizontal momentum equations, in which Coriolis forces balancing pressure forces, indicates a streamfunction: $u_p \sim \epsilon_{pqk} \hat{\Omega}_k \psi_{,q}$. The hydrostatic balance of the vertical momentum equation relates the pressure (streamfunction) to the fluid depth: $\psi \sim h$. The vertical component of the vorticity is given by the horizontal Laplacian of the streamfunction $\omega_3 = -\nabla_H^2 \psi \sim -\nabla_H^2 h$ and the system is closed: the evolution of the system is described by the vertical vorticity equation which has become an equation for h . The point is that if the horizontal divergence vanishes, or equivalently $\frac{D}{Dt} h = 0$, the flow is frame-indifferent and any modeled form of the equations should reflect this fact.

Frame-invariance of the second order equations

Our interest lies with constructing a turbulence closure consistent with physical principles: if the horizontal divergence vanishes (equivalently the axial stretching of vorticity) then the evolution equations for the turbulence must

be frame invariant. Thus any closure for the second-order moment equations must satisfy this invariance principle.

An investigation of the frame invariance of the second-moment equations is now described. It will be shown (1) how the geostrophic balance manifests itself in the second moment equations, and (2) what constraints a closure for the rapid-pressure covariances must satisfy.

It should be clear that a geostrophic turbulence is one whose horizontal divergence is small because its Rossby number is small reflecting a pressure-Coriolis balance $2\epsilon_{ikp}u_p\Omega_p \simeq -p_{,i}$. However any flow with vanishing horizontal divergence (arbitrary Rossby number) also satisfies the geostrophic constraint. Both have second-moment evolution equations that are frame-invariant.

In the second-order moment equations for an incompressible turbulence, Ristorcelli (1995, 1996, 1997), these issues of invariance appear in the pressure-strain and pressure-temperature gradient correlations, $-[\langle p_{,i}u_i \rangle + \langle p_{,i}u_j \rangle] = -[\langle pu_i \rangle_{,j} + \langle pu_j \rangle_{,i}] + \langle ps_{ij} \rangle$ and $\langle p_i\theta \rangle = \langle p_i\theta \rangle_{,i} - \langle p\theta_{,i} \rangle$. An equation for the pressure fluctuations comes from the divergence of the Navier-Stokes equations for the fluctuating velocity

$$u_{i,t} + u_j U_{i,j} + U_j u_{i,j} + u_j u_{i,j} - \langle u_i u_j \rangle_{,j} + 2\epsilon_{ikp}\hat{\Omega}_k u_p Ro^{-1} = -p_{,i} + \theta\beta_i + Re^{-1}u_{i,j} \quad (18)$$

which produces a Poisson equation for fluctuating pressure. The standard linear decomposition recognizes three terms

$$-p^r_{,ii} = 2[U_{i,p} + \epsilon_{pik}\hat{\Omega}_k Ro^{-1}]u_{p,i} \quad (19)$$

$$-p^s_{,ii} = u_{i,j}u_{j,i} - \langle u_{i,j}u_{j,i} \rangle \quad (20)$$

$$p^b_{,ii} = \beta_i\theta_{,i} \quad (21)$$

where p^r, p^s, p^b are respectively the rapid-pressure, the slow or return to isotropy pressure, and the buoyancy-pressure. The effects of rotation are felt through the rapid-pressure, p^r . Solution of the Poisson equation for the rapid-pressure is by application of Green's theorem

$$\phi(\mathbf{x}) = -(4\pi)^{-1} \int \phi(\mathbf{x}')_{,jj} \frac{d\mathbf{x}'}{|\mathbf{x}-\mathbf{x}'|}.$$

It is the moments of the solution that are required to close the second-order equations. For a homogeneous mean field a straightforward interchange of the order integration and averaging produces:

$$\langle p^r s_{ij} \rangle = -2[U_{q,p} + \epsilon_{pqk}\hat{\Omega}_k Ro^{-1}][X_{ipqj} + X_{jpqi}] \quad (22)$$

$$\langle p^r \theta_{,i} \rangle = -2[U_{q,p} + \epsilon_{pqk}\hat{\Omega}_k Ro^{-1}]X_{pqi} \quad (23)$$

where $s_{ij} = \frac{1}{2}[u_{i,j} + u_{j,i}]$ and

$$X_{piq} = (4\pi)^{-1} \int \langle \theta(\mathbf{x})u_p(\mathbf{x}') \rangle_{,i'q'} \frac{d\mathbf{x}'}{|\mathbf{x}-\mathbf{x}'|} \quad (24)$$

$$X_{ipqj} = (4\pi)^{-1} \int \langle u_i(\mathbf{x})u_p(\mathbf{x}') \rangle_{,j'q'} \frac{d\mathbf{x}'}{|\mathbf{x}-\mathbf{x}'|}. \quad (25)$$

By continuity $s_{jj} = 0$; $\langle ps_{ij} \rangle$ interchanges energy between the different components of the Reynolds stress but does not contribute to the kinetic energy of the turbulence. In drawing the mean velocity gradient outside the integral the assumption of quasi-homogeneity has been made: the length scale of the inhomogeneity of the mean field is large compared to the integral scale of the turbulence. The primary contribution to the integral will then come from regions within an integral length scale of the local position over which the velocity gradient is approximately constant.

Consider the portion of the rapid-pressure correlation associated with the rotation

$$\begin{aligned} & \epsilon_{pqk}\hat{\Omega}_k Ro^{-1}X_{ipqj} = \\ & = \frac{1}{4\pi Ro} \int \epsilon_{pqk}\hat{\Omega}_k \langle u_i(\mathbf{x})u_p(\mathbf{x}') \rangle_{,j'q'} \frac{d\mathbf{x}'}{|\mathbf{x}-\mathbf{x}'|}. \end{aligned} \quad (26)$$

A horizontally divergence free velocity field has, to within an arbitrary additive scalar function, the representation

$$u_p = \epsilon_{pqk}\hat{\Omega}_k \psi_{,q}, \quad (27)$$

$$\psi_{,p} = \epsilon_{qpk}\hat{\Omega}_k u_q + \hat{\Omega}_p \hat{\Omega}_q \psi, \quad (28)$$

for $\psi = \psi(x, y, z)$. The flow along the rotation axis is specified by an additive scalar function. In the stably stratified case in which there is a horizontal divergence associated with potential field the analysis is the same: the potential makes no contribution to the integral. A proof of the frame-invariance of the second-moment equations when the velocity field has the representation $\psi = \psi(x, y)$ is straightforward. Insert the expression for the velocity field into the integral and contract to produce, in the integrand, the Laplacian of the streamfunction, $\psi_{,p} = \epsilon_{qpk}\hat{\Omega}_k u_q$ which reduces the volume integral of a two-point statistic to a one-point statistic which is identical with the Coriolis term,

$$\begin{aligned} & \frac{1}{4\pi} \int \epsilon_{pqk}\hat{\Omega}_k \langle u_i(\mathbf{x})u_p(\mathbf{x}') \rangle_{,j'q'} \frac{d\mathbf{x}'}{|\mathbf{x}-\mathbf{x}'|} = \\ & = \langle u_i \psi_{,j} \rangle = \epsilon_{pjk}\hat{\Omega}_k \langle u_i u_p \rangle. \end{aligned} \quad (29)$$

This analysis and a similar one for the heat flux equations produce the geostrophic constraints

$$\epsilon_{pqn}\Omega_n X_{ipqj} = \epsilon_{qjn}\Omega_n \langle u_i u_q \rangle \quad (30)$$

$$\epsilon_{pqn}\Omega_n X_{pqi} = \epsilon_{qin}\Omega_n \langle u_q \theta \rangle. \quad (31)$$

These are constraints reflecting the geostrophic balance of the second-moments of the fluctuating field: any model for the rapid-pressure strain covariance, X_{ipqj} and X_{pqi} used for geophysical flows must satisfy geostrophic constraint. This is not an invocation of the principle of material-frame-indifference, Lumley (1970), used in rational mechanics to construct a constitutive relation. It is a constraint, derivable from first principles, that any constitutive relation for the rapid-pressure strain must satisfy if the evolution equations are to be frame-invariant in the limit of a two-dimensional or a two-componential turbulence.

Summary and Conclusions

Three examples of flows that readily approach the horizontally divergent free conditions – the rotating tank, the rotating heated annulus and the stratified grid turbulence – have been described. These cases cover three very basic classes of flows: rotating turbulence (in a finite domain), baroclinic turbulence (rotation with horizontal temperature gradient) and stably stratified turbulence. In the limit of small Rossby number or small Froude number these flows exhibit equilibrium states that are horizontally divergence-free and therefore frame-indifferent. If the second-moment equations are to be frame-invariant when the flow is horizontally divergence free then rapid pressure-strain covariance must satisfy the following constraint:

$$\epsilon_{pqn}\Omega_n X_{ipqj} = \epsilon_{qjn}\Omega_n \langle u_i u_q \rangle \quad (32)$$

$$\epsilon_{pqn}\Omega_n X_{pqi} = \epsilon_{qin}\Omega_n \langle u_q \theta \rangle. \quad (33)$$

This equality, which assures the frame-invariance of the second-order equations, is called the geostrophic constraint as it reflects the small Rossby number geostrophic balance of the momentum equations, $2\epsilon_{ikp}u_p\Omega_p \simeq -p_{,i}$. The geostrophic constraint must, however, be satisfied by any flow with a vanishing horizontal divergence for arbitrary Rossby number; this is a manifestation of the fact that, in the absence of vortex stretching along the axis of rotation, that the evolution equations are frame-invariant. This is not an application of the material-frame-indifference principle of rational mechanics, Lumley (1970), as a modeling principle; it is a rigorous consequence of the Navier-Stokes equations. The evolution equations are quite dependent on rotation as long as the flow is not horizontally

divergence free. The principle of frame-indifference in the two-dimensional limit, Speziale (1981), is a special case of this invariance relevant to a purely mechanical turbulence. Here the flow may have a vertical structure as might occur in stratified or baroclinic situations. The fundamental quantity is the vanishing of the stretching of the vorticity along an arbitrary axis. This is indicated by the vanishing of the concomitant diagonal component of the strain.

Acknowledgements : The basic aspects of the work were completed at Cornell University during the PhD studies of J.R.R. During that time support was primarily from the U.S. National Science Foundation Grant No. MSM-8611164 for Czochralski crystal growth and from U.S. Office of Naval Research under the programs Physical Oceanography (Code 422PO). Subsequent developments have been carried out while at ICASE.

References

- Browand, F.K., E.J. Hopfinger (1982). The inhibition of vertical turbulent scales by stable stratification. "Turbulence and diffusion in Stable Environments", IMA Publication, Clarendon, Oxford.
- Browand, F.K., D. Guyomar, S.-C. Yoon (1987). The behavior of a turbulent front in a stratified fluid: experiments with an oscillating grid. *J. Geophys. Res.* 92:5329.
- Buzyna, G., R.L. Pfeffer, R. Kung (1984). Transition to geostrophic turbulence in a rotating differentially heated annulus of fluid. *J. Fluid Mech.* 145:377.
- Fein, J.S., R.L. Pfeffer (1976). An experimental study of the effects of Prandtl number on thermal convection in a rotating differentially heated cylindrical annulus of fluid. *J. Fluid Mech.* 75:81.
- Greenspan, H.P. (1968). "Theory of Rotating Fluids." Cambridge U. Press.
- Gill, A.E. (1982). "Atmosphere-Ocean Dynamics". Academic Press.
- Hopfinger, E.J., F.K. Browand, Y. Gagne (1982). Turbulence and waves in a rotating tank. *J. Fluid Mech.* 52:609.
- Hopfinger, E.J. (1987). Turbulence in stratified fluids: a review. *J. Geophys. Res.* 92:5287.
- Hide, R., P.J. Mason (1975). Sloping convection in a rotating fluid. *Adv. Physics* 24:47.
- Hide, R. (1977). Experiments in rotating fluids. *Q. J. Met. Soc.* 103:1.
- Lin, J.-T., Y.-H. Pao (1979). Wakes in stratified fluids. *Ann. Rev. Fluid Mech.* 11:317.
- Lumley, J.L. (1970). Towards a turbulence constitutive relation. *J. Fluid Mech.* 41:413.
- Reynolds, W.C. (1989). Effect of rotation on homogeneous turbulence. 10th Australian Fluid Mechanics Conference, Melbourne, Australia.
- Riley, J.J., R.W. Metcalf, M.A. Weissman (1981). Direct numerical simulation of homogeneous stratified turbulence in density stratified fluids. In *Proc. of the AIP Conference on Nonlinear Properties of Internal Waves*, ed. B.J. West, AIP NY, p. 79.
- Ristorcelli, J.R. (1987). A realizable rapid-pressure model satisfying two-dimensional frame-indifference and valid for three-dimensional three-component turbulence. Sibley School of Mechanical and Aerospace Engineering, FDA-87-19, Cornell University, Ithaca, NY.
- Ristorcelli, J.R., J.L. Lumley (1991b). Synopsis of a rapid-pressure model materially frame indifferent in the 2D limit. FDA-91-15, Sibley School of Mechanical and Aerospace Engineering, Cornell, Ithaca, NY.
- Ristorcelli, J.R., J.L. Lumley, R. Abid (1995). A rapid-pressure covariance representation consistent with the Taylor-Proudman theorem materially-frame-indifferent in the 2D limit. *J. Fluid Mechanics* 292:111-152.
- Ristorcelli, J.R. (1996). "Toward a turbulence constitutive relation for rotating flows. ICASE Report 96-66. To appear in proceedings of "New Directions in Geophysical Fluid Dynamics and Turbulence", Arizona State University May 1996. *Theor. Comp. Fluid Dyn* 9: (1997).
- Thorpe, S.A. (1987). Transitional phenomena and the development of turbulence in stratified fluids: a review. *J. Geophys. Res.* 92:5287.
- Xu, Y., H.J.S. Fernando, D.L. Boyer (1995). Turbulent wakes in stratified flow past a cylinder. *Phys. Fluids* 7:2243.
- Speziale, C.G. (1981). Some interesting properties of two-dimensional turbulence. *Phys. Fluids A* 24:1425.

LOW-REYNOLDS-NUMBER SECOND-MOMENT CLOSURE WITHOUT WALL-REFLECTION REDISTRIBUTION TERMS

Nobuyuki Shima

Department of Mechanical Engineering

Shizuoka University

Johoku 3-5-1

Hamamatsu, 432

Japan

ABSTRACT

A full second-moment turbulence closure applicable right up to a wall is proposed. The closure adopts a quasi-linear rapid model, but does not contain wall-reflection redistribution terms. We test the turbulence model in fully-developed channel flow, boundary layers in zero, adverse and favorable pressure gradients, and plane and round jets. The predictions are generally in good agreement with experiments and DNS, though discrepancies are present in normal stress profiles.

INTRODUCTION

The "basic" second-moment turbulence closure (see Launder, 1989) and its low-Reynolds-number versions (e.g. Launder and Shima, 1989) have been widely used with success to calculate various turbulent flows. A weakness of these models is that they contain wall-reflection redistribution terms which are formulated using the wall-normal vector and the distance from the wall. In principle, these elements are inappropriate in invariant modeling. In practice, due to these elements, it is difficult to apply the models to flows with complex wall geometries. Clearly it is desirable to eliminate such wall-reflection terms, if possible.

Our aim in the present study is to develop a simple second-moment closure applicable right up to a wall without the use of wall-reflection redistribution terms. The model is tested in fully-developed channel flow, in three boundary layers, i.e. the flat-plate boundary layer without pressure gradient, a boundary layer in adverse pressure gradient and a sink flow boundary layer, and in two free flows, i.e. a plane jet and a round jet in stagnant surroundings.

MODELING

For incompressible flows the exact equation governing the Reynolds stress transport may be written as

$$\frac{D}{Dt} \overline{u_i u_j} = P_{ij} - \epsilon_{ij} + \phi_{ij} + T_{ij} + V_{ij} \quad (1)$$

$$P_{ij} = - \left(\overline{u_j u_k} \frac{\partial U_i}{\partial x_k} + \overline{u_i u_k} \frac{\partial U_j}{\partial x_k} \right) \quad (2)$$

$$\epsilon_{ij} = 2\nu \overline{\frac{\partial u_i}{\partial x_k} \frac{\partial u_j}{\partial x_k}} \quad (3)$$

$$\phi_{ij} = \frac{1}{\rho} \overline{p \left(\frac{\partial u_i}{\partial x_j} + \frac{\partial u_j}{\partial x_i} \right)} \quad (4)$$

$$T_{ij} = - \frac{\partial}{\partial x_k} \left[\overline{u_i u_j u_k} + \frac{1}{\rho} \overline{p (u_j \delta_{ik} + u_i \delta_{jk})} \right] \quad (5)$$

$$V_{ij} = \nu \frac{\partial^2}{\partial x_k \partial x_k} \overline{u_i u_j} \quad (6)$$

where U_i and u_i denote the mean and fluctuating velocity vectors, respectively, p the pressure fluctuation, ν the kinematic viscosity, ρ the density, and the overbar implies the ensemble averaging. The terms P_{ij} , ϵ_{ij} , ϕ_{ij} , T_{ij} and V_{ij} are identified as production, dissipation, redistribution, turbulent diffusion including the pressure diffusion, and viscous diffusion, respectively.

For the turbulent diffusion we adopt the simple gradient diffusion model of Daly and Harlow (1970):

$$T_{ij} = \frac{\partial}{\partial x_k} \left(C_s \frac{k}{\epsilon} \overline{u_k u_l} \frac{\partial \overline{u_i u_j}}{\partial x_l} \right) \quad (7)$$

with $C_s = 0.22$, where k is the turbulence energy and ϵ is its dissipation rate.

The sum of the dissipation and redistribution terms is expressed as

$$-\epsilon_{ij} + \phi_{ij} = -\frac{2}{3} \delta_{ij} \epsilon + \phi_{(1)ij} + \phi_{(2)ij} \quad (8)$$

where $\phi_{(1)ij}$ is the slow redistribution term including the anisotropic part of dissipation, and $\phi_{(2)ij}$ is the rapid redistribution term. For these redistribution terms we adopt the following simple models.

$$\phi_{(1)ij} = -C_1 \frac{\epsilon}{k} \left(\overline{u_i u_j} - \frac{2}{3} k \delta_{ij} \right) \quad (9)$$

$$\phi_{(2)ij} = -C_2 \left(P_{ij} - \frac{2}{3} \delta_{ij} P \right) - C_3 \left(D_{ij} - \frac{2}{3} \delta_{ij} P \right) - C_4 k \left(\frac{\partial U_i}{\partial x_j} + \frac{\partial U_j}{\partial x_i} \right) \quad (10)$$

where $P = P_{kk}/2$ is the production rate of k , and

$$D_{ij} = - \left(\frac{\overline{u_j u_k}}{\partial x_i} \frac{\partial U_k}{\partial x_i} + \frac{\overline{u_i u_k}}{\partial x_j} \frac{\partial U_k}{\partial x_j} \right) \quad (11)$$

Equation (9) is the Rotta model, and equation (10) is the most general rapid model that is linear in the Reynolds stress. The coefficients $C_1 \sim C_4$ will be determined as model functions of the stress invariants. Hence the present model is quasi-linear in the Reynolds stress.

As is well known (Launder, Reece and Rodi, 1975: LRR), under the assumption of homogeneity, the three rapid-part coefficients $C_2 \sim C_4$ reduce to only one due to the "normalization" or Green's condition. Then any linear or quasi-linear model reduces to the form of the QI (Quasi-Isotropic) model (Model 1 of LRR), which cannot reproduce the relative stress levels in the log-layer without introducing wall-reflection terms. Nonlinear models may resolve this problem (Launder and Li, 1994), but our position in this study is to develop a simple quasi-linear model by discarding the "normalization" constraint. Note that the "basic model" adopts the IP (Isotropization of Production) rapid model (Model 2 of LRR) which does not satisfy the constraint. The well-known quasi-linear rapid model of Speziale, Sarkar and Gatski (1991) also discards this constraint.

For the slow-part coefficient we assume

$$C_1 = C_1(A, A_2, R_T) \quad (12)$$

where A and A_2 are the invariants of the stress anisotropy tensor $a_{ij} = \overline{u_i u_j}/k - 2\delta_{ij}/3$ defined by

$$A = 1 - 9A_2/8 + 9A_3/8 \quad (13)$$

$$A_2 = a_{ij}a_{ji}, \quad A_3 = a_{ij}a_{jk}a_{ki} \quad (14)(15)$$

and $R_T = k^2/\nu\epsilon$ is the turbulence Reynolds number. The invariant A introduced by Lumley (1978) plays an important role in modeling; $A = 0$ in the two-component limit and $A = 1$ in the isotropic limit.

According to Lumley (1978), we impose the following requirements.

$$C_1(0, A_2, R_T) = C_1(1, 0, \infty) = C_1(A, A_2, 0) = 1 \quad (16)$$

For the rapid-part coefficients, it can readily be shown that the realizability condition requires

$$C_2 + C_3 = 0, \quad C_4 = 0 \quad \text{in the two-component limit} \quad (17)$$

According to Mansour, Kim and Moin's (1988) analysis of DNS data, for the ϕ_{22} component in the log-layer, the contribution of the rapid part is negligibly small. Within the framework of the present model, this implies

$$C_3 \simeq C_2/2 \quad \text{in the log-layer} \quad (18)$$

If we neglect transport terms, the relative stress levels in the log-layer are algebraically related to the coefficients $C_1 \sim C_4$. Then, using equation (18) and Kim's DNS data (from CTTM Data Library; see REFERENCES), i.e.

$\overline{u^2}/k = 1.02$, $\overline{v^2}/k = 0.40$, $\overline{w^2}/k = 0.58$, $-\overline{uv}/k = 0.29$, we obtain the values of the coefficients in the log-layer:

$$C_1 \simeq 2.50, \quad C_2 \simeq 0.45, \quad C_3 \simeq 0.23, \quad C_4 \simeq 0.22 \quad (19)$$

Note that, from the above-mentioned stress levels, $A = 0.64$ and $A_2 = 0.36$ in the log-layer.

Assuming the forms of the coefficients based on the above constraints and conditions and making tuning computations in the six different flows, we have arrived at

$$C_1 = 1 + 2.45A_2^{1/4}A^{3/4}[1 - \exp\{-(7A)^2\}] \times [1 - \exp\{-(R_T/60)^2\}] \quad (20)$$

$$C_2 = 0.7A, \quad C_3 = 0.3A^{1/2} \quad (21)(22)$$

$$C_4 = 0.65A(0.23C_1 + C_2 - 1) + 1.3A_2^{1/4}C_3 \quad (23)$$

The form of C_4 is designed to reproduce a desired shear-stress behavior in a near-wall region where the log-law holds but the relative stress levels vary significantly, i.e. $40 < y^+ < 80$. If we neglect transport terms, the present model yields

$$-\overline{uv} = \frac{1}{C_1} \left[(1 - C_2) \frac{\overline{v^2}}{k} - C_3 \frac{\overline{u^2}}{k} + C_4 \right] \frac{k^2}{\epsilon} \frac{\partial U}{\partial y} \quad (24)$$

In that region, the stress levels can be approximated as $\overline{v^2}/k \simeq 0.65A$ and $\overline{u^2}/k \simeq 1.3A_2^{1/4}$ from DNS data. Therefore the shear stress is expected to behave as

$$-\overline{uv} = 0.23 \frac{\overline{v^2}}{k} \frac{k^2}{\epsilon} \frac{\partial U}{\partial y} \quad (25)$$

This gives the standard value to the coefficient C_μ of the k - ϵ model in the region where $\overline{v^2}/k \simeq 0.4$, with a desired damping toward the wall.

Launder and Shima (1989) employ the following ϵ transport equation.

$$\frac{D\epsilon}{Dt} = C_{\epsilon 1} \frac{\epsilon}{k} P - C_{\epsilon 2} \frac{\epsilon \tilde{\epsilon}}{k} + \frac{\partial}{\partial x_k} \left(C_{\epsilon} \frac{k}{\epsilon} \overline{u_k u_l} \frac{\partial \epsilon}{\partial x_l} + \nu \frac{\partial \epsilon}{\partial x_k} \right) \quad (26)$$

where

$$\tilde{\epsilon} = \epsilon - 2\nu \left(\frac{\partial k^{1/2}}{\partial x_1} \right)^2 \quad (27)$$

We adopt this transport model with the coefficients different from those of Launder and Shima. The coefficients $C_{\epsilon 2}$ and C_ϵ are assigned standard values, i.e. $C_{\epsilon 2} = 1.92$ and $C_\epsilon = 0.15$. For the coefficient $C_{\epsilon 1}$, possible forms are assumed and tested to give correct length scales in the six different flows. The form reached is

$$C_{\epsilon 1} = 1.44 + \beta_1 + \beta_2 \quad (28)$$

$$\beta_1 = 0.25A \min(\lambda/2.5 - 1, 0) - 1.4A \min(P/\epsilon - 1, 0) \quad (29)$$

$$\beta_2 = 1.0A \lambda^2 \max(\lambda/2.5 - 1, 0) \quad (30)$$

$$\lambda = \min(\lambda^*, 4), \quad \lambda^* = \left[\frac{\partial}{\partial x_i} \left(\frac{k^{3/2}}{\epsilon} \right) \frac{\partial}{\partial x_i} \left(\frac{k^{3/2}}{\epsilon} \right) \right]^{1/2} \quad (31)(32)$$

The factor β_1 works mainly to reproduce the spreading rate of jets, as explained later. The factor β_2 acts to suppress an excessive increase in the length scale in the boundary layer in adverse pressure gradients.

The numerical solutions are obtained with an adapted version of the parabolic solver PASSABLE (Leschziner,

1982). For details of the procedure, see Launder and Shima (1989) and Shima (1993).

TESTING

Figure 1 compares the present model with Kim's DNS data for fully developed channel flow at $U_m a / \nu = 6880$ (from CTTM Data Library; see REFERENCES), where U_m is the bulk mean velocity and a is the channel half-width. The model gives $U_\tau a / \nu = 388$, slightly lower than the DNS value, 395. Figure 2 shows the comparison of the prediction with experimental data by Wiegardt (from Kline, Cantwell and Lilley, 1981) and Klebanoff (1955) for the boundary layer without pressure gradient. In both flows, the model performance is good in the wall shear stress and in the mean velocity and shear stress profiles. An obvious deficiency is that the present model does not reproduce the high anisotropy in turbulence intensities in the buffer layer in the vicinity of the wall.

The performance in a boundary layer with adverse pressure gradient is shown in Fig. 3, where the prediction is compared with experimental data of Samuel and Joubert (1974). The skin friction coefficient is here defined using a fixed reference velocity U_r , and U_e denotes the free-stream velocity. Due to the factor β_2 given by equation (30), the present model reproduces the variation of skin friction well. The model slightly overpredicts the wall shear stress at the downstream end. It should be noted, however, that there exist experiments (e.g. Nagano, Tagawa and Tsuji, 1992) which show a deviation from the log-law in the velocity profile, contrary to the experimental profile in Fig. 3(b). The peak value of the shear stress across the boundary layer is overpredicted considerably. If we adjust the model function β_2 to reproduce the peak value, then too high wall shear stresses return. For the turbulence intensities, the model again does not capture the measured behavior in the vicinity of the wall.

Table 1 compares the prediction of the skin friction coefficient for sink flow boundary layers with DNS data by Spalart (1986), where K is the acceleration parameter defined as $K = \nu U_e^{-2} dU_e/dx$. The predicted values are close to the DNS data, though the relaminarization occurs at slightly higher value of K . The element $[1 - \exp\{-(7A)^2\}]$ in equation (20) is introduced to control the critical K value for relaminarization. Figure 4 shows the results for the case of $K = 2.75 \times 10^{-6}$. Figure 4(a), where U_{r0} denotes the initial value of friction velocity, also includes the prediction for $K = 3.1 \times 10^{-6}$, which exhibits the relaminarizing behavior. Overall, the model reproduces the DNS data closely, though discrepancies are present in the turbulence intensities.

Turning to free flows, Table 2 shows the spreading rate of the plane and round jets in stagnant surroundings defined by $dy_{1/2}/dx$ and $dr_{1/2}/dx$, the experimental values being a consensus of data. Here, $y_{1/2}$ and $r_{1/2}$ denote the location where the streamwise velocity U equals half the centerline velocity U_0 . As is well known, the "basic" model and the standard $k-\epsilon$ model yield the result that the spreading rate of the round jet is greater than that of the plane jet. As is seen from Table 2, the anomaly has been suppressed in the present model. To produce the rather low spreading rate of the round jet, the generation coefficient $C_{\epsilon 1}$ in the ϵ transport equation (26) should be greater than the standard value if $C_{\epsilon 2}$ is fixed. The present model achieves this with the second term on the right side of equation

(29), which increases $C_{\epsilon 1}$ with the departure from the local equilibrium. In the plane jet, this effect is relatively weak and is compensated by the first term on the right side of equation (29). Craft and Launder (1996) pointed out that parabolic solvers such as used in the present study gives somewhat too large spreading rate, especially in the round jet. Therefore, the predicted values themselves are not entirely conclusive.

Figure 5 shows experimental and predicted profiles for the case of plane jet. The experimental data are collected from LRR and Jones and Musonge (1988). The predicted mean velocity and shear stress approach zero too slowly as y increases. For $y/y_{1/2} < 1.2$, the model closely reproduces the mean velocity profile. Figure 5(c) includes two sets of experimental data for the normal stresses. The two data sets are much different, and the prediction is relatively close to Heskestad's data.

Figure 6 compares the prediction and Panchapakesan and Lumley's experimental data for the round jet (from CTTM Data Library). The predicted profiles near the outer edge suffer from a numerical problem; there the length scale varies very rapidly. This is the reason for limiting the magnitude of λ by equation (31); for all the other flows tested in this study, the results with $\lambda = \lambda^*$ are the same as those with equations (31) and (32). The profiles for $r/r_{1/2} < 1.4$ are not affected by the problem, and overall good agreement is obtained between the data and prediction.

CONCLUDING REMARKS

As we have seen, the performance of the present model in six different flows are overall good, though some disagreements with experiments and DNS are present. More testing is needed before the model claims to be definitely useful, but the present study shows that it is possible to establish a simple second-moment closure for both wall and free flows which eliminates wall-reflection redistribution terms, adopts a quasi-linear rapid model and can be integrated up to walls.

REFERENCES

- Craft, T.J., and Launder, B.E., 1996, A Special Seminar: Present Status and Future Directions of Modeling Complex Turbulent Flow and Heat Transfer, JSME Text of Course, No. 96-47, pp. 16-30.
- CTTM (Collaborative Testing of Turbulence Models) Data Library, 1993, Mech. Eng. Dept., Stanford Univ.
- Daly, B.J., and Harlow, F.H., 1970, *Phys. Fluids*, Vol. 13, pp. 2634-2649.
- Jones, W.P., and Musonge, P., 1988, *Phys. Fluids*, Vol. 31, pp. 3589-3604.
- Klebanoff, P.S., 1955, NACA Rep. 1247.
- Kline, S.J., Cantwell, B.J., and Lilley, G.M., ed., 1981, *Proc. 1980-81 AFOSR-HTTM-Stanford Conf. on Complex Turbulent Flows*.
- Launder, B.E., 1989, *Whither Turbulence? Turbulence at the Crossroads*, J.L. Lumley, ed., Springer-Verlag, pp. 439-485.
- Launder, B.E., and Li, S.-P., 1994, *Phys. Fluids*, Vol. 6, pp. 999-1006.
- Launder, B.E., Reece, G.J., and Rodi, W., 1975, *J. Fluid Mech.*, Vol. 68, pp. 537-566.
- Launder, B.E., and Shima, N., 1989, *AIAA J.*, Vol. 27, pp. 1319-1325.

Leschziner, M.A., 1982, An Introduction and Guide to PASSABLE, Thermofluids Div., Dept. Mech. Eng., UMIST.

Lumley, J.L., 1978, *Advances in Applied Mechanics* 18, C.-S. Yih, ed., Academic, pp.123-176.

Mansour, N.N., Kim, J., and Moin, P., 1988, *J. Fluid Mech.*, Vol.194, pp.15-44.

Nagano, Y., Tagawa, M., and Tsuji, T., 1992, *Turbulent Shear Flows 8*, F.Durst et al., ed., Springer-Verlag, pp.7-21.

Samuel, A.E., and Joubert, P.N., 1974, *J. Fluid Mech.*, Vol.66, pp.481-505.

Shima, N., 1993, *ASME J. Fluids Eng.*, Vol.115, pp.56-69.

Spalart, P.L., 1986, *J. Fluid Mech.*, Vol.172, pp.307-328.

Speziale, C.G., Sarkar, S., and Gatski, T.B., 1991, *J. Fluid Mech.*, Vol.227, pp.245-272.

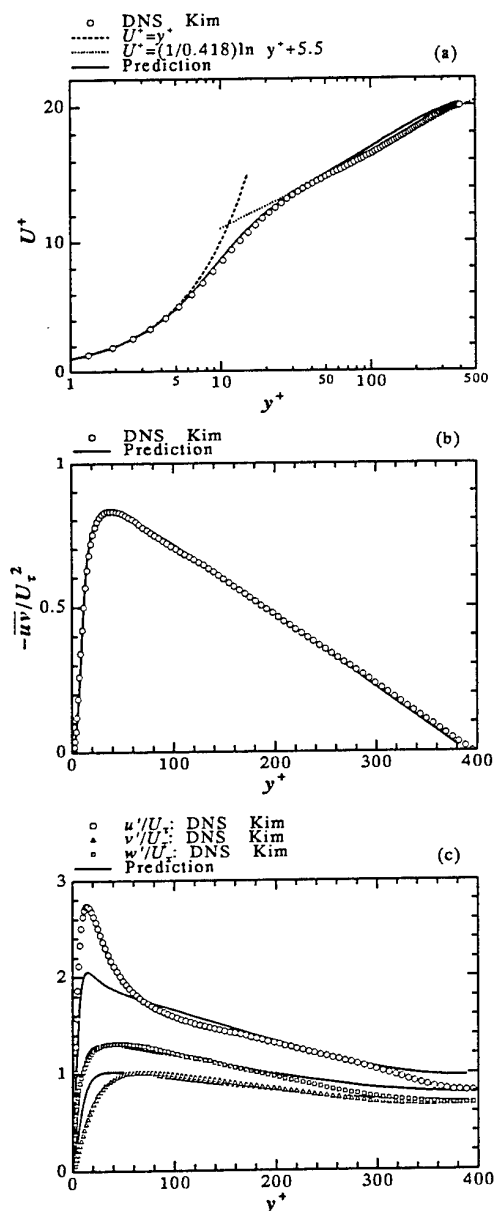


FIG.1 CHANNEL FLOW: (a)MEAN VELOCITY (b)SHEAR STRESS (c)TURBULENCE INTENSITIES

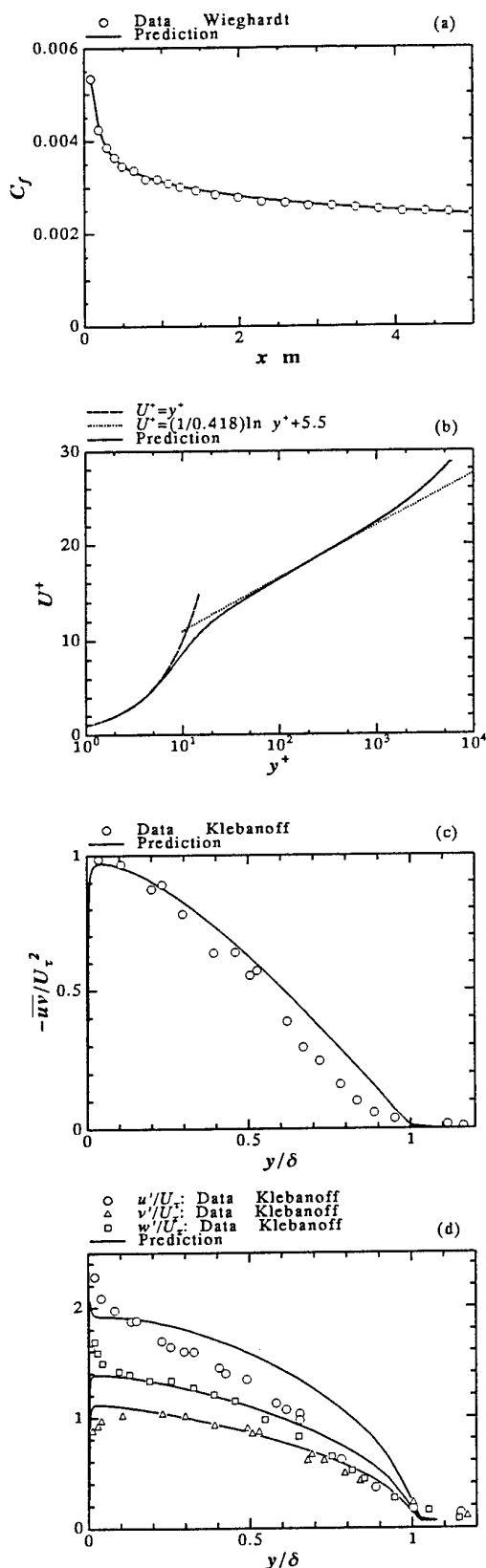


FIG.2 FLAT PLATE BOUNDARY LAYER: (a)SKIN FRICTION COEFFICIENT (b)MEAN VELOCITY (c)SHEAR STRESS (d)TURBULENCE INTENSITIES

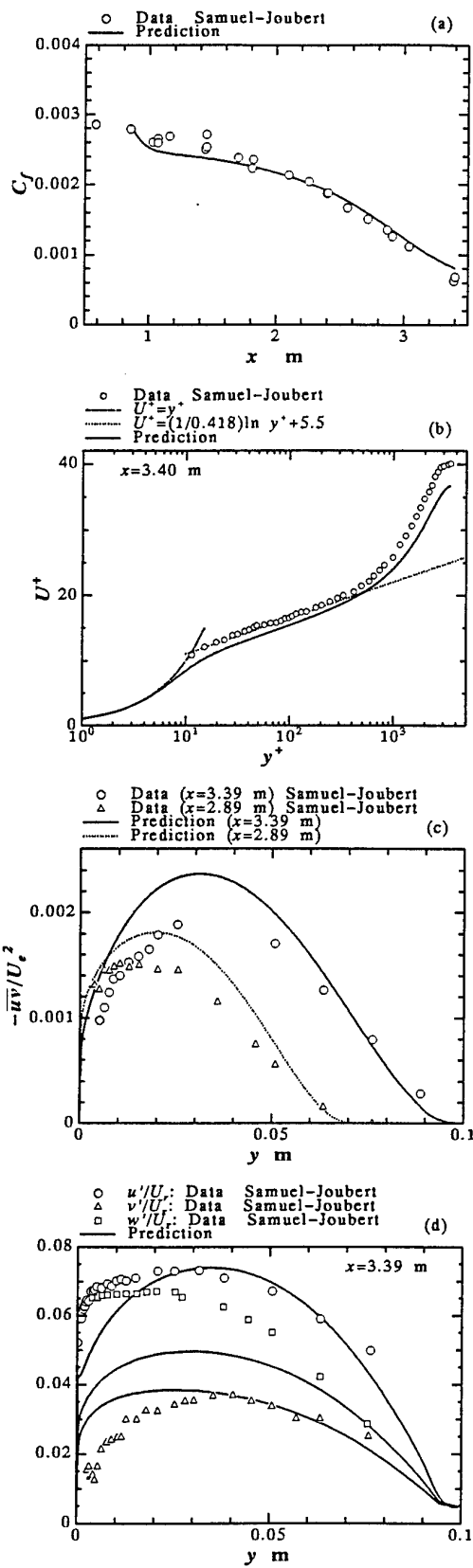


FIG.3 BOUNDARY LAYER IN ADVERSE PRESSURE GRADIENT: (a)SKIN FRICTION COEFFICIENT (b)MEAN VELOCITY (c)SHEAR STRESS (d)TURBULENCE INTENSITIES

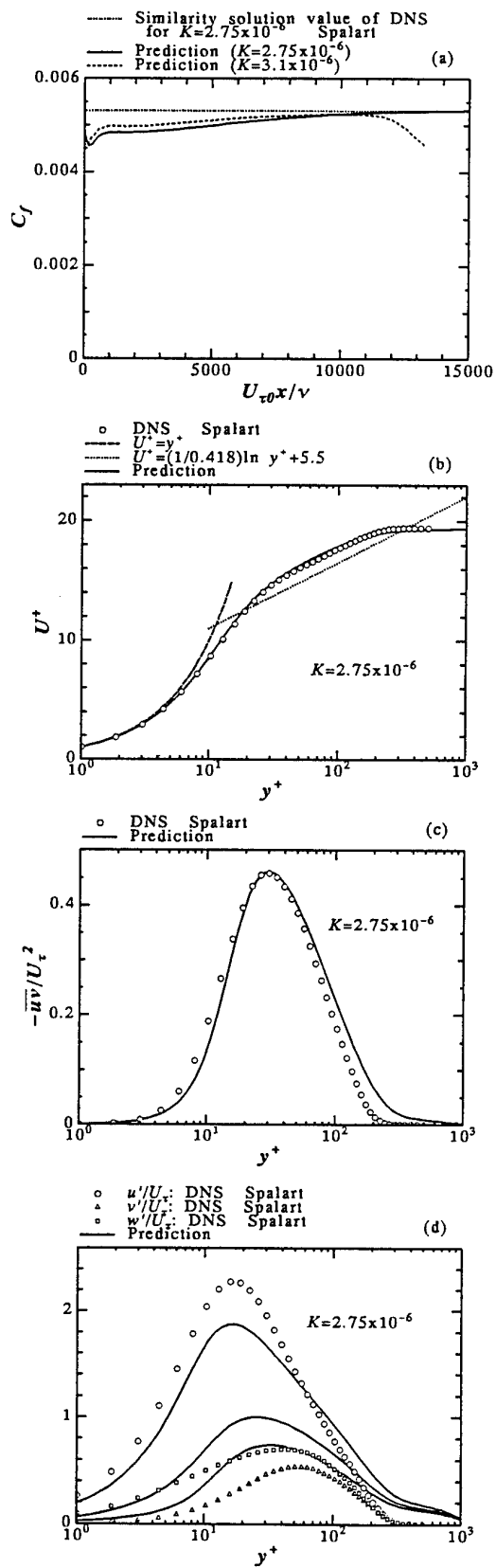


FIG.4 SINK FLOW BOUNDARY LAYER: (a)SKIN FRICTION COEFFICIENT (b)MEAN VELOCITY (c)SHEAR STRESS (d)TURBULENCE INTENSITIES

TABLE 1 SKIN FRICTION COEFFICIENT FOR
SINK-FLOW BOUNDARY LAYERS

$K \times 10^6$	DNS	Model
1.5	0.00499	0.00485
2.5	0.00522	0.00524
2.75	0.00530	0.00531
3.0	laminarization	0.00538
3.1	—	laminarization

TABLE 2 SPREADING RATE OF JETS

	Experiment	Model
Plane Jet	0.110	0.108
Round Jet	0.093	0.100

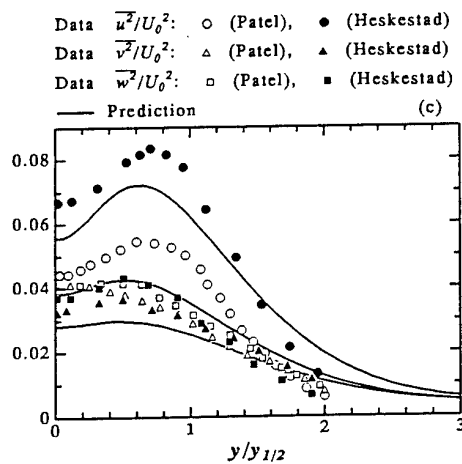
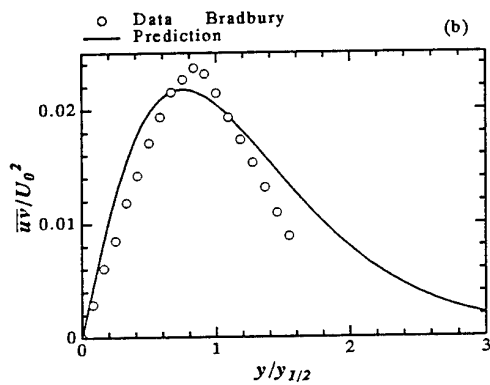
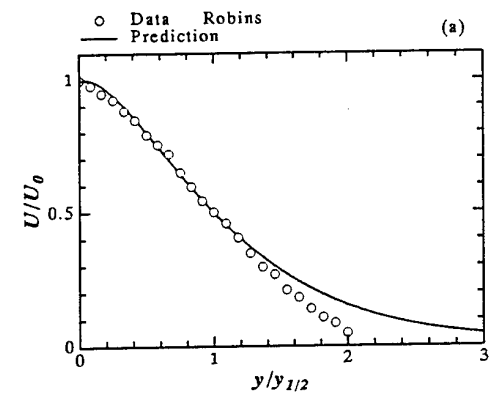


FIG.5 PLANE JET: (a)MEAN VELOCITY (b)SHEAR STRESS
(c)NORMAL STRESSES

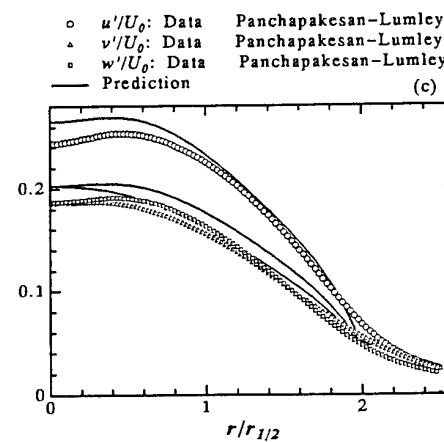
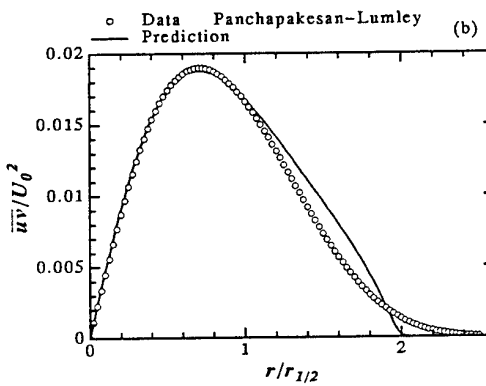
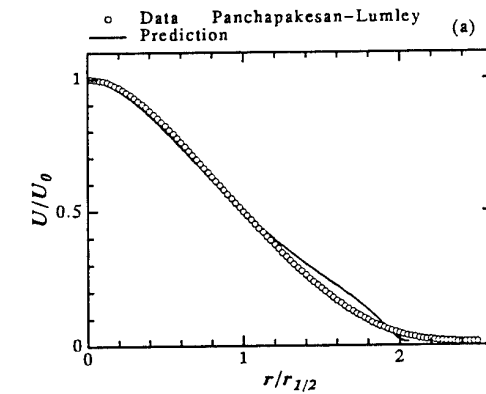


FIG.6 ROUND JET: (a)MEAN VELOCITY (b)SHEAR STRESS
(c)TURBULENCE INTENSITIES

A TWO-SCALE MODEL FOR A PASSIVE SCALAR FIELD UNDERGOING A SPHERICAL COMPRESSION

J. Pinheiro⁽¹⁾, M. Gonzalez⁽¹⁾, R. Borghi⁽²⁾

⁽¹⁾ UMR CNRS 6614/CORIA

Université de Rouen
76821 Mt St Aignan
France

⁽²⁾ ESM2

Institut Méditerranéen de Technologie
13451 Marseille
France

ABSTRACT

This paper describes the problem of modeling the passive scalar field subjected to a spherical compression. The analytical equation for the scalar fluctuations is found using a rescaling which makes the Navier-Stokes equation invariant in the case of a spherical compression neglecting the variations of diffusivity. Then, the time variations of diffusivity are taken into account in the equation of the scalar dissipation rate derived using the scalar enstrophy equation. The analytical expression of the scalar energy is derived using the scalar dissipation rate equation of Zeman and Lumley. The time variations of the diffusivity imply that the kinetic energy variance spectrum is evolving at the smallest scales. Using the same formalism as Le Penven and Serre (1991) for the turbulent dynamics, a new multi-scale model for the scalar field is derived.

INTRODUCTION

The problem of modeling the spherical compression at low Mach number has been approached in different ways. Reynolds (1980) has used the rapid distortion theory to modify the closure equation of the dissipation rate ϵ of the turbulent kinetic energy. Coleman and Mansour (1991) have generalized the Reynolds analysis in order to take into account the variations of kinematic viscosity during the compression. Spherical compression of turbulence was also studied by Wu *et al* (1985) who have derived a three equation scheme. Le Penven and Serre (1991) have presented a generalized $(k - \epsilon)$ model for the spherical compression also based on three equations. Good agreement was obtained between the model and the DNS data of Wu *et al*. (1985)

The purpose of this paper is to present a multi-scale model for a passive scalar field subjected to a spherical compression using the same formalism as Le Penven and Serre. By the term passive scalar, we mean a quantity that does not influence the dynamics. The Schmidt number will be assumed equal to one.

CAMBON ANALYSIS

We consider homogeneous compressible turbulence at

small fluctuation Mach number. A rescaling of the velocity fluctuations, space-coordinates and time used by Cambon *et al*. (1992,1993) makes the Navier-Stokes equation invariant in the case of a spherical compression:

$$\begin{cases} \vec{x}^\circ = J^{-1/3}(t)\vec{x} \\ t^\circ = \int_0^t J^{-2/3}(s)ds \\ u_i^\circ(\vec{x}^\circ, t^\circ) = J^{1/3}(t)u_i(\vec{x}, t) \end{cases} \quad (1)$$

where $J(t) = \rho(0)/\rho(t)$ is the reciprocal of the compression ratio. This transformation is the same used by Kurskov and Ozernoi (1974) to investigate the theory of isotropic turbulence in an expanding universe due to Nariai (1956). The coordinates \vec{x}_i° are the comoving coordinates.

The transport equation for the passive scalar fluctuations subjected to a spherical compression is:

$$\frac{\partial n'}{\partial t} - c(t)x_j \frac{\partial n'}{\partial x_j} + u_j' \frac{\partial n'}{\partial x_j} = D(t) \frac{\partial^2 n'}{\partial x_j^2}, \quad (2)$$

where $D(t)$ is the diffusivity. The mean field is $\overline{U}_i = -c(t)\delta_{ij}x_j$, where $c(t)$ is the compression rate. After applying rescaling (1) to equation (2), the scalar fluctuation equation is written, in the comoving frame:

$$\frac{\partial n'^\circ}{\partial t^\circ} = -u_j'^\circ \frac{\partial n'^\circ}{\partial x_j^\circ} + D(t^\circ) \frac{\partial^2 n'^\circ}{\partial x_j^{\circ 2}}. \quad (3)$$

Note that scalar fluctuation is invariant under the above defined rescaling: $n'^\circ(\vec{x}^\circ, t^\circ) = n'(\vec{x}, t)$. If the diffusivity is assumed to be time-independent, the treatment of the passive scalar is identical to the usual theory of the passive scalar. Then, we can suppose that the scalar variance follows, in the comoving frame, a power law with an exponent $-m$:

$$k_n^\circ = \overline{n'^{\circ 2}}/2 = B_n(t^\circ - t_o)^{-m}, \quad (4)$$

where B_n and t_o are constants. Then, the expression for k_n in the physical frame is, since $k_n^\circ(t^\circ) = k_n(t)$:

$$k_n = B_n \left(\int_0^t J^{-2/3}(s)ds - t_o \right)^{-m}. \quad (5)$$

If c is constant, we get $J = e^{-3ct}$ and the solution is

$$k_n = B_n \left(\frac{e^{2ct} - 1}{2c} - t_0 \right)^{-m}. \quad (6)$$

At the final period of decay, k_n varies like e^{-2cmt} in the case of a compression ($c > 0$). In the case of an expansion ($c < 0$), k_n tends to $B_n(-1/(2c) - t_0)^{-m}$. This latest result is unexpected since the variance does not tend to zero but to a constant value. In the next section, it will be shown that this unphysical behavior can be relaxed by allowing for time variation of diffusivity.

COLEMAN AND MANSOUR ANALYSIS

Following the analysis of Coleman and Mansour (1991) for the dissipation rate equation of the kinetic energy, the equation for the scalar enstrophy $\omega_n = (\partial n' / \partial x_j)^2$ is used to obtain the equation for the scalar dissipation rate $\varepsilon_n = D\omega_n$ which takes into account the time variations of the diffusivity:

$$\begin{aligned} \frac{\partial \varepsilon_{nd}}{\partial t} = & \frac{\varepsilon_{nd}}{D} \frac{\partial D}{\partial t} - 2D \frac{\partial n'}{\partial x_i} \frac{\partial n'}{\partial x_j} \frac{\partial \bar{U}_j}{\partial x_i} \\ & - 2D \frac{\partial n'}{\partial x_i} \frac{\partial n'}{\partial x_j} \frac{\partial u'_j}{\partial x_i} - 2D^2 \frac{\partial^2 n'}{\partial x_i \partial x_j} \frac{\partial^2 n'}{\partial x_i \partial x_j}. \end{aligned} \quad (7)$$

The A correlation $-2D \frac{\partial n'}{\partial x_i} \frac{\partial n'}{\partial x_j} \frac{\partial \bar{U}_j}{\partial x_i}$ describes a linear action of the mean velocity field on the dissipative scales. Since the compression is isotropic, the A correlation is proportional to $\delta_{ij}\varepsilon_n$:

$$A = -\frac{2}{3}\varepsilon_n \bar{U}_{k,k}, \quad (8)$$

$$\bar{U}_{k,k} = -3c(t). \quad (9)$$

The B correlations $-2D \frac{\partial n'}{\partial x_i} \frac{\partial n'}{\partial x_j} \frac{\partial u'_j}{\partial x_i} - 2D^2 \frac{\partial^2 n'}{\partial x_i \partial x_j} \frac{\partial^2 n'}{\partial x_i \partial x_j}$ represent the competition between the stretching and the destruction by the smallest scales. Several closures for this term are available in the literature. Lumley and Khajeh-Nouri (1974) were the first to give a closure for this terms:

$$B = -2b\varepsilon_n \frac{\varepsilon}{k}, \quad (10)$$

where b is a constant.

The usual closure for this term is due to Zeman and Lumley (1976a,b):

$$B = -CD_1 \frac{\varepsilon_n^2}{k_n} - CD_2 \frac{\varepsilon}{k} \varepsilon_n. \quad (11)$$

Lumley (1978) proposed to choose the constants such that the ratio r of velocity to scalar time scale is constant and equal to the initial time scale ratio. The constants given by Newman *et al.* (1981) are such that the time scale ratio tends to an asymptotic value.

Mantel *et al.* (1993) propose to model separately the dissipation and stretching terms:

$$B = \alpha \varepsilon_n \frac{\varepsilon}{k} Re^{1/2} - \frac{\beta}{2} \varepsilon_n \frac{\varepsilon_n}{k_n} Re^{1/2}, \quad (12)$$

where Re is the turbulence Reynolds number. The difference will be of order Re^0 while the ratio r is constant, of the order of $2\alpha/\beta$.

We suppose that the Schmidt number is equal to one, hence the diffusivity is identical to the kinematic viscosity. The viscosity for a perfect gas is given by (C_p constant):

$$\mu(T) = \mu(T_0)(T/T_0)^{0.5}. \quad (13)$$

The equation for the kinematic viscosity is derived using the equation for the temperature and assuming that γ is constant:

$$\frac{1}{\nu} \frac{d\nu}{dt} = (1 - 0.5(\gamma - 1))(-3c). \quad (14)$$

So we can derived the analytical expressions for the scalar variance with the different modelings for the scalar dissipation rate. With the constants used by Lumley (1978) in the Zeman Lumley equation, the expression for k_n is:

$$k_n = k_{n0} \left(1 + \frac{1}{n} \frac{\varepsilon_0}{k_0} \left(\frac{e^{c(2-3a)t} - 1}{c(2-3a)} \right) \right)^{-m_0}, \quad (15)$$

where $a = 1/D(\partial D)/(\partial t)/(-3c)$ is assumed to be constant, and m_0 is the initial power law decay $m_0 = n(\varepsilon_n/k_n)/(\varepsilon/k)$. Then, in the case of an expansion, it is proved that the scalar variance tends to zero when the effects of the kinematic viscosity are taken into account since $a > 2/3$. This resolves the unphysical result that we have reported in the introduction about the scalar variance in the case of an expansion with ν assumed to be constant (see Figure 1).

THE TWO-SCALE MODEL

We have assumed that the diffusivity does not influence the spectrum of the variance. During a rapid compression, the diffusivity varies rapidly which affects the dissipation rate and the spectrum is not in a stationary state. In this section, we describe briefly the generalized model of Serre and Le Penven (1991,1994) for the dynamics and the new generalized model for the scalar field that we have derived.

The Serre and Le Penven model

The time variations of the kinematic viscosity during the compression implies that the turbulence is not in an equilibrium state. It is very important to distinguish between the kinetic energy spectral flux ε_f and the dissipation rate ε_d . The model of Le Penven and Serre (Serre, 1994) is:

$$\begin{cases} \frac{dk}{dt} = 2c(t)k - \varepsilon_d \\ \frac{d\varepsilon_f}{dt} = 4c(t)\varepsilon_f - C_{\varepsilon 2} \frac{\varepsilon_d}{k} \varepsilon_f \\ \frac{\varepsilon_f}{\varepsilon_d} \frac{d}{dt} \left(\frac{\varepsilon_d}{\varepsilon_f} \right) = \frac{1}{\nu} \frac{d\nu}{dt} - b \left(\frac{\varepsilon_d}{\varepsilon_f} - 1 \right) \sqrt{\frac{\varepsilon_d}{\nu}} \end{cases} \quad (16)$$

The second equation is the equation for the kinetic energy spectral flux, and it states that it is only determined by the largest scales of the turbulence. We find the usual dissipation rate when ε_f equals ε_d . The last equation is the equation for the scalar dissipation rate, expressed through its ratio with the kinetic energy spectral flux.

The first term in the equation for the ratio of the kinetic energy spectral flux to the energy dissipation rate represents the variations of the kinematic viscosity which are responsible for the nonequilibrium. The second term is a relaxation term. The model constant b has been adjusted with the DNS data of Wu *et al* (1985), the best value was found to be 0.22.

A Two-Scale Model For The Scalar Field

Using the same formalism as Serre and Le Penven for the velocity field, a new multi-scale model for the scalar field is derived.

When a fluid is subjected to a compression, the density increases and the kinematic viscosity decreases, affecting

the scalar dissipation rate whereas ε_{nf} does not respond instantaneously to its variation. We need an equation for the scalar dissipation rate and another for the scalar spectral flux. If the viscosity falls rapidly then, the dissipation decreases instantaneously. Afterward, the dissipation relaxes until it equilibrates again with the scalar spectral flux.

The multi-scale model is based on three equations. The equation for the scalar variance is exact and gives the definition for the scalar dissipation rate:

$$\frac{d\overline{n^2}}{dt} = -2\varepsilon_{nd}. \quad (17)$$

In the following, two other equations are derived, one for the ratio of the scalar dissipation rate to the scalar spectral flux, and another for the scalar spectral flux.

We treat the problem in the comoving frame. The superscript \circ is omitted in the next section.

Equation For The Scalar Spectral Flux. An equation for the scalar spectral flux must be modeled. The scalar spectral flux equation can be derived from the standard equations for the scalar dissipation. However, a more appealing approach is to derive the scalar spectral flux equation from the evolution of the largest turbulent scales.

The ideas of Kolmogorov were used by Obukhov (1949) and Corrsin (1951) to derive the scalar variance spectrum. They proposed that the diffusivity produces a diffusion cut-off with the characteristic length scale:

$$\eta_n = \left(\frac{\varepsilon}{D^3}\right)^{1/4}. \quad (18)$$

In the limit of infinite Reynolds number, the dimensional analysis gives that $E_n(K)$, the spectral density of the scalar fluctuations energy is:

$$E_n(K) = C_{Co}\varepsilon_n\varepsilon^{-1/3}K^{-5/3}, \quad (19)$$

where C_{Co} is the Obukhov-Corrsin constant and K is the wavenumber.

For large but finite Reynolds number, the Obukhov-Corrsin spectrum is modified to take the form :

$$E_n(K) = C_{Co}\varepsilon_n\varepsilon^{-1/3}K^{-5/3}g(K\eta_n), \quad (20)$$

where g is a universal function.

As Lesieur *et al.* (1979), we assume that, for infinite Reynolds number, the spectrum as the form of equation (19) in the inertial range and, for very low wave number, a power law :

$$E_n(K, t) = C_s(t)K^{s'}, \text{ for } K \leq K_n \quad (21a)$$

$$E_n(K, t) = C_{Co}\varepsilon_n\varepsilon_f^{-1/3}K^{-5/3}, \text{ for } K \geq K_n \quad (21b)$$

where K_n is the scalar peak wave number. And the kinetic energy spectrum is given by:

$$E(K, t) = C_s(t)K^s, \text{ for } K \leq K_{max} \quad (22a)$$

$$E(K, t) = C_K\varepsilon_f^{2/3}K^{-5/3}, \text{ for } K \geq K_{max} \quad (22b)$$

where K_{max} is the kinetic energy peak wave number. By definition:

$$\frac{\overline{n^2}}{2} = \int_0^\infty E_n(K) dK. \quad (23)$$

Neglecting the energy contained in the lower wavenumber part of the spectrum and assuming large Reynolds number lead to:

$$\frac{\overline{n^2}}{2} \simeq 3/2 C_{Co}\varepsilon_n\varepsilon_f^{-1/3}K_n^{-2/3}. \quad (24)$$

Matching (21a) and (21b) for $K = K_n$, and using (24) give :

$$C_s'(t) \simeq C_{Co}\varepsilon_n\varepsilon_f^{-\frac{-3s'+3}{2}}\varepsilon_f^{\frac{3s'+3}{6}}\frac{3s'+5}{n^2} \quad (25)$$

Similarly, integrating the kinetic energy between K_{max} and the Kolmogorov wave number K_{Ko} , and matching (22a) and (22b) at K_{max} , give:

$$C_s(t) \sim C_K\varepsilon_f^{-s-1}\frac{3s+5}{q^2}. \quad (26)$$

We obtain the equation of the spectral flux ε_f if we assume that C_s is constant that is, that the energy containing eddies are permanent which is true if $s < 4$ (Lesieur and Schertzer, 1978):

$$\frac{d\varepsilon_f}{dt} = -\frac{3s+5}{s+1}\frac{\varepsilon_d}{q^2}\varepsilon_f. \quad (27)$$

Deriving (25) and assuming that C_s' is constant which is true if $s' < 4$, the scalar spectral flux equation is obtained:

$$\frac{d\varepsilon_{nf}}{dt} = \frac{1}{3} \left\{ -\frac{3s+5}{s+1}\frac{\varepsilon_d}{q^2} - \frac{3s'+5}{s'+1}\frac{2\varepsilon_{nd}}{n^2} \right\} \varepsilon_{nf}. \quad (28)$$

The transport equation for the scalar dissipation rate obtained is almost the same as the Zeman and Lumley equation. This simple model fails to corroborate the Mantel *et al.* (1993) modeling of the scalar dissipation rate equation.

Equation For The Scalar Dissipation Rate.

In this section, the equation for the scalar dissipation rate is derived.

In the case of nonequilibrium, the scalar spectrum of Corrsin and Obukhov given by equation (20) is generalized. The scaling gives:

$$E_n(K, t) = E_n(K)g(K\eta_n, \frac{\varepsilon_f}{\varepsilon_d}, \frac{\varepsilon_{nf}}{\varepsilon_{nd}}). \quad (29)$$

As Serre and Le Penven did for the dynamics, we simplify the different group as follows:

$$E_n(k, t) = C_{Co}\varepsilon_n\varepsilon^{-1/3}K^{-5/3}g(K\tilde{\eta}_n). \quad (30)$$

The spectrum is defined with only one length scale $\tilde{\eta}_n$. Let $P = K\tilde{\eta}_n$.

The scalar dissipation rate is defined by:

$$\varepsilon_{nd} = 2D \int_0^\infty K^2 E_n(K) dK. \quad (31)$$

Thus, with equation (30), the scalar dissipation rate is:

$$\varepsilon_{nd} = 2D \left(\frac{\varepsilon_n\varepsilon_f^{-1/3}}{\tilde{\eta}_n^{4/3}} \right) C_A, \quad (32)$$

$$\text{with } C_A = C_{Co} \int_0^\infty P^{1/3} g(P) dP. \quad (33)$$

We obtain the generalized Obukhov-Corrsin length scale $\tilde{\eta}_n$:

$$\tilde{\eta}_n = \left(2C_A \frac{\varepsilon_{nf}}{\varepsilon_{nd}}\right)^{3/4} \left(\frac{D^3}{\varepsilon_f}\right)^{1/4}. \quad (34)$$

The equation for the spectrum is:

$$\frac{dE_n(K, t)}{dt} = T_n(K, t) - 2DK^2 E_n(K, t), \quad (35)$$

where T_n is the spectral transfer.

For large Reynolds number, the inertial-convective range and the dissipative range are clearly separated. We can define a wave number K_n^o in the inertial range, such that $T_n(K_n^o) = 0$. Then, the scalar spectral flux is the rate at which energy is transferred from modes $K < K_n^o$ to modes $K > K_n^o$:

$$\varepsilon_{nf} = - \int_0^{K_n^o} T_n(K) dK = \int_{K_n^o}^{\infty} T_n(K) dK, \quad (36)$$

and we can approximate the dissipation by:

$$\varepsilon_{nd} = \int_{K_n^o}^{\infty} 2DK^2 E_n(K) dK. \quad (37)$$

The equation (35) is integrated from K_n^o to ∞ :

$$\begin{aligned} \frac{d}{dt} \int_{K_n^o}^{\infty} E_n(K, t) dK &= \int_{K_n^o}^{\infty} T_n(K, t) dK \\ &- \int_{K_n^o}^{\infty} 2K^2 E_n(K, t) dK. \end{aligned} \quad (38)$$

Subtracting ε_{nf} and ε_{nd} :

$$\varepsilon_{nf} - \varepsilon_{nd} = \int_{K_n^o}^{\infty} \frac{dE_n}{dt}. \quad (39)$$

Using the expression (30) for $E_n(K)$ in (39), and assuming ε_{nf} and ε_f are time-independent, it comes:

$$\varepsilon_{nf} - \varepsilon_{nd} = \varepsilon_{nf} \varepsilon_f^{-1/3} \tilde{\eta}_n^{-1/3} C_B(K_o \tilde{\eta}_n) \frac{d\tilde{\eta}_n}{dt}, \quad (40)$$

$$\text{with } C_B(K_o \tilde{\eta}_n) = \int_{K_n^o \tilde{\eta}_n}^{\infty} P^{-2/3} \frac{dg(P)}{dP} dP. \quad (41)$$

C_B will be assumed to be constant in this model. Using equation (39), (40) and (34), the equation for $(\varepsilon_{nd})/(\varepsilon_{nf})$ is derived. In fact, the spectrum is evolving with time, so a correction term c^* is needed. The correction term is determined when the diffusivity is constant, that is $\varepsilon_{nf} = \varepsilon_{nd}$:

$$c^* = \frac{1}{\varepsilon_{nf}} \frac{d\varepsilon_{nf}}{dt}. \quad (42)$$

The equation for the ratio $\varepsilon_{nd}/\varepsilon_{nf}$ is:

$$\begin{aligned} \frac{\varepsilon_{nf}}{\varepsilon_{nd}} \frac{d}{dt} \left(\frac{\varepsilon_{nd}}{\varepsilon_{nf}} \right) &= \frac{1}{D} \frac{dD}{dt} \\ -b_n \left(\frac{\varepsilon_{nd}/\varepsilon_{nf}}{\varepsilon_d/\varepsilon_f} \right)^{1/2} &\left(\frac{\varepsilon_{nd}}{\varepsilon_{nf}} - 1 \right) \sqrt{\frac{\varepsilon_d}{D}}, \end{aligned} \quad (43)$$

$$\text{with } b_n = -\frac{4}{3C_B(2C_A)^{1/2}}.$$

We obtain an equation which is quite similar to that derived by Serre and Le Penven, except for the extra term $((\varepsilon_{nd}/\varepsilon_{nf})/(\varepsilon_d/\varepsilon_f))^{1/2}$. The scalar dissipation is directly

affected by the variation of the diffusivity. If the constant b_n is equal to zero, the ratio of the scalar dissipation rate to the spectral flux will be governed by the variation of the diffusivity. If the scalar spectral flux increases, the scalar dissipation will increase until it reaches a new equilibrium state.

The constant b_n is estimated with different form for the function g .

In the limit of infinite Reynolds number, the function g is given by the even Heaviside function. The scalar spectrum is truncated at $K = 1/\tilde{\eta}_n$.

$$g(H) = \begin{cases} 0, & \text{for } H > 1 \\ 1, & \text{for } H < 1 \end{cases} \quad (44)$$

$$\begin{aligned} C_B &= -C_{Co} \\ C_A &= 3/4 C_{Co} \\ b_n &= 0.77 C_{Co}^{-1/2} \end{aligned}$$

If $C_{Co} = 1$ then $b_n = 0.77$.

For large but finite Reynolds number, the function is, in general, given by an exponential. With the spectrum given by Pao (1965):

$$g_n(P) = C_{Co} \exp(-\frac{3}{2} C_{Co} P^{4/3}), \quad (45)$$

$$C_A = \frac{2}{3} C_{Co}, \quad (46)$$

$$C_B = -\left(\frac{3}{2}\right)^{1/2} C_{Co}^{3/2} \Gamma\left(\frac{1}{2}\right), \quad (47)$$

$$b_n = \frac{2}{3} \sqrt{2} \frac{C_{Co}^{-2}}{\Gamma(\frac{1}{2})}. \quad (48)$$

If $C_{Co} = 1$, we have:

$$b_n = 0.53. \quad (49)$$

Both calculations give a value of b_n greater than b . A value of 0.6 is chosen.

The Scalar Two-Scale Model

Rewriting the equations (28) and (43) in the physical frame, we obtain the following two-scale model for the scalar field:

$$\frac{dk_n}{dt} = -\varepsilon_{nd} \quad (50)$$

$$\frac{d\varepsilon_{nf}}{dt} = 2c(t)\varepsilon_{nf} - C_{D1} \frac{\varepsilon_{nd}}{k_n} \varepsilon_{nf} - C_{D2} \frac{\varepsilon_d}{k} \varepsilon_{nf} \quad (51)$$

$$\begin{aligned} \frac{\varepsilon_{nf}}{\varepsilon_{nd}} \frac{\partial}{\partial t} \left(\frac{\varepsilon_{nd}}{\varepsilon_{nf}} \right) &= \frac{1}{D} \frac{\partial D}{\partial t} \\ -b_n \left(\frac{\varepsilon_{nd}/\varepsilon_{nf}}{\varepsilon_d/\varepsilon_f} \right)^{1/2} &\left(\frac{\varepsilon_{nd}}{\varepsilon_{nf}} - 1 \right) \sqrt{\frac{\varepsilon_d}{D}} \end{aligned} \quad (52)$$

Equation For r_d . We can define two ratio $r_d = \frac{\varepsilon_{nd}/k_n}{\varepsilon_d/k}$ and $r_f = \frac{\varepsilon_{nf}/k_n}{\varepsilon_f/k}$. The equation for r_f is similar to the equation for r .

The equation for r_d is in the case of $Sc = 1$:

$$\frac{1}{r_d} \frac{\partial r_d}{\partial t} = \frac{1}{r_f} \frac{\partial r_f}{\partial t} + \sqrt{\frac{\varepsilon_f}{\nu}} \left\{ b \left(\frac{\varepsilon_d}{\varepsilon_f} \right)^{1/2} \left(\frac{\varepsilon_d}{\varepsilon_f} - 1 \right) - b_n \left(\frac{\varepsilon_{nd}}{\varepsilon_{nf}} \right)^{1/2} \left(\frac{\varepsilon_{nd}}{\varepsilon_{nf}} - 1 \right) \right\}$$

If $b_n \neq b$, the respective nonequilibrium states for the dynamic and scalar field have antagonistic effects on r_d .

If $b = b_n$ (and $\frac{\varepsilon_d}{\varepsilon_f} = \frac{\varepsilon_{nd}}{\varepsilon_{nf}}$), then $r_d = r_f$.

We can introduce a scalar field in the dynamics given by Wu *et al.* (1985) subjected to a spherical compression. The turbulent field is compressed with a compression velocity V_p in a box of length L_o . The gradient is:

$$c = -\frac{\partial \bar{U}_i}{\partial x_i} = \frac{V_p}{L_o - V_p t}. \quad (53)$$

Simulation	$V_p(m/s)$	$L_o(m)$
SQF	-5.60	0.30
SQG	-1.00	1.00
SQH	-0.06	0.30
SQI	-0.012	0.30

The initial conditions are :

$$k(0) = (0.2856)^2 / 2, \varepsilon_f(0) = 1.43 \times 0.0324, \frac{\varepsilon_d}{\varepsilon_f} = 0.699,$$

$$k_n = 1, \varepsilon_{nf}(0) = 1, \frac{\varepsilon_f}{k} k_n, \frac{\varepsilon_{nd}}{\varepsilon_{nf}} = 0.699.$$

With the constant b_n estimated, we see that in Figures (2), (3), (4) and (5) the time scale ratio r_d increases in the different cases. If b_n were lower than b then the ratio r_d would increase with time. And if b_n were equal to b , r_d would be equal to r , (see Figure (6), for the case SQI).

CONCLUSION

The Serre and Le Penven formalism was adopted to carry out a consistent treatment for the scalar field undergoing a spherical compression. The main result is that a new generalized model for the scalar field has been presented. This work suggests that the ratio of the velocity to scalar time scales will increase with the compression. It should be noted, however, that this conclusion is based on the fact that b_n is greater b .

Acknowledgements : This work was supported by Peugeot-SA, Renault and the ECOTECH program of CNRS.

REFERENCES

- C. Cambon, Y. Mao, D. Jeandel, 1992, "On the application of time dependent scaling to the modelling of turbulence undergoing compression", *Eur. J. Mech. B/Fluids*, Vol. 11, Issue: 6, pp. 683-703.
- C. Cambon, G. N. Coleman, N. N. Mansour, 1993, "RDT analysis and direct simulation of compressible homogeneous turbulence at finite Mach number", *J. Fluid Mech.*, Vol. 257,
- G. N. Coleman, N. N. Mansour, 1991, "Modeling the rapid spherical compression of isotropic turbulence", *Physics of Fluids A*, vol. 3, Sept., p. 2255-2259.
- S. Corrsin, 1951, "On the spectrum of isotropic temperature fluctuations in isotropic turbulence", *Journal of Applied Physics*, Vol. 22, pp. 469-473.
- A. A. Kurskov and L. M. Ozernoy, 1974, "Evolution of cosmological turbulence. I - Inertial redistribution of vortex spectrum", (1974, *Astronomicheskii Zhurnal*, Vol. 51, pp. 270-280.) *Soviet Astron. (A.J.)*, Vol. 18, pp. 157-163. Translation
- L. Le Penven and G. Serre, 1991, "A generalized $(k - \varepsilon)$ model for compressed turbulence", Eurotherm 15, Toulouse, France.
- M. Lesieur, D. Schertzer, 1978, "Self-similar damping of turbulence at large Reynolds number", : *Journal de Mécanique*, Vol. 17, no. 4, pp. 609-646.
- M. Lesieur, J. P. Chollet, J. C. André, D. Schertzer, U. Frisch, M. Larchèveque, 1979, "The eddy-damped quasi-normal Markovian approximation applied to three-dimensional fully developed turbulence", *2nd Symposium on Turbulent Shear Flows*, London, England, Proceedings.
- J. L. Lumley, 1978, "Computational modeling of turbulent flows", *Advances in applied Mechanics*, Vol. 18, pp. 123-176.
- J. L. Lumley, B. Khajeh-Nouri, 1974, "Computational modeling of turbulent transport", *Adv. Geophys.*, Vol. 18, pp. 169-192.
- T. Mantel, R. Borghi, and A. Picart, 1993, "Turbulent premixed propagation revisited results with a new model", *9th Symposium on Turbulent Shear Flows*, pp. 28-1-1-28-1-6.
- H. Nariai, 1956, "On the cosmic turbulence. I", *Sci. Rep. I*, Vol. 39, pp. 213-235.
- G. R. Newman, B. E. Launder, J. L. Lumley, 1981, "Modelling the behaviour of homogeneous scalar turbulence", *Journal of Fluid Mechanics*, Vol. 111, pp. 217-232.
- A. M. Obukhov, 1949, "Structure of the temperature field in turbulent flows", *Izv. Akad. Nauk SSSR*, Vol. 13, pp. 58-69.
- Y. H. Pao, 1965, "Structure of turbulent velocity and scalar fields at large wavenumbers", *The Physics of Fluids*, Vol. 8, pp. 1063-1075.
- W. C. Reynolds, 1980, "Modeling of fluid motion in engines- An introductory overview", in "Combustion modeling in reciprocating engines", Ed. J. N. Mattavi, Plenum Press New-York, London.
- G. Serre, 1994, "Étude expérimentale et modélisation de la turbulence homogène compressée", Ph. D. Thesis, École Centrale de Lyon, Lyon, France.
- C. T. Wu, J. H. Ferziger and D. R. Chapman, 1985, "Simulation and modeling of homogeneous, compressed turbulence", *Report TF-21 NASA*, Stanford Univ. (CA, United States)
- O. Zeman and J. L. Lumley, 1976a, "Buoyancy effects in entraining turbulent boundary layers: a second order closure study", *Turbulent shear flows*, Vol I, pp. 295-306.
- O. Zeman and J. L. Lumley, 1976b, "Modeling buoyancy driven layers", *Journal of the Atmospheric Sciences*, Vol. 33, pp. 1974-1988.

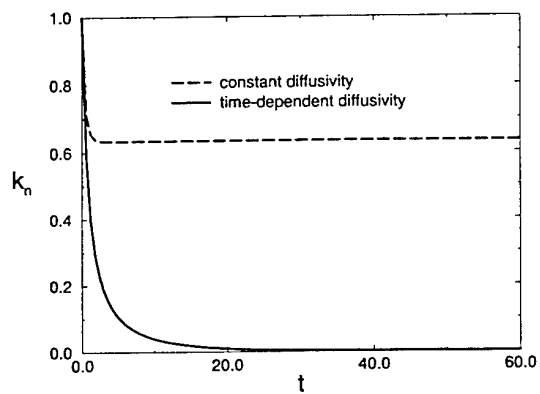


Figure 1: Scalar variance during an expansion. $c = -1, \gamma = 1.4$.

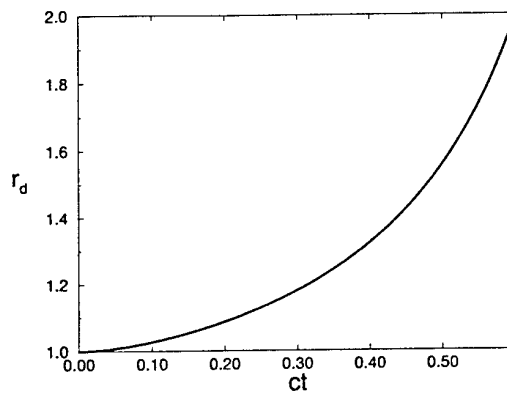


Figure 4: time scale ratio r_d . Case SQH

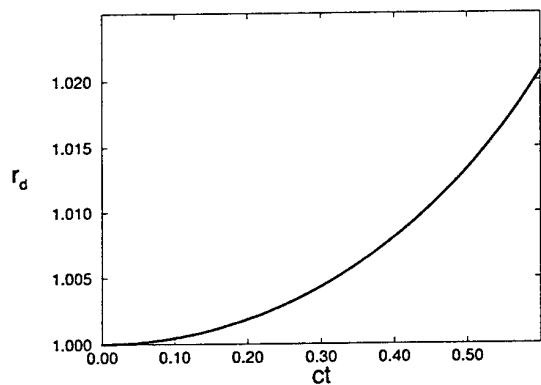


Figure 2: time scale ratio r_d . Case SQF.

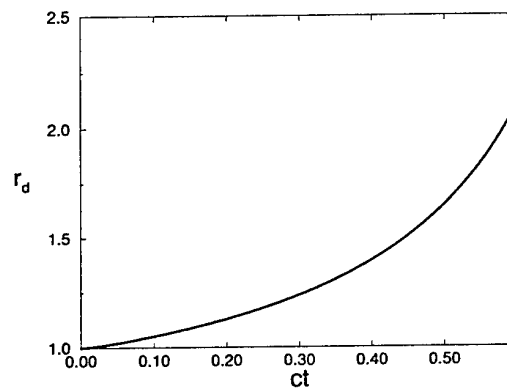


Figure 5: time scale ratio r_d . Case SQT.

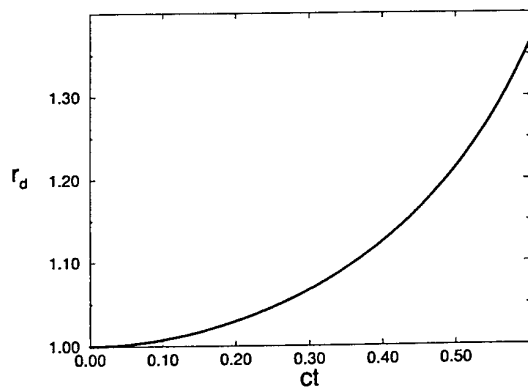


Figure 3: time scale ratio r_d . Case SQG.

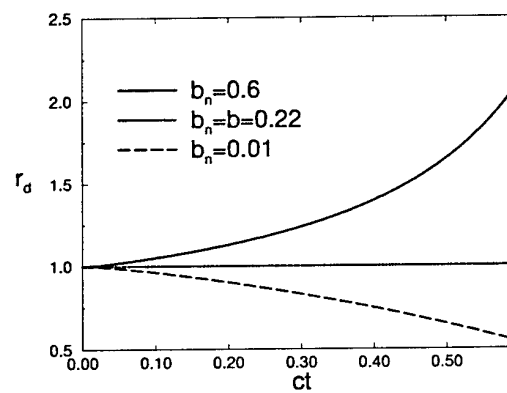


Figure 6: time scale ratio r_d . Case SQF.

ON THE MODELLING OF CONDITIONAL SCALAR DISSIPATION IN LOCALLY SELF-SIMILAR FLOWS

A. Kronenburg, R. W. Bilger and J. H. Kent
Department of Mechanical and Mechatronic Engineering
The University of Sydney, NSW, 2006
Australia

ABSTRACT

The modelling of conditional scalar dissipation in locally self-similar turbulent reacting jets is considered. The streamwise dependence in the transport equation of the conserved scalar pdf is represented by a function solely dependent on centreline mixture fraction. This procedure provides a simple model suitable for non-homogeneous flows and ensures positive values for conditional scalar dissipation. It has been tested in pure hydrogen-air jet diffusion flames using a Conditional Moment Closure method with detailed twelve species, twenty-three reactions chemistry. The calculations show good agreement of the averaged scalar dissipation with reference values and the model proves to be superior to previous models based on homogeneous flows if the distribution of the conditional scalar dissipation in mixture fraction space is compared with experimental results. A dependence of NO predictions on the model of conditional scalar dissipation can be observed.

INTRODUCTION

Scalar dissipation, χ , describes the scalar mixing of small scale structures in turbulent flows and is strongly related to the reaction rate as was shown by Bilger (1976) for the fast chemistry limit. Because of that it plays a significant role in the understanding and modelling of combustion problems and appears explicitly as an unclosed term in many models like the flamelet concept (Peters 1986), pdf methods (Pope 1985) or the Conditional Moment Closure method (Klimenko 1990, Bilger 1993a). Hence, accurate closure of χ is of vital importance for the performance of each of these combustion models. Of particular interest is the average of the scalar dissipation conditional on the scalar having a particular value. We confine ourselves here to consideration of conserved scalars such as mixture fraction.

Existing models for conditional scalar dissipation are – among others – Amplitude Mapping Closure (AMC) (Chen *et al.* 1989) and a model derived by Girimaji (1992) which is based on β -pdf distribution of mixture fraction. AMC can be derived by solving the scalar transport equation for mixture fraction for counterflow and has been validated by DNS results. However, both models are based on assumptions which may not be satisfied in turbulent jet flames.

Strictly speaking, AMC is only valid if some unmixed fluid is still present and Girimaji's model assumes homogeneous flow conditions that are certainly not present in shear layers such as jets.

In this paper we do not make either of these assumptions but show how to compute conditional scalar dissipation assuming local self-similarity of the flow. As shown by Klimenko *et al.* (1995) we can expect a functional interdependence of the conserved scalar pdf and conditional scalar dissipation in turbulent shear flows. These authors also derive analytical solutions for the self-similar regions of the flow. In this study we proceed differently. The idea is to uncouple the dependence of the conserved scalar pdf on spatial coordinates and mixture fraction. We aim at getting a relatively simple expression for the integrated pdf transport equation so that conditional scalar dissipation can be computed accurately. In the first section of this paper a quasi-selfsimilar solution of the pdf transport equation will be expressed in terms of integrals across the flow. This solution is a model for the conditional scalar dissipation. Then, the consistency of this model with the self-similar solution by Klimenko *et al.* (1995) is shown. Finally, the performance of different models will be tested in axisymmetric turbulent H_2 -Air jet flames with different jet exit velocities (150-300 m/s) and different nozzle diameters (3.75-7.62 mm) by comparing the CMC predictions with experimental data.

PDF TRANSPORT EQUATION IN LOCALLY SELF-SIMILAR FLOW

The transport equation for the conserved scalar pdf $P_\eta = P_\eta(\xi, x, r)$ provides the means for determining the conditional scalar dissipation, defined as $\langle \chi | \eta \rangle \equiv 2D \langle \nabla \xi \nabla \xi | \xi = \eta \rangle$, where angular brackets denote ensemble average of χ conditional on the expression to the right of the vertical bar. ξ is mixture fraction, D is the molecular diffusion coefficient and x and r denote the spatial coordinates in streamwise and radial direction, respectively. The pdf transport equation can be written in the form

$$\frac{\partial \rho(\eta) P_\eta}{\partial t} + \nabla \cdot (\langle \rho \underline{u} | \eta \rangle P_\eta) + \frac{1}{2} \frac{\partial^2}{\partial \eta^2} (\langle \rho \chi | \eta \rangle P_\eta)$$

$$= \nabla \cdot (\langle \rho D | \eta \rangle P_\eta). \quad (1)$$

In high Reynolds number flows the right hand side term of equation (1) can be neglected and, if we assume stationary flow, conditional scalar dissipation can be obtained from

$$-\frac{1}{2} \frac{\partial^2}{\partial \eta^2} (\langle \rho \chi | \eta \rangle P_\eta) = \nabla \cdot (\langle \rho \underline{u} | \eta \rangle P_\eta). \quad (2)$$

It is important to note that density-weighted Favre averaging is usually used to solve the momentum equations and the scalar transport equations for ξ and ξ''^2 . Therefore, we compute the Favre pdf \tilde{P}_η where

$$\tilde{P}_\eta = \langle \rho | \eta \rangle P_\eta. \quad (3)$$

In equation (2) $\langle \rho \underline{u} | \eta \rangle$ is taken as $\langle \rho | \eta \rangle \langle \underline{u} | \eta \rangle$, i.e. the correlation of the fluctuations of ρ and \underline{u} about their conditional means is neglected. Then we can write equation (2) after integration across the flow as

$$-\frac{1}{2} \frac{\partial^2}{\partial \eta^2} \{ \tilde{P}_\eta(\chi | \eta) \}_R = \frac{\partial}{\partial x} \{ \tilde{P}_\eta(\underline{u} | \eta) \}_R. \quad (4)$$

Here, we used the relationship of equation (3) and curly brackets $\{ \}_R$ denote integrals across the flow. These integrals are functions of x and η only.

Mixture fraction dependence of velocity can be approximated by assuming a linear dependence in η -space and $\langle \underline{u} | \eta \rangle$ can be written as $\langle \underline{u} | \eta \rangle \approx \tilde{u} + \frac{\underline{u}'' \xi''}{\xi''^2} (\eta - \xi)$. Then, double integration of eq. (4) in mixture fraction space gives

$$\begin{aligned} \{ \tilde{P}_\eta(\chi | \eta) \}_R &= -2 \frac{\partial}{\partial x} \left\{ \tilde{P}_\eta \int_\eta^1 \int_{\eta'}^1 \tilde{P}_\eta(\eta'', r) d\eta'' d\eta' \right\}_R \\ &- 2 \frac{\partial}{\partial x} \left\{ \tilde{P}_\eta \frac{\underline{u}'' \xi''}{\xi''^2} \int_\eta^1 \int_{\eta'}^1 \tilde{P}_\eta(\eta'', r) (\eta'' - \xi) d\eta'' d\eta' \right\}_R. \end{aligned} \quad (5)$$

The second term on the RHS of eq. (5) is expected to be small and will be neglected from here on. Integration by parts leads to

$$\{ \tilde{P}_\eta(\chi | \eta) \}_R = 2 \frac{\partial}{\partial x} \left\{ \tilde{P}_\eta \int_\eta^1 \tilde{P}_\eta(\eta', r) (\eta - \eta') d\eta' \right\}_R. \quad (6)$$

This derivation invokes the use of the following boundary conditions: $\partial \{ \tilde{P}_\eta(\chi | \eta) \}_R / \partial \eta \rightarrow 0$ and $\{ \tilde{P}_\eta(\chi | \eta) \}_R \rightarrow 0$ as $\eta \rightarrow 1$ as shown in Klimenko and Bilger (1993). Note the integration from η to 1. Since we consider mixture fraction fields in the downstream region of the jet where no pure hydrogen exists, the pdf is expected to peak near $\eta = 0$ but tends to 0 as $\eta \rightarrow 1$. Hence, pdf integrals from η to 1 can be resolved more accurately than integrals from 0 to η .

The function $f(\eta, x) = \left\{ \tilde{P}_\eta \int_\eta^1 \tilde{P}_\eta(\eta - \eta') d\eta' \right\}_R$ can be written without loss of generality as function $f(\hat{\eta} \xi_{ref}(x), x) = f^*(\hat{\eta}, x)$, where $\hat{\eta} \equiv \eta / \xi_{ref}$. The reference value to be used, ξ_{ref} , will be the centreline mean mixture fraction $\tilde{\xi}_0(x)$. With this transformation the differential of eq. (6) may be written as

$$\frac{\partial}{\partial x} |_\eta = \frac{\partial}{\partial x} |_{\hat{\eta}} - \frac{d \ln \tilde{\xi}_0}{dx} \hat{\eta} \frac{\partial}{\partial \hat{\eta}} |_x. \quad (7)$$

After some algebraic manipulations and transformation back into $\eta - x$ -space, the pdf-weighted area average of the conditional dissipation rate can be calculated as

$$\begin{aligned} \{ \tilde{P}_\eta(\chi | \eta) \}_R &= -2 \frac{d \ln \tilde{\xi}_0}{dx} \left\{ \tilde{P}_\eta \int_\eta^1 \tilde{P}_\eta(\eta', r) d\eta' \right\}_R \\ &+ 2 \frac{\partial}{\partial x} |_{\hat{\eta}} \left\{ \tilde{P}_\eta \tilde{\xi}_0 \int_{\hat{\eta}}^{\frac{1}{\tilde{\xi}_0}} \tilde{P}_\eta(\eta', r) (\hat{\eta} - \eta') d\eta' \right\}_R. \end{aligned} \quad (8)$$

Self-similarity of the flow implies that quantities like \tilde{P}_η , $\tilde{\chi}$ and $\tilde{\xi}''^2$ can be scaled in a way that they are locally only functions of one normalized conserved scalar variable which will be $\hat{\eta}$. Then $f^*(\hat{\eta}, x)$ will be only a function of $\hat{\eta}$ but not of x and the partial derivative in x in eq. (8) will vanish. Hence, the first term on the RHS gives the solution for the self-similar case. The second term accounts for deviations from self-similarity. This becomes more evident if we write for self-similar flows:

$$\begin{aligned} \tilde{\xi} / \tilde{\xi}_0 &= F_1(\hat{r}), \\ (\tilde{P}_\eta) / (\tilde{P}_0 \tilde{u}_0) &= F_2(\hat{r}) \end{aligned}$$

and

$$\tilde{P}_\eta = \tilde{P}_\eta(\hat{\eta}, \hat{r}) / \tilde{\xi}_0 = F^*(\hat{\eta}, \hat{r}).$$

F_1 and F^* will be only functions of $\hat{r} \equiv \frac{r}{L_0}$ and $(\hat{\eta}, \hat{r})$, respectively. The reference values are centreline mixture fraction, centreline density and velocity, and the radial position $L_0(x)$ where mixture fraction is half of its centreline value. Then we can write the integrand of the RHS of eq. (6) as

$$\begin{aligned} \left\{ \tilde{P}_\eta \int_\eta^1 \tilde{P}_\eta(\eta', r) (\eta - \eta') d\eta' \right\}_R &= 2\pi \tilde{P}_0 \tilde{u}_0 \tilde{\xi}_0 L_0^2 \times \\ &\times \int_{\hat{\eta}}^{1/\tilde{\xi}_0} \int_0^{R/L_0} F_2(\hat{r}) F^*(\eta', \hat{r}) \hat{r} d\hat{r} (\hat{\eta} - \eta') d\eta'. \end{aligned} \quad (9)$$

We note that $\tilde{P}_0 \tilde{u}_0 \tilde{\xi}_0 L_0^2$ is constant if F_1 and F_2 are truly functions of \hat{r} only, due to conservation of flux of mixture fraction. Then, the integrand is a function of $\hat{\eta}$ and independent of x ; only the first term on the RHS of eq. (8) deviates from zero as required for truly self-similar flow. Eq. (8) is exact for flows that are not self-similar in this way, but is structured such that the first term on the RHS will be dominant where the flow is locally close to being self-similar. We call eq. (8) with only the first term on the RHS the quasi-self-similar model for the conditional scalar dissipation.

COMPARISON TO THE INTEGRATED SELF-SIMILAR PDE

Using equation (4) a self-similar form of equation (2) can be obtained (Klimenko *et al.* 1995), viz

$$\lambda \hat{U} \hat{P} + \beta \frac{\partial}{\partial \hat{\eta}} (\hat{\eta} \hat{U} \hat{P}) + \frac{\partial^2}{\partial \hat{\eta}^2} (\hat{N} \hat{P}) = 0, \quad (10)$$

where N denotes scalar dissipation $N = 0.5\chi$. \hat{U} , \hat{P} and \hat{N} are functions of the normalized variable $\hat{\eta} \equiv \frac{\eta}{\tilde{\xi}_0(x)}$. If power law scaling is assumed these functions satisfy the following set of equations:

$$\begin{aligned} \hat{\eta} &\equiv \eta_R X^{-\beta} \\ U^* &= U_R X^{-\beta_u} \hat{U} \\ \hat{P}^* &= L^2 / \hat{\eta} X^{\beta_p} \hat{P} \\ N^* &= (U_R \eta_R^2 / L) X^{-\beta_N} \hat{N}. \end{aligned}$$

where $X = x/L$ and U_R, L and η_R are constants. $P^* = \{ \tilde{P}_\eta \}_R$, $N^* = \{ \tilde{N} \tilde{P}_\eta \}_R / P^*$ and $U^* = \{ \tilde{P}_\eta \tilde{u} \}_R / P^*$ denote averages across the flow. In turbulent axisymmetric jets $\lambda = \beta_p - \beta_u = 1$ and $\beta = 1$ holds and integration of eq. (10) gives (Klimenko *et al.* 1995)

$$\hat{N} \hat{P} = \hat{\eta} \int_{\hat{\eta}}^{\hat{\eta}_{max}} \hat{U} \hat{P} d\hat{\eta}. \quad (11)$$

Our purpose here is to show consistency of eq. (8) with eq. (11). Eq. (11) can be rewritten as

$$\begin{aligned} N^* P^* &= \frac{U_R \eta_R^2}{U_R L} \frac{X^{-\beta_N}}{X^{-\beta_u}} \frac{\eta}{\tilde{\eta}} \int_{\eta}^1 U^* P^* d\frac{\eta}{\tilde{\eta}} \\ \Leftrightarrow \{\bar{\rho} \tilde{N}_\eta \tilde{P}_\eta\}_R &= \frac{X^{-\beta_N + \beta_u + 2\beta}}{L} \eta \int_{\eta}^1 \{\bar{\rho} \tilde{u} \tilde{P}_\eta\}_R d\eta \\ &= x^{-1} \left\{ \bar{\rho} \tilde{u} \eta \int_{\eta}^1 \tilde{P}_\eta d\eta \right\}_R \end{aligned} \quad (12)$$

Here, $\beta_N = 4$ and $\beta_u = 1$ has been employed. Eq. (12) is consistent with the self-similar solution of eq. (8) since $-\frac{d \ln \tilde{\xi}_0}{dx} = -\frac{1}{\xi_0 L} \frac{d \tilde{\xi}_0}{dx/L} = \frac{\beta}{L} \frac{X^{-\beta-1}}{X^{-\beta}} = x^{-1}$. Note that an expression similar to eq. (11) can be derived for self-similar flows without assuming power-law scaling (Klimenko 1996).

RESULTS FOR TURBULENT JET FLAMES

Axisymmetric turbulent H_2 -Air jet flames are studied using a standard $k - \epsilon - g$ -flow field solver (Kent and Bilger 1973) to predict the flow field and the mixing field ($\tilde{\xi}(x, r), \tilde{\xi}''(x, r)$). The reactive scalar and enthalpy transport equations have been solved using the Conditional Moment Closure (CMC) approach where the instantaneous governing equations are conditionally averaged on mixture fraction (Klimenko 1990, Bilger 1993a). A twelve species, twenty-three reactions mechanism has been employed to simulate the chemical kinetics accurately and radiation losses were considered using the simple model suggested by Kuznetsov and Sabel'nikov (1989). Multiplication of the CMC equation (cf. Bilger 1993a and Smith *et al.* 1995) by $P(\eta, r)$, integration across the flow and using eq. (3) gives the appropriate shear flow equation, viz

$$\begin{aligned} \{\bar{\rho} \tilde{u} \tilde{P}_\eta\}_R \frac{\partial Q_i}{\partial x} &= \frac{1}{2} \{\bar{\rho}(\chi | \eta) \tilde{P}_\eta\}_R \frac{\partial^2 Q_i}{\partial \eta^2} \\ &+ \frac{1}{\langle \rho | \eta \rangle} \{\bar{\rho} \tilde{P}_\eta\}_R \langle w_i | \eta \rangle, \end{aligned} \quad (13)$$

where $\langle w_i | \eta \rangle$ is the production rate of species i conditionally averaged on mixture fraction. Details about the validity of this form of the CMC equation can be found elsewhere (Klimenko 1995). A β -pdf distribution $\tilde{P}_\eta = \eta^{\beta_1-1} (1-\eta)^{\beta_2-1} / I$ of mixture fraction is assumed. The parameters β_1 and β_2 are defined as $\beta_1 \equiv \tilde{\xi} (\tilde{\xi}(1-\tilde{\xi})/\tilde{\xi}''^2 - 1)$ and $\beta_2 \equiv (1-\tilde{\xi}) (\tilde{\xi}(1-\tilde{\xi})/\tilde{\xi}''^2 - 1)$ and the normalization factor I can be computed using $I = \Gamma(\beta_1)\Gamma(\beta_2)/\Gamma(\beta_1 + \beta_2)$. We use the equations mentioned in the last section to calculate the conditional scalar dissipation averaged across the flow. It is well known that simple numerical integration of eq. (8) may lead to unsatisfactory results if β_1 and/or β_2 are less than unity (Girimaji 1992). Substitution of $\ln \eta = -\zeta^n$ and $\ln(1-\eta) = -\zeta^n$, respectively, has been suggested (Swaminathan 1996) and the integral in eq. (8) can be evaluated by

$$\begin{aligned} \int_{\eta}^1 \tilde{P}_\eta d\eta &= \frac{n}{I} \left[\int_{(-\ln 0.5)^{1/n}}^{(-\ln \eta)^{1/n}} \zeta^{n-1} e^{-\beta_1 \zeta^n} (1 - e^{-\zeta^n})^{\beta_2-1} d\zeta \right. \\ &\quad \left. + \int_{(-\ln 0.5)^{1/n}}^{\infty} \zeta^{n-1} e^{-\beta_2 \zeta^n} (1 - e^{-\zeta^n})^{\beta_1-1} d\zeta \right] \end{aligned}$$

if $\eta < 0.5$ and

$$\int_{\eta}^1 \tilde{P}_\eta d\eta = \frac{n}{I} \int_{(-\ln \eta)^{1/n}}^{\infty} \zeta^{n-1} e^{-\beta_2 \zeta^n} (1 - e^{-\zeta^n})^{\beta_1-1} d\zeta$$

if $\eta > 0.5$. The exponent n is chosen to be $n = 3$ and infinity can be approximated by $-\beta_i \zeta^n = 10 (i = 1, 2)$. Maximum relative errors in evaluating of these integrals of $\approx 3\%$ can be observed.

Unconditionally averaged scalar dissipation can be obtained by integrating over mixture fraction space,

$$\{\bar{\rho} \tilde{\chi}\}_R = \int_0^1 \{\bar{\rho}(\chi | \eta) \tilde{P}_\eta\}_R d\eta \quad (14)$$

This is the density weighted scalar dissipation. First, the unconditionally averaged scalar dissipation is compared with a reference value, χ_{ref} obtained from the CFD calculation where it is calculated assuming that the time scale ratio

$$R = \frac{\tilde{k}}{\tilde{\epsilon}} \frac{\chi_{ref}}{\xi^{1/2}}$$

has a constant value of 1.82. Here, \tilde{k} is the Favre averaged kinetic energy and $\tilde{\epsilon}$ its rate of dissipation. χ_{ref} is a function of r and the reference value corresponding to eq. (14) can be evaluated as $\{\bar{\rho} \tilde{\chi}_{ref}\}_R$. Results for the averaged scalar dissipation are shown in Figure 1 as a function of the normalized downstream location X/D . Jet exit velocity is 150 m/s, co-flow velocity is 10 m/s and nozzle diameter is 7.62 mm. Results for simulations of other flames are comparable in error to the case presented here. We can see very good agreement between the quasi-self-similar model and the reference values after approximately 20 diameters downstream. The accuracy of the quasi-self-similar model then deteriorates as we proceed further downstream. Finally, at the end of the calculation ($X/D = 200$), the relative error is about 11%. The solid line shows the quasi-self-similar model with the correction term. As we can see, the resulting relative error decreases to less than 2%. This may be fortuitous. It indicates, however, that the assumption of $\langle \bar{\rho} \tilde{u} | \eta \rangle \approx \bar{\rho}(\eta) \tilde{u}$ is accurate enough. Tests have been carried out taking into account the mixture fraction dependence of velocity (cf. the second RHS term of eq. (5)). $\bar{\rho} \tilde{u}'' \tilde{\xi}''$ can be approximated by $\bar{\rho} \tilde{u}'' \tilde{\xi}'' = -\frac{\mu_t}{\sigma_\xi} \frac{\partial \tilde{\xi}}{\partial x}$, where μ_t denotes turbulent viscosity and $\sigma_\xi = 0.7$. Effects of mixture fraction dependence are up to 10% close to the nozzle but become negligible for $X/D > 20$. Note that solution of equation (6), which we shall call the 'direct' method, gives good agreement with the reference values (less than 9% deviation at $X/D = 200$). This is similar to the inaccuracies obtained using models for homogeneous flow. It is not clear where these errors come from. They may be due to inaccuracies when integrating the pdf in η -space. It is important to stress that the 'direct' method does not give always positive values for the conditional scalar dissipation rate. However, it gives approximately exact values in high probability regions and can be taken there as an alternative reference value.

Figure 2 shows the conditional scalar dissipation averaged across the flow as a function of mixture fraction for different downstream locations. The square symbols represent conditional scalar dissipation calculated with Girimaji's model for homogeneous flow (see Girimaji 1992) for the exact expression of his model for conditional scalar dissipation; the above mentioned logarithmic transformations have been used to calculate the integrals in mixture fraction space. Circles show the quasi-self-similar model results. The 'direct' method gives good reference values in the high probability region close to $\eta = 0$ and is depicted for comparison. The 'direct' method and the self-similar solution agree well in the high probability region but deviate by up to 30% for larger η towards the end of the simulation. The difference between the self-similar solution and the homogeneous solution can be clearly seen at all times. The former gives scalar dissipation more evenly distributed in mixture fraction space, whereas Girimaji's

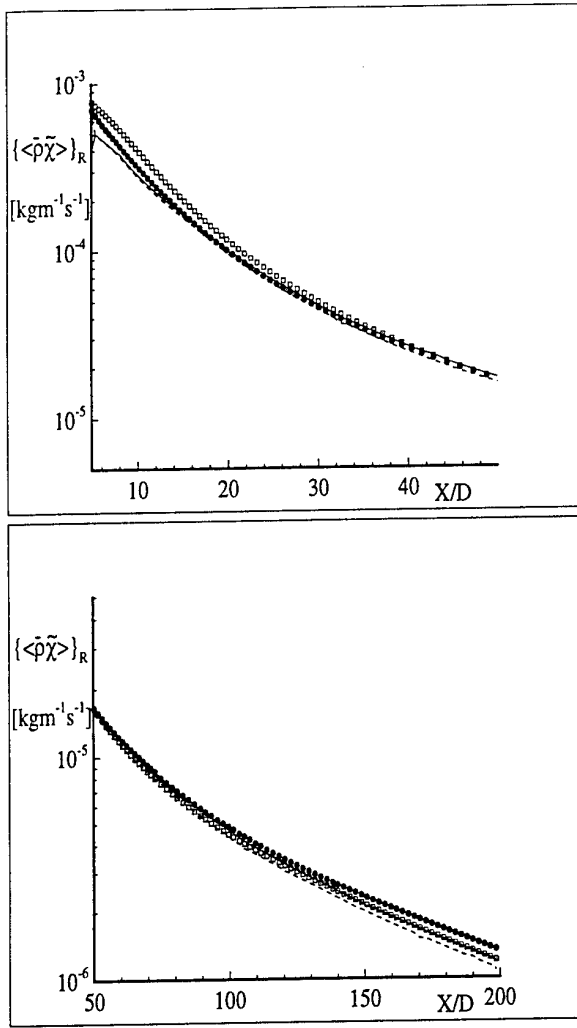


Figure 1: Averaged scalar dissipation as a function of the normalized streamwise distance. Reference value (squares), 'direct' method (dashed line), quasi-self-similar model (circles) and quasi-self-similar model plus correction term (solid line).

model predicts a more 'spiky' distribution of $\langle \tilde{\chi} | \eta \rangle$ with its maximum close to $\eta = 0.5$.

COMPARISON WITH EXPERIMENTAL RESULTS

Stärner *et al.* (1996) obtained conditional statistics of scalar dissipation for turbulent H_2 -Air jet diffusion flames. Direct quantitative comparison with their data is difficult since only conditional mean scalar dissipation normalized by its local unconditionally averaged mean value is shown. However, their measurements of $\langle \tilde{\chi} | \eta \rangle$ at an axial location of 25 jet diameters give information about the distribution in mixture fraction space and support the validity of our model. $\langle \tilde{\chi} | \eta \rangle$ peaks at values $\eta \approx 0.3$. This is consistent with the shift of $\langle \tilde{\chi} | \eta \rangle_{max}$ from $\eta = 0.5$ to $\eta \approx 0.3$ if we replace Girmaji's model by the model based on self-similarity assumptions. This may be very important if differential diffusion effects have to be included into CMC modelling. Differential conditional diffusion is proportional to the derivative of $\chi_\eta P_\eta$ in mixture fraction space and the influence of different models of χ_η on modelling of differential diffusion has to be investigated further.

The effects of different modelling of conditional scalar

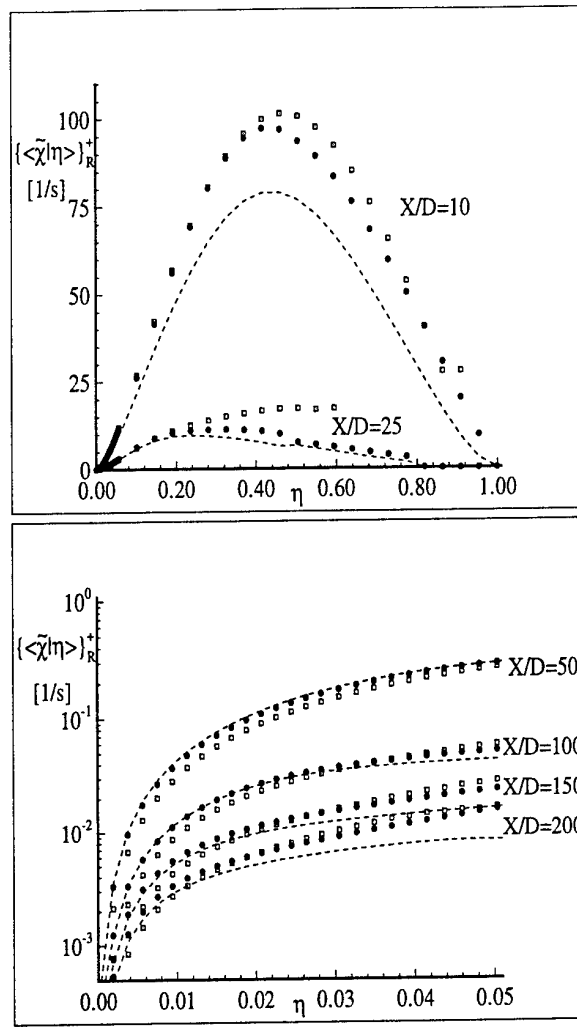


Figure 2: Conditional scalar dissipation $\langle \tilde{\chi} | \eta \rangle_R^+ = \int_0^R \bar{\rho}(\chi | \eta) \tilde{P}_\eta r dr / \int_0^R \bar{\rho} \tilde{P}_\eta r dr$ as a function of mixture fraction at different downstream locations. 'Direct' method (dashed line), quasi-self-similar model (circles) and Girmaji's model (squares).

dissipation can be seen if we compare our results with experimental data (Barlow and Carter 1994). Smith *et al.* (1995) investigated turbulent hydrogen jet flames with exit velocities of approximately 300m/s into coflowing air. Coflow velocity is 1m/s and nozzle diameter is 3.75mm. They compared CMC modelling predictions with LIF/Raman measurements. It has been shown that CMC is capable of predicting temperature and mass fraction fields of major species and radicals quite accurately. For nitric oxide, NO, formation, however, only trends could be simulated and NO levels at the visible flame length ($X/D \approx 180$) were overpredicted by up to 40%. Close to the nozzle predicted NO concentrations were much below the measured values. It has been suggested by Bilger (1993b) that rates of NO formation may require consideration of the second moments of temperature and O radical levels in the closure. Also differential diffusion effects, which are strongest close to the inlet, may influence NO formation. Numerical analysis has shown that NO production is dominated by a diffusive-reactive balance near the nozzle while further downstream the convective and reactive terms balance each other. We can conclude that accurate modelling of $\{\bar{\rho} \tilde{\chi}_\eta\}_R$ must be important close to the

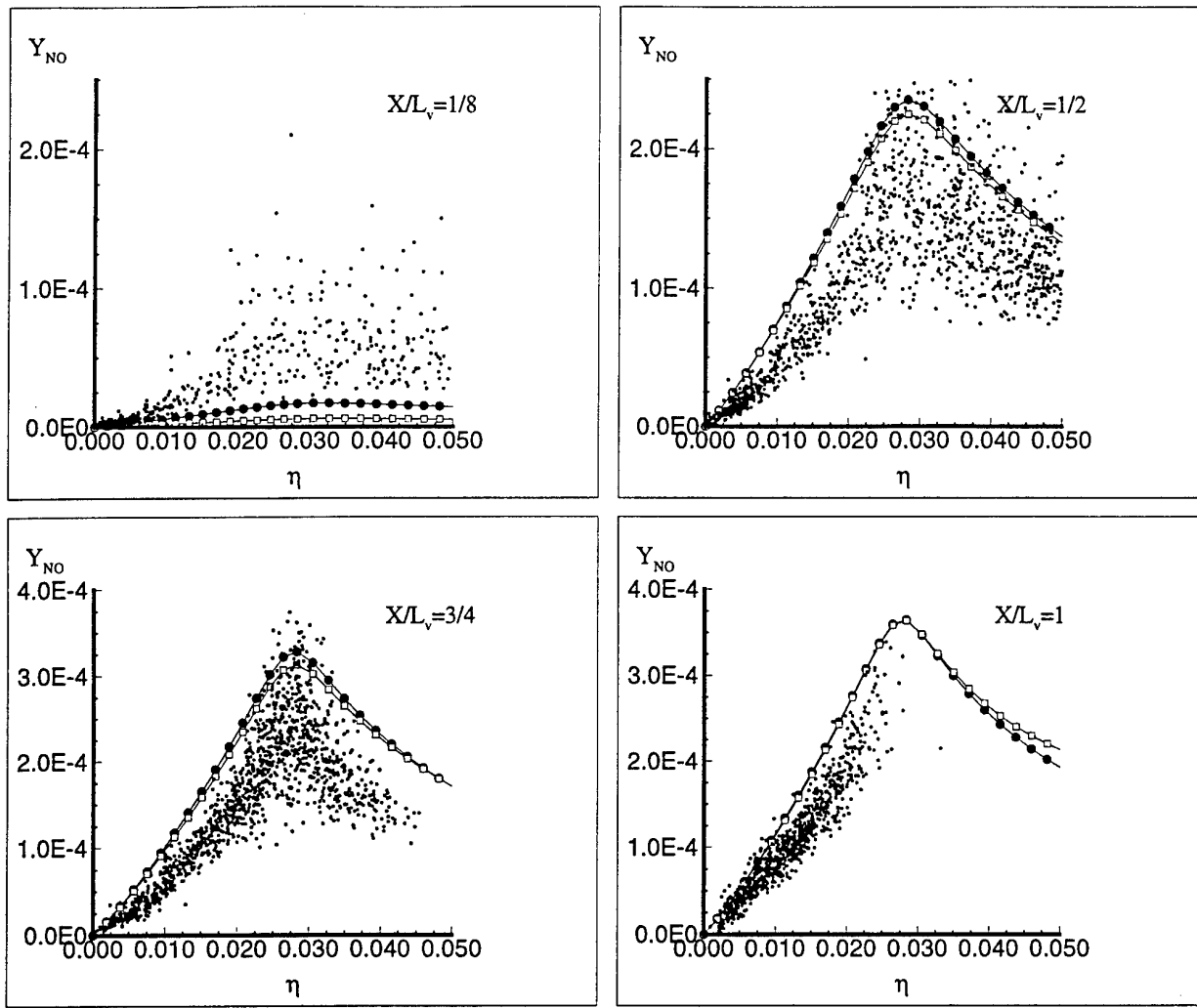


Figure 3: Comparison of the conditionally averaged NO mole fraction profiles at different axial locations. Dots represent experimental data by Barlow and Carter (1994), squares represent CMC calculations using Girimaji's model and circles represent CMC calculations based on self-similarity assumptions.

nozzle. Fig. 3 shows NO profiles of calculations in comparison with experimental data at different downstream locations. The squares represent results when Girimaji's model is used. The second set of data is obtained using the quasi-self-similar model. Tests have shown that mixture fraction dependence of velocity does not markedly influence predictions of species concentrations and have therefore been neglected. Fig. 3 clearly shows the influence of the different models on NO levels early in the flow. Still, measured NO concentrations are at least twice as high. This difference can be attributed mainly to the fact that we neglect temperature fluctuations. The conditional reaction rate $\langle w_i | \eta \rangle = \langle \rho A_0 T^\alpha \exp(-T_\alpha/T) Y_A Y_B | \eta \rangle$ can be expanded as

$$\begin{aligned} \langle w_i | \eta \rangle = & \rho_\eta k(Q_T) Q_A Q_B \left\{ 1 + \frac{\langle Y_A'' Y_B'' | \eta \rangle}{Q_A Q_B} \right. \\ & + \left(\alpha + \frac{T_\alpha}{Q_T} \right) \left(\frac{\langle Y_A'' T'' | \eta \rangle}{Q_A Q_T} + \frac{\langle Y_B'' T'' | \eta \rangle}{Q_B Q_T} \right) \\ & \left. + \frac{1}{2} \left[\alpha(\alpha - 1) + \frac{2(\alpha - 1)T_\alpha}{Q_T} + \frac{T_\alpha^2}{Q_T^2} \right] \frac{\langle T''^2 | \eta \rangle}{Q_T^2} \right\}. \end{aligned}$$

Experimental data (Barlow and Carter 1994) show that $\frac{T_\alpha^2}{Q_T^2} \frac{\langle T''^2 | \eta \rangle}{Q_T^2}$ can contribute significantly to NO formation

and increases the reaction rate term by a factor of up to 1.8 at $x/L_v = 1/8$. The correlation of T'' and O'' is expected to decrease the reaction rate slightly. However, a factor of approximately 2, which may be higher closer to the nozzle, may explain the underprediction of our calculations by a factor of 2–3. CMC can simulate NO mass fractions with satisfactory agreement further downstream and NO levels are insensitive to the model. NO is overpredicted by up to 20%. Reasons for this are discussed elsewhere (Smith *et al.* 1995). Note that using the 'direct' method gives slightly higher NO levels at $x/L_v = 1/8$ but it can only be used for the first 25 diameters since it gives negative values for conditional scalar dissipation over a wide range in mixture fraction space further downstream.

The temperature profiles could explain the trends in the NO predictions (not shown). Underprediction of T is consistent with underprediction of NO at $x/L_v = 1/8$ and the opposite can be observed at $x/L_v = 1/2, 3/4$ and 1. However, it shall be noted that numerical experiments do not confirm this conclusion. Temperature levels can be increased by increasing the reaction rates of the recombination reactions. Even if temperature is raised above the measured temperature levels, predicted NO mass fractions do not increase significantly at $x/L_v = 1/8$. Hence, a second order closure seems to be necessary if NO is to be predicted accurately near the nozzle. In general major species

and radical concentrations can be predicted well using the simple first order closure. It is pointed out that the relative errors of the predictions are approximately half those of previous CMC simulations (Smith *et al.* 1995). This can be attributed to the use of the $k - \epsilon - g$ -flowfield solver, the assumed β -pdf distribution and -in the region near the nozzle- to the more accurate quasi-self-similar model of conditional scalar dissipation.

CONCLUSION

Different methods have been used to compute conditional scalar dissipation for approximately self-similar flows. A new method has been developed that accounts for non-homogeneities of the flow and represents the dependence of scalar dissipation on its conditioning value more accurately than previous models. Relative errors of up to 15% seem to be acceptable since they only appear at far downstream locations in low probability regions. Use of this method is necessary since direct double integration in mixture fraction space and subsequent differentiation in axial direction of the pdf transport equation does not ensure positive values for conditional scalar dissipation. Comparison with experiments shows that predictions of NO mass fractions are sensitive to the modelling of $\{\bar{\rho}\tilde{\chi}_\eta\}_R$ in the region near the nozzle. NO levels are increased by a factor of 2 at $x/L_v = 1/8$ but measured NO concentrations are still 2 - 3 times higher. This error can be attributed mainly to the omission of second order moments in the computation of the reaction rate term of NO formation. NO levels further downstream can be predicted more satisfactorily but are insensitive to the model used for the conditional scalar dissipation. Hence, a second order closure seems to be necessary to predict NO levels accurately at all places in the flame.

Acknowledgements: Helpful discussions with Dr. A. Yu. Klimenko are highly appreciated. Mr. M.R. Roomina's assistance with the computations is acknowledged with thanks. This work was supported by the Australian Research Council.

REFERENCES

- Barlow, R.S. and Carter, C.D (1994). "Raman/Rayleigh/LIF Measurements of Nitric Oxide Formation in Turbulent Hydrogen Jet Flames", *Combustion and Flame*, 97, pp.261-280.
- Bilger, R.W. (1976). "The Structure of Diffusion Flames", *Combust.Sci.Tech.*,13, pp.155-170.
- Bilger, R.W. (1993a). "Conditional Moment Closure for Turbulent Reacting Flow", *Phys. Fluids*, A 5, pp.434.
- Bilger, R.W. (1993b). "Conditional Moment Closure Modelling and Advanced Laser Measurements", in *Turbulence and Molecular Processes in Combustion*, Takenko T. (ed.), Elsevier Science Publishers BV.
- Chen, H., Chen, S. and Kraichnan, R.H. (1989). "Probability distribution of a stochastically advected scalar field", *Phys. Rev. Lett.*, 63, pp. 2657.
- Girimaji, S.S. (1992). "On the modelling of scalar diffusion in isotropic turbulence", *Phys. Fluids*, A 4, pp.2529-2537.
- Kent, J.H. and Bilger, R.W. (1973). "Turbulent Diffusion Flames", *Fourteenth Symposium (Int'l) on Combustion*, The Combustion Institute, pp.615-625.
- Klimenko, A.Yu.(1990). "Multicomponent Diffusion of Various Scalars in Turbulent Flow", *Fluid Dyn.*,25, pp.327.
- Klimenko, A.Yu. and Bilger, R.W. (1993). "Relationship between conserved scalar pdfs and scalar dissipation in turbulent flows", *Charles Kolling Research Laboratory Report TN F-100*, The University of Sydney.
- Klimenko, A. Yu (1995). "Note on the conditional moment closure in turbulent shear flows", *Phys. Fluids*, 7, pp.446-448.
- Klimenko, A.Yu., Bilger, R.W. and Roomina, M.R. (1995). "Some PDF Integrals for Self-Similar Turbulent Flows", *Combust.Sci.Tech.*,107, pp.403-410.
- Klimenko, A.Yu. (1996). "Personal communication".
- Kuznetsov, V.R. and Sabel'nikov, V.A. (1989), *Turbulence and Combustion*, (Hemisphere, New York).
- Peters, N. (1986) "Laminar Flamelet Concepts in Turbulent Combustion", *Twenty-first Symposium (Int'l) on Combustion*, The Combustion Institute, pp. 1231-1250.
- Pope, S.B. (1985). "PDF Methods for Turbulent Reacting Flows", *Prog.Energy Combust.Sci.*,11, pp.119-192.
- Smith, N.S.A., Bilger, R.W., Carter, C.D., Barlow, R.S. and Chen, J.-Y. (1995). "A Comparison of CMC and PDF Modelling Predictions with Experimental Nitric Oxide LIF/Raman Measurements in a Turbulent H_2 Jet Flame", *Combust. Sci. Tech.*, 105, pp. 357.
- Stärner, S.H., Bilger, R.W., Long, M.B., Frank, J.H. and Marran, D.F. (1996). "Scalar Dissipation Measurements in Turbulent Jet Diffusion Flames of Air Diluted Methane and Hydrogen", *submitted to Combust. Sci. Tech.*.
- Swaminathan, N. (1996). "Personal communication".

SESSION 8 - HEAT AND MASS TRANSFER

MEASUREMENTS AND MODELING OF HEAT-FLUX TRANSPORT IN A HEATED CYLINDER WAKE

P. M. Wikström, M. Hallbäck, A. V. Johansson

Department of Mechanics

KTH

100 44 Stockholm

Sweden

ABSTRACT

Hot-wire measurements of velocity and temperature fluctuations have been made in the self preserving turbulent wake region of a heated cylinder. Second order statistics including Reynolds fluxes, $\overline{u_i \theta}$, are determined along with relevant triple correlations appearing in the Reynolds stress and Reynolds flux transport equations. The primary aim with these measurements is to study different modeling levels for passive scalar quantities. Models for the pressure scalar-gradient correlation, appearing in the transport equation of the Reynolds fluxes, are compared to measured data. A significant improvement to the simplest model, $-c_1 \tau \frac{1}{\tau} \overline{\theta u_i}$, is found to be achieved by including an 'isotropization-of-production'-like model for the rapid term, $c_2 \tau \overline{\theta u_j U_{i,j}}$. The mixed timescale, $\sqrt{k \theta^2 / \epsilon \epsilon_\theta}$, seems to be an appropriate choice for τ . Also models for the triple correlations, $\overline{u_i u_j \theta}$, are compared with the experiments.

EXPERIMENTAL SET-UP

A wind tunnel with a 7.0 m long test section of $1.2 \times 0.8 \text{ m}^2$ cross section and a free stream turbulence level less than 0.05% was used in the experiments. The diameter of the wake-generating cylinder was 6.4 mm and all the measurements were made at a velocity U_0 of 10.1 m/s giving a maximum mean velocity deficit of 0.5 m/s at $x/d=400$. The present Reynolds number, $U_0 d / \nu = 4300$, is about three times higher than that of Browne and Antonia (1986). The cylinder was electrically heated giving a maximum mean temperature excess Θ_s of 0.8°C above the ambient air temperature at $x/d=400$. Measurements were made at the following four different downstream positions: $x/d=200, 400, 600$ and 800 . The streamwise variations of the maximum velocity defect, U_s , the maximum temperature excess, Θ_s , and the velocity defect half-width, l , are in good agreement with those of Browne and Antonia, (Wikström et al. 1996). The results presented below are obtained from data at $x/d=400$, where the turbulent Reynolds number, $4k^2/\nu\epsilon$, is about 3200 at the location of maximum production. Here k is the turbulent kinetic energy and ϵ is the dissipation rate of k .

MEASUREMENT TECHNIQUE

The simultaneous measurements of velocity and temperature statistics were made using a three-wire probe configuration consisting of an X-probe for velocity measurements and a single cold wire for temperature detection, located 0.5 mm in front of the X-wire mid point. The hot wires had a length of 0.5 mm and a diameter of $2.5 \mu\text{m}$. The corresponding dimensions for the cold wire were 1.0 mm and $0.63 \mu\text{m}$. Voltages from the constant temperature and constant current circuits were sampled at 10 kHz and filtered at 5 kHz.

Cross-stream derivatives of measured quantities were obtained by use of cubic-spline smoothing fits to the experimental data. Derivatives in the streamwise direction, needed for deriving advective terms, were obtained by assuming self-similarity. The validity of this assumption, at $x/d=400$, was demonstrated.

THE HEAT-FLUX EQUATION

The transport equation for the scalar fluxes, $\overline{u_i \theta}$, is given by

$$\frac{\partial \overline{u_i \theta}}{\partial t} + U_i \frac{\partial \overline{u_i \theta}}{\partial x_i} = -\overline{u_i u_i} \frac{\partial \Theta}{\partial x_i} - \overline{\theta u_i} \frac{\partial U_i}{\partial x_i} - \frac{\partial}{\partial x_i} (\overline{\theta u_i u_i} - \alpha \frac{\partial \overline{\theta}}{\partial x_i} u_i - \nu \theta \frac{\partial u_i}{\partial x_i}) + \Psi_i \quad (1)$$

$$\Psi_i = -\frac{\partial}{\partial x_i} \left(\frac{\overline{p \theta \delta_{il}}}{\rho} \right) + \frac{\overline{p \theta}}{\rho} \frac{\partial \overline{\theta}}{\partial x_i} - (\alpha + \nu) \frac{\partial \overline{\theta}}{\partial x_i} \frac{\partial u_i}{\partial x_i} \quad (2)$$

The right hand side of the transport equation contains: two production terms; a transport term consisting of one turbulent and two molecular diffusion terms; a pressure-transport term; a pressure scalar-gradient correlation term and diffusive and viscous destruction. The sum of these three last terms is here denoted by Ψ_i . At high Reynolds numbers the molecular diffusion terms are small compared to the turbulent ones and may be neglected. Also the viscous and diffusive destruction terms should then be negligible, since the small scales are nearly isotropic at high Reynolds numbers. By modeling the turbulent diffusion, $-\frac{\partial}{\partial x_i} (\overline{\theta u_i u_i})$, and Ψ_i a modeled partial differential trans-

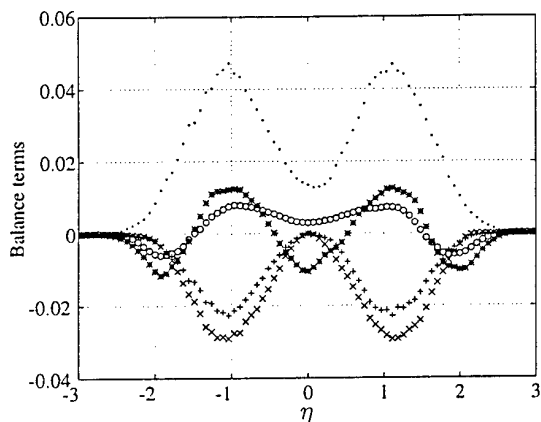


Figure 1: The dominating terms in the transport equation of $\overline{u\theta}$ normalized by $\frac{U_*^2 \Theta_*}{l}$, where l is the velocity defect half-width and $\eta = y/l$. \circ , $U \frac{\partial \overline{u\theta}}{\partial x}$; $+$, $-\overline{uv} \frac{\partial \Theta}{\partial y}$; \times , $-\overline{v\theta} \frac{\partial U}{\partial y}$; $*$, $-\frac{\partial}{\partial y} \overline{uv\theta}$; \cdot , Ψ_1 .

port equation for the scalar fluxes is obtained. The scalar fluxes may also be obtained from an algebraic scalar-flux model in which a model for the Ψ_i -tensor is needed.

RESULTS

In Figs. 1–2 the dominating terms in the transport equations for $\overline{u\theta}$ and $\overline{v\theta}$ are shown. The molecular diffusion as well as terms involving streamwise derivatives may be neglected. All terms are measured except Ψ_i which is obtained by balancing Eq. 1. These terms are of the same order as the rest of the terms, and may not be neglected. In the case of Ψ_1 , though, the inhomogeneous term, $-\frac{\partial}{\partial x} (\frac{\bar{\rho}}{\rho} \theta)$, may be neglected in the present flow situation. Measurements of $\frac{\partial \theta}{\partial t} \frac{\partial u_i}{\partial t}$ indicate that about 3% of Ψ_1 and 15% of Ψ_2 are contributions from the destruction terms in the present experiment. Figs. 1–2 also show that the turbulent diffusion terms are significant and may not be neglected.

Model comparison 1

In Fig. 3 the inclination angles of the turbulent scalar flux, $u_i \theta$, and Ψ_i are compared. In this figure we see that Ψ_i is approximately parallel to the heat-flux vector and oriented in the opposite direction. This result is similar to what has been found by Rogers, Mansour and Reynolds (1989). A linear relaxation relation, $\Psi_i = -c_{1T} \frac{1}{\tau} \overline{\theta u_i}$, seems from this figure to be a good candidate for modeling Ψ_i , where τ often is taken as the dynamical timescale, k/ε .

The following, more general, model for Ψ_i will be compared with the present data:

$$\Psi_i = -c_{1T} \frac{1}{\tau} \overline{\theta u_i} + c_{2T} \overline{\theta u_j} U_{i,j} + c_{3T} \overline{\theta u_j} U_{j,i} \quad (3)$$

This form is obtained by neglecting the destruction and the pressure-diffusion terms in Eq. 2, and modeling the slow part of the pressure scalar-gradient term by the first term on the right hand side of Eq. 3, and the rapid part by the second and third terms. In the present plane shear flow the c_{2T} term contributes only to the Ψ_1 component and the c_{3T} term contributes only to the Ψ_2 component.

The DNS of homogeneous shear flow by Rogers et al. gives a constant timescale ratio, $\overline{\theta^2} \varepsilon / k \varepsilon_\theta$, of about 1.2, where ε_θ is the dissipation rate of $\frac{1}{2} \overline{\theta^2}$. An estimation of ε has been made from the present data by balancing

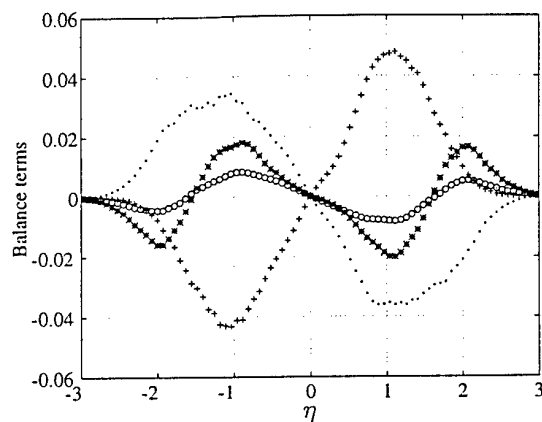


Figure 2: The dominating terms in the transport equation of $\overline{v\theta}$ normalized by $\frac{U_*^2 \Theta_*}{l}$, where l is the velocity defect half-width and $\eta = y/l$. \circ , $U \frac{\partial \overline{v\theta}}{\partial x}$; $+$, $-\overline{v^2} \frac{\partial \Theta}{\partial y}$; $*$, $-\frac{\partial}{\partial y} \overline{v^2 \theta}$; \cdot , Ψ_2 .

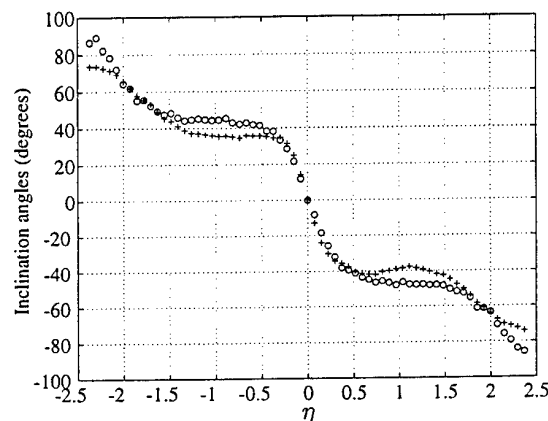


Figure 3: Comparison between the inclination angles of the turbulent scalar flux, $u_i \theta$, and Ψ_i . \circ , $\tan^{-1}(\overline{v\theta}/\overline{u\theta})$; $+$, $\tan^{-1}(\Psi_2/\Psi_1)$.

the transport equation of k and neglecting the pressure-diffusion term. The timescale ratio, based on this estimate, ranges from about 0.9 at the centerline to 0.6 at the point of maximum production. The timescale ratio is thus not constant in the present wake flow. In the comparisons below three different timescales will be used for τ : the dynamical timescale, k/ε , the thermal timescale, $\overline{\theta^2}/\varepsilon_\theta$, where ε_θ was determined from the $\overline{\theta^2}$ -equation, and a mixed timescale, $\sqrt{k \overline{\theta^2} / \varepsilon \varepsilon_\theta}$, which blends both thermal and mechanical contributions.

In Figs. 4–9 Ψ_1 and Ψ_2 obtained from the measured data are compared with those obtained from Eq. 3 using the values of c_{1T} , c_{2T} and c_{3T} given in Table 1 and the three different choices of the timescale. c_{1T} is the same, 3.2, for all models, whereas c_{2T} and c_{3T} are varied. In model (a) c_{2T} and c_{3T} are set to zero and Eq. 3 then gives a model of Ψ_i aligned with the heat-flux vector. The parameter choice of model (b) is $c_{1T} = 3.2$, $c_{2T} = 0.50$ and $c_{3T} = 0$. If the timescale is taken to be the dynamical timescale, k/ε , we have the Launder (1975) model. By formal solution of the Poisson equation for the rapid pressure a linear model for $\frac{\partial}{\partial x_i} \frac{\partial \theta}{\partial x_i}$ may be derived, see e.g. Shih (1996). Mathematical constraints then give $c_{2T} = \frac{4}{5}$ and $c_{3T} = -\frac{1}{5}$. These parameter choices are used in model (c).

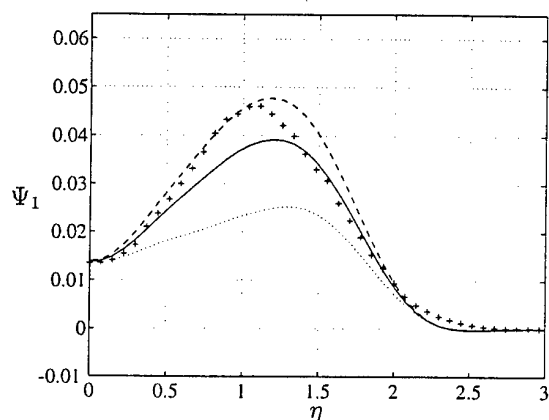


Figure 4: Comparison between Ψ_1 (normalized by $\frac{U_s^2 \theta_s}{l}$) obtained from the experimental data and that obtained from Eq. 3 using the parameter values of c_{1T} , c_{2T} and c_{3T} given in Table 1. +, experimental data; ····, (a); —, (b); ---, (c), with $\tau = k/\varepsilon$.

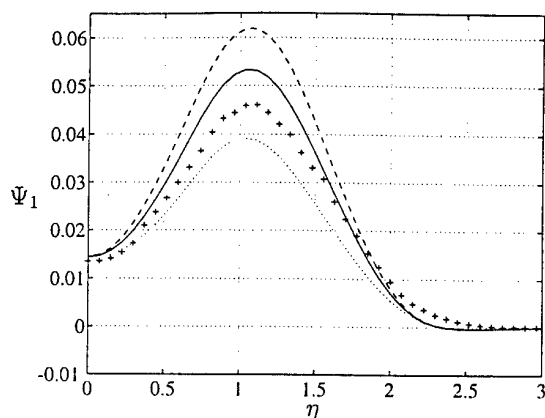


Figure 6: Comparison between Ψ_1 (normalized by $\frac{U_s^2 \theta_s}{l}$) obtained from the experimental data and that obtained from Eq. 3 using the parameter values of c_{1T} , c_{2T} and c_{3T} given in Table 1. +, experimental data; ····, (a); —, (b); ---, (c), with $\tau = \bar{\theta}^2/\varepsilon_\theta$.

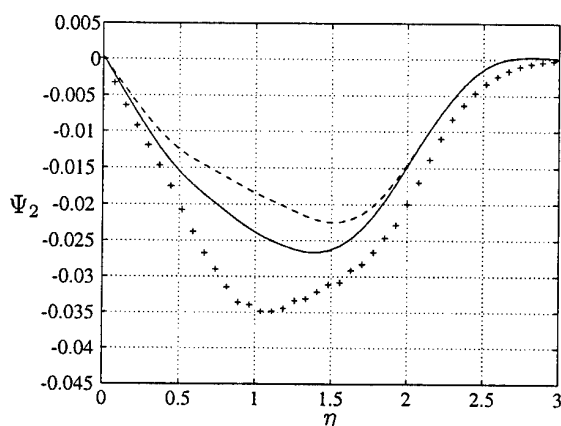


Figure 5: Comparison between Ψ_2 (normalized by $\frac{U_s^2 \theta_s}{l}$) obtained from the experimental data and that obtained from Eq. 3 using the parameter values of c_{1T} , c_{2T} and c_{3T} given in Table 1. +, experimental data; —, (a) and (b); ---, (c), with $\tau = k/\varepsilon$.

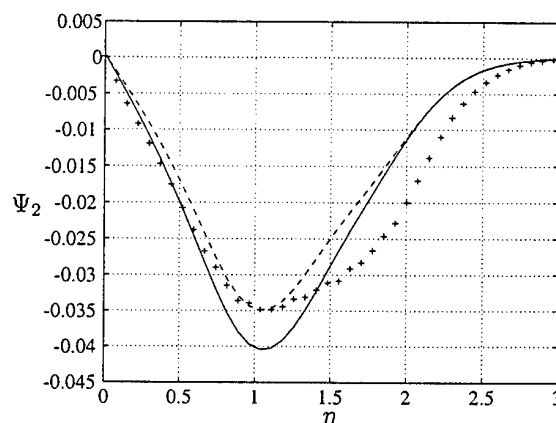


Figure 7: Comparison between Ψ_2 (normalized by $\frac{U_s^2 \theta_s}{l}$) obtained from the experimental data and that obtained from Eq. 3 using the parameter values of c_{1T} , c_{2T} and c_{3T} given in Table 1. —, (a) and (b); ---, (c), with $\tau = \bar{\theta}^2/\varepsilon_\theta$.

In Figs. 4–5 the timescale τ is taken to be k/ε as in the Launder model. All models give a very good agreement at the centerline, which simply reflects that an appropriate value of c_{1T} has been chosen. Model (a) underpredicts both the Ψ_1 and Ψ_2 components. The Launder model, (b), gives the same prediction as the previous one in the case of the Ψ_2 component, but improves the prediction of the Ψ_1 component. Hence, inclusion of the rapid term gives an improvement. Model (c) is unable to predict the two components simultaneously and gives a severe underprediction of the Ψ_2 term. The Launder model could give a better compromise for the components by increasing c_{1T} to 4.0, though, resulting in an overprediction of about 20% of the Ψ_1 component at the centerline.

For the models in Figs. 4–5 the prediction of the peak is displaced towards the freestream compared to the measured data. This could be due to the neglect of the pressure-diffusion term when determining ε needed in the dynamical timescale, k/ε . A comparison has been made with the model predictions obtained when using the directly measured ε of Aronson and Löfdahl (1994) in the timescale, k/ε . In this case the displacement of the peaks

Table 1: The different combinations of the model constants used in Eq. 3. Models (a) and (b) are equivalent for the Ψ_2 -component.

model	c_{1T}	c_{2T}	c_{3T}
(a)	3.2	0	0
(b)	3.2	0.50	0
(c)	3.2	$\frac{4}{5}$	$-\frac{1}{5}$

is not obtained, whereas the maximum amplitudes will be the same as with the estimate of ε from the present data.

In Figs. 6–7 the timescale τ is taken to be the thermal timescale, $\bar{\theta}^2/\varepsilon_\theta$. Since the timescale ratio is 0.9 at the centerline all models give good agreement here as in the previous case. Model (c) gives a good prediction of the maximum amplitude of the Ψ_2 component, whereas the Ψ_1 component is overpredicted. Model (b) gives an overprediction of both components. The larger values at $\eta=1$,

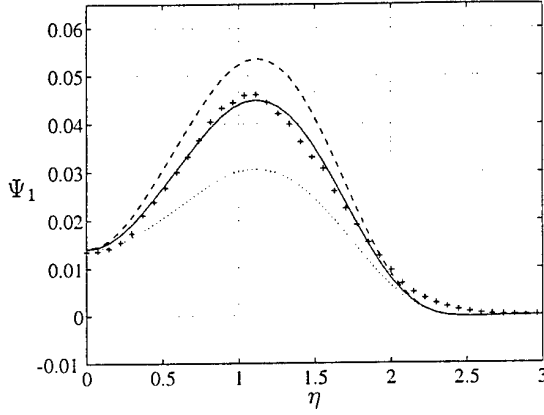


Figure 8: Comparison between Ψ_1 (normalized by $\frac{U^2 \Theta_s}{l}$) obtained from the experimental data and that obtained from Eq. 3 using the parameter values of c_{1T} , c_{2T} and c_{3T} given in Table 1. +, experimental data; ···, (a); —, (b); ---, (c), with $\tau = \sqrt{k\theta^2}/\varepsilon\epsilon_\theta$.

compared to the previous case, of all model predictions are due to that the timescale ratio is 0.6 at this position. By using $c_{1T}=2.8$ instead of 3.2 in model (b) the behavior of both components is well captured.

In Figs. 8–9 the timescale τ is taken to be the mixed timescale $\sqrt{k\theta^2}/\varepsilon\epsilon_\theta$. As in the previous cases models (a) and (c) are unable to predict the two components simultaneously and all models give good agreement at the centerline. Model (b) gives a very good prediction of the Ψ_1 component, whereas Ψ_2 is slightly underpredicted. This could be due to the fact that Ψ_2 contains also a pressure-diffusion term and the experimental data of this component seems to be more contaminated by the destruction term. Using $c_{1T}=3.5$ instead of 3.2 in model (b), a better compromise for the two components is obtained, while by choosing c_{3T} in model (b) to be 0.15 instead of 0, the prediction of Ψ_2 can be improved while the prediction of Ψ_1 is unchanged.

Model comparison 2

The following model for the triple correlations, $\overline{u_i u_j \theta}$, is here compared to the experimental data.

$$\begin{aligned} \overline{u_i u_j \theta} = & \alpha_1 k \tau (\overline{\theta u_k})_{,k} \delta_{ij} + \alpha_2 k \tau \left[(\overline{\theta u_i})_{,j} + (\overline{\theta u_j})_{,i} \right] \\ & + \tau \left\{ \alpha_3 \left[\overline{u_i u_k} (\overline{\theta u_j})_{,k} + \overline{u_j u_k} (\overline{\theta u_i})_{,k} \right] \right. \\ & + \alpha_4 \overline{u_i u_j} (\overline{\theta u_k})_{,k} \\ & + \alpha_5 \left[\overline{u_i u_k} (\overline{\theta u_k})_{,j} + \overline{u_j u_k} (\overline{\theta u_k})_{,i} \right] \\ & + \alpha_6 \overline{\theta u_k} (\overline{u_i u_j})_{,k} \\ & + \alpha_7 \left[\overline{\theta u_i} (\overline{u_j u_k})_{,k} + \overline{\theta u_j} (\overline{u_i u_k})_{,k} \right] \\ & + \alpha_8 \left[\overline{\theta u_k} (\overline{u_j u_k})_{,i} + \overline{\theta u_k} (\overline{u_i u_k})_{,j} \right] \\ & \left. + \alpha_9 \left[\overline{\theta u_j} (\overline{u_k u_k})_{,i} + \overline{\theta u_i} (\overline{u_k u_k})_{,j} \right] \right\} \end{aligned} \quad (4)$$

All the coefficients may be seen as functions of the invariants of the tensors in Eq. 4 but will here be considered as constants. If the timescale, τ , is taken as the dynamical timescale, the Shih (1996) model is obtained, where also higher order terms may be included. In a plane wake flow this model gives a zero prediction of the triple correlations $\overline{uw\theta}$ and $\overline{vw\theta}$, which is expected and in agreement with the experimental data. The other four nonzero compo-

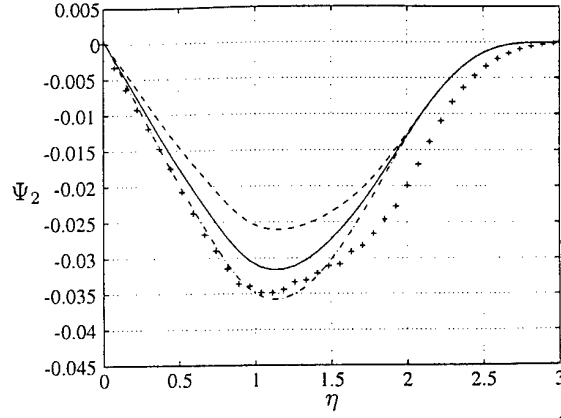


Figure 9: Comparison between Ψ_2 (normalized by $\frac{U^2 \Theta_s}{l}$) obtained from the experimental data and that obtained from Eq. 3 using the parameter values of c_{1T} , c_{2T} and c_{3T} given in Table 1. +, experimental data; —, (a) and (b); ···, (c); ···, $c_{1T}=3.2$, $c_{2T}=0.50$ and $c_{3T}=0.15$, with $\tau = \sqrt{k\theta^2}/\varepsilon\epsilon_\theta$.

nents, $\overline{u^2 \theta}$, $\overline{v^2 \theta}$, $\overline{w^2 \theta}$ and $\overline{uv \theta}$, are shown in Figs. 10–13. The derivatives $-\frac{\partial}{\partial y} \overline{v^2 \theta}$ and $-\frac{\partial}{\partial y} \overline{uv \theta}$ appear as the diffusion terms in the transport equations of the heat fluxes, in the present flow case. Figs. 10–13 also shows the prediction of Eq. 4 using the parameter values given in Table 2. The parameters of model (a) are obtained by a least-square fit to all four nonzero components simultaneously, using the mixed timescale, $\sqrt{k\theta^2}/\varepsilon\epsilon_\theta$. This model predicts all components quite well, though, the behavior of $\overline{u^2 \theta}$ and $\overline{w^2 \theta}$ are somewhat mispredicted for $\eta < 1$. Model (b) is also a least-square fit to the experimental data, but here only the α_2 and α_6 terms are included. This model gives predictions quite close to those of model (a) for all four components considering that only two model parameters are used instead of nine. Using the α_3 -term instead of the α_2 -term, gives approximately the same predictions as that of model (b). The inclusion of a tensor eddy diffusivity thus makes no major difference in the present flow case. The α_3 -term could of course be of importance in a flow with a higher degree of anisotropy. In the present flow case the α_6 -term seems to be of major importance. This term as well as the α_4 -term are the only ones giving a nonzero prediction of the $\overline{w^2 \theta}$ component in the present flow case. If the dynamical timescale is used instead of the mixed timescale when deriving the two least-square fits to the experimental data, approximately the same model predictions are obtained but with different values of the model parameters. For example the parameters of model (b) would then be $\alpha_2 = -0.064$ and $\alpha_6 = -0.43$.

Table 2: The parameter values in Eq. 4 obtained from a least-square fit to the experimental data using all nine terms, (a), and only two terms, (b), with $\tau = \sqrt{k\theta^2}/\varepsilon\epsilon_\theta$.

model	α_1	α_2	α_3	α_4	α_5
(a)	0.017	-0.12	-0.064	0.028	0.093
(b)	0	-0.072	0	0	0

model	α_6	α_7	α_8	α_9
(a)	-0.51	-0.0072	0.10	-0.062
(b)	-0.54	0	0	0

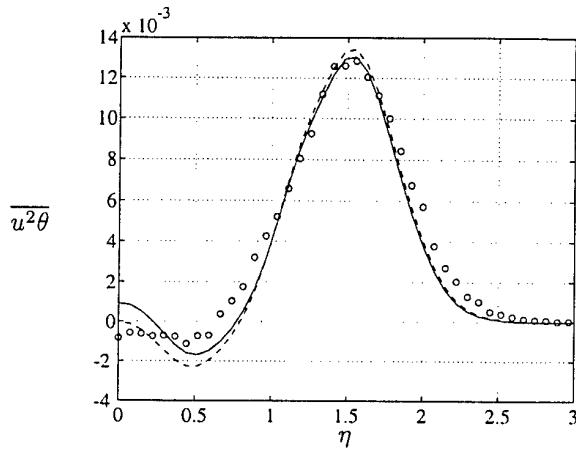


Figure 10: Comparison between $\overline{u^2\theta}$ (normalized by $U_s^2\Theta_s$) obtained from the experimental data and that obtained from Eq. 4 using the parameter values given in Table 2. \circ , experimental data; —, (a); ---, (b), with $\tau = \sqrt{k\theta^2/\varepsilon\varepsilon_\theta}$.

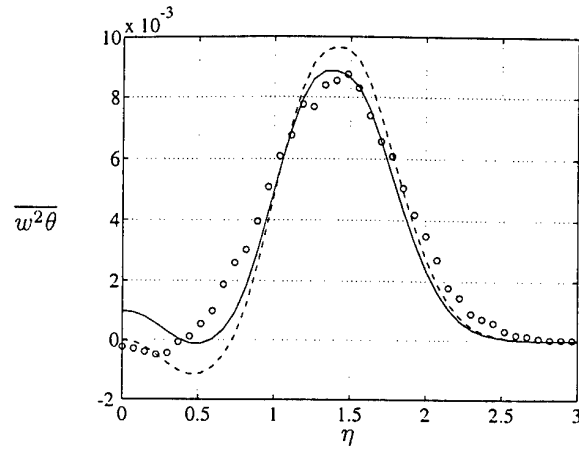


Figure 12: Comparison between $\overline{w^2\theta}$ (normalized by $U_s^2\Theta_s$) obtained from the experimental data and that obtained from Eq. 4 using the parameter values given in Table 2. \circ , experimental data; —, (a); ---, (b), with $\tau = \sqrt{k\theta^2/\varepsilon\varepsilon_\theta}$.

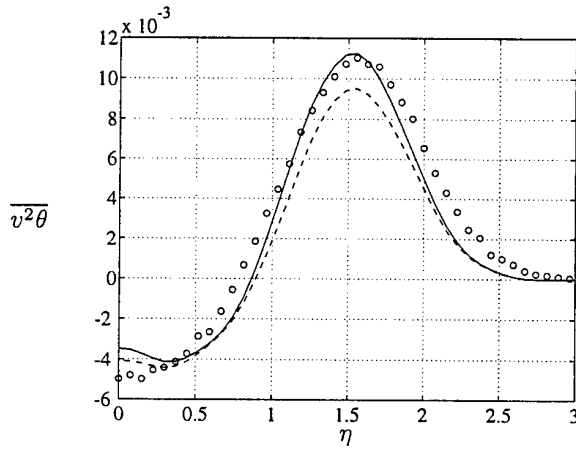


Figure 11: Comparison between $\overline{v^2\theta}$ (normalized by $U_s^2\Theta_s$) obtained from the experimental data and that obtained from Eq. 4 using the parameter values given in Table 2. \circ , experimental data; —, (a); ---, (b), with $\tau = \sqrt{k\theta^2/\varepsilon\varepsilon_\theta}$.

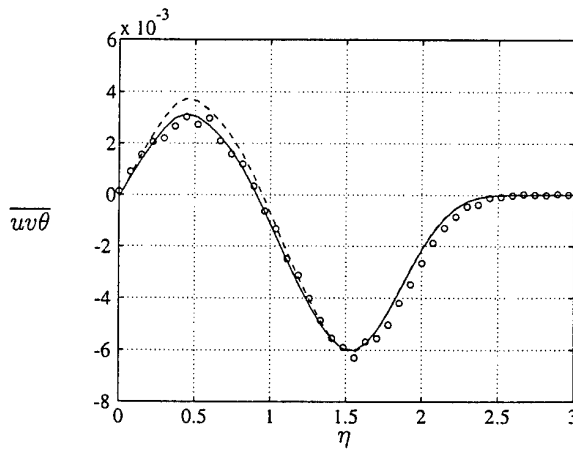


Figure 13: Comparison between $\overline{uv\theta}$ (normalized by $U_s^2\Theta_s$) obtained from the experimental data and that obtained from Eq. 4 using the parameter values given in Table 2. \circ , experimental data; —, (a); ---, (b), with $\tau = \sqrt{k\theta^2/\varepsilon\varepsilon_\theta}$.

CONCLUSIONS

From the present experimental data it seems clear that a significant improvement to the simplest model, $\Psi_i = -c_{1T}\frac{1}{\tau}\theta u_i$, can be achieved by including an 'isotropization-of-production'-like model for the rapid term, $c_{2T}\theta u_j U_{i,j}$. By using a mixed timescale, $\sqrt{k\theta^2/\varepsilon\varepsilon_\theta}$, the curves of the two components of Ψ_i are best captured. With this choice of the timescale the following parameter choice gives the most satisfactory model prediction for this flow situation: $c_{1T}=3.2$, $c_{2T}=0.50$, $c_{3T}=0.15$. In a DNS of scalar transport in homogeneous turbulence by Kawamura and Ihira (1996) it was found that c_{1T} depends on the turbulent Reynolds number and has a value of 3.8, using the dynamical timescale, for high Reynolds numbers. In the present case the Launder model gives a reasonably good compromise for both the components of Ψ_i by increasing c_{1T} from 3.2 to 4.0.

When using the truncated Shih model for the triple correlations, $u_i u_j \theta$, given in Eq. 4, only two of the terms may give approximately as good predictions as those of a model including all nine terms. These two terms are the α_2 -term and α_6 -term, where the latter ensures a nonzero predic-

tion of $\overline{w^2\theta}$ in the present flow case. A simple gradient diffusion model, though, given by the α_2 -term, using a constant eddy-diffusivity, or the α_3 -term, using a tensor eddy-diffusivity, are here unable to capture the behavior of this component. Inclusion of a tensor eddy-diffusivity, i.e., using the α_3 instead of the α_2 -term together with the α_6 -term, gives no improvement and thus seems to be of less importance in the present wake flow.

REFERENCES

- Aronson, D., and Löfdahl, L., 1994, "The plane wake of a cylinder: An estimate of the pressure-strain rate tensor", *J. Fluid Mech.*, Vol. 67, pp. 569–581.
- Browne, L. W. B., and Antonia, R. A., 1986, "Reynolds shear stress and heat flux measurements in a cylinder wake", *Phys. Fluids A*, Vol. 29, pp. 709–713.
- Kawamura, H., and Ihira, H., 1996, "DNS and modeling of scalar transport in homogeneous turbulence", *In Engineering Turbulence Modelling and Experiments 3*, pp. 239–249. Rodi and Bergeles, eds., Elsevier.
- Launder, B. E., 1975, "An algebraic model for the turbulent flux of a passive scalar", *J. Fluid Mech.*, Vol. 67, pp. 569–581.

Rogers, M. M., Mansour, N. N., and Reynolds, W. C., 1989, "An algebraic model for the turbulent flux of a passive scalar", *J. Fluid Mech.*, Vol. 203, pp. 77-101.

Shih, T. H., 1996, *Chapter 4 of Turbulence and transition modeling* Hallbäck et al., eds., *Kluwer EROFTAC Series*.

Wikstöm, P. M., Hallbäck, M., and Johansson, A. V., 1996, "Measurements and modeling of temperature fluctuations in a heated cylinder wake", *In Flow Modeling and Turbulence Measurements VI.*, pp. 143-150. Chen et al., eds., *Balkema*.

DNS OF TURBULENT HEAT TRANSFER IN CHANNEL FLOW WITH LOW TO MEDIUM-HIGH PRANDTL NUMBER FLUID

Hiroshi Kawamura and Kouichi Ohsaka,
Department of Mechanical Engineering, Science University of Tokyo
Noda-shi, Chiba-ken, 278
Japan

Kiyoshi Yamamoto
National Aerospace Laboratory
Choufu-shi, Tokyo, 182
Japan

ABSTRACT

The direct numerical simulation (DNS) of the turbulent heat transfer for various Prandtl numbers ranging from 0.025 to 5 are performed to obtain statistical quantities such as turbulent heat flux, temperature variance and their budget terms. The configuration is the fully developed channel flow with uniform heating from both walls. Budget of wall-normal heat flux shows that the TPG (temperature-pressure gradient correlation) and the dissipation terms become comparative around $Pr=0.2$. The Prandtl number of 5, which is equivalent to the water, is the highest value ever calculated for the turbulent heat transfer in the channel flow.

INTRODUCTION

Turbulent heat transfer is characterized not only by the Reynolds number (Re) but also by the Prandtl number (Pr) of the fluids. Several DNS's of the heat transfer in the turbulent channel flow were performed. Kim et al. (1989) made simulations for Prandtl numbers $Pr = 0.1, 0.71$ and 2 . They obtained profiles of the mean temperature, temperature variance and turbulent heat flux; but detailed budget of those quantities was not reported. Kasagi et al. (1992) and Kasagi-Ohtsubo (1993) performed DNS for $Pr = 0.025$ and 0.71 . They obtained the budget of the transport equation for the temperature variance and the turbulent heat fluxes. In summary the DNS's were performed for the heat transfer of liquid metal ($Pr = 0.025$) and gas ($Pr = 1$) up to now. However, the heat transfer of water ($Pr = 5 \sim 7$) has not yet been done; this is because the increase of the Prandtl number requires a larger mesh number.

In the present work, DNS of the turbulent heat transfer for various Prandtl numbers ranging from 0.025 to 5 are performed to obtain turbulence quantities such as turbulent heat flux, temperature variance, their budget terms and turbulent Prandtl number. The data for the middle Prandtl number such as $Pr =$

0.1, 0.2, 0.4 are rather difficult to be obtained experimentally. The Prandtl number of 5 is the highest value ever calculated for the turbulent heat transfer, to the authors' knowledge.

It is known that the smallest scale in the temperature fluctuation decreases with the increase of the Prandtl number inversely proportionally to $Pr^{1/2}$. Thus, in the calculation of $Pr = 5$ the mesh number is doubled in each direction. This causes roughly ten times calculation cost, which is the reason why the DNS for this range of the Prandtl number has not been made hitherto. The present calculation has been enabled by means of a super parallel computer "Numerical Wind Tunnel (NWT)" using about eight million mesh points and 1 GB main memory.

NUMERICAL PROCEDURE

DNS is often performed with the spectral method because of its higher accuracy. The finite-difference method (FDM), on the other hand, has an advantage to be potentially applicable for complex geometries. In the present study, the finite-difference method is applied to the DNS of turbulent heat transfer in a channel flow.

The configuration is the fully developed channel flow (Fig.1). The computational domain is $6.4\delta, 2\delta, 3.2\delta$ in the axial (x), wall-normal (y), and spanwise (z) directions, respectively. The mean flow is in x direction. The channel flow is heated with a uniform heat flux q_w from both of the walls. The fundamental equations are

Continuity equation:

$$\frac{\partial U_i^*}{\partial x_i} = 0 \quad (1)$$

Navier-Stokes equation:

$$\frac{\partial U_i^*}{\partial t^*} + U_j^* \frac{\partial U_i^*}{\partial x_j} = -\frac{\partial P^*}{\partial x_i} + \frac{1}{Re_\tau} \frac{\partial^2 U_i^*}{\partial x_j^2} \quad (2)$$

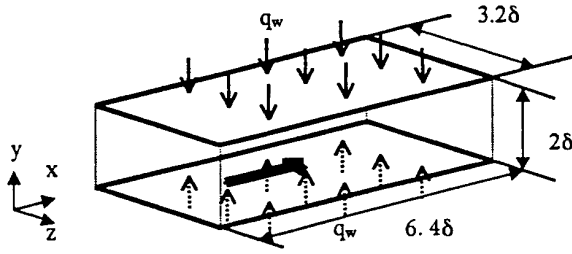


FIG.1 CONFIGURATION OF DNS

Energy equation:

$$\frac{\partial \Theta^*}{\partial t^*} + U_j^* \frac{\partial \Theta^*}{\partial x_j^*} = \frac{1}{Re_\tau \cdot Pr} \frac{\partial^2 \Theta^*}{\partial x_j^{*2}} + \frac{u_1^*}{\langle U^* \rangle} \quad (3)$$

where x^* , U^* , Θ^* and P^* are the distance, the instantaneous velocity, temperature and pressure, which are nondimensionalized by the channel half width δ , friction velocity u^* , the kinematic viscosity ν , and the density ρ . The Reynolds number is defined as $Re_\tau = u^* \delta / \nu$, and $\langle U^* \rangle$ is the average velocity over the channel section.

The boundary conditions are

$$U_i^* = 0, \Theta^* = 0 \quad y (=x_2) = 0, 2\delta \quad (4)$$

The above equations are discretized with the use of the finite difference method. A numerical scheme consistent with the analytical operation (Kawamura, 1995) is employed to ensure the balance of the transport equations for the statistical correlations such as the turbulent heat flux and the temperature variance. The method was well examined in comparison with the spectral method (Kawamura, Kondoh, 1996). The computational conditions are given in Table 1.

The mean temperature profile is given in Fig. 2. The results agree well with the Kader's correlation. The mean temperature profile is plotted again in Fig. 3 with an emphasis on the conduction region. This figure clearly indicates that the conduction region penetrates more deeply towards the center of the channel in case of the low Prandtl number fluid. Figure 4 shows the turbulent heat flux. The nondimensional turbulent heat flux increases with the increase of the Prandtl number, which is of course balanced by the decrease in the molecular transport.

In the wall vicinity, the fluctuations of the velocity u^* , v^* and temperature θ^* can be expanded in terms of y^* as

$$u^* = b_1 y^* + b_2 y^{*2} + \dots \quad (5)$$

$$v^* = c_2 y^{*2} + d_1 y^{*3} + \dots \quad (6)$$

$$\theta^* = b_0 y^* + d_0 y^{*3} + \dots \quad (7)$$

TABLE 1 COMPUTATIONAL CONDITIONS

Reynolds number	$Re_\tau = 180$
Mesh	Staggered Mesh
Coupling algorithm	Fractional Step method
Time advancement	2nd-order Adams-Bashforth method
Convective term	2nd Central (consistent scheme)
Other terms	2nd Central
Boundary conditions	Periodic (x, z direction) Non-slip (y direction)
Computational volume	$6.4 \delta \times 2 \delta \times 3.2 \delta$
Grid number	$128 \times 66 \times 128$ ($Pr \leq 1.5$) $256 \times 128 \times 256$ ($Pr = 5.0$)

On the other hand, the gradient of the instantaneous temperature Θ^* over the heating boundary satisfies the relation

$$\frac{1}{Pr} \frac{d\Theta^*}{dy^*} = 1 + \frac{q_w'}{q_w} \quad y = 0 \quad (8)$$

where $\overline{q_w}$ is the average heat flux and q_w' is its fluctuation. Inspection of the above equation indicates that both the mean and the fluctuation temperatures can be expanded in terms of y^* as

$$\overline{\Theta^*} = Pr y^* + \dots \quad (9)$$

$$\Theta^* = Pr b_0 y^* + \dots \quad (10)$$

With the use of Eqs. (6) and (10), the turbulent heat flux can be expressed as

$$-\overline{v^* \Theta^*} = Pr \overline{b_0 c_2} y^{*3} + Pr \overline{b_0 d_2} y^{*4} + \dots \quad (11)$$

Thus one can expect that $-\overline{v^* \Theta^*} / Pr$ varies as y^{*3} in the wall vicinity. Figure 5 illustrates this relation. Indeed, $-\overline{v^* \Theta^*} / Pr$ is proportional to y^{*3} with its correlation coefficient $\overline{b_0 c_2} = 7 \times 10^{-4}$.

The turbulent Prandtl number is defined as

$$Pr_t = \frac{v_t}{a_t} = \frac{\overline{u^* v^*} \left(\frac{d\overline{\Theta^*}}{dy^*} \right)}{\overline{v^* \Theta^*} \left(\frac{du^*}{dy^*} \right)} \quad (12)$$

With the use of Eqs. (5), (6), (9) and (11), one finds that

$$Pr_t = \frac{\overline{b_1 c_2}}{Pr \overline{b_0 c_2}} \frac{Pr}{1} = \frac{\overline{b_1 c_2}}{\overline{b_0 c_2}} \quad (y^* \rightarrow 0) \quad (13)$$

Since $\overline{b_1 c_2} = 7 \times 10^{-4}$ (Mansour et al, 1988), Pr_t tends to be 1.0 as the wall is approached. Moreover the above

consideration indicates that the wall asymptotic value of the turbulent Prandtl number is independent of the molecular Prandtl number. This feature was suggested in the analysis by Antonia (1991) up to $Pr = 2$; and it is confirmed and extended here to a higher Prandtl number.

The turbulent Prandtl numbers obtained through the present DNS are shown in Fig. 6. Indeed, the wall asymptotic value of Pr is independent of Prandtl number except for very low Prandtl numbers such as $Pr < 0.1$. This conclusion supports the widely used practice to employ a constant turbulent Prandtl number in the calculation of heat transfer with normal to high Prandtl number fluids.

The budget of the transport equation for the turbulent heat flux is given in Figs. 7 a to d. The production term is negative in this case. It is well known that, in the normal fluid, the dissipation

$$\epsilon_{\theta} = (a + \nu) \frac{\partial u_i}{\partial x_j} \frac{\partial \theta}{\partial x_j} \quad (14)$$

is negligible because of the isotropy in the dissipation scale. It is actually seen that the dissipation is negligibly small for $Pr = 5.0$ (Fig. 7 d) except in the wall vicinity. Thus, the production is balanced with the temperature pressure-gradient correlation (TPG) term:

$$\phi_{\theta} = -\theta \frac{\partial P}{\partial x_i} \quad (15)$$

In a low Prandtl number fluid, on the other hand, the dissipation is dominant because it takes place in eddies of a larger scale (see Fig. 7 a). Indeed, Figs. 7c, d show that the TPG term is dominant for $Pr=5.0$, 0.4 and the dissipation term is overwhelming for $Pr=0.05$. It is interesting to note that the TPG and the dissipation terms become comparative at $Pr=0.2$ as seen in Fig. 7 b. The instantaneous contour surfaces of the production, dissipation and TPG are visualized and shown in Figs. 8 a-d for $Pr=0.05$, 0.2, 0.4 and 5.0. As discussed above, the dissipation overcomes the TPG in $Pr=0.05$. On the other hand, their magnitude is inverted in $Pr=0.4$, and they are roughly balanced in $Pr=0.2$. In the high Prandtl number of $Pr=5.0$, the TPG dominates and the dissipation is hardly visible. Moreover, the structure of the TPG is seen to become streamwisely longer and spanwisely finer with the increase of the Prandtl number.

The temperature variance is illustrated in Fig. 9 for various Prandtl numbers. The peak of the temperature variance (θ^2) becomes higher and moves closer to a wall as the Prandtl number increases.

The budget terms of the transport equation of the temperature variance is given in Figs. 10 a, b and c. The production term is mostly balanced with the dissipation for all the Prandtl number calculated. A closer inspection, however, indicates that the turbulent and molecular diffusion terms plays a more significant role with increase of the Prandtl number. In case of $Pr=5.0$, the diffusion terms becomes even comparative with the dissipation, which has never been seen in the simulation of the lower Prandtl number cases.

It is seen in Figs. 10 a, b and c that the peak in the production term increases and moves towards the wall with increasing Prandtl number. If the energy equation Eq. (3) is

ensemble averaged and the assumption of the fully developed flow is considered, it becomes

$$\frac{d}{dy^+} \left[\frac{1}{Pr} \frac{d\bar{\theta}^+}{dy^+} - \overline{v^+ \theta^+} \right] + \frac{\bar{u}^+}{Re_\delta} = 0 \quad (16)$$

where $Re_\delta = \langle U \rangle \delta / \nu$ and the distance is nondimensionalized with ν / u^+ instead of δ . Since $\bar{u}^+ = y^+$ in the wall vicinity, Eq.(16) can be integrated with respect to y^+ as

$$\frac{1}{Pr} \frac{d\bar{\theta}^+}{dy^+} = 1 - \left(-\overline{v^+ \theta^+} \right) - \frac{1}{2 Re_\delta} y^{+2} \quad (17)$$

The last term in the right hand side is negligible compared to the other terms since $Re_\delta \approx 1400$ and $y^+ \approx 10$. Then the production term of the temperature variance can be expressed simply as

$$P_\theta = -\overline{v^+ \theta^+} \frac{d\bar{\theta}^+}{dy^+} = Pr \left(-\overline{v^+ \theta^+} \right) \left[1 - \left(-\overline{v^+ \theta^+} \right) \right] \quad (18)$$

It is easily found that the maximum in P_θ arises at $-\overline{v^+ \theta^+} = 0.5$ with its peak value of

$$P_{\theta \max} = Pr/4 \quad (Pr \gg 1.0) \quad (19)$$

If only the first term in Eq.(11) is adopted for simplicity, the position of peak can be approximated as

$$y_{\max}^+ = \frac{1}{2(b_\theta c_2)^{1/3}} \frac{1}{Pr^{1/3}} \quad (Pr \gg 1.0) \quad (20)$$

Thus, P_θ / Pr is plotted versus $Pr^{1/3} y^+$ in Fig. 10. It is found in Fig. 10 that, expect for low Prandtl number such as $Pr < 0.1$, the peak in the production rate tends to $Pr/4$ indeed and its position can also be well normalized with the above treatment.

CONCLUSIONS

1. DNS of the turbulent heat transfer in channel flow was performed for more than two decades of the Prandtl number from 0.025 to 5; the largest one ($Pr = 5$) is, to the author's knowledge, the highest Prandtl number calculated hitherto.
2. The budget terms of the transport equations for the turbulent heat flux and the temperature variance were obtained and visualized. The effect of the Prandtl number was examined.
3. The near wall behaviour of the turbulent quantities were analyzed and statistical correlation coefficients were obtained for the above range of Pr .
4. The wall limiting value of the turbulent Prandtl number was proved to be independent of the molecular Prandtl

number except for a low Prandtl number fluid. This conclusion gives a theoretical basis on the widely employed practice to use a constant value in the heat transfer analysis of the fluids with the normal to high molecular Prandtl number.

The present data base is made available on a web site. The detailed information is given at
<http://muraibm.me.noda.sut.ac.jp/e-page1.html>

REFERENCES

- Antonia, R. A. and Kim, J., 1991, "Turbulent Prandtl number in the near-wall region of a turbulent channel flow", *Int. J. Heat Mass Transfer*, Vol. 34, pp. 1905-1908.
- Kasagi, N., et al., 1992, "Direct Numerical Simulation of Passive Scalar Field in a Turbulent Channel Flow", *ASME, J. Heat Transfer*, Vol. 114, pp. 598-606.
- Kasagi, N. and Ohtsubo, Y., 1993, "Direct Numerical Simulation of Low Prandtl Number Thermal Field in a Turbulent Channel Flow", *Turbulent Shear Flows 8*, Springer, pp. 97-119.
- Kawamura, H., 1995, "Direct Numerical Simulation of Turbulence by Finite Difference Scheme" *The Recent Developments in Turbulence Research*, pp. 54-60, International Academic Publishers.
- Kawamura, H. and Kondoh, Y., 1996, "Application of Consistent Finite Difference Scheme to DNS of Turbulent Heat Transfer in Channel Flow", *The 3rd KSME-JSME Thermal Engineering Conference*, Vol. 1, pp. 53-58.
- Kim, J. and Moin, P., 1989, "Transport of Passive Scalars in a Turbulent Channel Flow", *Turbulent Shear Flows 6*, Springer, pp. 85-96.
- Mansour, N., Kim, J. and Moin, P., 1988, "Reynolds-stress and dissipation-rate budgets in a turbulent channel flow", *J. Fluid Mech.*, vol. 194, pp. 15-44.

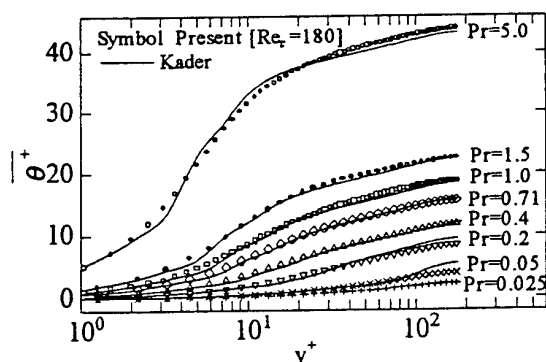


FIG. 2 MEAN TEMPERATURE PROFILE WITH AN EMPHASIS ON THE LOGARITHMIC REGION

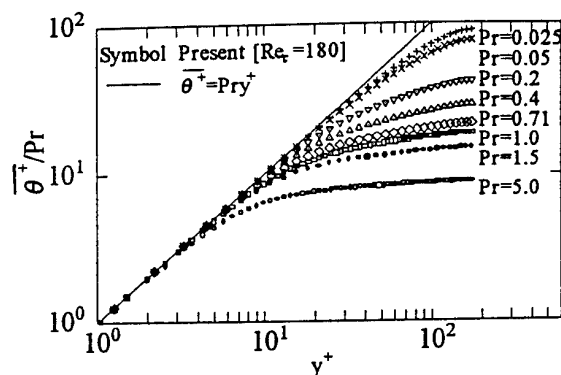


FIG. 3 MEAN TEMPERATURE PROFILE WITH AN EMPHASIS ON THE CONDUCTION REGION

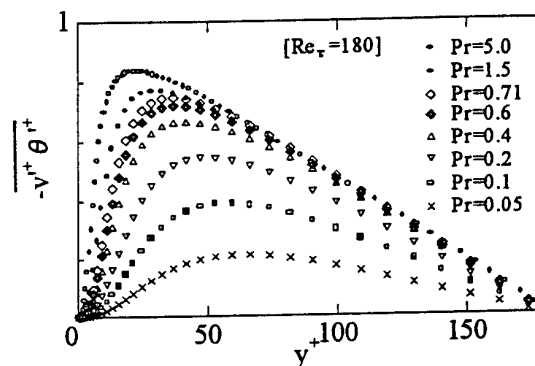


FIG. 4 TURBULENT HEAT FLUX FOR VARIOUS PRANDTL NUMBERS

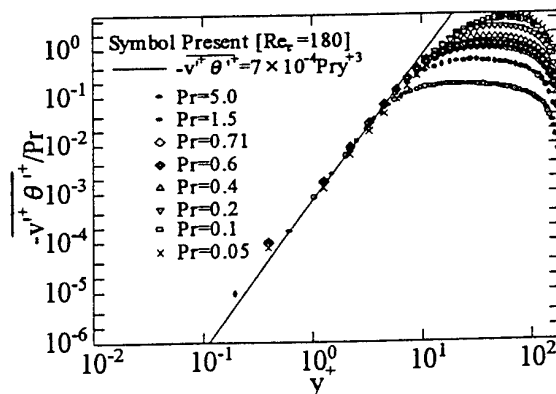


FIG. 5 TURBULENT HEAT FLUX INDICATING $y^+{}^3$ DEPENDENCE

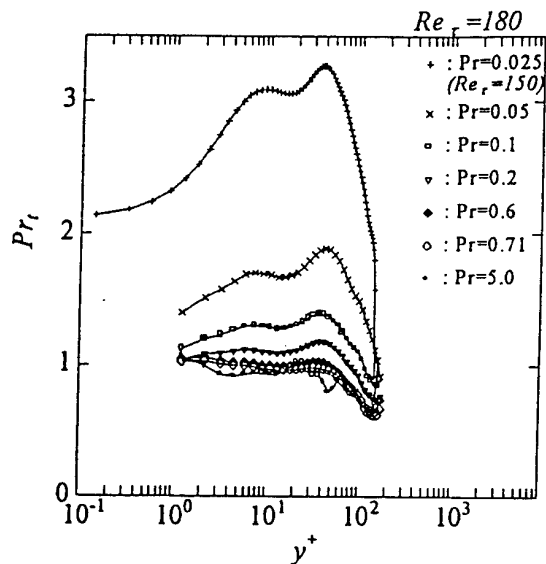


FIG. 6 TURBULENT PRANDTL NUMBER ($Pr=0.025$ by Kasagi(1993))

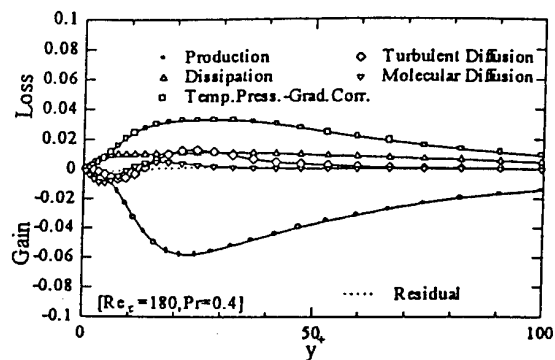


FIG. 7c BUDGET OF THE TRANSPORT EQUATION FOR THE TURBULENT HEAT FLUX ($Pr=0.4$)

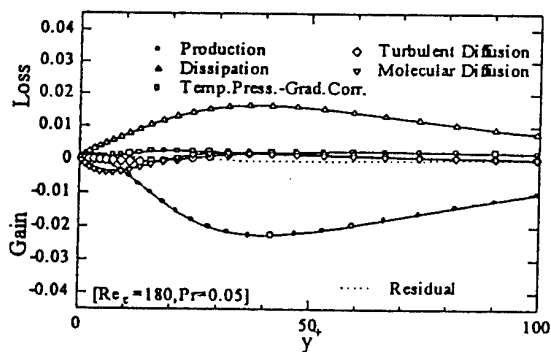


FIG. 7a BUDGET OF THE TRANSPORT EQUATION FOR THE TURBULENT HEAT FLUX ($Pr=0.05$)

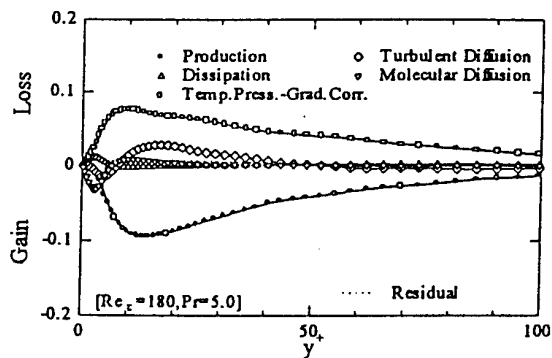


FIG. 7d BUDGET OF THE TRANSPORT EQUATION FOR THE TURBULENT HEAT FLUX ($Pr=5.0$)

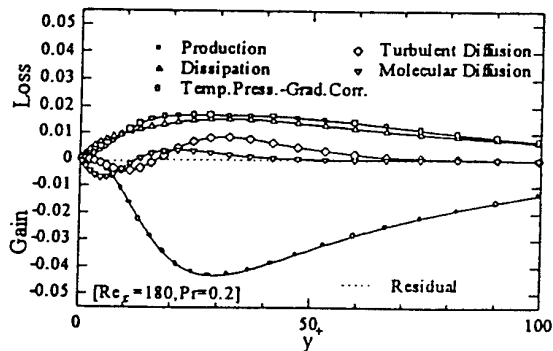


FIG. 7b BUDGET OF THE TRANSPORT EQUATION FOR THE TURBULENT HEAT FLUX ($Pr=0.2$)

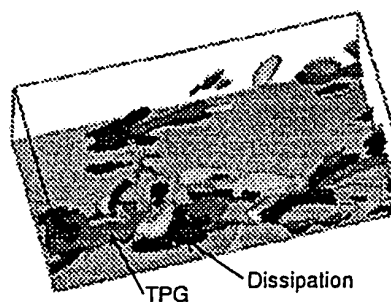


FIG. 8a CONTOUR SURFACES OF BUDGET TERMS OF TURBULENT HEAT FLUX ($Pr=0.05$, WHITE; LOW PRESSURE)

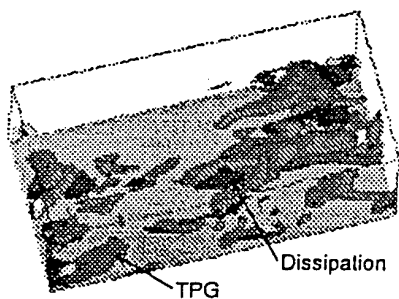


FIG. 8b CONTOUR SURFACES OF BUDGET TERMS OF TURBULENT HEAT FLUX ($Pr=0.2$, WHITE; LOW PRESSURE)

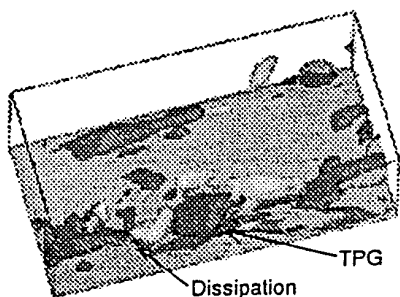


FIG. 8c CONTOUR SURFACES OF BUDGET TERMS OF TURBULENT HEAT FLUX ($Pr=0.4$, WHITE; LOW PRESSURE)

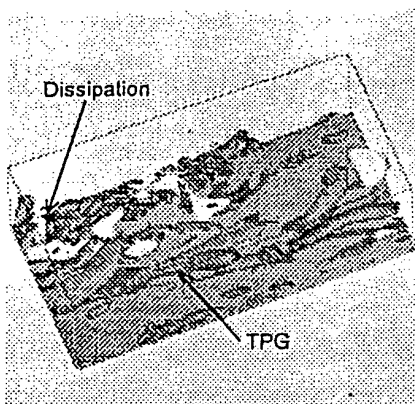


FIG. 8d CONTOUR SURFACES OF BUDGET TERMS OF TURBULENT HEAT FLUX ($Pr=5.0$, WHITE; LOW PRESSURE)

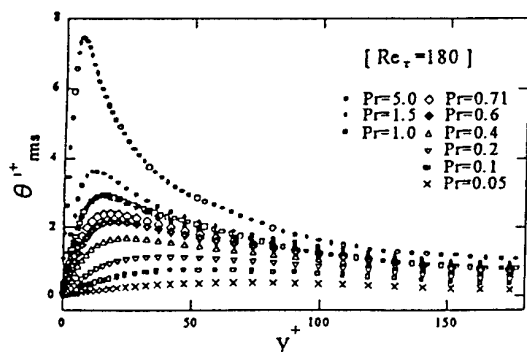


FIG. 9 TEMPERATURE VARIANCE FOR VARIOUS PRANDTL NUMBERS

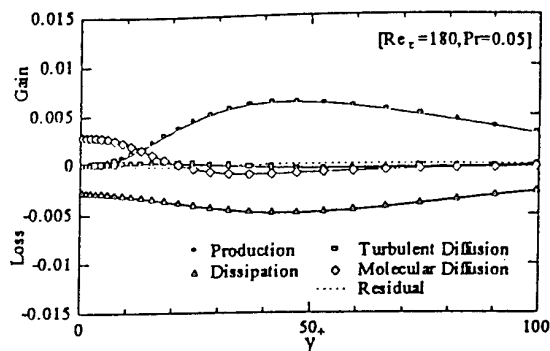


FIG. 10a BUDGET OF THE TRANSPORT EQUATION FOR THE TEMPERATURE VARIANCE ($Pr=0.05$)

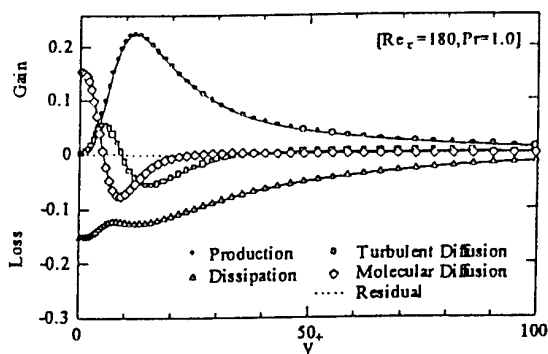


FIG. 10b BUDGET OF THE TRANSPORT EQUATION FOR THE TEMPERATURE VARIANCE ($Pr=1.0$)

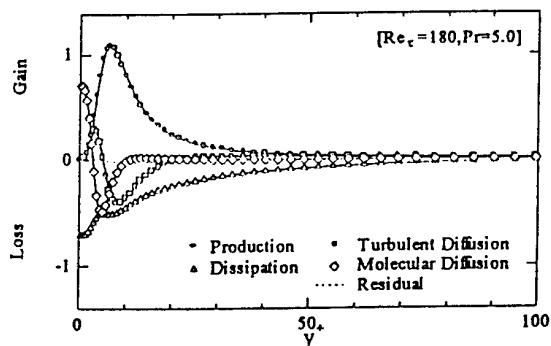


FIG. 10c BUDGET OF THE TRANSPORT EQUATION FOR THE TEMPERATURE VARIANCE ($Pr=5.0$)

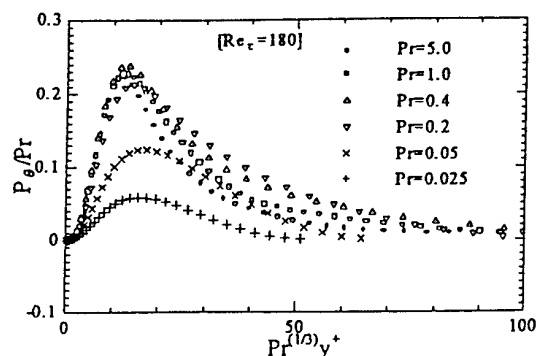


FIG. 11 NORMALIZED PROFILE OF PRODUCTION RATE OF THE TEMPERATURE VARIANCE

TURBULENT HEAT FLUX MEASUREMENTS ON A ROTATING DISK

Christopher J. Elkins and John K. Eaton

Department of Mechanical Engineering

Stanford University

Bldg. 500

Stanford, CA 94305-3030

U.S.A.

ABSTRACT

The vertical mixing of momentum in three-dimensional boundary layers differs significantly from that in two-dimensional boundary layers due to the presence of cross flow. It is hypothesized that the vertical mixing of heat in three-dimensional boundary layers differs as well. To test this hypothesis, the momentum and thermal boundary layers on a rotating disk with a constant heat flux surface have been studied for Reynolds numbers up to 10^6 . Measurements included the surface heat transfer coefficients, mean velocities and temperatures in turbulent and laminar flow, all six Reynolds stresses, turbulent temperature fluctuations, and three turbulent heat fluxes. It appears that the heat flux and momentum are both altered due to the three-dimensionality of the disk flow, but in the outer half of the boundary layer, the transport of momentum is affected more than the transport of heat. This is confirmed by the turbulent Prandtl number, which agrees with 2DBL values low in the outer region but is reduced from the 2DBL values higher in the boundary layer.

INTRODUCTION

The flow on a disk in an otherwise quiescent environment is one of the simplest examples of a three-dimensional turbulent boundary layer (3DTBL). The flow exhibits skewing of the velocity vector across the boundary layer which is the defining characteristic of 3DTBLs, but it is simpler than other 3DTBLs because there is no variation of the turbulence statistics in the tangential direction and the variations in the radial direction are small. The disk flow is thus of interest as both a simple flow for investigating 3DTBL physics and because of its direct relevance to rotating machinery.

Earlier work in our laboratory examined structural features of the disk boundary layer in an effort to explain reduced shear stress levels observed in previous 3DTBL experiments. Littell and Eaton (1991) measured single point and 2 point statistics in an air-flow apparatus and Chiang and Eaton (1993) made a flow visualization study of the near wall structure in a water-flow apparatus. These studies led to the conclusion that gradients in the cross-flow velocity profile render the near-wall structures less

efficient at producing sweeps and bursts, the two events associated with large shear stress production in turbulent boundary layers. The outer layer turbulence was also found to be considerably less coherent than in 2DTBLs with the level of $a_1 = -\overline{u'v'}/q^2$ (q^2 is twice the turbulent kinetic energy) being much lower in the disk flow. These findings led to the prediction that the turbulent heat flux in the disk boundary layer would be lower than might be predicted by conventional models. The objectives of this experiment were to measure all components of the turbulent heat flux and to calculate the turbulent Prandtl number which indicates the relative strengths of turbulent mixing of heat and momentum.

BACKGROUND

A comprehensive review of isothermal 3DBL studies made prior to 1991 can be found in Littell and Eaton (1991). Most of the significant 3D studies made after 1991 are discussed by Johnston and Flack (1996) who review 11 recent 3DTBL experiments. One significant conclusion made by Johnston and Flack is that the stronger the cross stream pressure gradient, the more skewing there is in the inner layer and the larger the reduction in a_1 .

The effect that three-dimensionality has on turbulent heat transport has been investigated in only one experiment by Abrahamson and Eaton (1991) who measured surface heat transfer and mean temperature profiles for the flow around a 60° and a 90° wedge. Their results showed that the increase in spanwise pressure gradient provided by the 90° wedge resulted in a decrease in surface heat transfer suggesting that an increase in the three-dimensionality of the flow adversely affects the turbulent mixing of heat. However, because their measurements did not include turbulent heat fluxes, it is difficult to understand the physical mechanisms for such reductions in the heat transfer.

Heated two-dimensional turbulent boundary layer cases are well-documented in the experiments of Antonia, Danh, and Prabhu (1977), Subramanian and Antonia (1981), Gibson and Veriopoulos (1984), and many others. By comparing the results of the present experiment to the 2DTBL data, the affects of the three-dimensionality may be evaluated.

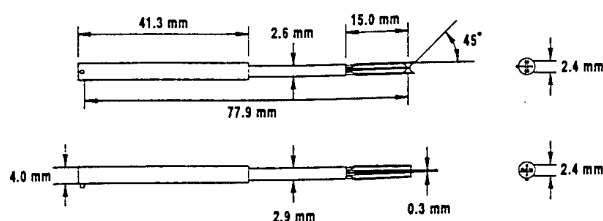


Figure 1: Triple wire heat flux probe used to measure Reynolds stresses and heat fluxes.

EXPERIMENTAL SETUP

The experiment was conducted using a 1 m diameter heated disk rotating in still air. The disk had a composite construction with a 13 mm thick aluminum base disk, a 13 mm thick insulating layer of balsa wood, a thermofilm heater supplying an approximately constant heat flux, and a 1 mm thick layer of stainless steel which served as the surface for the boundary layer. Disk temperatures were measured with type T thermocouples placed on the interior surfaces of the stainless steel and aluminum. The disk was mounted to a steel spindle supported by a steel frame. A 2 hp DC motor rotated the disk up to 1000 rpm giving a maximum $Re_{tip} = 1.6 \times 10^6$. Further details of the rotating disk construction and apparatus may be found in Elkins and Eaton (1994).

Constant temperature thermal anemometers (TSI Model IFA-100) were used to measure velocity, and a custom constant current anemometer was used to measure temperature. A dual 45° probe strung with 5 μm wire was used to measure mean velocity and temperature profiles. This probe consisted of two wires with $l/d = 270$ lying in the same plane parallel to the disk surface but oriented at $\pm 45^\circ$ to the probe axis. A single 1 μm Pt-10%Rh cold wire ($l/d = 900$) was used to measure the mean temperature and turbulent temperature fluctuations. A triple wire heat flux probe shown in Figure 1 was used to measure Reynolds stresses and heat fluxes. This probe consisted of two 2.5 μm hot wires separated by 0.35 mm in a cross wire formation with a 2.5 μm cold wire placed 0.55 mm upstream of the geometric center of the cross wire and perpendicular to the plane of measurement of the cross wire. This probe could be oriented in four different roll positions each separated by 45° in order to measure all six Reynolds stresses.

The probe signals were conditioned with Frequency Devices model 901F1 low-pass 8-pole Butterworth filters with cutoff frequencies of 10 kHz. The signals were sampled using a MSE 386 pc clone and a Metrabyte DAS-20 12 bit A/D board and a SSH-4 simultaneous sample and hold card. The cold wire signals were post-processed to compensate for the frequency response of the probes using a method based on Wroblewski and Eibeck (1990). The signals were compensated up to 3 kHz which was the necessary bandwidth to capture the energy containing fluctuations. This bandwidth was estimated from the power spectrum of the streamwise velocity fluctuations. A complete description of the frequency compensation procedure can be found in Elkins and Eaton (1997).

EXPERIMENTAL PROCEDURE

Profiles were measured at a 0.4 m radius for two different Reynolds numbers: 6.5×10^5 and 10^6 . In each case, two boundary conditions were used. The first boundary condition (BC1) is a constant heat flux surface for $r = 0.08 - 0.48$ m. The second boundary condition (BC2) had a constant heat flux surface over the annular region

from $r = 0.20 - 0.48$ m. The first condition heated the region of the disk with laminar, transitional, and turbulent flow while the second heated only the turbulent region. These two different boundary conditions allowed us to assess the effects that the large transition vortices might have on the heat transfer in the turbulence at higher Re .

For each profile, the disk was run for approximately 1 hour until the surface temperature profiles reached a steady state. For all the boundary layer measurements, the probes were aligned with the local mean flow direction. This was especially important when the heat flux probe was used since it helped reduce cross flow contamination of the velocity signals. The disk boundary layer is unusual because in the lab frame of reference there is high velocity close to the disk and zero velocity far from the disk. This presented many difficulties in measuring the turbulent heat fluxes, one of which was the contamination of the cold wire signal from the hot wire thermal wakes in low velocity regions of the flow. Due to this problem, heat fluxes could only be measured to $y/\delta_2 \approx 6$ corresponding approximately to $y/\delta_{99} \approx 0.6$.

The mean velocities and temperatures measured with the 45° probe were calculated from 4000 samples. The data used to calculate temperature fluctuations and heat fluxes consisted of 100 records 4096 samples long. The data were sampled at 20 kHz for the purposes of compensating the cold wire temperature signal. The uncertainty in the mean velocity is estimated to be 3% and 4% for the mean temperature difference above ambient. Uncertainty in the Reynolds stresses is estimated at 5% for the normal stresses and 10% for the shear stresses. Uncertainty in $\overline{\theta'^2}$ measured with the 1 μm cold wire is 5%. Finally, the uncertainty in the heat fluxes is 6% and is due mainly to uncertainty in the compensation process.

RESULTS AND DISCUSSION

The results are presented in the disk frame of reference. For convenience in comparing these results with results from other studies, the cylindrical coordinates and velocities are redefined in terms of Cartesian coordinates and velocities. The frame of reference is right-handed and has its origin at the measurement radius. The $+y$ direction is vertically upward, the $+x$ coordinate is in the tangential direction, and the $+z$ coordinate is in the radial direction pointing at the axis of rotation. The velocities v, u, w correspond to these coordinates, respectively.

In the lab frame, the velocity at the edge of the boundary layer is zero which makes it difficult to measure a height at which the velocity is 1% of the disk speed. This height is the equivalent of δ_{99} . An alternative boundary layer length scale is provided by the momentum thickness based on the velocity vector magnitude denoted by δ_2 . This can be determined with better certainty in the disk flow and will be used to normalize most of the results that follow.

The laminar boundary layer on a rotating disk has an analytic solution that provides a convenient way of testing instrumentation and measurement techniques. The mean velocity, flow angle, and temperature measured with the 45° probe at $Re = 1.5 \times 10^5$ agreed well with the analytic solution validating our methods in the heated flow.

Profiles for the mean velocity vector magnitude in wall coordinates for $Re = 6.5 \times 10^5$ and 10^6 are shown in Figure 2. Littell showed that with an appropriate choice of skin friction coefficient, the mean total velocity was fit by the conventional log-law with constants $\kappa = 0.41$ and $C = 5.0$. The present results compare well with those of Littell and Eaton (1991) for similar values of u_τ for both Reynolds numbers. The radial velocities and mean flow angles also compared well with earlier results indicating that heating the flow did not alter the velocity field of the boundary layer. One noteworthy characteristic of the mean velocity

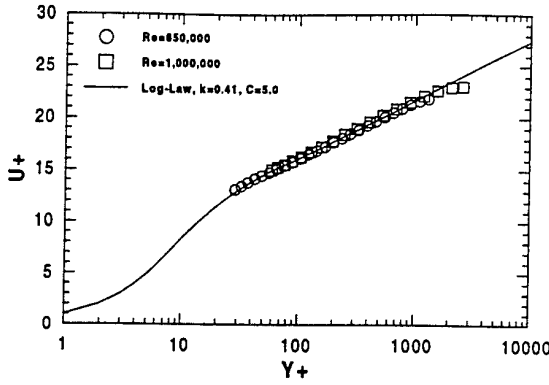


Figure 2: Mean total velocity in the rotating frame plotted in wall coordinates for turbulent flow with $Re = 6.5 \times 10^5$ and 10^6 .

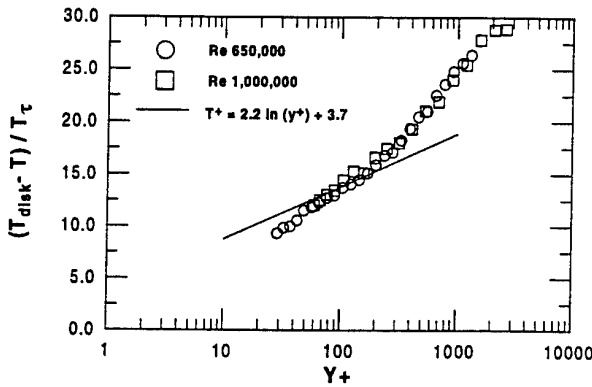


Figure 3: Mean temperature difference measured with the $5 \mu\text{m}$ dia. cold wire plotted in wall coordinates for $Re = 6.5 \times 10^5$ and 10^6 with BC1.

profiles is the lack of a wake profile.

Figure 3 shows the mean temperature profiles measured with the $5 \mu\text{m}$ cold wire for both Reynolds numbers and BC1. For comparison, the standard thermal log-law from Kays and Crawford (1980) is also shown. The log-law constants recommended by Kays and Crawford for the flat plate thermal boundary layer are $\kappa_\theta = 0.46$ and $C_\theta = 3.6$. While the present data and the thermal log-law intersect around $y^+ = 100$, the overall agreement between the data and the log-law is poor. Note that there is a wake profile in the temperature measurements but the velocity profile showed no wake profile. This is an indication that in the outer layer, the boundary layer dynamics are different for momentum and passive scalars such as temperature. From the results of measurements with BC2, we also observed that the upstream thermal boundary condition has a strong effect on the temperature profile in wall coordinates. The scaling for T^+ , which utilizes the wall heat flux, should remove the differences between the cases with BC1 and BC2, but it does not. For the heated disk boundary layer, we see that the scaling behind the thermal law of the wall can not account for upstream history effects.

In Figure 4, the three normal Reynolds stresses are shown for both boundary conditions at $Re = 10^6$. The results at the lower Reynolds number are similar, and these measurements agree well with those from Littell and Eaton except that $\overline{u'^2}$ is 5% lower. Figure 5 compares the present experiment results for $-\overline{u'v'}$ to the results from Littell and Eaton. The agreement is good and the same is true for the

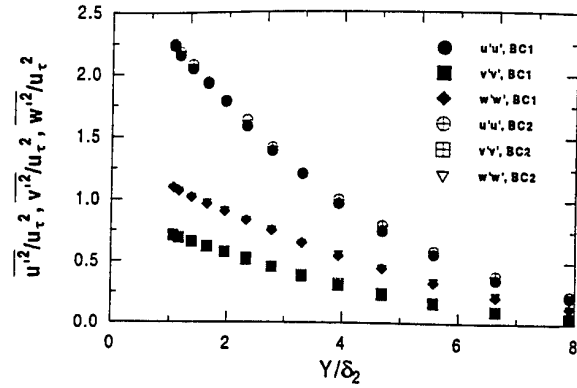


Figure 4: Normal Reynolds stresses for $Re = 10^6$ and BC1 and BC2.

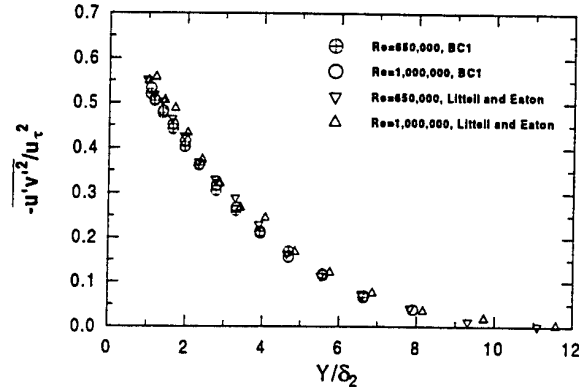


Figure 5: Reynolds shear stress $-\overline{u'v'}$ for $Re = 6.5 \times 10^5$ and 10^6 and BC1 compared to results from Littell and Eaton (1991).

other two shear stress components $-\overline{v'w'}$ and $\overline{u'w'}$. The primary shear stress component, $-\overline{u'v'}$ differs significantly from its values in 2DTBLs. Subramanian and Antonia (1981) show $-\overline{u'v'}/u_\tau^2$ nearly constant and equal to 1 at $y/\delta_2 \approx 1$. In Figure 5, the value of $-\overline{u'v'}/u_\tau^2$ is only 0.5 at $y/\delta_2 = 1$. This is a strong indication that the mixing of momentum in the disk boundary layer is different than it is in 2DTBLs. Nearly the same results are obtained if one considers the wall-parallel shear stress magnitude since values for $-\overline{v'w'}$ are small.

Figure 6 shows the $\sqrt{\theta'^2}$ data normalized by the friction temperature taken with the $1 \mu\text{m}$ cold wire for both Reynolds numbers and boundary conditions. In the disk boundary layer, the turbulent temperature fluctuations start high close to the disk, then decrease slightly and rise to a broad peak in the outer layer. Temperature fluctuation profiles in 2DBLs at high Reynolds number have a plateau in the outer layer, but do not show a peak. This figure also shows peakier profiles occur for the two Reynolds numbers with BC1. Note that these profiles are very different from what is observed in 2DTBLs due to the presence of the broad outer layer peak. Figure 6 shows that the temperature fluctuations are a strong function of boundary condition. The close agreement between the BC1 cases suggests that the highly peaked θ' profile is independent of Reynolds number.

Figure 7 shows the turbulent heat flux measurements for $Re = 10^6$ and both thermal boundary conditions. The results for the lower Reynolds number were similar. A signif-

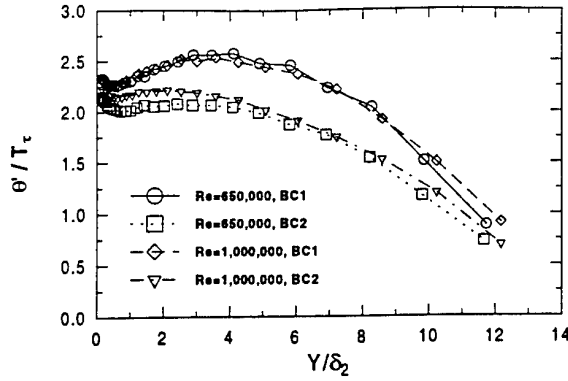


Figure 6: 1 μm cold wire results for $\sqrt{\theta'^2}$ for all cases.

ificant difference between these measurements and 2DTBLs is the existence of the cross stream heat flux $-\overline{w'\theta'}$ which is zero for 2DBLs.

The profiles for $\overline{v'\theta'}$ and $-\overline{w'\theta'}$ with BC1 cross around $y/\delta_2 = 2 - 3$ while the two profiles with BC2 cross at a slightly higher value for y/δ_2 and agree more closely. The similarity between values for $\overline{v'\theta'}$ and $-\overline{w'\theta'}$ indicates that the vertical and radial turbulent transport of heat are both important in the outer layer.

The values of several correlation coefficients and structural parameters were calculated for comparison to two-dimensional boundary layer flows. The behavior of these parameters is so consistent in simple boundary layers that they are widely used in turbulence models. However, there is no direct evidence that the same parameters can be used in 3DTBLs.

Figure 8 shows the ratio of the wall-parallel normal stresses to the vertical normal stress,

$$\frac{\overline{u'^2} + \overline{w'^2}}{\overline{v'^2}}$$

The results from the heated disk boundary layer agree well with the measurements of Littell and Eaton. Note that the wall-parallel stress is defined for a 3DBL as the magnitude of the wall-parallel stress vector. The behavior of this ratio is very different from its behavior in 2DTBLs and other 3DTBLs in which the ratio starts high, typically between 5 and 7, and monotonically decreases to around 2 at the outer edge of the boundary layer. In isotropic flow, this parameter has a value of 2. In the disk flow, the parameter starts between 4 and 5 and increases before peaking in the outer layer. Figure 8 shows that the vertical motion is strong close to the disk but decreases relative to the streamwise motion in the outer part of the flow.

The correlation coefficients $R_{u\theta}$ and $R_{v\theta}$ reported in 2D studies take on the following definitions in the 3D disk flow:

$$R_{u\theta} = \frac{\sqrt{\overline{u'\theta'^2} + \overline{w'\theta'^2}}}{\theta' \sqrt{\overline{u'^2} + \overline{w'^2}}}$$

and

$$R_{v\theta} = \frac{\overline{v'\theta'}}{\theta' (\overline{v'^2})^{1/2}}$$

In studies of 2DTBLs such as Subramanian and Antonia (1981) and Wroblewski and Eibeck (1990), $R_{u\theta}$ is normally constant and between 0.6 and 0.8 while $R_{v\theta}$ is constant as well and approximately 0.40-0.45. Figure 9 contains the results from both Reynolds numbers and thermal boundary conditions. The plots show there is a region where

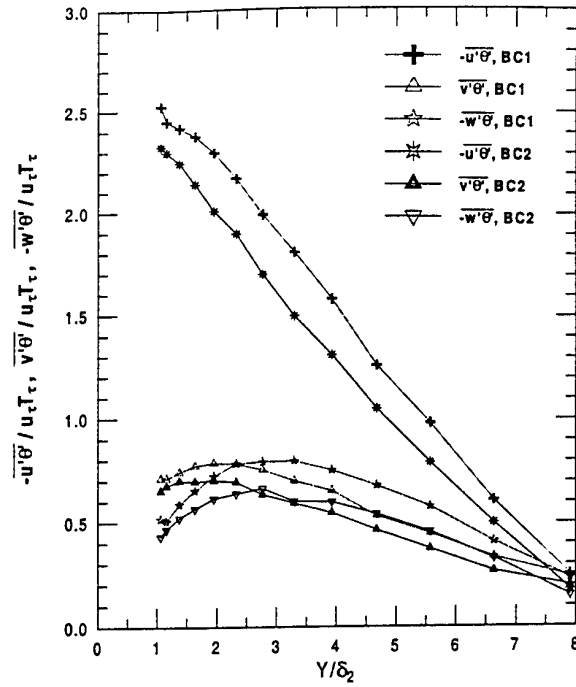


Figure 7: The turbulent heat fluxes $-\overline{u'\theta'}$, $\overline{v'\theta'}$, and $-\overline{w'\theta'}$ for $Re = 10^6$ and BC1 and BC2.

$R_{u\theta} \approx 0.5$ below $y/\delta_2 \approx 4$ but then the profiles decrease significantly with y . This decrease above $y/\delta_2 = 4$ corresponds to the increase in $\overline{u'^2} + \overline{w'^2}$ shown in Figure 8. The significantly low values for $R_{u\theta}$ which are only 0.5 instead of 0.7-0.8 indicate the turbulent transport of heat is low for the level of velocity and temperature fluctuations in the turbulence.

Figure 10 shows the values for $R_{v\theta}$ which are small close to the disk but monotonically rise to a constant value between 0.4-0.45 in agreement with the 2DBL value. Again, the small values below $y/\delta_2 = 4$ are surprising because of the strength of the vertical fluctuations indicated in Figure 8 and the large temperature fluctuations evident in Figure 6. This is another testament to the fact that although there is significant turbulence in the boundary layer, the structures do not seem to be transporting heat at the same rate as analogous structures in 2DBLs.

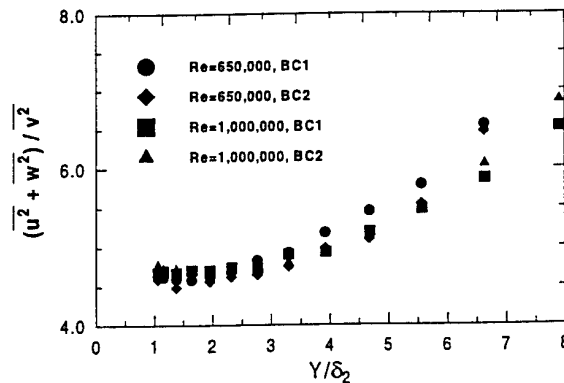


Figure 8: The structure parameter $\frac{\overline{u'^2} + \overline{w'^2}}{\overline{v'^2}}$ for all cases.

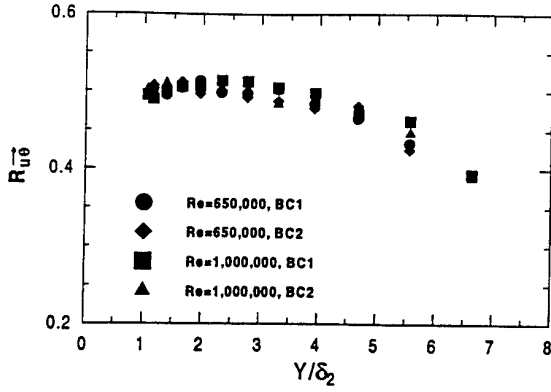


Figure 9: The correlation coefficient $R_{u\theta}$ for all cases.

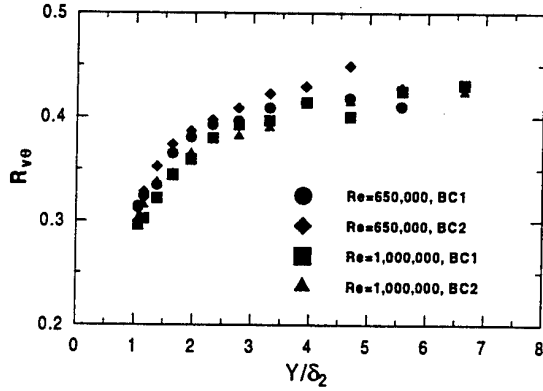


Figure 10: The correlation coefficient $R_{v\theta}$ for all cases.

Two other parameters similar to $R_{v\theta}$ are A_θ and $A_{1\theta}$ defined, respectively, as

$$A_\theta = \frac{\overline{v'\theta'}}{\theta' (k^2)^{1/2}}$$

and

$$A_{1\theta} = \frac{\overline{v'\theta'}}{\theta' (\overline{u'u'^2} + \overline{v'v'^2})^{1/4}}$$

The behavior of these parameters is similar to that of $R_{v\theta}$. In the constant region above $y/\delta_2 = 4$, A_θ is slightly lower than the constant value of 0.22 observed across 2D boundary layers, and $A_{1\theta}$ has a constant value between 0.45-0.5 which agrees well with the 2D values. The agreement between the constant values for the parameters $R_{v\theta}$, A_θ , and $A_{1\theta}$ with the values measured in 2DTBLs indicate that normalizing the vertical heat flux by v' or the wall-parallel shear stress works well in generalizing parameters for 2DBLs and the outer region in the disk boundary layer, but using k^2 or other quantities containing u' and w' does not work.

An important parameter used in calculating thermal boundary layers is the turbulent Prandtl number which is defined as the ratio of the eddy diffusivity for momentum to the eddy diffusivity for heat, or

$$Pr_t = \frac{\varepsilon_M}{\varepsilon_H} = \frac{\frac{-\overline{u'v'}}{\partial \overline{U}/\partial y}}{\frac{\overline{v'\theta'}}{\partial \overline{T}/\partial y}}$$

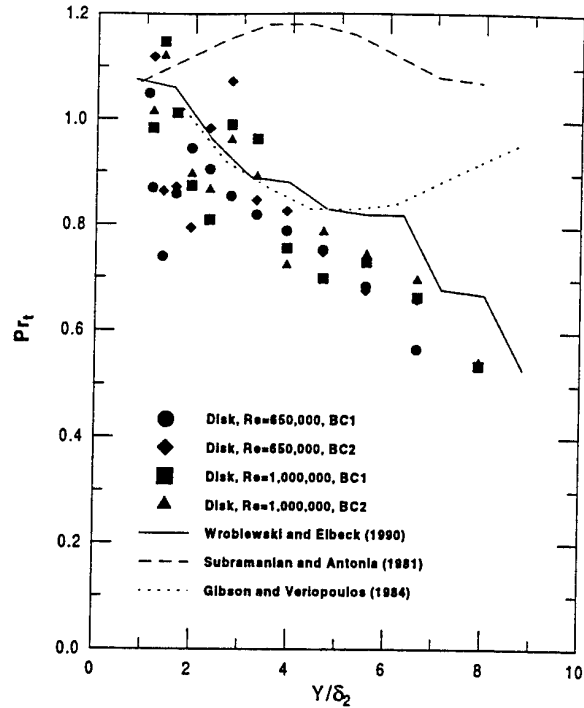


Figure 11: The turbulent Prandtl number (Pr_t) for all cases compared to results from several 2DBL studies.

The turbulent Prandtl number represents the relative effectiveness of the turbulent transport of momentum to the transport of heat and is typically assumed to be 1 in accordance with the Reynolds analogy. Many 2DBL studies have observed Pr_t to start slightly above 1 around $y/\delta_2 = 1$ and either stay constant or slowly decrease to 0.8 at the edge of the boundary layer. The results of the present study and three 2DTBL studies are shown in Figure 11. The values for Pr_t in other flows such as the disk flow are not well known, but are important for modelers who calculate ε_H from Pr_t and ε_M . For instance, Ong and Owen (1991) assumed $Pr_t = 0.9$ in their calculation of the turbulent disk flow. The measurements shown in Figure 11 indicate that 0.9 may not be a bad value for $y/\delta_2 < 4$, but over most of the outer layer this value is too high. The measurements also show that setting Pr_t to a constant value is not realistic.

One of the objectives of this experiment was to evaluate the amount of change in turbulent heat fluxes relative to the previously observed reduction in turbulent shear stress in 3DTBLs. The turbulent Prandtl number allows for the direct evaluation of the relative effects that the three dimensionality has on the turbulent heat flux. Since Pr_t in the disk flow is slightly lower than the measurements of Wroblewski and even smaller than the other measurements made in 2DBLs, the results indicate that the diffusivity for momentum is reduced slightly more than the diffusivity for heat. This indicates that the turbulent mixing of momentum is suppressed slightly more than the mixing of heat in the disk boundary layer.

CONCLUSIONS

The significant conclusions from this experiment are summarized as follows:

- The mean temperature profile contains a wake profile while the mean velocity profile does not. This indicates a difference between the transport of heat and

momentum in the outer layer of the disk boundary layer. It also indicates a major difference from 2D flat plate boundary layers. Moreover, the mean temperature profiles in wall coordinates differed from the 2D thermal log law and showed a strong dependence on the flow type, flow history, and the boundary condition.

- The turbulent temperature fluctuation profiles have a broad peak throughout the outer layer of the boundary layer. This is very different from what is observed in 2DBLs and indicates a fundamental difference in the process by which passive scalars are transported by the turbulence. The peak was shown to be related to a decrease in the turbulent diffusion term in the transport equation for θ'^2 .
- The correlation coefficients, $R_{v\theta}$ and $R_{u\theta}$, and structure parameters, A_θ and $A_{1\theta}$, related to the turbulent heat fluxes showed both similarities and differences compared to the quantities typically found in 2DT-BLs. These quantities are typically constant across the boundary layer, but in the disk flow, these parameters were not constant across the whole layer. $R_{u\theta}$ was constant below $y/\delta_2 = 3$ but decreased with y above that point. $R_{v\theta}$, A_θ , and $A_{1\theta}$ started low, increased with y up to $y/\delta_2 = 3$, and then became constant. Moreover, the constant values for these parameters were smaller than the 2DBL values. The basic reduction in the values for these quantities indicates that the correlated behavior between the temperature and velocity results in a lower net vertical transport of heat in the disk boundary layer compared to 2DBLs. This confirms our hypothesis that the turbulent transport of heat is adversely affected in the three-dimensional disk flow.
- The turbulent Prandtl number calculated directly from the heat flux probe measurements showed fairly close agreement with the 2D flat plate boundary layer results from Wroblewski (1990) below $y/\delta_2 = 3$. Above this height Pr_t is slightly lower than the 2D level and becomes increasingly lower with distance from the disk. Since the turbulent Prandtl number indicates the ratio of the strength of the turbulent mixing of momentum to that of heat, the slightly low value for Pr_t above $y/\delta_2 = 3$ suggests that the three-dimensionality of the disk flow affects the momentum transport process more than the heat transport process.

ACKNOWLEDGMENTS

We gratefully acknowledge support from the Department of Energy Division of Basic Energy Sciences under grant number DEFG0393ER14317. The first author also thanks the Air Force Office of Scientific Research for support from a Graduate Laboratory Fellowship.

REFERENCES

- Abrahamson, S., and Eaton, J. K., 1991, "Heat Transfer Through a Pressure-Driven Three-Dimensional Boundary Layer," *J. Heat Transfer*, Vol. 113, pp. 355-362.
- Antonia, R. A., Danh, H. Q., and Prabhu, A., 1977, "Response of a Turbulent Boundary Layer to a Step Change in Surface Heat Flux," *J. Fluid Mech.*, Vol. 80, pp. 153-177.
- Chiang, C., and Eaton, J. K., 1993, "An Experimental Investigation of Corotating Disks and Single Disk Flow Structures," Thermosciences Division Report MD-62, Department of Mechanical Engineering, Stanford University, Stanford, CA.
- Elkins, C. J., and Eaton, J. K., 1994, "Heat Transfer Measurements in the Boundary Layer on a Rotating Disk," ASME HTD-Vol. 271, pp. 193-200.
- Elkins, C. J., and Eaton, J. K., 1997, "Heat Transfer in the Rotating Disk Boundary Layer," Thermosciences Division Report TSD-103, Department of Mechanical Engineering, Stanford University, Stanford, CA.
- Gibson, M. M., and Verriopoulos, C. A., 1984, "Turbulent Boundary Layer on a Mildly Curved Surface: Part 2: Temperature Field Measurements," *Exp. Fluids*, Vol. 2, pp. 73-80.
- Johnston, J. P., and Flack, K. A., 1996, "Advances in Three-Dimensional Turbulent Boundary Layers with Emphasis on the Wall-Layer Regions," *J. Fluids Engr.*, Vol. 118, p. 219.
- Kays, W. M., and Crawford, M. E., 1980, *Convective Heat and Mass Transfer*, McGraw-Hill, New York.
- Littell, H. S., and Eaton, J. K., 1991, "An Experimental Investigation of the Three-Dimensional Boundary Layer on a Rotating Disk," Thermosciences Division Report MD-60, Department of Mechanical Engineering, Stanford University, Stanford, CA.
- Ong, C. L., and Owen, J. M., 1991, "Computation of the Flow and Heat Transfer Due to a Rotating Disc," *Int. J. Heat and Fluid Flow*, Vol. 12, pp. 106-115.
- Subramanian, C. S., and Antonia, R. A., 1981, "Effect of Reynolds Number on a Slightly Heated Turbulent Boundary Layer," *Int. J. Heat Mass Transfer*, Vol. 24, no. 11, pp. 1833-1846.
- Wroblewski, D. E., and Eibeck, P. A., 1990, "An Experimental Investigation of Turbulent Heat Transport in a Boundary Layer with an Embedded Streamwise Vortex," Ph.D. Thesis, Mechanical Engineering Department, University of California at Berkeley, Berkeley, CA.

JOINT SCALAR - SCALAR DISSIPATION MEASUREMENTS AT THE EXIT OF A TURBULENT JET

Katerina Sardi and Alexander M. K. P. Taylor
Mechanical Engineering Department
Imperial College of Science, Technology and Medicine
Exhibition Road
London SW7 2BX
United Kingdom

ABSTRACT

Cold wire measurements of a passive scalar, temperature, its fluctuations and the radial component of the scalar dissipation at five axial locations within the first two diameters downstream the exit plane of a slightly heated turbulent jet are reported and the correlation between the scalar fluctuations and their dissipation is examined. It is shown that in the first diameter downstream the exit plane, the scalar fluctuations and their dissipation were strongly correlated with their correlation coefficient varying from unity at the edges of the mixing layer to approximately -0.3 within the half width of the mixing layer. At larger axial distances, the correlation coefficient at the edges of the mixing layer progressively decreased and achieved the value of 0.5 at two diameters from the jet exit, suggesting that the assumption of statistical independence between the scalar fluctuations and their dissipation was better satisfied with increasing distance from the exit plane. The distribution of the mean scalar dissipation conditional on the scalar fluctuations was \cap -shaped with the maximum corresponding to almost zero or small values of the scalar fluctuations and decreasing towards the larger fluctuations from the colder or hotter side of the mixing layer. The measurements revealed that the mean conditional dissipation can be an order of magnitude larger than the respective unconditional value but that the difference decreased with increasing distance from the exit plane.

INTRODUCTION

Information on the extinction of turbulent jet diffusion flames may contribute to the design of stable operation of practical combustors. In the context of flame extinction modelling, a number of theoretical approaches have been introduced and these include the laminar flamelet formulation of Peters (1983), the Quasi-Equilibrium Distributed Reaction theory of Bilger (1988), the Conditional Moment Closure of Klimenko (1990) and Bilger (1991) and the use of pdf transport equations by Pope (1983). A common feature of all approaches is the

requirement for a detailed description of the conditional statistics of the scalar dissipation, that is the joint probability of the fuel mixture fraction and the scalar dissipation and also of the mean scalar dissipation *conditional* on the stoichiometric fuel mixture fraction.

Measurements of the structure of a passive scalar and its dissipation has been acquired in non-combusting jets in terms of temperature in the presence of non-combusting flows by a cold wire technique. Several publications report measurements of a scalar and its dissipation in non-reacting jets, but conditional scalar dissipation statistics are reported in few only cases, Anselmet & Antonia (1985), Kailasnath *et al.* (1993), Anselmet *et al.* (1994), Mi *et al.* (1995), and these refer to the far-downstream self-preserving region and are confined either to the jet axis, which is almost always far from the reaction zone, or at only a few selected off-axis locations which cannot provide a complete description of the mixing layer.

In this work, scalar dissipation has been measured at locations which are usually critical to flame stability, namely the first two diameters downstream the exit of a to provide new measurements of the statistical relationship between the scalar fluctuations and their dissipation and on the evolution of the mean conditional scalar dissipation as a function of mixture fraction.

EXPERIMENTAL ARRANGEMENT

The flow configuration comprised a 90 mm long contoured nozzle with area contraction ratio 9 followed by a 50 mm straight section of 30 mm diameter, d . To enhance turbulence, a perforated plate of 4mm hole diameter and 45% solidity was fitted upstream the straight section of the nozzle. The jet was heated to $25 \pm 1^\circ\text{C}$ above ambient, and the mean temperature distribution, measured with a single cold wire of $1\mu\text{m}$ in diameter and 0.4 mm long, was uniform to $\pm 2\%$ and the r.m.s. of the temperature fluctuations at the exit plane was less than 0.05 % of the mean value at the centreline, as shown in figure 1.

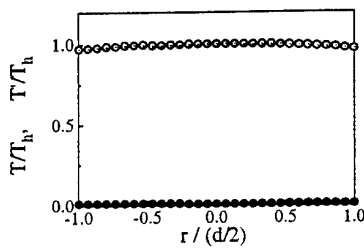


FIGURE 1: RADIAL PROFILES OF THE MEAN (OPEN CIRCLES) AND R.M.S. (BLOCKED CIRCLES) TEMPERATURE AT THE JET EXIT

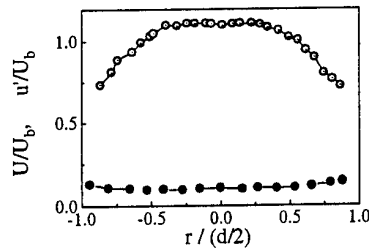


FIGURE 2: RADIAL PROFILES OF THE MEAN (OPEN CIRCLES) AND R.M.S. (BLOCKED CIRCLES) AXIAL VELOCITY COMPONENT AT THE JET EXIT.

The jet bulk velocity, U_b , was 4.1 m/s, metered by a calibrated sonic nozzle, and the mean and r.m.s. profiles of the axial velocity component at the exit plane, measured with a tungsten hot wire probe (DANTEC 55P11) connected to a bridge (DISA 55M10) and operating with an overheat ratio of 1.8, are shown in figure 2. It can be seen that the mean velocity profiles were flat for more than 45% of the nozzle radius and that the normalised r.m.s. of the axial turbulent fluctuations, u'/U_b , was 0.11. The integral length scale, L_t , at the jet exit can be taken as equal to 70% of the hole diameter of the perforated plate, as has been measured by Cho *et al.* (1988) and Kostiuk (1991). The turbulent Reynolds number, R_t , based on the integral length scale and the axial velocity fluctuations was equal to 73, the large eddy turn over time, $t_w = L_t/u'$, was about 7.2 ms and the Kolmogorov microscale was estimated to be of the order of 0.13 mm.

Parallel, fully etched, platinum cold wires (AUSPEX, Pennsylvania, USA, Dantec Compatible, A55P71) and a custom-built constant current circuit were used to measure the instantaneous passive scalar statistics considered in terms of a mixture fraction $\Theta = (T - T_c)/(T_h - T_c)$ deduced from the instantaneous temperature, T , the temperature, T_h , at the centreline of the heated jet and the temperature, T_c , of the cold ambient air. The passive scalar fluctuations, θ , from the mean scalar value were also measured as well as the radial component of their dissipation, $\chi_r = 2D_t(\partial\theta/\partial r)^2$, where D_t is the air thermal diffusivity assumed constant and equal to $2.2 \cdot 10^{-5} \text{ m}^2/\text{s}$. The cold wire prongs were tapered to a tip diameter of $75 \mu\text{m}$ and the sensors were $0.5 \mu\text{m}$ in diameter and 0.6 mm long resulting to a maximum wire length to diameter ratio, L_w/d_w , of 1200, and to a wire length to Kolmogorov length scale ratio, L_w/λ_k , of 4.6. The uncertainty in the measurements of the

scalar and the dissipation, due to end conduction effects and the influence of the thermal boundary layer created on the prongs, was estimated to be of the order of 15%, Parathoen *et al.* (1982), Tsuji *et al.* (1993), while the spatial attenuation was of the order of 20%, Wyngaard (1971a). The separation between the two parallel sensors was fixed at 0.3 mm and was selected, Sardi (1997), after measuring the radial squared gradient of the temperature fluctuations at each point along the centreline by parallel probes of spacing in the range of 0.2-0.4 mm, according to the procedure proposed by Anselmet *et al.* (1994). The time constant of the sensors in the vicinity of the stagnation plane, evaluated from the relation proposed by Collis & Williams (1959), was $20 \mu\text{s}$ resulting in a cut-off frequency of 8 kHz, approximately a factor of two higher than the estimated Kolmogorov frequency of 4.7 kHz and so that no compensation was required.

The constant current circuit comprised two, nominally identical, electronic circuits, one for each sensor of the twin probe. In each circuit, a constant voltage power supply drove a constant current chip providing 0.1 mA constant to $\pm 0.5 \mu\text{A}$, so that the velocity sensitivity of the sensors was of the order of 1%, Wyngaard (1971b). The signal was amplified and offset to increase the resolution and was interfaced to an Personal Computer (INTEL 486, 33 MHz) by a 16-bit A/D card (ANALOGIC HSDAS). The sampling rate was 8 kHz and 2^{18} samples were obtained at each point so as to ensure statistical convergence for the unconditional and the conditional values of the scalar dissipation.

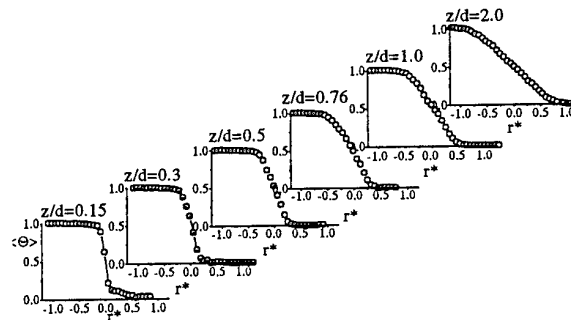


FIGURE 3: MEAN SCALAR RADIAL DISTRIBUTION.

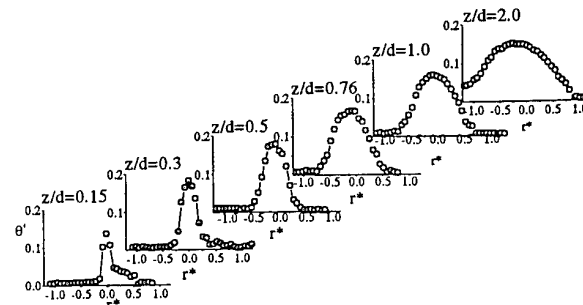


FIGURE 4: R.M.S. SCALAR RADIAL DISTRIBUTION.

RESULTS AND DISCUSSION

The measurements revealed that the radial distribution of the mean normalised temperature, $\langle\Theta\rangle$, can be approximated by an error function, with zero and unity at the cold and hot boundaries as shown in figure 3, in which the radial distance from the centreline has been normalised as $r^* = (r - r_d)/(r_d/2)$, where r_d corresponds to a mean scalar value of 0.5. Thus r^*

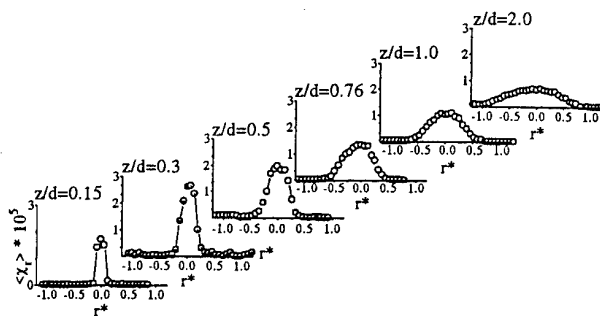


FIGURE 5: RADIAL DISTRIBUTION OF THE MEAN RADIAL SCALAR DISSIPATION COMPONENT.

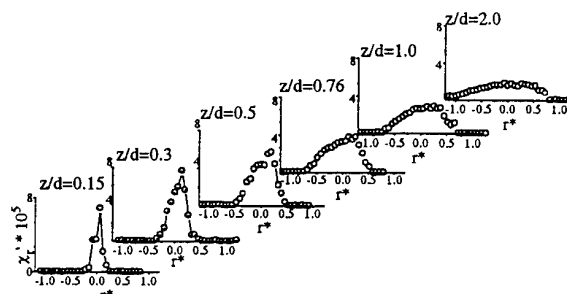


FIGURE 6: RADIAL DISTRIBUTION OF THE R.M.S. RADIAL SCALAR DISSIPATION COMPONENT.

ranges from -1.0 to 1.0 in the region of interest. The r.m.s. of the scalar fluctuations, θ' , achieved their maximum value at the mean scalar value of 0.5 as shown in figures 4. As it can be seen from figures 3 and 4, the width of the mixing layer between the cold and the heated fluid increased with distance downstream of the jet exit.

The distributions of the radial mean, $\langle \chi_r \rangle$, and r.m.s., χ'_r , scalar dissipation components are shown in figures 5 and 6 and are largest at $\langle \Theta \rangle = 0.5$ with maximum values that decrease as the distance from the jet increased, since the increase in the width of the mixing layer resulted in smoothening of the scalar gradients.

In order to ensure mathematical tractability in CFD approaches, it is common to assume that the scalar fluctuations and their dissipation are statistically independent so that the mean scalar dissipation conditional on the stoichiometric fuel mixture fraction may be estimated as equal to the unconditional mean, Bilger (1980). Figure 7 shows that in the first half diameter downstream the nozzle exit, the correlation coefficient, ρ_{θ, χ_r} , between scalar fluctuations and the radial component of their dissipation, defined as

$$\rho_{\theta, \chi_r} = \frac{\langle \theta^2 (\chi_r - \langle \chi_r \rangle) \rangle}{\theta'^2 \chi'_r} \quad (1)$$

varied from unity at the edges of the mixing layer (i.e. $r^* = \pm 0.5$) to approximately -0.3 at $r^* = 0$ implying that scalar fluctuations and scalar dissipation are *not* statistically independent but on the contrary they can - at the edges of the mixing layer - be perfectly correlated. At larger axial distances, the correlation coefficient at the boundaries of the mixing layer progressively decreased to a maximum value of

about 0.5 at two diameters downstream the jet exit suggesting that statistical independence is approached as the distance from the jet exit increases. This is in accord with the measurements of Anselmet *et al.* (1994) and Mi *et al.* (1996) in the self preserving region of square and round jets who report values of the correlation coefficient as low as 0.04. The absence of statistical independence between the scalar fluctuations and their dissipation in the vicinity of the exit of a turbulent jet can be related to the fact that the flow is rapidly distorted, with the residence time in the mixing layer being smaller than the eddy turn over time, so that there is not enough time for the 'cascade process' to propagate down to the smallest eddies, Anand & Pope (1988), Hunt & Garruthers (1990). Hence small scale variables such as the scalar dissipation can be locally determined by the large energy containing scales. The distribution of the correlation coefficient within the first diameter downstream the exit plane is similar to that measured by Sardi *et al.* (1997) along the centreline between two opposed jets where one jet was slightly heated and where it was reported that ρ_{θ, χ_r} varied from unity at the edges of the mixing layer to a negative value at the stagnation plane. The opposed jets flow was also shown to be rapidly distorted, so that the scalar turbulence was 'young', and this provides further experimental evidence that the statistical dependence of the scalar dissipation on the scalar fluctuations can be attributed to short residence times within the scalar interface.

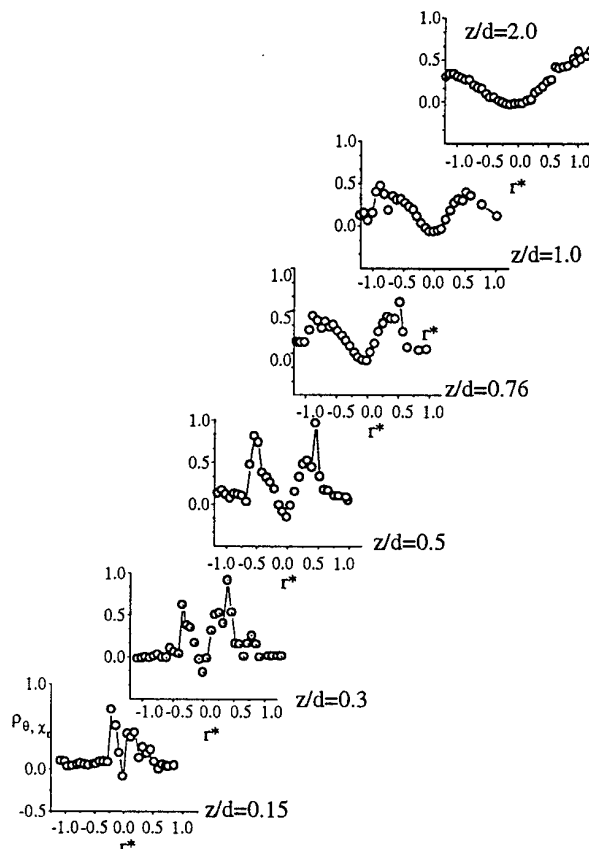


FIGURE 7: CORRELATION COEFFICIENT OF THE SCALAR FLUCTUATIONS AND THE RADIAL COMPONENT OF THEIR DISSIPATION.

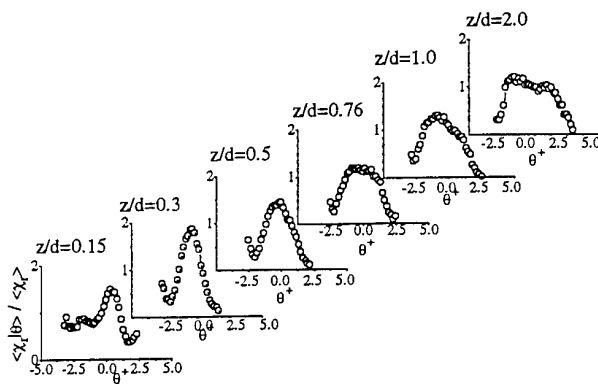


FIGURE 8: AXIAL DISTRIBUTION OF THE MEAN CONDITIONAL SCALAR DISSIPATION AT $\langle \Theta \rangle = 0.5$.

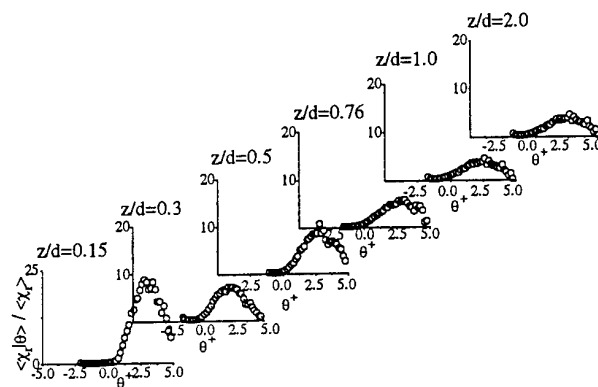


FIGURE 9: AXIAL DISTRIBUTION OF THE MEAN CONDITIONAL SCALAR DISSIPATION AT $\langle \Theta \rangle = 0.3$.

This finding is also supported by the direct numerical simulations of Eswaran and Pope (1988) who show that statistical independence between an initially binary scalar and the dissipation rate of its fluctuations is reached in stationary, homogeneous and isotropic turbulence when the time from the release of the scalar becomes asymptotically large.

The implications of this finding in the modelling of turbulent combustion and flame extinction can be quantified by estimating the mean conditional dissipation and comparing it to the unconditional mean. This is particularly true if combustion takes place in the flamelet regime, Peters (1983, 1984), where the flame thickness is assumed to be of the order of the Kolmogorov microscale so that the residence times in the mixing layer are short and the scalar fluctuations and their dissipation are likely to be statistically dependent. Figures 8 and 9 present the distributions of the mean radial scalar dissipation, $\langle \chi_r | \theta \rangle$, conditional on the scalar fluctuations,

$$\langle \chi_r | \theta \rangle = \frac{1}{N_{st}} \sum_{i=1}^{N_{st}} (\chi_r | \theta)_i \quad (2)$$

evaluated at five axial locations downstream the jet exit and corresponding to mean scalar values of $\langle \Theta \rangle \approx 0.5$ and $\langle \Theta \rangle \approx 0.3$. In equation (2), N_{st} is the number of scalar dissipation samples, $(\chi_r | \theta)_i$, conditional on a particular value of the scalar fluctuations, θ , and estimated for a bin width of $\pm 5\%$ of θ resulting in a statistical uncertainty in the value of the mean

conditional dissipation of less than 5%, Girimett & Stirzaker (1992). In all graphs of figures 8 and 9 the mean conditional dissipation has been normalised by the respective mean unconditional scalar dissipation value $\langle \chi_r \rangle$ so that $\langle \chi_r | \theta \rangle / \langle \chi_r \rangle = 1$ if statistical independence were satisfied. The scalar fluctuations are reported in terms of a centred variable defined as $\theta^+ = \theta / \theta^*$. Figures 8 and 9 show that the mean conditional dissipation has a parabolic shape, with the maximum at zero (figure 8) or small positive scalar fluctuations from the mean (figure 9) and decreasing towards large positive and negative values of θ . A similar distribution for the mean conditional scalar dissipation has also been measured by Sardi *et al.* (1997) in an opposed jet flow while the measurements of Jayesh and Warhaft (1992) and Anselmet *et al.* (1994) in the self-preserving region of grid generated turbulence and square jet respectively reveal a U-shape distribution where, in contrast to figures 8 and 9, the largest dissipation values result from the largest positive and negative scalar fluctuations. Eswaran and Pope (1988) and Jiang & O'Brien (1991) used direct numerical simulation and the mapping closure formulation respectively to study the temporal evolution of the moments of an initially binary scalar field and concluded that the distributions of figure 8 and 9 are representative of early time scalar mixing where thin diffusive layers separate regions of approximate homogeneity. Figure 8 shows that depending on the value of the scalar fluctuations, the mean conditional dissipation can vary from two times the unconditional mean to as low as one tenth the value of $\langle \chi_r \rangle$ while from figure 9 it is clear that the maximum values of the mean conditional dissipation, due to the occurrence of packets of heated fluid, can be an order of magnitude larger than the respective unconditional mean value within the first diameter from the exit plane. The differences between the conditional and the unconditional scalar dissipation values depend on the value of the scalar fluctuation used as the conditioning value and decrease with distance from the exit plane as was also demonstrated by figure 7.

In order to demonstrate further this effect figures 10 and 11 present the contours of the mean scalar dissipation conditional for instantaneous scalar value of 0.055 and 0.3, corresponding to the stoichiometric mixture fraction of methane and CO/H_2 flames respectively. It can be seen that for $\Theta = 0.055$ the mean conditional scalar dissipation can be up to a factor of ten larger than the respective unconditional value in the vicinity of the jet exit with consequent large misrepresentation of extinction limits. In contrast the difference between the conditional and the unconditional mean is only up to a factor of five for the $\Theta = 0.3$.

CONCLUSIONS

Cold wire measurements of a scalar, temperature, its fluctuations and the radial component within the first two diameters downstream the exit plane of a slightly heated turbulent jet revealed that the scalar fluctuations and their dissipation were strongly correlated within the first diameter downstream the exit plane and that the correlation decreased with increasing distance from the jet exit. The correlation between the scalar and its dissipation was related to the short fluid particle residence times in the mixing layer in comparison to the eddy turn over time so that this result is likely to hold in other flows characterised by 'young' scalar turbulence.

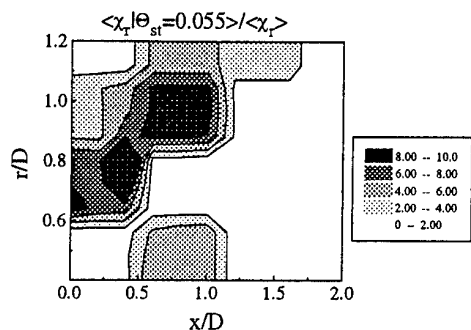


FIGURE 10: CONTOURS OF THE MEAN SCALAR DISSIPATION CONDITIONAL ON A MEAN MIXTURE FRACTION OF 0.055.

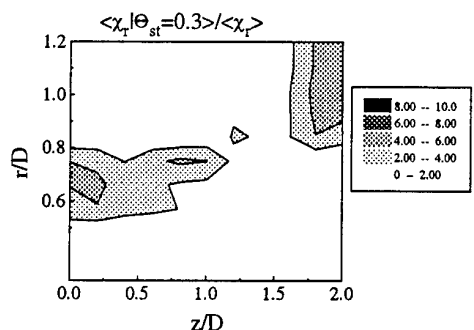


FIGURE 11: CONTOURS OF THE MEAN SCALAR DISSIPATION CONDITIONAL ON A MEAN MIXTURE FRACTION OF 0.3.

The mean scalar dissipation conditional on the scalar fluctuations was parabolically distributed with the maximum corresponding to almost zero values of the scalar fluctuations at the mean scalar value of 0.5 and to large heated or cold scalar fluctuations if measured in the cold or heated side of the mixing layer. The measurements revealed that the mean conditional dissipation can differ by an order of magnitude than the respective unconditional value but the difference decreased with distance from the exit plane.

REFERENCES

- Anand, A. and Pope, S.B., 1985, "Diffusion behind a line source in grid turbulence", *Turbulent Shear Flows 4*, Bradberry, L.J.S., Durst, F., Launder, B.E., Schmidt, F.W. and Whitelaw, J.H. (Eds), Springer Verlag, Berlin.
- Anselmet, F. and Antonia, R.A., 1985, "Joint statistics between temperature and its dissipation in a turbulent jet", *Phys. Fluids* Vol. 28, pp. 1048.
- Anselmet, F., Djeridi, H. and Fulachier, L., 1994, "Joint statistics of a passive scalar and its dissipation in turbulent flow", *J. Fluid Mech.*, Vol. 280, pp. 173.
- Bilger, R.W., 1980, "Turbulent flames with non-premixed reactants", In *Turbulent Reacting Flows*, Libby, P.A. & Williams, F.A. (Eds.), Springer Verlag, Berlin.
- Bilger, R.W., 1989, "Turbulent diffusion flames", *Ann. Rev. Fluid Mech.*, Vol. 21, pp. 101.
- Bilger, R.W., 1993, "Conditional moment closure for turbulent reacting flow", *Phys. Fluids A*, Vol. 5, pp. 436.
- Cho, P., Law, C.K., Cheng, R.K. & Shepherd, I.G., 1988, "Velocity and scalar fields of turbulent premixed flames in a stagnation flow", *Twenty-second Symposium (International) on Combustion*, The Combustion Institute, Pittsburgh, pp. 739-745.
- Collis, D.C. & Williams, M.J. (1959) "Two dimensional convection from heated wires at low Reynolds number", *J. Fluid Mech.*, Vol. 6, pp 357.
- Eswaran, V. and Pope, S.B., 1988, "Direct numerical simulations of the turbulent mixing of a passive scalar", *Phys. Fluids*, Vol. 31, pp. 506.
- Girimmet, G.R. and Stirzaker, D.R., 1992, "Probability and Random Processes", Clarendon Press, Oxford.
- Hunt, J.C.R. and Carruthers, D.J., 1990, "Rapid distortion theory and the 'problems' of turbulence", *J. Fluid Mech.*, Vol. 212, pp. 497.
- Jayesh & Warhaft, Z., 1992, "Probability distribution, conditional dissipation and transport of passive temperature fluctuations in grid generated turbulence", *Phys. Fluids A*, Vol. 4, pp. 2292.
- Jiang, T.L. and O'Brien, E.E., 1991, "Simulation of scalar mixing by stationary isotropic turbulence", *Phys. Fluids A* Vol. 3, pp. 1612.
- Kailasnath, P., Sreenivasan, K.R. and Saylor, J. R., 1993, "Conditional scalar dissipation rates in turbulent wakes, jets and boundary layers", *Phys. Fluids A*, Vol. 5, pp. 3207.
- Klimenko, A.Y., 1990, "Multicomponent diffusion of various admixtures in turbulent flow", *Fluid Dyn.*, Vol. 25, pp. 327.
- Kostiuk, L.W., 1991, "Premixed Turbulent Combustion in Counterflowing Streams", PhD Thesis, University of Cambridge.
- Mi, J., Antonia, R.A. and Anselmet, F., 1995, "Joint statistics between temperature and its dissipation rate components in a round jet", *Phys. of Fluids A*, Vol. 7, pp. 1665.
- Paranthoen, P., Petit, C. and Lecordier, J.C., 1982, "The effect of thermal prong-wire interaction on the response of a cold wire in gaseous flows (air, argon and helium)", *J. Fluid Mech.*, Vol. 124, pp. 457.
- Peters, N., 1983, "Local turbulent quenching due to flame stretch and non-premixed turbulent combustion", *Combust. Sci. and Tech.* Vol. 30, pp. 1.
- Peters, N., 1986, "Laminar flamelet concepts in turbulent combustion", *Twenty-first Symposium (International) on Combustion*, The Combustion Institute, Pittsburgh, pp. 1231.
- Pope, S.B., 1983, "PDF methods for turbulent reactive flows", *Prog. Energy Comb. Science* Vol. 11, pp. 119.
- Sardi, K., 1997, "Turbulent flame extinction in unforced and periodically forced counterflows", PhD Thesis, University of London.
- Sardi, K., Taylor, A.M.K.P. and Whitelaw, J.H., 1997, "Conditional scalar dissipation statistics in a turbulent counterflow and implications for flame extinction", in preparation.
- Tsuji, T., Nagano, Y. and Tagawa, M., 1992, "Frequency response and instantaneous temperature profile of cold-wire sensors for fluid temperature fluctuation measurements", *Exp. Fluids*, 13:171.
- Wyngaard, J.C., 1971a, "The effect of velocity sensitivity on temperature derivative statistics in isotropic turbulence", *J. Fluid Mech.*, Vol. 48, pp. 763.
- Wyngaard, J.C., 1971b, "Spatial resolution of a resistance wire temperature sensor", *Phys. Fluids*, Vol. 4, pp. 2052.

HIGH-SCHMIDT NUMBER MASS TRANSFER THROUGH TURBULENT GAS-LIQUID INTERFACES

Isabelle Calmet

Ecole Centrale de Nantes, UMR 6598
1 rue de la Noe 44321 Nantes cedex 3
France

Jacques Magnaudet

Institut de Mécanique des Fluides de Toulouse, UMR 5502
2 avenue Camille Soula 31400 Toulouse
France

ABSTRACT

This paper reports some new results concerning the structure of the concentration field and the mechanisms of mass transfer at flat gas-liquid interfaces, especially in the limit of high Schmidt numbers. The problem is investigated using the Large Eddy Simulation technique applied to two different interfaces, namely a sheared-driven surface and a shear-free surface. It appears that in the shear-free case the concentration field close to the interface is organized in large patches that mirror the upwelling structures coming from the core of the flow. In contrast at a sheared interface the concentration field is organized in streaks of much smaller spanwise extent. In both cases it is found that the concentration fluctuations are closely related to the horizontal turbulent motions that stretch the interface. The results of the simulations are used to check several mass transfer models.

1 - INTRODUCTION

Diffusion at high Schmidt numbers through turbulent gas-liquid interfaces occurs in many geophysical or industrial processes. It is for example the basic situation encountered in the exchange of slightly soluble gases like O_2 or CO_2 between the atmosphere and the oceans or the lakes. For such gases the diffusive sublayer in the liquid is so thin that the transfer is entirely governed by the structure of the turbulent field in the immediate vicinity of the interface. To understand such gas transfers, it is obviously highly desirable to perform simultaneous analyses of concentration and velocity fluctuations in the interfacial region in terms of both statistics and turbulent structures. Unfortunately this goal is very difficult to achieve experimentally: instantaneous measurement of concentration by means of microprobes is still under development and parasitic phenomena like interface contamination by impurities or capillary ripples occur very frequently in these experiments. Direct Numerical Simulation would be a perfect tool for that purpose but is very limited in practice since

the number of grid points required to capture the smallest scalar scales grows with the Reynolds (Re) and Schmidt (Sc) numbers like $Sc^3 Re^{9/4}$. Nevertheless, the same kind of information can be obtained by using the Large Eddy Simulation technique which avoids this limitation, provided the small scales do not prevail in the transfer process and their major effects on the large scales are correctly modelled. Recently this approach has been proved to provide very good results in the study of mass transfer at a solid wall: *Calmet* (1995) and *Calmet & Magnaudet* (1997) have shown that the LES approach using recent advances made in the formulation of subgrid-scale models gives mass transfer rates and characteristics of the mean and fluctuating concentration fields in very good agreement with the most advanced experimental studies.

The present paper reports some results obtained using the same technique for studying diffusion through flat gas-liquid interfaces at two different Schmidt numbers, namely $Sc=1$ and $Sc=200$. Two kinds of interfaces (i.e. sheared or shear-free) are considered by computing two different high- Re turbulent flows, namely a liquid layer driven by the interfacial shear and an open channel where turbulence is created at the bottom wall (Fig. 1). In both cases tangential velocity fluctuations can subsist up to the surface whereas a constant concentration is imposed on this surface.

2 - DESCRIPTION OF THE COMPUTATIONS

The flows fields are computed with the LES code developed at IMFT (*Calmet*, 1995). Basically this code solves the three-dimensional governing equations filtered in space by the computational grid, namely

$$\frac{\partial \bar{v}_i}{\partial x_i} = 0 \quad (1a)$$

$$\frac{\partial \bar{V}_i}{\partial t} + \frac{\partial}{\partial x_j} (\bar{V}_i \bar{V}_j) = -\frac{\partial \bar{P}}{\partial x_i} + \frac{\partial}{\partial x_j} [2\nu \bar{S}_{ij} - \tau_{ij}] \quad (1b)$$

$$\frac{\partial \bar{C}}{\partial t} + \frac{\partial}{\partial x_j} (\bar{C} \bar{V}_j) = \frac{\partial}{\partial x_j} \left[D_\mu \frac{\partial \bar{C}}{\partial x_j} - q_j \right] \quad (1c)$$

where $\bar{S}_{ij} = \frac{1}{2} \left(\frac{\partial \bar{V}_i}{\partial x_j} + \frac{\partial \bar{V}_j}{\partial x_i} \right)$ denotes the resolved strain rate tensor. The effect of the unresolved subgrid-scales appears in (1b) and (1c) through the subgrid stress $\tau_{ij} = \bar{V}_i \bar{V}_j - \bar{V}_i \bar{V}_j$ and the subgrid flux $q_j = \bar{C} \bar{V}_j - \bar{C} \bar{V}_j$. These subgrid scale terms are closed using the Dynamic Mixed Model (DMM) developed by Zang *et al.* (1993) and extended to the subgrid scalar flux by Calmet and Magnaudet (1997). In this model the anisotropic part of τ_{ij} is written under the form

$$\tau_{ij} - \frac{1}{3} \tau_{kk} \delta_{ij} = L_{ij} - \frac{1}{3} L_{kk} \delta_{ij} - 2\nu_T \bar{S}_{ij} \quad (2a)$$

with $L_{ij} = \bar{V}_i \bar{V}_j - \bar{V}_i \bar{V}_j$. Similarly the scalar flux is written

$$q_j = -D_T \frac{\partial \bar{C}}{\partial x_j} + L_{cj} \quad (2b)$$

with $L_{cj} = \bar{C} \bar{V}_j - \bar{C} \bar{V}_j$. The important feature of the DMM is that the Leonard terms L_{ij} and L_{cj} which are by far the most important subgrid-scale contribution in that formulation (see Calmet 1995) are computed explicitly by re-filtering the resolved fields \bar{V}_i and \bar{C} and their products on the computational grid. Consequently the subgrid-scale stress (resp. flux) is not forced to align with the resolved rate-of-strain (resp. concentration gradient). Following Smagorinsky the subgrid viscosity and diffusivity are connected to the local grid scale $\bar{\Delta} = (\bar{\Delta}_1 \bar{\Delta}_2 \bar{\Delta}_3)^{1/3}$ and to the local strain rate $|\bar{S}| = (2\bar{S}_{ij} \bar{S}_{ij})^{1/2}$ through the well-known expressions:

$$\nu_T = C \bar{\Delta}^2 |\bar{S}| \quad \text{and} \quad D_T = C_c \bar{\Delta}^2 |\bar{S}| \quad (3)$$

where C and C_c are the dimensionless coefficients to be determined dynamically. The computation of C and C_c is carried out using Germano's (1992) identity and the double-filtering procedure first proposed by Germano *et al.* (1991). A thorough description of this dynamic computation is given in Calmet and Magnaudet (1997) to which the reader is referred. The result of this procedure is to produce subgrid-scale coefficients which vary in both time and space. It is worth noting that no averaging procedure in planes of homogeneity is used here, so that the values of C and C_c used in the computations are actually closely related to the local and instantaneous features of the turbulent field.

The flows are studied at a single Reynolds number $Re^* = 1280$, based on the total depth 2δ and the friction velocity u^* (at the bottom wall or the

interface, respectively). The computational box of size $2\pi\delta \times 2\delta \times 3/4\pi\delta$ is discretized with a $32 \times 86 \times 64$ grid. This grid is uniform in the streamwise and spanwise directions and highly stretched in the normal direction in order to resolve properly the diffusive sublayer up to $y^+ = 0.02$ for $Sc = 200$. The boundary conditions are specified in Fig. 1. They assume periodicity of all variables (except the mean pressure) in the streamwise and spanwise directions. No-slip conditions are imposed at the bottom wall. In contrast the conditions imposed on both interfaces (upper plane) state that the normal velocity as well as the fluctuating shear stresses are zero, allowing the tangential velocity fluctuations u' and w' to subsist up to the surface.

3 - STATISTICS OF THE CONCENTRATION FIELD

In the immediate vicinity of the interface it can be shown (Calmet, 1995) that the velocity fluctuations obey $u' = a_0 + a_2 y^{+2} + \dots$, $v' = b_1 y^+ + b_3 y^{+3} + \dots$ and $w' = c_0 + c_2 y^{+2} + \dots$ while the concentration fluctuations obey $c' = d_1 y^+ + d_3 y^{+3} + \dots$. Using these expansions one can demonstrate that the diffusive sublayer thickness δ_c^+ is related to the viscous sublayer thickness δ_u^+ through

$$\delta_c^+ \propto \sqrt{\delta_u^+} Sc^{-1/2} \quad (4)$$

In Fig. 2 the mean concentration C^+ is plotted vs. the normalised interfacial distance $y^+ = (\delta - y)u^*/\nu$. Since the diffusive sublayer is the region where the concentration profile typically evolves like $Sc y^+$, δ_c^+ can be directly estimated graphically. One finds $\delta_c^+ \approx 1.9$ at $Sc = 1$ and $\delta_c^+ \approx 0.12$ at $Sc = 200$ near the sheared interface. Close to the shear-free surface the same technique yields $\delta_c^+ \approx 5$ at $Sc = 1$ and $\delta_c^+ \approx 0.35$ at $Sc = 200$. Below the sheared interface, the simulation indicates $\delta_u^+ \approx 3$ in accordance with the measurements of Mc Leish and Putland (1975). This value is smaller than the one found near a rigid wall because, close to an interface viscous effects only affect the slope of the velocity fluctuations but have little effects on their magnitude. Injecting this value in the theoretical law (4) yields $\delta_c^+ \approx 1.73$ at $Sc = 1$ and $\delta_c^+ \approx 0.12$ at $Sc = 200$, in good agreement with the graphical estimates. For a shear-free surface, the value of δ_u^+ cannot be determined through the velocity profile. However once δ_c^+ is known it can be estimated through (4). Using both Sc numbers one finds $\delta_u^+ \approx 25$. This very large value is due to the lack of small scale structures in the absence of shear (Hunt, 1984).

The r.m.s. fluctuations c' normalized by the difference of concentration between the interface and the bulk are presented in Fig. 3. They reach a well defined maximum in the buffer region of C^+ , i.e. between the diffusive sublayer where $C^+ = Sc y^+$ and the log-layer where $C^+ \propto \text{Log}(y^+)$. Owing to the $Sc^{-1/2}$ dependency of the diffusive sublayer

thickness, this maximum is reached much closer to the interface at $Sc=200$ than at $Sc=1$. Below the sheared interface this maximum is about 0.25 for both Schmidt numbers. Turbulence characteristics in the buffer region of concentration greatly influences the fluctuations c' . Indeed, in the sheared case, the fluctuations of velocity reaching their maximum right at the interface, the maximum of c' at $Sc=200$ is somewhat higher than at $Sc=1$ (0.28 instead of 0.25). In contrast near the shear-free surface, the turbulence decays when the interface is approached. Consequently an opposite behavior of c' is found, i.e. the maximum of c' is 0.38 at $Sc=1$ whereas it decreases to 0.31 at $Sc=200$. Moving away from the interface, c' becomes nearly zero at $Sc=200$ since the mean concentration is essentially constant over most of the flow. In contrast for $Sc=1$, a mean concentration gradient persists throughout the bulk because the mass flux crossing the flow from $y=\delta$ to $y=-\delta$ is much larger than in the high- Sc case. As can be seen in Fig. 3 this gradient induces significant r.m.s. intensities far from the interface. Although turbulence is weaker near the shear-free surface than near the sheared interface, c' is more intense in the first case owing to the presence of much larger, nearly non-dissipative eddies. This trend is confirmed by the budget of $\langle c'^2 \rangle$ (not shown here) where the ratio between production and dissipation is found to reach significantly higher values below the shear-free interface.

Near the interface, the skewness factors $S(c')$ and $S(v')$ shown in Fig. 4 indicate that the largest events in the concentration fluctuations are directly related to the largest events of the normal velocity fluctuation v' . As will be seen below, the events responsible for the asymmetry of the concentration field are either turbulent structures ejected from the bottom wall and reaching the shear-free interface, or sweeping events following the ejection process below the sheared interface. So, in both cases $S(c')$ is negative close to the interface since the upwelling velocities responsible for $S(v') > 0$ carry concentrations which are smaller than the average concentration.

4 - RELATION BETWEEN TURBULENT STRUCTURES AND CONCENTRATION FIELD

Figure 5 represents the instantaneous iso-contours of the vertical velocity v' and the concentration c' at $Sc=200$ in horizontal planes located in the diffusive sublayer. A direct comparison of the iso-contours of v' and c' reveals that the dynamics of the concentration field is highly correlated with the coherent structures present near each interface. The large patches that reach the shear-free surface and go away carry low and high concentration, respectively. In this case, the dynamics is simple enough to observe a mirror-image between the iso-contours of v' and those of the concentration fluctuation. This means that in that case the driving mechanism of the mass transfer is the renewal of the surface by the bursts coming from the bottom wall. It is particularly interesting to observe the horizontal motions on the interface itself. For that purpose the instantaneous streamlines corresponding to Fig. 5 are plotted in Fig. 6. The relation between the horizontal interfacial motions and the turbulent events can be quantified by

introducing the so-called surface divergence defined by

$$\nabla_s \cdot \mathbf{v}_s = \beta(x, z, t) = \left\{ \partial u' / \partial x + \partial w' / \partial z \right\}_s = - \left\{ \partial v' / \partial y \right\}_s \quad (5)$$

The sources where $\beta > 0$ (resp. the sinks where $\beta < 0$) corresponding to upwelling (resp. downwelling) motions are easily seen in Fig. 6. Coming back to the isocontours of c' it appears that concentration fluctuations are very closely related to the compression and dilation of the interface.

Near the sheared interface, the normal velocity fluctuations induced by the bursts have a very different structure: iso-contours of v' (Fig. 7) show that these events have a small lateral extent and are elongated in the streamwise direction. The same is true for c' but the concentration seems to be less organized and the relation between the two pictures is less simple than in the shear-free case. In contrast iso-contours of the streamwise fluctuations (not shown here) reveals that u' is clearly organized in regular streaks very similar to those present in usual boundary layers. A cross-section of c' and u' (not shown here) demonstrates that c' is actually also organized in streaks. There is no doubt that the vertical motions reaching the interface (which result from the cycle of life of the streaks) are also the source of the concentration fluctuations in that case. However, once c' has been created by v' in the diffusive sublayer, these fluctuations are transported and stretched by the large scales of the turbulent field and especially by the longitudinal streaks. Thus the structure of the concentration field is a mixture between the structure of v' in the viscous sublayer and the streaky structure of u' , giving a more complicated picture.

5 - COMPARISON WITH SOME MASS TRANSFER MODELS

Deriving simple predictive mass transfer models has been a subject of great importance in chemical engineering for a long time. Generally mass transfer efficiency is measured by defining a mass transfer velocity, K_L , directly proportional to the mass flux entering the liquid. Most of the mass transfer models state that the transfer is controlled by the molecular diffusivity D_μ and by a so-called renewal time τ . From dimensional evidence one then obtains (Danckwerts, 1951)

$$K_L = (D_\mu / \tau)^{1/2} \quad (6)$$

The key problem in such models lies obviously in the prediction of τ . One can distinguish between models based on a *global* property of turbulence, such as the turbulent Reynolds number Re_T defined with the aid of the integral scale L_∞ and some velocity scale u' , and models based on a *local* property able to characterize the turbulence on the interface itself.

The oldest and most simple models are of course those based on a global property of the turbulence. Depending on the range of scales which are assumed to govern the transfer, two kinds of models have emerged. If one assumes that the large scales dominate the transfer one obtains $\tau \propto L_\infty / u^*$. This yields (Fortescue and Pearson, 1970)

$$K_L / u^* = C_{LS} Sc^{-1/2} Re_T^{-1/2} \quad (7)$$

where the constant C_{LS} is generally set to 1.07. In contrast if one assumes that the transfer is governed by the small scales, the relevant time scale becomes $\tau \propto (\nu/\epsilon)^{1/2}$ where ϵ denotes the dissipation rate. Then one obtains (Banerjee et al. 1968, Lamont and Scott 1970)

$$K_L / u^* = C_{SS} Sc^{-1/2} Re_T^{-1/4} \quad (8)$$

where the constant C_{SS} is generally set to 0.25. Therefore the two models differ essentially by the exponent of the turbulent Reynolds number.

More recently several models based on a local property of the turbulence right at the interface have appeared. The simplest one was proposed by Banerjee (1990). This author simply assumes that the turbulent events that control mass transfer are the large-scale bursts coming either from the interfacial region when turbulence is produced directly at the interface or from the bottom of the flow when no shear acts on the free surface. Thus, denoting by f_B the bursting frequency, and assuming that $\tau \propto f_B^{-1}$, the mass transfer coefficient is given by

$$K_L / u^* = (f_B^{-1} u^{*2} / \nu)^{-1/2} Sc^{-1/2} \quad (9)$$

McCready et al. (1986) derived a more sophisticated model taking into account all the turbulent scales by solving the instantaneous concentration equation in the diffusive sublayer. For that purpose they injected in this equation a normal velocity signal recorded experimentally. This signal evolved linearly according to the law $v' = \beta(t)y$. In this approach the characteristic time is obviously $\tau \propto \langle \beta^2 \rangle^{-1/2}$. The results obtained by McCready et al. showed that the mass transfer coefficient followed the law

$$K_L / u^* = 0.71 \langle \beta^2 \rangle^{1/4} Sc^{-1/2} \quad (10)$$

Having recalled the form and the assumptions associated to these models, it is of particular interest to compare the values of the mass transfer coefficient K_L / u^* they predict with the one obtained in the present approach for $Sc=200$. Nevertheless before discussing this comparison some comments about the values of K_L / u^* given by the computations are in order. First of all, comparison of the results obtained for $Sc=1$ (not reported here) and for $Sc=200$ confirms that the LES values follow a dependency very close to $Sc^{-1/2}$. Moreover in the sheared case many experimental results are available. Hanratty (1991) compiled a lot of these results and concluded that the mass transfer coefficient follows the law $K_L / u^* = \alpha Sc^{-1/2}$ with α ranging between 0.12 and 0.15. The present result reported in Table 1 indicates $\alpha=0.131$, showing that the predictions of the LES approach are very accurate.

To compare these numerical predictions with available models it is necessary to know the turbulent Reynolds number Re_T , the r.m.s. value of β and the bursting frequency. The integral scale required to estimate Re_T is obtained by defining the scale l related to the dissipation rate ϵ through $\epsilon = u'^3 / l$ and using the isotropic relation $L_\infty = l/2$. The value of

$\langle \beta^2 \rangle^{1/2}$ follows directly from the asymptotic behavior of the normal velocity fluctuation since it is given by the slope of $\langle v'^2 \rangle^{1/2}$ in the viscous sublayer. Finally the bursting time can be estimated by determining the average distance between the bursts present at the surface and dividing by the mean streamwise velocity at the interface.

The key difficulty with the "global" models lies in the location where Re_T is determined. Basically these models assume that the turbulence is homogeneous and isotropic while this is obviously not the case in the interfacial region. For example if one determines Re_T at a distance L_∞ from the interface (where the assumption of homogeneity is better verified), one finds $Re_T=440$ for the sheared interface and $Re_T=390$ for the shear-free case. Inserting these values in models (7) and (8) yields $5.1 \cdot 10^{-3} \leq K_L / u^* \leq 5.5 \cdot 10^{-3}$ and $2.7 \cdot 10^{-3} \leq K_L / u^* \leq 2.8 \cdot 10^{-3}$, respectively. It is obvious that these results underpredict significantly those found in the simulations. In contrast if one estimate the typical magnitude of the velocity fluctuation right at the interface, much higher values of Re_T emerge. Using these values one obtains the estimates of K_L / u^* reported in Table 1. These values are in much better agreement with those given by the simulations. One can remark that both models give fairly close predictions. This means that it is not possible to discriminate between the 'large scale' and 'small scale' models from the present simulations. Actually the two exponents of Re_T which appear in these models are rather close and the predictions become significantly different only for much higher Reynolds numbers (Brumley and Jirka 1988).

When the model (9) is applied to the sheared interface, Table 1 shows that the result is in very good agreement with the simulations. This confirms that the bursting events play a central role in the transfer. The problem is more complicated in the shear-free case. In that situation, a direct application of (9) leads to $K_L / u^* = 8.8 \cdot 10^{-3}$. This value clearly overestimates the result given by the LES. Banerjee (1990) observed a similar disagreement when he tried to apply his model to shear-free experiments. He argued that in that case only one part of the interface is covered by large-scale structures which are active in the transfer, the remaining part being nearly inactive. This is clearly the case here as shown by Fig. 5. Banerjee overcame the problem by multiplying the value predicted by (9) by the percentage of 'active' surface. In the present case this percentage lies between 40 and 50%. The result of the 'corrected' model reported in Table 1 is then in good agreement with the simulation. Nevertheless the problem encountered in the application of model (9) to a shear-free interface underlines the intrinsic difficulty of the description of such interfacial conditions. Basically, this kind of turbulence is not produced in the vicinity of the interface, in contrast with the case where a strong interfacial shear is present. Thus the characteristics of this interfacial turbulence depends not only on the turbulence source itself (here the bottom wall) but also on the 'life' (and possibly 'death') of the turbulence during its transport towards the interface. This means that at least an additional parameter like

parameter like the depth of the flow is needed to describe this situation.

Finally when the model (10) is applied, the results for the two flow configurations are found to be in very good agreement with the simulations. Keeping in mind that this model is based on the r.m.s. value of β with is nothing else that the divergence of the interfacial motions, this agreement in two contrasted situations shows that β is indeed the key local parameter that governs the mass transfer rate. In other words if one knows the rate at which the interface is dilated and compressed by the horizontal turbulent motions, the mass transfer efficiency can be readily predicted.

6 - CONCLUSIONS

Large Eddy Simulation has been used to investigate high-Schmidt number mass transfer at a gas-liquid interface with or without shear. Comparison with the theoretical predictions has shown that the influence of the Schmidt number is correctly captured. Statistics of the fluctuating concentration have revealed the influence of both the Schmidt number and the local state of the turbulence. The mechanisms governing the mass transfer have been clarified by examining the spatial structure of v' and c' close to both interfaces. It has been made clear that the turbulent events impacting the interface are the source of the concentration fluctuations. A comparison of mass transfer coefficients given by the present approach with those predicted by simple available models has been carried out. The difficulties encountered with some of these models have been underlined and the central role of the surface divergence which is directly related to v' has been confirmed.

REFERENCES

- Banerjee, S. 1990 Turbulence structure and transport mechanisms at interfaces, *Proc. Int. Conf. Heat Transfer, Jerusalem*.
- Banerjee, S., Scott, D. & Rhodes, E. 1968 Mass transfer to falling wavy liquid films in turbulent flow, *Ind. Eng. Chem. Fundamentals*, Vol. 7, pp. 22-27.
- Calmet, I. 1995 Analyse par simulation des grandes échelles des mouvements turbulents et du transfert de masse sous une interface plane, Ph.D. Thesis, Inst. Nat. Polytech. Toulouse, France.
- Calmet, I. & Magnaudet, J. 1997 Large Eddy Simulation of high-Schmidt number mass transfer in a turbulent channel flow, *Phys. Fluids*, Vol. 9, pp. 438-455.
- Dankwerts, P. V. 1951 Significance of liquid film coefficients in gas absorption, *Ind. Eng. Chem.*, Vol. 43, pp. 1460-1466.
- Fortescue, G. E. & Pearson, J.R.A. 1970 On gas absorption into a turbulent liquid, *Chem. Eng. Science*, Vol. 22, pp. 1163-1176.
- Germano, M. 1992 Turbulence: the filtering approach, *J. Fluid Mech.* Vol. 238, pp. 325-336.
- Germano, M., Piomelli, U., Moin, P. & Cabot, W. 1991 *Phys. Fluids A*, Vol. 3, pp. 1760-1765.
- Hanratty, T.J. 1991 Effect of gas flow on physical absorption, In *Air-Water Gas Transfer*. S.C. Wilhelms & J.S. Gulliver eds., ASCE.
- Lamont, J. C. & Scott, D. S. 1970 An eddy cell model of mass transfer into the surface of a turbulent liquid, *AIChE J.*, Vol. 16, pp. 513-519.
- McCready, M.J., Vassiliadou, E. & Hanratty, T.J. 1986 Computer simulation of turbulent mass transfer at a mobile interface, *AIChE J.*, Vol. 32, pp. 1108-1115.
- Hunt, J.C.R. 1984 Turbulence structure and turbulent diffusion near gas-liquid interfaces, In *Gas transfer at water surfaces*, Brutsaert & Jirka eds., pp. 67-82.
- McLeish, W. & Putland, G. E. 1975 Measurements of wind-driven flow profiles in the top millimeter of water, *J. Phys. Ocean.*, Vol. 5, pp. 516-518.
- Zang, Y., Street, R.L. & Kossseff, J.R. 1993 A dynamic mixed subgrid scale model and its application to turbulent recirculating flows, *Phys. Fluids A*, Vol. 5, pp. 3186-3196.

	Shear-free	Sheared
LES prediction	$3.70 \cdot 10^{-3}$	$9.29 \cdot 10^{-3}$
Large Eddies (7)	$3.10 \cdot 10^{-3}$	$8.50 \cdot 10^{-3}$
Small eddies (8)	$3.40 \cdot 10^{-3}$	$1.17 \cdot 10^{-2}$
Bursting frequency (9)	$3.50 \text{ to } 4.40 \cdot 10^{-3}$	$1.00 \cdot 10^{-2}$
Surface divergence (10)	$4.36 \cdot 10^{-3}$	$1.00 \cdot 10^{-2}$

Table 1. Mass transfer coefficient predictions.

FIGURES

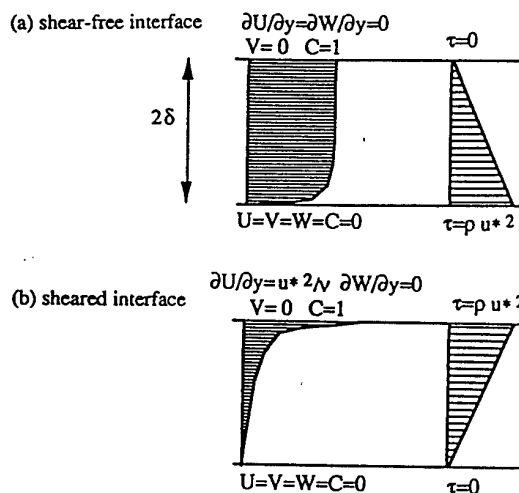


Figure 1. Sketch of the flow configurations.

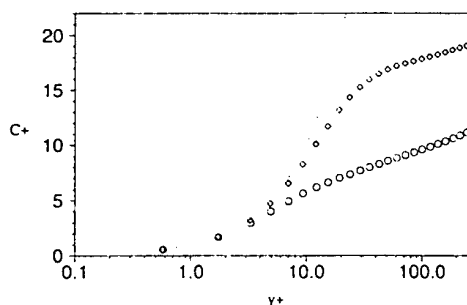


Figure 2a. Mean concentration profiles at $Sc=1$: \diamond Shear-free surface; \circ Sheared interface; $C^+ = Sc \ y^+$.

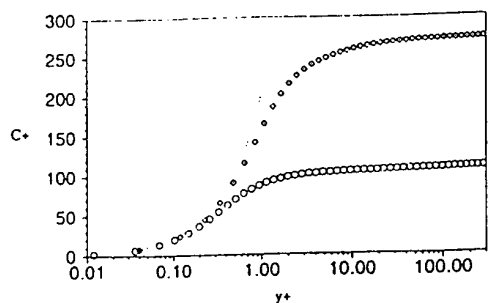


Figure 2b. Mean concentration profiles at $Sc=200$: ◇ Shear-free surface; ○ Sheared interface; $C^+ = Sc y^+$.

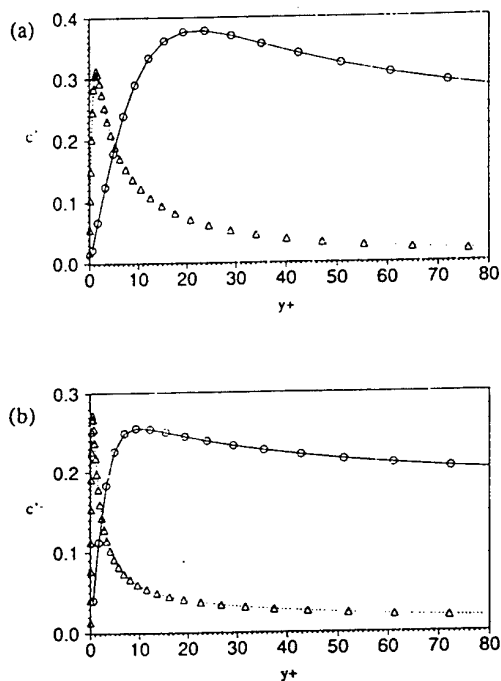


Figure 3. Fluctuations of concentration below (a) the shear-free surface, (b) the sheared interface : ○-○ $Sc=1$; Δ-Δ $Sc=200$.

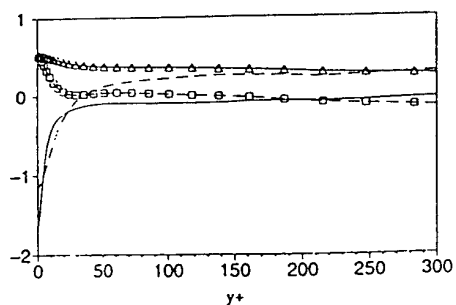


Figure 4. Skewness factors below the shear-free surface : Δ $S(v')$; --- $S(c')$ ($Sc=1$) and below the sheared interface : □ $S(v')$; — $S(c')$ ($Sc=1$).

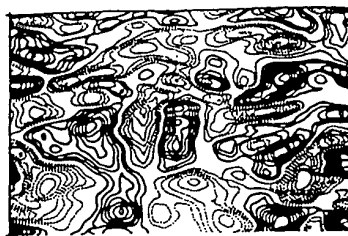


Figure 5a. Instantaneous iso-values of v' very close to the shear-free interface.



Figure 5b. Instantaneous iso-values of c' very close to the shear-free interface.

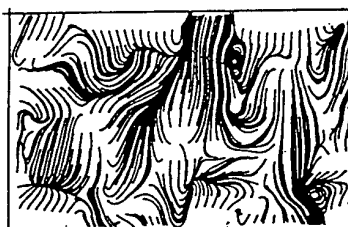


Figure 6. Instantaneous streamlines on the shear-free interface



Figure 7a. Instantaneous iso-values of v' very close to the sheared interface.

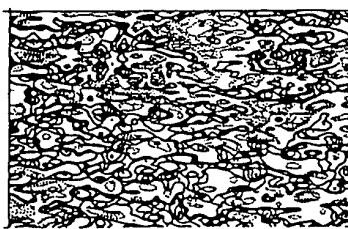


Figure 7b. Instantaneous iso-values of c' very close to the sheared interface.

SESSION 9 - FLOW MANAGEMENT

CONTROL OF DRAG BY TIME-SPACE PERIODICAL SUCTION AND BLOWING

Sedat Tardu

Laboratoire des Ecoulements Géophysiques et Industriels
Institut de Mécanique de Grenoble
INPG, UJF, CNRS
Grenoble - France

ABSTRACT

The effect of time periodical blowing through a slot on the spatio-temporal characteristics of the wall shear stress and the turbulence in the buffer layer is experimentally investigated. It is shown that the local imposed unsteadiness affects considerably the fine structure of the near wall turbulence. The drag is reduced by steady blowing, essentially because of a different redistribution of the quadrant events. The unsteady blowing affects the vorticity generation mechanism, without appreciably interacting with this redistribution.

INTRODUCTION

Aim of the research

Intensive research carried on the passive means of managing the near wall turbulence with the main goal of reducing the skin-friction has given somewhat deceptive results. Indeed, surface mounted longitudinal grooves, although being most successful, cannot achieve skin-friction reduction larger than 10% and their capacity of reducing drag is constrained to within a small range of the riblets spacing and heights being therefore quite sensitive to the changements of external flow conditions or the Reynolds number. The large eddy break up devices, on the other hand, do not result in a net reduction of the skin friction according to a consensus largely established by now.

The active and passive management of the turbulent wall shear stress is ultimately related to the interaction of the coherent structures present in the inner layer with the near wall flow. The ad-hoc out of phase active control scheme reported by Choi and al. (1994) may easily be replaced in this context. The wall shear stress τ is instantaneously enhanced in the regions wherein the spanwise vorticity $\omega_{z,0}$ is stretched due to the stagnation flow induced by the quasi-streamwise vortices - QSW (Tardu, 1995, p. 378). A simple

analysis conducted by Orlandi and Jiménez (1994) establishes the close relationship between τ and the characteristics of the QSW through $\tau^+ \propto \sqrt{R_{vqs}} \frac{u^+(2y^+)}{y^+}$. In

this relationship, R_{vqs} and y^+ are respectively the mean Reynolds number and the distance to the wall of the QS vortical structures. According to this relationship, the drag reduction may be achieved either by decreasing the intensity of the QSV's or by pushing them away from the wall. The objective of this study is to explore the capacity of time and space periodical suction and blowing to increase y^+ and achieve drag reduction. The reasons of using such a scheme are summarized hereafter.

Control strategy

The model suggested here is essentially based on the results reported recently by Acton and Dhanak (1993) although it differs basically in the methodology. We consider a distribution of sources and sinks which are uniformly periodical in space and whose intensities $C_n(t)$ (related to the suction and blowing velocities) are sinusoidal in time (Fig. 1). One has therefore N sources and sinks by wave length Λ with $C_n(t) = C_{n+N}(t)$. We deal with the periodicity in the streamwise direction at the present moment, but the same scheme will be applied to the periodical suction-blowing in the spanwise direction too. The temporal variation is choosen as $C_n(t) = (-1)^n C_0 \left[1 - \cos \left(2\pi f_e t - 2\pi \frac{n}{N} + \Phi_n \right) \right]$. In

this expression f_e stands for the ejection frequency in the inner layer, C_0 and Φ_n are respectively the amplitude and phase of the suction and blowing. This distribution represents an injection i followed by an aspiration $i+1$ with a phase shift of $\frac{-2\pi}{N} + \Phi_{i+1} - \Phi_i$. An inviscid computation of the effect of this management on the distance of a "street" of vortical structures shows that the former varies in time with:

$$K y_v = \ln \left[\alpha - \frac{1}{2} K^2 C_0 t \sum_{n=0}^{n=N-1} (-1)^n \cos \Phi_n \right] + \tilde{F}(t/T)$$

where $F(t/T)$ is a periodical function with periodicity $T=1/f_e$. This relationship is similar to that given by Acton et Dhanak (1993, p. 245). It is clearly seen that if the phases are manipulated according to $\sum_{n=0}^{n=N-1} (-1)^n \cos \Phi_n < 0$, the

distance y_v of the vortical structures will presumably increased once these structures interact intermittently with the pulsed surface. The expected consequence of this intervention is a reduction of drag according to the discussion made in the first section. It is without saying that the reaction of the near wall turbulence to this intervention may not be predicted by such a simple analysis and a detailed study is undoubtedly necessary.

The present steady deals with the effect of a local unsteady forcing on the wall turbulence. The main aim is to investigate the time-space relaxation of the near wall flow manipulated by a time varying blowing through a localized spanwise slit.

DEFINITIONS, EXPERIMENTAL SET-UP and DATA REDUCTION

An experimental model has been developed in the low-speed wind tunnel of our laboratory (Fig.2). The blowing and suction at the wall are done through spanwise slots of dimensions 0.6×100 mm which correspond to 10×1667 in wall units. There are one blowing and one suction slot by wavelength $\Lambda = 45$ mm. ($\Lambda^+ = 750$) and the pulsed surface recovers a total length of 3Λ i.e 2250 in wall units (Fig. 2, see Tardu, 1997 for further details). Hereafter (+) denotes values nondimensionalized with the inner variables, i.e the shear velocity $u_\tau = \sqrt{\frac{\tau}{\rho}}$ and the kinematic viscosity ν .

A special pulsating device has been designed for the present purpose. Quite satisfactory sinusoidal waveforms of the suction/blowing wall normal velocities have been obtained this way for the amplitude of the imposed velocities up to $A_{v,y^+=0} = \hat{A} = 1.5$ m/s ($\hat{A}^+ = 6$) and the imposed frequency $10\text{Hz} < f < 50\text{Hz}$ ($2.5 \times 10^{-3} < f^+ < 12.5 \times 10^{-3}$).

The wall shear stress measurements have been performed by means of a Cousteix-Houdeville wall hot-wire gauge (HWG) to avoid problems caused by the conduction into the substrate. The length of the sensing element is $200 \mu\text{m}$ which corresponds to a spanwise extend of $\Delta z^+ \approx 5$ at $X=1$ m. from the transition point with $\bar{U}_\infty = 6$ m/s. The total duration of each record is $T_{\text{tot}} \approx 5000 T_\infty$ where $T_\infty = \frac{\delta}{U_\infty}$ is the

outer time scale. This is enough to ensure the convergence of the statistics up to 4-th order moments including those of the time derivative of the fluctuating signals.

One should be careful in the interpretation of data in the presence of an organized motion as is the case with unsteady blowing in this study. In order to extract the deterministic and deduce the undeterministic part of the flow quantities the classical triple decomposition is used. A flow quantity $q(\vec{x}, t; T)$ is decomposed into a time mean \bar{q} an oscillating \tilde{q} and a fluctuating q' part :

$$q(\vec{x}, t; T) = \bar{q}(\vec{x}) + \tilde{q}(\vec{x}, t/T) + q'(\vec{x}, t)$$

where T stands for the period of the oscillating blowing. The ensemble or the phase average is performed in order to compute the amplitude $A_{\tilde{q}}$ and phase $\Phi_{\tilde{q}}$ of the oscillating part \tilde{q} from which the instantaneous fluctuating part q' is adequately determined. The beginning of each cycle was provided by a pulse from a photoelectric cell triggered by the pulsator, and the trigger signal was also recorded. The

modulation characteristics have been determined through a least square Fourier analysis. The procedure is the same as in Tardu et al. (1994) wherein further details are provided.

Blowing severity

In flows with uniformly distributed continuous blowing/suction (transpired layers through porous surface), the parameter which characterizes the intervention at the

wall is given by $B_f = \frac{\bar{v}_0 \bar{U}_\infty}{\bar{u}_\tau^2} = \bar{v}_0^+ \bar{U}_\infty^+$ where \bar{v}_0 stands for the

injection/suction velocity at the wall. This is expected, since B_f appears directly in the momentum integral equation of the transpired boundary layer and plays a role similar to the Clauser pressure-gradient parameter. However, the characterization of the severity of local blowing/suction by strips is not straightforward and B_f is not suitable for describing the flow characteristics past the local intervention, as clearly shown by Sano and Hirayama (1985) and Sokolov and Antonia (1993). Indeed, the local suction/blowing involves phenomena related to the relaxation of near wall turbulence downstream of the intervention zone. When \bar{v}_0^+ is high, but the injection is done over large areas, the flow has enough time to relax and reach its equilibrium state rapidly. On the other hand, in case of large injection velocities \bar{v}_0^+ over short distances, the near wall turbulence can hardly maintain its equilibrium state and its structure is expected to be strongly affected. The ratio of the injection or suction flow to the incoming flow

rate, i.e $\Theta = v_0 L_x / \int_0^\infty \bar{U} dy$ is therefore introduced and proved to be adequate to measure the blowing/suction severity.

We proceeded with particularly small slot widths compared with previous studies quoted above. For instance, the experiments reported by Sano and Hirayama have been conducted with two different configurations wherein L_x was respectively 50 and 25 mm corresponding to $L_x^+ \approx 2000$ and $L_x^+ \approx 1000$ under their experimental conditions. Recall that the slit width is only $L_x^+ = 7$ here. As a consequence, the severity parameter is low. The injection velocity in steady blowing experiments investigated here is $\bar{v}_0 = 1$ m/s and the severity parameter is only $\Theta = 0.006$. The shape parameter just downstream of the slit at $x/\delta = 0.1$ is $H = 1.4$ under these circumstances. In unsteady blowing experiments, the injection velocity $\langle v_0 \rangle$ changes in a cyclic manner between 0 and 2 m/s. The maximum value of the severity parameter in the oscillation cycle is therefore $\Theta = 0.012$. The shape parameter measured at the same station increased to $H = 1.7$ at $\bar{v}_0 = 2$ m/s but still remained below the critical value corresponding to flows prone to separate.

RESULTS

One of the main aims of this study is to determine whether a periodic time-varying blowing of the form $\bar{v}_0^+ = \hat{A}^+ (1 - \cos 2\pi f^+ t^+)$ affects the near wall turbulence characteristics when compared with a steady injection by slot with the same time-mean blowing velocity $\bar{v}_0 = \bar{v}_0^+ = \hat{A}$ resulting in the same time mean severity parameter $\Theta = \langle \Theta \rangle$. In other words, the question is whether the near wall flow interacts with the imposed unsteadiness or not. Therefore, we will systematically compare the mean flow characteristics obtained with unsteady and steady blowing hereafter. Before discussing the results, the notation needs to be clarified. Here, an asterisk (*) refers to quantities

measured in the manipulated boundary layer, while the subscript S indicates steady blowing. Thus $\frac{\bar{\tau}_s}{\bar{\tau}}$ is the ratio of the time-mean wall shear stress in the presence of local steady blowing to the wall shear stress of standard boundary layer (SBL), and $\frac{\bar{f}_s}{\bar{f}_e}$ is the ratio of the frequency of the energetic events, etc. In a similar manner, the subindex U corresponds to unsteady blowing, i.e. $\bar{\tau}_U$ and $\bar{\tau}'\tau'_U$ represent respectively the wall shear stress and the wall shear stress intensity in the boundary layer manipulated by time periodical local injection.

Wall shear stress characteristics

Fig. 3 shows the profiles of the ratios $\frac{\bar{\tau}_s}{\bar{\tau}}$ and $\frac{\sqrt{\bar{\tau}'\tau'_s}}{\sqrt{\bar{\tau}'\tau'}}$ and illustrates the effect of steady and unsteady manipulations on the wall shear stress and wall shear stress intensity. The open symbols correspond to time-periodic blowing. It is seen that both steady and unsteady local blowing decreases the drag appreciably. This decrease is persistent up to $X^+ = 500$ downstream of the slot. The average drag reduction is approximately 20%. The imposed unsteadiness is slightly less efficient, but the differences between $\bar{\tau}_U$ and $\bar{\tau}_s$ are always less than 9%.

The first significant difference between time-periodic and steady local injection is in the reaction of the wall shear stress intensity (Fig. 3b). The wall shear stress intensity is significantly less reduced by unsteady blowing, compared with steady blowing. A similar reaction has been observed in the measurements of the streamwise turbulence intensity performed at $y^+ = 10$ and $X^+ = 30$. These measurements will be discussed in the next section.

The decrease of the wall shear stress intensity by steady blowing appears surprising at a first glance, since one expects an increase of the turbulent intensities in the presence of local injection. However, the effect of blowing on the turbulent intensities is most significant beyond the viscous layer ($y^+ > 50$) according to Sano and Hirayama. These authors have shown that the profiles of $\bar{u}^+ s$ and $\frac{\sqrt{\bar{u}'u'}}{U_{\infty s}}$ collapse fairly well with those of SBL when plotted

against $y^+ = y \frac{\bar{u}_\tau}{v}$ near the wall (their fig. 5 and 9). It is easy to show, that under these circumstances $\frac{\sqrt{\bar{u}'u'} s}{\sqrt{\bar{u}'u'}} = \frac{u_\tau}{\bar{u}}$. Since, $\frac{\sqrt{\bar{\tau}'\tau'_s}}{\bar{\tau}} = \frac{\sqrt{\bar{u}'u'}}{\bar{u}}$ as $y^+ \rightarrow 0$ the last

relationship results in $\frac{\sqrt{\bar{\tau}'\tau'_s}}{\sqrt{\bar{\tau}'\tau'}} = \sqrt{\frac{\bar{u}_\tau}{\bar{u}}}$. The measurements

reported here are in good quantitative agreement with this estimation when the blowing is unsteady, but this correspondance is only qualitative in the case of steady injection. It has to be noted that detailed measurements very close to the wall are needed in order to confirm the analysis above, and the closest point to the wall in the data of Sano and Hirayama is only $y^+ \approx 5$.

The effect of the unsteadiness is more pronounced with respect to the fine structure of τ' . Fig. 4a shows that the skewness of the wall shear stress is increased by a factor 1.8 near the slot when the blowing is steady. In contrast, when the injection is unsteady the skewness of τ' is only slightly affected. The mechanism of drag reduction is therefore

certainly different in both manipulations. The increase of S_τ^* s may be interpreted either as the strengthening of the quadrant 4 events with $\tau' > 0$ (sweeps), or equivalently the inhibition of the quadrant 2 events with $\tau' < 0$ (ejections). We therefore suspect that the steady blowing decreases the drag by modifying the inner structure of the flow through the distribution of the quadrant contributions. This is only speculative at the present moment and in order to give a clear answer to this question more detailed measurements have to be performed. The imposed unsteadiness presumably does not affect the quadrant distribution, although measurements of conditional Reynolds stresses may provide a definitive answer to this speculation. It will be shown in the next section that the unsteadiness interacts strongly with the vorticity generation mechanism near the wall.

The flatness of the fluctuating wall shear stress reacts in a manner similar to S_τ^* (Fig. 4b). F_τ^* s increases significantly near $x=0$ while the unsteady blowing does not affect appreciably the spotty character of the fluctuating wall shear stress.

The skewness S_u^* and flatness F_u^* measured at $y^+ = 10$ and shown by squares in Fig. 4 behave in the same manner as S_τ^* and F_τ^* . The comments are therefore similar. The increase of S_u^* s may be interpreted as the enhancement of the convective diffusion by turbulence, i.e. the term

$$-\frac{\partial}{\partial x} \frac{u' q^2}{2} = -\frac{1}{2} \frac{\partial}{\partial x} \{ \bar{u}^3 + \bar{u}'u'^2 + \bar{u}'u'w'^2 \}$$

of the turbulence energy, q^2 , equation. This term is an order of magnitude smaller in the canonical boundary layer compared with

$$-\frac{\partial}{\partial y} \frac{v' q^2}{2},$$

but it is certainly important near the slot in the presence of injection. The integration of the equation $\frac{D}{Dt} \frac{q^2}{2}$

between two planes $x/\delta = 0$ at the injection point, and at $x/\delta = 2$ downstream where the flow reaches its equilibrium state, shows that there is a net contribution to the flux of energy of the order of $\left(\frac{1}{2} \bar{u}^3 \right)_{x/\delta=0} = \frac{1}{2} \bar{u}^{2/3} S_u^*$ due to the

transfer from regions of large intensity to regions of smaller intensity as imposed by the local injection at the wall. The results presented here show that in the case of steady injection there is an increase of the convective flux and this is in agreement with Sano and Hirayama (1983) who reported that the (steady) blowing increases the values of each term in the turbulent energy equation. There are two additional terms in the equation governing the mean turbulent kinetic energy

q^2 for unsteady blowing. These are respectively in the advective and the production terms and they result from the interactions between deterministic parts of the corresponding components. The turbulent diffusion term is however of the same form as in $\frac{D}{Dt} \frac{q^2}{2}$. Since the

skewness factors are only slightly affected by unsteady blowing, one may conclude that the imposed unsteadiness inhibits considerably the streamwise convective flux of energy.

Modulation characteristics

It was found that the streamwise velocity is modulated but that a_q^* does not exceed 0.20. The response of $\langle u \rangle$ is nonlinear and harmonics larger than one are of importance in the high imposed frequency regime.

Fig. 5a shows the phase averages of $\langle u'u' \rangle / \overline{u'u'}$ measured at $y^+ = 10$ and $x^+ = 44$, for respectively $f^+ = 0.01$ and $f^+ = 0.017$. The first striking feature of this Fig. is the occurrence of unexpectedly large modulations of the turbulence intensities which lead to relative amplitudes as high as $a_{\tilde{u}u} \approx 0.8$. It is quite surprising to note such severe effects on the turbulence when one recalls that the unsteady $\langle v \rangle$ forcing is only local. These large modulations point at the existence of a *relaminarization* phase during the cyclic oscillations. The second interesting observation drawn from Fig. 5a is the high sensitivity of the near wall activity response to the imposed frequency. Note indeed that $\langle u'u' \rangle$ at $f^+ = 0.017$ is in opposition of phase with $\langle u'u' \rangle$ at $f^+ = 0.01$.

The strong modification of the wall turbulence structure is better captured in Fig. 5b which shows the phase average of the skewness of du/dt and of the ejection frequency $\langle f_e^+ \rangle$ identified by the modified u' -level technique at $f^+ = 0.017$ and using the phase averaged thresholds. Recall that $S_{du/dt}$ is related to the vorticity stretching and the non linearity in the inner layer. Fig. 5b shows that both the vorticity generation and production mechanisms are altered at high blowing frequency during almost the half of the oscillation cycle.

The effect of the imposed unsteadiness on the vorticity stretching mechanism was further investigated by examining the behaviour of $S_{du/dt}^+ U$ at $y^+ = 10$ versus the imposed frequency (Fig. 6). It is found that the steady blowing does not affect the skewness of du/dt . The changes of $S_{du/dt}^+ U$ indicate therefore a direct effect of the imposed unsteadiness. Fig. 6 shows that in the low imposed frequency regime there is no effect of the oscillations on $S_{du/dt}^+ U$ and $S_{du/dt}^+ U$ which is close to the value in SBL. The skewness $S_{du/dt}^+ U$ decreases steadily once $f^+ > 0.005$ and this constitutes one of the most interesting results inferred from this study. The vorticity stretching mechanism and therefore the nonlinearity are weakened by oscillating blowing by a factor of 3 in the high imposed frequency regime (Fig. 6). This effect is saturated once $f^+ > 0.007$. Note also that there does appear to be a slight kink in the data near $f^+ \approx f_{cr}^+ = 0.01$.

CONCLUSION

*The unsteady blowing decreases the wall shear stress without affecting the skewness. In other words and presumably, it does not affect the distributions in the quadrants. This conclusion has to be checked further by detailed $\langle u'v' \rangle$ measurements.

* There is a clear effect of the imposed unsteadiness on the time mean flow and therefore a clear coupling between the imposed oscillating blowing and the near wall turbulence.

* The modulation of $\partial \tilde{v} / \partial y$ is confined in a layer of thickness $\delta_{uns}^+ \propto 1/\sqrt{f^+}$ and the amplitude of the shear increases with imposed frequency. There is subsequently an oscillating pressure gradient resulting from continuity. This imposed nonhomogeneous and time varying pressure gradient affects locally the time-space development of the coherent structures. On the other hand, if it is argued that the suction essentially removes vorticity near the wall, the unsteady suction may allow us to control the thickness of the boundary layer to manipulate. The unsteady suction deserves in this sense a detailed study.

* The high sensitivity of $\langle u'u' \rangle$ to the imposed frequency (Fig. 5a) suggests the possibility of management of the near wall turbulence in an interesting way. The unsteady blowing

through spanwise slits separated by $x^+ = 50$ and through which the blowing at one slot is in opposition of phase with the other, may result in important reduction of the near wall turbulence activity.

* Finally, the investigation of the same technique by making use of streamwise slits to affect the quasi-streamwise structures may reveal further interesting features.

References

- Acton E., Dhanak, M.-R. " The motion and stability of a vortex array above a pulsed surface" J. Fluid Mech. 247, pp. 231-245; 1993
- Bewley T., Choi H., Temam R., Moin P. " Optimal feedback control of turbulent channel flow" Annual Research Briefs, CTR; pp. 3-14 ; 1993
- Choi H., Moin P., Kim J. "Active control for drag reduction in wall-bounded flows" J. Fluid Mech., 262, pp. 75-110; 1994
- Kim J., Moin P., Moser R., 1987 " Turbulence statistics in fully developed channel flow at low Reynolds number" J. Fluid Mech., 177, 133
- Orlandi P., Jiménez J., 1994 " On the generation of turbulent wall friction" Phys. Fluids, 6, pp. 634-641
- Sano M., Hirayama N., 1985 " Turbulent boundary layers with injection and suction through a slit" Bulletin of JSME, vol.28, pp.807-814
- Sokolov M., Antonia R.-A. " Response of a turbulent boundary layer to intensive suction through a porous strip" Ninth Symp. on Turbulent Shear Flows, Kyoto, pp. 5-3-1 to 5-3-6, 1993.
- Tardu, S., Binder G., Blackwelder R. "Turbulent channel flow with large amplitude velocity oscillations" J. Fluid Mech., 267, pp. 109-151
- Tardu, S., 1995 "Coherent structures and riblets" Appl. Sc. Research. , 54, pp. 349-385
- Tardu, S., 1997 "Near wall turbulence control by local time-periodical blowing" To appear in Exp. Th. Fluid Science.

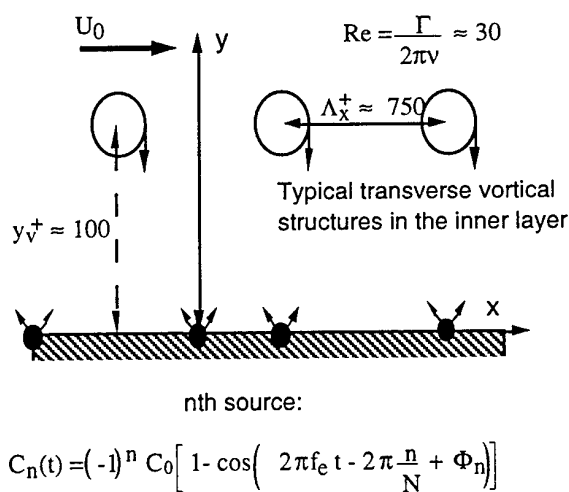


Figure 1 Control strategy

MANIPULATED ZONE

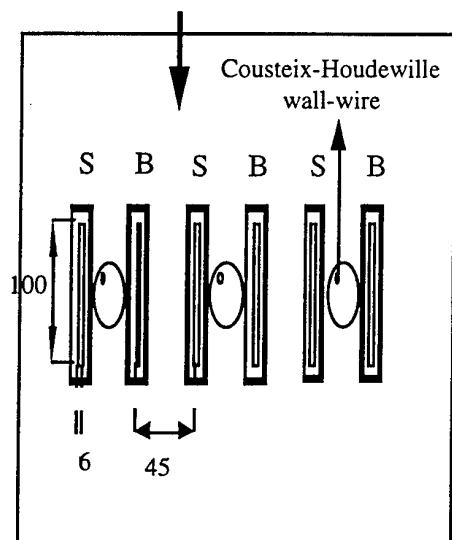


Figure 2 Are shown the slots and their dimensions in mm . S and B refers respectively to suction and blowing.

b-

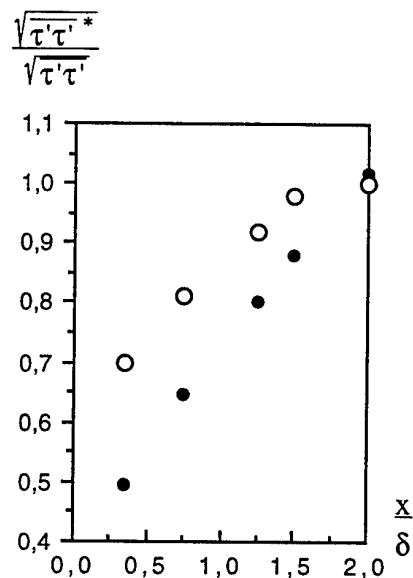
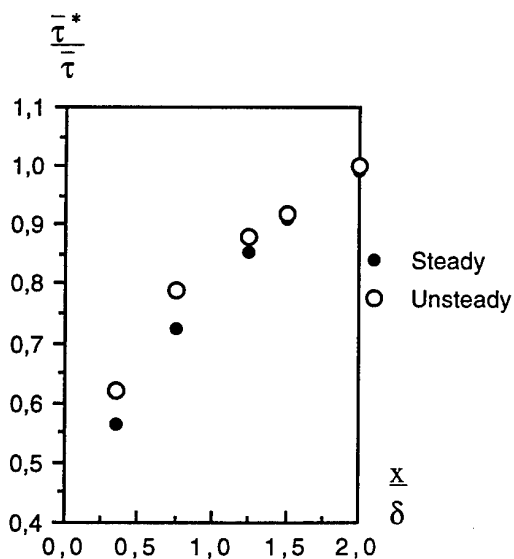
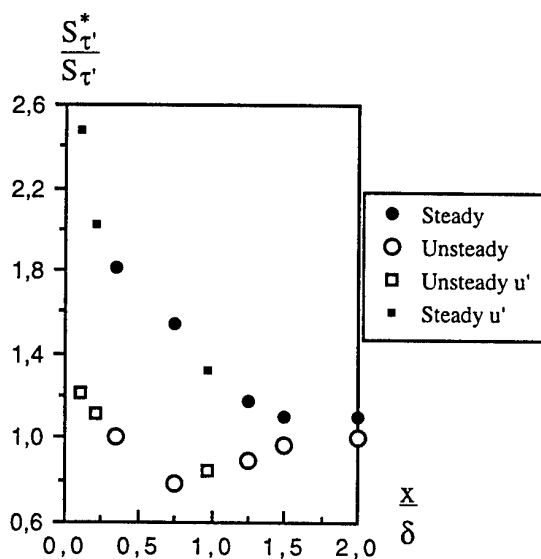


Figure 3 Ratio of (a) the time mean wall shear stress and (b) the wall shear stress intensity (b) in the manipulated versus standard boundary layers. Comparison of steady and unsteady blowing; $f^+ = 0.0072$ and $\hat{A}^+ = 5.4$ for different x stations downstream of the slot; δ is the local boundary layer thickness.

a-



a-



b-

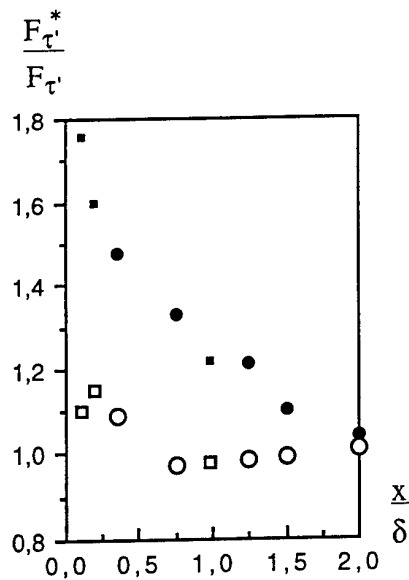


Figure 4 -Ratio of (a) the skewness and (b) flatness of the instantaneous wall shear stress in the manipulated and unmanipulated boundary layer. Comparison of steady and unsteady blowing; $f^+ = 0.0072$ and $\hat{A}^+ = 5.4$. Also shown the corresponding statistics of u' measured at $y^+ = 10$. See (a) for captions.

b-

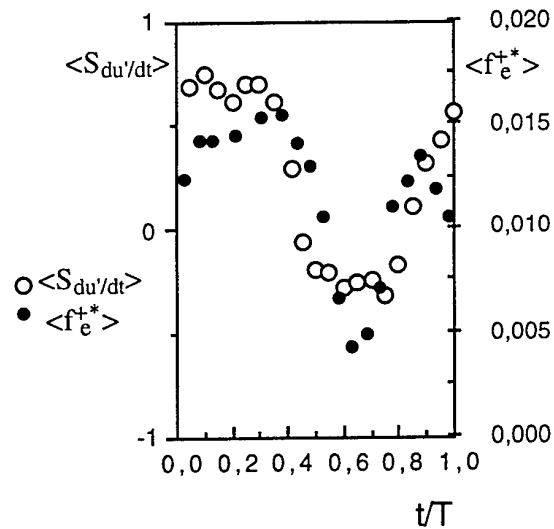


Figure 5 Phase averages at $y^+ = 10$ and $x^+ = 44$: a- Turbulence intensity at $f^+ = 0.017$ and $f^+ = 0.01$; b- Skewness of time derivative of u' and the ejection frequency determined by μ -l technique; the imposed frequency for (b) is $f^+ = 0.017$.

a-

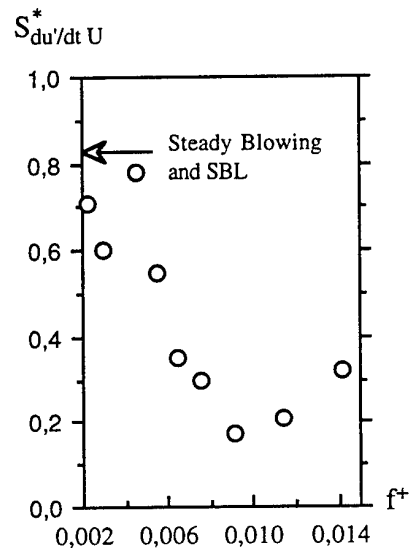
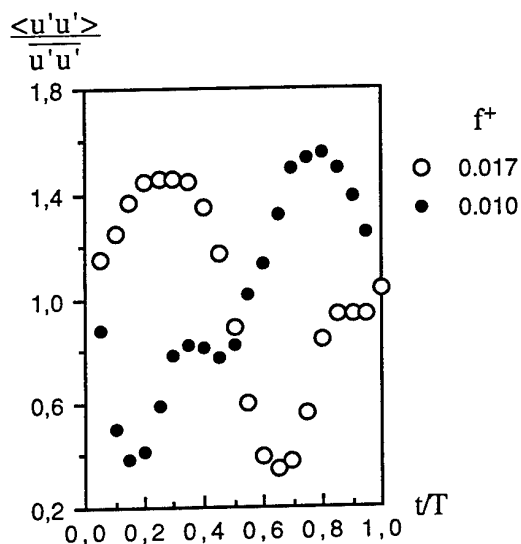


Figure 6 Skewness of the streamwise velocity time derivative at $y^+ = 10$ under unsteady blowing vs. the imposed frequency. $\hat{A}^+ = 5.4$; $U_\infty = 4$ m/s.

Turbulence Modification with Streamwise-uniform Sinusoidal Wall-oscillation

Yoichi MITO and Nobuhide KASAGI
Department of Mechanical Engineering
The University of Tokyo
Hongo 7-3-1
Bunkyo-ku, Tokyo 113
Japan

ABSTRACT

In pursuit of a possible active feedback turbulence control with a flexible wall, a simple oscillatory mode of wall deformation is tested in a turbulent channel flow by using direct numerical simulation. The deformation is spatio-temporally sinusoidal and its parametric conditions are determined with reference to the mean spatio-temporal scales of the quasi-coherent turbulent structures. The substantial influences are observed in the mean flow properties as well as instantaneous flow structures. Among the parameters of the wall deformation, the spanwise wavelength is more effective to the skin friction alteration than the time period. At the moderate strain rate caused by the wall deformation, both skin friction reduction and enhancement are achieved. The turbulent structures are found to be dependent on the scales of the wall deformation at both their enhanced and damped phases.

INTRODUCTION

Technological benefits such as skin friction reduction and heat transfer augmentation can be often achieved by turbulence modification, particularly by altering the turbulent coherent structures, which are known to play central roles in turbulent transport mechanism. For the sake of skin friction reduction, Jung *et al.* (1992) applied spanwise wall oscillations and Choi *et al.* (1994) employed local wall blowing and suction to turbulent channel flows in their recent direct numerical simulations (DNS, hereafter). On the other hand, turbulent heat transfer can be enhanced by using various kinds of vortex generators (Jacobi & Shah 1995) and roughness element (Webb 1987). Among various modes of flow actuation, active wall deformation would be a plausible method. The purpose of this work is to examine the effects of relatively simple wall oscillation modes on the structure of a canonical wall-bounded shear flow.

Presently, by using DNS, this turbulence modification scheme has been tested in a plane channel, of which one of the two walls is subject to deformation. The mode of oscillatory deformation is assumed to be spatio-temporally sinusoidal, and uniform in the streamwise direction. These assumptions reduce the number of parameters prescribed for the flow control and facilitate a parametric analysis. The streamwise uniformity of the wall deformation is intended for its possible interaction with the turbulent structures elongated or long-lived in the streamwise direction. In this work, the discussion is limited to the modification of turbulent momentum transport, although scalar transport is also of great interest. The alteration of skin friction, statistics and turbulent structures is studied to explore the relation between the parameters of wall oscillation and the resultant major influences. A possibility of selective modification among various scales of turbulence is also discussed, through which turbulence

may be distinctly enhanced or attenuated by a particular wall deformation mode.

NUMERICAL SCHEMES

DNS has been extensively used for understanding the fundamental physics of turbulent shear flows (see, e.g., Moin & Spalart (1989) and Kasagi & Shikazono (1995)). The most prevailing means for DNS is to utilize a semi-implicit method for the temporal discretization, by which the solution of the Navier-Stokes equations could be linearized. Presently, the modified Crank-Nicolson type fractional-step method (Choi & Moin 1994), which adopts a delta-form for pressure gradient terms with a more accurate and stable trapezoidal integration scheme, is used for the temporal discretization. By considering the temporal phase of each operator in a fractional-step method (Chorin 1969), it is presently extended to a moving coordinate system as follows:

$$\frac{\hat{q} - q^n}{\Delta\tau} = -\frac{1}{2}(T^{n+1}(\hat{q}) + T^n(q^n)) - \frac{1}{2}(N^{n+1}(\hat{q}) + N^n(q^n)) + \frac{1}{2}(L^{n+1}(\hat{q}) + L^n(q^n)) - G^n(\phi^n), \quad (1)$$

$$\frac{q^* - \hat{q}}{\Delta\tau} = G^n(\phi^n), \quad (2)$$

$$\frac{q^{n+1} - q^*}{\Delta\tau} = -G^{n+1}(\phi^{n+1}), \quad (3)$$

where T , N , L and G denote the moving coordinate terms, convection terms, viscous diffusion terms and gradient operators, respectively. In the above equations, q , \hat{q} and q^* are the volume flux (Rosenfeld *et al.* 1991) and two intermediate vector functions, respectively. The superscript indices, n and $n+1$, denote the reference time steps, τ^n and τ^{n+1} . The scalar function of ϕ^{n+1} in equation (3) can be solved by the following equation,

$$(DG)^{n+1}\phi^{n+1} = \frac{1}{\Delta\tau}Dq^*, \quad (4)$$

where D is a divergence operator. When equation (4) is derived, the continuity equation is used.

A second-order finite difference scheme is used for the spatial discretization of both flow variables and metrics. To compensate data and grid points near a wall, biased interpolative discretization schemes are used. A staggered mesh system is used with additional grid points near the wall to preserve an interpolative discretization manner. For the staggered mesh system, second-order accurate interpolations are necessary in the convective term of a conservative form. In the channel core region, a third-order (four-point for one dimension) interpolation is used to preserve symmetric discretization, whereas second-order accurate (three-point for one dimension) biased interpolative schemes are used

in the near-wall region. Equations (1) and (4) are solved by a Newton method combined with an approximate factorization technique (Choi *et al.* 1992), and by an incomplete LU conjugate gradient squared (ILUCGS) method and a fast Fourier transform algorithm, respectively.

The flow geometry and the coordinate system are shown in figure 1. A fully developed turbulent channel flow is assumed, and periodic boundary conditions are used in the streamwise (x_1) and spanwise (x_3) directions. The simulation is performed under the condition of a constant flow rate throughout the present study. The Reynolds number is 4600 based on the bulk mean velocity U_b and the channel width 2δ (about 150 based on the friction velocity and the channel half-width for the unactuated turbulent channel flow). Hereafter, u_τ represents the friction velocity in the unactuated channel flow, whilst all the data with a superscript + represent quantities non-dimensionalized by u_τ and the kinematic viscosity ν .

The size of the computational volume is $1.25\pi\delta$ in the streamwise direction and $0.375\pi\delta$ in the spanwise direction, which correspond to about 590 and 180 ν/u_τ , respectively. It is about 2.5 and 1.5 times larger than the so-called minimal flow unit (Jiménez & Moin 1991). The number of grid points is $48 \times 97 \times 48$ in the x_1 , x_2 and x_3 directions. Uniform meshes are used in the streamwise and spanwise directions with spacings $\Delta x_1^+ = 12$ and $\Delta x_3^+ = 3.7$, respectively. A non-uniform mesh with a hyperbolic tangent distribution is used in the x_2 direction. The first mesh point away from the wall is given at $x_2^+ = 0.25$. The computational time step is $0.33 \nu/u_\tau^2$. An instantaneous flow field of a fully-developed turbulent channel flow was used for the initial condition. After an initial period of $1300 \nu/u_\tau^2$, statistical averages over a time span of $6500 \nu/u_\tau^2$ were calculated for each case.

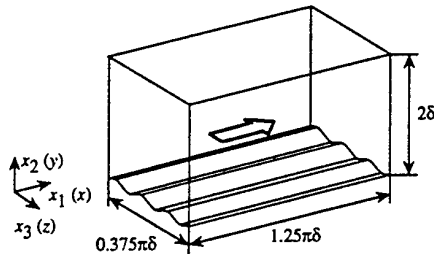


Figure 1 Flow geometry and coordinate system.

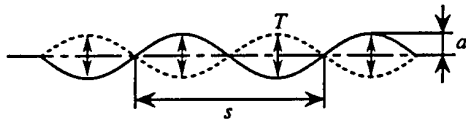


Figure 2 Wall deformation mode.

WALL DEFORMATION MODE

In the present study, one side wall is actuated, whilst the other is kept flat and stationary. The streamwise uniform wall displacement (y_w, z_w) is given by:

$$y_w = a \sin \frac{2\pi x}{s} \sin \frac{2\pi t}{T}, \quad z_w = 0, \quad (5)$$

where a , s and T are the amplitude, spanwise wavelength and time period of the wall oscillation, respectively, as shown in figure 2. With this deformation mode, the cross sectional area of the channel is kept constant. We focus on a possibility of effective turbulence control by acting on turbulent coherent structures, particularly on the longitudinal vortical structures, so that the values of the above parameters are specified by referring to their typical scales (Robinson 1991), e.g., the mean spanwise spacing

of low-speed streaks, $\lambda = 100 \nu/u_\tau$ (Smith & Metzler 1983), the mean diameter of longitudinal vortices, $30 \nu/u_\tau$ (Kim *et al.* 1987), and the time period of longitudinal vortices, $100 \nu/u_\tau^2$ deduced from the mean circulation of longitudinal vortices, 100ν .

As listed in table 1, two spanwise wavelengths are chosen: $s^+ = 90$, which is almost equal to λ , and $s^+ = 45$, which is almost equal to the diameter of vortices. Similarly, but based on the time scale of longitudinal vortices, two time periods are also selected: $T^+ = 50$ and 100 . The oscillatory amplitudes are assumed to be $a^+ = 2.5$ and 5.0 , which are comparable with the thickness of the viscous sublayer. This final assumption has come from an observation that the seeds of turbulence-producing eddies, i.e., longitudinal vortices, lie in the viscous region close to the wall (Brook & Hanratty 1992). Thus, the present mode and parameters for wall oscillation have been designed so that the origin or the initial stage of evolution of the turbulence-producing eddies should be a major control target.

Table 1 Wall deformation parameters.

s^+	T^+	a^+
45, 90	50, 100	2.5, 5.0

SKIN FRICTION

The skin friction coefficient on the oscillating wall, C_{f1} , and the mean skin friction coefficient averaged over the two walls, $C_{f\tau}$, are summarized in table 2. The former is defined as follows:

$$C_{f1} = \left[\frac{1}{\Delta T} \int_{\Delta T} d\tau \cdot \int_{\Gamma_w} \tau_w d\Gamma / \Gamma_{w0} \right] / \left(\rho U_b^2 / 2 \right), \quad (6)$$

where ΔT , Γ_w , Γ_{w0} and τ_w denote the time span of averaging, the instantaneous wall surface area, its projection onto the x_1 - x_3 plane, and the local streamwise wall-shear stress on the oscillating wall, respectively. In table 2, the two Reynolds numbers are also included: $Re_{\tau1}$ and $Re_{\tau\tau}$, based on the friction on the oscillating wall and the mean friction averaged over the two walls, respectively. Presently, three kinds of secondary parameters are calculated as shown in table 2: i.e., a^+/s^+ , a^+/T^+ and a^2/T^+s^+ , which characterize the gradient, the velocity and the strain rate associated with the wall deformation, respectively. The third parameter can also be considered as an specific streamwise vorticity on the deformed wall.

When the same flow rate is given in a laminar flow, the skin friction coefficient is 2.59×10^{-3} . For the present range of parameters, a small extent of skin friction reduction on the oscillating wall is achieved at $(s^+, T^+, a^+) = (45, 50, 2.5)$, $(90, 50, 5.0)$ and $(90, 100, 5.0)$. On the other hand, the skin friction is most enhanced at $(s^+, T^+, a^+) = (45, 100, 5.0)$. Obvious dependence of the skin friction on a^+/s^+ is observed except in the case of $(s^+, T^+, a^+) = (45, 100, 2.5)$, i.e., the skin friction becomes larger in the cases of $a^+/s^+ = 0.113$ than in the cases of $a^+/s^+ = 0.057$, whereas no systematic correlation is observed between the skin friction and a^+/T^+ . The moderate value of a^2/T^+s^+ around 5×10^{-3} is found to be effective to the skin friction alteration, e.g., in the cases of $(s^+, T^+, a^+) = (45, 100, 5.0)$ and $(90, 100, 5.0)$, where the skin friction is noticeably enhanced and reduced. Hence, the following comparison and discussion are restricted to the cases of the larger amplitude, $a^+ = 5.0$, with which the skin friction is altered distinctly.

For the present wall deformation modes, the ratio of actuating power input to the main flow pumping power, ϕ , is defined as:

$$\phi = - \int_{\Gamma_w} \left(u_n k + u_n p - \frac{1}{Re} \frac{\partial k}{\partial n} \right) d\Gamma / Q \Delta p_1, \quad (7)$$

Table 2 Skin friction coefficients.

s^*	T^*	a^*	a^*/s^*	a^*/T^*	a^{*2}/T^*s^*	C_{f1}	$Re_{\tau 1}$	C_{fT}	$Re_{\tau T}$
unactuated									
45	50	2.5	0.057	0.048	2.7×10^{-3}	8.46×10^{-3}	151	8.53×10^{-3}	151
		5.0	0.113	0.096	10.8	8.71	153	8.59	152
	100	2.5	0.057	0.026	1.4	8.64	152	8.51	151
		5.0	0.113	0.051	5.8	9.20	157	8.90	155
90	50	5.0	0.057	0.096	5.4	8.46	151	8.48	151
	100	5.0	0.057	0.051	2.9	8.46	151	8.60	152

where k , Δp_1 , Q and n denote the kinetic energy, the pressure drop in the streamwise direction, the total flow rate and the wall-normal, respectively. The above ratio reaches around a percent at the instantaneous maximum in the case of $(s^*, T^*, a^*) = (90, 50, 5.0)$, but all of the averaged values are found to be about 0.1 percent. Thus, the extra power input for the present turbulence modification remains negligibly small.

STATISTICS

The time-averaged statistics have been obtained by interpolating data at each distance from the mean height of the oscillating wall. The third-order and second-order interpolations are used in the channel-core and near-wall regions, respectively. Thus, the local zones covered by the wall oscillation are excluded from the averaging.

The mean velocity profiles on the oscillating walls are shown in figure 3. In all cases with wall oscillation, the mean flows are decelerated to almost the same extent compared with the unactuated case, although there are obvious differences in the skin friction coefficients as shown in table 2. This fact means that an intrusion of high momentum fluid is impeded with the wall oscillation, and this leads to a shift of the virtual origin from the mean height of the wall.

Figures 4 to 6 show the distributions of root-mean-square velocity fluctuations on the oscillating walls. There is observed little difference in the streamwise velocity fluctuations (figure 4), whereas the wall-normal (figure 5) and spanwise (figure 6) components are much enhanced in the case of $(s^*, T^*, a^*) = (45, 100, 5.0)$ and reduced in the case of $(s^*, T^*, a^*) = (90, 100, 5.0)$. In these two cases, the skin friction have been likewise enhanced and reduced, respectively, as shown in table 2.

The increase and decrease of the cross-stream velocity fluctuations are also reflected in the Reynolds shear stress distributions on the oscillating walls as shown in figure 7. In the case of the increased skin friction when $(s^*, T^*, a^*) = (45, 100, 5.0)$, the Reynolds shear stress is markedly increased, whereas it is decreased when $(s^*, T^*, a^*) = (90, 100, 5.0)$.

For these two extreme cases, the vorticity distribution on the oscillating wall is shown in figure 8. In general, the vorticity fluctuations are enhanced with the wall deformation. It is evident, however, that a difference exists between the two cases in figure 8. When $s^* = 45$, with the marked increase in ω_{x+}^{*rms} , both ω_{y+}^{*rms} and ω_{z+}^{*rms} are even more increased. On the other hand, ω_{x+}^{*rms} is little changed when $s^* = 90$, although two other components show appreciable increase. It is noted that ω_{x+}^* is the vorticity component induced by the wall deformation, and hence there is much difference in the degrees of receptivity of the near-wall region in these two cases with $s^* = 45$ and 90.

TEMPORAL EVOLUTION

Skin Friction

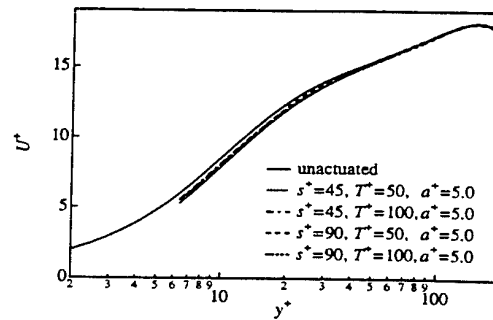


Figure 3 Mean velocity profiles.

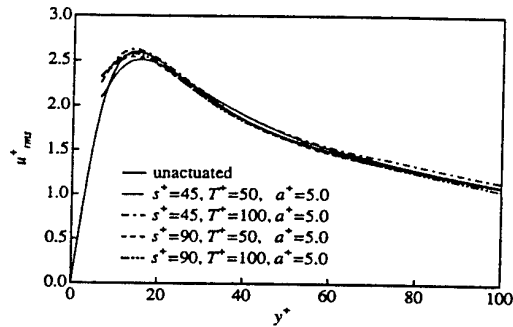


Figure 4 Rms streamwise velocity fluctuations.

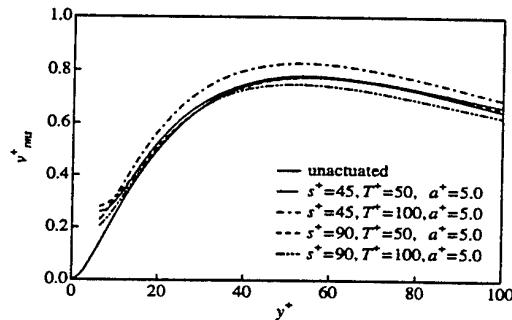


Figure 5 Rms wall-normal velocity fluctuations.

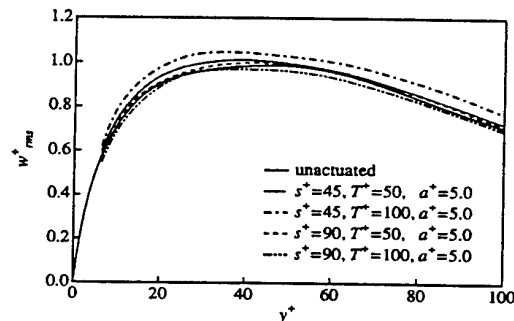


Figure 6 Rms spanwise velocity fluctuations.

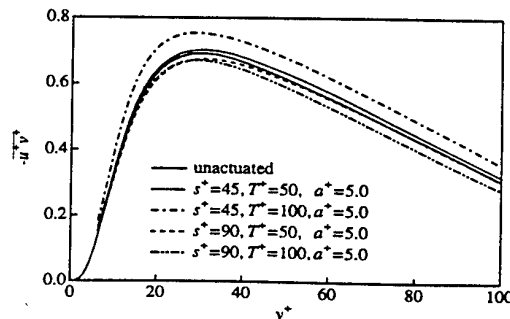


Figure 7 Reynolds shear stresses.

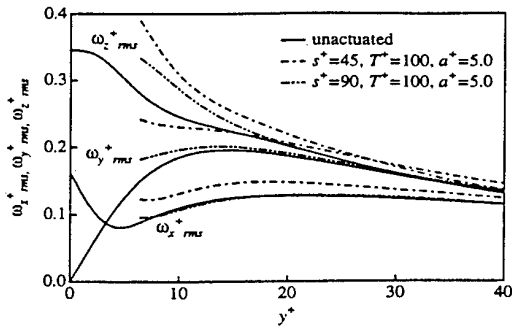


Figure 8 Rms vorticity fluctuations.

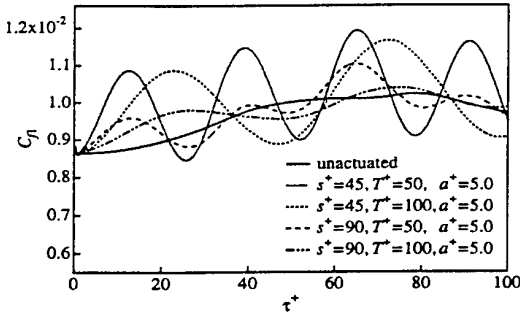


Figure 9 Time trace of skin friction coefficient in the initial period of flow control.

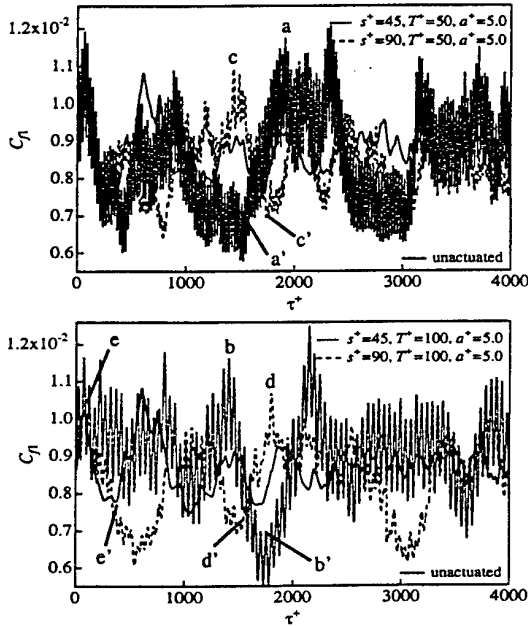


Figure 10 Time trace of skin friction coefficient. Indices a to e and a' to e' represent the time instants of the instantaneous flow fields shown in figures 11 to 14.

Figure 9 shows the initial time trace of instantaneous skin friction coefficient on the oscillating wall after the wall oscillation is started. Figure 10 shows the long-range time traces of skin friction coefficient on the oscillating wall. Each time trace has two undulations during each time period of wall oscillation because of the symmetric effects of the former and latter halves of the wall oscillation period. The amplitude of these short-period undulation of the skin friction coefficient becomes larger for the smaller spanwise wavelength of $s^+ = 45$ than for the larger wavelength of $s^+ = 90$. In addition to the short-period undulations shown in figure 9, there exist long-period undulations caused by the structural alteration of turbulence, which is illustrated by their

visualization in the next section. With these long-period undulations, the skin friction coefficient sometimes leaps to a much larger extent of reduction or enhancement than that in the unactuated case.

Turbulent Coherent Structures

Figures 11a to 11d show the turbulent structures over the oscillating walls at the maximum displacement phase of wall oscillation in the periods of increased skin friction. Figure 11e shows the turbulent structures also in a period of large skin friction in the unactuated channel. The time instant for each case is referred to as indices a to e in figure 10. The low-pressure regions, low-speed streaks and high-speed regions are visualized in these figures, where the fluctuations are calculated based on the mean value at the equivalent dimensionless height, $x_z^+/(2\delta-y_w^+)$ in the unactuated case. The low-pressure regions mostly correspond to vortex core regions (Robinson 1991, Kasagi *et al.* 1995). In these periods, the turbulent structures seem to be much enhanced compared to those visualized in the periods of smaller skin friction. With the smaller spanwise wavelength $s^+ = 45$, the smaller-scale turbulent structures are frequently induced and intensified on the oscillating walls. On the other hand, no apparent dependence on the time period of the wall oscillation is discerned as long as the instantaneous turbulent structures are concerned.

The velocity vector distributions in the cross sections, which are denoted in figure 11, are shown in figure 12 with the gradation contours of the streamwise velocity fluctuation. Only the three cases in figure 11 are chosen here, i.e., 11b, d and e in which turbulence is enhanced, suppressed and unactuated, respectively. In general, the high-speed region often emerges on the crest of wall deformation, whereas the low-speed region is frequently formed in the valley. This fact is also illustrated in the wall-shear distributions on the oscillating walls in figure 13. By imposing the wall oscillation, the cross-stream fluctuations are largely enhanced close to the walls (see, figures 5 and 6), which sometimes leads to intrusions of high-speed fluid into the valleys as shown in 12b and 12d. Although many small longitudinal vortices are found in figure 12d, large-scale high-momentum regions seem to be kept away from the wall. The similar effect has been observed by Choi *et al.* (1993).

The enhanced turbulent structures shown in figures 11 to 13 are markedly damped at the periods of reduced skin friction as shown in figure 14. Each picture is taken again at the maximum displacement phase of wall oscillation. Figure 14e' shows the turbulent structures in the unactuated case. These time instant are also indicated to as indices a' to e' in figure 10. From the comparison of these pictures with those in figure 11, it is obvious that the difference between the turbulent structures observed in the periods of the increased and decreased skin friction is much larger in the actuated channels than in the unactuated one. In the former, the turbulent energy-producing vortices, denoted as the low-pressure regions, are hardly visible, although the elongated streaky structures are still formed being well aligned with the streamwise-uniform deformation of the wall. These streaky structures become gradually unstable and produce new growing vortices with time, and eventually the whole flow field returns to the activated state at the period of increased skin friction.

CONCLUSIONS

Direct numerical simulation of turbulent channel flow with a oscillatorily deformed wall has been performed by using a temporally rigorous numerical scheme. The time traces of the skin friction coefficient and the evolution of the turbulent

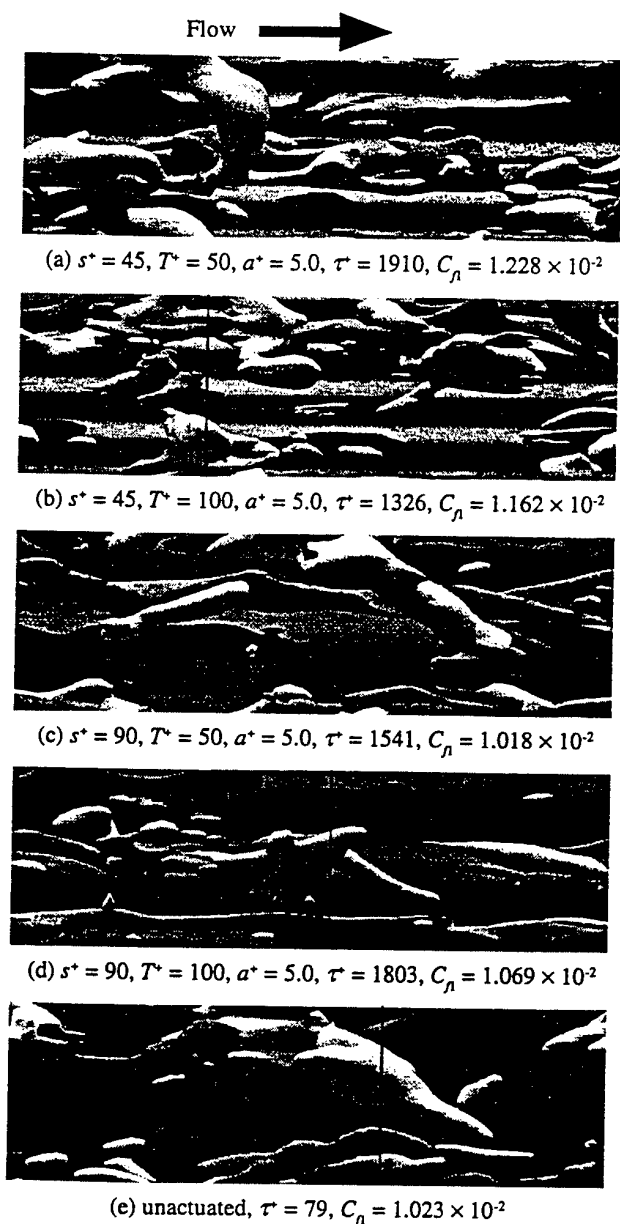


Figure 11 Turbulent coherent structures on the oscillating walls at large skin-friction instants shown in figure 10. Cases a to d correspond to the phase of the maximum displacement for each wall oscillation mode. White: $p^* = -2.5$, light gray: $u^* = -3.5$, dark gray: $u^* = 3.5$.

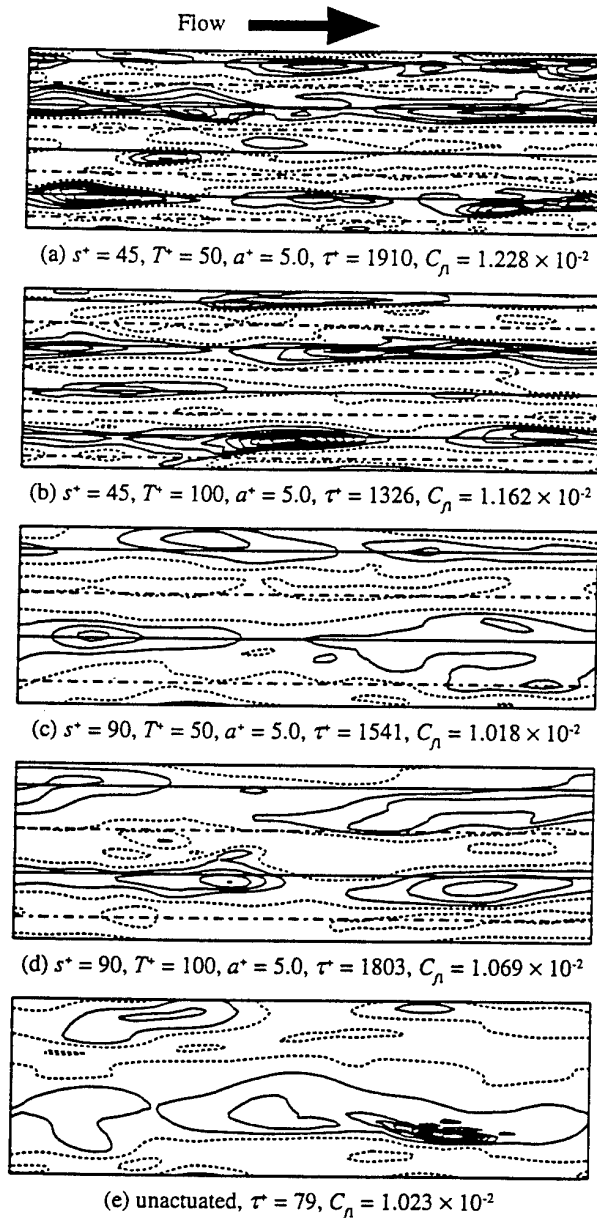


Figure 13 Wall shear stress τ_w^+ distributions on the oscillating walls at the same instants with figure 11. The contour levels range from 0.5 to 5.0 by increments of 0.5. Smaller contours, 0.5 and 1.0, are dotted. Crests and valleys of wall deformation are also shown by solid and dashed lines, respectively.

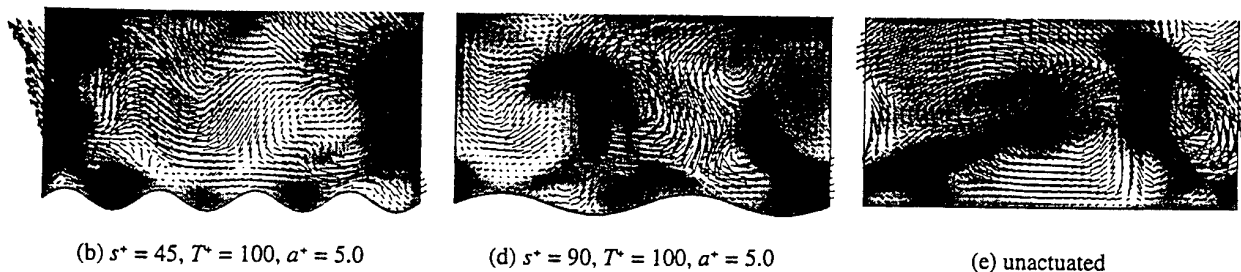
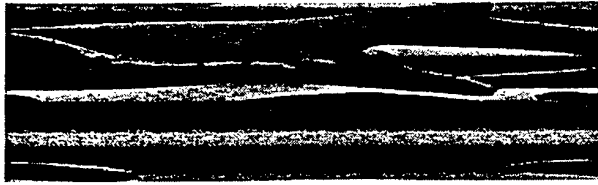


Figure 12 Low-speed streaks and velocity vectors on the oscillating walls in the cross sections shown in figure 11. Black to white: $u^* = -3.5$ to 3.5.

Flow →



(a') $s^+ = 45$, $T^+ = 50$, $a^+ = 5.0$, $\tau^+ = 1488$, $C_f = 7.60 \times 10^{-3}$



(b') $s^+ = 45$, $T^+ = 100$, $a^+ = 5.0$, $\tau^+ = 1705$, $C_f = 6.96 \times 10^{-3}$



(c') $s^+ = 90$, $T^+ = 50$, $a^+ = 5.0$, $\tau^+ = 1572$, $C_f = 7.25 \times 10^{-3}$



(d') $s^+ = 90$, $T^+ = 100$, $a^+ = 5.0$, $\tau^+ = 1507$, $C_f = 7.28 \times 10^{-3}$



(e') unactuated, $\tau^+ = 362$, $C_f = 7.78 \times 10^{-3}$

Figure 14 Turbulent coherent structures on the oscillating walls at small skin-friction instants shown in figure 10. Cases a' to d' correspond to the phase of the maximum displacement for each wall oscillation mode. White: $p^+ = -2.5$, light gray: $u^+ = -3.5$, dark gray: $u^+ = 3.5$.

structures on the oscillating wall have been drastically changed by imposing a streamwise-uniform sinusoidal wall oscillation. Among the present parameters, the spatial scale, i.e., the spanwise wavelength, is more effective to the turbulence modification than the temporal scale, i.e., the time period. Both the skin friction reduction and enhancement can be achieved at the moderate strain rate of the wall deformation. The skin friction alteration is also reflected on ω_{rms}^+ as a consequence of the receptivity of near wall region. Visualization of turbulent structures has illustrated that the turbulence structures are largely dependent on the spatial scales of the wall deformation. The difference between the turbulent structures observed in the periods of the increased and decreased skin friction become much larger in the actuated channels than in the unactuated one.

This work was supported by Ministry of Education, Science,

Culture and Sports through the Grant-in-Aid for Developmental Scientific Research (No. 08455102).

REFERENCES

- Brook, J. W., and Hanratty, T. J., 1993, "Origin of Turbulence-Producing Eddies in a Channel Flow," *Physics of Fluids A*, Vol. 5, pp. 1011-1022.
- Choi, H., Moin, P., and Kim, J., 1992, "Turbulent Drag Reduction: Studies of Feedback Control and Flow over Riblets," Rep. TF-55, Department of Mechanical Engineering, Stanford University.
- Choi, H., Moin, P., and Kim, J., 1993, "Direct Numerical Simulation of Turbulent Flow over Riblets," *Journal of Fluid Mechanics*, Vol. 255, pp. 503-539.
- Choi, H., and Moin, P., 1994, "Effects of the Computational Time Step on Numerical Solutions of Turbulent Flow," *Journal of Computational Physics*, Vol. 113, pp. 1-4.
- Choi, H., Moin, P., and Kim, J., 1994, "Active Turbulence Control for Drag Reduction in Wall-Bounded Flows," *Journal of Fluid Mechanics*, Vol. 262, pp. 75-110.
- Chorin, A. J., 1969, "On the Convergence of Discrete Approximations to the Navier-Stokes Equations," *Mathematics of Computation*, Vol. 23, pp. 341-353.
- Jacobi, A. M., and Shah, R. K., 1995, "Heat Transfer Surface Enhancement through the Use of Longitudinal Vortices: A Review of Recent Progress," *Experimental Thermal and Fluid Science*, Vol. 11, pp. 295-309.
- Jiménez, J., and Moin, P., 1991, "The Minimal Flow Unit in Near-Wall Turbulence," *Journal of Fluid Mechanics*, Vol. 225, pp. 213-240.
- Jung, W. J., Mangiavacchi, N., and Akhavan, R., 1992, "Suppression of Turbulence in Wall-Bounded Flows by High-Frequency spanwise oscillations," *Physics of Fluids A*, Vol. 8, pp. 1605-1607.
- Moin, P., and Spalart, P. R., 1989 "Contributions of Numerical Simulation Data Bases to the Physics, Modeling, and Measurement of Turbulence," *Advances in Turbulence*, edited by George, W. K., and Arndt, R., Hemisphere, New York, pp. 11-38.
- Kasagi, N., Sumitani, Y., Suzuki, Y., and Iida, O., 1995, "Kinematics of the Quasi-coherent Vortical Structure in Near-wall Turbulence," *International Journal of Heat and Fluid Flow*, Vol. 16, pp. 2-10.
- Kasagi, N., and Shikazono, N., 1995, "Contribution of Direct Numerical Simulation to Understanding and Modelling Turbulent Transport," *Proceedings of the Royal Society of London A*, Vol. 451, pp. 257-292.
- Kim, J., Moin, P., and Moser, R., 1987, "Turbulence Statistics in Fully Developed Channel Flow at Low Reynolds Number," *Journal of Fluid Mechanics*, Vol. 177, pp. 133-166.
- Robinson, S. K., 1991, "The Kinematics of Turbulent Boundary Layer Structure," NASA TM-103859.
- Rosenfeld, M., Kwak, D., and Vinokur, M., 1991, "A Fractional Step Solution Method for the Unsteady Incompressible Navier-Stokes Equations in Generalized Coordinate Systems," *Journal of Computational Physics*, Vol. 94, pp. 102-137.
- Smith, C. R., and Metzler, S. P., 1983, "The Characteristics of Low-Speed Streaks in the Near-Wall Region of a Turbulent Boundary Layer," *Journal of Fluid Mechanics*, Vol. 129, pp. 27-54.
- Webb, R. L., 1987 "Enhancement of single-phase heat transfer," *Handbook of Single-Phase Convective Heat Transfer*, edited by Kakaç S., Shah, R. K., and Aung, W., John Wiley & Sons, New York, pp. 17.1-17.62.

OPTIMUM FEEDBACK CONTROL OF VORTEX SHEDDING FROM A CIRCULAR CYLINDER BY ROTARY OSCILLATIONS USING A NEURAL NETWORK

N. FUJISAWA

Department of Mechanical Engineering
Niigata University
8050, Ikarashi-nino-chou
Niigata, 950-21
Japan

T. Nakabayashi

Department of Mechanical Engineering
Gunma University
1-5-1 Tenjin
Kiryu, 376
Japan

ABSTRACT

The active feedback control of vortex shedding from a circular cylinder by rotary cylinder oscillations is studied experimentally using neural networks, which optimizes automatically the control parameters such as the phase lag and the feedback coefficient. This optimization procedure is applied to find out an optimum position of reference probe to attenuate the vortex shedding effectively. The attenuation effect of vortex shedding under this control is investigated by measuring the velocity fluctuations in the cylinder wake and the oscillating pressure distributions over the cylinder surface. It is found that the drag and lift forces acting on the cylinder are reduced under the optimum reference control in comparison with the control with other reference positions as well as those of the stationary cylinder. The attenuation mechanism of vortex shedding is discussed based on the measured pressure distributions and the flow visualization results.

INTRODUCTION

Vortex streets are formed in the wake of a bluff body over a wide range of Reynolds numbers. The formation of vortex streets may cause the vortex induced vibration on the bluff body structure, which appears strongly when the frequency of vortex shedding approaches close to the natural frequency of structures. When the oscillation of the bluff body structure is synchronized to the vortex shedding, the vorticity is intensified and the velocity fluctuations in the cylinder wake are magnified. This dynamic state of flow is known to have adverse effects on engineering structures arousing an interest in the control of vortex shedding (Blevins, 1990). Passive method for attenuating the vortex shedding from the bluff body structure has been developed through ad hoc experiments, but it is rather difficult to obtain a high performance of vortex attenuation, so that the research attention is shifted to the active controls. Recently, active methods for controlling the vortex shedding from a circular cylinder are investigated by simple rotary oscillations and the results are summarized in a review paper by Griffin and Hall (1994). More recently, the active feedback control of vortex shedding from a circular cylinder is investigated by using acoustic sounds (Ffowcs-Williams and Zhao 1989), cross-flow cylinder oscillations (Warui and Fujisawa 1995) and rotary cylinder oscillations (Fujisawa and Kawaji 1995). They adopt a reference velocity signal in the cylinder wake and the signal is fed back to the supplied sounds or the cylinder motions. The feedback signal is multiplied by a factor of feedback coefficient with a certain phase between the reference signal and the control signal. However, the optimum control parameters of feedback coefficient

and phase lag are expected to vary with the geometry of bluff body and the flow conditions. They can be determined from optimization experiments by varying the feedback coefficients and phase lags in a wide range, but it is not convenient for practical applications. Therefore, it is useful to discuss an automatic optimization technique to determine the control parameters of the active feedback controls.

The objective of the present paper is to investigate the automatic optimization procedures with neural networks for determining the control parameters in active feedback controls. This procedure is applied to an active feedback control of vortex shedding by rotary cylinder oscillations and the optimum position of reference probe is discussed to attenuate the vortex shedding effectively. Further, the attenuation mechanism is studied based on the measured pressure distributions and visualized flow field.

EXPERIMENTAL APPARATUS AND PROCEDURES

Experimental Techniques

Figure 1 shows an illustration of the test section and the velocity feedback mechanism employed in the present study. The coordinate system is chosen in such a way that x-axis is along the flow direction, y-axis is in the vertical direction perpendicular to the flow, and the origin is located at the center of the cylinder. The experiments are carried out in a low-speed wind tunnel with a test-section of square cross-section of $0.5\text{m} \times 0.5\text{m}$ and 1.5m long providing a uniform flow velocity. A smooth circular cylinder of radius $R=50\text{mm}$ is positioned at the center of the open test-section with two side walls, spanning the axis normal to the flow direction. Two hot-wires are positioned in the cylinder wake, one for detecting the reference velocity signal in the cylinder wake for the feedback control and the other for measuring the velocity fluctuations in the cylinder wake in response to the control. The former probe can be traversed in the cylinder wake, while the latter probe is fixed at the lower shear layer ($x/R=3$, $y/R=-1.6$) to observe the typical response of the wake. The reference velocity at the shear layer from the cylinder is processed through linearizer, high pass filter and low pass filter to a microcomputer fitted with AD and DA converter. The output signal from the DA converter is supplied to the AC servo motor, which provides a rotary oscillation of a circular cylinder. The phase lag ϕ between the velocity signal and the monitored angular velocity signal and the feedback coefficient α ($=R \delta \omega / \delta u_r$) are set in the computer, where ω is an angular velocity of the cylinder and u_r is a fluctuating reference velocity. More details of the feedback control are described by Fujisawa and Kawaji (1995).

Measurements of pressure distributions over the cylinder surface are carried out to estimate the aerodynamic performance of the cylinder, which is performed at the free stream velocity $U=3\text{m/s}$. In order to obtain an insight into the flow mechanism of the vortex evolution and the corresponding formation, the flow field around the cylinder is visualized by smoke-wire method and the cylinder motion is evaluated by the simultaneous data sampling technique. The visualization study is made at the free stream velocity $U=1\text{m/s}$. More details of the experimental techniques are described by Fujisawa and Kawaji(1995).

Neural Networks

Figure 2 shows an illustration of the neural networks used in the present study, which consists of three layers of neurons with back propagation algorithm. There are 2 units for the input layer, 3 for the hidden layer, and 1 for the output layer. The phase lag ϕ and the feedback coefficient α are selected as the input parameters. They are modified by minimizing the error function $E=(J-O)^2/2$ and changing the weights between each unit and also the input parameters, where J is a evaluation function and O is an object function. It is noted that the weight and the input parameters are modified by the delta rule. Details of the neural network model are described by Li and Nagaya (1995). For application of this model to the present study, the evaluation function is expressed as $J=\int_0^T u_i^2 dt$ and the object function is set to zero, where u_i is the velocity fluctuations at the reference probe, t is the time, and T is the integration time. Therefore, the error function is minimized by modifying the input parameters ϕ and α for every estimation of weights by back propagation algorithm. The selection of the integration time is important to stabilize the neural network model. When the integration time T is set to less than 20 wave lengths, the neural network is unstable, which is due to the unsteadiness of the velocity fluctuations in the cylinder wake. It is found that an increase in the integration time stabilizes the neural networks, but the increase in the integration time enlarges the computing time of neural network and the response to the disturbance becomes too slow. Therefore, the integration time is reduced to 7 wave lengths and the evaluation function is averaged over previous 5 set of evaluation functions, which improves both the stability and the response.

RESULTS AND DISCUSSIONS

Effect of Active Control on Vortex Shedding

Figure 3(a),(b) shows the effect of phase lag ϕ (a) and feedback coefficient (b) of the active control on the mean and fluctuating velocities at the fixed probe ($x/R=3, y/R=1.6$), respectively, which are shown for the three reference probe positions, that is at ($x/R=3, y/R=-1.6$), ($x/R=4, y/R=-2.4$), ($x/R=3, y/R=0$). Here, the feedback coefficient α in Fig.3(a) is set to 0.48 and the phase lag ϕ in Fig.3(b) is fixed to the optimum phase, where the minimum velocity fluctuations are observed in Fig.3(a). It is clearly seen from these figures that the velocity fluctuations at the fixed probe is strongly influenced by the variations of phase lag and feedback coefficient. The minimum velocity fluctuations under the control with optimum control parameters is smaller than that of the stationary cylinder, which indicates the attenuation of vortex shedding. Among the results of three reference probe positions, the smallest velocity fluctuations are observed at the reference probe position ($x/R=4, y/R=-2.4$). Therefore, the results indicate that the performance of the active feedback control depends on the control parameters and the reference probe position.

Optimization of Control Effect by Neural Networks

Figure 4(a)-(c) shows a typical example of flow response by the active feedback control with neural networks and the corresponding variations of phase lag ϕ and feedback coefficient α , respectively, which are plotted against the time after the start of the control. Here, the reference probe is set to ($x/R=4, y/R=-2.4$). As can be seen in Fig.4(a), the control effect can be recognized on the traces of velocity fluctuations at the fixed probe around the time $t=150\text{ sec.}$, in comparison with the stationary cylinder. Hereafter, the control effect is strengthened as the time increases and reaches a steady state for further increase in time. Corresponding to the reduction in velocity fluctuations in Fig.4(a), the phase lag ϕ decreases from the initial value as shown in Fig.4(b) and the feedback coefficient increases as shown in

Fig.4(c). However, these changes in the velocity fluctuations and control parameters are fluctuating unsteadily, reflecting the unsteady nature of the cylinder wake.

Figure 5(a)-(c) indicates the map of optimized velocity fluctuations at the fixed probe, the corresponding values of phase lag and feedback coefficient, respectively, which are obtained from the present optimization with neural networks. These results are obtained by traversing the reference probe in the cylinder wake in a range of $x/R=0-6$ and $y/R=-3-0$. Figure 5(a) indicates that the smallest velocity fluctuations are obtained when the reference probe is set around ($x/R=4, y/R=-2.5$) and the area of small velocity fluctuations extends from the cylinder side to the downstream inclining to the outward. On the other hand, the optimization study with neural networks is not applicable to the shaded area behind the cylinder, because the variations of velocity fluctuations with the control parameters are very small to find out the optimum values in Fig. 3. It should be noted that the control effect on the vortex shedding is not expected for the reference probe behind the cylinder, as can be seen in Fig.3. The optimum phase lag is found around $\phi=180^\circ$ and the optimum feedback coefficient is near $\alpha=0.45$. The optimum phase lag decreases as the reference probe moves downstream and the optimum feedback coefficient increases in the outside of the cylinder wake, reflecting the distance between the reference probe and the cylinder and the distributions of velocity fluctuations in the cylinder wake, respectively.

Fluid Force Characteristics

Figure 6 indicates the distributions of drag and lift coefficient $C_d (=F_x/\rho U^2 R)$, $C_l (=F_y/\rho U^2 R)$ acting on the cylinder with and without active control, which are plotted against the phase angle ψ of vortex shedding. Here, F_x and F_y are streamwise and normal fluid forces acting on the cylinder, respectively, and the phase angle ψ is defined in the reference fluctuating velocity distributions, that is, $\psi=0^\circ$ is the phase angle where the fluctuating velocity changes from negative to positive and $\phi=360^\circ$ for the 1 wave length. The active control results in this figure is for the two reference probe positions ($x/R=3, y/R=-1.6$) and ($x/R=4, y/R=-2.4$). It is clearly seen that the aerodynamic performance of the cylinder is improved by the present active controls, in comparison with the stationary cylinder. The comparison between the active controls at two different reference probe position indicates that a better aerodynamic performance appears in the result of the reference probe position ($x/R=4, y/R=-2.4$) than that of ($x/R=3, y/R=-1.6$), reflecting the map of optimized velocity fluctuations in Fig.5. These results indicate that the aerodynamic performance of the cylinder is much improved by the active feedback control with optimum reference probe position, suggesting the usefulness of the present neural network optimization procedures.

Variations of Pressure Distributions and Flow Fields

The phase-averaged pressure distributions over the cylinder surface and the visualized flow field with and without the active control are given in Fig. 7(a),(b) and Fig.8(a),(b) for various phase angles $\psi=0^\circ, 90^\circ, 180^\circ, 270^\circ$ of vortex shedding, respectively. The pressure distributions over the cylinder surface are modified by the active control to reduce the variations of pressure distributions, which appears strongly on both sides of the cylinder where the flow separation occurs. It is expected that the unsteady movement of the separation point over the cylinder surface is suppressed by the active feedback control. Corresponding variations of flow field are recognized on the visualization results. That is, the roll up and roll down motion of vortex shedding in the near wake as clearly seen in the stationary cylinder are weakened by the active control effect, so that the cylinder wake develops almost straight in the downstream under the control. It can be considered that the vortex shedding from a circular cylinder is dynamically attenuated by the oscillating cylinder motion of active feedback control, which acts to attenuate the movement of separation point over the cylinder surface.

CONCLUSIONS

The active control of vortex shedding from a circular cylinder by rotary oscillations is studied experimentally using a neural network for optimizing the control parameters, such as the phase

(4) The mechanism of vortex shedding attenuation by the active feedback control is investigated based on the measured pressure distributions and flow visualizations around the cylinder. It is found that the movement of the separation point over the cylinder surface is suppressed and the roll-up and roll-down motion of the vortex formation near the cylinder is effectively weakened by the rotary cylinder motion.

Warui, H.M. and Fujisawa, N., 1996, "Feedback Control of Vortex Shedding from a Circular Cylinder by Cross-Flow Cylinder Oscillations" Experiments in Fluids, Vol.21, pp.49-56.

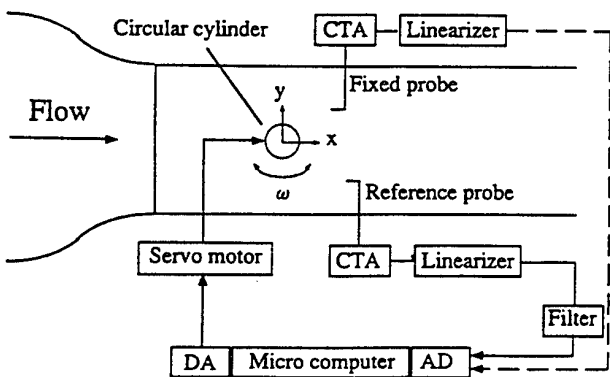


Diagram illustrating a neural network structure with three layers: Input layer, Hidden layer, and Output layer.

- Input layer:** Contains nodes 0, 1, and 2.
- Hidden layer:** Contains nodes 0, 1, 2, and 3.
- Output layer:** Contains node 1.

Connections and weights are shown:

- Node 0 in the Input layer connects to nodes 0 and 1 in the Hidden layer with weights of -1.
- Node 1 in the Input layer connects to nodes 1, 2, and 3 in the Hidden layer with weights of 1.
- Node 2 in the Input layer connects to nodes 2 and 3 in the Hidden layer with weights of 1.
- Node 1 in the Output layer receives input from node 1 in the Hidden layer and an external input J .
- The output of the network is O .
- A feedback loop labeled α and ϕ connects the output O back to the input nodes 1 and 2.

Figure 10 consists of two subplots, (a) and (b), showing the normalized root-mean-square velocity fluctuation $\sqrt{u_f^2}/U$ on the y-axis (ranging from 0.1 to 0.4).

Subplot (a) shows the fluctuation as a function of the azimuthal angle ϕ (in degrees) on the x-axis (ranging from 100 to 800). Three data series are plotted:

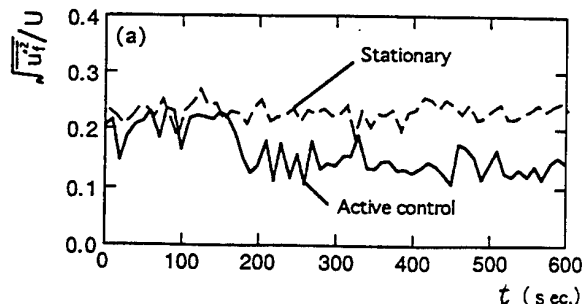
- $(3R, -1.6R)$: represented by solid circles, showing a fluctuation that peaks around $\phi = 550^\circ$ and dips around $\phi = 250^\circ$.
- $(4R, -2.4R)$: represented by open squares, showing a fluctuation that peaks around $\phi = 450^\circ$ and dips around $\phi = 200^\circ$.
- $(3R, 0)$: represented by open triangles, showing a fluctuation that is relatively constant around 0.22.

 A horizontal line at $\sqrt{u_f^2}/U \approx 0.22$ is labeled "Stationary".

Subplot (b) shows the fluctuation as a function of the angle α on the x-axis (ranging from 0.0 to 1.0). The same three data series are plotted:

- $(3R, -1.6R)$: represented by solid circles, showing a fluctuation that generally increases with α .
- $(4R, -2.4R)$: represented by open squares, showing a fluctuation that generally decreases with α .
- $(3R, 0)$: represented by open triangles, showing a fluctuation that is relatively constant around 0.22.

Figure 3: Effect of control parameters on velocity fluctuations at fixed probe $\sqrt{u_1'^2}/U$
(a) Phase lag ϕ , (b) Feedback coefficient α .



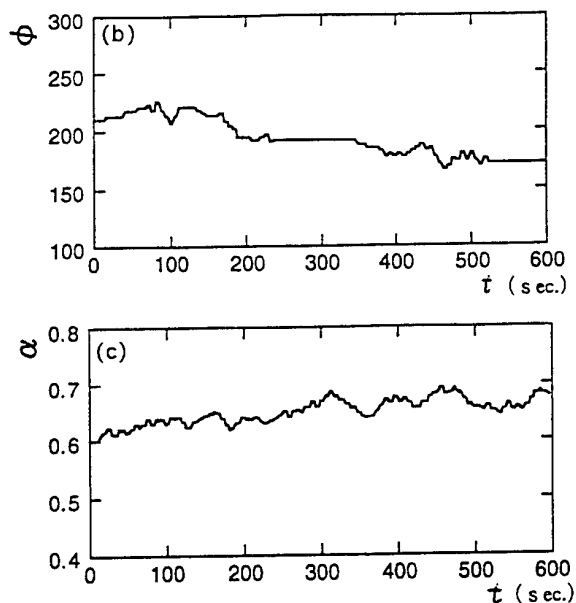


Figure 4: Time variations of reference velocity fluctuations and control parameters under active feedback control with neural network.
(a) Velocity fluctuations $\sqrt{u_r^2}/U$, (b) Phase lag ϕ , (c) Feedback coefficient α

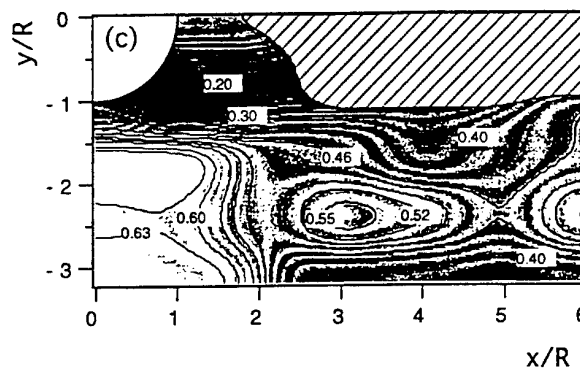
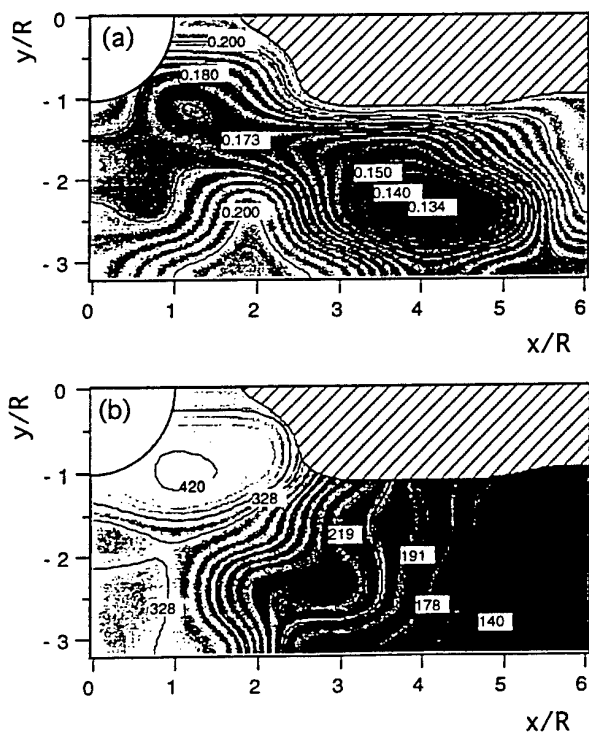


Figure 5: Distributions of optimum velocity fluctuations at fixed probe and optimum control parameters obtained from active control with neural network.
(a) Velocity fluctuations $\sqrt{u_r^2}/U$, (b) Phase lag ϕ , (c) Feedback coefficient α

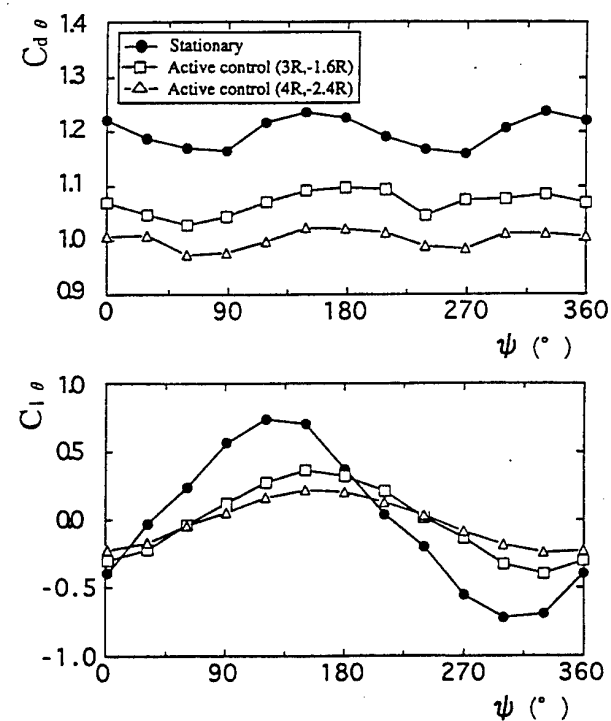


Figure 6: Phase-averaged drag and lift coefficient $C_{d\theta}, C_{l\theta}$ in relation to phase angle ψ of vortex shedding.
(a) Drag coefficient $C_{d\theta}$, (b) Lift coefficient $C_{l\theta}$

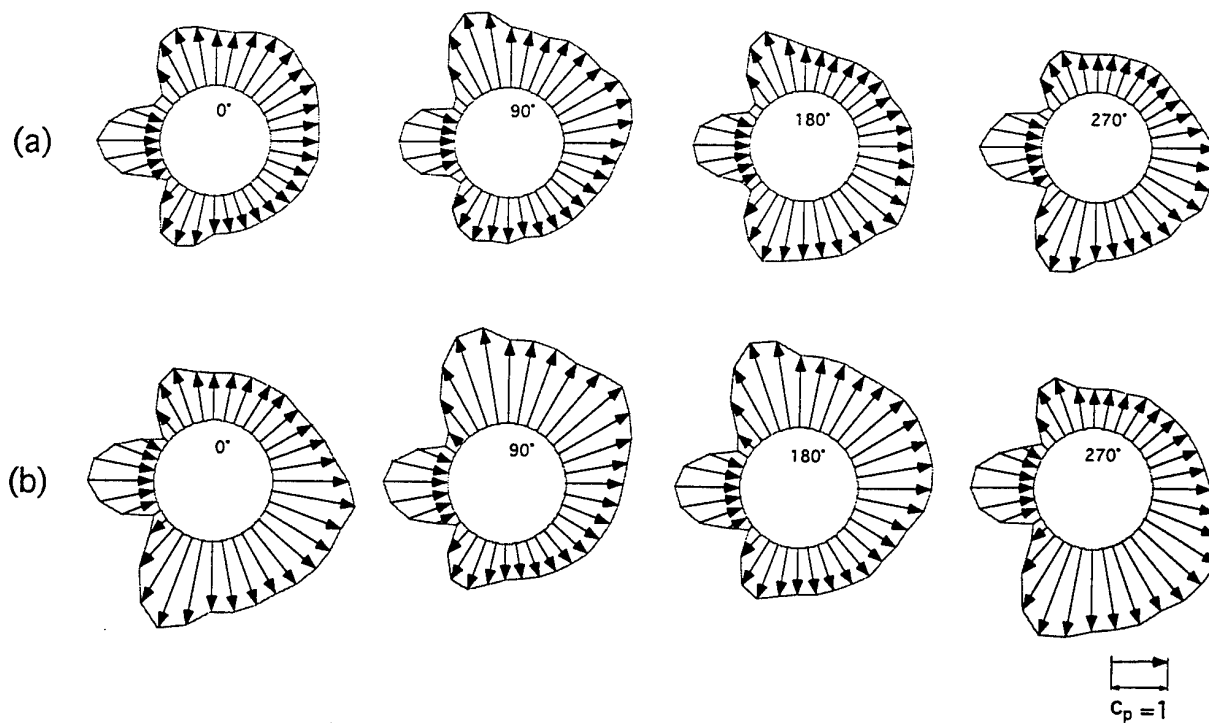


Figure 7: Pressure distributions over cylinder surface with and without control.
 (a) Optimum reference control, (b) Stationary cylinder

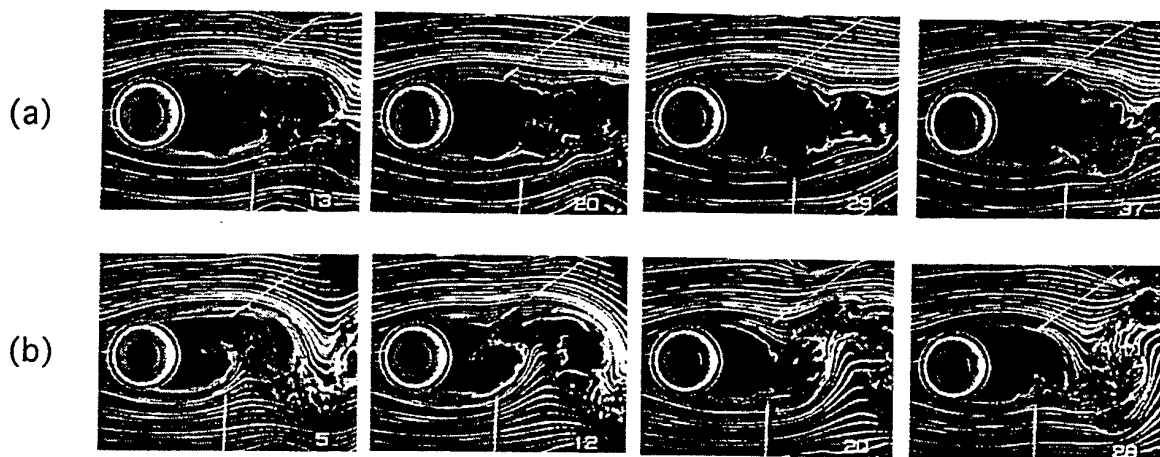


Figure 8: Flow visualization of cylinder wake with and without control.
 (a) Optimum reference control, (b) Stationary cylinder

ACTIVE FLOW CONTROL WITH NEURAL NETWORK AND ITS APPLICATION TO VORTEX SHEDDING

Yuji SUZUKI and Nobuhide KASAGI

Department of Mechanical Engineering
The University of Tokyo
Hongo, Bunkyo-ku, Tokyo 113
Japan

ABSTRACT

A new method for designing neural network (NN) architecture is proposed based on the finite difference form of dynamical equations. The generalization of system NNs can be markedly improved by using the present architecture. The optimal control algorithm proposed by Yoshida & Nagato (1992) was applied to the heat conduction and the Burgers equations. The response of the presently designed NN controller is in good agreement with existing control theories. The optimal control method is then applied to the management of velocity fluctuations downstream of a cylinder. When the system NN is employed as the plant model, the total cost is reduced to 20%. Although the control performance is deteriorated for the physical experiments at this state, the present control algorithm seems to be promising for many future applications.

1. INTRODUCTION

Among various turbulent management techniques, active feedback control with distributed sensors and actuators is the most promising method, since it has a large potential to alter a flow field with a small control input (Wilkinson, 1990; Gad-el-Hak, 1994; Moin & Bewley, 1994). Recently, Choi et al. (1993) proposed a powerful sub-optimal/optimal control algorithm, which is applicable to turbulent flows, and obtained 50% drag reduction in turbulent channel flow (Moin & Bewley, 1995). However, the computational load to determine control through their procedure is enormous, so that control algorithms based on a certain kind of state feedback are desired for real applications.

Neural network (hereafter, NN) is a possible candidate to develop such kind of control systems. Jacobson & Reynolds (1993) used the adaptive inverse control with NN (Widrow, 1986) and the forward model control algorithm (Jordan & Rumelhart, 1992) for controlling a 2-D model of near-wall vortical structures. They obtained 8% reduction in the wall-shear stress. Lee et al. (1997) employed NNs to predict wall-normal velocity fluctuations v at a prescribed wall elevation from the spanwise wall-shear stresses. They showed from direct numerical simulations of turbulent channel flow that turbulent drag is reduced by the wall blowing/suction with an opposite sign to the predicted v (Choi et al., 1994). They also applied the adaptive inverse control to determine blowing/suction rate based on wall-shear stresses.

In the inverse and forward model algorithms, however, con-

trol signals are determined based on the desired plant output, which cannot be uniquely defined beforehand. Moreover, the cost for control is not taken into account, so that the magnitude of the control signal tends to be larger than that derived from optimal control. In the optimal control procedure, a cost function, which is generally a function of the state and the control input, is introduced, and the control input is determined by minimizing this function. Yoshida & Nagato (1992) proposed an optimal control algorithm with NN, and found their method was effective for controlling linear/nonlinear mechanical vibrations.

For any control algorithms based on NN, the learning procedure is most important; the synaptic weights have to be trained properly to mimic the response of the system considered. In general, backpropagation learning algorithm is employed with a descent method, but convergence is not always guaranteed, especially for complex systems. Since there is no general rule to design the architecture of NN, one has to resort to his experience or intuition when optimizing various parameters such as the number of layers and the number of neurons in hidden layers.

The objectives of the present study are to develop a new method of designing architectures for plant-model NNs, and to evaluate the optimal control algorithm proposed by Yoshida & Nagato (1992) for its application to active flow control. To do this, we apply their method to the heat conduction and Burgers equations, and examine the network architectures derived. Moreover, we apply their algorithm to a physical experiment to control vortex shedding from a square cylinder.

2. DYNAMICAL-EQUATION-BASED NEURAL NETWORK ARCHITECTURE

Even though turbulence is a very complex system, we have a good deal of knowledge of its governing equation, i.e., the Navier-Stokes equation. Therefore, if the characteristics of the equation are properly incorporated into the architecture of NN, the learning performance should be markedly improved.

Let us consider the one-dimensional Burgers equation,

$$\frac{\partial u(x,t)}{\partial t} + \frac{\partial}{\partial x} \left(\frac{u(x,t)^2}{2} \right) = \nu \frac{\partial^2 u(x,t)}{\partial x^2}. \quad (1)$$

To mimic the response of the system, multilayer nonlinear recurrent NN (RNN) shown in Fig. 1(a) is often employed with a hyperbolic-tangent activation function. The velocity increment

Δu_i^n at time step n at the i -th point is calculated with u_i^n ($i = 0, \dots, L$), where velocity is sampled at $(L+1)$ locations. A neuron having a fixed output of unity is added to the input and also to the hidden layer to account for bias of the threshold.

Equation (1) can be discretized with the second-order central difference scheme as follows:

$$u_i^{n+1} - u_i^n = -\frac{\Delta t}{2\Delta x} \left\{ \left(u_{i+1}^n \right)^2 - \left(u_{i-1}^n \right)^2 \right\} + \frac{v\Delta t}{\Delta x^2} \left\{ u_{i+1}^n - 2u_i^n + u_{i-1}^n \right\} \quad (2)$$

As can be seen in Eq. (2), the increment Δu_i^n depends only on quantities at the neighboring three points at time n , i.e., u_{i+1}^n , u_i^n , and u_{i-1}^n . Therefore, the network architecture can be designed as shown in Fig. 1(b). For the viscous term in Eq. (2), a linear NN with no hidden layer can be used. On the other hand,

nonlinear neurons are needed for the convection terms $\left(u_{i+1}^n \right)^2$

and $\left(u_{i-1}^n \right)^2$. Since each term is a square of velocity, a neuron which outputs square of an input is employed to account for nonlinearity. Note that any kind of explicit finite difference scheme can be applied; once the discretization scheme is chosen, the basic architecture is uniquely determined. The output of the present NN is expected to be almost equivalent to the solution of the finite difference scheme. However, the advantage of using the NN instead of the governing equation itself is that flow parameters such as v and Δx can be adapted through learning process, and unexpected effects such as unequal distribution of sensors and measurement error can be compensated when NNs are trained sufficiently.

The quantities v , Δx and Δt were chosen as $1/20$, $1/16$, 0.001 , respectively. The number of neurons in the hidden layer for the nonlinear NN is chosen as 4. The synaptic weights were trained with velocity evolution for the initial and boundary conditions,

$$\begin{cases} u(x, 0) = \sin(2\pi x), \\ u(0, t) = u(1, t) = 0. \end{cases} \quad (3)$$

Figure 2(a) shows the response of the NN with the trained weights to the training signal. The agreement of the NN output with the desired response is remarkable for both NN architectures. Figure 2(b) shows the velocity evolution with different initial and/or boundary condition,

$$\begin{cases} u(x, 0) = \cos(2\pi x), \\ u(0, t) = u(1, t) = 0, \end{cases} \quad (4)$$

predicted by the NNs having the weights trained for Eq. (3). It is found that the velocity evolution predicted with the present NN (Fig. 1b) is in good agreement with the desired response. However, the performance of the NN with the general architecture (Fig. 1a) is considerably deteriorated in this case. Since NNs are considered to interpolate the training signal that they have observed during the learning process, a variety of training data set should be required to obtain generalization, if conventional NNs are used. On the other hand, the present NN is designed with the knowledge of the governing equation, generalization can be obtained with a less amount of training signal.

3. OPTIMAL CONTROL WITH NEURAL NETWORK

3.1 Algorithm

In the NN optimal control method proposed by Yoshida & Nagato (1992), two kinds of NN, i.e., a system NN that mimics the response of the plant considered, and a NN controller, are

employed as shown in Fig. 3. The procedure is divided into three specific periods; a system identification period, a training period, and a control period.

In the system identification period, the procedure is the same as that used for the forward model control; random forcing is imposed on the plant as well as the system NN, and the synaptic weights in the NN are trained by using the deviation of NN outputs over the desired response in such a way that the NN mimic the dynamics of the plant being controlled. It is noted that system NNs must have recurrent connections between the input and the output layers to ensure precise prediction of future plant response for some successive time period.

Once a cost function is defined, the NN controller is trained with a help of the system NN. The NN controller is trained to

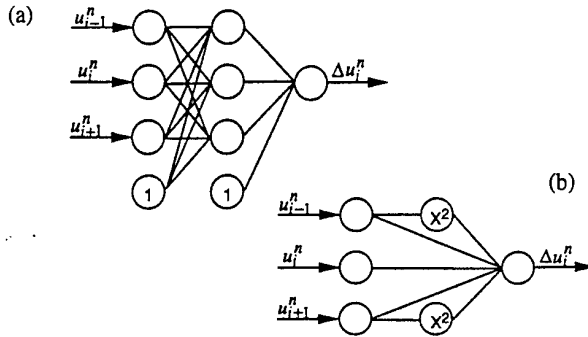


Figure 1: Neural network architecture for the Burgers equation: (a) Conventional architecture, (b) Present architecture. Symbol X^2 denotes neurons having a square activation function.

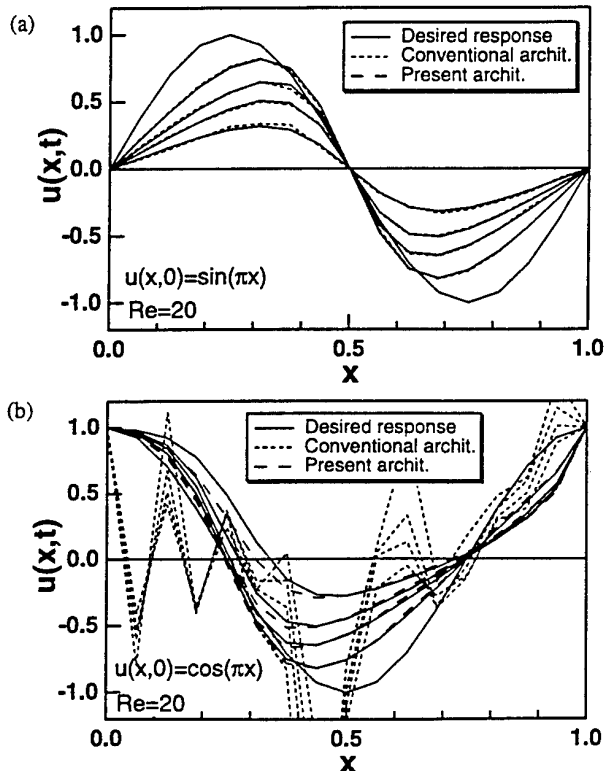


Figure 2: The response of RNN trained for the Burgers equation. Both NN were trained with the teach signal for $u(x, 0) = \sin(2\pi x)$: (a) $u(x, 0) = \sin(2\pi x)$, (b) $u(x, 0) = \cos(2\pi x)$.

minimize the cost function,

$$J = \sum_{k=1}^N \{J_{NS}(k) + J_{NU}(k-1)\}, \quad (5)$$

where J_{NS} and J_{NU} denote the cost for the state vector $x(k)$ and that for the control forcing $F(k)$ at time step k , respectively. These cost for the system can be written with the output of the system NN and that of the NN controller. The synaptic weights of the NN controller w_j ($j=1,2,3,\dots$) are trained with the steepest descent method:

$$w_j = w_j + \sum_{k=1}^N \Delta w_j(k), \quad \Delta w_j(k) = -\epsilon \frac{\partial J}{\partial w_j}. \quad (6)$$

Generally speaking, it is difficult to determine derivatives of the cost function with respect to control parameters. However, once the system NN is trained sufficiently, it is straightforward to determine them, since the functional relation between the input and output of NNs are known; by using the chain rule, the gradients $\partial J / \partial w_j$ can be expressed in terms of the derivatives of the cost function with respect to outputs of the NNs:

$$y_i^1(k) = \frac{\partial J_{NS}(k)}{\partial o_i^S(k)}, \quad \text{and} \quad y_i^2(k) = \frac{\partial J_{NU}(k)}{\partial o_i^C(k)}, \quad (7)$$

where $o_i^S(k)$ and $o_i^C(k)$ are the i -th output of the system NN and the controller, respectively. Since the decomposition of $\partial J / \partial w_j$ into $y_i^1(k)$ and $y_i^2(k)$ is equivalent with propagating two terms in Eq. (7) backwards through the system NN and the NN controller. Therefore, the synaptic weights in the NN controller are trained iteratively by using the backpropagation from the last time step N backward to the first time step. For more details, see Nagato & Yoshida (1992).

In the control period, the NN controller gives the optimum control vector $F(k)$ through forward propagation of the state vector $x(k)$. The advantage of this approach is that the control signal is readily determined as a state feedback. Therefore, the computational load in the control period is much less than that needed for solving the Riccati-type equation at each time instant.

3.2 Boundary Control of 1-D Partial Differential Equations

The optimal control algorithm was applied to boundary control of the unsteady heat conduction and the Burgers equations. The control to be optimized is the quantities at both ends ($x=0$,

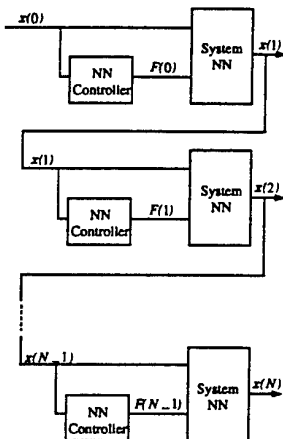


Figure 3: Optimal control with neural network controller proposed by Yoshida & Nagato (1992).

1), and the cost function is chosen as a quadratic form, i.e.,

$$J = \sum_{n=1}^N \left[\sum_{i=1}^{L-1} (u_i^n)^2 + R \left\{ (u_0^{n-1})^2 + (u_L^{n-1})^2 \right\} \right] \Delta t, \quad (8)$$

where R is the parameter accounting for the relative cost of the control signal to that of the state, while L , Δt and N denotes the number of nodes, the time step, and the number of time steps during the control, respectively. The system NN architecture is designed with the procedure mentioned above, while conventional architecture was employed for the NN controller. The number of sigmoidal neurons in the hidden layer is chosen as 4, while the linear activation function is adopted for neurons in the output layer. The quantities Δx and Δt are chosen as 1/16 and 0.001, respectively.

Figures 4(a) and (b) show the temporal evolution of the temperature and the control for the heat conduction equation. The initial temperature distribution is chosen as $u(x,0)=\sin(2\pi x)$ with $N=100$ and $R=1$. Without control, the total cost (Eq. (8)) is $J=0.099$. The response of the system and the control obtained with the NN controller are in good agreement with the results calculated from the Riccati equation, which is derived from the optimal control theory for the linear-quadratic problem. The cost with the NN controller is 0.083, while it is 0.080 with the control using the solution of the Riccati equation. It is also noted that the magnitude of J_{NS} and J_{NU} for both control cases is also in good agreement with each other.

Figure 4(c) shows the temporal evolution of the control with an initial temperature distribution $u(x,0)=\sin(\pi x)$ with the same N and R . The fixed weights optimized for the aforementioned case were employed for the NN controller. The performance of the NN controller is deteriorated in this case; the control at both ends is markedly underestimated in this case, though the overall tendency is similar. The cost is respectively 0.34, 0.29, and 0.25 for no control, NN control, and optimal control theory. On the other hand, the cost is reduced to 0.26 by using the NN controller trained with this initial condition. Therefore, some sort of algorithm should be developed for designing the architecture of NN controller in order to improve generalization.

We also applied the present control procedure to the Burgers equation. The quantities $v(=1/Re)$, N , and R is respectively 1/20, 500 and 1. The system NN was trained for the initial condition $u(x,0)=\sin(2\pi x)$, and the NN controller was developed for $u(x,0)=\sin(3\pi x)$. Figure 5 shows the temporal evolution of control. The response of the system and the control obtained with the NN controller are in accordance with the results obtained from the optimal control procedure proposed by Abergel & Temam (1990). The cost for both control agrees well each other, while it is 8% smaller than that without control.

4. SYSTEM IDENTIFICATION AND CONTROL OF FLOW AROUND SQUARE CYLINDER

The present control procedure based on NN is applied to the control of vortex shedding from a square cylinder. The objective of the present control is to reduce velocity fluctuations downstream of a cylinder with a minimum rotation of the cylinder itself. In previous studies (e.g., Tokumaru & Dimotakis, 1991; Gopalkrishnan et al., 1994; Warui & Fujisawa, 1996), it is found that flow modification can be achieved with rotary oscillation, flapping foil, oscillation in cross-flow, and so on. While they employed some prescribed feedback rule, the control in the present study is determined with a NN controller, which minimizes the cost function defined with instantaneous velocities and the rotation angle of the cylinder.

4.1 Flow Facility and Experimental Technique

The experiment was performed in an open channel water flow facility with a test section having a square cross-section of $0.2 \times 0.2 \text{ m}^2$ and a length of 0.5 m . The freestream velocity U_0 is about 33 mm/s and the turbulent intensity is $2\text{-}5\%$. A square cylinder, of which side D is 5 mm and 200 mm in length is placed at the center of the test section. The Reynolds number based on the freestream velocity and the side is 170 . The natural frequency of vortex shedding measured is about 0.95 Hz , which corresponds to the Strouhal number of 0.14 .

Figure 6 shows the schematic of the flow and the real-time control system. In the present study, instantaneous velocities are obtained by using a two-dimensional particle tracking velocimetry (2-D PTV) in real time. The PTV system consists of a CCD camera, a frame grabber, three RISC processors (Al-

pha Data System Inc., $\alpha 21066$, 233 MHz , 150 MFLOPS), and a digital I/O board. The data transfer rate between processors is nominally 20 MB/s . The square cylinder is connected to a stepping motor located above and can be rotated around its axis.

Nylon 12 spherical particles, of which specific density is 1.02 , are used as flow tracers. The mean diameter of particles is about $120 \mu\text{m}$. Measurement area is about $40 \times 40 \text{ mm}^2$, and an Ar-ion laser sheet is used for illumination. The uncertainty interval for velocity measurements is estimated as $0.05 U_0$.

Instantaneous velocity vectors are calculated from two successive images of tracer particles, and a binary correlation method for 2-D PTV (Yamamoto et al., 1991) is employed to track each particle. Up to 400 instantaneous 2-D vectors in a full frame

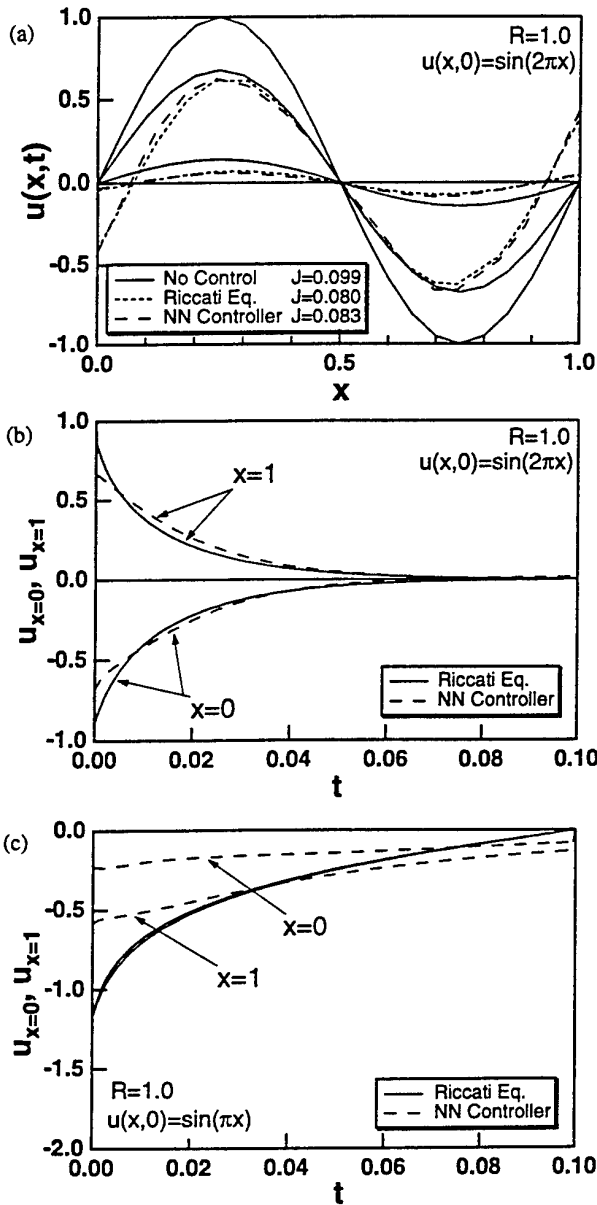


Figure 4: The response of NN controller for boundary control of heat conduction equation. (a) Temporal evolution of temperature distribution, (b) control with an initial condition $u(x,0)=\sin(2\pi x)$, (c) Temporal evolution of control with $u(x,0)=\sin(\pi x)$.

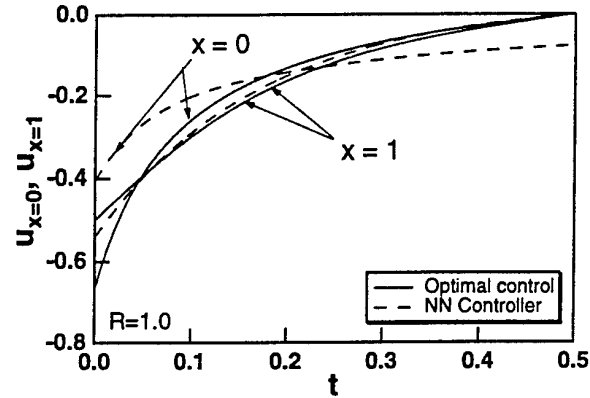


Figure 5: Temporal evolution of control with NN controller for the Burgers equation with an initial condition $u(x,0)=\sin(3\pi x)$

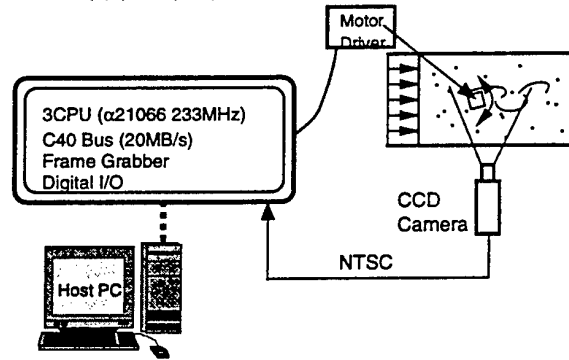


Figure 6: Parallel processing system for real-time vortex-shedding control.

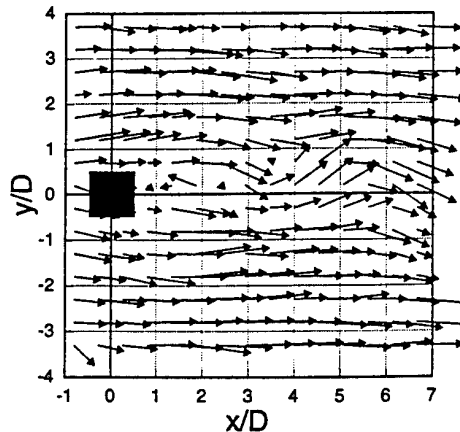


Figure 7: Distribution of interpolated instantaneous vectors obtained with the real-time 2-D PTV.

(512 x 480 pixels) can be obtained every 133 ms. To avoid somewhat large time lag, 1/3 frame (512 x 160 pixels) is employed in the present study. In this case, 100 vectors are obtained within 66 ms, and the total time lag from the image capturing until the onset of the cylinder rotation is less than 100 ms including the computation for the NN controller.

In the present study, velocity vectors at grid points are determined by using a least-square fit to a 3-D plane with the nearest 4 vectors randomly distributed in the measurement area. The spacing of the grids is respectively $0.6D$ and $0.56D$ in the streamwise and the cross-stream direction, and 15×15 grid points are employed. Figure 7 shows a distribution of the interpolated vectors. The origin of the coordinate system is chosen at the center of the cylinder as shown in Fig. 7.

4.2 System Identification of the Flow

To mimic temporal evolution of the flow around the cylinder, a system NN having conventional architecture (Fig. 8a) was employed at the first attempt. The input data to the system NN are the velocity information and the rotation angle of the cylinder θ . The streamwise (u) and cross-stream (v) velocity components at 3×3 grid points in the region of $2.7 < x/D < 3.9$ and $-0.34 < y/D < 0.79$ were employed. Before being transferred to the NN, input data are normalized in such a way that the magnitude is less than unity. The number of neurons in the input layer is 20 including the bias neuron, while 7 neurons is employed in

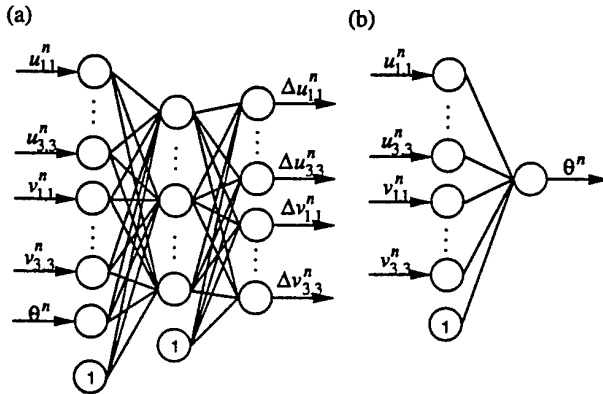


Figure 8: Neural network architecture for flow in physical experiments: (a) System NN, (b) NN controller.

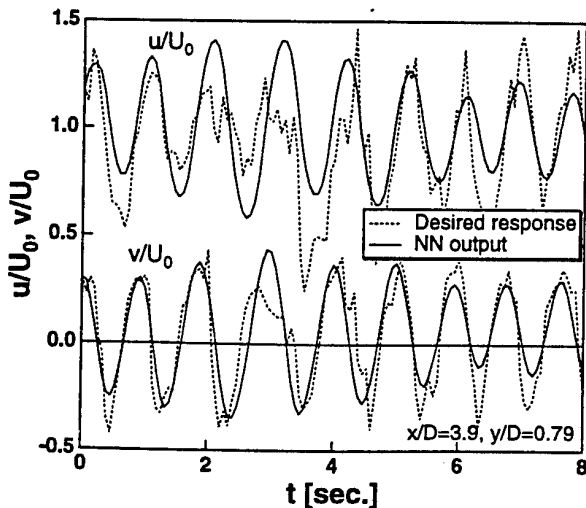


Figure 9: Response of system NN for the flow behind a square cylinder at $x/D=3.9$ and $y/D=0.79$.

the hidden layer. The simulated annealing method is employed for the training to elude local minima. Since the training signal may contain a measurement error as large as $0.05U_0$ as mentioned above, the system NN possibly follows the random noise. To avoid this unwanted effect and improve robustness in prediction, a smoothing regularization method (Wu & Moody, 1996), which inhibits the synaptic weights from growing rapidly, is implemented. About 1000 frames are captured while rotating the square cylinder in somewhat random manner, and the velocity data measured are used for the off-line training of the system NN.

Figure 9 shows the output of the system NN at $x/D=2.7$ and $y/D=0.79$ with weights optimized for the training signal $0 < t < 8$ (120 time step). The NN gives output with the desired response is reasonably well. Note that the NN output does not follow high-frequency fluctuations in the training signal. It is noted that the response of the system NN is also in good accordance with the desired response at other grid points, although not shown here.

4.3 Development of NN Controller

The objective of the present control is to reduce v_{rms} with minimal motion of the cylinder. Thus, the cost function is defined as follows:

$$J = \frac{1}{N} \sum_{k=1}^N \left[\sum_{i=1}^3 \sum_{j=1}^3 \left(\frac{v_{i,j}(k)}{U_0} \right)^2 + R \cdot \left(\frac{\theta(k-1)}{\theta_0} \right)^2 \right] \quad (9)$$

where N, θ_0 and R are chosen as 120, 30.0 and 0.89, respec-

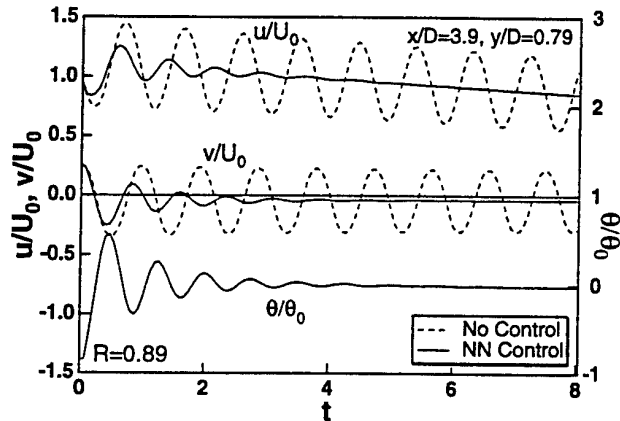


Figure 10: Response of the system NN with the NN controller for $x/D=3.9$ and $y/D=0.79$.

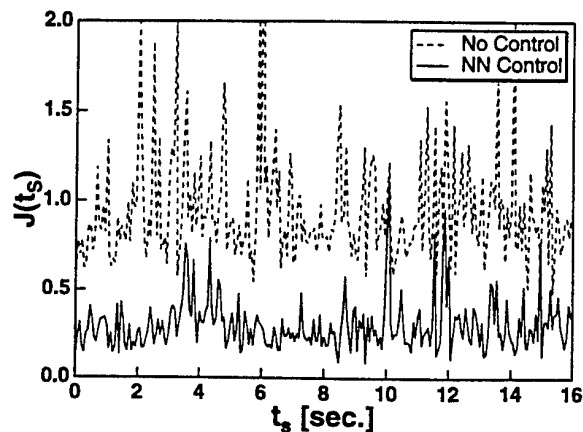


Figure 11: The effect of initial time step on the total cost.

tively. In the present study, a two-layer linear NN is employed as a controller as shown in Fig. 8(b).

The performance of the NN controller is examined by using the system NN as a plant model. Figure 10 shows the temporal evolution of u and v at $x/D=3.9$ and $y/D=0.79$. The velocity fluctuations are rapidly decreased once the control is started. The total cost defined by Eq. (9) is reduced to 20% compared with that without control. The cost for control is about 40% of the total cost. As shown in Fig. 10, the angle of the cylinder is negative (clockwise rotation from the right angle) for positive v at this location, and vice versa. Since a linear NN is employed for the controller, the magnitude of weight is proportional to the contribution of the velocity to the control. If a small number of weights are dominant, then it might be possible to deduce a simple feedback rule by using the corresponding velocity information only. However, most of the weights remain on the same order, so that the input data have almost equal contribution to the decision of control.

The NN controller was trained with the initial condition at $t=0$, and the performance might be depends on the flow patterns when the control starts. Figure 11 shows the effect of the initial time of control t_s on the total cost with the period for the optimization kept unchanged. For most cases, the cost is significantly decreased, thus the controller seems to be robust in this case.

The NN controller with the fixed weights was then applied to the real-time feedback control in the physical experiment. The cost was determined with a time average of quantities for 60 s. Unlike the control of the system NN, the cylinder was rotated continuously with large amplitude, and more velocity fluctuation was generated. Therefore, the NN controller failed in both reducing the total cost and damping the v fluctuations. At this moment, it is difficult to determine the major cause responsible for this unsuccessful result, but the performance could be improved if the system NN is trained with better generalization.

5. CONCLUSION

A new method for designing NN architectures was proposed based on the dynamical equations. The optimal control algorithm proposed by Yoshida & Nagato (1992) was applied to the heat conduction and the Burgers equations. Their method was also implemented in a physical experiment of flow around a square cylinder. The following conclusions can be derived:

- 1) The generalization of system NNs can be markedly improved by using the architecture based on the finite difference form of the governing equations.
- 2) The response of the NN controller is in good agreement with existing control theories. However, it is difficult to obtain generalization for the NN controller, when the conventional architecture is employed.
- 3) The optimal control method was successfully applied to suppressing the velocity fluctuations behind the cylinder. When the system NN was employed as the plant model, the total cost is reduced to 20%. Although the performance of the control was deteriorated in the physical experiment at this moment, the present control algorithm seems to be promising for many future applications.

The authors acknowledge the financial supports through the Grant-in Aids for General Scientific Research (No. 08455102) and for Exploratory Research (No. 08875043) by the Ministry of Education, Science, Sports and Culture, and also by TEPCO Research Foundation.

REFERENCES

- Abergel, F., and Temam, R., 1990, "On Some Control Problems in Fluid Mechanics," *Theoret. Comput. Fluid Dynamics*, 1, pp. 303-325.
- Bewley, T., Choi, H., Temam, R., and Moin, P., 1993, "Optimal Feedback Control of Turbulent Channel Flow," *Annual Research Briefs*, CTR, Stanford, pp. 3-14.
- Choi, H., Temam, R., Moin, P., and Kim, J., 1993, "Feedback Control for Unsteady Flow and its Application to the Stochastic Burgers Equation," *J. Fluid Mech.*, 253, pp. 509-543.
- Choi, H., Moin, P., and Kim, J., 1994, "Active Turbulence Control for Drag Reduction in Wall-Bounded Flows," *J. Fluid Mech.*, 262, pp. 75-110.
- Gad-el-Hak, M., 1994, "Interactive Control of Turbulent Boundary Layers: A Futuristic Overview," *AIAA J.*, 32, pp. 1753-1765.
- Gopalkrishnan, R., Triantafyllou, M. S., Triantafyllou, G. S., and Barrett, D., 1994, "Active Vorticity Control in a Shear Flow Using a Flapping Foil," *J. Fluid Mech.*, 274, pp. 1-21.
- Jacobson, S. A., and Reynolds, W. C., 1993, "Active Control of Boundary Layer Wall Shear Stress Using Self-Learning Neural Networks," *AIAA Paper*, 93-3272.
- Jordan, M. I., and Rumelhart, D. E., 1992, "Forward models: Supervised learning with a distal teacher," *Cognitive Sciences*, 16, pp. 307-354.
- Kim, J., Babcock, D., Gupta, B., and Goodman, R., 1994, "Application of a Neural Network to Turbulence Control," *APS Annual Meeting*.
- Lee, C., Kim, J., Babcock, D., and Goodman, R., 1997, "Application of Neural Networks to Turbulence Control for Drag Reduction," *Phys. Fluids*, in press.
- Moin, P., and Bewley, T., 1994, "Feedback control of turbulence," *Appl. Mech. Rev.*, 47, pp. S3-S13.
- Moin, P., and Bewley, T., 1995, "Application of Control Theory to Turbulence," *Proc. Twelfth Australasian Fluid Mechanics Conference*, Sydney.
- Nagato, H., and Yoshida, K., 1992, "Optimal Control of Non-linear Systems by Neural Network," *Trans. JSME C*, 58, pp. 171-177.
- Tokumaru, P. T., and Dimotakis, P. E., 1991, "Rotary Oscillation Control of a Cylinder Wake," *J. Fluid Mech.*, 224, pp. 77-90.
- Warui, H. M., and Fujisawa, N., "Feedback Control of Vortex Shedding From a Circular Cylinder by Cross-Flow Cylinder Oscillations," *Exp. Fluids*, 21, (1996), pp. 49-56.
- Widrow, B., 1986, "Adaptive Inverse Control," in *Adaptive Systems in Control and Signal Processing 1986*, IFAC, Astrom, K. J., and Wittenmark, B., eds., Pergamon Press.
- Wilkinson, S. P., 1990, "Interactive Wall Turbulence Control," *Prog. Astronautics and Aeronautics: Viscous Drag Reduction in Boundary Layers*, Bushnell, D. M., and Hefner, J. N., eds., 123, pp. 479-509, AIAA.
- Wu, L., and Moody, J., 1996, "A Smoothing Regularizer for Feedforward and Recurrent Neural Networks," *Neural Computation*, 8, pp. 463-491.
- Yamamoto, F., Uemura, T., Iguchi, T., and Morita, Z., 1991, "A Binary Correlation Method Using a Proximity Function for 2-D and 3-D PTV," *Exp. Numerical Flow Vis.*, Khalighi, B., et al. eds., New York, ASME, pp. 23-28.
- Yoshida, K., and Nagato, H., 1992, "Application of Neural Network to the Optimal Control of Active Dynamic Vibration Absorber," *Proc. 1st Int. Conf. Motion and Vibration Control*, pp. 947-951, Yokohama.

THE INFLUENCE OF POLYMER STRESSES IN DRAG-REDUCTION

Thomas J. Hanratty, Michael Warholic
Heshmat Massah

Department of Chemical Engineering
University of Illinois
600 South Mathews Avenue
Urbana, IL 61801
USA

ABSTRACT

The presence of long-chain polymers in a turbulent flow introduces added stresses. As a consequence, the sum of the Reynolds shear stress and the solvent shear stress is not equal to the total shear stress. Under conditions of maximum drag-reduction the Reynolds stress is close to zero. Because of the presence of time-averaged polymer shear stresses laminar flow is not realized when the Reynolds stresses are zero. The presence of turbulence under conditions of zero Reynolds stress suggests that turbulence can be produced by polymer stresses. This is explained by calculations that represent polymer molecules with FENE-P bead-spring chains. These show that the contraction of the polymer stress tensor with the tensor representing the fluctuations in the rate of strain can be positive (dissipates turbulence) or negative (produces turbulence).

INTRODUCTION

A remarkable discovery in turbulence is that the addition of long chain polymers in amounts of less than 1 ppm can cause significant changes in the drag of a turbulently flowing liquid on a plane solid surface. An explanation of this phenomenon requires the understanding of how turbulence changes the polymers and of how polymers change the turbulence. At the Ninth Symposium on Turbulent Shear Flow we explored the first of these questions by representing a polymer molecule by a FENE-P bead-spring chain and by examining how these chains change their configuration in the velocity field represented by a direct numerical simulation of turbulent flow of a Newtonian fluid in a channel.

This paper presents results of a continuation of this study in which we examine the added stresses associated with the configurational changes of dilute solutions of FENE-P bead-spring chains. Recent laboratory studies of the turbulence properties of dilute solutions of polyacrylamide are also discussed. Three issues are addressed: (1) the shear stress deficit, (2) the production of "turbulence" under conditions where the Reynolds stress is close to zero, and (3) possible effects of drag-reducing polymers on turbulence structure.

The work expands on previous studies by Tiederman (1990) and by Willmarth et al. (1987).

DESCRIPTION OF EXPERIMENTS

The experiments were carried out in a 5 x 50 cm rectangular channel in which polymer was injected through slots in the wall. The Reynolds number (defined with the average velocity, the half-height of channel, H , and the viscosity of the solvent) was held at 18,900. Concentrations of 2, 5, 10 and 90 ppm were used. Drag-reductions of 48, 58, 67, and 65 per cent were realized. Measured velocity profiles are shown in figure 1, where the velocity is normalized with the friction velocity and the distance from the wall, by the half height of the channel, H . The areas under the curves are measures of the drag-reduction, since they equal the ratio of the volumetric flow to the friction velocity. Figure 2 presents plots of the dimensionless velocity against the logarithm of the distance from the wall, made dimensionless with wall parameters. For water, the edge of the viscous wall region may be defined as $y^+ = 30$. The velocity at this location may be looked upon as an effective slip. The drag-reduction for 2.5 ppm (48%) is associated with a thickening of the viscous wall layer and an increase in this effective slip. For 5 ppm (58%) and 10 ppm (67%) one cannot distinguish between a viscous wall region and an outer flow. For 90 ppm (65%) the viscosity measured in a shear viscometer is larger than water and this value has been used in calculating y^+ .

REYNOLDS STRESSES AND POLYMER STRESSES

One of the interesting aspects of polymer drag-reduction is the occurrence of a stress deficit. A force balance defines the shear stress variation in a two-dimensional fully-developed channel flow as

$$\bar{\tau} = (H-y) \frac{d\bar{P}}{dx}$$

Here H is the half-height of the channel and y is the distance from the bottom wall. For a Newtonian fluid

$$\bar{\tau} = \bar{\tau}_s - \rho \bar{u}v$$

where $\bar{\tau}_s = \mu (d\bar{U}/dy)$ and $-\rho \bar{u}v$ is the Reynolds stress. Willmarth et al. (1987) have shown that this equality does not always hold for a polymer flow so that an added mean shear stress due to the polymers can be assumed to exist if the polymer concentration is large enough

$$\bar{\tau} = \bar{\tau}_s - \rho \bar{u}v + \bar{\tau}_p$$

Polymer drag-reduction is associated with a decrease in the Reynolds stress. However, the presence of polymer stresses, $\bar{\tau}_p$, has the effect of reducing the amount of drag-reduction. For example, if $\bar{u}v = 0$ the volumetric flow for a given wall stress would be less than what would be calculated for laminar flow if $\bar{\tau}_p \neq 0$. This explains why maximum drag-reduction is not associated with a return to laminar flow and suggests that maximum drag-reduction could depend on the polymer that is used.

Figure 3 shows measured values of $-\bar{u}v$. Of particular interest are the extremely small values of $-\bar{u}v$ for 10 ppm and 90 ppm. For 90 ppm, the Reynolds stresses are approximately zero. Figure 4 is a plot of $(\bar{\tau}_s - \rho \bar{u}v) / \bar{\tau}_w$ versus y/H . For a Newtonian fluid a linear relation which is zero at the center of the channel and unity at the wall is obtained. A stress deficit is clearly shown for polymer solutions.

INTERPRETATION

An interesting question is how turbulence is produced for cases where $\bar{u}v = 0$. A possible explanation is suggested from studies of the behavior of FENE-P chains in a turbulent field by Massah & Hanratty (1997). A consideration of the mechanical energy balance for a turbulent flow shows that turbulence is produced by Reynolds stresses through the term

$-\bar{u}v \frac{d\bar{U}}{dy}$. Dissipation is defined by the equation

$$\epsilon_v = \overline{\tau'_{ij} \frac{\partial u_i}{\partial x_j}}$$

where τ'_{ij} are the components of the fluctuating viscous stress given by

Because of the above relation ϵ_v is always positive.

If fluctuating polymer stresses are present the mechanical energy balance introduces an additional term

$$\tau'_{ij} = \mu \left(\frac{\partial u_i}{\partial x_j} + \frac{\partial u_j}{\partial x_i} \right)$$

$$\epsilon_p = \overline{\tau'_{ij} \frac{\partial u_i}{\partial x_j}}$$

This can be either plus or minus. When plus, ϵ_p introduces additional losses of turbulent energy. When minus, ϵ_p represents a transfer of mechanical energy from polymer chains to the fluid. This, then, provides a mechanism whereby polymer stresses can produce turbulence.

The study of the response of dilute solutions of FENE-P bead-spring chains to turbulent velocity fluctuations by Massah & Hanratty (1997) are a "thought" experiment in that the influence of the polymer stresses are not introduced into the momentum equations. They are a rheological study in which stresses associated with a given kinematic field are determined. Fluid particles were followed in the three-dimensional time-dependent, random velocity field given by a DNS of turbulent flow of a Newtonian fluid in a channel. The change of the rate of strain tensor and the behavior of a dilute solution of FENE-P bead-spring chains in these time-varying rates of strain are determined. A number of results are pertinent to the drag-reduction problem.

Large intermittent values of ϵ_p are calculated. Positive ϵ_p are often associated with the vortices that are producing turbulence in the viscous wall region. We speculate that the added dissipation will have the effect of increasing the size of the wall vortices, or of reducing their importance.

Large additional shear stresses, τ'_{xy} , are introduced. The calculations suggest that at a given y these have an average value which could explain the measured $\bar{\tau}_p$. Furthermore, the calculations suggest that close to the wall ϵ_p could, on average, be negative. That is, polymer stresses could be creating turbulence.

This occurs because the large shear rate, $\frac{d\bar{U}}{dy}$, close to the wall unravels the chains, and orients them in the flow direction. This introduces a positive normal stress τ'_{xx} . The "dissipation," ϵ_p , can then be plus or minus depending on the sign of $\partial u_x / \partial x$. The calculations suggest that, on average, ϵ_p will be negative close to the wall. This opens the possibility of polymer stresses producing large streamwise velocity fluctuations, that are noted for polymer solutions close to the wall (see figure 5).

ACKNOWLEDGMENT

This work is supported by the National Science Foundation under Grants NSF CTS 95 03000 and NSF CTS 95 00518.

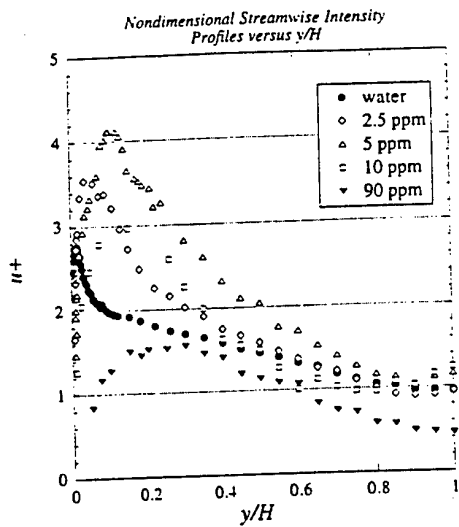


Figure 1. Plots of the dimensionless velocity against the distance from the wall, made dimensionless with the half-height of the channel.

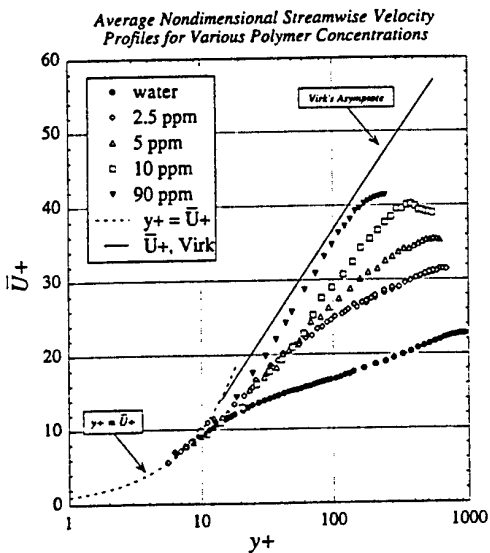


Figure 2. Effect of polymers on the mean velocity profile for an experiment in which the volumetric flow was kept constant.

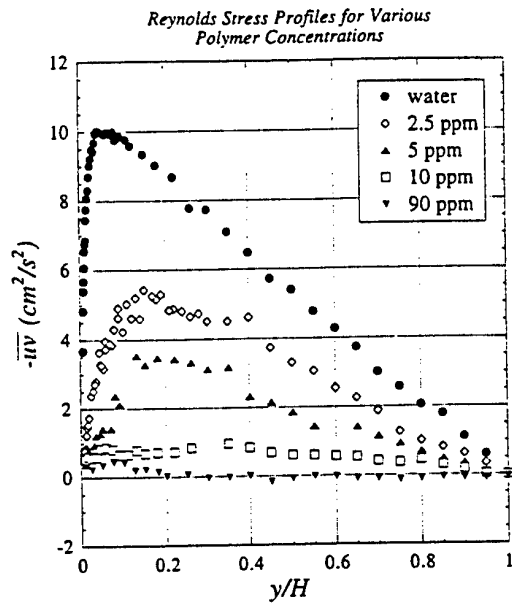


Figure 3. Effect of polymers on the Reynolds stress.

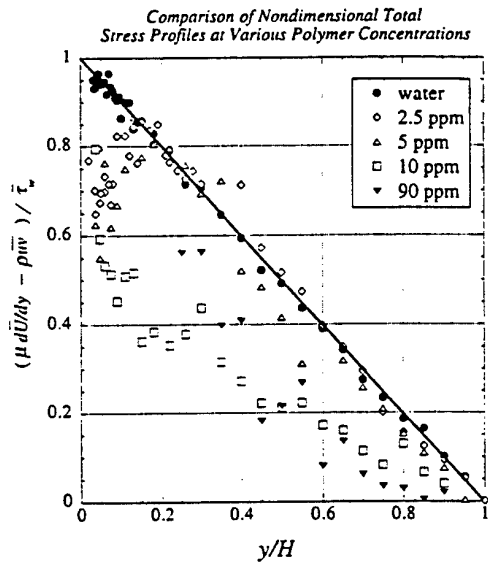


Figure 4. Stress deficits in polymer solutions.

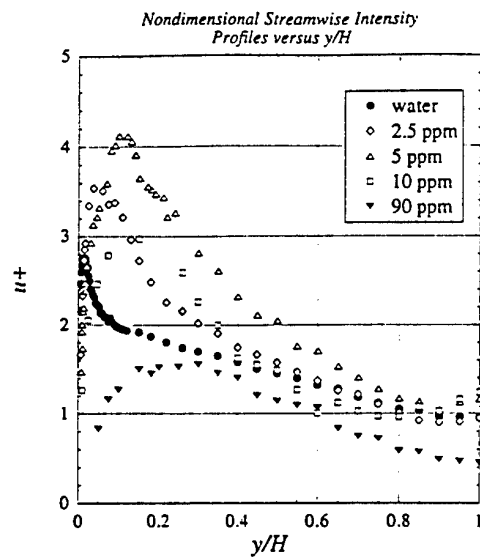


Figure 5. Effect of polymers on the streamwise velocity fluctuations.

REFERENCES

- Massah, H., and Hanratty, T. J., 1997, "Added Stresses Because of the Presence of FENE-P Bead-Spring Chains in a Random Velocity Field," *J. Fluid Mech.*, Vol. 337, pp. 67-101.
- Tiederman, W. G., 1990, "The Effect of Dilute Polymer Solutions on Viscous Drag and Turbulence Structure," In *Structure of Turbulence and Drag Reduction* (ed. A. Gyr), pp. 257-274, Springer.
- Willmarth, W. W., Wei, T. and Lee, C. O., 1987, "Laser Anemometer Measurements of Reynolds Stress in a Turbulence Channel Flow with Drag-Reducing Polymer Additions," *Phys. Fluids*, Vol. 30, pp. 933-935

SESSION 10 - FUNDAMENTALS II

STRETCHING OF VORTICITY GRADIENTS IN TWO-DIMENSIONAL WAKE FLOW

B. Protas⁽¹⁾⁽²⁾, J.E. Wesfreid⁽²⁾

(1) Department of Aerodynamics
Institute of Aeronautics and Applied Mechanics
Warsaw University of Technology
Nowowiejska 24, 00-665 Warsaw, Poland

(2) Laboratoire de Physique et Mécanique des Milieux Hétérogènes, C.N.R.S., U.R.A. 857
École Supérieure de Physique et Chimie Industrielles
10 rue Vauquelin, 75231 Paris Cedex 05, France

INTRODUCTION

One of the most intriguing features of developed turbulent flows is the phenomenon of intermittency. It is related to the presence of strongly non-uniform distributions of velocity increments in the flow field. The most straightforward way to study intermittency effects is to examine the anomalous scaling of the structure functions [1]. The two-dimensional (2D) and three-dimensional (3D) turbulent flows have clearly different scaling characteristics [1], [2]. Nevertheless, when the relative scaling is taken into account [3], then the differences cancel out and the intermittency corrections can be studied in the same way in the two cases [4].

Various forms of coherent structures are ubiquitous in all turbulent flows encountered in Nature. It is therefore of considerable theoretical and practical interest to determine how their presence influences the small scale intermittency in the flow. Turbulent wake flows appear to be particularly well suited to the investigation of the interaction between coherent structures and small scale statistics. They incorporate both forced and decaying regimes. In the wake flow one can find a whole panoply of eddies with varying degrees of regularity and coherence. These phenomena were investigated in a real laboratory experiment [5] and numerical 2D simulation of turbulent wake flow with developed enstrophy cascade [6]. Both these studies indicate that the intermittency correction (i.e. the deviation of the scaling exponent from the linear K41 prediction [7]) was different in various parts of the flow domain. In the vicinity of the obstacle, in the region dominated by large scale strain and anisotropy, the intermittency effects are considerably more pronounced. Motivated by these findings, below we will attempt to determine the mechanisms which may have some bearing on the origins of intermittency. In particular, we will focus on the stretching phenomena and the statistics of geometrical alignments. Comprehensive discussion of various stretching phenomena in hydrodynamics as well as their relation to the theory of dynamical systems can be found in [8] and [9].

STRETCHING OF VORTICITY GRADIENTS - KINEMATIC APPROACH

Generation of strong vorticity gradients is a generic feature of 2D turbulent flows [10]. Stretching and folding of vorticity layers results in that vorticity fronts with varying magnitudes are brought close together. According to [11], this is the way in which enstrophy is cascaded towards small scales. In [12] it was postulated that this phenomenon can be feasibly described by the equation for the inviscid evolution of vorticity gradients:

$$\frac{d}{dt} \nabla \omega = \left(\frac{\partial}{\partial t} + \mathbf{V} \cdot \nabla \right) \nabla \omega = -\nabla \mathbf{V} \cdot \nabla \omega. \quad (1)$$

This equation implies that, following a fluid particle, the vorticity gradient changes according to the local properties of the stretching term $-\nabla \mathbf{V} \cdot \nabla \omega$ (reminiscent of the *vortex stretching* term in the 3D vorticity equation). Consequently, this non-linear term sustains the enstrophy cascade and as such is responsible for the anomalies that can be observed in this process. In order to quantify these effects we will analyze the statistical properties of various parameters related to stretching of vorticity gradient $\nabla \omega$ [13]. An entirely equivalent description can be given with the use of *palinstrophy* η (defined as the curl of vorticity).

In [14] it was argued that, to the leading order, the straining field represented by $\nabla \mathbf{V}$ remains frozen with regard to the variations of $\nabla \omega$. This assumption implies the persistence of strain and is often referred to as the hypothesis of the separation of scales. Thus the equation (1) can be linearized

$$\frac{d}{dt} \nabla \omega = -\mathbf{A} \nabla \omega, \quad (2)$$

where:

$$A_{ij} = \left(\frac{\partial u_i}{\partial x_j} \right)_{t=t_0}, \quad i, j = 1, 2, \quad (3)$$

and integrated:

$$\nabla \omega(t) = \nabla \omega(0) e^{-\mathbf{A}t}, \quad t \rightarrow 0, \quad (4)$$

where $e^{-\mathbf{A}t}$ is a linear matrix operator [15]. The symbol $t \rightarrow 0$ implies that the above mentioned linearization may no longer be valid for big times. Consequently, the analysis will concern the statistics built out of instantaneous events.

The properties of the operators \mathbf{A} and $e^{-\mathbf{A}t}$ are crucial in the kinematics of stretching, therefore below we proceed to enumerate some of them. First, the velocity gradient ∇V can be rewritten in terms of strain and vorticity:

$$\nabla V = \frac{1}{2} \begin{bmatrix} s_{11} & s_{12} - \omega \\ s_{12} + \omega & -s_{11} \end{bmatrix}, \quad (5)$$

where:

$$s_{11} = 2 \frac{\partial u}{\partial x} = -2 \frac{\partial v}{\partial y}, \quad s_{12} = \frac{\partial u}{\partial y} + \frac{\partial v}{\partial x}, \quad (6)$$

$$\omega = \frac{\partial v}{\partial x} - \frac{\partial u}{\partial y}. \quad (7)$$

Its eigenvalues are given by:

$$\lambda_{\pm} = \pm \frac{1}{2} \sqrt{s_{11}^2 + s_{12}^2 - \omega^2} \quad (8)$$

and the associated (unnormalized) eigenvectors:

$$\begin{aligned} \mathbf{r}^1 &= \begin{bmatrix} s_{12} - \omega \\ \sqrt{s_{11}^2 + s_{12}^2 - \omega^2} - s_{11} \end{bmatrix}, \\ \mathbf{r}^2 &= \begin{bmatrix} \omega - s_{12} \\ \sqrt{s_{11}^2 + s_{12}^2 - \omega^2} + s_{11} \end{bmatrix}, \end{aligned} \quad (9)$$

corresponding to the positive λ_+ and negative λ_- eigenvalue. Henceforth we will use the denotation $\lambda = \lambda_+ = -\lambda_-$. The eigenvectors of $e^{-\mathbf{A}t}$ are also given by the relations (9). In this basis $e^{-\mathbf{A}t}$ can be written as:

$$e^{-\mathbf{A}t} = \begin{bmatrix} e^{-\lambda t} & 0 \\ 0 & e^{\lambda t} \end{bmatrix}. \quad (10)$$

In the Cartesian basis $e^{-\mathbf{A}t}$ takes the form:

$$e^{-\mathbf{A}t} = \cosh(\lambda t) \cdot \mathbf{I} - \frac{1}{2} \frac{\sinh(\lambda t)}{\lambda} \cdot \mathbf{A}. \quad (11)$$

Depending on the relative significance of strain and vorticity, the eigenvalues λ can be either purely real or purely imaginary. From equation (??) it follows that in the first case the vorticity gradients can be exponentially amplified, whereas in the second they just rotate and oscillate. These two regimes are referred to as *hyperbolic* and *elliptic*, respectively [12]. Growth of vorticity gradients is characteristic of developed enstrophy cascade. These regions are therefore of primary dynamical significance and on this case we will exclusively focus in the following.

Every tensor can be decomposed into symmetric \mathbf{D} and antisymmetric part $\mathbf{\Omega}$:

$$\nabla V = \mathbf{D} + \mathbf{\Omega}, \quad (12)$$

where

$$\begin{aligned} \mathbf{D} &= \frac{1}{2} (\nabla V + \nabla V^T), \\ \mathbf{\Omega} &= \frac{1}{2} (\nabla V - \nabla V^T). \end{aligned} \quad (13)$$

The stretching properties are associated only with the symmetric part \mathbf{D} . For the antisymmetric part $\mathbf{\Omega}$ one always has $\mathbf{n}^T \mathbf{\Omega} \mathbf{n} \equiv 0$ for any vector \mathbf{n} . The directions of maximum stretching and compression are orthogonal and are given by the eigenvectors of \mathbf{D} :

$$\begin{aligned} \mathbf{d}^1 &= \begin{bmatrix} s_{12} \\ \sqrt{s_{11}^2 + s_{12}^2} - s_{11} \end{bmatrix}, \\ \mathbf{d}^2 &= \begin{bmatrix} -s_{12} \\ \sqrt{s_{11}^2 + s_{12}^2} + s_{11} \end{bmatrix}. \end{aligned} \quad (14)$$

The rates of strain are equal to the eigenvalues of \mathbf{D} $\sigma_{\pm} = \pm \frac{1}{2} \sqrt{s_{11}^2 + s_{12}^2}$. The actual stretching efficiency depends on the alignment of $\nabla \omega$ with respect to the direction of maximum stretching. Two parameters can be introduced to quantify these effects [13]. The instantaneous stretching efficiency κ represents the combined effects of strain magnitude and geometrical alignments:

$$\begin{aligned} \kappa &= \frac{d \ln |\nabla \omega|}{dt} = -\mathbf{m}^T \mathbf{D} \mathbf{m} \\ &= \sqrt{s_{11}^2 + s_{12}^2} \cos(2\alpha), \end{aligned} \quad (15)$$

where $\mathbf{m} = \frac{\nabla \omega}{|\nabla \omega|}$ and $\alpha = \angle(\nabla \omega, \mathbf{d}^1)$ is the angle between the vorticity gradient and the extensional eigenvector of \mathbf{D} . The formula on the right hand side corresponds to the 2D incompressible case. The pure effect of geometrical alignments is given by the normalized instantaneous stretching efficiency e :

$$e = \frac{-\mathbf{m}^T \mathbf{D} \mathbf{m}}{(\mathbf{D} : \mathbf{D})^{\frac{1}{2}}} = \frac{\sqrt{2}}{2} \cos(2\alpha). \quad (16)$$

It is visible that, in order to be stretched, $\nabla \omega$ must lie within the range of $\frac{\pi}{4}$ from the direction of \mathbf{d}^1 . In the stretching process the role of vorticity is to re-orient the stretched vector with respect to the principal directions of strain $\{\mathbf{d}^1, \mathbf{d}^2\}$. For finite times (cf. equation (4)) this can be a source of considerable complexity in the history of stretching.

At this stage one can enumerate agents necessary for robust stretching:

- (i) non-vanishing $|\nabla \omega|$,
- (ii) *hyperbolicity*, i.e. dominance of strain over vorticity,
- (iii) $\nabla \omega$ aligned possibly close to \mathbf{d}^1 (the direction of maximum stretching).

It is obvious that all the three conditions must be satisfied simultaneously. Below we will present an analysis of the flow pattern in the 2D turbulent wake in terms of the conditions (i)-(iii).

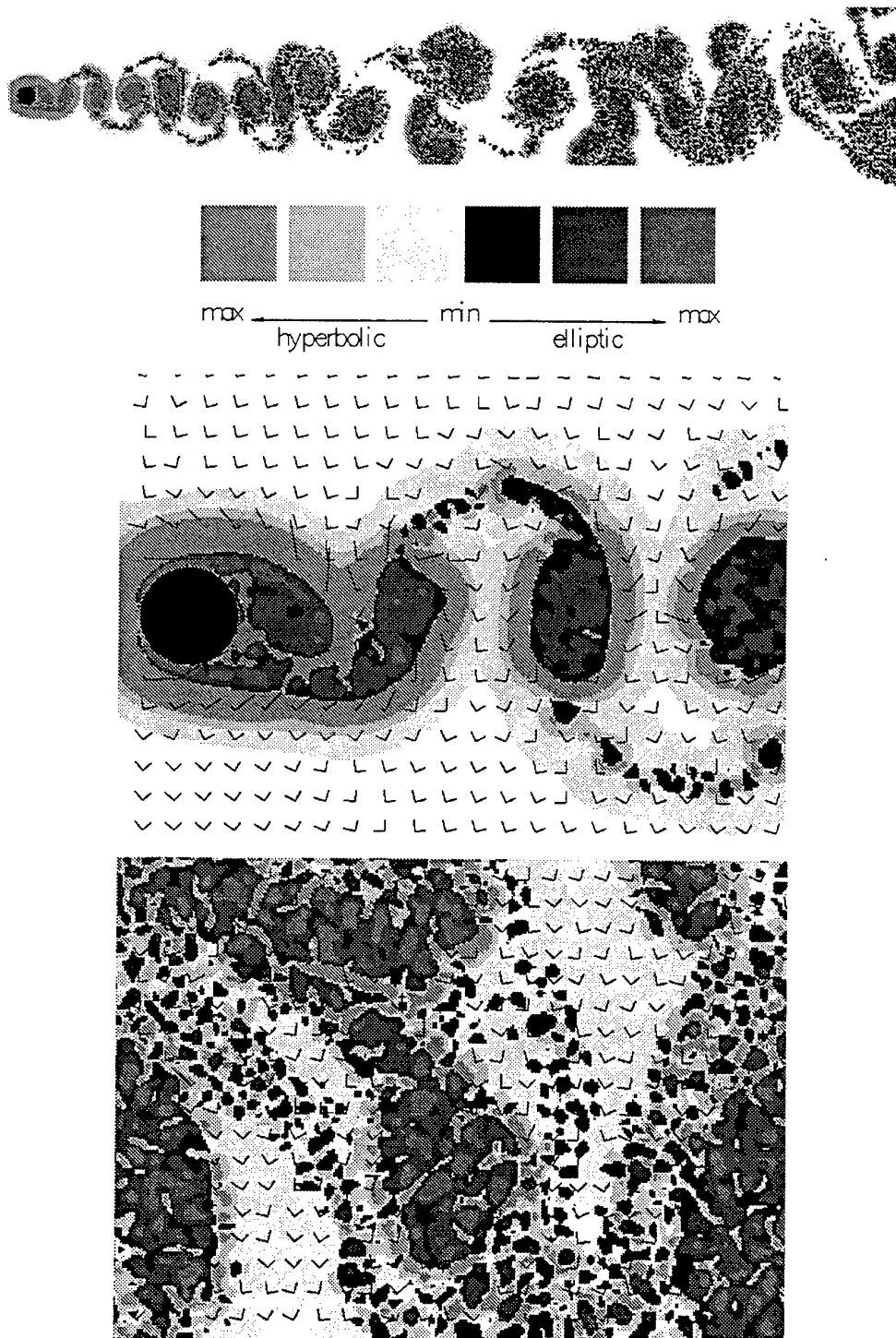


Figure 1: Instantaneous contours of the eigenvalue λ in the wake flow. The near and far wake region are shown in magnification in the middle (b) and bottom (c) figure respectively. In Figs. (b) and (c) the eigenvectors $\{d^1, d^2\}$ are displayed.

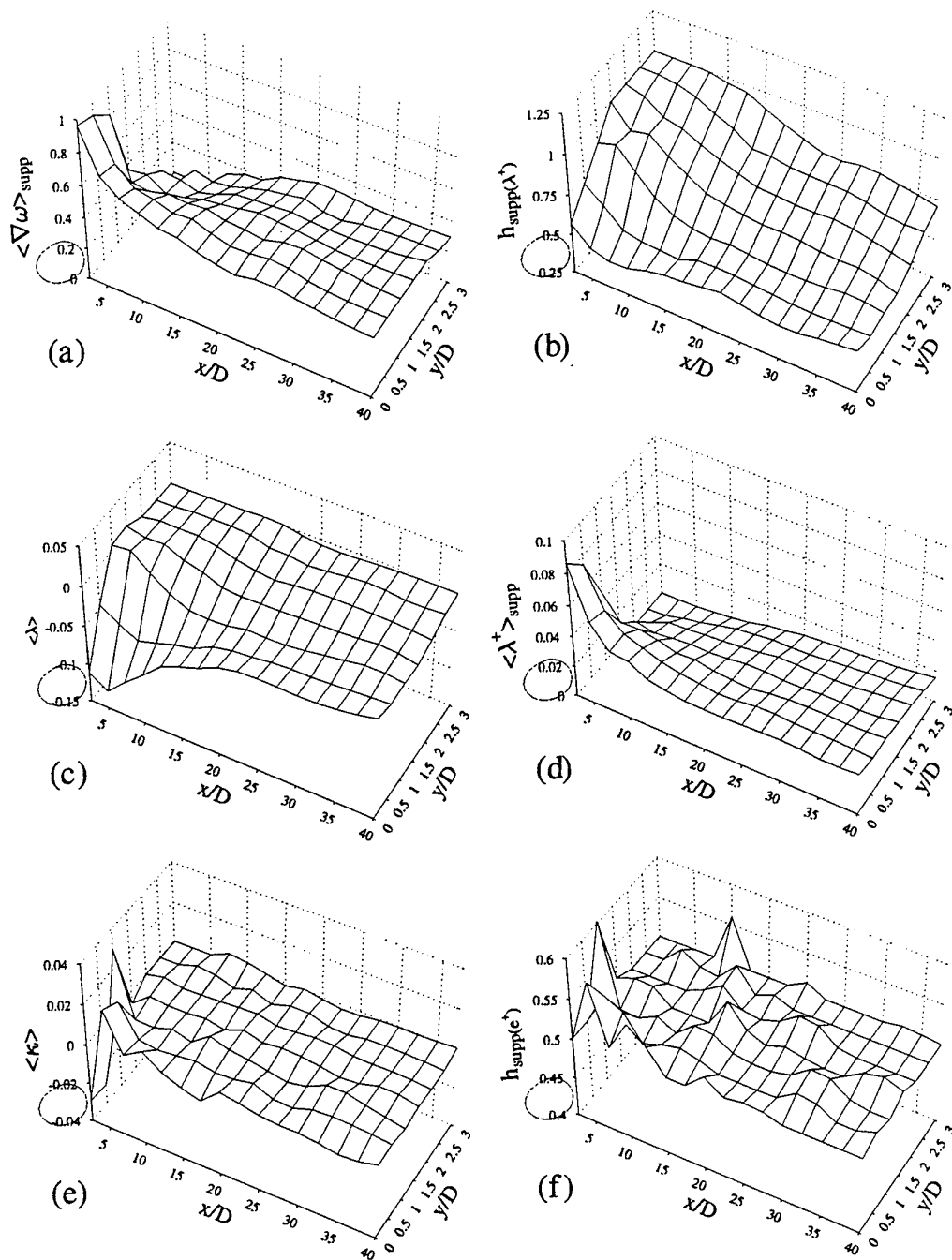


Figure 2: Dependence of the statistical parameters related to the conditions (i)–(iii) (see texts for exact definitions) on the downstream x and spanwise y distance. The circular contour near the origin represents the approximate location of the obstacle. Plots are stretched in the spanwise direction.

RESULTS

RANDOM VORTEX BLOB method was used in the simulation of unsteady 2D turbulent wake flow. Overview of these methods is given in [16]. Details of the current implementation can be found in [17]. Comprehensive discussion of the results will be reported elsewhere. Here only the main points are summarized.

In Fig (1) we present the instantaneous contours of the eigenvalue λ . As indicated on the inset, the two grayscales represent the *hyperbolic* and *elliptic* regimes. The near and far wake regions are shown in magnification. In the hyperbolic parts of the flow domain the eigenvectors $\{d^1, d^2\}$ are shown with lengths corresponding to the exponential of the rate of strain $e^{\pm\sigma}$.

In Fig (2) we present distributions in the wake of certain statistical parameters. First, in a number of control points in the wake the time series of various quantities were recorded (ω , s_{11} , s_{12} , etc.). Then appropriate statistics of instantaneous events were computed. Because of assumed statistical symmetry with respect to the $y = 0$ axis, the mesh covers only one half of the flow domain (corresponding to positive y). Comparing to the actual proportions, the plots are stretched in the spanwise y direction. The circular contour near the origin represents the approximate location of the obstacle. In Fig. 2a (top left) $\langle \nabla \omega \rangle_{supp}$ is presented. It is the average magnitude of $|\nabla \omega|$ computed with respect to the intervals of time when it was non-vanishing:

$$\langle \nabla \omega \rangle_{supp} = \frac{\int_{supp(\nabla \omega)} |\nabla \omega(\tau)| d\tau}{\mu(supp(\nabla \omega))}, \quad (17)$$

where $\mu(supp(\nabla \omega))$ is the overall measure of the time intervals when $\nabla \omega$ was non-vanishing. Next, in order to be able to compute the parameters related to λ , the following auxiliary quantities have to be introduced:

$$\lambda^+ = \begin{cases} \lambda & \text{if } \lambda^2 > 0 \\ 0 & \text{elsewhere,} \end{cases} \quad (18)$$

$$\lambda^- = \begin{cases} -Im(\lambda) & \text{if } \lambda^2 < 0 \\ 0 & \text{elsewhere,} \end{cases}$$

$$\lambda^* = \lambda^+ + \lambda^-. \quad (19)$$

λ^* is thus positive or negative depending on whether λ is real or imaginary.

Fraction of time spent in the *hyperbolic* regime $h_{supp(\lambda^+)}$ is shown in Fig. 2b (top right). In Fig. 2c (middle left) the mean eigenvalue $\langle \lambda \rangle$ is presented. It does not however give much information about the intensity of stretching, as it appears to be dominated by coherent eddy (i.e. *elliptic*) effects. Therefore in the following Fig. 2d (middle right) we give the average of *hyperbolic* effects. It is defined as the mean value of λ^+ conditioned to the *hyperbolic* regime:

$$\langle \lambda^+ \rangle_{supp} = \frac{\int_{supp(\lambda^+)} \lambda^+(\tau) d\tau}{\mu(supp(\lambda^+))}. \quad (20)$$

The mean instantaneous stretching efficiency $\langle \kappa \rangle$ (cf. equation (16)) is given in Fig. 2e (bottom left). It represents the combined influence of strain magnitude and geometrical alignments. Finally, In Fig. 2 (bottom right) we

present $h_{supp(e^+)}$ which in our notation represents the fraction of time when $\nabla \omega$ was aligned in a way that resulted in it being stretched.

CONCLUSIONS

In the instantaneous plots (Fig. 1) it is visible that the regions of the most intense *hyperbolic* activity are concentrated on the perimeters of the big eddies and along the thin vorticity filaments. These are the locations where the most robust stretching takes place. Further downstream the distributions of λ become less regular and small scales start to be involved. This qualitative change is also reflected in the statistical results shown in Fig. (2). In Fig. (2a) one can see that the vorticity gradients $|\nabla \omega|$ are sharpest in the vicinity of the obstacle. The near wake region is, in the mean sense, dominated by coherent eddies (Figs. 2b,c). It is interesting that, at the same time, the *hyperbolic* effects are most concentrated in this region and gradually decay further downstream (Fig. 2d). This is also indicated in Fig. (2e), which shows that in the near wake region the stretching efficiency is higher than elsewhere. All these facts imply that in the vicinity of the obstacle stretching of vorticity gradients proceeds in a significantly more intensive way. As it will be discussed at length elsewhere, this is indeed correlated with an increased intermittency correction observed in scaling exponents [5], [6]. Finally, it should be noted (Fig. 2f) that in the near wake there is a tendency of vorticity gradient $\nabla \omega$ to be aligned so that it is stretched. This implies increased organization of the flow on small scales.

ACKNOWLEDGMENTS

The first author is grateful to the PMMH / ESPCI Laboratory for hospitality. The support was provided by the TEMPUS Programme (JEP 08029-94). We acknowledge the discussions A. Babiano and J. Szumbarski.

REFERENCES

- [1] U. Frisch, *Turbulence: the legacy of A. N. Kolmogorov*, (Cambridge University Press, Cambridge, 1995).
- [2] R.H. Kraichnan, Phys. Fluids **10**, 1417 (1967).
- [3] R. Benzi, S. Ciliberto, C. Baudet, G. R. Chavarria, R. Tripiccone, Europhys. Lett. **24** (4), 275 (1993).
- [4] A. Babiano, B. Dubrulle, P. Frick, Phys. Rev. E **52**, 4 (1995).
- [5] E. Gaudin, S. Goujon-Durand, B. Protas, J. E. Wesfreid, J. Wojciechowski (preprint A 96/57 PMMH - ESPCI).
- [6] B. Protas, S. Goujon-Durand, J.E. Wesfreid, Phys. Rev. E (in press).
- [7] A. N. Kolmogorov, C.R. Acad. Sci. URSS **30**, 301 (1941).
- [8] E. Dresselhaus and M. Tabor, J. Fluid Mech. **236**, 415 (1991).
- [9] M. Tabor and I. Klapper, Chaos, Solitons Fractals **4**, 1031 (1994).
- [10] B. Legras, D. Dritschel, Appl. Sci. Res. **51**, 445 (1993).
- [11] P.G. Saffman, Stud. Appl. Math. **50**, 377 (1971).
- [12] J. Weiss, Physica D **48**, 273 (1991).
- [13] J. M. Ottino, *The kinematics of mixing: stretching, chaos and transport*, (Cambridge University Press, Cambridge, 1995).

- [14] M.E. Brachet, M. Meneguzzi, H. Politano, P.L. Sulem, *J. Fluid Mech.* **194**, 333 (1988).
- [15] W.I. Arnold, *Ordinary Differential Equations* (in Russian), Nauka (1971).
- [16] *Vortex Methods and Vortex Motion*, ed. K. E. Gustafson, J. A. Sethian, SIAM, Philadelphia 1991.
- [17] A. Styczek, J. Szumbariski, P. Wald, in *Japanese-Polish Joint Seminar on Advanced Computer Simulation, Tokyo, 1993*, (Tokyo, 1993).

HYPERVISCOUS DYNAMICS OF TWO-DIMENSIONAL TURBULENCE

V. Herbert and M. Larchêveque

Laboratoire de Modélisation en Mécanique URA-CNRS 229

Boîte 162

Université Pierre et Marie Curie

4 place Jussieu

75252 PARIS cédex 05

France

C. Staquet

Laboratoire de Physique

Ecole normale supérieure de Lyon

46 allée d'Italie

69364 Lyon cédex 07

France

ABSTRACT

Two-dimensional turbulence has been investigated by many authors using a hyperviscous operator. This dissipation operator, introduced by Basdevant *et al.* (1983), parameterizes the unresolved subgrid scales. Recent studies by Mariotti *et al.* (1994) and Jiménez (1995) have however put forward spurious effects attributed to this hyperviscous operator. The purpose of the present work is to investigate in detail these effects in comparison with simulations using an ordinary laplacian operator. For this comparison to be physically meaningful, we first introduce the concept of flows that are "equivalent", from a turbulent point of view. We next proceed to comparison between equivalent flows, either simulated using an ordinary laplacian diffusion or using a hyperviscous operator. For this purpose, we analyse in detail the topology and distribution of coherent vortices in the flow.

INTRODUCTION

The dynamics of the atmosphere at large scales can be modelled, in a simplified way, by two-dimensional turbulence (e.g. McWilliams 1983). Two-dimensional turbulence has also been the subject of numerous fundamental studies, through theoretical, experimental and numerical works. The two-dimensional Euler equations are characterized by the conservation of an infinite number of invariants, namely the integral kinetic energy and any integral function of the vorticity. Among the latter is the enstrophy (integral of the squared vorticity), whereof importance stems from the fact that its conservation prohibits kinetic energy from being transferred toward small scales. Only enstrophy can be transferred toward small scales. In a numerical model, the number of dynamical scales is finite and the transfer of enstrophy toward the subgrid scales across the smallest computed scale may be modelled by a high order linear operator (Basdevant *et al.*, 1983). Such a hyperviscous operator dissipates the enstrophy at this smallest scale while ensuring a quasi conservation of the kinetic energy. It writes

$$-\nu_p(-\Delta)^p, \quad \text{with } p \geq 2. \quad (1)$$

Almost all numerical studies of two-dimensional turbulence deal with the Navier-Stokes equations with the classical laplacian operator $\nu\Delta$ replaced by this hyperviscous operator. However, recent studies (Mariotti *et al.* 1994, Jiménez 1995) have revealed spurious small scale effects when this type of diffusion is used. In particular, vorticity about the vortex center is found to be pumped out toward the vortex center and toward its frontier.

The purpose of our study is to examine the influence of such a hyperviscous on the behavior of a two-dimensional decaying turbulent flow, using 512^2 numerical simulations. A difficulty in this study is to produce turbulent flows with different operators (laplacian and hyperviscous ones) whereof properties can be compared. Indeed, for this comparison to be possible, these flows have to be in the same turbulent state at a given time. A new concept of flows that are *equivalent* from a turbulent point of view is introduced in the next section. We next briefly present the two-dimensional flows that we simulate numerically. The influence of the hyperviscous operators upon their dynamics is next described in detail, through the topology and distribution of the coherent structures.

A NEW CONCEPT: EQUIVALENT TURBULENT FLOWS.

At a given time, we say that two-dimensional turbulent flows are in the same turbulent state, or are *equivalent* from a turbulent point of view, if their inertial range and enstrophy dissipation rate are the same. The dissipation rate of enstrophy is defined by:

$$\beta_p = -\frac{dZ}{dt} = 2\nu_p \int_0^{k_{max}} k^{2p+2} E_p(k) dk, \quad (2)$$

for a hyperviscous operator of order p (note that the ordinary laplacian operator is recovered for $p = 1$). The conditions $\beta_p = \beta$ and $E_p(k) = E(k)$, where the absence

of the p index refers to $p = 1$, yields:

$$\nu_p = \nu \frac{\int_0^{k_{max}} k^4 E(k) dk}{\int_0^{k_{max}} k^{2p+2} E(k) dk} \quad (3)$$

Relation (3) is valid at any time. Thus, we are able at any time to define a hyperviscous flow *equivalent* to a viscous flow. It is the subsequent evolutions of these flows that we wish to compare.

Figure 1, which displays ν_p/ν as a function of time, shows that the hyperviscosity ν_p reaches an absolute minimum value whatever the value of p at a time independent of p .

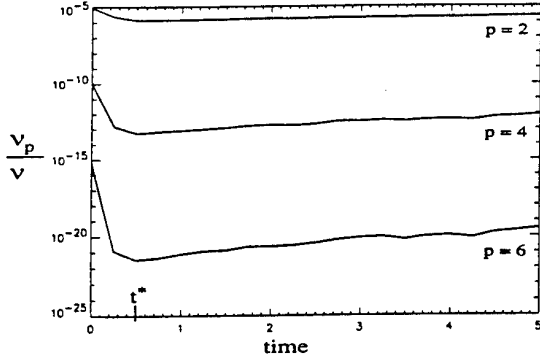


FIGURE 1: Temporal evolution of the ratio ν_p / ν , for $p = 2, 4$ and 6 . The minimum of the ratio is reached for $t = t^* = 0.5$.

At that time, denoted t^* , the two-dimensional skewness factor of the $p = 1$ flow reaches a maximum value, meaning that the enstrophy has reached the smallest dissipative scales and that, therefore, a developed spectrum has set up (Brachet *et al.* 1988). The relation between this skewness factor and ν_p is unclear yet. From a practical point of view, we carry out a simulation with a laplacian diffusion ($p = 1$ simulation) starting from a given initial condition (specified below). At time t^* , we define *equivalent* hyperviscous flows as stated above and next continue the simulations of these different flows with $p = 1, 2$ and 4 .

DIRECT NUMERICAL SIMULATIONS: INITIAL CONDITIONS AND FLOW PARAMETERS.

The initial condition ($t = 0$) of two-dimensional turbulence is prescribed in Fourier space by a kinetic energy spectrum strongly peaked about the wavenumber $k_0 = 8$:

$$E(k) = v_0^2 \frac{k}{k_0} \exp\left(-\frac{k^2}{k_0^2}\right) \quad (4)$$

with $v_0 = 0.4$. The molecular viscosity ν has the value $1/500$ and the resolution of all calculations is 512^2 . The Navier-Stokes equations with periodic boundary conditions are solved in Fourier space using a standard pseudo-spectral algorithm (e.g. Canuto *et al.* 1988). Time advancement is made through a third order Adams-Bashforth scheme and the viscous terms are solved explicitly (no difference with the use of a second order implicit Crank-Nicholson algorithm has been found, the Reynolds number of the flow being large enough for the stability condition to be imposed by the advective time scale and not by the diffusive one).

NUMERICAL RESULTS

The influence of a hyperviscous operator ($p = 2$ and $p = 4$) upon the dynamics of two-dimensional turbulence

is first investigated through the temporal evolution of the quadratic invariants of the flow, (in the absence of viscous effects) namely the kinetic energy E and the enstrophy Z averaged over the numerical domain.

E and Z are plotted in figures 2 and 3 respectively. Their $p = 1$ evolution is also drawn for comparison

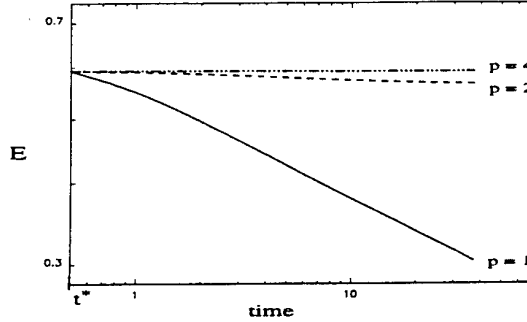


FIGURE 2: Kinetic energy E for $p = 1, 2$ and 4 .

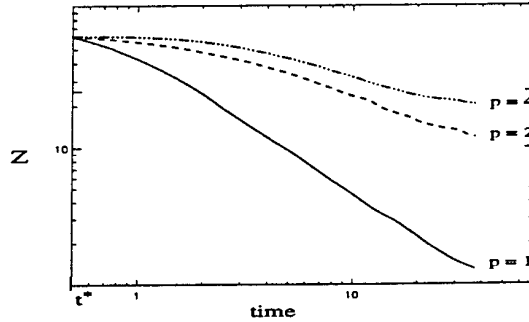


FIGURE 3: Enstrophy Z for $p = 1, 2$ and 4 .

Figure 2 shows that the dramatic decrease of E when an ordinary laplacian diffusion is used is halted for $p = 4$ because of the local action in Fourier space of the hyperviscous operator, at the largest wavenumbers. The enstrophy displays the same trend though the hyperviscous diffusion operator was designed so as to parameterize enstrophy transfers toward subgrid scales across the wavenumber cut-off. The reason for the lesser decay of Z as p increases, as shown below, is that the total enstrophy is mostly contributed by vortex maxima, which decrease much less as time elapses for $p = 2, 4$.

Studies of two-dimensional turbulence have mostly focused upon the coherent structures of the flow, through detailed diagnostic analysis (Weiss 1981, Benzi *et al.* 1988, Mc Williams 1990, Elhamaïdi *et al.* 1993). These structures account for the most part of the flow vorticity. It is therefore of interest to explore the influence of a hyperviscous operator on these structures. Before presenting our results, we first need to present the method we have used to identify the vortices.

The identification of a vortex is still a matter of debate but the most common definition uses Weiss criterion: a vortex is defined by the region of the flow where the Hessian of the stream function is strictly positive:

$$H(\psi) = \frac{\partial^2 \psi}{\partial x^2} \cdot \frac{\partial^2 \psi}{\partial y^2} - \left(\frac{\partial^2 \psi}{\partial x \partial y} \right)^2 > 0. \quad (5)$$

Larchevêque (1993) suggested to rather define the structures by the hessian of the *vorticity* to be strictly positive. The frontier of the vortex becomes the line where the hessian vanishes and more physically, where $\|\nabla\omega\|$ is maximum. Larchevêque also proved that vortex lines are closed lines within this frontier. Using high resolution numerical simulations, Herbert *et al.* (1996) showed that this new criterion better educes the vortex cores than the Weiss criterion. This new criterion has been used in the present case to detect the vortices of the flow, along with a threshold test on the ellipticity of the structures to eliminate vorticity filaments.

The density of vortices ρ is plotted in figure 4.

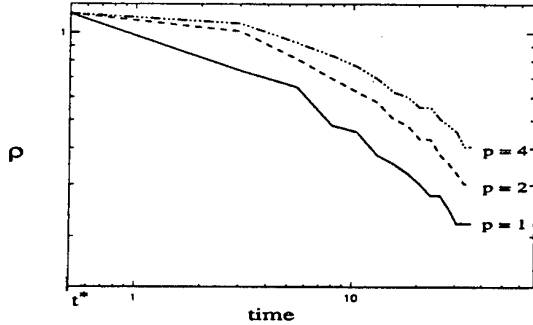


FIGURE 4: Vortex density ρ for $p = 1, 2$ and 4 .

The vortex density increases with order p . The reason is that the hyperviscous operator acts locally in Fourier space, at high wavenumbers only, as said above; in physical space, this action affects all regions where strong vorticity gradient exists, as in the periphery of vortex centers. Thus, the hyperviscous operator tends to smooth out more rapidly the vortex periphery and, consequently, to isolate the vortices in preventing pairing from occurring. In other words, this hyperviscous operator promotes intermittency. Another consequence is that the mean radius R of the vortices (figure 5) increases much less for higher values of p , pairing being the primary mechanism for the growth of the vortices. The value found for $p = 2$ is in agreement with the hyperviscous simulations of McWilliams (1990).

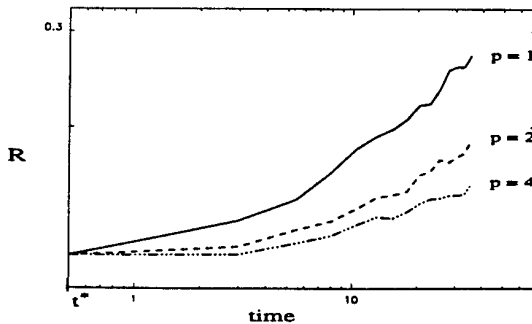


FIGURE 5: Mean radius R of the vortex for $p = 1, 2$ and 4 .

Finally, the mean value ω_{ext} for the vortex maxima is plotted in figure 6. We observe that this mean value remains close to its initial value for $p=2$ and 4 only, which is consistent with figure 3.

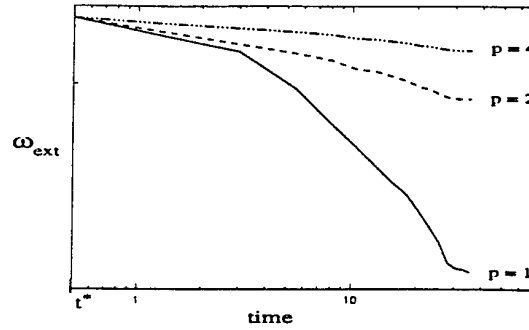


FIGURE 6: Mean value of the vortex maxima ω_{ext} for $p = 1, 2$ and 4 .

CONCLUSIONS

We have investigated the dependency of two-dimensional homogeneous isotropic turbulence upon a hyperviscous operator $-(\Delta)^p$, using 512^2 numerical simulations. For this purpose, we have introduced the concept of flows that are *equivalent* from a turbulent point of view. This concept permits us to infer a hyperviscous flow from (and equivalent to) a viscous flow, at a given time. We next compare the development of both viscous and hyperviscous flows from that time. A strong effect of the hyperviscous operator upon the coherent structures of the flow is found: because it smoothes locally strong vorticity gradients, this hyperviscous operator isolates the structures and thus prevents pairing from occurring. As a consequence, intermittency increases: the hyperviscous flow becomes made of small vortices -i.e. with a smaller radius than in the simulations using an ordinary laplacian operator- with strong vorticity maxima -close to their initial value- embedded in a nearly irrotational flow. The reduction of pairing events also decreases the transfers of enstrophy toward small scales, which steepens the energy density spectra and thus leads to discrepancy with predictions by theories of turbulence, in which spatial homogeneity of the fluctuations is assumed.

ACKNOWLEDGEMENTS

This work has been supported by the Groupement de Recherche (GDR) Mécanique des Fluides Numériques of CNRS. Computation time has been allocated by the scientific council of IDRIS (CNRS computer center), through contracts nos 960389 and 970389.

REFERENCES

- Basdevant C. and Sadourny R., 1983, "Ergodic properties of inviscid truncated models of two-dimensional incompressible flows", *J. Fluid Mech.*, A 69, p. 673-688.
- Benzi R., Paternello S. et Santangelo P., 1988, "Self-similar coherent structures in two-dimensional decaying turbulence", *J. Phys A : Math. Gen.*, 21, 1221-1237.
- Brachet M. E., Meneguzzi H., Politano and P. L. Sulem, 1988, "The dynamics of freely decaying turbulence", *J. Fluid Mech.*, 194, p. 333-349.
- Canuto, C., Hussaini, M.Y., Quarteroni A., and Zang T.A., 1988, "Spectral methods in fluid dynamics", *Springer series in computational physics*, Springer Verlag, Berlin.
- Elhmaïdi D., Provenzale A. and Babiano A., 1993, "Elementary topology of two-dimensional turbulent flows and single particle dispersion". *J. Fluid Mech.*, 251, p. 533-558.
- Herbert V., Larchevêque M. et Staquet C., 1996, "Identification des structures organisées en écoulement bidimen-

sionnel", *C. R. Acad. Sci. Paris*, 323 Série II b, p. 519-526.

Jiménez J., 1995, "Hyperviscous vortices", *J. Fluid Mech.*, 279, p. 169-176.

Larchevêque M., 1993, "Pressure field, vorticity field, and coherent structures in a two-dimensional incompressible turbulent flow", *Theoret. Comput. Fluid Dynamics*, 5, p. 215-222.

Marrioti A., Legras B. and Drichtel D.G., 1994, "Vortex stripping and erosion of coherent structures in two-dimensional flows", *Phys. Fluid A*, 6, p. 3954-3962.

Mc Williams J.C., 1983, "On the relevance of two-dimensional turbulence to geophysical fluid motions", *Journal Mécanique Théor. Appl.*, special issue of Two-Dimensional Turbulence, p. 83-97.

Mc Williams J.C., 1990, "The vortices of two-dimensional turbulence", *J. Fluid Mech.*, 219, p. 361-385.

Weiss J., 1991, "The dynamic of enstrophy transfert in two-dimensional hydrodynamics", *Physica D*, 48, p. 273-294.

MODEL OF TWO-DIMENSIONAL TURBULENCE FOR LIQUID METAL FLOWS IN A MAGNETIC FIELD

J. SOMMERIA

Laboratoire de Physique
Ecole Normale Supérieure de Lyon
46 allée d'Italie
69364 Lyon cdx 07
France

T. DUMONT, R. ROBERT

Laboratoire d'Analyse Numérique
Univ. Lyon 1,
69 622 Villeurbanne Cedex
France

ABSTRACT

We model a laboratory experiment of turbulent shear flow in a layer of conducting fluid subjected to a transverse magnetic field. The turbulence has very specific properties due to its two-dimensional structure. It organizes into a ring of a few coherent vortices. Furthermore heat transfer measurements indicate a very weak turbulent heat flux. We first explain these properties by statistical mechanics of vorticity. The flow organization appears as the consequence of optimal vorticity mixing with the constraint due to the conserved quantities like energy, circulation, and angular momentum. The flow does not really reach this equilibrium, but tends to it under the effect of turbulent stirring. We use this property to derive a Large Eddy Simulation of the system.

INTRODUCTION

For a conducting fluid in a magnetic field, usual turbulence is damped by Joule dissipation in eddy currents. However two-dimensional turbulence persists with weak energy dissipation, in the case of a fluid layer submitted to a uniform transverse magnetic field (Sommeria & Moreau, 1982, Buhler, 1996). There is therefore an interesting analogy with geophysical flows. Moreover, this property could be useful to enhance heat transfers in liquid lithium blankets around tokamacs designed for nuclear fusion. Usual turbulence models, adapted to three-dimensional turbulence, are inappropriate. We here propose a theoretical modelling of such two-dimensional shear flows, and test it by comparison with the laboratory experiments reported in this conference by Alboussière et al. (1997). A circular shear flow is electrically driven in a annular horizontal mercury layer, subjected to a vertical magnetic field.

The flow is modelled by the two-dimensional Navier-Stokes equations, with forcing and friction terms. The forcing term accounts for the interaction of injected electrical currents with the magnetic field. The friction term represents the effect of the horizontal (Hartmann) boundary layers, vertically transferred to the whole fluid layer by the "rigidity" due to the magnetic field.

Horizontal viscosity effects are small (the Reynolds number is typically 10^5), so that small scale vorticity fluctuations develop, and some statistical modelling is needed. The energy cascade toward small scales is forbidden (as vorticity is conserved by the non-linear transfer terms), and the flow tends to be organized in large vortices. This organization has been explained by equilibrium statistical mechanics for a model of point vortices (Onsager, 1949, Montgomery & Joyce, 1974). A generalization to continuous vorticity fields has been more recently developed (Robert & Sommeria, 1991). The organized vortices are predicted as states of maximum vorticity mixing compatible with the conservation of energy. We first discuss these equilibrium states, using a highly simplified model.

Statistical equilibrium is not really reached in the presence of forcing and friction. However turbulent mixing is expected to drive the system towards this equilibrium. This idea can be used for turbulence modeling in a Large Eddy Simulation, using the approach of non-equilibrium linear thermodynamics. Like diffusivity drives the system toward the thermodynamic equilibrium, with uniform concentration, the eddy fluxes should drive the system towards the statistical equilibrium. This equilibrium is non-trivial, involving organized vortices, so that the resulting turbulence model does not reduce to an eddy diffusivity. Robert & Sommeria (1992) developed this idea, proposing a principle of maximum entropy production: eddy fluxes of vorticity increase entropy at an optimal rate, while exactly conserving energy. This LES model, consistent with the specific conservation properties of two-dimensional turbulence, has been successfully tested on vortex interactions by Robert & Rosier (1997), and on a simplified model of oceanic circulation by Kazantsev et al. (1997). We apply here a similar LES model for the M.H.D. experiments.

THE PHYSICAL MODEL

The experimental geometry is sketched in Fig. 1 (together with the numerical grid used for computations). An electric current is flowing from the circular line of electrodes to the outer frame. The interaction of this radial

current with the vertical magnetic field generates an azimuthal jet along the outer rim. This jet becomes turbulent by shear instability, but this turbulence remains mainly two-dimensional due to the effect of the magnetic field.

Mercury is used, with density $\rho = 1.36 \times 10^4 \text{ kg m}^{-3}$, viscosity $\nu = 1.17 \times 10^{-7} \text{ m}^2 \text{ s}^{-1}$, electrical conductivity $\sigma = 1.05 \times 10^6 \Omega^{-1} \text{ m}^{-1}$. The magnetic field is $B = 0.17$ Tesla, the layer thickness $a = 10^{-2} \text{ m}$. The radius of the cell is $R = 11 \text{ cm}$, and the current is injected at the radius $r_e = 9.3 \text{ cm}$. The Hartmann number M and interaction parameter N , characterizing the importance of electromagnetic forces in comparison with viscous and inertial effects respectively, are

$$M = \left[\frac{\sigma B^2 a^2}{\rho \nu} \right]^{1/2} = 43.7, \quad N = \frac{\sigma B^2 a}{\rho U} = 0.22 \quad (1)$$

where we have assumed a typical velocity scale $U = 0.1 \text{ m/s}$.

At high Hartmann number, the velocity is quasi-uniform along the direction of the magnetic field (vertical), except for a thin Hartmann layer near horizontal walls (the Hartmann layer thickness is $a/M = 0.23 \text{ mm}$ in the considered experiments). Furthermore for a sufficiently high interaction parameters N , the flow can be modelled by the two-dimensional Navier-Stokes equation with a electric forcing term, and a term of friction in the Hartmann boundary layer. Following Sommeria (1988), we write a two-dimensional equation of motion for the divergenceless horizontal velocity field $\mathbf{u}(x, y, t)$ in the core

$$(\partial/\partial t + \mathbf{u} \cdot \nabla) \mathbf{u} = -\nabla P/\rho + \mathbf{f}(x, y) - \mathbf{u}/t_H \quad (2)$$

The driving term $\mathbf{f} = \mathbf{J} \times \mathbf{B}/\rho$ results from the (vertically averaged) horizontal current density \mathbf{J} introduced by the electrodes. Its horizontal divergence is proportional to the current density j_z injected through the bottom plate, $\nabla \cdot \mathbf{J} = j_z/a$, due to the conservation of the electric current. As a consequence $\nabla \times \mathbf{f} = -j_z \mathbf{B}/(\rho a)$. In the considered geometry, the current density can be considered as a Dirac δ function, centered at the injection radius r_e , with integral equal to the injected current I ,

$$j_z = \frac{I}{2\pi r_e} \delta(r - r_e) \quad (3)$$

and \mathbf{f} is purely azimuthal, with value

$$f_\theta = -\frac{IB}{2\pi \rho a r} \quad (4)$$

The last term in (2) is the Hartmann friction, with characteristic time

$$t_H = (\rho/\sigma \nu)^{1/2} a/(2B). \quad (5)$$

The upper surface is free, but covered by a thin rigid (oxyde) film, so that a no slip condition must be used (and we neglect the vertical deformation of the surface). Therefore, two Hartmann layers, at the bottom plate and the upper surface, contribute to the friction, yielding the factor 2 in the expression for t_H .

We shall use the equation of motion in term of vorticity ω and stream function ψ , writing the advective term with the Jacobian J ,

$$\frac{\partial \omega}{\partial t} + J(\psi, \omega) = -j_z(B/\rho a) - \frac{\omega}{t_H} \quad (6)$$

The velocity is $\mathbf{u} = \nabla \times \psi \mathbf{z}$, where \mathbf{z} is the upward vertical unit vector, and $\omega = (\nabla \times \mathbf{u}) \cdot \mathbf{z}$, so that

$$\omega = -\Delta \psi. \quad (7)$$

Equation (2) or (6) needs to be solved numerically, but general results can be obtained by the conservation laws.

Indeed the following quantities are conserved by the advective term: the total circulation Γ (and the integral of any function of the vorticity), the angular momentum L , the energy E , respectively defined as

$$\Gamma = \int \omega d^2 \mathbf{r} \quad (8)$$

$$L = \int u_\theta r d^2 \mathbf{r} = \int \frac{1}{2} \omega (R^2 - r^2) d^2 \mathbf{r} \quad (9)$$

$$E = \frac{1}{2} \int u^2 d^2 \mathbf{r} = \frac{1}{2} \int \psi \omega d^2 \mathbf{r} \quad (10)$$

Under the effect of a horizontal viscosity ν , energy decays, but at a rate $-\nu \int \omega^2 d^2 \mathbf{r}$ which tends to zero in the limit of small viscosity (since $\nu \int \omega^2 d^2 \mathbf{r}$ remains bounded). Similarly the angular momentum is conserved in the limit of a small viscosity. Indeed the rate of change of the angular momentum is the torque due to the viscous stress $\nu \partial u_\theta / \partial r$ at the outer wall. A boundary layer with minimum thickness $\delta \sim (\nu R/u_\theta)^{1/2}$ (corresponding to the width of diffusion during the period of rotation $\sim R/u_\theta$) is formed near this wall. This leads to a torque $\sim \nu u_\theta R^2/\delta \sim \nu^{1/2} (Ru_\theta)^{3/2}$, tending to zero in the limit of small viscosity. The circulation is maintained equal to zero by a small viscosity, because of the no-slip boundary condition: the vorticity in the interior is balanced by an opposite vorticity in the boundary layer. If this vorticity remains in the boundary layer, without detachment, the circulation in the interior is conserved. We shall make this hypothesis, and therefore assume that Γ , L , and E are not modified by the small horizontal viscosity effects.

Then these three quantities are set in the steady regime by a global balance between forcing and Hartmann friction. This balance writes, introducing (8-10) in (2) or (6),

$$\Gamma = -t_H IB/(\rho a) \quad (11)$$

$$L = t_H \int r f_\theta d^2 \mathbf{r} = -\frac{t_H IB}{2\rho a} (R^2 - r_e^2) \quad (12)$$

$$E = (t_H/2) \int \mathbf{f} \cdot \mathbf{u} d^2 \mathbf{r} = \Gamma/(4\pi) \int \psi(r_e, \theta) d\theta \quad (13)$$

In the considered experiments, the interaction parameter N is of order 1, so the validity of the 2D model (2) or (6) is questionable. In particular Ekman recirculation effects are expected in vortices (as discussed by Sommeria & Moreau, 1982), leading to additional dissipation. Furthermore, the Hartmann boundary layer may become unstable, exciting small eddies at scale a/M , which would also increase energy dissipation. The practical threshold of instability, obtained from duct flow experiments, is $Re/M \equiv M/N = 250$, as discussed by Sommeria (1988). This threshold corresponds to a velocity $U = 12.5 \text{ cm/s}$ in the experimental conditions, so it is exceeded in most cases (with velocities up to 30 cm/s in some experiments). Despite these caveats, we know that shallow water experiments are reasonably described by a two-dimensional model of the form (2) or (6), even without magnetic field. Therefore we expect that such a two-dimensional model is a good approach, possibly with additional friction effects due to three-dimensional perturbations (the friction time becoming shorter than t_H).

STATISTICAL EQUILIBRIUM STATES

The electrical forcing generates an annular shear, with vorticity localized over the electrode ring. This shear is unstable, and produces classical Kelvin-Helmholtz vortices. After successive merging, the turbulence organizes in a robust pattern of a few vortices. This remarkable behavior is common to various experiments producing two-dimensional annular shears in different physical conditions.

Although turbulent fluctuations remain, the very weak heat transfer measured in the experiment suggest that fluid particle mainly oscillate around some equilibrium position.

Statistical mechanics of vorticity provides a general understanding of this flow organization, in the frame of an inviscid theory. We first consider the case of a free flow evolution, from some initial condition, instead of the permanently forced case. A steady flow is predicted as the most probable final outcome of complex vorticity stirring, with the constraint due to the conservation laws of the Euler equations. Vorticity fluctuations remain at small scale, but they generate a coherent large scale steady flow. It is characterized by a relationship between vorticity and stream function

$$-\Delta\psi = f(\psi') \quad (14)$$

where ψ' is the stream function in some rotating frame of reference. This function f must be monotonic, with values bounded by the minimum and maximum vorticity of the initial condition. It is implicitly determined by the respective area occupied by the different vorticity levels. For a vorticity strip with small area and high vorticity, it simplifies to

$$-\Delta\psi = \exp[-\alpha - \beta(\psi + \Omega r^2/2)] \quad (15)$$

where the constants α , β , and Ω are indirectly set by the values of circulation, angular momentum and energy, given by the initial condition. Notice that the expression (15) is also obtained from point vortex statistical mechanics, but more general results can be obtained in other cases.

The statistical equilibrium obtained from an initial strip of vorticity initially at radius r_e is shown in Fig. 2. Part of the vorticity spreads around the cell, but part of it remains in an isolated coherent vortex. While entropy maximization favors an even spreading of vorticity, mixed with the irrotational fluid, the constraints on energy and angular momentum lead to the persistence of the organized vortex, close to the outer rim. This statistical equilibrium represents the trend towards which turbulent stirring should drive the system. It naturally explains the formation of large vortices, and their merging to form larger ones. In next section, we shall present a numerical simulation of the system with forcing and friction, modelling subgrid scale turbulence as a force driving the system towards the statistical equilibrium.

NUMERICAL SIMULATIONS IN THE FORCED CASE

The equation of motion (6) involves fine scale vorticity fluctuations which we do not resolve explicitly. They produce an eddy flux of vorticity $J_\omega = \tilde{u}\tilde{\omega}$ (denoting by a tilde the subgrid scale fluctuations). To determine this flux, we use a Maximum Entropy Production Principle, as discussed by Robert & Sommeria (1992), Robert & Rosier (1997), Chavanis & Sommeria (1997). In general the system is described in term of the local probability distribution of vorticity levels, which generally requires many variables at each grid point. We use here an approximation, expressed only in term of the local vorticity ω (averaged over the subgrid scales), and the fluctuation variance $\omega_2 = \tilde{\omega}^2$. The eddy flux is expressed as

$$J_\omega = -A_E(\nabla\omega - \omega_2(\beta\nabla\psi + \gamma\tau)) \quad (16)$$

where β satisfies the system

$$\begin{aligned} \beta \int \omega_2(\nabla\psi)^2 d^2\mathbf{r} + \gamma \int \omega_2 \mathbf{r} \cdot \nabla\psi d^2\mathbf{r} &= - \int \nabla\psi \cdot \nabla\omega d^2\mathbf{r} \\ \beta \int \omega_2 \mathbf{r} \cdot \nabla\psi d^2\mathbf{r} + \gamma \int \omega_2 r^2 d^2\mathbf{r} &= - \int \mathbf{r} \cdot \nabla\omega d^2\mathbf{r} \end{aligned} \quad (17)$$

The first term in the expression of J_ω represents a usual diffusion, and the second term a systematic drift, whose coefficient b is determined by (17) to exactly satisfy the energy conservation and angular momentum. The vorticity ω and local variance ω_2 satisfy the following pair of evolution equations,

$$\frac{\partial\omega}{\partial t} + J(\psi, \omega) = -\nabla \cdot J_\omega - j_z B/(\rho a) - \omega/t_H \quad (18)$$

$$\frac{\partial\omega_2}{\partial t} + J(\psi, \omega_2) = \nabla \cdot (A_E \nabla\omega_2) - 2J_\omega \cdot \nabla\omega - 2\omega_2/t_H \quad (19)$$

The first and second terms in the right hand side of (19) respectively stand for the eddy diffusion of vorticity variance, and its production by the eddy fluxes of vorticity. The diffusion coefficient A_E depends on the local vorticity fluctuations as

$$A_E = k\epsilon^2\omega_2^{1/2} \quad (20)$$

where ϵ is a typical mesh size (here $0.02R$), and $k = 0.25$ an empirical non-dimensional constant. With $\omega_2 \sim 1s^{-1}$, this yields a typical eddy diffusivity $1.2 \times 10^{-6} m^2 s^{-2}$ about 10 times higher than the molecular viscosity (which is neglected).

The impermeability boundary condition imposes a constant streamfunction, set equal to zero, at the boundary. Physically, the no slip condition is also imposed by viscous effects. However the boundary layers have a three-dimensional structure, influenced by the magnetic field. Therefore the boundary condition required for the two-dimensional model, describing only the interior flow (outside the boundary layer), does not need to be no-slip. For a similar experiment, Verron & Sommeria (1987) found that a free slip condition is more appropriate, but not necessarily the best choice. The MEP principle naturally provides a boundary condition for the inviscid model, without additional hypothesis. Indeed stating that the normal flux for both ω and ω_2 vanish at the boundary yields (with \mathbf{n} the normal unit vector)

$$\psi|_{\partial\mathcal{D}} = 0 \quad (21)$$

$$\mathbf{n} \cdot \nabla\psi|_{\partial\mathcal{D}} = b g_2 \mathbf{n} \cdot \nabla\psi|_{\partial\mathcal{D}} \quad (22)$$

$$\mathbf{n} \cdot \nabla\omega_2|_{\partial\mathcal{D}} = 0 \quad (23)$$

Note that condition (22) is not standard: the normal vorticity gradient is proportional to the tangential velocity.

We numerically solve these equations with a finite element code, allowing easy adaptation to different geometries. Vorticity is injected along a circle by the electrical forcing. We find that this shear layer is unstable, producing a ring of vortices (Fig. 3a), increasing in width by successive merging events. A permanent regime involving a ring of large steady vortices is eventually obtained (Fig. 3b). As the forcing is increased, the flow is more inertial, and merging leads to a steady ring with fewer vortices, until a state of two vortices is obtained at high forcing (Fig. 3c). These findings are basically in agreement with the experiments.

The radial profile of azimuthal velocity is in good agreement with the experiments, but the velocity is typically twice larger for a given current. It appears that the angular momentum in the experiments is also about half the one predicted by relation (12). Since this relation does not rely on the numerical resolution of the two-dimensional model, we can conclude that the friction time is actually twice shorter than t_H . This is not really surprising as the interaction parameter is smaller than 1, which invalidates the derivation of the two-dimensional model. However reasonable agreement with experiments is obtained by adjusting the friction time to fit the experimentally obtained angular momentum.

CONCLUSIONS

The organization of turbulence into coherent vortices is understood by the statistical theory. It provides a natural explanation for the weak heat transfer measured in the experiments: a fluid particle containing vorticity do not move freely, but remains bounded (in the average) to a coherent vortex, so it cannot transport heat efficiently, in spite of the strong turbulent motion. Heat transfer computations are in progress to make this statement more precise.

Numerical computations give result in good agreement with the experiments, but with velocity typically twice larger, for a given driving current. This must be due additional friction effects, not taken into account in the model (2). A more systematic comparison is in progress to better characterize this discrepancy as a function of the parameters.

ACKNOWLEDGEMENTS

This work has been supported by the EEC grant CIPA-CT-93-0080.

REFERENCES

- Alboussière T., Uspenski V. & Moreau R. "Quasi-2D MHD turbulent free shear layers" Communication submitted to the 11th Symposium on Turbulent Shear Flows.
- Buhler L. (1996) "Instabilities in quasi-two-dimensional magnetohydrodynamic flows" *J. Fluid Mech.* 326, 125-150.
- Chavanis & Sommeria (1997) "A thermodynamic approach to small scale parametrization in 2D turbulence" *Phys. Rev. Letters* 28, 3302-3305.
- Kazantsev E., Sommeria J., Verron J. (1997) "Subgrid scale eddy parametrization by statistical mechanics in a barotropic ocean model" submitted *J. Phys. Ocean.*
- Montgomery D. & Joyce G. (1974) "Statistical mechanics of negative temperature states" *Phys. Fluids* 17, 1139-1145.
- Onsager (1949) "Statistical hydrodynamics" *Nuovo Cimento Suppl.* 6, 279-287.
- Robert R. & Rosier C. (1997) "The modelling of small scales in 2D turbulent flows: a statistical mechanics approach", *J. Stat. Phys.*
- Robert R. & Sommeria J. (1991) "Statistical equilibrium states for two-dimensional flows" *J. Fluid Mech.* 229, 291-310.
- R. Robert and J. Sommeria (1992), *Phys. Rev. Letters*, 69 2776-2779.
- Sommeria J. and Moreau R. (1982) "Why, how, and when, MHD turbulence becomes two-dimensional" *J. Fluid Mech.* 118, 507-518.
- Sommeria J. (1988) "Electrically driven vortices in a strong magnetic field", *J. Fluid Mech.* 189, 553-569.
- Verron J. and Sommeria J. (1987) "Numerical simulation of the two-dimensional turbulence experiment in magnetohydrodynamics" *Phys. Fluids* 30, 732-739.

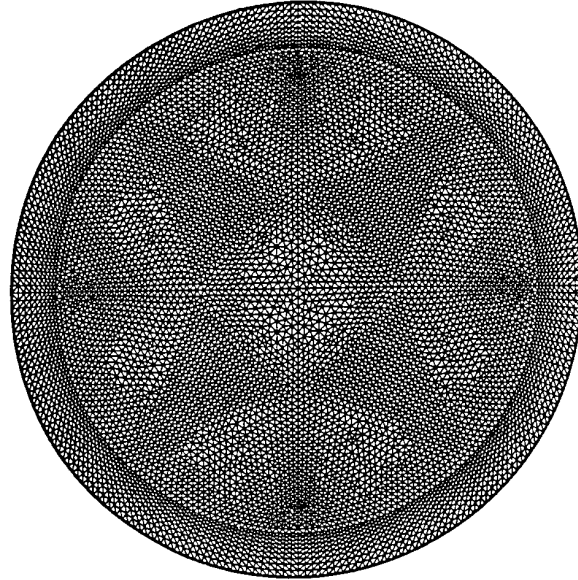
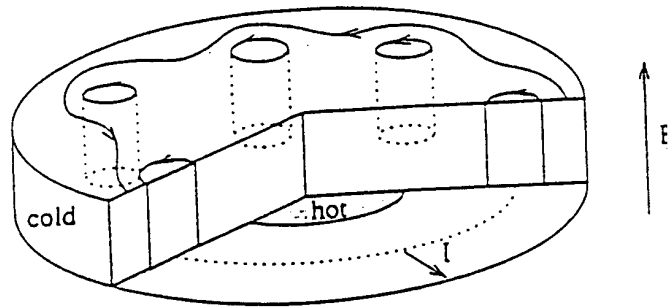


Figure 1: a) Sketch of the mean flow and two-dimensional organized vortices in the experimental cell of Alboussière et al. (1997). We have also represented the line of electrodes injecting the current I at the radius $r_e=9.3$ cm, while the cell radius is $R=11$ cm. b) Numerical grid used for the computations with the finite element method.

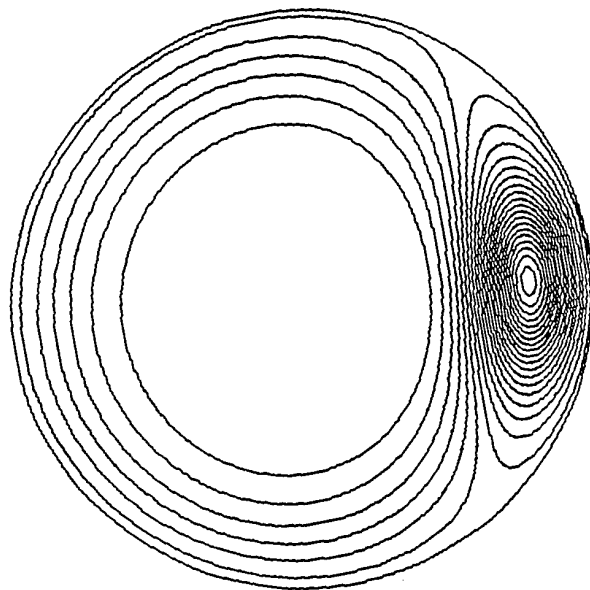


Figure 2: Statistical equilibrium state (isovorticity contours) calculated from the free inertial evolution from a thin vorticity sheet located at the radius r_e (corresponding to the vorticity injection in the laboratory experiment).

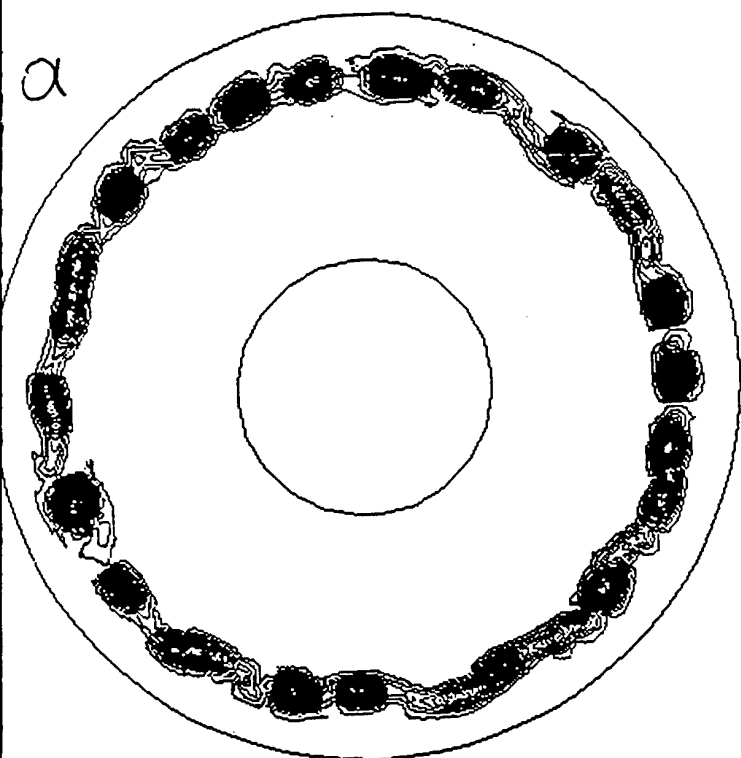
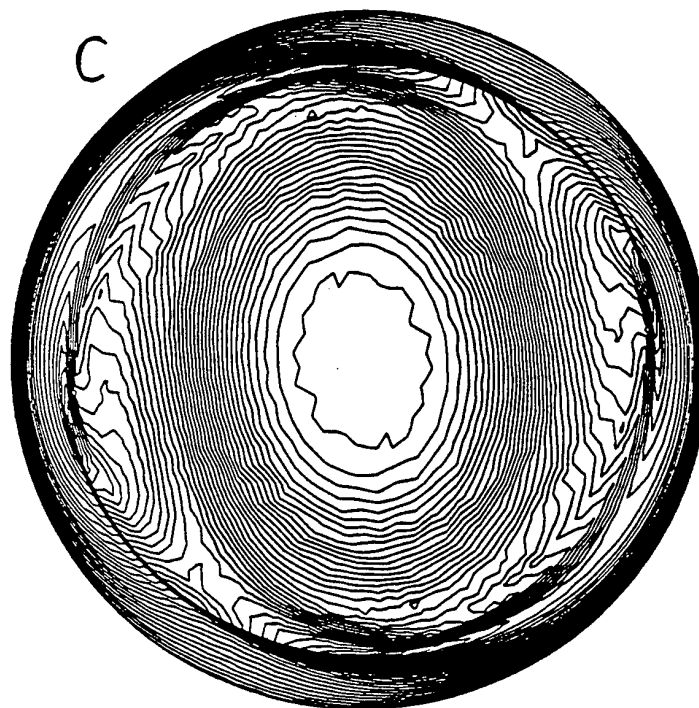
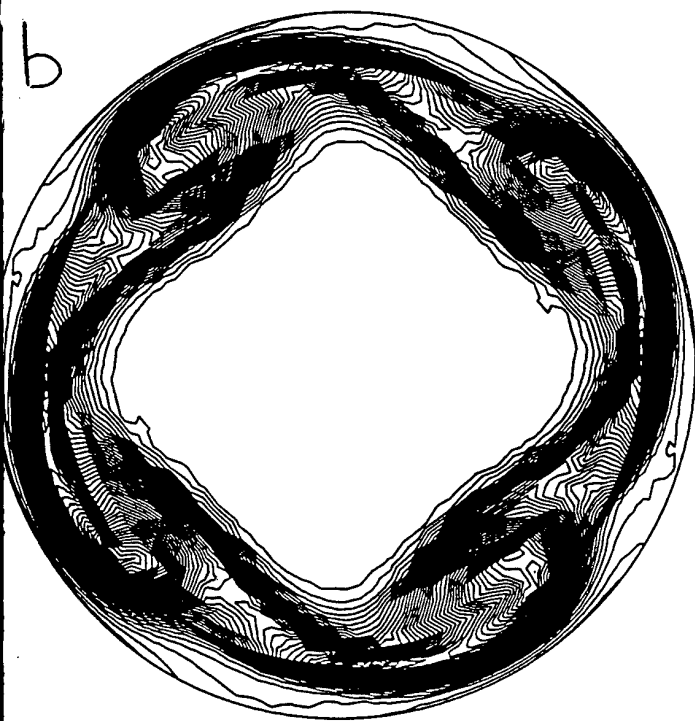


Figure 3: Numerical computation with the actual experimental forcing (vorticity contours). a) Initial development of the shear instability; b) Organization into a quasi-steady ring of four vortices, at moderate forcing ($I=2.5$ A); c) Organization into a two-vortex state at higher forcing ($I=20$ A)



VORTICITY MEASUREMENTS IN A TURBULENT GRID FLOW

Y. Zhu[†], T. Zhou and R. A. Antonia

Department of Mechanical Engineering,
The University of Newcastle, N.S.W., 2308, Australia

[†]Current Address: Department of Mechanical Engineering,
Johns Hopkins University, Baltimore, MD 21218, USA

ABSTRACT

All three velocity components and all three vorticity components in decaying grid turbulence have been measured with a 4-X-wire vorticity probe. The measurements indicate that local isotropy is more closely satisfied than global isotropy. The velocity and vorticity fluctuations exhibit the same rate of decay with power-law exponents of about 1.25 and about 1 respectively. These exponents are consistent with the isotropic form of the vorticity equation.

INTRODUCTION

Measurements of one, two and in some cases all three components of the vorticity vector ω_i ($\equiv \epsilon_{ijk}u_{k,j}$, where ϵ_{ijk} is the alternating tensor and $u_{k,j} = \partial u_k / \partial x_j$) have been reported in different flows using different types of hot wire probes (e.g. Wallace and Foss, 1995; Antonia et al., 1996; Zhu and Antonia, 1996a,b). An accurate measurement of ω_i is important for studying various aspects of turbulence, such as helicity, the turbulent/non-turbulent interface and small-scale intermittency. Batchelor and Townsend (1947) examined the decay of vorticity in grid turbulence by measuring the longitudinal velocity fluctuation u_1 and by assuming isotropy. Various studies (e.g. Comte-Bellot and Corrsin, 1966 and more recently Mydlarski and Warhaft, 1996) have demonstrated that isotropy is not precisely satisfied. The direct measurement of vorticity should provide a more stringent quantification of the de-

cay law since vorticity is closely associated with the small scale structure of turbulence and local isotropy is more likely to be satisfied than isotropy. Kit et al. (1988) and Fan (1991) examined the decay of the streamwise vorticity ω_1 in grid turbulence. Although a linear decay behavior was verified, i.e. $d(1/\omega'_1)/dt = \text{constant}$ (hereafter a prime denotes a rms value), the constant was not evaluated. The determination is important since it can provide a stringent test of the vorticity transport equation. The main aim of the present study is to quantify the vorticity decay in grid turbulence.

MEASUREMENT DETAILS

Measurements were made along the centerline of the wind tunnel at several locations downstream of a biplane grid ($x_1/M = 20 \sim 80$, where x_1 is measured from the grid plane and the mesh size M is 24.76 mm. The grid consists rods of 4.76 mm diameter, yielding a solidity of 0.35. The mean flow velocity U was 12.3 m/s and the Reynolds number R_M ($\equiv UM/\nu$) was 20300. At this speed, the Kolmogorov length scale η varies from 0.17 mm at $x_1/M = 20$ to 0.4 mm $x_1/M = 80$.

The vorticity probe consists of 4 X-probes, two placed in the $x_1 - x_2$ plane and separated in x_3 direction; the other two placed in the $x_1 - x_3$ plane and separated in the x_2 direction (Zhu and Antonia, 1996a,b). It is assumed that each X-probe measures two velocity fluctuation components at the centre of the probe. For each X-probe, the

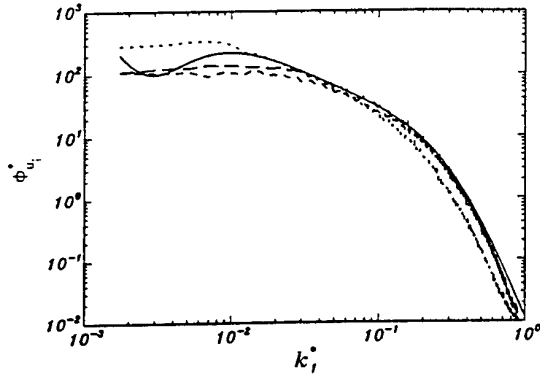


Figure 1: Spectra of velocity components., $i = 1$; ---, $i = 2$; —, $i = 3$; —, Isotropic calculation for $i = 2$ or 3 using Eq. 1.

binormal velocity effect is assumed to be negligible compared with the two other components and the mean velocity gradient acting on each X-probe is assumed to be zero. The wire length is about 0.5 mm for all the eight wires. The separation between two inclined wires in each X-probe is 0.6 mm. The separations between centres of X-probes are 2.1 and 2.2 mm in x_2 and x_3 directions, respectively. The effective angle for each inclined wire was about 50° . For the present flow conditions, the spatial resolution of the probe is in the range of $(5.2 - 13)\eta$.

The hot wires were operated with in-house constant temperature circuits at an overheat ratio of 0.5. Output voltages from the anemometers were passed through buck and gain circuits and low-pass filtered at a cut-off frequency f_c of 5 kHz \sim 10 kHz. The value of f_c was chosen to correspond approximately to the Kolmogorov frequency f_K ($\equiv U/2\pi\eta$). The filtered signals were subsequently sampled at a frequency of $f_s \approx 2f_c$ into a personal computer (NEC 486) using a 12-bit A/D converter (RC Electronics). Yaw and velocity calibrations were carried out also using the NEC 486. Subsequent processing of the data was done on a VAX 8550 computer.

RESULTS

Grid turbulence is only approximately isotropic. Comte-Bellot and Corrsin (1966) found that $\overline{u_1^2}$, the variance of the streamwise velocity component, was about 12 \sim 15% larger than $\overline{u_2^2}$, the transverse velocity component variance. The present measurements indicated that $\overline{u_3^2}$ is about 12% smaller than $\overline{u_1^2}$ whereas $\overline{u_2^2}$ is about 28% smaller than $\overline{u_1^2}$.

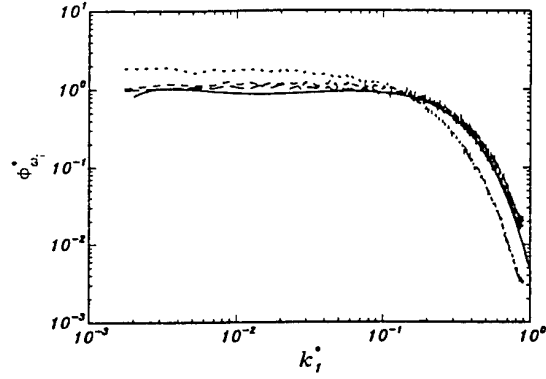


Figure 2: Spectra of vorticity components., $i = 1$; ---, $i = 2$; —, $i = 3$; —, Isotropic calculation for $i = 2$ or 3 using Eq. 1 (replacing u with ω).

Figure 1 shows spectra of the three velocity components, i.e. $\phi_{u_1}^*$, $\phi_{u_2}^*$ and $\phi_{u_3}^*$ and the isotropic calculation of the spectra of lateral components, via.

$$\phi_{u_2}^* = \phi_{u_3}^* = \frac{1}{2}\phi_{u_1}^* - \frac{1}{2}k_1^* \frac{\partial \phi_{u_1}^*}{\partial k_1^*}, \quad (1)$$

where an asterisk denotes normalisation by Kolmogorov scales, i.e. the velocity scale $u_k \equiv (\nu\bar{\epsilon})^{1/4}$, the length scale $\eta \equiv \nu^{3/4}\bar{\epsilon}^{-1/4}$ and the kinematic viscosity ν ($\bar{\epsilon}$ is the average energy dissipation rate). $\phi_{u_2}^*$ and $\phi_{u_3}^*$ show a significant departure from the corresponding isotropic calculation at small wavenumbers, reflecting the anisotropy of larger scales. The departure observed at very large wavenumbers is mainly due to noise contamination and effect of the cross-talk of the two hot wires in each X-probe (e.g. Zhu and Antonia, 1995). Due to the cross-talk, $\phi_{u_1}^*$ is overestimated at high wavenumbers while $\phi_{u_2}^*$ and $\phi_{u_3}^*$ are underestimated in this wavenumber region. After correcting for the cross-talk, $\phi_{u_2}^*$ and $\phi_{u_3}^*$ are in better agreement with the calculation. The variances of velocity derivatives and vorticity components also show some degree of departure from isotropy. However, the departure is smaller than for the velocity variances. For example, the data from the 4-X-wire probe showed that the isotropic equality $\overline{\omega_1^2} = \overline{\omega_2^2} = \overline{\omega_3^2}$ is satisfied to within $\pm 10\%$.

The spectra of ω_i are shown in Figure 2. The spectra are corrected for the effect of spatial resolution (see Zhu and Antonia, 1996b for details). At large wavenumbers, ϕ_{ω_2} and ϕ_{ω_3} have slightly different magnitude. This discrepancy may be due to errors in the measurement (e.g. electronic noise, thermal interference between sensors). In

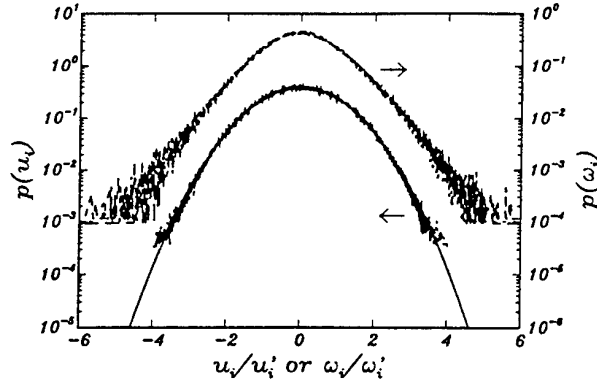


Figure 3: PDF of velocity component $p(u_i)$ and $p(\omega_i)$.
 \cdots , $i = 1$; $---$, $i = 2$; $- \cdot -$, $i = 3$; $---$, Gaussian distribution.

order to ensure that the probe performs adequately, the present vorticity spectra were also compared with the corresponding data from the direct numerical simulation (DNS) (Kim et al., 1987; Antonia and Kim, 1994) of a fully developed turbulent channel flow at approximately the same Reynolds number ($R_\lambda = 55$). The agreement is reasonably well (Figure not shown here) and reflects the encouraging performance of the probe. Figure 2 indicates that the spectra of ω_i show a smaller departure from isotropy in comparison with those of u_i , especially at small wavenumbers. This is not surprising since vorticity (and its components) characterises better the small scale structure of turbulence, which is more likely to be isotropic than the large scales. The spectra of velocity derivatives also satisfy the isotropic relations reasonably well.

Figure 3 shows the probability density functions (pdf) of u_i and ω_i . The pdfs of ω_i follow each other remarkably well. Such a behaviour is also observed for the pdfs of u_i . The pdf of u_i is closely Gaussian while the pdfs of ω_i is exponential when $|\omega_i/\omega'_i| \geq 3$. The near symmetry of the pdfs implies that the skewness is very small, which is consistent with the isotropic value of zero.

Figure 4 shows the present distributions of u'_i as a function of x_1/M . Also shown are the data of Comte-Bellot and Corrsin (1966), Van Atta and Chen (1969), Mohamed and LaRue (1990) and Fan (1991). The Reynolds numbers R_M for these studies are 33900, 25600, 14000 and 12800, respectively. It is clear that u_i has a power-law decay and the magnitude of the normalised velocity variances depends on the Reynolds number. Comte-Bellot and Corrsin (1966) noted that

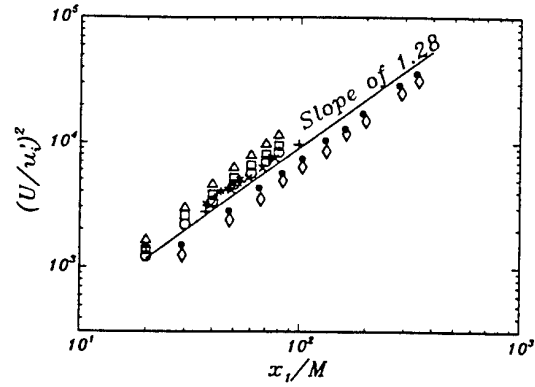


Figure 4: Variation of normalised velocity variance $(U/u'_i)^2$ with x_1/M .

Present: \circ , $i = 1$; Δ , $i = 2$; \bullet , $i = 3$. Comte-Bellot and Corrsin (1966): \diamond , $i = 1$; \circ , $i = 2$. Fan (1991): $+$, $i = 1$. Mohamed and LaRue (1990): \times , $i = 1$. Van Atta and Chen (1969): $*$, $i = 1$.

$$\left(\frac{U}{u'_i}\right)^2 \sim \left(\frac{x_1}{M} - \frac{x_0}{M}\right)^n, \quad (2)$$

where x_0 is the virtual origin. They also found that the values of x_0 and n differed for each velocity component. However, if x_0 is not subtracted from the data, each data set follows a straight line in the region $x_1/M > 30$ and these lines have approximately the same power-law, i.e. $\sim x_1^{1.28}$ for all components and all the data quoted here. The magnitude of n depends normally on the choice of x_0 . Using the trial and error method suggested by Comte-Bellot and Corrsin (1966), we estimated that x_0/M is 3 and n is 1.26. Varying x_0 by ± 1 only leads to a marginal change in n ($\pm 3\%$). Mohamed and LaRue (1990) estimated x_0 and n by selecting data only in the range where the ratio $(-dq^2/dt)/2\bar{\epsilon}$ is nearly 1 (where $\bar{\epsilon} = 15\nu(\partial u_1/\partial x_1)^2$ is the isotropic average energy dissipation rate). This method was also used here for estimating x_0 . The present data show that the ratio is satisfied to within $\pm 10\%$ for $x_1/M > 30$. Using the data in this range, a value of 1.25 was obtained for n . The Comte-Bellot and Corrsin method yielded values n in the range 1.24 \sim 1.27.

The decay of vorticity can be examined by considering the vorticity transport equation. Using the assumptions of homogeneity and isotropy, Batchelor and Townsend (1947) simplified this equation to

$$\frac{d\omega'_i{}^2}{dt} = -\frac{7}{3\sqrt{5}}\omega'_i{}^3(S + 2G/R_\lambda), \quad (3)$$

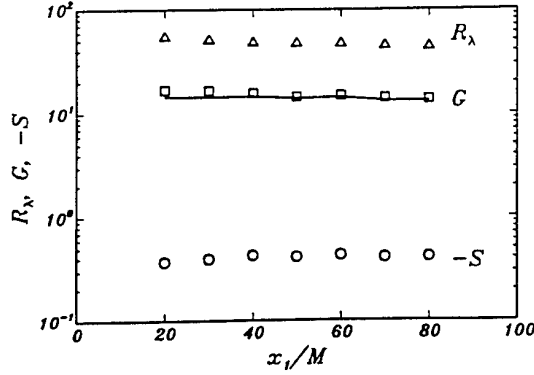


Figure 5: Variation of $-S$, G and R_λ with x_1/M . \circ , $-S$; \square , G ; \triangle , R_λ ; —, G calculated using Eq. 7.

where S is the skewness of $u_{1,1}$; R_λ is the turbulence Reynolds number based on the Taylor microscale λ and $G = \overline{u_1^2 u_{1,1}^2} / (\overline{u_{1,1}^2})^2$. They verified the equation by replacing ω_i' with $\sqrt{5}u_{1,1}'$ and using measurements in grid turbulence with a single hot wire. Eq. (3) can be rewritten as

$$\frac{d(1/\omega_i'^+)}{dx_1^+} = -\frac{7}{6\sqrt{5}}(S + 2G/R_\lambda), \quad (4)$$

where Taylor's hypothesis $\partial/\partial x_1 = -U^{-1}\partial/\partial t$ is used and the superscript $+$ denotes normalisation by U and M . When isotropy is assumed, $\omega_1' = \omega_2' = \omega_3' = \omega'/\sqrt{3}$ and Eq. (3) can be rewritten as

$$\frac{d(1/\omega'^+)}{dx_1^+} = -\frac{7}{6\sqrt{15}}(S + 2G/R_\lambda). \quad (5)$$

The values of S , G and R_λ values are shown in Figure 5. The skewness of $u_{1,1}$ is about -0.4 in the range $20 \leq x_1/M \leq 80$. This magnitude is very close to that measured by Batchelor and Townsend (1947). However, the measurement of Mohamed and LaRue (1990) indicated a higher value $-0.50 \sim -0.5$ in the range $x_1/M > 30$. The estimation of G involved the calculation of $u_{1,1}^2$. This quantity is inferred from the spectrum of $u_{1,1}$, via.

$$\overline{u_{1,1}^2} = \int_0^\infty k_1^2 \phi_{u_{1,1}} dk_1. \quad (6)$$

The integrand $k_1^2 \phi_{u_{1,1}}$ shows good closure at large wavenumbers. The present values of G and R_λ also agree well with those by Batchelor and Townsend (1947) at approximately the same Reynolds number. For isotropic turbulence, the

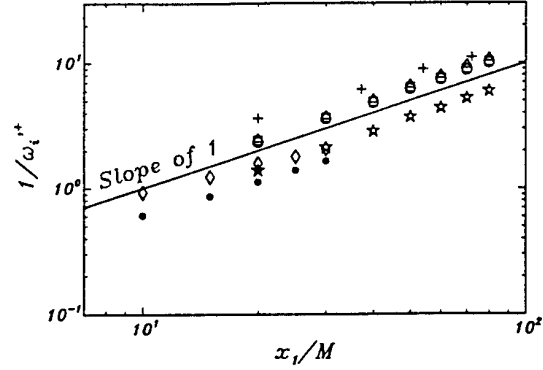


Figure 6: Variation of $1/\omega_i'^+$ with x_1/M .

Present: \circ , $i = 1$; \triangle , $i = 2$; \star , ω . Comte-Bellot and Corrsin (1966): \diamond , $i = 1$; \bullet , $i = 2$. Fan (1991): $+$, $i = 1$. Mohamed and LaRue (1990): \times , $i = 1$. Van Atta and Chen (1969): $*$, $i = 1$.

three quantities S , G and R_λ should satisfy the relation

$$G = 30/7 + R_\lambda S/2. \quad (7)$$

While the present values of G depart from the calculations at small x_1/M values, the agreement is better than 15% in the region $x_1/M \geq 30$.

Figure 6 shows the distribution of $1/\omega_i'^+$ as a function of x_1/M . The slight difference in the magnitude of the present vorticity components may be due to the measurement uncertainty as well as the slight departure from local isotropy. It is clear that $1/\omega_i'$ varies linearly with x_1/M . Such a behavior was also observed for ω_1' measured by Kit et al. (1988) and Fan (1991). The Reynolds number R_M for Kit et al.'s data is about 25000. The present data indicate a slope of 1 for the rms value of the total vorticity and its components in the range $x_1/M \geq 30$. However, the data by Fan (1991) and the small rod (diameter = 8mm) grid data by Kit et al. (1988) show a smaller slope. Kit et al.'s large rod (diameter = 16 mm) data exhibit a slope of 1 although the magnitude is smaller than their small rod data. The slope of 1 is consistent with Eqs. (3-4) since S and the ratio G/R_λ are almost constant over the measurement range.

Further justification of Eqs. (3)-(5) is presented in Figure 7. The decay rate of vorticity, i.e. the left-hand side of the equations, was inferred from the slope of the vorticity rms distributions in Figure 6. The right-hand side of Eqs. (3)-(5), estimated from the distributions of S , G and R_λ , agrees to within 15% with the decay rate of vorticity and its components.

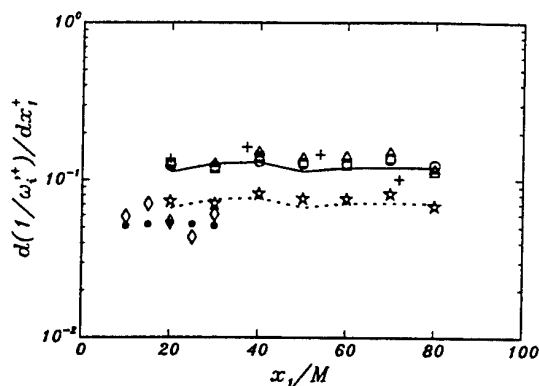


Figure 7: Variation of the vorticity decay rate with x_1/M .

Symbols as in Figure 6; —, right side of Eq. 4; ····, right side of Eq. 5.

CONCLUSIONS

The decay of vorticity in grid turbulence has been studied using three-dimensional vorticity data obtained with a 4-X-wire probe. The velocity fluctuations exhibit a power-law decay and the exponents are about 1.25, close to the values obtained by Comte-Bellot and Corrsin (1966) and Mohamed and LaRue (1990). A power-law is also observed for the vorticity and its components. The decay constant agrees reasonably well with the transport equation.

ACKNOWLEDGMENT

The support of the Australian Research Council is gratefully acknowledged.

REFERENCES

- J. Kim and R. A. Antonia. A numerical study of local isotropy of turbulence. *Phys. Fluids A*, Vol. 6, pp.834-841, 1994.
- R. A. Antonia, Y. Zhu, and H. S. Shafi. Lateral vorticity measurements in a turbulent wake. *J. Fluid Mech.*, Vol. 323, pp.173-200, 1996.
- G. K. Batchelor and A. A. Townsend. Decay of vorticity in isotropic turbulence. *Proc. Roy. Soc. Lond. A*, Vol. 190, pp.534-550, 1947.
- G. Comte-Bellot and S. Corrsin. The use of a contraction to improve the isotropy of grid-generated turbulence. *J. Fluid Mech.*, Vol. 25, pp.657-682, 1966.
- M. Fan. *Features of Vorticity in Fully Turbulent Flows*. PhD thesis, Yale University, 1991.

J. Kim, P. Moin and R. Moser. Turbulent statistics in fully developed channel flow at low Reynolds number. *J. Fluid Mech.*, Vol. 177, pp.133-166, 1987.

E. Kit, A. Tsinober, M. Teitel, J. L. Balint, J. M. Wallace, and E. Levich. Vorticity measurements in turbulent grid flows. *Fluid Dyn. Res.*, Vol. 3, pp.289-294, 1988.

M. S. Mohamed and J. C. LaRue. The decay power law in grid-generated turbulence. *J. Fluid Mech.*, Vol. 219, pp.195-214, 1990.

L. Mydlarski and Z. Warhaft. On the onset of high-Reynolds-number grid-generated wind tunnel turbulence. *J. Fluid Mech.*, Vol. 320, pp.331-368, 1996.

C. W. Van Atta and W. Chen. Measurements of spectral energy transfer in grid turbulence. *J. Fluid Mech.*, Vol. 38, pp.743-763, 1969.

J. M. Wallace and J. F. Foss. The measurements of vorticity in turbulent flows. *Ann. Rev. Fluid Mech.*, Vol. 27, pp.467-514, 1995.

Y. Zhu and R. A. Antonia. Effect of wire separation on X-probe measurements in a turbulent flow. *J. Fluid Mech.*, Vol. 287, pp.199-223, 1995.

Y. Zhu and R. A. Antonia. Correlation between the enstrophy and the energy dissipation rate in a turbulent wake. In S. Gavrilakis, L. Machiels, and P. A. Monkewitz, editors, *Advances in Turbulence VI*, pages 507-510. Kluwer Academic Publishers, 1996a.

Y. Zhu and R. A. Antonia. Spatial resolution of a 4-X-wire vorticity probe. *Meas. Sci. & Technol.*, Vol. 7, pp.1492-1497, 1996b.

GENERALIZED THEORY FOR SYMMETRIES IN INHOMOGENEOUS TURBULENT SHEAR FLOWS

M. Oberlack[†]

Center for Turbulence Research
Stanford University
California 94305-3030
USA

ABSTRACT

A new turbulence theory based on Lie-group analysis is presented. This theory unifies a large set of self-similar solutions for the mean velocity of stationary parallel turbulent shear flows. The theory is derived from the Reynolds averaged Navier-Stokes equations, the fluctuation equations, and the velocity product equations, which are the dyad product of the velocity fluctuations with the equations for the velocity fluctuations. For the plane case the results include the logarithmic law of the wall, an algebraic law, the viscous sublayer, the linear region in the centre of a Couette flow and in the centre of a rotating channel flow, and a new exponential mean velocity profile that is found in the mid-wake region of high Reynolds number flat-plate boundary layers. The algebraic scaling law is confirmed in both the centre and the near wall regions in both experimental and DNS data of turbulent channel flows. For a non-rotating and a moderately rotating pipe about its axis an algebraic law was found for the axial and the azimuthal velocity near the pipe-axis with both laws having equal scaling exponents. In case of a rapidly rotating pipe a new logarithmic scaling law for the axial velocity is developed.

INTRODUCTION

The logarithmic law was first derived by von Kármán (1930) using empirical models and dimensional arguments. Later Millikan (1939) derived the law of the wall more formally using the so called "velocity defect law", which was also introduced by von Kármán (1930). Even though Millikan's derivation was much more comprehensive from a mathematical point of view, it still had no link to the Navier-Stokes equations. Recently, some doubts have been expressed as to whether the appropriate wall-layer form is logarithmic or algebraic (see e.g. George *et al.* 1996). In the present approach it will be shown by investigating plane and circular shear flows that von Kármán's law of the wall is by no means the only non-trivial self-similar mean velocity profile which may be given explicitly. Almost all scaling laws which will be derived in the present analysis will be empirically verified in certain flow domains.

The main purpose using Lie group analysis to derive self-similar solutions is that it overcomes the limitation of guessing ansatz functions and dimensional analysis. The primary advantage of using Lie group theory is that it guarantees to obtain all similarity solutions admitted by the set of equation under investigation which are here the Reynolds averaged Navier-Stokes equations and the equations for the fluctuations.

GOVERNING EQUATIONS

The subsequent Lie group analysis is based on the Reynolds averaged Navier-Stokes equations

$$\begin{aligned} \bar{N}_i = & \frac{\partial \bar{u}_i}{\partial t} + \bar{u}_k \frac{\partial \bar{u}_i}{\partial x_k} + \frac{\partial \bar{p}}{\partial x_i} - \nu \frac{\partial^2 \bar{u}_i}{\partial x_k^2} \\ & + \frac{\partial \tau_{ik}}{\partial x_k} + 2 \Omega_k e_{ikl} \bar{u}_l = 0, \end{aligned} \quad (1)$$

the equations for the velocity fluctuations

$$\begin{aligned} \mathcal{N}_i = & \frac{\partial u_i}{\partial t} + \bar{u}_k \frac{\partial u_i}{\partial x_k} + u_k \frac{\partial \bar{u}_i}{\partial x_k} - \frac{\partial \tau_{ik}}{\partial x_k} + \frac{\partial u_i u_k}{\partial x_k} \\ & + \frac{\partial p}{\partial x_i} - \nu \frac{\partial^2 u_i}{\partial x_k^2} + 2 \Omega_k e_{ikl} u_l = 0 \end{aligned} \quad (2)$$

and the mean and fluctuation continuity equations

$$\bar{C} = \frac{\partial \bar{u}_k}{\partial x_k} = 0 \text{ and } C = \frac{\partial u_k}{\partial x_k} = 0. \quad (3)$$

In the latter equations $t, \mathbf{x}, \bar{\mathbf{u}}, \bar{p}, \boldsymbol{\tau}, \mathbf{u}, p$ and $\boldsymbol{\Omega}$ are, respectively, time, the spatial coordinate, the mean velocity, the mean pressure, the Reynolds stress tensor, the fluctuating velocity, the fluctuating pressure and the rotation rate of the coordinate system with respect to an inertial frame.

The set of equations (1)–(3) is underdetermined in the sense that it contains more dependent variables than equations. In the classical approach of finding turbulent scaling laws, this difficulty has motivated the introduction of second moment equations. In the next section, the above set of equations (1)–(3) will be analysed with regard to its symmetry properties alone, without introduction of higher

[†] present address: Institut für Technische Mechanik, RWTH Aachen, Templergraben 64, 52056 Aachen, Germany

order correlation equations which contain more unclosed terms.

Instead an additional equation is introduced in the subsequent analysis which is the velocity product equation

$$\mathcal{N}_i u_j + \mathcal{N}_j u_i = 0. \quad (4)$$

Using the latter equation in the similarity analysis leads to two major differences between the present and the classical similarity approach using the ensemble averaged Reynolds stress transport equations only. First, in the present approach, only the Reynolds stresses appear as unclosed terms in the equations, and no higher order correlations need to be considered. Hence, only a finite number of variables are present in the system to be analysed.

Second, it is shown in Oberlack (1997a) that any scaling law for the velocity fluctuation and the second order velocity product equations (4) is also a scaling law for all n^{th} order velocity product equations. In the classical approach using correlation functions, it may be difficult to show that all higher order velocity correlations are consistent with the scaling in the Reynolds stress equations.

LIE POINT SYMMETRIES IN TURBULENT SHEAR FLOWS

Lie group analysis as used in this section is described e.g. in Bluman (1989). The set of variables considered in the subsequent calculation consists of

$$\mathbf{y} = \{t, x, \nu, \bar{u}, \bar{p}, \tau, u, p\}. \quad (5)$$

The purpose of the symmetry analysis is to find all those invertible transformations

$$\mathbf{y}^* = \{t^*, x^*, \nu^*, \bar{u}^*, \bar{p}^*, \tau^*, u^*, p^*\} = \mathbf{f}(\mathbf{y}; \epsilon) \quad (6)$$

which preserve the functional form of (1)–(4), written in the new variable \mathbf{y}^* :

$$\begin{aligned} \mathcal{N}_i &= \mathcal{N}_i^*, \quad \bar{C} = \bar{C}^*, \quad \mathcal{N}_i = \mathcal{N}_i^*, \quad C = C^*, \\ (\mathcal{N}_i u_j + \mathcal{N}_j u_i) &= (\mathcal{N}_i u_j + \mathcal{N}_j u_i)^*. \end{aligned} \quad (7)$$

The superscript * of any quantity denotes its evaluation according to the transformation (6). The transformation \mathbf{f} is an invertible mapping which depends on the group parameter ϵ . Lie gave an infinitesimal form of the transformation (6)

$$\mathbf{y}^* = \mathbf{y} + \epsilon \left. \frac{\partial \mathbf{f}}{\partial \epsilon} \right|_{\epsilon=0} + \mathcal{O}(\epsilon^2). \quad (8)$$

and it can be shown that from the expansion only the terms to order ϵ need to be considered. Hence, (8) is rewritten as

$$\begin{aligned} t^* &= t + \epsilon \xi_t, \quad x^* = x + \epsilon \xi_x, \quad \nu^* = \nu + \epsilon \xi_\nu, \\ \bar{u}^* &= \bar{u} + \epsilon \eta_{\bar{u}}, \quad \bar{p}^* = \bar{p} + \epsilon \eta_{\bar{p}}, \quad \tau^* = \tau + \epsilon \eta_\tau, \\ u^* &= u + \epsilon \eta_u, \quad p^* = p + \epsilon \eta_p, \end{aligned} \quad (9)$$

where, instead of the mapping \mathbf{f} , only the infinitesimal generators $\xi(\mathbf{y})$ and $\eta(\mathbf{y})$ need to be determined. Given the infinitesimal generators, the global transformation \mathbf{f} is uniquely determined. The major advantage of the infinitesimal approach is that the equations for the infinitesimal generators are linear and, generally, easy to solve.

Practically speaking, it is impossible to find \mathbf{f} from (7) using the global transformation (6) directly, as this results in a large, over-determined system of non-linear PDE's for \mathbf{f} which is intractable to solve.

If all the infinitesimal generators ξ and η in (9) are calculated, the self-similar solutions of the equations (1)–(4) can be obtained from the invariant surface condition (ISC) (see e.g. Bluman 1989). In the following three sub-sections the new theory will be tested by analysing several different inhomogeneous shear flows: plane parallel shear flows in an

inertial frame and in a rotating frame, and non-rotating and rotating pipe flow.

Recall that, in the first step of the current approach the infinitesimal generators must be determined from the equations (7). This is accomplished using SYMM-GRP-MAX, a package for MACSYMA written by Champagne *et al.* (1991). As a result, for each of the test cases an over-determined set of more than one hundred linear PDE's are obtained, whose solutions are calculated manually. The solutions are given in Oberlack (1997a) and Oberlack (1997b). The present purpose is to investigate scaling laws for the mean flow. Hence, the following results contain only a restricted set of equations from the ISC.

Plane shear flows in an inertial frame

The ISC and the infinitesimal generators for x_2 and \bar{u}_1 in Oberlack (1997a) can be combined to

$$\frac{dx_2}{a_1 x_2 + a_2} = \frac{d\bar{u}_1}{[a_1 - a_3]\bar{u}_1 + a_4}, \quad (10)$$

where \bar{u}_1 is the mean velocity in the x_1 -direction and x_2 is perpendicular to it. Integrating (10) results in several fundamentally different self-similar solutions for certain values of the parameters a_1 – a_4 .

The physical interpretation of the scaling parameters a_1 and a_3 is crucial in order to understand each scaling law to follow. As an example consider the parameter a_1 . It appears as a factor of all spatial coordinates in the generators (see Oberlack 1997a). This means that all spatial coordinates can be scaled by a certain factor if also the appropriate velocity scale is introduced. Suppose a given external length scale l is present in the flow under investigation. As a consequence, the scaling symmetry with respect to the spatial coordinates is lost since l is a fixed quantity. Consequently, a_1 can only be zero. Subsequently, any of the parameters being zero is referred to as a "broken symmetry".

Each of the velocity profiles to be computed below and its associated symmetries, may be interpreted in terms of a given external length, time or velocity scale breaking some of the scaling symmetries. If $a_1 = a_3$ the scaling symmetry for the velocities is broken as can be taken from (10). Subsequently the C_i are integration constants.

Algebraic mean velocity profile. ($a_1 \neq a_3 \neq 0$ and $a_4 \neq 0$) The present case is the most general one. No scaling symmetry is broken. As a result, the mean velocity \bar{u}_1 has the following form

$$\bar{u}_1 = C_1 \left(x_2 + \frac{a_2}{a_1} \right)^{1 - \frac{a_3}{a_1}} - \frac{a_4}{a_1 - a_3}. \quad (11)$$

In the domain of its validity, there is no external length or velocity scale acting directly on the flow.

Logarithmic mean velocity profile. ($a_1 = a_3 \neq 0$ and $a_4 \neq 0$) For the present combination of parameters an external velocity scale is symmetry breaking. The mean velocity \bar{u}_1 may be integrated to a generalized form of the familiar log-law

$$\bar{u}_1 = \frac{a_4}{a_1} \log \left(x_2 + \frac{a_2}{a_1} \right) + C_2. \quad (12)$$

In case of the classical logarithmic law of the wall, it is the friction velocity u_τ that is symmetry breaking.

Since the scaling symmetry with respect to the spatial variables ($a_1 \neq 0$) is still retained the length scale varies linearly with the distance to the wall. This is an assumption in the classical derivation of the log law of the wall but is a result of the present analysis.

Exponential mean velocity profile. ($a_1 = 0$ and $a_3 \neq a_4 \neq 0$) Since a_1 is zero in the present case, there exists an external length scale which is symmetry breaking. The mean velocity \bar{u}_1 turns out to have the following form

$$\bar{u}_1 = \frac{a_4}{a_3} + \exp\left(-\frac{a_3}{a_2} x_2\right) C_3. \quad (13)$$

It will be shown in the next section that the present case applies to the flat plate high Reynolds number boundary layer flow. It appears that the boundary layer thickness is the external length scale which is symmetry breaking.

Linear mean velocity profile. ($a_1 = a_3 = 0$ and $a_4 \neq a_2 \neq 0$) In the present case there is an external velocity and length scale present in the flow and only the linear mean velocity profile is a self-similar solution

$$\bar{u}_1 = \frac{a_4}{a_2} x_2 + C_4. \quad (14)$$

The latter profile applies in the viscous sublayer and in the centre of a turbulent Couette flow.

Plane shear flows in a rotating frame

Here, the symmetries of plane parallel shear flow with system rotation normal to the mean shear is considered ($\Omega_3 \neq 0$). The most important difference to the previous cases is that $a_3 = 0$, and hence the scaling symmetry with respect to the time is lost. As a result the mean velocity is given by

$$\bar{u}_1 = C_5 \Omega_3 x_2 + C_6. \quad (15)$$

The present case is distinguished from the previous linear mean velocity profiles, since a scaling of the spatial coordinates still holds ($a_1 \neq 0$).

Non-rotating and rotating pipe flow

In case of a circular shear flow the infinitesimal generators in Oberlack (1997b) and the ISC for the axial and the azimuthal mean velocity, \bar{u}_z and \bar{u}_ϕ respectively, are combined to

$$\begin{aligned} \frac{dr}{b_1 r} &= \frac{d\bar{u}_z}{[b_1 - b_3]\bar{u}_z + b_4}, \\ \frac{dr}{b_1 r} &= \frac{d\bar{u}_\phi}{[b_1 - b_3]\bar{u}_\phi - b_3 r \Omega} \end{aligned} \quad (16)$$

where Ω is the rotation rate of the coordinate system about the axis of symmetry. Three scaling laws need to be distinguished:

Algebraic mean velocity profiles. ($b_1 \neq b_3 \neq 0$ and $b_4 \neq 0$) As for (11), there is no symmetry breaking scale imposed on the flow. Equation (16) can be integrated for the axial and azimuthal mean velocity

$$\bar{u}_z = -\frac{b_4}{b_1 - b_3} + C_6 r^{1 - \frac{b_3}{b_1}} \quad (17)$$

and

$$\bar{u}_\phi = C_7 r^{1 - \frac{b_3}{b_1}} - \Omega r, \quad (18)$$

respectively, where C_6 and C_7 are constants.

Logarithmic axial mean velocity profile. ($b_1 = b_3 \neq 0$ and $b_4 \neq 0$) This combination of parameters applies if an external velocity scale acts on the flow. As in the case of a plane parallel shear flow, this results in a logarithmic mean velocity profile

$$\bar{u}_z = \frac{b_4}{b_1} \ln(r) + C_8. \quad (19)$$

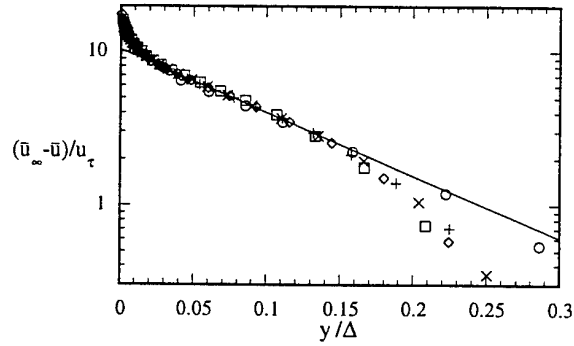


Figure 1: Mean velocity of the zero-pressure gradient turbulent boundary layer flow: \circ , $Re_\theta = 370000$ Saddoughi *et al.* (1994); \square , \diamond , $Re_\theta = 60000$ Fernholz *et al.* (1995); $+$, $Re_\theta = 15000$, \times , $Re_\theta = 20000$ DeGraaff (1996); —, $10.34 \exp(-9.46y/\Delta)$.

It is important to note that this does not correspond to the classical law of the wall, since the singularity appears on the pipe axis. Subsequently it will be referred to as “circular log-law”. It appears that (19) applies on some section of the radius for rapidly rotating pipes, in which the wall velocity is the symmetry breaking velocity scale. The corresponding azimuthal velocity is given by

$$\bar{u}_\phi = -\Omega r + C_9, \quad (20)$$

which is also singular at the centreline.

Hyperbolic mean velocity profiles. ($b_3 = 2b_1 \neq 0$ and $b_4 \neq 0$) For this parameter combination the axial mean velocity can be computed to be

$$\bar{u}_z = \frac{b_4}{b_1} + \frac{C_{10}}{r} \quad (21)$$

and the corresponding azimuthal velocity is the potential vortex as given by

$$\bar{u}_\phi = \frac{C_{11}}{r} - \Omega r. \quad (22)$$

For the subsequent comparison with data, the system rotation in the circular case does not need to be considered since only solid-body rotation terms appear in the scaling laws for the azimuthal velocities. Hence, without loss of generality one can take $\Omega = 0$.

VERIFICATION OF THE SCALING LAWS

In the present section experimental and DNS data will be presented to give an empirical verification of the scaling laws (11)-(15) and (17)-(22).

The logarithmic law of the wall which has been verified in a large number of experiments will not be investigated here. The linear mean velocity in the viscous sublayer and in the centre of a turbulent Couette flow will not be verified either. Both have been shown by experimental and DNS data (see e.g. Bech *et al.* 1995 and Kim *et al.* 1987). In both linear cases, there are a length and a velocity scale dominating the flow and hence two scale symmetries are broken. In the viscous sublayer the length and the velocity scales are ν/u_τ and u_τ , and in the turbulent Couette flow they are b and u_w , the channel width and the wall velocity, respectively.

From a similarity point of view the linear region in the centre of a rotating channel flow is distinct from the previous two cases. Here the external time scale Ω^{-1} acts on the flow, which results in $a_4 = 0$. However, a scaling

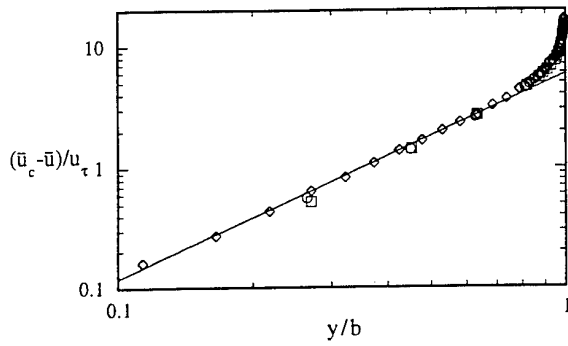


Figure 2: Mean velocity of the turbulent channel flow: \circ , $Re_c = 40000$; \square , $Re_c = 23000$ Wei & Willmarth (1989); \diamond , $Re_c = 18000$ Niederschulte (1996); —, $5.83 (y/b)^{1.69}$.

symmetry with respect to the spatial coordinates still exists. The linear mean velocity as given by equation (15) is well documented in experimental and DNS data (see e.g. Kristoffersen & Andersson 1993).

From the circular cases the potential vortex (22) will not be investigated here. So far, only the axial mean velocity profile (21) could not be assigned to any specific turbulent flow. In order to avoid the duplication of well documented invariant solutions, it is focused on three plane and three circular cases.

Flat plate turbulent boundary layer flow

Three sets of experimental data at medium to high Reynolds numbers have been chosen for comparison with the exponential velocity profile. The data of DeGraaff (1996), Fernholz *et al.* (1995) and Saddoughi & Veeravalli (1994) cover the Reynolds number range $Re_\theta = 15000 - 370000$, where $\theta = \int_0^\infty (1 - \bar{u}/\bar{u}_\infty) \bar{u}/\bar{u}_\infty dy$ is the momentum thickness and \bar{u}_∞ is the free stream velocity.

As has been pointed out above, it appears that the exponential law (13) describes the outer part of a high Reynolds number flat plate boundary layer flow. In order to match the theory and the data, the exponential mean velocity profile in equation (13) will be written in outer scaling

$$\frac{\bar{u}_\infty - \bar{u}}{u_\tau} = \alpha \exp\left(-\beta \frac{y}{\Delta}\right), \quad (23)$$

where α and β are universal constants, $\Delta = \int_0^\infty (\bar{u}_\infty - \bar{u})/u_\tau dy$ is the Rotta-Clausner length scale and u_τ is the friction velocity.

In figure 1 the turbulent boundary layer data are plotted as $\log[(\bar{u}_\infty - \bar{u})/u_\tau]$ vs. y/Δ . All the data appear to converge to a straight line in the region $y/\Delta \approx 0.025 - 0.15$. The data of Saddoughi & Veeravalli (1994) show an extended region for the exponential law up to about $y/\Delta \approx 0.23$. With increasing Reynolds number the applicability of the exponential law appears to increase. The log region is valid within $y/\Delta \approx 0 - 0.025$ and does not follow the exponential (23). The applicability of the exponential region is approximately five to eight times longer than the logarithmic law.

If the exponential velocity profile (23) were valid over the entire boundary layer, an integration of (23) from zero to infinity would give $\alpha = \beta$. A least square fit of the presented data leads to approximately the latter equivalence with $\alpha = 10.34$ and $\beta = 9.46$.

Two dimensional turbulent channel flow

Here the experimental data of Niederschulte (1996), Wei & Willmarth (1989) and the low Reynolds number DNS

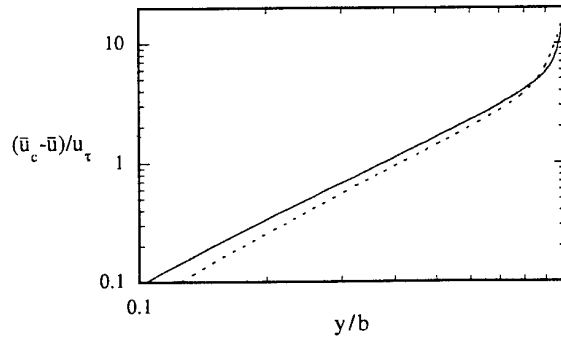


Figure 3: Mean velocity of the turbulent channel flow from Kim *et al.* (1987): —, $Re_c = 7900$; ---, $Re_c = 3300$.

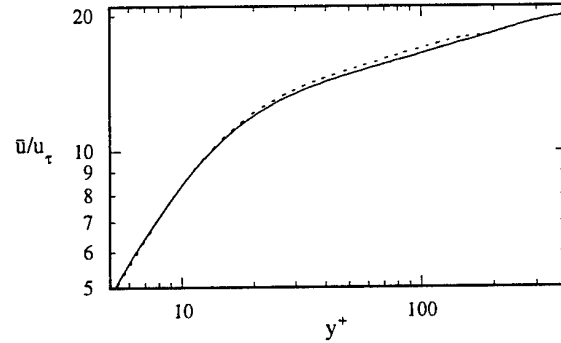


Figure 4: Mean velocity of the turbulent channel flow from Kim *et al.* (1987): —, $Re_c = 7900$; ---, $Re_c = 3300$.

data of Kim *et al.* (1987) will be used for the investigation of the algebraic scaling law.

Here two algebraic regimes have been detected: one where the origin of the independent coordinate is at the wall and one where it is at the centre of the channel. The region of validity of an algebraic scaling law near the centre-line appears to be more clear than for the near wall region. Since for the algebraic scaling law (11), both constants a_1 and a_4 have to be non-zero and distinct, the region for which the algebraic scaling law applies has the highest degree of symmetry. The centre region seems to be more suitable for that, since in the near-wall region the friction velocity u_τ is symmetry breaking.

Regarding the algebraic law in the centre of the channel, the appropriate outer scaling for the channel is

$$\frac{\bar{u}_c - \bar{u}}{u_\tau} = \varphi \left(\frac{y}{b}\right)^\gamma, \quad (24)$$

where φ and γ are constants, y originates on the channel centre line, \bar{u}_c is the centre line velocity and b is the channel half width.

In figure 2 the data of Niederschulte (1996) and Wei & Willmarth (1989) have been plotted in log-log scaling for the Reynolds number range $Re_c = 18000 - 40000$, where Re_c is based on the centre line velocity and channel half width. There is some obvious indication that the centre region up to about $y/b \approx 0.8$ closely follows an algebraic scaling law given by (24). The unknown constants in (24) have been fitted to $\varphi = 5.83$ and $\gamma = 1.69$ the data.

An even more profound indication regarding the algebraic law may be obtained from the DNS data of Kim *et al.* (1987). In figure 3, the data are plotted with log-log scaling and an almost perfectly straight line is visible for both $Re_c = 3300$ and 7900 from the centreline up to about $y/b = 0.75$. The scaling extends slightly further out for the $Re_c = 7900$ case. Since both Reynolds numbers in the

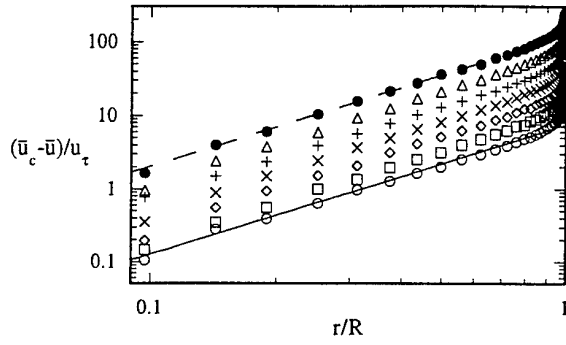


Figure 5: Mean velocity of the turbulent pipe flow from Zagarola (1996): \bullet , Δ , $+$, \times , \diamond , \square , \circ , $Re_m = 4.2 \cdot 10^4 - -3.5 \cdot 10^7$; —, $7.5 (r/R)^{1.77}$; ---, $10^{1.27.5} (r/R)^{1.77}$. The data are shifted vertically by the factor $10^{0.2}$.

DNS are low, a weak Reynolds number dependence of both φ and γ exists.

Figure 4 shows a log-log plot of the mean velocity of the channel flow data in wall units. Up to about $y^+ = 3$ the linear law of the viscous sublayer is valid. In the range $50 < y^+ < 250$ for $Re_c = 7900$ an almost perfectly straight line is visible and a least square fit of an algebraic law in this range results in a much higher correlation coefficient than a least square fit of a logarithmic function.

Non-rotating pipe flow

From the invariant solution (17), the proposed new defect law for the pipe flow is given by

$$\frac{\bar{u}_c - \bar{u}_z}{u_\tau} = \chi \left(\frac{r}{R} \right)^\psi, \quad (25)$$

where χ and ψ are constants. In contrast to the usual defect law for the pipe flow, the coordinate r has its origin at the pipe centre rather than at the pipe wall.

In figure 5 the data of Zagarola (1996) for medium to high-Reynolds-number turbulent pipe flows are plotted in the form suggested by equation (25). (Note that the individual curves are shifted vertically.)

It is apparent from figure 5 that in the range $0.1 \leq r/R \leq 0.8$ all data vary linearly. The deviation for $r/R \leq 0.1$ may be due to the large amplification of errors when plotting the difference between \bar{u}_c and \bar{u}_z in log coordinates. The data of Zagarola (1996) suggest that the constants in (25) are $\chi = 7.5$ and $\psi = 1.77$.

Rotating pipe flow

In contrast to the laminar flow in a rotating pipe, where the azimuthal velocity closely follows solid-body rotation (see e.g. Reich 1988), in the turbulent flow case, an algebraic scaling law (18) with an exponent larger than one is apparent in many experimental and DNS data. This can be rewritten as

$$\frac{\bar{u}_\phi}{u_w} = \zeta \left(\frac{r}{R} \right)^\psi, \quad (26)$$

where u_w is the azimuthal velocity at the wall and ζ and ψ are constants.

In figure 6 experimental data for the azimuthal mean velocity in rotating pipes at moderate rotation numbers are presented. This indicates that for the outer part of the pipe radius the data closely follow an algebraic scaling law, and the range of validity depends on Reynolds number and rotation number $N = u_w/\bar{u}_m$. The inner region of the rotating pipe exhibits a significant deviation from the power law. This is due to solid-body rotation near the pipe

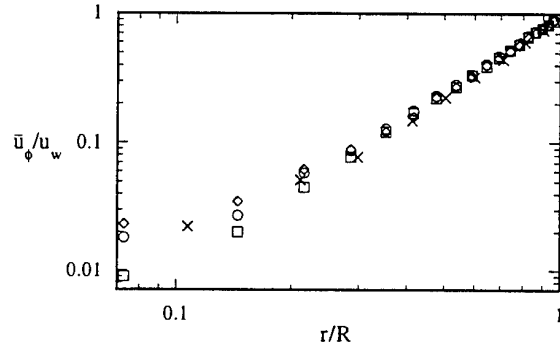


Figure 6: Azimuthal mean velocity in a rotating pipe flow: \circ , $Re_m = 20000$, $N = 0.5$; \square , $Re_m = 20000$, $N = 1.0$; \diamond , $Re_m = 50000$, $N = 0.5$ (Reich 1988); \times , $Re_m = 50000$, $N = 1.0$ (Kikuyama 1983).

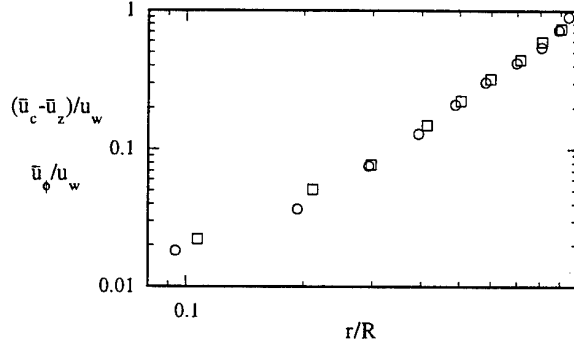


Figure 7: Axial and azimuthal mean velocity in a rotating pipe from Kikuyama *et al.* (1983) for $Re_m = 50000$ and $N = 1.0$: \circ , $(\bar{u}_c - \bar{u}_z)/u_w$; \square , \bar{u}_ϕ/u_w .

axis. The extension towards the pipe axis is affected by the Reynolds and the rotation number.

One can deduce from the two invariant solutions (17) and (18) that the exponent ψ of the scaling law for the axial velocity in (25) is also a constant that has the same value as $\hat{\psi}$. The scaling law in equation (25) has to be extended to account for rotation effects in the pre-factor χ . Since an additional velocity scale u_w is induced at the wall, a modified scaling law for axial mean velocity is proposed by

$$\frac{\bar{u}_c - \bar{u}_z}{u_\tau} = \hat{\chi} \left(\frac{u_w}{u_\tau} \right) \left(\frac{r}{R} \right)^\psi, \quad (27)$$

where $\hat{\chi}$ is not a constant but rather a function of the velocity ratio.

In figure 7 experimental data of the axial and azimuthal mean velocity have been plotted in log-log scaling for a moderate rotation number. The two curves are parallel and straight for some part of the pipe radius as suggested by (26) and (27). No functional form has been assigned to $\hat{\chi}(u_w/u_\tau)$ from the present form of the Lie group theory.

As the rotation number increases, the rotating wall velocity u_w becomes the dominant velocity scale at the wall and the axial velocity changes to a circular log law (19). The suggested scaling law is

$$\frac{\bar{u}_z}{u_w} = \lambda \log \left(\frac{r}{R} \right) + \omega \quad (28)$$

In figure 8 the axial mean velocity data of Orlandi & Fatica (1996) are plotted in semi-log scaling, corresponding to (28). A straight line matches about 30% of the pipe radius in the range $0.5 \leq r/R \leq 0.8$. The region of applicability of this new log-region is different from the logarithmic law of the wall which is valid for $0.8 \leq r/R \leq 1.0$. Also the

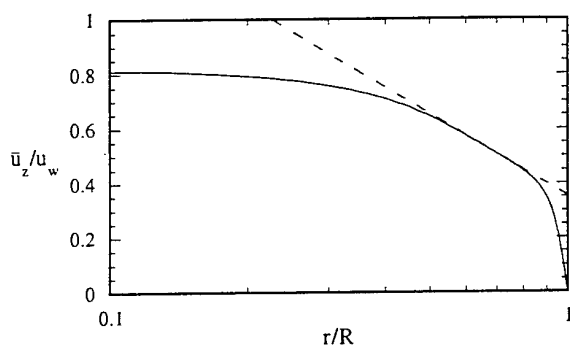


Figure 8: Axial mean velocity in a rotating pipe from Orlandi & Fatica (1996) for $Re_m = 4900$ and $N = 2$: —, \bar{u}_z/u_w from DNS: ---, $\bar{u}_z/u_w = -\log(r/R) + 0.354$.

coefficient λ in (28) is negative and approximately equal to -1 . The additive constant ω is about 0.354.

SUMMARY

It has been demonstrated by the application of Lie group analysis to parallel turbulent shear flows that a large class of invariant solutions for the mean velocity can be computed. For the plane case these solutions include the logarithmic law of the wall, an algebraic law, and a linear profile; a new exponential mean profile has also been found. The circular scaling laws include an algebraic law for the axial and the azimuthal velocity, the potential vortex and a circular log law.

Using DNS and experimental data the exponential and algebraic laws have been demonstrated to be valid in the outer part of boundary layer and channel flows respectively. For the turbulent boundary layer, high quality data are available, and there is little doubt regarding the existence of an exponential region. For the turbulent channel flow, the DNS data exhibit an almost perfect algebraic centre region, but the data are at low Reynolds number and show Reynolds number dependence of the scaling law parameters. The experimental data also clearly show the algebraic region, but contain more scatter.

Another algebraic scaling law in the vicinity of the wall has also been confirmed in the present investigation using the low Reynolds number DNS data of Kim *et al.* (1987).

To avoid duplication, the verification of the linear mean velocity profile in the viscous sublayer and in the centre region of a turbulent Couette flow have not been investigated in the present study. In experiments and DNS data of a rotating channel flow a linear mean velocity profile has been found with its slope scaling with Ω . This third linear mean velocity is distinct from the two other cases since only one scaling symmetry with respect to the time is lost.

In a non-rotating pipe, the algebraic law for the axial velocity covers about 80% of the pipe radius. This was confirmed for three decades of Reynolds number by using the data of Zagarola (1996). In the case of the rotating pipe flow the algebraic law for the azimuthal velocity was confirmed for a range of Reynolds numbers and rotation numbers for at least 70% of the radius. Based on experimental and DNS data it was concluded that, except in the central region of the pipe, these scaling laws were independent of Re and Ω .

For high rotation numbers, the azimuthal velocity at the wall (rather than the friction velocity) becomes the dominant velocity scale imposed on the flow, and in this case a new circular logarithmic law is found. The validity of this law was demonstrated by using the DNS data of Orlandi & Fatica (1996) at the rotation number $N = 2$. The new circular log-law differs from the usual log-law of the wall because it scales with the radius and its location is closer

to the pipe axis and has a wider extent.

An important application of the present theory is turbulence modelling. Common statistical turbulence models may not be consistent with all the symmetries calculated in the present theory and hence can not capture the associated scaling laws. It is proposed that turbulence models should have the symmetry properties computed in the present analysis. This is a necessary condition in order to capture the turbulent scaling laws and the associated turbulent flows present herein. The presented symmetry properties in turbulent flows may be considered as a new realizability concept.

REFERENCES

- Bech, K. H., Tillmark N., Alfredsson, P. H. & Andersson, H. I., 1995, "An investigation of turbulent plane Couette flow at low Reynolds numbers", *J. Fluid Mech.*, Vol. 286, pp. 291–325.
- Bluman, G. W. & Kumei S., 1989, "Symmetries and Differential Equations", Applied mathematical sciences, Vol. 81, Springer.
- Champagne, B., Hereman, W. & Winternitz, P., 1991, "The computer calculation of Lie point symmetries of large systems of differential equations", *Comp. Phys. Comm.* Vol. 66, pp. 319–340.
- DeGraaff, D., 1996, "private communication".
- Fernholz, H. H., Krause, E., Nockemann, M. & Schober, M., 1995, "Comparative measurements in the canonical boundary layer at $Re_{\delta_2} \leq 6 \times 10^4$ on the wall of the German-Dutch windtunnel", *Phys. Fluids*, Vol. 7(6), pp. 1275–1281.
- George, W. K., Castillo, L. & Knecht, P., 1996, "The zero pressure-gradient turbulent boundary layer", Turbulence Research Laboratory, School of Engineering and Applied Sciences, SUNY Buffalo, NY.. Tech. Rep. No. TRL-153.
- von Kármán, Th., 1930, "Mechanische Ähnlichkeit und Turbulenz", *Nachr. Ges. Wiss. Göttingen*, Vol. 68.
- Kikuyama, K., Murakami, M., Nishibori, K. & Maeda, K., 1983, "Flow in axially rotating pipe", *Bulletin JSME*, Vol. 26, No. 214.
- Kim, J., Moin, P. & Moser, R., 1987, "Turbulence statistics in fully developed channel flow at low Reynolds number", *J. Fluid Mech.*, Vol. 177, pp. 133–166.
- Kristoffersen, R. & Andersson H. I., 1993, "Direct simulations of low-Reynolds-number turbulent flow in a rotating channel", *J. Fluid Mech.*, Vol. 256, pp. 163–197.
- Millikan, C. B., 1939, "A critical discussion of turbulent flows in channels and circular tubes", *Proc. 5rd Int. Congr. Appl. Mech.*, Cambridge.
- Niederschulte, G. L., 1996, "Turbulent flow through a rectangular channel", Ph. D. thesis, University of Illinois, Department of Theoretical and Applied Mechanics.
- Oberlack, M., 1997a, "Unified theory for symmetries in plane parallel turbulent shear flows", *submitted to J. Fluid Mech.*
- Oberlack, M., 1997b, "Similarity in non-rotating and rotating turbulent pipe flows", *submitted to J. Fluid Mech.*
- Orlandi, P. & Fatica M., 1996, "Direct simulation of a turbulent pipe rotating along the axis", *submitted to J. Fluid Mech.*
- Saddoughi, S. G. & Veeravalli S. V., 1994, "Local isotropy in turbulent boundary layers at high Reynolds number", *J. Fluid Mech.*, Vol. 268, pp. 333–372.
- Wei, T. & Willmarth, W. W., 1989, "Reynolds-number effects on the structure of a turbulent channel flow", *J. Fluid Mech.*, Vol. 204, pp. 57–95.
- Zagarola, M. V., 1996, "Mean-flow scaling of turbulent pipe flow", Dissertation at Princeton University.

POSTER SESSION - 1

NUMERICAL PREDICTION OF TURBULENT HEAT TRANSFER IN A ROTATING SQUARE DUCT WITH NONLINEAR K- ϵ MODEL

A. F. Abdel Gawad⁽¹⁾, O. E. Abdel Latif⁽²⁾, Saad A. Ragab⁽¹⁾, M. R. Shaalan⁽³⁾

⁽¹⁾ ESM Dept., Virginia Tech., Blacksburg, VA 24061-0219,
USA

⁽²⁾ Dept. of Mech. Eng., Shobra Faculty of Eng.,
Egypt

⁽³⁾ Dept. of Power Mech. Eng., Zagazig University,
Egypt

ABSTRACT

This work is concerned with the numerical prediction of fully developed turbulent flow through square straight cooling passages rotating in an orthogonal mode using a nonlinear k- ϵ model. The normal Reynolds stresses are found by the nonlinear model developed by Speziale (1987). The closure of the energy equation is presented at the two-equation level of turbulence modeling as developed by Nagano and kim (1988). With any buoyancy effect neglected, temperature was considered as a passive scalar. The momentum equations and the turbulence kinetic energy and its dissipation rate equations are expanded to include Coriolis forces. The primary objective of this modeling effort is to validate the numerical modeling in an attempt to fill the gap between model predictions and the experimental data for flow and heat transfer in rotating systems. The obtained results contained time-mean velocity, wall shear stresses, time-mean temperature distributions and Nusselt numbers. The results showed that there is a significant effect of rotation on both the flow and thermal fields. Very good agreement is noticed between the present results and the recently published data (Tekriwal, 1994, Iacovides & Launder, 1991, and Wagner et al., 1991).

INTRODUCTION

In order to increase the thermodynamic efficiency of a gas turbine engine, a high turbine inlet temperature is required. A high inlet temperature demands enhanced cooling of the turbine blade with minimum coolant flow rate. This can be achieved in different ways such as film cooling and convective heat transfer to the gas flowing through the internal ducts of the blade (see Fig.(1)). These internal ducts may be smooth or sometimes may have turbulators such as an array of cross-ribs to further enhance cooling. As shown in Fig.(1), the cross section of the internal ducts may vary from circular at the leading edge of the blade to rectangular or square in the middle section to triangular at the trailing edge.

Thus, to predict the operational life of the blade, stresses must be determined. The temperature distribution should also be known prior to the stress determination. A heat conduction analysis of the blade will require boundary con-

ditions on its internal and external surfaces. To this end, therefore, heat transfer coefficient values must be determined either experimentally or analytically on the blade surfaces. Clearly, analytical predictive methods verified by experimental data will permit faster and more economic cooling design evaluation. Indeed, modern computerized methods of design evaluation have resulted in substantial reduction of development cost of design, (Medwell et al., 1991). In the current work an attempt has been made to model and predict flow field and heat transfer due to air flow in a radial cooling duct rotating about an axis perpendicular to its own-a condition known as orthogonal mode rotation. The duct is smooth and the flow is radially outward as shown in Fig. (2). The flow condition depicted in Fig. (2) is one encountered in gas turbine blades (see Fig. (1)). Wherever it is possible, comparisons are made with the available published results.

GOVERNING EQUATIONS

Nonlinear K- ϵ Model

A two-equation model uses the concept of eddy viscosity ν_t so as to describe the magnitude of turbulence intensity and its spatial extent. In the K- ϵ model, the reference velocity of turbulence is represented by $K^{0.5}$ determined from the turbulence kinetic energy (K). The characteristic length scale is given by the eddy length scale $L_\epsilon = K^{0.5}/\epsilon$.

The complete model is:

- Continuity equation:

$$\frac{\partial U}{\partial x} + \frac{\partial V}{\partial y} + \frac{\partial W}{\partial z} = 0 \quad (1)$$

- Momentum equations:

$$\begin{aligned} \frac{\partial U^2}{\partial x} + \frac{\partial UV}{\partial y} + \frac{\partial UW}{\partial z} &= -\frac{1}{\rho} \frac{\partial P}{\partial x} \\ &+ \left[\frac{\partial}{\partial x} \left(\nu \frac{\partial U}{\partial x} \right) + \frac{\partial}{\partial y} \left(\nu \frac{\partial U}{\partial y} \right) \right] - \\ &\left[\frac{\partial}{\partial x} \overline{u^2} + \frac{\partial}{\partial y} \overline{uv} \right] + \Omega^2 x - 2 \Omega W \end{aligned} \quad (2)$$

$$\begin{aligned} \frac{\partial UV}{\partial x} + \frac{\partial V^2}{\partial y} + \frac{\partial VW}{\partial z} &= -\frac{1}{\rho} \frac{\partial P}{\partial y} \\ &+ \left[\frac{\partial}{\partial x} \left(\nu \frac{\partial V}{\partial x} \right) + \frac{\partial}{\partial y} \left(\nu \frac{\partial V}{\partial y} \right) \right] - \\ &\left[\frac{\partial}{\partial x} \overline{uv} + \frac{\partial}{\partial y} \overline{v^2} \right] \end{aligned} \quad (3)$$

$$\begin{aligned} \frac{\partial UW}{\partial x} + \frac{\partial VW}{\partial y} + \frac{\partial W^2}{\partial z} &= -\frac{1}{\rho} \frac{dP}{dz} \\ &+ \left[\frac{\partial}{\partial x} \left(\nu \frac{\partial W}{\partial x} \right) + \frac{\partial}{\partial y} \left(\nu \frac{\partial W}{\partial y} \right) \right] - \\ &\left[\frac{\partial}{\partial x} \overline{uw} + \frac{\partial}{\partial y} \overline{vw} \right] + \Omega^2 z + 2 \Omega U \end{aligned} \quad (4)$$

- K-equation:

$$\begin{aligned} U_i \frac{\partial k}{\partial x_i} &= \frac{\partial}{\partial x_i} \left[\left(\frac{\nu_t}{\sigma_k} \right) \frac{\partial k}{\partial x_i} \right] - \epsilon \\ &+ \frac{1}{\rho} G + G_k \end{aligned} \quad (5)$$

- ϵ -equation:

$$\begin{aligned} U_i \frac{\partial \epsilon}{\partial x_i} &= \frac{\partial}{\partial x_i} \left(\frac{\nu_t}{\sigma_\epsilon} \frac{\partial \epsilon}{\partial x_i} \right) + \\ \frac{\epsilon}{k} [C_{\epsilon 1} \frac{G}{\rho} + G_k - (1 + G_\epsilon) C_{\epsilon 2} \epsilon] \end{aligned} \quad (6)$$

where $G = -\rho \overline{u_i u_j} \left(\frac{\partial U_i}{\partial x_j} \right)$ is a turbulent generation term.
 G_k, G_ϵ : are the turbulence production terms that have been added to account for Coriolis effect.

$G_k = 0.0$

$G_\epsilon = C_r [2 \Omega \left(\frac{K}{\epsilon} \right)^2 \left(\frac{\partial W}{\partial z} \right)]$
 (Howard et al., 1980)

- Turbulent Viscosity Equation:

$$\nu_t = C_\mu \frac{K^2}{\epsilon} \quad (7)$$

where C_μ is a model constant.

- Nonlinear representation of Reynolds stresses ($-\overline{u_i u_j}$):

$$\begin{aligned} -\overline{u_i u_j} &= C \frac{k^3}{\epsilon^2} [(\overline{D_{im}} \overline{D_{mj}} - \\ &\frac{1}{3} \overline{D_{mm}} \overline{D_{nn}} \delta_{ij}) + (\overline{D_{ij}} - \frac{1}{3} \overline{D_{mm}} \delta_{ij})] \\ &+ \nu_t \left(\frac{\partial U_i}{\partial x_j} + \frac{\partial U_j}{\partial x_i} \right) - \frac{2}{3} \delta_{ij} k \end{aligned} \quad (8)$$

C is a numerical constant obtained from numerical optimization and from comparison with the experimental data. where,

$$\begin{aligned} \overline{D_{mn}} \overline{D_{mn}} &= \frac{1}{4} \left(\frac{\partial U_m}{\partial x_n} + \frac{\partial U_n}{\partial x_m} \right)^2 \\ &= \left(\frac{\partial U}{\partial x} \right)^2 + \left(\frac{\partial V}{\partial y} \right)^2 + \left(\frac{\partial W}{\partial z} \right)^2 \\ &+ \left(\frac{\partial U}{\partial y} \frac{\partial V}{\partial x} \right) + \left(\frac{\partial U}{\partial z} \frac{\partial W}{\partial x} \right) + \\ &\left(\frac{\partial V}{\partial z} \frac{\partial W}{\partial y} \right) + \frac{1}{2} \left[\left(\frac{\partial U}{\partial y} \right)^2 + \left(\frac{\partial U}{\partial z} \right)^2 \right. \\ &+ \left. \left(\frac{\partial V}{\partial x} \right)^2 + \left(\frac{\partial V}{\partial z} \right)^2 + \left(\frac{\partial W}{\partial x} \right)^2 + \right. \\ &\left. \left(\frac{\partial W}{\partial y} \right)^2 \right] \end{aligned} \quad (9)$$

$$\begin{aligned} \overline{D_{mn}} &= \frac{\partial}{\partial t} (\overline{D_{mn}}) + U \frac{\partial}{\partial x} (\overline{D_{mn}}) + \\ &V \frac{\partial}{\partial y} (\overline{D_{mn}}) + W \frac{\partial}{\partial z} (\overline{D_{mn}}) - \\ &\left(\frac{\partial U_m}{\partial x_k} \right) \overline{D_{kn}} - \left(\frac{\partial U_n}{\partial x_m} \right) \overline{D_{mk}} \end{aligned} \quad (10)$$

$$\begin{aligned} \overline{D_{mm}} &= \frac{\partial}{\partial t} (\overline{D_{mm}}) + U \frac{\partial}{\partial x} (\overline{D_{mm}}) + \\ &V \frac{\partial}{\partial y} (\overline{D_{mm}}) + W \frac{\partial}{\partial z} (\overline{D_{mm}}) - \\ &\left(\frac{\partial U_m}{\partial x_k} \right) \overline{D_{km}} - \left(\frac{\partial U_m}{\partial x_m} \right) \overline{D_{mk}} \end{aligned} \quad (11)$$

for steady flow: $\overline{D_{mm}} = \frac{\partial U_m}{\partial x_m} = 0$

In the above set, the values of the constants are: $\sigma_k = 1.0$, $\sigma_\epsilon = 1.3$, $C_{\epsilon 1} = 1.44$, $C_{\epsilon 2} = 1.92$, $C_\mu = 0.09$, $k=0.42$, $C = 1.69$

Two-Equation Model for Temperature Field

When temperature is regarded as a passive scalar, the transport equations are expressed as :

- Energy equation:

$$U_j \frac{\partial T}{\partial x_j} = \frac{\partial}{\partial x_j} \left(\alpha \frac{\partial T}{\partial x_j} - \overline{u_j t} \right) \quad (12)$$

- Temperature variance ($\overline{t^2}$) equation:

$$\begin{aligned} U_j \frac{\partial \overline{t^2}}{\partial x_j} &= \frac{\partial}{\partial x_j} \left[\left(\alpha + \frac{\alpha_t}{\sigma_h} \right) \frac{\partial \overline{t^2}}{\partial x_j} \right] - \\ &2 \overline{u_j t} \frac{\partial T}{\partial x_j} - 2 \epsilon_t - 2 \alpha \left(\frac{\sqrt{\overline{t^2}}}{\partial x_j} \right)^2 \end{aligned} \quad (13)$$

- Temperature variance dissipation rate (ϵ_t) equation:

$$\begin{aligned} U_j \frac{\partial \epsilon_t}{\partial x_j} &= \frac{\partial}{\partial x_j} \left[\left(\alpha + \frac{\alpha_t}{\sigma_\phi} \right) \frac{\partial \epsilon_t}{\partial x_j} \right] - \\ &C_{p1} f_{p1} \left(\frac{\epsilon_t}{\overline{t^2}} \right) \overline{u_j t} \frac{\partial T}{\partial x_j} - \\ &C_{p2} f_{p2} \left(\frac{\epsilon_t}{k} \right) \overline{u_i u_j} \left(\frac{\partial U_i}{\partial x_j} \right) \\ &- C_{D1} f_{D1} \frac{(\epsilon_t)^2}{\overline{t^2}} - C_{D2} f_{D2} \epsilon \frac{\epsilon_t}{k} + \\ &\alpha \alpha_t (1 - f_\lambda) \left(\frac{\partial^2 T}{\partial x_j \partial x_k} \right)^2 \end{aligned} \quad (14)$$

- Turbulent heat flux ($-\overline{u_j t}$) equation:

$$-\overline{u_j t} = \alpha_t \left(\frac{\partial T}{\partial x_j} \right) \quad (15)$$

- Eddy diffusivity for heat (α_t) equation:

$$\frac{\alpha_t}{\nu} = C_\lambda f_\lambda Re_h \quad (16)$$

where $Re_h = K \left(\sqrt{\frac{K \overline{t^2}}{\epsilon_t}} \right) / \nu$

In the above model, the values of the constants and the model functions which account for wall-proximity effects are:

$C_\lambda = 0.11$, $f_\lambda = (1 - \exp(-2(Pr)^{0.5} St y^+ / (30.5 C_f)))^2$,
 $\sigma_\phi = 1.0$, $f_{p1} = 1.0$, $f_{p2} = 1.0$, $f_{D1} = 1.0$, $f_{D2} = 1.0$,
 $A = 30.5$, $C_{D1} = 2.2$, $C_{D2} = 0.8$, $C_{p1} = 1.8$, $C_{p2} = 0.72$

COMPUTATIONAL DETAILS

Calculation Domain

For fully developed turbulent flow, the flow pattern is similar at any cross-sectional plane in the main flow (streamwise) direction. So, the flow domain of interest is a two dimensional plane (x-y cross-sectional plane) which is normal to the main flow direction (z-direction), Fig. (2).

Boundary Conditions

The boundary conditions of the rotating duct walls involve the following two main items: all components of velocity are zero and wall temperatures are constant at certain value. The effect of the wall was introduced mainly via the logarithmic wall function, Launder and Spalding (1972). Special care was taken when considering kinetic energy (K) and its rate of dissipation (ϵ) as well as Reynolds stresses near the wall. For the thermal field, the wall proximity effects on the turbulent heat flux ($u_i \bar{t}$), the temperature variance (\bar{t}^2) and the dissipation rate of temperature fluctuations (ϵ_t) are considered by the above mentioned f_λ -function and a group of constants (f_{p1} , f_{p2} , f_{D1} and f_{D2}).

Grid and Accuracy

Preliminary calculations were carried out using the grid systems (20×20), (30×30), and (40×40). No significant grid number effects were observed on the results, except that both the secondary velocities and the thermal field results were found to be more sensitive to the grid dimension than the mean axial velocity profile. However, the 30×30 grid was used to obtain more accurate resolution near the corners of the duct.

Calculation Sequence

Calculation starts with solving the cross-flow momentum equations (Eqs. (2) and (3)), and subsequently this estimated cross-flow velocity field is corrected by the pressure correction so that the velocity field fulfills the continuity principle. Then, the streamwise momentum equation (Eq. (4)) is solved. The turbulence quantities K and ϵ are next solved. Finally, the thermal equations such as energy equation (Eq. (12)), temperature variance equation (Eq. (13)) and temperature variance dissipation (Eq. (14)) are solved. This iteration sequence is repeated until convergence is achieved. Convergence is measured in terms of the maximum change in each variable during an iteration. The maximum change allowed for the convergence check is set to 10^{-5} .

RESULTS AND DISCUSSION

Air was chosen as a test fluid, and the molecular Prandtl number (Pr) was 0.71.

Flow Field

Mean Axial Velocity. Fig. (3) represents the predicted mean axial velocity distributions at $Re=25000$. Three values of Rossby number (0.0, 0.042, 0.12) are selected to illustrate the effect of rotation on the mean axial velocity profiles. The obvious effect of rotation is to cause a shift in the location of maximum axial velocity towards the trailing edge (pressure side). This means that the boundary layer becomes thinner there but on the leading edge (suction side) the boundary layer is seen to be thicker than the stationary flow. In the case of a stationary duct ($Ro = 0.0$), the differences between the predictions of the linear and nonlinear models are due to the fact that

the nonlinear model is the one which is capable of predicting the turbulence-driven motion. At the higher rotation speed ($Ro = 0.042$), some differences are still noticed, especially in the near-wall regions where the turbulence- and the pressure-driven motions are approximately of the same order. As the Rossby number increases, the pressure-driven motion dominates and the profiles of the two models become closer. It is noticed that as the Rossby number increases the mean axial velocity profile tends to have a flat central portion. Fig.(4) represents a comparison between the contours of the normalized mean axial velocity (W/W_s) predicted by both the linear and nonlinear models at $Re = 25000$ for a Rossby number of 0.042. The effect of the turbulence-driven motion is more pronounced near the leading edge (suction side). Fig.(5) shows a qualitative comparison between the present nonlinear predictions and the predictions of Iacovides and Launder (1991) at $Re = 32500$ and $Ro = 0.075$.

Shear Stresses Distributions. Fig. (6) demonstrates the effect of rotation on wall shear stress. The present predictions are compared with the results of Iacovides and Launder (1991) for a Reynolds number of 32500. The friction coefficient (C_f) is normalized by the same quantity as the case of a stationary duct for the same Reynolds number. The results include the skin friction coefficient of the trailing wall (pressure side), the leading wall (suction side), side wall and the four walls of the duct (overall). On the pressure side rotation enhances turbulent activity and increases the wall shear stress. The reverse is noticed on the suction side where the wall shear stress is reduced. The increase of the Rossby number increases the wall shear stress on the top wall and the overall shear stress.

Secondary Flow. The existence of the Coriolis force causes the formation of two-vortex structure (one on each side of the symmetry plane). The secondary flow moves adjacent to the side walls from the high-pressure region (trailing wall) to the low pressure one (leading wall) and returns in the opposite direction in the central region of the duct to satisfy continuity. The increase of rotation velocity increases the rate of secondary flow circulation. The transport of relatively cooler fluid from the central core region to the trailing wall enhances the heat transfer on the trailing wall as will be seen later. Fig. (7) represents a qualitative comparison between the present predictions and those predicted by Iacovides and Launder (1991) at a Reynolds number of 97500 and a Rossby number of 0.05. Good agreement is noticed between the two predictions.

Thermal Field

The turbulent Prandtl number (Pr_t) in the turbulent part of the wall region had a maximum value of 1.05.

Mean Temperature. The contours of the normalized mean temperature (T/T_w) in the cross-sectional plane X-Y at a Reynolds number of 25000 for two Rossby numbers (0.0 and 0.042) are shown in Fig. (8). When comparing with the case of the stationary duct ($Ro = 0.0$), the rotation causes the central core to enlarge and shift towards the trailing wall of the duct. The increase of the rotation rate increases the area of the core. As stated before, for the velocity field, with the increase of the rotation rate, the pressure-driven motion dominates. Thus, the contours of the normalized temperature predicted by both the linear and nonlinear models become closer. So, for high rotation rates, it is quite satisfactory to use the linear model to predict the temperature distribution. Fig. (9) shows a comparison of the normalized mean temperature (T/T_w)

between the present predictions of the normalized (T/T_w) and those of Dutta et al. (1994). The Reynolds number is 25000 and the Rossby number is 0.24. Very good agreement is noticed between the two predictions especially at the core and the leading wall.

Nusselt Number Distributions. Figure (10) shows the effect of Rossby number on the values of Nusselt number $(Nu = q_w D / (k(T_w - T_b)))$.

Where D : is the hydraulic diameter of the duct.

k : is the thermal conductivity of fluid.

T_w : is the wall temperature.

T_b : is the bulk (average temperature over the duct cross-section).

The values are normalized by the value of Nusselt number for the stationary duct at the same Reynolds number (25000) and the same Rossby numbers. It can be concluded from the figure that the rotation greatly enhances the heat transfer on the trailing wall and impairs it on the leading wall. At a Rossby number of 0.12 the Nusselt number on the trailing wall is some 80 percent higher than for the stationary duct. The value on the leading wall is about 20 percent lower than for the stationary duct. On the trailing side, Nusselt number increases continuously with the Rossby number. But on the leading side it asymptotes to a constant value (0.8). Very good agreement is noticed with the predictions of Tekriwal (1994) and the experimental data of Wagner et al. (1991) at the same Reynolds number (25000) as well as the predictions of Iacovides and Launder (1991) at a Reynolds number of 32500.

CONCLUSIONS

In this work the results of the nonlinear $K-\epsilon$ model of turbulence in conjunction with the thermal model for a rotating square duct were presented. Emphasis has been placed on the prediction of the effects of Coriolis forces on fully developed flows for the situations published in the literature. Special care was paid to the effect of Rossby number on both the flow and thermal fields.

The following conclusions are derived from the present modeling effort:

- 1- The rotation causes the point of maximum mean axial velocity to be displaced towards the trailing wall (pressure side).
- 2- The wall shear stress increases above the non-rotating levels on both the pressure side and the side walls (top and bottom walls). It decreases on the suction side.
- 3- Heat transfer is enhanced on the trailing wall (pressure side) due to rotational effects (Coriolis-induced secondary flow). While it is impaired on the leading wall (suction side).
- 4- The variation of the heat transfer (Nusselt number) on the leading wall appears to be less sensitive to Reynolds number (not shown here) and Rossby number.
- 5- The heat transfer rates on the pressure side continue to increase, even at higher rotational speeds.
- 6- The present predictions are in good agreement with the existing published results.

From these standpoints, the utilized modeling scheme may be regarded as a turbulence model of considerable accuracy and cost efficiency.

REFERENCES

Dutta, S., Andrews, M. J., and Han, J. C., 1994, "Numerical Prediction of Turbulent Heat Transfer in a Rotating Square Duct with Variable Buoyancy Effects," *Proceedings of the AIAA/ASME 6th Thermophysics and Heat Transfer Conference (Colorado Springs, Co), General Papers in Heat and Mass Transfer, Insulation, and Turbomachinery, HTD*, Vol. 271, pp. 161-170.

Howard, J. H., Patanker, S. V. and Bordyniuk, R. M.,

1980, "Flow Prediction in Rotating Ducts Using Coriolis Modified Turbulence Model," *ASME J. Fluids Engineering*, Vol. 102, pp. 456-461.

Iacovides, H. and Launder, B. E., 1991, "Parametric and Numerical Study of Fully Developed Flow and Heat Transfer in Rotating Rectangular Ducts," *ASME J. Turbomachinery*, Vol. 113, pp. 331-338.

Launder, B. E. and Spalding, D. B., 1972, "Mathematical Models of Turbulence," *Academic Press, London, U. K.*

Medwell, J. O., Morris, W. D., Xia, J. Y., and Taylor, C., 1991, "An Investigation of Convective Heat Transfer in Rotating Coolant Channel," *ASME J. Turbomachinery*, Vol. 113, pp. 354-359.

Nagano, Y. and Kim, C., 1988, "A Two-Equation Model for Heat Transport in Wall Turbulent Shear Flows," *ASME J. Heat Transfer*, Vol. 110, pp. 583-589.

Speziale, C. G., 1987, "On Nonlinear $k-L$ and $k-\epsilon$ models of Turbulence," *J. Fluid Mechanics*, Vol. 178, pp. 459-475.

Tekriwal, P., 1994, "Heat Transfer Predictions with Extended $K-\epsilon$ Turbulence Model in Radial Cooling Ducts Rotating in Orthogonal Mode," *ASME J. Heat Transfer*, Vol. 116, pp. 369-380.

Wagner, J. H., Johnson, B. V., and Hajek, T. J., 1991, "Heat Transfer in Rotating Passages with Smooth Walls and Radial Outward Flow," *ASME J. of Turbomachinery*, Vol. 113, pp. 42-51.

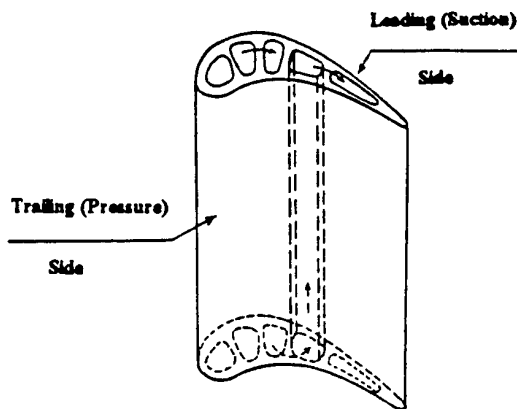


Figure 1: Internal Cooling Passages in a Turbine Blade.

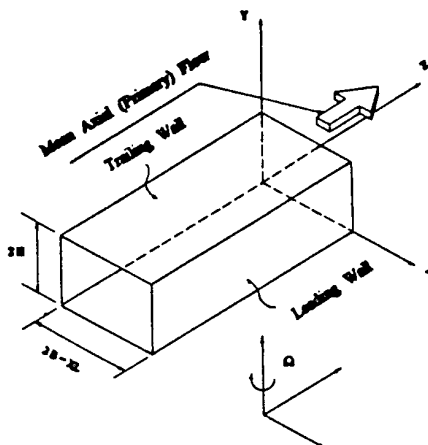


Figure 2: The Coordinate System and Flow Configuration of a Rotating Duct.

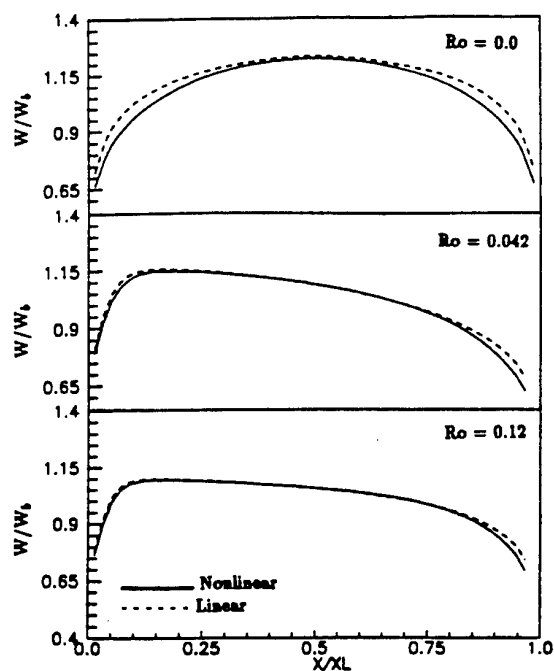


Figure 3: Rotation Effect on Mean Axial Velocity Profiles in a Square Duct, $Re = 25,000$.

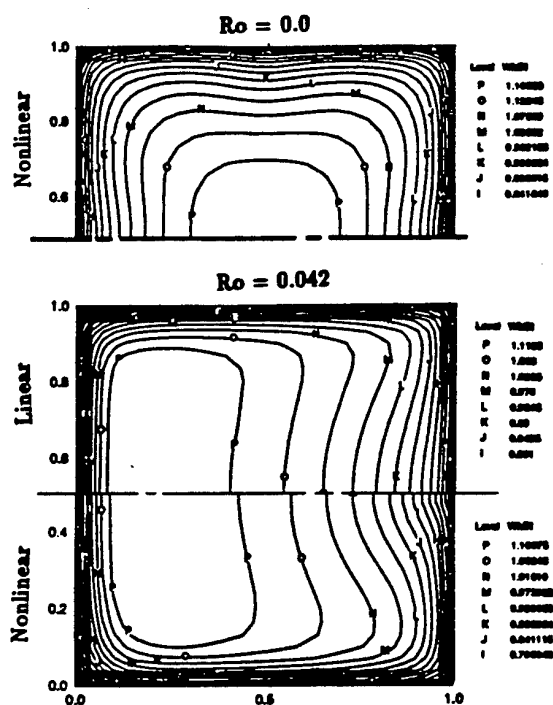


Figure 4: Contours of Normalized Mean Axial Velocity (W/W_b) in a Square Duct for Two Rossby Numbers, $Re = 25,000$.

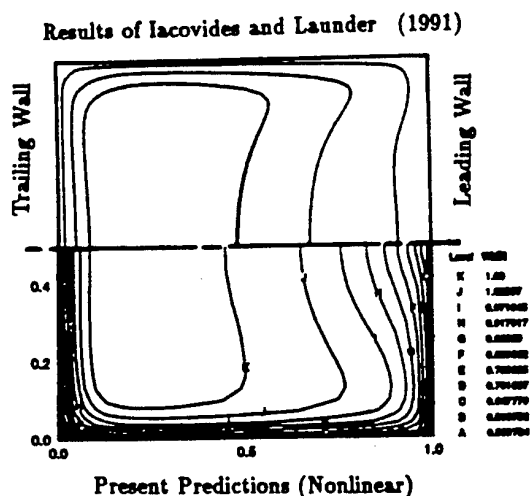


Figure 5: Comparison Between Present Predictions and the Results of Iacovides and Launder (1991) for Normalized Mean Axial Velocity (W/W_b), $Re = 32,500$ & $Ro = 0.075$.

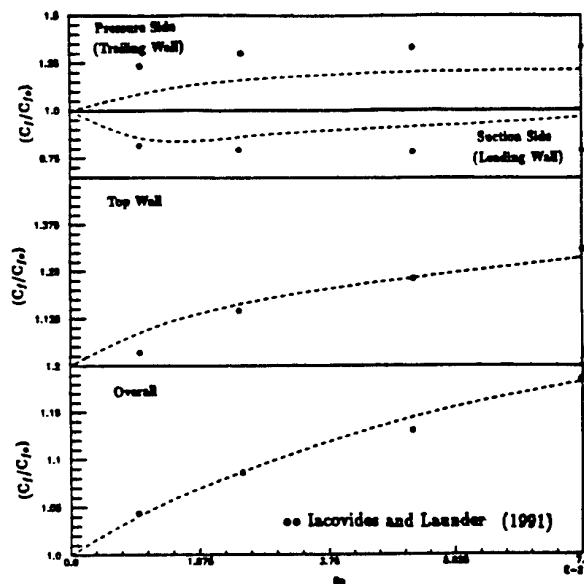


Figure 6: Comparison Between Present Nonlinear Predictions and the Results of Iacovides and Launder (1991) for Normalized Skin Friction Coefficient at Different Rossby Numbers, $Re = 32,500$.

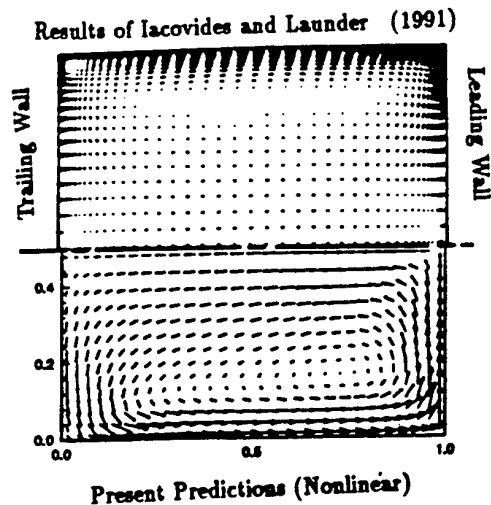


Figure 7: Comparison Between Present Nonlinear Predictions and the Results of Iacovides and Launder (1991) for Secondary Flow, $Re = 97,500$ & $Ro = 0.05$.

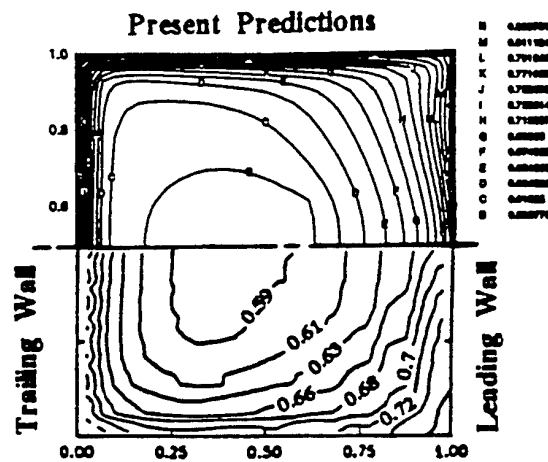


Figure 9: Comparison between Present Predictions and the Predicted Results of Dutta et al. (1994) for the Normalized Mean Temperature (T/T_w), $Re = 25,000$ & $Ro = 0.24$.

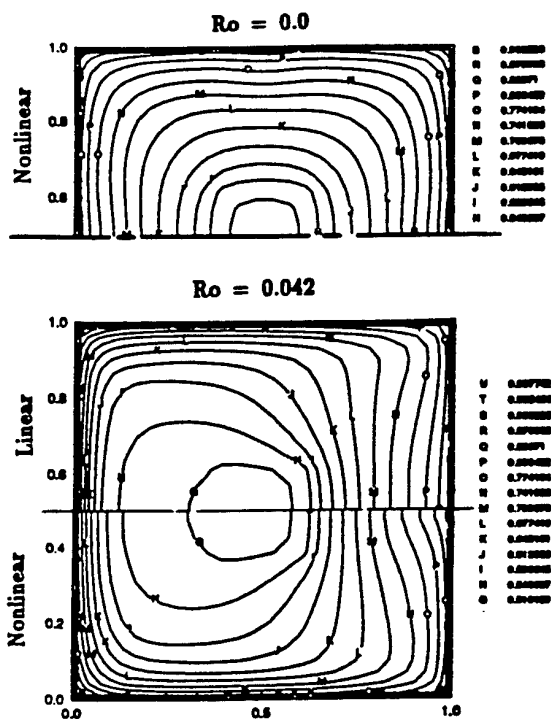


Figure 8: Contour Map of Normalized Mean Temperature (T/T_w) for Different Rossby Numbers, $Re = 25,000$.

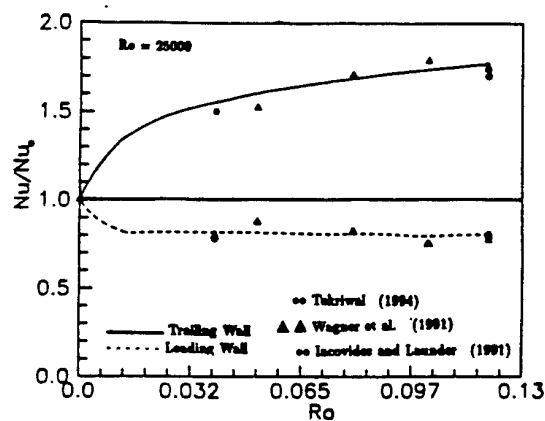


Figure 10: The Effect of Rossby Number on the Values of Nusselt Number for the Square Duct.

EXPLOITING THE FLEXIBILITY OF UNSTRUCTURED GRIDS FOR COMPUTING COMPLEX FLOW PATTERNS MORE PRECISELY

C.-H. Rexroth, R. Koch, S. Wittig
Lehrstuhl und Institut für Thermische Strömungsmaschinen
Universität Karlsruhe (TH)
D-76128 Karlsruhe
Germany

ABSTRACT

In comparison to structured meshes, the most important advantage of unstructured grids is geometrical flexibility. The present work proposes techniques to exploit this feature by generating and optimizing unstructured meshes to achieve more accurate results in less computing time. Several test cases and a demanding application are selected to demonstrate the effectiveness of these methods.

INTRODUCTION

For the design of modern gas turbines, numerical methods for the simulation of flow problems are indispensable tools. Because of the complex geometries there is a growing tendency to unstructured grids instead of their structured predecessors. This choice is often accompanied by losses in precision and computational efficiency. However, specific properties of unstructured meshes offer the chance to temper or even overcome these drawbacks. This paper discusses some of these approaches with special emphasis on turbomachinery application.

SPATIAL DISCRETIZATION

It is well known that triangles can cover two-dimensional domains of arbitrary shape without any difficulty. The vertices of the triangles serve as nodes in the computational grid. For a Finite Volume method, it is necessary to construct control volumes. A second mesh is applied to define these volumes. Fig. 1 shows the formation of the dual mesh inside and at the boundaries of a domain. Differing from bare triangles, the resulting polygonal Finite Volume mesh assures a strong coupling of the transport variables in adjacent control volumes.

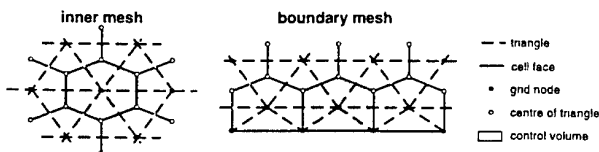


Fig. 1: Topology of control volumes (duals)

NUMERICAL ALGORITHM

In continuing earlier work (Noll and Wittig, 1991; Kurreck and Wittig, 1994), a Navier-Stokes code using the Finite Volume method on two-dimensional unstructured

grids has been developed to meet the requirements arising from flow problems in turbomachinery (Rexroth and Wittig, 1995). The governing transport equations are solved in a blockiterative manner. The velocity field is derived from Reynolds-averaged Navier-Stokes equations. A pressure distribution is calculated by a SIMPLE(C)-type correction algorithm (Patankar, 1981; Van Doormaal and Raithby, 1984) where a special interpolation of cell face velocities (Rhie and Chow, 1983) prevents chess-board oscillations on the collocated grid. An extension for the treatment of compressibility has also been implemented (Karki and Patankar, 1989). Turbulent quantities are calculated by applying the standard k, ϵ model together with wall function. A transport equation for the enthalpy accounts for an exchange of energy. For stable and accurate modelling of the convective terms, the new DISC discretization scheme is available (Rexroth *et al.*, 1997).

To assure a fast implicit solution of the linear equations the iterative BiCGSTAB algorithm (Van der Vorst, 1992) combined with a reduced ILU decomposition is applied. It rarely takes more than one iteration of BiCGSTAB to solve a linear system for a single transport variable.

EXPLOITING FLEXIBILITY

Already at the stage of grid generation, it is possible to profit from the geometrical flexibility of unstructured meshes. Based on a rough estimation, the spatial resolution of a grid can be chosen according to the mean flow pattern. Another possibility is the acceleration of convergence (AC) by a special grid design. Both methods are capable to reduce memory and time requirements. Existing meshes can be optimized by adapting the grid density to the character of the calculated flow field. The pay off is a significant gain in accuracy, if the basic grid is relatively coarse.

Grid generation

Fig. 2 presents two different grids for the simulation of a turbulent flow over a backward facing step (Eaton and Johnston, 1980). First, there is a section of a conventional mesh with uniform spatial resolution consisting of 9695 nodes. The second grid takes advantage of the assumption, that near the centre line of the domain no steep gradients in flow quantities will be found. By prescribing a coarser resolution in this region, the number of grid nodes can be reduced to 6924 without loss of information inside the boundary layers.

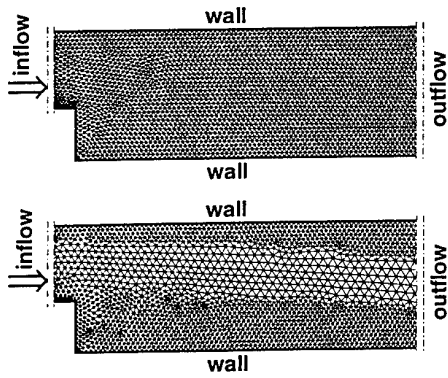


Fig. 2: Conventional grid and AC grid for step flow

As a side effect, the number of mesh cells the flow has to pass on its way from inflow to outflow boundary is reduced in the coarse grid area. Therefore, information can travel much easier enhancing the coupling between the different parts of the domain. Consequently, as a further advantage, convergence is accelerated (AC). The corresponding convergence history in terms of normalized pressure residual (Res) and number of outer iterations can be found in Fig. 3.

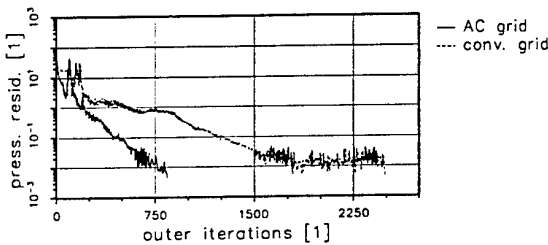


Fig. 3: Convergence of step flow calculations

On the conventional grid 2490 blockiterations and 165.5 min of computing time on a workstation are required to achieve the stopping criterion of $Res \leq 5 \cdot 10^{-3}$. With the AC new grid, the whole procedure just takes 842 loops and 33.6 min.

In Fig. 4, numerical and experimental results for the axial component U of the velocity are compared at two positions located 4.0 and 8.0 step heights s downstream of the expansion. In spite of reducing the numerical effort to 20%, the AC grid arrives at almost exactly the same results as the conventional approach.

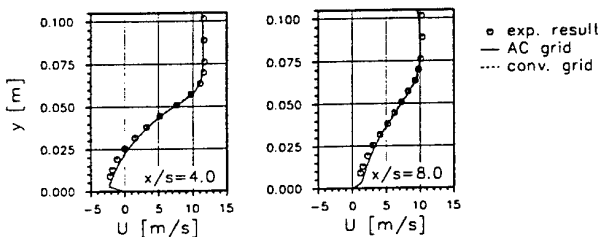


Fig. 4: Velocity profiles for step flow

In cases, where a comparison with measurements is not possible, the response of the AC solution to successive refinement and optimization of the grid has to be monitored carefully.

Grid optimization

To modify the spatial resolution of a mesh, grid nodes can be added or removed. The methods used are designed to preserve the connectivity of existing nodes as far as possible.

As can be seen from Fig. 5, a new node P is inserted at the centre of the triangle ABC . Afterwards the surrounding triangles are checked. If the new triangulation is of better quality, the corresponding old edges are removed and the new triangles are fixed.

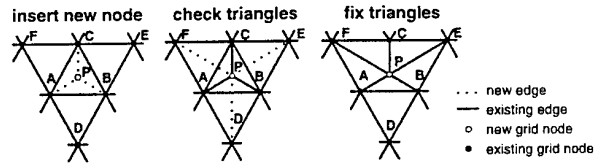


Fig. 5: Adding new grid nodes

The technique to delete grid nodes is shown in Fig. 6. In the first step a new node P is inserted, too. Then its three neighbours are deleted and P is connected to all surrounding nodes. What remains to be done is checking and fixing the triangles. Both procedures are finished by smoothing the modified mesh.

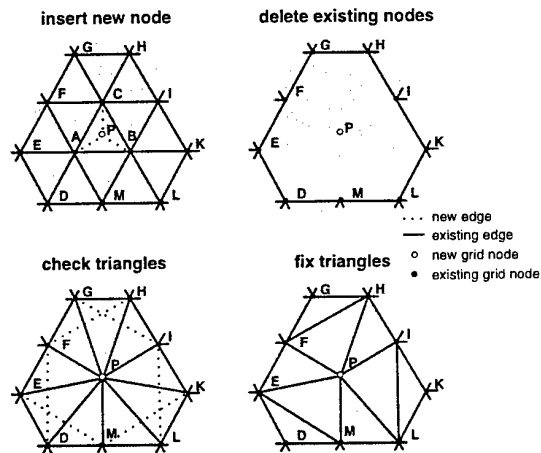


Fig. 6: Removing existing grid nodes

A grid can be optimized either under complete control of the user or automatically by the program. In each case various options are at hand. For an automatic adaption to the pattern of a calculated flow field, non-dimensional gradients P_i of the transport variables ϕ_i are used.

$$P_i = \left[\left| \frac{\partial \phi_i}{\partial x} \right| + \left| \frac{\partial \phi_i}{\partial y} \right| \right] \cdot \frac{D}{|\phi_{i,ref}|} \quad (1)$$

P_i is evaluated at the grid nodes from spatial derivatives $\frac{\partial \phi_i}{\partial x_j}$, the mean diameter D and a reference value $\phi_{i,ref}$ at the corresponding mesh cell. The expressions $\frac{\partial \phi_i}{\partial x_j} \cdot D$ may be interpreted as first order terms of a Taylor expansion for ϕ_i . At locations, where the grid density is insufficient, strong variations of ϕ_i are associated with high values of P_i . In these areas, there is the probability of numerical inaccuracies. Therefore, P_i can be regarded as an indicator for the local discretization error of ϕ_i . For high values of P_i grid refinement is required, whereas low values permit coarsening.

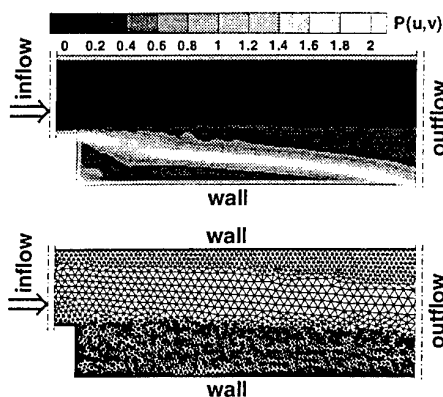


Fig. 7: $P(u,v)$ and modified AC grid

Fig. 7 illustrates the distribution of $P(u,v)$ on the basic AC grid as well as the adapted mesh for the backward facing step. Refinement was performed downstream of the expansion where flow separation provokes a high level of $P(u,v)$. Besides recirculation zones, $P(u,v)$ is sensitive to boundary layers and stagnation points.

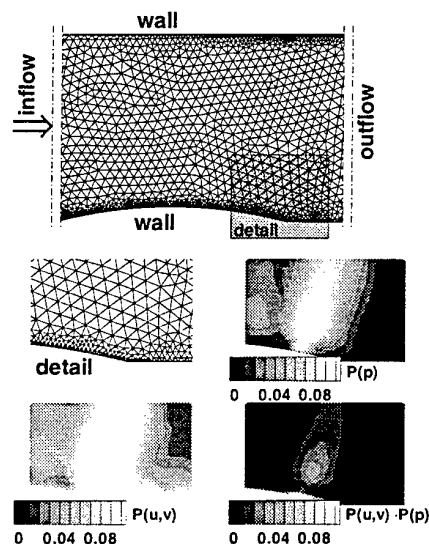


Fig. 8: Basic grid and $P(\phi)$ for channel flow

In transonic flows, this grid optimization procedure can be applied for shock capturing. As an example, the basic grid and evaluations of different adaption parameters P_i are shown in Fig. 8 for a channel flow (Liu et al., 1988).

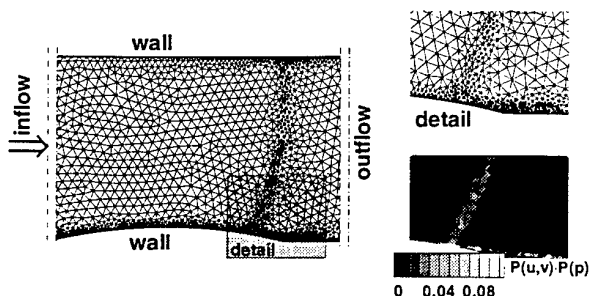


Fig. 9: Modif. grid and $P(u,v) \cdot P(p)$ for channel flow

Over a circular arc at the bottom wall of the channel, the flow accelerates to transonic speed. Near the trailing edge of the profile recompression takes place. $P(u,v)$ and $P(p)$ are able to locate the shock, but the product $P(u,v) \cdot P(p)$ of both quantities leads to contours which are more sharply confined.

Fig. 9 presents the same mesh after optimization based on the former criterion. The position of the shock itself and an induced flow separation near the bottom wall are clearly visible from grid resolution. The peak values of the optimization parameter $P(u,v) \cdot P(p)$ have also been reduced significantly.

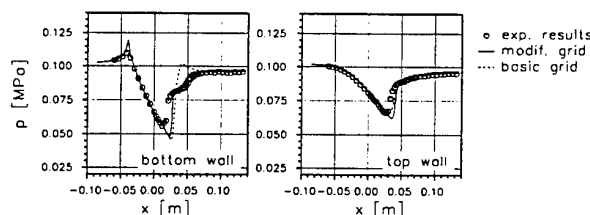


Fig. 10: Wall pressure for channel flow

To demonstrate the improvement of accuracy gained by the refinement, Fig. 10 shows a comparison of the pressure distributions calculated along the top and the bottom wall with experimental findings. On the modified grid, the shock has moved a little further downstream at the top of the channel, but the flow separation at the trailing edge of the arc is resolved now.

PRACTICAL APPLICATION

As an example for the effectiveness of grid optimization in practical applications, the flow through a cascade of film cooled gas turbine blades has been selected (Beeck et al., 1992). The basic mesh with 5787 grid nodes can be seen in Fig. 11.

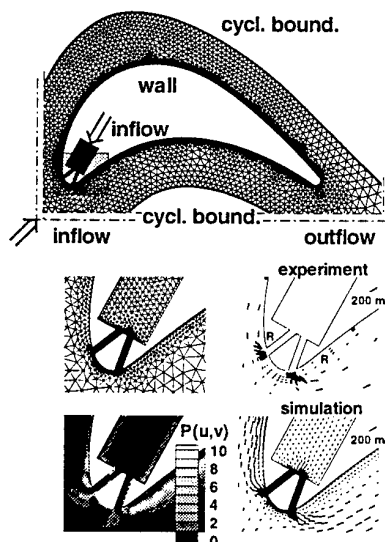


Fig. 11: Basic grid, velocity and $P(u,v)$ at LE for cascade

It consists of the outer domain, the two cooling air channels near the leading edge of the blade (LE) and a plenum where the cooling flow enters. Experiments were carried out at a blowing ratio $M = \frac{(\rho|\vec{u}|)_{cool}}{(\rho|\vec{u}|)_{\infty}}$ of 1.14. Downstream of both cooling air injections, large separation bubbles were found. These characteristic features of the flow

field are already present in the simulation on the basic grid. By the optimization parameter $P(u, v)$ critical mesh areas are identified in front of the cooling jets and inside the recirculation zones.

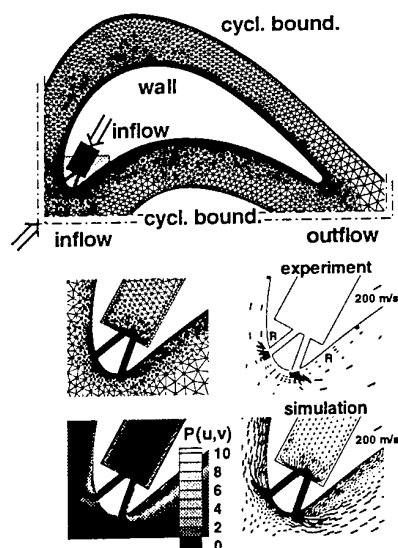


Fig. 12: Modif. grid, velocity and $P(u, v)$ at LE for cascade

By evaluating $P(u, v)$, the mesh was refined by 2262 additional nodes. Fig. 12 shows, how the spatial resolution has been adapted, especially in the vicinity of the leading edge of the profile (LE). Therefore, the structure of flow separation is predicted much more detailed. According to the new contours of $P(u, v)$ the extension of critical area has been reduced, too.

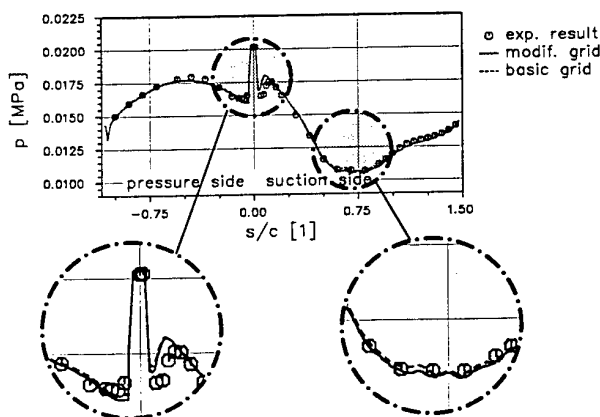


Fig. 13: Wall pressure for filmcooled cascade

For a quantitative rating of accuracy, Fig. 13 presents measured and calculated profiles of the pressure along the surface of the blade. The surface coordinate s has been normalized by the chord length c . Results from basic and modified grid are in very good agreement with the measurements. The adapted mesh improves accuracy inside both separation zones and near the pressure minimum on the suction side.

CONCLUSION

The geometrical flexibility of unstructured grids can be exploited to enhance accuracy and computing time of flow calculations. Time requirements are cut down by prescribing a spatial resolution of the mesh that is capable to accelerate convergence by enhancing the exchange of information inside the domain. A gain in accuracy is attained by adapting the mesh to the character of the simulated flow field. The optimization criteria presented in this paper are able to identify critical zones inside a domain, for example flow separations, shocks, stagnation points and boundary layers.

Acknowledgements : This work was supported by a grant of the Deutsche Forschungsgemeinschaft in the context of the Graduiertenkolleg 'Energie- und Umwelttechnik' and the Sonderforschungsbereich 167 'Hochbelastete Brennräume'.

REFERENCES

- Beeck, A., Fottner, L., Benz, E. and Wittig, S., 1992, "The aerodynamic effect of coolant ejection in the leading edge region of a film-cooled turbine blade", *Proceedings of 80th. Int. Symp. Heat Transfer and Cooling in Gas Turbines, Antalya, Turkey*.
- Eaton, J. K. and Johnston, J. P., 1980, "Turbulent flow reattachment: An experimental study of the flow and structure behind a backward facing step", *Stanford University Department of Mechanical Engineering, Report MD-39*.
- Karki, K. C. and Patankar, S. V., 1989, "Pressure based calculation procedure for viscous flows at all speeds in arbitrary configurations", *AIAA Journal*, Vol. 27, pp. 1167-1174.
- Kurreck, M. and Wittig, S., 1994, "Numerical simulation of combustor flows on parallel computers: Potential limitations and practical experience", *ASME Paper 94-GT-404*.
- Liu, X. and Squire, L. C., 1988, "An investigation of shock/boundary-layer interactions on curved surfaces at transonic speeds", *Journal of Fluid Mechanics*, Vol. 187, pp. 67-486.
- Noll, B. E. and Wittig, S., 1991, "A generalized conjugate gradient method for the efficient solution of three-dimensional fluid flow problems", *Numerical Heat Transfer*, Vol. 20, pp. 207-221.
- Patankar, S. V., 1981, "A calculation procedure for two-dimensional elliptic situations", *Numerical Heat Transfer*, Vol. 4, pp. 409-425.
- Rexroth, C.-H. and Wittig, S., 1995, "Improved accuracy and effectiveness for Navier-Stokes solvers on unstructured grids", *Numerical Methods for Fluid Dynamics V, Oxford Science Publications*, pp. 549-556.
- Rexroth, C.-H., Bauer, H.-J. and Wittig, S., 1997, "DISC-An efficient method for the discretization of convection on unstructured grids", *Aerospace Science and Technology*, accepted for publication.
- Rhie, C. M. and Chow, W. L., 1983, "Numerical study of the turbulent flow past an airfoil with trailing edge separation", *AIAA Journal*, Vol. 21, pp. 1525-1532.
- Van der Vorst, H. A., 1992, "Bi-CGSTAB: A fast and smoothly converging variant of Bi-CG for the solution of nonsymmetric linear systems", *SIAM Journal on Scientific and Statistical Computing*, Vol. 13, pp. 631-644.
- Van Doormaal, J. P. and Raithby, G. D., 1984, "Enhancement of the SIMPLE method for predicting incompressible fluid flows", *Numerical Heat Transfer*, Vol. 7, pp. 147-163.

COMPUTATION OF THE UNSTEADY AND LAMINAR-TURBULENT FLOW IN A LOW-PRESSURE TURBINE

Frank Eulitz and Karl Engel

Institute for Propulsion Technology
DLR German Aerospace Research Establishment
Linder Höhe
51147 Köln
Germany

ABSTRACT

A three-dimensional time-accurate Reynolds averaged Navier-Stokes solver is applied to study the wake interaction in a low pressure turbine along a precalculated streamtube near midspan. The model turbine configuration consists of three stator and two rotor rows of equal pitch.

Laminar-turbulent transition phenomena are incorporated qualitatively by coupling the Abu-Ghanam Shaw transition correlation with a two-layer version of the Spalart and Allmaras one-equation turbulence model. In order to account for by-pass transition induced by migrating wakes, the transport equation for the turbulent kinetic energy is solved in addition.

The numerical methods used to obtain, first, a steady-state initialization and, then, the time-periodic solution are shortly described.

Instantaneous entropy plots are presented to monitor the wake migration and interaction with downstream boundary layers and wakes. It is shown that the interaction gives rise to a substantial variation of the skin friction parameter (order of 40 per cent).

INTRODUCTION

Presently, many research activities are involved with the measurement and modeling of wake/blade row interaction in axial compressors and turbines (e.g. Fan and Lakshminarayana 1996, Dawes 1996, Halstead et al. 1997). Sharma and Ni (1994) show efficiency measurements of a turbine in which the inlet guide vanes are clocked relative to the second stage stator. Results of this experiment, carried out at NASA during 1991, indicate that the performance of the turbine can be optimized by adjusting the relative position of the stator blades, i.e. by appropriate clocking. The phenomenon, which is obviously a result of the altered wake/blade row interaction between two stators, however, is not fully understood yet. As Greitzer et al. (1994) remark, the physical mechanism responsible for the efficiency variation may or may not be associated with unsteadiness.

Time-accurate CFD studies on the subject using different numerical methods and levels of turbulence modeling (Sharma,

Dorney, Eulitz 1996b) uniformly conclude that an increase of the efficiency is observed when the wake of the first stage stator impinges on the (clocked) second stage stator blade. Whereas Dorney's turbulent flow results are based on the Baldwin-Lomax model, the previous work by the authors is based on the one-equation transport model by Spalart and Allmaras (1992). In all of these works, transition phenomena were neglected although the turbine flow typically exhibits various forms of transition (Mayle, 1991). In particular, transition induced by migrating wakes from upstream rows is an inherent part of wake interaction, and the effect on the unsteady loss production can be large (Denton, 1993).

The aim of the present work is to present a robust solution method which incorporates important unsteady transition effects and to apply it to the study of wake interaction in a 2-1/2 stages low pressure turbine operating at a low Reynolds number (order of 300,000). The well known transition criterion by Abu-Ghanam Shaw (1980) in a formulation by Drela (1995) has been implemented into the present time-accurate Navier-Stokes solver (Engel, Eulitz 1996). Before, Rodi (1989) and Cho (1993) went a similar route to simulate the transitional flow over a flat plate and through a turbine cascade subject to a time-periodic wake disturbance. To the authors' knowledge, Rodi's approach is the only one documented which is based on the solution of the RANS and a turbulence transport model for the complete integration domain. Other approaches either use algebraic turbulence modeling in conjunction with the intermittency approach to describe the transitional flow region (e.g. Ameri and Arnoult 1994) or inviscid/viscous schemes with advanced two-equation models (e.g. Fan and Lakshminarayana 1996).

First, the computational methods for the steady-state and time-accurate calculation are briefly described. The former is needed as an initialization for the time-accurate integration. Then, the coupling of the transition criterion with a two-layer formulation of the Spalart-Allmaras turbulence (1992) model will be presented. Finally, computational results for a multistage turbine will be presented in form of instantaneous entropy and skin friction plots.

One word of caution is in order beforehand. Within the

framework of a Reynolds-averaged approach and the use of a simple Boussinesq turbulence model the study of wake/blade row interaction can only be of qualitative and approximate nature. The approach is only justified in light of the tremendous computational costs involved with more rigorous approaches as LES or DNS (see AGARD Rep. 1994).

BASIC EQUATIONS

The unsteady flow is solved along a three-dimensional streamtube with varying radial thickness and radius as given by a design calculation procedure. Instead of using transformed coordinates for a stream surface, as for instance Chima (1987), the fully three-dimensional flow equations are the basis of the present investigation (Eulitz 1996). Since highly stretched grids are used, the so-called full-thin-layer-approximation of the viscous fluxes is employed.

COMPUTATIONAL METHOD

The used multi-block flow solver is parallelized based on domain decomposition and message passing using communication routines of the PVM or MPI library. To achieve a good parallel efficiency, explicit or block local solution strategies are implemented.

The convective fluxes are discretized using Roe's upwind scheme (1981) in combination with van Leer's (1979) MUSCL extrapolation for second order accuracy in space. The viscous fluxes are discretized using central differences (Engel and Eulitz 1996).

For initialization, the flow solver is first run in a steady-state multistage mode with a four-stage Runge-Kutta scheme using local time stepping, implicit residual smoothing (von Lavante 1990) and non-reflecting formulations for the inlet/outlet and mixing plane boundaries (Saxer and Giles 1993).

For the unsteady calculation, a second-order time accurate four stage Runge-Kutta scheme is applied in conjunction with He's (1993) two-grid acceleration method. The time-accurate two-grid approach by He is justified when highly stretched grids are used, and if one is only interested in time scales which can be resolved by the outer "inviscid" grid. This is the case here. The mesh (shown in figure 3) is condensed near the blade surface to allow for the resolution of the laminar sublayer. The y^+ values of the first mesh points off the surface are inbetween 1 and 3. (This has been shown sufficient for the Spalart & Allmaras turbulence model, Eulitz 1996). And we wish to accurately resolve time scales in the order of the blade passing frequency. Smaller time scales like Tollmien-Schlichting waves are excluded anyway in the present study by the ensemble-averaged approach that we take.

BOUNDARY CONDITIONS

At the airfoil boundary, the no slip condition is enforced. At the streamtube boundaries facing hub and tip, only the normal velocity components vanish. The wall pressure is found via the momentum equation normal to the wall.

For the steady state multistage calculation, quasi-three dimensional non-reflecting boundary conditions according to Saxer and Giles (1993) are used at the inlet and outlet boundaries of the computational domain. Part of this technique is that the solution vector at the boundary is decomposed into spatial Fourier modes. Whereas the higher harmonics are treated in a non-reflecting sense, the zeroth mode is coupled to the prescribed physical boundary condition. At the exit boundary, for example, the average change of the downstream running acoustic wave is related to the specified exit pressure. At the

stator/rotor or rotor/stator mixing plane, the zeroth mode is prescribed by a flux-averaging technique in order to preserve mass, momentum and energy. As a result, a wake will be mixed out at the interface plane (figure 4). When starting the unsteady calculation with a steady-state multistage solution thus obtained, a time periodic solution does not evolve until all wakes are convected through the entire computational domain.

For the unsteady calculation, other formulations are used at the inlet/outlet boundaries and the mixing planes. A time accurate coupling at the moving and non-moving grid interface is possible by virtue of the sheared-cell technique according to Giles (1989). Therefore, the computational mesh (figure 3) has been made equidistant at the blade row boundaries. At the inlet and outlet boundaries, the non-reflecting method of Acton and Cargill (1988) is employed. Here, the amplitudes of the upstream and downstream running waves are given by a partial differential equation system.

TREATMENT OF TURBULENCE

Turbulence effects are accounted for by a one-equation transport model formulated for the eddy viscosity according to Spalart and Allmaras (1992).

Since we are interested in the unsteady behavior of a laminar or turbulent boundary layer, which may be separated or attached, the use of wall functions is ruled out and the laminar sublayer has to be resolved in our study. As the model shares the treatment of the inner layer with an algebraic model it does not require any finer mesh resolution. Note, that many two-equation models require very fine resolution of the laminar sublayer (y^+ in the range of 0.2, Wilcox 1993) which leads to unacceptable low time steps. For a discussion of the one-equation model, the reader is referred to the works of Spalart and Allmaras 1992, Birch 1993, Menter 1996, Shur et al 1996. The predictive capabilities and the numerical robustness make the Spalart & Allmaras model a very attractive candidate for unsteady flow calculations. The version which is used here is valid for free shear flows and the near-wall region outside the viscous sublayer,

$$\frac{Dv_t}{Dt} = c_{b1}|\omega|v_t - c_{w1}f_w\left[\frac{v_t}{d}\right]^2 + [\nabla(v_t \cdot \nabla v_t) + c_{b2}(\nabla v_t)^2] \quad (1)$$

where v_t , $|\omega|$, d denote the eddy viscosity, magnitude of vorticity, and wall distance, respectively. In their Low-Reynolds variant, Spalart and Allmaras (1992) express (1) in terms of \tilde{v} and employ the damping function from Mellor and Herring (1973) to obtain the eddy viscosity $v_t = f_{v1}\tilde{v}$. It reads

$$f_{v1} = \frac{\chi^3}{\chi^3 + c_{v1}^3}, \quad \chi = \frac{v_t}{v} \quad (2)$$

where a value of 7.1 is used for the constant c_{v1} . The damping is not valid at the outer edge of a boundary layer or wake. In steady flows where turbulence is only emanating from the profile and the mean flow gradients are small it has virtually no effect. In our case, however, it does affect the outer edge of a wake which migrates through several passages, and interacts with the outer part of the boundary layer. Therefore, the twolayer formulation as proposed in (Eulitz 1996a) is adopted here for the treatment of the laminar sublayer. The convective term in (1) is discretized using second order accurate upwind differences instead of the

usual first-order accuracy so that with central differences for the diffusion term the model is integrated with second order accuracy.

Transition effects

Transition onset is determined from a correlation as proposed by Drela (1995) for his viscous/inviscid interaction code MISES. It reads

$$Re_{\theta,s} = 163 + 74.3 \left[0.55 \tanh\left(\frac{10}{H_{12}-1} - 5.5\right) + 1 \right] \times [0.94 \cdot n_{crit} + 1] \quad (3)$$

where $Re_{\theta,s}$ is the momentum Reynoldsnumber at transition start, H_{12} is the form parameter, and the n_{crit} is related to the freestream turbulence level Tu by Mack's relation

$$n_{crit} = -8.43 - 2.4 \ln(Tu) . \quad (4)$$

Correlation (3) is a modification of the well known Abu-Ghanam Shaw (AGS) criterium (1980). In effect, the form parameter H_{12} is used to replace the Thwaites' parameter λ of the original formulation which was found to be ill-posed when applied to Drela's viscous/inviscid interaction code. It is adopted here for the physical reasons given by Drela in that it is in better accordance with linear stability theory. By inspection of the Orr-Sommerfeld equation (see Mack 1984) one can see that the profile shape is of primary importance for the growth of initial disturbances in a laminar boundary layer (Tollmien-Schlichting waves). In non-equilibrium or separated flows this is better described by H_{12} than by λ .

For unsteady flow, the use of (3) which is based on steady-state experiments is surely debatable. It is nevertheless applied here and implemented in a Lagrangian fashion as described by Cho and Rodi (1993).

In order to account for the effect of varying freestream turbulence intensity induced by the migrating wakes of upstream blade rows, a transport equation for the turbulent kinetic energy is solved. Doing this, no attention is paid to the behavior in the laminar sublayer, since it is only used in (4).

Transition is now obtained as follows: In the laminar part of the boundary layer the transport model (1) is solved with zero production term which results in low values for the eddy viscosity (in the order of $1.e-3$). We have found that this laminar "zero-solution" does not impair the good numerical stability characteristics of (1). When (3) signals the start of transition, the production term is turned on and the eddy viscosity gradually increases.

VALIDATION OF COMPUTATIONAL METHOD

The computational method has been systematically validated for many types of flows starting from twodimensional inviscid steady and unsteady flow. The following test cases have been considered for the present problem:

- 1) Unsteady inviscid flat-plate cascade flow excited by external disturbances (Engel 1994, Eulitz 1996c)
- 2) Steady boundary layer transition on a flat plate.
- 3) Steady boundary layer transition in a turbine cascade. (Eulitz 1997)
- 4) Unsteady boundary layer transition in a turbine cascade subject to a wake perturbation by a moving bar (see Eulitz 1997).

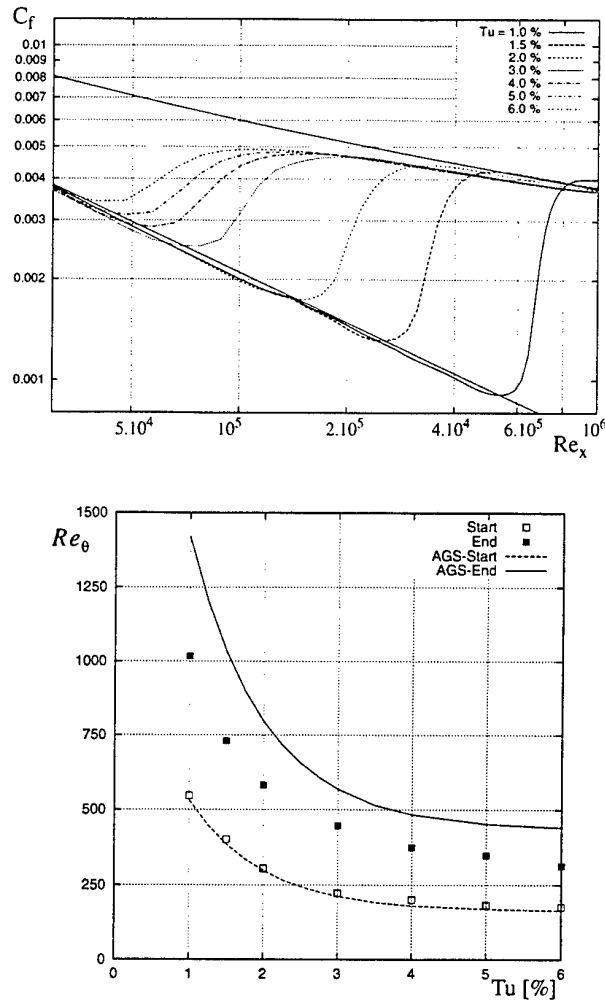


Figure 1: Transition in a steady boundary layer: (top) skin friction coefficient with laminar and turbulent correlation, (bottom) start and end of transition with AGS correlation.

The implementation of the turbulence model has been validated for many other steady and unsteady turbomachinery test cases (e.g. Eulitz 1996a, Weber 1996, Küsters 1997). The numerical studies indicated that the model is numerically robust and produces grid independent solutions. Due to the limited space, most of the above cases can not be reported here. Therefore, reference to the relevant publications is given above.

Figure 1 shows the skin friction distribution on a flat plate for various freestream turbulence levels. For orientation, the laminar and turbulent correlations (straight lines) have been included. Assuming that transition starts and ends where the minimum and maximum skin friction is obtained, respectively, one can compare the predicted transition lengths in terms of the momentum Reynolds number against the AGS correlation. As expected, transition occurs too rapid (the ratio of the momentum Reynolds numbers at the end and the beginning of transition is around 1.9, whereas the AGS-correlation requires 2.667). But it is by far not as rapid as reported for the $k-\epsilon$ model by Schmidt & Patankar (1991, part 1) and Fan & Lakshminarayana (1996, part 1).

RESULTS

In figure 4, Mach number contours of the steady-state solution are shown. The solution has become perfectly periodical in time after computation of approximately 16 periods (figure 6). The downstream influence of the wakes leads to a substantial variation of the passage averaged Mach number (between 4 and 10 per cent in the mixing planes and the exit plane) and the flow angle (not shown here). As a result, the blades experience large oscillations in skin friction (shown in figure 7 for the first two guide vanes). Comparatively small appears the variation in the entry plane which is solely a result of potential upstream influence. The instantaneous entropy contours shown in figure 5 provide an overview of the unsteady flow field. Figure 8 shows separation bubble induced transition on the pressure side of the second stator.

CONCLUDING REMARKS

A three-dimensional time-accurate Navier-Stokes solver has been applied to the study of wake interaction in a multistage low pressure turbine. The turbulence and transition modeling is based on the Spalart & Allmaras one-equation model and a transition correlation by Abu-Ghanam Shaw. The approach is numerically robust (apart from the need to determine integral boundary layer parameters) and found to be suitable for qualitative studies of unsteady transitional flow. For steady flows, the method produces results in good agreement with experimental data. For unsteady flows, however, the usefulness of the Abu-Ghanam Shaw correlation still needs to be clarified.

ACKNOWLEDGEMENTS

The work is part of a common research project with MTU Motoren- und Turbinen-Union München GmbH. The support by Dr. A. Fiala and the permission to publish the results are gratefully acknowledged.

REFERENCES

- Abu-Ghanam, B., and Shaw, R., 1980, "Natural Transition of Boundary Layers - The Effects of Turbulence, Pressure Gradient, and Flow History", *J. of Mech. Eng. Science*, Vol. 22, pp. 213-228.
- AGARD-Rep. No. 793, 1994, "Progress in Transition Research".
- Ameri A.A., Arnone A., 1994, "Transition Modeling Effects on Turbine Rotor Blade Heat Transfer Predictions", ASME paper 94-GT-22.
- Cho, N., Liu, X., Rodi, W., and Schönung, B., 1993, "Calculation of Wake-Induced Unsteady Flow in a Turbine Cascade", *ASME J. of Turbomachinery*, Vol. 115, pp 675-686.
- Drela M., 1995, "MISES Implementation of Modified Abu-Ghanam/Shaw Transition Criterion", MIT Aero-Astro.
- Denton, J. D., 1993, "Loss Mechanisms in Turbomachines", *ASME J. of Turbomachinery*, Vol. 115, pp. 621-656.
- Engel K., Eulitz F., Faden, M., and Pokorný, S., 1994, "Validation of Different TVD-Schemes for the Calculation of the Unsteady Turbomachinery Flow", 14. ICNMF, Bangalore, India.
- Engel, K., Eulitz, F., Faden, M., and Pokorný, S., 1994, "Numerical Investigation of the Rotor-Stator Interaction in a Transonic Compressor Stage", AIAA-94-2834.
- Eulitz F., Engel K., and Gebing, H., 1996a, "Application of a one-equation eddy-viscosity model to unsteady turbomachinery flow", *Proc. of 3rd Int. Symp. on Eng. Turbulence Modelling and Measurements*, ed. H.W. Rodi, Elsevier Science.
- Eulitz F., Engel K., and Gebing, H., 1996b, "Numerical Investigation of the Clocking Effects in a Multistage Turbine", ASME Paper No. 96-GT-26.
- Eulitz F., Engel K., and Pokorný S., 1996c, "Numerical Investigation of Inviscid and Viscous Interaction in a Transonic Compressor", in *Loss Mechanisms and Unsteady Flows in Turbomachines*, AGARD-CP 571, paper 38.
- Eulitz F., Engel K., 1997, "Numerical Investigation of Wake Interaction in a Low-Pressure Turbine", to be published as AIAA-paper 97-3027.
- Fan S., Lakshminarayana B., 1996, "Computation and Simulation of Wake-Generated Unsteady Pressure and Boundary Layers in Cascades: Part 1 and Part 2", *ASME J. of Turbomachinery*, Vol. 118, pp. 96-121.
- Greitzer, E.M., Wisler, D.C., and Adamczyk, J.J., 1994, "Unsteady Flow in Turbomachines: Where's the Beef?", AD-Vol. 40, *ASME CP Unsteady Flows in Aeropropulsion*.
- Giles, M.B., 1988, "Non-Reflecting Boundary Conditions for the Euler Equations", CFDL-TR-88-1.
- Mack L.M., "Boundary-Layer Linear Stability Theory" in *A Special Course on Stability and Transition of Laminar Flow*, AGARD-Rep. No. 709, part 3, 1984.
- Mayle, R.E., 1991, "The Role of Laminar-Turbulent Transition in Gas Turbine Engines", *ASME J. of Turbomachinery*, Vol. 113, pp. 509-537.
- Mellor G.L. and Herring H.J., "A Survey of Mean Turbulent Field Closure Models", *AIAA J.*, Vol. 11, pp. 590-599.
- Halstead D.E., Wisler D.C., Okiishi T.H., Walker G.J., Hodson H.P., Shin H.-W., 1997a, "Boundary Layer Development in Axial Compressors and Turbines: Part 1 of 4 - Composite Picture" and "Part 4 of 4 - Computations and Analyses", *ASME J. of Turbomachinery*, Vol. 119, pp. 114-127.
- Küsters B., Schreiber H.A., 1997, "Numerical Investigation of Compressor Cascade Flow with Strong Shock-Wave Boundary-Layer Interaction", to be published as AIAA-paper 97-2882.
- Menter F., 1996, "On the Connection between One- and Two-Equation Models of Turbulence", in *Engineering Turbulence Modelling and Measurements 3*, Editor H.W. Rodi, Elsevier, Amsterdam.
- Roe P., 1981, "Approximative Riemann Solvers, Parameter Vector and Difference Schemes", *Journal on Computational Physics*, 43, pp. 357-372.
- Schmidt R.C., Patankar S.V., 1991, "Simulating Boundary Layer Transition With Low-Reynoldsnumber k- ϵ Turbulence Models: Part 1 - An Evaluation of Prediction Characteristic" and "Part 2 - An Approach to Improving the Predictions", *ASME J. of Turbomachinery*, Vol. 113, pp. 10-26.
- Shur M., Strelets M., Travin A., Zaikov L., 1996, "Comparative Study of One- and Two-Equation Turbulence Models for Incompressible and Transonic Flows with Separation and Reattachment", in *Engineering Turbulence Modelling and Measurements 3*, Editor H.W. Rodi, Elsevier, Amsterdam.
- Spalart, P., and Allmaras, S., 1992, "A One-Equation Turbulence Model for Aerodynamic Flows", AIAA-92-0439.
- van Leer, B., 1979, "Towards the Ultimate Conservation Difference Scheme V, A Second-Order Sequel to Godunov's Method", *J. Comp. Phys.*, Vol. 32, pp. 101-136.
- Weber, A., 1996, "Validierung von drei Navier-Stokes-Codes an einem transsonischen Verdichtergitter unter rein zweidimensionalen Bedingungen", DLR-report, IB-325-09-96.
- Wilcox D.C., 1993, "Turbulence Modeling for CFD", DCW Industries, Inc..

FIGURES

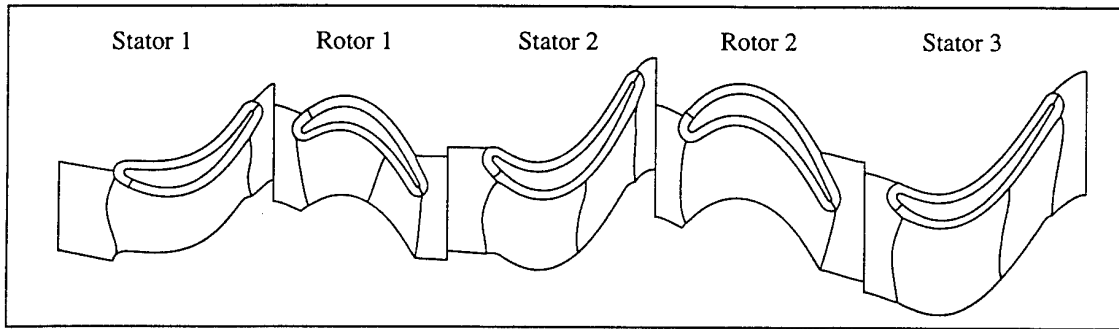


Figure 2. Investigated low pressure model turbine and used mesh topology (O/H-Blocks) along a streamtube near mid-span.

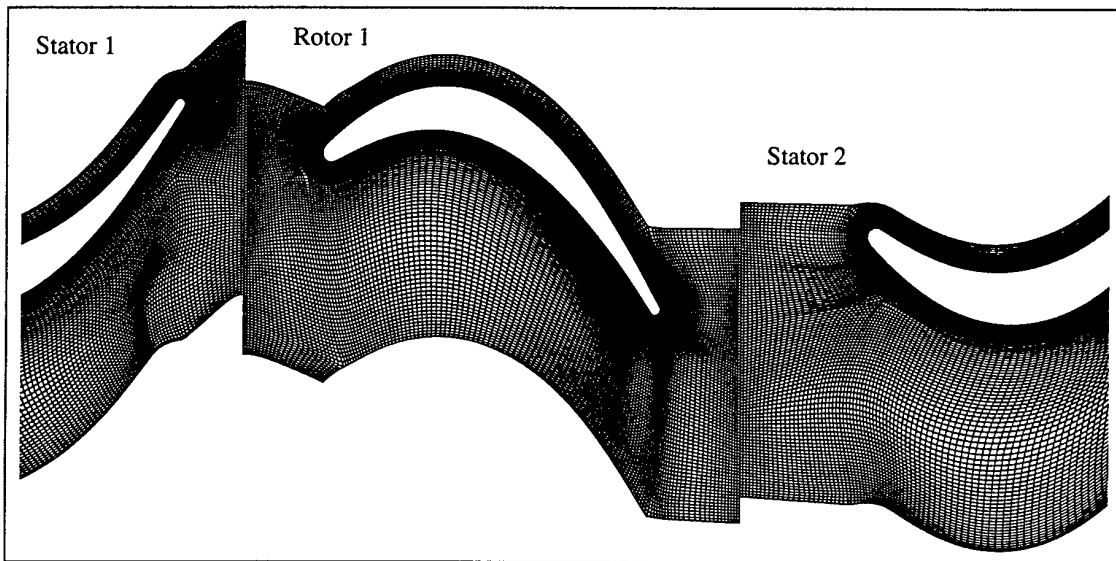


Figure 3. Detail of computational mesh of first rotor. In total 100,000 nodes are considered. The mesh cells at the mixing planes are equispaced. The grid is condensed near the blade surfaces to allow for the resolution of the laminar sublayer.

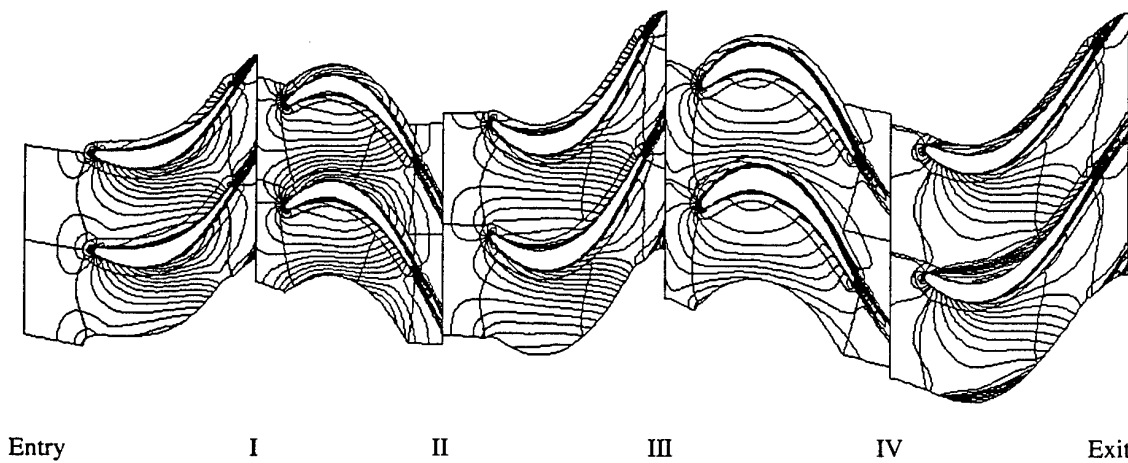
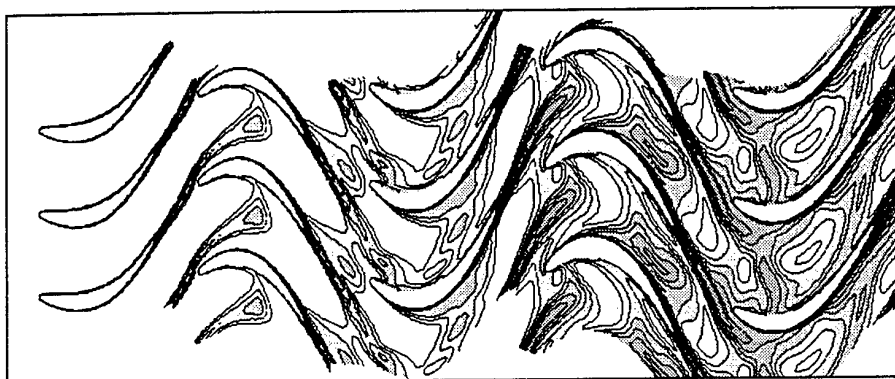


Figure 4. Mach number contours in the relative frame of reference as a result of a steady-state multistage calculation.

$t = 0$



$t = T/4$



$t = T/2$



$t = 3T/4$



Figure 5. Instantaneous entropy contours during a blade passing period T .

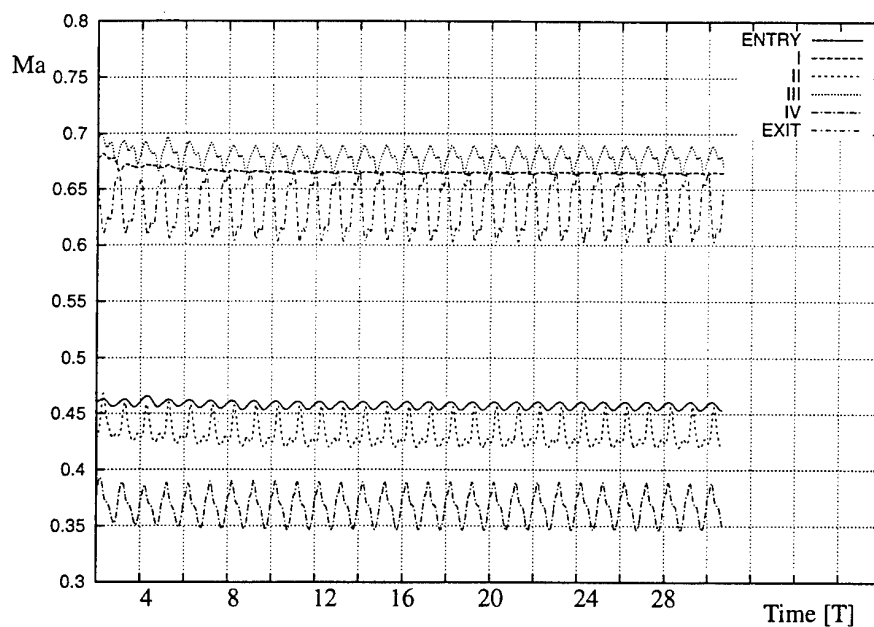


Figure 6. Evolution of the passage-averaged Machnumber at various downstream positions.

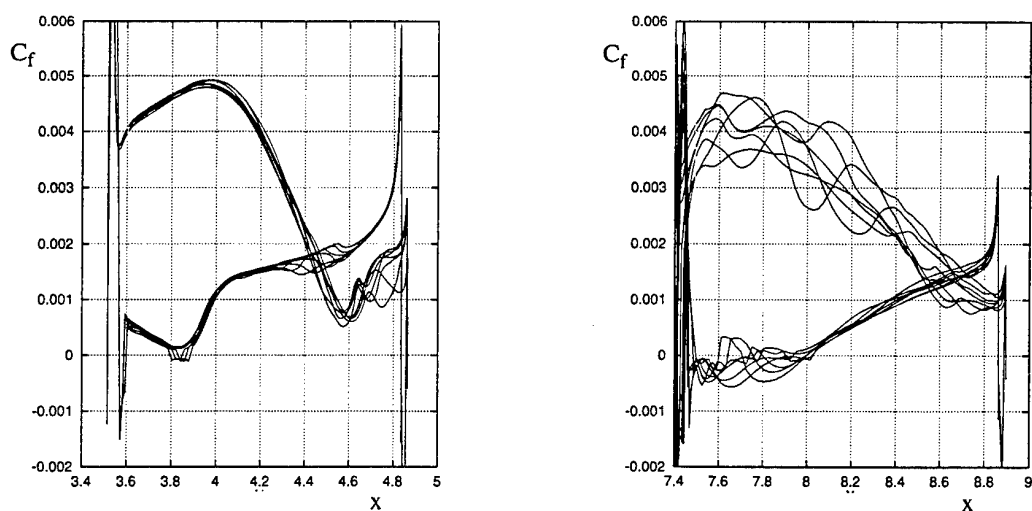


Figure 7. Evolution of the skin friction for the guide vanes 1 (left) and vane 2 (right) during a blade passing period T.

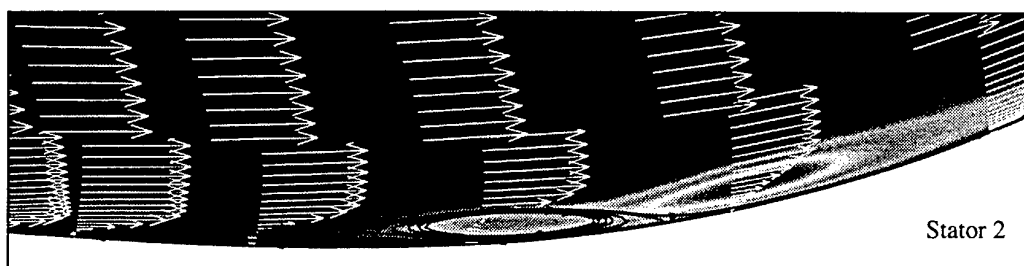


Figure 8. Eddy viscosity contours and every second velocity vector: Laminar separation and turbulent reattachment on the pressure side of stator 2.

STEAM TURBINE-ROTOR BLADE OSCILLATION

R. S. Amano, B. Lin

Mechanical Engineering Department
University of Wisconsin - Milwaukee
P.O. Box 784
Milwaukee, WI 53201
U.S.A.

See late papers

EFFECTS OF FIRST-ORDER TURBULENCE MODELS APPLIED TO FLOWS AROUND LIFTING AIRFOILS

S. Khris, J. Marcillat

Goupe Aérodynamique Numérique
Institut de Recherche sur les Phénomènes Hors Equilibre
Unité Mixte de Recherche N°6594
CNRS - Université de la Méditerranée et de Provence
1, rue Honnorat
13003 Marseille
France

ABSTRACT

A numerical study is conducted in order to evaluate the ability of different turbulence models, based on the eddy viscosity concept, to predict two air flows that are trailing edge breakdown and a transition bubble separation. The used models are deduced from the arrangement of Boussinesq linear and Speziale non-linear Reynolds stresses with standard $k - \epsilon$ and RNG $k - \epsilon$ models. The obtained results point out the mean flow prediction improvements, especially the intensity of the backflow, effected by taking in account the RNG $k - \epsilon$ model associated with the non-linear Reynolds stress formulation. On the other hand, the normal stress anisotropy level can not be accurately predicted by any used model.

INTRODUCTION

The option calling on the turbulence modelling based on the eddy-viscosity concept is without any doubt the only approach, among the current models, that can allow to solve the practical industrial problems involving complex geometries. The $k - \epsilon$ model is undoubtedly in the more general use among the proposed formulations; in conjunction with linear Boussinesq Reynolds stresses model, it is suitable to simple shear flows description. Nevertheless, the most industrial applications involve pressure gradients and strains excluding the ones appearing in the Boussinesq assumption. These strains are initiated by different physical phenomena such as streamlines curvature, separation, reattachment and recirculating flow zones of which turbulence structure and especially its anisotropy are dependent.

The standard approach ($k - \epsilon$, Boussinesq assumption) disadvantages are characterized by insensitiveness to above mentioned effects, of which making the model purely dissipative and ignoring rotation rate presence (see Speziale (1991) and Leschziner (1994)). In order to cope with these difficulties, while keeping the modelling order, two improving propositions have been developed. The first is concerned with Reynolds stresses expression through models establishment including a non-linear dependence with respect to deformation and/or vorticity invariants respectively for Speziale (1987) and Craft et al. (1993) anisotropic models. The model constants are fitted

by means of experimental results.

The second is based on the modelling of the kinetic energy dissipation rate transport equation. Firstly by implementation of an additional source term, allowing to cope with the purely dissipative nature of the standard model such as the Chen et al. (1987) model. Secondly, by making this equation coefficient C_{ϵ_2} dependent of anisotropy invariants (see Schiestel (1993)) enabling the modelling of the near wall anisotropy through the improvement of the Reynolds stresses redistribution process as explained by Leschziner (1995). Finally, from the RNG theory, based on an asymptotic development and having the particular characteristic that the dissipation complementary production contribution through mean field effect accounting, making in doubt the local isotropy assumption (referred to Yakhot et al. (1992)).

In order to estimate the different turbulence models behaviour, two external aerodynamic flow configuration types, involving different non-equilibrium phenomena have been chosen: 1) the turbulent flow around a NACA-4412 airfoil, placed at the 13.87° incidence in a 1.52×10^6 Reynolds number flow, corresponding to the airfoil stall situation, 2) the reduced Reynolds number ($1. \times 10^5$) flow around a NACA-0012 airfoil, characterized by a transition bubble.

TRANSPORT EQUATIONS - MODELLING

Reynolds equations closure, through the turbulent viscosity concept, needs the resolution of the following equations system that establishes the momentum and mass conservation with respect to the mean field and the kinetic energy and dissipation rate transport with respect to the turbulent field, which return as follows:

$$U_{i,t} + U_j U_{i,j} = -\frac{1}{\rho} P_{,i} + (\nu (U_{i,j} + U_{j,i}) - R_{ij})_{,j} \quad (1)$$

with $R_{ij} = \overline{u_i u_j}$ Reynolds stress

$$U_{i,i} = 0 \quad (2)$$

$$k_{i,t} + U_j k_{i,j} = -R_{ij} U_{i,j} + \left(\frac{\nu_t}{\sigma_k} k_{,i} \right)_{,i} - \epsilon \quad (3)$$

$$\epsilon_{i,t} + U_j \epsilon_{i,j} = -C_{\epsilon_1} \frac{\epsilon}{k} R_{ij} U_{i,j} - C_{\epsilon_2} \frac{\epsilon^2}{k} + \left(\frac{\nu_t}{\sigma_\epsilon} \epsilon_{,i} \right)_{,i} \quad (4)$$

where U_i is the velocity component in the direction x_i , P is the pressure, ρ is the specific mass, ν is the molecular viscosity, k is the turbulence kinetic energy and ϵ its dissipation rate. The turbulent viscosity is expressed by:

$$\nu_t = C_\mu \frac{k^2}{\epsilon} \quad (5)$$

The different numerical values of the coefficients which involve in the turbulent field expressions are the result of experiments data in association with numerical optimisation procedure. According to Launder (1975), the following values are proposed:

$$C_\mu = 0.09, \sigma_k = 1.00, \sigma_\epsilon = 1.30, C_{\epsilon_1} = 1.44, C_{\epsilon_2} = 1.92.$$

The $k-\epsilon$ model defined by the equations (??) and (??) with the previous coefficients values, is in its standard form.

Reynolds stresses model

The turbulent constraints, that become apparent as a consequence of the Navier-Stokes equations non-linearity, can be linked to the mean field by means of these models through the turbulent viscosity concept.

Boussinesq linear model.

The original idea is based on analogy with the viscous stresses expression involving in laminar flows:

$$R_{ij} = \frac{2}{3} k \delta_{ij} - 2 \nu_t S_{ij} \quad (6)$$

where $S_{ij} = \frac{1}{2} (U_{i,j} + U_{j,i})$ is the mean field strain rate.

Speziale non-linear model.

This model derives from the Reynolds stresses generalized form established by Lumley (1970), by taking into account the invariance through a coordinate framework change in the limit of a two-dimensional turbulence. It represents a simplified version of a more complex model proposed by Yoshizawa (1984) and can be expressed as follows:

$$\begin{aligned} R_{ij} = & \frac{2}{3} k \delta_{ij} - 2 \nu_t S_{ij} \\ & - 4 C_D C_\mu \frac{k}{\epsilon} \nu_t \left(S_{ik} S_{kj} - \frac{S_{mn} S_{mn}}{3} \delta_{ij} \right) \\ & - 4 C_E C_\mu \frac{k}{\epsilon} \nu_t \left(\dot{S}_{ij} - \frac{\dot{S}_{mn}}{3} \delta_{ij} \right) \end{aligned} \quad (7)$$

where $\dot{S}_{ij} = -U_{i,k} S_{kj} - U_{j,k} S_{ki}$ is the Olroyd derivative of the mean field strain rate for which the convective derivative has been neglected. In comparison with the linear model, the Speziale formulation introduces an additional coefficient $C_D = C_E = 1.68$ (see Speziale (1987)). This value has been appraised from turbulent flow between two infinite plates experiments.

$k-\epsilon$ models

Standard model.

In the standard model, described by equations (??) and (??), the viscous diffusion term, concerned with each equation, has been neglected with respect to turbulent diffusion term because of the high Reynolds number value assumption. This turbulent diffusion term is modelled by means of a gradient transport hypothesis for each of the two equations.

RNG model.

The RNG formalism, as proposed by Yakhot et al. (1992), introduces an additional production contribution $(-\pi)$ in the dissipation rate equation ??:

$$\pi = C_\mu \eta^3 \frac{(1 - \eta/\eta_0) \epsilon^2}{(1 + \beta \eta^3) k} = B \frac{\epsilon^2}{k} \quad (8)$$

where $\eta = \frac{k}{\epsilon} \sqrt{2 S_{ij} S_{ij}}$ is the parameter which characterizes the mean field shear. The homogeneous and isotropic turbulence enables the fixed point $\eta_0 = \sqrt{\frac{C_{\epsilon_2} - 1}{C_\mu (C_{\epsilon_1} - 1)}}$ determination. The coefficient C_{ϵ_1} can be rewritten as follows: $C_{\epsilon_1}^* = C_{\epsilon_1} - \eta \frac{(1 - \eta/\eta_0)}{1 + \beta \eta^3}$. With the boundary layer equilibrium assumption where $\eta = \frac{1}{\sqrt{C_\mu}}$, a relation between the Von Karman constant κ and the coefficient β can be deduced and written as follows: $\kappa = (\sigma_\epsilon (C_{\epsilon_1} - C_{\epsilon_1}^*) \sqrt{C_\mu})^{1/2}$. The numerical coefficients values are determined by an explicit way as follow:

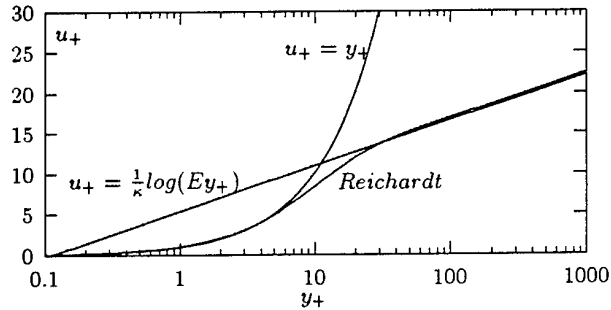
$$C_\mu = 0.085, \quad C_{\epsilon_1} = 1.42, \quad C_{\epsilon_2} = 1.68, \quad \sigma_k = 0.718, \quad \sigma_\epsilon = 0.718, \quad \kappa = 0.387, \quad \eta_0 = 4.38, \quad \beta = 0.012.$$

Near wall region

The wall effect is taken into account by the use of universal velocity profile expressed in the semi-empiric form following the Reichardt development (see Haroutunian et al. (1992)). This form enables to account for the three sub-layers (laminar, buffer and turbulent) and ensures the profile continuity, as it is shown in the figure below. Its expression is written as:

$$\begin{aligned} u_+ = & \frac{1}{\kappa} \log(1 + \kappa y_+) \\ & + 7.8 \left(1 - \exp\left(\frac{-y_+}{11}\right) - \frac{y_+}{11} \exp(-0.33 y_+) \right) \end{aligned} \quad (9)$$

where $u_+ = U/u_\tau$, $y_+ = y u_\tau / \nu$ and u_τ is the skin friction velocity. The coefficients κ and E take respectively the values 0.41 and 9.



Concerning the turbulent viscosity in the near wall region, it is appraised from the algebraic Van Driest mixing length model:

$$l_m = \kappa y (1 - \exp(-y_+/A)) \quad (10)$$

where the coefficient A takes the value 26.

NUMERICAL APPROACH

The different transport equations discretisation is carried out by means of the FIDAP numerical code, based on the finite elements method. The large computation domains areas as well as strong gradients, arising at the neighboring of walls and in the near wake, involve a very

high number of discretisation nodes. To cope with this difficulty, a segregated algorithm has been used, in connection with iterative solvers, allowing to reduce memory size and computer time. As a continuation of Haroutounian et al. (1992) work, a preliminary study has been carried out, precisely about solvers and algorithm choice. As a result, it appears that the more convenient approach is the consistent variant of the SIMPLER algorithm, with an implicit relaxation of the different variables, associated with the iterative solvers "CR" and "CGS" (arising from conjugated gradients method), respectively for Poisson equation and advection-diffusion equations.

The used meshes are based on unstructured type, which has the particularity, especially in external flow configuration, to be able to focus a high cells density within strong gradients areas, whereas this condition is less and less required in coming up to the external boundaries.

Boundary conditions

Provided that the variable are dimensionless, the boundary conditions prescribed along the inlet section are Dirichlet's ones and expressed as follows:

$$U = \cos(\alpha), \quad V = \sin(\alpha), \quad k = 1.5 (IU_\infty)^2, \quad \varepsilon = \frac{k^{3/2}}{0.1\Delta},$$

where α is the profile angle of attack, I the upstream turbulence intensity, U_∞ the upstream flow velocity and Δ the turbulent characteristic length scale. Free conditions are applied at the outlet boundary, such as:

$$-P + \frac{2\mu^*}{Re} U_{,x} = 0, \quad \frac{\mu^*}{Re} (U_{,y} + V_{,x}) = 0, \quad k_{,x} = 0, \quad \varepsilon_{,x} = 0,$$

where $\mu^* = 1 + \mu_t/\mu_0$ and Re is the Reynolds number. Finally, adherence and equilibrium conditions are applied at the foil wall and at first cell boundary respectively for velocities and turbulent variables:

$$U = 0, \quad V = 0, \quad k_{,y_n} = 0, \quad \varepsilon = \frac{(C_\mu^{1/2} k_1)^{3/2}}{\kappa y_n},$$

where, y_n is the normal to the wall ordinate and k_1 the kinetic energy value at the first cell boundary.

RESULTS AND DISCUSSION

The four model combinations used involve linear and non-linear Speziale Reynolds stress forms and standard and RNG $k - \varepsilon$ models. They are identified as follow:

STD-B: standard $k - \varepsilon$ associated to Boussinesq assumption,
RNG-B: RNG $k - \varepsilon$ associated to Boussinesq assumption,
STD-S: standard $k - \varepsilon$ associated to Speziale non-linear model,
RNG-S: RNG $k - \varepsilon$ associated Speziale non-linear model.

NACA-4412 profile

This flow configuration has been subject to experiments by Coles et al. (1979) by means of flying hot wire anemometry technique and constitutes a test case at the 1968 Stanford Conference. The foil is placed at the angle of attack of 13.87° in a wind tunnel test section regulated in order to obtain a two-dimensional upstream flow characterized by the Reynolds number value $1.52e + 06$ and a turbulent intensity of 1.5 per cent. The experimental results are delivered in a coordinate framework based on the foil chord, as well around the profile as in the wake, and its origin is located at the leading edge. In order to consider faithfully experience conditions and particularly blockage effect, the wind tunnel walls have been taken in account during computations. The generated mesh for this flow configuration

is shown in figure ?? : the nodes number is about $5.e + 04$ and the first cell thickness at the wall is equal to $1.e - 03$ in term of profile chord length. The stall occurring in this flow type is a direct consequence of a trailing edge separation of the boundary layer developed along profile upper face.

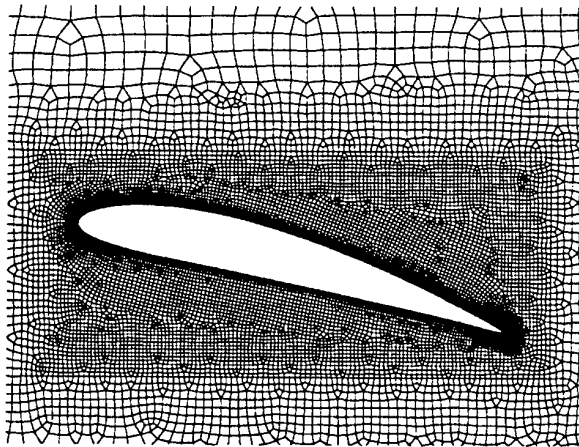


Figure 1: Unstructured mesh around the foil

The experimental suction side pressure distribution data (Fig. ??) points out a very low pressure zone close to the leading edge, followed by a recompression along about $0.8 C$ and finally, a constant pressure zone, spreading up to the trailing edge, highlighting boundary layer separation.

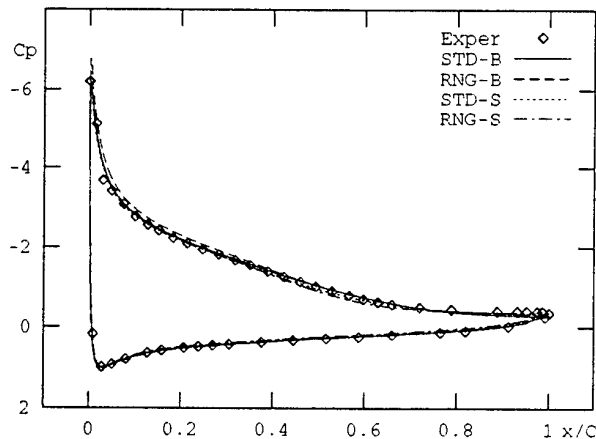


Figure 2: Pressure coefficient distributions

The adverse pressure gradient effect generates an important boundary layer thickening in the streamwise direction and, downstream of separation point, a recirculation region near the trailing edge, as it is shown by the streamline plot in figure ??.



Figure 3: Streamline contour - RNG-S model

The skin friction distribution reveals this separation and, furthermore, enables the separation point localisation. As showed in figure ?? this one is situated at the abscissa

$x/C = 0.7$ when the *RNG-S* form is used, which seems to be premature as will be shown latter with the streamwise velocity profiles.

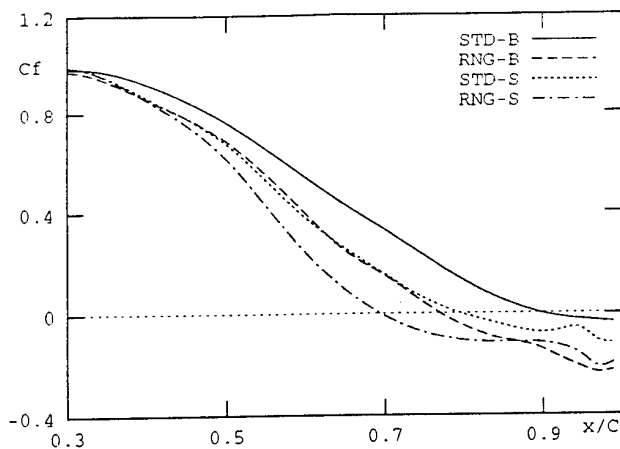


Figure 4: Skin friction coefficient distributions ($1.e+03$)

On the other hand, this point is moved away with the STD-B model ($x/C = 0.9$) making the recirculation zone less important. This recirculation zone extend upstream when the Speziale invariants (STD-S) are used and more with the RNG-B model. A contra-rotary secondary eddy is detected near the trailing edge with the Speziale Reynolds stresses ($0.95 \leq x/C \leq 1$). Its size is less important in the case of the STD-S and less more with the RNG-B model.

A comparison set of the streamwise velocity component and the three Reynolds stress tensor components has been carried out at three longitudinal locations: just upstream of the separation point ($x/C = 0.731$), right in the separation zone ($x/C = 0.997$) and in the near wake region ($x/C = 1.063$). At the first location ($x/C = 0.731$) none of the models returns an entirely satisfactory representation of streamwise velocity profile, as it is shown in figure ???. The model STD-B predicts an attached boundary layer characterized by a velocity profile in good agreement with experiments in the region very close to the wall. Indeed, up to a distance about the boundary layer thickness tenth, this model returns a noticeably velocity defect, especially in the middle region. The π parameter contribution in the dissipation rate equation (RNG-B model), improves the streamwise velocity profile within upper boundary layer part ($y/C \geq 0.095$) in comparison to the STD-B model. Nevertheless, the inner part prediction by the RNG-B variant is less satisfactory, insofar as the computation underestimates experimental profile more than STD-B one. This behaviour is due, probably, to the shear parameter evolution η through the boundary layer. As a matter of fact, if $\eta \leq \eta_0$, the coefficient $C_{\epsilon_2}^* = C_{\epsilon_2} + B$ (equation ??), which arises by factorizing the ϵ^2/k term in the dissipation rate equation, is larger than 1.68, and tends to approach and even to exceed the 1.92 value suggested in the standard model. In that last case, the higher dissipation destruction causes an evident dissipation decreasing and generally a kinetic energy increasing, but the present computations lead, at this location, to a slight kinetic energy reduction. These mechanisms involve a turbulent viscosity increasing, according to its definition ??, that can provide the explanation of inertia gain within this boundary layer part. On the other hand, the reciprocal effect occurs near the wall, with a velocity defect as a consequence. Through their gradients in momentum diffusion process, the Reynolds stresses effect on velocity profiles is found

to be noticeable. The use of the Speziale deformation invariants formulation with the standard turbulent transport equations, increases the velocity defect along about 90 per cent boundary layer thickness. This behaviour is notably generated by the shear stress evolution (Fig. ??), which on the one hand under-estimates widely experimental values and on the other presents a maximum value more further from the wall with respect to STD-B and RNG-B models. This maximum location is corroborated by the rising displacement of the velocity profile inflexion point, which seems located very close to the shear and R_{11} normal stress maximum point. This model (STD-S) allows nevertheless to correct the stresses anisotropy, especially with regard to R_{11} intensity, which is not the case when the RNG-B model is used, for which any relevant difference was observed as compared with STD-B model. The combined RNG-S form manifests itself through a backflow beginning near the wall, that seems to indicate an advanced boundary layer separation. Corresponding velocity profile is characterized by a combination of aforementioned effects with regard to RNG-B and STD-B forms. Indeed, the obtained profile shape is similar to that obtained by RNG-B use, with a defect enlarging such as it was generated by STD-B form use. The obtained Reynolds stresses are found to be quite similar to the ones resulting from STD-B form use.

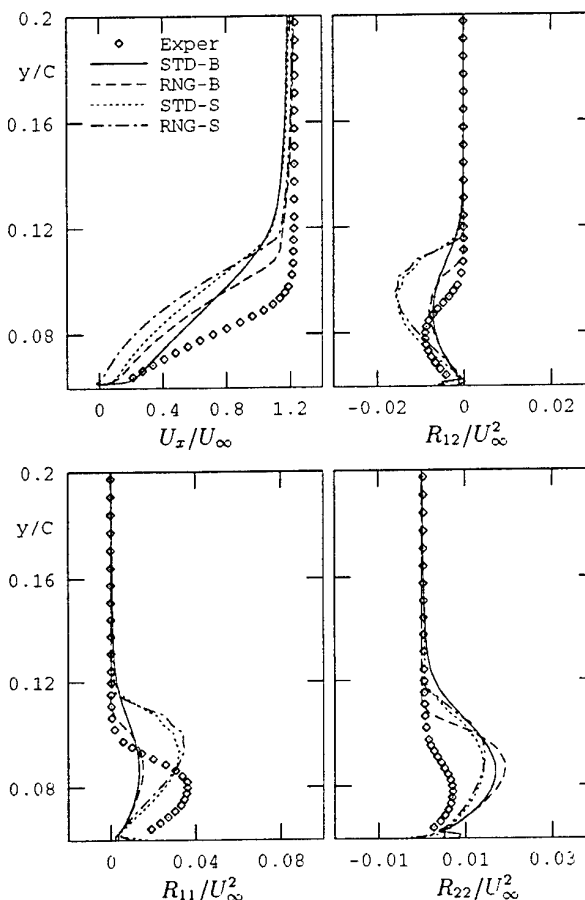


Figure 5: Streamwise velocity and Reynolds stresses at $x/C=0.731$.

Within the recirculating region ($x/C = 0.997$) all versions return the same velocity profiles general trend (Fig. ??). A weakness arising from the STD-B model is that the recirculating flow near the wall is under-estimated. This behaviour seems to result from an important diffusion at this location, providing the explanation of the low shear

stress level. The recirculating flow intensity is higher when the RNG model is connected with Speziale stresses formulation and is found to be in very good agreement with experimental data. Nevertheless, significant velocity defects are observed within shear layer, probably generated on the one hand by the low obtained anisotropy level although Speziale invariants enable to rectify stresses, especially R_{11} component and on the other hand by the shear stress maximum change of location farther from the wall.

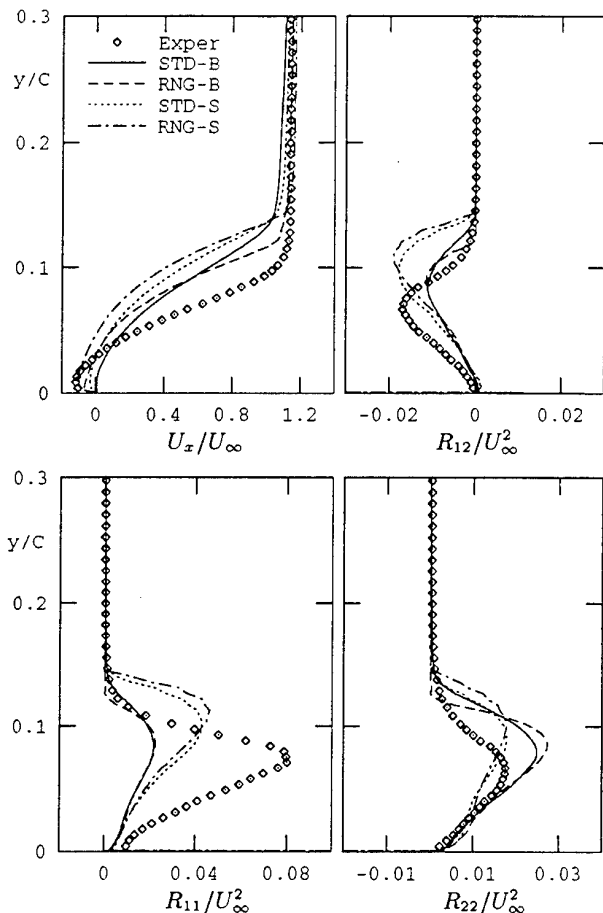


Figure 6: Streamwise velocity and Reynolds stresses at $x/C=0.997$.

Finally, at the last location ($x/C = 1.063$), velocity defect is always present over the greater part of the shear layer previously developed over the foil upper wall (Fig. ??) whatever the model may be used. Velocity profiles highlight an under-estimated minimum value, slightly set to the foil lower side when the RNG form is used, whereas the opposite behaviour is observed with standard approach. This result points out a poor lower side shear layer representation when the RNG model is used and is confirmed by the under-estimation of shear stresses and stress anisotropy within the lower shear layer.

NACA-0012 profile

The low Reynolds number flows around such airfoils are particularly characterized by a separation bubble appearance from the profile upper side, even for small incidence values. The bubble size and location are strongly dependent on angle of attack, Reynolds number and turbulence intensity. Such bubble generates a laminar-turbulent transition process, of which the origin point corresponds to the recirculating flow core location. The bubble is made

up first of a part of stagnant fluid, just downstream of the separation point, and then of a recirculating fluid vortex, of which the boundary determines the size.

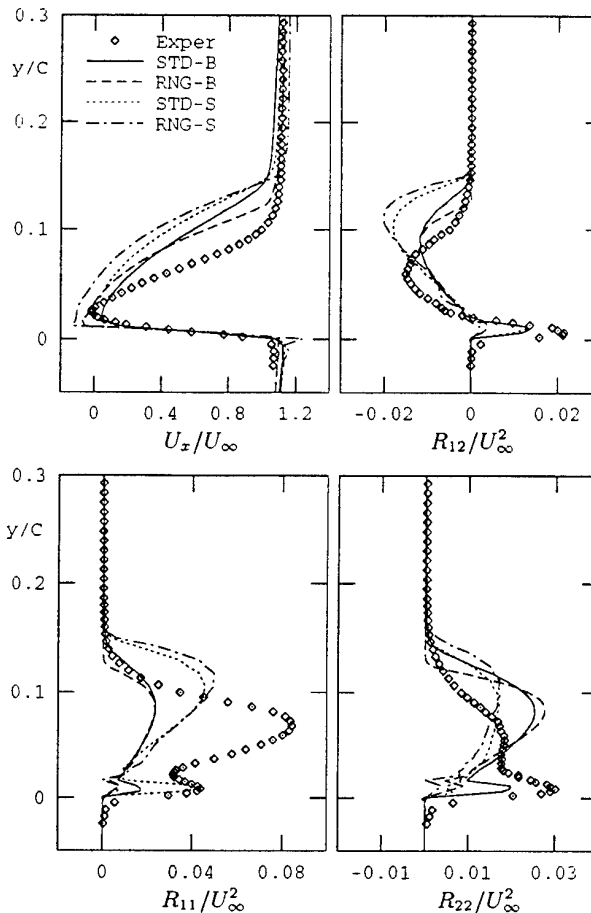


Figure 7: Streamwise velocity and Reynolds stresses at $x/C=1.063$.

The shear layer flowing over the bubble, is apt either to reattach itself at the wall and then develop as turbulent boundary layer or, if the profile is in a stalling situation, to break down and to generate, probably, a vortex sheet in the downstream direction. With the object to assess the turbulence modelling effect on such a phenomenon, the four approaches described before have been used. The above models and variants are applied to the flow around a NACA-0012 foil, placed at the angle of attack value 8° in an infinite flow characterized by a Reynolds number value of $1.e + 05$ and a turbulence intensity of 1 per cent: these conditions correspond to the experimental works of Decaix (1992).

The streamwise pressure coefficient distribution is shown in figure ?? in order to characterize this bubble. Its occurring is shown up by a constant pressure zone ($0.09 \leq x/C \leq 0.2$), and confirmed by skin friction coefficient distribution (Fig. ??) from which the bubble size and location can be determined. Pressure distribution well highlights the incapacity of classical STD-B model for predicting this bubble, since pressure distribution shows a continuously increasing trend with streamwise direction, and the skin friction evolution indicate that the boundary layer is attached to the wall. The RNG-B model also can not predict the bubble presence. In comparison to the STD-B model, small pressure and skin friction distributions modifications are obtained. On the other hand, the stresses anisotropy (STD-S) enables bubble presence detection. In fact, the

skin friction distribution shows the boundary layer separation and reattachment, as well as the pressure evolution predicts a plateau area which is placed between the separation and reattachment points.

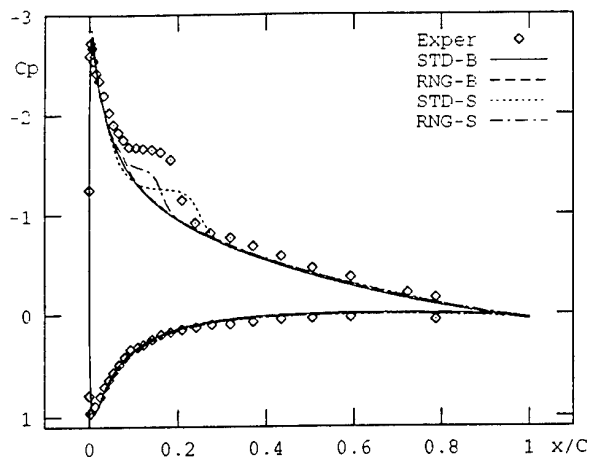


Figure 8: Pressure coefficient distributions

Nevertheless, the bubble intensity is under-estimated and its position is translated ($0.1 C$) towards the trailing-edge. Instead, the RNG form used in connection with the Speziale invariants (RNG-S) allows to improve the bubble core position prediction but its intensity as well as its length decreased comparing to previous model.

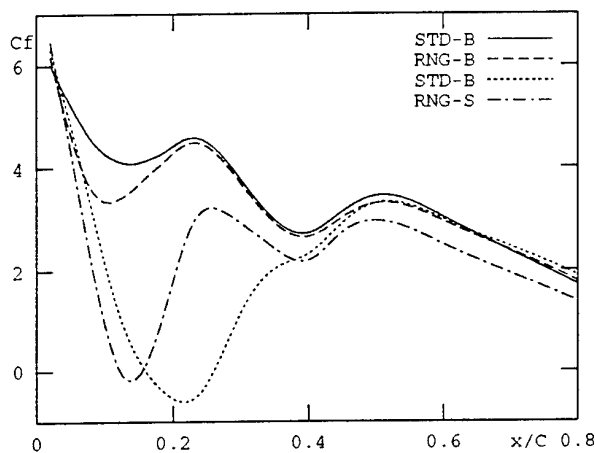


Figure 9: Skin friction coefficient distributions ($1.e+03$)

CONCLUSIONS

In order to provide needs of turbulent flow accurate predictions, the present study has in aim to evaluate several turbulence models performances based on the eddy-viscosity approach and applied to non-equilibrium phenomena. These models combine the standard and RNG $k - \epsilon$ transport equations with linear and Speziale non-linear Reynolds stresses.

Generally every model shows common discrepancies with experimental data consisting in velocity defect and maximum shear and streamwise normal stresses value position farther from the wall.

The standard $k - \epsilon$ model and Boussinesq assumption association is unable to reproduce non-equilibrium phenom-

ena such as trailing-edge breakdown or separation bubble. The RNG linear form does not change fundamentally previous Reynolds stresses and especially its anisotropy; nevertheless differences between these models appear in improving of the primary eddy backflow intensity. Speziale non-linear Reynolds stress contribution emphasizes secondary eddy presence coming closer to experimental one. The same trend becomes apparent about normal stress anisotropy and shear stress. The RNG formalism connected with Speziale Reynolds stresses formulation is characterized by streamwise velocity component prediction improvement within the very near wall region and by stresses anisotropy correction, too. Nevertheless the unsatisfactory anisotropy level prediction affects this model because of its strong interaction with the curvature deformation and its influence on shear stress.

Finally it is impossible to confirm the absolute superiority of a model between the tested ones.

REFERENCES

- Y. S. Chen and S. W. Kim. Computation of turbulent flows using an extended ($k - \epsilon$) turbulence closure model. CR 179204, NASA, 1987.
- D. Coles and A. J. Wadcock. Flying-hot-wire study of flow past an naca 4412 airfoil at maximum lift. *AIAA*, 17(4), 1979.
- A. F. Decaix. *Etude numérique et expérimentale de l'écoulement instationnaire autour de profils portant*. PhD thesis, Institut de Mécanique des Fluides de Marseille, 1992.
- V. Haroutunian and M. Engelman. On modelling wall-bound turbulent flows using specialized near wall finite elements and the standard $k - \epsilon$ turbulence model. *Symposium on advances in numerical calculation of turbulent flows*, Portland, Oregon, June 24-26, 1991.
- M. A. Leschziner. Refined turbulence modelling for engineering flows. *Computational Fluid Dynamics*, 1994.
- M. A. Leschziner. Computation of aerodynamic flows with turbulence-transport models based on second-moment closure. *Computers & Fluids*, 24(4):377-392, 1995.
- R. Schiestel. Modélisation et simulation des écoulements turbulents. *Editions Hermes*, 1993.
- C. G. Speziale. On nonlinear ($k - l$) and ($k - \epsilon$) models of turbulence. *J. Fluid Mech.*, 178:459-475, 1987.
- C. G. Speziale. Analytical methods for the development of Reynolds-stress closures in turbulence. *Annual Review of Fluid Mechanics*, 23:107-157, 1991.
- V. Yakhot, S. A. Orszag, S. Thangam, T. B. Gatski and C. G. Speziale. Development of turbulence models for shear flows by a double expansion technique. *Physics of Fluids*, A (4), 1992.
- J. Craft, B. E. Launder and K. Suga. Extending the applicability of eddy-viscosity models through the use of deformation invariants and non-linear elements. *5th Conference on refined flow modelling and turbulence measurements*, 1993.

INVESTIGATION OF THE TURBULENT WIND ON THE AERODYNAMIC CHARACTERISTICS OF WIND TURBINES AND SAILS

C. Bréard , S.G. Voutsinas

Fluids Section, Department of Mechanical Engineering
National Technical University of Athens
P.O. Box 64070
Athens, 15710
Greece

F. Hauville, S. Huberson

Laboratoire de Mécanique
University of Le Havre
BP 540
Le Havre 76058
France

INTRODUCTION

We are interested in the study of turbulent effects on lifting surfaces, by numerical simulations. The fluid modelling is based on the vortex element method (VEM). These methods are suitable for external flows when the vorticity support is bounded. It is the case for lifting surfaces, where the turbulent shear flow along the surface and the wake formed by the vortex shedded along the trailing edge are represented by dipole surface distribution and vortex sheets, respectively. During the last ten years, this methodology was successfully validated and was able to capture dynamic wake effects in details. (See Voutsinas et al. 1994).

However, in all these works, it was only dedicated to stationary inflow conditions. In order to extend the range of applicability of this method, we will be considered in this paper stochastic inflow conditions.

The coupling of this turbulent inflow and the vortex particle method was straightforward. However, some assumptions has been required for the modelization of the convection of the velocity fluctuations in the wake, and for the non-linear deformation term of the Helmholtz's equation. Moreover, due to the Helmholtz's decomposition theorem, the turbulent inflow which is rotational, was assumed small enough compared to the rotational part of the flow induced by the vortex shedded into the wake from the lifting body.

Finally, the interaction of the small scales of the turbulence was introduced by modelling the subgrid scales stress.

have sometimes been considered. Except when writing this Kutta condition, the flow has been assumed inviscid. The lifting problem is solved by means of a boundary integral method : the surface of the body is represented using panels of rectangular shape which are used to satisfy potential the slip conditions. Specifically, a dipole strength was associated with each panel, and the strength of the dipole was adjusted by imposing that the normal velocity component at the surface of the body must vanish at control points (c.f. Fig. 1 ; Eqs. 4, 5). The wake has been modelized by means of the particle method itself (Rehbach, 1977). In this method, the vorticity distribution within the wake is described by means of particles carrying vortex. The motion of particles is computed in a Lagrangian framework. The vorticity on each particle has to satisfy the Helmholtz equation.

According to the Helmholtz's decomposition theorem, the velocity field \underline{U} takes the form :

$$\underline{U} = \underline{U}_{\infty} + \underline{U}_{\omega} + \underline{U}_{\phi} + \underline{U}_{ext} \quad (1)$$

where \underline{U}_{∞} represents the inflow velocity, \underline{U}_{ϕ} which is derived from a scalar potential ϕ , and \underline{U}_{ω} , which is derived from a potential vector $\underline{\psi}$, representing respectively the body's influence and the wake's influence and \underline{U}_{ext} is the velocity field induced for example by an another lifting body with its wake.

The Euler equations in velocity-vorticity formulation for particle i are expressed in Lagrangian coordinates. \underline{X}_i denotes the position of the particle and Ω_i the "weight" of

METHODOLOGY

Boundary and Vortex Element Methods

The basic method is made of two parts : a lifting body problem and a wake problem. These two problems are coupled by means of a kind of Kutta condition which has been derived from the kinematic and dynamic conditions along the separation lines. Usually, these lines reduced to the trailing edges although more complicated situations

the particle. The evolution equation for $\underline{X}_i, \underline{\Omega}_i$ are :

$$\begin{cases} \frac{D\underline{X}_i}{Dt} = (\underline{U}_\omega + \underline{U}_\phi + \underline{U}_\infty + \underline{U}_{ext})(\underline{X}_i, t) \\ \frac{D\underline{\Omega}_i}{Dt} = -\frac{1}{4\pi} \sum_{\substack{p=1 \\ p \neq i}}^{N_j + N_p(t)} \dots \\ \left(\frac{3}{|\underline{X}_p - \underline{X}_i|^5} (\underline{X}_p - \underline{X}_i)(\underline{\Omega}_i \cdot (\underline{\Omega}_p \wedge (\underline{X}_p - \underline{X}_i))) \right. \\ \left. + \frac{1}{|\underline{X}_p - \underline{X}_i|^3} (\underline{\Omega}_p \wedge \underline{\Omega}_i) \right) \\ + (\underline{\Omega}_i \cdot \nabla)(\underline{U}_\infty + \underline{U}_{ext})(\underline{X}_i, t) + \nu \Delta \underline{\Omega}_i \end{cases} \quad (2)$$

N_j is the number of bound vortex particles equivalent to the dipole (Hess, 1973), $N_p(t)$ is the number of free vortex particles and N_f the number of panels :

$$\underline{U}_\omega(\underline{X}_i, t) = -\frac{1}{4\pi} \sum_{\substack{p=1 \\ p \neq i}}^{N_p(t)} \frac{\underline{\Omega}_p(t) \wedge (\underline{X}_p - \underline{X}_i)}{|\underline{X}_p - \underline{X}_i|^3} \quad (3)$$

$$\underline{U}_\phi(\underline{X}_i, t) = -\frac{1}{4\pi} \sum_{\substack{p=1 \\ p \neq i}}^{N_j} \mu_p(t) \sum_{n=1}^4 \underline{U}_{ip}^n \quad (c.f. \text{ fig. 1}) \quad (4)$$

$$\underline{U}_{ip}^n = \frac{\underline{r}_{ip}^{n1} \wedge \underline{r}_{ip}^{n2}}{|\underline{r}_{ip}^{n1} \wedge \underline{r}_{ip}^{n2}|^2} [|\underline{r}_{ip}^{n1}| + |\underline{r}_{ip}^{n2}|] \left[1 - \frac{\underline{r}_{ip}^{n1} \cdot \underline{r}_{ip}^{n2}}{|\underline{r}_{ip}^{n1}| |\underline{r}_{ip}^{n2}|} \right] \quad (5)$$

The dipole distribution μ on the surface of the body, which is used to compute \underline{U}_ϕ , has been set in order to satisfy the non-penetration condition. It is obtained by solving the full matrix linear system :

$$[\mathcal{A}][\mu] = [S] \quad (6)$$

Where μ is the unknown vector of the system, S the known vector of boundary conditions $(-\underline{U}_\infty + \underline{U}_\omega + \underline{U}_{ext}) \cdot \underline{n}$, and \mathcal{A} a square matrix called "influence matrix". \mathcal{A} depends only on the body geometry. The a_{ij} term of this matrix represents the influence of the unknown μ_j on the boundary condition term S_i . It is obtained by computing the normal velocity induced by a unit of dipole strength μ_j at the control point of panel i :

$$a_{ij} = \frac{\underline{n}_i}{4\pi} \cdot \sum_{n=1}^4 \underline{U}_{ij}^n \quad c.f. (5) \quad (7)$$

The singular behaviour of these equations when \underline{X}_p tends to \underline{X}_i leads to the introduction of a regularisation function ξ_δ which tends to a Dirac measure ξ when $\delta \rightarrow 0$. Thus have replaced the singular kernel (c.f. 5) by the convolution product of this kernel by ξ_δ where :

$$\xi(r) = \frac{3}{4\pi} \frac{1}{(1+r^6)^{\frac{3}{2}}} \quad \text{et} \quad f(r) = \frac{r^3}{(1+r^6)^{\frac{1}{2}}}$$

We set for the desingularized Biot-Savart law :

$$\begin{aligned} \underline{U}_\omega(\underline{X}_i, t) &= -\frac{1}{4\pi} \sum_{\substack{p=1 \\ p \neq i}}^{N_p(t)} f\left(\frac{|\underline{X}_p - \underline{X}_i|}{\delta_i}\right) \frac{\underline{\Omega}_p(t) \wedge (\underline{X}_p - \underline{X}_i)}{|\underline{X}_p - \underline{X}_i|^3} \\ &= -\frac{1}{4\pi} \sum_{p=1}^{N_p(t)} \frac{\underline{\Omega}_p(t) \wedge (\underline{X}_p - \underline{X}_i)}{((\underline{X}_p - \underline{X}_i)^6 + \delta_i^6)^{\frac{1}{2}}} \end{aligned}$$

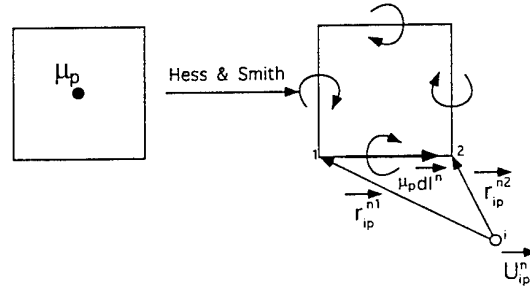


Figure 1: Dipole-vortex equivalence

The amount of vorticity initially contained in the particle is obtained by application of the Bernoulli relation on the separation line (with $\underline{U}_{te} = \frac{1}{2}(\underline{U}^+ + \underline{U}^-)$, the trailing edge velocity) :

$$\frac{\partial \mu}{\partial t} + \underline{U}_{te} \cdot \nabla \mu = 0$$

So during one step time δt , we evaluate the position and the vorticity of the new vortex particle by the following equations :

$$\begin{cases} \underline{\Omega}_i = [\delta l_i (\mu_i(t + \Delta t) - \mu_i(t))] \underline{i} \\ \quad + \left[\Delta t |\underline{U}_{te}| \frac{\mu_{i+1} - \mu_{i-1}}{2} \right] \underline{j} \\ \underline{X}_i = \underline{X}_{te} + \underline{U}_{te} \frac{\Delta t}{2} \end{cases} \quad (9)$$

δl_i is the length of the side of panel i which is a part of the trailing edge.

Fluid/Structure Interaction

The fluid/structure interaction has been taken into account by two different modelling corresponding to two applications.

For the wind turbines case, the vortex particle method is coupled with a beam model which satisfies two conditions, one for the forces or pressures (dynamic conditions) and an other one for the velocities (kinematic condition). The complete aeroelastic problem is solved in the time domain by considering successively the aerodynamic and elastodynamic problems.

For the sails problem, only the dynamic condition is satisfied and a new geometry of the sails is calculated. For the structural problem, we have used a non-linear model of string deformation in large displacements. It leads to a non convex variational principle connected to the minimisation of the non convex energy of the structure (the sail is considered as a network of stress-unilateral elastic strings). More details about this model could be found in Le Maitre et al. (1997).

Turbulent Inflow

In order to describe the turbulent inflow, a statistical approach has been chosen. Such approach is tractable if the turbulence nature of the flow is well known. This is the case of the turbulence shear flows in the Atmospheric Boundary Layer for flat terrain. For atmospheric turbulent flows, the spectrum and coherency function are well known. A suitable method based on the work of Shinosuka (1972) consists in generating time series of the velocity field by considering a set of homogeneous Gaussian processes. Similar methods were developed by Veers (1988) and Winkelaar (1992).

The numerical model, requires several data related to the spectrum and coherency function which are supposed to be well described by the Von Karman spectrum and the Davenport coherency function.

A similar method was developed by Mann (1994). Based on the work of Townsend, Mann solves the linearised Navier-Stokes equation of the fluctuation in the frequency domain by introducing a eddy life time concept. Only linear shear has been considered and the Taylor's hypothesis is required in order to link space and time. However this method has the advantage of simulating the full 3D velocity field.

The statistical concept has enabled us to describe the turbulence of the inflow velocity field. It is noticed that this velocity should be a small disturbance of the flow compared to the rotational part of the flow in relation (1) :

$$|\underline{U}'_{\infty}| \ll |\underline{U}_{\infty}|$$

where \underline{U}'_{∞} represents the fluctuation of the inflow velocity.

Then, within the framework of the Boundary and Vortex Element methods, the inflow velocity should be estimated on a grid for the lifting body problem and the wake problem, respectively.

Concerning the lifting problem, the positions of the control points are supposed to be known even if they are moving because of the elastic deformations, this one, in return, depends on the inflow condition. These deformations are considered small enough so that the control points position can be determined before the aeroelastic simulation. We have build a grid which contain all the possible sail configuration. On this grid, the times series are generated

Wake is presumed to be "known", a set of the stochastic times series could be also computed on the grid for the wake problem. Moreover, such simulation would have required very long computational time in practice.

Thus a local Taylor's hypothesis is used in order to estimate the inflow velocity for each particle in the wake. It consists in attributing the corresponding inflow velocity to the emitted particles by interpolation from the times series grid. Then it is conserved along the particles trajectories.

A simple LES modelling with the 3D VEM

There is an obvious interaction between the inflow which is represented by the times series and the vortex particles flow. A 3D Reynolds Averaged Navier-Stokes (RANS) method within the Lagrangian Framework has been developed. Turbulent transport for the scalars (as $k - \epsilon$) with particles have been investigated and interaction with the vorticity was described via a turbulent eddy-viscosity (Bréard, 1996).

Besides this, we have also implemented the Smagorinsky model of the turbulent eddy-viscosity (Meneveau et al. 1995) which requires less computational effort compared to the RANS method. In this method, a simple form is used for ν_t :

$$\nu_t = (C_s \delta_t)^2 (2S_{ij}S_{ij})^{\frac{1}{2}} \quad (10)$$

where C_s denotes the Smagorinsky constant which lies with the range 0.1-0.24, and S_{ij} is the rate of strain tensor. The Eulerian grid filter δ_t is replaced by the particle core size δ used in the vortex particle method.

It is clear that this simple eddy-viscosity hypothesis is arbitrary, and some progress might be achieved. However, only an extension to the vortex particle with stochastic

conditions is considered here after. In the second equation of (2) the diffusion term has been replaced by a turbulent diffusive term and is modelized by means of an equivalent diffusion velocity as defined by the following :

$$\nabla(\nu_t \nabla \otimes \underline{\omega}) = \nabla(\underline{U}_d \otimes \underline{\omega}) \quad (11)$$

In the case of wake flows, the component orthogonal to $\underline{\omega}$ have been considered to be very small due the filament structure of the vorticity field. Therefore only the component parallel to $\underline{\omega}$ is computed :

$$\underline{U}_d^{\parallel} = \nu_t \frac{(\nabla \otimes \underline{\omega}) \cdot \underline{\omega}}{|\underline{\omega}|^2}$$

RESULTS

First of all, the model presented above has been thoroughly checked for self-consistency. Concerning wind turbines, a large amount of test was done during the last year and the aeroelastic modelling was successfully validated. Most of these validation concern stationary conditions. More details can be found in Belessis et al. (1994) and Voutsinas et al. (1996).

Concerning sails, although very few data are available, good agreements with existing measurement was found in Charvet, (1992) and Hauville, (1996).

In the case of a turbulent inflow, the comparison is not so easy. The wind and the configuration should be represent as well as possible the condition which have been measured (pitch, yaw related with the wind direction, length scale, turbulent intensity, decay factor of the coherency function, shear law, etc ...). Some assumptions are necessary, and herein this paper, some tendency will be selected in order to give an indication of the turbulence effect. Two runs were performed for each case with and without the turbulent inflow conditions. Both calculations has taken into account the shear of the inflow described by :

$$U = \bar{U}_{\infty(z_{ref})} \frac{\ln(\frac{z}{z_o})}{\ln(\frac{z_{ref}}{z_o})} \quad (12)$$

where z_o is the roughness parameter, z_{ref} the reference height at which the mean wind speed is $\bar{U}_{\infty(z_{ref})}$ and z , the height.

Sails

We have used harmonic motions of the sail in order to estimate the importance of unsteady forces on sails. The most important effect is probably due to the unsteady motion of the hull. This latter is strongly related to the waves characteristics so it could be roughly simulated by imposing a harmonic pitching motion. It is well known that this kind of motion is directly responsible for the efficiency loss of higher sails in waves. This is a limitation to the use of high rigs since this configuration should have a better propulsive efficiency due to the wind vertical gradient. As a result, it is of some interest to derive a design tool which provides an evaluation of the respective magnitudes of these two competitive effects.

The pitching motion is described by the angle between the mast and the normal to the mean sea surface, which is expressed in the form of a sinusoidal law (the center of rotation is the boat center of inertia) :

$$\alpha = \alpha_o \sin(2\pi t/T)$$

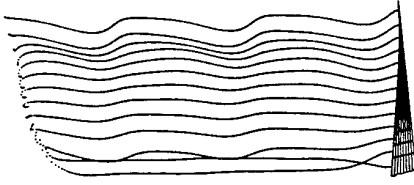


Figure 2: Wake and grid mesh sail in pitching motion under wind shear conditions

The ratio between the mast height and a length scale is obtained as the product of the period of the oscillations and the unperturbed stream velocity :

$$\mathcal{R} = \frac{z_{mast}}{U_{\infty} T}$$

We consider a pitching motion at $\mathcal{R} = 1$ and $\alpha_o = 10^\circ$ in the two cases (Stochastic problem and wind shear) for a "First Class 8" sail. We impose a $7ms^{-1}$ mean wind speed at $10m$ height. The angle of attack of the sail is approximatively 10 degrees.

Initially, the sail geometry is shaped with the Fluid/Structure interaction model without the pitching motion, but with the shear of the inflow described by (12). In the second time, when we imposed the motion, it has been assumed that the shape remains constant.

The two original runs described above are split into two additional cases : with and without the pitching motion.

Figure 2 represents the position of the vortex particle and the sail grid mesh. On Figures 3 and 4 we show the propulsive force during one period of the motion : on Figure 3, the inflow conditions are the same for both two curves with pitching motion only on the solid curve. On Figure 4, we have pitching motion for both two curves with wind shear condition on the solid curve and mean shear inflow conditions on the dotted curve. The fluctuation is asymmetric. When the sail moves down ($\approx \frac{5T}{8}$), in the direction of the wake (left direction on the figure 2) the effect of the wake becomes more important, therefore the propulsive force decreases. When the sail moves in the opposite direction ($\approx \frac{T}{8}$) the propulsive force increases but with different amplitudes due to the non-linear behaviour. The same kind of results are presented in Figures 5 and 6 but with the turbulent inflow. The pitching effect is amplified by unsteady inflow conditions. This is an important consequence for the sails designers.

Wind Turbines

The turbulent inflow is the main excitation for wind turbines. Also the tower perturbs the flow and its shadow effect is modelled by superposing a deficit velocity approximated by a potential theory. The data for the turbulent inflow are : the mean wind speed of 9 m/s at hub height (60 m), the turbulent intensity is 10%. In the sequel, we will address some results concerning the wake properties with different computing configuration. Concerning the loads

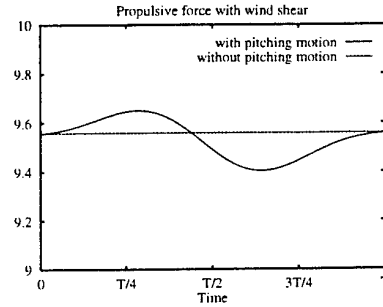


Figure 3: Propulsive force under wind shear condition with and without pitching motion

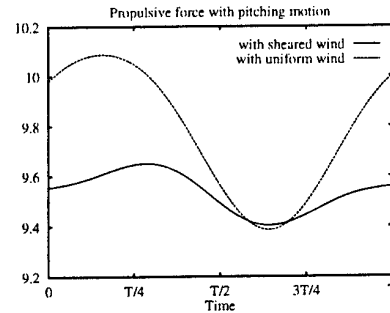


Figure 4: Propulsive with pitching motion under wind shear and uniform wind condition

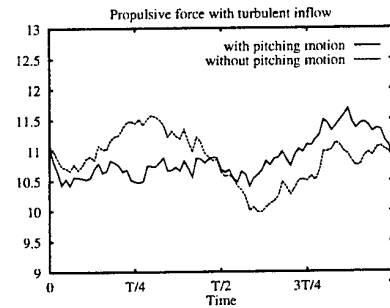


Figure 5: Propulsive force under stochastic condition with and without pitching motion



Figure 6: Wake and grid mesh sail in pitching motion under stochastic conditions

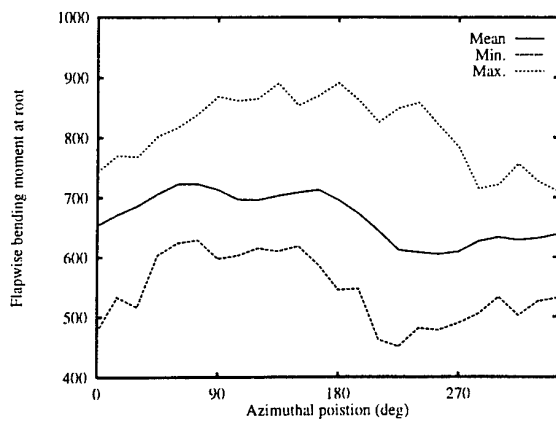


Figure 7: Bin process of the flapwise bending moment at root in case of stochastic inflow condition

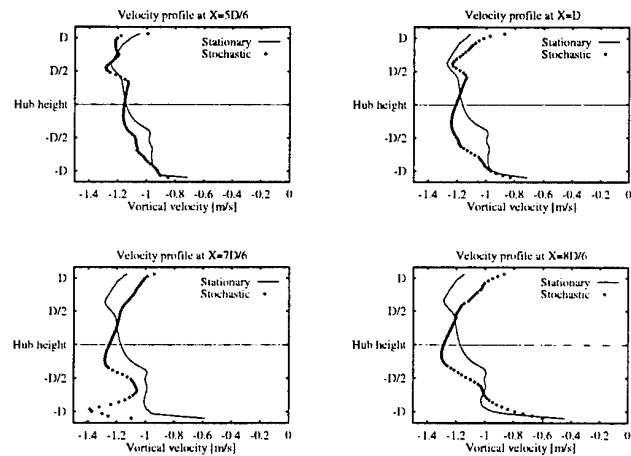


Figure 9: Axial vortical velocity profile at different positions downstream the wind turbine (5D/6, 6D/6, 7D/6, 8D/6)

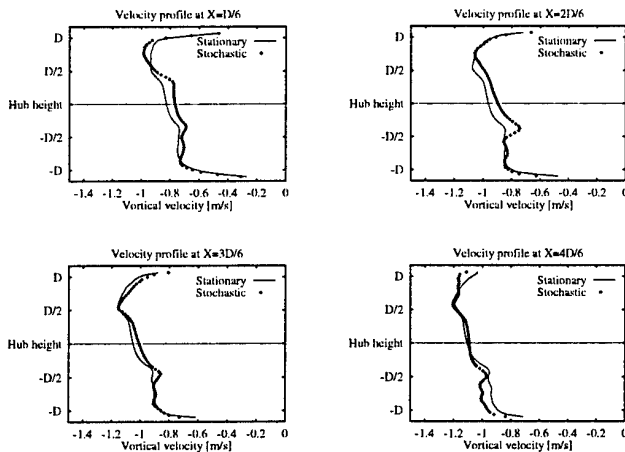


Figure 8: Axial vortical velocity profile at different positions downstream the wind turbine (D/6, 2D/6, 3D/6, 4D/6)

on the blade and their spectra, other results can be found in Bréard et al. (1997).

We present the bin process of the flapwise bending moment at root in Figure 7. The amplitudes given by the maximum and the minimum value at a specific azimuthal position is of the same order as the deterministic response due to the gradient.

Results from the axial vortical part of the velocity \underline{U}_w are shown from the two runs described above in Figures 8 and 9. When a turbulent inflow is considered, the profile of the velocity deficit differs significantly. The difference becomes more important as the distance of one diameter. It is noted that the profile corresponds to instantaneous velocity profile, and comparisons are difficult. However, the result give a clear indication how the particle vortex method is able to transport the information of the turbulent inflow. Further downstream the wind turbine, the deficit could reach 0.5 m/s less than given by the deterministic simulation.

The turbulent inflow has a significant impact on the wake of the wind turbine, and such impact must be carefully modelled when interaction between wind turbines are considered as it is the case for wind parks.

CONCLUSION

An extension to the aeroelastic codes based on the vortex particle and boundary element methods is proposed in

order to account for atmospheric turbulence. Also the interaction between the turbulent inflow and the turbulent wake is considered by a simple LES model. It is believed that such a methodology will permit the simulation of 3-D unsteady problems of engineering interests. It has been applied to wind turbines and sails and the following findings :

- Concerning sails, our purpose to build a numerical model including the utmost real conditions experienced by a sailing boat is still far from being achieved. Since very few data are available, the present result only provide "qualitative" informations.
- Concerning wind turbines, the turbulence affects considerably the aerodynamic of the blade. The wind simulator appears as crucial specially if complex terrain have to be considered. Several project are under development in order to estimate the quality of the wind simulation for mountainous sites. The elastic modelling of the whole system (drive-train, tower and blades) contributes to some particular improvement. The turbulent modelling does not affect directly the loads but the wake (far from the wind turbine) is altered. This is particularly important for the implementation of wind parks.

In both cases, the wake flow computation requires particular attention. For sailing boats in racing conditions or wind turbines operating in wind park, the vortical flow interaction added to the turbulent inflow contributes to strong turbulent wakes. Thus the generator of stochastic times series is useful tool for the study of unsteady flows around lifting bodies.

Acknowledgements : The authors would like to thank V. Riziotis from National Technical University of Athens which provided details concerning wind turbines and many usefull comments. Some computations were carried out at the NTUA, Fluids Section.

REFERENCES

- Bréard, C., 1996, "*Non-linear aeroelasticity modelling*", PhD Thesis, University of Le Havre, France.
- Bréard, C., Huberson, S., Belessis, M.A., Voutsinas, S.G., 1997, "*Non-linear aeroelastic modelling of wind turbines rotors*" Submitted to Journal of Fluids and Structures.
- Hauville, F., 1996, "*Optimisation des méthodes de calculs d'écoulements tourbillonnaires instationnaires*", PhD Thesis, University of Le Havre, France.
- Charvet, T., 1992, "*Résolution numérique de problèmes liés au comportement des voiles de bateau*", PhD Thesis, University of Le Havre, France.
- Hess, L.S., 1973, "*Calculation of potential flow about arbitrary 3-D lifting bodies*", Mc Donnell Douglas n° MDC J5679-01.
- Le Maître, O., Huberson, S., Souza de Cursi, J.E., 1996, "*Large Displacement Analysis For Ideally Flexible Sails*", ECCOMAS, Paris.
- Mann, J., 1994, "*Models in Micrometeorology*", PhD Thesis, Riso National Laboratory, Denmark.
- Meneveau, C., Mansfield, J., Knio, O., 1995, "*Towards Lagrangian large vortex simulation*" Wrk. Int. Workshop on Vortex Flows and Related Numerical Method, Montréal.
- Rehbach, C., 1977, "*Calcul numérique d'écoulements tridimensionnels instationnaires avec nappes tourbillonnaires*", La Recherche Aérospatiale, 5:289-298.
- Shinozuka, M., Jan, C.M. "*Digital simulation of random processes and its applications*" J. of Sound and Vibrations, Vol. 25, pp.111-128.
- Townsend, A.A., 1976 "*The structure of turbulent shear flow*", 2nd ed., Cambridge University Press.
- Veers, P.S., "*Three-Dimensional Wind Simulation*, 1988, Sandia Report SAND88-0152
- Voutsinas, S.G., Belessis, A.M., Rados, K.G., 1994, "Investigation of the yawed operation of wind turbines by means of a vortex particle method." 75th AGARD Fluid Dynamics Panel Symposium, Aerodynamics and Aeroacoustics of Rotorcraft, paper n° 11.
- Voutsinas, S.G., Riziotis, V.A., 1996, "*Vortex particle modelling of stall of rotors. Applications to wind turbines*", Proceedings of the ASME Fluids Engineering Division Summer Meeting, Vortex Flows and Vortex Methods, San Diego, USA, Vol. 3, p. 25-32.
- Winkelaar, D., "*SWIFT: Program for three-dimensional wind simulation*", 1992, ECN-Report.

3D DIRECT SIMULATION OF THE SHOCK-BOUNDARY LAYER INTERACTION AND VON KARMAN INSTABILITY IN TRANSONIC FLOW AROUND A WING

A. Bouhadji, M. Braza

Institut de Mécanique des Fluides de Toulouse

UMR CNRS-INPT 5502

Av. du Prof. Camille Soula 31400 Toulouse Cedex

France

ABSTRACT

The numerical simulation of a transonic flow around a wing of constant section (NACA0012) is performed at Mach number 0.85, Reynolds number 10,000 and zero angle of incidence. The full time-dependent Navier-Stokes equations are solved in two and three dimensions by using a finite-difference method. This flow shows the spontaneous appearance of a von-Kármán instability in the near wake. It is found that this instability results from the shock-boundary-layer interaction, occurring in the vicinity of the trailing edge. The natural disturbances due to this interaction lead further downstream to amplification of the instability, which leads to appearance of an alternating vortex pattern. The spacial evolution of this mode is studied and its maximum amplification rate is localized in the near wake. A thorough study of the instability process is performed in the 2D and 3D flow configurations. A detailed cartography of the flow through the instantaneous three-dimensional and two-dimensional fields of Mach number, density, temperature, velocity components and pressure allow the tracking of the shock-boundary-layer interaction and of the formation of coherent vortices.

INTRODUCTION

The investigation of transonic flows around aerofoils and wings has been the objective of numerous numerical and experimental studies over the last thirty years, because of the high interest of this kind of flows in the domain of aeronautical applications. Although there is a number of studies devoted to the analysis of the shock-boundary-layer interaction, the majority of them use the steady-state approach. There are very few studies, to our knowledge, examining the unsteady character of this interaction and especially its impact to a von Kármán instability. A few 2D numerical simulations of this flow by different numerical schemes report the onset of this instability downstream the shock, in the vicinity of the trailing edge (Bristeau et al. (1987), Lanteri (1990), Satofuka et al. (1987)). However, these studies were limited to a brief observation of this physical phenomenon, insisting rather to the numerical methodology aspects. Moreover, there are not, to our knowledge, numerical studies of this kind of transonic flow

in three dimensions. This is the objective of the present study, which is devoted to analyse the appearance of an alternating vortex pattern downstream the shock and to relate this to the interaction with the boundary layer, under the influence of three-dimensionality.

GOVERNING EQUATIONS AND NUMERICAL IMPLEMENTATION

In three dimensions, the time-dependent Navier-Stokes equations for a compressible, viscous fluid can be written under conservative and non-dimensional form, for a general, non-orthogonal, curvilinear coordinates system as follows:

$$\frac{\partial \hat{q}}{\partial t} + \frac{\partial \hat{E}}{\partial \xi} + \frac{\partial \hat{F}}{\partial \eta} + \frac{\partial \hat{H}}{\partial \zeta} = \frac{1}{Re} \left(\frac{\partial \hat{G}}{\partial \xi} + \frac{\partial \hat{R}}{\partial \eta} + \frac{\partial \hat{S}}{\partial \zeta} \right) \quad (1)$$

$$\hat{q} = J \begin{bmatrix} \rho \\ \rho u \\ \rho v \\ \rho w \\ e \end{bmatrix} \quad \hat{E} = J \begin{bmatrix} \rho U \\ \rho u U + \xi_x p \\ \rho v U + \xi_y p \\ \rho w U + \xi_z p \\ (e + p) U \end{bmatrix}$$

$$\hat{F} = J \begin{bmatrix} \rho V \\ \rho u V + \eta_x p \\ \rho v V + \eta_y p \\ \rho w V + \eta_z p \\ (e + p) V \end{bmatrix} \quad \hat{H} = J \begin{bmatrix} \rho W \\ \rho u W + \zeta_x p \\ \rho v W + \zeta_y p \\ \rho w W + \zeta_z p \\ (e + p) W \end{bmatrix}$$

$$\hat{G} = J \begin{bmatrix} 0 \\ \xi_x \tau_{xx} + \xi_y \tau_{xy} + \xi_z \tau_{xz} \\ \xi_x \tau_{yx} + \xi_y \tau_{yy} + \xi_z \tau_{yz} \\ \xi_x \tau_{zx} + \xi_y \tau_{zy} + \xi_z \tau_{zz} \\ \xi_x \beta_x + \xi_y \beta_y + \xi_z \beta_z \end{bmatrix}$$

$$\hat{R} = J \begin{bmatrix} 0 \\ \eta_x \tau_{xx} + \eta_y \tau_{xy} + \eta_z \tau_{xz} \\ \eta_x \tau_{yx} + \eta_y \tau_{yy} + \eta_z \tau_{yz} \\ \eta_x \tau_{zx} + \eta_y \tau_{zy} + \eta_z \tau_{zz} \\ \eta_x \beta_x + \eta_y \beta_y + \eta_z \beta_z \end{bmatrix}$$

$$\hat{S} = J \begin{bmatrix} 0 \\ \zeta_x \tau_{xx} + \zeta_y \tau_{xy} + \zeta_z \tau_{xz} \\ \zeta_x \tau_{yx} + \zeta_y \tau_{yy} + \zeta_z \tau_{yz} \\ \zeta_x \tau_{zx} + \zeta_y \tau_{zy} + \zeta_z \tau_{zz} \\ \zeta_x \beta_x + \zeta_y \beta_y + \zeta_z \beta_z \end{bmatrix}$$

where \hat{q} is the unknown vector, \hat{E} , \hat{F} , \hat{H} and \hat{G} , \hat{R} , \hat{S} are the inviscid and the viscous fluxes, respectively. u, v, w are the cartesian velocity components in x, y , and z direction, ρ the density, p the pressure and e the total energy per unit volume. U, V, W are the so-called contravariant velocities along ξ and η and ζ . We define β_x as $\frac{\gamma\mu}{Pr}e_{ix} + u\tau_{xx} + v\tau_{xy} + w\tau_{xz}$. Re, Pr, γ and μ are respectively, the Reynolds number, the Prandtl number, the ratio of specific heat, and the dynamic viscosity. We can define the dimensionless laminar viscosity by the Sutherland law.

Finally, the pressure p is related to e , and ρ by the perfect gas equation of state:

$$p = (\gamma - 1) \rho e; \quad (2)$$

The dimensionless variables are specified through the chord length, the uniform stream velocity, density and temperature.

A C-type mesh (fig.1) is generated by using the mesh-generation technique developed by Thompson *et al.* (1977) and solving a system of Poisson equations.

The numerical method uses an explicit four-stage Runge-Kutta scheme for the time discretization and an upwind Roe's scheme (1981) for the approximation of the convective terms, the extension to the second order spacial accuracy is provided by the MUSCL approach (1979). The diffusive derivatives are discretized by second order central differences.

In the x, y planes, Dirichlet free-stream conditions are adopted. At the outlet boundary, first-order extrapolation boundary conditions are applied, as well as at the edges of the spanwise direction. At time $t=0$, uniform fields are defined from the inflow conditions and are imposed as initial conditions.

On the wing surface, no-slip conditions are prescribed and a constant temperature wall is considered, while the pressure is deduced from the momentum equations written for the solid boundary.

RESULTS

2D Results

Firstly, a 2D study has been accomplished. A detailed numerical study has been performed for the grid-dependence and for the choice of the optimum numerical parameters.

A grid sensitivity study is done for three different grids. The grids used are 169x49, 241x90 and 351x85. The Strouhal number and the mean drag coefficient obtained are shown in table 1. From the two last fine grids, it is shown that the grid independency is achieved.

Grid	St	C_d
169x49	0.7568	0.0996
241x90	0.7813	0.0998
351x85	0.7813	0.0101

Table 1: Grid-dependence study

Figure 2 shows the time-dependent evolution of the lift coefficient according to the grid 241x90. After a significant number of time steps, a regular oscillatory character is obtained. The amplitudes of the oscillation reach an

established state after a dimensionless time value of 70 approximately. The unsteady behavior of the flow displays the onset of a von Kármán instability, in a similar way as in the flow behind bluff bodies at much lower Reynolds number. In figure 3, the shock-boundary layer interaction and the formation of coherent structures are clearly identified. The instantaneous field of the Mach number and the temperature are selected in five equidistant instants in a period (fig.4). These figures clearly show the periodic vortex pattern. The oscillatory motion downstream the trailing edge is obtained. Especially, the temperature shows that the centers of the vortices carry maximum temperature values (of the same order as at the wall), because of the almost zero relative velocity near eddies centers. Furthermore, the temperature variations as a function of time are opposite in phase relatively to the Mach number variation.

In order to study in detail the space evolution of the von Kármán mode in the near wake, a spectral analysis of the time-domain properties is provided. A fast Fourier transform (FFT) is operated on each time-domain signal, along a characteristic line at the near wake ($y/c=0.052$). v -component spectra are especially produced, because of the sensitivity of this component to the shedding of the alternating vortices. Along all the mesh points of the selected line, the spectral amplitude corresponding to the fundamental frequency is evaluated as a function of x/c (fig.5). The variation of the spectral amplitude shows an increase towards $x/c=1.35$ and displays a maximum plateau region up to $x/c=1.68$. This is the region along which the effects of the von Kármán mode are the most prominent in the rear wake. Downstream, the variation decreases because of the loss of coherence in the flow structure, due to the effect of diffusion. This curve provides a cartography of the von Kármán mode in the near wake for the present transonic flow. It displays qualitatively a similar behavior as a number of experimental and numerical studies in lower Reynolds number incompressible flows (Persillon *et al.* (1995), Goujon-Durand *et al.* (1994), although in the present transonic flow case, the maximum region appears more broadened.

3D Results

The grid of (169x49x32) is used for the 3D study (fig.1), in order to have a reasonable CPU time. The 3D numerical simulation shows that the alternating vortex pattern persists, as it is shown on the time-dependent evolution of lift coefficient (fig.11). This is also indicated by the anti-symmetric variations of v component along the rear axis, presented on figure 6.

In addition, the onset of three-dimensionality progressively appears in the flow field. Figure 7 and 8 show the iso- w velocity component in (x, z) plan for $y/c = 0$ and $y/c = 0.1$ values. It is remarkable that this component displays formation of organized cells along the spanwise direction. The wavelength of this pattern (λ/c) is found 0.45. The kernels of the recirculation regions correspond alternatively to maximum and minimum values of w component. This spatial oscillation is also found on fig.9 where a temporal periodicity of w component is also developed. A phase opposition by 180deg approximately is obtained between the w variations at $z/c = 1.95$ and $z/c = 2.25$. This figure shows a progressive amplification of the oscillations of w component which is organized in respect to a regular oscillatory behavior. The iso-contours of w component are shown also in (x, y) plan (fig.10). It is noticeable that the alternating vortex shedding pattern governs the variations of this velocity component in the near wake.

Figs 11, 12, 13 and 14 show the time-dependent evolution of global and local quantities in the wake, in the middle spanwise section. A frequency modulation is obtained in the 3D case of the simulations, ($St=0.7407$), comparing to the frequency value (0.7568) in the 2D case. This frequency

decrease in 3D case may be attributed to a decrease of the energy amount devoted to sustain the alternating pattern, on the profit of the simultaneous development of the three-dimensional motion.

CONCLUSION

This numerical study analyses the inherently unsteady behavior of a transonic flow around a NACA0012 airfoil at zero angle of incidence, Reynolds number 10^4 and upstream Mach number 0.85. It is found that the flow develops an inherently oscillating character and it is organized according to a Bénard-von Kármán mode. This is confirmed by employing different meshes and this study provides grid-independent results. It is noticeable that the present inherent unsteadiness develops after a long transient phase. The spatial evolution (amplification and decay) of this mode is quantified in the vicinity of the rear axis in the present study. The location of maximum spectral amplitude of this fundamental mode is found to occur at $x/c=1.68$. It is worthy to mention that the present study provides the spatial evolution of the Bénard-von Kármán mode under the action of the compressibility effects, and this, by using the non-linear approach, offered by the system of the Navier-Stokes equations. This study indicates the mutual influence between the shock formation and the von Kármán mode which mode would not be developed at zero angle of incidence for the present wing configuration without the shock formation, this last one due to transonic flow conditions and to the body shape. The von Kármán mode formation can be seen as a consequence of perturbations induced by the shock discontinuity and due to the relatively high value of the nominal Reynolds number. It is found that this mode persists in the 3D case, simultaneously with the appearance of an oscillatory pattern in the spanwise direction having a characteristic wavelength. The von Kármán mode and the spanwise oscillation coexist with the formation of the shock wave which also persists in the third direction.

Acknowledgements : The present work has been carried out in the group Ecoulements Monophasiques, Transitionnels et Turbulents (EMT2) of the Institut de Mécanique des Fluides de Toulouse (IMFT). The authors are grateful to the personnel of the two National Computer Centres of France, CNUSC and IDRIS for the computational time and the precious assistance provided to carry out this work. The authors express many thanks to Dr A. Dervieux, Dr B. Koobus and Dr S.Lanteri (INRIA-Sophia Antipolis France) and to Professors B. van Leer and P.Roe (Dept. of Aerospace, University of Michigan), for their useful discussions. They are also grateful to Professors H. Boisson, P. Chassaing and Ha Minh (IMFT) for their encouragements to carry out this work in the group EMT2.

REFERENCES

- Bristeau, M. O., Glowinski, R., Periaux, J., Viviand, H., 1987 "Numerical simulation of compressible Navier-Stokes flows", *Notes on Numerical Fluid Mechanics*, Vol.18, Vieweg, Braunschweig.
- Goujon-Durand, S., Jenffer, P., Wesfreid, J. E., 1994 "Downstream evolution of the Bénard-von Kármán instability", *Phys.Rev.Lett.*, Vol.50.
- Lanteri, S., 1990 "Simulation d'écoulements aérodynamiques instationnaires sur une architecture S.I.M.D massivement parallèle" Thèse de Doctorat, Université de Nice Sophia-Antipolis.
- Persillon, H., Braza, M., Ha Minh, H., Williamson, C., 1995, "Non-linear instability and three-dimensional transition in the flow past a circular cylinder at low Reynolds number", *IUTAM Symposium, Non-linear instability and transition in three-dimensional boundary layers*, Ed.Kluwer, selected papers, Manchester, pp. 207-216.

lected papers, Manchester, pp. 207-216.

Roe, P. L., 1981 "Approximate Riemann solvers, parameters vectors and difference schemes." *J.Comput.Phys.*, Vol.43

Satofuka, N., Morinishi, K., Nishida, Y., 1987 "Numerical solution of two-dimensional compressible Navier-Stokes equations using rational Runge-Kutta method" *Notes on Numerical Fluid Mechanics*, Vol.18, Vieweg, Braunschweig.

Thompson, J. F., Thames, F. C., Mastin, C. W., 1977 "Boundary-fitted curvilinear coordinate systems for solution of partial differential equations on fields containing any number of arbitrary two-dimensional bodies" NASA CR-2729.

Van Leer, B., 1979 "Towards the ultimate conservation difference scheme V: a second-order sequel to Godunov's method", *J.Comp.Phys.*, Vol.32, pp.101-136.

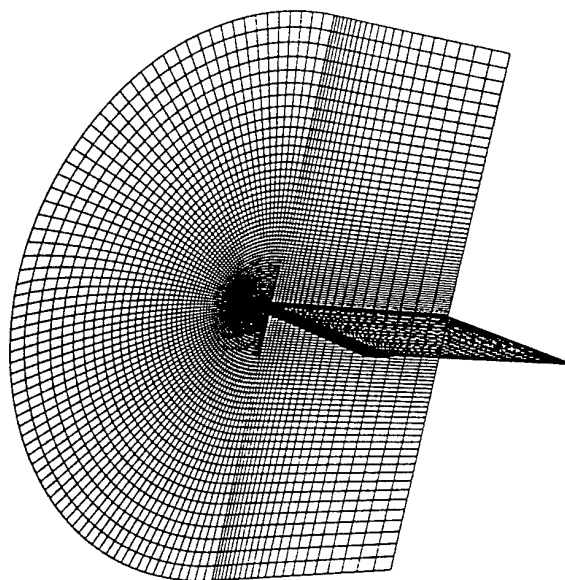


Figure 1: The C-type grid

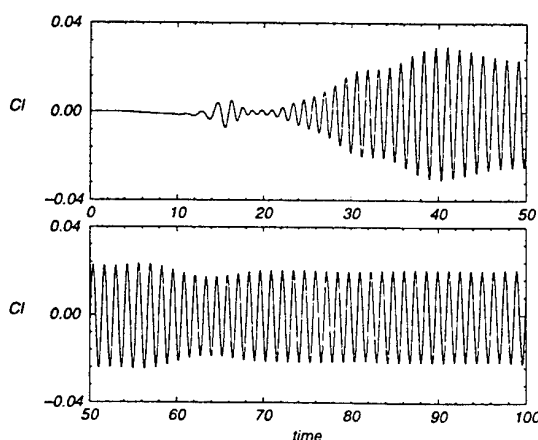


Figure 2: Time-dependent evolution of lift coefficient (grid 241x90)

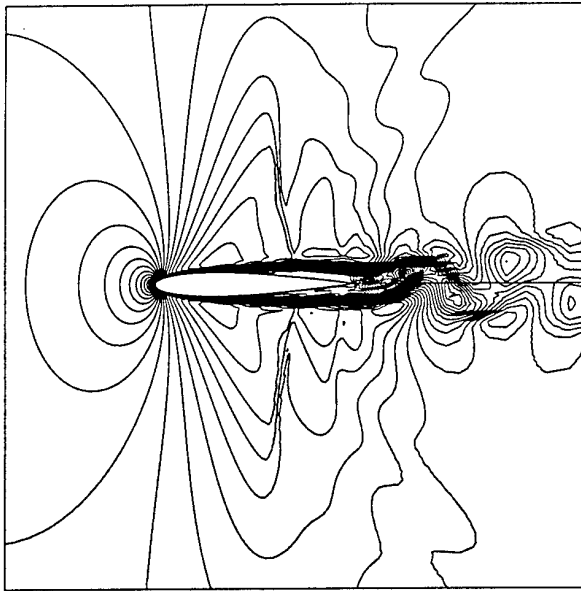


Figure 3: Iso-Mach number contours of the established phase at time=100

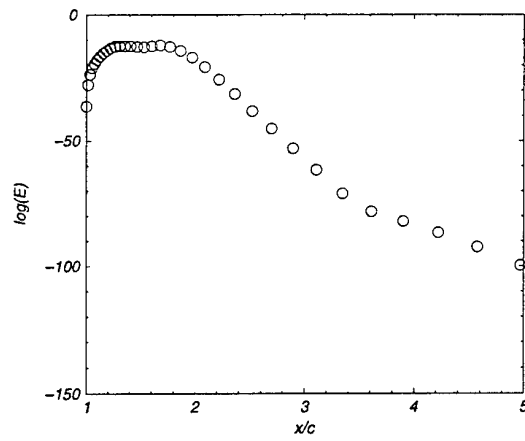


Figure 5: Spectral amplitude of the fundamental frequency versus x/c along $y/c=0.052$

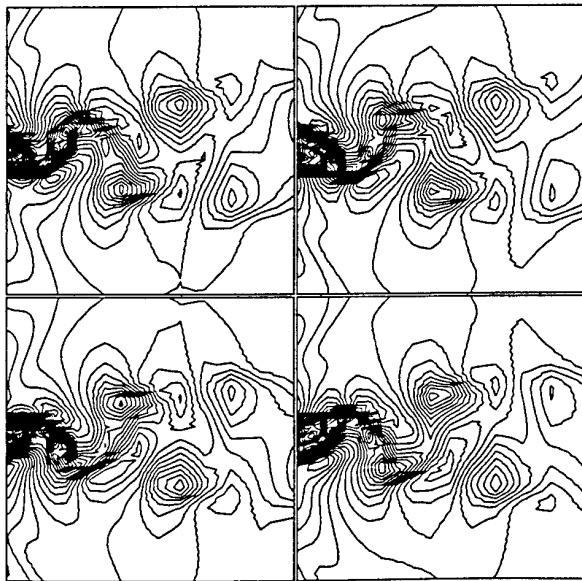


Figure 4: Time-dependent evolution of alternating coherent structures (Iso-Mach number contours)

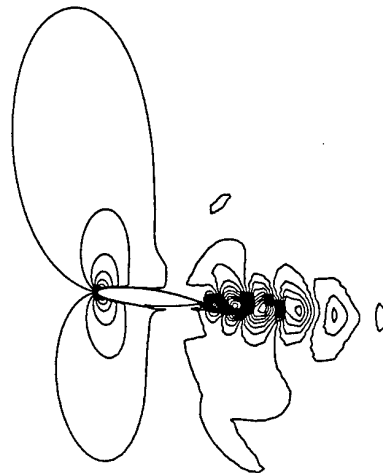


Figure 6: Iso- v component velocity contours (Zoom of the 3D field at $z/c = 2.25$)

pb_3d

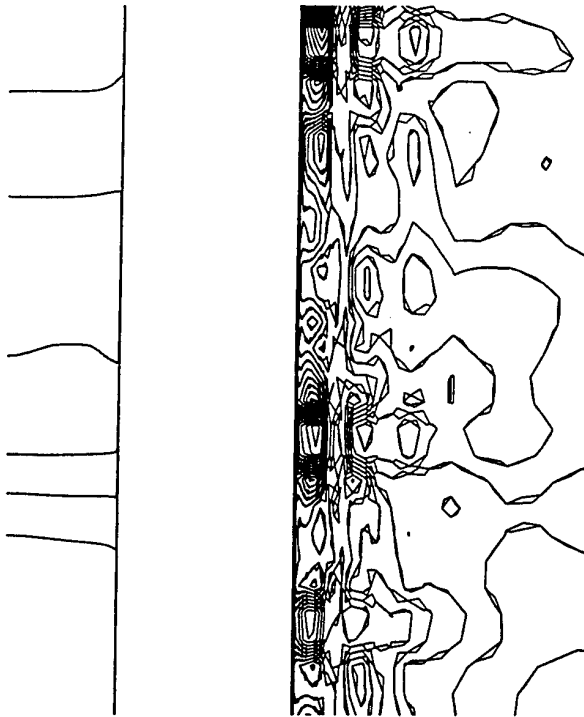


Figure 7: Iso-w component velocity contours in (x, z) plan for $y/c = 0$

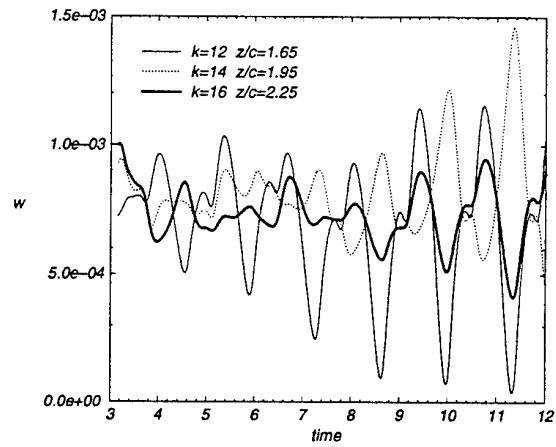


Figure 9: Time-dependent evolution of w component velocity at $x/c=1.24$ $y/c=0.054$ in three spanwise sections

pb_3d

pb_3d

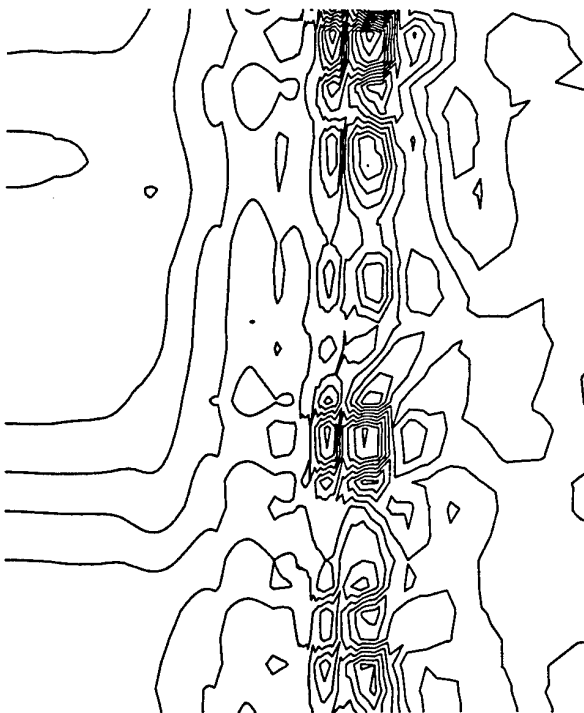


Figure 8: Iso-w component velocity contours in (x, z) plan for $y/c = 0.1$

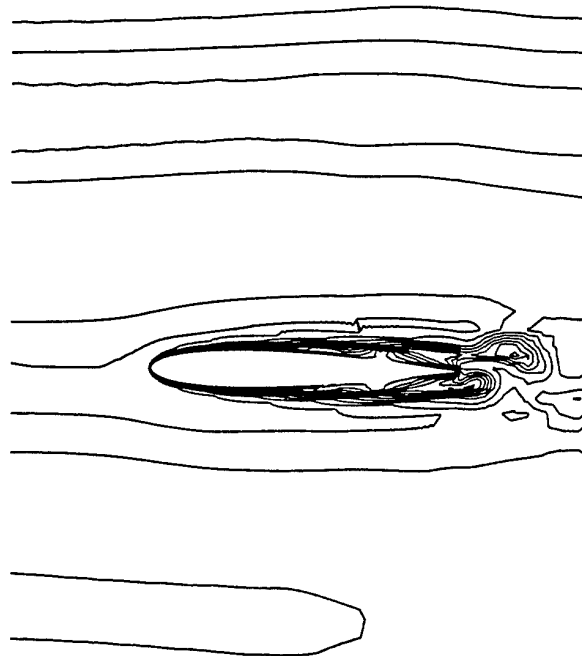


Figure 10: Iso-w component velocity contours in (x, y) plan in the middle spanwise section

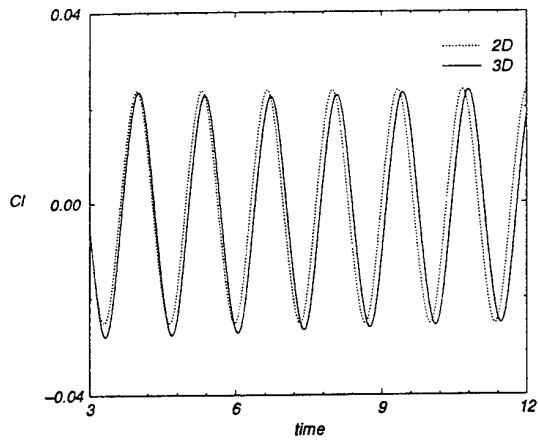


Figure 11: 2D and 3D time-dependent evolution of lift coefficient

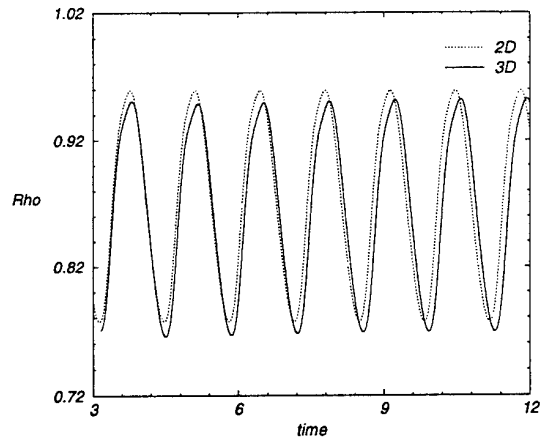


Figure 13: 2D and 3D time-dependent evolution of density at $x/c=1.24$, $y/c=0.088$, $z/c = 2.25$

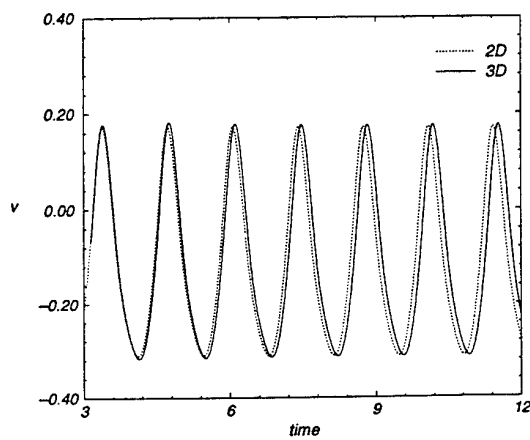


Figure 12: 2D and 3D time-dependent evolution of v component velocity at $x/c=1.24$, $y/c=0.088$, $z/c = 2.25$

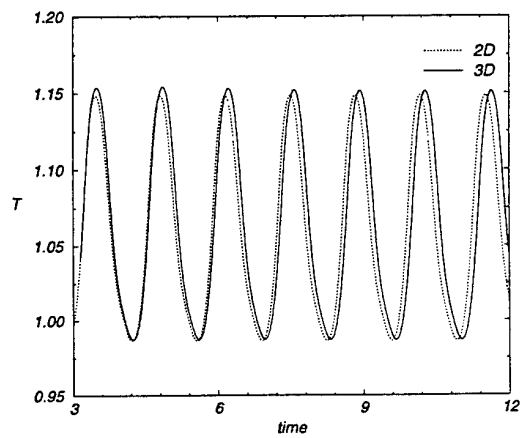


Figure 14: 2D and 3D time-dependent evolution of temperature at $x/c=1.24$, $y/c=0.088$, $z/c = 2.25$

EFFECTS OF BLOWING/SUCTION FROM A SPANWISE SLOT ON A TURBULENT BOUNDARY LAYER FLOW

H. Choi, J. Park, S. Hahn

Department of Mechanical Engineering
Seoul National University
Seoul 151-742
Korea

ABSTRACT

Effects of uniform blowing/suction from a spanwise slot on a turbulent boundary layer are investigated using the direct numerical simulation technique. Even though the magnitude of blowing/suction is very small, it significantly changes the skin friction as well as the streamwise vortex above the wall. In the case of uniform blowing, the skin friction on the slot is significantly decreased. Streamwise vortices above the wall are lifted up by blowing, and thus the interaction of the vortices with the wall is reduced. Therefore, the lifted vortices become stronger, resulting in the increase of the turbulence intensity as well as the skin friction downstream of the slot. The opposite effects are observed in the case of uniform suction.

INTRODUCTION

Flow above the flat plate changes from laminar to turbulent as it moves downstream, and then a significant increase in the skin-friction drag occurs. This increase is due to the downward motion induced from streamwise vortices very near the wall. Therefore, the skin friction on the wall may be reduced by weakening or annihilating the near-wall streamwise vortices. This concept was used by Choi, Moin & Kim (1994). They applied active blowing/suction on the wall such that the wall-normal velocity on the wall matches the normal velocity at $y^+ = 10$ with an opposite sign. The magnitude of their blowing and suction was about two orders of magnitude smaller than the free-stream velocity. As a result, they obtained about 25% drag reduction in turbulent channel flow. It was shown that the near-wall streamwise vortices are significantly weakened by the active control scheme.

It is known that a uniform blowing from the wall decreases the skin friction and increases the strength of the fluctuating quantities, while a uniform suction has nearly the opposite effect. However, the increase of the turbulent fluctuations from the blowing may cause an increase of drag in the downstream due to strong turbulent motion there. In the case of suction, the downstream skin friction may be reduced due to the stabilization of the turbulence even though the skin friction increases near the place of the suction. Furthermore, it is not clear how near-wall turbu-

lence structure interacts with uniform blowing or suction. These kinds of questions have been around so many years, but no clear answer has been presented so far. Choi, Moin & Kim (1994) tried to investigate this issue but could not reach any conclusion because their flow geometry was a turbulent channel flow where the mass flow rate should be kept constant during the blowing/suction.

The effects of wall suction/blowing have been studied on various flow fields experimentally or numerically: i.e. turbulent pipe flow (Schildknecht *et al.* 1979; Sofialidis & Prinos 1996), turbulent channel flow (Piomelli 1987; Sumitani & Kasagi 1995) and turbulent boundary layer flow (Antonia & Fulachier 1989; Mariani *et al.* 1993). Suction through a porous strip or slot in a laminar/turbulent boundary layer has been studied for drag reduction: i.e. extension of laminar flow region (Schlichting 1965), separation delay (Sano & Hirayama 1985), relaminarization of turbulent flow (Narasimha & Sreenivasan 1979; Antonia *et al.* 1995). However those studies involve rather large magnitudes of the wall-normal velocity.

In the present study, we are mainly interested in the change of near-wall turbulence structures due to a small amount of blowing and suction. The magnitude of blowing/suction is two orders of magnitude smaller than the free-stream velocity, which is nearly the same as that used in Choi *et al.* (1994).

COMPUTATIONAL DETAILS

The direct numerical simulation technique is used in this study. The integration method used to solve the the Navier-Stokes equations is based on a fully implicit, fractional step method (Choi & Moin 1994); all terms are advanced with the Crank-Nicolson method in time and are resolved with the second-order central difference scheme in space. The number of grids points used is $352 \times 64 \times 128$ in the streamwise (x), wall-normal (y) and spanwise (z) directions, respectively. The spacing between grid points, in wall units, is $\Delta x^+ = 18.4$, $\Delta y_{min}^+ = 0.17$, $\Delta y_{max}^+ = 22.4$, $\Delta z^+ = 5.3$, and there are 45 grid points in the wall-normal direction in the boundary layer at the flow inlet.

The computational domain size is $(240\delta^*, 19\delta^*, 25\delta^*)$ in (x, y, z) directions, where δ^* denotes the displacement

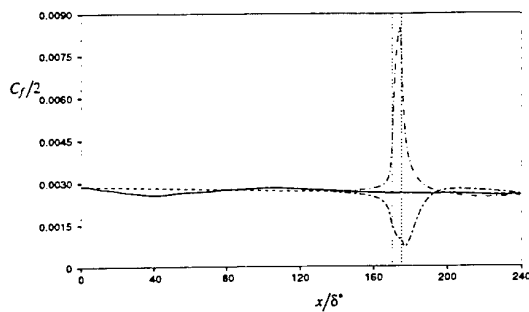


Figure 1: Variation of the skin friction coefficient due to blowing and suction: —, no blowing/suction; ----, seventh law; - · -, uniform blowing; · · · ·, uniform suction. Dotted lines denote the location of the spanwise slot.

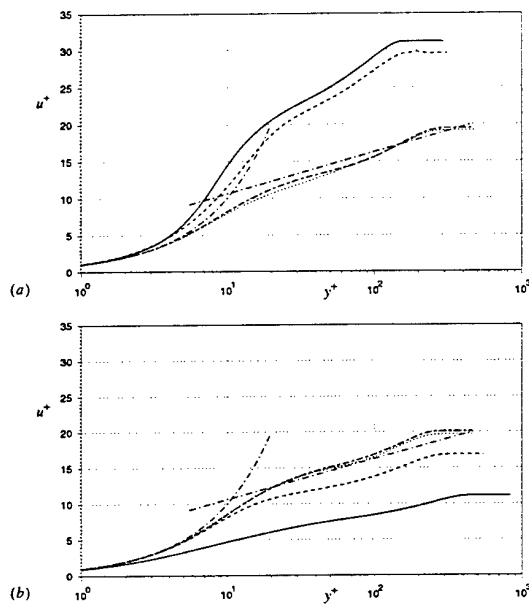


Figure 2: Mean velocity profiles in wall coordinate: —, $x = 172\delta^*$; ----, $x = 180\delta^*$; - · -, $x = 200\delta^*$; · · · ·, $x = 230\delta^*$; ----, law of the wall. (a) uniform blowing; (b) uniform suction.

thickness at the flow inlet. The nondimensional timestep $\Delta t u_\infty / \delta^*$ is 0.3 ($\Delta t^+ \approx 0.4$), and then the maximum local CFL number is about 3.

Inflow boundary condition is based on the method by Na & Moin (1996), where they applied amplitude jittering on the fluctuation components of Spalart's database (1988). The inlet Reynolds number based on the displacement thickness and free-stream velocity is 500. A convective outflow boundary condition is used at the exit. A transition length of $l = 120\delta^*$ from the artificial flow inlet was necessary to obtain a fully developed turbulent boundary layer flow at the upstream of the slot.

The uniform blowing or suction is applied from a spanwise slot ($x = 170\delta^*$ to $175\delta^*$), where $x = 0$ corresponds to the flow inlet. The slot width (L) is about 100 in wall units and there are 8 grid points in the streamwise direction on the slot. Kravchenko *et al.* (1993) studied the relation between the wall skin friction and near-wall streamwise vortices and showed that high skin friction regions on the wall are strongly correlated with streamwise vortices whose longitudinal length is approximately 100 wall

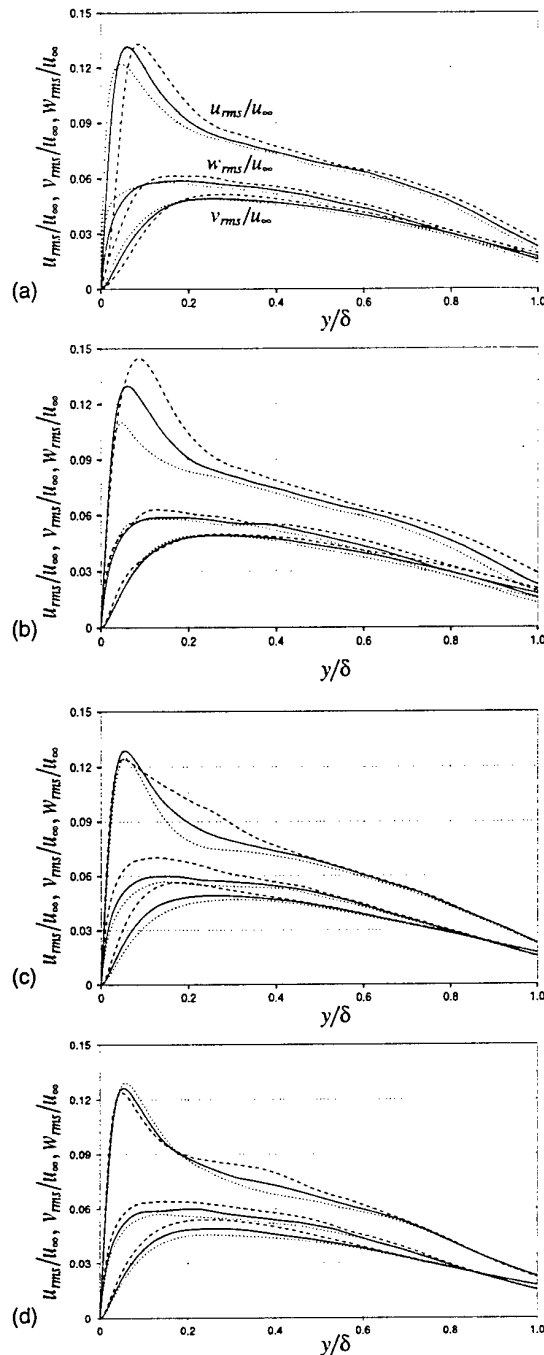


Figure 3: Variation of the turbulence intensities due to blowing and suction: —, no blowing/suction; ----, uniform blowing; - · -, uniform suction. (a) $x = 172\delta^*$; (b) $x = 180\delta^*$; (c) $x = 200\delta^*$; (d) $x = 230\delta^*$.

units. The magnitude of uniform blowing and suction was fixed to be the magnitude of v_{rms} at $y^+ = 10$ from the unmodified turbulent boundary layer flow, which is two orders of magnitude smaller than the free-stream velocity ($|v_w| = 0.018u_\infty$). Therefore, changes in turbulence quantities may be restricted to the near wall region only.

RESULTS

Some key features of the flow fields obtained by using blowing/suction were studied to investigate the effect of

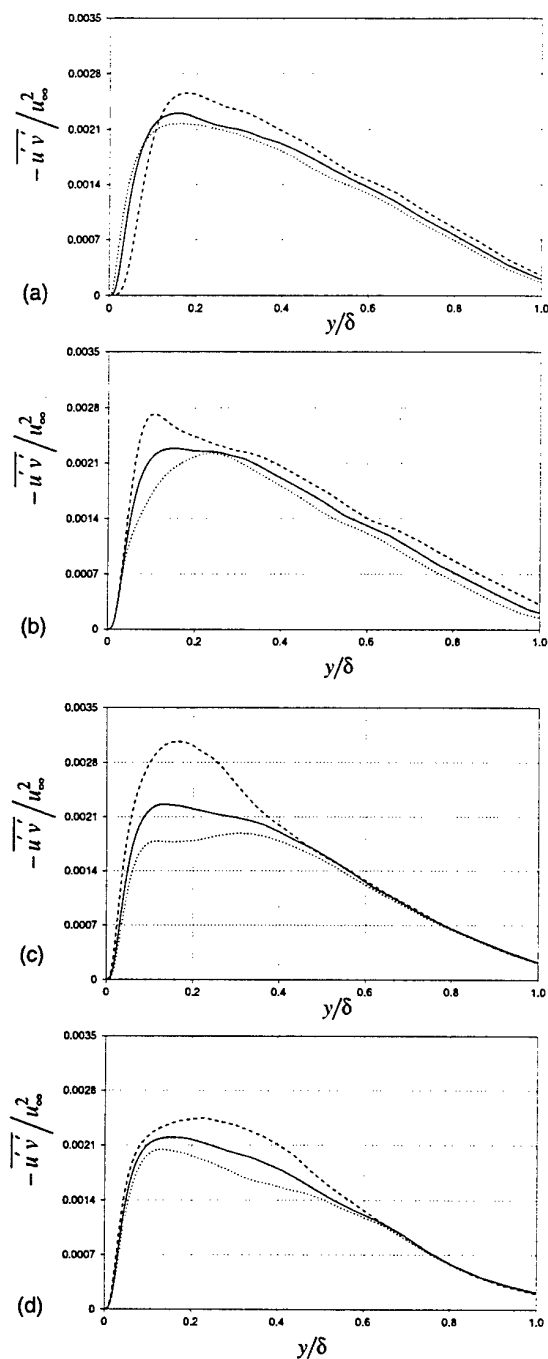


Figure 4: Variation of the Reynolds shear stress due to blowing and suction: —, no blowing/suction; ----, uniform blowing; ·····, uniform suction. (a) $x = 172\delta^*$; (b) $x = 180\delta^*$; (c) $x = 200\delta^*$; (d) $x = 230\delta^*$.

uniform blowing/suction on the modification of turbulent boundary layer flow. The statistics of the modified turbulent boundary layer flows were compared to those of the unmodified turbulent boundary layer flow at four different points: i.e. above the slot, L downstream, $5L$ downstream, and $11L$ downstream.

Figure 1 shows the variation of the skin friction according to the blowing or suction. It is seen that the skin friction without blowing/suction matches very well with the existing formula after $x = 120\delta^*$. Drag rapidly increases in the case of suction and decreases in the case of blowing near

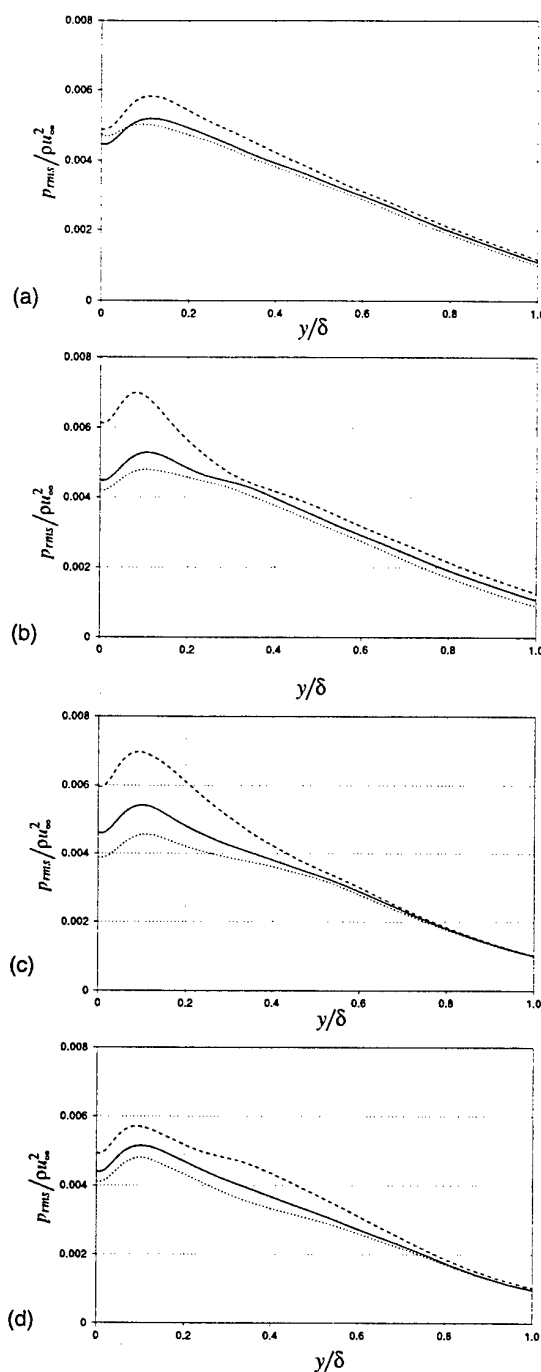


Figure 5: Variation of the pressure fluctuations due to blowing and suction: —, no blowing/suction; ----, uniform blowing; ·····, uniform suction. (a) $x = 172\delta^*$; (b) $x = 180\delta^*$; (c) $x = 200\delta^*$; (d) $x = 230\delta^*$.

the slot. It is also interesting to note that the skin friction in the downstream location from the slot shows the opposite: i.e. the skin friction increases in the case of blowing, while it decreases in the case of suction. It turns out that this is due to the flow stabilization and destabilization from suction and blowing, respectively (see below).

The mean-velocity profiles are shown in figure 2. In the case of blowing, upward shift is observed near the slot and downward shift is observed in the downstream. This upward shift in the log layer has previously been observed

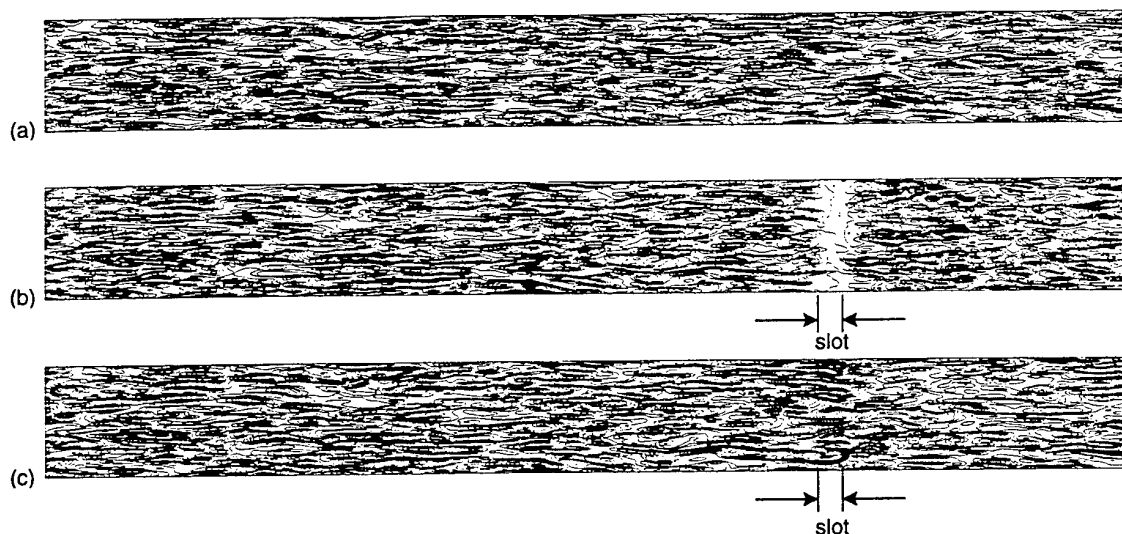


Figure 6: Contours of the streamwise velocity at $y \approx 0.04\delta^*$: (a) no blowing/suction; (b) uniform blowing; (c) uniform suction. Contour levels are from 0 to 0.2 by increments of 0.01.

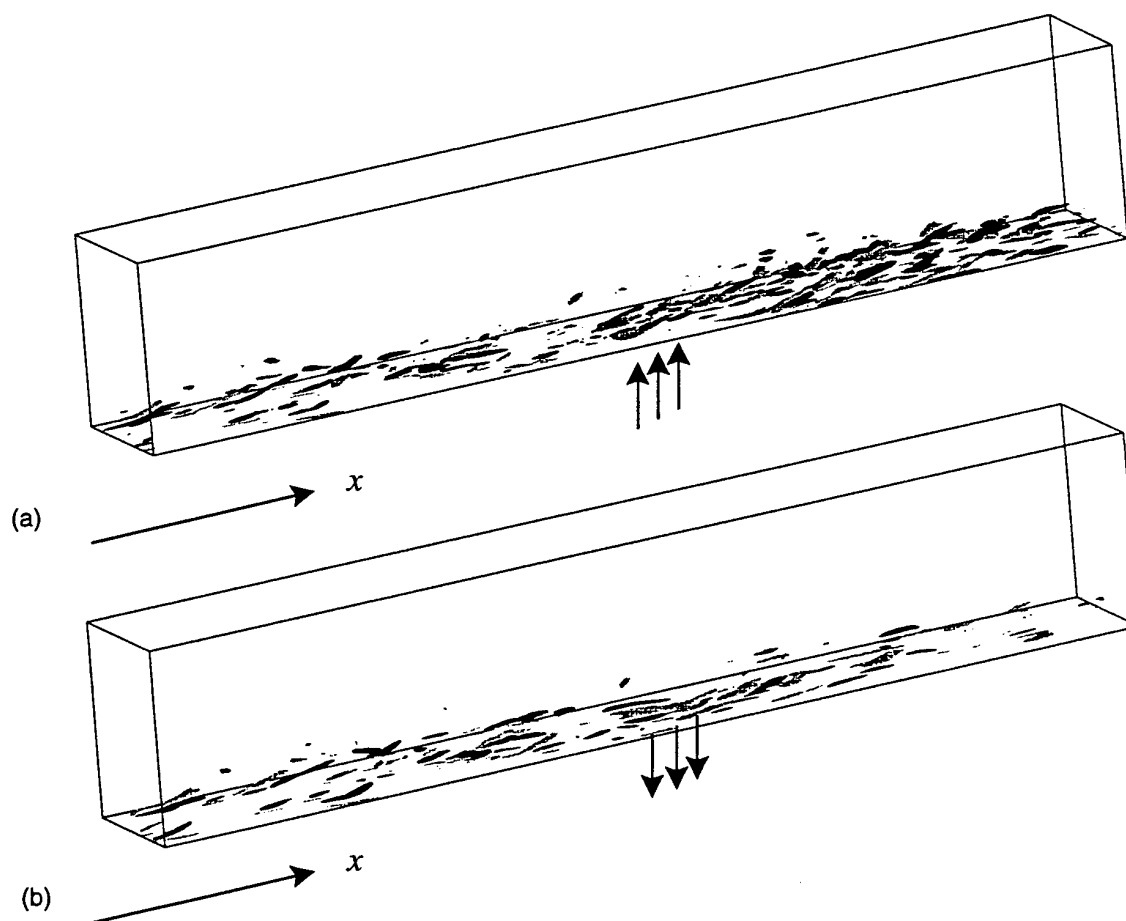


Figure 7: Three dimensional view of the streamwise vortices very near the wall: (a) uniform blowing; (b) uniform suction. The contour levels of the streamwise vorticity are $-0.5u_\infty/\delta^*$ (black) and $0.5u_\infty/\delta^*$ (grey).

in drag-reduced flows such as large-eddy breakup devices (Bandyopadhyay 1986), riblets (Choi 1989; Choi *et al.* 1993), and polymers (Lumley 1973; Virk 1975). In the case

of suction, downward shift is observed near the slot and upward shift in the downstream. These are consistent with the skin-friction variation with respect to blowing/suction.

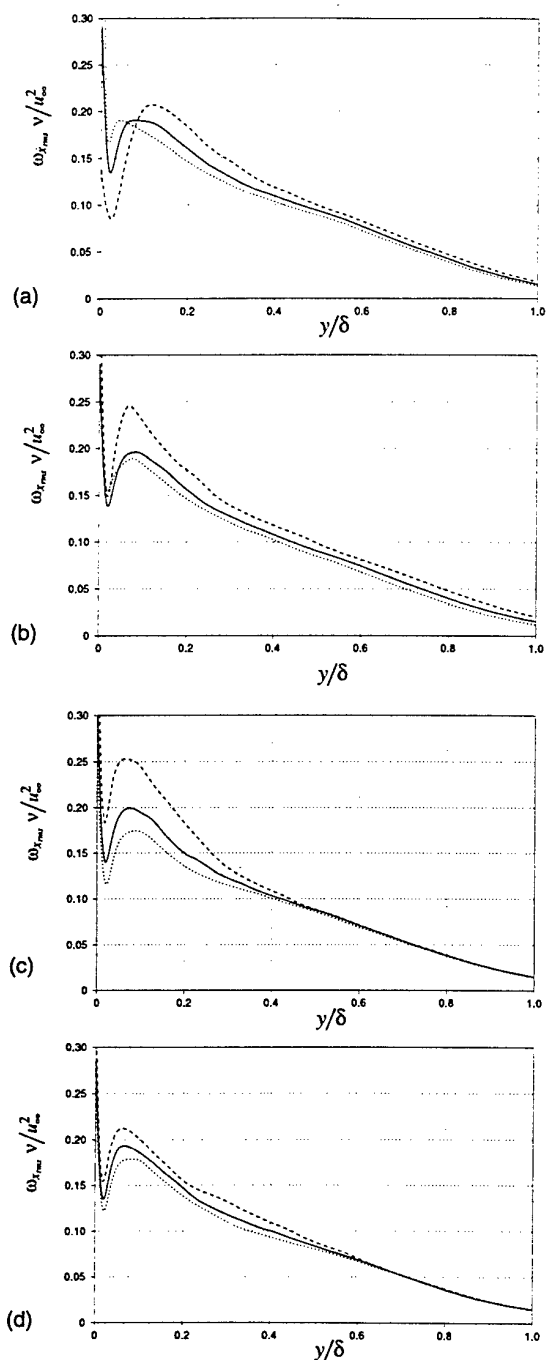


Figure 8: Variation of the streamwise vorticity fluctuations due to blowing and suction: —, no blowing/suction; ---, uniform blowing; ·····, uniform suction. (a) $x = 172\delta^*$; (b) $x = 180\delta^*$; (c) $x = 200\delta^*$; (d) $x = 230\delta^*$.

Figure 3 shows the modified profiles of the velocity fluctuations due to blowing or suction. It is clear that suction decreases the magnitude of the velocity fluctuations, while blowing increases them. Besides, suction shifts the profiles toward the wall and blowing away from the wall. The maximum change of u_{rms} from blowing or suction occurs at $x = 180\delta^*$, while the maximum change of v_{rms} and w_{rms} occurs at $x = 200\delta^*$. At $x = 200\delta^*$, the y -location where turbulent intensities are maximum becomes nearly the same irrespective of blowing/suction. Changes in the

Reynolds shear stress shown in Figure 4 are similar to those of the wall-normal velocity fluctuations. Therefore, blowing/suction affects the Reynolds stresses differently in time. Antonia *et al.* (1995), from their experiment using a short porous wall strip ($v_w = -0.181u_\infty, -0.361u_\infty, -0.451u_\infty$), reported that the longitudinal turbulent intensity recovers relatively quickly in the case of suction while the wall-normal turbulence intensity and Reynolds shear stress are significantly affected by suction and slowly recover. They also assumed that the spanwise turbulent intensity would be affected in a similar fashion to the longitudinal turbulent intensity. However, in the present study, w_{rms} shows a similar behavior to v_{rms} and the Reynolds shear stress.

Figure 5 shows the modified profiles of the pressure fluctuations due to blowing or suction. It is notable that the modification of the surface pressure fluctuations lasts long in the downstream. It shows that suction reduces the flow-induced noise, while blowing does the opposite.

Figure 6 shows contours of the streamwise velocity very near the wall. The streaky structure is clearly broken above the slot in the case of blowing and gets strong in the downstream direction. The suction shows the opposite. Note that the streaky structure is mainly due to the strong streamwise vortices present near the wall. Therefore, it will be interesting to see the interaction of the near-wall streamwise vortices with blowing or suction. A three dimensional view of this interaction is shown in figure 7. The near-wall vortical structure is clearly affected by blowing and suction. In the case of blowing, the vortical structure becomes strong after the slot. In the case of suction, however, some streamwise vortices disappear near the slot and thus flow becomes much calm after the slot. These become more clear in figure 8 which shows the variation of the streamwise vorticity fluctuations. In the case of blowing, above the slot ($x = 172\delta^*$), the local maximum point (center of streamwise vortices) moves away from the wall, i.e. the near-wall streamwise vortices are lifted up. On the other hand, suction makes the center of streamwise vortices closer to the wall. Because the magnitude of the streamwise vorticity at the wall is determined from vortices above the wall with no slip condition, in the case of blowing the magnitude of the streamwise vorticity at wall is smaller than that of the unmodified case (figure 8 (a)). Hence, the interaction between the main and secondary vortices at wall becomes weaker. Therefore the lifted vortices due to blowing get stronger, resulting in the increase of the turbulence intensity as well as the skin friction downstream of the slot. The opposite effect is observed in the case of suction. In the downstream of the slot, the center of the streamwise vortices returns to nearly the same y -location as the unmanipulated case but with different magnitudes in both cases of blowing and suction.

CONCLUSION

In the present study, we investigated effects of blowing/suction from a spanwise slot of $L^+ \simeq 100$ on a turbulent boundary layer using the direct numerical simulation technique. Even though the magnitude of uniform blowing/suction was very small, $|v_w| = 0.018u_\infty$, it significantly changed the skin friction as well as the streamwise vortex above the wall. In the case of uniform blowing, the skin friction on the slot was significantly decreased. On the other hand, the streamwise vortices above the wall were lifted up by blowing, and thus the interaction of the vortices with the wall was reduced. Therefore, the lifted vortices became stronger, resulting in the increase of the turbulence intensity as well as the skin friction downstream of the slot. In the case of uniform suction, the skin friction on the slot was increased, while the intensity of the streamwise vortices and turbulence intensities were reduced, resulting in the decrease of the skin friction downstream of the slot.

Acknowledgements : This work is sponsored by the Cray Research, Inc. The use of the supercomputer facilities from SERI is appreciated.

REFERENCES

- Antonia, R. A., and Fulachier, L., 1989, "Topology of a boundary layer with and without wall suction," *J. Fluid Mech.*, Vol. 198, 429.
- Antonia, R. A., Zhu, Y., and Sokolov, M., 1995, "Effect of concentrated wall suction on a turbulent boundary layer," *Phys. Fluids*, Vol. 7, 2465.
- Bandyopadhyay, P. R., 1986, "Review - mean low in turbulent boundary layers disturbed to alter skin friction," *Trans. ASME I: J. Fluids Eng.*, Vol. 108, 127.
- Choi, H., Moin, P., and Kim, J., 1993, "Direct numerical simulation of turbulent flow over riblets," *J. Fluid Mech.*, Vol. 255, 503.
- Choi, H., Moin, P., and Kim, J., 1994, "Active turbulence control for drag reduction in wall-bounded flows," *J. Fluid Mech.*, Vol. 262, 75.
- Choi, H., and Moin, P., 1994, "Effects of the computational time step on numerical solutions of turbulent flow," *J. Comp. Phys.*, Vol. 113, 1.
- Choi, K.-S., 1989, "Near-wall structure of a turbulent boundary layer with riblets," *J. Fluid Mech.*, Vol. 208, 417.
- Kravchenko, A. G., Choi, H., and Moin, P., 1993, "On the relation of near-wall streamwise vortices to wall skin friction in turbulent boundary layers," *Phys. Fluids A*, Vol. 5, 3307.
- Lumley, J. L., 1973, "Drag reduction in turbulent flow by polymer additives," *J. Polymer Sci. D: Macromol. Rev.* Vol. 7, 263.
- Mariani, P., Spalart, P., and Kollmann, W., 1993, "Direct simulation of a turbulent boundary layer with suction," *Near-Wall Turbulent Flows*, edited by R. M. C. So, C. G. Speziale, and B. E. Launder, Elsevier, Amsterdam, 347.
- Na, Y., and Moin, P., 1996, "Direct numerical simulation of turbulent boundary layers with adverse pressure gradient and separations," Report No. TF-68, Thermosciences Division, Dept. of Mechanical Eng., Stanford University.
- Narasimha, R., and Sreenivasan, K. R., 1979, "Relaminarization of fluid flows," *Adv. Appl. Mech.*, Vol. 19, 221.
- Piomelli, U., 1987, "Models for large eddy simulations of turbulent channel flows including transpiration," Ph. D. Thesis, Stanford Univ., Stanford, CA.
- Sano, M., and Hirayama, N., 1985, "Turbulent boundary layers with injection and suction through a slit. First report: Mean and turbulence characteristics," *Bull. J. Soc. Mech. Eng.*, Vol. 28, 807.
- Schlichting, H., 1965, *Boundary Layer Theory*, McGraw-Hill, New-York.
- Schildknecht, M., Miller, J. A., and Meier, G. E. A., 1979, "The influence of suction on the structure of turbulence in fully developed pipe flow," *J. Fluid Mech.*, Vol. 90, 67.
- Sofialidis, D., and Prinos, P., 1996, "Wall suction effects on the structure of fully developed turbulent pipe flow," *J. Fluids Eng.*, Vol. 118, 33.
- Spalart, P. R., 1988, "Direct numerical simulation of a turbulent boundary layer up to $Re_\theta = 1410$," *J. Fluid Mech.*, Vol. 187, 61.
- Sumitani, Y., and Kasagi, N., 1995, "Direct numerical simulation of turbulent transport with uniform wall injection and suction," *AIAA J.*, Vol. 33, 1220.
- Virk, P. S., 1975, "Drag reduction fundamentals," *AIChE J.* Vol. 21, 625.

SUBOPTIMAL TURBULENCE CONTROL WITH THE BODY FORCE OF SELECTIVE VELOCITY DAMPING LOCALIZED TO THE NEAR-WALL REGION

Shin-ichi Satake

Department of Mechanical Systems Engineering
Kogakuin University
Nishi-shinjuku, Shinjuku-ku, Tokyo 163-91
Japan

and

Nobuhide Kasagi

Department of Mechanical Engineering
The University of Tokyo
Hongo, Bunkyo-ku, Tokyo 113
Japan

ABSTRACT

A suboptimal control theory is adopted to maximize the performance of an active turbulence control in the fully developed channel flow. The control input is a virtual body force field, which damps the spanwise velocity fluctuations within a thin layer adjacent to the wall. The method used is to minimize a cost functional, which is constructed so as to represent a balance of the body force strength and the square spanwise velocity gradient; the latter stands for the dominant component of either the streamwise vorticity or the strain rate, which are associated with the near-wall vortical structures. From a series of direct numerical simulations, it is found that the suboptimal control achieves the turbulent drag reduction as large as that obtained by an unoptimized active control, but its damping effect is concentrated at the regions beneath the near-wall vortical structures.

INTRODUCTION

Turbulence control has been one of the central issues in modern scientific, engineering and environmental research efforts. Its potential benefits can be easily recognized if one thinks about the significance of the artificial manipulation of turbulent drag, noise, heat transfer as well as chemical reaction, to name a few. Although there is considerable empirical knowledge on how to attenuate or enhance these processes, the underlying mechanisms in most cases have not been fully explored. Hence, any attempt at optimizing the turbulence control is likely to be based on empiricism or intuition. A good example of the use of engineering intuition in the design of the flow control schemes is the active cancellation of the effect of near-wall vortices employed by Choi et al. (1994). This scheme, being applied to a turbulent channel flow, demonstrated about 20% drag reduction, and the sensing location at $y^+ = 10$ achieved the best result.

Recently, Choi et al. (1993) devised a suboptimal and feedback control algorithm for the Navier-Stokes equations and applied it to the stochastic Burgers equation. As a result, the proposed control method produced significant reductions in the cost functions defined. Their suboptimal control algorithm can be implemented in real applications in contrast to the optimal control theory suggested by Aberger & Temam (1990). The latter provides more ideally optimized control distributions, but can not be exploited in reality. Choi (1995) applied the developed suboptimal control algorithm to a turbulent channel flow and a vortex

shedding behind a circular cylinder. The control method used in his study is an extended version of the algorithm developed by Choi et al. (1993) and Bewley et al. (1993).

The knowledge on the quasi-coherent structures in wall turbulence (Cantwell, 1981; Robinson, 1991; Kasagi et al., 1995) provides a physical target for the control schemes to be developed. The control efforts should be coordinated to manipulate these turbulent structures. For example, referring to the drag reduction mechanisms on the riblet surface deduced by Suzuki & Kasagi (1994), Satake & Kasagi (1995) found that a drag reduction as much as about 15 % in the fully developed channel flow could be achieved by damping selectively the spanwise velocity component in a limited region adjacent to the wall ($0 < y^+ < 10$). This control method turned out to be very effective in terms of the ratio of the pumping power saved to the required work, which reached as much as 80.

In the present study, we extend our work mentioned above and assume a virtual body force field damping the spanwise velocity component in a thin layer attached to the wall. Although the strength of this force field was assumed to be constant in the previous study, its spatio-temporal distribution is now designed by the suboptimal control theory of Choi et al. (1993). Trial cost functional to be minimized is defined by referring to the dominant kinematics of the quasi-coherent vortical structures. The suboptimal control scheme is implemented numerically in the direct numerical simulation (DNS) of turbulent channel flow. The present results are compared with the authors' previous DNS (Satake & Kasagi, 1995), in which the body force strength parameter has been kept constant.

FORMULATION OF SUBOPTIMAL CONTROL

The governing equations of a plane channel flow are

$$\frac{\partial u_i}{\partial t} + \frac{\partial u_i u_j}{\partial x_j} = -\frac{\partial p}{\partial x_i} + \frac{1}{Re_\tau} \frac{\partial^2 u_i}{\partial x_j^2} - \alpha u_i \delta_{3i}, \quad (1)$$

$$\frac{\partial u_i}{\partial x_i} = 0, \quad (2)$$

with a no-slip boundary condition on the two walls, where x_i ($i = 1, 2, 3$) denote the streamwise, wall-normal and spanwise directions, respectively. Here, the velocities are non-dimensionalized by the friction velocity u_w in the uncontrolled channel. The last term on the RHS of equation (1) is the virtual body force term,

whose strength is given by a dimensionless parameter α . This parameter is a function of time and location, but has non-zero values only in the region of $0 < y^+ < 10$ and its value is to be determined by the suboptimal control algorithm (Choi et al., 1993). In the previous study it was assumed constant ($\alpha = 0 \sim 4$), but larger constant values are also tested in this study.

Presently, the control is aimed to minimize two kinds of the spanwise velocity components in the near-wall region, since the reduction of such components is expected to result in the attenuation of the near-wall vortices. We test two cost functionals defined as:

$$J_1(\alpha) = \frac{\ell}{2} \int_V \alpha^2 C(x_2) dv + \frac{m}{2} \int_V \left(\frac{\partial u_3}{\partial x_2} \right)^2 C(x_2) dv, \quad (3)$$

$$J_2(\alpha) = \frac{\ell}{2} \int_V \alpha^2 C(x_2) dv + \frac{m}{2} \int_V \left(\frac{\partial u_2}{\partial x_3} \right)^2 C(x_2) dv, \quad (4)$$

where ℓ and m are weighting parameters, and V denotes the computational volume, respectively. These equations are multiplied by $C(x_2)$ to restrict the damping effect to the zone of $0 < y^+ < 10$. This function is 1 at $0 < y^+ < 10$ and otherwise zero. The first terms in Eqs. (3) and (4) are a measure of the magnitude of the control, whereas the second terms represent the quantities to be reduced. It is noted that the latter terms correspond to the major components of the rotation and strain rates, respectively, that are associated with the quasi-coherent streamwise vortex near the wall (Iida & Kasagi, 1993). These components are schematically illustrated in Fig. 1. The deformation components around streamwise vortex represented as:

$$\begin{pmatrix} 0 & 0 & 0 \\ 0 & \frac{\partial u_2}{\partial x_2} & \Omega_1 \\ 0 & -\Omega_1 & -\frac{\partial u_2}{\partial x_3} \end{pmatrix} = \begin{pmatrix} 0 & 0 & 0 \\ 0 & 0 & \frac{1}{2} \left(\frac{\partial u_2}{\partial x_3} - \frac{\partial u_3}{\partial x_2} \right) \\ 0 & -\frac{1}{2} \left(\frac{\partial u_2}{\partial x_3} - \frac{\partial u_3}{\partial x_2} \right) & 0 \end{pmatrix} + \begin{pmatrix} 0 & 0 & 0 \\ 0 & \frac{\partial u_2}{\partial x_2} & 0 \\ 0 & 0 & -\frac{\partial u_2}{\partial x_3} \end{pmatrix}. \quad (5)$$

Thus, we consider two forms of cost functional; one contains the term of $\partial u_3 / \partial x_2$, which is dominant in the streamwise vorticity component, and the other the $\partial u_2 / \partial x_3$ term, which represents the redistribution (pressure-strain) mechanism for the spanwise turbulent kinetic energy.

If the viscous terms in the wall-normal direction and the body force term in Eq. (1) are approximated by the Crank-Nicolson method and the other terms by the Adams-Bashforth method, then the resulting equations are

$$u_i^n - \frac{\Delta t}{2Re_\tau} \frac{\partial^2 u_i^n}{\partial x_j^2} + \frac{\Delta t}{2} \alpha u_i^n \delta_{3i} C(x_2) + \Delta t \frac{\partial p^n}{\partial x_i} = Q_i^{n-1}, \quad (6)$$

where n denotes the current time step, whilst Q_i^{n-1} represents all the terms evaluated at the time step $n-1$. Taking a Frechet deriva-

tive (Finlayson, 1972) of Eq. (6) against an infinitesimal change of the force strength parameter $\hat{\alpha}$ gives

$$\eta_i^n - \frac{\Delta t}{2Re_\tau} \frac{\partial^2 \eta_i^n}{\partial x_j^2} + \frac{\Delta t}{2} \hat{\alpha} u_i^n \delta_{3i} C(x_2) + \frac{\Delta t}{2} \alpha \eta_i^n \delta_{3i} C(x_2) + \Delta t \frac{\partial p_\eta^n}{\partial x_i} = 0, \quad (7)$$

where $\eta_i^n \equiv \frac{Du_i^n}{D\alpha} \hat{\alpha}$, and $p_\eta^n \equiv \frac{Dp^n}{D\alpha} \hat{\alpha}$. When the cost functional given by Eq. (3) is adopted, the adjoint equation corresponding to Eq. (7) is derived as:

$$\zeta_i^n - \frac{\Delta t}{2Re_\tau} \frac{\partial^2 \zeta_i^n}{\partial x_j^2} + \frac{\Delta t}{2} \alpha \zeta_i^n \delta_{3i} C(x_2) + \Delta t \frac{\partial p_\zeta^n}{\partial x_i} = -\frac{\partial^2 u_i^n}{\partial x_j^2} \delta_{3i} C(x_2), \quad (8)$$

$$\frac{\partial \zeta_i^n}{\partial x_i} = 0. \quad (9)$$

Here, Eqs. (7) and (8) must satisfy the following relationship:

$$\langle A \eta_i^n, \zeta_i^n \rangle = \langle \eta_i^n, A^* \zeta_i^n \rangle + b, \quad (10)$$

where $\langle \cdot \rangle$ is a inner product, and A^* is an adjoint operator. The boundary term b is set to be zero, and then the boundary condition for Eq. (8) leads to $\zeta_i^n = 0$ on the walls.

The Frechet derivative of the cost functional is given as:

$$\begin{aligned} \frac{DJ_1(\alpha)}{D\alpha} \hat{\alpha} &= \lim_{\epsilon \rightarrow 0} \frac{J_1(\alpha + \epsilon \hat{\alpha}) - J_1(\alpha)}{\epsilon} \\ &= \ell \int_V \alpha \hat{\alpha} C(x_2) dv + m \int_V \frac{\partial}{\partial x_2} \left(\frac{Du_3}{D\alpha} \hat{\alpha} \right) C(x_2) dv \\ &= \ell \int_V \alpha \hat{\alpha} C(x_2) dv + m \int_V \frac{\partial \eta_3}{\partial x_2} \hat{\alpha} C(x_2) dv \\ &= \ell \int_V \alpha \hat{\alpha} C(x_2) dv - m \int_V \frac{\Delta t}{2} u_3 \zeta_3 \hat{\alpha} C(x_2) dv. \end{aligned} \quad (11)$$

Then, the gradient of the cost functional becomes

$$\frac{DJ_1}{D\alpha} = \ell \alpha C(x_2) - \frac{\Delta t}{2} m u_3 \zeta_3 C(x_2). \quad (12)$$

Finally, the gradient algorithm, by which the distribution of α is renewed at each time step, is written as:

$$\begin{aligned} \alpha^{k+1} &= \alpha^k - \rho \frac{DJ_1(\alpha)}{D\alpha} \\ &= \alpha^k - \rho \left(\ell \alpha^k C(x_2) - \frac{\Delta t}{2} m u_3 \zeta_3 C(x_2) \right), \end{aligned} \quad (13)$$

where the superscript k indicates an iteration step. In this study, we restrict the number of the iteration to be only one.

NUMERICAL PROCEDURE

The convective terms, the pressure terms in the momentum equations (1) and the continue equation (2) are discretized by using the fourth-order central finite difference method proposed by Morinishi (1995) on the staggered grid. This scheme has been proved to be conservative for higher-order accurate finite difference schemes. For time integration, the Crank-Nicolson scheme and the second-order Adams-Bashforth scheme are employed for the viscous terms in the wall-normal direction and the other terms,

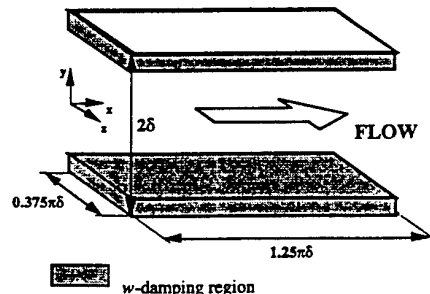


Figure 2. Computational domain.

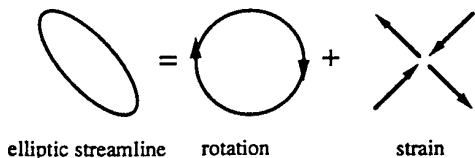


Figure 1. Schematic view of a strained streamwise vortex.

Table 1 Parameter for suboptimal control

Case	Cost Functional	ℓ	m	ρ
1	$J_1(\alpha)$	1	1000	0.01
2	$J_2(\alpha)$	1	1000	0.01
3	$J_1(\alpha)$	0	1	10
4	$J_2(\alpha)$	0	1	10

respectively. The time integration is made by the partially implicit fractional step method developed by Kim & Moin (1985). The discretized pressure Poisson equation is solved by a Fast Fourier Transform in the streamwise and spanwise directions and by a septa-diagonal matrix algorithm in the wall-normal direction. The viscous terms in the wall-normal direction is solved implicitly by a penta-diagonal matrix algorithm. The adjoint equation and its solver are coded with a method analogous to that for the flow solver.

COMPUTATIONAL CONDITIONS

The flow geometry and the coordinate system are shown in Fig. 2. The uncontrolled channel flow simulation is used as a baseline for comparison. In the control simulations, the skin-friction reduction has been observed in terms of the change in the mean pressure gradient, which is required to drive the flow at a fixed mass flow rate. The Reynolds number, which is based on the bulk mean velocity u_b and the channel width 2δ , is assumed to be 4365. The streamwise and spanwise computational periods are $1.25\pi\delta$ and $0.375\pi\delta$ (589 and 176 wall units), respectively. The number of grid points is $48 \times 97 \times 36$ in the x -, y - and z -directions, respectively.

Starting from the same initial state reached by the uncontrolled channel flow simulation, several trial controls are repeated. In addition to the suboptimal control, some constant values of α are tested. All the results shown in the following section are non-dimensionalized by the initial wall friction velocity u_w and the kinematic viscosity ν . Presently, we examine four different cases for two cost functionals with two weighting parameters as listed in Table 1. The relative magnitude of ℓ against m should be modified according to the cost and the degree of importance of the control; ℓ can be very small when the control is cheap and easy to implement. However, these values of ℓ and m are quite arbitrarily chosen. Another parameter ρ in Table 1 is a descent coefficient in Eq. (13), of which value has been determined by

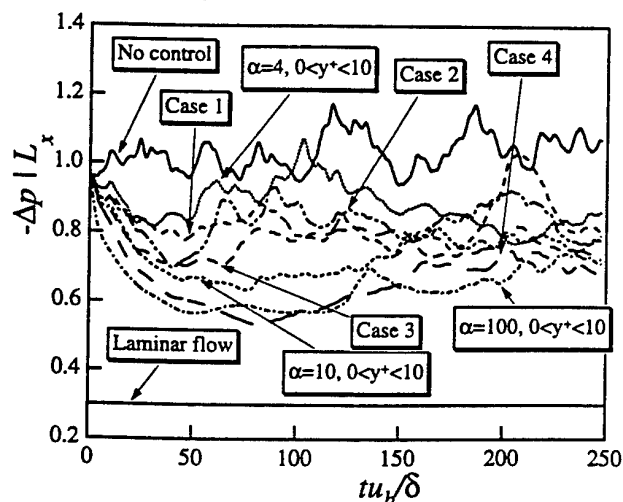


Figure 3. Time trace of mean pressure gradient.

trial and error. The suboptimal control results are compared with those that have been obtained by assuming constant α , i.e., $\alpha = 4, 10$, and 100 .

RESULTS AND DISCUSSION

The time traces of the volume-averaged pressure gradient with and without control are shown in Fig. 3, in which also included are those with α kept constant as $\alpha = 4, 10$, and 100 . In all cases tested, the effect of control readily becomes evident once the control is started. Initially, Case 4 and the case of the largest $\alpha (=100)$ seem most effective and give a drag reduction as much as 40%, but later both curves tend to return to a level of about 25% reduction. For the bulk Reynolds number considered here, the maximum turbulent drag reduction possible is about 70%, which would correspond to a laminar flow state. Case 3 becomes eventually effective to the same degree as Case 4, although the initial effect is not so large as in Case 4. It is noted that, in Cases 3 and 4, the cost of the control has not been accounted for. Cases 1 and 2 are less effective than Cases 3 and 4, but they become equally effective at the later period. When α is kept constant, the drag is simply decreased as α is increased.

Figure 4 shows the cumulative time-averaged gain in the pumping work (or work saved), which is defined as:

$$\bar{G} = \frac{1}{T} \int_0^T \left(-\frac{dp}{dx}_u + \frac{dp}{dx}_d \right) u_b dt, \quad (14)$$

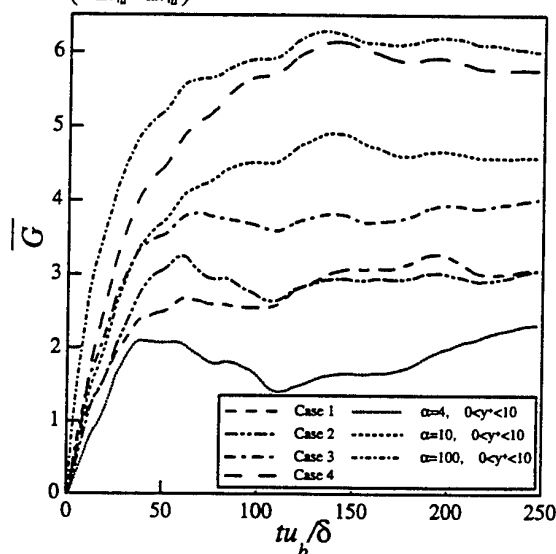


Figure 4. Time-averaged gain in pumping work.

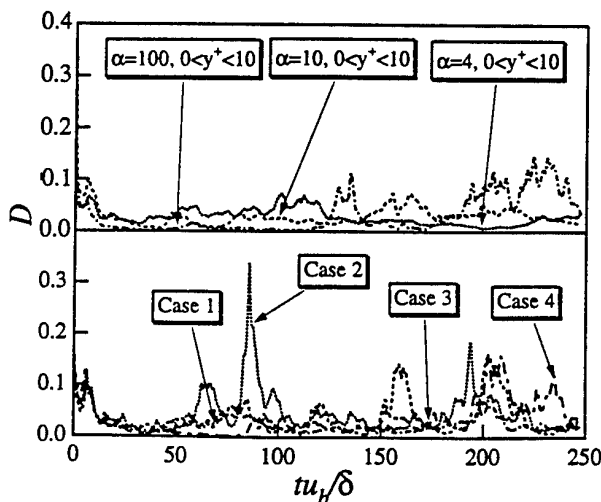


Figure 5. Damping dissipation.

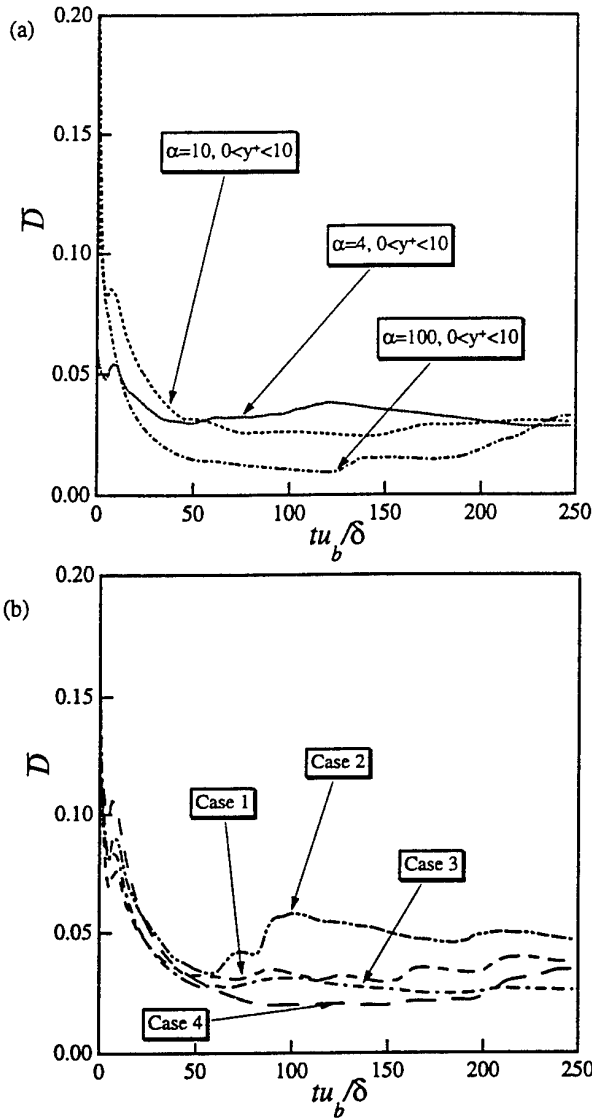


Figure 6. Time-averaged damping dissipation: (a) constant α control and (b) suboptimal control.

where $-dp/dx|_u$ and $-dp/dx|_d$ are the mean pressure gradients in the uncontrolled and controlled channels, respectively. This quantity \bar{G} initially increases with time, but eventually levels off at a constant, which depends on the control condition. Among the suboptimal controls, Case 4 gives the best result, which is comparable to the case with $\alpha = 100$, and the second best is Case 3. Here, the better result has been obtained by the cost functional of $J_2(\alpha)$. Case 1 exhibits almost the same degree of the work saved as in Case 2; the difference due to the different cost functionals seems small in these cases.

Figure 5 shows the time traces of the damping dissipation defined as:

$$D = \frac{1}{V} \int_V \alpha \omega_3^2 C(x_2) dv, \quad (15)$$

which is interpreted as the instantaneous dissipative work per volume done against the imposed force field. In general, it is initially very large ($tu_b/\delta < 10$, say), particularly in the case of a large damping parameter ($\alpha = 100$), but later becomes small. Thus, once the turbulence is reduced to some degree (see Fig. 3), it may not be necessary to continuously damp the turbulence strongly. However, the turbulence survives longer and sometimes grows

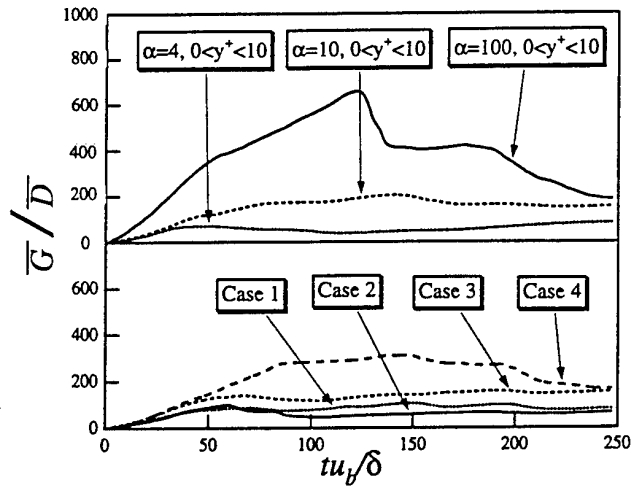


Figure 7. The efficiency of the control.

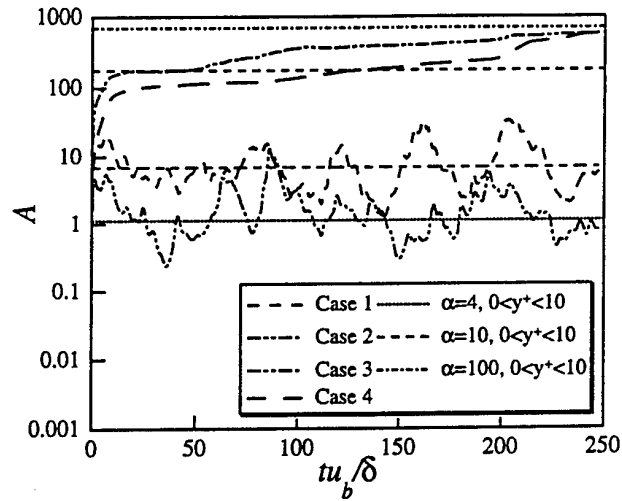


Figure 8. Time trace of mean-square damping parameter, Eq. (17).

markedly at a late period, and then the damping dissipation leaps to a high level as shown in Fig. 5. Figure 6 shows the cumulative time-averaged damping dissipation defined as:

$$\bar{D} = \frac{1}{T} \int_0^T \frac{1}{V} \int_V \alpha \omega_3^2 C(x_2) dv dt. \quad (16)$$

This work is again initially very large, particularly in the case of $\alpha = 100$, but levels off to a smaller value later.

The efficiency of the control, which is defined as the ratio of the pumping power saved to the the damping dissipation, is shown in Fig. 7. This ratio fluctuates considerably, and it is found that the total length of time integral has not been sufficiently long. Despite this fact, the efficiency seems better with larger α among the cases of constant α , whilst Case 4 seems to give the best result, which is comparable with that of $\alpha = 100$, among the suboptimal controls. It is noted, however, that the comparison between Cases 3 and 4 should also depend on the value of the descent parameter of ρ .

Figure 8 shows the volume-averaged square damping force parameter defined as:

$$A = \frac{1}{V} \int_V \alpha^2 C(x_2) dv. \quad (17)$$

The straight lines represent the cases in which α is constant time. In Cases 3 and 4, A approaches asymptotically some constant value,

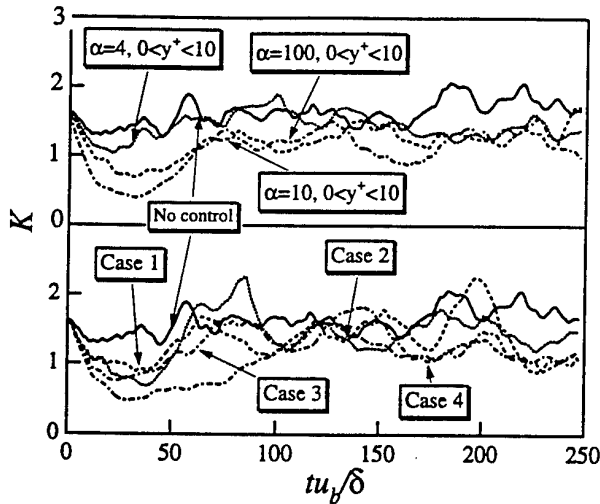


Figure 9. Volume-averaged turbulent kinetic energy.

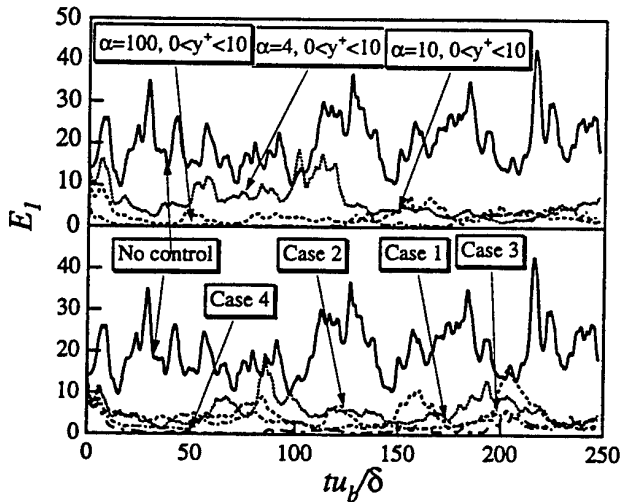


Figure 10. Time-trace of E_1 .

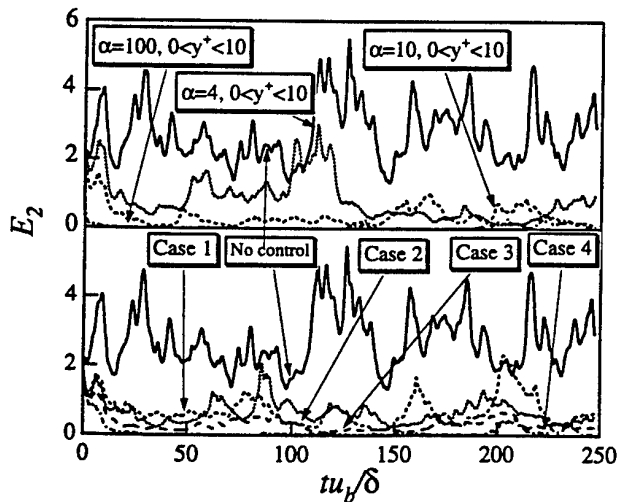


Figure 11. Time-trace of E_2 .

which is a little smaller than that of $\alpha = 100$. However, α in Cases 1 and 2 are much smaller than in Cases 3 and 4, and oscillates in time. This is because the parameter ℓ is not zero in Cases 1 and 2, so that the magnitude of α is also minimized.

The volume-averaged turbulent kinetic energy defined as:

$$K = \frac{1}{V} \int_V u'_i u'_i / 2 \, dv, \quad (18)$$

is shown in Fig. 9. In the suboptimal control cases and the cases with larger damping parameters, K is initially diminished effectively. In most cases, however, K approaches eventually almost the same steady level, which is still appreciably smaller than that without control.

Figure 10 shows the time histories of the square spanwise velocity gradient:

$$E_1 = \frac{1}{V} \int_V \left(\frac{du_3}{dx_2} \right)^2 dv, \quad (19)$$

which is one of the two terms in the cost functional of $J_1(\alpha)$ and is interpreted as an index of the streamwise vorticity. Initially, this quantity is decreased drastically by all suboptimal controls regardless of the adopted definitions of the cost functionals, but later it fluctuates considerably. However, the dependence upon the weighting parameters is visible. Thus, the performance of the suboptimal control can be improved by carefully tuning the cost functional. In Fig. 11, the square spanwise velocity gradient defined as:

$$E_2 = \frac{1}{V} \int_V \left(\frac{du_3}{dx_3} \right)^2 dv, \quad (20)$$

for $J_2(\alpha)$ is shown. This quantity can be interpreted as an index of the pressure strain correlation associated with the near-wall streamwise vortices. It behaves in a manner similar to E_1 , but the order of magnitude of E_2 is much smaller.

Figure 12(a) shows instantaneous velocity vectors and the gradation contour of $\partial u_3 / \partial x_2$ in the $x_2 - x_3$ plane in Case 3 at $tu_y / \delta = 0.06$, which is at the very initial stage of the evolution of the controlled flow field. As seen in this figure, a strongly negative value of $\partial u_3 / \partial x_2$ can be found in the central region of a vortex, whereas strongly positive regions are also found on the upper and lower sides of the vortex. In addition, there are some regions of large magnitudes of $\partial u_3 / \partial x_2$ in the thin layer of damping. The optimized distribution of the damping force at the same instant is shown in Fig. 12(b). As is expected, the damping force is strong where the vorticity component is large in Fig. 12(a), regardless whether the vortex exists above the thin layer or not. Thus, in this control mode, the streamwise vorticity component is distinctly suppressed unlike the cases of constant α , where the spanwise velocity itself is suppressed.

The similar results in Case 4 are shown in Figs. 13(a) and (b), where the large magnitude of $\partial u_3 / \partial x_3$ well corresponds to that of $-\alpha u'_3$ beneath a vortical structure. In this case, the intercomponent transfer of turbulent kinetic energy to the spanwise component is limited by the control.

Finally, instantaneous velocity vectors and the damping force of $-\alpha u'_3$ in the $x_2 - x_3$ plane when $\alpha = 10$ are shown in Fig. 14. The magnitude of the damping force is very large regardless its sign throughout the whole damping region, since its distribution has not been optimized.

CONCLUSIONS

A suboptimal control theory is adopted to maximize the performance of an active turbulence control in the fully developed turbulent channel flow. The control input is a virtual body force field, which damps the spanwise velocity fluctuations within a thin layer adjacent to the wall. Two kinds of cost functional forms are employed and tested. The functionals are constructed so as to represent a balance of the body force strength and the square spanwise velocity gradient. The numerical results obtained by direct numerical simulations are presented.

It is found that the suboptimal control achieves the turbulent drag reduction as large as that obtained by the unoptimized active control. The control efficiency is also comparable in the suboptimal and constant- α cases. It is seen that, in the suboptimal con-

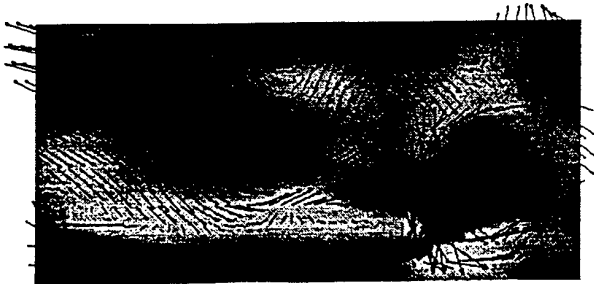


Figure 12(a). Instantaneous velocity vector and $\partial u_3 / \partial x_2$ in the x_2 - x_3 plane at $tu_f / \delta = 0.06$ in Case 3: gray to white; $\partial u_3 / \partial x_2 = 0$ to +3, gray to black; $\partial u_3 / \partial x_2 = 0$ to -3.

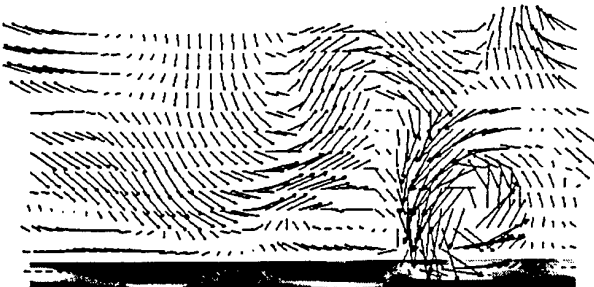


Figure 12(b). Instantaneous velocity vector and $-au_3$ in the x_2 - x_3 plane at $tu_f / \delta = 0.06$ in Case 3: gray to white; $-au_3 = 0$ to +3, gray to black; $-au_3 = 0$ to -3.

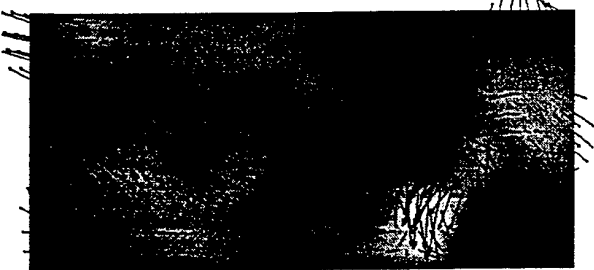


Figure 13(a). Instantaneous velocity vector and $\partial u_3 / \partial x_3$ in the x_2 - x_3 plane at $tu_f / \delta = 0.06$ in Case 4: gray to white; $\partial u_3 / \partial x_3 = 0$ to +3, gray to black; $\partial u_3 / \partial x_3 = 0$ to -3.

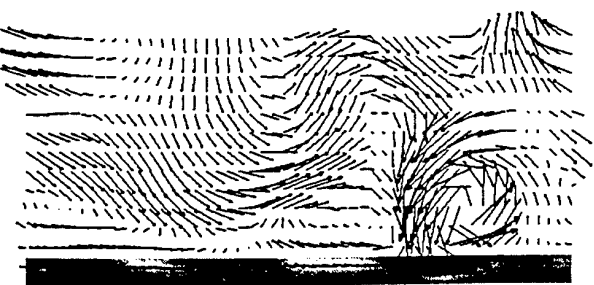


Figure 13(b). Instantaneous velocity vector and $-au_3$ in the x_2 - x_3 plane at $tu_f / \delta = 0.06$ in Case 4: gray to white; $-au_3 = 0$ to +3, gray to black; $-au_3 = 0$ to -3.

control, the damping force distribution has high correlation with that of the velocity deformation component, which has been introduced into the cost functional. Thus, damping effect is concentrated on the region beneath the streamwise vortex unlike the cases with α kept constant, where the damping force appears large regardless of the existence of the vortex.

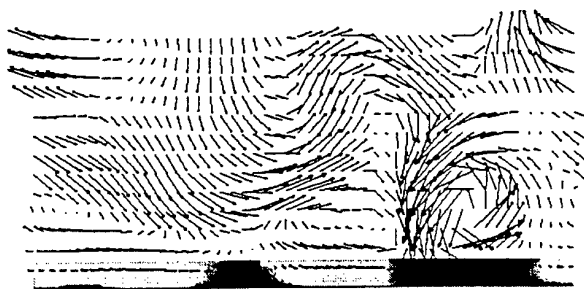


Figure 14. Instantaneous velocity vector and $-au_3$ in the x_2 - x_3 plane at $tu_f / \delta = 0.06$ in the case of $\alpha = 10$: gray to white; $-au_3 = 0$ to +3, gray to black; $-au_3 = 0$ to -3.

ACKNOWLEDGMENTS

The authors are grateful to Professor Haecheon Choi at Seoul National University for his discussions on the suboptimal control theory and also to Professor Youhei Morinishi at Nagoya Institute of Technology for his suggestion on the fourth-order central finite difference scheme. This work was supported through the Grant-in-Aids for Scientific Research on Priority Areas (No. 05240103) and for Encouragement of Young Scientists (No. 06003542) by the Ministry of Education, Science and Culture.

REFERENCES

- Abergel, F. and Temam, R., 1990, "On some control problems in fluid mechanics," *Theor. Comput. Fluid Dyn.* 1, p. 303.
- Bewley, T., Choi, H., Temam, R. and Moin, P., 1993, "Optimal feedback control for turbulent channel flow," *CTR Annual Research Briefs 1993*, pp. 3-14.
- Cantwell, B., 1981, "Organized motion in turbulent flows," *Annu. Rev. Fluid Mech.*, J. L. Lumley, M. Van Dyke and H. L. Reed, (eds), Vol. 13, pp. 457-515.
- Choi, H., Moin, P. and Kim, J., "1994. Active turbulence control for drag reduction in wall-bounded flows," *J. Fluid Mech.*, Vol. 262, pp. 75-110.
- Choi, H., Temam, R., Moin, P. and Kim, J., 1993, "Feed back control for unsteady flow and its application to the stochastic Burgers equation," *J. Fluid Mech.*, Vol. 253, pp. 509-543.
- Choi, H., 1995, "Suboptimal control of turbulent flow using control theory," *Proc. of the International Symp. on Mathematical Modeling of Turbulent Flows*, Tokyo, Japan, pp. 131 - 138.
- Finlayson, B. A., 1972, "The method of weighted residuals and variational principles," Academic Press.
- Iida, O. and Kasagi, N., 1993, "Redistribution of the Reynolds stresses and destruction of the turbulent heat flux in homogeneous decaying turbulence," *Proc. 9th Turbulent Shear Flows*, Kyoto, 24-4-1.
- Kasagi, N., Sumitani, Y., Suzuki, Y. and Iida, O., 1995, "Kinematics of the quasi-coherent vortical structure in near-wall turbulence," *Int. J. Heat & Fluid Flow*, Vol. 16, pp. 2-10.
- Kim, J. and Moin, P., 1985, "Application of a fractional-step method to incompressible Navier-Stokes equations," *J. Comp. Phys.*, Vol. 59, pp. 308-323.
- Lee, M. J. and Hunt, J. C. R., 1988, "The structure of sheared turbulence near a plane boundary," *Proc. CTR Summer Program*, CTR, Stanford University, CA, pp. 221-241.
- Morinishi, Y., 1995, "Conservative properties of finite difference schemes for incompressible flow," *CTR Annual Research Briefs 1995*, pp. 121-132.
- Robinson, S.K., 1991, "The kinematics of a turbulent boundary layer structures," *NASA TM-103859*.
- Satake, S. and Kasagi, N., 1995, "Turbulence control with a wall-adjacent thin Layer Spanwise Damping Force," *Int. J. Heat & Fluid Flow*, Vol. 17, pp. 343-352.
- Suzuki, Y. and Kasagi, N., 1994, "On the turbulent drag reduction mechanism above a riblet surface," *AIAA J.*, Vol. 32, No. 9, pp. 1781-1790.

TURBULENT CHARACTERISTICS IN TRANSITION REGION OF DILUTE SURFACTANT DRAG REDUCING FLOWS

Yasuo Kawaguchi¹⁾, Hisashi Daisaka²⁾, Akira Yabe¹⁾,
Koichi Hishida²⁾ and Masanobu Maeda²⁾

1) Department of Energy Engineering,
Mechanical Engineering Laboratory, AIST MITI,
1-2 Namiki, Tsukuba 305 Japan

2) Department of System Design Engineering,
Keio University,
3-14-1 Hiyoshi, Yokohama 223 Japan

ABSTRACT

Turbulent characteristics of a dilute surfactant/water solution in a two-dimensional channel have been experimentally investigated. Mean velocity and turbulent stress distributions were examined in the Reynolds number range from 0.93×10^4 to 6.83×10^4 using a two component LDV system.

The friction factor behavior for the surfactant solution flow showed a critical phenomena wherein the drag reduction effectiveness disappeared at critical Reynolds number, Re_c . To gain insight into this phenomena, turbulent characteristics and shear viscosity of the solution were examined near the critical Reynolds number.

There was no remarkable structural change indicated by the shear viscosity behavior around Re_c even large change of friction factor appeared. Based on the observation of friction factor, mean velocity profile and turbulence characteristics, we can divide the Reynolds number range into three regimes. Each of these regimes have been characterized in this report. In the region where large drag reduction existed, the streamwise and vertical turbulent normal stress components were suppressed and the Reynolds shear stress disappeared. It was found that suppression of Reynolds shear stress in drag reducing flow can be related to suppressed ejection and sweep events and intensified interaction events.

NOMENCLATURE

Latin Letters

$DR\% = 100 \frac{f_0 - f}{f_0}$ percentage drag reduction

$f = \frac{\tau_w}{0.5\rho_s U_b^2}$ friction factor

H channel height (m)

$Re = \frac{U_b H}{\nu_s}$ Reynolds number

U streamwise mean velocity (m/s)

u' streamwise velocity fluctuation intensity (m/s)

$U_\tau = \sqrt{\frac{\tau_w}{\rho}}$ friction velocity (m/s)

v' normal velocity fluctuation intensity (m/s)
 x, y, z coordinates in the streamwise, normal and spanwise directions respectively (m)

W channel width (m)

Greek Letters

ν kinematic viscosity (m^2/s)
 τ frictional stress (Pa)

Subscripts and Superscript

b bulk
 c critical
 w value at the wall
 s solvent (=water)
 0 reference
 $+$ normalized by inner scale U_τ and ν

1. INTRODUCTION

When drag reducing additives, such as surfactants, are added to water, they suppress turbulence even at high Reynolds numbers (Gyr and Bewersdorff). They have been shown to exhibit remarkable effectiveness in reducing frictional drag in pipes, and since the lifetime is fairly long, they can be used in closed systems such as district heating/cooling systems (Hammer, Pollert et al.), and they can be expected to help conserve energy needed for water recirculation. When surfactants are used in district heating and cooling systems, dilute solutions are preferred because they reduce environmental impact and prevent corrosion in the system.

In previous studies, the authors conducted LDV measurements of the turbulence of drag reducing flow in a two-dimensional water channel (Kawaguchi et al. 1996a) and examined turbulent characteristics including Reynolds shear stress. Kawaguchi et al. (1996b) also experimentally

Surfactant	Cetyltrimethyl ammonium chloride (CTAC)
Product name	Catinar CTC-70ET
Supplier	Toho Kagaku Co. (Japan)
Chemical Formula	$C_{16}H_{33}N(CH_3)_3Cl$ (MW=320.00)

Table 1 DESCRIPTION OF SURFACTANT ADDITIVE

investigated the instabilities of drag reducing flow caused by a heater element on the channel wall, for the purpose of heat transfer enhancement in drag reducing flow.

The friction factor behavior for the surfactant solution flow shows a critical phenomena wherein the drag reduction effectiveness disappeared at critical Reynolds number, Re_c . Recently, Kawaguchi *et al.* (1997) performed a study of heat transfer characteristics in a dilute surfactant solution and found that Re_c could be controlled by changing the flow temperature slightly. Specifically, the heat transfer coefficient and friction factor tripled over a surprisingly small 3°C fluid temperature increase. Similar effects could be obtained by applying mechanical treatments such as preshear, vibration and so on.

As the first step in studying such active control method, this report will clarify the turbulent characteristics by focusing on phenomena around the critical Reynolds number through investigation using LDV and rheological measurements.

2. EXPERIMENTAL FACILITIES AND PROCEDURES

2.1 Surfactant Additives

Measurements were made using the quaternary ammonium salt detailed in Table 1. The surfactant solution was prepared by adding a weight concentration of 50ppm CTAC and 50ppm Sodium Salicylate (156 μ moles/312 μ moles) in tap water. The same additives at the same molar ratio were employed in the preceding studies by Kawaguchi *et al.* (1995, 1996a, 1996b).

2.2 Viscometer

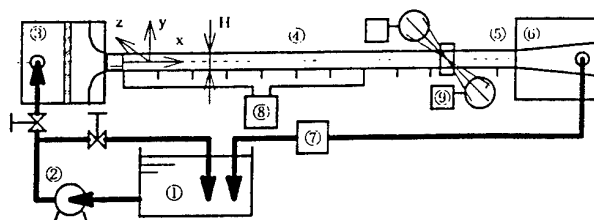
A capillary viscometer having 1.5mm diameter and 1.5m length was used to measure the shear rate dependency of the apparent shear viscosity of the surfactant solution.

2.3 Water Channel

The present experiments were carried out in the closed loop fluid flow facility shown schematically in Figure 1. The basic configuration of the channel and LDV system was unchanged from previous work (Kawaguchi *et al.* 1996a). The test section is 40mm high (H), 500mm wide (W), and 6m long (inside measurements). The LDV measurement position is 5000mm ($\approx 125H$) downstream from the inlet of the test section, and measurements were made across the half height ($H/2$) in the center of the channel ($W/2$). Both sides of the LDV measuring position were fitted with rectangular glass windows. For measurement of pressure drop, a high-precision differential pressure meter was used. The flow rate was measured by an electro-magnetic flow meter.

2.4 LDV System

The LDV measurement system consisted of an argon-ion laser, standard DANTEC 55X optics working in a two-color three-beam mode, forward scatter configuration, two photomultipliers, and two counter-processors. A double beam



① STORAGE TANK ② PUMP ③ CONTRACTION
④ TWO DIMENSIONAL CHANNEL ⑤ LDV MEASURING SECTION ⑥ DIFFUSER ⑦ FLOW METER ⑧ PRESSURE GAGE ⑨ LDV

FIGURE 1. SCHEMATIC DIAGRAM OF THE CLOSED LOOP FLOW FACILITY

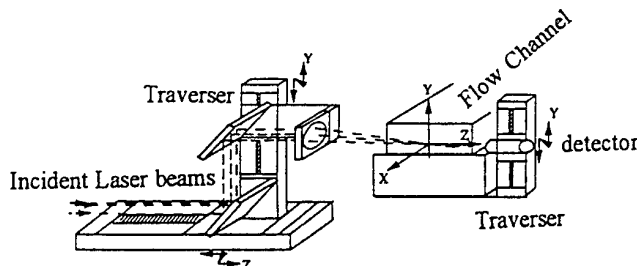


FIGURE 2. LDV MEASUREMENT SYSTEM SHOWING THE COORDINATE FRAMES AND TRAVERSER DIRECTIONS

expander was used to minimize the measurement volume size. The probe volume was 1.3 mm long and the beam waist diameter was 0.08 mm. Coincidence between the two channels was required for the data to be validated and transferred to the acquisition computer. For measurement at each location, 20,000 data points were recorded and analyzed. The sampling frequency was on the order of 10 Hz for most cases.

The LDV and water channel configurations and axes are shown in Figure 2. For the scattering particles, polyethylene beads (Seitetsu Kagaku Co., Flow Beads #1013) were used, which had a diameter of 5 μ m and density of 0.95.

3. RESULT AND DISCUSSION

3.1 Friction Factor

The relationship between the friction factor f of the surfactant solution channel flow and the Reynolds number Re is shown in Figure 3. The values of solution viscosity estimated at a wall shear rate of $\dot{\gamma}_s$, bulk mean velocity U_b , and channel height H were used for characteristic scales. The figure shows that in the region below the critical Reynolds number Re_c , the friction factor is about 75% less than the value for water. When the Reynolds number exceeded Re_c , the drag reducing effect gradually disappeared, causing the friction coefficient f and the wall shear stress τ_w increase asymptotically to the value for water. The friction factor increased fourfold over a relatively narrow Reynolds number range near Re_c , which makes this phenomena interesting from the viewpoint of turbulence control. Furthermore, we can see that increasing the surfactant concentration led to an increase in the critical Reynolds number.

Three types of flow regions can be identified, with respect to Reynolds number, namely (1) Incomplete drag reduction

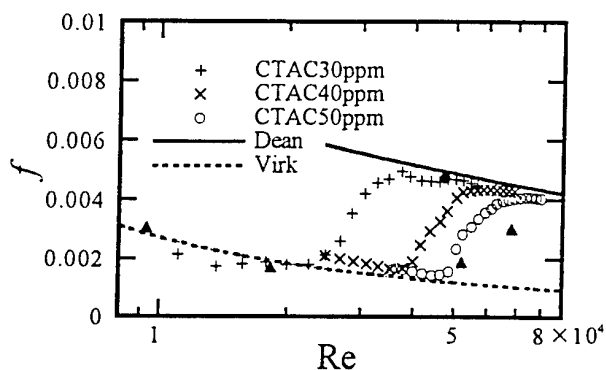


FIGURE 3. EFFECT OF SURFACTANT CONCENTRATION FOR FRICTION FACTOR BEHAVIOR

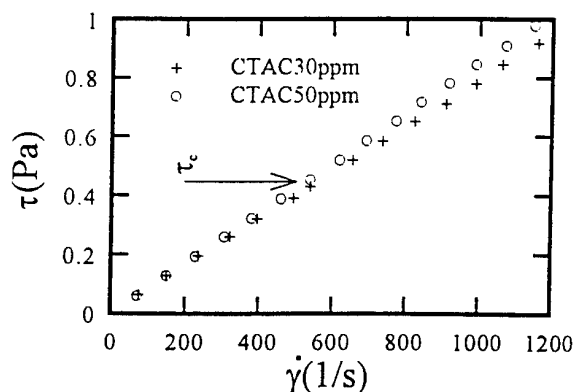


FIGURE 4. SHEAR STRESS/SHEAR RATE DIAGRAM FOR DILUTE SURFACTANT SOLUTION (→: CRITICAL WALL SHEAR STRESS FOR 50PPM)

(DR) region, (2) Complete DR region and (3) Post DR region. Detailed characteristics of mean velocity and turbulent quantities in each region will be examined in the following sections.

3.2 Critical Shear Stress

The critical wall shear stress τ_{wc} corresponding to flow transition has been reported to be unaffected by the diameter of the pipe (Savins). Recently, Usui *et al.* (1996) showed that the friction factor - Re relation for surfactant solution pipe flow can be predicted by accounting for the nonlinear viscosity effect in a viscoelastic dumping factor model. Loss of drag reduction phenomenon was especially conspicuous in water-based polymer solutions, being equivalent to the mechanical destruction of additives. Therefore, a capillary viscometer was used to determine whether or not changes in viscosity appeared near the critical shear stress τ_c . The relationship between shear stress τ and shear rate $\dot{\gamma}$ is usually shown by a rheogram, such as the plot shown in Figure 4 for two concentrations of surfactant solution. Although τ tends to exhibit a slight stress thinning at the low shear rate, the shear viscosity becomes constant when $\dot{\gamma}$ exceeds a certain value. The viscosity here approaches the value for water. The value indicated by the arrow in the figure shows the critical wall shear stress τ_c for a 50ppm CTAC solution in the channel. At this shear rate, the shear viscosity is unchanged, and this indicated that the critical shear rate has no direct relation to fluid property changes in the dilute surfactant solution.

3.3 Mean Velocity Profiles for Surfactant Solution

Measurements of mean velocity and turbulence quantities for surfactant solution flow was made for four cases A to D at different Reynolds numbers. For comparison, experiments using water only (Case W) were also made. Experimental conditions and measured friction factor values are tabulated in Table 2. Friction factor was determined from the pressure drop between the pressure holes on the channel. Shear viscosity was estimated at the shear rate at the wall.

Initially, the effect of Reynolds number on the streamwise mean velocity profile was examined. In Figure 5, velocity profiles for cases A, B, C, and D are shown normalized by inner layer scales. Lines corresponding to velocity profiles for

the viscous sublayer and outer layer of a Newtonian fluid are also shown in the figure. These relations obtained are:

$$U^+ = y^+ \quad [1]$$

$$U^+ = 2.5 \ln y^+ + 5.5 \quad [2]$$

It can be seen that in the region below $y^+ = 12$, a viscous sublayer akin to a Newtonian fluid [1] can be seen for all four cases. In cases A and B, the velocity profile shows an S-shaped curve in the semi-log plot. There exists an outer region for cases A and B where the $U^+ - \ln y^+$ gradient is similar to that of a Newtonian flow [2]. The profile in the outer region can be written as:

$$U^+ = 2.5 \ln y^+ + 5.5 + \Delta B \quad [3]$$

Between these regions, an interactive zone can be seen, the presence of which is characteristic of drag reduction, and is sometimes called the elastic layer. Virk proposed the "Ultimate Profile" for this region, which is written as:

$$U^+ = 11.7 \ln y^+ - 17.0 \quad [4]$$

In the case C, there is no outer region and the velocity profile is covered by Virk's ultimate profile. In contrast with case C, the outer region of case D is described by equation [3] instead of [4]. The diminishing of the elastic layer corresponds to a decrease in drag reduction effect.

3.4 Turbulence Characteristics for Surfactant Solution

Figures 6 to 9 show the effect of Reynolds number on turbulence characteristics. The following comparisons are based on the turbulence intensity normalized by friction velocity. It is necessary here to remember that the turbulence intensity normalized by bulk mean velocity is rather small

Key, Symbol	CTAC concentration (wppm)	T (°C)	U_b (m/s)	Re ($\times 10^4$)	f ($\times 10^{-3}$)	DR%
A, +	50	23.0	0.233	0.93	3.08	57.8
B, x	50	22.0	0.458	1.83	1.71	72.5
C, o	50	23.0	1.300	5.20	1.19	74.7
D, ▲	50	24.0	1.708	6.83	3.17	27.9
W, —	0 (water)	23.0	1.083	4.73	4.74	0

TABLE 2 DESCRIPTION OF EXPERIMENTAL CONDITION

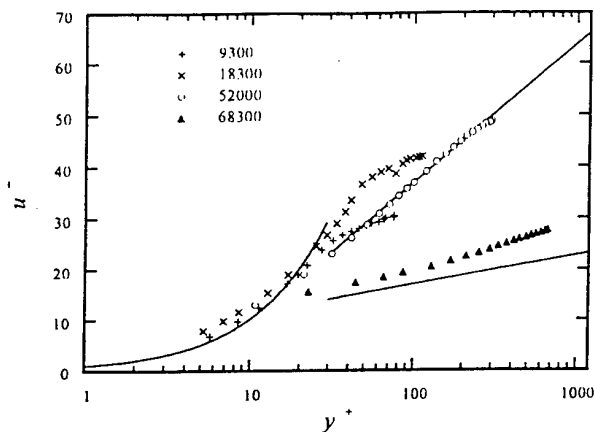


FIGURE 5. EFFECT OF REYNOLDS NUMBER FOR MEAN VELOCITY PROFILES, CTAC 50PPM

when surfactant is added. In the following figures, the results for water are shown by the solid line in each figure. Figure 6 shows the Reynolds number dependency of streamwise turbulence intensity u' . Experiments in the water flow revealed that u'/u_τ takes on a value of 3 at the peak located around $y^+=15$. The u' profile for case D is similar to one normally observed in a Newtonian flow, and value of u'/u_τ for cases A, B, and C becomes equal to or smaller than the case D values at the same y^+ position. Profiles of the vertical component of turbulence intensity are shown in Figure 7. The v' profile for case D is again similar to that in a Newtonian fluid flow. For the other cases, v'/u_τ is about half of that seen in case D for most y^+ positions. As a result of v' suppression, the v'/u' ratio drops to lower values than observed in Newtonian fluid flow. This suggests that anisotropy near the wall is enhanced in the drag reducing flow, which originates from inhibition of the redistribution process.

Figure 8 shows results of Reynolds shear stress measurements at the highly drag reducing case C. Here we can see that the Reynolds shear stress is subdued over the entire channel section. According to investigations of the joint probability density function, this phenomenon is caused by the loss of correlation between the two components of velocity fluctuation u' and v' , and was affected by an extensive attenuation of the organizational structure near the wall. In the case of drag reducing flow, it is known that the shear stress cannot balance the sum of viscous shear stress and turbulent shear stress. Therefore, G , sometimes called the "elastic stress" and defined by the following equation, is not restricted to zero.

$$G = \tau_w \{1 - y/(H/2)\} / \rho \{v(y) \frac{dU}{dy} - \overline{uv}\} \quad [5]$$

The presence of G is not strange for the elastic fluid. As the elasticity means capacity to store energy, deformation and stress can be out of phase in turbulent flow. Therefore, there will be a correlation between velocity fluctuation and elastic stress G in much complicated fashion than the correlation in Newtonian turbulence.

Profiles of G normalized by friction velocity for cases A through D are plotted in Figure 9. As G becomes zero in steady flow, there is a possibility to correlate this with turbulent fluctuation time scale relating to energy storage and some scale. It is seen that G can be correlated by y^+ near the wall and correlated by $y/(H/2)$ in outer layer. It is also interesting to note

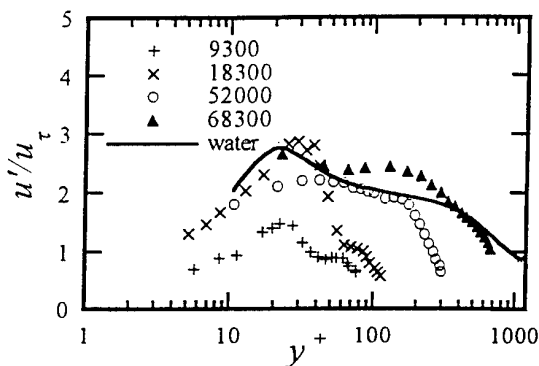


FIGURE 6. EFFECT OF REYNOLDS NUMBER FOR TURBULENT INTENSITY u' PROFILES, CTAC 50PPM

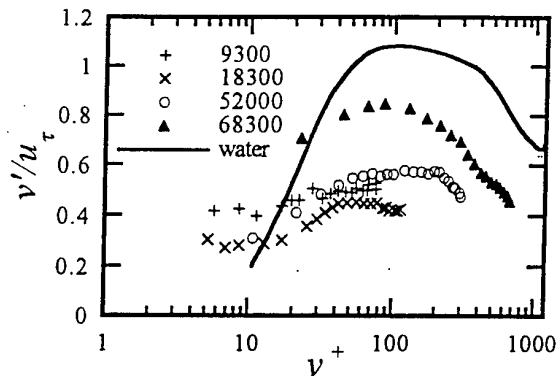


FIGURE 7. EFFECT OF REYNOLDS NUMBER FOR TURBULENT INTENSITY v' PROFILES, CTAC 50PPM

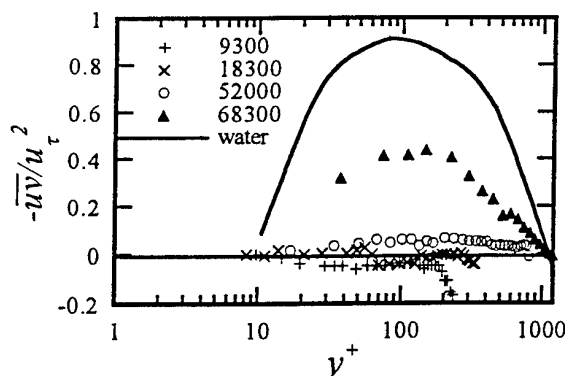


FIGURE 8. EFFECT OF REYNOLDS NUMBER FOR REYNOLDS SHEAR STRESS ($-\overline{uv}$) PROFILES, CTAC 50PPM

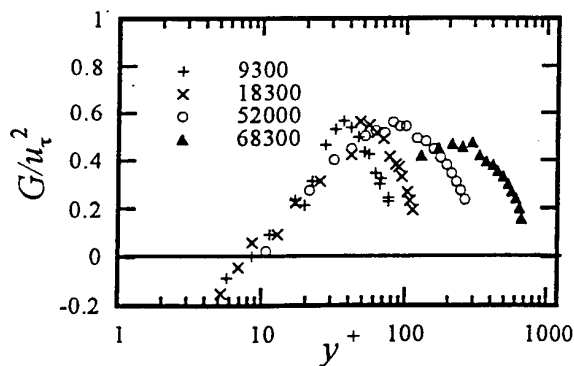


FIGURE 9. EFFECT OF REYNOLDS NUMBER FOR ELASTIC STRESS G PROFILES, CTAC 50PPM

Region	DR%	mean velocity profile	u'/U_τ at the peak	v'/U_τ at the peak	$-uv/U_\tau^2$ at the peak
1) Incomplete DR (Case A and B)	60%/70%	[1]+[4]+[3]	1.0/3.0	~ 0.4	~ 0
2) Complete DR (Case C)	$\sim 75\%$	[1]+[4]	~ 2.0	~ 0.5	~ 0
3) Post DR (Case D)	$\sim 30\%$	[1]+[3]	~ 3.0	~ 0.8	~ 0.4
Water (Newtonian)	0%	[1]+[2]	~ 3.0	~ 1.0	~ 0.9

TABLE 3 CHARACTERISTICS OF REGION 1) TO 3) (\sim : between, \sim : approximately, [n]: profile given by equation [n])

that G is non-zero for case D where drag reduction is not substantial. Therefore, some effect of elasticity is remaining in the turbulence characteristics for case D.

Three types of flow regions were identified from the behavior of friction factor. Major characteristics of mean velocity profile and turbulent quantities of each region are summarized in Table 3. From this table, the following things can be concluded.

1) In the region of incomplete DR, although the outer layer can be regarded as the coexistence of elastic layer and Newtonian outer layer, turbulence characteristics are similar to complete DR region. 2) In the complete DR region, the streamwise and vertical turbulent normal stress components were suppressed and the Reynolds shear stress diminished. 3) In the post DR region, mean velocity profile, turbulent quantities including Reynolds shear stress looks like on the way to recovering and approaching to Newtonian fluid turbulence.

Drag reduction effectiveness is closely related to the diminish of Reynolds shear stress $-uv$. Both components of turbulent intensity u' and v' has finite value even if the Reynolds shear stress diminishes.

3.5 Quadrant Analysis

To investigate the behavior of the Reynolds shear stress more precisely, quadrant analysis proposed by Lu and Willmarth was applied to drag reducing flow. The conditional average of uv normalized by $u'v'$ is shown in figures 10a to 10c, corresponding to case C, case D and the water case, respectively. Contribution from each quadrant \tilde{uv}_i is defined as follows.

$$\tilde{uv}_i = \sum I_q uv \quad [6]$$

$$I_q = \begin{cases} 1 & \text{(if signs of } u \text{ and } v \text{ corresponds to } i \text{ th quadrant)} \\ 0 & \text{(otherwise)} \end{cases}$$

By the definition, total contribution from four quadrant equal to cross correlation coefficient at each y^+ positions.

In case C, shown in Figure 10a, which is characterized by large drag reduction, the contribution from four quadrant has similar magnitude. This suggests uv product fluctuates around evenly around zero. It can be understood that interactive events are intensified and give a negative contribution to Reynolds shear stress. As the result of this, Reynolds shear stress becomes almost zero in this case. This is in contrast to the water case, where contribution from ejection-like or sweep-like

i	sign of u	sign of v	name of fluid motion
1	+	+	outward interaction
2	-	+	ejection-like motion
3	-	-	wallward interaction
4	+	-	sweep-like motion

TABLE 4. CLASSIFICATION OF EVENTS

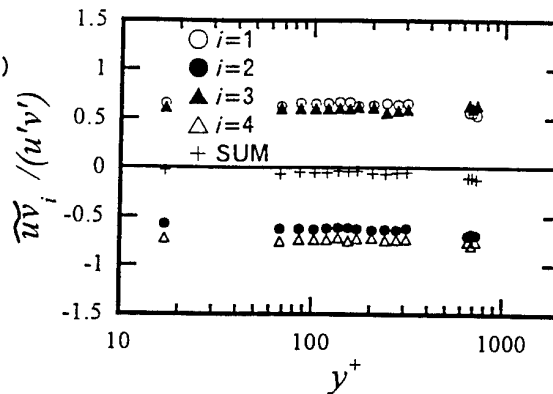


FIGURE 10a. CONTRIBUTIONS FROM QUADRANTS TO REYNOLDS SHEAR STRESS (CTAC 50PPM, CASE C)

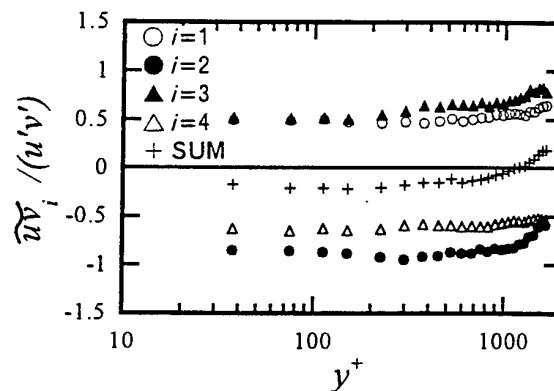


FIGURE 10b. CONTRIBUTIONS FROM QUADRANTS TO REYNOLDS SHEAR STRESS (CTAC 50PPM, CASE D)

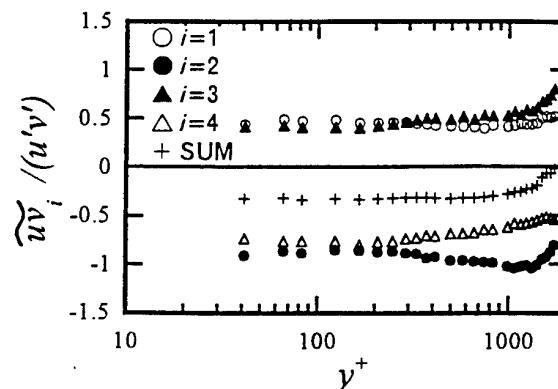


FIGURE 10c. CONTRIBUTIONS FROM QUADRANTS TO REYNOLDS SHEAR STRESS (WATER, CASE W)

motion has about twice magnitude to contribution from interaction motion. This feature of uv product is a general observation for Newtonian wall turbulence, but is not observed in drag reducing flows.

Figure 10b shows the contribution from four quadrant record for case D. It is evident that this diagram is similar to water case shown in Figure 10c. It suggests that the coupling feature between the u and v is approaching to water case. The reason that the Reynolds shear stress has about the half value of that in water case is coming from suppression of turbulent intensity.

The occurrence of interactive events in Newtonian fluid shear flows having gradient of $\partial U/\partial y > 0$ is not significant because the turbulent eddies move in a random fashion. Then, sweep (coupling of negative u and positive v) and ejection (coupling of positive u and negative v) become significant. In the case of drag reducing flows, probably due to the effect of fluid elasticity, an initial fluid motion characterized by a sweep-like motion will be followed by outward or wallward interaction such as bounding in fluid. A similar sequence may exist for ejection-like motion followed by interaction. This conjecture is based on the presence of force not directly related to local velocity fluctuation. Direct visual flow observation, where slow wavy motion was seen to be significant, supports this hypothesis. Although this hypothesis is not proven quantitatively, investigation of velocity patterns and spatial correlation in drag reducing flows will be an interesting future research theme.

4. CONCLUSION

Turbulent characteristics of a dilute surfactant/water solution in a two dimensional channel have been experimentally investigated over the Reynolds number range from 0.93×10^4 to 6.83×10^4 .

The friction factor behavior for the surfactant solution flow shows a critical phenomena where drag reduction effectiveness disappears above a certain Reynolds number Re_c . Since the friction factor quadruples over a relatively narrow Reynolds number range including Re_c , this phenomena is interesting from the viewpoint of turbulence control. There was no evidence found of structural change from the shear viscosity behavior at Re_c .

Distributions of mean velocity and turbulence stress components showed that in the region where large drag reduction exists, the streamwise and vertical components of turbulent normal stress were suppressed and Reynolds shear stress disappeared. Three types of flow regions can be identified, with respect to Reynolds number, namely 1) Incomplete drag reduction (DR) region, 2) Complete DR region and 3) Post DR region. Although each region are characterized by the mean velocity profile, turbulent characteristics of region 1) and region 2) are in common. In the post DR region 3), mean velocity profile, turbulent quantities including Reynolds shear stress looks like on the way to recovering and approaching to Newtonian fluid turbulence.

It was found that suppression of Reynolds shear stress in drag reducing flow can be related to suppressed ejection and sweep events and intensified interaction events.

5. REFERENCE

- Dean, R.B., 1978, "Reynolds number dependence of skin friction and other bulk flow variables in two-dimensional rectangular duct flow", *Journal of Fluid Engineering*, vol. 100, pp. 215-223
- Gyr, A. and Bewersdorff, H. -W., 1995, "Drag Reduction of Turbulent Flows by Additives", Kluwer Academic Publishers, Dordrecht
- Hammer, F., 1991, "Demonstration of smooth water in the district heating system of Herning, Denmark", *Proceedings, Nordic Council of Minister's International Symposium on Fluids for District Heating*
- Kawaguchi, Y., Tawaraya, Y. and Tanaka, M., 1995, "Viscosity measurements of CTAC:NaSal/W micelle solution - temperature effect and wall effect of viscometer", *Journal of Mechanical Engineering Laboratory*, Vol. 49-4, pp. 12-21
- Kawaguchi, Y., Tawaraya, Y., Yabe, A., Hishida, K. and Maeda, M., 1996a, "Turbulent Transport Mechanism in a Drag Reducing Flow with Surfactant Additive Investigated by Two Component LDV", *Proceedings, 8th International Symposium on Application of Laser Techniques to Fluid Mechanics, Lisbon*, pp. 29.4.1-29.4.7
- Kawaguchi, Y., Tawaraya, Y., Yabe, A., Hishida, K. and Maeda, M., 1996b, "Active control of turbulent drag reduction in surfactant solutions by wall hearing", *ASME 1996 Fluid Engineering Division Conference*, FED-Vol. 236, pp. 47-52
- Kawaguchi, Y., Daisaka, H., Yabe, A., Hishida, K. and Maeda, M., 1997, "Existence of Double diffusivity Fluid Layers and Heat Transfer Characteristics in Drag Reducing Channel Flow", *Proceedings, 2nd International Symposium on Turbulence, Heat and Mass Transfer (in printing)*
- Lu, S. S. and Willmarth, W. W., 1973, "Measurements of the structure of the Reynolds stress in a turbulent boundary layer", *Journal of Fluid Mechanics*, 60-3, p481
- Pollert, J., Zakin, J. L., Myška, J. and Kratochvil, P., 1994, "Use of friction reducing additives in district heating system field test at Kladono - Krocchlavy, Czech republic", *Proceedings, International District Heating and Cooling 1994 conference*, pp. 141-156
- Savins, J. G., 1967, "A Stress Controlled Drag Reduction Phenomenon", *Rheological Acta*, 6, p. 323
- Usui H., Itoh T. and Saeki, T., 1996, "Drag reducing pipe flow of surfactant solutions", *ASME 1996 Fluid Engineering Division Conference*, FED-Vol. 236, pp. 31-36
- Virk, P. S., 1975, "Drag reduction fundamentals", *AIChE Journal*, vol. 21, No. 4, pp. 625-656

KINETIC ENERGY BALANCE IN A TURBULENT BOUNDARY LAYER DISTURBED BY A CIRCULAR CYLINDER: CLASSICAL AND CONDITIONAL APPROACH

F. de Souza^{(1) (2)}, J. Delville⁽¹⁾, J.P. Bonnet⁽¹⁾

⁽¹⁾ LEA/CEAT
43 Route de l'Aérodrome
86036 Poitiers Cédex
France

⁽²⁾ Present address: Institute for Aerospace Research
National Research Council Canada
Ottawa, Ontario, K1A 0R6
Canada

INTRODUCTION

The effect of external manipulators on turbulent boundary layers has been the subject of several studies in the past (see Coustols and Savill, 1992; Hamdouni and Bonnet, 1993; Lemay *et al.*, 1995). Interest in such manipulators originally stemmed from their ability to reduce turbulent skin friction drag. It has been shown since that the considerable reduction in local skin friction (of the order of 10%) that can be obtained is at best equivalent to the form drag of the manipulator itself, leading to no net reduction in drag. However, most outer layer manipulators have been shown to reduce the wall heat transfer as well, making them attractive in terms of thermal applications.

In this paper, a specific configuration is examined where an increase in heat transfer is produced despite the skin friction drag reduction. The Reynolds analogy seems then to be violated. This flow has been quantified by Marumo *et al.* (1978, 1985) and Suzuki *et al.* (1989). Initial investigations of the cause of this apparent dissimilarity between heat and momentum transfer have involved quadrant analysis applied to single-point measurements of velocity and temperature fluctuations (Kawaguchi *et al.*, 1984; Suzuki *et al.*, 1988). However, analysis of the turbulent kinetic energy budget, which previously has led to valuable insight into the flow structure modification by a thin ribbon-type boundary layer manipulator (Lemay *et al.*, 1990), has never before been attempted for the case of a circular cylinder.

The goal of the present study is thus to attempt to explain the observed dissimilarity in terms of the various processes of loss and gain of turbulent kinetic energy in the disturbed boundary layer. In addition to classical methods, a "spectral filtering" technique is used to approach the kinetic energy balance from a conditional point of view. Specifically, the individual contributions of the coherent and non-coherent velocity fields to the production, convection and diffusion of turbulent kinetic energy are evaluated using the equations derived by Reynolds and Hussain (1972).

The present analysis has been found to complement an investigation of the observed dissimilarity in terms of the large scale organization of the flow (de Souza *et al.*, 1997).

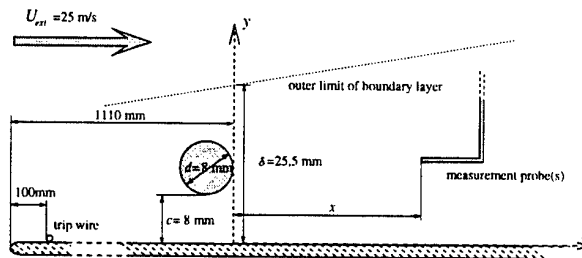


Figure 1: Schematic description of the experimental configuration.

EXPERIMENTAL DETAILS

Experimental Configuration

The experimental configuration is the same as that reported in de Souza *et al.* (1997). Experiments were performed in a closed circuit, subsonic wind tunnel with a square test section of cross-sectional dimensions 300 mm \times 300 mm and length 2 m. The boundary layer developed on a flat plate placed horizontally at about 100 mm above the test section floor. The circular cylinder lay parallel to the wall and perpendicular to the streamwise direction. The cylinder diameter, as well as the vertical gap between the cylinder and the wall, was equal to approximately one-third of the thickness of the unmanipulated, fully turbulent boundary layer at the streamwise location of the cylinder (figure 1). At this location, the unmanipulated boundary layer conditions were: thickness $\delta = 25.5$ mm, and Reynolds number (based on momentum thickness) $Re_\theta = 4500$. The free stream velocity was set at $U_{\infty} = 25$ m/s, and the corresponding turbulence intensity was less than 0.25%.

Flow qualification

Flow qualification involved skin friction measurements using the Preston tube technique, and velocity measurements using pitot tubes as well as single and x-type hot-wire probes. These measurements were consistent with

those reported in the literature (Marumo *et al.*, 1978, 1985, Suzuki *et al.* 1989). The nature of the observed dissimilarity is revealed from our own experimental results (de Souza, 1996) and those obtained by Suzuki *et al.* (1989), who also investigated the streamwise evolution of the local heat transfer coefficient h_x . The maximum reduction in the local skin friction coefficient C_f is of the order of 30% and is located at $x \sim 20$ diameters from cylinder, whereas the maximum heat transfer increase is of the order of 60% and occurs very close to the manipulator ($x \sim 5d$). Further details on the flow qualification can be found in de Souza *et al.* (1997) or de Souza (1996).

Measurements

Measurements of the quantities required to evaluate the kinetic energy budget were obtained via hot-wire anemometry, using a T.S.I. model 1248 T1.5 x-wire probe and a modified T.S.I. model 1260 T1.5 single-wire probe, both operating with platinum-coated tungsten wires. Wire diameters and lengths were respectively 2.5 μm and 0.35 mm for the single-wire probe, and 5.0 μm and 1.25 mm for the x-wire probe.

The x-wire measurements were acquired at a sampling rate of 20 kHz per channel, and low-pass filtered at 10 kHz. The single-wire measurements, which were used to estimate the dissipation of turbulent kinetic energy, were acquired at 100 kHz and low-pass filtered at 50 kHz. At each measurement position 131 072 data samples were obtained. Further details are provided by de Souza (1996).

TURBULENT KINETIC ENERGY BUDGET

General form of the transport equation

The transport equation for the turbulent kinetic energy, defined by:

$$k = \frac{1}{2} \overline{u_i' u_i'} = \frac{1}{2} (\overline{u'^2} + \overline{v'^2} + \overline{w'^2}) \quad (1)$$

can be expressed in the following general form:

$$\underbrace{\frac{\partial \bar{k}}{\partial t} + \bar{U}_j \frac{\partial \bar{k}}{\partial x_j}}_I = \underbrace{-\overline{u_i' u_j'} \frac{\partial \bar{U}_i}{\partial x_j}}_{II} - \underbrace{\frac{\partial}{\partial x_j} \overline{k' u_j'}}_{III} - \underbrace{\frac{1}{\rho} \frac{\partial}{\partial x_j} (\overline{p' u_j'})}_{IV} + \underbrace{\nu \left[\frac{\partial^2 \bar{k}}{\partial x_j \partial x_j} + \frac{\partial^2 \overline{u_i' u_j'}}{\partial x_i \partial x_j} \right]}_V - \underbrace{\frac{1}{2} \nu \left(\overline{\frac{\partial u_i'}{\partial x_j} + \frac{\partial u_j'}{\partial x_i}}^2 \right)}_{VI} \quad (2)$$

The various terms of equation (2) correspond to:

- *I* : The total rate of change of turbulent kinetic energy, which includes the temporal variation as well as convection by the mean velocity field.
- *II* : Energy production by the interaction of the Reynolds stresses with mean velocity gradients.
- *III* : Energy diffusion due to velocity fluctuations.
- *IV* : Energy transport due to pressure-velocity correlations.
- *V* : The work of viscous stresses, or alternatively, energy transport by viscous effects.
- *VI* : The dissipation of turbulent kinetic energy into heat through the action of viscosity.

Explicit form for the studied flow

For the given flow configuration(s), it is assumed that the mean flow is stationary and two-dimensional, and that the Reynolds number is large. These assumptions lead to the following explicit forms for each of the terms of equation (2):

$$\begin{aligned} \bullet I &: \bar{U} \frac{\partial \bar{k}}{\partial x} + \bar{V} \frac{\partial \bar{k}}{\partial y} \\ \bullet II &: -(\overline{u'^2} - \overline{v'^2}) \frac{\partial \bar{U}}{\partial x} - \overline{u'v'} \left(\frac{\partial \bar{U}}{\partial y} + \frac{\partial \bar{V}}{\partial x} \right) \\ \bullet III &: -\frac{1}{2} \frac{\partial}{\partial x} (\overline{u'^3} + \overline{u'v'^2} + \overline{u'w'^2}) \\ &\quad -\frac{1}{2} \frac{\partial}{\partial y} (\overline{u'^2 v'} + \overline{v'^3} + \overline{v'w'^2}) \end{aligned}$$

These first three terms can be measured fairly easily.

$$\bullet IV : -\frac{1}{\rho} \frac{\partial \overline{p' u'}}{\partial x} - \frac{1}{\rho} \frac{\partial \overline{p' v'}}{\partial y}$$

This term is difficult, if not impossible, to measure. It thus can only be estimated from the balance, or "remainder", of equation (2).

• *V* : This term is negligible at high Reynolds number, as in the present flow configuration.

• *VI* : This term, generally denoted ϵ , is evaluated by assuming that the flow is locally isotropic. The dissipation can be expressed then in the following manner:

$$\epsilon = 15 \nu \overline{\left(\frac{\partial u'}{\partial x} \right)^2}$$

By applying Taylor's hypothesis: $\frac{\partial}{\partial t} = -\bar{U} \frac{\partial}{\partial x}$, we obtain an expression for ϵ in terms of a temporal gradient:

$$\epsilon = \frac{15 \nu}{\bar{U}^2} \overline{\left(\frac{\partial u'}{\partial t} \right)^2} = \frac{60 \nu \pi^2}{\bar{U}^2} \int_0^\infty f^2 E_u(f) df,$$

where $E_u(f)$ is the energy spectral density of the streamwise velocity component.

Evaluation of the various terms.

The various moments of velocity which appear in the energy transport equation were evaluated using three x-wire probe configurations, corresponding to different orientations of the plane of the wires with respect to the flow, with the probe body always aligned with the streamwise direction. The detailed procedure has been described by Lemay *et al.* (1990). Derivatives with respect to x and y were evaluated respectively using 2nd and 4th order finite difference schemes. The spectra of the streamwise velocity component were evaluated using the single-wire probe.

Results of the classical analysis

The turbulent kinetic energy budget was evaluated for the manipulated boundary layer (MBL) at 4.25, 24.25 and 49.25 diameters downstream of the cylinder (figure 2). The first station is located in the near wake of the cylinder, where the skin friction coefficient C_f decreases with streamwise distance. The second station is situated close to the location where the manipulator wake reaches the wall, which corresponds to the point of maximum skin friction reduction, as shown by de Souza (1996). Finally, the third station is located in the region of relaxation of C_f . For comparison, measurements were repeated at the same streamwise stations in the isolated cylinder wake (IW). The

results obtained at the first station are presented in figure 3. Also shown in figure 3 is the kinetic energy balance evaluated by Lemay *et al.* (1990) for a turbulent boundary layer manipulated by a thin ribbon (LEBU). The thickness of the unmanipulated boundary layer, δ_n , was used to normalize the results presented in figure 2. For the IW configuration, the characteristic wake thickness b was used as a normalizing length scale. Lemay *et al.* use the boundary layer thickness δ .

There are significant qualitative as well as quantitative differences between the results obtained in the MBL at $x/d = 4.25$ and those measured further downstream. Whereas the energy balances established at $x/d = 24.25$ and especially at $x/d = 49.25$ are similar to those obtained in the thin ribbon-manipulated boundary layer, the results evaluated at $x/d = 4.25$ closely resemble those corresponding to the isolated wake (IW) configuration (figure 3). This resemblance is particularly evident in the region $y/b > 1.5$. For the region close to the cylinder, therefore, it can be concluded that the wake structure dominates the boundary layer structure, and that wall effects are relatively insignificant. In fact, the influence of the wall is only evident below the cylinder axis, where energy production and diffusion are attenuated and energy dissipation is slightly higher than in the IW configuration (figure 2a and 3). The term which seems to be the least influenced by wall effects is convection. In particular, it retains its symmetry about the cylinder axis, as in the IW configuration. Further downstream, the resemblance between the MBL and IW flows diminishes. In this region, the boundary layer is characterized by very strong production, while the isolated wake is marked by strong convection (figures 2b,c and 3a).

Energy production and transport.

Detailed analysis reveals that wake and wall effects do not influence the production and transport terms to the same extent, depending on the downstream region considered. At $x/d = 4.25$, the MBL and IW flow configurations are comparable. Wall effects are evident only at less than $1.5b$ above the cylinder axis.

Further downstream, in the upper half-wake of the cylinder within the boundary layer, it can be noted that the convection and diffusion terms are of comparable amplitude, and that the general appearance of these curves does not change significantly with downstream distance. The qualitative aspect of these curves is comparable to that which can be observed in the IW configuration (cf. figures 2b,c and 3a). It can be postulated that the mechanisms of energy diffusion and convection in the MBL configuration are similar to those which exist in the isolated wake.

On the other hand, still considering only the upper half-wake of the cylindrical manipulator, the amplitude of the production of turbulent energy, which at $x/d = 4.25$ is largely inferior to those of energy transport by convection and diffusion, is more than double those of the transport terms at the second station. Further, maximum energy production in the MBL configuration is more than 5 times greater than in the IW configuration at this station (de Souza, 1996). It is evident that at $x/d = 24.25$, there is little resemblance between the energy production curve in the MBL configuration and that typical of a wake flow (figures 2b and 3a). On the contrary, the dominance of the production term in the MBL is more typical of the energy balance in the natural boundary layer (cf. figure 3c). There are nevertheless important differences. With respect to the NBL configuration, a large surplus of energy production immediately above the cylinder axis, as well as a region of deficit below, can be observed in the MBL. This increase in energy production above the manipulator axis, relative to the IW case, is balanced in part by an increased dissipation rate but also by an increased diffusion of energy towards the outer regions of the wake (figures 2b,c

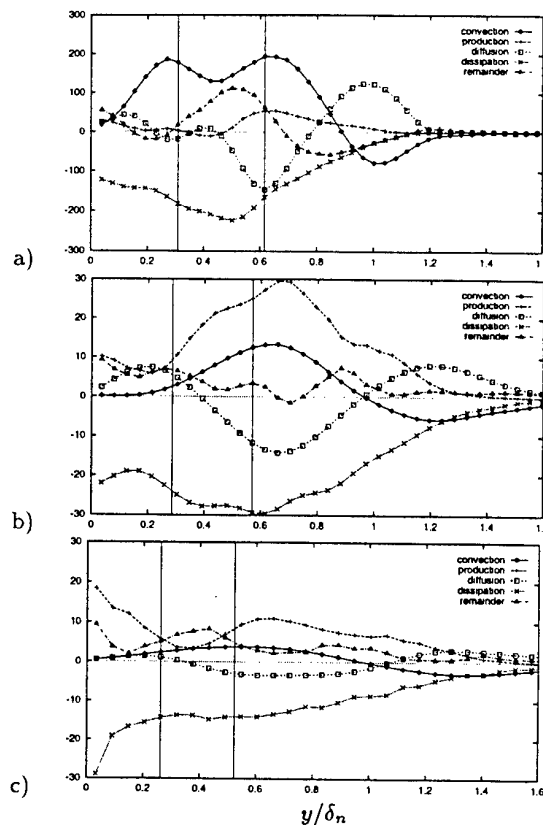


Figure 2: Turbulent kinetic energy balance normalized by $\delta_n/U_{ext}^3 \times 10^4$. MBL configuration. The vertical lines indicate the extent of the cylinder. a) $x/d = 4.25$. b) $x/d = 24.25$. c) $x/d = 49.25$.

and 3a). The energy thus diffused towards the wall seems to be dissipated fairly rapidly. However, the increased diffusion towards the outer region of the MBL is accompanied by an increased convection towards the cylinder axis.

These results suggest that in the MBL, wall effects lead to an increase in energy transport in the transverse y direction with respect to the IW configuration. It is recalled that energy transport in the transverse direction is typically greater in a wake flow than in a wall flow. The cylinder thus increases the transverse transport of energy in the boundary layer, but wall effects actually improve the energy transport mechanism proper to the cylinder wake.

Energy dissipation.

Given that significant assumptions were made (in particular that of local isotropy¹) in order to estimate the turbulent dissipation rate from single-wire measurements, we limit the discussion here to a comparative analysis of the different flow configurations (for which the same procedure was used to evaluate the dissipation). The results indicate that as of the first measurement station, energy dissipation in the MBL flow is much greater than in the IW. This is evident over a large portion of the upper half-wake of the cylinder, and especially in the near-wall region. Similarly, the dissipation rate in the MBL is significantly higher than in the NBL. We can conclude from this analysis that the cylinder wake tends to accelerate the development of

¹According to Browne *et al.* (1987), the dissipation rate in a wake flow tends to be underestimated when evaluated under the assumption of local isotropy.

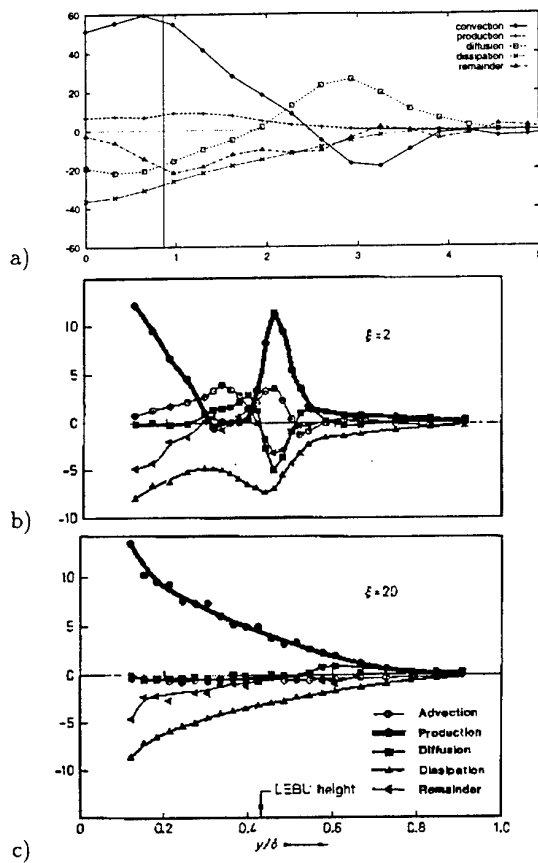


Figure 3: Turbulent kinetic energy balance measured: a) in the near wake of the isolated cylinder (IW); b) in the near wake of a thin ribbon-type boundary layer manipulator (LEBU); c) in the far wake of the LEBU, which is identical to the energy balance in the natural boundary layer (NBL). LEBU results are from Lemay *et al.* (1990).

turbulence in the boundary layer, which is equivalent to concluding that wall effects tend to accelerate the development of the wake turbulence. The growth of the integral scales of the turbulence can thus be expected to be more rapid in the MBL than in the NBL or the IW configurations.

Summary of the results of the classical analysis.

Classical analysis of the kinetic energy balance shows that energy production and dissipation are qualitatively much more sensitive to wall effects (and thus less dominated by wake effects) than energy transport by convection and diffusion. In other words, although the wake turbulence structure seems to take precedence over that of the wall turbulence, the influence of the wall on the production and dissipation terms remains considerable. It is proposed that this observed dissimilarity between the mechanisms of energy production and transport is related to the fact that the cylindrical manipulator produces contradictory effects on the heat transfer and the shear stress at the wall. In the IW case, numerous studies (Townsend, 1949, Ferre *et al.*, 1990) have shown that the heat transfer in the transverse direction is related to the turbulent energy diffusion, in that both are favored by large scale structures, and in particular by the large spanwise vortices which are typical of this flow configuration. At the same time, it is well accepted that wall shear stress (and hence skin friction) is

related to turbulent energy production at the wall.

CONDITIONAL APPROACH

To analyze more closely the influence of the large scale wake structure on the energy production and transport processes, the kinetic energy balance is approached from a conditional point of view via the triple decomposition technique proposed by Reynolds and Hussain (1972).

Triple Decomposition

The triple decomposition technique consists of decomposing the instantaneous contribution of each velocity component $u_i(y, t)$ into three components. The mean value is extracted as defined by the Reynolds decomposition $\overline{u_i(y)}$, while the residual fluctuating component $u_i(y, t) = u_i(y, t) - \overline{u_i(y)}$ is further decomposed into "coherent" $u_{ci}(y, t)$ and "random" $u_{ri}(y, t)$ contributions. Instantaneous decomposition of the fluctuating field is performed using the "spectral filtering" method which is described in detail by de Souza *et al.* (1997). Briefly, this method is based on the principle that the coherent structures are considerably localized in the spectral domain for the given flow configuration. This is true of the vortices shed from the cylinder. By isolating the well-defined peaks of the energy spectral density, the spectral filter can extract the instantaneous contribution of the "coherent" velocity field, which would thus be mainly associated with the large-scale wake turbulence.

According to the triple decomposition technique, the total turbulent kinetic energy must be equal to the sum of the energies corresponding to the three fields (mean, coherent and random):

$$\frac{1}{2} \overline{u_i u_i} = \frac{1}{2} \overline{U_i U_i} + \frac{1}{2} \overline{u_{ci} u_{ci}} + \frac{1}{2} \overline{u_{ri} u_{ri}}$$

By applying this decomposition to the kinetic energy transport equation (2), we obtain expressions for the triple decomposition of the convection, production and diffusion terms:

i) Convection of energy by the mean flow:

$$U_j \frac{\partial}{\partial x_j} \left(\frac{1}{2} \overline{u'_i u'_i} \right) = \underbrace{U_j \frac{\partial}{\partial x_j} \left(\frac{1}{2} \overline{u_{ci} u_{ci}} \right)}_{\text{coherent}} + \underbrace{U_j \frac{\partial}{\partial x_j} \left(\frac{1}{2} \overline{u_{ri} u_{ri}} \right)}_{\text{random}} \quad (3)$$

ii) Production of energy by the mean flow:

$$\underbrace{-\overline{u'_i u'_j} \frac{\partial U_i}{\partial x_j}}_{\text{total}} = \underbrace{-\overline{u_{ci} u_{cj}} \frac{\partial U_i}{\partial x_j}}_{\text{coherent}} + \underbrace{-\overline{u_{ri} u_{rj}} \frac{\partial U_i}{\partial x_j}}_{\text{random}} \quad (4)$$

iii) Diffusion of energy through velocity fluctuations:

$$\underbrace{-\frac{\partial}{\partial x_j} \left[\overline{u'_j \left(\frac{1}{2} u'_i u'_i \right)} \right]}_{\text{total}} = \underbrace{-\frac{\partial}{\partial x_j} \left[\overline{u_{cj} \left(\frac{1}{2} u_{ci} u_{ci} \right)} \right]}_{\text{coherent}} + \underbrace{-\frac{\partial}{\partial x_j} \left[\overline{u_{rj} \left(\frac{1}{2} u_{ri} u_{ri} \right)} \right]}_{\text{random}} \quad (5)$$

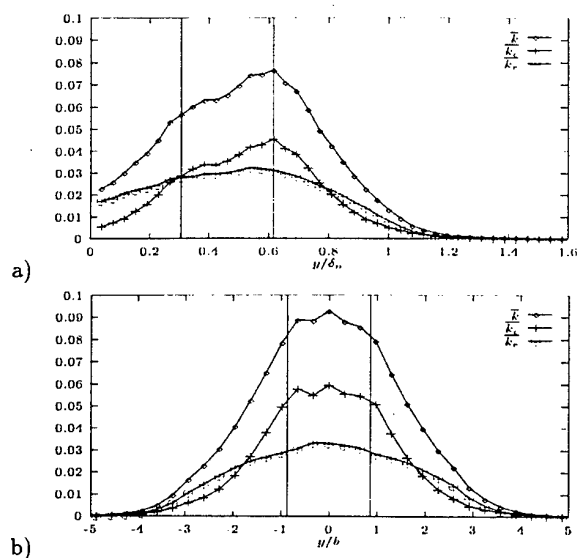


Figure 4: Triple decomposition of the turbulent kinetic energy (normalized by U_{ext}^2) measured in the: a) MBL; b) IW. The vertical lines indicate the extent of the cylinder.

Results of the conditional analysis

The importance of wake effects on the energy processes in the MBL can be made evident by considering the contribution of the coherent flow field to the total turbulent energy. Figure 4 shows the mean contributions of both the coherent and incoherent components to the total energy in the near wake of the cylinder for the MBL and IW configurations. Whereas the profiles of coherent and incoherent energy in both configurations are very comparable for the upper portion of the wake, significant differences can be observed below the cylinder axis. In particular, the incoherent turbulence accounts for almost all of the turbulent kinetic energy in the lower part of the MBL, the coherent energy being significantly attenuated in this region.

Energy production and transport.

The results obtained from the triple decomposition of the energy convection, production and diffusion terms are shown in figures 5 and 6. In this section, the contributions of the coherent and incoherent fields are analyzed for each term individually. This analysis will be used to support the conclusions drawn from the classical energy balance.

a) Convection The coherent turbulence appears to be responsible for most of the energy convection in the MBL. Comparison with the IW configuration suggests that the coherent structures which dominate the convection process are almost exclusively related to wake effects. The convection of incoherent energy is relatively weak, and is only significant towards the outer portion of the upper wake in both flow configurations. Nevertheless, similarity between the two configurations suggests that the incoherent convection is also mainly related to wake effects. Wall effects are limited to the region very close to the wall, where the convection of incoherent turbulence is weaker than at the corresponding distance above the cylinder axis.

b) Production The turbulent energy production in the MBL, unlike convection, is mostly assured by the incoherent field, except very close to the wake axis. This is not the case, however, in the IW. In the central region of the IW,

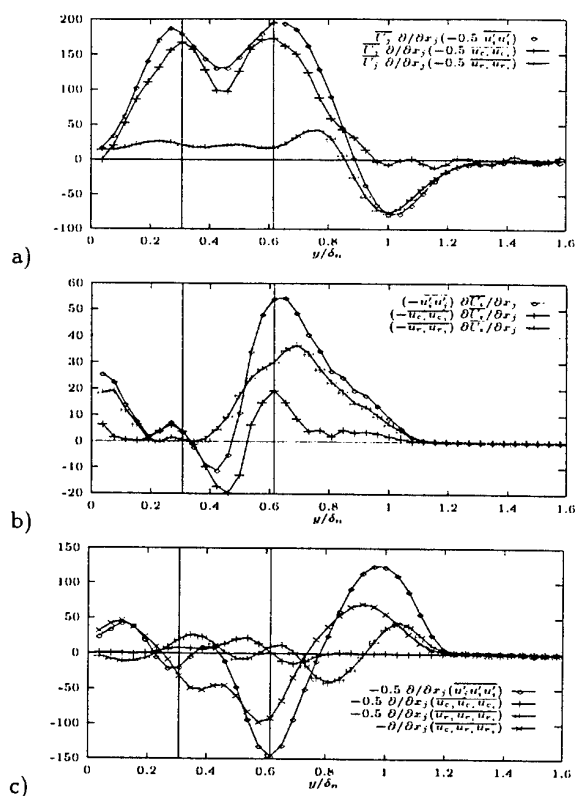


Figure 5: Triple decomposition of the terms of the kinetic energy budget measured in the MBL, normalized by $\delta_n/U_{ext}^3 \times 10^4$. The vertical lines indicate the extent of the cylinder. a) Convection. b) Production. c) Diffusion.

the production process involves mostly the coherent field. Towards the outer portion of the IW, the contribution of the coherent field becomes less significant, but is nevertheless comparable to that of the incoherent field. It is evident, therefore, that the energy production mechanisms are not identical in the two flow configurations. In fact, the strong resemblance between the production of incoherent energy in figure 5b and the total energy production in the near wake of the thin ribbon-type manipulator (figure 3b), where the flow disturbance is less significant, indicates that the production process is less influenced by wake effects than by wall effects, contrarily to the convection process.

c) Diffusion Triple decomposition of the turbulent energy diffusion is more difficult to obtain from one-point measurements. Only the first and third terms on the right hand side of equation (5) were evaluated directly, making no further assumptions about the flow. An estimation for the second term, which represents the diffusion of coherent energy by the "incoherent" turbulence, was obtained by neglecting the contribution of the term $-0.5 \frac{\partial}{\partial y} \overline{w_c w_r v_r}$. This part of the term can only be evaluated if the transverse v and spanwise w velocity components are measured simultaneously, which is not possible to do with a simple x-wire probe. Nevertheless, it is likely that this derivative is much less significant than the rest of the second term. The last term of equation (5) is impossible to evaluate, even approximately, from single point x-wire measurements.

Figures 5c and 6c show that the diffusion of coherent energy contributes the most to the total energy diffusion. This remark is especially valid in the near wall region of the MBL. More specifically, the diffusion of coherent energy

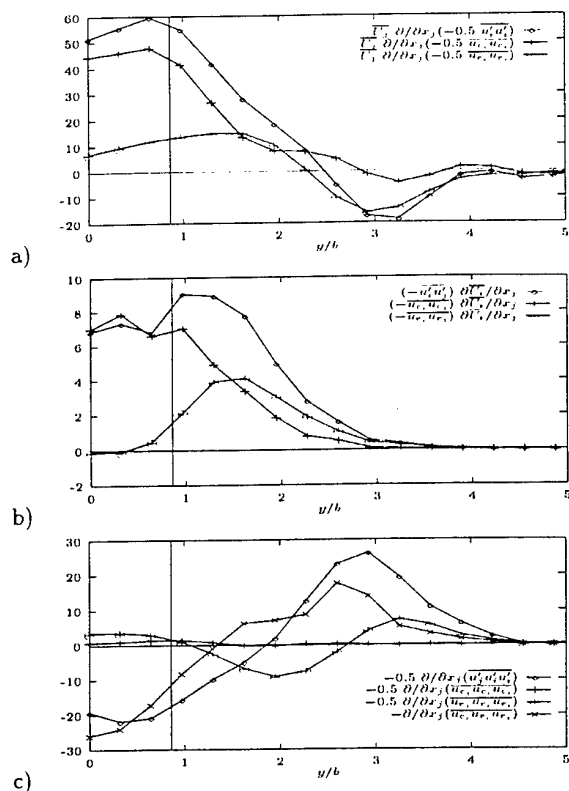


Figure 6: Triple decomposition of the terms of the kinetic energy budget measured in the IW, normalized by $b/U_{ext}^3 \times 10^4$. $y/b = 0$ on the cylinder axis; the vertical line indicates the upper limit of the cylinder. a) Convection. b) Production. c) Diffusion.

by the incoherent turbulence dominates largely the other terms on the right hand side of equation (5). The term involving exclusively the incoherent flow field becomes significant mainly near the outer limit of the MBL, as is the case for the NBL configuration. It can be concluded that the diffusion process in the MBL, like that of convection, is largely determined by the coherent structure dynamics, which in turn are characteristic of the wake turbulence. The influence of wall turbulence appears to be relatively insignificant. These remarks are consistent with the fact that large scale vortical structures associated with the cylinder wake dominate the coherent flow field, as demonstrated by the conditional analysis of de Souza *et al.* (1997).

CONCLUSIONS

The present results suggest that the observed dissimilarity between heat and momentum transfer in the considered flow is related to the fact that the two basic flow types involved in the wake/boundary layer interaction impose their influence on distinct energy processes. Specifically, wall effects influence mainly the production process, which is related to wall skin friction, whereas the transport processes, related to heat transfer, are largely determined by wake effects. Further, it can be inferred from the results that the mechanism of energy production, and thus of skin friction reduction, may be at least partly similar to that which exists in the case of a thin ribbon-type manipulator. de Souza *et al.* (1997) show that this mechanism is enhanced by the cylinder wake-type turbulence. On the other hand, the mechanism of energy transport, and thus of heat transfer, is likely typical of an isolated wake flow.

Triple decomposition of the energy transport equation permitted analysis of the individual contributions of the "coherent" and "incoherent" turbulence to the energy production and transport processes. A "spectral filter" separated the effects of the large-scale "coherent" wake structures from those of the background "incoherent" turbulence. This conditional approach confirmed the above conclusions drawn from the classical kinetic energy balance.

Acknowledgements : Special thanks are due to H. Garem for his help with the experimental arrangement.

REFERENCES

- Browne, L.W.B., Antonia, R.A. and Shah, D.A., 1987, "Turbulent energy dissipation in a wake", *J. Fluid Mech.*, Vol. 179, pp. 307-326.
- Coustols, E. and Savill, A.M., 1992, "Turbulent skin friction drag reduction by active and passive means", AGARD FDP/VKI Special Course on Skin Friction Drag Reduction, March 2-6, Von Karman Institute, Brussels, Belgium.
- de Souza, F., 1996, "Experimental study of the wake/wall interaction in a turbulent boundary layer manipulated by a circular cylinder", Ph. D. Thesis, Université de Poitiers, France (in French).
- de Souza, F., Delville, J. and Bonnet, J.P., 1997, "On the large scale organization of a turbulent boundary layer disturbed by a circular cylinder", *Eleventh Symposium on Turbulent Shear Flows*, Grenoble, France.
- Ferré, J.A., Mumford, J.C., Savill, A.M. and Giralt, F., 1990, "Three-dimensional large-eddy motions and fine-scale activity in a plane turbulent wake", *J. Fluid Mech.*, Vol. 210, pp. 371-414.
- Hamdouni, A. and Bonnet, J.P., 1993, "Effect of external manipulators on the heat transfer on a flat plate turbulent boundary layer", *Appl. Sci. Res.*, Vol. 50, pp. 369-385.
- Kawaguchi, Y., Matsumori, Y. and Suzuki, K., 1984, "Structural study of momentum and heat transport in the near wall region of a disturbed turbulent boundary layer", *Proc. 9th Biennial Symp. on Turbulence*, pp. 28.1-28.10.
- Lemay, J., Bonnet, J.P. and Delville, J., 1995, "Experimental Testing of Diffusion Models in a Manipulated Turbulent Boundary Layer", *AIAA J.*, Vol. 33, no. 9, pp. 1597-1603.
- Lemay, J., Delville, J. and Bonnet, J.P., 1990, "Turbulent kinetic energy balance in a LEBU modified turbulent boundary layer", *Exp. Fluids*, Vol. 9, pp. 301-308.
- Marumo, E., Suzuki, K. and Sato, T., 1978, "A turbulent boundary layer disturbed by a cylinder", *J. Fluid Mech.*, Vol. 87, pp. 121-141.
- Marumo, E., Suzuki, K. and Sato, T., 1985, "Turbulent heat transfer in a flat plate boundary layer disturbed by a cylinder", *Int. J. Heat & Fluid Flow*, Vol. 6, no. 4, pp. 241-248.
- Reynolds, W.C. and Hussain, A.K.M.F., 1972, "The mechanics of an organized wave in turbulent shear flow. Part 3. Theoretical models and comparisons with experiments.", *J. Fluid Mech.*, Vol. 54, part 2, pp. 263-288.
- Suzuki, K., Suzuki, H., Kikkawa, Y. and Kigawa, H., 1989, "Study on a turbulent boundary layer disturbed by a cylinder - effect of cylinder size and position", *Seventh Symposium on Turbulent Shear Flows*, Stanford University, pp. 8.5.1 - 8.5.6.
- Suzuki, H., Suzuki, K. and Sato, T., 1988, "Dissimilarity between heat and momentum transfer in a turbulent boundary layer disturbed by a cylinder", *Int. J. Heat Mass Transfer*, Vol. 31, no. 2, pp. 259-265.
- Townsend, A.A., 1949, "The fully developed turbulent wake of a circular cylinder", *Austral. J. Sci. Res.*, Vol. 2, pp. 451-468.

VERIFICATION OF A TURBULENT DISPERSION MODEL THROUGH COMPARISON WITH THE RESULTS OF A FIELD TRACER EXPERIMENT IN A COMPLEX TERRAIN

Yoichi Ichikawa, Koichi Sada and Kazuo Asakura
Atmospheric Science Department, Komae Research Laboratory
Central Research Institute of Electric Power Industry
2-11-1 Iwado Kita,
Komae-shi, Tokyo 201
Japan

ABSTRACT

A Lagrangian particle dispersion model was developed to predict concentrations of air pollutants in complex terrain. The governing equations of the model are stochastic differential equations which represent the random motion of a particle. The equations include coefficients which describe the effects of dynamic characteristics and noise. These coefficients were determined from turbulent statistics predicted by a turbulence closure model which is based on the Reynolds stress model. The dispersion model was applied to the prediction of concentration distribution over actual topography in Japan. Field tracer experiments were conducted in a mountainous coastal area of western Japan in order to verify the dispersion model. The results obtained using the dispersion model were accurate.

INTRODUCTION

The Lagrangian particle dispersion model is one of the best numerical models of atmospheric dispersion, and is applicable to complicated flow fields generated by topography and heat (e.g., Wilson and Sawford, 1996). The model presented by Thomson (1987) is superior to conventional Lagrangian particle dispersion models in its applicability to non-Gaussian and inhomogeneous turbulent fields, and its use of Gaussian random numbers. The Thomson model has been applied to analyses of dispersion in a convective boundary layer (e.g. Luhar and Britter, 1989; Weil, 1990) but not to the prediction of dispersion phenomena over topography. The authors (Ichikawa et al, 1996) developed a Lagrangian particle model to predict three-dimensional dispersion in complex terrain using the Thomson's approach and evaluated the model through comparison with the results of a wind tunnel experiment. In this paper, field tracer experiments were conducted in a mountainous coastal area of western Japan in order to verify the model.

DISPERSION MODEL

The governing equations of the Lagrangian particle dispersion model are stochastic differential equations which represent the random motion of a particle (Thomson, 1987):

$$du^i = a^i(x, u, t) dt + b^{ij}(x, u, t) d\xi^j, \quad (1)$$

$$dx = u dt, \quad (2)$$

where u and x are the velocity and position of a fluid element or particle, respectively, t is time, and $d\xi^j$ is the increment of an Wiener process. The coefficients a and b describe the effects of dynamic characteristics and noise, respectively. Equations (1) and (2) imply that the density function $g(x, u, t)$ of the (x, u) -space distribution of all the particles satisfies the Fokker-Planck equation

$$\frac{\partial g}{\partial t} = -\frac{\partial}{\partial x^i} (u^i g) - \frac{\partial}{\partial u^i} \{a^i(x, u, t) g\} + \frac{\partial^2}{\partial u^i \partial u^j} \{B^{ij}(x, u, t) g\}. \quad (3)$$

In this equation, B^{ij} is used to denote $b^i b^j / 2$. The following conditions should be satisfied:

$$g(x, u, t) = g_u(x, u, t) \quad (4)$$

$$a^i g_u = \frac{\partial}{\partial u^j} (B^{ij} g_u) + \Phi^i(x, u, t), \quad (5)$$

where g_u is the density function of the distribution of the fluid elements and Φ satisfies

$$\frac{\partial \Phi^i}{\partial u^j} = -\frac{\partial g_u}{\partial t} - \frac{\partial}{\partial x^i} (u^i g_u). \quad (6)$$

$$2\langle B^{ij} \rangle = \delta^{ij} C_{\phi\phi}, \quad (7)$$

where $\langle \rangle$ indicates the ensemble average, δ_{ij} is Kronecker's delta, ϵ is the energy dissipation rate, and C_0 is a universal constant, the value of which is 1.0 in our calculation.

Thomson proposed a formulation of ϕ for Gaussian turbulence given by

$$\frac{\phi^i}{g_*} = \frac{1}{2} \frac{\partial V^{11}}{\partial x^1} + \frac{\partial U^1}{\partial t} + U^1 \frac{\partial U^1}{\partial x^1} + \left\{ \frac{1}{2} (V^{-1})^{1j} \left(\frac{\partial V^{11}}{\partial t} + U^1 \frac{\partial V^{11}}{\partial x^1} \right) + \frac{\partial U^1}{\partial x^j} \right\} (u^1 - U^1) + \frac{1}{2} (V^{-1})^{1j} \frac{\partial V^{11}}{\partial x^k} (u^j - U^j) (u^k - U^k), \quad (8)$$

where

$$g_* = \frac{\langle \rho \rangle}{(2\pi)^{3/2} (\det V)^{1/2}} \exp \left\{ -\frac{1}{2} (u^i - U^i) (V^{-1})^{ij} (u^j - U^j) \right\}. \quad (9)$$

a^i is given by

$$a^i = -B^{1j} (V^{-1})^{jk} (u^k - U^k) + \phi^i / g_*. \quad (10)$$

In Eqs.(8) ~ (10),

$$U = \langle \rho u_e \rangle / \langle \rho \rangle, \quad (11)$$

$$V^{ij} = \langle \rho (u_e^i - U^i) (u_e^j - U^j) \rangle / \langle \rho \rangle. \quad (12)$$

Each particle is assumed to be reflected perfectly at the earth's surface according to the incline of the topography. The position of the particle after reflection, x' , is calculated by

$$x' = x - 2n \{ n \cdot (x - x_s) \}, \quad (13)$$

where x is the position of the particle in the case of no reflection, x_s is the position of the reflection point, and n is the normal unit vector given by

$$n = \frac{-z_x i - z_y j + k}{(1 + z_x^2 + z_y^2)^{1/2}}, \quad (14)$$

where $z_i = z_i(x, y)$ is the elevation of the topography, and z_x and z_y are the partial derivatives of z_i in the x and y directions, respectively. The velocity vector, u' , of the particle after reflection is calculated by

$$u' = u - 2n (n \cdot u), \quad (15)$$

where u is the velocity vector of the particle in the case of no reflection.

In order to consider unsteady wind direction, the direction of the movement of a particle at the release point was calculated according to the probability given by

$$w(\psi) = \frac{1}{\sqrt{2\pi} \sigma_\psi} \exp \left(-\frac{\psi^2}{2\sigma_\psi^2} \right), \quad (16)$$

$w(\phi)$ is the frequency distribution of wind directions ϕ and σ_ψ is the standard deviation of the wind direction fluctuations.

Turbulent statistics such as the mean velocity, the full tensor form of stress and the energy dissipation rate required for the calculation of dispersion were predicted using the turbulence closure model. This model is based on the Reynolds stress model developed by Gibson and Launder (1978). The advection and diffusion terms of the Reynolds stress equations were simplified and the Reynolds stresses were expressed in terms of algebraic equations. The boundary layer approximation was used and the hydrostatic assumption was applied to the vertical component of wind motion. The four-dimensional data assimilation technique was incorporated into the horizontal momentum equations.

FIELD TRACER EXPERIMENT

Field tracer experiments were conducted in a mountainous coastal area of western Japan on 26 August 1994 to verify the dispersion model. The three-dimensional perspective in Fig.1 and the dotted contour lines in Fig.2 show the topographical features of the region. Figure 1 shows the topography as seen from the northeast. The interval between the contour lines in Fig.2 is 100m. The eastern part of the region was sea and the western part was land. The maximum elevation of the topography was higher than 500m. The point at which the tracer gas was released is indicated by the star (\star) in Fig.2. SF₆ tracer gas was released from an outlet mounted at a height of 180m on a stack and sampled at ground level. We used 5 sampling arcs, each of which had about 10 sampling points. The approximate distances of the arcs from the source were 1.5, 3, 4.5, 6 and 10 km, respectively. We also obtained meteorological data using equipment such as a radiosonde, ultrasonic anemometer, and Doppler sodar during the tracer experiment. The location of meteorological observation points are shown in Fig.2. The meteorological observations included the average of and fluctuations in wind direction and velocity, and temperature on the ground and in the upper atmosphere. These data were used for the calculation of the turbulence closure model. The tracer gas began to be released at 10 a.m. and sampling of the tracer gas was carried out from 11 a.m. to 3 p.m. The duration of each sampling was 30 minutes. That is, 8 sets of experimental data were obtained in one day. Due to the unstable thermal condition, a sea breeze occurred and thermal internal boundary layer developed.

CALCULATION RESULTS OF DISPERSION

Dispersion calculation was carried out under unsteady meteorological conditions. One hundred particles per second were used in the calculation and the time step was 4 seconds. The turbulence statistics were obtained every 10 minutes from the turbulence closure model. The standard deviation of the wind direction fluctuations in Eq. (16) was obtained using ultrasonic anemometer at the release point of tracer gas. The standard deviation of the horizontal wind angle was 10 ~ 20°. An example of the calculated particle trajectories over the topography is presented in Fig. 1.

Figure 2 shows an example of the comparison of the calculated and experimental concentrations on the ground surface. The concentration values were averaged over a period of 30 minutes from 12:00 to 12:30. In the figure, the solid contour lines show the concentration distribution calculated using the dispersion model; the concentration values are 10,

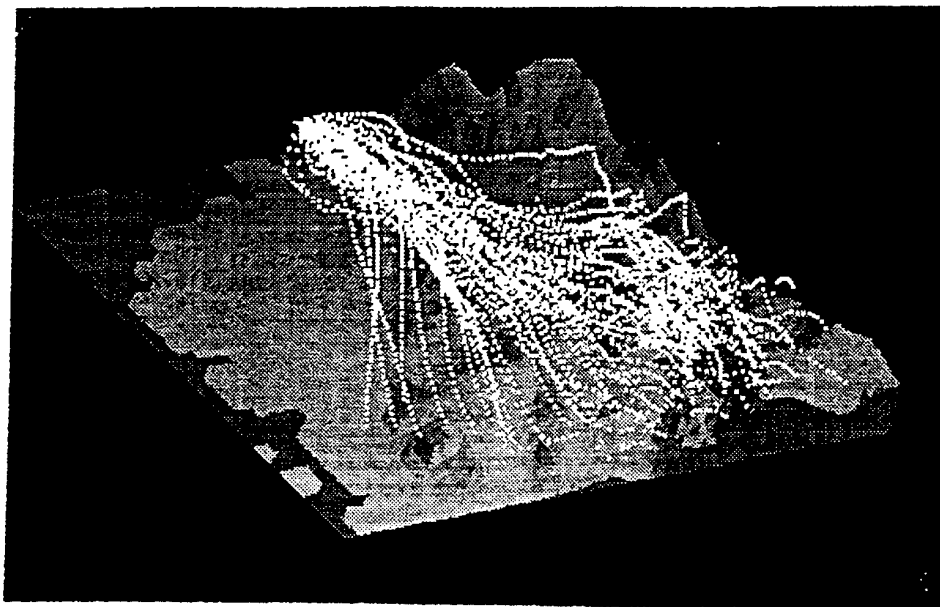


Fig. 1 Three-dimensional perspective of the topography as seen from the northeast and an example of the calculated particle trajectories.

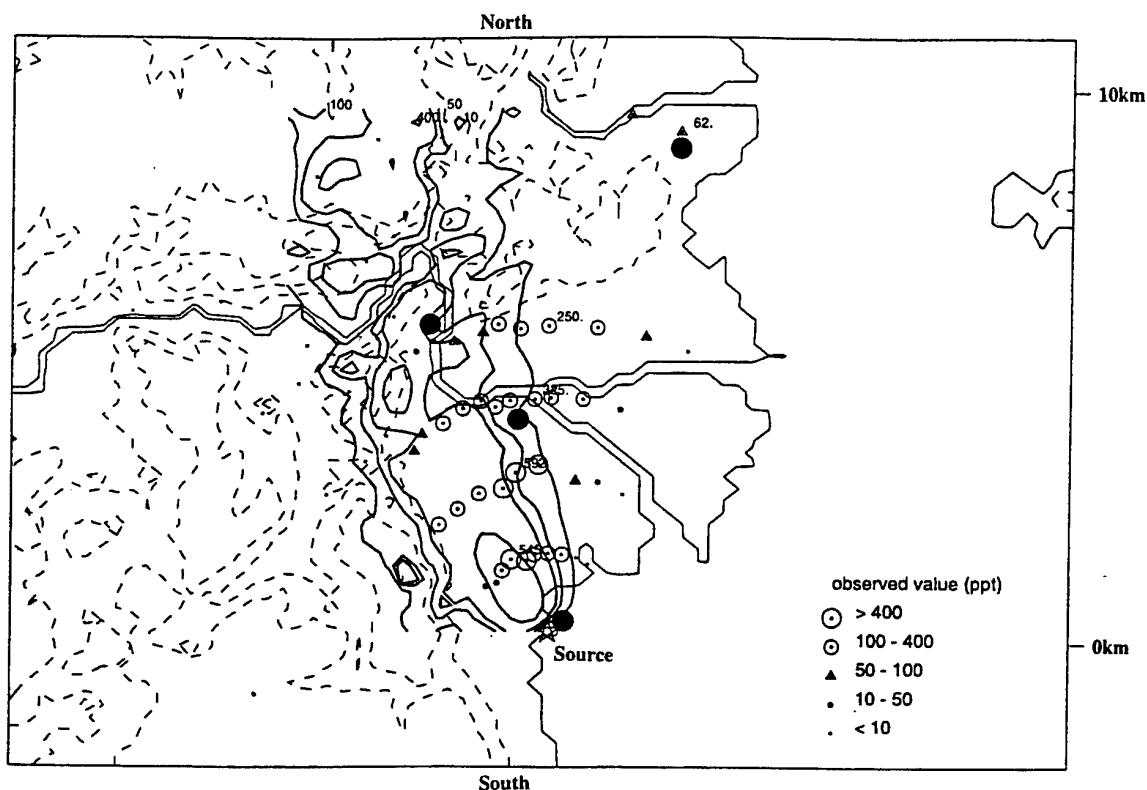


Fig. 2 Comparison of the ground surface concentrations obtained by calculation and in the field tracer experiment. The solid contour lines show the calculated results. The concentrations are 10, 50, 100 and 400 ppt, respectively, from the outside. ☆ and ● indicate the release point of the tracer and the locations of meteorological stations, respectively.

50, 100 and 400 ppt, respectively, from the outside. The circles, triangles and dots indicate the experimental results, and their values are shown. The calculated plume axis moves inland slightly compared to the experimental result, due to the fact that the sea breeze predicted by the turbulence closure model was stronger than that observed. However, the overall patterns of concentration distribution obtained using the dispersion model and in the field tracer experiment are in good agreement.

Figure 3 shows the comparison of the concentration distributions along the surface plume axis obtained by calculation and in the field tracer experiment. The plume axis represents the locations of the peak concentration at downwind distances from the source. There was a difference in the plume axes of the calculation and the experiment. The 8 figures in Fig.3 express the time series of 30-minute averages of calculated and observed concentrations. Both the calculated and observed peak concentrations are found within

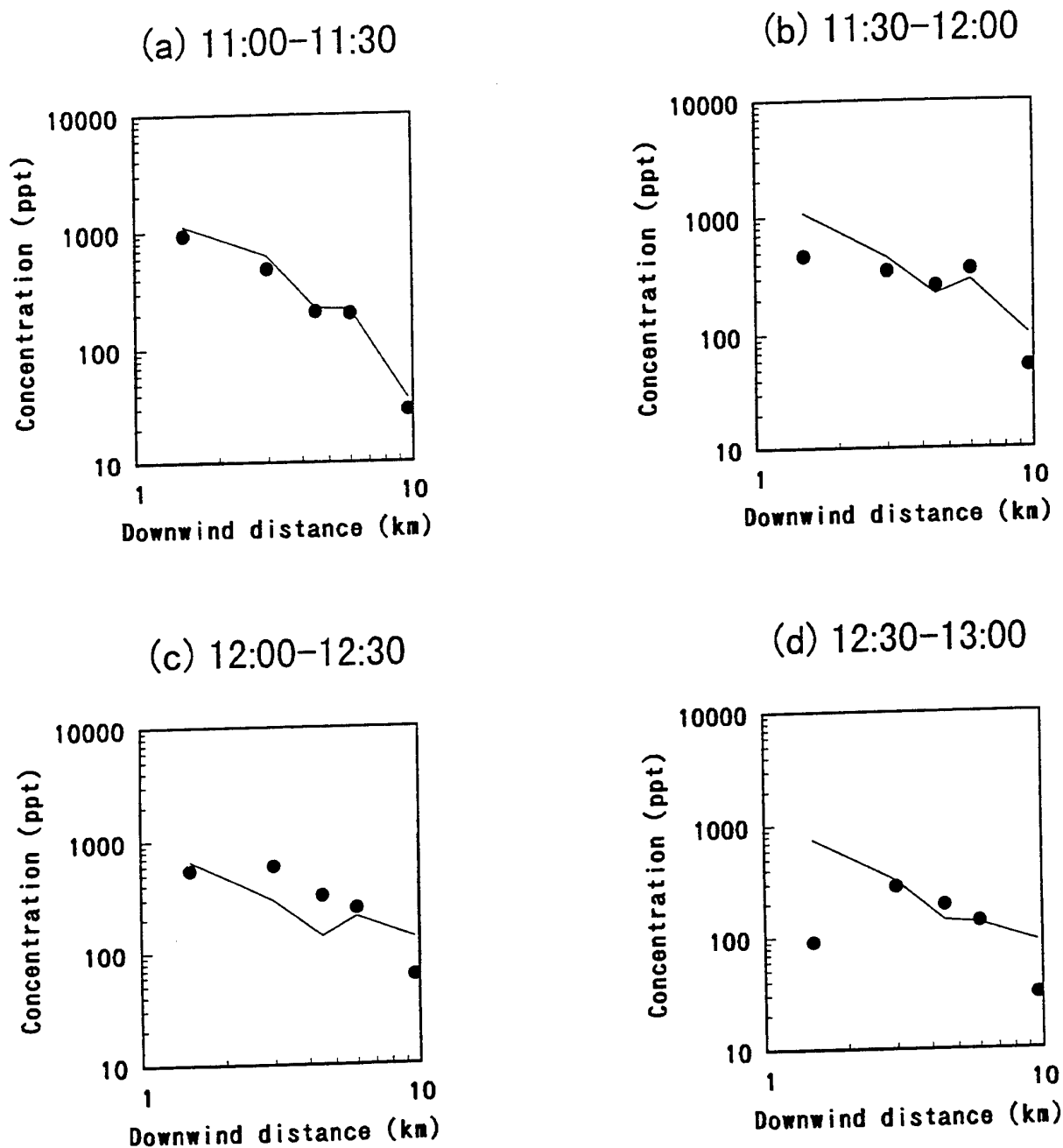
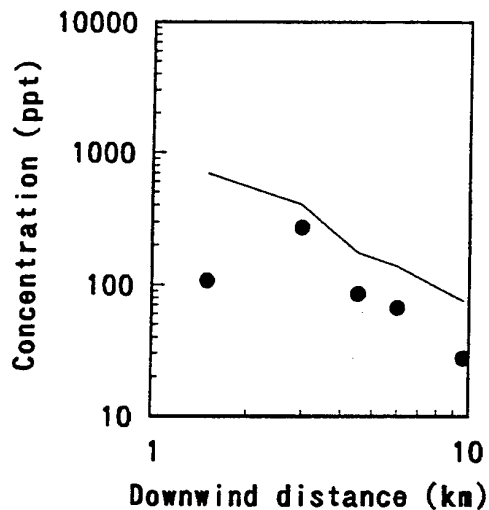
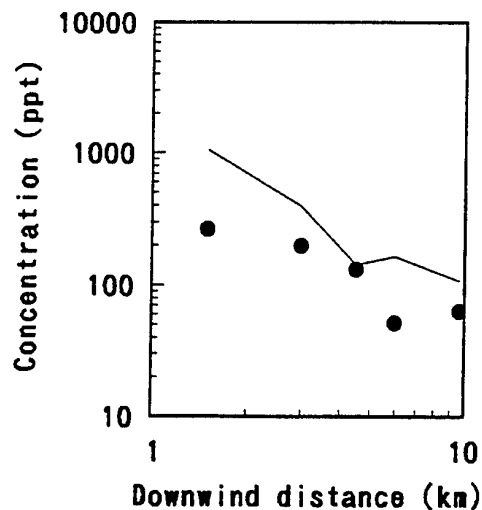


Fig. 3 Comparison of the concentration distributions along the surface plume axis, obtained by calculation and in the field tracer experiment. Solid line: calculation, ●: experiment.

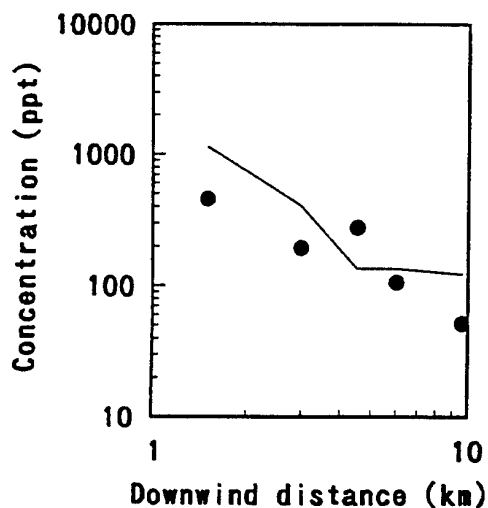
(e) 13:00-13:30



(f) 13:30-14:00



(g) 14:00-14:30



(h) 14:30-15:00

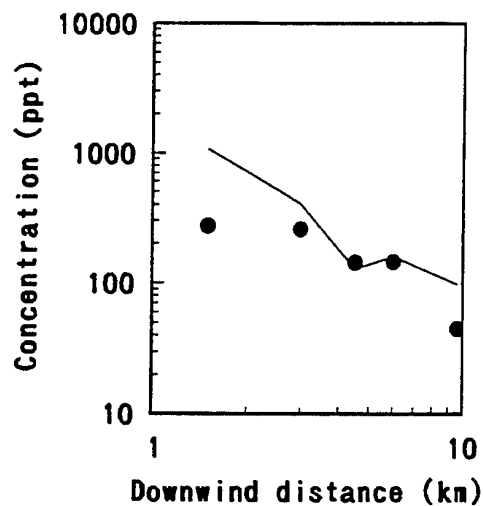


Fig. 3 Continued.

the downwind distance of 1.5 km for almost all periods. The calculated concentration distribution along the surface plume axis agrees well with the observed one for the period from 11:00 to 12:30. After 12:30, the dispersion model slightly overpredicts the concentration. A plot of observed peak concentrations at each sampling arc against calculated values is shown in Fig.4. Also shown are the lines of slope 1:1, 1:2

and 2:1. The average calculated-to-observed ratio is 1.6 and there is a high number of cases with calculations within a factor of 2 of observations. Although the dispersion model shows a tendency of slight overprediction, we can conclude that generally there is a good agreement between calculated and observed results.

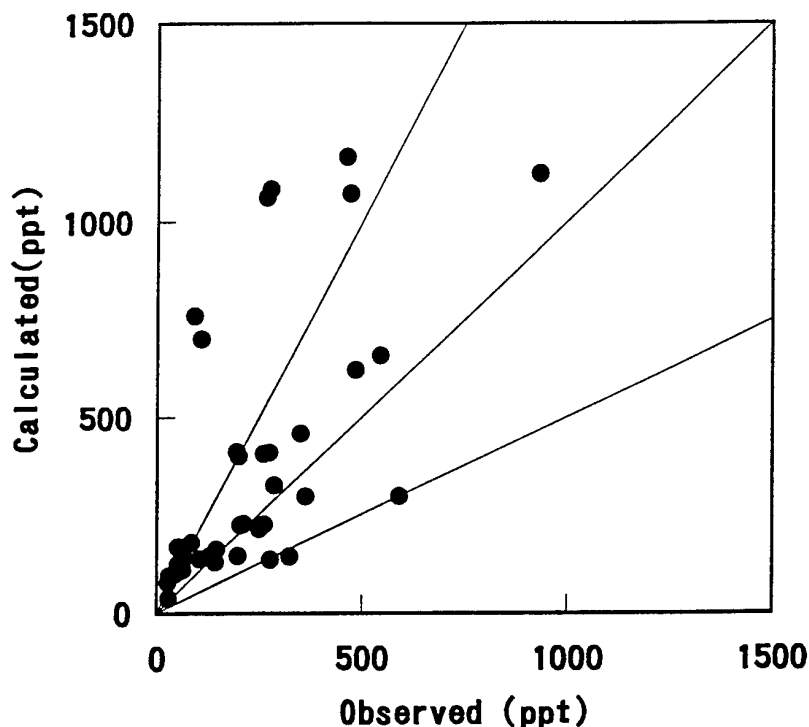


Fig. 4 Comparison of the peak concentrations at each sampling arc obtained by calculation and in the field tracer experiment:

CONCLUSION

A Lagrangian particle dispersion model was developed to predict concentrations of air pollutants in complex terrain. The dispersion model was applied to the prediction of concentration distribution over actual topography in Japan. Field tracer experiments were conducted in a mountainous coastal area of western Japan in order to verify the dispersion model. The thermal conditions were unstable. Dispersion calculation was carried out under unsteady meteorological conditions. The overall pattern of concentration distributions on the ground surface obtained using the dispersion model and in the field tracer experiment were in good agreement. The calculated results of concentration distribution along the surface plume axis and peak concentrations at each sampling arc agree well with the observed ones. It can be concluded that the dispersion model showed relatively high accuracy of prediction.

ACKNOWLEDGMENTS

This research was commissioned by the Agency of Natural Resources and Energy, of the Ministry of International Trade and Industry of Japan.

REFERENCES

- Gibson, M. M. and Launder, B. E., 1978, "Ground Effects on Pressure Fluctuations in the Atmospheric Boundary Layer," *J. Fluid Mech.* Vol. 86, pp. 491-511.
- Ichikawa, Y., Sada, K. and Asakura, K., 1996, "Simulation of Turbulent Dispersion Phenomena in a Complex Terrain using a Lagrangian Particle Dispersion Model," *Proceedings, 6th International Symposium on Flow Modeling and Turbulence Measurements*, Chen, C.-J. et al., ed., A. A. Balkema Publishers, Rotterdam, pp. 739-746.
- Luhar, A. K. and Britter, R. E., 1989, "A Random Walk Model for Dispersion in Inhomogeneous Turbulence in a Convective Boundary Layer," *Atmos. Environ.*, Vol. 23, pp. 1911-1924.
- Thomson, D. J., 1987, "Criteria for the Selection of Stochastic Models of Particle Trajectories in Turbulent Flows," *J. Fluid Mech.*, Vol. 180, pp. 529-556.
- Weil, J. C., 1990, "A Diagnosis of the Asymmetry in Top-Down and Bottom-Up diffusion using a Lagrangian Stochastic Model," *J. Atmos. Sci.*, Vol. 47, pp. 501-515.
- Wilson, J. D. and Sawford, B. L., "Review of Lagrangian Stochastic Models for Trajectories in the Turbulent Atmosphere," *Boundary-Layer Meteorol.*, Vol. 78, pp. 191-210.

A MODIFIED CONTINUOUS IN TIME STOCHASTIC MIXING MODEL : APPLICATION TO A SIMPLE ATMOSPHERIC CHEMICAL REACTION.

Christophe MICHELOT, Serge SIMOËNS,
Michel AYRAULT

LMFA, UMR CNRS 5509,
36, avenue Guy de Collongues , BP 163, 69131 - Ecully Cedex

Vladimir SABELNIKOV

Central Aerohydrodynamic Institute (TsAGI)
Zhukovsky, Moscow Region, Russia 140160

ABSTRACT

Concerning atmospheric problems, chemical reactions leading to pollutant emissions is greatly function of turbulent flow where species evolved. Particularly the turbulent micromixing effects are of great importance. The aim of this paper is to develop a new stochastic mixing model which is close to the experimental observations. This model theoretically shows its ability to recover correctly the experimental results concerning the relaxation of the probability density function (pdf) in homogeneous turbulence. Furthermore it shows a good agreement with experimental data concerning second order chemical reactions in turbulent mixing layer and two-dimensional source in homogeneous turbulence.

INTRODUCTION

Both Lagrangian stochastic models and Eulerian models for probability density function (pdf) transport equation are applied to turbulent reactive flows and then need some additional closure hypothesis for turbulent micromixing (i.e. mixing at molecular scale). Mixing models currently in use were reviewed by Dopazo (1994). One of the main problem is their discontinuity in time. This has been bypassed by the Monte-Carlo model of Hsu and Chen (1991). Unfortunately, applied to the case of a passive scalar diffusing in isotropic turbulence, this model does not lead to a pdf of concentration relaxing towards a Gaussian shape as experimentally observed by Jayesh and Warhaft (1992).

The continuous mixing Hsu and Chen model (HCM) is revisited and extended in the present paper. In first part theoretical analysis for obtaining the new model is developed. We show that it is function of a single parameter ψ (eq. 1) and that original HCM is a particular case of it. A self-similar solution of the pdf transport equation, which is obtained from equation (1), for the case of a passive scalar diffusing in isotropic turbulence is determined. It is shown that in most of the cases, the asymptotic pdf is quite far from Gaussian and has unbounded normalized moments. Only in the case of the deterministic parameter ψ the asymptotic pdf is Gaussian. In the second part, the new continuous stochastic model with ψ deterministic is applied to the case of mixing with chemical reaction between NO and O_3 . Two cases are studied:

1- mixing layer between two homogeneous flows of NO and O_3

2- homogeneous grid generated turbulence with the main flow doped with O_3 and a line source of NO .

These numerical results are compared to the experimental data of Bilger et al. (1991) for mixing layer, and of Li and Bilger (1996) for a line source. Our results are in good agreement with the experimental data.

THEORY

According to Hsu and Chen model (1991) the relationship between the concentration contained in two randomly selected particles m and n is described as follows :

$$\begin{aligned}\frac{dc_m(t)}{dt} &= \psi(c_n(t) - c_m(t)) \\ \frac{dc_n(t)}{dt} &= \psi(c_m(t) - c_n(t))\end{aligned}\quad (1)$$

where ψ is equal to ξ/T_d (T_d being the integral concentration fluctuation time scale and ξ a uniform random variable uniformly distributed in the range $[0,1]$). The equations of the system (1) are solved numerically using time discretisation. The time step τ used is such that $\tau \ll T_d$. Following Pope (1982) the pdf Concentration change for this time step τ is given by

$$p_c(\theta; t + \tau) = p_c(\theta; t) + \frac{1}{2} \int_{-\infty}^{\infty} \int_{-\infty}^{\infty} \int_{-\infty}^{\infty} p_c(c_m(t); t) p_c(c_n(t); t) A(\xi; t) \left[\delta(\theta - c_m(t+\tau)) + \delta(\theta - c_n(t+\tau)) - \delta(\theta - c_m(t)) - \delta(\theta - c_n(t)) \right] dc_m dc_n d\xi \quad (2)$$

where $A(\xi; t)$ is the pdf of the random variable ξ and $\delta(\cdot)$ is a Dirac function. From this equation, performing the second order Taylor expansions of $\delta(\cdot)$, $p_c(\cdot)$, $c_m(\cdot)$, $c_n(\cdot)$ and using the hypothesis that the random variable ξ is independent of the concentrations, we derive the following differential equations for pdf in homogeneous turbulence (more details can be found in Michelot et al. (1997))

$$\begin{aligned}\frac{\partial p_c}{\partial t} + \frac{\tau}{2} \frac{\partial^2 p_c}{\partial t^2} &= \langle \psi \rangle + \tau \left(\frac{1}{2} \frac{d\langle \psi \rangle}{dt} - \langle \psi^2 \rangle \right) \frac{\partial}{\partial \theta} ((\theta - \langle c \rangle) p_c) \\ &+ \frac{1}{2} \langle \psi^2 \rangle \tau \frac{\partial^2}{\partial \theta^2} ((\theta - \langle c \rangle)^2 + \sigma_\theta^2) p_c + O(\tau^2)\end{aligned}\quad (3)$$

After some calculations we obtain that to the first order, pdf obeys the diffusion equation with the concentration dependent coefficient of diffusion :

$$\frac{\partial p_c}{\partial t} = \left[\langle \psi \rangle + \left(\frac{\langle \psi \rangle^2}{2} - \langle \psi^2 \rangle \right) \tau \right] \frac{\partial}{\partial \theta} ((\theta - \langle c \rangle) p_c) + \frac{\tau}{2} \frac{\partial^2}{\partial \theta^2} \left((\sigma_\psi^2 (\theta - \langle c \rangle)^2 + \langle \psi^2 \rangle \sigma_\theta^2) p_c \right) + O(\tau^2) \quad (4)$$

The analysis of the equation (4), carried out by the authors, shows that the asymptotic (self-similar) pdf of decaying fluctuations of a passive scalar c in homogeneous turbulence is given by

$$p(c, t) = \frac{1}{\sigma(t)} g_0 \left[\left(\frac{c - \langle c \rangle}{\sigma} \right)^2 + \left(\frac{\langle \psi^2 \rangle}{\sigma_\psi^2} \right) \right]^{-\left(1 + \frac{\sigma_\psi^2 + \langle \psi^2 \rangle}{2\sigma_\psi^2}\right)} \quad (5)$$

where $\langle c \rangle$ and σ are, respectively, the mean value and the standard deviation of the concentration fluctuations; g_0 a constant determined by normalisation condition $\langle c \rangle$.

When ψ is a deterministic coefficient, the asymptotic pdf is Gaussian

$$p(c, t) = \frac{1}{\sqrt{2\pi}} \exp\left(-\frac{1}{2} \left(\frac{c - \langle c \rangle}{\sigma} \right)^2\right) \quad (6)$$

In particular one can conclude from equations (5) that in the case of HCM the normalized moments of even order greater than four diverge. Thus, to be in correspondance with experimental data which show that pdf tends to a Gaussian in isotropic turbulence, a deterministic coefficient ψ is recommended to use in continuous stochastic model described by the equations of the system (1).

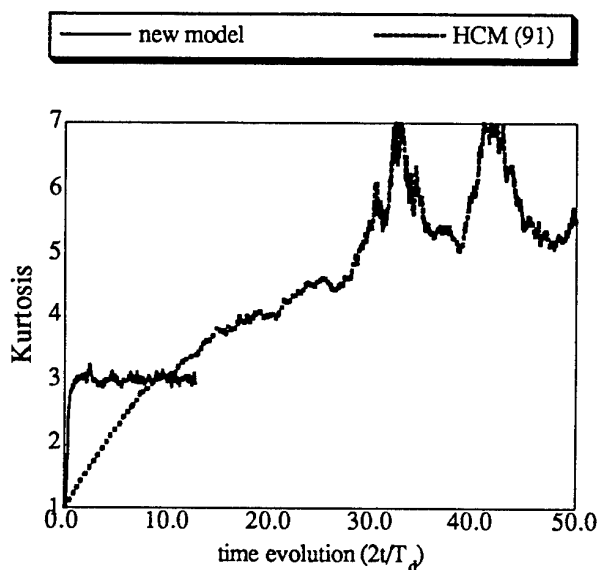
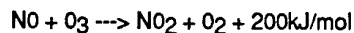


Figure 1 : comparison between concentration kurtosis obtain from HCM and the new model.

A comparison of the kurtosis obtained for deterministic coefficient ψ equal to 0.5 (our model) and random coefficient ξ uniformly distributed in $[0,1]$ (HCM) is given in figure 1 (the time step τ of numerical integration of equation (1) was equal to $0.05 T_L$) for initial Binary scalar field.

APPLICATION TO MIXING WITH IRREVERSIBLE CHEMICAL REACTION

We consider the following irreversible atmospheric reaction :



with k_0 the rate constant equal to $3.7 \cdot 10^{-1} \text{ ppm}^{-1} \text{ s}^{-1}$ at 293K. Different turbulent flows are considered : mixing layer between two turbulent homogeneous flows of NO and O_3 and the line source of NO emitting in a turbulence homogeneous flow doped with O_3 .

A Lagrangian stochastic model (Michelot, 1996) was used to describe the hydrodynamical part of the flows. The input parameters of this model (kinetic energy, dissipation and velocity variances were taken from experimental data (Bilger et al., 1991; Li and Bilger, 1996). More details could be found in (Michelot, 1996). Molecular mixing and chemical reaction are described by the stochastic model (1) with ξ equal to 0.5 and added terms corresponding to the chemical source included (i.e. $k_0 C_{\text{NO}} C_{\text{O}_3}$).

Different probability density functions, mean concentration, correlations and moments of higher orders were determined using numerical simulations. All the numerical results are in a quite good agreement with the experimental data of Bilger et al. (1991), and Li and Bilger (1996). In figure 2 some results of numerical simulation and comparisons with experimental data are presented.

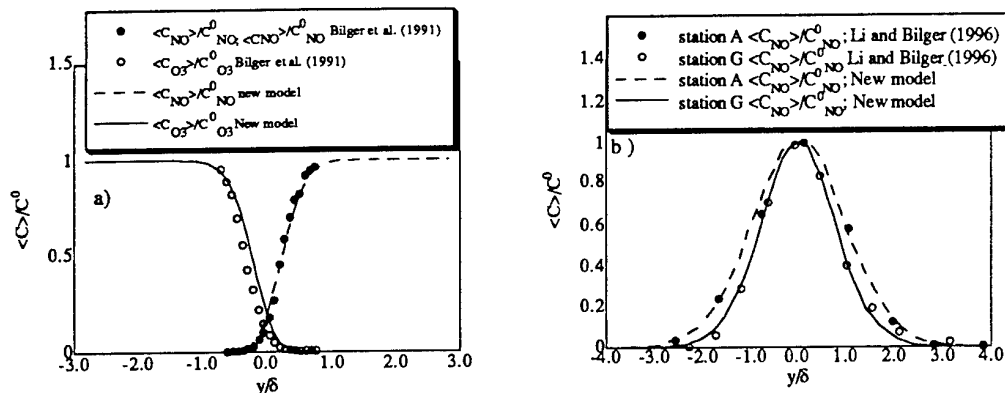


Figure 2: transverse mean concentration profiles for : a) NO and O3 at $x/M = 21$, Bilger et al. (1991) mixing layer experiment b) NO for the far field, Li and Bilger (1996). Comparison between experimental data and results from the new model.

CONCLUSION

The continuous in time stochastic mixing model of Hsu and Chen (1991) with deterministic coefficient ψ (originally in HCM ψ was considered as a random variable) is a promising tool for the description of molecular mixing and chemical reactions in turbulent flows. It provides a qualitative right relaxation of pdf in the case of a passive scalar diffusing in isotropic turbulent flow. Furthermore validation of this model including chemical reaction terms enable us to furnish good results in the case of chemical reaction issue from mixing of different species in homogeneous turbulent flow.

ACKNOWLEDGEMENTS

The authors are grateful to Prs. Li and Bilger for providing experimental data concerning the line source experiment (1996).

REFERENCES

- Bilger R.W., Sae tran L.R. and Krishnamoorthy L.V. , 1991, "Reaction in a scalar mixing layer", J. Fluid Mech. 233, 211 - 242.
- Dopazo C. , 1994, "Recent developments in pdf methods in turbulent reacting flows", Ch. 7. Ed. P.A. Libby, F.A. Williams Academic Press.
- Hsu A.T. and Chen J.Y. , 1991, "A continuous mixing model for pdf simulations and its application to combustng shear flows", Paper 22 - 4 , 22 - 4.1, 22 4.5, 8th Symp. on Turbulent shear flows, Terminal University, Munich, Germany, 9 - 11 september.
- Jayesh and Warhaft, 1992, "Probability distribution, conditional dissipation, and transport of passive temperature fluctuations in grid-generated turbulence", Phys. Fluids A4, 2292-2307.
- Li T.D. and Bilger R.W., 1996, "The diffusion of conserved and reactive scalars behind line sources in homogeneous turbulence", submitted to Journal of Fluid Mechanics .
- Li T.D., Brown R. J. and Bilger R.W. , 1992, "Experimental study of a scalar mixing layer using reactive and passive scalar", 11th Australasian Fluid Mechanics Conference, pp 159-162", .
- Michelot C., 1996, "Développement d'un modèle stochastique lagrangien : Application à la dispersion et à la chimie atmosphérique", Thèse de Docteur de l'Ecole Centrale de Lyon, 13th December.
- Michelot C., Simoëns S., Ayrault M. and Sabel'nikov V., 1997, "A continuous in time stochastic mixing model; Application to rapid chemical reaction in turbulent flows", submitted to Phys. Fluids A.
- Pope S.B., 1982, "An improved turbulent mixing model", Combust. Sci. and Tech. 28, 131.

TURBULENT FLOW AND HEAT TRANSFER FROM AN OBLIQUE FLAT PLATE TO A TWO-DIMENSIONAL WALL ATTACHING OFFSET JET

Heung Bok Song, Dae Seong Kim, Soon Hyun Yoon
School of mechanical engineering
Pusan National University, 609-735, Pusan, KOREA

Dae Hee Lee
School of mechanical and automotive engineering
Inje University, 621-749, Kimhae, KOREA

ABSTRACT

Turbulent flow and heat transfer characteristics of a two-dimensional oblique wall attaching offset jet were experimentally investigated. The local Nusselt number distributions were measured using liquid crystal as a temperature sensor. The jet mean velocity, turbulent intensity, and wall static pressure coefficient profiles were measured at the Reynolds number Re (based on the nozzle width, D) ranging from 17700 to 53200, the offset ratio H/D from 0 to 10, and the oblique angle α from 0° to 40° . It is observed that the time-averaged reattachment point nearly coincides with the maximum Nusselt number point for all oblique angles, and the maximum pressure position only for $\alpha < 20^\circ$. The decays of the maximum jet velocity in the streamwise direction obey the conventional $-1/2$ power law of the wall attaching offset jet for $\alpha \leq 30^\circ$. The reattachment position and maximum pressure position are well correlated with offset ratio and oblique angle. The correlations between the maximum Nusselt number and Reynolds number, offset ratio, and oblique angle are presented.

INTRODUCTION

The Oblique Wall Attaching Offset Jet (OWAOJ) is a two-dimensional slot jet issued into quiescent surroundings above an inclined plate. As depicted in a schematic diagram of the OWAOJ in fig. 1, when the jet discharges from the nozzle, the so-called "coanda effect" causes the jet to deflect towards the wall boundary and reattach to the plate wall. The jet redevelops in the wall jet region after its reattachment to the wall.

OWAOJ is frequently encountered in numerous industrial applications such as the cooling of a combustion chamber wall in a gas turbine, an air deflector as a circulation controller, an automobile demister, and a moisture remover in the car washer. In spite of its wide application to practical engineering problems, however, no previous research on the OWAOJ has been found in the literature search.

In the mean time, numerous studies on the wall attaching offset jet (WAOJ) have been performed. Borque and Newman

(1960) and Sawyer (1963) studied the mean flow characteristics of the WAOJ. Hoch and Jiji (1981a) numerically predicted the jet trajectory, jet reattachment length, wall pressure distribution, and maximum axial velocity decay. Pelfray and Liburdy (1986) provided the mean velocity and turbulent intensity profiles in the recirculation and impingement regions. Yoon *et al* (1993) presented the detailed flow data in the entire region of the WAOJ.

Kumada *et al* (1973) measured the mass transfer coefficients using the naphthalene sublimation technique. Hoch and Jiji (1981b), and Holland and Liburdy (1990) studied the thermal characteristics of the heated WAOJ, and the temperature and energy distributions of the heated WAOJ, respectively. Most recently, Kim *et al* (1996) investigated the flow and heat transfer characteristics of the WAOJ and found that a dividing streamline of the jet unstably reattaches in the impingement region. They also found that the jet reattachment point nearly coincides with the maximum Nusselt number position and

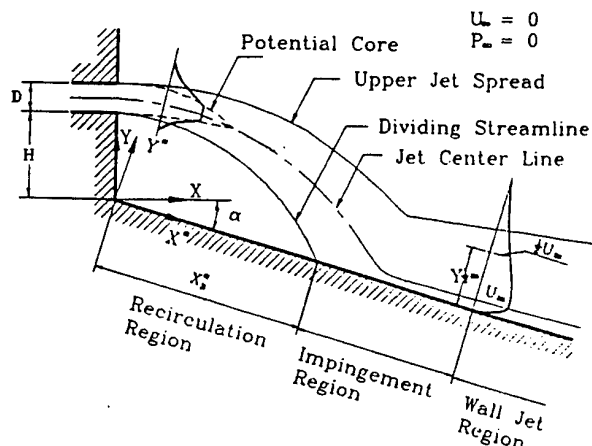


FIG.1 DEFINITION SKETCH OF THE WALL
ATTACHING OFFSET JET FLOW

presented correlations between the local Nusselt number distributions and the Reynolds number, the offset ratio, and the streamwise distance.

In the present study, the mean velocities, turbulent intensities, wall static pressure coefficients, and local heat transfer coefficients in the entire region of the OWAJO are measured by employing a split film probe and thermochromic liquid crystal. The Reynolds number ranges from 17700 to 53200, the offset ratio from 0 to 10, the oblique angle from 0° to 40°. This research is an extension of the previous work by Kim *et al.* (1996) in that it investigates the effect of the oblique angle on the flow and heat transfer characteristics of the two-dimensional WAOJ.

EXPERIMENTAL APPARATUS

Measurements are made in a low speed blow-down wind tunnel. Air is moved by 5HP centrifugal fan and the fan speed is controlled by an inverter. The wind tunnel consists of a diffuser, a plenum chamber and a contraction nozzle. A size of the plenum chamber is 300mm x 300 mm and a size of the nozzle is 300mm x 25mm, resulting in an aspect ratio of 12. The jet velocity U_j at the nozzle exit is measured with a pitot tube to an accuracy of $\pm 2\%$. The initial turbulent intensities at the nozzle exit are $u/U_j = 0.1\%$, $v/U_j = 0.2\%$ and $w/U_j = 0.15\%$, respectively. The test plate on which the discharged jet attaches is made of 300mm high 1.8m long and 10mm thick plexiglass. The test plate surface was heated with gold film Intrex (a very thin gold-coated polyester substrate sheet) by passing a DC Current, which created a uniform heat flux boundary condition on the plate surface. The liquid crystal used in this experiment is "R35C3W" micro-encapsulated thermochromic liquid crystal. Since the actual color image is affected by factors such as the angle and distance of the light illuminating the liquid crystal covered surface, and aging effects, a careful color calibration was carried out. In order to accurately determine the spatial location of the particular color and to minimize a visual bias, a true color image processing system was utilized. The flow measurements were made a Reynolds number of $Re = 53200$, the offset ratio of $H/D = 5.0$ and, the oblique angle of $\alpha = 0^\circ$ to 40° . Heat transfer measurement were made for the Reynolds numbers ranging from 17700 to 53200, the offset ratio from 0 to 5 and the oblique angles ranging from 0° to 40° .

DATA REDUCTION

Details of the flow and heat transfer measurement technique used in this study are described by Yoon (1993) and Lee *et al.* (1994), respectively. For flow field measurements in the OWAJO, a split film probe (TSI-1288) which is an end-flow-type, 0.15mm diameter and 2mm long, was used. The probe calibration method used was the same as that described by Yoon (1993). A location of the reattachment point was estimated by a forward flow fraction, γ_w , which was defined as a fraction of time duration of which the flow is directed towards downstream. The streamwise and crosswise turbulent velocity components in the OWAJO were measured using a constant temperature anemometer (TSI, IFA300). A calibrated 0.025cm diameter Chromel-Alumel thermocouple measured the jet exit temperature to an accuracy of $\pm 0.1^\circ\text{C}$. By electrically heating a very thin gold-coating on the Intrex, an essentially uniform

wall heat flux condition is established. The heat flux can be adjusted by changing the current through the Intrex, which changes the surface temperature. Under the constant heat flux condition, an isotherm on the Intrex surface corresponds to a contour of a constant heat transfer coefficients. As the heat flux changes, the position of the color isotherm is also moved. The local heat transfer coefficient at the position of the particular color being observed is calculated from

$$h = \frac{q_v}{(T_w - T_j)} \quad (1)$$

where, T_w is the wall temperature determined by liquid crystal, T_j is the jet temperature, q_v is the net heat flux which is obtained by subtracting the radiation and conduction heat losses from the total heat flux through the Intrex, i.e.

$$q_v = \frac{IV}{A} - \epsilon\sigma(T_w^4 - T_a^4) - q_c \quad (2)$$

where, variables I , V , A , ϵ , σ , T_a , and q_c are the current across the Intrex, voltage across the Intrex, surface area of the Intrex, emissivity of liquid crystal on the plate surface, Stefan-Boltzmann constant, ambient temperature, and the conduction heat loss, respectively. The uncertainty estimates calculated by Kline and Mcclintock (1953) show that the uncertainty in the mean velocity at the maximum pitch angle of above $\pm 70^\circ$ is less than 5% and the uncertainty of Nusselt number for $H/D=5$, $\alpha=0^\circ$, and $X/D=12$ at $Re=53200$ is less than 4%. The uncertainty in the wall temperature factor is the largest contribution to the total uncertainty. Another source of the large uncertainty is the gold coating uniformity.

RESULT AND DISCUSSION

Flow characteristics

The pressure distributions along the plate are shown in Fig. 2, for $Re=53200$, $H/D=5$, and $\alpha=0^\circ$ to 40° . The wall static pressure coefficient is defined by,

$$C_{PW} = \frac{(P_w - P_\infty)}{1/2\rho U_j^2} \quad (3)$$

where, P_w is a static pressure on the wall and P_∞ is the atmospheric pressure. It can be observed from Fig. 2 that with an oblique angle increasing from $\alpha=0^\circ$ to 40° in the recirculation region, the maximum pressure position on the plate shifts downstream and the magnitude of the maximum pressure coefficient decreases. On the other hand, the minimum pressure position also shifts downstream with an increasing oblique angle, but the magnitude of the minimum pressure coefficient remains nearly unchanged.

Fig. 3 shows variations of the reattachment length, X_R^* . The maximum Nusselt number position, $X_{N_{max}}^*$, and the maximum pressure position, $X_{P_{max}}^*$, with the offset ratio for $\alpha = 0^\circ$ to 40° and $Re=53200$. In general, the reattachment point has been used as an important parameter to better understand the flow characteristics of the WAOJ. According to our previous WAOJ research results (Kim *et al.*: 1996), the WAOJ flow reattachment is a very unsteady process, resulting in a wide

reattaching region. In spite of the unsteadiness of the reattachment region, Kim *et al.* (1996) estimated the reattachment length by considering the point where the mean skin friction coefficient vanishes (i.e., the γ_w value becomes 0.5) as the time-averaged reattachment point of the unsteady reattaching flow. They showed that the reattaching length increases with an increasing offset ratio. The similar flow behaviors can be expected for the OWAOJ since the WAOJ is a limiting case ($\alpha=0^\circ$) of the OWAOJ.

It is shown from Fig. 3 that the reattachment length increases with an increasing offset ratio and oblique angle. The reattachment length for the case of $\alpha=0^\circ$ in the present experiment is in a good agreement with those of Borque and Newsman (1960) and Hoch and Jiji (1981a). Fig. 3 also shows the position of the time-averaged reattachment point nearly coincides with the maximum Nusselt number position. Vogel and Eaton (1985) and Baughn *et al.* (1987) have demonstrated that the maximum Nusselt number position closely agrees with the reattachment point, and in the light of the close similarity of the flows, it can be assumed that the same is true for the OWAOJ.

It should also be noted from Figs. 2 and 3 that the reattachment point nearly coincide with the maximum wall pressure position for $\alpha < 20^\circ$. However, as the oblique angle increases $\alpha = 20^\circ$, the reattachment point more closely coincides with the point where the pressure coefficient changes from negative to positive value than with the maximum pressure position. A similar behavior can be seen from Fig. 4. As the oblique angle increases from $\alpha = 20^\circ$, the gap between the reattachment position and the maximum pressure position is progressively widening. According to Fig. 4, the reattachment position and maximum pressure position are well correlated by the following expressions:

$$X_R^\alpha / D = 4.854 (H/D)^{0.6} \cos(\alpha)^{-3.02} \quad (4)$$

and

$$X_{Cpmax}^\alpha / D = 4.975 (H/D)^{0.6} \cos(\alpha)^{-3.52} \quad (5)$$

These correlations are valid for $2.5 \leq H/D \leq 10$, $0^\circ \leq \alpha \leq 40^\circ$,

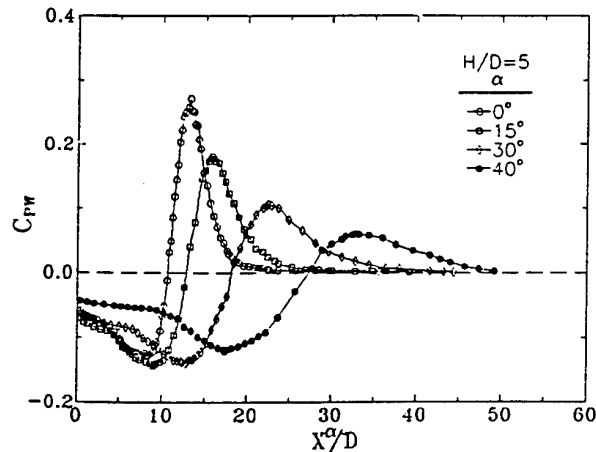


FIG.2 DISTRIBUTIONS WALL STATIC PRESSURE COEFFICIENT FOR $H/D=5.0$, $Re=53200$, AND $\alpha=10^\circ$ TO 40°

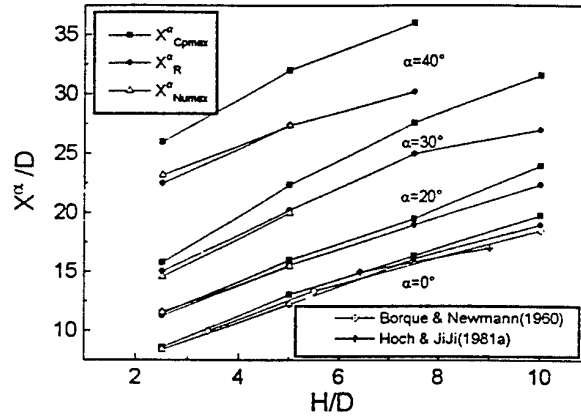


FIG.3 VARIATIONS OF THE REATTACHMENT LENGTH, Nu_{max} POSITION, AND Cp_{max} POSITION WITH OFFSET RATIO FOR $\alpha=10^\circ$ TO 40°

and $Re=53200$. The mean velocity vector profiles in the initial flow development region of the OWAOJ for $H/D=5$ and $\alpha=20^\circ$ are shown in Fig. 5. The primary jet flow appears to curve gradually in the recirculation region and turns downward as the jet impinges on the plate. To investigate the flow characteristics of the OWAOJ in the far downstream region, the mean velocity profiles for different oblique angles are plotted along the vertical distance in Fig. 6. According to Rajaratnam and Subramanya (1968) who performed the plane turbulent attached wall jet experiment, the mean velocity profiles in the wall jet region become similar in the region corresponding to $x^a \geq 20D$. A similar behaviour is also observed both in the WAOJ experiment by Kim *et al.* (1996) and in the present experiment for $\alpha=0^\circ$. However, as the oblique angle increases, a starting position of the velocity similarity moves further downstream, and for $\alpha=40^\circ$, the velocity similarity would not be observed until $x^a=50D$.

The decays of the maximum axial velocity, U_m , of the OWAOJ are displayed in log scales in Fig. 7. Within the

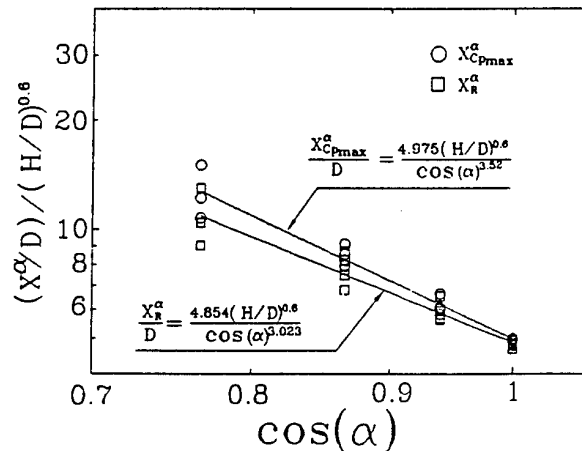


FIG.4 EFFECT OF THE OBLIQUE ANGLE ON THE REATTACHMENT POINT AND MAXIMUM PRESSURE POSITION FOR $Re=53200$

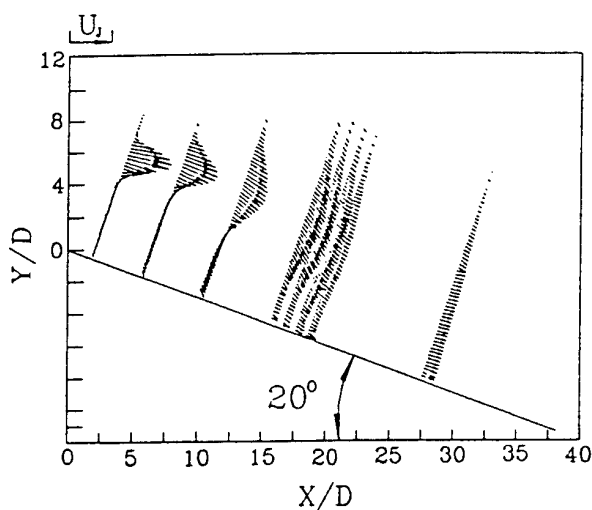


FIG. 5 MEAN VELOCITY VECTOR PROFILES FOR $H/D=5$, $Re=53200$ AND $\alpha=20^\circ$

the maximum axial velocity decays with $\sqrt{X^\alpha}$). However, for $\alpha=40^\circ$, the maximum velocity decay profile is deviated from the typical fully developed wall jet. Thus, it can be speculated that when the oblique angle is greater than 40° , the flow completely departs from the WAOJ.

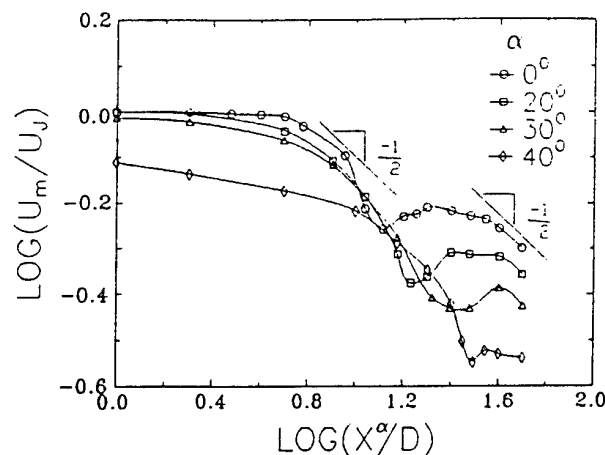


FIG. 7 LOGARITHMIC PLOTS OF THE MAXIMUM VELOCITY VARIATIONS TO SHOW A POWER LAW DECAY FOR $H/D=5$, $Re=53200$ AND $\alpha=0^\circ$ TO 40°

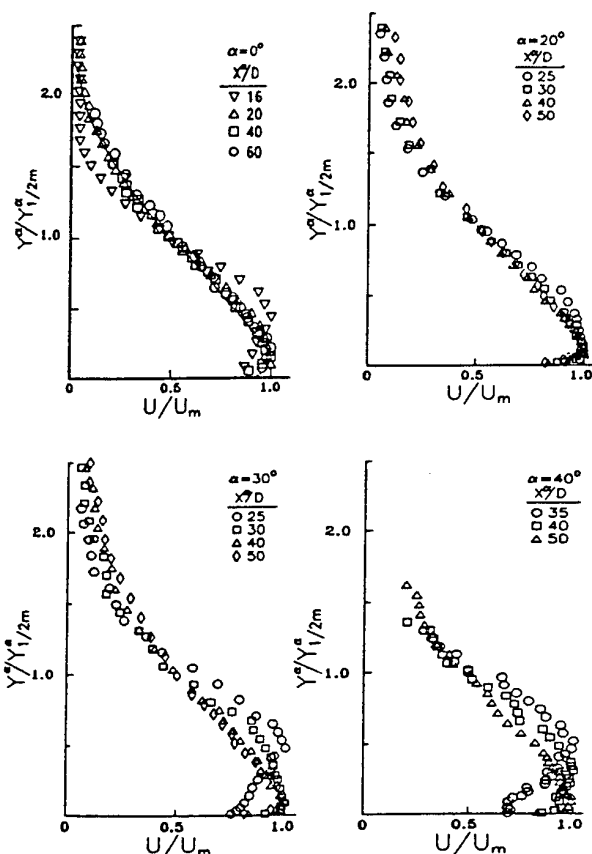


FIG. 6 NON-DIMENSIONAL MEAN VELOCITY DISTRIBUTIONS FOR $H/D=5$, $Re=53200$ AND $\alpha=0^\circ$ TO 40°

experimental uncertainty, it may be concluded that for $\alpha=0^\circ$ to 30° , the maximum velocity decay of the OWAOJ, both in the initial development region and in the wall jet region, obeys the conventional $-1/2$ power law of the wall attaching offset jet (i.e.,

Heat transfer characteristics

The local Nusselt number distributions along the plate are presented in Fig. 8 for three offset ratios, one Reynolds number $Re=53200$ and five oblique angles. In general, the position and magnitude of the maximum Nusselt number are much influenced by oblique angle and offset ratio. The local Nusselt number in the recirculation region increases due to turbulent mixing processes by the recirculation bubble and reaches a maximum value at the point where the jet flow reattaches. The Nusselt number in the wall jet region begins to decrease monotonically from the maximum value at the reattachment point and likely converged (except for $\alpha=40^\circ$) to approximately the same value as the flow redevelops far downstream.

It should be noted from Fig. 8 that the minimum Nusselt number occurs between $X^\alpha/D \approx 1.0$ and $X^\alpha/D \approx 5.0$ for the offset ratios and oblique angles tested, with an increase of the Nusselt number as the upstream inclined wall is approached. This increase of the Nusselt number is attributed to an additional mixing of the flow caused by a secondary recirculation in the upstream corner near the step of the of the inclined wall. The existence of the secondary recirculation is also observed by the color display of liquid crystal on the plate wall.

Variations of the maximum Nusselt number, Nu_{max} with jet Reynolds number and oblique angle are shown Fig. 9 for two offset ratios of $H/D=2.5$ and 5.0 . The maximum Nusselt number varies according to $Nu_{max} \propto (Re)^{0.52-0.65}$ and for $Nu_{max} \propto (Re)^{0.52-0.65} H/D=2.5$ and 5.0 , respectively. The exponents to Reynolds number corresponds to each oblique angle of $\alpha=0^\circ$ to 40° . As shown in Fig. 3, the maximum Nusselt number position nearly coincides with the reattachment point and the reattachment point formed by the OWAOJ can be considered to be the stagnation point in the impinging jet. Our

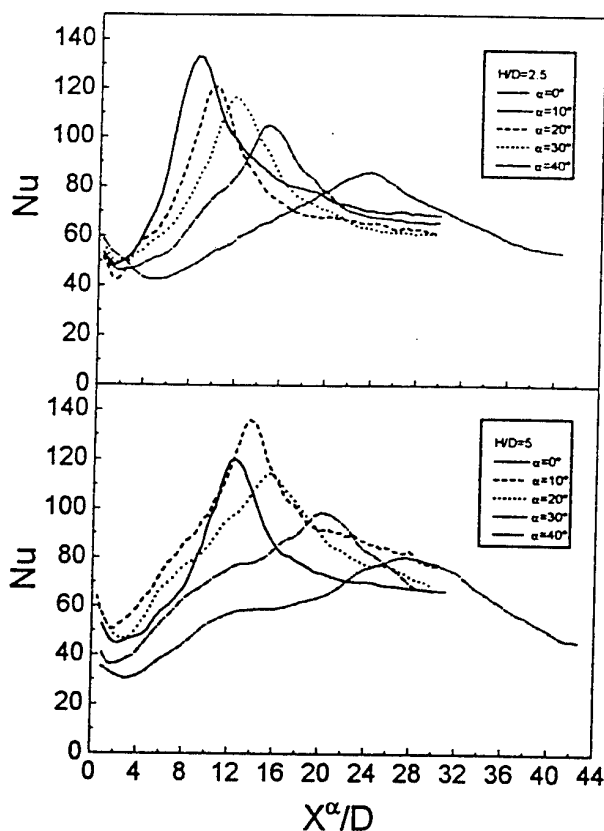


FIG. 8 STREAMWISE VARIATIONS OF THE LOCAL NUSSELT NUMBER WITH OBLIQUE ANGLE AND OFFSET RATIO FOR $Re=53200$

results approximately agree with those of impinging jet flow studies by Lee *et al.* (1995) and Hollworth and Gero (1985) for which the exponents to Reynolds number varied from 0.5 to 0.67 depending on the nozzle-to-plate distances and Reynolds number tested. Kumada *et al.* (1973) also reported in their mass transfer study with WAOJ that the maximum Sherwood number depends on $Re^{0.58}$ for the offset ratios ranging from 2.5 to 24.5.

Fig. 10 depicts a dependence of heat transfer parameter Nu_{max}/Re^n on the oblique angle for $H/D=2.5$ and 5.0 the maximum Nusselt number distributions have the following correlations:

$$Nu_{max} = 0.367 (Re)^{0.54} \cos(\alpha)^{1.817} \quad H/D=2.5 \quad (6)$$

and

$$Nu_{max} = 0.176 (Re)^{0.60} \cos(\alpha)^{1.50} \quad H/D=5 \quad (7)$$

These correlation indicate that for larger offset ratio of $H/D=5.0$, the Reynolds number dependence of Nu_{max} is stronger. This may be due to an increase of turbulence in the approaching jet as a result of stronger exchange of momentum with surrounding air, since in the case of larger offset ratio, the jet travels a longer distance before impinging on the plate. Meanwhile, the oblique angle dependence of Nu_{max} is stronger for $H/D=2.5$

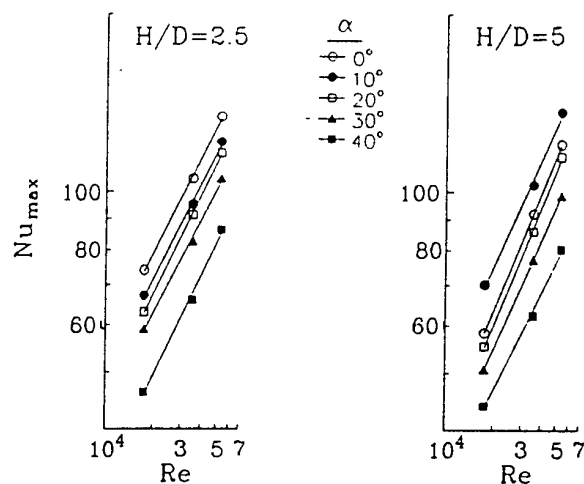


FIG. 9 EFFECT OF REYNOLDS NUMBER AND OBLIQUE ANGLE ON THE MAXIMUM NUSSELT NUMBER FOR $H/D=2.5$ AND 5.0

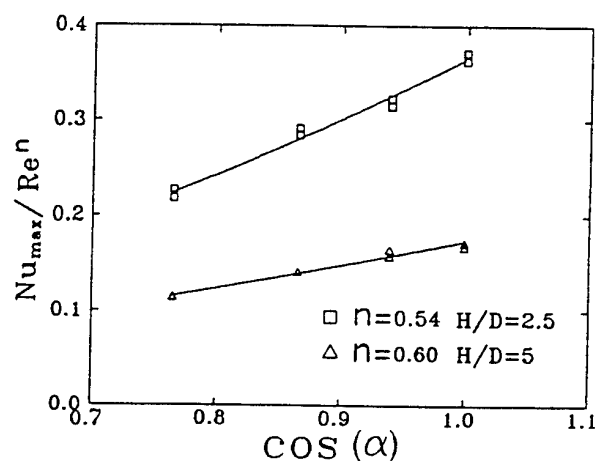


FIG. 10 VARIATIONS OF THE MAXIMUM NUSSELT WITH OBLIQUE ANGLE AND REYNOLDS NUMBER FOR $H/D=2.5$ AND 5.0

than $H/D=5.0$.

Fig. 11 shows variations of the mean Nusselt number with the oblique angle in the initial development region corresponding to $X^a \leq 31D$. The mean Nusselt number is defined as

$$Nu_{mean} = \frac{1}{x^a} \int_0^{x^a} Nu \, dx \quad (8)$$

The results show that the largest Nu_{mean} occurs at $\alpha=0^\circ$, and $\alpha=10^\circ$ for $H/D=2.5, 5.0$ respectively. The magnitudes of Nu_{mean} are larger for $H/D=2.5$ than for $H/D=5.0$ at $\alpha=0^\circ$, and $\alpha>30^\circ$. This may be due to a large downstream shift of the reattachment point for $\alpha>30^\circ$ and $H/D=5.0$

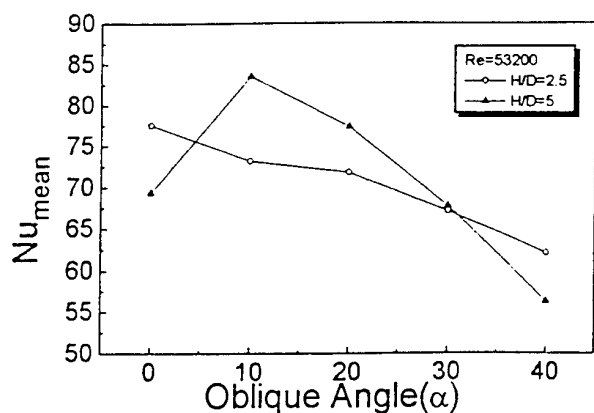


FIG.11 VARIATIONS OF THE MEAN NUSSELT NUMBER WITH OBLIQUE ANGLE FOR $H/D=2.5$ AND 5.0 AND $Re=53200$

CONCLUSION

Turbulent flow and heat transfer characteristics of a two-dimensional oblique wall attaching offset jet (OWAOJ) have been experimentally investigated. The results show that the maximum pressure on the plate shift downstream and the magnitude of the maximum pressure coefficient decreases with an increasing oblique angle in the recirculation region. But, the magnitude of the minimum pressure coefficient remains unchanged.

It is found that the time-averaged reattachment point nearly coincides with the maximum Nusselt number point for all oblique angle tested and the maximum pressure position for $\alpha < 20^\circ$. The flow similarity in the wall jet region is observed for $X^+ < 20^\circ$. The flow similarity in the wall jet region is observed for $X^+ \geq 20^\circ$ at $\alpha = 0^\circ$. But, as the oblique angle increases, the position of similarity moves further downstream, and for $\alpha = 40^\circ$, the flow similarity is not observed until $X^+ = 50D$. The decays of the maximum axial velocity of the OWAOJ obey the $-1/2$ power law of the wall attaching offset jet for $X^+ \leq 30^\circ$.

The local Nusselt number in the recirculation region increases due to turbulent mixing processes by the recirculation bubble and reaches a maximum value at the reattachment point. The maximum Nusselt number varies according to $Nu_{max} \propto (Re)^{0.52-0.56}$, and $Nu_{max} \propto (Re)^{0.55-0.65}$ for $H/D=2.5, 5$ respectively. It is observed that the Reynolds number dependence of Nu_{max} is stronger for larger offset ratio of $H/D=5.0$. This is attributed to an increase of turbulence in the approaching jet as a result of more active exchange of momentum with surrounding air. It is also observed that the minimum Nusselt number occurs between $X^+/D \approx 1.0$ and $X^+/D \approx 5.0$ for all H/D and α tested, with an increase of the Nusselt number as the upstream inclined wall is approached, which is due to an additional mixing caused by the secondary recirculation.

REFERENCE

Baughn, J. W. and Shimizu, S., 1989, "Heat transfer measurements from a surface with uniform heat flux and an

impinging jet", *J. Heat Transfer* 111, 1096-1098

Baughn, J. W., Hoffman, M. A., Launder, B.E., Lee, D. and Yap, C., 1989, "Heat transfer and velocity measurements downstream of an abrupt of an abrupt expansion in a circular tube at a uniform wall temperature", *J. Heat Transfer* 111,

Borque, and Newmann, G., 1960, "Reattachment of a two-dimensional incompressible jet to an adjacent flat plate", *Aerion Quat.* 11, 201-232

Hoch, J. and Jiji, M., 1981, "Two-dimensional turbulent offset jet boundary interaction", *J. Fluids Engng* 103, 154-161

Hoch, J. and Jiji, M., 1981, "Theoretical and experimental temperature distribution in two-dimensional turbulent jet boundary interaction", *J. Heat Transfer* 103, 331-336

Holland, J. T. and Liburdy, J. A., 1990, "Measurements of the thermal characteristics of heated offset jet", *Int. J. Heat Mass Transfer* 33, 69-78

Hollworth, B. R. and Gero, L. R., 1985, "Entrainment effects on impingement heat transfer :part2-local heat transfer measurements," *ASME J. of heat transfer*, vol. 107. Pp. 910-915

Kim, D. S., Yoon, S. H., Lee, D. H. and Kim, K. C., 1996, "Flow and heat transfer measurements of a wall attaching offset jet", *Int. J. Heat Mass Transfer*, Vol. 39, No. 14, pp.2907-2913

Kim, K., 1991, "A new hue-capturing technique for the quantitative interpretation of liquid crystal images used in convective heat transfer studies", Ph. D. Thesis, The Pennsylvania State University, PA

Kline, S. J. and McKlintock, F. A., 1953, "Describing uncertainties in single sample experiments", *Mech. Eng* 5, 3-8

Kumada, M., Mabuchi, I. and Oyakawa, K., 1973, "Studies in heat transfer to turbulent jets with adjacent boundaries (3rd report mass transfer to plane turbulent jet reattachment on an offset parallel plate)", *Bull. JSME* 16, 1712-1722

Lee, S. J., Lee, J. H. and Lee, D. H., 1994, "Local heat transfer measurements from an elliptic jet impinging on a flat plate using liquid crystal", *Int. J. Heat Mass Transfer* 37, 967-976

Lee, D. H., Greif, R., Lee, S. J. and Lee, J. H., 1995, "heat transfer from a flat plate to a fully developed axisymmetric impinging jet," *ASME J. of heat transfer* vol. 117, pp. 772-776

Pelfray, J.R. R. and Liburdy, J. A., 1986, "Mean flow characteristics of a turbulent offset jet", *J. Fluids Engng* 108, 82-88

Ra, S. H., Chang, P. K. and Park, S. O., 1990, "A modified calibration technique for the split film sensor", *Meas. Sci. Technol.* 1, 1156-1161

Rajaratnam, N. and Subramanya, N., 1968, "Plane turbulent reattached wall jet", *J. Hydraulic Div.* 94, 95-112

Sawyer, R. A., 1963, "Two-dimensional reattachment jet flows including the effect of curvature on entertainment", *J. Fluid Mech.* 17, 481-498

Yoon, S. H., 1992, "Investigation on the turbulence structure of a wall-attaching offset jet", Ph. D. Thesis, Korea Advanced Institute of Science and Technology, Taejeon

Yoon, S. H., Kim, K. C., Kim, D. S. and Chung, M. K., 1993, "Comparative study of a turbulent wall-attaching offset jet and a plane wall jet", *Trans. KSME J.* 7, 101-112

Vogel, J. C. and Eaton, J. K., 1985, "Combined heat transfer and fluid dynamic measurements downstream of a backward-facing step", *J. Heat Transfer* 107,992- 929.

CONCENTRATION FLUCTUATION CHARACTERISTICS AROUND A CUBIC OBSTACLE

Ryusuke Yasuda, Yukoh Ikeda
College of Engineering, Osaka Prefecture University
1-1, Gakuen-cho Sakai, Osaka, 593
JAPAN

ABSTRACT

To investigate the fundamental property of concentration fluctuation around a surface mounted obstacle, and to get a quantitative reference data set for the verification of numerical simulation, a wind tunnel experiment was performed. In this study, we focused on the turbulent diffusion of passive pollutant around a surface mounted cube. A continuous point source was located on the roof of it.

The distribution pattern of the mean concentration near the ground surface was not so sensitive to the detailed location of the emission source as far as it was set on the roof. The instantaneous concentration measurements showed large fluctuation and highly intermittent character.

As far as our experimental configuration, clipped-normal distribution did not fit so well to the cumulative distribution of instantaneous concentration. Log-normal distribution seems to be more preferable for the use of environmental assessment.

The frequency weighted power spectra obtained at the adjacent points of the emission source seems to suggest the existence of "inertial-meandering" subrange.

INTRODUCTION

Recently, concentration prediction of pollutants around buildings has become an important issue associated with the use of co-generation systems, which promote energy efficiency. In such cases, a large amount of exhaust gas flows out from vents of a building and relatively high concentrations might occur around it. In urban areas it is especially important to be able to predict the concentration distribution in the vicinity of buildings because the activity area of our life surrounds them. Many studies have been made to establish a mean concentration prediction model around a building and several methods have been proposed (e.g. Huber and Snyder(1982); Wilson and Lamb(1994)). Though these models may give good estimations for the situations on which they based, further fundamental investigation seem to be required to expand their applicability and to develop an evaluation method for concentration fluctuation around buildings.

In the recent years, several research groups (e.g. Sykes and Henn(1992); Mylne et al.(1996)) have investigated the

statistical characteristics of the concentration fluctuation over a flat plane and some types of probability density functions were proposed for the frequency of the instantaneous concentration occurrence. There are few studies about the concentration fluctuation around obstacles, however, the detailed characters of it have not been understood well.

Understanding of the behavior of the instantaneous concentration around buildings is very important for a risk assessment of an accidental leakage of toxic or inflammable contaminants. Fundamental knowledge about it is also required for a verification stage of a numerical results, obtained by unsteady calculations such as a Large Eddy Simulation, as a reference, and for the construction of a closure scheme, which will be employed in Reynolds-average based models.

In this study we aimed to investigate the fundamental statistical characteristics (The fluctuation intensity, the power spectrum, the PDF etc.) of the concentration fluctuation around a surface mounted cube and the wake region of it.

EXPERIMENTAL ARRANGEMENT

The experiments were carried out in the closed-circuit, low speed, atmospheric environment wind tunnel of SHIMIZ Co., which has a test section of the dimension 15.0m long(x) \times 2.6m wide(y) \times 2.4m high(z). We focused on a pollution case around a surface mounted cube located in a well developed turbulent boundary layer. The cube, 0.12m on each edge($= H$), was located at the ground. On the upwind side of the cube, roughness elements were placed to generate a thick boundary layer. The height of the boundary layer was more than ten times higher than that of the cube. A schematic diagram of the experiment is shown in Figure 1, and the coordinate system and the measuring cross sections were shown in Figure 2.

Horizontal velocity at the cube's height was set to 3m/s ($= U_b$). The Reynolds number based on H and U_b is 24,000, which assures that the flow characteristics are not sensitive to the number. A X-probe hot wire anemometer was used for the wind profile measurement. The sampling time was 90s at each point with 2kHz sampling frequency.

The diffusion experiment was executed for two types of

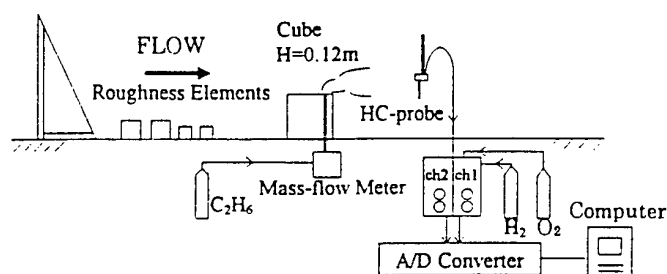


Figure 1: A schematic diagram of the experiment

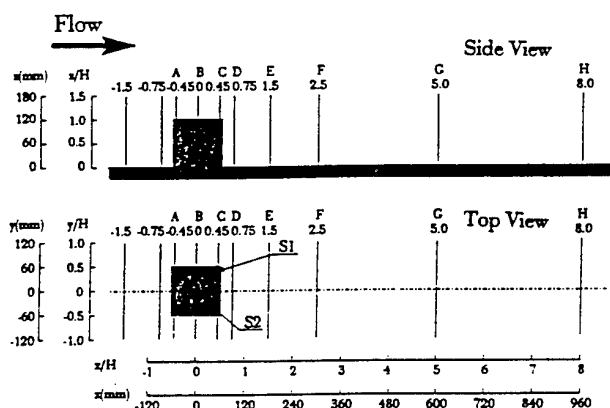


Figure 2: The measuring cross sections

emission source locations. In the first case, Case 1, an emission vent was located at the downstream side on the roof of the cube ($0.167H \times 0.167H$ away from a downstream corner). This design was often seen in actual buildings we have investigated. In the second case, Case 2, as a reference, an emission vent was located at the center of the cube's roof. A circular vent with $0.1H$ diameter was used in both of the cases. Tracer gas (100 %- C_2H_6) with no thermal buoyancy was continuously released from the vent at a low effluent velocity ($0.01U_b$). A high-frequency-response Flame Ionization Detector (FID) was used to get instantaneous concentration measurements. The sampling time was 60s at each point with 1kHz sampling frequency. In the post processing, every five data were averaged into one sample in consideration of the FID response.

Mean concentration distribution were investigated for both of cases, but the instantaneous concentration was saved and analyzed for Case 1 only. All of the concentration measurements were normalized by $C_n = CU_b H^2 / Q$, where C_n is the normalized concentration, C is the measurement value in ppm, Q is the emission intensity. After normalizing, background concentration was subtracted from each measurement value. Intermittency factor (γ ; = Total time of zero concentration appearance / Total time of the measurement) will largely depend on the determination of the threshold signal level corresponding to zero concentration. We defined twice the standard deviation of the background signal noise measured before the tracer gas release as the threshold signal level (i.e. the concentration measurements below twice the standard deviation of background noise were replaced by zero). Except PDF fitting, all statistics were based on unconditional samples (i.e. including zero concentration data).

WIND VELOCITY PROFILES

Wind velocity measurement was carried out only for two points. One of them is an upstream point of the cube (P1: $x/H = -1, y/H = 0$). At this point the measure-

ment was done without a cube to investigate the property of the approach flow. Another measuring point is set on the lee side of the cube (P2: $x/H = 2.5, y/H = 0$). Figure 3 shows the vertical profiles of (a) the mean streamwise velocity, and (b) its standard deviation.

For the approach flow, the mean streamwise velocity profile almost agrees with 1/4 power law profile, which can be often observed in urban areas. The turbulence intensity (σ_u/U_b) at the cube's height is 17%.

In comparison the mean velocity profile obtained at P2 with that of at P1, we can see that a uniform velocity deficit of 1m/s exists below the roof level, and the influence of the obstacle extends to the height of $2.5H$ approximately. In Fig.3(b), we can see that the all components of the turbulent intensities are enhanced significantly by the obstacle especially in $z/H < 1.5$. At Point P2, σ_u has a clear peak around $z/H = 1$, but the value of σ_w is nearly uniform in $0.75 < z/H < 1$.

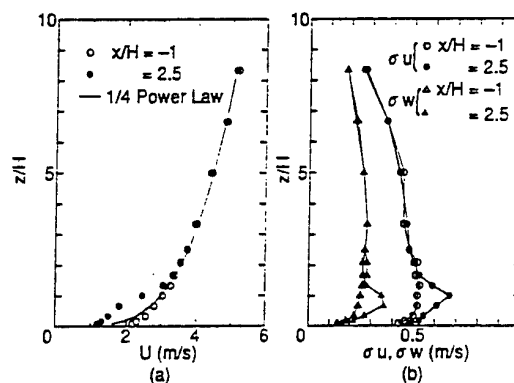


Figure 3: Vertical profiles of (a) mean streamwise velocity and (b) standard deviation of velocity measured at P1 ($x/H = -1, y/H = 0$) and P2 ($x/H = 2.5, y/H = 0$).

MEAN CONCENTRATION

Case 1

A Horizontal distribution of the mean concentration at the ground is shown in Figure 4. In spite of the biased location of the emission vent, the distribution pattern of the mean concentration is almost symmetrical in the lee side of the cube. Due to the strong horizontal mixing caused by the lee side arch vortices, the pattern of the mean ground concentration distribution is not so sensitive to the detailed location of the emission source, as far as the source is set on the roof. Asymmetry of the concentration distribution pattern at the ground is most prominent near the point just downstream side of the reattachment point of flow ($x/H = 2.5, y/H \sim 0.25$), and the asymmetry decreases as downwind distance increases. The asymmetry also decreases from that point to the foot of the cube. This tendency suggests that most part of the emitted tracer is straightforwardly convected and falls on to the ground directly, then it is drawn back toward the cube by reverse flow, and be mixed horizontally by the strong arch vortices being just behind the cube.

Figure 5 shows the horizontal profiles of mean concentration at the roof level ($z/H = 1$). At this height, the biased location of the emission source affects the pattern of the mean concentration distribution in the near wake region. Since the effect of source location almost disappears at cross section G ($x/H = 5$), it may be reasonable to neglect the detailed source location for the prediction of the mean concentration distribution in $x/H \geq 5$.

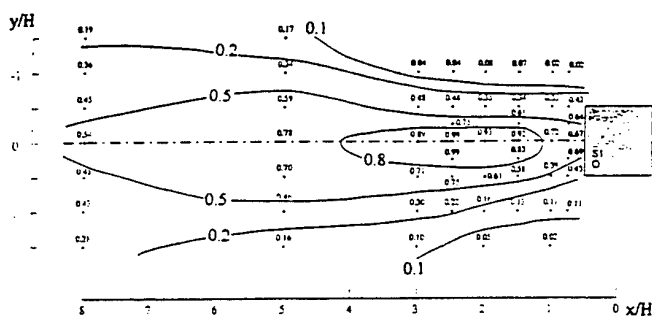


Figure 4: Horizontal distribution of mean concentration near the ground surface($z/H = 0.083$).

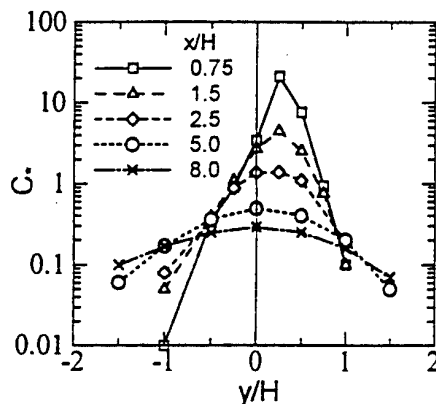


Figure 5: Horizontal profiles of mean concentration at the roof level of the cube($z/H = 1$).

Case 2

In Case 2, the value of the maximum ground concentration is lower, and the distance from the cube to the point where the maximum ground concentration occurs is shorter ($x/H \sim 2.0, y/H = 0$) than those of Case 1. The most significant difference between Case 1 and Case 2 is the pattern of the concentration distribution on the roof of the cube. In contrast to Case 1 (the tracer gas emitted from the corner vent is mainly convected to the downstream side), tracer gas emitted from the center vent is taken into the reverse flow very often and causes extremely high concentration on the upstream side of the emission source.

INSTANTANEOUS CONCENTRATION

The time series variation

Figure 6(a)(b)(c) show the time series variations of instantaneous concentration. Each time series was obtained (a) on the roof of the cube($0.45H, 0.1.08H$), (b) at the bottom of lee side cavity region($0.75H, 0.0.08H$), (c) in the far wake region($5H, 0.0.08H$). In Figure 6(a), the variation of the instantaneous concentration shows highly intermittent character because the extremely high concentration can be observed only when the meandering instantaneous plume passes the probe. No periodicity can be found for this intermittency. The interval of high concentration occurrence is much longer (20~100 times) than the characteristic time scale($= H/U_b$) of the flow field. This means that, in an unsteady calculation such as LES, the integral time must be extremely long to obtain well established mean concentration distribution on the roof.

In Figure 6(b), relatively high concentrations occur intermittently, and low level fluctuation continuously co-exists. This two-phase fluctuation in the cavity region can be

understood that it formed by a superimposing; i.e. the high concentration caused by the intermittent entrainment of the dense plume rides on the background low level fluctuation, which is yielded by broken puffs.

Figure 6(c) shows the stage that the turbulent diffusion has proceeded farther. Zero concentration can hardly be seen here because the instantaneous plume has spreaded and dense puffs have diffused through the cascade process.

The fluctuation intensity

We define the fluctuation intensity of instantaneous concentration as a ratio of the second central moment of concentration fluctuation to the mean concentration($= \overline{c'^2}/\overline{C}$). Figure 7 shows the vertical profiles of the concentration fluctuation intensity at the various downwind distances from the cube. On the roof of the cube, where the fluctuation intensity has its largest value, the value of more than 7 can be observed because the meandering instantaneous plume is dense and thin. In the cavity region, the fluctuation intensity is almost uniform and has a value less than 2.

The intermittency factor and the peak factor

Figure 8 shows the vertical profiles of the intermittency factor($=\gamma$). In this experiment, all of the measuring points show more or less intermittent character. The lowest intermittency is observed at the lee side bottom of the cube. In general, the ground surface area along the centerline of the cube is less intermittent, $\gamma < 3\%$, and the intermittency factor rapidly increases as the distance from the centerline increases. The intermittency factor is more than 90% on the roof of the cube because the instantaneous plume is thin and meanders to every direction.

Figure 9 shows a scatter plot of the intermittency factor vs. the fluctuation intensity. We can see a clear relationship between them. Though this relationship has already been suggested by Lewellen and Sykes(1986) as one of the basic assumptions for the clipped-normal distribution, it has not been examined for complex flow configuration.

Here, we define a peak factor as a ratio of the concentration value at 98% cumulative probability to its mean value. Figure 10 shows the vertical profiles of the peak factor obtained at various downwind distances. The values of the peak factor range from 10 to 15 on the roof surface. In the lee side cavity region the value of the peak factor is less than 5, but the value reaches to 10 and more in the outside area above the cavity region. In far wake region($x/H \geq 5$), the value of the peak factor near the ground is about 3.

The integral time scale

The Eulerian integral time scale is defined as $T_E = \int_0^\infty R(\tau) d\tau$, where $R(\tau)$ denotes the auto correlation coefficient of concentration fluctuation. Figure 11 shows the vertical profiles of the Eulerian integral time scale obtained at various downwind positions. At point D, T_E in $z/H < 0.5$ is much longer than that of the other points. Especially at the bottom of the cube ($0.75H, 0.0.08H$), the T_E is $4.3H/U_b$, which corresponds to the value of 0.23 in Strouhal number, so it seems that the long term concentration fluctuation may be dominated by the vortex shedding at this point. The entrainment of instantaneous plume into the cavity region doesn't have an explicit periodicity, so T_E rapidly decreases as the distance from the lee side arch vortices increases by its disturbance. The value of T_E obtained at the point on the roof is less than H/U_b , and the T_E at this height is not so much increases as the downstream distance increases.

The probability distribution

Sykes and Henn(1992) investigated the cumulative probability distribution of the instantaneous concentration based on their LES results for the dispersing plume in a plain turbulent boundary layer. They concluded that the probability distribution was well represented by the clipped-normal distribution near the source and the distribution asymptotes to the log-normal distribution as the downwind distance increases.

The clipped-normal distribution has a Gaussian PDF where the concentration is positive, but the part of negative concentration is clipped. At zero concentration, a delta function PDF is added to this clipped Gaussian distribution to represent the intermittency. The integrated value of the delta function corresponds to the probability of negative concentration occurrence in un-clipped Gaussian distribution. By the use of the zero order moment(γ), the first moment(μ) and the second central moment(σ), the PDF parameters of the clipped-normal distribution can be described as follows.

$$p(x) = \frac{1}{\sqrt{2\pi}\sigma_0} \exp\left[-\frac{(x - \mu_0)^2}{2\sigma_0^2}\right], \quad x > 0 \quad (1)$$

$$= \frac{1}{2} \left[1 + \operatorname{erf}\left(\frac{\mu_0}{\sqrt{2}\sigma_0}\right) \right] (\gamma = 1 - \gamma), \quad x = 0 \quad (2)$$

Here we examined two types of PDFs, (1)clipped-normal distribution (2)log-normal distribution, for the cumulative probability of instantaneous concentration near the source. Note that the clipped-normal distribution is fitted to the unconditional probability, but the log-normal distribution is fitted to the conditional one (i.e. zero concentrations were excluded in the cumulative probability estimation).

Figure 12(a) shows the fitting results of the clipped-normal distribution at roof level point in the lee side of the cube($0.75H, 0, H$). The fitting result of the clipped-normal distribution is not so good. In our experiment, the clipped-normal distribution seems to underestimate the 98% value of the unconditional cumulative probability. From the practical point of view, this tendency is not preferable to use in an environment assessment. Though the clipped-normal distribution fits well in the region where the value of the intermittency factor is not so large ($\gamma < 10\%$), it is not so much different to use usual Gaussian PDF in such situation. So we don't have enough reason to do use the clipped-normal distribution.

Figure 12(b) shows the result of the log-normal distribution fitting at the same point. Though this fitting is based on the conditional samples rather than unconditional samples, the log-normal distribution gives good estimation to the cumulative probability distribution. Contrary to the result of clipped-normal distribution, log-normal distribution tends to overestimates the probability of higher concentration as the downwind distance increases. This fact implies that the PDF of the instantaneous concentration approaches to the Gaussian distribution in the far wake region.

The power spectrum

Figure 13(a) shows the power spectrum (frequency weighted) of the concentration fluctuation obtained on the roof of the cube($0.45H, 0.25H, 1.08H$). A narrow band of inertial subrange can be seen in the range where the non-dimensional frequency(fH/U_b) is higher than 2. In our results, no prominent peak can be seen in the power spectrum obtained on the roof surface.

Figure 13(b) shows the power spectrum which obtained at the lee side of the cube($0.75H, 0, H$). We can see -2/3 decay behavior in $fH/U_b > 1$. The portion with -2/3 decay is wider than that of the spectrum obtained on the

roof surface. In figure 13(b) we can also see a +2/3 decay range in the relatively lower frequency. This +2/3 behavior seems to suggest the existence of "inertial-meandering" subrange, proposed by Thomson(1996).

Figure 13(c) also shows the power spectrum obtained at the far wake region($5H, 0, 0.08H$). This power spectrum has a wide range of -2/3 decay in $fH/U_b > 0.2$.

CONCLUSIONS

In this experiment, the distribution pattern of the mean concentration near the ground surface was not so sensitive to the detailed location of the emission source as far as it was set on the roof. In spite of the biased location of the emission source, the pattern of the mean concentration is almost symmetrical in the lee side of the cube, due to the strong horizontal mixing caused by the lee side arch vortices.

Instantaneous concentration measurements show large fluctuation and highly intermittent character especially on the roof of the cube. As the fluctuation on the roof surface doesn't have an explicit period and the intensity of the fluctuation is very large, the integration time in LES must be extremely long to obtain well established mean concentration distribution.

A clear relationship can be seen between intermittency factor and concentration fluctuation intensity. Though the function form of their relationship has not been determined here, the exclusion of the intermittency factor in the determination of PDF for instantaneous concentration has justified if we choose the mean concentration and its standard deviation as the fundamental parameters.

Sykes and Henn have reported that cumulative probability distribution of instantaneous concentration fits the clipped-normal distribution near the source, and the distribution function gradually changes from clipped-normal to log-normal as the downstream distance increases. Against their results, clipped-normal distribution didn't show a good applicability for the concentration fluctuation around a cube, except far wake region where the intermittency is relatively low. From the practical point of view in environment assessment, log-normal distribution is more preferable to use for the prediction of the peak concentration level near the emission source, as far as our experimental condition.

The frequency weighted power spectrum, obtained at just downstream side of the emission source, seems to suggest the existence of "inertial-meandering" subrange proposed by Thomson.

REFERENCES

- Huber, A.H., Snyder, Q.H., 1982, "Wind tunnel investigation of the effects of a rectangular-shaped building on dispersion of effluents from short adjacent stacks", *Atmos. Env.*, Vol.16, pp.2837-2848
- Wilson, D.J., Lumb, B.K., 1994, "Dispersion of exhaust gases from roof-level stacks and vents on a laboratory building", *Atmos. Env.*, Vol.28, pp.3099-3111
- Sykes, R.I., Henn, D.S., 1992, "Large-eddy simulation of concentration fluctuations in a dispersing plume", *Atmos. Env.*, Vol.26A, pp.3127-3144
- Mylne, K.R., Davidson, M.J., Thomson, D.J., 1996, "Concentration fluctuation measurements in tracer plumes using high and low frequency response detectors", *Bound. Lay. Meteorol.*, Vol.79, pp.225-242
- Thomson, D.J., 1996, "The second-order moment structure of dispersing plumes and puffs", *J. Fluid Mech.*, Vol.320, pp.305-329
- Lewellen, W.S., Sykes, R.I., 1986, "Analysis of concentration fluctuation from lidar observations of atmospheric plumes", *J. Climate Appl. Meteor.*, Vol.25, pp.1145-1154

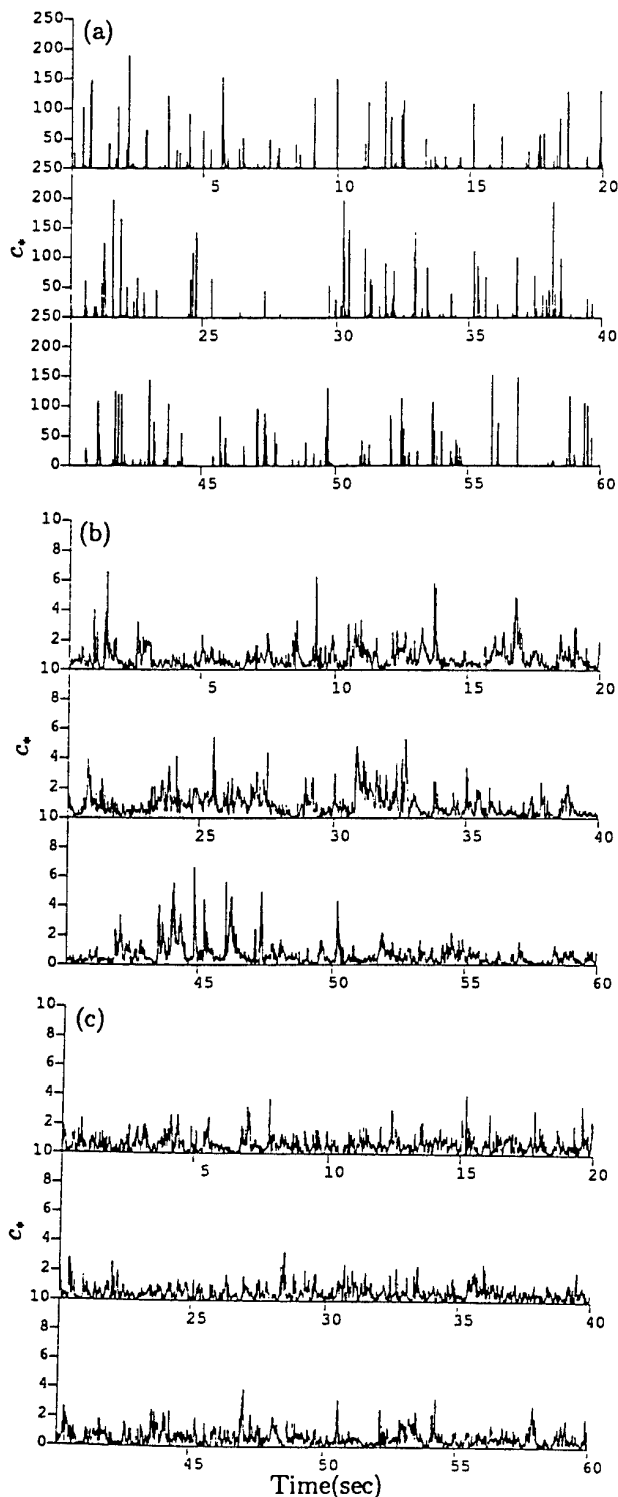


Figure 6: The time series variation of instantaneous concentration.(a)on roof the cube($0.45H, 0.1.08H$), (b)in the lee side cavity region($0.75H, 0.0.08H$), (c)in the far wake region($5H, 0.0.08H$).

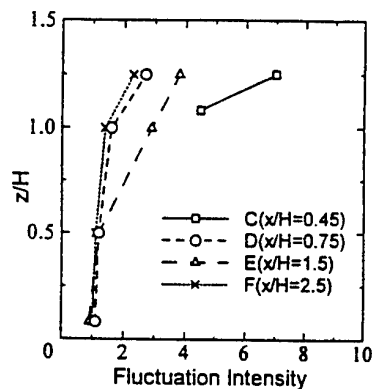


Figure 7: The vertical profiles of the concentration fluctuation intensity at the various downwind distances along the centerline($y/H = 0$).

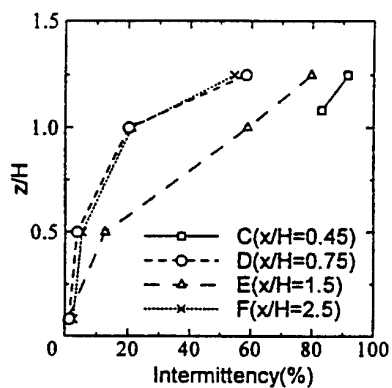


Figure 8: The vertical profiles of the intermittency factor at the various downwind distances along the centerline($y/H = 0$).

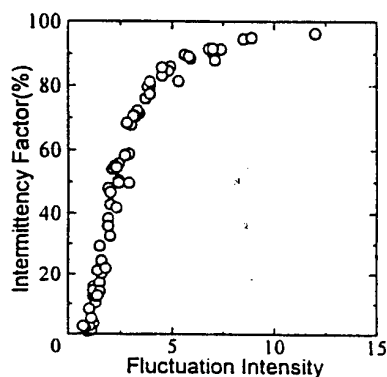


Figure 9: The relationship between concentration fluctuation intensity and intermittency factor.

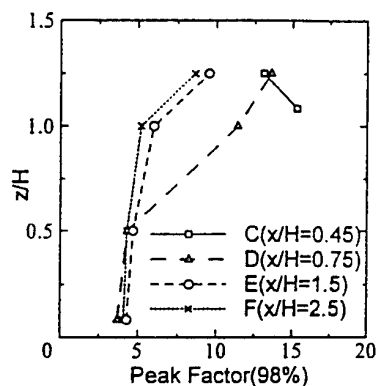


Figure 10: The vertical profiles of the peak factor at the various downwind distances along the centerline($y/H = 0$).

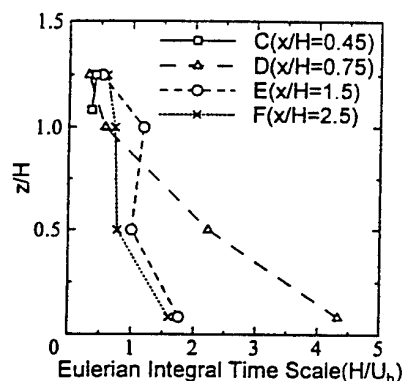


Figure 11: The vertical profiles of the Eulerian integral time scale at the various downwind distances along the centerline($y/H = 0$).

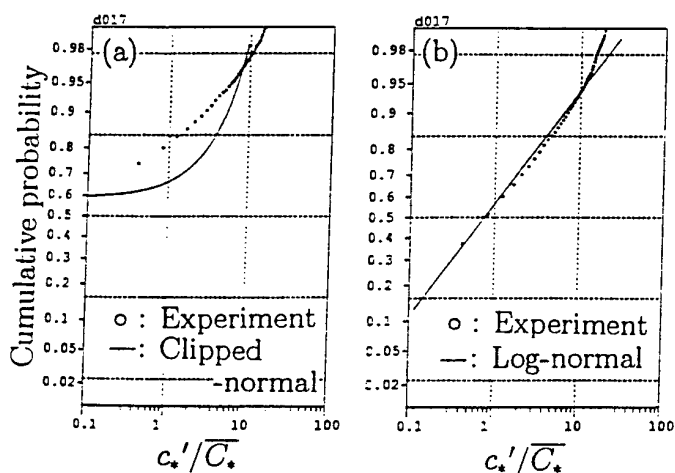


Figure 12: Cumulative probability distribution of instantaneous concentration at the point just behind the emission source($0.75H, 0, H$). (a) the fitting result of clipped-normal distribution(based on unconditional samples), and (b) the fitting result of log-normal distribution(based on conditional samples).

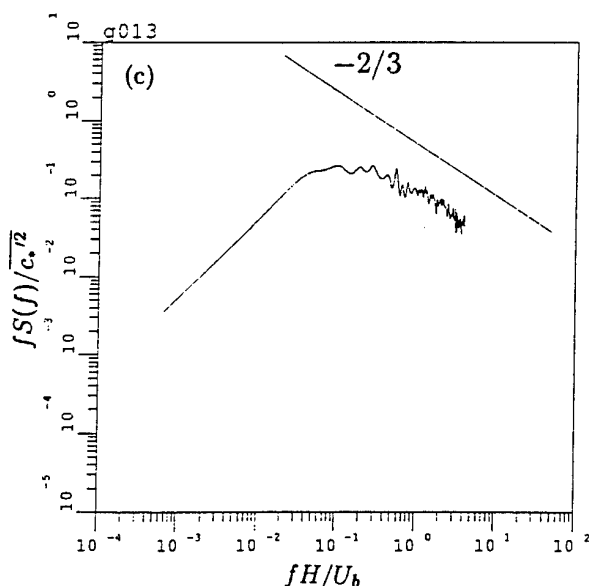
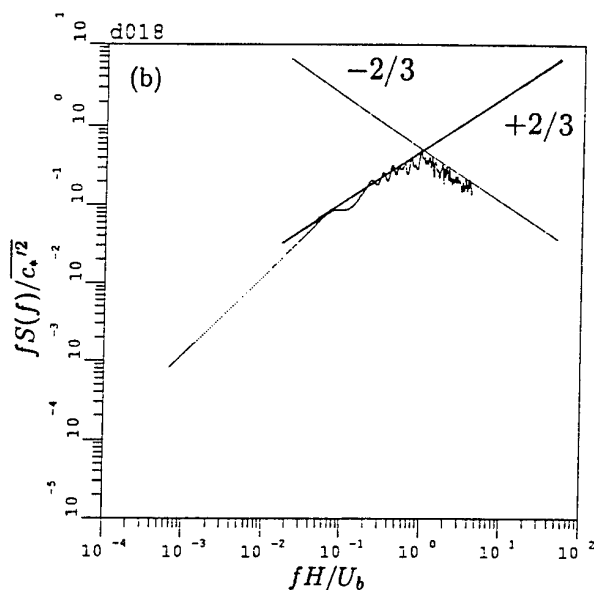
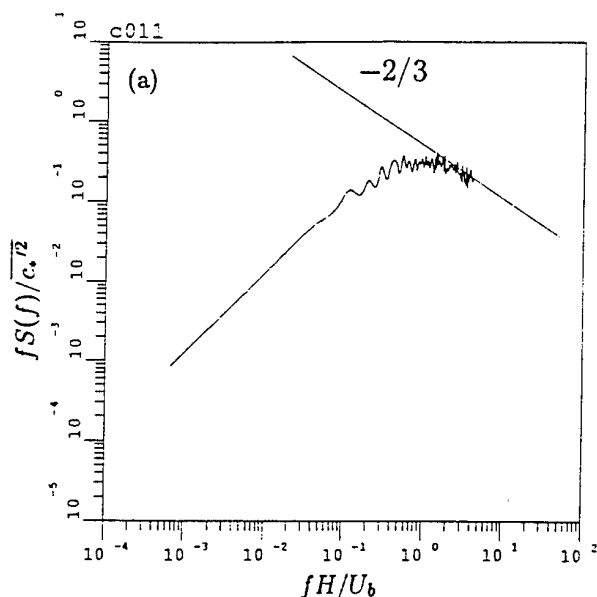


Figure 13: The power spectra of the concentration fluctuation obtained (a) on the roof of the cube ($0.45H, 0.25H, 1.08H$), (b) at lee side of the cube ($0.75H, 0, H$), (c) at the far wake region ($5H, 0, 0.08H$).

TURBULENT WALL SHEAR FLOW IN A VERTICAL TUBE WITH COMBINED HEAT AND MASS TRANSFER

Shuisheng He, Pei An, Jiankang Li and J.D. Jackson
School of Engineering
University of Manchester
Manchester M13 9PL
U.K.

ABSTRACT

A computational modelling study is reported of buoyancy-influenced turbulent shear flow with heat and mass transfer for the case of upward flow of air and water vapour in a heated vertical tube in the presence of a falling film of water on the wall. Procedures have been successfully developed which enable this complex problem to be simulated using turbulence modelling.

1. INTRODUCTION

Combined experimental and computational studies of water film cooling have been undertaken by the authors in connection with the evaluation of ideas for passive cooling of advanced, inherently safe, nuclear reactors. The computational study is reported in this paper and comparisons are made with measured data.

The experimental arrangement involved a long vertical tube, which was electrically heated in a uniform manner along the whole of its length. Radial jets of water were sprayed onto the inside surface of the tube at the top, so as to form a thin uniform film which ran down the tube wall. An upward flow of air and vapour was created in the tube by supplying air from a compressor to a settling box, which enclosed a bellmouth intake at the bottom of the tube. The top of the tube was open to the atmosphere. A sketch of the rig is shown in Figure 1. In order to simulate the experiments, the governing equations for the turbulent flow, heat and mass transfer in the air/vapour mixture have been solved using a finite volume method in an elliptic scheme. Incorporated in these equations was the Launder-Sharma low Reynolds number $k-\epsilon$ turbulence model. The motion of the downward flowing water film was determined analytically assuming that effect of the thermal field could be neglected. The temperature field within the water flow was computed by solving the energy equation for that region simultaneously with that for the air/vapour field.

Water film cooling mechanisms have been studied by a number of researchers. Examples of such work include studies of combined heat and mass transfer in laminar natural convection for flow along a vertical wall by Gebhart and Pera (1971) and

flow along a vertical cylinder by Chen and Yuh (1980). Both studies utilised the Boussinesq approximation, which enabled the governing equations to be reduced to a form, which had a similarity solution. Thus, the flow was treated in a manner similar to those involving just one mechanism of buoyancy influence. In an interesting study of natural convection flow in an open vertical tube, resulting from combined buoyancy effects of thermal and mass diffusion, Chang et al (1986) solved the Navier-Stokes equations with the thin shear flow assumptions. In their study, the wall of the tube was covered by a stationary water film at a specified uniform temperature. This study was extended later by Chiang and Kleinstreuer (1991) by allowing the liquid film to fall and removing the thin shear flow assumptions. Both studies involved the Boussinesq approximation and were carried out for laminar flow. Studies of convective heat and mass transfer along an inclined heated plate with film evaporation were conducted by Yan and Soong (1995). The flow in both the water and gas phases was considered to be turbulent and the thin shear flow assumption was employed. A modified Van Driest model and a $k-\epsilon$ turbulence model were used for the water and gas flow regions respectively. The calculations were conducted for the forced convection condition, i.e., buoyancy effects were not taken into account.

A more complete study, including simultaneously the influences of buoyancy forces and turbulence, remains to be done. It is known that the interaction between buoyancy and turbulence can be important in some situations. The present study was undertaken to fulfil this need.

2. ANALYSIS

2.1 Water flow field

The water film flow is gravity driven. However, it is influenced by the gas phase flow through two mechanisms, namely shear at the interface between the two phases and the axial pressure gradient needed to produce the gas phase flow. The shear between the two flow surfaces implies a non-zero velocity gradient at the interface whereas for the situation where the free surface is not subject to a shear, the velocity gradient would be zero. The axial pressure gradient influences the flow in a similar

way to the body force due to gravity, and can be incorporated in the gravity term. In the present experiments, both the effects have been found to be very small, the former being generally less than 0.2% and the latter less than about 1.5%. They can be ignored without introducing significant error. Another matter, which needs to be considered is the effect of the evaporation of water from the film on its thickness. This was also found to be small.

Neglecting the effects mentioned above, the water flow can be considered as being unaffected by the thermal field and the gas flow. Under such conditions, the following analytical solution for the velocity distribution in the water is applicable:

$$U = \frac{\rho g}{\mu} \left(\delta y - \frac{y^2}{2} \right) \quad (1)$$

in which δ is the water film thickness ($= [3\mu V_m / \rho g]^{1/3}$ where V_m is the mean velocity).

2.2 Temperature Field in the Water

The water flow is subjected to a uniformly imposed heat flux from the steel wall. It loses heat to the gas phase flow through convection and evaporation at the air-water interface. The rate at which heat is lost to the gas phase through these two mechanisms is largely dependent on the flow and temperature fields in the gas phase. The temperature field in the water flow is therefore closely coupled with the gas phase flow and heat transfer processes and it should be solved for simultaneously with the gas flow and thermal fields.

2.3 The Gas Phase Flow

The gas phase is affected by the processes of turbulent heat and mass transfer and evaporation of water at the interface. Effects of buoyancy are present due to the non-uniformity of temperature and vapour concentration and they might be significant due to the fact that the flow rate is low. At the gas-water interface, the vertical velocity components of the gas and water are the same and non-zero. Although strictly speaking the value is influenced by the coupling of the two flows, it is mainly dependent on the water phase flow. As mentioned earlier, the water phase is hardly affected by the interfacial shear. A radial velocity in the gas flow results from the generation of vapour due to evaporation of water at the interface.

The gas phase receives energy from the water phase at the interface as a result of convection and the evaporation of water. Both mechanisms are dependent on the velocity and temperature fields within the two flows and the mass concentration field in the gas phase. Within the flow, energy is transferred through molecular and turbulent diffusion and by convection. Strictly speaking, diffusion of species is accompanied by energy transfer but this is a very small effect.

Assuming thermodynamic equilibrium, the partial pressure of the vapour at the interface is the saturated vapour pressure at the interfacial temperature. The mass fraction of vapour at the interface is therefore defined once temperature is known. Within the gas flow, the mass transfer process is similar to that of heat transfer and is governed by a balance between molecular and turbulent diffusion and convection.

It is clear that the velocity, temperature and species fields are closely coupled and that their transport equations must be solved simultaneously.

The gas flow is considered as incompressible, two dimensional and axisymmetric. The Reynolds averaged equations for such a flow written in a cylindrical co-ordinate system are:

Continuity

$$\frac{1}{r} \left\{ \frac{\partial}{\partial x} (\rho r U) + \frac{\partial}{\partial r} (\rho r V) \right\} = 0 \quad (2)$$

U-momentum

$$\frac{1}{r} \left\{ \frac{\partial}{\partial x} (\rho r U^2) + \frac{\partial}{\partial r} (\rho r V U) \right\} = -\frac{\partial p}{\partial x} + \rho g + \frac{1}{r} \left\{ 2 \frac{\partial}{\partial x} \left[r \mu_e \left(\frac{\partial U}{\partial x} \right) \right] + \frac{\partial}{\partial r} \left[r \mu_e \left(\frac{\partial U}{\partial r} + \frac{\partial V}{\partial x} \right) \right] \right\} \quad (3)$$

V-momentum

$$\frac{1}{r} \left\{ \frac{\partial}{\partial x} (\rho r U V) + \frac{\partial}{\partial r} (\rho r V^2) \right\} = -\frac{\partial p}{\partial r} + \frac{1}{r} \left\{ \frac{\partial}{\partial x} \left[r \mu_e \left(\frac{\partial V}{\partial x} + \frac{\partial U}{\partial r} \right) \right] + 2 \frac{\partial}{\partial r} \left[r \mu_e \left(\frac{\partial V}{\partial r} \right) \right] \right\} - 2 \frac{\mu_e V}{r^2} \quad (4)$$

in which μ_e is the effective viscosity defined as $\mu_e = \mu + \mu_T$, where μ_T is the turbulent viscosity, ρ is density and p is pressure.

The energy equation for axisymmetric flow written using a cylindrical co-ordinate system is shown below. It can be used for both the water and gas flows:

Energy Equation

$$\frac{1}{r} \left\{ \frac{\partial}{\partial x} (\rho r U T) + \frac{\partial}{\partial r} (\rho r V T) \right\} = \frac{1}{r} \left\{ \frac{\partial}{\partial x} \left[r \left(\frac{\mu}{Pr} + \frac{\mu_T}{\sigma_T} \right) \frac{\partial T}{\partial x} \right] + \frac{\partial}{\partial r} \left[r \left(\frac{\mu}{Pr} + \frac{\mu_T}{\sigma_T} \right) \frac{\partial T}{\partial r} \right] \right\} \quad (5)$$

Pr is the molecular Prandtl number and σ_T the turbulent Prandtl number. For the water phase flow, $\mu_T = 0$ (laminar flow).

The vapour mass transport equation for axisymmetric flow written using a cylindrical co-ordinate system, is as follows:

Mass Transfer Equation

$$\frac{1}{r} \left\{ \frac{\partial}{\partial x} (\rho r U \omega) + \frac{\partial}{\partial r} (\rho r V \omega) \right\} = \frac{1}{r} \left\{ \frac{\partial}{\partial x} \left[r \left(\frac{\mu}{Sc} + \frac{\mu_T}{\sigma_\omega} \right) \frac{\partial \omega}{\partial x} \right] + \frac{\partial}{\partial r} \left[r \left(\frac{\mu}{Sc} + \frac{\mu_T}{\sigma_\omega} \right) \frac{\partial \omega}{\partial r} \right] \right\} \quad (6)$$

Sc is the Schmidt number and σ_ω the turbulent Schmidt number.

The vapour fraction ω is defined as the ratio of the density of the vapour to the density of the air/vapour mixture.

2.4 Turbulence Model and Numerical Method

The low Reynolds number k- ϵ turbulence model due to Launder and Sharma (1974) has been used in this study to account for the turbulent transport. This model has been found in our earlier work to perform well in single phase mixed convection flows. The transport equations for the turbulent quantities as well as those for the mean flow properties (Equations 2 to 6) have been discretised using the finite volume scheme and solved, coupled, using an elliptical SIMPLE procedure.

2.5 Boundary Conditions at the Interfacial Cells

a) The Vapour Fraction at the Interface. Assuming thermodynamic equilibrium, the vapour pressure is the saturated vapour pressure corresponding to the local temperature. The vapour mass fraction at the interface can therefore be calculated as:

$$\omega_i = \frac{M_v P_v}{M_v P_v + M_a (p - P_v)} \quad (7)$$

where p and P_v are the absolute pressure and the vapour pressure at the interface, respectively. M_a and M_v are molecular weights of air and vapour.

b) Velocity at the Interface. The axial velocity component is calculated using Equation 1. The radial velocity component is non-zero due to the generation of vapour at the interface. Assuming that the gas-water interface is semi-permeable (that is, the solubility of air is negligibly small with the air being stationary at the interface), the velocity of water vapour at the interface can be written as:

$$v_i = -\frac{D}{(1-\omega_i)} \frac{\partial \omega}{\partial y} \Big|_{y=0} \quad (8)$$

in which D is the mass diffusivity.

c) Energy Balance at the Interface. At the interface, the law of energy conservation requires that the energy diffused towards the interface from both sides equals the energy used for the generation of vapour at the interface:

$$\lambda_{\text{water}} \frac{\partial T}{\partial y} \Big|_{\delta^-} - \lambda_{\text{gas}} \frac{\partial T}{\partial y} \Big|_{\delta^+} = \dot{m} \gamma \quad (9)$$

in which γ is the enthalpy of evaporation and \dot{m} is the vapour generation rate ($= \rho_{\text{vapour}} v_i$).

3. RESULTS¹

3.1 Simulations of Wall Temperature and Comparisons with Experimental Data

Figures 2 to 4 show comparisons between predicted variations of wall temperature along the tube and those measured experimentally for a number of conditions. Referring first to Figure 2, the air flow rate was varied, whilst other conditions, such as, the power input and mass flow rate and temperature of the cooling water, were kept fixed. Figure 3 shows the effects of varying the power input and the mass flow rate of water and Figure 4 shows the effect of varying the inlet temperature of the cooling water. It is clear that the simulations do reproduce observed behaviour quite well and that the computed results are generally in good quantitative agreement with the experimental data. However, in Figure 2 an exception is clearly apparent in the case of the lowest air flow rate (Curve 1). The computed wall temperature is too high. It seems that in the simulation for that case, the turbulence model over-responded to buoyancy influences causing the flow to be almost laminarized. This resulted in the effectiveness of the heat transfer being significantly reduced. The results of a simulation with buoyancy effects switched off are also shown in the figure (Curve 1a). The latter is clearly much closer to the experimental data. In this simulation the flow remained turbulent. A further example of a simulation with buoyancy force switched off is shown in Figure 3 as Curve 1a. In this case the buoyancy influence is much weaker. For all the other cases reported here, the effect of buoyancy is similarly weak.

3.2 Detailed Flow and Thermal Fields

Figure 5 illustrates the development of the velocity of the air/vapour mixture along the tube. The result is a typical one. The uniform inlet velocity profile adjusts to become a turbulent profile within the first 20 diameters or so from the inlet. The velocity then increases steadily because the concentration of vapour builds up due to evaporation from the water film and the density of the air decreases due to the increase of its temperature. The shape of the profile remains similar.

Figure 6 illustrates the development of turbulence along the tube. The low level of turbulence specified at the inlet in this case remains low for the first 20 diameters or so, after which it builds up quickly. The reason for the turbulence level remaining low is that the initial uniform velocity distribution is not effective in producing turbulence. Later, as the velocity profile takes on its shape and a wall shear layer is formed, turbulence is produced and the level builds up. The steady increase of turbulence in the remaining part of the flow is associated with an increase of local Reynolds number. A low level turbulence in the inlet region is a general feature of flows with a uniform velocity specified at inlet. When a higher level of turbulence is specified at inlet, such as in the example shown in Figure 7, it is damped out initially before building up later. The effect of varying the specified inlet conditions (shape of the velocity profile, turbulence level and air temperature) on wall temperature profile have been investigated and some typical results are shown in Figure 8.

Two patterns of development of temperature have been found in the simulations, typical examples of which are shown in Figures 9 and 10. When the temperature of the water film at inlet is relatively high, the temperature of the wall and that of the air both increase monotonically with distance up the tube (Figure 9). The temperature of the wall is higher than the temperature of the air at the same cross section and the diffusion of heat is outwards from the wall. When the temperature of the water at inlet is relatively low, the variation of wall temperature is non-monotonic. It increases slightly first and then decreases. In the upper section of the tube, the temperature of the air may be higher than the temperature of the wall at the same axial position. In this situation, the diffusion of heat is towards the wall (Figure 10).

3.3 Heat Transfer Mechanisms and Water Film Cooling Modes

It is of interest to consider the energy transfer in the case of the water film. An energy balance for an element of unit length with one surface coinciding with the wall and one with the air-water interface can be expressed as follows:

$$\text{Heat released from wall to water film} + \text{Convection of heat in water film} - \text{Energy loss to air/vapour mixture due to evaporation} - \text{Energy loss to air/vapour mixture due to convection} = 0$$

Figures 11 and 12 show examples of such energy transfers for two typical cases. When the temperature of the water at the inlet is high (Figure 11), the saturated vapour pressure at the water-air interface is high, which means that there is plenty of evaporation of water, and therefore effective heat transfer from the wall. Evaporation of the water film then serves as the main mechanism for heat removal. The temperature of the water decreases as it runs down the wall and the contribution by convection in the water to heat removal from the wall is negative, i.e., the water actually releases energy. We can describe the system as working in an *evaporation mode*. In contrast, when the water at inlet is at relatively low temperature as in the typical case shown in Figure 12, the saturated vapour pressure is low and evaporation ceases to be a major mechanism for heat removal from the wall. The heat flux released by the wall is mainly carried away by the water film itself as it falls and the air/vapour mixture transfers only a small portion of the heat released by the wall. Such a system can be described as working in a *water film cooling mode*. Under such conditions an increase of mass flow rate of water will cause a reduction of wall temperature. For water film cooling in both modes, the heat removal which can be directly attributed to convective heat transfer in the air/vapour mixture flow is small. However, the

¹ Unless otherwise specified, the experimental conditions for the typical cases presented here are as follows: Flow rate of air: 0.015 kg/s (Re=13800), power input: 3000 W, flow rate of water: 27 g/s.

turbulent flow process in the air/vapour mixture is of crucial importance when the system is working in the evaporation mode because the rate of evaporation of liquid depends on the rate at which the vapour is transferred from the water-air interface by turbulence. For systems working in the water film cooling mode, changing the air flow rate does not have much influence on the effectiveness of heat transfer.

Figures 13 and 14 show vapour concentration distributions along the whole length of the tube for cases corresponding to those shown in Figures 11 and 12. It can be seen from Figure 13 that the vapour concentration is high (5% to 20%) when the system is working in the evaporation mode. From the gradient of concentration it is apparent that vapour is being transmitted away from the water film surface at all locations along the tube. In the case shown in Figure 14, the vapour concentration at the interface is much lower (from 2.4% down to about 1%). From the gradient of concentration, it can be seen that vapour is being transmitted away from the water film surface in the lower part of the tube and towards it in the upper section. Thus the water is being evaporated from the film in the lower section and vapour is condensing on the film in the upper section.

4. CONCLUSIONS

Modelling procedures have been successfully developed which enable satisfactory simulations to be made of water film cooling experiments involving buoyancy-influenced turbulent flow in a vertical pipe with heat and mass transfer. The Launder-Sharma turbulence model is generally able to respond well to the influences of the buoyancy present under the mixed convection conditions in the complex combined heat and mass situation studied. However, there is evidence that in some situations the turbulence model does over-respond to the buoyancy influences and causes laminarization of the flow to occur when this did not happen in practice. Some useful understanding of the heat transfer physics involved in the problem studied here was obtained from the detailed profiles of velocity, turbulence, temperature and concentration produced in the simulations. Two very different modes of heat transfer were identified, the *evaporation mode* and the *water film cooling mode*.

When the cooling water is supplied at relatively high temperature, the system operates in the evaporation mode. Energy supplied by the wall is mainly absorbed by evaporation from the water film. The water temperature (which determines the saturated vapour pressure at the water-air interface) and the air flow rate (which determines the effectiveness of turbulent diffusion of vapour away from the film surface) are important factors controlling the effectiveness of heat transfer under such conditions. An increase in the rate at which water is supplied to the system generally leads to an increase of wall temperature.

In contrast, when the temperature at which the water is supplied is relatively low, the system operates in the water film cooling mode. The convection of heat in the flowing water film becomes the main mechanism for heat removal from the wall. Only a small part of the heat input to the water passes to the air/vapour mixture. The greater the mass flow rate of water, the lower is the wall temperature. Under such conditions, a change of air flow rate does not significantly affect heat transfer.

REFERENCES

Chang, C.J., Lin, T.F. and Yan, W.M. (1986) 'Natural convection flows in a vertical, open tube resulting from combined buoyancy effects of thermal and mass diffusion', *Int. J. Heat Mass Transfer*, Vol. 29, No. 10, pp 1543-1552

Chen, T.S. and Yuh, C.F. (1980) 'Combined heat and mass transfer in natural convection along a vertical cylinder', *Int. J. Heat Mass transfer*, Vol. 23, pp 451-461

Chiang, H. and Kleinstreuer, C. (1991) 'Analysis of passive cooling in a vertical finite channel using a falling liquid film and buoyancy-induced gas-vapour flow', *Int. J. Heat Mass Transfer*, Vol. 34, No. 9, pp 2389-2349

Gebhart, B. and Pera, L. (1971) 'The nature of vertical natural convection flows resulting from the combined buoyancy effects of thermal and mass diffusion', *Int. J. Heat Mass Transfer*, Vol. 14, pp 2025-2050

Launder, B.E. and Sharma, B.I. (1974) 'Application of the energy-dissipation of turbulence to calculation of low near a spinning disc', *Lett. Heat Mass Transfer*, 1, pp.131-138.

Yan, We-Mon and Soong, Chyi-Yeou (1995) 'Convective heat and mass transfer along an inclined heated plate with film evaporation', *Int. J. Heat and Mass Transfer*, v38, n7, pp1261-1269

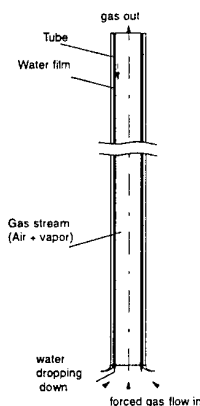


Figure 1. Test Section

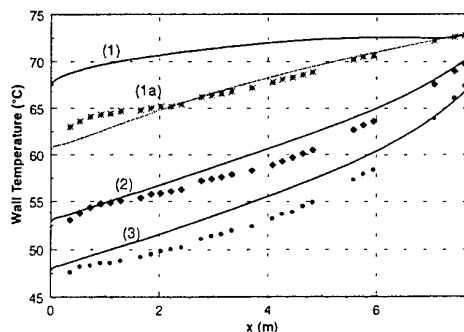


Figure 2. Variation of wall temperature along the tube - Effect of varying the air flow rate. [Curves: (1) Flowrate=0.005kg/s; (1a) Flowrate=0.005kg/s (no buoyancy effect); (2) Flowrate=0.01kg/s & (3) Flowrate=0.015kg/s] (Other conditions: $P=1350$ W; $F_{\text{water}}=27$ g/s, $T_{\text{water,in}}=70^{\circ}\text{C}$, $T_{\text{air}}=30^{\circ}\text{C}$)

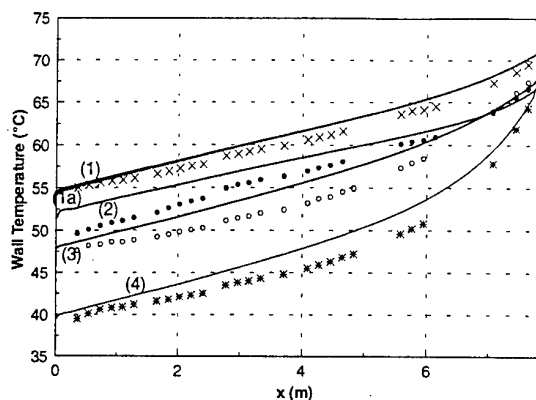


Figure 3. Variation of wall temperature along the tube - Effect of varying power input and mass flow rate of cooling water. [Curves: (1) $P=3000$ W, $F_{\text{water}}=27$ g/s; (1a) $P=3000$ W, $F_{\text{water}}=27$ g/s (no buoyancy effect); (2) $P=3000$ W, $F_{\text{water}}=13$ g/s; (3) $P=1350$ W, $F_{\text{water}}=27$ g/s; (4) $P=1350$ W, $F_{\text{water}}=13$ g/s] (Other conditions: Air Flowrate= 0.015 kg/s, $T_{\text{water,in}}=70^{\circ}\text{C}$, $T_{\text{air}}=30^{\circ}\text{C}$)

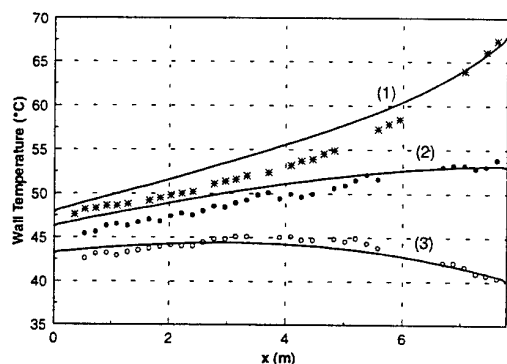


Figure 4. Variation of wall temperature along the tube - Effect of varying the temperature of the cooling water. [Curves: (1) $T_{\text{w,in}}=70^{\circ}\text{C}$; (2) $T_{\text{w,in}}=55^{\circ}\text{C}$; (3) $T_{\text{w,in}}=40^{\circ}\text{C}$] (Other conditions: Air Flowrate= 0.015 kg/s; $P=3000$ W; $F_{\text{water}}=27$ g/s)

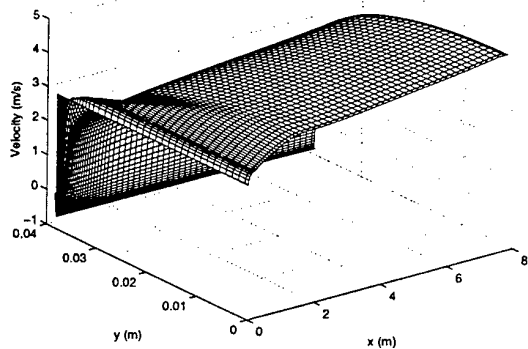


Figure 5. Development of velocity profile along the tube ($T_{\text{water,in}}=70$)

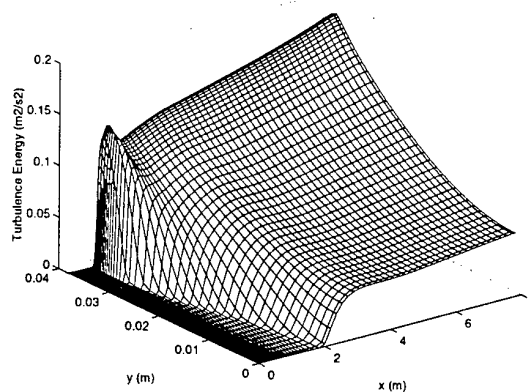


Figure 6. Development of turbulence along the tube ($T_{\text{water,in}}=70$, $T_{k,in}=0.03\%$)

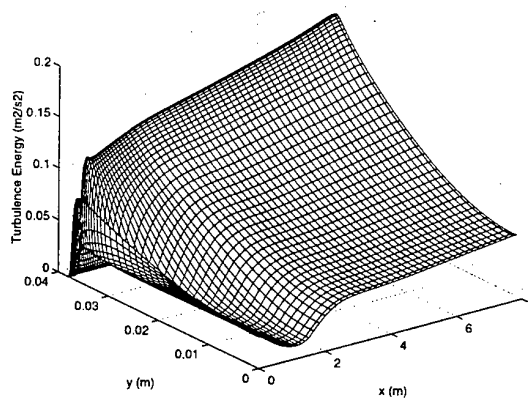


Figure 7. Development of turbulence along the tube ($T_{\text{water,in}}=70^{\circ}\text{C}$, $T_{k,in}=1\%$)

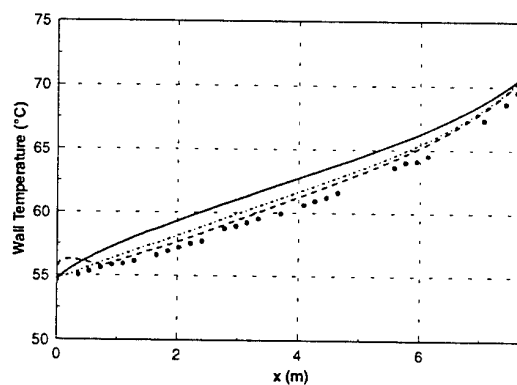


Figure 8. Variation of wall temperature along the tube - Effect of assumed inlet flow conditions. [a) solid-line: fully developed velocity profile; b) dashed-line: uniform velocity profile, 1% turbulence; c) chain-line: uniform velocity profile, 0.03% turbulence; d) dotted-line: uniform velocity profile, 0.03% turbulence].

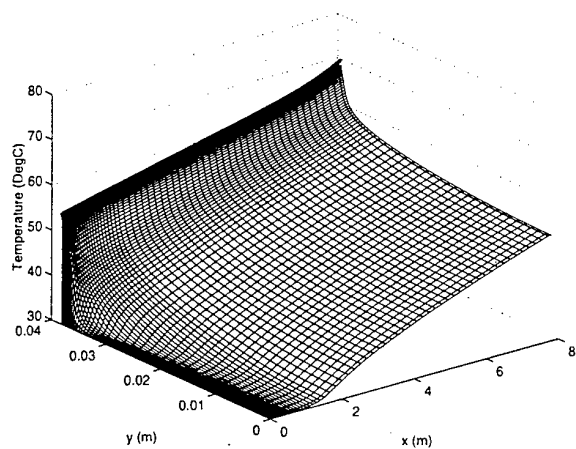


Figure 9. Development of fluid (air and water) temperature ($T_{\text{water, in}}=70^{\circ}\text{C}$)

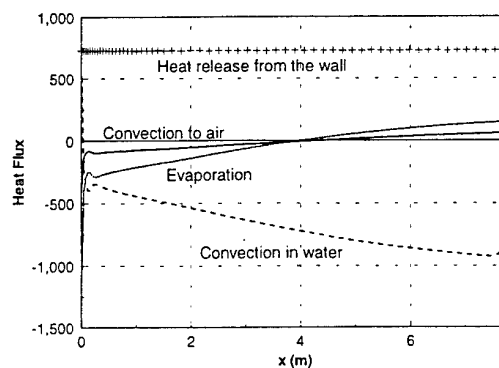


Figure 12. Energy balance for the water film ($T_{\text{water, in}}=20^{\circ}\text{C}$)

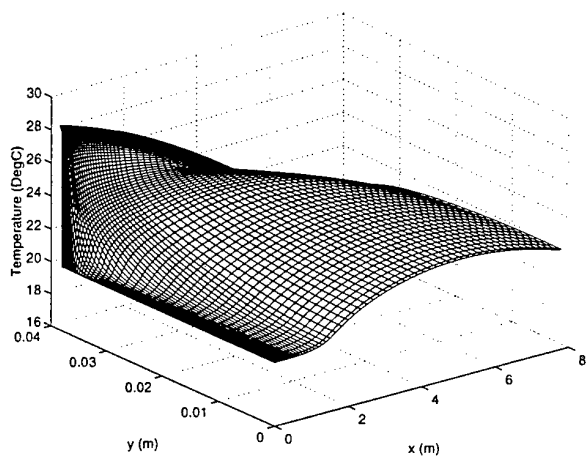


Figure 10. Development of fluid (air and water) temperature ($T_{\text{water, in}}=20^{\circ}\text{C}$)

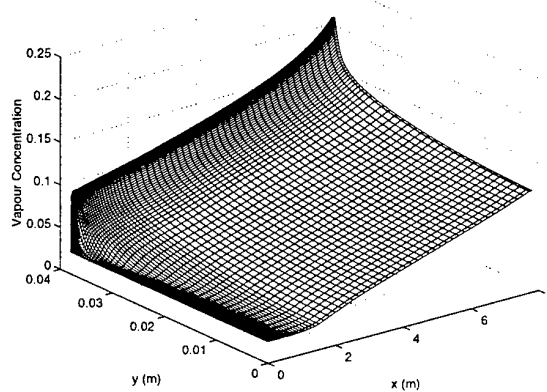


Figure 13. Vapour concentration ($T_{\text{water, in}}=70^{\circ}\text{C}$)

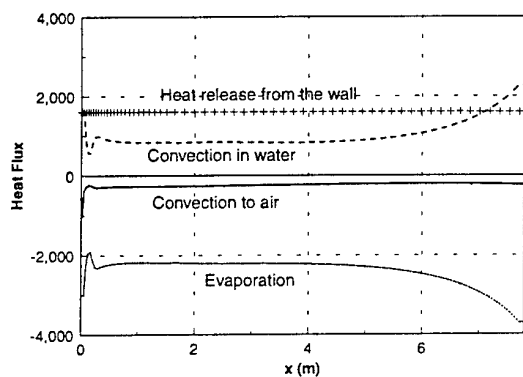


Figure 11. Energy balance for the water film ($T_{\text{water, in}}=70^{\circ}\text{C}$)

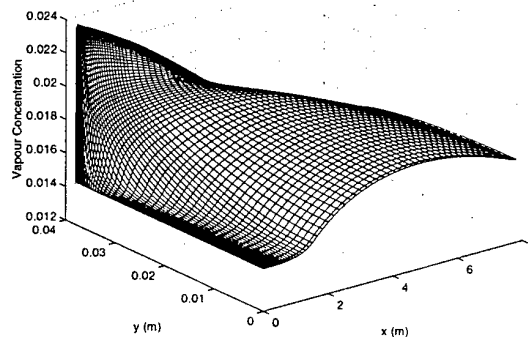


Figure 14. Vapour concentration ($T_{\text{water, in}}=20^{\circ}\text{C}$)

VELOCITY MEASUREMENTS IN THE WAKE OF A PAIR OF CYLINDERS IN HIGH INTERACTION CONFIGURATION

Christophe Brun, Michel Picut

DRN/DTP/SETEX

Laboratoire d'Etudes Thermohydrauliques des Systèmes

CEA-Grenoble

17, rue des Martyrs

Grenoble, 38054 cedex 09

France

ABSTRACT

We studied the near wake development behind two cylinders side by side with high interaction (tubes gap $g=0.583d$) in the low subcritical Reynolds number regime, using Laser Doppler Velocimetry. At this small gap we noticed that the jet created between the two tubes was deflected on a side. The main results focus on the stability of this gap jet deflection depending from the Reynolds number. Considering the frequency characteristics of the flow, we found a high dependence between the Strouhal number and the Reynolds number investigated. We ascribed this phenomenon to the stability degree and to the deflection rate of the jet. Finally we concluded that these flow behaviours were governed by the transition to turbulence location which is known to be highly changing for this Reynolds number range: It evolves between the separated shear layer in the near wake and the separation point on the tubes.

INTRODUCTION

The interaction between two cylinders placed side by side in a uniform flow is of a great interest in fluid engineering. It has been essentially investigated in terms of frequency and pressure forcing induced by the flow configuration.

When studying the case of low interaction for which $g^* > 1$, where $g^*=g/d$ is the dimensionless gap between the two cylinders, the frequency peak encountered in the wake reaches around $St_o=0.21$ (St_o based on the cylinder diameter d and on the inlet flow U_o) as for a unique cylinder Karman vortex street.

A few studies, generally using hot wire measurements, investigated the near wake behind a pair of parallel cylinders in the case of high interaction: $0.1 < g^* < 1$. The Reynolds numbers (based on the cylinder diameter and the inlet velocity) were ranging from 100 to 5.10^5 . Most of these studies determined two of the three following peculiar frequencies characterising vortex structures in the wake of both cylinders: around $St_o=0.1$,

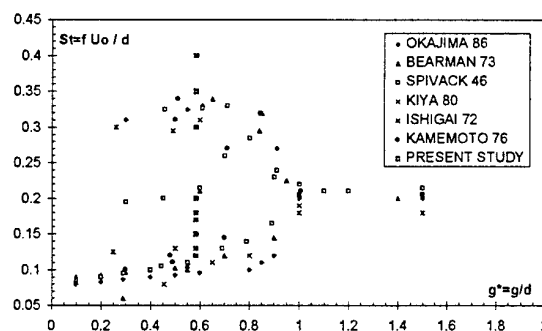


Figure 1: Near wake Strouhal number evolution with the dimensionless gap g^* between the two tubes at various Reynolds numbers ranging from 660 to 97000

$St_o=0.2$ and $St_o=0.3$. Figure 1 is a compilation of various experiments. One can see a large dispersion of the frequency results when not paying attention to the Reynolds number which lies in the subcritical regime. Kamemoto (Kamemoto, K., 1976) investigated two opposite regimes, the first at $Re=600$ and the second at $Re=30000$; Spivack (Williamson, C., H., K., et al. 1985) went as far as $Re=93000$; Okajima (Ohya & al, 1989) made measurements at more than $Re=70000$; Ishigai (Ishigai, S., 1972) did not experiment over $Re=4000$; Kiya (Kiya, M., et al, 1980) and Bearman (Bearman, P., W., et al., 1973) studied the case of respectively $Re=15800$ and $Re=25000$. Finally, the present study is in the range from $Re=1000$ to $Re=14300$. As pointed out by these numerous different results, it may be necessary to take into account the Reynolds number effect. The purpose of our study is to investigate the near wake zone past the two obstacles in order to clarify the influence of the Reynolds number on the Strouhal number for $g^*=0.583$ and to understand the jet deflection

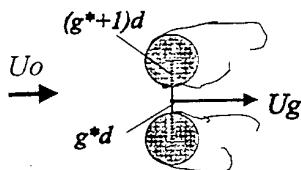


Figure 2: tubes geometrical and flow field configuration

phenomenon pointed out in the literature and its stability conditions.

For this type of arrangement very little is known about the shape of the wake: Laser Doppler Velocimetry measurements have been done at IMST (Béguier, C., 1994) just for the low interaction case. In our context, LDV brought crucial quantitative information about the flow behaviour in the near wake of the pair of cylinders in high interaction.

EXPERIMENTAL FACILITY

The configuration of the two cylinders is shown on Figure 2. Let d be the tube diameter and $g=g*d$ the gap between the tubes (So that $g*+1$ represents the dimensionless transversal spacing between the two cylinders). Using mass conservation arguments it is possible to join the velocity gap Ug with the free stream velocity Uo : $Ug=(g*+1)/g*Uo=2.71Uo$ in our case.

Using a green Argon LASER ($P=300mW$, measuring volume: $300\mu m$; fringe spacing: $3.74\mu m$; seed size: $2\mu m$) we measured axial instantaneous velocity in the near wake of the two obstacles (diameter: $d=12mm$; low gap: $g*=0.583$; high aspect ratio: $H/d=10$; low blockage: $L/d=14$) placed in a water channel down a convergent ($S1/S0=10$) and several grids and honeycomb structures ($Tu=0.5\%$; $Uo=10$ to $60cm/s$; $T=16$ to $52^\circ C$). The domain investigated is extended in the middle plan of the channel ($z=H/2$) transversally from $y=-5d$ to $y=+5d$ and axially from $x=0.6d$ to $x=20d$.

Statistical procedure gave us information about the mean values $\langle u \rangle$, $\langle u^2 \rangle$, $\langle u^3 \rangle$, $\langle u^4 \rangle$, the probability density function, and the Strouhal number deduced from longitudinal velocity energy spectrum. Several Reynolds numbers based on Uo and d , ranging from 1000 to 14300 have been studied in order to determine their influence on the near wake development.

Mean pressure distribution around the tubes was measured by a water column manometer connected to a pressure tap (diameter: $0.3mm$) performed on the rotating tubes. For the lowest Reynolds number investigated, pressure measurements have not been performed because of the lack of resolution of the manometer compared to the low flow dynamic pressure (around $5mmH_2O$).

RESULTS

For all the Reynolds numbers investigated, a flow jet is created in the gap between the two tubes and more or less deflected on one side. Nevertheless, we found two flow behaviour regimes: A stable one at $Re=1000$ and an unstable one at $Re=14300$. The cases at $Re=5100$ and $Re=10000$ are characterised by an intermediate behaviour between these two situations. In order to analyse each Reynolds number regime, we compare instantaneous velocity samples, velocity frequency spectra, radial mean velocity profile in the near wake and mean pressure distribution around the tubes.

As the flow behaviour is different for a Reynolds number case to another, we first present and analyse each wake

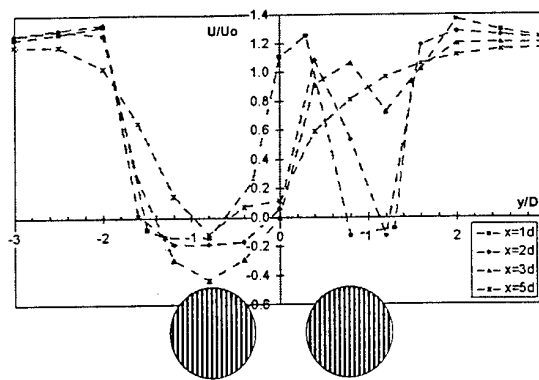


Figure 3: Transversal mean axial velocity profile at $x=1d$, $x=2d$, $x=3d$ and $x=5d$, for $Re=1000$.

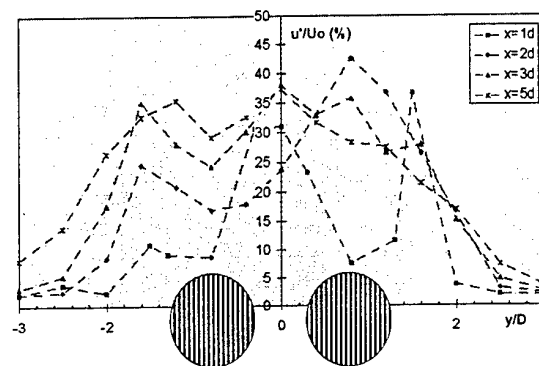


Figure 4: Transversal profile of the axial velocity fluctuations at $x=1d$, $x=2d$, $x=3d$ and $x=5d$, for $Re=1000$.

configuration. Then we discuss the evolution with growing Reynolds number and suggest a relation between the different cases. In the last section, we describe the similar flow behaviour tending for all the cases to a unique symmetric wake configuration in the zone between $x=7d$ and $x=20d$.

The Stable Biased Gap Jet: $Re=1000$

The instantaneous flow velocity field LDV measurements let us access to the transversal mean and RMS axial velocity profile in the near wakes of the two tubes. Figure 3 and Figure 4 represent the evolution of respectively $U_{MEAN}(y)$ and $u_{RMS}(y)$ at 4 successive longitudinal stations: $x=1d$, $x=2d$, $x=3d$ and $x=5d$. In the near wake of the tubes, a recirculation zone appears near each tube. A flow jet, created in the gap between the two tubes is slightly biased on one side of the double wake. With an increasing value of x/d , this gap jet becomes more and more biased on one side. At the same time, the two wakes tend to be asymmetric in strength and size: A narrow wake appears on the side where the gap flow is deflected as a wide wake is observed on the other side. For $x=5d$, only the wider wake which has asymmetrically growth on the other side remains.

The fast Fourier transform analysis of each temporal velocity field allows us to access to the spectral energy density distribution for each measurement sample. As in most of the previous studies two typical frequencies due to the vortex shedding taking place in the rear of the tubes have been encountered in the flow: The first one is around $0.97Hz$ and the second one is around $3.10Hz$. Figure 5 is a map of the flow configuration where we represent the two different Strouhal

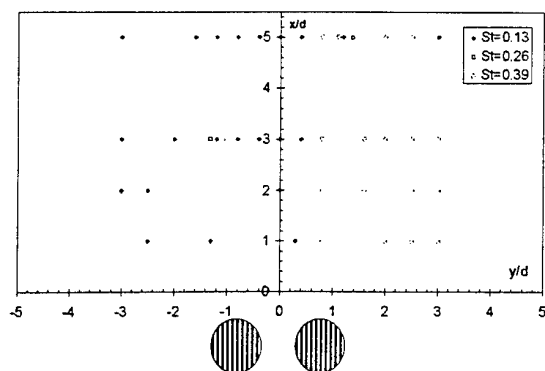


Figure 5: Strouhal number map in the near wake of the two tubes at $Re=1000$.

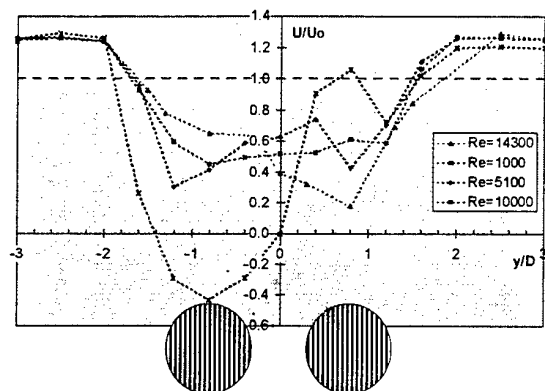


Figure 6: Transversal mean axial velocity profile at $x=3d$, for $Re=1000$, $Re=5100$, $Re=10000$ and $Re=14300$.

numbers deduced from spectrum. As pointed out by Kamemoto who made similar experiments (Kamemoto, K., 1976) at $Re=662$ with a spacing gap $g^*=0.5$, we encountered a higher strouhal number around $St=0.39=1/T_1$ on the side of the smaller wake (Kamemoto found $St=0.34$) and a lower one around $St=0.13=1/T_0$ on the side of the larger wake (Kamemoto found $St=0.08$). This seems to be dimensionally predictable if we consider that the low velocities of the larger wake correspond to the low frequencies ($f=U/d$) and vice versa. An important notice confirms the observations made in the last section: The frequency peaks in the spectrum distribution were always unique and very local (in frequency space). The two high and low Strouhal number zones never mix, the two wake zones never change side and the gap jet deflection is stable on a side during all the time measurement $\Delta t=180s=540T_1=180T_0$.

The analysis of two instantaneous velocity field located at $(x=3d, y=0.8d)$, and $(x=3d, y=-0.8d)$ shows that the biased flow in the near wake is stable. The single bump shape of the velocity probability density function confirms this information. Nevertheless, we considered the flow behaviour as a bistable one because a large perturbation (as a brutal variation of the free stream velocity) got the gap jet biased from one side to the other.

The transversal profiles of the axial velocity fluctuations (Figure 4) points out the four shear zones on each side of the two wakes: The mean velocity profiles characteristics, as well as the maxima for the fluctuations are asymmetrically located in the wakes. The amplitude of fluctuations is first larger on the side of the narrower wake, where the instantaneous velocity field temporally and spatially fast evolves. But it changes

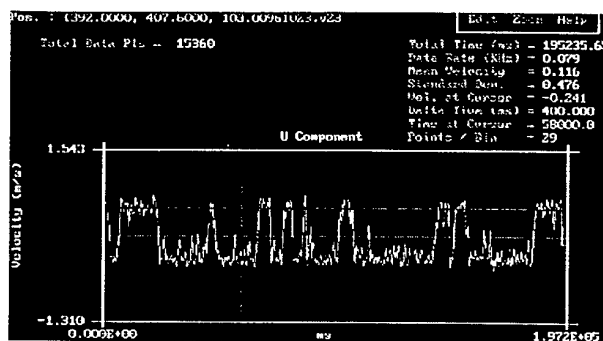


Figure 7: Instantaneous velocity sample in $x=3d$, $y=0.8d$ at $Re=14300$.

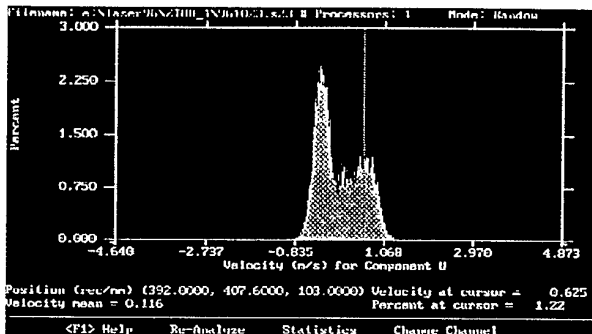


Figure 8: Velocity probability density function in $x=3d$, $y=0.8d$ AT $Re=14300$.

around $x=3d$, when the turbulence transition has taken place in the shear zones. At $x=5d$, only two shear zones are localised on each part of the remaining asymmetrical wake.

Considering the flow behind a cylinder alone at a Reynolds number range around 1000 (Coutanceau, M., 1993), the turbulence transition occurs down the boundary layer separation in the free shear layer. The transposition to our configuration suggests us that the instabilities development only appears after the boundary layer separation, in the near wake of each tube as suggested by the turbulence level evolution. Once the jet is biased, the turbulence instabilities are not able to make it change from one side to another because of their late development downstream of the tubes. If nothing changes in the flow up to the cylinders, the biased gap jet remains in a stable situation.

The Unstable Biased Gap Jet: $Re=14300$

We compiled on Figure 6 the transverse mean axial velocity profiles measured at $x=3d$ and Reynolds number $Re=1000$, $Re=5100$, $Re=10000$ and $Re=14300$. The two different wakes behind each tube really appear only for the case $Re=1000$. At $Re=14300$, we just see a low asymmetry on a side which may indicate that the jet is lightly deflected on one side. Looking at an instantaneous velocity sample during $\Delta t=195s=3800T_1=1404T_0$ (T_1 and T_0 being the two vortex shedding period described in the previous section) at $Re=14300$ and $(x=3d, y=0.8d)$ (Figure 7) one can draw a velocity probability density function diagram (Figure 8) where a double velocity bump appears. Actually, it is obvious that the flow hesitates between two velocity positions around $u=62cm.s^{-1}$ which corresponds to the velocity bulk samples ($U/U_0=93\%$) and around $u=-31cm.s^{-1}$ which corresponds to the

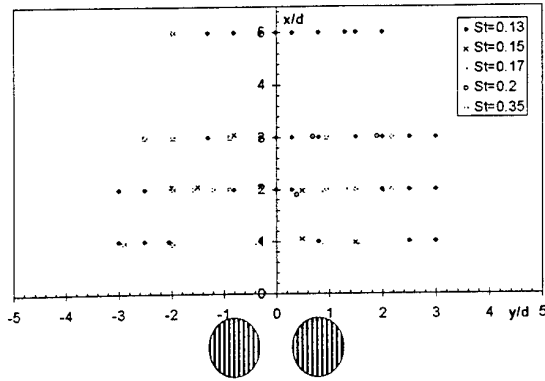


Figure 9: Strouhal number map in the near wake of the two tubes at $Re=14300$.

velocity wake samples ($U/U_0=-47\%$). We retrieve the unstable situation described by Ohya et al. at a Reynolds number around $Re=100000$ (Ohya, Y. et al., 1989) who stated that the biased gap flow changed side deflection at nonregular and numerous intervals of time. When averaging the whole velocity sample without separating the parts due to each jet deflection position, we obtained (Figure 7) $U/U_0=19\%$ which is not a realistic result. Nevertheless, it shows that the gap jet never stay at the same side without being submitted to important perturbations: One can talk about unstable bistable situation.

This last point is confirmed when studying the Strouhal number map corresponding to this measurement configuration (Figure 9). Essentially two frequencies emerged from spectral analysis, one around 7.2Hz ($St=0.13=1/T'_0$) and the other one around 19.3Hz ($St=0.28=1/T'_1$), as encountered in Kiya study (Kiya, M., et al, 1980) whose investigation configuration was $g^*=0.65$ at $Re=15800$. Kiya found two frequency peaks around $St=0.11$ and $St=0.31$ and considered it as the sign of the jet deflection, the lower Strouhal number corresponding to the wider wake, and the higher Strouhal number corresponding to the narrower wake as described for the case at $Re=1000$.

Nevertheless, the spatial distribution of Strouhal numbers is different compared to the previous case: The two main frequencies cited above are encountered in the same measurement location down $x=3d$. This confirms again the unstable deflection phenomenon described on Figures 7 and 8. Applying the fast Fourier transform procedure to one of the two parts (with jet deflection either on one side, or on the other side) of a velocity sample, one may obtain either the higher frequency or the lower one.

As for the previous case, one may explain this unstable flapping from a side to another by the location of transition to turbulence in the flow. With increasing Reynolds number higher from $Re=1000$, considering again the analogy with a unique cylinder shedding vorticity structures, the first point transition comes back to the tube and contaminates the boundary layer before separation. The transposition to our configuration makes us consider that the first vortex shedding takes place immediately past the two cylinders at $Re=14300$. A small instability may be amplified in the turbulent boundary layer and may cause the jet deflect from one side to the other at random time interval. This may be a reason why the jet deflection is unstable for this Reynolds number range.

Few spectral analysis pointed out frequency peaks corresponding to $St=0.2$ as encountered by Bearman (Bearman,

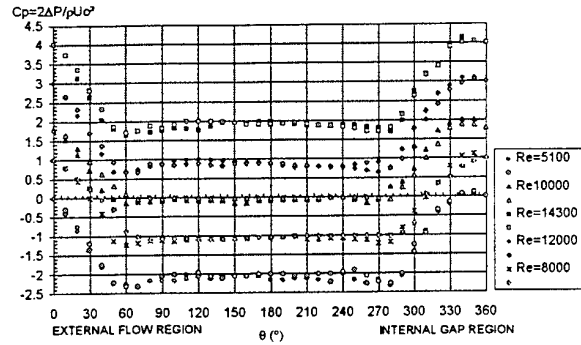


Figure 10: Pressure coefficient distribution around the two tubes (one tube being referred by open symbols, the other one by solid symbols) at Reynolds number ranging from $Re=5100$ to $Re=14300$.

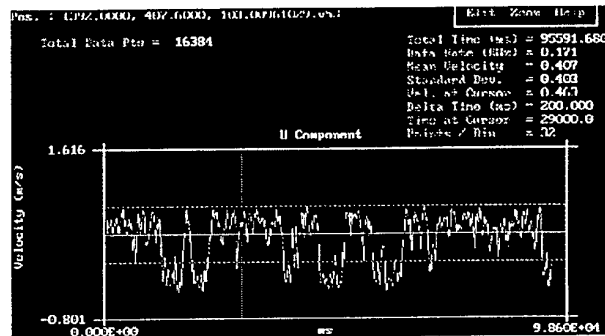


Figure 11: Instantaneous velocity sample in $x=3d$, $y=0.8d$ AT $Re=10000$.

P., W., et al., 1973) and Spivack (Williamson, C., H., K., et al. 1985) with $g^*=0.6$, at higher Reynolds numbers respectively $Re=25000$, and $Re=93000$. Is this last frequency emergence due to a Reynolds number effect? It seems to be a good reason, considering Ohya investigations (Ohya & al, 1989) in the critical regime ($Re=340000$ and $Re=450000$): He found respectively $St=0.21$ and $St=0.23$ for dimensionless tubes space around $g^*=0.7$.

The Unstable Quasi Symmetric Gap Jet: Around $Re=10000$

Mean pressure measurements have been performed around the two cylinders for Reynolds numbers ranging from $Re=5100$ to $Re=14300$, as reported in Figure 10. The angle of measurement is referred to the point of the cylinder in front of the flow; The direction of rotation always goes from the outlet flow to the inlet gap jet. We choose a pressure coefficient depending on the free stream velocity: $C_p=2(P-P_{ref})/\rho U_0^2$. The mean pressure distribution is globally independent from the investigated Reynolds number. The two tubes have a similar behaviour. The front stagnation point is located around $\theta=-15^\circ$; this is a sign of the high interaction between the tubes which pushes one over the other. Nevertheless, the maximum pressure variation (around $\Delta C_p=2.5$) is not locally influenced by the gap jet developed between the two tubes ($U_g=2.71U_0$); Actually, the whole distribution is modified, compared to the one around a unique cylinder at an equivalent Reynolds number regime for which maximum pressure variation is around $\Delta C_p=2$. Considering this last value, one can propose an equivalent

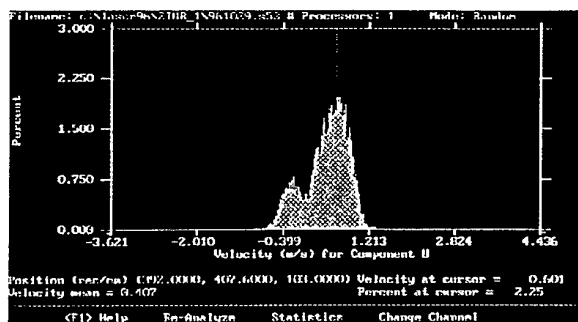


Figure 12: velocity probability density function in $x=3d$, $y=0.8d$ AT $Re=10000$.

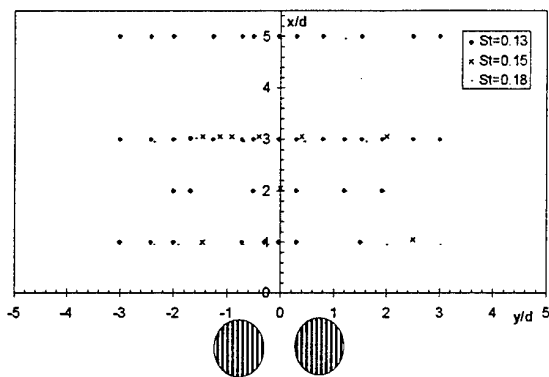


Figure 13: Strouhal number map in the near wake of the two tubes at $Re=10000$.

velocity value U_p characterising this interaction ($2(P - P_{ref})/\rho U_p^2 = 2$) and obtain $U_p = 1.12U_o$ which represents the modified velocity field around the tubes. The inlet boundary layer separation seems to be situated around $\theta = -100^\circ$, and the outlet boundary layer one around $\theta = 80^\circ$. Between those two points, at the rear of the tubes, the pressure distribution does not evolve; Nevertheless, on each measurement case, we can see irregular variations from one point to another due to the vortex shedding phenomenon (and maybe also the gap jet flapping) which amplitude is not damped by the manometer measurement system.

Like the mean pressure distribution, the mean velocity profile in $x=3d$, at $Re=5100$ and $Re=10000$ are quasi-symmetric (Figure 6) and similar to the shape of the wake past a unique cylinder.

Actually, a study of the instantaneous velocity field during $\Delta t = 95s = 700T''_0$ (Figure 11) is once again necessary to determine the position and the stability of the gap jet. As pointed out by the double bump appearing on the velocity probability density function (pdf) diagram on Figure 12, the flow hesitates between two velocity values, that is to say the jet hesitates (as at higher Reynolds number) between two positions, one leading to the development of a wake zone around the measurement point and the other one feeding the flow velocity. Contrary to the previous case, the velocity pdf are weakly influenced by the lowest velocities; This may indicate that the wakes made from each part of the gap jet are weakly developed, that is to say the gap jet flapping has a low amplitude. The flow is not far away from a symmetric double wake situation in spite of the random unstable jet deflection.

The frequency map has a real peculiar feature at this Reynolds number range compared to the two previous cases. As

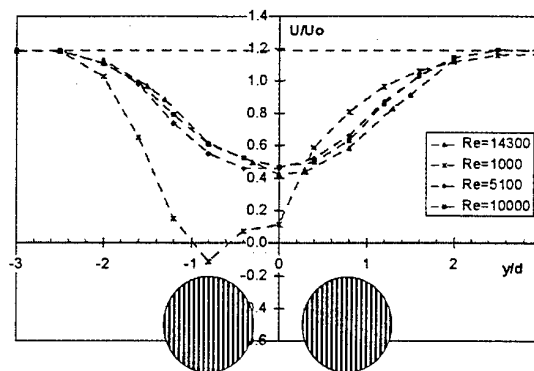


Figure 14: Transversal mean axial velocity profile at $x=5d$, for $Re=1000$, $Re=5100$, $Re=10000$ and $Re=14300$.

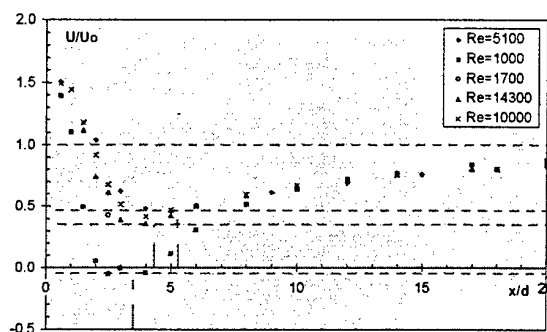


Figure 15: Axial evolution of longitudinal fluctuation velocity on the median axis of the two tubes ($y=0$) for $Re=1000$, $Re=5100$, $Re=10000$ and $Re=14300$.

one can see on Figure 13, there are no more high frequency locations around $St=0.35$. Looking at the velocity energy spectrum, one can observe a large energetic bump around the same low frequency value as described in the previous sections, with a stronger peak at $St=0.13=1/T''_0$ and spreading up to $St=0.18$.

This frequency behaviour is encountered equally on each side of the parallel cylinders as for the case $Re=14300$. Therefore we can consider that it is due to the mixing of the two parts of the signals between which the flow oscillates randomly. Separating those two velocity levels would give us each one of the two frequency peaks. Using dimension argument ($f=U/d$) as described in the first chapter, one may obtain two similar velocity wakes. This frequency proximity between the two possible states of the flow would confirm that the two wakes past the tubes are similar in size and amplitude, due to a low gap jet deflection.

The Intermediate Wake Zone: Return To a Symmetric Unique Wake Configuration.

At all the Reynolds numbers studied, we noticed a similar behaviour in the intermediate wake: The flow tends to a symmetric unique wake which characteristics are quasi-independent from the Reynolds number range.

Figure 14 compares the transverse mean axial velocity profile at $x=5d$ for different Reynolds numbers. The highest Reynolds

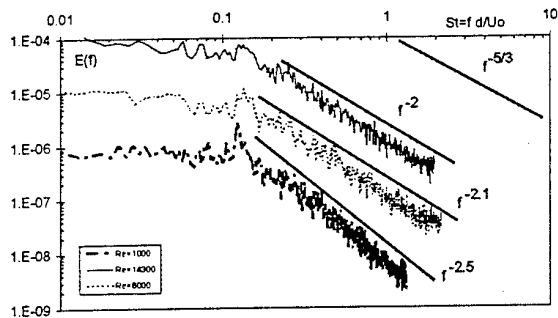


Figure 16: Longitudinal velocity energy spectrum at $x=12d$, $y=0$, for $Re=1000$, $Re=8000$, and $Re=14300$.

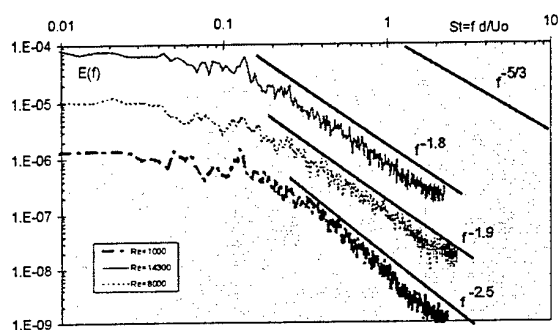


Figure 17: Longitudinal velocity energy spectrum at $x=20d$, $y=0$, for $Re=1000$, $Re=8000$ and $Re=14300$.

number cases are quasi symmetric and identical, with no more random flapping jet phenomenon (the gap jet spread and vanishes in the whole near wake region). The flow behaviour seems to be different for the lowest Reynolds number case. The gap jet deflection is stronger and stable as described in the first chapter creating a large asymmetric unique wake from $x=5d$ (Figure 14) up to $x=10d$.

In the same time, the axial velocity fluctuations level (Figure 15) slowly reduces, reaching 15% at $x=20d$ independently from the Reynolds number investigated. A statistic study of the velocity samples obtained in this intermediate wake let us access to turbulence characteristics as skewness and flatness coefficients which respectively tend to around $Su=0$ and $Fu=3$.

This decreasing turbulence situation is a sign of a certain energetic equilibrium reached by the flow after the first phase governed by high interaction phenomenon as jet deflection or flapping. A spectral analysis of the situation at $x=12d$ and $x=20d$ (Figure 16 and 17), shows the emergence of a unique general Strouhal number around $St_0=0.13$. This value corresponds to the Strouhal number encountered in the wake of a unique cylinder which diameter is around the double of the present one. This confirms the visualisations made by Williamson at low Reynolds number around $Re=100$ (Williamson, C. H. K., et al. 1985) who pointed out an amalgam between vortices. These structures were shed and advected in the rear of the tubes and coalesced to form a large scale single vortex street.

On the other hand, an energetic transfer phenomenon from large shear structures to small ones appears on the velocity

spectrum. In the case of $Re=1000$ an energetic transfer zone is beginning its development around $x=12d$. At $x=20d$ the energy spectrum reaches a $E(f) \propto f^{-2.5}$ law, sign of a turbulent non equilibrium situation. For higher Reynolds number cases, the jet flapping may contribute in structures mixing. For $Re=14300$, an $E(f) \propto f^{-2}$ law is developing from $x=12d$ on one decade at least and reaches an $E(f) \propto f^{-1.8}$ at $x=20d$. The highest energetic frequencies vanishing may participate in the spectrum spreading by a backscatter phenomenon encountered when small eddy structures coalesce and form a larger one. This would accelerate the appearance of a fully developed turbulent flow regime.

DISCUSSION AND CONCLUSION

We studied the deflection mechanism developed in the case of a high interaction phenomenon between two tubes side by side. As assumed by Ohya (Ohya, Y., et al., 1989) the gap jet deflection seems to be stimulated by the way the flow instabilities are developed during the wake transition to turbulence, and not essentially by a Coanda effect as described by several authors. Thus we pointed out the importance of the flow Reynolds number, in particular in the low subcritical regime studied here ($Re < 20000$). With increasing Reynolds number the transition location comes back to the cylinders, as for a unique obstacle, and may have contaminated the separated boundary layer on the tubes at $Re=14300$. From our point of view, this evolutionary behaviour of the transition to turbulence is the reason why we obtain both a changing amplitude and an uncertain stability of the gap jet deflection. In case of transition in the wake (lower Reynolds number) instabilities are developed too late to make the jet change side: the deflection is stable. In case of transition near the boundary layer separation (higher Reynolds number), instabilities may increase and randomly let the jet deflect from one side to another: the deflection is unstable. In the intermediate case (Reynolds number around $Re=10000$) instabilities rapidly spread in the two separated shear layers on each side of the gap jet letting it biased both weakly and randomly.

REFERENCES

- Bearman, P. W., and Wadcock, A. J., 1973, "The Interaction Between a Pair of Circular Cylinders Normal to a Stream", *Journal of Fluid Mechanics*, Vol. 61, n° 3, pp. 499-511.
- Béguier, C., 1994, "The Double Wake Turbulent Mixing", Les Houches 1994, *Computational Fluid Dynamics*.
- Coutanceau, M., 1993, "Structure des Sillages à l'Aval d'Obstacles Rigides", Cours de DEA de l'université de Poitiers.
- Ishigai, S., Nishikawa, E., Nishimura, H., and Cho, K., 1972, "Experimental Study on Structure of Gas Flow in Tube Banks with Tube Axes Normal to Flow", *Bulletin of the JSME*, vol. 15, n° 86, pp 949-956.
- Kamemoto, K., 1976, "Formation and Interaction of Two Parallel Vortex Streets", *Bulletin of the JSME*, vol. 19, n° 129, pp 283-290.
- Kiya, M., Arie, M., Tamura, K., and Mori, H., 1980, "Vortex shedding for two circular cylinders in staggered arrangement", *Journal of Fluid Engineering (ASME)*, vol 102, pp 166-173.
- Ohya, Y., Okajima, A., and Hayashi, M., 1989, "Wake Interference and Vortex Shedding", *Encyclopedia of Fluid Mechanics*, Vol. 2, pp. 323-389.
- Williamson, C. H. K., 1985, "Evolution of a Single Wake behind a Pair of Bluff Bodies", *Journal of Fluid Mechanics*, Vol. 159, pp. 1-18.

ON THE CONFIGURATION OF THREE-DIMENSIONAL INTERMITTENT TURBULENT BULGES IN A FAR WAKE

Gregory A. Kopp, Francesc Giralt, Josep A. Ferré

Escola Tècnica Superior d'Enginyeria Química

Universitat Rovira i Virgili

Carretera de Salou, s/n

43006 Tarragona, Catalunya

Spain

James F. Keffer

Department of Mechanical and Industrial Engineering

University of Toronto

5 King's College Road

Toronto, Ontario, M5S 1A4

Canada

ABSTRACT

The spatial distribution of the turbulent bulges in the far region of a plane turbulent wake was obtained by using data from 16 normal wires placed in the horizontal (homogeneous) plane where the intermittency factor was 0.5. By using a new technique to identify the presence of the bulges, it was found that the probability density function of bulge sizes is considerably different than that obtained by using a single probe because the PDF from a single probe underestimates the true bulge sizes. This is due to quiescent regions within the turbulent bulges. Statistics relating to the turbulent bulges are consistent with the presence of double roller structures, previously identified with a pattern-recognition technique, indicating that the turbulent bulges are these structures.

INTRODUCTION

Early investigations of free turbulent shear flows identified the existence of a sharp interface between turbulent and non-turbulent fluid (e.g., Corrsin and Kistler, 1955; Kovaszny et al., 1970) by utilizing a turbulence indicator function based on velocity signals. This interface was found to be characterized by rather large turbulent bulges, between which there was found quiescent fluid.

More recent research along this line has gone in at least two different directions. The first, which began with the work of Theodorsen (1952) and Townsend (1956), has focused on identifying large-scale coherent structures within the turbulent region of these flows. The resulting energy balances and momentum transfer analyses relating to these structures have answered many questions about the dynamics of the interior motions (e.g., Antonia et al., 1987).

Although a connection between these inner structures and the outer turbulent bulges has been inferred, the connection has not been explicitly investigated in fully-developed turbulence.

The second line of research has remained explicitly concerned with the identification and nature of the turbulent/non-turbulent interface by examining its fractal properties. The pioneering work of Mandelbrot (1974) was greatly extended by the series of papers by Sreenivasan's group (e.g., Prasad and Sreenivasan, 1990; Sreenivasan, 1991), and others, who used digital image analysis to identify the interface and obtain its fractal dimension in a variety of turbulent flows. The fact that the turbulent interface is a fractal means that there is a self-similarity between the large and small scales of the interface. This, too, implies a relationship between the coherent structures and the large and small scales at the interface. An investigation of the relationship between coherent motions and fractal geometry has been performed by Tsuji and Nakamura (1994) who identified the fractal dimension of iso-velocity surfaces associated with the bursting event, as identified by quadrant analysis, in a turbulent boundary layer.

Several questions obviously remain. The present work is a preliminary effort to make an explicit connection between the coherent structures and the turbulent/non-turbulent interface. A new technique is developed to identify turbulent bulges from multi-point measurements and the results are compared with those from single point measurements. A connection between these bulges and the inner double roller structure is made.

EXPERIMENTAL DETAILS

Experiments were performed in the plane turbulent wake generated by a circular cylinder mounted flush with the tunnel walls. The cylinder diameter, D , was 11.6 mm and the freestream velocity, U_0 , was 9.0 m/s so that the Reynolds number, Re , was 6700. Measurements were made at $x=170 D$, downstream of the cylinder.

A rake of 16 normal wires were placed in the horizontal (x^*-z^*) plane at the lateral (y^*) location where the intermittency factor was about 0.5. The co-ordinates are normalized such that $z^* = z/l_0$, $y^* = y/l_0$ and $x^* = -U_0 t/l_0$ where the mean velocity half-width length scale, l_0 , is 44 mm. The lateral location where the intermittency factor is about 0.5 is called the half-intermittency point, l_h . The conversion of the time co-ordinate into a spatial one assumes Taylor's hypothesis. Note that x^* defined in this manner is not to be confused with x/D . The probes were separated by 6 mm in the spanwise (z^*) direction which corresponds to a non-dimensional spacing, Δz^* , of 0.14. Thus, the total span of the rake was $2.1 l_0$. It should be noted that by using Taylor's hypothesis to convert time into the streamwise (x^*) co-ordinate, the sampling rate ($\Delta t=0.2$ msec) corresponds to streamwise spacing of $\Delta x^*=0.041$ ($\approx 1/3 \Delta z^*$). A definition sketch is shown in Fig. 1 while further details about the various scales in this flow can be found in Table 1.

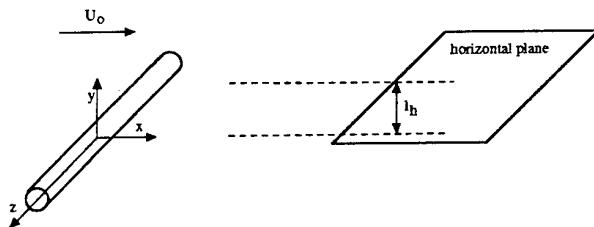


Fig. 1. A definition sketch showing the plane of measurement for the 16 normal wires.

TABLE 1. Details of the Wake at $x/D=170$.

cylinder diameter, D	11.6 mm
freestream velocity, U_0	9.0 m/s
Taylor macro-scale, T	3.6 ms
Taylor micro-scale, λ	1.0 ms
Kolmogorov length scale, $\eta=(\nu^3/\epsilon)^{1/4}$	0.4 mm
dissipation, $\epsilon=(u')^3/T$	0.1 m ² /s ³
$\lambda_k=2\pi\eta/U_0^*$	0.3 ms
l_h/l_0	1.6
$Re=U_0 D/\nu$	6700
$Re=u'T/\nu$	320

* see Meneveau and Sreenivasan (1991)

The measurements were made in the open-circuit, variable-speed, low turbulence wind tunnel at Universitat Rovira i Virgili. This tunnel has a test section 60x60 cm square and 300 cm long and the freestream velocity can be adjusted between 5 and 20 m/s. There is a 9:1 contraction downstream of a honeycomb and six screens. The freestream turbulence intensity is about 0.1% while the variation of mean velocity across the tunnel is about 1% at 9 m/s. The room temperature

can vary by up to 0.5K during the time required to set the resistances, calibrate the probes and make the measurements. The aspect ratio of the cylinder is about 50 and the tunnel blockage is 2%.

DISA 55M01/10 and 56C01/17 anemometers and bridges were used with Dantec 55P11 normal wire probes. The voltage signals from the anemometers were amplified by 10, low-pass filtered at 2 kHz and digitally sampled at 5000 points per second per channel for 40 seconds. The signal conditioners were built in-house. The normal wires were calibrated using a Pitot tube and King's law in a part of the wind tunnel unaffected by the wake. The data were stored on optical disk for later processing.

IDENTIFICATION OF TURBULENT BULGES

Turbulence Indicator Function

Since turbulence is characterized by random vorticity fluctuations, identification of the interface separating turbulent and non-turbulent (or "potential") fluid domains would be best accomplished via the instantaneous vorticity signal because there are effectively zero levels of random vorticity in the potential stream and non-zero levels within the turbulent flow. Thus, the random vorticity signal would provide a rational basis for a turbulence indicator function, which is defined as

$$I(x, y, z, t) = \begin{cases} 1, & \text{turbulent} \\ 0, & \text{otherwise} \end{cases} \quad (1)$$

Thus, the turbulence indicator function, which is a random square wave, is the time history of the turbulent/non-turbulent interface. Obtaining the random vorticity signal, however, requires the use of special probes like, for example, the 4-wire probe of Haw et al. (1989). Our desire to investigate the instantaneous spatial distribution of the interface would be severely limited using such probes, thus, the identification of turbulent zones is made using the streamwise velocity component obtained from a normal wire.

The intermittency factor, $\bar{I}(x, y, z)$ is the time-average of $I(x, y, z, t)$ at a point. In addition, the turbulence burst rate is defined to be the average number of transitions from zero to unity per unit time, namely,

$$\bar{f}(x, y, z) = \frac{Q}{T} \quad (2)$$

where Q is the total number of zero to unity transitions in time, T . Twice the value of the turbulence burst rate represents the average number of times that the interface between the turbulent and non-turbulent domains passes the probe per unit time. Previously, it was assumed that the turbulence burst rate was an indication of the number of turbulent bulges passing the probe per unit time (Kawall and Keffer, 1979) with each square wave of the instantaneous indicator function defining a bulge. The average turbulent zone length (or average bulge size) and potential zone length are defined to be, respectively,

$$\bar{z}_t(x, y, z) = \frac{1}{Q} \sum_{i=1}^Q (z_t)_i = \frac{\bar{I}(x, y, z)}{\bar{f}(x, y, z)} \quad (3)$$

$$\bar{z}_p(x, y, z) = \frac{1 - \bar{I}(x, y, z)}{\bar{f}(x, y, z)} \quad (4)$$

where z_t and z_p are the turbulent and potential zone lengths, respectively.

Obtaining the turbulence indicator function from a velocity signal is not straightforward because velocity fluctuations at a point can legitimately occur in both the turbulent and non-turbulent flow domains. Thus, an intermittently turbulent velocity signal needs to be sensitized to the presence of turbulence so that the probability density functions (PDF) of the turbulent and non-turbulent regions are sufficiently separated (Kawall and Keffer, 1980). Typically, detector functions are based on the square of the first or second time derivative of the streamwise velocity. Tabatabai et al. (1989) used, for example, $((U - U_0)(\partial U / \partial t))^2$ while Hedley and Keffer (1974) used $(\partial U / \partial t)^2 + (\partial V / \partial t)^2$. Thus, the detector function of Tabatabai et al. (1989) with digitally sampled data at a fixed location is,

$$D(t_j) = \left\{ (U_j - U_0) \left(\frac{\Delta U_j}{\Delta t} \right) \right\}^2 \quad (5)$$

where U_j is the instantaneous streamwise velocity, j varies from 1 to N , and N is the number of points sampled.

Two types of problems arise from the use of any real detector function. In the first type of problem, termed the signal dropout problem, there will be occasions when the detector function takes on zero values within legitimately turbulent regions. In the second type of problem, termed the signal noise problem, there will be occasions when the detector function takes on non-zero values within non-turbulent regions due to the low-level background turbulence, legitimate velocity fluctuations within the ambient fluid and electronic noise. In addition, it seems likely that time derivatives of velocity signals do not fully reflect the random vorticity fluctuations which characterize turbulence.

There are several methods for avoiding the signal dropout problem, as discussed by Kawall and Keffer (1980), but smoothing of the detector function is generally accepted to be an effective technique. Smoothing involves a short-time averaging (or short-time integration) of the detector function. With digitally sampled data at a fixed location one obtains,

$$S(t_j) = \frac{1}{T_s} \sum_{i=j-M/2}^{i=j+M/2} D(t_i) \quad (6)$$

where $T_s = M\Delta t$ is termed the hold time or smoothing time. The resulting smoothed signal is called the criterion function by Hedley and Keffer (1974). Note that the criterion function is dependent on past and future velocities and that the holdtime may be dependent on the sampling rate.

The method for solving the signal noise problem is to apply a threshold to the criterion function such that the turbulence indicator function, at a given point in space, is

$$I(t_j) = \begin{cases} 1, & \text{when } S(t_j) \geq C_1 \\ 0, & \text{otherwise} \end{cases} \quad (7)$$

where C_1 is the threshold. Selection of the threshold is somewhat arbitrary and a completely objective technique does not exist. Selection procedures vary from choosing C_1 "by eye", invariance of the potential zone length (Hedley and Keffer, 1974), the technique of Kawall and Keffer (1980) which is described below, and others.

Kawall and Keffer (1980) based their choice of threshold on the fact that in the freestream the intermittency factor, I_0 , should be zero and the intermittency factor on the centreline, I_1 , should be unity. Basically, C_1 and T_s are determined such that they are high enough so that I_0 is approximately zero and low enough so that I_1 is approximately unity. C_1 and T_s ,

once chosen, are invariant across the flow. However, Prasad and Sreenivasan (1990) show that for a turbulent jet the intermittency factor I_1 is not really unity on the centreline and this may be the case for the far wake as well.

In the present work, the indicator function is obtained via the detector function of Tabatabai et al. (1989), namely, $((U - U_0)(\partial U / \partial t))^2$. The technique of Kawall and Keffer (1980) is used to determine the threshold level (C_1) and hold time (T_s). Tabatabai et al. (1989) found that the present detector function allows for a shorter hold time to be used so that there is less dependence on past and future events. In the present work, the hold time has been determined to be 1.2 msec so that, in effect, the streamwise resolution is $\Delta x^* = 0.25$ ($= 1.7 \Delta z^*$). Thus, the difference in the spatial resolution in time (or the streamwise direction) and in the spanwise direction is not large.

With appropriately selected values for C_1 and T_s , the curvature in plots of intermittency factor and burst rate versus threshold is small for the data from the intermittent region of the flow. The threshold chosen is observed to be that where the curvature begins to be constant. Thus, the present technique for choosing the threshold is consistent with that of Hedley and Keffer (1974). It should be noted that the burst rate decreases with increasing hold times. Thus, any non-turbulent regions surrounded by turbulent that remain in the indicator function (after choosing a fairly large hold time) must be considered real.

An obvious flaw in this technique is that the hold time is 4 times larger than the Kolmogorov scale estimated in Table 1. Thus, the interface is not marked with Kolmogorov scale resolution. Nevertheless, since our objective is to investigate the relationship between the coherent structures and the large-scale bulges (and not to determine the fractal dimension of the interface), this should not be too great a problem.

Identification Technique

The first work identifying turbulent bulges and the turbulent/non-turbulent interface focused on the indicator function obtained from a single probe (e.g., Corrsin and Kistler, 1955) (although it is noted that Paizis and Schwarz, 1974, used data from a rake of probes to identify the slope of the interface). Since a single indicator function gives the time history of the passage of the interface passing the probe it was assumed that each zero-to-one transition followed by a one-to-zero transition was a turbulent bulge. More recent work has concentrated on identifying the interface from digital images obtained in a single plane of the flow illuminated by the laser induced fluorescence technique (e.g., Prasad and Sreenivasan, 1990). The present technique falls somewhere between the two.

In order to develop a technique which identifies turbulent bulges it is assumed that the bulges are spatially separated from one another by quiescent regions and that the bulges do not overlap. With this technique we are primarily concerned with identifying where the bulges are located and not where the interface is explicitly with regard to the bulge. (The turbulence indicator function is assumed to mark the interface explicitly, however.)

We define an intermittency factor which is obtained by averaging the indicator function over a relatively large scale of the flow, such that

$$I_{ls} = \frac{1}{n_{ls} n_z} \sum_{i=1}^{i=n_{ls}} \sum_{k=1}^{k=n_z} (I_{i,k}) \quad (8)$$

where I_{ls} is the spatially averaged indicator function, n_{ls} is the number of points corresponding to the streamwise extent of the largest scale structures and n_z is the number of probes in the fixed rake. A similar spatial average can be defined at a smaller scale, such that

$$I_{ss} = \frac{1}{n_{ss} n_z} \sum_{i=1}^{i=n_{ss}} \sum_{k=1}^{k=n_z} (I_{i,k}) \quad (9)$$

where n_{ss} is the number of points for the minimum length of the quiescent region between bulges.

It seems reasonable to expect that there is bulge present when I_{ls} is near unity and that there is a quiescent zone when I_{ss} is near zero. The actual values for n_{ls} and n_{ss} were chosen as $n_{ls}=0.8 l_0=1.0 T$ and $n_{ss}=0.1 l_0=2 \lambda_k$. The actual value of n_{ls} is not critical as long as it is large enough to identify the smallest large-scale bulges but not so long that it approaches the global time-average.

A portion of the time history of I_{ls} is given in Fig. 2. This figure shows that there are regions within the data set that have values near unity and regions that have values near zero. Because the peaks exhibit a variety of levels, it is necessary to choose a threshold, C_{ls} , in order to identify the bulges. With C_{ls} chosen as 0.7 the regions with bulges can be identified. Three bulges with a peak above C_{ls} can be identified in Fig. 2.

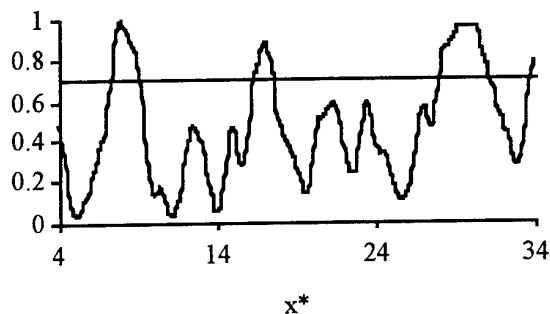


Fig. 2. A portion of the variation of I_{ls} (see Eqn. 8) with x^* .

Once a bulge has been identified its edges, i.e., fronts and backs, need to be located. Determining the exact locations of the fronts and backs is somewhat more difficult, however, because the interface is rather irregular. The intermittency factor, I_{ss} , which is averaged over a smaller spatial scale is used for this purpose. A portion of I_{ss} is given in Fig. 3. This signal has a higher rms. value than I_{ls} but is remarkably similar because the actual bulges in these figures are much larger than the scales used to determine I_{ls} and I_{ss} . Since I_{ss} is used to mark the edges (fronts and backs) of the bulges a threshold, C_{ss} , near zero is necessary. With C_{ss} chosen as 0.3 the fronts and backs of any bulge identified by a peak in I_{ls} can be identified. Choosing a lower value of C_{ss} would lead to longer bulges being identified.

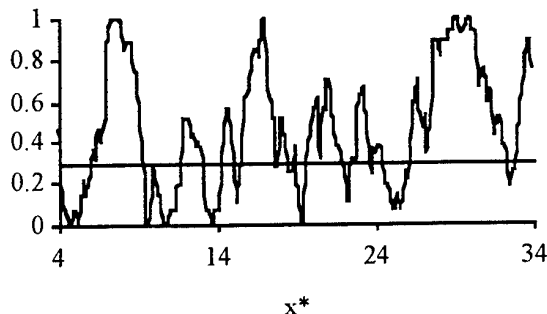


Fig. 3. A portion of the variation of I_{ss} (see Eqn. 9) with x^* .

DISCUSSION OF RESULTS

Figure 4 depicts the probability density functions of bulge sizes obtained with the present technique and with the single wire technique of Kawall and Keffer (1979). The shape of the PDF from a single wire, or in other words, the PDF of the turbulent zone lengths, z_t , is similar to that obtained by Kawall and Keffer (1979). What is interesting is that the streamwise scale where this PDF is maximum is much smaller than that obtained from the rake technique, with significant values from $x^*=0$ to 3 and a peak value at about $x^*=0.5$. On the other hand, the rake technique gives a peak at $x^*=2$ with significant values from $x^*=1.5$ to 7. For the minimum size allowed by the technique (determined by n_{ls}), no bulges are detected, suggesting that the shape of the PDF is not dependent on the choice of n_{ls} .

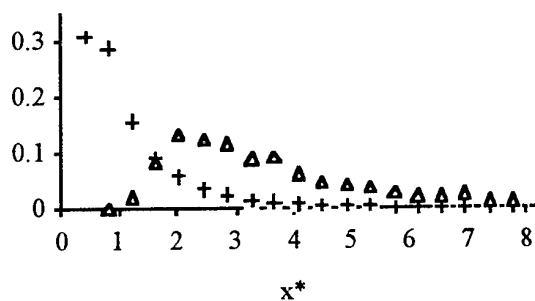


Fig. 4. Probability density functions of bulge sizes (or turbulent zone lengths) from the single probe, +, and the multi-probe, Δ , techniques.

In addition, Kawall and Keffer (1979) found that the average turbulent zone length, z_t , decreased rapidly from a value approaching infinity at the wake centreline (because $I_1=1$) to a value approaching zero in the freestream (because $I_0=0$). At the edge of the turbulent core, at say $y^*=1$, which is the average location of the "base" of the bulges and where many of the previous structural analyses have been performed (see Vernet et al, 1997a for a recent discussion), the average turbulent zone length is about 15 times larger than that at the half-intermittency point ($y^*=1.6$). However, examination of pattern-recognition results (see Vernet et al., 1997b) show

structures which do not appear to be much different in size between $y^*=1.0$ and 1.6 . Thus, one would expect quiescent regions within the turbulent structures at their outer edges.

In order to investigate this point it is useful to examine some of the individual bulges. Figure 5 shows the instantaneous turbulence indicator function, I , for a typical bulge identified with the present technique. In this figure the white regions are turbulent ($I=1$) and the black regions are "potential" or quiescent ($I=0$). It is observed that there is a large turbulent region within the bulge with no encapsulated quiescent regions, while the rest of the bulge has patches of quiescence and turbulence. It seems reasonably clear that these "patches" of turbulence must be considered as parts of the same bulge, not as individual bulges because they are all connected. Thus, the effect of using a single wire to obtain the PDF of bulge sizes is clear. Without the additional spanwise information one would conclude that each individual indicator function making up Fig. 5 contains many bulges. The scale of the bulges identified with multi-probe technique must be larger because this effect is taken into account.

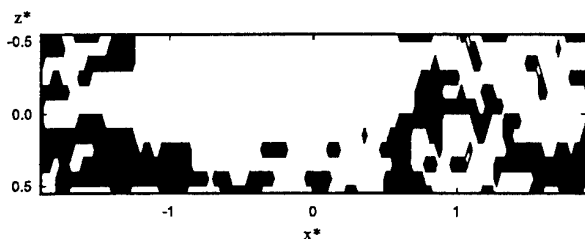


Fig. 5. An instantaneous spatial distribution of the turbulence indicator function selected by the multi-probe identification technique.

Figure 6 shows the streamwise velocity fluctuations corresponding to Fig. 5 where the mean velocity has been subtracted from the instantaneous velocity to obtain the fluctuations. It is observed that the turbulent region without encapsulated quiescent regions contains negative velocity fluctuations of large magnitude, with the peak negative fluctuation more than four times larger than the rms. level. Clearly there are huge amounts of turbulence energy contained within this region as well. The remainder of the plot contains primarily positive velocity fluctuations, but of a much smaller relative magnitude, near the edges of this bulge. The region of negative streamwise velocity fluctuations seems likely to be the fluid ejected outwards from the central region of a double roller structure which exists in the fully turbulent core (e.g., Vernet et al., 1997b).

In order to investigate the behaviour of the velocity fluctuations for all of the bulges identified, the conditional velocity fluctuations, u_b and their square were ensemble-averaged. These ensemble-averages were obtained using the velocities fluctuations, u , within a bulge when the turbulence indicator function was unity. Figures 7 and 8 show the resulting distributions of $\overline{u_b}/u'$ and $\overline{u_b^2}/(u')^2$, respectively, where u' is the rms. value of the streamwise velocity.

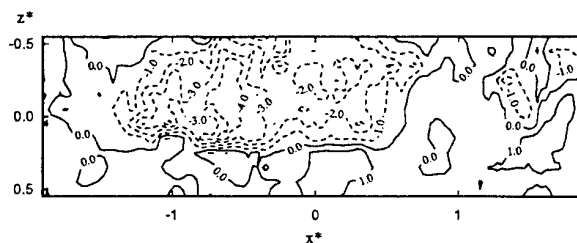


Fig. 6. The streamwise velocity fluctuations, u/u' , associated with the bulge in Fig. 5.

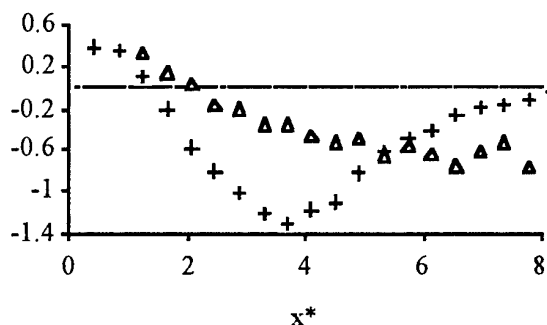


Fig. 7. Ensemble-averaged streamwise velocity fluctuations, $\overline{u_b}/u'$, from the single probe, +, and the multi-probe, Δ , techniques.

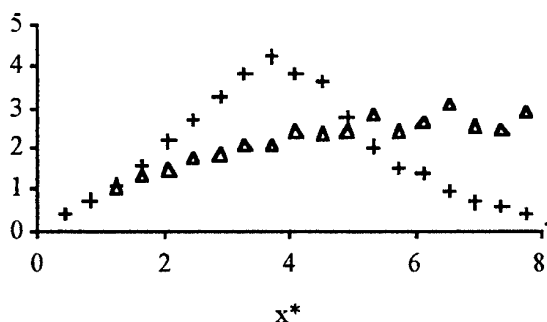


Fig. 8. Ensemble-average streamwise velocity fluctuations squared, $\overline{u_b^2}/(u')^2$, from the single probe, +, and the multi-probe, Δ , techniques.

For the bulges identified with the present technique, it is observed that those with a time extent longer than $2 l_0$ have negative average velocities. In addition, the larger the bulge the larger this deficit of momentum. It is further observed that the larger bulges have more energy.

Pattern-recognition results (Vernet et al., 1997ab) show that the dominant feature in the far wake structures is the outward ejection of highly turbulent fluid from the central

region of a double roller/horseshoe-like structure. This turbulence is produced in the fully turbulent region of the flow (i.e., $\bar{I}=1$) by the motions in the symmetry plane region of the double roller structures. The ejections have a deficit of streamwise momentum and a great deal of "incoherent" or small-scale energy. Thus, it seems reasonable that the bulges of a size greater than $2 l_0$ are these ejections. Because the production of turbulence (both coherent and small-scale) is primarily in the symmetry region of the horseshoe structures (Vernet et al., 1997b), it also seems reasonable that the turbulence being ejected outwards would be fully turbulent, i.e., that there would not be patches of "potential fluid" being ejected. Our conclusion is that the central region of the double roller/horseshoe structure forms the core of these large-scale turbulent bulges.

ACKNOWLEDGEMENTS

This work was financially supported by DGICYT project PB91-0551 and NATO Collaborative Research Grant 960142. The hardware and a portion of the software were supported by PB93-0656-C02-01. Computer support was granted by the Servei de Tecnologia Química of the Universitat Rovira i Virgili. G.A. Kopp was financially supported by NSERC Canada and URV.

REFERENCES

- Antonia, R.A., Browne, L.W.B., Bisset, D.K. and Fulachier, L., 1987, "A description of the organized motion in the turbulent far wake of a cylinder at low Reynolds number," *Journal of Fluid Mechanics*, vol. 184, pp. 423-444.
- Barsoum, M.L., Kawall, J.G. and Keffer, J.F., 1978, "Spanwise structure of the plane turbulent wake," *Physics of Fluids*, vol. 21, pp. 157-161.
- Corrsin, S. and Kistler, A.L., 1955, "Free stream boundaries of turbulent flows," NACA Report No. 1244.
- Haw, R.C., Foss, J.K. and Foss, J.F., 1989, "Vorticity based intermittency measurements in a single stream shear layer," *Advances in Turbulence 2*, ed., Fernholz, H.-H. and Fiedler, H.E., Springer-Verlag, Heidelberg, pp. 90-95.
- Hedley, T.B. and Keffer, J.F., 1974, "Turbulent/non-turbulent decisions in an intermittent flow," *Journal of Fluid Mechanics*, vol. 64, pp. 625-644.
- Kawall, J.G. and Keffer, J.F., 1979, "Interface statistics of a uniformly distorted heated turbulent wake," *Physics of Fluids*, vol. 22, pp. 31-39.
- Kawall, J.G. and Keffer, J.F., 1980, "Techniques of generating turbulence indicator functions," *Anales de Fisica*, vol. 76, pp. 253-260.
- Kovaszny, L.S.G., Kiebens, V. and Blackwelder, R.F., 1970, *Journal of Fluid Mechanics*, vol. 41, pp. 283.
- Mandelbrot, B.B., 1974, "Intermittent turbulence in self-similar cascades: divergence of high moments and dimension of the carrier," *Journal of Fluid Mechanics*, vol. 62, pp. 331-358.
- Meneveau, C. and Sreenivasan, K.R., 1991, "The multifractal nature of turbulent energy dissipation," *Journal of Fluid Mechanics*, vol. 224, pp. 429-484.
- Paizis, S.T. and Schwarz, W.H., 1974, "An investigation of the topography and motion of the turbulent interface," *Journal of Fluid Mechanics*, vol. 63, pp. 315-343.
- Prasad, R.R. and Sreenivasan, K.R., 1990, "The measurement and interpretation of fractal dimensions of the scalar interface in turbulent flows," *Physics of Fluids A*, vol. 2, pp. 792-807.
- Sreenivasan, K.R., 1991, "Fractals and multifractals in fluid turbulence," *Annual Review of Fluid Mechanics*, vol. 23, pp. 539-600.
- Tabatabai, M., Kawall, J.G. and Keffer, J.F., 1989, "Choice of the threshold in a velocity-based conditional sampling procedure," *Physics of Fluids A*, vol. 1, pp. 307-311.
- Theodorsen, T., 1952, "Mechanism of turbulence," *Proceedings, 2nd Midwestern Conference of Fluid Mechanics*, Ohio State University, Columbus.
- Townsend, A.A., 1956, *The Structure of Turbulent Shear Flow*, Cambridge University Press, Cambridge.
- Tsuji, Y. and Nakamura, I., 1994, "The fractal aspect of an isovelocity set and its relationship to bursting phenomena in the turbulent boundary layer," *Physics of Fluids*, vol. 6, pp. 3429-3441.
- Vernet, A., Kopp, G.A., Ferré, J.A. and Giralt, F., 1997a, "Simultaneous velocity and temperature patterns in the far region of a turbulent cylinder wake," *ASME Journal of Fluids Engineering*, vol. 118.
- Vernet, A., Kopp, G.A., Ferré, J.A. and Giralt, F., 1997b, "The average three-dimensional structure and momentum transfer in the far region of a turbulent cylinder wake," *Proceedings, 4th World Conference on Heat Transfer, Fluid Mechanics and Thermodynamics*, Brussels.

**LOW DIMENSIONAL DESCRIPTION OF LARGE SCALE STRUCTURES DYNAMICS
IN A PLANE TURBULENT MIXING LAYER**

L. Cordier, J. Delville, C. Tenaud

CEAT - Laboratoire d'Etude Aérodynamique
Université de Poitiers
86036 Poitiers
France

See late papers

DANGERS OF TURBULENCE DESCRIPTION BY MEANS OF NAVIER-STOKES SOLUTIONS WITH A PRIORI SYMMETRY RESTRICTIONS

V.G. Priymak⁽¹⁾, T. Miyazaki⁽²⁾

⁽¹⁾ Institute for Mathematical Modeling
Russian Academy of Sciences
Miusskaya Square 4-A, Moscow 125047
Russia

⁽²⁾ Department of Mechanical Engineering
Kokushikan University
4-28-1, Setagaya, Setagaya-ku, Tokyo 154
Japan

INTRODUCTION

We analyze the correctness of certain mathematical models based on Navier-Stokes equations and intended to describe turbulent viscous fluid and gas flows in cylindrical coordinates r, φ, z . We consider the case where the integration domain includes singularity along the polar axis $r = 0$ and where the dependence of flow field on azimuth angle φ can be represented as a Fourier series due to physical symmetry of the problem. Such important flow configurations as incompressible and compressible turbulent flows in circular pipes and round jets satisfy these conditions.

For the above-mentioned flows Navier-Stokes equations and boundary conditions formally preserve symmetry relations of the form

$$\begin{aligned} v(r, \varphi, z, t) &= v(r, -\varphi, z, t), \\ w(r, \varphi, z, t) &= -w(r, -\varphi, z, t), \\ u(r, \varphi, z, t) &= u(r, -\varphi, z, t), \end{aligned} \quad (1)$$

where v, w and u are radial, azimuthal and streamwise components of the velocity $\mathbf{v} = v\mathbf{e}_r + w\mathbf{e}_\varphi + u\mathbf{e}_z = (v, w, u)^T$. From the computational point of view it is rather tempting to assume *a priori* that the flow field may have such a symmetry. Indeed, in this case one can exploit the sparse set of Fourier modes instead of general representation

$$\mathbf{v} = \sum_{n=0}^{\infty} \mathbf{v}_n^C(r, z, t) \cos n\varphi + \sum_{n=1}^{\infty} \mathbf{v}_n^S(r, z, t) \sin n\varphi. \quad (2)$$

As it follows from Eqs. (2) and (1)

$$v_n^S(r, z, t) \equiv 0, \quad w_n^C(r, z, t) \equiv 0, \quad u_n^S(r, z, t) \equiv 0. \quad (3)$$

so that the computational complexity of simulation may be considerably reduced.

Similar hypotheses are often made in the course of boundary layer and channel flow simulations when the flow field is assumed to be symmetric with respect to the plane $x = 0$, x being the spanwise coordinate (see, e.g., Henningson *et al.*, 1987; Sandham and Kleiser, 1992).

In Cartesian coordinates the spanwise-symmetric Navier-Stokes solutions seem to be adequate: comparison of the computed turbulent flow characteristics with those of obtained in the laboratory gives satisfactory results.

Below we show analytically and numerically that turbulent viscous flows in cylindrical geometry with coordinate singularities cannot be adequately described by means of Navier-Stokes solutions having certain symmetries (e.g., incorporating the φ -expansion restrictions).

BEHAVIOUR OF ANALYTIC FUNCTIONS NEAR THE SINGULARITY

In contrast to Cartesian coordinates we can produce certain reasons justifying the inability of the Navier-Stokes solutions (1) to describe actual turbulent flows in cylindrical geometry with coordinate singularities. Our consideration is based on the well known (see, e.g., Garg and Rouleau, 1972) asymptotic behaviour of analytic functions at $r \rightarrow 0$. To make the article self-contained we include the following lemma.

Lemma 1 Suppose that vector $\mathbf{v}(x, y, z) = v_x\mathbf{e}_x + v_y\mathbf{e}_y + v_z\mathbf{e}_z$, and scalar $p(x, y, z)$ functions of Cartesian coordinates are analytic for $(x^2 + y^2)^{1/2} < \varepsilon$ (some $\varepsilon > 0$). Then, as functions of cylindrical coordinates, $\mathbf{v}(r, \varphi, z) = v\mathbf{e}_r + w\mathbf{e}_\varphi + u\mathbf{e}_z$, $f(r, \varphi, z) = v + iw$, $g(r, \varphi, z) = v - iw$ and $p(r, \varphi, z)$ satisfy the relations ($0 \leq r < \varepsilon$):

$$q(r, \varphi, z) = \sum_{n=-\infty}^{\infty} q_n(r, z) \exp(in\varphi), \quad q = (f, g, p, v, w, u)^T,$$

$$f_n = r^{|n+1|} \hat{f}_n(r, z), \quad g_n = r^{|n-1|} \hat{g}_n(r, z),$$

$$(p_n, u_n) = r^{|n|} (\hat{p}_n(r, z), \hat{u}_n(r, z)),$$

$$(v_n, w_n) = r^{|n|-1} (\hat{v}_n(r, z), \hat{w}_n(r, z)), \quad n \neq 0, \quad (4)$$

$$(v_0, w_0) = r (\hat{v}_0(r, z), \hat{w}_0(r, z)),$$

where

$$\hat{q}_n = \sum_{k=0}^{\infty} \hat{q}_{nk}(z) r^{2k}, \quad \hat{q} = (\hat{f}, \hat{g}, \hat{p}, \hat{v}, \hat{w}, \hat{u})^T.$$

Notice, that all these statements can be derived solely from the analysis of Taylor expansions of vector and scalar functions in the vicinity of polar axis (see also Priymak and Miyazaki, 1995).

From Eqs. (3),(4) one can immediately obtain (at $r = 0$) for the streamwise component ω_z of vorticity $\omega = (\omega_r, \omega_\varphi, \omega_z)^T = \nabla \times \mathbf{v}$:

$$\omega_z(r, \varphi, z, t) = r(\bar{\omega}_z)_1^S \sin \varphi + r^2 \sum_{n=2}^{\infty} (\bar{\omega}_z)_n^S \sin n\varphi. \quad (5)$$

where $(\bar{\omega}_z)_n^S(r, z, t)$ are smooth regular functions of r -variable. Note, that as it follows from Eq. (5), the instantaneous values as well as the root-mean-square fluctuations of the streamwise vorticity become zero at the polar axis.

The latter property contradicts with certain known computational results for the turbulent flow vorticity values. Indeed, in channel flow calculations (Kim et al., 1987) all three components of the fluctuating vorticity have almost equal nonzero values at the channel centerline. Analogous result (Fig. 3(a)) is obtained in the present investigation for the r.m.s. vorticity values at the polar axis in the case of general Navier-Stokes solutions in a circular pipe $\mathcal{G} = \{\mathbf{r} = (r, \varphi, z) : 0 \leq r \leq R, 0 \leq \varphi < 2\pi, |z| < \infty\}$. In addition, such a behaviour of vorticity components looks very plausible from the physical point of view.

NUMERICAL RESULTS

To clarify the issue, i.e. to understand if the azimuthally-symmetric Navier-Stokes solutions (1) really exist and what is their relationship with actual turbulent flows, we have carried out special investigation. For definiteness we considered the model problem of pressure driven incompressible flows in an infinite circular pipe \mathcal{G} at Reynolds number of 4000 based on the mean velocity and pipe diameter.

The stability problem for Poiseuille flow

$$\mathbf{V}^0 = U^0(r)\mathbf{e}_z = -\frac{R^2}{4\nu\rho} \frac{dP_0}{dz} (1 - r^2/R^2)\mathbf{e}_z, \quad (6a)$$

$$\frac{dP_0}{dz} = \text{const}, \quad \mathbf{e}_z = (0, 0, 1), \quad (6b)$$

in \mathcal{G} may be set up as the initial boundary-value problem for the Navier-Stokes equations

$$\frac{\partial \mathbf{v}}{\partial t} = -\nabla \Pi + \nu \Delta \mathbf{v} + \mathbf{D}(\mathbf{v}), \quad (7a)$$

$$\nabla \cdot \mathbf{v} = 0, \quad (7b)$$

$$\mathbf{v}|_{r=R} = 0, \quad \mathbf{v}|_{t=0} = \mathbf{V}^0 + \mathbf{v}_0(r), \quad \nabla \cdot \mathbf{v}_0 = 0, \quad (7c)$$

where $\mathbf{v} = (v, w, u)^T$; $\mathbf{D} = \mathbf{v} \times \boldsymbol{\omega}$; $\boldsymbol{\omega} = \nabla \times \mathbf{v}$; Π is the total pressure; ρ and ν are the constant density and kinematic viscosity and $\mathbf{v}_0 \neq 0$ is a certain initial disturbance of Poiseuille flow.

Since the flow is homogeneous in z -direction, equations (7) are supplemented with the following boundary conditions

$$\mathbf{v}(\mathbf{r}, t) = \mathbf{v}(r, \varphi, z + Z, t), \quad (8a)$$

$$\Pi = p_z(t)z + p(r, t), \quad p(r, t) = p(r, \varphi, z + Z, t), \quad (8b)$$

$$U(t) \stackrel{\text{def}}{=} \frac{1}{\pi R^2} \int_0^R r dr \int_0^{2\pi} d\varphi u(r, t) = \frac{2}{R^2} \int_0^R U^0 r dr. \quad (8c)$$

Here the streamwise period Z is the parameter of the mathematical model, $p_z(t)$ has the meaning of space averaged pressure gradient and Eq. (8c) is the condition of volume flux (mean velocity \bar{U}) constancy.

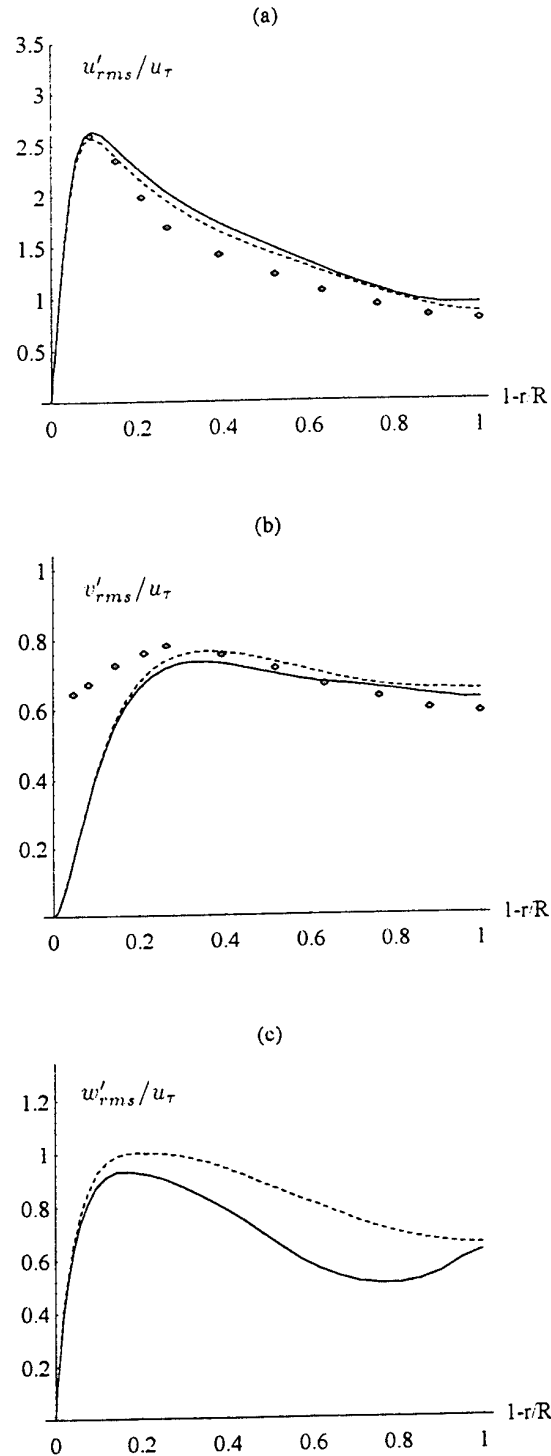


Figure 1: Comparison of the r.m.s. velocity distributions corresponding to Navier-Stokes solutions of general and azimuthally-symmetric forms: \diamond Shemer et al.(1985), $Re = 4000$; Present, General form; — Present, Azimuthally symmetric.

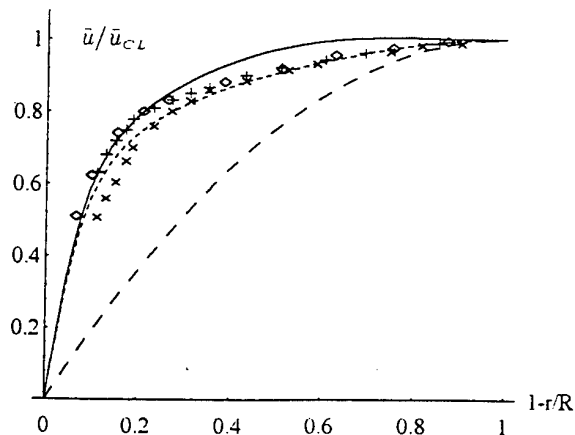


Figure 2: Mean velocity profiles corresponding to Navier-Stokes solutions of general and azimuthally-symmetric forms: \diamond Shemer et al. (1985), $Re = 4000$; $+$ Patel and Head (1969), $Re = 4430$; \times Patel and Head (1969), $Re = 2975$; $---$ Parabolic profile; \cdots Present, General form; $—$ Present, Azimuthally-symmetric.

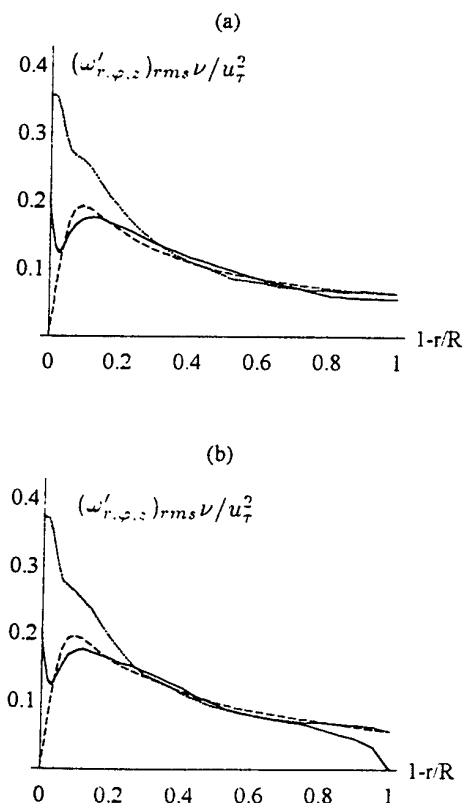


Figure 3: R.m.s. vorticity fluctuations corresponding to Navier-Stokes solutions of general (a) and azimuthally-symmetric (b) forms: \cdots $(\omega'_{r,\phi,z})_{rms} \nu / u_\tau^2$; $---$ $(\omega'_r)_{rms} \nu / u_\tau^2$; $—$ $(\omega'_z)_{rms} \nu / u_\tau^2$.

Computations were carried out with $33 \times 41 \times 41$ basis functions in r, ϕ, z by means of pseudospectral algorithm developed by Priymak and Miyazaki (1995) at $Re = 4000$ ($Re_{CL} = \bar{u}_{CL} D / \nu \approx 5432$, $Re_\tau = u_\tau D / \nu \approx 289$ for the established turbulent flow regime) and $Z = 2\pi R$ ($Z^+ = Z u_\tau / \nu \approx 907$). Here \bar{u}_{CL} and u_τ are the mean centreline and wall-shear velocities. Minimum and maximum grid spacings in r were $0.17\nu/u_\tau$ (the first mesh point away from the wall) and $7.09\nu/u_\tau$. The minimal resolved wavelengths in ϕ (at $r = R$, along the pipe surface) and z were about $45.36\nu/u_\tau$. The total integration time was $\Delta T \approx 54R/u_\tau$ with the averaging time (to compute turbulence statistics) of $18R/u_\tau \approx 2659\nu/u_\tau^2$ and computational time step of about $9.03 \times 10^{-4} R/u_\tau \approx 0.13\nu/u_\tau^2$.

As a result we can conclude that the use of symmetry relations (1) turns to be very insidious. First of all, the numerical Navier-Stokes solutions (1) do exist: pipe Poiseuille flow is unstable with respect to finite amplitude azimuthally-symmetric disturbances and statistically steady ("turbulent") solutions can be really computed. Secondly, certain basic turbulence characteristics are almost insensitive to the incorporation of symmetry relations into the numerical model (e.g., skin-friction coefficient, Reynolds shear stress as well as the root-mean-square fluctuations of streamwise and radial velocity components shown in Figs. 1(a), 1(b)). At the same time there exist such well-established flow characteristics that cannot be adequately described by the azimuthally-symmetric solutions. Among them are the r.m.s. fluctuations of azimuthal component of velocity and the mean velocity profile (Figs. 1(c), 2). The most striking disagreement between general and azimuthally-symmetric cases is observed for the computed r.m.s. fluctuations of the streamwise vorticity ω_z near the pipe axis (cf. Figs. 3(a) and 3(b)).

Thus, in contrast to Cartesian coordinates, the "span-wise" (azimuthally) symmetric Navier-Stokes solutions fail to describe some of the basic turbulent flow characteristics in the presence of coordinate singularities.

OTHER POSSIBLE SYMMETRIES FOR INCOMPRESSIBLE PIPE FLOW

Approximate solutions of Eqs. (7), (8) we represent by the truncated Fourier series

$$\begin{aligned} \mathbf{v} &= \sum_{n=-N}^N \sum_{m=-M}^M \mathbf{v}_{nm}^F(r, t) \exp(i\alpha_m z + in\phi) \\ &= \sum_{n=0}^N \sum_{m=0}^M \mathbf{v}_{nm}(r, \phi, z, t), \end{aligned} \quad (9)$$

$$(\mathbf{v}_{nm}^F)^* = \mathbf{v}_{-n, -m}^F, \quad i^2 = -1, \quad \alpha_m = 2\pi m/Z,$$

with an analogous representation for $p(r, t)$. One more symmetry group allowed by the Navier-Stokes equations and boundary conditions (7), (8) is defined by the solutions (9) with

$$\mathbf{v}_{2k, 2l+1}(r, \phi, z, t) = 0, \quad \mathbf{v}_{2k+1, 2l}(r, \phi, z, t) = 0, \quad (10)$$

$$k = 0, 1, \dots, \quad l = 0, 1, \dots$$

Nonstationary Navier-Stokes solutions with symmetry restrictions (10) were computed (among others) using one of the previous versions of our numerical method (see algorithm A in Priymak, 1995). These long-life (i.e., undamped at least for about $\Delta T \approx O(Re)$) solutions describe statistically steady flow regimes in \mathcal{G} with the same skin-friction coefficient, averaged pressure gradient and kinetic energy of velocity fluctuations as in the case of general Navier-Stokes solutions without any symmetry

restrictions. The detailed comparison of turbulence statistics computed by means of symmetric and general solutions was not conducted.

Notice also the following computational peculiarity of the symmetry conditions (10). If we take the velocity field satisfying Eqs. (10) as an initial condition for the Navier-Stokes integration in time, we may reproduce these symmetry relations for arbitrary time even when we use an universal computer code. We may even do not suspect that one half of our Fourier modes remains equal zero in the course of calculation. For example, if our initial condition is the superposition of the base parabolic flow and any eigensolution corresponding to wavenumbers $(m, n) = (1, 1)$ we'll be able to compute only solutions belonging to the class of functions (10). Roundoff errors may not play usual destabilizing role here because the result of multiplication of nonzero value by the machine zero is often interpreted as the zero constant by the computer. That is just the case when we compute the quadratic nonlinear terms of the Navier-Stokes equations.

Of course, the foregoing investigation of some symmetry relations and their suitability for the Navier-Stokes turbulent flow simulation is incomplete. In the present investigation we intended to show possible difficulties as well as the existence of certain solutions in principle. Is there any relation between symmetry and some special physics? Are symmetric solutions stable with respect to disturbances of general form? Are there any simplifications of the space-time structure of velocity and pressure fields described by the symmetric solutions compared with those of general form? These problems require additional thorough investigation.

Acknowledgements : We thank B.L. Rozhdestvensky, S.G. Ponomarev, and M.I. Stoykov for valuable discussions and suggestions.

This research was supported in part by the Russian Fundamental Science Foundation Grant No. 96-01-01468.

REFERENCES

- Garg, V.K., and Rouleau, W.T., 1972, "Linear spatial stability of pipe Poiseuille flow," *J. Fluid Mech.*, Vol. 54, pp. 113-127.
- Henningson, D., Spalart, P., and Kim, J., 1987, "Numerical simulations of turbulent spots in plane Poiseuille and boundary-layer flow," *Phys. Fluids*, Vol. 30, pp. 2914-2917.
- Kim, J., Moin, P., and Moser, R.D., 1987, "Turbulence statistics in fully developed channel flow at low Reynolds number," *J. Fluid Mech.*, Vol. 177, pp. 133-166.
- Patel, V.C., and Head, M.R., 1969, "Some observations on skin friction and velocity profiles in fully developed pipe and channel flows," *J. Fluid Mech.*, Vol. 38, pp. 181-201.
- Priymak, V.G., 1995, "Pseudospectral algorithms for Navier-Stokes simulation of turbulent flows in cylindrical geometry with coordinate singularities," *J. Comput. Phys.*, Vol. 118, pp. 366-379.
- Priymak, V.G., and Miyazaki, T., 1995, "Efficient implementation of influence matrices and collocation technique in cylindrical coordinates," *Proceedings, 6th International Symposium on Computational Fluid Dynamics* (Sept. 4-8, 1995, Lake Tahoe, Nevada U.S.A.), Vol. 2, pp. 958-963.
- Sandham, N.D., and Kleiser, L., 1992, "The late stages of transition to turbulence in channel flow," *J. Fluid Mech.*, Vol. 245, pp. 319-348.
- Shemer, L., Wignanski, I., and Kit, E., 1985, "Pulsating flow in a pipe," *J. Fluid Mech.*, Vol. 153, pp. 313-337.

COUPLED RESONANT TRIADS INTERACTIONS IN PHASE-LOCKED EVOLUTION

G.Sciortino¹, M.A.Boniforti², M.Morganti¹

¹Dipartimento di Scienze dell'Ingegneria Civile
III Università di Roma,
via Segre 60,
Roma, Italy

²Dipartimento di Idraulica, Trasporti e Strade
Università di Roma La Sapienza,
via Eudossiana 18,
00184 Roma, Italy

ABSTRACT

In this paper, a *nonlinear* resonance criterion allowed us for selecting coupled resonant triads to model interactions among two-dimensional waves and oblique shedding waves which travel in *phase-locked* evolution in a wake flow. The local time evolution of oblique three-dimensional modes was simulated by integrating low-dimensional dynamical systems which correspond to the selected coupled triads of modes. To check the validity of our theoretical approach, an experimental investigation was used as data test. A comparison between numerical and experimental results showed an interesting qualitative agreement in particular referring to the energy spectral distribution of the temporal evolution of modes activated by the physical process. Furthermore, the *phase-locked* condition taken together with our resonance criterion, eliminates most of arbitrariness in identifying leading modes whose dynamics can describe the physical process, simplifying the path which has to be followed in characterising the dynamical system.

INTRODUCTION

Recently, a number of studies seem to confirm that the subharmonic triadic resonance proposed by Craik (1971) cannot explain important transition phenomena (Williamson and Prasad 1993 *a,b*, Wu and Stewart 1996, Corke, Krull and Ghassemi 1992). This kind of resonance is a particular case of a general triadic resonance condition which involves only frequencies predicted by the linear theory (Craik, 1985). Nevertheless, only in a weakly nonlinear approach does this last condition have full meaning. On the other hand, triadic resonance can be observed in strongly nonlinear phenomena as well; in this case, experimentally observed frequencies do not necessarily coincide with the predicted linear ones but can be shifted - even considerably - due to the effects of nonlinear interactions. In this last case, a resonance condition which does

not base itself on the weakly nonlinear approach is necessary (Boniforti, Morganti and Sciortino 1996). In this work, we propose to extend this *nonlinear* resonance criterion to the case of several coupled triadic systems. Then, a nonlinear dynamical analysis was carried out to investigate the local time evolution of three-dimensional disturbances in a transitional wake flow. Nonlinear wave interactions were simulated using a three-dimensional theoretical model which coincides with Craik's in the two-dimensional case (Craik 1985, Boniforti, Magini and Sciortino 1994).

An incisive experimental study by Williamson and Prasad (1993 *a,b*) showed the extreme sensitivity of the far wake dynamics to free stream disturbances, that is its dependence on the particular environment in which it is observed. Background noise turned out to be the link between the near and far wake. In the observed experimental conditions, waves linked to oblique Kármán shedding interact with free stream noise producing a regular three-dimensional pattern corresponding physically to oblique resonance waves. These oblique resonances turned out to be quite different from the subharmonic resonance models used to represent the rapid growth of three-dimensional disturbances in the far wake.

The experimental results by Williamson and Prasad (1993 *b*) were used as a starting point in this work to prove the validity of both the low-dimensional dynamical system approach and the resonance criterion in modelling strong nonlinear phenomena. These experimental data allowed us to select some triadic sets of modes using the proposed temporal condition of nonlinear triadic resonance. As experimentally observed, a sequence of resonances occurs as the wake travels downstream, so that, starting from a suitable streamwise location, velocity fluctuation spectra highlight several peaks whose frequencies are linked among themselves through mechanisms of coupled triadic resonance. Nonlinear quadratic interactions between oblique shedding waves and two-dimensional waves were then modelled by coupled triadic dynamical systems.

Numerical integration of these low-dimensional dynamical systems showed interesting results that are in good qualitative agreement with the conclusive considerations of Williamson and Prasad's investigation (1993 b). In particular, varying the ratio f_T / f_K , where f_T is the free-stream frequency and f_K is the Kármán shedding frequency, dynamics with a spectral energy distribution similar to the one experimentally observed were obtained. This seemed to validate the resonance criterion which, together with the theoretical model, proved to be an appropriate tool for describing the local evolution of large scale structures in shear flows.

THEORETICAL MODEL

The theoretical model used in this work falls into the category of the *Dynamical System Approach* method. Accordingly, a necessary condition for describing large-scale dynamics is that only a few modes capture most of the kinetic energy of the flow. If this condition is fulfilled a low dimensional approach can be a suitable tool for investigating the dynamics of the physical process.

By using eigenfunctions of the linear problem, a solenoidal disturbance $V(x, t)$ superimposed on a basic shear flow $V_0(x) \equiv (U(y), 0, 0)$, $x \equiv (x, y, z)$, can be decomposed into a sum of linear eigenfunctions:

$$V = \nabla \wedge \sum_k W_k e^{i k \cdot x}$$

$$W_k(y, t) = \sum_{n=1}^{\infty} \epsilon_k^{(n)}(t) w_k^{(n)}(y)$$

where $W_{-k} = \tilde{W}_k$ (\sim indicates complex conjugation), $w_k^{(n)}(y)$ is n -th eigenvector and $\epsilon_k^{(n)}(t)$ is the n -th unknown eigenmode amplitude linked to the wave vector $k \equiv (\alpha, \beta, 0)$.

It can be shown that $\epsilon_k^{(n)}(t)$ must satisfy the following nonlinear dynamical system (Boniforti, Morganti and Sciortino 1996)

$$\left(\frac{d}{dt} + i \omega_k^{(m)} \right) \epsilon_k^{(m)}(t) = - \sum_{p, q=1}^{\infty} \sigma_{k1}^{(m, p, q)} \epsilon_{k-p}^{(p)}(t) \epsilon_1^{(q)}(t) \quad (1)$$

where $\sigma_{k1}^{(m, p, q)}$ are complex coefficients which accounts for nonlinear interactions and $\omega_k^{(m)}$ are the eigenvalues linked to $w_k^{(m)}(y)$ eigenvectors.

A truncated form of system (1) with $\sum_{k, m} \text{im}[\omega_k^{(m)}] < 0$, namely a dissipative system, is used in this work to investigate large-scale dynamics ($\text{im}[\#]$ is the imaginary part of $\#$).

RESONANCE CRITERION

Owing to the structure of the system itself, a generic truncated form of system (1) is characterised by one or more triadic coupled systems.

If we consider a generic system of M coupled triadic equations, the spatial resonance condition among modes of each triad

$$k_{1,j} + k_{2,j} = k_{3,j} \quad j = 1, 2, \dots, M \quad (2)$$

must be fulfilled. Not all $k_{p,j}$ are distinct because we are considering coupled triads, namely triads with some modes in common.

The following coupled equations can be obtained from system (1):

$$\begin{cases} d\epsilon_{1,j} / dt = -i\omega_{1,j} \epsilon_{1,j} + \sum_{s_1} \lambda_{1,s_1} \tilde{\epsilon}_{2,s_1} \epsilon_{3,s_1} \\ d\epsilon_{2,j} / dt = -i\omega_{2,j} \epsilon_{2,j} + \sum_{s_2} \lambda_{2,s_2} \tilde{\epsilon}_{1,s_2} \epsilon_{3,s_2} \\ d\epsilon_{3,j} / dt = -i\omega_{3,j} \epsilon_{3,j} + \sum_{s_3} \lambda_{3,s_3} \epsilon_{1,s_3} \epsilon_{2,s_3} \end{cases} \quad (3)$$

$$j = 1, 2, \dots, M$$

where the index s_p ($p=1,2,3$) denotes those spatial resonance equations (2) which have the $k_{p,j}$ wave vector in common (for the sake of simplicity we have written λ instead of the corresponding σ of the system (1)).

A temporal resonance condition has to be imposed to simulate what is highlighted by the physical process. To take into account the effects of coupled nonlinear interactions, we used a generalisation of our *nonlinear* resonance criterion.

This criterion allows us to consider under which conditions system (3) admits solutions of the form :

$$\epsilon_{p,j}(t) = \rho_{p,j} e^{i(-\Omega_{p,j} t + \varphi_{p,j})} \quad (4)$$

where $\rho_{p,j}$, $\Omega_{p,j}$ and $\varphi_{p,j}$ are real constants with $\rho_{p,j} > 0$. Substituting (4) into equations (3) it can be shown that the conditions

$$\Omega_{1,j} + \Omega_{2,j} = \Omega_{3,j} \quad j = 1, 2, \dots, M \quad (5)$$

together with the following set of nonlinear algebraic equations which involves the unknowns $\rho_{p,j}$, $\Omega_{p,j}$ and $\varphi_{p,j}$

$$\begin{cases} \rho_{1,j}(\Omega_{1,j} - \omega_{1,j}) = i \sum_{s_1} \lambda_{1,s_1} \rho_{2,s_1} \rho_{3,s_1} e^{i(\varphi_{3,s_1} - \varphi_{1,j} - \varphi_{2,s_1})} \\ \rho_{2,j}(\Omega_{2,j} - \omega_{2,j}) = i \sum_{s_2} \lambda_{2,s_2} \rho_{1,s_2} \rho_{3,s_2} e^{i(\varphi_{3,s_2} - \varphi_{2,j} - \varphi_{1,s_2})} \\ \rho_{3,j}(\Omega_{3,j} - \omega_{3,j}) = i \sum_{s_3} \lambda_{3,s_3} \rho_{1,s_3} \rho_{2,s_3} e^{i(\varphi_{1,s_3} - \varphi_{3,j} + \varphi_{2,s_3})} \end{cases}$$

$$j = 1, 2, \dots, M$$

must be satisfied.

The nonlinear algebraic equations together with the (5) define our resonance equations. If these admits solutions in the space

$$S = \left\{ (\rho_{p,j}, \Omega_{p,j}, \varphi_{p,j}) \mid \rho_{p,j} > 0, \Omega_{p,j}, \varphi_{p,j} \in \mathbb{R}, p = 1, 2, 3 \right. \\ \left. j = 1, 2, \dots, M \right\}$$

system (3) is taken to verify our *nonlinear* temporal resonance condition. As shown from the above set of algebraic equations, frequencies $\Omega_{p,j}$ differ from the linear ones ($\text{re}[\omega_{p,j}]$) by a correction term linked to nonlinear interactions (Boniforti, Morganti and Sciortino 1996). Numerical tests performed on a

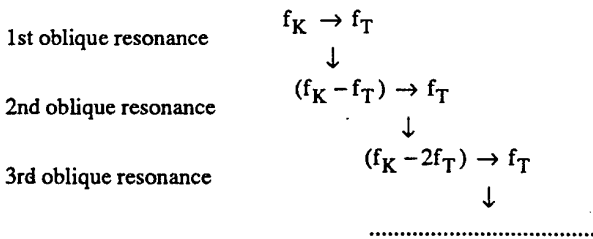
number of dynamical systems have revealed that if there are dominant peaks in the power spectra linked to some frequencies, they are nearer to the $\Omega_{p,j}$ than to the $\text{re}[\omega_{p,j}]$. The difference between $\Omega_{p,j}$ and $\text{re}[\omega_{p,j}]$ are negligible in weakly nonlinear dynamics.

In order to characterise the low-dimensional dynamical systems of type (3) that can be used to model large-scale dynamics of the physical process, the mathematical properties of the resonance equations are linked to experimental observations by requiring $\Omega_{p,j}$ frequencies to be close to the experimental ones.

RESULTS

The aim of this work is to support the validity of both the proposed resonance criterion and the theoretical model extended to the case of a number of coupled triadic systems. As experimentally underlined by Williamson and Prasad, varying a suitable parameter F , defined by the ratio between free-stream frequency f_T and Kármán frequency f_K , causes a number of different scenarios to arise in the power spectra in the far wake of a cylinder. These can be described by a sequences of resonances produced by the nonlinear interaction between the two-dimensional forcing mode and the oblique three-dimensional modes as they arise. The structure of this sequence of resonances reflects the kind of nonlinearity of Navier-Stokes equations, that is, it contains quadratic nonlinear terms. As a result, by varying F , different scenarios may be modelled by several coupled triadic systems, given the same coupling mechanisms in both the physical process and the structure of the dynamical system.

The sequence of resonances, as experimentally observed, may be summarised in the following (Williamson and Prasad, 1993 b):



For a fixed F value, this sequence activates oblique modes, the last of which exhibits a frequency $f_K - nf_T$, where $n=n(F)$ is the last integer which verifies the inequality

$$F < 1/n.$$

In the present numerical investigation, resonant modes were selected in the following way. Firstly, for a fixed value F , and a known f_K frequency for the examined Reynolds cylinder number, all the frequencies $f_T, f_K - f_T, \dots, f_K - nf_T$, are known.

Moreover, the spatial resonance condition which is implicit in our theoretical model must be fulfilled and the modes must be *phase-locked*, namely the phase speed of the waves must be equal. The spatial resonance condition and the phase-locked condition can be written respectively as follows:

$$k_n + nk_T = k_0 \Leftrightarrow k_n + k_T = k_{n-1}$$

$$f_T / \alpha_T = (f_K - f_T) / \alpha_1 = \dots = (f_K - nf_T) / \alpha_n = c = \text{const.}$$

where $k_1 = (\alpha_1, 0, 0)$ is the wave vector of the 2D mode and $k_j = (\alpha_j, \beta_j, 0)$ is the wave vector of the j -th oblique mode linked to the frequency $f_K - jf_T$ ($j=0, \dots, n$).

From the resonance condition, it follows that $\beta_0 = \beta_1 = \dots = \beta_n = \beta$, and taking the *phase-locked* condition into account we have $\beta = (f_K / c) \tan \vartheta$, where ϑ is the fixed oblique angle of the Kármán shedding waves.

In order to model this kind of oblique resonance, at least one of the eigenmodes linked to $k_j = (\alpha_j, \beta_j, 0)$ wave vector must be

unstable. Denoting the corresponding frequency with $f_K - if_T$, we selected, varying α_i , eigenmodes linked to the wave vector $(\alpha_i, f_K \tan \vartheta \alpha_i / (f_K - if_T))$ whose eigenvalue ω has a real part $\text{re}[\omega] \approx 2\pi(f_K - if_T)$ and an imaginary part $\text{im}[\omega] > 0$.

Our numerical investigation showed that, for a fixed i , all these conditions, if verified, univocally characterise the unstable eigenmode.

From this value of α_i we obtain $\beta = f_K \tan \vartheta \alpha_i / (f_K - if_T)$, and the all the other α_j , $j \neq i$ from the *phase-locked* condition. Finally, for each of the wave vectors $(\alpha_j, \beta, 0)$ we

selected the eigenmodes with $\text{re}[\omega] \approx 2\pi(f_K - jf_T)$.

All these conditions permitted us to locate a set of dynamical systems, each of which is characterised by $n(F)$ coupled triadic systems. A further selection among these dynamical systems was carried out to take only dissipative systems into account. Finally, our *nonlinear* resonance condition allowed us to locate dynamical systems whose evolution equations are able to model the local large-scale dynamics experimentally observed. Following this way, some coupled triadic sets of eigenmodes were selected and the corresponding evolution equations were numerically integrated. This analysis was performed at a distance $x/D=150$ downstream in the far wake of a cylinder, where D is the cylinder diameter, and for a Reynolds number $R = U_\infty D / \nu = 150$. A non-dimensional wake profile $U = U_0 / U_* + \tanh^2(2y/\delta)$ - where U_0 is the centreline velocity, $U_* = U_\infty - U_0$, U_∞ is the free-stream velocity and δ is the width of the wake - was used to obtain eigenmodes from the linear problem.

Numerical investigation was performed for different F values in the range (0.2, 0.8). As observed by Williamson and Prasad, higher order modes linked to $f_K - nf_T$ frequencies appear to exhibit peak response at lower F . In particular, when $F \approx 1/(2r)$, ($r=1, 2, \dots$), the $f_K - rf_T$ frequencies are dominant in the power spectrum.

Numerical integration of the selected low-dimensional dynamical systems showed interesting results that are in good qualitative agreement with the conclusive consideration of Williamson and Prasad's investigation (1993 b). In particular, figure 1 shows power spectra corresponding to different F values. In the case $F=0.55$ the spectrum is obtained from analysis of the temporal evolution of a dynamical system characterised by a single triad of eigenmodes. This numerical spectrum shows three dominant peaks linked to the frequencies $f_K - f_T, f_T, f_K$. The corresponding wave vectors k_1, k_T, k_0 must satisfy the following spatial resonance condition:

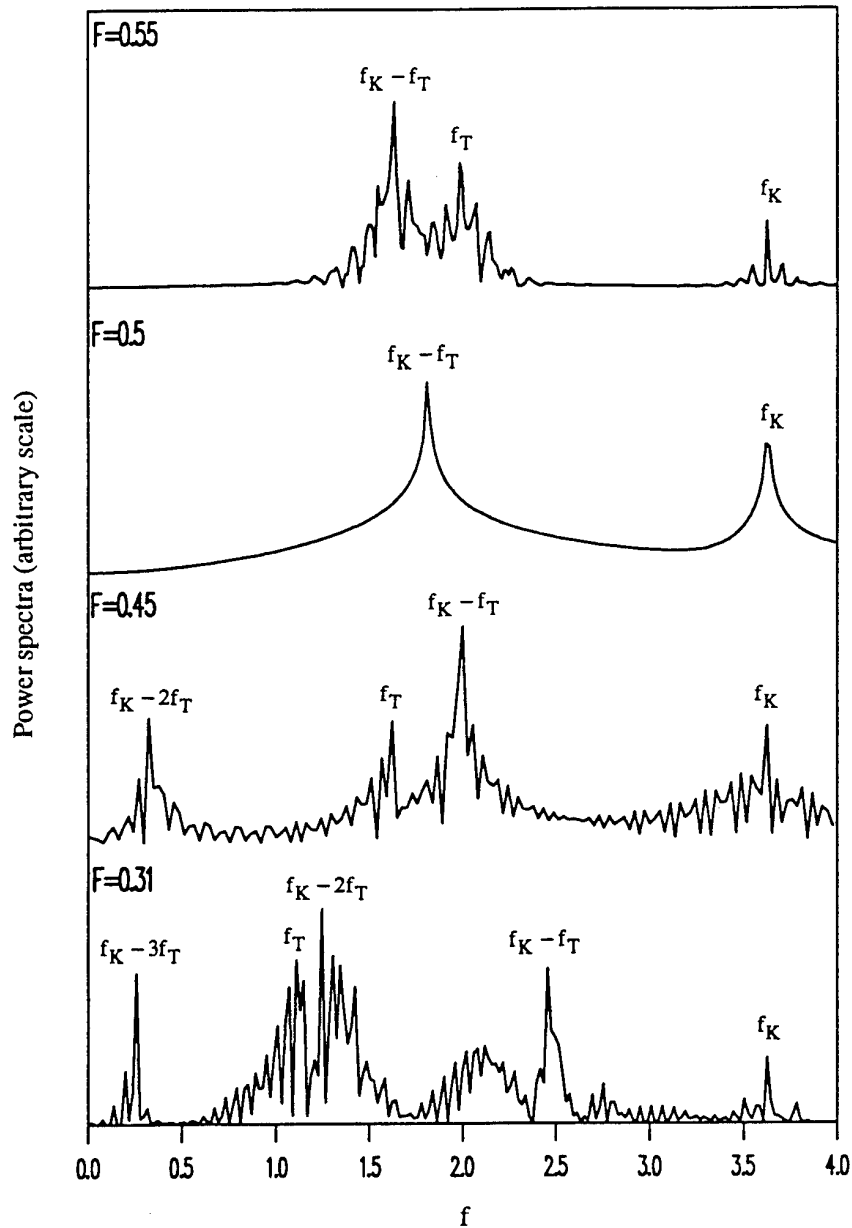


FIGURE 1 - POWER VELOCITY SPECTRA FOR DIFFERENT F VALUES ($F = f_T / f_K$) AT A STREAMWISE DISTANCE FROM THE CYLINDER $X/D=150$ AND FOR A REYNOLDS NUMBER $R=150$. THE NON-DIMENSIONAL FREQUENCY f IS DEFINED BY $f = \delta / (U_\infty - U_0)$, WHERE f IS THE DIMENSIONAL FREQUENCY, U_∞ IS THE FREE-STREAM VELOCITY, U_0 IS THE CENTRELINE VELOCITY AND δ IS THE WIDTH OF THE WAKE.

$$\mathbf{k}_1 + \mathbf{k}_T = \mathbf{k}_0.$$

In this case ($F=0.55$) the two frequencies $f_K - f_T$ and f_T are distinct and the dominant peak is the one linked to the $f_K - f_T$ frequency, in qualitative agreement with the experimental law establishing that when $F=0.5$ the $f_K - f_T$ frequency is the most amplified irrespective of the mode it represents.

When $F=0.5$ we have two peaks, one at frequency $f_T = f_K - f_T$ and the other at frequency $2(f_K - f_T) = f_K$. In this case it is not possible to separate the single spectral contributions of the two-dimensional mode, linked to f_T frequency, from that of the oblique mode, linked to $f_K - f_T$ frequency. The dynamical system associated to this scenario was selected by using our *nonlinear* resonance criterion and requiring a single triadic system to exhibit three nonlinear Ω -frequencies, coinciding with the experimental ones, two of which with the same value. Moreover, the shape of this spectrum shows a strong regular temporal evolution of the corresponding modes.

For $F=0.45$, $n=n(F)$ is equal to 2, so that the physical process (Williamson and Prasad 1993 *b*) highlights two resonant oblique modes corresponding to the frequencies $f_K - f_T$ and $f_K - 2f_T$, the first of which is dominant. Two secondary peaks at frequency f_T and f_K also appear in the spectrum.

In order to model this kind of resonance, a dynamical system defined by two coupled triadic systems was used. Nevertheless only four modes are distinct and linked to the previous frequencies so that the corresponding wave vectors $\mathbf{k}_1, \mathbf{k}_2, \mathbf{k}_T, \mathbf{k}_0$ must satisfy the following spatial resonance conditions:

$$\begin{cases} \mathbf{k}_1 + \mathbf{k}_T = \mathbf{k}_0 \\ \mathbf{k}_2 + \mathbf{k}_T = \mathbf{k}_1 \end{cases}$$

The dynamical system was selected by requiring that nonlinear Ω -frequencies, derived from the solutions of the resonance equations, for which

$$\begin{cases} \Omega_1 + \Omega_T = \Omega_0 \\ \Omega_2 + \Omega_T = \Omega_1 \end{cases}$$

coincide with those experimentally observed. The numerical integration of this system enhanced a temporal evolution whose power spectrum shows dominant peaks at the same frequencies as the experimental ones with an energy distribution in qualitative agreement (Fig.1, $F=0.45$).

In the last case, $F=0.31$, $n=n(F)$ is equal to 3. At this value, peaks corresponding to three oblique mode linked to the frequencies $f_K - f_T$, $f_K - 2f_T$, $f_K - 3f_T$ may be observed in the numerical power spectrum. The spectral energy distribution is in good qualitative agreement with experimental observation. In particular, the dominant peak is associated to the $f_K - 2f_T$ frequency. These results were obtained by using a nonlinear dynamical system structured by three coupled triadic systems with five distinct modes, as shown by experimental investigation. Related wave vectors $\mathbf{k}_1, \mathbf{k}_2, \mathbf{k}_3, \mathbf{k}_T, \mathbf{k}_0$ and nonlinear Ω -frequencies satisfy the conditions:

$$\begin{cases} \mathbf{k}_1 + \mathbf{k}_T = \mathbf{k}_0 \\ \mathbf{k}_2 + \mathbf{k}_T = \mathbf{k}_1 \\ \mathbf{k}_3 + \mathbf{k}_T = \mathbf{k}_2 \end{cases} \quad \begin{cases} \Omega_1 + \Omega_T = \Omega_0 \\ \Omega_2 + \Omega_T = \Omega_1 \\ \Omega_3 + \Omega_T = \Omega_2 \end{cases}$$

It must be emphasised that these two resonance conditions have the same form but arise in a substantially different manner. In fact, while the spatial resonance condition is a consequence of the separation of the Fourier components of the vorticity equation (Boniforti, Morganti and Sciortino 1996), the temporal resonance condition is a consequence of a heuristic truncation criterion used to select *leading* modes able to span large-scale dynamics.

It must be also observed that even if the temporal condition is deduced from mathematical criteria, that is, the existence of periodic solutions of equations (3), it reflects the same nonlinear mechanisms as that of the experimental investigation. Moreover, it can be shown that fulfilment of this temporal resonance condition requires that a dynamical system of type (1) with five distinct modes must be characterised by at least three coupled triads, as suggested by the sequence of resonances experimentally observed.

CONCLUSIONS

By using the experimental results of Williamson and Prasad, an analytical and numerical study was performed in this work to describe local wave interactions. A dynamical system approach permitted us to analyse the temporal *phase-locked* evolution of modes coupled by resonant triadic equations. In order to characterise this physical process by low-dimensional nonlinear systems, a new criterion of *nonlinear* resonance was used. This *nonlinear* criterion is both a truncation criterion, in that by linking mathematical properties of the dynamical system to experimental observations it allows for representation of the essential features of large-scale structures, and a resonance criterion, in that it make it possible to select those modes whose nonlinear interactions give rise to non-explosive dynamics with a well defined physical meaning. At a fixed distance downstream in the far wake of a cylinder ($x/D=150$), we performed a local analysis of the wake at a Reynolds cylinder number $R=150$. Varying the ratio $F=f_T/f_K$ where f_T is the free-stream frequency and f_K the Kármán shedding frequency, local time evolution of oblique modes, activated by nonlinear interactions between modes linked to f_T and f_K frequencies, was simulated. Varying F , the different scenarios numerically modelled show a spectral energy distribution in qualitative agreement with the one experimentally observed. Decreasing F , more resonant oblique modes are activated and an increasing number of degrees of freedom of the dynamical system must be taken into account. In particular, wave interactions corresponding to F values near 0.5 ($F=0.55$, $F=0.5$, $F=0.45$), that is the case when the oblique and the two-dimensional waves have the same frequency, were examined. In modelling the physical process, one or more coupled triads, as suggested by the experimental spectra, were used. Numerical investigation highlighted that in the neighbourhood of the value $F=0.5$, all scenarios are characterised by an energy spectral distribution in which the energy of the oblique waves at frequency $f_K - f_T$ is dominant. When $F=0.31$ the dominant mode is linked to the $f_K - 2f_T$ frequency. In order to model a sequence of three oblique resonances in this case, three coupled triadic systems with five distinct *phase-locked* modes must be considered. In this case,

our resonance criterion allows for global investigation of the resonance interactions among all modes activated by the physical process without requiring an artificial subdivision into single triads which does not account for the important effects of coupled interactions. The phase-locked evolution of modes which characterise the rapid growth of three-dimensional disturbances in the far wake downstream from a cylinder was shown to be an important dynamic feature in clarifying the amplification mechanism of the amplitude of three-dimensional modes (Wu and Stewart 1996). In our work this condition is shown to be an essential mathematical requisite for identifying modes defining the low-dimensional model. Furthermore, this *phase-locked* condition, taken together with our resonance criterion, eliminates most of arbitrariness in identifying modes that could describe the physical process, simplifying the path which has to be followed in characterising the dynamical system.

REFERENCES

- Boniforti, M.A., Magini, R. and Sciortino, G., 1994, "Transitional flow as a nonlinear dynamical system," *Advances in Turbulence V*, Kluwer Academic Publishers, pp.36-40.
- Boniforti, M.A., Morganti, M. and Sciortino, G., 1996, "Triadic resonant modes: dynamical model and truncation criterion," *Fluid Dynamics Research* (to appear).
- Corke, T., Krull, J.D. and Ghassemi, M., 1992, "Three-dimensional mode resonance in the far wake", *J.Fluid Mech.*, Vol.239, pp. 99.
- Craik, A.D.D., 1985, "Wave interactions and fluid flows", Cambridge University Press.
- Craik, A.D.D., 1971, "Nonlinear resonant instability in boundary layers", *J.Fluid Mech.*, Vol.50, pp.393-413.
- Sciortino, G., 1995, "Evoluzione dinamica di moti di larga scala: modello per la simulazione numerica", Tesi di Dottorato di Ricerca, Università *La Sapienza* di Roma, Italy.
- Williamson, C.H.K. and Prasad, A., 1993a, "A new mechanism for oblique wave resonance in the 'natural' far wake", *J.Fluid Mech.*, Vol. 256, pp.269-313.
- Williamson, C.H.K. and Prasad, A., 1993b, "Acoustic forcing of oblique wave resonance in the far wake", *J.Fluid Mech.*, Vol. 256, pp.315-341.
- Wu, X. and Stewart, P.A., 1996, "Interaction of phase-locked modes: a new mechanism for the rapid growth of three-dimensional disturbances", *J.Fluid Mech.*, Vol. 316, pp.335-372.

COMPUTATION OF TURBULENT CHANNEL FLOW USING PDF METHOD

J.P. Minier⁽¹⁾ and J. Pozorski⁽²⁾

⁽¹⁾ Laboratoire National d'Hydraulique, Electricité de France
6 quai Watier, 78400 Chatou, France
Fax: +33 1 30877253, e-mail: Jean-Pierre.Minier@der.edf.gdfr.fr

⁽²⁾ Instytut Maszyn Przepływowych, Polska Akademia Nauk
Fiszera 14, 80952 Gdańsk, Poland
Fax: +48 58 416144, e-mail: jp@galia.imp.pg.gda.pl

ABSTRACT

An application of a Lagrangian stochastic model to the case of turbulent channel flow is presented. A recent model of Pope (1991) for the joint pdf of velocity and dissipation rate in turbulent flows is used for the purpose. Boundary conditions for particles are formulated to simulate wall-bounded flows. Obtained results for the first and second order velocity moments compare well with available experimental data. Moreover, higher-order moments (skewness and flatness) of velocity components, otherwise unavailable from more standard second-order closures, are found to agree, at least qualitatively, with experimental results.

INTRODUCTION

The paper discusses computation results obtained with a Probability Density Function (PDF) approach. The main idea of the PDF method (for a review see Pope 1994) is to propose a closed evolution equation for the one-point joint probability density (pdf) of variables describing the flow (here, instantaneous velocity and the turbulent energy dissipation rate). The equation is solved by means of the so-called particle representation (Monte Carlo method). The method therefore consists in simulating the behaviour of a large number of notional (stochastic) fluid particles. A number of variables (location, velocity, dissipation rate, scalars,...) can be attached to each particle. The time evolution of these variables is governed by modelled stochastic differential equations. They are shown to be equivalent to the evolution equation for the pdf. Equations for the moments of the random variables are easily obtained from the closed pdf equation. For first-order velocity statistics, equations are identical with Reynolds equations and in the second order they give some Reynolds stress transport (RSM) model. However, in the PDF approach, contrary to the RSM closure, triple correlations do not need to be modelled and evolution of higher-order statistics, such as velocity skewness and flatness, can also be followed.

The work presented here is a continuation of the authors' effort towards a development of a numerical tool to compute turbulent flows, possibly in geometries of practical interest, with the use of the PDF method. Previous results (Pozorski & Minier 1994, Minier & Pozorski 1995)

concerned free-shear flows. The method is now extended to take wall effects into account. Particularities of the numerical treatment of wall-bounded flows, as opposed to the self-similar regions of free-shear mixing layers or wakes, manifest themselves in the pressure algorithm as well as in the need for an appropriate statement and application of the boundary conditions.

STOCHASTIC MODELLING

The starting point are instantaneous evolution equations for variables describing the fluid motion in the Lagrangian formulation (a "+" sign denotes values taken along a particle trajectory):

$$\begin{aligned} dx^+ &= U^+(t) dt, \\ dU^+ &= \left(-\frac{1}{\rho} \frac{\partial p}{\partial x} + \nu \Delta U \right)^+ dt. \end{aligned} \quad (1)$$

Reynolds averaging applied to the momentum equation results in unknown terms involving fluctuating quantities. Closure amounts to replacing these terms by increments of a stochastic process. Consequently, evolution equations for the stochastic fluid particles, denoted by a "*" superscript, are written in the Lagrangian way as follows:

$$dx^* = U^*(t) dt \quad (2)$$

$$dU_i^* = -\frac{1}{\rho} \frac{\partial \langle p \rangle}{\partial x_i} dt + dA_i^*(t) \quad (3)$$

$$d\epsilon^* = dA_\epsilon^*(t). \quad (4)$$

The first equation expresses that convection is treated exactly. In the particle equation of motion, the mean viscous term and gravity are disregarded. Evolution equation for the turbulent energy dissipation rate ϵ has to be modelled altogether since it only involves small-scale quantities (dissipation due to the mean velocity gradients is negligible compared to that caused by fluctuating velocity).

Generally, the above set of equations can be thought of as describing a vector stochastic diffusion process, its evolution equation taking the form

$$dA = D(t, A) dt + B(t, A)^{1/2} dW \quad (5)$$

where \mathbf{A} stands for a vector of variables describing the flow. \mathbf{D} and B denote respectively the drift vector and the diffusion matrix; dW is a white-noise (Wiener process). To be precise, \mathbf{D} and B depend not only on instantaneous values of \mathbf{A} , but also on some moments (depending on the modelling) of the distribution of \mathbf{A} . It is thus more appropriate to think about the drift term and the diffusion matrix as being functionally dependent on the pdf of \mathbf{A} .

The model we apply here was developed by Pope and coworkers (Haworth & Pope 1986, Pope & Tchen 1990, Pope 1991). The state vector \mathbf{A} comprises position \mathbf{x} , velocity \mathbf{U} and turbulent frequency $\omega = \epsilon/k'$ (the inverse of the turbulent time scale).

The evolution equation for particle velocities writes :

$$d\mathbf{U}_i^* = -\frac{1}{\rho} \frac{\partial \langle p \rangle}{\partial x_i} dt + G_{ij}(U_i - \langle U_i \rangle) dt + \sqrt{\left(C_0 + \frac{2}{3}\beta \frac{P}{\langle \epsilon \rangle}\right) k \langle \omega^* \rangle dW_i} \quad (6)$$

Here, the fluctuating part of the drift term has been gathered in a general matrix G which writes:

$$G_{ij} = -\left(\frac{1}{2} + \frac{3}{4}C_0\right) \frac{\epsilon}{k} \delta_{ij} + \beta \frac{\partial \langle U_i \rangle}{\partial x_j} \quad (7)$$

where C_0 and β are constants of the model and P is the turbulent energy production rate.

The ω -equation has the form:

$$d\omega^* = -\omega^* \langle \omega \rangle \times \left\{ S_\omega + C_\chi \left[\ln \left(\frac{\omega^*}{\langle \omega \rangle} \right) - \left\langle \frac{\omega}{\langle \omega \rangle} \ln \left(\frac{\omega}{\langle \omega \rangle} \right) \right\rangle \right] \right\} dt + \omega^* \sqrt{2C_\chi \langle \omega \rangle \sigma^2} dW \quad (8)$$

In this equation, σ^2 is the variance of $\chi = \ln(\omega/\langle \omega \rangle)$, C_χ is a constant.

The above (Eqs. 2, 6 and 8) have to be understood as the governing equations for the dynamics of an ensemble of virtual (or stochastic) fluid particles representing a turbulent flow. The modeling assumption for the momentum equation is that the sum of the fluctuating pressure term and the fluctuating viscous term can be expressed by a stochastic diffusion process. A derivation of this model has recently been put forward (Minier & Pozorski 1997). A more traditional argument in favor of such modelling is that the sample paths of the process are continuous and the second-order Lagrangian velocity structure function in the inertial range is in accord with Kolmogorov theory. Equation for ω has been modelled so that the evolution of $\langle \omega \rangle$ agrees with the standard form known from the k - ϵ turbulence model; the instantaneous dissipation rate ϵ^* is used according to the refined Kolmogorov hypothesis (1962).

WALL BOUNDARY CONDITIONS

Wall boundaries require specific conditions. The aim is not to simulate the complete boundary layer (down to the no-slip condition) but to represent the momentum exchange by bridging over the viscous layer. The boundary conditions are applied to the instantaneous variables attached to each particle that crosses the boundaries. The presence of the wall is taken into account by formulating the conditions for the boundary of the computational domain, placed in the constant-stress region of the turbulent boundary layer (the so-called logarithmic layer). The only important parameter that represents the effect of wall proximity is the friction velocity u_* . Shear stress is assumed to be equal to $-u_*^2$.

We consider a plane wall, at y_{min} (in the constant-stress region of the TBL). Every time a particle crosses the boundary, it is reflected in the domain so as to ensure zero mass flux at the wall. The detailed conditions for the incoming particle are written in terms of the outgoing one as :

$$\begin{aligned} y_{in} &= 2y_{min} - y_{out} \\ v_{in} &= -v_{out} \\ U_{in} &= U_{out} - 2\frac{\langle uv \rangle}{\sigma_v^2} v_{out} \\ \omega_{in} &= \omega_{out} - 2\frac{\langle \omega v \rangle}{\sigma_v^2} v_{out} \end{aligned} \quad (9)$$

or, alternatively for the last condition

$$\chi_{in} = \chi_{out} - 2\frac{\langle \chi v \rangle}{\sigma_v^2} v_{out} \quad (10)$$

These conditions assure that ensemble averages over the flux of particles that cross the domain boundary, denoted by $\langle \cdot \rangle_b$, satisfy the conditions:

$$\begin{aligned} \langle v_{in} \rangle_b &= -\langle v_{out} \rangle_b \\ \langle u_{in} \rangle_b &= -\langle u_{out} \rangle_b \\ \langle v_{in}^2 \rangle_b &= \langle v_{out}^2 \rangle_b \\ \langle u_{in}^2 \rangle_b &= \langle u_{out}^2 \rangle_b \\ \langle u_{in} v_{in} \rangle_b &= \langle u_{out} v_{out} \rangle_b \\ \langle \chi_{in} \rangle_b &= -\langle \chi_{out} \rangle_b, \text{ etc.} \end{aligned} \quad (11)$$

Relationships (11) can be proven as follows. Given the pdf $f(u, v)$, the mean value of any function $Q(u, v)$ over the particles crossing the domain boundary, $\langle Q \rangle_b$, is defined:

$$\langle Q \rangle_b = \frac{1}{C} \int_0^\infty dv \int_{-\infty}^\infty du v Q(u, v) f(u, v) \quad (12)$$

where

$$C = \int_0^\infty dv \int_{-\infty}^\infty du v f(u, v) \quad (13)$$

is a normalisation constant.

Supposing that $f(u, v)$ is a joint-normal pdf,

$$\mathcal{N}(\langle U \rangle, 0, \sigma_u, \sigma_v, r_{uv}),$$

with obviously

$$r_{uv} = \langle uv \rangle / (\sigma_u \sigma_v),$$

we obtain

$$\begin{aligned} \langle u_{in} \rangle_b &= \frac{1}{2} \sqrt{2\pi} r_{uv} \sigma_u \\ \langle v_{in} \rangle_b &= \frac{1}{2} \sqrt{2\pi} \sigma_v \\ \langle u_{in}^2 \rangle_b &= (1 + r_{uv}^2) \sigma_u^2 \\ \langle v_{in}^2 \rangle_b &= 2\sigma_v^2 \\ \langle u_{in} v_{in} \rangle_b &= 2r_{uv} \sigma_u \sigma_v \end{aligned} \quad (14)$$

Analogously, supposing that $f(v, \chi)$ is also a joint-normal pdf, $\mathcal{N}(0, \sigma_\chi^2/2, \sigma_v, \sigma_\chi, r_{v\chi})$, we obtain

$$\begin{aligned} \langle \chi_{in}^2 \rangle_b &= (1 + r_{v\chi}^2) \sigma_\chi^2 \\ \langle v_{in} \chi_{in} \rangle_b &= 2r_{v\chi} \sigma_v \sigma_\chi \end{aligned} \quad (15)$$

Now, applying the operator $\langle \cdot \rangle_b$ to (9) and substituting from (14), we obtain (11).

To determine the values of the constants, we have performed computational test of the TBL. We have placed the upper boundary of the layer in the constant-stress region and applied there the same limit conditions as for the other

Statistics	Present work	Pope (1991)	Experiment
k/u_*^2	3.35	3.4	3.8
$\langle u^2 \rangle / u_*^2$	2.85	2.99	4.3
$\langle v^2 \rangle / u_*^2$	1.95	1.96	1.0
$\langle w^2 \rangle / u_*^2$	1.95	1.96	2.4

Table 1: Results for the constant-stress region of the turbulent boundary layer: u_* - friction velocity.

boundary close to the wall. The results of computation are presented in Table 1 and compared to the experimental data (after Tennekes & Lumley 1972). They are expected to be the same as the results of Pope (1991) and differences are supposedly due to the statistical noise.

It has to be noted here that similar results can be obtained for several sets of constants (they are not independent), e.g. ($C_\lambda = 1.6$, $C_0 = 3.5$, $C_{w1} = 1.15$) or ($C_\lambda = 6.0$, $C_0 = 3.5$, $C_{w1} = 1.45$). The second set has been used for the following calculations.

BOUNDARY CONDITIONS FOR THE CHANNEL FLOW

Plane turbulent channel flow (TCF) is of both academic and technical relevance; its geometry is simple (Fig. 1), but a non-trivial spatial distribution of flow parameters makes it a sound test of any turbulence model. Different boundary conditions are used for the particles. Particles are first initialized with uniform concentration and with respect to given initial fields. At the outlet, particles leaving the domain are replaced at the inlet of the computed section. This corresponds to periodic conditions and implies that particles are marched to an homogeneous solution (in the longitudinal direction). The wall boundary conditions are those of the previous section. Half a channel is computed and symmetry conditions are applied at the channel centerline $y/h = 1$

$$\begin{aligned} v_{in} &= -v_{out} \\ U_{in} &= U_{out} \\ \omega_{in} &= \omega_{out} \end{aligned} \quad (16)$$

PRESSURE CORRECTION ALGORITHM

Considerable effort has been devoted to the development of the pressure-correction algorithm. The algorithm is used to satisfy continuity conditions which take a two-fold aspect in PDF modelling: uniform concentration of particles (for inert incompressible flows) and zero divergence of mean velocities. The channel flow has been computed with two numerical approaches. The simpler version is a 1D calculation with a one dimensional grid in the y -direction. Cross-stream velocity corrections are derived to ensure uniform particle distribution while streamwise particle velocities are corrected to respect the mass flow rate. The second version corresponds to the general 2D algorithm. At every time step, particle locations are corrected first to assure the uniform mean fluid density throughout the computational domain. Then, particle velocities are corrected in order to satisfy the mean continuity equation. Poisson solver is used for the purpose. Both corrections need a few (typically 2-3) internal iterations at every time step.

RESULTS

Although particle methods are basically grid-free, it is a standard technique to introduce a computational grid in order to solve the Poisson equation (unless pressure enters the vector of stochastic variables attached to the particle); statistical averages are also computed for every grid cell (however, smoothed-particle hydrodynamics provides

an alternative). We usually used 10×15 grid with roughly 10 000 particles to achieve a reasonable trade-off between the computational cost and the statistical noise level. On the HP 9000/735 machine, it typically takes a few CPU minutes to achieve convergence towards the steady state for the above parameters.

The computations have been performed for the channel of $h = 0.09m$ half-width at the Reynolds number $Re = U_b h / \nu = 120\,000$, U_b being the bulk velocity. These conditions are identical to those used in Comte-Bellot (1965) measurements. Consequently, all results have been compared to these data.

A few PDF closures proposed by Pope (1990,1991,1994) have been considered in computations. Results have been obtained with so-called Simplified Langevin Model (SLM, $C_0 = 3.5$, $\beta = 0$ in Eq. 7) and Isotropisation-of-Production Model (IPM, $C_0 = 2.1$, $\beta = 0.5$). No noticeable improvements have been observed when using more complicated (and computationally expensive) Refined Langevin Model (RLM). However, this might be no longer true in a more complex flow case.

The plots shown in Fig. 2 present mean streamwise velocity as well as second-order statistics, i.e. components of the Reynolds stress tensor R_{ij} and the turbulent kinetic energy as functions of the cross-stream coordinate normalised by the channel half-width. These results have been obtained with an IPM form of the Langevin equation (Pope, 1994) and from the 2D computation using the SLM model. It is noticed that the shear stress R_{12} and the turbulent kinetic energy k are in good agreement with experiment. On the other hand, a discrepancy in the distribution of this energy between the diagonal components of the Reynolds stress tensor is observed. The numerical values obtained at the wall boundaries reflect the model predictions of a turbulent boundary layer (see Table 1 for the SLM model) that can be theoretically derived. Contrary to the experimental evidence, the transverse and the spanwise components of the Reynolds stress tensor are predicted to be equal. This is an inherent feature of the models used here.

To illustrate the capacities of the PDF approach, higher-order statistics, unavailable in the RSM closures, have also been computed. As shown in Fig. 3, qualitative agreement with experimental data is satisfying.

CONCLUSION

Particle boundary conditions have been derived. They reproduce all known statistics of the logarithmic near-wall region and correspond to wall-functions in the PDF context. A general pressure-gradient algorithm has also been implemented. Both developments allow wall-bounded non-homogeneous turbulent flows to be computed with a full 2D PDF approach. Numerical results have been obtained in the case of a high-Reynolds channel flow and compared to experimental results. Current developments aim at improving computational efficiency using techniques such as Variance Reduction Techniques, at pursuing validation with different turbulent flows (recirculating flows for example) and at introducing numerical models for inert and/or reactive variables for which PDF methods take their full value.

REFERENCES

- Comte-Bellot, G., 1965, "Ecoulement turbulent entre deux parois paralleles", *Publ. Sci. Techn. Min. Air*, Paris, 246.
- Haworth D.C. & Pope, S.B., 1986, "A generalized Langevin model for turbulent flows", *Phys. Fluids* **29**, pp. 387-405.
- Minier, J.-P. & Pozorski, J. 1995, "Analysis of a PDF model in a mixing layer case," *10th Symposium on Turbulent Shear Flows*, The Pennsylvania State University, University Park, PA, pp. 26-25.
- Minier, J.-P. & Pozorski, J., 1997, "Derivation of a PDF model for turbulent flows based on principles from statistical physics," *Phys. Fluids* **9**, No. 6, pp. ?-?.
- Pope, S.B., 1991, "Application of the velocity-dissipation probability density function model to inhomogeneous turbulent flows," *Phys. Fluids A* **3**, pp. 1947-1957.
- Pope, S.B., 1994, "Lagrangian PDF methods for turbulent flows," *Annu. Rev. Fluid Mech.* **26**, pp. 23-63.
- Pope, S.B. & Tchen, Y.L., 1990, "The velocity-dissipation probability density function model for turbulent flows," *Phys. Fluids A* **2**, pp. 1437-1449.
- Pozorski, J. & Minier, J.-P., 1994, "Lagrangian modelling of turbulent flows," *Rep. No. HE-44/94.016*, Electricité de France, Chatou.
- Tennekes, H. & Lumley, J.L., 1972, *A First Course in Turbulence*, MIT Press, Cambridge, Mass.

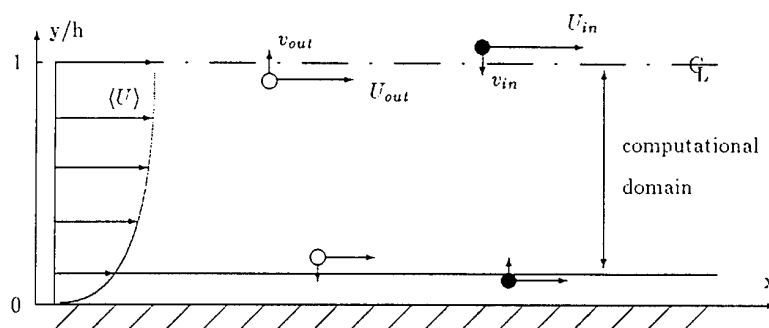


Figure 1: Sketch of the turbulent channel flow.

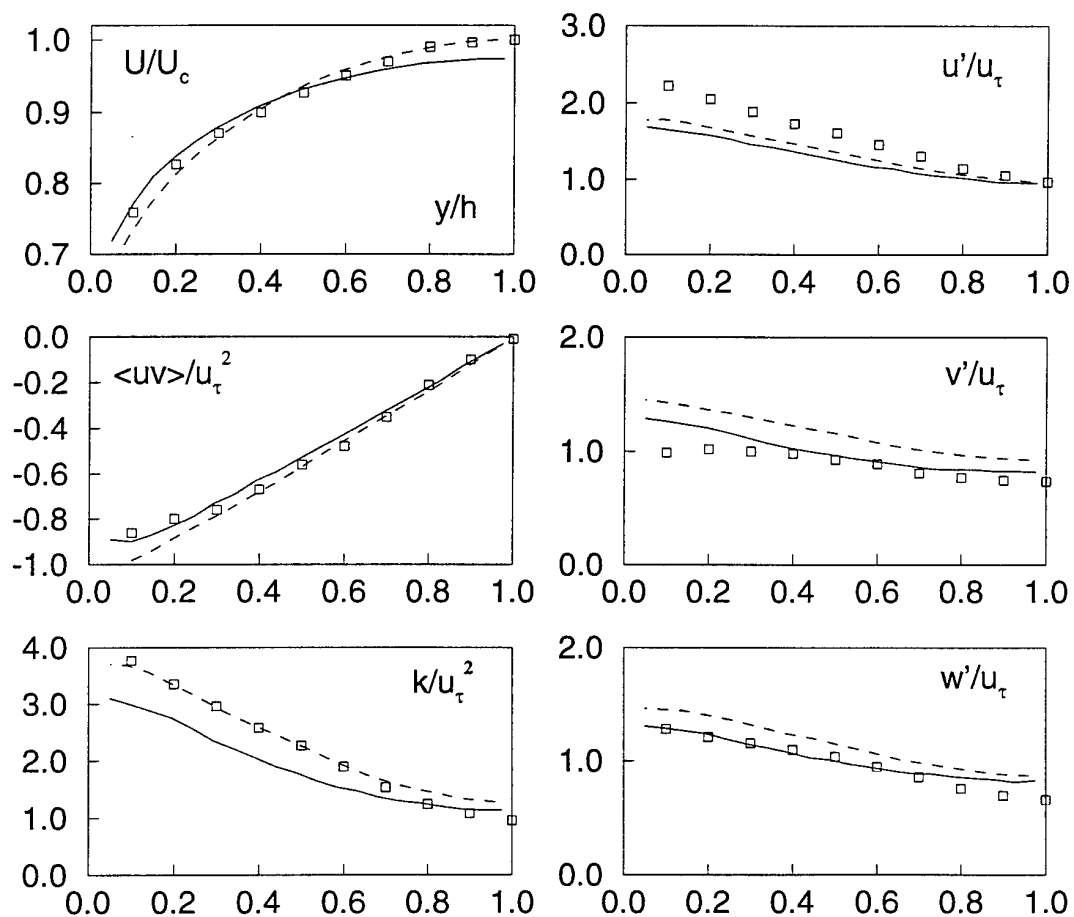


Figure 2: Streamwise mean velocity and Reynolds stress tensor components plotted as a function of the normalized cross-stream coordinate. Comparison with the Comte-Bellot (\square) experiment. Solid line - SLM 2D computation, dashed line - IPM 1D computation.

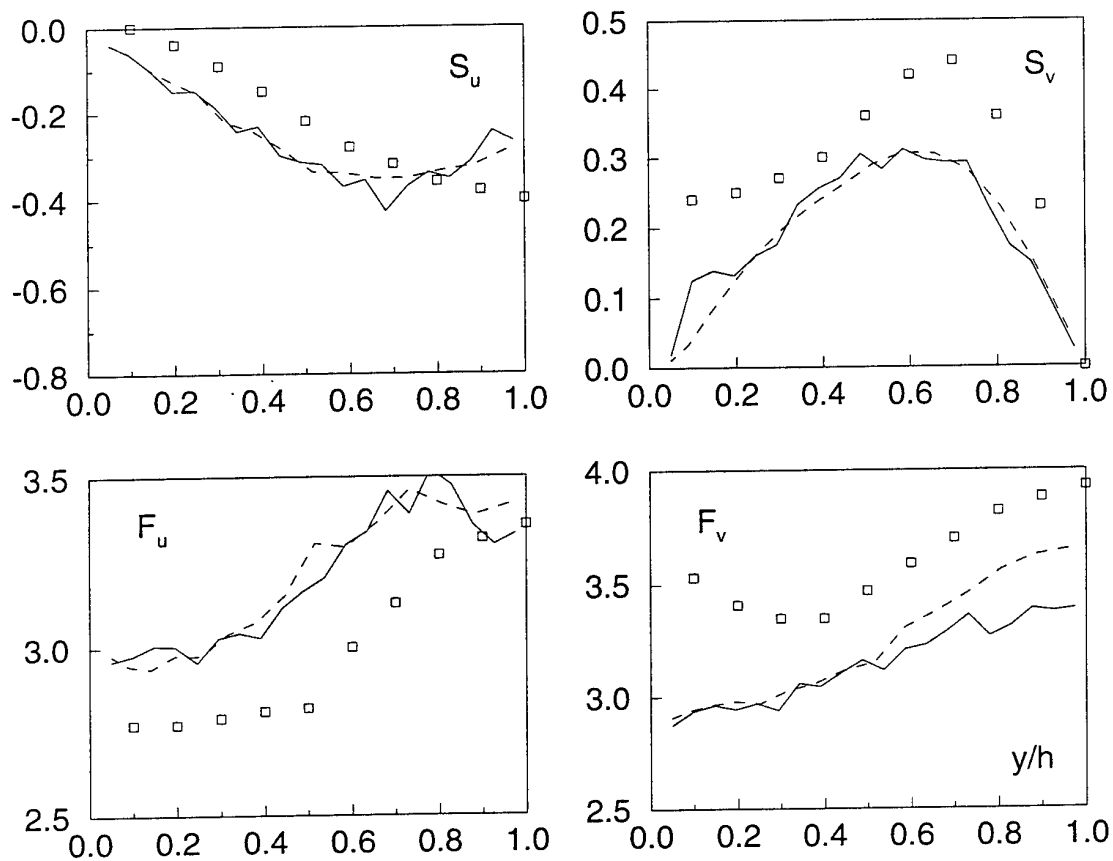


Figure 3: Skewness and flatness factors of the streamwise and the cross-stream velocity components as a function of the normalized wall distance. Comparison with the Comte-Bellot (\square) experiment. Solid line - SLM 2D computation, dashed line - IPM 1D computation.

DYNAMICAL SYSTEM ANALYSIS OF REYNOLDS STRESS CLOSURE EQUATIONS

Sharath S. Girimaji

Institute for Computer Applications in Science and Engineering
NASA Langley Research Center
Hampton, Virginia 23693
USA

INTRODUCTION

The equilibrium states of benchmark turbulent homogeneous flows have long been used to develop, calibrate and validate pressure-strain correlation models, Speziale *et al* (1991). The benchmark flows have typically been strain-rate dominated flows such as plane shear, plane strain and axisymmetric expansion/contraction. When these pressure-strain models are used to compute slightly more complex flows which contain the effects of both rotation and strain (elliptic flows), the model results are inconsistent with linear stability theory and direct numerical simulation (DNS) data, (Speziale *et al* 1996, Blaisdell and Shariff, 1996). Improved predictive capability of elliptic flows requires a better understanding of the physics of turbulence as well as the dynamics of the model equations. This calls for an intimate understanding of the model equations, especially the causality between the model constants and the predicted long-time behavior. For the special case of shear flow in rotating coordinate frame, the equilibrium state predicted by two-equation turbulence models and linear pressure-strain models have been investigated by Speziale and Mac Giolla Mhuiris (1989, 1990). These studies have lead to models with better predictive capability in those selected flows.

The objective of the present study is to perform dynamical system analysis, i.e., fixed point and bifurcation analyses, of the anisotropy, kinetic energy and dissipation closure equations with aid of representation theory for all elliptic flows (with two-dimensional mean velocity field) to establish for the first time exact (analytical) relationship between turbulence model (pressure-strain correlation and dissipation equation) coefficients and the asymptotic behavior of the equation set. The results from our study enables us to classify completely the turbulent asymptotic state predicted by a model as a function of the mean strain and rotation rates. The knowledge of this causality can be used in closure model development to yield the required asymptotic (equilibrium) behavior. Quasilinear pressure-strain model which includes the entire class of Launder, Reece and Rodi (1975), referred to as LRR, models are considered here. This study also sheds light on the strategies that can be employed to develop non-equilibrium al-

gebraic Reynolds stress models starting from the Reynolds stress closure equations.

In this study we will restrict ourselves to turbulence in inertial frame which includes elliptic flows. Turbulence modeling in non-inertial rotating frames will be considered in future work.

TURBULENCE CLOSURE EQUATIONS

In homogeneous turbulence, the exact Reynolds stress transport equation in an arbitrary inertial reference frame is given by

$$\frac{d\overline{u_i u_j}}{dt^*} = P_{ij} - \varepsilon_{ij} + \phi_{ij}. \quad (1)$$

The terms, respectively, are the time rate of change, production (P_{ij}), dissipation (ε_{ij}) and pressure-strain correlation (ϕ_{ij}) of Reynolds stress:

$$\begin{aligned} P_{ij} &= -\overline{u_i u_k} \frac{\partial U_j}{\partial x_k} - \overline{u_j u_k} \frac{\partial U_i}{\partial x_k}; \\ \varepsilon_{ij} &= 2\nu \frac{\partial u_i}{\partial x_k} \frac{\partial u_j}{\partial x_k}; \quad \phi_{ij} = p \left(\frac{\partial u_i}{\partial x_j} + \frac{\partial u_j}{\partial x_i} \right). \end{aligned} \quad (2)$$

The production and dissipation rate of turbulent kinetic energy are, respectively, $P = \frac{1}{2} P_{ii}$ and $\varepsilon = \frac{1}{2} \varepsilon_{ii}$. In high Reynolds number flows, dissipation is generally treated as being isotropic:

$$\varepsilon_{ij} = \frac{2}{3} \varepsilon \delta_{ij}. \quad (3)$$

Closure models are needed for the pressure-strain correlation (ϕ_{ij}) and dissipation rate (ε).

In this study, we focus on the quasilinear class of pressure-strain correlations models of the general form:

$$\begin{aligned} \phi_{ij} &= -(C_1^0 \varepsilon + C_1^1 P) b_{ij} + C_2 K S_{ij} + \\ &C_3 K (b_{ik} S_{jk}^* + b_{jk} S_{ik}^* - \frac{2}{3} b_{mn} S_{mn}^* \delta_{ij}) + \\ &C_4 K (b_{ik} W_{jk}^* + b_{jk} W_{ik}^*), \end{aligned} \quad (4)$$

where the C 's are numerical constants and

$$\begin{aligned} S_{ij}^* &= \frac{1}{2} \left(\frac{\partial U_i}{\partial x_j} + \frac{\partial U_j}{\partial x_i} \right); \quad W_{ij}^* = \frac{1}{2} \left(\frac{\partial U_i}{\partial x_j} - \frac{\partial U_j}{\partial x_i} \right); (5) \\ b_{ij} &= \frac{\bar{u}_i \bar{u}_j}{2K} - \frac{1}{3} \delta_{ij}. \end{aligned}$$

We choose this form of the pressure-strain model for two reasons. First, this form of the model permits analytical treatment of the asymptotic behavior. Second, this is the form most frequently used in practical Reynolds stress closure calculations: this form includes all linear-pressure strain models (e.g. LRR model) and some of the non-linear models (such as the SSG model) can also be reduced to this form near equilibrium. For the LRR model, the coefficients are

$$C_1^0 = 3.0; C_1^1 = 0.; C_2 = 0.8; C_3 = 1.75; C_4 = 1.31$$

The coefficients for the Gibson and Launder (1978) model are

$$C_1^0 = 3.6; C_1^1 = 0.; C_2 = 0.8; C_3 = 1.2; C_4 = 1.2$$

For the quasilinearized SSG model, the coefficients are

$$C_1^0 = 3.4; C_1^1 = 1.8; C_2 = 0.36; C_3 = 1.25; C_4 = 0.4$$

The anisotropy evolution equation can be derived from the Reynolds stress equation and the pressure strain correlation model:

$$\begin{aligned} \frac{db_{ij}}{dt^*} &= -b_{ij}(L_1^0 \frac{\epsilon}{K} - L_1^1 b_{mn} S_{mn}^*) + L_2 S_{ij}^* \\ &+ L_3 (b_{ik} S_{jk}^* + b_{jk} S_{ik}^* - \frac{2}{3} b_{lm} S_{lm}^* \delta_{ij}) \\ &+ L_4 (b_{ik} W_{jk}^* + b_{jk} W_{ik}^*) \end{aligned} \quad (6)$$

The pressure-strain correlation model coefficients are redefined as:

$$\begin{aligned} L_1^0 &\equiv C_1^0 - 2; \quad L_1^1 \equiv 2C_1^1 + 4; \quad L_2 \equiv C_2 - \frac{4}{3}; \quad (7) \\ L_3 &\equiv C_3 - 2; \quad L_4 \equiv C_4 - 2. \end{aligned}$$

The turbulent kinetic energy evolves according to

$$\frac{dK}{dt^*} = P - \epsilon, \quad (8)$$

and the modeled evolution equation of dissipation is

$$\frac{d\epsilon}{dt^*} = C_{e1} \frac{\epsilon}{K} P - C_{e2} \frac{\epsilon^2}{K}. \quad (9)$$

The model constants C_{e1} and C_{e2} are typically given values of 1.44 and 1.90 respectively.

Equations (6), (8) and (9) constitute the second order closure equations in homogeneous turbulence. These equations can be non-dimensionalized using the norm of the deformation rate tensor:

$$\eta = S_{ij}^* S_{ij}^* + W_{ij}^* W_{ij}^*, \quad (10)$$

The non-dimensional quantities are

$$\begin{aligned} S_{ij} &= S_{ij}^* / \sqrt{\eta}; \quad W_{ij} = W_{ij}^* / \sqrt{\eta}; \\ dt &= \sqrt{\eta} dt^*; \quad \omega = \epsilon / (\sqrt{\eta} K), \end{aligned} \quad (11)$$

where ω is the relative strain rate, i.e., the ratio of the turbulence to mean flow strain rates. In the above equations, asterisk is used to represent dimensional quantities and the corresponding non-dimensional quantity is written

without the asterisk. In dimensionless time, the anisotropy transport equation is

$$\begin{aligned} \frac{db_{ij}}{dt} &= -b_{ij}(L_1^0 \omega - L_1^1 b_{mn} S_{mn}) + L_2 S_{ij} \\ &+ L_3 (S_{ik} b_{kj} + b_{ik} S_{kj} - \frac{2}{3} b_{mn} S_{mn} \delta_{ij}) \\ &+ L_4 (W_{ik} b_{kj} - b_{ik} W_{kj}). \end{aligned} \quad (12)$$

Two points are worthy of note here. In dimensionless time the anisotropy evolution is (i) independent of the magnitude of deformation (η) and depends only on the ratio of strain to rotation rate; and (ii) dependent only on the relative strain rate and not individually on kinetic energy and dissipation. The evolution equation of the relative strain rate, ω , is easily obtained from those of the turbulent kinetic energy and dissipation:

$$\frac{d\omega}{dt} = -2\omega(C_{e1} - 1)b_{mn} S_{mn} - (C_{e2} - 1)\omega^2. \quad (13)$$

The first term on the right hand side of equation (13) represents the production of the relative strain rate whereas the second terms represents its destruction.

In homogeneous turbulence, the above non-linear dynamical system of equations represents an initial value problem. The Reynolds stress, kinetic energy and dissipation may grow unbounded from their initial values. However, it is known that for some benchmark flows such as (homogeneous) plane shear, plane strain and axisymmetric expansion/contraction the normalized turbulence parameters b_{ij} and ω evolve from their specified initial conditions according to the equations and asymptote to finite-valued fixed points (equilibrium turbulence), provided such a state exists. The fixed point or the equilibrium state of turbulence is described by

$$\frac{db_{ij}}{dt} = 0; \quad \text{and} \quad \frac{d\omega}{dt} = 0. \quad (14)$$

Representation theory

We are only interested in the asymptotic behavior, long after the influence of the initial conditions has diminished. At this stage of evolution, it can be argued that the Reynolds stress can be tensorial function only of the mean strain and rotation rates. Representation theory can then be invoked to determine the most general tensor function that can be constructed with the strain and rotation rates. The most general, physically permissible tensor representation for the Reynolds stress anisotropy in terms of the strain and rotation rates in the case of two-dimensional mean flow is given by (Girimaji 1996a)

$$\begin{aligned} b_{ij} &= G_1 S_{ij} + G_2 (S_{ik} W_{kj} - W_{ik} S_{kj}) \\ &+ G_3 (S_{ik} S_{kj} - \frac{1}{3} \eta_1 \delta_{ij}), \end{aligned} \quad (15)$$

where,

$$\eta_1 = S_{ij} S_{ij}; \quad \text{and} \quad \eta_2 = W_{ij} W_{ij}. \quad (16)$$

In the above equations $G_1 - G_3$ are yet to be determined scalar functions of the invariants of strain and rotation rate tensors. During b_{ij} evolution, $G_1 - G_3$ will be functions of time as well. Also note that, by definition, $\eta_1 + \eta_2 = 1$.

The representation for b_{ij} is now substituted into equation (12) and the resulting equation is simplified using the following identities valid for all two-dimensional mean flows:

$$\begin{aligned} S_{ik} S_{kj} &= \frac{1}{2} \eta_1 \delta_{ij}^{(2)}; \quad W_{ik} W_{kj} = -\frac{1}{2} \eta_2 \delta_{ij}^{(2)}; \quad (17) \\ S_{ik} S_{kl} S_{lj} &= \frac{1}{2} \eta_1 S_{ij}; \quad S_{ik} W_{kl} S_{lj} = -\frac{1}{2} \eta_1 W_{ij}; \\ W_{ik} S_{kl} W_{lj} &= \frac{1}{2} \eta_2 S_{ij}; \quad S_{mn} b_{mn} = G_1 \eta_1, \end{aligned}$$

where $\delta_{ij}^{(2)}$ and δ_{ij} are two and three dimensional delta functions respectively. We retain terms up to quadratic power (in strain and rotation rate) in their original form and invoke their two-dimensional property only when these terms appear in cubic and higher power terms. For example, $S_{ik}S_{kj}$ is retained as such when it appears by itself: whereas, when it appears as a part of a cubic or higher power term we invoke $S_{ik}S_{kj} = \frac{1}{2}\eta_1\delta_{ij}^{(2)}$ to write $S_{ik}S_{kj}S_{jl} = \frac{1}{2}\eta_1S_{il}$. By invoking the two-dimensional property for reducing only cubic and higher power terms, it is hoped that the three-dimensional effect is approximately accounted for upto the quadratic term. Using these rules, we write

$$\begin{aligned} S_{ik}b_{kj} + b_{ik}S_{kj} - \frac{2}{3}b_{mn}S_{mn}\delta_{ij} &= \frac{1}{3}\eta_1G_3S_{ij} \quad (18) \\ &+ 2G_1(S_{ik}S_{kj} - \frac{1}{3}\eta_1\delta_{ij}) \\ W_{ik}b_{kj} - b_{ik}W_{kj} &= -G_1(S_{ik}W_{kj} - W_{ik}S_{kj}) \\ &+ 2\eta_2G_2S_{ij}. \end{aligned}$$

Substitution of equation (15) into equation (12) yields the anisotropy evolution equation in terms of coefficients $G_1 - G_3$. After substitution, the coefficient of each tensor on either side of equation (12) has to be equal due to the linear independence of the representation tensors. Comparing the coefficients of the three representation tensors on either side we get

$$\begin{aligned} \frac{dG_1}{dt} + G_1(L_1^0\omega - L_1^1G_1\eta_1) &= L_2 + \frac{1}{3}L_3G_3\eta_1 \quad (19) \\ &+ 2L_4\eta_2G_2 \\ \frac{dG_2}{dt} + G_2(L_1^0\omega - L_1^1G_1\eta_1) &= -G_1L_4, \\ \frac{dG_3}{dt} + G_3(L_1^0\omega - L_1^1G_1\eta_1) &= 2G_1L_3. \end{aligned}$$

Equations (19) along with (13) constitute the new non-linear system of evolution equations for Reynolds stresses in homogeneous turbulence. Fixed point and bifurcation analyses of this system is now performed.

DYNAMICAL SYSTEM ANALYSIS

Fixed point and bifurcation analyses of the new system is now performed.

The fixed point equations (14) can now be restated as

$$\frac{dG_1}{dt} = \frac{dG_2}{dt} = \frac{dG_3}{dt} = \frac{d\omega}{dt} = 0. \quad (20)$$

Using the notation that the fixed point values are denoted by a superscript 0, the algebraic fixed point relations are (using $b_{mn}S_{mn} = G_1\eta_1$):

$$\begin{aligned} 0 &= 2\omega^0(C_{e1} - 1)G_1^0\eta_1 + (C_{e2} - 1)(\omega^0)^2 \quad (21) \\ 0 &= -G_1^0(L_1^0\omega - L_1^1G_1^0\eta_1) + L_2 + \frac{1}{3}L_3G_3^0\eta_1 \\ &+ 2L_4\eta_2G_2^0 \\ 0 &= G_2^0(L_1^0\omega - L_1^1G_1^0\eta_1) + G_1^0L_4 \\ 0 &= G_3^0(L_1^0\omega - L_1^1G_1^0\eta_1) - 2G_1^0L_3 \end{aligned}$$

This system of equations leads to five fixed points:

$$\begin{aligned} [\omega^0 = 0, G_1^0 = 0, L_2 + \frac{1}{3}L_3G_3\eta_1 + 2L_4\eta_2G_2 = 0]; \\ [\omega^0 = 0, G_1^0 = -\frac{1}{\sqrt{\eta_1}}Q_1, G_2^0 = \frac{L_4}{L^*\eta_1}, G_3^0 = -\frac{2L_3}{L^*\eta_1}]; \\ [\omega^0 = 0, G_1^0 = +\frac{1}{\sqrt{\eta_1}}Q_1, G_2^0 = \frac{L_4}{L^*\eta_1}, G_3^0 = -\frac{2L_3}{L^*\eta_1}]; \\ [\omega^0 = -2\frac{C_{e1}-1}{C_{e2}-1}G_1^0\eta_1, G_1^0 = -\frac{Q^*}{\sqrt{\eta_1}}, G_2^0 = \frac{L_4}{L^*\eta_1}, G_3^0 = -\frac{2L_3}{L^*\eta_1}]; \\ [\omega^0 = -2\frac{C_{e1}-1}{C_{e2}-1}G_1^0\eta_1, G_1^0 = +\frac{Q^*}{\sqrt{\eta_1}}, G_2^0 = \frac{L_4}{L^*\eta_1}, G_3^0 = -\frac{2L_3}{L^*\eta_1}]. \end{aligned}$$

In the above equations Q_1 and Q^* are defined as

$$\begin{aligned} Q_1 &= \sqrt{-\frac{L_2}{L_1^1} + \frac{2}{3}(\frac{L_3}{L_1^1})^2 - 2(\frac{L_4}{L_1^1})^2 \frac{1-\eta_1}{\eta_1}}, \quad (22) \\ Q^* &= \sqrt{-\frac{L_2}{L^*} + \frac{2}{3}\frac{L_3^2}{L^{*2}} - 2\frac{L_4^2}{L^{*2}} \frac{1-\eta_1}{\eta_1}}, \end{aligned}$$

where

$$L^* = 2L_1^0\frac{C_{e1}-1}{C_{e2}-1} + L_1^1. \quad (23)$$

It should be pointed out that a negative value of G_1^0 is consistent with gradient-diffusion type effect. A positive value would imply a negative value of kinetic energy production - i.e, flow of energy from the turbulent fluctuations to the mean flow.

Bifurcation analysis

The qualitative behavior of the solution of a set of differential equations may depend on the parameters of the system. For example, the nature and even the number of fixed points of a system can change with changing parameter values (bifurcation). The parameters of the present system of equations are the constants of the pressure-strain correlation model and the mean strain-rate to total deformation ratio η_1 . (Note that, by definition, $\eta_2 = 1 - \eta_1$, and hence η_2 is not considered an independent parameter.) In this paper, we restrict our attention to bifurcation due to η_1 alone for a given pressure-strain correlation model.

The system has five fixed points when η_1 is such that both Q_1 and Q^* are real. If only one of Q_1 or Q^* is real, then the system has three fixed points. If both are not real, then there is only one fixed point. Therefore, it is important to establish the conditions under which Q_1 and Q^* are real.

For Q_1 to be real we need

$$-\frac{L_2}{L_1^1} + \frac{2}{3}(\frac{L_3}{L_1^1})^2 - 2(\frac{L_4}{L_1^1})^2 \frac{1-\eta_1}{\eta_1} \geq 0, \quad (24)$$

implying that η_1 should be greater than a critical value η_1^a :

$$\eta_1 \geq \eta_1^a = \frac{2L_4^2}{-L_2L_1^1 + \frac{2}{3}L_3^2 + 2L_4^2}. \quad (25)$$

Similarly, Q^* is real only when

$$\eta_1 \geq \eta_1^b = \frac{2L_4^2}{-L_2L^* + \frac{2}{3}L_3^2 + 2L_4^2}. \quad (26)$$

For all the pressure-strain correlation models considered in this paper, L_2 is negative and $L^* > L_1^1$ leading to

$$1 > \eta_1^a > \eta_1^b > 0. \quad (27)$$

When η_1 is in the interval $(1, \eta_1^a)$, the system has five fixed points. The system has three fixed points in the interval (η_1^a, η_1^b) . Finally, for $\eta_1 < \eta_1^b$, the system has only one fixed point.

In summary, the nonlinear set of equations governing the (modeled) evolution of the Reynolds stress has two bifurcation points η_1^a and η_1^b . The behavior of the solution for various values of η_1 depends upon the stability of the various fixed points.

Stability of fixed points

In order to establish the stability of a fixed point, we need examine if any small perturbation of the system away from a fixed point eventually returns to the fixed point after a sufficiently long time. The most expeditious way of establishing this is by investigating the Jacobian of the

system at the fixed point. If an eigenvalue of the Jacobian is negative, solution trajectories are attracted towards the fixed point along the corresponding eigenvector. On the other hand, if an eigenvalue is positive, the solution trajectory is repelled away from the fixed point along the corresponding eigenvector. For a fixed point to be stable all the eigenvalues must be negative, so that all trajectories in the neighborhood of the fixed point are attracted towards the fixed point. If all permissible initial conditions are attracted to the fixed point, such a fixed point is called globally asymptotically stable. The set of all initial conditions that ultimately evolve to a stable fixed point is called the basin of attraction of that fixed point. For a nonlinear set of equations, such as the one considered here, it is difficult to establish the basin of attraction and will not be attempted here. We will only seek to establish the local asymptotic stability of each of the fixed points. First, the various types of fixed points are listed.

1. When all the eigenvalues of the Jacobian are real and negative, then the fixed point is a stable fixed point also called an attractor or a sink.
2. If all the eigenvalues are real and positive, then the fixed point is a source or repeller. All solution trajectories in the neighborhood of the fixed point are repelled away from it.
3. If the eigenvalues are real with some positive and the others negative, then the fixed point is of the saddle type. The solution trajectories are attracted towards the fixed point in some directions and repelled away in other directions.
4. If the eigenvalues are complex and the real part is positive, then the fixed point is a spiral source. The solution to the system fluctuates about the fixed point with the amplitude of the fluctuation getting larger with time.
5. If the eigenvalues are complex with a negative real part, then the fixed point is a spiral sink. The solution is oscillatory with decreasing magnitude about the fixed point.
6. If the eigenvalues are purely imaginary, then the fixed point is classified as a center. The asymptotic solution then displays an oscillatory behavior.

The sink and spiral sink fixed points are attracting fixed points and, hence, stable. Saddle and source fixed points are unstable.

Fixed point # 1. This fixed point is given by

$$\omega^0 = 0, \quad G_1^0 = 0, \quad L_2 + \frac{1}{3}L_3G_3\eta_1 + 2L_4\eta_2G_2 = 0.$$

This is the only fixed point that exists for the entire range of η_1 values.

The Jacobian at this fixed point is

$$\begin{pmatrix} 0 & 0 & 0 & 0 \\ 0 & 0 & 2L_4(1-\eta_1) & \frac{1}{3}L_3\eta_1 \\ 0 & L_1^1\eta_1G_2^0 - L_4 & 0 & 0 \\ 0 & L_1^1\eta_1G_3^0 + 2L_3 & 0 & 0 \end{pmatrix} \quad (28)$$

The eigenvalues of the Jacobian are

$$\lambda_1 = 0, \quad \lambda_2 = 0, \quad \lambda_3 = +\sqrt{\eta_1}L_1^1Q, \quad \lambda_4 = -\sqrt{\eta_1}L_1^1Q,$$

and the corresponding eigenvectors are

$$\begin{aligned} \mathbf{v}_1 &= [1, 0, 0, 0], \\ \mathbf{v}_2 &= [0, 0, -\frac{L_3\eta_1}{6L_4(1-\eta_1)}, 1], \\ \mathbf{v}_3 &= [0, +\sqrt{\eta_1}L_1^1Q, L_1^1\eta_1G_2^0 - L_4, L_1^1\eta_1G_3^0 + 2L_3], \\ \mathbf{v}_4 &= [0, -\sqrt{\eta_1}L_1^1Q, L_1^1\eta_1G_2^0 - L_4, L_1^1\eta_1G_3^0 + 2L_3]. \end{aligned} \quad (29)$$

Since two of the eigenvalues are zero, this fixed point is classified as a non-hyperbolic fixed point. So long as Q is real ($\eta_1 \geq \eta_1^b$), λ_3 is positive and λ_4 is negative leading to this fixed point being a saddle and hence unstable. When $\eta_1 < \eta_1^b$ the eigenvalues λ_3 and λ_4 are both purely imaginary; the fixed point is a center and the asymptotic solution is oscillatory. The stability of non-hyperbolic center fixed point cannot be gleaned from a linear approximation. The stability can be evaluated only from a center manifold theory which is not attempted here. Details of the center manifold analysis is given in Girimaji (1997). It suffices here to say that for $\eta_1 < \eta_1^b$, the long-time behavior of the Reynolds stress in oscillatory.

Fixed points #2 and #3. These fixed points are given by

$$\omega^0 = 0, \quad G_1^0 = \pm \frac{1}{\sqrt{\eta_1}}Q_1, \quad G_2^0 = \frac{L_4}{L^*\eta_1}, \quad G_3^0 = -\frac{2L_3}{L^*\eta_1},$$

and exist only in the range $\eta_1 \geq \eta_1^a$. The Jacobian at this fixed point is

$$\begin{pmatrix} 0 & 0 & 0 & 0 \\ -G_1^0 & 2G^* & 2L_4(1-\eta_1) & \frac{1}{3}L_3\eta_1 \\ -G_1^0 & 0 & G^{**} & 0 \\ -G_1^0 & 0 & 0 & G^{**} \end{pmatrix} \quad (30)$$

where $G^* = G_1^0\eta_1(L_1^1 + C_{e1} - 1)$ and $G^{**} = G_1^0\eta_1(L_1^1 + 2C_{e1} - 2)$.

The eigenvalues are given by

$$\begin{aligned} \lambda_1 &= -2(C_{e1} - 1)G_1^0\eta_1, \quad \lambda_2 = 2L_1^1G_1^0\eta_1, \\ \lambda_3 &= \lambda_4 = L_1^1G_1^0\eta_1. \end{aligned} \quad (31)$$

The eigenvectors are,

$$\begin{aligned} \mathbf{v}_1 &= [\frac{\eta_1}{L_1^0}(L_1^1 + 2C_{e1} - 2), \\ &\quad \frac{G_1^0\eta_1(L_1^1 + 2C_{e2} - 2) + 2L_4\eta_2 + \frac{1}{3}L_3\eta_1}{2G_1^0\eta_1(L_1^1 + C_{e1} - 1)}, 1, 1], \\ \mathbf{v}_2 &= [0, 1, 0, 0], \\ \mathbf{v}_3 &= [0, -\frac{2L_4(1-\eta_1)}{G_1^0L_1^1\eta_1}, 1, 0], \\ \mathbf{v}_4 &= [0, \frac{L_3}{3G_1^0L_1^1}, 0, 1]. \end{aligned} \quad (32)$$

Since all the eigenvalues are non-zero this is a hyperbolic fixed point. In all the models considered, L_1^1 and $(C_{e1} - 1)$ are both positive and η_1 is positive by definition. As a result, irrespective of the sign of G_1^0 , some of the eigenvalues will be positive and others negative and, hence, the fixed point is of the saddle type. These two fixed points are unstable when $\eta_1 > \eta_1^a$ and do not exist otherwise. They do not play an important role in the long-time behavior of the Reynolds stresses.

Fixed point #4. This fixed point is given by

$$\begin{aligned} \omega^0 &= -2\frac{C_{e1}-1}{C_{e2}-1}G_1^0\eta_1, \quad G_1^0 = -\frac{1}{\sqrt{\eta_1}}Q^* \\ G_2^0 &= \frac{L_4}{L^*\eta_1}, \quad G_3^0 = -\frac{2L_3}{L^*\eta_1}. \end{aligned} \quad (33)$$

This fixed point exists only for $\eta_1 \geq \eta_1^b$. Due to the complex nature of the Jacobian, it is difficult to obtain all the eigenvalues and eigenvectors symbolically. However, one eigenvalue is easily obtained by inspection:

$$\lambda_1 = G_1^0\eta_1L^*; \quad \mathbf{v}_1 = [0, 0, 1, -6\frac{L_4(1-\eta_1)}{L_3\eta_1}]. \quad (34)$$

The eigenvalues evaluated numerically are plotted in Figure 1(a) as a function of the parameter η_1 for the linearized-SSG pressure-strain correlation model. All of the eigenvalues are non-zero (hyperbolic fixed point) and negative indicating that this is an attractor. (Note that the quantity plotted is the negative of the actual eigenvalues.) Another important point to be gleaned from the figure is that eigenvalue λ_4 is always about an order of magnitude smaller than the other eigenvalues. This indicates that the evolution equations evolve slowly along the eigenvector associated with λ_4 and rapidly along all other direction. The eigenvector direction corresponding to λ_4 is shown in Figure 1(b) and it is almost coincident with the ω axis. The behavior of the eigenvalues of this fixed point with LRR pressure-strain correlation model is qualitatively and, even, quantitatively similar to that of SSG model.

Fixed point #5. This fixed point

$$\begin{aligned}\omega^0 &= -2 \frac{C_{e1}-1}{C_{e2}-1} G_1^0 \eta_1, \quad G_1^0 = + \frac{1}{\sqrt{\eta_1}} Q^* \\ G_2^0 &= \frac{L_4}{L^* \eta_1}, \quad G_3^0 = - \frac{2L_3}{L^* \eta_1}.\end{aligned}\quad (35)$$

also exists only for $\eta_1 \geq \eta_1^b$. The eigenvalues calculated numerically are all positive indicating that the fixed point is a source or a repeller and, hence, unstable.

All the stability and bifurcation results for G_1 are summarized in Figure 2. The bifurcation diagram of ω is given in Figure 3.

SUMMARY AND DISCUSSION

The long-time behavior of the standard Reynolds stress closure equation depends upon the value of the parameter η_1 , the mean strain to total deformation ratio. The asymptotic behavior undergoes bifurcation at $\eta_1 = \eta_1^b$.

Asymptotic behavior for $\eta_1 > \eta_1^b$. The solution is attracted to fixed point 4. The production to dissipation ratio at this equilibrium state is

$$\frac{P}{\epsilon}(\text{equilibrium}) = \frac{C_{e2}-1}{C_{e1}-1} \quad (36)$$

independent of η_1 . In appropriately normalized time, the turbulent kinetic energy and dissipation grow exponentially at rates independent of η_1 :

$$\frac{d \ln K}{d\tau} = \frac{P}{\epsilon} - 1; \quad \frac{d \ln \epsilon}{d\tau} = C_{e1} \frac{P}{\epsilon} - C_{e2}, \quad (37)$$

where $\tau = \omega_0 t$.

Longtime behavior for $\eta_1 < \eta_1^b$. The long-time behavior in this case is dictated by fixed point 1 which is non-hyperbolic (has zero eigenvalues). Linear analysis about the fixed point is inadequate to determine its stability. Numerical calculations indicate that (i) ω decays monotonically (exponentially?) to zero, (ii) G_1 oscillates about zero, (iii) G_2 and G_3 converge to non-zero values, (iv) with decreasing η_1 the asymptotic growth rates of kinetic energy and dissipation decrease. In fact, for small enough η_1 values kinetic energy and dissipation decay in time leading to relaminarization.

Implications to pressure-strain correlation modeling. It is reasonable to demand that future models yield bifurcation diagrams consistent with experimentally (laboratory and numerical) observed behavior of the Navier-Stokes equation. At the very least, for the sake of qualitative consistency with true physics, the bifurcation

points of the model equation set should coincide with that of Navier-Stokes statistics.

The DNS data of Blaisdell and Shariff (1996) appears to indicate that the asymptotic growth rate of kinetic energy is always positive and nearly independent of η_1 :

$$\frac{d \ln K}{dt} \approx \text{Const.}(>0), \text{ for } 1 \geq \eta_1 > 0, \quad (38)$$

a result that is consistent with linear stability analysis. The lack of qualitative (or, even, quantitative) change in the behavior of the kinetic energy growth rate appears to imply that there is no bifurcation, contrary to model predictions. This can be interpreted as the bifurcation taking place at $\eta_1 = 0$. If this is indeed true (further work is currently underway), then, in order for the pressure strain model to be consistent with physics we need:

$$\eta_1^b = \frac{2L_4^2}{-L_2 L^* + \frac{2}{3} L_3^2 + 2L_4^2} = 0, \quad (39)$$

leading to $L_4 = 0$, implying $C_4 = 2$.

The consequence of changing the value of C_4 should be examined thoroughly and this certainly would require recalibration of the other model constants to preserve the agreement in other important cases. In particular, the performance of the present pressure-strain models in turbulent flows with coordinate frame rotation depends heavily on C_4 .

Non-equilibrium algebraic stress modeling.

Non-equilibrium algebraic Reynolds stress model can be considered as the approximate solution of the Reynolds stress closure equations away from the equilibrium state. When $\eta_1 > \eta_1^b$, the solution approaches the equilibrium state (fixed point 4) along the invariant manifold corresponding to eigenvector \mathbf{v}_4 for nearly all initial conditions. This is because the corresponding eigenvalue (λ_4) is much smaller than the rest (Figure 1a). (From a random initial condition, the solution evolution along the other eigenvector directions is very rapid, so that the trajectory after a short initial stage is nearly aligned with the slowest eigen direction.) In Girimaji (1996b), it was suggested that the invariant manifold of \mathbf{v}_4 be used as the non-equilibrium Reynolds stress model and a strategy for determining the manifold was presented. When $\eta_1 < \eta_1^b$, the strategy for non-equilibrium algebraic modeling is not yet clear. Central manifold reduction may be the answer and that approach is currently under investigation.

Acknowledgements : This work was supported by the National Aeronautics and Space Administration under NASA Contract No. NAS1-19480.

REFERENCES

- R. Abid, and C. G. Speziale, 1993, 'Predicting equilibrium states with Reynolds stress closure in channel and homogeneous shear flows', *Phys. Fluids A* Vol. 5, pp. 1776-1782.
- G. A. Blaisdell and K. Shariff, 1996, 'Simulation and modeling of elliptic streamline flow', Center for Turbulence Research, Proceedings of the Summer Program 1996.
- M. M. Gibson and B. E. Launder, 1978, 'Ground effects of pressure fluctuations in the atmospheric boundary layer', *J. Fluid Mech.*, Vol. 86, pp 491-511.
- S. S. Girimaji, 1996a, 'Fully explicit and self-consistent algebraic Reynolds stress model', *Theoret. Comput. Fluid Dynamics*, Vol. 8, pp 387-402.
- S. S. Girimaji, 1996b, 'Non-equilibrium algebraic Reynolds stress model', *Bulletin of the Amer. Physical Soc.*, Vol. 41 (9), pp 1813.

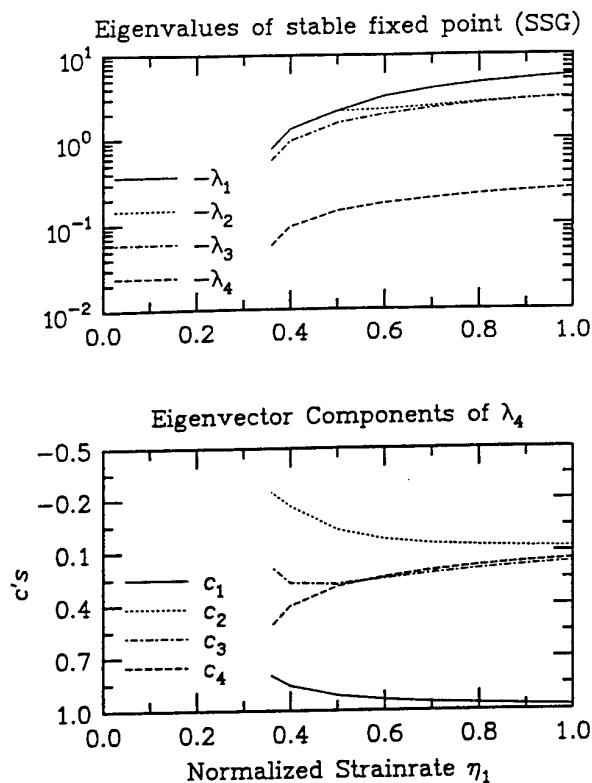


Figure 1: (a) Eigenvalues of fixed point 4 as a function of η . (b) Components of eigenvector corresponding to eigenvalue λ_4 .

S. S. Girimaji, 1997, 'Long-time behavior of Reynolds stress in homogeneous turbulence; Classification and prediction'. Manuscript under preparation.

B. E. Launder, G. J. Reece and W. Rodi, 1975, 'Progress in the Development of Reynolds Stress Turbulence Closure', *J. Fluid Mech.*, Vol. 68, pp 537-566.

C. G. Speziale, R. Abid and G. A. Blaisdell, 1996, "On the consistency of Reynolds stress turbulence closures with hydrodynamic stability theory", *Phys. Fluids*, Vol. 8, pp 781-788.

C. G. Speziale and N. Mac Giolla Mhuiris, 1989, "On the prediction of the equilibrium states in homogeneous turbulence", 1989, *J. Fluid Mech.*, Vol. 209, pp. 591-615.

C. G. Speziale and N. Mac Giolla Mhuiris, 1990, "Scaling laws for homogeneous turbulent shear flows in a rotating frame", *Phys. Fluids A*, Vol. 1, pp. 294-301.

C. G. Speziale, S. Sarkar and T. B. Gatski, 1991, "Modeling the pressure-strain correlation of turbulence: an invariant dynamical system approach", *J. Fluid Mech.*, Vol. 227, pp. 245-272.

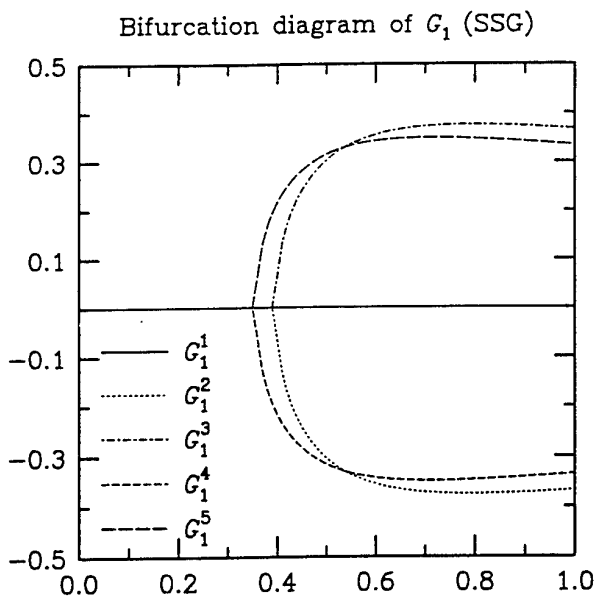


Figure 2: Bifurcation diagram of G_1 . Fixed point G_1^1 : unstable (saddle) for $\eta \geq \eta_1^b$ and center for $\eta < \eta_1^b$. G_2 : unstable (saddle). G_4 : stable (attractor). G_5 : unstable (repellor).

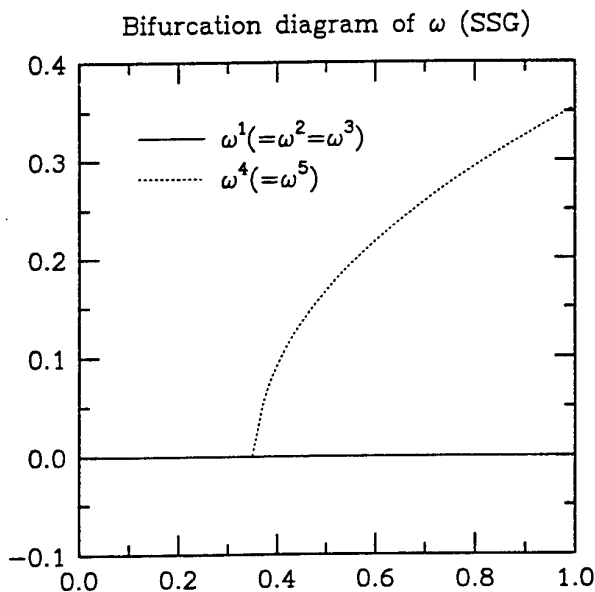


Figure 3: Bifurcation diagram of ω . Fixed point $\omega^1 (= \omega^2 = \omega^3)$ is unstable (saddle) for $\eta \geq \eta_1^b$ and stable for $\eta < \eta_1^b$. $\omega^4 (= \omega^5)$ is stable (attractor).